IONIC LIQUIDS: PROPERTIES AND APPLICATIONS

EDITED BY: Francesca D'Anna and Jason Harper
PUBLISHED IN: Frontiers in Chemistry

frontiers Research Topics

About Frontiers

Frontiers is more than just an open-access publisher of scholarly articles: it is a pioneering approach to the world of academia, radically improving the way scholarly research is managed. The grand vision of Frontiers is a world where all people have an equal opportunity to seek, share and generate knowledge. Frontiers provides immediate and permanent online open access to all its publications, but this alone is not enough to realize our grand goals.

Frontiers Journal Series

The Frontiers Journal Series is a multi-tier and interdisciplinary set of open-access, online journals, promising a paradigm shift from the current review, selection and dissemination processes in academic publishing. All Frontiers journals are driven by researchers for researchers; therefore, they constitute a service to the scholarly community. At the same time, the Frontiers Journal Series operates on a revolutionary invention, the tiered publishing system, initially addressing specific communities of scholars, and gradually climbing up to broader public understanding, thus serving the interests of the lay society, too.

Dedication to Quality

Each Frontiers article is a landmark of the highest quality, thanks to genuinely collaborative interactions between authors and review editors, who include some of the world's best academicians. Research must be certified by peers before entering a stream of knowledge that may eventually reach the public - and shape society; therefore, Frontiers only applies the most rigorous and unbiased reviews.
Frontiers revolutionizes research publishing by freely delivering the most outstanding research, evaluated with no bias from both the academic and social point of view. By applying the most advanced information technologies, Frontiers is catapulting scholarly publishing into a new generation.

What are Frontiers Research Topics?

Frontiers Research Topics are very popular trademarks of the Frontiers Journals Series: they are collections of at least ten articles, all centered on a particular subject. With their unique mix of varied contributions from Original Research to Review Articles, Frontiers Research Topics unify the most influential researchers, the latest key findings and historical advances in a hot research area! Find out more on how to host your own Frontiers Research Topic or contribute to one as an author by contacting the Frontiers Editorial Office: researchtopics@frontiersin.org

IONIC LIQUIDS: PROPERTIES AND APPLICATIONS

Topic Editors:
Francesca D'Anna, Università degli Studi di Palermo, Italy
Jason Harper, UNSW, Australia

Sustainability, defined as the way to meet the needs of the present generation without compromising the ability of future ones to meet their own, is one of the main challenges of modern society. Within this context, chemistry plays a significant role, and solvent nature as well as its environmental impact are pivotal issues frequently addressed.

Ionic liquids, i.e. organic salts that have melting temperatures lower than 100 °C, have been frequently hailed as alternatives to conventional organic solvents. Their greenness has been mainly ascribed to their low vapor pressure and flammability. However, in addition to this, their high solubilizing ability and low miscibility with conventional organic solvents frequently allow for reducing the amount used, as well as for their recycling. Ionic liquids, especially the ones featured by aromatic cations, are frequently described as "polymeric supramolecular fluids" constructed through the establishment of feeble but cooperative supramolecular interactions like Coulomb and π-π interactions, as well as hydrogen bonds.

In general, ionic liquids are also indicated as "designer solvents" as it is possible to tailor their features to specific applications by simply modifying their cation or anion structure. In this way, small changes in the ion's structure can give rise to solvents showing very different properties.

The above premises widely justify the growing interest in the properties and applications of ionic liquids, seen in recent literature (according to Scopus, more than 27,000 papers published in the last five years have "ionic liquids" as a keyword). Thanks to their properties, they have been variously used as solvent media, solvents for the obtainment of gel phases, components in the building of dye-sensitized solar cells, media for the preparation of thermochromic materials, etc.

This Research Topic aims to present how structural features can determine not only the properties of ionic liquids, but also their possible employment. In this latter case, the interest arises from their ability to affect the outcome of a given reaction in terms of rate, yield, and nature of the products obtained for general use in the field of materials chemistry.

This article collection is dedicated to Prof. Kenneth R. Seddon for his outstanding contribution to the formation and development of the ionic liquids community.

Table of Contents

Anomalous and Not-So-Common Behavior in Common Ionic Liquids and Ionic Liquid-Containing Systems

José M. S. S. Esperança[1]*, Mohammad Tariq[1], Ana B. Pereiro[1], João M. M. Araújo[1], Kenneth R. Seddon[2†] and Luis Paulo N. Rebelo[1]*

[1] *LAQV/REQUIMTE, Faculdade de Ciências e Tecnologia da Universidade Nova de Lisboa, Caparica, Portugal,* [2] *QUILL Research Centre, the Queen's University of Belfast, Belfast, United Kingdom*

This work highlights unexpected, not so well known responses of ionic liquids and ionic liquid-containing systems, which are reported in a collective manner, as a short review. Examples include: (i) Minima in the temperature dependence of the isobaric thermal expansion coefficient of some ILs; (ii) Viscosity Minima in binary mixtures of IL + Molecular solvents; (iii) Anomalies in the surface tension within a family of ILs; (iv) The constancy among IL substitution of C_p/V_m at and around room temperature; (v) ILs as glass forming liquids; (vi) Alternate odd-even side alkyl chain length effects; (vii) Absolute negative pressures in ILs and IL-containing systems; (viii) Reversed-charged ionic liquid pairs; (ix) LCST immiscibility behavior in IL + solvent systems.

Keywords: ionic liquids, unusual behavior, thermal expansion coefficient, viscosity, surface tension, odd-even effects, reversed charge ILs, LCST

INTRODUCTION

Ionic Liquids (ILs) are constituted quasi-exclusively by anions and cations, melting at temperatures that are much lower than those of their conventional, inorganic salts counterparts. For instance, "table salt" (NaCl) melts at about 800°C. In contrast, many ILs present melting points lower than room temperature. Generally, ILs have a large liquid range and, some of them do not easily crystallize on cooling, instead they supercool and undergo a glass transition.

Several high quality reviews (Welton, 1999, 2018; Plechkova and Seddon, 2008; Armand et al., 2009; Hallett and Welton, 2011; Niedermeyer et al., 2012; Tariq et al., 2012; Chatel et al., 2014; Hayes et al., 2015; Hunt et al., 2015; Podgoršek et al., 2016; Kar et al., 2019) are available. No review focused on the unexpected behavior of ILs has been published, where a scrutiny of their not so well known physical chemistry responses is made. This work constitutes a first attempt in this direction.

With the upsurge in the research activity around these novel salts during the last two decades, peculiar, unique and interesting behavior of these complex materials have been revealed. ILs are considered a link between molten salts and molecular solvents (Leal et al., 2009).

Lopes and Pádua (2006) using MD simulations and Triolo et al. (2007) using experimental X-ray data have demonstrated that ILs, even in their pure state, contain nanostructured organization at a molecular level. In addition, this very distinct feature has been confirmed using experimental thermodynamic approaches (Pereiro et al., 2013; Rocha et al., 2013). This phenomenon is responsible for many of their peculiar behavior. Also, how a particular IL interacts with the co-solvent is very unique and depends on the interactions between the IL and the chemical nature of the other component: polar/apolar/associated fluids (Lopes et al., 2006; Pádua et al., 2007).

The topics tackled in this contribution are not comprehensive. Examples not herein presented include: their ability to form halogen-bonds (Bernardes and Canongia Lopes, 2017; Saccone et al., 2017; Cavallo et al., 2018; Lodeiro et al., 2018), the formation of liquid crystals (Alvarez Fernandez and Kouwer, 2016; Goossens et al., 2016), the total miscibility in water of fluorinated ILs (Pereiro et al., 2015; de Ferro et al., 2018), and other unexpected behavior in respect to their physical properties (Singh et al., 2015, 2017; Dzida et al., 2018; Rahman and Senapati, 2018). Zwitterionic liquids (Blesic et al., 2017; Ohno et al., 2018; Wu et al., 2018), which fill the gap between small-ion ILs and ILs with strong H-bonds, as well as hydrated ILs (Haberler et al., 2012; Fujita et al., 2016), where H-bonds between one or both of the ions and a small number of water molecules is sufficient to produce new materials with superior properties, constitute other examples of not so-well-known behavior.

MINIMA IN THE TEMPERATURE DEPENDENCE OF THE ISOBARIC THERMAL EXPANSION COEFFICIENT OF SOME ILs

For most liquids the isobaric thermal expansion coefficient, α_p, is positive and increases with increasing temperature as it has to diverge to a positive infinite value at the critical point. The best well-known example of a distinct behavior is that of water, in which α_p at about atmospheric pressure is negative at temperatures between 0 and 3.98°C, meaning a contraction on heating. At the temperature of maximum density, 3.98°C, α_p reaches a null value, becoming positive for higher temperatures. Despite this "anomaly," the α_p of water always increases with increasing temperature. In this section, we highlight examples of the anomalous behavior of α_p with temperature increase for some ionic liquids. The results discussed in this section are the first examples of substances that show a minimum in α_p as temperature increases.

Conflicting results were reported earlier about the temperature dependence of α_p of ILs (Rebelo et al., 2004). Later some reports for a small set of ILs have shown that it is possible to obtain negative values for $(\partial\alpha_p/\partial T)_p$ (Rodríguez and Brennecke, 2006; Sanmamed et al., 2007). Accurate determinations of this property may be difficult since the determination of α_p from the temperature dependence of density, $\rho(T)$, can produce numerical artifacts (Cerdeirina et al., 2001; Troncoso et al., 2010). Most often the density of ILs is measured using a vibrating tube densimeter. Their high viscosity may influence the determination of the density and, if viscosity corrections are not taken into consideration, erroneous $\alpha_p(T)$ values may be obtained (Sanmamed et al., 2007).

Systematic studies on the measurements of density along a homologous series and wide temperature and pressure conditions are not commonly reported. In order to fill this gap, the densities of a series of ILs in a wide temperature and pressure range were reported. Tariq et al. (2010) have measured the densities of imidazolium bistriflimide ILs, $[C_nC_1im][Ntf_2]$, where $n = 2$–14 in the temperature range of 283–483 K. This dataset was the largest one both in terms of an extended homologous series of ILs, as well as in a large temperature interval, enabling the authors to study subtle specificities of their thermal response. Nieto de Castro et al. (2010) have carried out high-precision density measurements over broad temperature (293–473 K) and pressure (0.1–60 MPa) ranges on four ILs, namely $[C_4C_1im][Ntf_2]$, $[C_4C_1im][dca]$, $[C_2C_1im][C_2SO_4]$, and [Aliquat][dca].

It has been demonstrated (Tariq et al., 2010) that in the $[C_nC_1im][Ntf_2]$ series, an increase in temperature results on a small decrease in the values of α_p. This inverse proportionality between α_p and T constitutes an anomalous behavior and is observed at "low-temperature." Since thermodynamics impose that at the liquid–vapor critical point, a divergence to $+\infty$ in α_p ought to occur, at some lower temperature a minimum in $\alpha_p = f(T)$ is obtained (**Figure 1A**).

Similarly, densities of four ILs in wide pressure and temperature ranges were measured (Nieto de Castro et al., 2010). Again, α_p decreases as temperature increases in the low-T range (**Figure 1B**). Navia et al. (2010a), Navia et al. (2010b) also obtained data for a large set of ILs confirming negative $(\partial\alpha_p/\partial T)_p$ values at low temperatures.

These works have shown that the temperature derivative of the thermal expansion coefficient, $(\partial\alpha_p/\partial T)_p$, of some ILs changes sign at a temperature that depends both on pressure and IL nature.

VISCOSITY MINIMA IN BINARY MIXTURES OF IL + MOLECULAR SOLVENTS (MSs)

Most models for the viscosity of a mixture predict that the mixture's viscosity of two components with identical viscosities is invariant along the whole composition range.

A minimum in viscosity-composition plots of binary mixtures is an unusual phenomenon, which has been observed for some non-polar + polar systems (Kouris and Panaylotou, 1989; Papanastaaiou and Ziogas, 1991; Laesecke et al., 2007). However, the molecular reasoning behind this phenomenon is not very well understood (Srinivas et al., 2001; Abraham et al., 2007) and thereby it is hard to model the viscosity values of such mixtures using existing mixing rules and predictive methods (Qunfang and Yu-Chun, 1999). Such uncommon phenomenon has been shown for the first time in systems containing ionic liquids (ILs) + molecular solvents (MSs) (Tariq et al., 2015).

Tariq et al. (2015) selected four binary IL+MS systems composed of a molecular solvent (2-amino-ethanol (2AE) or 3-amino-1-propanol (3AP)) and an IL (from the 1-alkyl-3-methylimidazolium family ($[C_nmim]^+$) using dicyanamide ([DCA]) or bistriflimide ($[Ntf_2]$) as the anion). All the components forming the four binary systems are completely miscible in the entire composition range and show crossover temperatures where the IL and MS viscosity values are identical (**Figure 2**).

The $\eta(T,x)$ plots presented in **Figure 3** reveal that (i) there is a viscosity minimum at low temperatures for IL-rich mixtures and that (ii) the viscosity minimum is centered around the
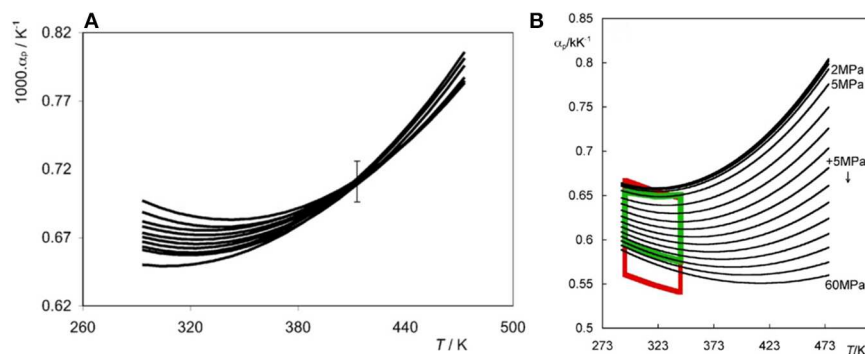
FIGURE 1 | (A) Thermal expansion coefficient, α_p as a function of temperature and at atmospheric pressure for each member of the $[C_nC_1im][Ntf_2]$ family (C_{14}-C_2 from top to bottom). The error bar corresponds to an average uncertainty for all fits. (Reprinted from Tariq et al., 2010 with permission from Elsevier) **(B)** α_p for $[C_4C_1im][Ntf_2]$ as a function of temperature at different pressures. The top four unlabeled isobars in the right panel correspond to pressures of 0.1, 0.25, 0.5, and 1 MPa. The red lines represent the boundaries of the data presented by Navia et al. (2010a), Navia et al. (2010b) (isotherms between 293 and 353 K and isobars between 5 and 50 MPa). The green lines highlight the same boundaries for the set of data measured by Nieto de Castro et al. (2010). (Reprinted from Nieto de Castro et al., 2010 with permission from Elsevier).
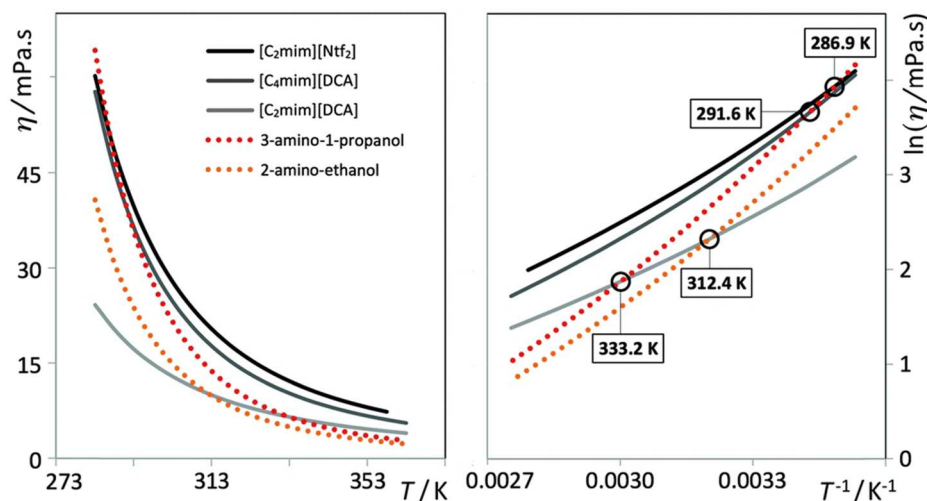
FIGURE 2 | Experimental viscosity data, $\eta/mPa\cdot s$, of the three ILs ($[C_2mim][Ntf_2]$, $[C_2mim][DCA]$, and $[C_4mim][DCA]$) and two molecular solvents (2AE and 3AP) studied in this work as a function of temperature. The right-hand plot shows the logarithm of viscosity as a function of the reciprocal of temperature. The circles indicate the viscosity cross-over temperatures. (Reprinted from Tariq et al., 2015 with permission from Royal Society of Chemistry).

equimolar composition as one approaches the temperature at which both components present identical viscosities. The overall viscosity trend for these systems is similar along the composition/temperature surface.

The origin of the viscosity minima is 2-fold: (i) it comes from the different cohesive energies of both pure MSs and ILs and (ii) from changes in the structure and interactions of the mixtures compared to the pure components.

The molecular interactions between the molecules can be revealed by comparison of the cohesive energies of the two classes of components (obtained through vaporization enthalpies at room temperature). The values of the vaporization enthalpies of the MSs are in the range of 60–70 kJ mol^{-1} (Marsh et al., 2004; Yaws, 2009; Acree and Chickos, 2010). In contrast, ILs present vaporization enthalpies above 135 kJ mol^{-1} (Marsh et al., 2004; Esperança et al., 2010). In the case of these MSs, the cohesive energy is largely related to the intra-hydrogen bonding between the functional groups of each molecule. In the case of ILs, MD simulations (Santos et al., 2007; Shimizu et al., 2010) have revealed that Coulomb forces play an important role, contributing substantially for their enhanced cohesive energy.

H-bonds between the different ILs and MSs and the structural differences between the mixture and the pure molecular components originates a reduction on the viscosity of the mixtures. Other type of uncommon behavior of IL containing binary mixtures has been reported by Andrzejewska et al. (2009) and Trivedi and Pandey (2011), where a maximum in the viscosity has been found in mixtures of IL + polymers. It should
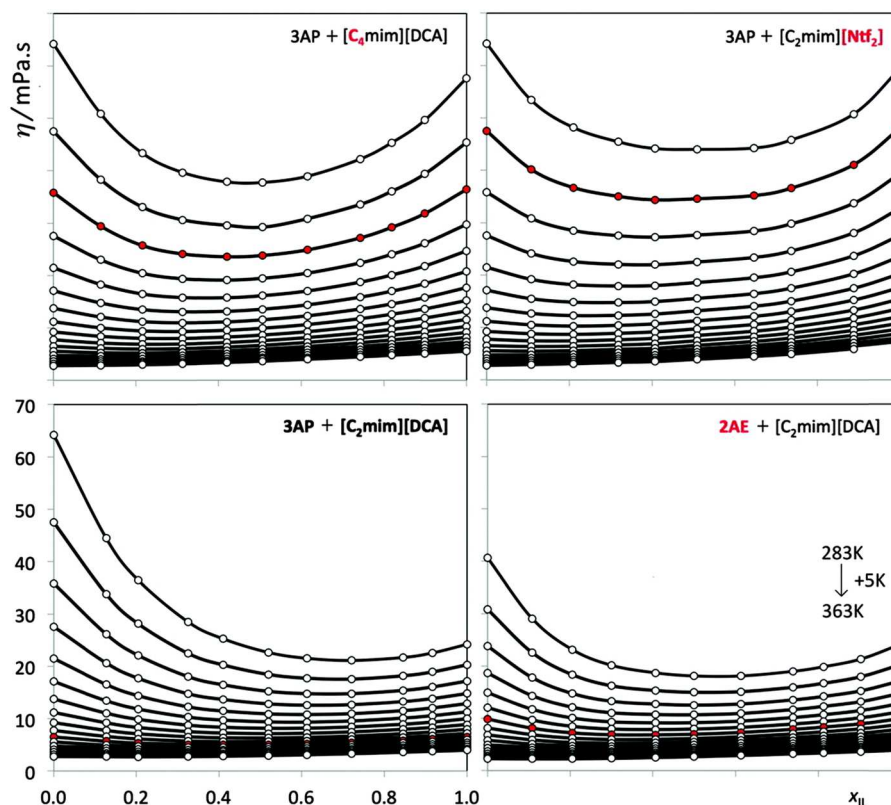
FIGURE 3 | Experimental viscosity data, $\eta/\text{mPa·s}$, of four (ionic liquid plus molecular solvent) binary mixtures as a function of the ionic liquid mole fraction, x_{IL}. The curves represent different isotherms. The red circles denote for each system the isotherm closest to the viscosity crossover temperature. (Reprinted from Tariq et al., 2015 with permission from Royal Society of Chemistry).

be noted that systems containing polymers are known to show non-Newtonian behavior.

ANOMALIES IN THE SURFACE TENSION WITHIN A FAMILY OF ILs

The values of the surface tension of most ILs fall in between those of water and molecular solvents. One interesting trend has been found in the 1-alkyl-3-methylimidazolium bistriflimide, $[C_nC_1im][Ntf_2]$ family (Carvalho et al., 2008; Kolbeck et al., 2010; Tariq et al., 2010; Haddad et al., 2018; Shimizu et al., 2018). Carvalho et al. (2008) were the first to report that the surface tension values of $[C_nC_1im][Ntf_2]$ series do not decrease linearly with the alkyl chain length increase ($n = 2$–10), but rather reach a plateau for long cation side alkyl chains. Later, Tariq et al. (2010) measured the surface tension for C_2-C_{14} within a broad temperature range of 303–493 K and Kolbeck et al. (2010) measured it at room temperature for C_1-C_{12}. Both confirmed these trends (**Figure 4A**).

The trend is not regular, and was checked out by three distinct works: there is a substantial decrease in the surface tension value from $[C_2C_1im][Ntf_2]$ to $[C_5C_1im][Ntf_2]$ and a relatively lower decrease from $[C_6C_1im][Ntf_2]$ to $[C_{12}C_1im][Ntf_2]$. Changes in the ratio of prominence of non-polar to polar moieties of the

ILs at the surface are a consequence of the length of the alkyl side chains. MD simulations and X-ray diffraction studies (Lopes and Pádua, 2006; Triolo et al., 2007) have shown the creation of a second nanostructured domain (formation of non-polar continuous domains) for ILs with alkyl chain length equal or >6 carbon atoms.

Recently, Shimizu et al. (2018) have been able to predict the surface tension of the 1-alkyl-3-methylimidazolium bistriflimide family by combining angle-resolved X-ray photoelectron spectroscopy data and MD simulations results using the Langmuir principle.

Haddad et al. (2018) have also used angstrom-resolution X-ray methods to understand the reason behind the peculiar behavior of the surface tension within the $[C_nC_1im][Ntf_2]$ homologous series. They also found a distinct behavior for ILs with alkyl chain length equal or longer than six carbon atoms due to the formation of nanosegregated domains (polar/apolar) which create alternating layers at the surface. This study clarifies the liquid–air interface structure for a common homologous series of ILs. By varying the cation's alkyl chain length one can tune the interactions's importance, from long-range coulombic forces to short-range van der Waals interactions. Such variation causes the interface structure to turn from simple, to layered, to liquid crystalline. The quantitative results obtained from this work may constitute a reference for validating simulations and theory.

An even more peculiar behavior of the surface tension within a homologous series has been reported by Luís et al. (2016) for $[C_nC_1im]$ cation based ILs (where $n = 2–12$) combined with perfluorobutanesulfonate anions. Instead of a plateau, a minimum in the surface tension is observed for a cation alkyl side chain of 8 (**Figure 4B**). The existence of three nanosegregated domains (polar, apolar, and fluorinated) for the long cation's alkyl chain length is the main reason for this distinctive trend. More specifically, it results from the competition between the diverse domains for the gas-liquid interface. Their surface entropy is the lowest when compared to conventional ILs.

THE CONSTANCY AMONG IL SUBSTITUTION OF C_P/V_M AT AND AROUND ROOM TEMPERATURE

The temperature dependence of the enthalpy is known as heat capacity. Some heat capacity changes may indicate the occurrence of a phase transition and enable to understand variations in the structure of the compounds.

Zabransky et al. (1990) and Domalski and Hearing (1996) compiled and analyzed, independently, the heat capacity data for a huge number of substances. To the best of our knowledge, group contribution methods and/or corresponding state principal based methods are the approaches generally used to estimate liquid heat capacities.

For ionic liquids, Strechan et al. (2008) and Gardas and Coutinho (2008) demonstrated independently that there is a linear relationship between the heat capacities and the molar volumes of imidazolum, pyridinium, and pyrrolidinium based-ILs (**Figure 5**). They have used the dataset of limited number of ILs to establish this correlation and propose that the volumetric heat capacity of ILs is almost invariant at 298.15 K.

Later, Paulechka et al. (2010) have refined this relation by carefully selecting dataset of 19 ILs (for which the precise density data was available) and measured their heat capacity with an

uncertainty of ($\pm 1\%$). They have also witnessed that there is constancy among the volumetric heat capacities of ILs. The average value at 298.15 K is:

$$C_p/V_m = 1.95 \pm 0.02 \ (JK^{-1}cm^{-3}) \tag{1}$$

This average value agrees well with those of Gardas and Coutinho (2008). The difference between the experimental volumetric heat capacities and this C_p/V_m value was found to be $< \pm 5\%$. Contrarily to molecular solvents, a simple rule exists to predict the heat capacity of distinct ILs.

It has been demonstrated that C_p/V_m is basically independent of the structure of the IL. Therefore, Paulechka et al. (2010) concluded that ILs used for application as heat accumulators

FIGURE 5 | IL heat capacity as a function of the molar volume (T = 298.15 K). [Drawn using the data presented in Paulechka et al. (2010)].

FIGURE 4 | (A) Surface tension values vs. the size of the alkyl chain, n, for $[C_nC_1im][Ntf_2]$ family from different authors measured at 293 K showing clearly a break around C_5-C_6. **(B)** Surface tension values as a function of the alkyl chain, n, for the $[C_nC_1im][C_4F_9SO_3]$ family at 313 K. (Reprinted with permission from Luís et al., 2016. Copyright (2016) American Chemical Society).

should be chosen on the basis of other parameters such as thermal stability, viscosity, thermal conductivity, to name a few.

ILs AS GLASS FORMING MATERIALS

ILs have low melting points (Tm) when compared to conventional inorganic salts. This fact gives them the status of a unique class of ionic materials composed almost solely of cations and anions that exist in the liquid state at or near room-temperature. Many ILs that do exist in the liquid state

FIGURE 6 | Glass transition temperatures (T$_g$) for the [C$_n$C$_1$im][Ntf$_2$] (black circles) and [C$_n$C$_n$im][Ntf$_2$] (red squares) series as a function of n (number of carbon atoms in one alkyl side chain); [C$_1$C$_1$im][Ntf$_2$] (gray circle). (Reprinted from (Rodrigues and Santos, 2016) with permission from John Wiley and Sons).

never crystallize and thus do not show any melting point, instead, on cooling they show a glass transition (Tg). Most ILs (Valderrama et al., 2017) show a glass transition temperature in the 150–250 K range.

It is easier to accurately determine melting points (typically for ILs a good (±5 K) uncertainty is obtained) than those of vitrification—large discrepancies (up to 20%) have been found in reported Tg values. Glass transitions do not occur at a specified fixed temperature as they are not first-order changes (Brandrup et al., 1999), and are kinetically dependent. The dependence of Tg of ILs on the scan rate has thoroughly been investigated (Gómez et al., 2013; Tao et al., 2017).

Blokhin et al. (2006) and Rodrigues and Santos (2016) have continuously presented high quality thermal properties data of ILs and the latter demonstrated how the nanostructuration of [C$_n$C$_1$im][NTf$_2$] and [C$_n$C$_n$im][NTf$_2$] family influences their glass and melting temperatures. The work demonstrates a variation of the Tg behavior at the critical alkyl size, when $n = 6$ (Figure 6). T$_g$ increases as the alkyl side chain of the imidazolium cation grows, mainly due to the enhancement of the van der Waals interactions. For alkyl chains longer than $n = 6$, a plateau in the Tg values after nano-structuration is observed.

Some works have tackled the prediction of the Tg of ILs (Mirkhani et al., 2012; Valderrama et al., 2017). Other studies have identified difficulties behind observing IL's crystallization (Serra et al., 2017; Ferreira et al., 2019).

Lima et al. (2018) have measured the Tg and Tm of a pyrrolodinium based-IL, [C$_4$C$_1$Pyrr][Ntf$_2$], from atmospheric pressure up to an extremely high pressure of 2 GPa using X-ray diffraction and Raman scattering techniques. They have found that Tg and Tm both follow similar pressure dependences.

At atmospheric pressure, most compounds seem to follow the well-known "2/3 golden rule" meaning that the ratio of glass

FIGURE 7 | (A) Melting points vs. glass transition temperatures for PILs reported by Belieres and Angell (2007). (Reprinted with permission from Belieres and Angell, 2007. Copyright (2007) American Chemical Society) (B) T$_g$ values as a function of molar volume (V$_m$) for PILs reported by Xu and Angell (2003). The line through the points is a guide to the eye. [From Xu and Angell (2003). Reprinted with permission from AAAS].

transition temperature (Tg) to that of melting (Tm), Tg/Tm, for all compounds should be around 0.66. Belieres and Angell (2007) have collected data for several protic ionic liquids (PILs) and showed that similar to other materials, most of the PILs fall in the 2/3 line (**Figure 7A**). However, there are outliers that can reach a ratio as high as 3/4. Xu and Angell (2003) have discussed the Tg dependence on the molar volume (**Figure 7B**). Recently, Ferreira et al. (2019) and Serra et al. (2017) have shown that many of the aprotic ILs show high Tg/Tm values that are close to the $\frac{3}{4}$ value.

ALTERNATE ODD-EVEN SIDE ALKYL CHAIN LENGTH EFFECTS

Whenever the thermophysical characterization of the members of a family of ILs within a homologous series is performed, odd members are often neglected (Tariq et al., 2009). The main difficulty in the synthesis of ILs with alkyl chains, C_n, where n is an odd number, is the high cost of their chemical precursors.

Adamová et al. (2011) have measured the densities of a series of alkyltrioctylphosphonium chloride, [P8 8 8 n]Cl based ILs and found that the density values show a clear odd-even chain length alternation effect (**Figure 8A**). There are two independent trends: one for the odd and another one for the even-numbered

compounds. This was observed up to $n = 9$. Data analyzed in terms of their molar volume, $Vm = M/\rho$, presents remarkably this see-saw effect (**Figure 8B**).

Adamova et al. (2014) have carried out *Ab initio* calculations and MD simulations to understand the molecular reasoning behind these effects. Simulation runs revealed that the type of conformation/packing of the liquid (transoid conformations of the cation and head-to-head packing) are responsible for the observed alternation effects. The unexpected results first seen for the [P8 8 8 n]Cl series, enabled the authors to reveal a similar trend for another IL family, $[C_nC_1im][NTf_2]$. Moreover, this see-saw effect, already known for the solid phase of linear alkanes and alkanols, was also seen in their liquid phase molar volume.

Very recently, it has been shown (Belchior et al., 2018) that diluted solutions of $[C_nC_1im]Cl$ ($n = 2$–14) used to form aqueous biphasic systems (ABS) with salts also exhibit such odd/even effects. The odd/even effect was observed in the Setschenow salting-out coefficients (ks) for systems containing water, $[C_nC_1im]Cl$ and K_2CO_3 (**Figure 9A**). The salting-out ability depends on the molar volume of the IL, and therefore the alternation odd-even volume pattern is reflected in the ks values. This is more prominently seen for ILs with alkyl side chain length up to $n = 6$. As for the CMC values of the $[C_nC_1im]Cl$ series
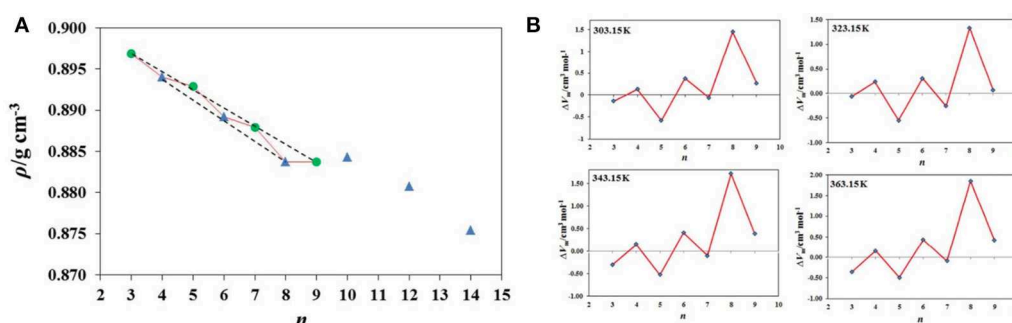
FIGURE 8 | (A) Experimental densities of [P_{888n}]Cl ionic liquids at 303.15 K, where $n = 3,5,7$, and 9 (green circles), $n = 4,6,8,10,12$, and 14 (blue triangles). (Reprinted from Adamová et al., 2011 with permission from Royal Society of Chemistry) **(B)** See-saw, even/odd alternation effect in the form of deviations (residuals) between experimental and fitted molar volume (V) data as a function of n, at four different temperatures. (Reprinted from Adamová et al., 2011 with permission from Royal Society of Chemistry).
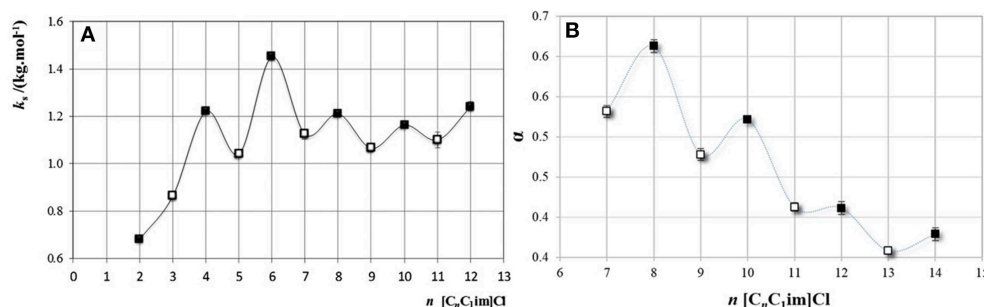
FIGURE 9 | (A) Setschenow constant, ks, as a function of the carbon number at the longest alkyl chain, n, in [C_nC_1im]Cl, for the ABS formed with the salt K_2CO_3. (Reprinted from Belchior et al., 2018 with the permission of AIP Publishing) **(B)** Degree of ionization as a function of the carbon number at the cation alkyl chain, n, in [C_nC_1im]Cl. (Reprinted from Belchior et al., 2018 with the permission of AIP Publishing).

this effect was not observed. In contrast, it was also shown that an odd-even effect occurs for properties, such as, the degree of ionization (**Figure 9B**), the molar conductivity, and the molar conductivity at infinite dilution.

In addition to the above-discussed cases, odd/even effects have also been encountered in several other IL properties, such as, viscosities (Rocha et al., 2013), entropy and enthalpy of vaporization (Rocha et al., 2012, 2014), glass forming behavior (Leys et al., 2014), and diffusion coefficients (Yang et al., 2016).

ABSOLUTE NEGATIVE PRESSURES IN ILs AND IL-CONTAINING SYSTEMS

Liquids can be mechanically stretched. If this is performed in an isotropic fashion it is possible to obtain absolute negative pressures. Most of the focus of negative pressure experiments was placed on water samples and only very recently some results for pure ionic liquids appeared. The results show that a variety of commonly used ionic liquids (ILs) can be stretched successfully to tensions of about −100 MPa in Pyrex glass capillaries of internal volume of ∼0.05 cm^3 (Silva et al., 2018). These results contrast with the ones obtained for water, in which the maximum stretching of samples of similar size was around −35 MPa (Visak et al., 2002, 2003).

The main reasons for achieving such enormous absolute negative pressures in ionic liquids appears to be a consequence of distinct properties, namely almost null volatility, increased viscosity compared to common liquids, low surface tension, enhanced wettability toward pyrex glass, and easiness to supercool.

Recent work by Silva et al. (2018) has shown that it is possible to use pulsed field gradient NMR spectroscopy to describe the change on the fluid molecular dynamics (transport response

FIGURE 10 | The Berthelot cycle used to obtain tensioning in the IL samples inside a glass capillary: liquid at L-V equilibrium **(A)**; the liquid fills in the entire internal volume at Tfill **(B)**; the liquid is forced along an isochore (constant volume) creating higher, positive pressures **(C)**; if the liquid adheres extremely well to the glass capillary walls, at point **(D)** the liquid is experiencing an isotropic, bulk tension (absolute negative pressure metastable state). At Tcav (cavitation temperature) it will collapse at point **(E)**, relaxing back to its stable condition located along its vapor pressure curve at **(F)**. (Reprinted from Silva et al., 2018).

FIGURE 11 | Relative cation's self-diffusion coefficients vs. temperature in positive, negative, and null pressure regimes. (Reprinted from Silva et al., 2018).

functions) of liquid salts under homogeneous negative pressure regimes (down to about −20 MPa). The experiments followed the thermodynamic Berthelot cycle (**Figure 10**) in order to pre-pressurize the samples and create the conditions to further enter, by cooling the sample, into negative pressure regimes. Negative pressures have been accurately estimated by using experimental values of thermal-pressure coefficients of each liquid at the
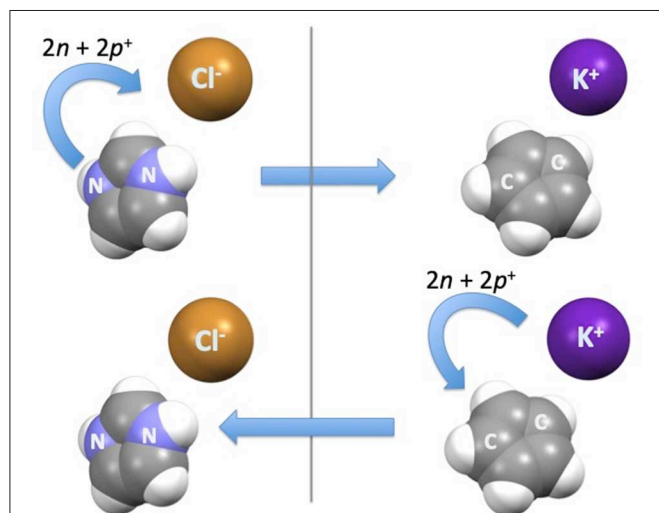
relevant-temperatures of the corresponding isochore. A marked augment in both anions' and cations' self-diffusion coefficients is observed as one enters the metastable negative pressure region as compared to the saturated liquid conditions. **Figure 11** shows the ratio between the cation's diffusion under isochoric conditions and the cation's diffusion under isobaric conditions. The vertical dotted line indicates the filling temperature of the samples, and consequently, data at higher temperatures represent the positive pressure regime while data below this temperature characterize the negative pressure region. It is important to note that for temperatures below 25.5°C ($p \sim$ −150 bar), the liquid salt has already cavitated to the L-V condition and, therefore, the ratio in D's was restored to 1.0. The results show a markedly decrease of the self-diffusion coefficient upon applied positive pressure and a steep increase in it for regimes of negative pressure. It is worth to note that a mild volumetric expansion of about 0.6–0.7% ($\Delta V/V\%$) per each Δp = −100 bar of applied negative pressure can be estimated. This contrasts with the increase in the self-diffusion coefficients of about 5% per each Δp = −100 bar, representing an almost 10-fold increase as compared to the volume expansion of the ionic liquid.

REVERSED-CHARGED IONIC LIQUID PAIRS

It is well-known that salts based on the halides' anions show much lower melting temperatures than those in which their isoelectronic alkyl metals counterparts are present as cations. For instance, already-known salts based on potassium are

FIGURE 12 | The conceptual transfer of two neutrons and two protons to obtain charge-inverted ionic pairs—the 1-alkyl-3-methylimidazolium chloride and its isoelectronic and isostructural counterpart, the potassium 1-alkyl-3-methylcyclopentadienyl.

FIGURE 13 | (A) Phase-separation temperature vs. water content in mixtures of amino acid based ILs. (Reprinted from Fukumoto and Ohno, 2007 with permission from John Wiley and Sons) **(B)** Cloud point data for different ([$N_{11 n2OH}$][Ntf_2] + ether) binary mixtures. Each panel depicts a given ether molecule: A = tert-butyl methyl ether; B = sec-butyl methyl ether; C = n-butyl methyl ether; D = tert-amyl methyl ether; E = cyclopentyl methyl ether and tert-butyl ethyl ether; F = diethyl ether. Each marker/color represents a different choline cation in the ionic liquid: blue triangles = [N_{1122OH}]$^+$ = C2ch; red squares = [N_{1152OH}]$^+$ = C5ch; green rhombs = [N_{1182OH}]$^+$ = C8ch. The arabic numerals indicate the number of phases present on each side of the boundaries defined by the cloud point data. (Reprinted from Costa et al., 2013 with permission from Royal Society of Chemistry).

not members of the ionic liquids family, whereas many with chloride are.

It was recently shown (Cruz et al., 2018, 2019) that using alkali metal cations with distinctive 1-alkyl-3-methylcyclopentadienyl anions it is possible to generate ILs. More specifically, if one uses the same isoelectronic concept as we do for alkali metals vs. halides (e.g., K^+ vs. Cl^-), it is possible to recognize the 1-alkyl-3-methylcyclopentadienyl anion as the isoelectronic and isostructural counterpart of the 1-alkyl-3-methylimidazolium cation (**Figure 12**). Conceptually, one simply has to transfer one proton and one neutron from each of the two nitrogen atoms of the imidazolium ring to the nucleus of the chloride anion. Differential scanning calorimetry has been used to show that $K[C_4C_1Cp]$ and $K[C_6C_1Cp]$ melt without decomposition at around $90°C$. Molecular Dynamics (MD) simulations were used to understand the structural differences between these two IL families. The marked structural differences between the $K[C_nC_1Cp]$ and $[C_nC_1im]Cl$ series is a consequence of the charge-reversion among ion pairs. In the case of these alkali metal based ILs, peculiarities of metal coordination chemistry enables the creation of new structural features. In conclusion, charge-inverted salts can also present low melting temperatures. This fact opens the door for the synthesis of new families of ILs.

LCST Immiscibility Behavior in IL + Solvent Systems

The liquid-liquid lower critical solution temperature (LCST) type of phase diagram rarely occurs. However, it is an important type of demixing that is the basis of several key applications (Albertsson, 1986). It means that phase separation occurs upon temperature increase, with the system attaining a higher order (as compared to the separated components). The closed-loop phase diagram (a temperature-composition island of immiscibility) is even rarer and appears as a result of a very subtle balance between enthalpic and entropic contributions to the Gibbs energy of a system as temperature is changed. It is characterized by a LCST at a given temperature followed by an upper critical solution temperature (UCST) at a higher temperature.

LCST-type of immiscibility was typically only found in some aqueous or (polymer + solvent) solutions. For the first time, Lachwa et al. (2005) have encountered both LCST and closed-loop type of behavior in binary and *quasi*-binary liquid solutions of alkylmethylimidazolium bistriflimide, $[C_nmim][Ntf_2]$, with chloroform or with (chloroform + carbon tetrachloride) mixtures. This study revealed the tunable character of the liquid–liquid phase diagrams involving ILs. Two variables were taken into account, first, in the solutions with chloroform, the number of the carbon atoms in the IL's cation alkyl side chain were varied and secondly the chain length was kept constant at $n = 5$, but the composition of the mixed solvent was altered by adding carbon tetrachloride to chloroform. This work has demonstrated the extreme sensitivity of the phase diagrams upon small changes of

two variables: long IL alkyl chain lengths promote better solubility; whereas addition of more CCl_4 to the $CHCl_3$ worsens the solubility.

Fukumoto and Ohno (2007) have presented another example of LCST behavior, which was related to the solutions of amino acid-based ILs and water (**Figure 13A**). The LCST temperatures of the solutions were tuned by changing the length of the alkyl side chains of either the phosphonium cation or the triflate-aminoacid anion. Longer alkyl chains lower the temperature of the phase separation due to enhanced hydrophobicity. The insertion of four methylene groups to one cation's alkyl side chain brings the LCST down from room temperature to the freezing temperature of water. The anion chain addition of only one $–CH_2-$ group lowers the LCST by about $15°C$. Insertion of a phenyl group with a CH_2 group attached to it also reduces the LCST by about $15°C$. The tuning of the LCST behavior has immense potential in extraction and separation processes.

Other cases of LCST behavior within solutions of ILs and polymer as two component systems were demonstrated independently by Ueki and Watanabe (2007) and Lee and Lodge (2011). Alkyl-methylimidazolium bistriflimide ILs, $[C_nmim][NTf_2]$, mixed with poly(benzyl-methacrylate) (Ueki and Watanabe, 2007) or poly(n-butyl methacrylate) (Lee and Lodge, 2011) show that the increase of the cation chain length, either in the pure IL or through a mixture of cations with different chains, provokes an opposite effect as compared to similar aqueous solutions. Thereby, longer alkyl chains exhibit better solubility and higher LCST. The authors related the improved solubility to the enhancement of the dispersive forces between the (longer) cation alkyl chains and the polymer chains.

Recently, Costa et al. (2013) have reported for the first time functionalized IL + ether systems exhibiting a LCST behavior. Investigating the phase behavior of binary mixtures of three N-alkyl-N,N-dimethyl-N-hydroxyethylammonium bis(trifluoromethane)sulfonylimide ILs, $[N_{11\,n2OH}][Ntf_2]$, with nine distinct ethers at atmospheric pressure, they have found that most systems exhibit unusual LCST-type of phase separation (**Figure 13B**). By increasing the alkyl side chain of the cholinium-derived cation, an enhancement of the mutual solubilities of ILs and ethers is attained. The availability of the oxygen atom of the ether molecule to perform hydrogen bonding with the IL cation and the size/ramification of the alkyl groups of the ether molecule are the key factors that control the solubility of these systems. This LCST behavior is a consequence of the disruption of the H-bond network between the hydroxyl group of the cholinium based cation and the oxygen atom of the ether molecule.

Other works also report systems showing LCST behavior containing mixtures of ILs with polymers, water, supramolecular compounds and other solvents and are summarized in a recent review (Qiao et al., 2017) which highlights their potential applications.

CONCLUDING REMARK

We have highlighted some unexpected features of ionic liquids and ionic liquid-containing systems which are not so well-known of the scientific community.

AUTHOR CONTRIBUTIONS

All authors listed have made a substantial, direct and intellectual contribution to the work, and approved it for publication.

FUNDING

ACKNOWLEDGMENTS

REFERENCES

Abraham, S. E., Chakrabarati, D., and Bagchi, B. (2007). Energy landscape view of nonideality in binary mixtures. *J. Chem. Phys.* 126:074501. doi: 10.1063/1.2434967

Acree, W Jr., and Chickos, J. S. (2010). Phase transition enthalpy measurements of organic and organometallic compounds. sublimation, vaporization and fusion enthalpies from 1880 to 2010. *J. Phys. Chem. Ref. Data* 39:043101. doi: 10.1063/1.3309507

Adamová, G., Gardas, R. L., Rebelo, L. P., Robertson, A. J., and Seddon, K. R. (2011). Alkyltrioctylphosphonium chloride ionic liquids: synthesis and physicochemical properties. *Dalton Trans.* 40, 12750–12764. doi: 10.1039/c1dt10332f

Adamova, G., Lopes, J. N. C., Rebelo, L. P. N., Santos, L. M. N. B., Seddon, K. R., and Shimizu, K. (2014). The alternation effect in ionic liquid homologous series. *Phys. Chem. Chem. Phys.* 16, 4033–4038. doi: 10.1039/C3CP54584A

Albertsson, P. A. (1986). *Partitioning of Cell Particles and Macromolecules, 3rd Edn.* New York, NY: John Wiley.

Alvarez Fernandez, A., and Kouwer, P. H. (2016). Key developments in ionic liquid crystals. *Int. J. Mol. Sci.* 17:731. doi: 10.3390/ijms17050731

Andrzejewska, E., Podgorska-Golubska, M., and Andrzejewski, M. (2009). Photoinitiated polymerization in ionic liquids: kinetics and viscosity effects. *Polymer* 50, 2040–2047. doi: 10.1016/j.polymer.2009.02.034

Armand, M., Endres, F., MacFarlane, D. R., Ohno, H., and Scrosati, B. (2009). Ionic-liquid materials for the electrochemical challenges of the future. *Nat. Mater.* 8, 621–629. doi: 10.1038/nmat2448

Belchior, D. C. V., Sintra, T. E., Carvalho, P. J., Soromenho, M. R. C., Esperança, J. M. S. S., Ventura, S. P. M., et al. (2018). Odd-even effect on the formation of aqueous biphasic systems formed by 1-alkyl-3- methylimidazolium chloride ionic liquids and salts. *J. Chem. Phys.* 148:193842. doi: 10.1063/1.5012020

Belieres, J. P., and Angell, C. A. (2007). Protic ionic liquids: preparation, characterization, and proton free energy level representation. *J. Phys. Chem. B* 111, 4926–4937. doi: 10.1021/jp067589u

Bernardes, C. E. S., and Canongia Lopes, J. N. (2017). Modeling halogen bonds in ionic liquids: a force field for imidazolium and halo-imidazolium derivatives. *J. Chem. Theory Comput.* 13, 6167–6176. doi: 10.1021/acs.jctc.7b00645

Blesic, M., Level, G., Gilmore, B. F., Holbrey, J. D., Jacquemin, J., Nockemann, P., et al. (2017). An introduction to zwitterionic salts. *Green Chem.* 19, 4007–4011. doi: 10.1039/C7GC01523B

Blokhin, A. V., Paulechka, Y. U., Strechan, A. A., and Kabo, G. J. (2006). Physicochemical properties, structure, and conformations of 1-butyl-3-methylimidazolium bis(trifluoromethanesulfonyl)imide [C4mim]Ntf2 ionic liquid. *J. Phys. Chem. B* 112, 4357–4364. doi: 10.1021/jp710872s

Brandrup, J., Immergut, E. H., and Grulke, E. A. (1999). *Polymer Handbook, 4th Edn.* New York, NY: John Wiley & Sons, Inc.

Carvalho, P. J., Freire, M. G., Marrucho, I. M., Queimada, A. J., and Coutinho, J. A. P. (2008). Surface tensions for the 1-Alkyl-3-methylimidazolium Bis(trifluoromethyl)imide ionic liquids. *J. Chem. Eng. Data* 53, 1346–1350. doi: 10.1021/je800069z

Cavallo, G., Bruce, D. W., Terraneo, G., Resnati, G., and Metrangolo, P. (2018). From molecules to materials: engineering new ionic liquid crystals through halogen bonding. *J. Vis. Exp.* 133:e55636. doi: 10.3791/55636

Cerdeirina, C. A., Tovar, C. A., Gonzalez-Salgado, D., Carballo, E., and Roman,í, L. (2001). Isobaric thermal expansivity and thermophysical characterization of liquids and liquid mixtures. *Phys. Chem. Chem. Phys.* 3, 5230–5236. doi: 10.1039/b104891k

Chatel, G., Pereira, J. F. B., Debbeti, V., Wang, H., and Rogers, R. D. (2014). Mixing ionic liquids – "simple mixtures" or "double salts"? *Green Chem.* 16, 2051–2083. doi: 10.1039/c3gc41389f

Costa, A. J. L., Soromenho, M. R. C., Shimizu, K., Esperança, J. M. S. S., Lopes, J. N. C., and Rebelo, L. P. N. (2013). Unusual LCST-type behaviour found in binary mixtures of choline-based ionic liquids with ethers. *RSC Adv.* 3, 10262–10271. doi: 10.1039/c3ra40327k

Cruz, T. F. C., Shimizu, K., Esperança, J. M. S. S., André, V., Duarte, M. T., Rebelo, L. P. N., et al. (2019). ILs in wonderland: from electrostatics to coordination chemistry. *J Phys. Chem. C* 123, 5804–5811. doi: 10.1021/acs.jpcc.9b00987

Cruz, T. F. C., Shimizu, K., Esperança, J. M. S. S., Rebelo, L. P. N., Gomes, P. T., and Canongia Lopes, J. N. (2018). ILs through the looking glass: electrostatics and structure probed using charge-inverted ionic liquid pairs. *Faraday Discuss.* 206, 203–218. doi: 10.1039/C7FD00139H

de Ferro, A. M., Reis, P. M., Soromenho, M. R. C., Bernardes, C. E. S., Shimizu, K., Freitas, A. A., et al. (2018). Designing the ammonium cation to achieve a higher hydrophilicity of bistriflimide-based ionic liquids. *Phys. Chem. Chem. Phys.* 20, 19307–19313. doi: 10.1039/C8CP03398F

Domalski, E. S., and Hearing, E. D. (1996). Heat capacities and entropies of organic compounds in the condensed phase volume III. *J. Phys. Chem. Ref. Data* 25, 1–523. doi: 10.1063/1.555985

Dzida, M., Musiał, M., Zorebski, E., Zorebski, M., Jacquemin, J., Goodrich, P., et al. (2018). Comparative study of effect of alkyl chain length on thermophysical characteristics of five N-alkylpyridinium bis(trifluoromethylsulfonyl)imides with selected imidazolium- based ionic liquids. *J. Mol. Liq.* 271, 401–412. doi: 10.1016/j.molliq.2019.01.022

Esperança, J. M. S. S., Canongia Lopes, J. N., Tariq, M., Santos, L. M. N. B. F., Magee, J. W., and Rebelo, L. P. N. (2010). Volatility of aprotic ionic liquids—a review. *J. Chem. Eng. Data* 55, 3–12. doi: 10.1021/je900458w

Ferreira, A. I. M. C. L., Rodrigues, A., Villas, M., Tojo, E., Rebelo, L. P. N., and Santos, L. M. N. B. F. (2019). Crystallization and glass-forming ability of ionic liquids: novel insights into their thermal behavior. *ACS Sust. Chem. Eng.* 7, 2989–2997. doi: 10.1021/acssuschemeng.8b04343

Fujita, K., Kajiyama, M., Liu, Y., Nakamura, N., and Ohno, H. (2016). Hydrated ionic liquids as a liquid chaperon for refolding of aggregated recombinant protein expressed in *Escherichia coli*. *Chem. Commun.* 13491–13494. doi: 10.1039/C6CC06999A

Fukumoto, K., and Ohno, H. (2007). LCST-type phase changes of a mixture of water and ionic liquids derived from amino acids. *Angew. Chem. Int. Ed.* 46, 1852–1855. doi: 10.1002/anie.200604402

Gardas, R. L., and Coutinho, J. A. P. (2008). A group contribution method for heat capacity estimation of ionic liquids. *Ind. Eng. Chem. Res.* 47, 5751–5757. doi: 10.1021/ie800330v

Gomez, E., Calvar, N., Domínguez, Á., and Macedo, E. A. (2013). Thermal analysis and heat capacities of 1-Alkyl-3-methylimidazolium ionic liquids with NTf2-, TFO-, and DCA- anions. *Ind. Eng. Chem. Res.* 52, 2103–2110. doi: 10.1021/ie3012193

Goossens, K., Lava, K., Bielawski, C. W., and Binnemans, K. (2016). Ionic liquid crystals: versatile materials. *Chem. Rev.* 116, 4643–4807. doi: 10.1021/cr400334b

Haberler, M., Schröder, C., and Steinhauser, O. (2012). Hydrated ionic liquids with and without solute: the influence of water content and protein solutes. *J. Chem. Theory Comput.* 8, 3911–3928. doi: 10.1021/ct300191s

Haddad, J., Pontoni, D., Murphy, B. M., Festersen, S., Runge, B., Magnussen, O. M., et al. (2018). Surface structure evolution in a homologous series of ionic liquids. *Proc. Nat. Acad. Sci. U. S. A.* 115, E1100–E1107. doi: 10.1073/pnas.1716418115

Hallett, J. P., and Welton, T. (2011). Room-temperature ionic liquids: solvents for synthesis and catalysis. 2. *Chem. Rev.* 111, 3508–3576. doi: 10.1021/cr1003248

Hayes, R., Warr, G. G., and Atkin, R. (2015). Structure and nanostructure in ionic liquids. *Chem. Rev.* 115, 6357–6426. doi: 10.1021/cr500411q

Hunt, P. A., Ashworth, C. R., and Matthews, R. P. (2015). Hydrogen bonding in ionic liquids. *Chem. Soc. Rev.* 44, 1257–1288. doi: 10.1039/C4CS00278D

Kar, M., Plechkova, N. V., Seddon, K. R., Pringle, J. M., and MacFarlane, D. R. (2019). Ionic liquids – further progress on the fundamental issues. *Aust. J. Chem.* 72, 3–10. doi: 10.1071/CH18541

Kolbeck, C., Lehmann, J., Lovelock, K. R., Cremer, T., Paape, N., Wasserscheid, P., et al. (2010). Density and surface tension of ionic liquids. *J. Phys. Chem. B* 114, 17025–17036. doi: 10.1021/jp1068413

Kouris, S., and Panaylotou, C. (1989). Dynamic viscosity of mixtures of benzene, ethanol and n-heptane at 298.15 K. *J. Chem. Eng. Data* 34, 200–203. doi: 10.1021/je00056a016

Lachwa, J., Szydlowski, J., Najdanovic-Visak, V., Rebelo, L. P., Seddon, K. R., da Ponte, M. N., et al. (2005). Evidence for lower critical solution behavior in ionic liquid solutions. *J. Am. Chem. Soc.* 127, 6542–6543. doi: 10.1021/ja0510257

Laesecke, A., Freund, M., and Morrison, E. (2007). "Molecular interactions in nonpolar+polar binary mixtures: measurements of N-hexadecane+butyl benzoate," in *AIChE Annu Meeting* (Salt Lake City, UT). 384b.

Leal, J. P., da Piedade, M. E., Lopes, J. N., Tomaszowska, A. A., Esperança, J. M., Rebelo, L. P. N., et al. (2009). Bridging the gap between ionic liquids and molten salts: group 1 metal salts of the bistriflamide anion in the gas phase. *J. Phys. Chem. B* 113, 3491–3498. doi: 10.1021/jp811039b

Lee, H. N., and Lodge, T. P. (2011). Poly(n-butyl methacrylate) in ionic liquids with tunable lower critical solution temperatures (LCST). *J. Phys. Chem. B* 115, 1971–1977. doi: 10.1021/jp1106058

Leys, J., Tripathi, C. S., Glorieux, C., Zahn, S., Kirchner, B., Longuemart, S., et al. (2014). Electrical conductivity and glass formation in nitrile-functionalized pyrrolidinium bis(trifluoromethylsulfonyl)imide ionic liquids: chain length and odd–even effects of the alkyl spacer between the pyrrolidinium ring and the nitrile group. *Phys. Chem. Chem. Phys.* 16, 10548–10557. doi: 10.1039/c4cp00259h

Lima, T. A., Faria, L. F. O., Paschoal, V. H., and Ribeiro, M. C. C. (2018). Glass transition and melting lines of an ionic liquid. *J. Chem. Phys.* 148:171101. doi: 10.1063/1.5030083

Lodeiro, L., Contreras, R., and Ormazábal-Toledo, R. (2018). How meaningful is the halogen bonding in 1-ethyl-3-methyl imidazolium-based ionic liquids for Co2 capture? *J. Phys. Chem. B* 122, 7907–7914. doi: 10.1021/acs.jpcb.8b04990

Lopes, J. N., Gomes, M. F., and Pádua, A. A. (2006). Nonpolar, polar, and associating solutes in ionic liquids. *J. Phys. Chem. B* 110, 16816–16818. doi: 10.1021/jp063603r

Lopes, J. N., and Pádua, A. A. (2006). Nanostructural organization in ionic liquids. *J. Phys. Chem. B* 110, 3330–3335. doi: 10.1021/jp056006y

Luís, A., Shimizu, K., Araújo, J. M. M., Carvalho, P. J., Lopes-da-Silva, J. A., Lopes, J. N., et al. (2016). Influence of nanosegregation on the surface tension of fluorinated ionic liquids. *Langmuir* 32, 6130–6139. doi: 10.1021/acs.langmuir.6b00209

Marsh, K. N., Boxall, J. A., and Lichtenthaler, R. (2004). Room temperature ionic liquids and their mixtures—a review. *Fluid Phase Equilib.* 219, 93–98. doi: 10.1016/j.fluid.2004.02.003

Mirkhani, S. A., Gharagheizi, F., Ilani-Kashkouli, P., and Farahani, N. (2012). Determination of the glass transition temperature of ionic liquids: a molecular approach. *Thermochimica Acta* 543, 88–95. doi: 10.1016/j.tca.2012.05.009

Navia, P., Troncoso, J., and Romaní, L. (2010a). Isobaric thermal expansivity for ionic liquids with a common cation as a function of temperature and pressure. *J. Chem. Eng. Data* 55, 590–594. doi: 10.1021/je900407u

Navia, P., Troncoso, J., and Romani, L. (2010b). Dependence against temperature and pressure of the isobaric thermal expansivity of room temperature ionic liquids. *J. Chem. Eng. Data* 55, 595–599. doi: 10.1021/je900482x

Niedermeyer, H., Hallett, J. P., Villar-Garcia, I. J., Hunt, P. A., and Welton, T. (2012). Mixtures of ionic liquids. *Chem. Soc. Rev.* 41, 7780–7802. doi: 10.1039/c2cs35177c

Nieto de Castro, C. A., Langa, E., Morais, A. L., Lopes, M. L. M., Lourenco, M. J. V., Santos, F. J. V., et al. (2010). Studies on the density, heat capacity, surface tension and infinite dilution diffusion with the ionic liquids [C4mim][NTf2], [C4mim][dca], [C2mim][EtOSO3], and [Aliquat][dca]. *Fluid Phase Equilib.* 294, 157–179. doi: 10.1016/j.fluid.2010.03.010

Ohno, H., Yoshizawa-Fujita, M., and Kohno, Y. (2018). Design and properties of functional zwitterions derived from ionic liquids. *Phys. Chem. Chem. Phys.* 20, 10978–10991. doi: 10.1039/C7CP08592C

Pádua, A. A., Costa Gomes, M. F., and Lopes, J. N. (2007). Molecular solutes in ionic liquids: a structural perspective. *Acc. Chem. Res.* 40, 1087–1096. doi: 10.1021/ar700050q

Papanastaaiou, G. E., and Ziogas, I. I. (1991). Physical behaviour of some reaction media. Density, viscosity, dielectric constant, and refractive index change of ethanol-cyclohexane mixtures at several temperatures. *J. Chem. Eng. Data* 36, 46–51. doi: 10.1021/je00001a014

Paulechka, Y. U., Kabo, A. G., Blokhin, A. V., Kabo, G. J., and Shevelyova, M. P. (2010). Heat capacity of ionic liquids: experimental determination and correlations with molar volume. *J. Chem. Eng. Data* 55, 2719–2724. doi: 10.1021/je900974u

Pereiro, A. B., Araújo, J. M. M., Teixeira, F. S., Marrucho, I. M., Piñeiro, M. M., and Rebelo, L. P. N. (2015). Aggregation behavior and total miscibility of fluorinated ionic liquids in water. *Langmuir* 31, 1283–1295. doi: 10.1021/la503961h

Pereiro, A. B., Pastoriza-Gallego, M. J., Shimizu, K., Marrucho, I. M., Canongia Lopes, J. N., Piñeiro, M. M., et al. (2013). On the formation of a third, nanostructured domain in ionic liquids. *J. Phys. Chem. B* 117, 10826–10833. doi: 10.1021/jp402300c

Plechkova, N. V., and Seddon, K. R. (2008). Applications of ionic liquids in the chemical industry. *Chem. Soc. Rev.* 37, 123–150. doi: 10.1039/B006677J

Podgoršek, A., Jacquemin, J., Pádua, A. A. H., and Costa Gomes, M. F. (2016). Mixing enthalpy for binary mixtures containing ionic liquids. *Chem. Rev.* 116, 6075–6106. doi: 10.1021/acs.chemrev.5b00379

Qiao, Y., Ma, W., Theyssen, N., Chen, C., and Hou, Z. (2017). Temperature-responsive ionic liquids: fundamental behaviors and catalytic applications. *Chem. Rev.* 117, 6881–6928. doi: 10.1021/acs.chemrev.6b00652

Qunfang, L., and Yu-Chun, H. (1999). Correlation of viscosity of binary liquid mixtures. *Fluid Phase Equilib.* 154, 153–163. doi: 10.1016/S0378-3812(98)00415-4

Rahman, M. H., and Senapati, S. (2018). Water clathrates in nanostructural organization of hydrated ionic liquids manifest in peculiar density trend. *J. Phys. Chem. B.* 123, 1592–1601. doi: 10.1021/acs.jpcb.8b08586

Rebelo, L. P. N., Najdanovic-Visak, V., Visak, Z. P., Nunes da Ponte, M., Szydlowski, J., Cerdeirina, C. A., et al. (2004). A detailed thermodynamic analysis of [C4mim][BF4] + water as a case study to model ionic liquid aqueous solutions. *Green Chem.* 6, 369–381. doi: 10.1039/B400374H

Rocha, M. A., Coutinho, J. A., and Santos, L. M. (2012). Cation symmetry effect on the volatility of ionic liquids. *J. Phys. Chem. B* 116, 10922–10927. doi: 10.1021/jp306937f

Rocha, M. A., Coutinho, J. A., and Santos, L. M. (2014). Vapor pressures of 1,3-dialkylimidazolium bis(trifluoromethylsulfonyl)imide ionic liquids with long alkyl chains. *J. Chem. Phys.* 141:134542. doi: 10.1063/1.4896704

Rocha, M. A., Neves, C. M., Freire, M. G., Russina, O., Triolo, A., Coutinho, J. A., et al. (2013). Alkylimidazolium based ionic liquids: impact of cation symmetry on their nanoscale structural organization. *J. Phys. Chem. B* 117, 10889–10897. doi: 10.1021/jp406374a

Rodrigues, A. S., and Santos, L. M. (2016). Nanostructuration effect on the thermal behavior of ionic liquids. *ChemPhysChem* 17, 1512–1517. doi: 10.1002/cphc.201501128

Rodríguez, H., and Brennecke, J. F. (2006). Temperature and composition dependence of the density and viscosity of binary mixtures of water + ionic liquid. *J. Chem. Eng. Data* 51, 2145–2155. doi: 10.1021/je0602824

Saccone, M., Palacio, F. F., Cavallo, G., Dichiarante, V., Virkki, M., Terraneo, G., et al. (2017). Photoresponsive ionic liquid crystals assembled via halogen bond: en route towards light-controllable ion transporters. *Faraday Discuss.* 203, 407–422. doi: 10.1039/C7FD00120G

Sanmamed, Y. A., Gonzalez-Salgado, D., Troncoso, J., Cerdeirina, C. A., and Romaní, L. (2007). Viscosity-induced errors in the density determination of room temperature ionic liquids using vibrating-tube densitometry. *Fluid Phase Equilib*. 252, 96–102. doi: 10.1016/j.fluid.2006.12.016

Santos, L. M. N. B. F., Canongia Lopes, J. N., Coutinho, J. A. P., Esperança, J. M. S. S. Gomes, L. R., Marrucho, I. M., et al. (2007). Ionic liquids: first direct determination of their cohesive energy. *J. Am. Chem. Soc.* 129, 284–285. doi: 10.1021/ja067427b

Serra, P. B. P., Ribeiro, F. M. S., Rocha, M. A. A., Fulem, M., RuŽicka, K., Coutinho, J. A. P., et al. (2017). Solid-liquid equilibrium and heat capacity trend in the alkylimidazolium PF6 series. *J. Mol. Liq.* 248, 678–687. doi: 10.1016/j.molliq.2017.10.042

Shimizu, K., Heller, B. S. J., Maier, F., Steinrück, H. P., and Lopes, J. N. (2018). Probing the surface tension of ionic liquids using the langmuir principle. *Langmuir* 34, 4408–4416. doi: 10.1021/acs.langmuir.7b04237

Shimizu, K., Tariq, M., Costa Gomes, M. F., Rebelo, L. P. N., and Lopes, J. N. C. (2010). Assessing the dispersive and electrostatic components of the cohesive energy of ionic liquids using molecular dynamics simulations and molar refraction data. J. Phys. *Chem. B* 114, 5831–5834. doi: 10.1021/jp101910c

Silva, W., Veiga, H. I. M., Tariq, M., Cabrita, E. J., Esperança, J. M. S. S., Canongia Lopes, J. N., et al. (2018). Negative pressure regimes in ionic liquids: structure and interactions in stretched liquids as probed by NMR. *ECS Trans.* 86, 141–147. doi: 10.1149/08614.0141ecst

Singh, A. P., Gardas, R. L., and Senapati, S. (2015). Divergent trend in density versus viscosity of ionic liquid/water mixtures: a molecular view from guanidinium ionic liquids. *Phys. Chem. Chem. Phys.* 17, 25037–25048. doi: 10.1039/C5CP02841H

Singh, A. P., Gardas, R. L., and Senapati, S. (2017). How water manifests the structural regimes in ionic liquids. *Soft Matter* 13, 2348–2361. doi: 10.1039/C6SM02539K

Srinivas, G., Mukherjee, A., and Bagchi, B. (2001). Nonideality in the composition dependence of viscosity in binary mixtures. *J. Chem. Phys.* 114:6220. doi: 10.1063/1.1354166

Strechan, A. A., Kabo, A. G., Paulechka, Y. U., Blokhin, A. V., Kabo, G. J., Shaplov, A. S., et al. (2008). Thermochemical properties of 1-butyl-3-methylimidazolium nitrate. *Thermochimica Acta* 474, 25–31. doi: 10.1016/j.tca.2008.05.002

Tao, R., Gurung, E., Cetin, M. M., Mayer, M. F., Quitevis, E. L., and Simon, S. L. (2017). Fragility of ionic liquids measured by Flash differential scanning calorimetry. *Thermochimica Acta* 654, 121–129. doi: 10.1016/j.tca.2017.05.008

Tariq, M., Forte, P. A. S., Gomes, M. F. C., Lopes, J. N. C., and Rebelo, L. P. N. (2009). Densities and refractive indices of imidazolium- and phosphonium-based ionic liquids: effect of temperature, alkyl chain length, and anion. *J. Chem. Thermodynamics* 41, 790–798. doi: 10.1016/j.jct.2009.01.012

Tariq, M., Freire, M. G., Saramago, B., Lopes, J. N., Coutinho, J. A. P., and Rebelo, L. P. N. (2012). Surface tension of ionic liquids and ionic liquid solutions. *Chem. Soc. Rev.* 41, 829–868. doi: 10.1039/C1CS15146K

Tariq, M., Serro, A. P., Mata, J. L., Saramago, B., Esperança, J. M. S. S., Lopes, J. N. C., et al. (2010). High-temperature surface tension and density measurements of 1-alkyl-3-methylimidazolium bistriflamide ionic liquids. *Fluid Phase Equilib.* 294, 131–138. doi: 10.1016/j.fluid.2010.02.020

Tariq, M., Shimizu, K., Esperança, J. M. S. S., Lopes, J. N. C., and Rebelo, L. P. N. (2015). Viscosity minima in binary mixtures of ionic liquids + molecular solvents. *Phys. Chem. Chem. Phys.* 17, 13480–13494. doi: 10.1039/C5CP01563D

Triolo, A., Russina, O., Bleif, H. J., and Di Cola, E. (2007). Nanoscale segregation in room temperature ionic liquids. *J. Phys. Chem. B* 111, 4641–4644. doi: 10.1021/jp067705t

Trivedi, S., and Pandey, S. (2011). Interactions within a [IonicLiquid+ Poly(ethylene glycol)] mixture revealed by temperature-dependent synergistic dynamic viscosity and probe-reported microviscosity. *J. Phys. Chem. B* 115, 7405–7416. doi: 10.1021/jp203079p

Troncoso, J., Cerdeirina, C. A., Navia, P., Sanmamed, Y. A., Gonzalez-Salgado, D., and Romani, L. (2010). Unusual behavior of the thermodynamic response functions of ionic liquids. *J. Phys. Chem. Lett.* 1, 211–214. doi: 10.1021/jz900049g

Ueki, T., and Watanabe, M. (2007). Lower critical solution temperature behavior of linear polymers in ionic liquids and the corresponding volume phase transition of polymer gels. *Langmuir* 23, 988–990. doi: 10.1021/la062986h

Valderrama, J. O., Campusano, R. A., and Rojas, R. E. (2017). Glass transition temperature of ionic liquids using molecular descriptors and artificial neural networks. *C. R. Chimie* 20, 573–584. doi: 10.1016/j.crci.2016.11.009

Visak, Z. P., Rebelo, L. P. N., and Szydlowski, J. (2002). Achieving absolute negative pressures in liquids: precipitation phenomena in solution. *J. Chem Educ.* 79, 869–873. doi: 10.1021/ed079p869

Visak, Z. P., Rebelo, L. P. N., and Szydlowski, J. (2003). The "hidden" phase diagram of water+3-methylpyridine at large absolute negative pressures. *J. Phys. Chem. B* 107, 9837–9846. doi: 10.1021/jp0223206

Welton, T. (1999). Room-temperature ionic liquids: solvents for synthesis and catalysis. *Chem. Rev.* 99, 2071–2084. doi: 10.1021/cr980032t

Welton, T. (2018). Ionic liquids: a brief history. *Biophys. Rev.* 10, 691–706. doi: 10.1007/s12551-018-0419-2

Wu, B., Kuroda, K., Takahashi, K., and Castner, E. W. (2018). Structural analysis of zwitterionic liquids vs. homologous ionic liquids. *J. Chem. Phys.*148:193807. doi: 10.1063/1.5010983

Xu, W., and Angell, C. A. (2003). Solvent-free electrolytes with aqueous solution–like conductivities. *Science* 302, 422–425. doi: 10.1126/science.1090287

Yang, K., Cai, Z., Tyagi, M., Feygenson, M., Neuefeind, J. C., Moore, J. S., et al. (2016). Odd–even structural sensitivity on dynamics in network-forming ionic liquids. *Chem. Mater.* 28, 3227–3233. doi: 10.1021/acs.chemmater.6b01429

Yaws, C. L. (2009). *Thermophysical Properties of Chemicals and Hydrocarbons*. Elsevier.

Zabransky, M., Ruzicka, V Jr., and Majer, V. (1990). Heat capacities of organic compounds in the liquid state I. C1 to C18 1-alkanols. *J. Phys. Chem. Ref. Data* 19, 719–762. doi: 10.1063/1.555860

Check for
updates

A Review of Solvate Ionic Liquids: Physical Parameters and Synthetic Applications

Daniel J. Eyckens* and Luke C. Henderson*

Institute for Frontier Materials, Deakin University, Geelong, VIC, Australia

Solvate Ionic Liquids (SILs) are a relatively new class of ionic liquids consisting of a coordinating solvent and salt, that give rise to a chelate complex with very similar properties to ionic liquids. Herein is the exploration of the reported Kamlet-Taft parameters, Gutmann Acceptor numbers and the investigation of chelating effects through NMR spectroscopy of multiple atomic nuclei. These properties are related to the application of SILs as reaction media for organic reactions. This area is also reviewed here, including the implication in catalysis for the Aldol and Kabachnik-Fields reactions and electrocyclization reactions such as Diels-Alder and [2+2] cycloaddition. Solvate ILs exhibit many interesting properties and hold great potential as a solvent for organic transformations.

Keywords: solvate ionic liquid, lithium TFSI, glyme complexes, chelation, solvatochromic properties

INTRODUCTION/CONTEXT

The context of this review is to examine the application of solvate ionic liquids as a reaction media. This extends to encompass the relevant physical parameters of hydrogen bonding characteristics, polarity and Lewis acidity. The use of these solvates as electrolytes for lithium ion batteries (Ueno et al., 2013; Kido et al., 2015; Nakazawa et al., 2016; Kawazoe et al., 2017), their microstructure (Murphy et al., 2016; Saito et al., 2016; Cook et al., 2017; Li H. et al., 2017) or indeed their thermoelectrochemical properties (Black et al., 2018) are not covered here. In addition to these applications, it may be of interest to note that they have also been evaluated as sizing agents for carbon fiber in resin composites, with good success (Eyckens et al., 2018).

It is important to note that while this review focusses on the use of SILs in organic and materials chemistry there has been substantial use of traditional ILs in both of these fields. There has been considerable work in the use of ionic liquids in the modification of graphene with imidazolium ionic liquids, one reporting a one-step functionalization procedure from graphite (Liu et al., 2008). The use of these materials has also seen a great amount of application in sensors of biological species such as NADH (Shan et al., 2010; Atta et al., 2017), hydrogen peroxide (Chen et al., 2018), bisphenol A (Wang et al., 2018), and glucose (Zhang et al., 2011). These materials have also seen use in nanocomposites still as electrodes for detection of chemical or biological species (Krampa et al., 2017; Li J. et al., 2017; Zad et al., 2018).

The work in materials science is also not limited to imidazolium-derived ionic liquids and interesting works in graphene exfoliation have been conducted in pyridinium and pyrrolidinium cation based ionic liquids (Chaban and Fileti, 2015). Examination of the difference between molecular liquids and ionic liquids has been reported (Bordes et al., 2018) and followed by exploring the difference between *N*-butylpyridinium *bis*(trifluoromethanesulfonyl)imide and 1-butyl-1-methylpyrrolidinium *bis*(trifluoromethanesulfonyl)imide (Chaban et al., 2017). Both of these ionic liquids were superior to the imidazolium-derived ionic liquid 1-ethyl-3-methylimidazolium tetrafluoroborate by ~20 kJ mol^{-1} nm^{-1}. Complementing this work is other investigations into pyridinium and pyrrolidinium-derived ionic liquids in various fields such as heat transfer processes (Musiał et al., 2017), super capacitors (Chee et al., 2016; Chaban et al., 2018), and graphene nanostructures (Atilhan and Aparicio, 2014).

Solvate Ionic Liquids

A recently reported (Tamura et al., 2010) class of ionic liquids known as solvate ionic liquids (SILs) is an area of study in its infancy, though investigations into to the field are rapidly increasing. Typically, SILs exist due to the diffusing of a cationic charge *via* the sequestering of a hard cation, often in an ethereal solvent (Austen Angell et al., 2012). The most prominent in the literature is the dissolution of lithium *bis*(trifluoromethanesulfonyl)imide (LiTFSI) in either triethylene glycol dimethyl ether or tetraethylene glycol dimethyl ether ([Li(G3)]TFSI (**1**) or [Li(G4)]TFSI (**2**), respectively, **Figure 1**).

The use of ionic liquids for organic transformations (Welton, 1999; Hallett and Welton, 2011), and their physical properties (Forsyth et al., 2002; Angell et al., 2007; Lee et al., 2008; Ferrara et al., 2017) have been well studied, though these solvate counterparts have a relatively low representation in the literature. Also well-established is the effect on reaction kinetics the use of ILs convey (Keaveney et al., 2017; Butler and Harper, 2018; Hawker et al., 2018), an area that has had, at the time of publishing, not been investigated in SILs.

The LiTFSI salt has been incorporated into polymer electrolytes for batteries, with good success (Watanabe and Nishimoto, 1995; Mary Sukeshini et al., 1996; Watanabe and Mizumura, 1996; Nishimoto et al., 1998), and the addition of boric acid ester monomers have assisted the solubility of the salt in these networks (Hirakimoto et al., 2001; Tabata et al., 2003). Henderson et al. first identified and characterized the chelation

of Li$^+$ salts in triglyme and tetraglyme (Henderson et al., 2003) but the salts studied in that work didn't include LiTFSI.

Both [Li(G3)]TFSI and [Li(G4)]TFSI satisfy the following criteria for solvate ILs outlined by Mandai et al. (2014): (1) A solvate compound is formed between an ion and a ligand(s) in a certain stoichiometric ratio (in this instance, 1:1). (2) Consist (almost) entirely of complex ions (solvates) and their counter ions in the molten state. (3) Show no physicochemical properties based on both pure ligands and precursor salts under using conditions. (4) Have a melting point below 100°C (which satisfies the criterion for typical room temperature ILs). (5) Have a negligible vapor pressure.

In relation to the third criterion, the equimolar mixture of LiTFSI and glyme forgoes any evaporation due to the lithium chelation, an effect not present when lesser concentrations of LiTFSI in glyme were assessed (Mandai et al., 2014).

The solvation occurs when the lone pairs on the oxygen atoms of the ether moieties act as a Lewis base, donating electrons to the Lewis acid (lithium) cation, chelating it (**Scheme 1**). This multidentate sequestration enables the dissolution of alkali metals, such as LiTFSI or lithium perchlorate (LiClO$_4$). In the case of LiTFSI, electron density of the nitrogen atom (of the anion) is attenuated due to the strongly electron withdrawing flanking groups [sulfur(VI)], heavily delocalising the anionic charge. This allows the oligo-ether groups to coordinate the lithium cation. The combination of these effects relieves the strong coulombic interactions of the naked LiTFSI salt, reducing the previously high melting point (234–238°C) to below room-temperature.

Changing the glyme or anion combination can produce highly variable results, exemplified by the crystal structure produced when LiClO$_4$ is dissolved in G3 (melting point = 103°C) compared with the room-temperature IL formed when dissolved in G4 (Ueno et al., 2012). The greater the ionic association of the salt in aprotic solvents, the less likely that chelation will occur, supported by the previous example by the greater Lewis basicity (association with cation) of the anion ClO$_4^-$ compared to TFSI$^-$ (Henderson, 2006). Further to this, employing a PF$_6^-$ anion may catalyze the decomposition of polyethylene oligomers to alkenes, with concimmitant HF and phosphorous containing by-products, according to **Scheme 2** (Abraham et al., 1997).

Background

Similar structures of Li$^+$ cations with oligoether-containing structures were investigated by Fujinami and Buzoujima (2003)

FIGURE 1 | Simplified structure of Lithium in G3 ([Li(G3)]TFSI, **1**), G4 ([Li(G4)]TFSI, **2**), and the TFSI$^-$ anion (**3**).

SCHEME 1 | Addition of Lewis acid and Lewis base to give a solvate ionic liquid. Anion not shown.
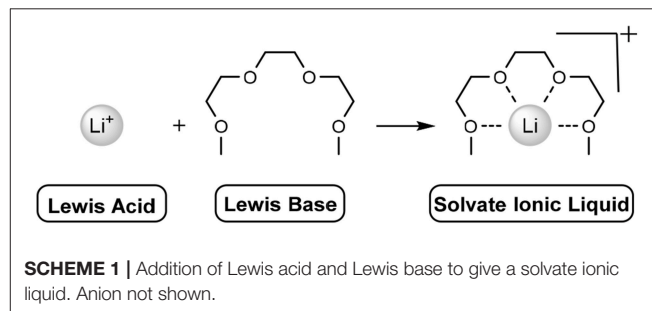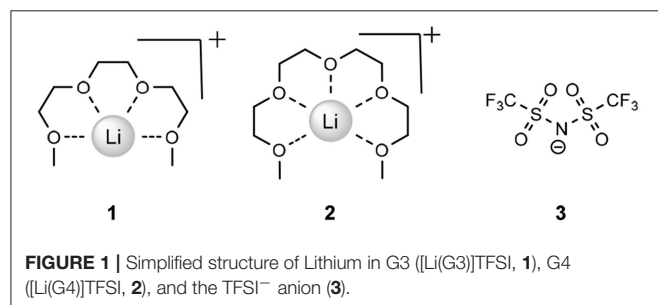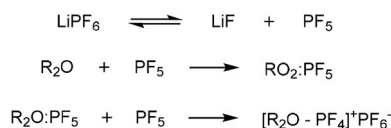
SCHEME 2 | Mechanism of decomposition of Glyme-like groups (R_2O) through reaction with the PF_6 anion (Abraham et al., 1997).

which consisted of two ethereal units and two electron withdrawing units attached to an aluminate anionic center (**4**) according to **Scheme 3**.

Comparatively, Shobukawa et al. demonstrated an analogous structure, though with a borate anionic center (**5**, **Figure 2**) (Shobukawa et al., 2004). The main difference here is that the latter example was fully characterized as an ionic liquid, and the former (aluminate solvate), was not formally characterized, though was referred to as a liquid salt in the manuscript (Fujinami and Buzoujima, 2003). Both structures exhibit similar glass transition states, far below 0°C (average $T_g \approx -50$°C across different length PEG groups) and the reduction in Lewis basicity of the anionic component of these solvates allow the Li^+ cation to be chelated by the ethereal units (Shobukawa et al., 2004).

Although these examples are similar in concept to the solvate ionic liquids explored here, Pappenfus et al. was the first to report the equimolar mixture of LiTFSI and tetraglyme as a room temperature (solvate) ionic liquid (Pappenfus et al., 2004). This was closely followed by the analysis of different length glyme oligomers with lithium salts (Henderson, 2006).

The chelation of the lithium cation by the glyme molecule characterizes the mixture as a solvate ionic liquid, not just a concentrated solution, as identified by Ueno et al. (2012) by exploring anion-dependent properties. It was determined that a weakly Lewis basic anion (TFSI-type anions and ClO_4) was required to allow the glyme-Li^+ chelation to dominate over the competitive cation-anion interactions. When anions of greater Lewis basicity were employed, the result was concentrated solutions of salt in glyme (**Table 1**, entries with asterisks).

In contrast to the concentrated solutions, the solvate ILs showed high thermal stability, high ionic conductivity, high viscosity, low volatility, low flammability as well as a wide electrochemical window, just like traditional ILs (Tamura et al., 2010; Seki et al., 2011; Ueno et al., 2012).

Table 1, below, shows the difference in melting point and density of equimolar mixtures of tri- or tetraglyme and lithium salts with a variety of anions.

As may be seen in the table, altering the anion has large effects on both melting point and density. The solvate ionic liquids explored in this work are in bold, and worth noting is the outcome that not all lithium salts present as liquids in both tri- and tetraglyme, and may only exist as such in one or the other with the alternative being a solid complex. These combinations are not shown in **Table 1**, but an example is [Li(G3)]ClO_4 which is solid above 100°C, whereas [Li(G4)]ClO_4 has a melting point of 28°C.

Raman spectroscopy of both [Li(G3)]TFSI and [Li(G4)]TFSI indicates a very negligible percentage of free glyme in these

equimolar mixtures (**Figure 3**), which is to be expected of solvate ILs (Ueno et al., 2015).

As identified earlier, some combinations of lithium salt and glyme do not result in solvate ionic liquids, only concentrated solutions, further confirmed by the large percentage of free glyme (not-chelating) in those examples (Ueno et al., 2015).

PHYSICAL CHEMICAL PROPERTIES

Kamlet-Taft Parameters

Sometimes referred to as solvatochromic parameters, the Kamlet-Taft parameters are determined spectrophotometrically *via* the addition of different dyes to solvents and subsequent UV-visible spectroscopy (Kamlet et al., 1977). The scale is based on linear solvation energy relationships (LSER) consisting of three complimentary solvent characteristics. These are the hydrogen-bond donating and accepting abilities (α and β values, respectively) and polarity/polarizability (π^* values). It is also possible to determine the $E_T(30)$ (solvent polarity) and the E_T^N (solvent polarity normalized against water) from one of the dyes used (Reichardt's dye).

This technique has previously been employed in molecular solvents (Kamlet and Taft, 1976; Taft and Kamlet, 1976; Kamlet et al., 1977), in non-aqueous binary mixtures of organic solvents (Reta et al., 2001), as well as for ionic liquids (Muldoon et al., 2001; Lee et al., 2008; Padró and Reta, 2016). In addition to the key characteristics that can be investigated through this technique, is the reactivity of anionic nucleophiles in ionic liquids (Crowhurst et al., 2006). All solvents must be appropriately anhydrous when employing these techniques, to reduce any augmentation of results.

The determination of the physical parameters of SILs is still in its infancy, though in regard to the Kamlet-Taft parameters, there have been three reports in the literature (Dolan et al., 2016; Eyckens et al., 2016b; Black et al., 2018). Each have had some slight difference in detection method, be it different dyes or different mole ratio of solvating glyme to LiTFSI salt. Due to this fact, the reported values have some slight variation from one another, though it is important to note that the trend of these parameters is of most importance when comparing these values, which is largely consistent.

The dyes used to determine the Kamlet-Taft parameters are traditionally *N,N*-diethyl-4-nitroaniline, 4-nitroaniline and Reichardt's dye. Burgess' dye may be used in place Reichardt's dye (**Figure 4**), if the latter is not sufficiently soluble in the given solvent, as was the case for Dolan et al. except for the glyme solvents (**Table 2**) (Dolan et al., 2016).

The solvents examined here are the neat glymes (tri- and tetraglyme, G3 and G4, respectively), LiTFSI versions of these ([Li(G3)]TFSI and [Li(G4)]TFSI), the LiBETI (lithium *bis*(pentafluoroethanesulfonyl)imide) versions ([Li(G3)]BETI and [Li(G4)]BETI), and for comparison to a traditional ionic liquid, [Bmim]TFSI (1-butyl-3-methylimidazolium *bis*(trifluoromethanesulfonyl)imide). For greater investigation of anion combinations, please refer to the literature (Dolan et al., 2016). Solvates consisting of the LiBETI salt are presented as the G4 varietal is reported to have a very low percentage of free
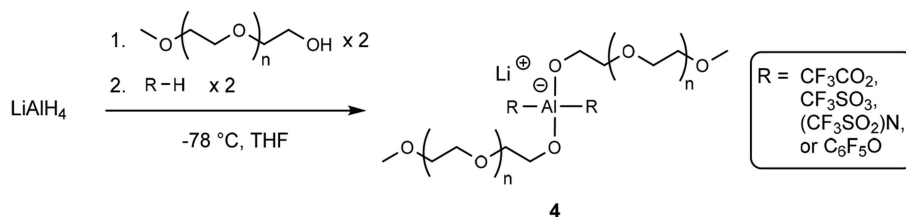
SCHEME 3 | Production of an aluminate-based lithium solvate salt (Fujinami and Buzoujima, 2003).
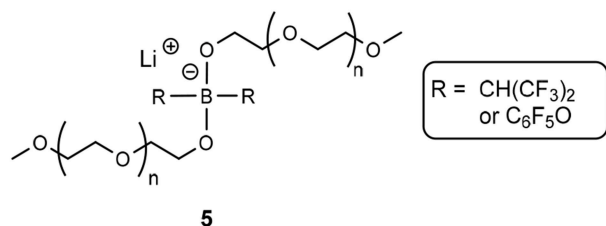
FIGURE 2 | Borate-based solvate ionic liquid produced by Shobukawa et al. (2004).

TABLE 1 | Properties of a range glyme-lithium salt mixtures.

Glyme-Li$^+$ salt mixture	T_m (°C)	ρ (g cm^{-3})
[Li(G3)]TFSI	**23**	**1.42**
[Li(G3)]FSI	56	1.36
[Li(G3)]OTf*	35	1.30
[Li(G3)]NO$_3$*	27	1.18
[Li(G3)]TFA*	n.d.	1.20
[Li(G4)]TFSI	**n.d.**	**1.40**
[Li(G4)]CTFSI	28	1.40
[Li(G4)]FSI	23	1.32
[Li(G4)]BETI	23	1.46
[Li(G4)]ClO$_4$	28	1.27
[Li(G4)]BF$_4$	39	1.22
[Li(G4)]NO$_3$*	n.d.	1.17
[Li(G4)]TFA*	n.d.	1.19

*Entries in bold are those most relevant to this review. *denotes concentrated solutions, not solvate ILs. TFSI, bis(trifluormethansulfonyl)imide; FSI, bis(fluorosulfonyl)imide; OTf, trifluoromethylsulfonate; NO$_3$, nitrate; TFA, trifluoroacetate; CTFSI, cyclic-TFSI derivative 1,2,3-dithiazolidine-4,4,5,5-tetrafluoro-1,1,3,3-tetraoxide; BETI, bis(pentafluoroethanesulfonyl)imide; ClO$_4$, perchlorate; BF$_4$, tetrafluoroborate; Adapted from Ueno et al. (2012).*

FIGURE 3 | Estimated amount of free glyme in solution for equimolar mixtures of tri- or tetraglyme with various lithium salts.
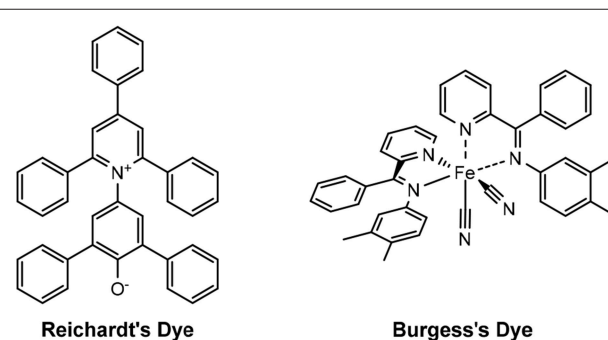
FIGURE 4 | Structures of Reichardt's and Burgess's dyes.

glyme (**Table 1**) (Ueno et al., 2015), and though this hasn't been reported for [Li(G3)]BETI (potentially due to the higher melting point, mp = 74°C) it has been included here for consistency.

The Kamlet-Taft parameters are measured on a scale generated by examining the wavelength exhibited by solvents of differing hydrogen bond characteristics in response to the presence of different dyes. Due to this, the values are measured in reference to a strongly hydrogen bond donating or accepting solvent, which is given the arbitrary value of 1.00. It is possible that a solvent of unknown hydrogen bonding properties may have a value of <1.00, meaning for example that it is a greater hydrogen bond donator than the given reference.

α-Values

Looking first at the α values (hydrogen bond donating), the tri- and tetraglyme both exhibit negligible values across all reports, as is anticipated judging from their structures and lack of acidic protons.

An unexpected result is the high α values for the SILs consisting of all glymes. This is attributed to the Lewis acidity

TABLE 2 | Reported Kamlet-Taft parameters of solvate ionic liquids.

Solvent	α			β			π^*		
	(i)	(ii)	(iii)	(i)	(ii)	(iii)	(i)	(ii)	(iii)
G3	0.10	0.04	−0.01	0.62	0.66	0.71	0.74	0.66	0.67
G4	0.03	0.02	−0.05	0.72	0.66	0.72	0.68	0.66	0.69
[Li(G3)]TFSI	1.03[a]	1.08	1.32	0.30	0.26	0.31	0.96	1.00	0.94
[Li(G4)]TFSI	0.77[a]	1.22[b]	1.35	0.24	0.27[b]	0.28	0.92	0.99[b]	0.91
[Li(G3)]BETI	0.88[a]	-	-	0.32	-	-	0.84	-	-
[Li(G4)]BETI	0.80[a]	-	-	0.36	-	-	0.86	-	-
[Bmim]TFSI	-	-	0.55	-	-	0.22	-	-	0.97

(i) (Dolan et al., 2016) (ii) (Black et al., 2018) (iii) (Eyckens et al., 2016b).
[a]Values determined with Burgess' dye in place of Reichardt's dye.
[b]Mole ratio of 4:5 (LiTFSI:G4) used instead of 1:1.

FIGURE 5 | Typical configuration predicted for the dye—Li$^+$ complex, showing additional coordination of three oxygen atoms provided by two TFSI molecules, taken from the [Li(G4)]TFSI liquid simulation. Remainder of the liquid not shown for clarity. Cyan = carbon, white = hydrogen, blue = nitrogen, red = oxygen, green = fluorine, yellow = sulfur and purple = Li$^+$ (Eyckens et al., 2016b).
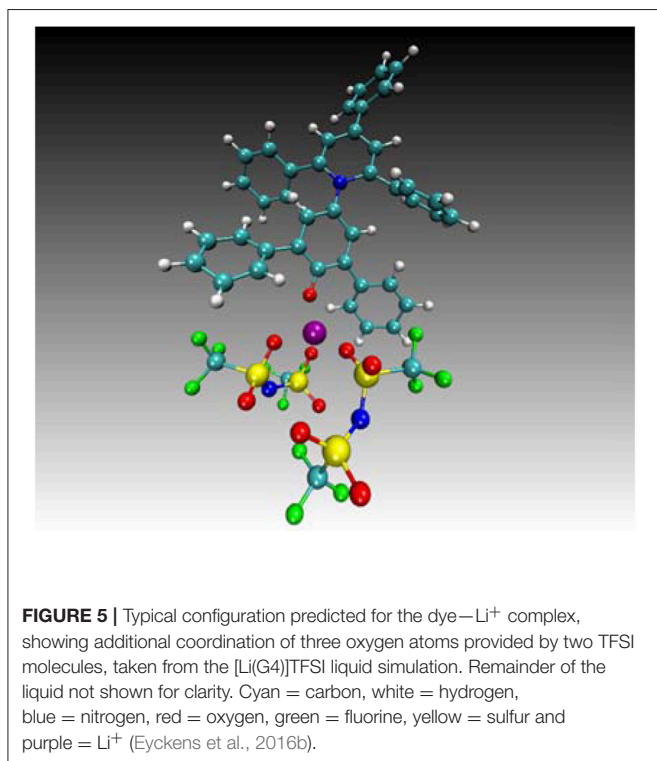
of the chelated lithium cation, which is acting as a surrogate hydrogen bond. This phenomenon was confirmed by molecular dynamics, simulating the interaction between the chelated lithium cation of [Li(G4)]TFSI and Reichardt's dye (**Figure 5**) (Eyckens et al., 2016b).

The α values of the LiBETI derivatives of SILs are lower than those with the TFSI$^-$ anion. This suggests there may be some greater attenuation of the cation in the presence of BETI$^-$, or possibly the relative increase in size of BETI$^-$ from TFSI$^-$ (pentafluoroethyl vs. trifluoromethyl) suppressing the interaction of cation and dye. Note also, the determination of the α values of the by Dolan et al. (2016) were performed using Burgess' dye rather than Reichardt's, and all SILs exhibit lower values than those reported by others (Eyckens et al., 2016b; Black et al., 2018).

The Kamlet-Taft parameters for a traditional, imidazolium-based ionic liquid, [Bmim]TFSI (1-butyl-3-methylimidazolium *bis*(trifluoromethylsulfonyl)imide) have been included here to give context to the values of the SILs. The α value for this IL is a little under half of that of the SILs with the same anion, which may be due to the diffusion of the positive charge around the imidazolium ring, the acidic hydrogens or a combination of both (Eyckens et al., 2016b). In any event, the α value suffers from the absence of the hard lithium cation.

β-Values

The β values (hydrogen bond accepting ability) of the solvents also demonstrated the effect of chelation of lithium by the glyme/glycol units, in that the observed values of the SILs are comparatively lower than those of the glyme solvents on their own. This reduced hydrogen bond accepting ability of the solvents is caused by the electrons of the ethereal oxygens being engaged with the lithium-glyme chelate, and therefore limited for other hydrogen bonding entities. This is true across all SILs from all reports.

A similar value is exhibited by [Bmim]TFSI, though slightly lower. The hydrogen bond accepting characteristic of this IL is due to the anion. In the case of the SILs the accepting ability of the anion is bolstered with that of the chelating glyme, giving the slightly increased β values.

π-Values

Finally, the π* (pi-star) values (polarity/polarizability) are the ability of the solvent to stabilize charge or become polarized. It would then follow that ionic compounds, like SILs, should have higher values than the solvating agents themselves. This observation is consistent across all reports with the introduction of either LiTFSI or LiBETI increasing the π* values by about a third when compared to the glymes. A high π* value is also observed for [Bmim]TFSI, which is typical for traditional ILs (Lee et al., 2008; Padró and Reta, 2016).

E$_T$(30) and E_T^N–Solvent Polarity and Normalized Solvent Polarity

The determination of the E$_T$(30) and the E_T^N (solvent polarity and normalized solvent polarity, respectively) does not require any

further measurements, only calculations using the data already obtained. The solvent polarity, $E_T(30)$, is referred to as such due to the betaine (Reichardt's dye) in the original report simply being the 30th dye investigated. This parameter is calculated using the maximum absorption of Reichardt's dye in the solvent which is then substituted into Equation 1 (Reichardt, 1994; Lee et al., 2008).

$$E_T(30)\ (kcal\ mol^{-1}) = \frac{28591}{\nu_{\max}(nm)} \quad (1)$$

The $E_T(30)$ gives no real context to the polarity of the solvent, so it is therefore necessary to normalize this value on a scale of trimethylsilane (TMS, least polar, $E_T^N = 0.000$) to water (most polar, $E_T^N = 1.000$). This is accomplished using Equation 2 (Reichardt, 1994; Lee et al., 2008).

$$E_T^N = \frac{E_T(solvent) - E_T(TMS)}{E_T(water) - E_T(TMS)} = \frac{E_T(solvent) - 30.7}{32.4} \quad (2)$$

The results of these calculations are summarized in **Table 3** (Eyckens et al., 2016b).

The E_T^N gives a relative scale of the polarity of solvents compared to water as the most polar, $E_T^N = 1.000$ (Entry 1, **Table 3**). [Li(G3)]TFSI and [Li(G4)]TFSI have E_T^N values of 1.028 and 1.033 (Entry 2 & 3, **Table 3**), greater than that of water. Given the nature of ionic liquids comprising entirely of ions, it is not unexpected that they would have a high degree of polarity. This is due to the full cationic and anionic charges present in the IL, rather than the dipole moment experienced by water. The tri- and tetraglyme compounds are both around a third of the polarity of water with E_T^N values of 0.301 and 0.284, respectively (Entry 4 & 5, **Table 3**). These ethereal solvents are expected to have a degree of polarity associated with them, due to the electronegativity of the oxygen atoms, and decreased E_T^N values compared to the solvate ILs is due to the absence of ions. [Bmim]TFSI has a markedly reduced E_T^N value compared to the solvate ILs, with 0.590 (Entry 6, **Table 3**), which is consistent with the higher α and β values of the solvate ILs.

NMR Studies

Investigations into the electronic effects on the chelation of the lithium cation have been conducted by Black et al. using nuclear magnetic resonance (NMR) spectroscopy of ^7Li, ^{17}O, ^1H and ^{13}C nuclei (Black et al., 2018).

When examining ^7Li in DMOS-d_6, there is a reduction in chemical shift (moving to the right) of the signal from LiTFSI compared to the reference (9.7 mol kg^{-1} LiCl in H_2O) (Black et al., 2018). This is due to the electron donation of the TFSI$^-$ anion to the lithium cation. The introduction of the G1 and G2 glyme solvents initially results in the largest change (upfield) in ppm of the ^7Li signal. This is attributed to the additive effect of the electron donation of the ethereal oxygens and the anion. This is true for both concentrations examined; 0.025 lithium atoms per oxygen atom, and 0.25 lithium atoms per oxygen atom.

Interestingly, the combination of the G3 and G4 solvents with LiTFSI demonstrated a less significant reduction in chemical shift, compared to that of the smaller glyme solvents. This is consistent with the chelation of the cation by the glyme having a greater effect, which may in part be due to the resulting steric bulk limiting anion-cation interaction.

A similar result is observed in the case of ^{17}O NMR, though only the lesser concentration of LiTFSI in glyme was able to accurately be examined. The larger concentration (0.25 lithium per oxygen) resulted in only a broad signal that was unable to be deconvoluted. Nonetheless, the lesser concentration gives a good indication of the trend that is likely occurring in both scenarios.

With the introduction of the LiTFSI salt, the ethereal oxygen signals exhibit an upfield shift due to the chelation of the cation, resulting in an electron-poor oxygen atom (Peng et al., 2016). While this effect is initially counterintuitive, it has been demonstrated previously in aliphatic ether systems, that withdrawal of electron density from the oxygen results in a more shielded system, manifesting as a lower chemical shift (Béraldin et al., 1982).

A point of difference is observed between the terminal oxygen atoms (closest to the methyl group) and those of the ethylene linker, where the former exhibit a smaller change in chemical shift in the presence of the lithium cation. This can be ascribed to the lower degree of coordination of lithium by the terminal oxygens and this effect is exacerbated with larger glyme molecules, as there are more "non-terminal" oxygens available for chelating.

In determining the changes in the ^1H NMR shifts of the glyme compounds, there is a trend of a decrease in chemical shift with the introduction of LiTFSI. Further, a greater change in ppm of the methyl protons than the signals corresponding to the methylene protons (relative to the pure glyme values) is observed.

This is again counterintuitive, as a coordination of the oxygen atoms to lithium should draw on electrons, shifting the signals of the relative protons downfield, and the draw of two oxygen atoms should have a greater effect on methylene protons than methyl. The effect is credited to interaction of protons with the TFSI$^-$ anion, effectively negating the electron withdrawing effect by donating electron density to these protons.

The more withdrawn the protons, as is the case with those of the methylene, the greater the susceptibility to anion interaction. These two processes effectively cancel each other out, resulting in the negligible change in shift for the methylene protons. In the case of the methyl protons however, the balance between effects is not as evenly matched, resulting in a more prominent change in signal resonance, albeit a small one. It may also be possible that the electron withdrawn nature of the protons with

TABLE 3 | The $E_T(30)$ (solvent polarity) and E_T^N (normalized solvent polarity) of solvents (Eyckens et al., 2016b).

Entry	Solvent	$E_T(30)$	E_T^N
1	Water	63.1	1.000
2	[Li(G3)]TFSI	64.0	1.028
3	[Li(G4)]TFSI	64.2	1.033
4	Triglyme	40.4	0.301
5	Tetraglyme	39.9	0.284
6	[Bmim]TFSI	49.8	0.590

the chelation of the lithium cation contributes to some degree to the unanticipatedly large α value exhibited by the SILs.

Notably, this phenomenon is somewhat reversed when exploring the effects through ^{13}C NMR. The carbons of the methyl groups show no significant change in chemical shift in the solvate ILs with respect to the pure glyme. For the methylene carbons however, there is a decrease in shift resulting from the balance of interaction with both the lithium cation and $TFSI^-$ anion.

This investigation clearly demonstrates the significant role played by the anion on the electronics of the SIL complex. These interactions between glyme ligand and cation become more significant with increasing glyme length, causing a reduction in cation-anion interaction.

The correlation of these observations with molecular modeling would potentially compliment these studies and provide potential insight into the intricacies of this system.

Gutmann Acceptor Number

Given the high α values of the SILs and the confirmation of this effect with molecular dynamics, the *pseudo*-hydrogen bonding may be attributed to Lewis acidity, which can be examined using a phosphorous-based probe, and it analysis *via* ^{31}P NMR. The Gutmann Acceptor Number is a measurement of the Lewis and measures the interaction of the desired solvent and a Lewis base, triethylphosphine oxide (Et_3PO) in a 3:1 ratio (solvent:base) dissolved in deuterated benzene (Mayer et al., 1975; Gutmann, 1976).

The Acceptor Number (AN) is determined by monitoring the shift of the phosphorous atom when introduced to a Lewis acid by polarization of the P=O bond. The greater the strength of the Lewis acid, the more electron withdrawn the phosphorous atom becomes, shifting the resonance of that atom in the ^{31}P NMR spectra downfield (to the left, **Figure 6**).

To accurately ascertain the degree of shift of the phosphorous resonance, the Lewis base must first be measured in relation to a non-Lewis acidic solvent, as a control measurement (*n*-heptane was used in this case).

The Acceptor Numbers of solvents are summarized in **Table 4** (Eyckens et al., 2016a).

It was of interest to determine the AN of the naked LiTFSI salt, to quantify the effect chelation had on the lithium cation. The salt exhibited an Acceptor Number of 41.84 (Entry 3, **Table 4**),
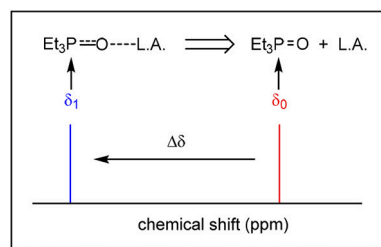
almost double that of the solvate ILs. Lithium has been shown to be a strong Lewis acid, often used as an additive for organic reactions (Springer et al., 1999), so in the non-chelated form, it is logical to expect this increase in Lewis acidity. [Li(G3)]TFSI and [Li(G4)]TFSI demonstrated identical AN with 26.53 each (Entry 4 & 5, **Table 4**). This represents the effect of chelation, as the lithium cation is not as free to interact with the Lewis base, the effect may be due to a combination of electronic and steric effects. The tri- and tetraglyme molecules showed the expected very low AN with 0.24 and 0.21, respectively (Entry 6 & 7, **Table 4**). The negligible Lewis acidity exhibited by these compounds, is to be expected due to the absence of electron-accepting functional groups. [Bmim]TFSI shows reduced Lewis acidity when compared to the solvate ILs with AN values of 11.90 and 3.10 (Entry 8, **Table 4**). The two chemical shifts are due to the nature of the cation, as Lewis acids are typically metal-based and the amine cation is not as efficient at accepting electrons. Presumably, the observed Lewis acidity of [Bmim]TFSI is dominated by hydrogen-bonding effects between the phosphine oxide and the acidic hydrogen atom at C2, and the pair at C4/C5 on the imidazolium ring (**Figure 7**), giving the two values.

In summary, solvate ionic liquids represent a unique class of liquids which possess interesting Lewis Acidic properties, with the typical features of ionic liquids being negligible vapor pressure and high polarity. These unique properties, in addition to their cryogenic melting points and absence of acidic protons, opens the potential of these liquids to be used as media for organic chemical transformations which are typically inaccessible using imidazolium-derived or protic ionic liquids. The first reports of SILs as reaction media

TABLE 4 | Acceptor Number (AN) of Solvate ILs (Eyckens et al., 2016a).

| Entry	Lewis acid	Et_3PO		AN
		$\delta(^{31}P)$	$\Delta\delta(^{31}P)$	
1	*n*-heptane	46.66	0.00	0.00
2	LiTFSI (salt)	64.48	17.82	41.84
3	[Li(G3)]TFSI	57.96	11.30	26.53
4	[Li(G4)]TFSI	57.96	11.30	26.53
5	Triglyme	46.76	0.10	0.24
6	Tetraglyme	46.75	0.09	0.21
7	[Bmim]TFSI	51.68, 47.94	5.07, 1.30	11.90, 3.10

FIGURE 6 | Representation of the effect of a Lewis acid on the chemical shift of phosphorous in the ^{31}P NMR spectrum.
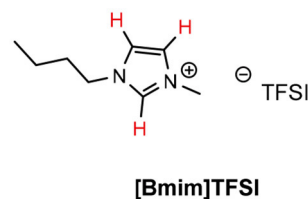
[Bmim]TFSI

FIGURE 7 | Acidic protons of [Bmim]TFSI shown in red.

and their effect on reaction outcome are reported in the following section.

APPLICATIONS IN SYNTHETIC CHEMISTRY

Ionic liquids as reaction mediums for organic transformations are already well-established in the literature, with many reviews available detailing their use (Welton, 1999; Wasserscheid and Keim, 2000; Hallett and Welton, 2011; Qureshi et al., 2014). In comparison, solvate ILs have seen very little representation in the literature, though the examples that do exist are reported here.

Organocatalysis

Juaristi and co-workers report a highly efficient, and stereoselective asymmetric aldol reaction when using (S)-proline in conjunction with solvate ionic liquids (**Table 5**, below) (Obregón-Zúñiga et al., 2017). The solvates explored are both the [Li(G3)]TFSI and [Li(G4)]TFSI, as well as the perchlorate versions; the [Li(G3)]ClO$_4$ and [Li(G4)]ClO$_4$. It should be noted that [Li(G3)]ClO$_4$ is reported as a solid (mp 103°C) (Ueno et al., 2012, 2015; Mandai et al., 2014; Obregón-Zúñiga et al., 2017), and [Li(G4)]ClO$_4$ is considered a concentrated solution, rather than a solvate ionic liquid, due to the excess of free glyme (~20%) in the system (Ueno et al., 2015).

Nevertheless, these particulars are of little consequence due to the greater performance exhibited by the TFSI$^-$ anion varietals compared to the ClO$_4^-$ versions (**Table 5**). It was found that an equimolar mixture of SIL and (S)-proline employed at 3 mol% with 1 equivalent of water was the optimal conditions for the aldol reaction to take place, at ambient temperature for 14 h (Obregón-Zúñiga et al., 2017).

Employing [Li(G3)]TFSI with (S)-proline exhibits an excellent yield (94%), *dr* (94:6) and *er* (98:2) in the aldol reaction between cyclohexanone **6** and 4-nitrobenzaldehyde **7** (Entry 1, **Table 5**). The yield is slightly improved (96%) with the use of the tetraglyme counterpart, [Li(G4)]TFSI, though both the diastereomeric ratio and enantiomeric ratio suffer (Entry 2, **Table 5**). this leads to the conclusion that, despite a slight reduction yield, [Li(G3)]TFSI is the better performing SIL.
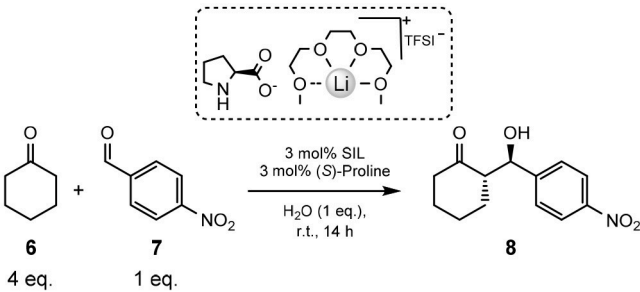
[Li(G3)]ClO$_4$ gives the lowest yield of all the additives (84%, Entry 3, **Table 5**), though does see an improvement in *dr* (93:7) when compared to [Li(G4)]TFSI (90:10), and the same *er* as [Li(G3)]TFSI (98:2). This may suggest some conformational benefit of the triglyme over the tetraglyme, as [Li(G4)]ClO$_4$ lead to worse *dr* and er, but a slight increase in yield (87%, Entry 4, **Table 5**).

To give these results context, the reaction was repeated without the addition of any SILs or water (Entry 5, **Table 5**). This instance shows, as expected, the lowest yield (18%), diastereomeric and enantiomeric ratios (64:36 and 88:12, respectively), and an increase in reaction time to 24 h. Immediate improvement is observed with the addition of 1 equivalent of water, with higher yield (67%) and better *dr* and *er* (82:18 and 92:8, respectively, Entry 6, **Table 5**).

The stereoselective advantage of [Li(G3)]TFSI in this aldol reaction is proposed to be the formation of a supramolecular aggregate between the SIL and (S)-proline (Obregón-Zúñiga et al., 2017).

This structure is supported by both ^{7}Li NMR and IR spectroscopic methods (Obregón-Zúñiga et al., 2017), and the

TABLE 5 | Evaluation of various SILs and blanks in the model aldol reaction (Obregón-Zúñiga et al., 2017).

Entry	SIL	Yield (%)[a]	dr (anti:syn)[b]	er (anti)[c]
1	[Li(G3)]TFSI	94	94:6	98:2
2	[Li(G4)]TFSI	96	90:10	96:4
3	[Li(G3)]ClO$_4$	84	93:7	98:2
4	[Li(G4)]ClO$_4$	87	89:11	94:6
5[d]	-	18	64:36	88:12
6	-	67	82:18	92:8

[a] Isolated yield.
[b] Determined by ^{1}H NMR from the crude reaction.
[c] Determined by HPLC with chiral stationary phase.
[d] No water added, 24 h of reaction.

transition state of the supramolecular ensemble containing ketone, aldehyde, water and the (*S*)-proline-[Li(G3)]TFSI complex was also modeled (Obregón-Zúñiga et al., 2017). The complex shows the 1 equivalent of water acting as a bridgehead between the carbonyls of the ketone and aldehyde.

The effect of [Li(G3)]TFSI in this aggregation is observed to be specific for SILs, as a comparison is conducted with a traditional IL; [Bmim]PF$_6$ and one without any ionic species present (Obregón-Zúñiga et al., 2017). This is also explored in the context of electron withdrawn, neutral and electron donating aldehydes with cyclohexanone.

In every case examined, [Li(G3)]TFSI was the best performing example with higher yields and diastereomeric and enantiomeric ratios. The best results obtained of the three types of aromatic aldehydes were those that are electron withdrawn, as may be expected. Further demonstrating the requirement for the SIL complex, is the poor result obtained when using the lithium carboxylate of (*S*)-proline as the catalyst, or just the LiTFSI.

This work demonstrates the advantage of SILs in an organic transformation, over a traditional IL ([Bmim]PF$_6$), [Li(G3)]ClO$_4$ or [Li(G4)]ClO$_4$. The latter proves the requirement for the solvation of the lithium cation, as it has been defined as a concentrated solution (Ueno et al., 2015).

Diels-Alder Reactions

To utilize the Lewis acidity of [Li(G3)]TFSI and [Li(G4)]TFSI, both SILs were assessed in their application as solvents for Diels–Alder reactions (Eyckens et al., 2016a). The [4+2] cycloadditions of a series of reactants are summarized in **Table 6**.

A similar solvent, 5.0 M Lithium Perchlorate in Diethyl Ether (5.0 M LPDE) saw good application for electrocyclization reactions in the 1990s to 2000s (Grieco et al., 1990; Forman and Dailey, 1991; Grieco and Moher, 1993; Heydari, 2002), but soon fell out of favor due to a lack of handleability and stability of the ClO$_4^-$ anion at elevated temperatures. It has been included here as the closest point of comparison to the SILs in terms of a reaction

medium. The limitation of not being able to heat 5.0 M LPDE due to potential explosion is not relevant to the solvate ILs, and thus this fact was exploited during reaction optimization.

The Diels–Alder reaction between isoprene and **9** is reported to proceed well at ambient temperature in 5.0 M LPDE (94% in 7 h, Entry 1, **Table 6**). It has also been shown to be successful in [Bmim]PF$_6$, with the addition of heat (96% in 2 h, Entry 2, **Table 6**). The reported conditions for the Diels–Alder reaction in ionic liquids use 5 equivalents of the diene, and this was kept consistent in this study to allow for greater comparison. However, isoprene was observed to be only sparingly soluble in the solvate ILs, forming a biphasic solution when added to the reaction vessel. This suggests that a much lower effective concentration was required to complete these reactions than in the instances of other ionic liquids, meaning fewer equivalents may have been able to be used to produce the same result.

Performing the reaction for 30 min at 100°C, using microwave irradiation (Entry 3 & 4, **Table 6**) gave good yields for both [Li(G3)]TFSI and [Li(G4)]TFSI (73 and 81%, respectively). This demonstrated the advantages of being able to heat these solvate ILs without limitation (such as those outlined for 5.0 M LPDE) as part of an optimization process.

The Diels–Alder reaction between isoprene and dimethyl maleate (**11a**) or dimethyl fumarate (**11b**) was also investigated. Previous reports (Renninger and Mcphee, 2008) of the Diels–Alder reaction between dimethyl maleate (**11a**) and isoprene required the use of extremely high temperatures to obtain good yields (cf. 195°C and 66%, respectively). Attempting the reaction in a molecular solvent (chloroform) proved the difficult nature of this reaction when only traces of the desired product **12** obtained (Entry 1, **Table 7**) despite relatively high temperatures. Employing [Li(G3)]TFSI and [Li(G4)]TFSI (Entry 2 & 3, **Table 7**) showed greater promise, with isolated yields of 73 and 21%, respectively. Despite this, it was found that the isolated product was **12b**, possessing the *trans* configuration of the esters and not the expected *cis* transfiguration of **12a**. This is unusual as stereochemistry is typically retained throughout the Diels-Alder reaction, and it was concluded that while the product **12a** may form initially, it is possible for this product to convert to the more thermodynamically stable **12b**.

This epimerization is presumed to be due to the higher temperature employed in this reaction. The dramatic reduction in yield in [Li(G4)]TFSI is unknown, but may be due to a slightly different solubility of isoprene in this IL compared to the [Li(G3)]TFSI variation.

This reaction was then repeated with **11a** at room temperature in [Li(G3)]TFSI overnight (Entry 4, **Table 7**) to minimize possible epimerization. Unfortunately, the reaction was unsuccessful and only starting material **11a** was isolated.

Dimethyl fumarate (**11b**) was then employed as the dienophile, and a much less pronounced improvement in yield was obtained in the solvate ILs, when compared to the molecular solvent (Entry 5, **Table 7** *vs*. Entry 6 & 7, **Table 7**). When

TABLE 6 | Diels–Alder reactions in solvate ionic liquids (Eyckens et al., 2016a).

Entry	Solvent	Time	Temp. (°C)[a]	Yield (%)[b]
1	5.0 M LPDE	7 h	r.t.	94[c]
2	[Bmim] PF$_6$	2 h	80[d]	96[e]
3	[Li(G3)]TFSI	30 min	100	73
4	[Li(G4)]TFSI	30 min	100	81

[a] Microwave irradiation.
[b] Isolated yield.
[c] Reported yield (Grieco et al., 1990).
[d] No microwave irradiation.
[e] Reported yield (Earle et al., 1999).

TABLE 7 | Diels–Alder reactions in solvate ionic liquids (Eyckens et al., 2016a).

isoprene (5 equiv.)   11a cis   11b trans   12a cis   12b trans

Entry	Reactant	Solvent	Time	Temp. (°C)[a]	Yield (%)[b]
1	11a	CHCl$_3$	20 min	100	<5
2	11a	[Li(G3)]TFSI	20 min	100	73[c]
3	11a	[Li(G4)]TFSI	20 min	100	21[c]
4	11a	[Li(G3)]TFSI	16 h	r.t.	0
5	11b	CHCl$_3$	20 min	100	45
6	11b	[Li(G3)]TFSI	20 min	100	74
7	11b	[Li(G4)]TFSI	20 min	100	65

[a] Microwave irradiation.
[b] Isolated yield.
[c] Only trans product isolated.

compared to previous reports (Lee et al., 2009) however (*cf.* 36 h, 70°C), the reaction required considerably less time to occur.

[2+2] Cycloaddition Cascade Formation of Dienes

Another electrocyclisation reaction attempted in the solvate ILs was the [2+2] reaction of dimethyl ketene (13) (generated *in situ* from isobutyryl chloride) and (*E*)-cinnamaldehyde (14) giving 15 after CO$_2$ extrusion (Eyckens et al., 2016a). This reaction is reported not to proceed in the absence of LiClO$_4$ and has been reported in 5.0 M LPDE, therefore is an obvious choice to compare the application of the solvate ILs.

Conducting the reaction in chloroform resulted in trace amounts of product formed, as was expected (Entry 1, **Table 8**). When repeating the literature conditions (Arrastia and Cossío, 1996), the high yield (95%) originally reported in 5.0 M LPDE was unable to be reproduced (Entry 2, **Table 8**). Employing freshly prepared 5.0 M LPDE, from extensively dried LiClO$_4$ and diethyl ether, saw highly variable yields at best. The yield of 15 in 5.0 M LPDE varied between 5–40%, with <20% being typical for repeated attempts. Despite the complete consumption of the aldehyde 14, a complex mixture of products was typically observed in the ^{1}H NMR spectra of the crude mixture.

The complete consumption of the aldehyde 14 was also observed in the ^{1}H NMR spectra of crude mixtures of the reactions carried out in [Li(G3)]TFSI and [Li(G4)]TFSI, though the isolated yields were greatly improved; 56% and 41%, respectively (Entry 3 & 4, **Table 8**). It was hypothesized that atmospheric water may be affecting the reaction outcomes. In an attempt to remedy this and improve yields, 4 Å molecular sieves were added to the reaction in [Li(G4)]TFSI to remove adventitious water, improving the yield to 60% (Entry 6, **Table 8**). Further to this, heating for the final hour of the reaction to 80°C in [Li(G3)]TFSI increased the yield to 70% (Entry 7, **Table 8**).

TABLE 8 | Comparison of solvents in [2+2] cascade formation of dienes (Eyckens et al., 2016a).

13   14   15

Entry	Solvent	Time (h)	Temp. (°C)	Yield (%)[a]
1	CHCl$_3$	6	r.t.	<5
2	5.0 M LPDE	6	r.t.	~20
3	[Li(G3)]TFSI	6	r.t.	56
4	[Li(G4)]TFSI	6	r.t.	41
6[b]	[Li(G3)]TFSI	6	r.t.	60
7	[Li(G3)]TFSI	6[c]	80	70

[a] Isolated yield.
[b] Activated molecular sieves (100 mg) were used throughout the reaction.
[c] The reaction mixture was heated for the finally hour of the specified time.

These reactions highlight the ease with which these SILs can be handled. The use of molecular sieves and heated using 5.0 M LPDE is not possible, due to precipitation of lithium perchlorate if taken out of inert atmosphere, and again the limitations of heating in this system.

α-Aminophosphonates

α-Aminophosphonates are small, phosphorous containing molecules, structurally analogous to naturally occurring α-amino acids.

Replacement of the carbonyl component of the amino acid with phosphorous has been shown to inhibit enzymes of receptors to which the natural amino acids bind (Cherkasov and Galkin, 1998). This lays the

TABLE 9 | Scoping of aniline derivatives to produce α-aminophosphonates in SILs (Eyckens and Henderson, 2017).

Entry	Solvent	Aniline	R_1^a	Yield (%)[b]	Entry	Aldehyde	R_2^a	Yield (%)[b]
1	[Li(G3)]TFSI	**16a**	4-NO$_2$	64	15	**17h**	4-Br	90
2	[Li(G4)]TFSI			25	16			91
3	[Li(G3)]TFSI	**16b**	4-OH	82	17	**17i**	4-Me	90
4	[Li(G4)]TFSI			92	18			86
5	[Li(G3)]TFSI	**16c**	4-F	84	19	**17j**	4-NO$_2$	69
6	[Li(G4)]TFSI			68	20			59[c]
7	[Li(G3)]TFSI	**16d**	4-Cl	96	21	**17k**	4-F	77
8	[Li(G4)]TFSI			96	22			78
9	[Li(G3)]TFSI	**16e**	3-Cl	83	23	**17l**	2-OH	84
10	[Li(G4)]TFSI			59	24			76
11	[Li(G3)]TFSI	**16f**	3-CF$_3$	86	25	**17m**	3,4-Cl	74
12	[Li(G4)]TFSI			81	26			79
13	[Li(G3)]TFSI	**16g**	3,5-CF$_3$	54				
14	[Li(G4)]TFSI			60				

[a] Alternate R group is hydrogen.

[b] Isolated yield.

[c] This material contained α-hydroxyphosphonate (17% by 1H NMR) resulting from direct attack of the phosphite on 4-nitrobenzaldehyde.

foundation for α-aminophosphonates to have medicinal or therapeutic applications.

These compounds are typically accessed *via* the Kabachnik-Fields reaction, discovered independently by both Kabachnik and Ya (1952) and Fields (1952). The reaction proceeds through condensing an amine with an aldehyde (either *in situ* or preformed), before reaction with a phosphonate.

Conducting this reaction in SILs at room temperature for 5 min demonstrated the broad scope of reactants suitable in these conditions. The advantage of SILs is evident as other reports of the synthesis of these molecules utilize increased reaction time [up to 7 days (Pettersen et al., 2006)], temperature (Guo et al., 2015), the use of boutique catalysts (Ambica et al., 2008; de Noronha et al., 2011; Heo et al., 2012; Li et al., 2016) or combinations thereof.

The success of the Kabachnik-Fields reaction in solvate ILs is demonstrated through the application of a range of substituted aldehydes and anilines with diphenyl phosphite (**Table 9**), (Eyckens and Henderson, 2017).

The production of a range of α-aminophosphonates with various electron withdrawing or donating functional groups on either the aniline or benzaldehyde was rapidly achieved, with overall excellent yields (**Table 9**). It was observed that, in general, [Li(G3)]TFSI proved to be the better performing solvent of the two SILs in most cases. This is consistent with previous findings when using these SILs as reaction solvents, although the difference between the two solvents is generally quite small.

In addition to the production of these *mono-α-*aminophosphonates, is the synthesis of *bis-*versions, utilizing arylenediamines (**Table 10**).

The synthesis of *bis-α-*aminophosphonates in SILs is demonstrated with good success (**Table 10**), maintaining the very concise reaction time and good substrate tolerance.

Unlike the earlier trend of [Li(G3)]TFSI outperforming [Li(G4)]TFSI in the production of *mono-α-*aminophosphonates, there seems a reversal in this trend when introducing substituted aldehydes into the *bis-*versions of these α-aminophosphonates **22b-c**.

In addition to the successful synthesis of *bis-*versions of α-aminophosphonates, the efficacy of producing a non-C$_2$-symmetric *bis-α-*aminophosphonate using two different aldehydes was investigated (**Scheme 4**).

The non-C$_2$-symmetric compound **24** was synthesized in good yields in both SILs (43% in [Li(G3)]TFSI and 26% in [Li(G4)]TFSI isolated yields), in only 10 min of total reaction time at room temperature. Each aldehyde was reacted for 5 min in a two-step, one-pot process. The use of 4-tolualdehyde served as a simple ^{1}H NMR handle to determine the incorporation of both aldehydes through comparison of integration ratios of the methyl signal and the protons attached to the tertiary carbon.

The use of SILs as solvents for organic reactions has shown great success, even in the limited number of reports available. The comparison to molecular solvents, other ionic liquids or even the use of catalysts has advocated strong advantage in the

Entry	Product	R	Solvent	Yield (%)[a]
1	**22a**	Ph	[Li(G3)]TFSI	64
2			[Li(G4)]TFSI	52
3	**22b**	4-BrPh	[Li(G3)]TFSI	36
4			[Li(G4)]TFSI	65
5	**22c**	4-NO$_2$Ph	[Li(G3)]TFSI	18
6			[Li(G4)]TFSI	33

[a] *Isolated yield.*

SCHEME 4 | Synthesis of a non-C$_2$-symmetric *bis*-α-aminophosphonate 24 from *p*-phenylenediamine and incorporating different aldehydes in the SILs (Eyckens and Henderson, 2017).
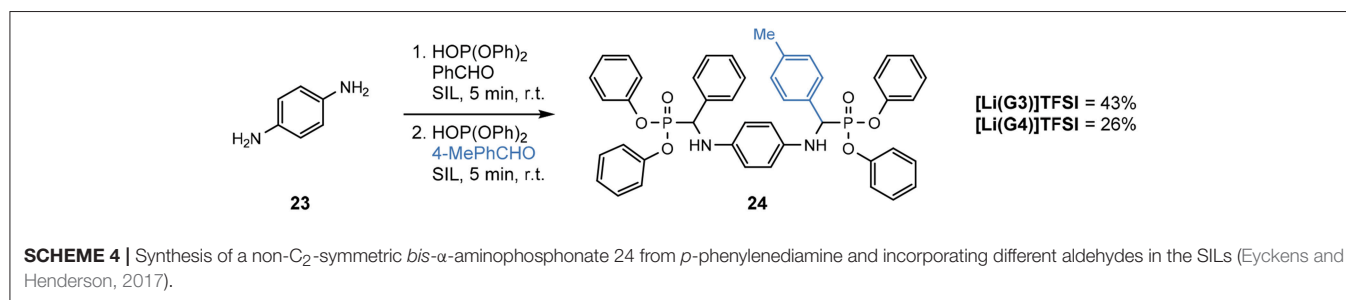
use of synthesis. The ability to access products of cycloaddition or condensation reactions using these solvents shows great versatility and utility.

CONCLUSIONS AND OUTLOOK

The physical parameters of solvate ionic liquids have been discussed here, as reported by a number of research groups. Consist findings of high α values (hydrogen bond donating) are recorded, despite the absence of acidic protons. This was largely attributed to the lithium cation acting as a surrogate hydrogen bond, which was confirmed by molecular dynamics simulations. The high α values were also consolidated by the determination of Lewis acidity (Gutmann Acceptor Number), revealing identical values for both SILs (AN = 26.5). This value was reduced in comparison to the naked LiTFSI salt and increased compared to that of the pure glymes.

The β values were reduced in comparison to the pure glyme solvents, anticipating the chelation of lithium by the ethereal oxygens, thereby limiting their availability for hydrogen bond accepting. This effect of chelation was also supported by NMR studies of all relevant nuclei. Finally, the π* values demonstrated the SILs' polarizability which was expectedly high due to their ionic character, and consistent with traditional ionic liquids. The SILs were also observed to be as polar (if not slightly more so) as water.

The application of SILs to effect reaction outcomes was validated in conjunction with a proline organocatalyst with excellent results in the aldol reaction. This success was further echoed by the use as a solvent for Diels-Alder and [2+2] cycloaddition reactions, with good yields reported.

The application to a different type of reaction in the Kabachnik-Fields reaction further conveyed the advantage of SILs, rapidly accessing α-aminophosphonates in excellent yields at room temperature, with good scope and the ability to produce *bis*-versions (including non-C$_2$-symmetric) of these compounds.

The foundational research explored here serves as a good basis for future investigations, and the use of these SILs as solvents for organic transformations is a field with huge potential. The potential to access molecules in less time, temperature or both is enticing and offers great advantage over previous methods.

AUTHOR CONTRIBUTIONS

All authors listed have made a substantial, direct and intellectual contribution to the work, and approved it for publication.

FUNDING

REFERENCES

Abraham, K. M., Jiang, Z., and Carroll, B. (1997). Highly conductive PEO-like polymer electrolytes. *Chem. Mater.* 9, 1978–1988. doi: 10.1021/cm970075a

Ambica, K. S., Taneja, S. C., Hundal, M. S., and Kapoor, K. K. (2008). One-pot synthesis of α-aminophosphonates catalyzed by antimony trichloride adsorbed on alumina. *Tetrahedron Lett.* 49, 2208–2212. doi: 10.1016/j.tetlet.2008.02.047

Angell, C. A., Byrne, N., and Belieres, J. P. (2007). Parallel developments in aprotic and protic ionic liquids, physical chemistry and applications. *Acc. Chem. Res.* 40, 1228–1236. doi: 10.1021/ar7001842

Arrastia, I., and Cossío, F. P. (1996). Tandem [2+2] cycloaddition-cycloreversion reactions in highly polar media: a convergent one-pot entry to substituted alkenes and dienes. *Tetrahedron Lett.* 37, 7143–7146. doi: 10.1016/0040-4039(96)01562-6

Atilhan, M., and Aparicio, S. (2014). Folding of graphene nanostructures driven by ionic liquids nanodroplets. *J. Phys. Chem. C.* 118, 21081–21091. doi: 10.1021/jp502303q

Atta, N. F., Abdel Gawad, S. A., El-Ads, E. H., El-Gohary, A. R. M., and Galal, A. (2017). A new strategy for NADH sensing using ionic liquid crystals-carbon nanotubes/nano-magnetite composite platform. *Sensors Actuators B Chem.* 251, 65–73. doi: 10.1016/j.snb.2017.05.026

Austen Angell, C., Ansari, Y., and Zhao, Z. (2012). Ionic liquids: past, present and future. *Faraday Discuss.* 154, 9–27. doi: 10.1039/C1FD00112D

Béraldin, M.-T., Vauthier, E., and Fliszár, S. (1982). Charge distributions and chemical effects. XXVI. Relationships between nuclear magnetic resonance shifts and atomic charges for 17O nuclei in ethers and carbonyl compounds. *Can. J. Chem.* 60, 106–110. doi: 10.1139/v82-020

Black, J. J., Dolan, A., Harper, J. B., and Aldous, L. (2018). Kamlet–Taft solvent parameters, NMR spectroscopic analysis and thermoelectrochemistry of lithium–glyme solvate ionic liquids and their dilute solutions. *Phys. Chem. Chem. Phys.* 20, 16558–16567. doi: 10.1039/C8CP02527D

Bordes, É., Szala-Bilnik, J., and Pádua, A. A. H. (2018). Exfoliation of graphene and fluorographene in molecular and ionic liquids. *Faraday Discuss.* 206, 61–75. doi: 10.1039/C7FD00169J

Butler, B. J., and Harper, J. B. (2018). The effect of the structure of the anion of an ionic liquid on the rate of reaction at a phosphorus centre. *J. Phys. Org. Chem.* 32:e3819. doi: 10.1002/poc.3819

Chaban, V. V., Andreeva, N. A., and Fileti, E. E. (2018). Graphene/ionic liquid ultracapacitors: does ionic size correlate with energy storage performance? *New J. Chem.* 42, 18409–18417. doi: 10.1039/C8NJ04399J

Chaban, V. V., and Fileti, E. E. (2015). Graphene exfoliation in ionic liquids: unified methodology. *RSC Adv.* 5, 81229–81234. doi: 10.1039/C5RA16857K

Chaban, V. V., Fileti, E. E., and Prezhdo, O. V. (2017). Exfoliation of graphene in ionic liquids: pyridinium versus pyrrolidinium. *J. Phys. Chem. C* 121, 911–917. doi: 10.1021/acs.jpcc.6b11003

Chee, W. K., Lim, H. N., Zainal, Z., Huang, N. M., Harrison, I., and Andou, Y. (2016). Flexible graphene-based supercapacitors: a review. *J. Phy. Chem. C.* 120, 4153–4172. doi: 10.1021/acs.jpcc.5b10187

Chen, D., Zhuang, X., Zhai, J., Zheng, Y., Lu, H., and Chen, L. (2018). Preparation of highly sensitive Pt nanoparticles-carbon quantum dots/ionic liquid functionalized graphene oxide nanocomposites and application for H2O2 detection. *Sens. Act. B: Chem.* 255, 1500–1506. doi: 10.1016/j.snb.2017.08.156

Cherkasov, R., and Galkin, V. I. (1998). The Kabachnik-fields reaction: synthetic potential and the problem of the mechanism. *Russian Chem. Rev.* 67, 857–882. doi: 10.1070/RC1998v067n10ABEH000421

Cook, A., Ueno, K., Watanabe, M., Atkin, R., and Li, H. (2017). Effect of variation in anion type and glyme length on the nanostructure of the solvate ionic liquid/graphite interface as a function of potential. *J. Phy. Chem. C.* 121, 15728–15734. doi: 10.1021/acs.jpcc.7b03414

Crowhurst, L., Falcone, R., Lancaster, N. L., Llopis-Mestre, V., and Welton, T. (2006). Using kamlet–taft solvent descriptors to explain the reactivity of anionic nucleophiles in ionic liquids. *J. Organ. Chem.* 71, 8847–8853. doi: 10.1021/jo0615302

de Noronha, R. G., Romão, C. C., and Fernandes, A. C. (2011). MoO2Cl2 as a novel catalyst for the synthesis of α-aminophosphonates. *Catal. Commun.* 12, 337–340. doi: 10.1016/j.catcom.2010.10.005

Dolan, D. A., Sherman, D. A., Atkin, R., and Warr, G. G. (2016). Kamlet–taft solvation parameters of solvate ionic liquids. *ChemPhysChem.* 17, 3096–3101. doi: 10.1002/cphc.201600361

Earle, J. M., McCormac, P. B., and Seddon, K. R. (1999). Diels-Alder reactions in ionic liquids . A safe recyclable alternative to lithium perchlorate-diethyl ether mixtures. *Green Chem.* 1, 23–25. doi: 10.1039/a808052f

Eyckens, D. J., Champion, M. E., Fox, B. L., Yoganantharajah, P., Gibert, Y., Welton, T., et al. (2016a). Solvate ionic liquids as reaction media for electrocyclic transformations. *Eur. J. Org. Chem.* 2016, 913–917. doi: 10.1002/ejoc.201501614

Eyckens, D. J., Demir, B., Walsh, T. R., Welton, T., and Henderson, L. C. (2016b). Determination of Kamlet–taft parameters for selected solvate ionic liquids. *Phy. Chem. Chemical Phy.* 18, 13153–13157. doi: 10.1039/C6CP01216G

Eyckens, D. J., and Henderson, L. C. (2017). Synthesis of α-aminophosphonates using solvate ionic liquids. *RSC Adv.* 7, 27900–27904. doi: 10.1039/C7RA04407K

Eyckens, D. J., Servinis, L., Scheffler, C., Wolfel, E., Demir, B., Walsh, T. R., et al. (2018). Synergistic interfacial effects of ionic liquids as sizing agents and surface modified carbon fibers. *J. Mater. Chem. A.* 6, 4504–4514. doi: 10.1039/C7TA10516A

Ferrara, C. V., Dall'Asta, Berbenni, V., Quartarone, E., and Mustarelli, P. (2017). Physicochemical characterization of AlCl3–1-Ethyl-3-methylimidazolium chloride ionic liquid electrolytes for aluminum rechargeable batteries. *J. Phy. Chem. C.* 121, 26607–26614. doi: 10.1021/acs.jpcc.7b07562

Fields, E. K. (1952). The synthesis of esters of substituted amino phosphonic acids. *J. Am. Chem. Soc.* 74, 1528–1531. doi: 10.1021/ja01126a054

Forman, M. A., and Dailey, W. P. (1991). The lithium perchlorate-diethyl ether rate acceleration of the Diels-Alder reaction: Lewis acid catalysis by lithium ion. *J. Am. Chem. Soc.* 113, 2761–2762. doi: 10.1021/ja00007a065

Forsyth, C. M., MacFarlane, D. R., Golding, J. J., Huang, J., Sun, J., and Forsyth, M. (2002). Structural characterization of novel ionic materials incorporating the Bis(trifluoromethanesulfonyl)amide anion. *Chem. Mater.* 14, 2103–2108. doi: 10.1021/cm0107777

Fujinami, T., and Buzoujima, Y. (2003). Novel lithium salts exhibiting high lithium ion transference numbers in polymer electrolytes. *J. Power Sources* 119-121, 438–441. doi: 10.1016/S0378-7753(03)00185-X

Grieco, P. A., and Moher, E. D. (1993). Lithium catalyzed hetero Diels-Alder reactions cyclocondensation of N-protected α-amino aldehydes with 1-methoxy-3-tert-butyldimethylsilyloxybutadiene in the presence of lithium perchlorate. *Tetrahedron Lett.* 34, 5567–5570. doi: 10.1016/S0040-4039(00)73883-4

Grieco, P. A., Nunes, J. J., and Gaul, M. D. (1990). Dramatic rate accelerations of Diels-Alder reactions in 5 M lithium perchlorate-diethyl ether: the cantharidin problem reexamined. *J. Am. Chem. Soc.* 112, 4595–4596. doi: 10.1021/ja00167a096

Guo, Y.-C., Li, J. J., Ma, L. Z., Yu, R. H., Wang, W. W., Zhu, J. X., et al. (2015). Synthesis and antitumor activity of α-aminophosphonate derivatives containing thieno[2,3-d]pyrimidines. *Chin. Chem. Lett.* 26, 755–758. doi: 10.1016/j.cclet.2015.03.026

Gutmann, V. (1976). Solvent effects on the reactivities of organometallic compounds. *Coordinat. Chem. Rev.* 18, 225–255. doi: 10.1016/S0010-8545(00)82045-7

Hallett, J. P., and Welton, T. (2011). Room-temperature ionic liquids: solvents for synthesis and catalysis. *Chem. Rev.* 111, 3508–3576. doi: 10.1021/cr1003248

Hawker, R. R., Haines, R. S., and Harper, J. B. (2018). The effect of varying the anion of an ionic liquid on the solvent effects on a nucleophilic aromatic substitution reaction. *Org. Biomol. Chem.* 16, 3453–3463. doi: 10.1039/C8OB00651B

Henderson, W. A. (2006). Glyme–lithium salt phase behavior. *J. Phys. Chem. B.* 110, 13177–13183. doi: 10.1021/jp061516t

Henderson, W. A., Brooks, N. R., and Young, V. G. (2003). Tetraglyme–Li+ cation solvate structures: models for amorphous concentrated liquid and polymer electrolytes (II). *Chem. Mater.* 15, 4685–4690. doi: 10.1021/cm034352r

Heo, Y., Cho, D. H., Mishra, M. K., and Jang, D. O. (2012). Efficient one-pot synthesis of α-aminophosphonates from aldehydes and ketones catalyzed by ytterbium(III) triflate. *Tetrahedron Lett.* 53, 3897–3899. doi: 10.1016/j.tetlet.2012.05.068

Heydari, A. (2002). Organic synthesis in an unconventional solvent, 5.0 M lithium perchlorate/diethyl ether. *Tetrahedron* 58, 6777–6793. doi: 10.1016/S0040-4020(02)00745-7

Hirakimoto, T., Nishiura, M., and Watanabe, M. (2001). Effects of addition of a boric acid ester monomer to electrolyte solutions and gel electrolytes on their ionic transport properties. *Electrochim. Acta* 46, 1609–1614. doi: 10.1016/S0013-4686(00)00760-X

Kabachnik, M. I. M., and Ya, T. (1952). A new method for the synthesis of α-amino phosphoric acids. *Doklady Akademii Nauk* 83:689.

Kamlet, M. J., Abboud, J. L., and Taft, R. W. (1977). The solvatochromic comparison method. 6. The .pi.* scale of solvent polarities. *J. Am. Chem. Soc.* 99, 6027–6038.

Kamlet, M. J., and Taft, R. W. (1976). The solvatochromic comparison method. I. The .beta.-scale of solvent hydrogen-bond acceptor (HBA) basicities. *J. Am. Chem. Soc.* 98, 377–383.

Kawazoe, T., Hashimoto, K., Kitazawa, Y., Kokubo, H., and Watanabe, M. (2017). A Polymer electrolyte containing solvate ionic liquid with increased mechanical strength formed by self-assembly of ABA-type ionomer triblock copolymer. *Electrochim. Acta* 235, 287–294. doi: 10.1016/j.electacta.2017.03.125

Keaveney, S. T., Haines, R. S., and Harper, J. B. (2017). Investigating solvent effects of an ionic liquid on pericyclic reactions through kinetic analyses of simple rearrangements. *ChemPlusChem.* 82, 449–457. doi: 10.1002/cplu.201600585

Kido, R., Ueno, K., Iwata, K., Kitazawa, Y., Imaizumi, S., Mandai, T., et al. (2015). Li+ ion transport in polymer electrolytes based on a glyme-Li salt solvate ionic liquid. *Electrochim. Acta* 175, 5–12. doi: 10.1016/j.electacta.2015.01.067

Krampa, F. D., Aniweh, Y., Awandare, G. A., and Kanyong, P. (2017). A Disposable amperometric sensor based on high-performance PEDOT:PSS/ionic liquid nanocomposite thin film-modified screen-printed electrode for the analysis of catechol in natural water samples. *Sensors* 17:1716. doi: 10.3390/s17081716

Lee, J.-M., Ruckes, S., and Prausnitz, J. M. (2008). Solvent polarities and kamlet–taft parameters for ionic liquids containing a pyridinium cation. *J. Phys. Chem. B.* 112, 1473–1476. doi: 10.1021/jp076895k

Lee, J. H., Kim, W. H., and Danishefsky, S. J. (2009). Syntheses of isomerically pure reference octalins and hydrindanes. *Tetrahedron Lett.* 50, 5482–5484. doi: 10.1016/j.tetlet.2009.07.068

Li, H., Rutland, M. W., Watanabe, M., and Atkin, R. (2017). Boundary layer friction of solvate ionic liquids as a function of potential. *Faraday Discuss.* 199, 311–322. doi: 10.1039/C6FD00236F

Li, J., Wang, Y., Sun, Y., Ding, C., Lin, Y., Sun, W., and Luo, C. (2017). A novel ionic liquid functionalized graphene oxide supported gold nanoparticle composite film for sensitive electrochemical detection of dopamine. *RSC Adv.* 7, 2315–2322. doi: 10.1039/C6RA25627A

Li, X.-C. S., Gong, S. D.-, Zeng, Y. Y.,You, H., and Sun, Q. (2016). Highly efficient synthesis of α-aminophosphonates catalyzed by hafnium(IV) chloride. *Tetrahedron Lett.* 57, 1782–1785. doi: 10.1016/j.tetlet.2016.03.033

Liu, N., Luo, F., Wu, H., Liu, Y., Zhang, C., and Chen, J. (2008). One-step ionic-liquid-assisted electrochemical synthesis of ionic-liquid-functionalized graphene sheets directly from graphite. *Adv Func Mater.* 18, 1518–1525. doi: 10.1002/adfm.200700797

Mandai, T., Yoshida, K., Ueno, K., Dokko, K., and Watanabe, M. (2014). Criteria for solvate ionic liquids. *Phys. Chem. Chem. Phys.* 16, 8761–8772. doi: 10.1039/c4cp00461b

Mary Sukeshini, A., Nishimoto, A., and Watanabe, M. (1996). Transport and electrochemical characterization of plasticized poly(vinyl chloride) solid electrolytes. *Solid State Ionics*, 86–88, 385–393. doi: 10.1016/0167-2738(96)00156-7

Mayer, U., Gutmann, V., and Gerger, W. (1975). The acceptor number — a quantitative empirical parameter for the electrophilic properties of solvents. *Monatshefte für Chemie.* 106, 1235–1257. doi: 10.1007/BF00913599

Muldoon, M. J., Gordon, C. M., and Dunkin, I. R. (2001). Investigations of solvent-solute interactions in room temperature ionic liquids using solvatochromic dyes. *J. Chem. Soc. Perkin Trans.* 2, 433–435. doi: 10.1039/b101449h

Murphy, T., Callear, S. K., Yepuri, N., Shimizu, K., Watanabe, M., Canongia Lopes, J. N., et al. (2016). Bulk nanostructure of the prototypical 'good' and 'poor' solvate ionic liquids [Li(G4)][TFSI] and [Li(G4)][NO3]. *Phys. Chem. Chem. Phy.* 18, 17224–17236. doi: 10.1039/c6cp00176a.

Musiał, M., Malarz, K., Mrozek-Wilczkiewicz, A., Musiol, R., Zorebski, E., and Dzida, M. (2017). Pyrrolidinium-based ionic liquids as sustainable

media in heat-transfer processes. *ACS Sustain. Chem. Eng.* 5, 11024–11033. doi: 10.1021/acssuschemeng.7b02918

Nakazawa, T., Ikoma, A., Kido, R., Ueno, K., Dokko, K., and Watanabe, M. (2016). Effects of compatibility of polymer binders with solvate ionic liquid electrolytes on discharge and charge reactions of lithium-sulfur batteries. *J. Power Sources.* 307, 746–752. doi: 10.1016/j.jpowsour.2016.01.045

Nishimoto, A., Watanabe, M., Ikeda, Y., and Kohjiya, S. (1998). High ionic conductivity of new polymer electrolytes based on high molecular weight polyether comb polymers. *Electrochimica Acta* 43, 1177–1184. doi: 10.1016/S0013-4686(97)10017-2

Obregón-Zúñiga, A., Milán, M., and Juaristi, E. (2017). Improving the catalytic performance of (S)-proline as organocatalyst in asymmetric aldol reactions in the presence of solvate ionic liquids, involvement of a supramolecular aggregate. *Org. Lett.* 19, 1108–1111. doi: 10.1021/acs.orglett.7b00129

Padró, J. M., and Reta, M. (2016). Solvatochromic parameters of imidazolium-, hydroxyammonium-, pyridinium- and phosphonium-based room temperature ionic liquids. *J. Mol. Liquids* 213, 107–114. doi: 10.1016/j.molliq.2015.10.055

Pappenfus, T. M., Henderson, W. A., Owens, B. B., Mann, K. R., and Smyrl, W. H. (2004). Complexes of lithium imide salts with tetraglyme and their polyelectrolyte composite materials. *J. Electrochem. Soc.* 151, A209–A215. doi: 10.1149/1.1635384

Peng, J., Carbone, L., Gobet, M., Hassoun, J., Devany, M., and Greenbaum, S. (2016). Natural Abundance oxygen-17 NMR investigation of lithium ion solvation in glyme-based electrolytes. *Electrochimica Acta.* 213, 606–612. doi: 10.1016/j.electacta.2016.07.144

Pettersen, D., Marcolini, M., Bernardi, L., Fini, F., Herrera, R. P., Sgarzani, V., et al. (2006). Direct access to enantiomerically enriched α-amino phosphonic acid derivatives by organocatalytic asymmetric hydrophosphonylation of imines. *J. Org. Chem.* 71, 6269–6272. doi: 10.1021/jo060708h

Qureshi, Z., Deshmukh, K., and Bhanage, B. (2014). Applications of ionic liquids in organic synthesis and catalysis. *Clean Technol. Environ. Policy.* 16, 1487–1513. doi: 10.1007/s10098-013-0660-0

Reichardt, C. (1994). Solvatochromic dyes as solvent polarity indicators. *Chem. Rev.* 94, 2319–2358. doi: 10.1021/cr00032a005

Renninger, N., and Mcphee, D. J. (2008). *Fuel Compositions Comprising Farnesane and Farnesane Derivatives and Method of Making and Using Same.* US. WO/2008/045555.

Reta, M., Cattana, R., and Silber, J. J. (2001). Kamlet–Taft's solvatochromic parameters for nonaqueous binary mixtures between n-hexane and 2-propanol, tetrahydrofurane, and ethyl acetate. *J. Sol. Chem.* 30, 237-252. doi: 10.1023/A:1005275432313

Saito, S., Watanabe, H., Hayashi, Y., Matsugami, M., Tsuzuki, S., Seki, S., et al. (2016). Li+ Local structure in Li–tetraglyme solvate ionic liquid revealed by neutron total scattering experiments with the 6/7Li isotopic substitution technique. *J. Phy. Chem. Lett.* 7, 2832–2837. doi: 10.1021/acs.jpclett.6b01266

Seki, S., Takei, K., Miyashiro, H., and Watanabe, M. (2011). Physicochemical and electrochemical properties of glyme-LiN(SO2F)2 complex for safe lithium-ion secondary battery electrolyte. *J. Electrochem. Soc.* 158, A769–A774. doi: 10.1149/1.3582822

Shan, C., Yang, H., Han, D., Zhang, Q., Ivaska, A., and Niu, L. (2010). Electrochemical determination of NADH and ethanol based on ionic liquid-functionalized graphene. *Biosens. Bioelectron.* 25, 1504–1508. doi: 10.1016/j.bios.2009.11.009

Shobukawa, H., Tokuda, H., S.-,Tabata, I., and Watanabe, M. (2004). Preparation and transport properties of novel lithium ionic liquids. *Electrochim. Acta.* 50, 305–309. doi: 10.1016/j.electacta.2004.01.096

Springer, G., Elam, C., Edwards, A., Bowe, C., Boyles, D., Bartmess, J., et al. (1999). Chemical and spectroscopic studies related to the lewis acidity of lithium perchlorate in diethyl ether. *J. Org. Chem.* 64, 2202–2210. doi: 10.1021/jo981042x

Tabata, S.-i., Hirakimoto, T., Nishiura, M., and Watanabe, M. (2003). Synthesis of a Lewis-acidic boric acid ester monomer and effect of its addition to electrolyte solutions and polymer gel electrolytes on their ion transport properties. *Electrochim. Acta* 48, 2105–2112. doi: 10.1016/S0013-4686(03)00192-0

Taft, R. W., and Kamlet, M. J. (1976). The solvatochromic comparison method. 2. The .alpha.-scale of solvent hydrogen-bond donor (HBD) acidities. *J. Am. Chem. Soc.* 98, 2886–2894.

Tamura, T., Yoshida, K., Hachida, T., Tsuchiya, M., Nakamura, M., Kazue, Y., et al. (2010). Physicochemical properties of glyme-Li salt complexes as a new family of room-temperature ionic liquids. *Chem. Lett.* 39, 753–755. doi: 10.1246/cl.2010.753

Ueno, K., Tatara, R., Tsuzuki, S., Saito, S., Doi, H., Yoshida, K., et al. (2015). Li+ solvation in glyme-Li salt solvate ionic liquids. *Phy. Chem. Chem. Phys.* 17, 8248–8257. doi: 10.1039/C4CP05943C

Ueno, K., Yoshida, K., Tsuchiya, M., Tachikawa, N., Dokko, K., and Watanabe, M. (2012). Glyme–lithium salt equimolar molten mixtures, concentrated solutions or solvate ionic liquids? *J. Phy. Chem. B.* 116, 11323–11331. doi: 10.1021/jp307378j

Ueno, K. J., Park, W., Yamazaki, A., Mandai, T., Tachikawa, N., Dokko, K., et al. (2013). Anionic effects on solvate ionic liquid electrolytes in rechargeable lithium–sulfur batteries. *J. Phy. Chem. C.* 117, 20509–20516. doi: 10.1021/jp407158y

Wang, Y., Li, C., Wu, T., and Ye, X. (2018). Polymerized ionic liquid functionalized graphene oxide nanosheets as a sensitive platform for bisphenol A sensing. *Carbon* 129, 21–28. doi: 10.1016/j.carbon.2017.11.090

Wasserscheid, P., and Keim, W. (2000). Ionic liquids—new solutions for transition metal catalysis. *Angew. Chem. Int. Ed.* 39, 3772–3789. doi: 10.1002/1521-3773(20001103)39:21<3772::AID-ANIE3772>3.0.CO;2-5

Watanabe, M., and Mizumura, T. (1996). Conductivity study on ionic liquid/polymer complexes. *Solid State Ionics*, 86-88, 353–356. doi: 10.1016/0167-2738(96)00136-1

Watanabe, M., and Nishimoto, A. (1995). Effects of network structures and incorporated salt species on electrochemical properties of polyether-based polymer electrolytes. *Solid State Ionics*, 79, 306–312. doi: 10.1016/0167-2738(95)00079-L

Welton, T. (1999). Room-temperature ionic liquids. solvents for synthesis and catalysis. *Chem. Rev.* 99, 2071–2084. doi: 10.1021/cr980032t

Zad, Z. R., Davarani, S. S. H., Taheri, A., and Bide, Y. (2018). A yolk shell Fe3O4 @PA-Ni@Pd/Chitosan nanocomposite -modified carbon ionic liquid electrode as a new sensor for the sensitive determination of fluconazole in pharmaceutical preparations and biological fluids. *J. Mol. Liq.* 253, 233–240. doi: 10.1016/j.molliq.2018.01.019

Zhang, Q., Wu, S., Zhang, L., Lu, J., Verproot, F., Liu, Y., et al. (2011). Fabrication of polymeric ionic liquid/graphene nanocomposite for glucose oxidase immobilization and direct electrochemistry. *Biosen. Bioelectron.* 26, 2632–2637. doi: 10.1016/j.bios.2010.11.024

frontiers
in Chemistry

NHC in Imidazolium Acetate Ionic Liquids: Actual or Potential Presence?

Isabella Chiarotto*, Leonardo Mattiello, Fabiana Pandolfi, Daniele Rocco and Marta Feroci*

Dipartimento di Scienze di Base e Applicate per l'Ingegneria, Sapienza University of Rome, Rome, Italy

Ionic liquids (ILs) are considered in the majority of cases green solvents, due to their virtually null vapor pressure and to the easiness in recycling them. In particular, imidazolium ILs are widely used in many fields of Chemistry, as solvents or precursors of N-heterocyclic carbenes (NHCs). The latter are easily obtained by deprotonation of the C2-H, usually using strong bases or cathodic reduction. Nevertheless, it is known that weaker bases (e.g., triethylamine) are able to promote C2-H/D exchange. From this perspective, the possibility of deprotonating C2-H group of an imidazolium cation by means of a basic counter-ion was seriously considered and led to the synthesis of imidazolium ILs spontaneously containing NHCs. The most famous of this class of ILs are N,N'-disubstituted imidazolium acetates. Due to the particular reactivity of this kind of ILs, they were appointed as "organocatalytic ionic liquids" or "proto-carbenes." Many papers report the use of these imidazolium acetates in organocatalytic reactions (i. e., catalyzed by NHC) or in stoichiometric NHC reactions (e.g., with elemental sulfur to yield the corresponding imidazole-2-thiones). Nevertheless, the actual presence of NHC in N,N'-disubstituted imidazolium acetate is still controversial. Moreover, theoretical studies seem to rule out the presence of NHC in such a polar environment as an IL. Aim of this Mini Review is to give the reader an up-to-date overview on the actual or potential presence of NHC in such an "organocatalytic ionic liquid," both from the experimental and theoretical point of view, without the intent to be exhaustive on N,N'-disubstituted imidazolium acetate applications.

Keywords: N-heterocyclic carbene, imidazolium acetate, NHC, basic anion, ionic liquids, C2-H deprotonation, organocatalytic ionic liquid

INTRODUCTION

Ionic liquids (ILs), salts constituted of a large organic cation and an organic or inorganic anion not coordinated (usually liquid below 100°C), are gaining more and more popularity in many fields of Chemistry (Handy, 2011; Vekariya, 2017; Watanabe et al., 2017). Due to their physico-chemical properties their use is advantageous in view of a "greener" way of thinking Chemistry (Mohammad and Inammudin, 2012; Feroci et al., 2013a) although there are not sufficient studies on their possible toxicity (Ostadjoo et al., 2018). In particular, their high solvation ability, their virtually null vapor pressure, the relative easiness in removing them from the reaction mixture and recycle them spurred chemists to revisit established chemical procedures using them both as solvents and

as reagents (Qureshi et al., 2014; Hajipour and Rafiee, 2015). Imidazolium ionic liquids are a class of ILs very often used in organic chemistry, as solvents and as precursors of N-heterocyclic carbenes (NHC), very efficient ligands and organocatalysts (Enders et al., 2007; Biju, 2019). In fact, the deprotonation of the C2-H in between the two imidazolium nitrogen atoms leads to the formation of a singlet carbene, which can act as a base and/or nucleophile. This deprotonation is usually carried out using strong bases (Sowmiah et al., 2009; Chiarotto et al., 2014) or by cathodic reduction (Gorodetsky et al., 2004; Feroci et al., 2016a), but it is known from decades (Olofson et al., 1964) that C2-H/D exchange can be induced by weaker bases, like Et$_3$N. This led to the awareness of the possibility to incorporate a weak base into the imidazolium salt structure, i.e., as counter-ion, in order to have in the same reagent the acid (imidazolium cation, precursor of carbene) and the base (acetate ion). Imidazolium acetates are currently used in many fields of organic chemistry, but the actual presence of NHC into such ionic liquids is still debated: is an imidazolium acetate a mixture of IL and NHC, or the basicity of the anion (with respect to the acidity of the imidazolium cation) is not strong enough for this deprotonation in such a polar environment as the ionic liquid? This question has been faced from both theoretical and experimental point of view.

THEORETICAL STUDIES

1-Ethyl-3-methylimidazolium acetate (EMIm-OAc) and 1-butyl-3-methylimidazolium acetate (BMIm-OAc) are among the most studied ILs potentially containing NHC, both theoretically and experimentally. The main question about the possibility of endogenous NHC in this kind of ILs arises from the very different pK$_a$ of the N,N'-dialkylimidazolium cation and of acetic acid (about 22 and 12.3 in DMSO, respectively), which seems to rule out the possibility of a deprotonation of the imidazolium cation by acetate ion (although the pK$_a$s in ILs are not known), leading to the formation of the corresponding NHC and acetic acid. To gain insights into the possibility of this proton transfer, Nyulászi and coworkers as early as 2010 studied computationally the system EMIm-OAc (at the B3LYP/6-31+G* level), starting from the premise that the imidazolium cation is a good hydrogen-bond donor, while acetate anion is a hydrogen-bond acceptor and thus this ion pair could be represented as hydrogen bonded in the gas phase (Hollóczki et al., 2010). The authors found that the relative energy of the two hydrogen bonded structures (RMIm-OAc and NHC-AcOH, **Scheme 1**, equation 1) are almost identical and the barrier for their isomerization is low (3.6 kcal mol^{-1}), rendering possible the existence of both isomers in the gas phase.

Qian et al. carried out quantum mechanical calculations to determine the reasons for the higher ability of imidazolium acetates over imidazolium chlorides in dissolving cellulose (Du and Qian, 2011). In this case also the effect of the solvent was evaluated. The authors calculated the free energy for the deprotonation reaction in the gas phase (-74.2 kcal mol^{-1}), while in the MMIm-OAc ionic liquid the same calculation gave a value of $+25.4$ kcal mol^{-1}, suggesting that the deprotonation

process is favorable in the gas phase, but unfavorable in IL (in fact, the reactant are charged while the products are neutral and a polar solvent stabilizes more charged species). Furthermore, *ab initio* calculations allowed the authors to suggest a reaction mechanism in which the NHC-AcOH hydrogen bonded complex dissociates into NHC and AcOH (**Scheme 1**, equation 2), rendering NHC free to react with cellulose.

Later, Hollóczki and Kirchner (Thomas et al., 2014) reconsider the system EMIm-OAc taking into account the NHC solvation in such an ionic liquid. Starting from previous experimental data, the authors investigated the possible hydrogen bond between NHC and the EMIm$^+$ cation (**Scheme 1**, equation 3) and its stabilizing effect. Unexpectedly, the authors found that such an interaction was not present in the studied system, as the C2-H site of the imidazolium cation was involved exclusively in an interaction with the acetate ion. This lack of stabilization is partially balanced out by a hydrogen bond between the carbene center and the alkyl substituent of the cation. The authors conclude that in a system like EMIm-OAc a latent carbene content can be observed, but due to the absence of a stabilizing effect by hydrogen bond between NHC and EMIm$^+$ cation, the proton transfer between C2-H and AcO$^-$ could be suppressed.

More recently (Gehrke and Hollóczki, 2017) Hollóczki and Gehrke questioned the actual presence of a NHC in an IL in which a weak base is present (starting from the high difference in pK$_a$), suggesting instead a concerted mechanism for the imidazolium cation deprotonation and reaction with the substrate to yield the organocatalysed reaction products.

EXPERIMENTAL STUDIES

Due to the experimental evidence that imidazolium acetate ionic liquids act as organocatalysts in organocatalytic reactions (e.g., the benzoin condensation), many attempts were made in order to prove the presence of NHC in such an ionic liquid. In fact, the presence of NHC and acetic acid in the gas phase (due to the evaporation under vacuum of EMIm-OAc) was proved by photoelectron spectroscopy and mass spectroscopy (Hollóczki et al., 2010), but in the liquid phase only an indirect evidence of NHC presence was obtained, as benzoin was isolated by reaction of EMIm-OAc and benzaldehyde (Kelemen et al., 2011). This result spurred the authors to refer to EMIm-OAc as an "organocatalytic ionic liquid." Almost at the same time, Rogers and coworkers (Rodríguez et al., 2011) confirmed the possibility to obtain NHC derived products (imidazole-2-thiones) by reaction of EMIm-OAc with elemental chalcogens, and suggesting for such an ionic liquid the name "proto-carbene." Moreover, the same authors studied the effect of the addition of a proton donor (acetic acid, water) on this reaction and proposed a mechanism for the stabilization in IL of the neutral products derived from the deprotonation of EMIm$^+$ cation by acetate anion. Such a mechanism (**Scheme 1**, equation 4) describes the formation of a hydrogen bonded dimer between acetic acid and acetate ion. On the other side, Welton and coworkers (Clough et al., 2013) carried out a study on the thermal degradation of EMIm-OAc with the identification of the neutral
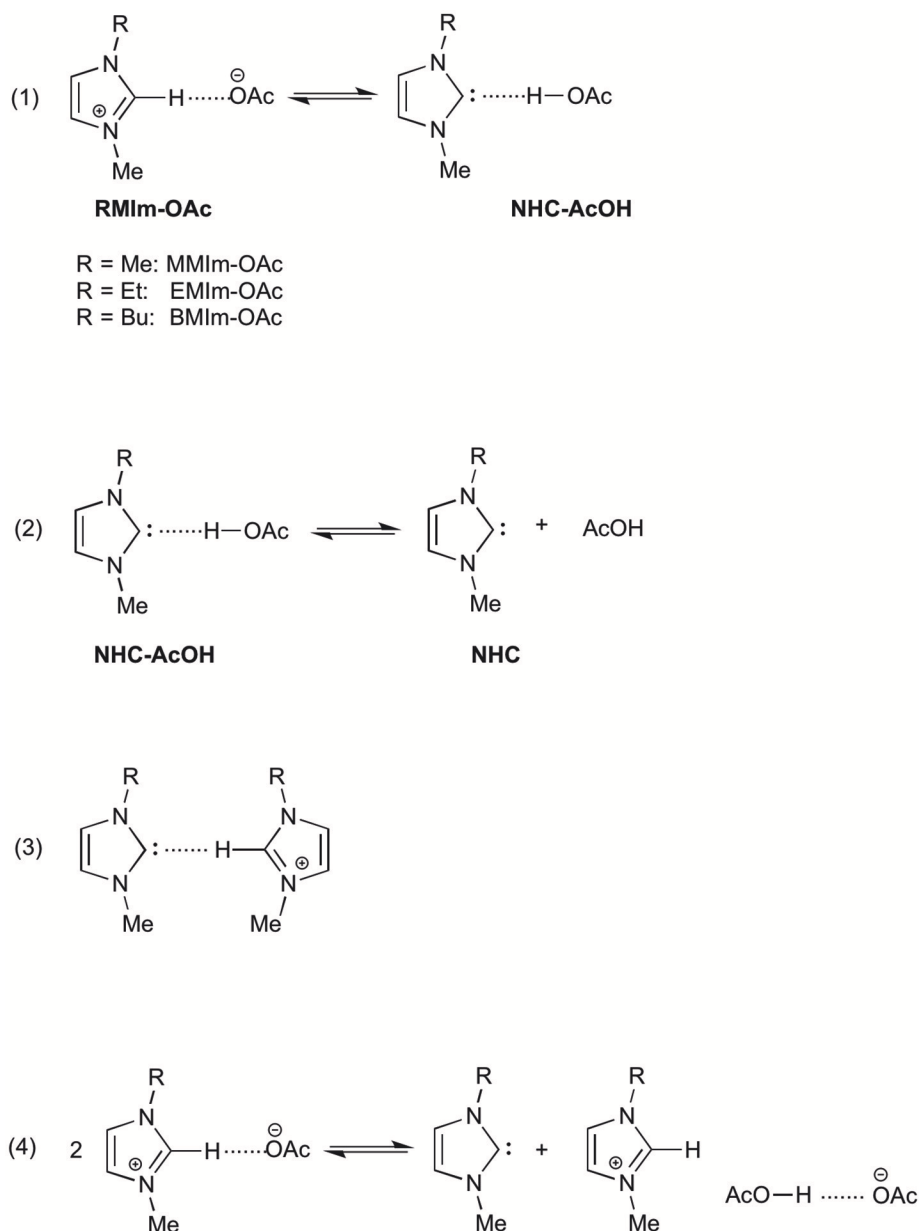
SCHEME 1 | Possible structures and equilibrium reactions present in imidazolium acetate ionic liquids.

products obtained at high temperature (by thermogravimetric analysis coupled with mass spectrometry) and found that the main products derived from dealkylation reactions, while NHC formation was occurring to a small extent.

Kar and Sander (2015) demonstrated the reversibility of the imidazolium deprotonation reaction by acetate anion (**Scheme 1**, equation 1), carrying out experiments at very low temperature (9 K), on gas and condensed phases, monitoring the system by IR spectroscopy. They found that for EMIm-OAc both ionic liquid and neutral species (NHC and AcOH) coexist at very low temperatures and if the vapor phase is condensed at 9 K, only NHC and acetic acid are present (and no ionic species).

Moreover, if the temperature is increased to room temperature, a proton transfer is active, leading again to the ionic liquid EMIm-OAc.

The demonstration of the potential presence of NHC in imidazolium acetates was obtained by many groups, carrying out successfully catalyzed or stoichiometric reactions (Lambert et al., 2016; Baumruck et al., 2017; Binks et al., 2018; Pandolfi et al., 2018), but in no case any attempt to evidence the actual presence of NHC was done. This last topic was faced in a few papers. Inesi and coworkers (Chiarotto et al., 2015, 2017) studied this question by cyclic voltammetry, starting from the fact that NHC is an electroactive species and it can be oxidized at the

anode at a potential around +0.5 V (vs. Ag), in pure imidazolium acetate ionic liquid. This investigation was carried out registering the cyclic voltammetries of pure IL at different temperatures and comparing the electrochemical behavior of BMIm-OAc with that of an imidazolium ionic liquid containing a less basic anion, BMIm-Cl. The authors found that at a temperature higher of 100°C the cyclic voltammetry of BMIm-OAc showed the presence of the corresponding carbene, while starting from the corresponding chloride ionic liquid, the oxidation peak of NHC was not present in 25–150°C interval of temperatures. The authors thus infer that the acetate anion is a base strong enough to deprotonate C2-H of the BMIm$^+$ cation and that this deprotonation reaction at temperatures higher than 100°C leads to the formation of a detectable amount of NHC. Suzer and coworkers (Gokturk et al., 2017) recently confirmed by XPS analysis the attribution of the anodic peak around +0.5 V to the oxidation of NHC, electrogenerated by cathodic reduction. In fact, imidazolium NHCs can also be generated by cathodic cleavage of the C2-H bond to yield NHC and molecular hydrogen (Gorodetsky et al., 2004; Feroci et al., 2016b,c).

Welton and coworkers (Daud et al., 2017) consider that all the observations reported in the literature about the presence of NHC in imidazolium acetate ionic liquids do not confirm the actual presence of carbenes in ILs, but just indicate their accessibility and that in order to have NHC derived products it is necessary the presence of a "NHC trap," i.e., a reagent or the electrode. Moreover, they believe that a concerted mechanism to NHC derived products can always be claimed in alternative to a multistep one (with the formation of NHC as a distinct molecule). In order to gain evidences on the actual or potential presence of NHC in EMIm-OAc, a kinetic study was carried out on a possible deuterium isotope effect in the formation of the adduct between NHC and an aromatic aldehyde (Breslow intermediate) starting from EMIm-OAc with a C2-D or C2-H group. The absence of a deuterium isotope effect allowed the authors to exclude a concerted mechanism and to confirm the actual presence of NHC in EMIm-OAc.

Apart from acetates (and other imidazolium organic carboxylates), other imidazolium ionic liquids containing basic anions are reported to be useful reagents for NHC derived reactions. Among them hydrogen carbonate and hydroxide are particularly important. As regards 1,3-dialkylimidazolium hydrogen carbonates, it is reported that these ionic liquids are in equilibrium with the corresponding NHC-CO$_2$ adducts (vide infra), demonstrating the possibility to afford NHCs (see for example: Fèvre et al., 2012; Zhao et al., 2017) by releasing of carbon dioxide due to high temperature effect or, at room temperature, using a solvent favoring the carbene generation (as THF or toluene).

As for 1,3-dialkylimidazolium hydroxides, it is a different story. In fact, although hydroxide anion is a noteworthy basic species (or precisely for this reason), imidazolium hydroxides are very rarely used as organocatalysts or reagents (see for example: Rajesh et al., 2012), due to their instability. In fact, the reaction between 1,3-dialkylimidazolium cation and hydroxide anion leads mainly to ring opening products (Yuen et al., 2013; Long and Pivovar, 2014), rendering in most of cases unuseful

this class of imidazolium ionic liquids (although the ring opening seems to be directly related to NHC formation, Hollóczki et al., 2011).

The literature survey on imidazolium ionic liquids containing basic anions other than acetate is not intended to be complete.

THE PRESENCE OF CO$_2$

Besides the various applications in organic chemistry, electrochemistry or material chemistry, ionic liquids gained popularity in the field of carbon dioxide capture and storage (CCS, e.g., in CO$_2$ absorption from industrial waste gases), as carbon dioxide catch and release reagents (de Robillard et al., 2013; Feroci et al., 2013b). Physisorption is the mechanism for such a CO$_2$ capture in ILs, but chemisorption was invoked for some functionalized ILs. In particular, the solubility of carbon dioxide in imidazolium acetate ionic liquids is remarkable and this very high solubility was charged to chemisorption. In order to fully understand the nature of such an interaction (with acetate anion, imidazolium cation or NHC), many theoretical and experimental studies have been carried out and such papers shed light on the presence of endogenous NHC in imidazolium acetate ILs. Rogers and coworkers (Gurau et al., 2011) reported the single-crystal X-ray structures of EMIm-OAc and EMIm-OAc-CO$_2$ mixture and found that no NHC was present when studying pure IL (as expected for the solid phase). On the contrary, after CO$_2$ bubbling the corresponding NHC-CO$_2$ adduct was present, along with the AcO$^-$/AcOH dimer (**Scheme 2**, equation 1), demonstrating the formation of NHC and suggesting a two-step mechanism (formation of NHC and then reaction with CO$_2$ to give the adduct).

Besnard and coworkers (Besnard et al., 2012; Cabaço et al., 2012) carried out theoretical (DFT) and experimental (Raman, NMR) studies to understand the high CO$_2$ solubility in BMIm-OAc and suggested a two-step mechanism dominated by an irreversible chemical reaction leading to the formation of the NHC-CO$_2$ adduct (**Scheme 2**, equation 2). In the suggested mechanism a first reaction leads to the formation of a transient NHC, stabilized by the interaction with carbon dioxide; although the NHC formation is not favored in the liquid phase, it is triggered by the interaction with CO$_2$. The transient intermediate then isomerizes to NHC-CO$_2$ adduct. Moreover, the acetic acid molecule produced in this reaction interacts with the acetate anion to give a hydrogen bonded dimer.

Kirchner and Hollóczki (Hollóczki et al., 2013a,b) studied the EMIm-OAc-CO$_2$ system by AIMD simulations and static quantum chemical calculations and found that in the liquid phase the NHC formation is facilitated by the physically absorbed carbon dioxide, leading to the chemically absorbed CO$_2$ (NHC-CO$_2$ adduct). Moreover, the authors underline the fact that the occurrence of NHC induced reactions in EMIm-OAc does not prove that NHC is present in this IL, but only that it is accessible.

DFT and ONIOM calculations on imidazolium acetate-CO$_2$ system, both in the gas phase and in the liquid phase, considering the one-step and the two step mechanisms (**Scheme 2**, equations 1 and 2) allowed Damodaran and coworkers (Mao et al., 2016) to
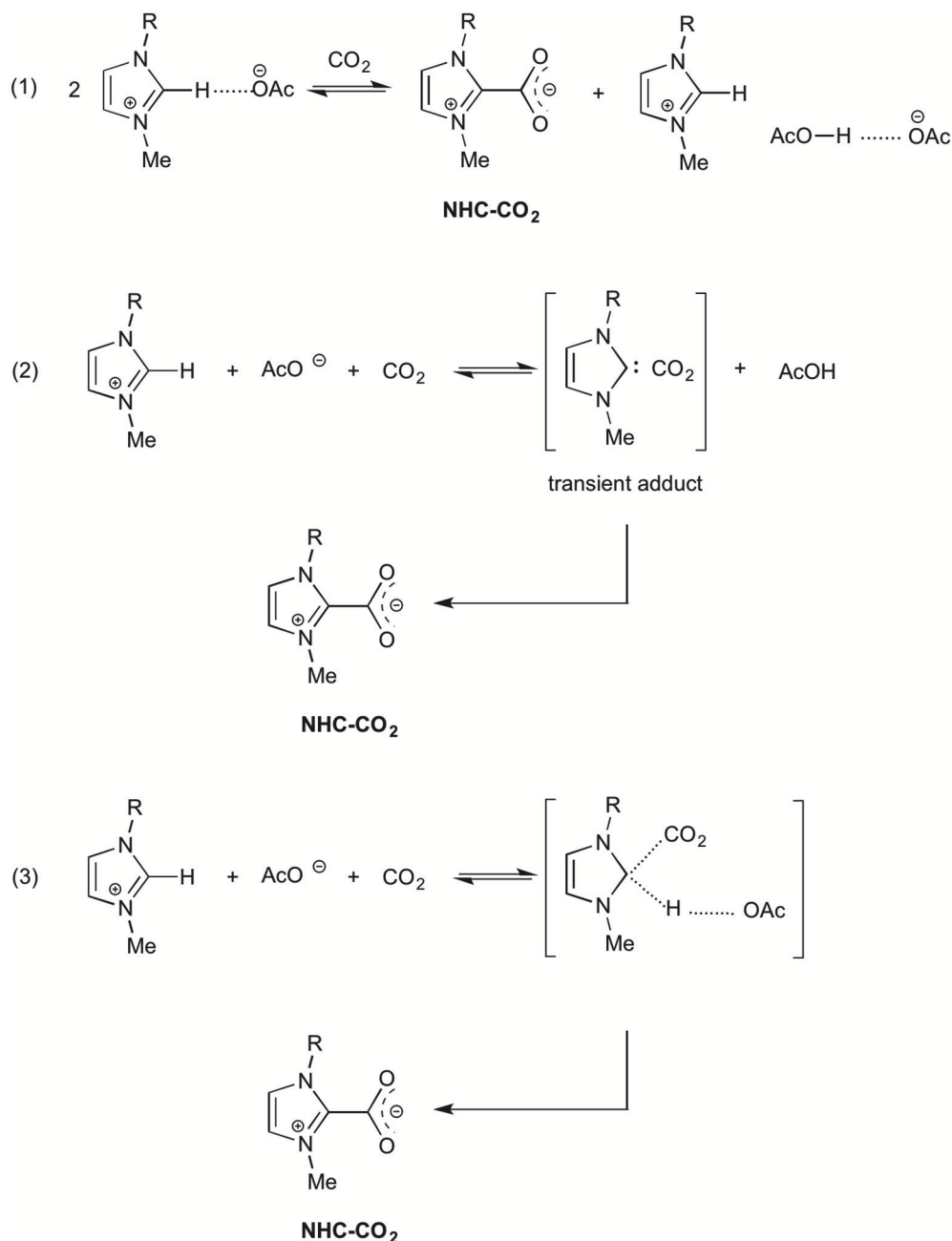
SCHEME 2 | Possible reactions in imidazolium acetate IL-CO$_2$ mixtures.

propose a new two-step reaction mechanism: at first the addition reaction between the imidazolium cation (at C2) and carbon dioxide, then the deprotonation of the C2-H of the adduct to yield NHC-CO$_2$. The authors emphasize the important role played by IL in the stabilization of the products.

In a recent paper, (Yan et al., 2017) reporting *ab initio* results on EMIm-OAc, the effect of solvation is underlined also by Kim and coworkers. The authors exclude the presence of NHC in such an ionic liquid and suggest that acetate anion can deprotonate

the imidazolium cation only in a non-polar or extremely weakly polar environment (solvent). Moreover they suggest that the reaction of EMIm-OAc with carbon dioxide to yield NHC-CO$_2$ adduct is a concerted process (**Scheme 2**, equation 3), in which the intermediate has a sp^3 C2 which subsequently evolves toward the NHC-CO$_2$ adduct.

These NHC-CO$_2$ adducts are also useful NHC masked organocatalysts for the carboxylation of organic compounds (see as examples: Tommasi and Sorrentino, 2006; Desens and Werner,

2016; Stewart et al., 2016) and NHC-transfer agent in the synthesis of NHC-metal complexes (see as examples: Voutchkova et al., 2007; Voutchkova and Crabtree, 2010; Li et al., 2011).

CONCLUSIONS

The overview of the last decade literature on the possible presence of NHC in imidazolium acetate ionic liquids evidences that the question of the actual or potential presence of NHC in such ionic liquids is still debated. On one side, theoretical calculations seem to exclude the possibility of NHC presence in imidazolium acetate, due to the highly polar environment which should strongly unfavor the proton transfer from imidazolium C2-H to acetate anion, and thus transform charged species into neutral molecules. On the other side, experimental studies demonstrate the possibility of using imidazolium acetates as a reservoir of NHC, giving rise to the formation of products in which it is necessary the formation of catalytic or stoichiometric amounts of carbene. It is still possible that the deprotonation equilibrium at room temperature lies far toward the charged species and the presence of a "carbene-trap" (always present in NHC-induced organic reactions) or an irreversible subsequent reaction is necessary in order to move such an equilibrium toward the formation of NHC and acetic acid. Moreover, it is possible that in some cases the reactions between NHC and its trap and NHC formation are concerted (as theorized for the reaction between NHC and CO_2), while in others they are a two-step process (as demonstrated in the Breslow intermediate formation). The present literature data exclude the possibility to isolate or even evidence the presence of NHC in imidazolium acetates (either for its presence as a strongly hydrogen bonded adduct, or for its very low concentration), but it is not to be excluded that in the future it would be possible to isolate from these systems stable NHCs (like Arduengo's ones).

Anyway, it is undeniable that imidazolium acetate ILs are "organocatalytic ionic liquids" or "proto-carbenes" and that their reactivity is so peculiar that their use is highly suggested in many fields of Chemistry.

AUTHOR CONTRIBUTIONS

All authors listed have made a substantial, direct, and intellectual contribution to the work, and approved it for publication.

REFERENCES

Baumruck, A. C., Tietze, D., Stark, A., and Tietze, A. A. (2017). Reactions of sulfur-containing organic compounds and peptides in 1-ethyl-3-methyl-imidazolium acetate. *J. Org. Chem.* 82, 7538–7545. doi: 10.1021/acs.joc.7b01272

Besnard, M., Cabaço, M. I., Vaca Chávez, F., Pinaud, N., Sebastião, P. J., Coutinho, J. A., et al. (2012). CO_2 in 1-butyl-3-methylimidazolium acetate. 2. NMR investigation of chemical reactions. *J. Phys. Chem. A.* 116, 4890–4901. doi: 10.1021/jp211689z

Biju, A. T. (2019). *N-Heterocyclic Carbenes in Organocatalysis*. Hoboken, NJ: John Wiley and Sons.

Binks, F. C., Cavalli, G., Henningsen, M., Howlin, B. J., and Hamerton, I. (2018), Investigating the mechanism through which ionic liquids initiate the polymerisation of epoxy resins. *Polymer* 139, 163–176. doi: 10.1016/j.polymer.2018.01.087

Cabaço, M. I., Besnard, M., Danten, Y., and Coutinho, J. A. P. (2012). Carbon dioxide in 1-butyl-3-methylimidazolium acetate. I. Unusual solubility investigated by Raman spectroscopy and DFT calculations. *J. Phys. Chem. A* 116, 1605–1620. doi: 10.1021/jp211211n

Chiarotto, I., Feroci, M., Forte, G., and Inesi, A. (2015). Stability of electrogenerated 1-butyl-3-methylimidazol-2-ylidene in DMF. Part 2. Role of acid substrates. *Electrochim. Acta* 176, 627–635 doi: 10.1016/j.electacta.2015.06.129

Chiarotto, I., Feroci, M., Forte, G., Orsini, M., and Inesi, A. (2014), Proton-exchange equilibrium between bases and [BMIm][BF₄]: an electrochemical procedure to evaluate the presence of carbenes for synthetic applications. *ChemElectroChem* 1, 1525–1530. doi: 10.1002/celc.201402134

Chiarotto, I., Feroci, M., and Inesi, A. (2017). First direct evidence of N-heterocyclic carbene in BMIm acetate ionic liquids. an electrochemical and chemical study on the role of temperature. *N J. Chem.* 41, 7840–7843. doi: 10.1039/C7NJ00779E

Clough, M. T., Geyer, K., Hunt, P. A., Mertes, J., and Welton, T. (2013). Thermal decomposition of carboxylate ionic liquids: trends and mechanisms. *Phys. Chem. Chem. Phys.* 15, 20480–20495. doi: 10.1039/c3cp53648c

Daud, N. M. A. N., Bakis, E., Hallett, J. P., Weber, C. C., and Welton, T. (2017). Evidence for the spontaneous formation of N-heterocyclic carbenes in imidazolium based ionic liquids. *Chem. Commun.* 53, 11154–11156. doi: 10.1039/C7CC06112A

de Robillard, G., Devillers, C. H., Kunz, D., Cattey, H., Digard, E., and Andrieu, J. (2013). Electrosynthesis of imidazolium carboxylates. *Org. Lett.* 15, 4410–4413. doi: 10.1021/ol401949f

Desens, W., and Werner, T. (2016). Convergent activation concept for CO_2 fixation in carbonates. *Adv. Synth. Catal.* 358, 622–630. doi: 10.1002/adsc.201500941

Du, H., and Qian, X. (2011). The effects of acetate anion on cellulose dissolution and reaction in imidazolium ionic liquids. *Carbohydr. Res.* 346, 1985–1990. doi: 10.1016/j.carres.2011.05.022

Enders, D., Niemeier, O., and Henseler, A. (2007). Organocatalysis by N-heterocyclic carbenes. *Chem. Rev.* 107, 5606–5655. doi: 10.1021/cr068372z

Feroci, M., Chiarotto, I., D'Anna, F., Gala, F., Noto, R., Ornano, L., et al. (2016b). N-heterocyclic carbenes and parent cations: acidity, nucleophilicity, stability, and hydrogen bonding-electrochemical study and Ab initio calculations. *ChemElectroChem* 3, 1133–1141. doi: 10.1002/celc.201600187

Feroci, M., Chiarotto, I., D'Anna, F., Ornano, L., Rizzo, C., and Inesi, A. (2016c). Azolium and acetate ions in DMF: formation of free N-heterocyclic carbene. A voltammetric analysis. *Electrochem. Comm.* 67, 55–58. doi: 10.1016/j.elecom.2016.03.012

Feroci, M., Chiarotto, I., Forte, G., and Inesi, A. (2013b). An electrochemical methodology for the cyclic CO2 "catch and release." The role of the electrogenerated N-heterocyclic carbene in BMIm-BF₄. *J. CO_2 Util.* 2, 29–34. doi: 10.1016/j.jcou.2013.07.002

Feroci, M., Chiarotto, I., and Inesi, A. (2013a). Electrolysis of ionic liquids. A possible keystone for the achievement of green solvent-catalyst systems. *Curr. Org. Chem.* 17, 204–219. doi: 10.2174/1385272811317030003

Feroci, M., Chiarotto, I., and Inesi, A. (2016a). Advances in the knowledge of N-heterocyclic carbenes properties. The backing of the electrochemical investigation. *Catalysts* 6:178 doi: 10.3390/catal6110178

Fèvre, M., Coupillaud, M. P., Miqueu, K., Sotiropoulos, J. M., Vignolle, J., and Taton, D. (2012). Imidazolium hydrogen carbonates versus imidazolium carboxylates as organic precatalysts for N-heterocyclic carbene catalyzed reactions. *J. Org. Chem.* 77, 10135–10144. doi: 10.1021/jo301597h

Gehrke, S., and Hollóczki, O. (2017). Are there carbenes in N-heterocyclic carbene organocatalysis? *Angew. Chem. Int. Ed.* 56, 16395–16398. doi: 10.1002/anie.201708305

Gokturk, P. A., Salzner, U., Nyulászi, L., Ulgut, B., Kocabas, C., and Suzer, S. (2017). XPS-evidence for in-situ electrochemically-generated carbene formation. *Electrochim. Acta* 234, 37–42. doi: 10.1016/j.electacta.2017.03.053

Gorodetsky, B., Ramnial, T., Branda, N. R., and Clyburne, J. A. C. (2004). Electrochemical reduction of an imidazolium cation: a convenient preparation of imidazol-2-ylidenes and their observation in an ionic liquid. *Chem. Commun.* 10, 1972–1973. doi: 10.1039/b407386j

Gurau, G., Rodríguez, H., Kelley, S. P., Janiczek, P., Kalb, R. S., and Rogers, R. D. (2011). Demonstration of chemisorption of carbon dioxide in 1,3-Dialkylimidazolium acetate ionic liquids. *Angew. Chem. Int. Ed.* 50, 12024–12026. doi: 10.1002/anie.201105198

Hajipour, A. R., and Rafiee, F. (2015). Recent progress in ionic liquids and their applications in organic synthesis. *Org. Prep. Proced. Int.* 47, 249–308. doi: 10.1080/00304948.2015.1052317

Handy, S. (2011). *Applications of Ionic Liquids in Science and Technology*. London: IntechOpen.

Hollóczki, O., Firaha, D. S., Friedrich, J., Brehm, M., Cybik, R., Wild, M. et al. (2013b). Carbene formation in ionic liquids: spontaneous, induced, or prohibited? *J. Phys. Chem. B* 117, 5898–5907. doi: 10.1021/jp4004399

Hollóczki, O., Gerhard, D., Massone, K., Szarvas, L., Németh, B., Veszprémi, T., et al. (2010). Carbenes in ionic liquids. *New J. Chem.* 34, 3004–3009. doi: 10.1039/c0nj00380h

Hollóczki, O., Kelemen, Z., Könczöl, L., Szieberth, D., Nyulászi, L., Stark, A., et al. (2013a). Significant cation effects in carbon dioxide–ionic liquid systems. *ChemPhysChem* 14, 315–320. doi: 10.1002/cphc.201200970

Hollóczki, O., Terleczky, P., Szieberth, D., Mourgas, G., Gudat, D., and Nyulászi, L. (2011). Hydrolysis of imidazole-2-ylidenes. *J. Am. Chem. Soc.* 133, 780–789. doi: 10.1021/ja103578y

Kar, B. P., and Sander, W. (2015). Reversible carbene formation in the ionic liquid 1-ethyl-3-methylimidazolium acetate by vaporization and condensation. *ChemPhysChem* 16, 3603–3606. doi: 10.1002/cphc.201500729

Kelemen, Z., Hollóczki, O., Nagy, J., and Nyulászi, L. (2011). An organocatalytic ionic liquid. *Org. Biomol. Chem.* 9, 5362–5364. doi: 10.1039/c1ob05639e

Lambert, R., Coupillaud, P., Wirotius, A. L., Vignolle, J., and Taton, D. (2016). Imidazolium-based poly(Ionic Liquid)s featuring acetate counter anions: thermally latent and recyclable precursors of polymer-supported N-heterocyclic carbenes for organocatalysis. *Macromol. Rapid Commun.* 37, 1143–1149. doi: 10.1002/marc.201600019

Li, J., Peng, J., Bai, Y., Lai, G., and Li, X. (2011). Synthesis of rhodium N-heterocyclic carbene complexes and their catalytic activity in the hydrosilylation of alkenes in ionic liquid medium. *J. Organomet. Chem.* 696, 2116–2121. doi: 10.1016/j.jorganchem.2010.11.017

Long, H., and Pivovar, B. (2014). Hydroxide degradation pathways for imidazolium cations: A DFT study. *J. Phys. Chem. C.* 118, 9880–9888. doi: 10.1021/jp501362y

Mao, J. X., Steckel, J. A., Yan, F., Dhumal, N., Kim, H., and Damodaran, K. (2016). Understanding the mechanism of CO_2 capture by 1,3 di-substituted imidazolium acetate based ionic liquids. *Phys. Chem. Chem. Phys.* 18, 1911–1917. doi: 10.1039/C5CP05713B

Mohammad, A., and Inammudin (2012). *Green Solvents. Properties and Applications of Ionic Liquids*. Dordrecht: Springer.

Olofson, R. A., Thompson, W. R., and Michelman, J. S. (1964). Heterocyclic nitrogen ylides. *J. Am. Chem. Soc.* 86, 1865–1866. doi: 10.1021/ja01063a051

Ostadjoo, S., Berton, P., Shamshina, J. L., and Rogers, R. D. (2018). Scaling-up ionic liquid-based technologies: how much do we care about their toxicity? prima facie information on 1-Ethyl-3-Methylimidazolium acetate. *Toxicol. Sci.* 161, 249–265. doi: 10.1093/toxsci/kfx172

Pandolfi, F., Feroci, M., and Chiarotto, I. (2018). Role of anion and cation in the 1-methyl-3-butyl imidazolium ionic liquids BMImX: the knoevenagel condensation. *ChemistrySelect* 3, 4745–4749. doi: 10.1002/slct.201800295

Qureshi, Z. S., Deshmukh, K. M., and Bhanage, B. M. (2014). Applications of ionic liquids in organic synthesis and catalysis *Clean Technol. Environ.* 16, 1487–1513. doi: 10.1007/s10098-013-0660-0

Rajesh, S. R., Perumal, S., Menéndez, J. C., Pandian, S., and Murugesan, R. (2012). Facile ionic liquid-mediated, three-component sequential reactions for the green, regio- and diastereoselective synthesis of furocoumarins. *Tetrahedron* 68, 5631–5636 doi: 10.1016/j.tet.2012.04.058

Rodríguez, H., Gurau, G., Holbrey, J. D., and Rogers, R. D. (2011). Reaction of elemental chalcogens with imidazolium acetates to yield imidazole-2-chalcogenones: direct evidence for ionic liquids as proto-carbenes. *Chem. Commun.* 47, 3222–3224. doi: 10.1039/c0cc05223j

Sowmiah, S., Srinivasadesikan, V., Tseng, M. C., and Chu, Y. H. (2009). On the chemical stabilities of ionic liquids. *Molecules* 14, 3780–3813. doi: 10.3390/molecules14093780

Stewart, J. A., Drexel, R., Arstad, B., Reubsaet, E., Weckhuysena, B. M., and Bruijnincx, P. C. A. (2016). Homogeneous and heterogenised masked N-heterocyclic carbenes for bio-based cyclic carbonate synthesis. *Green Chem.* 18, 1605–1618. doi: 10.1039/C5GC02046H

Thomas, M., Brehm, M., Hollóczki, O., and Kirchner, B. (2014). How can a carbene be active in an ionic liquid? *Chem. Eur. J.* 20, 1622–1629. doi: 10.1002/chem.201303329

Tommasi, I., and Sorrentino, F. (2006). Synthesis of 1,3-dialkylimidazolium-2-carboxylates by direct carboxylation of 1,3-dialkylimidazolium chlorides with CO_2. *Tetrahedron Lett.* 47, 6453–6456. doi: 10.1016/j.tetlet.2006.06.106

Vekariya, R. L. (2017). A review of ionic liquids: applications towards catalytic organic transformations. *J. Mol. Liq.* 227, 44–60. doi: 10.1016/j.molliq.2016.11.123

Voutchkova, A. M., and Crabtree, R. H. (2010). Rhodium and iridium N-heterocyclic carbene complexes from imidazolium carboxylates. *Inorg. Synth.* 35, 88–91. doi: 10.1002/9780470651568

Voutchkova, A. M., Feliz, M., Clot, E., Eisenstein, O., and Crabtree, R. H. (2007). Imidazolium carboxylates as versatile and selective N-heterocyclic carbene transfer agents: synthesis, mechanism, and applications. *J. Am. Chem. Soc.* 129, 12834–12846. doi: 10.1021/ja0742885

Watanabe, M., Thomas, M. L., Zhang, S., Ueno, K., Yasuda, T., and Dokko, K. (2017). Application of ionic liquids to energy storage and conversion materials and devices. *Chem. Rev.* 117, 7190–7239. doi: 10.1021/acs.chemrev.6b00504

Yan, F., Dhumala, N. R., and Kim, H. J. (2017). CO_2 capture in ionic liquid 1-alkyl-3- methylimidazolium acetate: a concerted mechanism without carbene. *Phys. Chem. Chem. Phys.* 19, 1361–1368. doi: 10.1039/C6CP06556B

Yuen, A. K. L., Masters, A. F., and Maschmeyer, T. (2013). 1,3-disubstituted imidazolium hydroxides: dry salts or wet carbenes? *Catal. Today* 200, 9–16. doi: 10.1016/j.cattod.2012.04.007

Zhao, T., Hu, X., Wu, D., Li, R., Yang, G., and Wu, Y. (2017). Direct synthesis of dimethyl carbonate from carbon dioxide and methanol at room temperature using imidazolium hydrogen carbonate ionic liquid as a recyclable catalyst and dehydrant. *ChemSusChem* 10, 2046–2052. doi: 10.1002/cssc.201700128

Ionic Liquids Catalysis for Carbon Dioxide Conversion With Nucleophiles

Shu-Mei Xia[1], Kai-Hong Chen[1], Hong-Chen Fu[1] and Liang-Nian He[1,2]*

[1] State Key Laboratory and Institute of Elemento-Organic Chemistry, College of Chemistry, Nankai University, Tianjin, China,
[2] Collaborative Innovation Center of Chemical Science and Engineering, Nankai University, Tianjin, China

Carbon dioxide, as a promising C_1 synthon, has attracted great interest in organic synthesis. Due to the thermodynamic stability and kinetic inertness of CO_2, developing efficient strategies for CO_2 activation and subsequent conversion is very crucial. In this context, Ionic liquids (ILs) show great potential for capturing and activating CO_2 owing to their unique structures and properties, making them become ideal alternatives to volatile organic solvents and/or catalysts for CO_2 transformation. This minireview aims at summarizing ILs-promoted reactions of CO_2 with *N*-nucleophiles (primary amines)/*O*-nucleophiles (primary alcohols, water). Two catalytic systems i.e., metal/ILs binary systems such as Cu/ILs systems and Ag/ILs systems as well as single ILs systems including anion-functionalized ILs and bifunctionalized ILs have been developed for CO_2 catalytic conversion, for instance, carboxylative cyclization of nucleophiles e.g., propargylic alcohols, amines, 2-aminobenzonitriles and *o*-aminobenzenethiol, and formylation of amines or 2-aminothiophenols with hydrosilanes to afford various value-added chemicals e.g., cyclic carbamates, unsymmetrical organic carbonates, α-hydroxyl ketones, and benzimidazolones. In a word, IL could provide a powerful tool for efficient CO_2 utilization.

Keywords: CO_2 conversion, carboxylative cyclization, catalysis, ionic liquids, green chemistry

INTRODUCTION

CCS strategy, carbon capture and storage/sequestration, has been proposed as a most potential invention to reduce or mitigate CO_2 emissions, including the capture of waste CO_2, the transportation and deposition of CO_2 in a safe place. Nevertheless, high cost and energy consumption of CCS process are the main obstacles. Carbon dioxide, as an abundant and non-poisonous C_1 resource, has shown significant potential for constructing new C–C, C–O, and C–N bond in chemical synthesis (Shi et al., 2003; Zhang et al., 2008; He et al., 2009, 2010; Aresta et al., 2014; Liu et al., 2015, 2016a, 2017a,b; Song et al., 2017). However, the inherent thermodynamic stability and kinetic limitation of CO_2 become the main barriers in transforming CO_2 into high value-added chemicals, fuels, and materials. Therefore, developing efficient strategies for CO_2 activation and conversion from environmental protection and economic perspectives is crucial. Carbon capture and utilization (CCU) strategy have been proposed by He group, which could be an ideal alternative to address the energy consumption problem in CCS (Yang et al., 2011a,b, 2012).

Ionic liquids (ILs) have attracted widespread attention as promising alternatives to solvents and catalysts on account of their unique properties such as the low melting point, unlimited tunability, negligible vapor pressure, and high stability (Zhang et al., 2006). As a novel green medium, ILs have been identified the outstanding performance in the absorption and conversion of CO_2 under mild conditions through tunning the structures of cations and anions (Jutz et al., 2011; Yang et al., 2011b; Liu et al., 2016b). ILs-promoted CCU processes have attracted numerous attentions owning to ILs' unique properties. In most cases, ILs can be used as solvent, dehydrate, or catalyst, and these roles are similar in CCU processes. Thus, we hope to be able to shed light on all ILs-promoted CCU processes by using these limited but systematic examples.

In this minireview, we aim at summarizing ILs-promoted reactions of CO_2 with some nucleophiles. We would like to divide this review into two parts that are metal/ILs binary systems such as Cu/ILs systems and Ag/ILs systems as well as single ILs systems including conventional ILs, anion-functionalized ILs, and bifunctionalized ILs. Selected carboxylative cyclization of nucleophiles, e.g., propargylic alcohols, amines, 2-aminobenzonitriles and *o*-aminobenzenethiol, and formylation of amines or 2-aminothiophenols with hydrosilanes, to afford various value-added chemicals are taken into consideration.

METAL/IONIC LIQUID BINARY CATALYTIC SYSTEM

Metal (Cu, Ag)-ILs system is an important part of the CO_2 capture and utilization. Since its ability to activate carbon-carbon triple bond, Cu/Ag has been used in various cyclization reactions of CO_2 as shown in **Scheme 1**.

Cu/Ionic Liquid Catalysis

The first example of the synthesis of α-methylene cyclic carbonates from CO_2 and propargylic alcohols in ILs is reported by Deng and co-workers (Gu et al., 2004; **Figure S1**). By screening of commercially available transition metal salts and ILs, [BMIm][PhSO$_3$]/CuCl system exhibits the best performance in this reaction with a yield of 97%. Thanks to the reusability
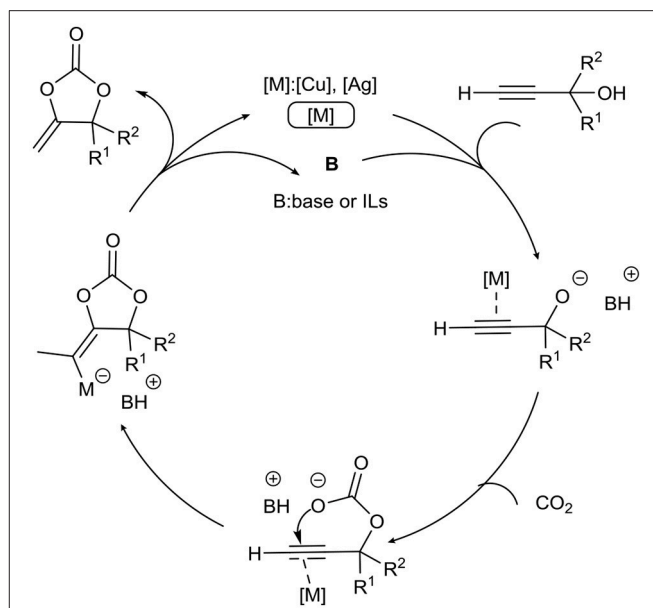
SCHEME 1 | Plausible reaction mechanism of propargylic alcohols and CO_2.

of ILs, CuCl can be reused 3 times without losing activity after immobilized in [BMIm][PhSO$_3$].

A similar system, [BMIm]BF$_4$/CuCl, is then used by the same group in a similar reaction (**Figure S1**; Gu et al., 2005). IL is used as the "green" reaction media and believed as the promoter for this three-component reaction of propargylic alcohols, primary amines and CO_2.

The synthesis of α-methylene oxazolidinones only from propargylic amines and CO_2 is reported by our group, in which bifunctional Cu(II)-polyoxometalate-based ILs is used as catalyst (**Figure S2**; Wang et al., 2016a). According to the experimental results and NMR studies, this IL is found to be able to activate propargylic amine and CO_2 at the same time (**Figure S3**). And both terminal and internal propargylic amines successfully deliver the corresponding 2-oxazolidinones in excellent yields.

Ag/Ionic Liquids Catalysis

Compared with copper, silver displays better reactivity in activation of carbon-carbon triple bond of propargylic amine/alcohol. Therefore, Ag-IL catalyst systems have also been widely applied for catalyzing cyclization propargylic amine/alcohols with CO_2.

In 2015, He et al. successfully developed a dual-component catalytic system comprising AgOAc and [(*n*-C$_7$H$_{15}$)$_4$N][Br], which could effectively catalyze CO_2 fixation with propargylic alcohols/amines to produce various cyclic carbonates/oxazolidinones in the absence of solvent, ligand or organic base (**Figure S4**; Song and He, 2016). This elegant system can achieve the TON of 6024. Through experimental results and DFT calculations, the cation with a longer alkyl chain can enhance the nucleophilicity of anion resulting in improving its activity.

Besides of cations, tuning structures of anions in ILs is another way that can control the activity of ILs. Recently, Wang group has developed an efficient AgOAc/ [P$_{66614}$][DEIm] (trihexyltetradecylphosphonium dimethyl 4,5-imidazoledicarboxylate) system for the synthesis of cyclic carbonates from propargylic alcohols with CO$_2$ under mild conditions (**Figure S5**; Chen et al., 2016a). The basicity of the IL is found to play a dramatic role: only when IL with moderate basicity, can it have excellent activity. According to DFT calculation and NMR spectroscopic analyzing, weaker basicity shows poor activity but stronger basicity will reduce the yield because of the polymerization of propargylic alcohols.

Similarly, AgI/[OAc] is disclosed as a robust catalyst system in the same reaction (**Figure S5**; Yuan et al., 2017). Only 1% of the catalyst is needed to obtain excellent yield of cyclic carbonates. The high concentration of [OAc] in this system is favorable for the activation of hydroxyl in the substrate and CO$_2$, which is also identified by Steckel (Steckel, 2012). Another Ag binary catalyst system, AgCl/[OAc], is reported by Han group in the reaction of CO$_2$, propargylic alcohols, and primary alcohols (**Figure S6**; Hu et al., 2017). AgCl/[BMIm][OAc] serves as both catalyst and solvent, and can be easily reused at least five times without reducing notably catalytic activity. The activation of alcoholic hydroxyl by [OAc] and the activation of triple bond by Ag salt are supposed as important steps in this reaction.

IONIC LIQUID CATALYSIS FOR CO$_2$ CONVERSION

Traditional Ionic Liquids

It has been a long time since ILs have been discovered the good solubility for CO$_2$ (Blanchard et al., 1999; Bates et al., 2002; Jessop et al., 2005). And this property can also make IL a nice catalyst for CO$_2$ conversion (Ma et al., 2017; Wang et al., 2018). Recently, two similar nonfunctional IL dual systems (CsOH or Co(acac)$_3$/[BMMIm][Cl]) have been reported by Deng et al. in the synthesis of symmetric urea derivatives from CO$_2$ and amines (**Figure S7**; Shi et al., 2003; Li et al., 2010). In the CsOH/[BMMIm][Cl] system, symmetric urea derivatives can be obtained in high yields, but no product is produced when without IL, indicating that IL is indispensable for this reaction. However, as a strong base, CsOH suffers from many weakness, such as corrosion, deactivation, and even destructive action to [BMMIm][Cl] under high temperature. In order to overcome these disadvantages, Co(acac)$_3$/[BMIm][Cl] system is developed for this reaction. In this catalyst system, [BMIm][Cl] is believed as a physical dehydrant, importantly, it can be reused while keeping high activity.

IL, such as [BMIm][Br], is also believed as an efficient dehydrant in the synthesis of cyclic urethanes from 2-aminoethanol and CO$_2$ (**Figure S8**; Fujita et al., 2006). K$_2$CO$_3$ is the catalyst in this reaction, while [BMIm][Br] acts as a recyclable dehydrant and can activate the carbonyl group. In another work to obtain oxazolidinone, Deng et al. develops an ILs-catalyzed efficient three-component reaction of propargylic alcohols, amines, and CO$_2$ (Zhang et al., 2005). Among all of the

SCHEME 2 | CO$_2$ conversions catalyzed by IL$_S$.
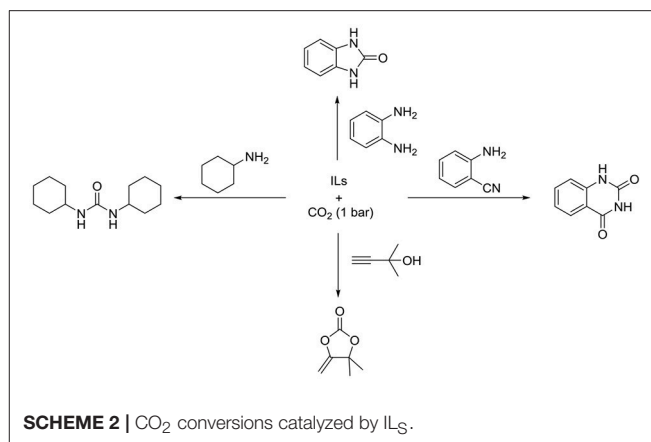
solvents they use, [DMIm][BF$_4$] exhibits the best performance, while traditional solvents like DMSO and toluene have no activity (**Figure S9**). Therefore, it is indicated that IL has a strong impact on this reaction. After recycling three times, high catalytic activity can be maintained for the [DMIm][BF$_4$].

Imidazole IL ([BMIm][Cl]) is also applied by Liu group in the reductive functionalization of CO$_2$ with amine**s** to afford formamide (Hao et al., 2015). The experimental results imply that both anions and cations of ILs play important roles in their activity. [BMIm][Cl] can activate not only the Si–H bond of phenylsilane to react with CO$_2$, but the amine through the hydrogen bond. In addition, [BMIm][Cl] can be reused for five times with high activity (**Figure S10**).

Anion-Functionalized Ionic Liquids

Although many CCU processes can be promoted by traditional ILs, most of them suffer from low ability for CO$_2$ activation, in which high pressure (>1 MPa) or additional metal catalysts will be needed. Recently, anion-functioanlized ILs are designed for CO$_2$ absorption and some of their CO$_2$ absorption capacities are even 100 times higher than traditional organic solvent (Gurkan et al., 2010; Wang et al., 2011b; Yang et al., 2011a,b; Lei et al., 2014; Cui et al., 2016; Song et al., 2017). In addition, compared with traditional ILs, anion-functioanlized ILs also exhibit higher catalytic activities even without metal catalyst (**Scheme 2**).

In 2009, Patil et al. developed an alternative method that can obtain quinazoline-2,4(1H,3H)-diones easily from CO$_2$ and 2-aminobenzonitriles by using [BMIm][OH] as catalyst (Patil et al., 2009). Except for [BMIm][OH], many inorganic bases, Et$_3$N or traditional ILs ([BMIm][BF$_4$] and [BMIm][HSO$_4$]) show weak or no activity (**Figure S11**). For the role of [BMIm][OH] in this process, they propose that [OH] will activate the 2-aminobenzonitrile to initiate the reaction, while [BMIm] can stabilize the intermediate.

To elucidate the mechanism of this reaction, Wu et al. conducts a systematic DFT calculation (Ren et al., 2011). In the beginning, the mechanism proposed by Patil et al. is calculated to be energy unfeasible. Inspired by NHCs–CO$_2$ adducts, they think these adducts might be a potential catalyst. Although the overall barrier is lower than the mechanism suggested by Patil

et al. it is also too high to be taken into consideration. Then, a new mechanism with a lower energy barrier (42.5 kcal/mol) is proposed that $[OH]^-$ initiated the reaction and the NHC, which is generated from [BMIm][OH], is the real catalyst for this process (**Figure S12**).

After that, in order to make catalyst's recycling easier, SiO_2 supported [HMIm][OH] is used by Bhanage group in the reaction of 2-aminobenzonitriles and CO_2 (Nale et al., 2014; **Figure S11**). This supported IL can be separated easily and only a minor change is found through FT-IR spectrum and surface areas analysis after using 3 times. Under optimized conditions, various electron-rich and electron-deficient groups on 2-aminobenzonitriles can react to give moderate to good yield.

Actually, imidazolium ILs are not stable under strong basicity conditions (Wang et al., 2017). Thus, many anions with weak basicity, such as acetate and azoles, are used instead of hydroxide. Han et al. discovers [Bmim][OAc] can catalyze the reaction of CO_2 and 2-aminobenzonitriles even under atmospheric pressure of CO_2 (**Figure S13**; Lu et al., 2014). Through screening different ILs, the anion in ILs is found to play a more significant role than the cation in this transformation. On the other hand, traditional organic/inorganic bases or non-functional ILs have no activity in this reaction.

Recently, Liu and coworkers utilize [BMIm][OAc] as catalyst in the cyclization of 2-aminothiophenols with CO_2 and hydrosilane (Gao et al., 2015). A variety of benzothiazoles are obtained in moderate to excellent yield in the presence of [BMIm][OAc] and CO_2 (**Figure S13**). Moreover, benzimidazoles can be also obtained in excellent yield by the same IL. Through ^1H NMR analysis, [BMIm][OAc] is found to be capable of activating CO_2, substrates and hydrosilane at the same time.

[BMIm][OAc] is found to promote the cross-link of chitosan by Guazzelli's group [**Figure S13**; (Mezzetta et al., 2017)]. Two amino groups in different chitosan chains can react with CO_2 to form urea in [BMIm][OAc]. However, no cross-linked chitosan is found when using N-methyl-2-pyrrolidone as solvent, showing the importance of ILs. Moreover, the resulting products have good stability under different conditions that would have potential utility in drug delivery.

Azole-functionalized ILs are another kind of versatile ILs that can be utilized in the absorption of different gases (Wang et al., 2011a,b; Chen et al., 2015, 2016c; Cui et al., 2016). Also in the formation of urea, Deng and co-workers investigate the performance of various ILs in the reaction of CO_2 with 1,6-hexamethylenediamine to form polyurea (Wang et al., 2016b). Since the importance of basicity of ILs is realized, $[P_{4446}][ATriz]$ is designed for this polymerization, and exhibits the best activity among the ILs used in this work (**Figure S14**).

Previous to this work, by using azole-functionalized ILs as catalysis, the group of Liu develops an efficient method to easily obtain α-ahydroxy ketones by the hydration of propargylic alcohol (Zhao et al., 2015; **Figure S15**). Azole-functionalized ILs are disclosed can promote this reaction even under atmospheric pressure of CO_2. Based on the experimental and NMR investigations, the anion in IL, $[Im]^-$, is proposed to capture CO_2 at the first and then attack the triple bond of the propargylic alcohol to start the reaction.

In this mechanism, α-alkylidene cyclic carbonate is one of intermediates. Recently, the same group discovers that this reaction can stop at α-alkylidene cyclic carbonate when in an anhydrous conditions, while $[P_{4444}][2\text{-}MIm]$ showes the highest activity (Zhao et al., 2016; **Figure S15**). More importantly, the similar reaction condition can be also utilized in other reactions, such as CO_2 with 2-aminobenzonitriles, o-phenylenediamines or 2-aminothiophenol. Since the ability to capture CO_2 from atmosphere, $[P_{4444}][2\text{-}MIm]$ is believed to absorb CO_2, then the formed carbamate intermediate would further react with substrates.

Although various kinds of substrates are suitable for this system, a high temperature (353 K) is needed to get α-alkylidene cyclic carbonate in that work. To lower down the energy demanding, they then use a new IL, $[Bu_4P]_3[2,4\text{-}OPym\text{-}5\text{-}Ac]$, as catalyst in the cyclization reaction of propargylic alcohols with CO_2 at ambient conditions (Wu et al., 2017; **Figure S15**). In addition, cations in ILs also exhibit a significant effect on this transformation, only the quaternary ammonium with C_4 chain can it have good activity.

Apart from these ILs, tungstate ILs are found to be also able to catalyze this reaction under mild conditions (Kimura et al., 2012b). Mizuno group calculates the natural bond orbital (NBO) charges of O on different tungstates at the first, and $[WO_4]^-$ is found to have more negative charges than others, suggesting that it should be the most basic among these tungstates. Then, in the reaction of 1,2-phenylenediamine with CO_2 to give 2-benzimidazolone, $[N_{4444}]_2[WO_4]$ exhibits the best performance. Importantly, quinazoline-2,4(1H,3H)-diones, cyclic carbonates, and urea derivatives can be also obtained in good to excellent yield by using $[N_{4444}]_2[WO_4]$ as catalyst. Through ^1H, ^{13}C and ^{183}W NMR spectra analysis, $[WO_4]^-$ is identified can activate not only substrates but CO_2. After that, this dual-functional role of $[WO_4]$ is also verified by DFT calculation in the reaction of CO_2 and 2-aminobenzonitriles (Kimura et al., 2012a).

Bifunctionalized Ionic Liquids

As noted above, anion-functionalized ILs can promote the CO_2 utilization because of their basicity. In many cases, however, cations in ILs are also helpful to lower down the energy barriers through forming hydrogen bond, and we call this kind of ILs as bifunctional ILs. Liu et al. have reported protic IL (PIL), $[HDBU^+][TFE]$, as catalyst that can simultaneously activate CO_2 and aminobenzonitriles to synthesize of quinazoline-2,4(1H,3H)-diones (Zhao et al., 2014). In the mechanism analysis, the hydrogen bond between [HDBU] and substrates is found to facilitate the nucleophilic attack of substrates to CO_2, which is activated by [TFE].

Using a similar IL, [DBUH][OAc], they disclose that o-phenylenediamines can react with CO_2 to obtain benzimidazolones in mild condition (Yu et al., 2013). In this reaction, three DBU-ILs with different anion and [n-Bu-DBUH][OAc] are synthesized, then the activity is showed in the order: [DBUH][Cl]< [n-BuDBU][OAc]< [DBUH][Lac]< [DBUH][OAc]. NMR spectra demonstrate that [DBUH][OAc] acts as a bifunctional catalyst: the cation [HDBU] activated effectively CO_2, while the nucleophilicity attack of

o-phenylenediamine to CO_2 is enhanced by hydrogen bond with [OAc] (**Figure S16**).

In 2014, Zheng et al. reported an IL-catalyzed route to fix CX_2 (O, S) with 2-aminobenzonitriles for the synthesis of quinazoline-2,4(1H,3H)-diones and quinazoline-2,4(1H,3H)-dithiones (Zheng et al., 2014). The ILs can be formed via the mixture of DBU and ethanol under bubbling atmospheric pressure of CO_2 or CS_2 (**Figure S17**), which act as both catalyst and solvent in CX_2 (O, S) conversion. As shown in previous, both of the cation and anion in this IL are significant in this reaction (**Figure S18**).

In 2015, Han and coworkers successfully developed a new method of synthesizing a series of 2-oxazolidinones from atmosphere CO_2 and propargylic amines by utilizing [DBUH][MIm] as both catalyst and solvent under mild conditions [**Figure S19**; (Hu et al., 2015)]. Based on the DFT investigation, [MIm]$^-$ can capture and activate CO_2, at the same time, the H atom on [DBUH]$^+$ can attack the triple bond, which promotes effectively the intramolecular cyclization step (**Figure S20**).

Subsequently, Wang and co-workers firstly realize ILs-catalyzed one-pot domino hydration of diyne alcohols to synthesize 3-(2H)-furanones (**Figure S21**), where H_2O acts as both a substrate and solvent under atmospheric pressure CO_2 (Chen et al., 2016b). This is the first time to predict the catalytic activity of ILs through quantum calculation, and [HDBU][BenIm] shows more effective on catalytic activity than other ILs. Based on NMR spectroscopic investigation and DFT calculation, both cations and anions in ILs are important to keep a moderate basicity so as to reach an excellent reactivity.

Apart from DBU-based ILs, He et al. report carboxylative cyclization of 2-aminobenzonitriles with ambient CO_2 by employing [HTMG][Im], as highly efficient and recyclable catalyst (Lang et al., 2016). This system has a broad substrate tolerance, and [HTMG][Im] exhibits excellent reusability.

Recently, Wang et al. developed an efficient strategy for generation of quinazoline-2,4(1H,3H)-diones from CO_2 through varying the cations to design hydroxyl functionalized ILs, in which the catalytic activity is affected by the basicity of cation and the hydrogen bond from cation shows great promotion for this reaction (Shi et al., 2018). The aprotic IL (2-hydroxyethyl)-trimethyl-ammonium imidazole, [Ch][Im], gives the best catalytic activity. In addition, the high yield of quinazoline 2,4-(1H,3H)-dione can be obtained under one-gram scale and flue gas simulation system using [Ch][Im] as catalyst.

CONCLUSION AND OUTLOOK

As a sustainable C_1 source, CO_2 capture and utilization is an attractive field in view of environmental protection. Lots of strategies have been developed for the utilization of CO_2, and the products have potential utility in biology and pharmacy. However, there is still a long way for most of these reactions to meet the requirement of industry, because of high cost and low efficiency. ILs-promoted CCU processes have attracted numerous attentions owning to ILs' unique properties. In most cases, ILs can be used as solvent, dehydrate, or catalyst, and these roles are similar in CCU processes. Thus, we hope to be able to shed light on all ILs-promoted CCU processes by using these limited but systematic examples. Owing to the nature of ILs, CO_2-philic functional groups, such as oxygen atoms, and amine groups, could be incorporated into the anion and/or cation in ILs. Functional ILs show great potential for the absorption and conversion of CO_2, and have been used as solvent, dehydrate, or catalyst in CCU processes. The anion-functionalized ILs exhibit better catalytic effect than the functionalization of cation part. We believe that ILs-promoted CCU protocol provides high efficient conversion of CO_2 to synthesize a series of oxazolidinones, ureas, etc. We believe this ILs-promoted CCU protocol will be widely applied in CO_2 chemistry, especially chemical utilization of CO_2 to produce added-value commodity chemicals in industry.

However, a few of interesting or important fields are still needed to explore. At first, the efficiency of these processes needs to be improved, either new efficient CO_2 utilized reaction or highly efficient and low-cost catalyst needs to be discovered. On the other hand, decreasing the cost of these reactions, such as lowering the pressure and temperature or using renewable energy (light or electricity), is a tendency for these researches. In addition, structures of ILs are related to their properties, which exhibit dramatically influence on their activity. Therefore, the investigation of the way structures affects their activity should have a profound significance in this field. Only when we obtain these answers, can we know how to design an efficient IL for specific reaction without basing on experience and experimental trial and error.

AUTHOR CONTRIBUTIONS

All authors contributed for the writing of the manuscript. L-NH designed this proposal and determined the contents. S-MX wrote the Abstract, Introduction, Ag/Ionic Liquids Catalysis, and Bifunctionalized Ionic Liquids. H-CF wrote the Cu/Ionic Liquid Catalysis and Traditional Ionic Liquids Parts. K-HC wrote Anion-Functionalized Ionic Liquids, Conclusion and Outlook. K-HC, L-NH, and S-MX revised the manuscript.

FUNDING

SUPPLEMENTARY MATERIAL

The Supplementary Material for this article can be found online at: https://www.frontiersin.org/articles/10.3389/fchem. 2018.00462/full#supplementary-material

REFERENCES

Aresta, M., Dibenedetto, A., and Angelini, A. (2014). Catalysis for the valorization of exhaust carbon: from CO$_2$ to chemicals, materials, and fuels. Technological use of CO$_2$. *Chem. Rev.* 114, 1709–1742. doi: 10.1021/cr4002758

Bates, E. D., Mayton, R. D., Ntai, I., and Davis, J. H. (2002). CO$_2$ capture by a task-specific ionic liquid. *J. Am. Chem. Soc.* 124, 926–927. doi: 10.1021/ja017593d

Blanchard, L. A., Hancu, D., Beckman, E. J., and Brennecke, J. F. (1999). Green processing using ionic liquids and CO$_2$. *Nature* 399, 28–29. doi: 10.1038/19887

Chen, K. H., Lin, W. J., Yu, X. N., Luo, X. Y., Ding, F., He, X., et al. (2015). Designing of anion-functionalized ionic liquids for efficient capture of SO$_2$ from flue gas. *AIChE J.* 61, 2028–2034. doi: 10.1002/aic.14793

Chen, K. H., Shi, G. L., Dao, R. N., Mei, K., Zhou, X. Y., Li, H. R., et al. (2016a). Tuning the basicity of ionic liquids for efficient synthesis of alkylidene carbonates from CO$_2$ at atmospheric pressure. *Chem. Commun.* 52, 7830–7833. doi: 10.1039/C6CC02853E

Chen, K. H., Shi, G. L., Zhang, W. D., Li, H. R., and Wang, C. M. (2016b). Computer-assisted design of ionic liquids for efficient synthesis of 3(2H)-furanones: a domino reaction triggered by CO$_2$. *J. Am. Chem. Soc.* 138, 14198–14201. doi: 10.1021/jacs.6b08895

Chen, K. H., Shi, G. L., Zhou, X. Y., Li, H. R., and Wang, C. M. (2016c). Highly efficient nitric oxide capture by azole-based ionic liquids through multiple-site absorption. *Angew. Chem. Int. Ed.* 55, 14362–14366. doi: 10.1002/anie.201607528

Cui, G. K., Wang, J. J., and Zhang, S. J. (2016). Active chemisorption sites in functionalized ionic liquids for carbon capture. *Chem. Soc. Rev.* 45, 4307–4339. doi: 10.1039/C5CS00462D

Fujita, S., Kanamaru, H., Senboku, H., and Arai, M. (2006). Preparation of cyclic urethanes from amino alcohols and carbon dioxide using ionic liquid catalysts with alkali metal promoters. *Int. J. Mol. Sci.* 7, 438–450. doi: 10.3390/i7100438

Gao, X., Yu, B., Yang, Z. Z., Zhao, Y. F., Zhang, H. G., Hao, L. D., et al. (2015). Ionic liquid-catalyzed C-S bond construction using CO$_2$ as a C$_1$ building block under mild conditions: a metal-free route to synthesis of benzothiazoles. *ACS Catal.* 5, 6648–6652. doi: 10.1021/acscatal.5b01874

Gu, Y. L., Shi, F., and Deng, Y. Q. (2004). Ionic liquid as an efficient promoting medium for fixation of CO$_2$: clean synthesis of alpha-methylene cyclic carbonates from CO$_2$ and propargyl alcohols catalyzed by metal salts under mild conditions. *J. Org. Chem.* 69, 391–394. doi: 10.1021/jo0351365

Gu, Y. L., Zhang, Q. H., Duan, Z. Y., Zhang, J., Zhang, S. G., and Deng, Y. Q. (2005). Ionic liquid as an efficient promoting medium for fixation of carbon dioxide: a clean method for the synthesis of 5-methylene-1,3-oxazolidin-2-ones from propargylic alcohols, amines, and carbon dioxide catalyzed by CuM under mild conditions. *J. Org. Chem.* 70, 7376–7380. doi: 10.1021/jo050802i

Gurkan, B. E., de la Fuente, J. C., Mindrup, E. M., Ficke, L. E., Goodrich, B. F., Price, E. A., et al. (2010). Equimolar CO$_2$ absorption by anion-functionalized ionic liquids. *J. Am. Chem. Soc.* 132, 2116–2117. doi: 10.1021/ja909305t

Hao, L. D., Zhao, Y. F., Yu, B., Yang, Z. Z., Zhang, H. Y., Han, B. X., et al. (2015). Imidazolium-based ionic liquids catalyzed formylation of amines using carbon dioxide and phenylsilane at room temperature. *ACS Catal.* 5, 4989–4993. doi: 10.1021/acscatal.5b01274

He, L. N., Wang, J. Q., and Wang, J. L. (2009). Carbon dioxide chemistry: examples and challenges in chemical utilization of carbon dioxide. *Pure Appl. Chem.* 81, 2069–2080. doi: 10.1351/PAC-CON-08-10-22

He, L. N., Yang, Z. Z., Liu, A. H., and Gao, J. (2010). "CO$_2$ chemistry at nankai group: catalytic conversion of CO$_2$ into value-added chemicals," in *Advances in CO$_2$ Conversion and Utilization*, ed Y. H. Hu (Washington, DC: American Chemical Society), 77–101.

Hu, J. Y., Ma, J., Lu, L. G., Qian, Q. L., Zhang, Z. F., Xie, C., et al. (2017). Synthesis of asymmetrical organic carbonates using CO$_2$ as a feedstock in AgCl/ionic liquid system at ambient conditions. *Chemsuschem* 10, 1292–1297. doi: 10.1002/cssc.201601773

Hu, J. Y., Ma, J., Zhu, Q. G., Zhang, Z. F., Wu, C. Y., and Han, B. X. (2015). Transformation of atmospheric CO$_2$ catalyzed by protic ionic liquids: efficient synthesis of 2-Oxazolidinones. *Angew. Chem. Int. Ed.* 54, 5399–5403. doi: 10.1002/anie.201411969

Jessop, P. G., Heldebrant, D. J., Li, X. W., Eckert, C. A., and Liotta, C. L. (2005). Green chemistry - reversible nonpolar-to-polar solvent. *Nat.* 436, 1102–1102. doi: 10.1038/4361102a

Jutz, F., Andanson, J. M., and Baiker, A. (2011). Ionic liquids and dense carbon dioxide: a beneficial biphasic system for catalysis. *Chem. Rev.* 111, 322–353. doi: 10.1021/cr100194q

Kimura, T., Kamata, K., and Mizuno, N. (2012a). A bifunctional tungstate catalyst for chemical fixation of CO$_2$ at atmospheric pressure. *Angew. Chem. Int. Ed.* 51, 6700–6703. doi: 10.1002/anie.201203189

Kimura, T., Sunaba, H., Kamata, K., and Mizuno, N. (2012b). Efficient [WO$_4$](2-)-catalyzed chemical fixation of carbon dioxide with 2-aminobenzonitriles to quinazoline-2,4(1H,3H)-diones. *Inorg. Chem.* 51, 13001–13008. doi: 10.1021/ic302110a

Lang, X. D., Yu, Y. C., Li, Z. M., and He, L. N. (2016). Protic ionic liquids-promoted efficient synthesis of quinazolines from 2-aminobenzonitriles and CO$_2$ at ambient conditions. *J. CO$_2$ Util.* 15, 115–122. doi: 10.1016/j.jcou.2016.03.002

Lei, Z. G., Dai, C. N., and Chen, B. H. (2014). Gas solubility in ionic liquids. *Chem. Rev.* 114, 1289–1326. doi: 10.1021/cr300497a

Li, J. A., Guo, X. G., Wang, L. G., Ma, X. Y., Zhang, Q. H., Shi, F., et al. (2010). Co(acac)$_3$/BMMImCl as a base-free catalyst system for clean syntheses of N,N'-disubstituted ureas from amines and CO$_2$. *Sci. China Chem.* 53, 1534–1540. doi: 10.1007/s11426-010-4026-8

Liu, M. S., Gao, K. Q., Liang, L., Sun, J. M., Sheng, L., and Arai, M. (2016a). Experimental and theoretical insights into binary Zn-SBA-15/KI catalysts for the selective coupling of CO$_2$ and epoxides into cyclic carbonates under mild conditions. *Catal. Sci. Technol.* 6, 6406–6416. doi: 10.1039/C6CY00725B

Liu, M. S., Lan, J. W., Liang, L., Sun, J. M., and Arai, M. (2017a). Heterogeneous catalytic conversion of CO$_2$ and epoxides to cyclic carbonates over multifunctional tri-s-triazine terminal-linked ionic liquids. *J.Catal.* 347, 138–147. doi: 10.1016/j.jcat.2016.11.038

Liu, M. S., Liang, L., Li, X., Gao, X. X., and Sun, J. M. (2016b). Novel urea derivative-based ionic liquids with dual-functions: CO$_2$ capture and conversion under metal- and solvent-free conditions. *Green Chem.* 18, 2851–2863. doi: 10.1039/C5GC02605A

Liu, M. S., Lu, X. Y., Shi, L., Wang, F. X., and Sun, J. (2017b). Periodic mesoporous organosilica with a basic urea-derived framework for enhanced carbon dioxide capture and conversion under mild conditions. *ChemSusChem* 10, 1110–1119. doi: 10.1002/cssc.201600973

Liu, Q., Wu, L. P., Jackstell, R., and Beller, M. (2015). Using carbon dioxide as a building block in organic synthesis. *Nat. Commun.* 6:5933. doi: 10.1038/ncomms6933

Lu, W. J., Ma, J., Hu, J. Y., Song, J. L., Zhang, Z. F., Yang, G. Y., et al. (2014). Efficient synthesis of quinazoline-2,4(1H,3H)-diones from CO$_2$ using ionic liquids as a dual solvent-catalyst at atmospheric pressure. *Green Chem.* 16, 221–225. doi: 10.1039/C3GC41467A

Ma, Y., Chen, C., Wang, T. F., Zhang, J. S., Wu, J. J., Liu, X. D., et al. (2017). Dialkylpyrazolium ionic liquids as novel catalyst for efficient fixation of CO$_2$ with metal- and solvent-free. *Appl. Catal. A Gen.* 547, 265–273. doi: 10.1016/j.apcata.2017.09.009

Mezzetta, A., Guazzelli, L., and Chiappe, C. (2017). Access to cross-linked chitosans by exploiting CO$_2$ and the double solvent-catalytic effect of ionic liquids. *Green Chem.* 19, 1235–1239. doi: 10.1039/C6GC02935C

Nale, D. B., Saigaonkar, S. D., and Bhanage, B. M. (2014). An efficient synthesis of quinazoline-2,4(1H)-dione from CO$_2$ and 2-aminobenzonitrile using [Hmim]OH/SiO$_2$ as a base functionalized supported ionic liquid phase catalyst. *J. CO$_2$ Util.* 8, 67–73. doi: 10.1016/j.jcou.2014.08.001

Patil, Y. P., Tambade, P. J., Deshmukh, K. M., and Bhanage, B. M. (2009). Synthesis of quinazoline-2,4(1H,3H)-diones from carbon dioxide and 2-aminobenzonitriles using [Bmim]OH as a homogeneous recyclable catalyst. *Catal. Today* 148, 355–360. doi: 10.1016/j.cattod.2009.06.010

Ren, Y., Meng, T. T., Jia, J. F., and Wu, H. S. (2011). A computational study on the chemical fixation of carbon dioxide with 2-aminobenzonitrile catalyzed by 1-butyl-3-methyl imidazolium hydroxide ionic liquids. *Comput. Theor. Chem.* 978, 47–56. doi: 10.1016/j.comptc.2011.09.032

Shi, F., Deng, Y. Q., SiMa, T. L., Peng, J. J., Gu, Y. L., and Qiao, B. T. (2003). Alternatives to phosgene and carbon monoxide: synthesis of symmetric urea derivatives with carbon dioxide in ionic liquids. *Angew. Chem. Int. Ed.* 42, 3257–3260. doi: 10.1002/anie.200351098

Shi, G. L., Chen, K. H., Wang, Y. T., Li, H. R., and Wang, C. M. (2018). Highly efficient synthesis of quinazoline-2,4(1H,3H)-diones from CO$_2$ by hydroxyl

functionalized aprotic Ionic Liquids. *ACS Sust. Chem. Eng.* 6, 5760–5765. doi: 10.1021/acssuschemeng.8b01109

Song, Q. W., and He, L. N. (2016). Robust silver(I) catalyst for the carboxylative cyclization of propargylic alcohols with carbon dioxide under ambient conditions. *Adv. Synth. Catal.* 358, 1251–1258. doi: 10.1002/adsc.201500639

Song, Q. W., Zhou, Z. H., and He, L. N. (2017). Efficient, selective and sustainable catalysis of carbon dioxide. *Green Chem.* 19, 3707–3728. doi: 10.1039/7GC00199A

Steckel, J. A. (2012). *Ab initio* calculations of the interaction between CO$_2$ and the acetate ion. *J. Phys. Chem. A* 116, 11643–11650. doi: 10.1021/jp306446d

Wang, B. S., Qin, L., Mu, T. C., Xue, Z. M., and Gao, G. H. (2017). Are ionic liquids chemically stable? *Chem. Rev.* 117, 7113–7131. doi: 10.1021/acs.chemrev.6b00594

Wang, C. M., Cui, G. K., Luo, X. Y., Xu, Y. J., Li, H. R., and Dai, S. (2011a). Highly efficient and reversible SO$_2$ capture by tunable azole-based ionic liquids through multiple-site chemical absorption. *J. Am. Chem. Soc.* 133, 11916–11919. doi: 10.1021/ja204808h

Wang, C. M., Luo, X. Y., Luo, H. M., Jiang, D. E., Li, H. R., and Dai, S. (2011b). Tuning the basicity of Ionic liquids for equimolar CO$_2$ capture. *Angew. Chem. Int. Ed.* 50, 4918–4922. doi: 10.1002/anie.201008151

Wang, M. Y., Song, Q. W., Ma, R., Xie, J. N., and He, L. N. (2016a). Efficient conversion of carbon dioxide at atmospheric pressure to 2-oxazolidinones promoted by bifunctional Cu(II)-substituted polyoxometalate-based ionic liquids. *Green Chem.* 18, 282–287. doi: 10.1039/C5GC02311D

Wang, P. X., Ma, X. Y., Li, Q. H., Yang, B. Q., Shang, J. P., and Deng, Y. Q. (2016b). Green synthesis of polyureas from CO$_2$ and diamines with a functional ionic liquid as the catalyst. *RSC Adv.* 6, 54013–54019. doi: 10.1039/C6RA07452A

Wang, T. F., Zheng, D. N., Zhang, J. S., Fan, B. W., Ma, Y., Ren, T. G., et al. (2018). Protic pyrazolium ionic liquids: an efficient catalyst for conversion of CO$_2$ in the absence of metal and solvent. *ACS Sust. Chem. Eng.* 6, 2574–2582. doi: 10.1021/acssuschemeng.7b04051

Wu, Y. Y., Zhao, Y. F., Li, R. P., Yu, B., Chen, Y., Liu, X. W., et al. (2017). Tetrabutylphosphonium-based ionic liquid catalyzed CO$_2$ transformation at ambient conditions: a case of synthesis of alpha-alkylidene cyclic carbonates. *ACS Catal.* 7, 6251–6255. doi: 10.1021/acscatal.7b01422

Yang, Z. Z., He, L. N., Gao, J., Liu, A. H., and Yu, B., (2012). Carbon dioxide utilization with C–N bond formation: carbon dioxide capture and subsequent conversion. *Energy Environ. Sci.* 5, 6602. doi: 10.1039/c2ee02774g

Yang, Z. Z., He, L. N., Zhao, Y. N., Li, B., and Yu, B. (2011a). CO$_2$ capture and activation by superbase/polyethylene glycol and its subsequent conversion. *Energy Environ. Sci.* 4, 3971–3975. doi: 10.1039/c1ee02156g

Yang, Z. Z., Zhao, Y. N., and He, L. N. (2011b). CO$_2$ chemistry: task-specific ionic liquids for CO$_2$ capture/activation and subsequent conversion. *RSC Adv.* 1, 545–567. doi: 10.1039/c1ra00307k

Yu, B., Zhang, H. Y., Zhao, Y. F., Chen, S., Xu, J. L., Hao, L. D., et al. (2013). DBU-based ionic-liquid-catalyzed carbonylation of o-phenylenediamines with CO$_2$ to 2-benzimidazolones under solvent-free conditions. *ACS Catal.* 3, 2076–2082. doi: 10.1021/cs400256j

Yuan, Y., Xie, Y., Zeng, C., Song, D. D., Chaemchuen, S., Chen, C., et al. (2017). A recyclable AgI/OAc$^-$ catalytic system for the efficient synthesis of α-alkylidene cyclic carbonates: carbon dioxide conversion at atmospheric pressure. *Green Chem.* 19, 2936–2940. doi: 10.1039/C7GC00276A

Zhang, Q. H., Shi, F., Gu, Y. L., Yang, J., and Deng, Y. Q. (2005). Efficient and eco-friendly process for the synthesis of N-substituted 4-methylene-2-oxazolidinones in ionic liquids. *Tetrahedron Lett.* 46, 5907–5911. doi: 10.1016/j.tetlet.2005.06.116

Zhang, S. J., Sun, N., He, X. Z., Lu, X. M., and Zhang, X. P. (2006). Physical properties of ionic liquids: database and evaluation. *J. Phys. Chem. Ref. Data* 35, 1475–1517. doi: 10.1063/1.2204959

Zhang, Z. F., Xie, E., Li, W. J., Hu, S. Q., Song, J. L., Jiang, T., et al. (2008). Hydrogenation of carbon dioxide is promoted by a task-specific ionic liquid. *Angew. Chem. Int. Ed.* 47, 1127–1129. doi: 10.1002/anie.200704487

Zhao, Y. F., Wu, Y. Y., Yuan, G. F., Hao, L. D., Gao, X., Yang, Z. Z., et al. (2016). Azole-anion-based aprotic ionic liquids: functional solvents for atmospheric CO$_2$ transformation into various heterocyclic compounds. *Chem. Asian J.* 11, 2735–2740. doi: 10.1002/asia.201600281

Zhao, Y. F., Yang, Z. Z., Yu, B., Zhang, H. Y., Xu, H. J., Hao, L. D., et al. (2015). Task-specific ionic liquid and CO$_2$-cocatalysed efficient hydration of propargylic alcohols to alpha-hydroxy ketones. *Chem. Sci.* 6, 2297–2301. doi: 10.1039/C5SC00040H

Zhao, Y. F., Yu, B., Yang, Z. Z., Zhang, H. Y., Hao, L. D., Gao, X., et al. (2014). A protic ionic liquid catalyzes CO$_2$ conversion at atmospheric pressure and room temperature: synthesis of quinazoline-2,4-(1H,3H)-diones. *Angew. Chem. Int. Ed.* 53, 5922–5925. doi: 10.1002/anie.201400521

Zheng, H., Cao, X., Du, K., Xu, J., and Zhang, P. (2014). A highly efficient way to capture CX$_2$ (O, S) mildly in reusable ReILs at atmospheric pressure. *Green Chem.* 16, 3142–3148. doi: 10.1039/c4gc00190g

CO$_2$ Electroreduction in Ionic Liquids

Deonildo Faggion Jr., Wellington D. G. Gonçalves and Jairton Dupont*

Laboratory of Molecular Catalysis, Institute of Chemistry, Universidade Federal do Rio Grande do Sul, Porto Alegre, Brazil

CO$_2$ electroreduction is among the most promising approaches used to transform this green-house gas into useful fuels and chemicals. Ionic liquids (ILs) have already proved to be the adequate media for CO$_2$ dissolution, activation, and stabilization of radical and ionic electrochemical active species in aqueous solutions. In general, IL electrolytes reduce the overpotential, increase the current density, and allow for the modulation of solution pH, driving product selectivity. However, little is known about the main role of these salts in the CO$_2$ reduction process the assumption that ILs form solvent-separated ions. However, most of the ILs in solution are better described as anisotropic fluids and display properties of an extended cooperative network of supramolecular species. That strongly reflects their mesoscopic and nanoscopic organization, inducing different processes in CO$_2$ reduction compared to those observed in classical electrolyte solutions. The major aspects concerning the relationship between the structural organization of ILs and the electrochemical reduction of CO$_2$ will be critically discussed considering selected recent examples.

Keywords: ionic liquids, carbon dioxide, electrochemistry, reduction, oxidation

INTRODUCTION

The reduction of atmospheric carbon dioxide (CO$_2$) is one of the major challenges of modern life. This is due to the atmospheric increase in this gas by contemporary industrial activity and its contribution to possible global warming issues, the consequences of which can affect the future generation (Mac Dowell et al., 2017). Hence, alternative sources of energy that decrease the use of fossil fuels, as well as the reduction of the CO$_2$ concentration in the air atmosphere, are required. One of the most elegant ways to achieve this objective is the catalytic transformation of CO$_2$ into C1 feedstocks and fuels.

Efforts have been undertaken to use the sustainable energy of sunlight, directly or indirectly, to convert CO$_2$ by photocatalytic chemistry (Sasirekha et al., 2006; Habisreutinger et al., 2013; Dong et al., 2018; Lin et al., 2018), electrochemical (Dong et al., 2018; Francke et al., 2018; Resasco et al., 2018; Yuan et al., 2018), and photo-electrochemical approaches (Barton et al., 2008; Kaneco et al., 2009; Sahara et al., 2016). For a sustainable and high energy efficiency process, CO$_2$ electrochemical reduction reaction (CO$_2$ERR) is expected to exhibit a high Faradaic efficiency at a low overpotential. In this vein, ionic liquids (ILs) are among the most promising materials under investigation due their unique physico-chemical properties.

This is mainly due to IL selectivity and relatively high CO$_2$ absorption capacity, as well as their ability to stabilize charged CO$_2$ species (Shkrob and Wishart, 2009). ILs also present a wide electrochemical window (Hayyan et al., 2013), thermal and chemical stability (Cao and Mu, 2014), negligible volatility (Anthony et al., 2001), and possible use as electron transfer mediators for redox catalysis (Balasubramanian et al., 2006), which makes them an interesting alternative to promote the CO$_2$ERR. The technology for using CO$_2$ as a renewable energy carrier is still far from practical application, making the design of novel electrochemistry technologies using ILs for the CO$_2$ERR a "hot" field for recent research.

The real challenge for sustainable and high energy efficiency processes, and turning them into practical alternatives, is to develop a way to lower the energy barrier for CO$_2$ERR due to the high stability of this compound. Decreasing the overvoltage of the reaction as much as possible will make the CO$_2$ fixation costs low enough for practical use (Haran et al., 1998).

The objective of the present review is to highlight the use of ILs for CO$_2$ERR, and the influence in the reactions that have been attempted to this purpose. CO$_2$ERR using ILs is able to provide high product selectivity and conversion efficiency (Alvarez-Guerra et al., 2015) **(Table 1)**. There are several reviews on electrochemistry in ILs, but the main aspects related to the roles of these fluids are only marginally treated for specific applications (Buzzeo et al., 2004; Silvester and Compton, 2006; Hapiot and Lagrost, 2008; Ohno and Fukumoto, 2008; Rees and Compton, 2011).

The role of the IL has been described as mainly absorbing CO$_2$ and stabilizing the CO$_2^{\bullet-}$ (radical anion) that is related to the electronic properties imposed by both the cation and anion. It appears that in ILs containing basic anions the role of the IL is not only related to the formation and stabilization of CO$_2^{\bullet-}$, but also the pH control of the reaction mixture. We will first briefly discuss the structural organization of bare ILs and solutions of ILs. Second, the formation and stabilization of CO$_2^-$ in solutions (aqueous and organic) of ILs associated with non-basic anions will be addressed. Thirdly, CO$_2$ERR employing ILs containing basic anions, in which the role of bicarbonate and buffering will be detailed. Finally, the influence of the macroscopic and nanoscopic properties of ILs in solution on CO$_2$ diffusion and electrochemical activation are discussed considering the most recently published results.

BARE ILS AND IL SOLUTIONS

The well-known and unique physical-chemical properties cited above are attributed to the structural organization of bare ILs, which are highly ordered fluids described as a well-organized hydrogen-bonded polymeric supramolecular structure in the solid, liquid phase and is apparently maintained to a great extent even in the gas phase. The most investigated classes of ILs are imidazolium salts, and their properties can be finely tuned by varying the N-alkylimidazolium substituents (Dupont, 2004).

However, taking into account that water-free ILs are extremely difficult to obtain, it is expected that even traces of water may present a profound effect on the organization and reactivity of ILs at the nanoscopic level. Hence, it is important to consider the presence of water when employing and analyzing physico-chemical IL properties (Zanatta et al., 2016).

In the case of an aqueous system, the values of standard reduction potentials (SRP) can be influenced by the water and proton concentration. This effect can be derived from the activity coefficients of the water and protons in solution. The consequence of 18 mol% water in 1-butyl-3-methylimidazolium tetrafluoroborate ([BMIM][BF$_4$]) is a 6 mV shift of the SRP for the bare IL, and the addition of 0.1 M HCl shifts the SRP by 28 mV (Kim et al., 2004; Matsubara et al., 2015). This

effect causes an imprecise determination of the real SRP in CO$_2$ERR, resulting in lower overpotentials in comparison to the real decreasing overpotential, making a precise comparison impossible (Matsubara et al., 2015).

When other molecules are introduced into this organization, a disruption of the hydrogen bond network occurs, generating nanostructures with polar and non-polar regions. Under this condition, the concept of polarity of the solvent, generally used to describe other solvents, cannot be applied to ILs (Dupont, 2004). This collapsed macrostructure starts to form contact ion pair structures, and in an infinite diluted solution can form a solvent-separated ion pair network (Stassen et al., 2015).

There is a general misunderstanding when correlating the physical-chemical properties attributed to bare ILs when the studies are made in a different concentration regime, i.e., with the addition of other species or solvents in the media (MacFarlane et al., 2017).

CO$_2^{\bullet-}$ RADICAL IN ILS

After the confirmation in 2007 that ILs are able to boost organic carbonate synthesis by electrochemistry under ambient conditions (Zhang et al., 2008) **(Table 1**, entry 1), CO$_2$ERR with ILs has grown exponentially due to the kinetic effects that minimize the energy necessary for intermediate CO$_2^{\bullet-}$ formation.

The 1-ethyl-3-methyl-imidazolium trifluorochloroborate ([EMIM][BF$_3$Cl]) IL can bind to CO$_2$ through a Lewis base adduct, becoming active for CO$_2$ERR and showing a high faradaic efficiency at low overpotentials (Snuffin et al., 2011) **(Table 1**, entry 2). The capability of lowering the overpotential for CO$_2$ERR was also confirmed when using [EMIM][BF$_4$] to "stabilize" CO$_2^{\bullet-}$ (Rosen et al., 2011).

The studies presented in this review have shown that ILs are among the most efficient materials as both electrolytes and active functionalized materials for CO$_2$ERR. Therefore, they may constitute a key compound in the development of new technologies for large-scale applicability. The most recent report showed that methylimidazolium groups can be attached to the periphery of an iron porphyrin, providing a pre-organized environment that presents excellent selectivity for CO production at low overpotentials, with water as a solvent and proton source (Khadhraoui et al., 2018).

However, until now, the precise mechanisms by which ILs decrease the overpotential have not been completely elucidated. In many cases, even the global electrochemical reactions were not clarified, making it difficult to determine the SRP and the real decrease in the reaction overpotential. It can be demonstrated by the simple modification of the imidazolium cation, able to act like a proton source to the CO$_2$RR (Matsubara et al., 2015), and changes the equilibrium potential of the CO$_2$/CO acting.

The lifetime of a radical is one important factor for the major efficiency in CO$_2$ERR. The lifetime of CO$_2^{\bullet-}$ was

TABLE 1 | Selected examples of CO$_2$ERR employing ionic liquids.

Entry	Electrode	Onset potential (V)	Electrolysis potential (V)	Faradaic efficiency product (%)	Current density (mA cm^{-2})	Electrolyte	References
1	Ag	reductive peak −1.61 V vs. Ag/AgI	−1.80 V vs. Ag/AgI	dimethyl carbonate (74)	charge passed, 1.0 F.mol^{-1}	Bare [BMIM][BF$_4$]	Zhang et al., 2008
2	Pt disk	reductive peak −1.8 V vs. silver wire	−1.8 V vs. silver wire	n/a	5.7	[EMIM][BF$_3$Cl]	Snuffin et al., 2011
3	Au	n/a	−1.16 vs. Ag/AgCl	CO (85)	7	0.1 mol dm^{-3} KHCO$_3$	Ohmori et al., 2001
4	Ag	n/a	−1.50 vs. cell potencial	CO (96)	n/a	18% [EMIM][BF$_4$] in water	Rosen et al., 2011
5	Bi-CMEC	−1.80 vs. SCE	−2.00 vs. SCE	CO (82)	31	[EMIM][PF$_6$]	Medina-Ramos et al., 2014
6	Bi-CMEC	−1.80 vs. SCE	−2.00 vs. SCE	CO (82)	26	[EMIM][BF$_4$]	Medina-Ramos et al., 2014
7	Bi-CMEC	−1.80 vs. SCE	−2.00 vs. SCE	CO (79)	17	[BMIM][Cl]	Medina-Ramos et al., 2014
8	Bi-CMEC	−1.80 vs. SCE	−2.00 vs. SCE	CO (74)	20	[BMIM][Br]	Medina-Ramos et al., 2014
9	Bi-CMEC	−1.80 vs. SCE	−2.00 vs. SCE	CO (87)	25	[BMIM][OTf]	Medina-Ramos et al., 2014
10	Imidazole incorporated into a phosphonium-type IL-modified Au electrode	−0.32 vs. Ag/AgCl	−0.80 vs. Ag/AgCl	CH$_3$OH (9) HCOOH (30) CO (5)	0.095	0.1 mol dm^{-3} NaClO$_4$	Iijima et al., 2018
11	Pb	−2.30 vs. Ag/AgNO$_3$	−2.40 vs. Ag/AgNO$_3$	Oxalate (78) CO (10)	0.6	0.1 mol dm^{-3} TEAP/ACN	Sun et al., 2014
12	Pb	−2.12 vs. Ag/AgNO$_3$	−2.25 vs. Ag/AgNO$_3$	Carboxylate (55) CO (42)	0.6	0.1 mol dm^{-3} [EMIM][NTf$_2$]/ACN	Sun et al., 2014
13	MoO$_2$/Pb	−2.22 vs. Fc/Fc+	−2.45 vs. Fc/Fc+	HCO$_2^-$ (38) C$_2$O$_4^{2-}$ (6) CO (41)	20	0.3 M [BMIM][PF$_6$] in ACN	Oh and Hu, 2015
14	MoO$_2$/Pb	−2.22 vs. Fc/Fc+	−2.45 vs. Fc/Fc+	HCO$_2^-$ (18) C$_2$O$_4^{2-}$ (5) CO (60) H$_2$ (12)	n/a	0.3 mol dm^{-3} [BMIM][PF$_6$] in ACN + 0.1 mol dm^{-3} water	Oh and Hu, 2015
15	MoO$_2$/Pb	−2.22 vs. Fc/Fc+	−2.45 vs. Fc/Fc+	HCO$_2^-$ (10) C$_2$O$_4^{2-}$ (5) CO (52) H$_2$ (25)	n/a	0.3 mol dm^{-3} [BMIM][PF$_6$] in ACN + 0.2 mol dm^{-3} water	Oh and Hu, 2015
15	MoO$_2$/Pb	−2.22 vs. Fc/Fc+	−2.45 vs. Fc/Fc+	HCO$_2^-$ (6) C$_2$O$_4^{2-}$ (4) CO (51) H$_2$ (29)	n/a	0.3 mol dm^{-3} [BMIM][PF$_6$] in ACN + 0.3 mol dm^{-3} water	Oh and Hu, 2015
16	Ag	∼ −0.62 vs. Ag/AgNO$_3$	−0.70 vs. Ag/AgNO$_3$	HCO$_2^-$ (95)	Charge (10 C)	0.1 mol dm^{-3} [P$_{66614}$][124Triz] in ACN + 0.7 mol dm^{-3} of water	Hollingsworth et al., 2015
17	Ag	∼ −0.62 vs. Ag/AgNO$_3$	−1.90 vs. Ag/AgNO$_3$	HCO$_2^-$ (6) CO (6) H$_2$ (41)	Charge (10 C)	0.1 mol dm^{-3} [P$_{66614}$][124Triz] in ACN + 0.7 mol dm^{-3} of water	Hollingsworth et al., 2015
18	Ag	reductive peak −1.5 V vs. Cc+/Cc	n/a	n/a	0.7 mA.cm^{-2}	Bare [PMIM][NTf$_2$]	Tanner et al., 2016

(Continued)

TABLE 1 | Continued

Entry	Electrode	Onset potential (V)	Electrolysis potential (V)	Faradaic efficiency product (%)	Current density (mA cm^{-2})	Electrolyte	References
19	Ag	reductive peak −1.5 V vs. Cc+ /Cc	n/a	n/a	−1.5	Bare [EMIM][NTf$_2$]	Tanner et al., 2016
20	Ag	reductive peak (−1.1 V vs. Cc$^+$/Cc)	n/a	n/a	−1.60	Bare [BMIM][NTf$_2$]	Tanner et al., 2016
21	Ag	reductive peak −1.05 V vs. Cc+ /Cc	n/a	n/a	−1.5	Bare[BMIM][NTf$_2$]	Tanner et al., 2016
22	Ag	reductive peak −1.05 V vs. Cc+ /Cc	n/a	n/a	−0.8	Bare [BMIM][BF$_4$]	Tanner et al., 2016
23	Ag	reductive peak −1.6 V vs. Cc+ /Cc	n/a	n/a	0.75	Bare [BMIM][FAP]	Tanner et al., 2016
24	Ag	−2.20 V vs. Fc+/Fc	−2.4 V vs. Fc+/Fc	n/a	∼10.0	0.1 M [Bu$_4$N][PF$_6$] + 0.02 M [Ethyl 2-Methyl Imimidazolium][BF$_4$] +	Lau et al., 2016
25	Ag	−2.15 V vs. Fc+/Fc	−2.4 V vs. Fc+/Fc	n/a	∼16.0	0.1 M [Bu$_4$N][PF$_6$] + 0.02 M [Ethyl 2,3-dimethyl Imimidazolium][BF$_4$]	Lau et al., 2016
26	Ag	−2.30 V vs. Fc+/Fc	−2.4 V vs. Fc+/Fc	n/a	∼5.5	0.1 M [Bu$_4$N][PF$_6$] + 0.02 M [Ethyl 2,3,4,5-tetramethyl Imimidazolium][BF$_4$][BF$_4$]	Lau et al., 2016

determined by pulse radiolysis time-resolved resonance Raman spectroscopy to be 10 ns (Janik and Tripathi, 2016). Furthermore, the dynamic effect of recombination depends on the surroundings **(Figure 1A)**. A change in the surroundings is possible by an alteration of the ILs (Strehmel, 2012).

The physical absorption of CO$_2$ is possible because of the ability of ILs to confine CO$_2$ inside cavities near alkyl groups and aromatic protons (H4 and H5) of the IL, an interaction that does not compete with the interaction of the IL counter ion (Corvo et al., 2013).

ILs also play a role similar to surfactants near the electrode **(Figure 1D)**, where imidazolium cations help the stabilization of CO2$^{\bullet-}$, avoiding the dimerization process, inhibiting oxalate production, favoring CO, and decreasing the overpotential (Sun et al., 2014) **(Table 1**, entry 11–12).

According to a proposed mechanism (Duong et al., 2004), ILs can chemically adsorb CO$_2$ through a carboxylation process on the imidazolium C2 position for the decreases in CO$_2$ERR overpotential and posterior formation of CO. Following this mechanism, other CO$_2$ERR studies were made with the IL C2 position protected with a methyl group to avoid the carboxylation process (Sun et al., 2014). Higher CO formation was observed, indicating that the process does not depend exclusively on carboxylation of the C2 position.

BASIC ILS AND THE BICARBONATE EFFECT

Anion basicity is also an important issue. By adjusting this property, it is possible to obtain high adsorption values and, in some cases, a positive effect in the presence of water (Wang et al., 2011; Taylor et al., 2015). Reversible carbonate formation when using gas mixture ILs has already been proposed, considering that CO$_2$ capture can form bicarbonate species in solution (Ma et al., 2011; Anderson et al., 2015). Bicarbonate species formation is more efficient and more frequent than expected when there is water contribution to the reactivity and self-organization of ILs, providing a third kind of sorption mechanism (Simon et al., 2017; Qadir et al., 2018).

The absorption parameters of CO$_2$ by ILs can make efficient diffusion mass transport to the electrode surface with high adsorption possible. There are two main processes of CO$_2$ adsorption by ILs: non-covalent interactions, i.e., physical adsorption of CO$_2$, mainly in ILs with non-basic nucleophilic anions, such as hexafluorophosphate and bis(trifluoromethyl) sulphonyl amide **(Figure 1A)**, and chemical adsorption by carboxylation and CO$_2$ conversion to bicarbonate in proton-rich media, occurring mainly in ILs with acid protons for easy deprotonation and basic anions, such as acetate and imidazolium **(Figure 1B)** (Simon et al., 2017).

FIGURE 1 | (A) CO$_2$ adsorption phenomena in ILs, **(B)** bicarbonate equilibrium for the acetate anion in the presence of water and CO$_2$, **(C)** Effect of lower viscosity and higher current density in ILs solutions and **(D)** a supramolecular-like effect near the electrode.
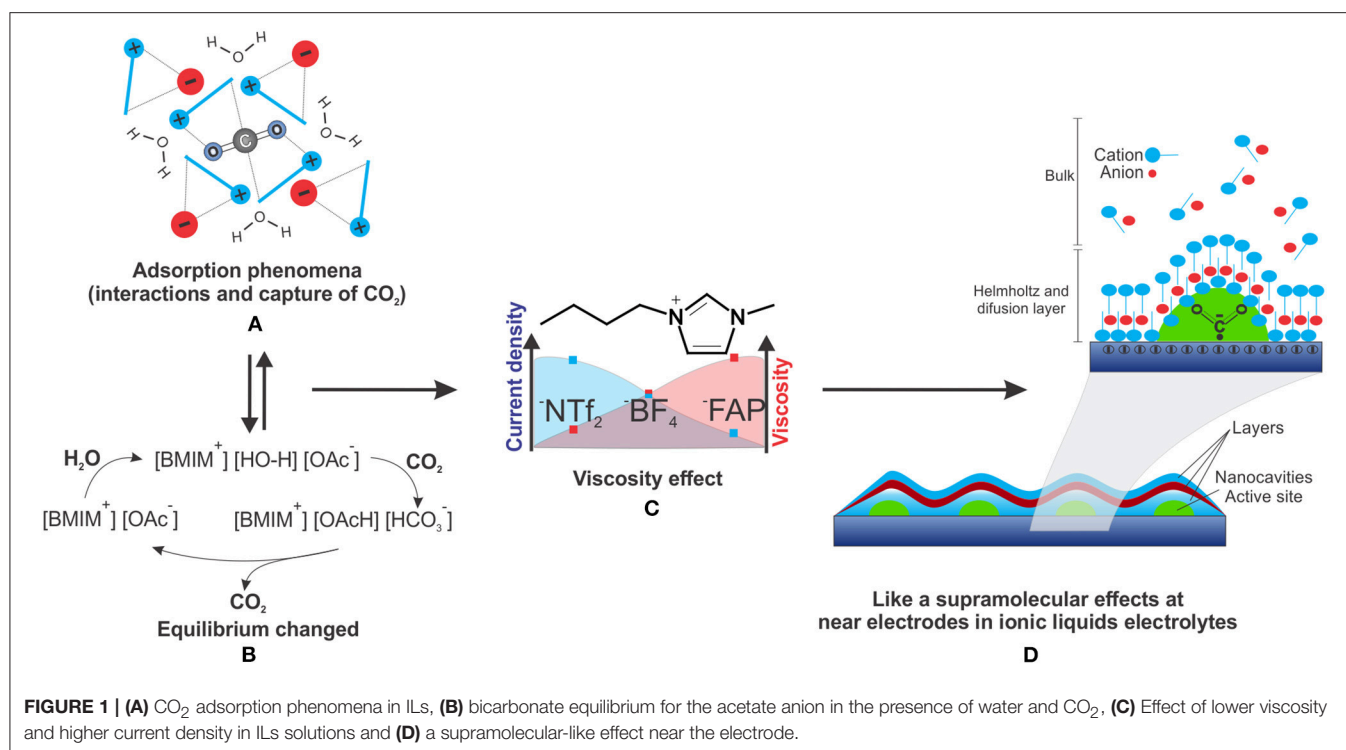
The role of water on CO$_2$ERR has been described (Simon et al., 2017), where depending on the IL anion structure, the reaction of CO$_2$ with the confined and "activated" water can shift the equilibrium to bicarbonate **(Figure 1B)**. Water activation can even occur in some IL aqueous solutions that act as a neutral base catalyst as well as a proton buffer.

In the same study, it was also reported that basic ILs with acetate and imidazolate anions in aqueous solutions can have buffer properties. It is possible, considering that the retained water molecules by the contact ion couple are active and react reversibly with CO$_2$, to form bicarbonate species in solution. Therefore, water and CO$_2$ are active species in these solutions and can modify the mechanistic steps from the bicarbonate formation.

NEAR ELECTRODE ORGANIZATION ILS

For desired applications, better understanding of the self-organization of ILs is crucial. Some properties, such as viscosity, conductivity, polarity, and thermic properties, are important for better understanding the ILs influences on the radical stabilization process for CO$_2$ERR (Strehmel, 2012).

The diffusion of species in ILs may be strongly affected by both the macroscopic viscosity of ILs and molecular parameters related to structural phenomena, like the microviscosity (Yago and Wakasa, 2011; Strehmel, 2012). These regions play an important role when confining species near the electrode in the Helmholtz plane and diffusion layer, favoring synergistic effects capable of inducing and catalyzing specific reactions.

It was proposed that the reduction in the overpotential for CO$_2$ERR when using [EMIM][BF$_4$] was a result of the cation complexing with CO$_2^{\bullet-}$ (Rosen et al., 2011). Indeed, when using 1-butyl-1-methylpyrrolodinium, a cation unable to realize π- π interactions (Tanner et al., 2016) (**Table 1**, entries 18–23), the overpotential decreases at comparable value than using cations able to realize it. This suggests that the interaction previously proposed by Rosen et al. (2011) is probably unlikely in the reduction of the overpotential. This leads to another assumption proposed by a different mechanism, which is an inner-sphere process (Tanner et al., 2016). This mechanism involves the previous desorption of the cation from the silver electrode surface, allowing CO$_2$ to access the surface, before the irreversible CO$_2$ERR. However, it is assumed in this case that ILs are free ions and not structured as ion pairs and aggregates, as usually observed in solution (Stassen et al., 2015).

When the anion of the [BMIM] IL was varied, the current density increase was observed in the following order: 1-butyl-3-methylimidazolium tris(pentafluoroethyl)trifluorophosphate ([BMIM][FAP]), [BMIM][BF$_4$], and 1-butyl-3-methylimidazolium bis(trifluoromethylsulfonyl)imide ([BMIM][NTf$_2$]) (Tanner et al., 2016) (**Figure 1C**). For the [BMIM] ILs with different anions the increase of density current (at high dilution) follows the same trend of viscosity decreasing (at low dilution) (Paduszynski and Domanska, 2014).

Such effects are also observed when varying the IL cation, with the same trend of increasing current density with the decrease in viscosity **(Figure 1C)** (Reche et al., 2014).

The solubility of CO$_2$ in conventional ILs, such as [BMIM] and [EMIM], can increase according to the alkyl chain increase

(Reche et al., 2014). The solubility is also correlated with the anion nature, increasing with the fluorination nature from the anion, indicating that CO$_2$ solubility increases with charge delocalization.

The viscosity effect on lifetime, mobility, dimerization, and radical coordination in ILs was evaluated (Strehmel, 2012), where the radical lifetime and the recombination dynamic are extremely dependent on the environment. An example of this recombination is that the increase in the IL concentration caused a decrease in oxalate production from CO$_2$ERR and an increase in CO (Sun et al., 2014). This indicated that the IL was able to immobilize CO$_2^{\bullet-}$ at the electrode surface, making the dimerization process more difficult and, consequently, decreasing oxalate production.

The interaction between [IM]$^+$ and CO$_2^{\bullet-}$ was also studied (Lau et al., 2016) and the 4 and 5 positions of [IM]$^+$ were able to make hydrogen bonds with the radical, providing higher current density compared to the substituted [IM]$^+$ at the same positions (**Table 1**, entries 24–26).

The radical stabilization, increase in lifetime, mobility, and the observation that ILs of [IM]$^+$ can promote hydrogen bonds with the radical lead to the idea that reactive microregions could be formed at the electrode surface.

The concept of microregions was demonstrated through theoretical calculations (Lim et al., 2018), wherein the formation of microenvironments promotes the formation of a "cage" capable of promoting CO$_2$ERR. It was also demonstrated through calculations that instead of the conventional idea of an intermolecular bond between the IL and CO$_2^{\bullet-}$, the microregion effect promotes better catalytically efficiency, even in diluted conditions. This mechanism suggests that even in high diluted solutions, there is an important relationship between the volume properties, such as resistance, solubility, gas diffusivity, and viscosity.

This corroborates the idea of a microenvironment, similar to the supramolecular structures formed in low diluted ILs. The increase in IL concentration near the electrode surface was proven by the Helmholtz and diffusion layer, which considerably increases the electrolyte concentration in this region (**Figure 1D**).

The idea that the electric field effect at near electrode surface leads to a local rise of the IL concentration (Lim et al., 2018), is supported by the relationship among current density, viscosity, reduction of dimerization effect, and microenvironments formation.

These increases in concentration, even in diluted solutions, are able to induce the formation of a thin organized structure on the double layer region and diffusion layer, promoting considerable local concentration increase in the solution (Yochelis et al., 2015).

The concept presented here brings a new point of view to CO$_2$ERR based on concepts already known regarding the supramolecular structures of ILs, taking a step forward toward the precise determination of the CO$_2$ERR mechanism in ILs based on macro and microstructuration.

CONCLUSIONS

For CO$_2$ERR, ILs play a significant role due their distinct physical chemistry properties, the tuning of the reactions conditions, the assistance with CO$_2^{\bullet-}$ stabilization, the decrease in overpotential, and the increase in faradaic efficiency and current density.

The basicity of the anion has been shown to play an important role in CO$_2$ERR, helping to obtain high adsorption values and positive effects in the presence of water. The CO$_2$ capture and formation of bicarbonate species combined with the reactivity and self-organization of ILs can exhibit a different sorption process in proton-rich media, occurring mainly in ILs with acid protons and basic anions, such as acetate and imidazolate. This equilibrium with bicarbonate can be shifted with confined water activation by the IL anion structure, which acts like a neutral base catalyst as well as a proton buffer.

ILs have shown notorious participation in CO$_2$ERR, being involved in distinct ways, from diluted to bare ILs. This capacity of self-organization is able to confine species and favor synergistic effects that are capable of inducing and catalyzing specific reactions. When ILs are exposed to an electric field in the case of electrocatalysis, the cited self-organization is able to form a microenvironment, even in diluted conditions, increasing the IL concentration near the electrode surface.

Further efforts are needed for understanding the global reaction mechanism, with the aim of improving the research and helping solve atmospheric CO$_2$ problems, especially with regards to the generation of clean energy carriers.

AUTHOR CONTRIBUTIONS

All authors listed have made a substantial, direct and intellectual contribution to the work, and approved it for publication.

ACKNOWLEDGMENTS

REFERENCES

Alvarez-Guerra, M., Albo, J., Alvarez-Guerra, E., and Irabien, A. (2015). Ionic liquids in the electrochemical valorisation of CO$_2$. *Energy Environ. Sci.* 8, 2574–2599. doi: 10.1039/c5ee01486g

Anderson, K., Atkins, M. P., Estager, J., Kuah, Y., Ng, S., Oliferenko, A. A., et al. (2015). Carbon dioxide uptake from natural gas by binary ionic liquid–water mixtures. *Green Chem.* 17, 4340–4354. doi: 10.1039/c5gc00720h

Anthony, J. L., Maginn, E. J., and Brennecke, J. F. (2001). Solution thermodynamics of imidazolium-based ionic liquids and water. *J. Phys. Chem. B* 105, 10942–10949. doi: 10.1021/jp0112368

Balasubramanian, R., Wang, W., and Murray, R. W. (2006). Redox ionic liquid phases: ferrocenated imidazoliums. *J. Am. Chem. Soc.* 128, 9994–9995. doi: 10.1021/ja0625327

Barton, E. E., Rampulla, D. M., and Bocarsly, A. B. (2008). Selective solar-driven reduction of CO$_2$ to methanol using a catalyzed p-GaP

based photoelectrochemical cell. *J. Am. Chem. Soc.* 130, 6342–6344. doi: 10.1021/ja0776327

Buzzeo, M. C., Evans, R. G., and Compton, R. G. (2004). Non-haloaluminate room-temperature ionic liquids in electrochemistry–a review. *Chemphyschem* 5, 1106–1120. doi: 10.1002/cphc.200301017

Cao, Y., and Mu, T. (2014). Comprehensive Investigation on the thermal stability of 66 ionic liquids by thermogravimetric analysis. *Ind. Eng. Chem. Res.* 53, 8651–8664. doi: 10.1021/ie5009597

Corvo, M. C., Sardinha, J., Menezes, S. C., Einloft, S., Seferin, M., Dupont, J., et al. (2013). Solvation of carbon dioxide in [C4 mim][BF(4)] and [C(4) mim][PF(6)] ionic liquids revealed by high-pressure NMR spectroscopy. *Angew. Chem. Int. Ed.* 52, 13024–13027. doi: 10.1002/anie.201305630

Dong, Y., Ghuman, K. K., Popescu, R., Duchesne, P. N., Zhou, W., Loh, J. Y. Y., et al. (2018). Tailoring surface frustrated lewis pairs of In$_2$O$_{3-x}$ (OH)$_y$ for gas-phase heterogeneous photocatalytic reduction of CO$_2$ by isomorphous substitution of In^{3+} with Bi^3. *Adv. Sci.* 5:1700732. doi: 10.1002/advs.201700732

Duong, H. A., Tekavec, T. N., Arif, A. M., and Louie, J. (2004). Reversible carboxylation of N-heterocyclic carbenes. *Chem. Commun.* 1, 112–113. doi: 10.1039/b311350g

Dupont, J. (2004). On the solid, liquid and solution structural organization of imidazolium ionic liquids. *J. Braz. Chem. Soc.* 15, 341–350. doi: 10.1590/s0103-50532004000300002

Francke, R., Schille, B., and Roemelt, M. (2018). Homogeneously catalyzed electroreduction of carbon dioxide-methods, mechanisms, and catalysts. *Chem. Rev.* 118, 4631–4701. doi: 10.1021/acs.chemrev.7b00459

Habisreutinger, S. N., Schmidt-Mende, L., and Stolarczyk, J. K. (2013). Photocatalytic reduction of CO$_2$ on TiO$_2$ and other semiconductors. *Angew. Chem. Int. Ed.* 52, 7372–7408. doi: 10.1002/anie.201207199

Hapiot, P., and Lagrost, C. (2008). Electrochemical reactivity in room-temperature ionic liquids. *Chem. Rev.* 108, 2238–2264. doi: 10.1021/cr0680686

Haran, B. S., Popov, B. N., and White, R. E. (1998). Determination of the hydrogen diffusion coefficient in metal hydrides by impedance spectroscopy. *J. Power Sources* 75, 56–63.

Hayyan, M., Mjalli, F. S., Hashim, M. A., AlNashef, I. M., and Mei, T. X. (2013). Investigating the electrochemical windows of ionic liquids. *J. Indus. Eng. Chem.* 19, 106–112. doi: 10.1016/j.jiec.2012.07.011

Hollingsworth, N., Taylor, S. F. R., Galante, M. T., Jacquemin, J., Longo, C., Holt, K. B., et al. (2015). Reduction of carbon dioxide to formate at low overpotential using a superbase ionic liquid. *Angew. Chem. Int. Ed.* 127, 14370–14374. doi: 10.1002/ange.201507629

Iijima, G., Kitagawa, T., Katayama, A., Inomata, T., Yamaguchi, H., Suzuki, K., et al. (2018). CO$_2$ Reduction promoted by imidazole supported on a phosphonium-type ionic liquid-modified Au electrode at a low overpotential. *ACS Catal.* 8, 1990–2000. doi: 10.1021/acscatal.7b03274

Janik, I., and Tripathi, G. N. (2016). The nature of the CO$_2^-$ radical anion in water. *J. Chem. Phys.* 144:154307. doi: 10.1063/1.4946868

Kaneco, S., Ueno, Y., Katsumata, H., Suzuki, T., and Ohta, K. (2009). Photoelectrochemical reduction of CO$_2$ at p-InP electrode in copper particle-suspended methanol. *Chem. Eng. J.* 148, 57–62. doi: 10.1016/j.cej.2008.07.038

Khadhraoui, A., Gotico, P., Boitrel, B., Leibl, W., Halime, Z., and Aukauloo, A. (2018). Local ionic liquid environment at a modified iron porphyrin catalyst enhances the electrocatalytic performance of CO$_2$ to CO reduction in water. *Chem. Commun.* 54, 11630–3. doi: 10.1039/C8CC06475J

Kim, K.-S., Park, S.-Y., Choi, S., and Lee, H. (2004). Vapor pressures of the 1-butyl-3-methylimidazolium bromide + water, 1-butyl-3-methylimidazolium tetrafluoroborate + water, and 1-(2-hydroxyethyl)-3-methylimidazolium tetrafluoroborate + water systems. *J. Chem. Eng. Data* 49, 1550–1553. doi: 10.1021/je034210d

Lau, G. P., Schreier, M., Vasilyev, D., Scopelliti, R., Gratzel, M., and Dyson, P. J. (2016). New insights into the role of imidazolium-based promoters for the electroreduction of CO$_2$ on a silver electrode. *J. Am. Chem. Soc.* 138, 7820–7823. doi: 10.1021/jacs.6b03366

Lim, H.-K., Kwon, Y., Kim, H. S., Jeon, J., Kim, Y.-H., Lim, J.-A., et al. (2018). Insight into the microenvironments of the metal–ionic liquid interface during electrochemical CO$_2$ reduction. *ACS Catal.* 8, 2420–2427. doi: 10.1021/acscatal.7b03777

Lin, L., Hou, C., Zhang, X., Wang, Y., Chen, Y., and He, T. (2018). Highly efficient visible-light driven photocatalytic reduction of CO$_2$

over g-C$_3$N$_4$ nanosheets/tetra(4-carboxyphenyl)porphyrin iron(III) chloride heterogeneous catalysts. *Appl. Catal. B Environ.* 221, 312–319. doi: 10.1016/j.apcatb.2017.09.033

Ma, J. W., Zhou, Z., Zhang, F., Fang, C. G., Wu, Y. T., Zhang, Z. B., et al. (2011). Ditetraalkylammonium amino acid ionic liquids as CO$_2$ absorbents of high capacity. *Environ. Sci. Technol.* 45, 10627–10633. doi: 10.1021/es201808e

Mac Dowell, N., Fennell, P. S., Shah, N., and Maitland, G. C. (2017). The role of CO$_2$ capture and utilization in mitigating climate change. *Nat. Clim. Chang.* 7, 243–249. doi: 10.1038/nclimate3231

MacFarlane, D. R., Chong, A. L., Forsyth, M., Kar, M., Vijayaraghavan, R., Somers, A., et al. (2017). New dimensions in salt-solvent mixtures: a 4th evolution of ionic liquids. *Farad. Discuss.* 206, 9–28. doi: 10.1039/c7fd00189d

Matsubara, Y., Grills, D. C., and Kuwahara, Y. (2015). Thermodynamic aspects of electrocatalytic CO$_2$ reduction in acetonitrile and with an ionic liquid as solvent or electrolyte. *ACS Catal.* 5, 6440–6452. doi: 10.1021/acscatal.5b00656

Medina-Ramos, J., DiMeglio, J. L., and Rosenthal, J. (2014). Efficient reduction of CO$_2$ to CO with high current density using *in situ* or *ex situ* prepared bi-based materials. *J. Am. Chem. Soc.* 136, 8361–8367. doi: 10.1021/ja501923g

Oh, Y., and Hu, X. (2015). Ionic liquids enhance the electrochemical CO$_2$ reduction catalyzed by MoO$_2$. *Chem. Commun.* 51, 13698–13701. doi: 10.1039/c5cc05263g

Ohmori, T., Nakayama, A., Mametsuka, H., and Suzuki, E. (2001). Influence of sputtering parameters on electrochemical CO$_2$ reduction in sputtered Au electrode. *J. Electroanal. Chem.* 514, 51–55. doi: 10.1016/s0022-0728(01)00624-6

Ohno, H., and Fukumoto, K. (2008). Progress in ionic liquids for electrochemical reaction matrices. *Electrochemistry* 76, 16–23. doi: 10.5796/electrochemistry.76.16

Paduszynski, K., and Domanska, U. (2014). Viscosity of ionic liquids: an extensive database and a new group contribution model based on a feed-forward artificial neural network. *J. Chem. Inform. Model* 54, 1311–1324. doi: 10.1021/ci500206u

Qadir, M. I., Weilhard, A., Fernandes, J. A., de Pedro, I., Vieira, B. J. C., Waerenborgh, J. C., et al. (2018). Selective carbon dioxide hydrogenation driven by ferromagnetic RuFe nanoparticles in ionic liquids. *ACS Catal.* 8, 1621–1627. doi: 10.1021/acscatal.7b03804

Reche, I., Gallardo, I., and Guirado, G. (2014). Electrochemical studies of CO$_2$ in imidazolium ionic liquids using silver as a working electrode: a suitable approach for determining diffusion coefficients, solubility values, and electrocatalytic effects. *RSC Adv.* 4, 65176–65183. doi: 10.1039/c4ra11297k

Rees, N. V., and Compton, R. G. (2011). Electrochemical CO2sequestration in ionic liquids; a perspective. *Energy Environ. Sci.* 4, 403–408. doi: 10.1039/c0ee00580k

Resasco, J., Lum, Y., Clark, E., Zeledon, J. Z., and Bell, A. T. (2018). Effects of anion identity and concentration on electrochemical reduction of CO$_2$. *ChemElectroChem* 5, 1064–1072. doi: 10.1002/celc.201701316

Rosen, B. A., Salehi-Khojin, A., Thorson, M. R., Zhu, W., Whipple, D. T., Kenis, P. J., et al. (2011). Ionic liquid-mediated selective conversion of CO$_{(2)}$ to CO at low overpotentials. *Science* 334, 643–644. doi: 10.1126/science.1209786

Sahara, G., Kumagai, H., Maeda, K., Kaeffer, N., Artero, V., Higashi, M., et al. (2016). Photoelectrochemical reduction of CO$_2$ coupled to water oxidation using a photocathode with a Ru(II)-Re(I) complex photocatalyst and a CoO$_x$/TaON photoanode. *J. Am. Chem. Soc.* 138, 14152–14154. doi: 10.1021/jacs.6b09212

Sasirekha, N., Basha, S., and Shanthi, K. (2006). Photocatalytic performance of Ru doped anatase mounted on silica for reduction of carbon dioxide. *Appl. Catal. B Environ.* 62, 169–180. doi: 10.1016/j.apcatb.2005.07.009

Shkrob, I. A., and Wishart, J. F. (2009). Charge trapping in imidazolium ionic liquids. *J. Phys. Chem. B* 113, 5582–5592. doi: 10.1021/jp811495e

Silvester, D. S., and Compton, R. G. (2006). Electrochemistry in room temperature ionic liquids: a review and some possible applications. *Zeitschr. für Physikal. Chem.* 220, 1247–1274. doi: 10.1524/zpch.2006.220.10.1247

Simon, N. M., Zanatta, M., Dos Santos, F. P., Corvo, M. C., Cabrita, E. J., and Dupont, J. (2017). Carbon dioxide capture by aqueous ionic liquid solutions. *ChemSusChem* 10, 4927–4933. doi: 10.1002/cssc.201701044

Snuffin, L. L., Whaley, L. W., and Yu, L. (2011). Catalytic electrochemical reduction of CO$_2$ in ionic liquid EMIMBF3Cl. *J. Electrochem. Soc.* 158:F155. doi: 10.1149/1.3606487

Stassen, H. K., Ludwig, R., Wulf, A., and Dupont, J. (2015). Imidazolium salt ion pairs in solution. *Chem. Eur. J.* 21, 8324–8335. doi: 10.1002/chem.201500239

Strehmel, V. (2012). Radicals in ionic liquids. *Chemphyschem* 13, 1649–1663. doi: 10.1002/cphc.201100982

Sun, L., Ramesha, G. K., Kamat, P. V., and Brennecke, J. F. (2014). Switching the reaction course of electrochemical CO$_2$ reduction with ionic liquids. *Langmuir* 30, 6302–6308. doi: 10.1021/la5009076

Tanner, E. E. L., Batchelor-McAuley, C., and Compton, R. G. (2016). Carbon dioxide reduction in room-temperature ionic liquids: the effect of the choice of electrode material, cation, and anion. *J. Phys. Chem. C* 120, 26442–26447. doi: 10.1021/acs.jpcc.6b10564

Taylor, S. F. R., McCrellis, C., McStay, C., Jacquemin, J., Hardacre, C., Mercy, M., et al. (2015). CO$_2$ Capture in wet and dry superbase ionic liquids. *J. Solution Chem.* 44, 511–527. doi: 10.1007/s10953-015-0319-z

Wang, C., Luo, X., Luo, H., Jiang, D. E., Li, H., and Dai, S. (2011). Tuning the basicity of ionic liquids for equimolar CO$_2$ capture. *Angew. Chem. Int. Ed.* 50, 4918–4922. doi: 10.1002/anie.201008151

Yago, T., and Wakasa, M. (2011). Nanoscale structure of ionic liquid and diffusion process as studied by the MFE probe. *J. Phys. Chem. C* 115, 2673–2678. doi: 10.1021/jp1108762

Yochelis, A., Singh, M. B., and Visoly-Fisher, I. (2015). Coupling bulk and near-electrode interfacial nanostructuring in ionic liquids. *Chem. Mater.* 27, 4169–4179. doi: 10.1021/acs.chemmater.5b00780

Yuan, J., Zhi, W.-Y., Liu, L., Yang, M.-P., Wang, H., and Lu, J.-X. (2018). Electrochemical reduction of CO$_2$ at metal-free N-functionalized graphene oxide electrodes. *Electrochim. Acta* 282, 694–701. doi: 10.1016/j.electacta.2018.06.107

Zanatta, M., Girard, A.-L., Marin, G., Ebeling, G., dos Santos, F. P., Valsecchi, C., et al. (2016). Confined water in imidazolium based ionic liquids: a supramolecular guest@host complex case. *Phys. Chem. Chem. Phys.* 18, 18297–18304. doi: 10.1039/C6CP03112A

Zhang, L., Niu, D., Zhang, K., Zhang, G., Luo, Y., and Lu, J. (2008). Electrochemical activation of CO$_2$ in ionic liquid (BMIMBF4): synthesis of organic carbonates under mild conditions. *Green Chem.* 10, 202–206. doi: 10.1039/b711981j

Check for
updates

Proteins in Ionic Liquids: Reactions, Applications, and Futures

Alexandra Schindl[1,2,3], Matthew L. Hagen[1,4], Shafaq Muzammal[1], Henadira A. D. Gunasekera[1,4] and Anna K. Croft[1]*

[1] Department of Chemical and Environmental Engineering, Faculty of Engineering, University of Nottingham, Nottingham, United Kingdom, [2] Faculty of Medicine & Health Sciences, School of Life Sciences, University of Nottingham, Nottingham, United Kingdom, [3] Faculty of Science, School of Pharmacy, University of Nottingham, Nottingham, United Kingdom, [4] Centre for Additive Manufacturing, Faculty of Engineering, University of Nottingham, Nottingham, United Kingdom

Biopolymer processing and handling is greatly facilitated by the use of ionic liquids, given the increased solubility, and in some cases, structural stability imparted to these molecules. Focussing on proteins, we highlight here not just the key drivers behind protein-ionic liquid interactions that facilitate these functionalities, but address relevant current and potential applications of protein-ionic liquid interactions, including areas of future interest.

Keywords: ionic liquids, enzymes, proteins, intermolecular interactions, reactions, molecular organization, physico-chemical relationships

INTRODUCTION

Proteins as both materials and catalysts have a number of practical features when considering global challenges such as developing a circular economy and minimization of environmental impacts. They are biodegradable and can be readily biosourced, are renewable, and can act as biocompatible scaffolds. Being polymeric materials consisting of combinations of around 20 main building blocks (amino acids), the range of materials properties that are accessible is substantial. The different amino acid functionalities lend these polymers to further post-processing, which can further extend the property scope. In addition to their catalytic properties as enzymes, proteins such as keratins, collagens, silks, and plant-fibers are strong, can be highly elastic, and possess many other desirable materials properties, including being suitable scaffolds for living cells. As such, these biopolymers have found significant use in the medical industries in particular, due to this biocompatibility and ability to replace or enhance existing tissues (Defrates et al., 2018).

Ionic liquids have firmly established themselves as useful industrial and laboratory solvents, reflected by substantial and ever-increasing literature in the area. Due to the reduced vapor pressure, arising from the strong electrostatic interactions of the constituent ions, they possess a number of useful properties, some of which underpin their "green" reputation. This includes minimal harmful vapor when handling, low flammability, and the lack of vaporization, which gives an opportunity to recycle these liquids across many cycles. The number of different ion combinations that can be considered leads to over 10^6 potential ionic liquids (Rogers and Seddon, 2003), before mixtures are even considered, each with different physical and chemical properties. Thus, in principle, tuning of the properties for a particular task can be achieved through judicious selection of ion combinations. They are especially good for the dissolution of recalcitrant materials, as the combination of electrostatic, hydrogen-bonding, π- and van der Waals interactions means that non-covalent (and sometimes covalent) interactions within these materials are more readily broken, with concomitant stabilization in the solution form.

The interaction of ionic liquids with proteins adds a significant new landscape for the understanding of ionic-liquid solute interactions. With the vast range of cation and anion combinations available (see **Figure 1** for those highlighted in this review) affording a differing balance of intermolecular interactions and thus interacting properties that can constitute an ionic liquid, not to mention mixtures of ions, the different anionic, cationic, hydrophobic, and polar interactions from each amino acid of a protein backbone becomes a many dimensional challenge.

STRUCTURAL PROTEINS

Keratins

Keratins are proteins that can be sourced from the skin, hair, horns, nails, beaks, and teeth of different mammals, reptiles, birds, and fish (Mckittrick et al., 2012), and constitute a significant biowaste stream (Zoccola et al., 2009; Sharma and Gupta, 2016; Holkar et al., 2018). As a natural fiber, wool is widely used commercially in the textile industry (Lewis and Rippon, 2013), and has found many uses ranging from biomedical and cosmetic applications (Rouse and Van Dyke, 2010; Silva et al., 2014; Sharma and Gupta, 2016), (being documented in medical use at least since ancient Greek times) (Alves et al., 2013), to fertilizers and flame retardants (Sharma and Gupta, 2016).

Keratins can be categorized as either hard or soft, depending on their sulfur content, with hard keratins, like wool, having a high sulfur content, and therefore more covalent (disulfide)

crosslinks (Simpson and Crawshaw, 2002; Zoccola et al., 2009; Mckittrick et al., 2012). Soft keratins can be found in the outer layer of the skin and have lower sulfur content and concomitantly fewer covalent (disulfide) crosslinks (Zoccola et al., 2009; Mckittrick et al., 2012). The disulfide bridges and strong inter- and intra-protein hydrogen-bonding of keratin proteins provide a significant processing challenge (Liu et al., 2018), often addressed through using mixtures of different solvents, with each solvent playing a key role in breaking covalent and/or non-covalent bonds (Xie et al., 2005). Volatility, corrosiveness, environmental impact, difficulty of recycling, and lack of renewability have all been highlighted as issues with these solvent regimes, in addition to the requirements for multi-step processes and resultant keratin degradation leading to regenerated keratin with a lower value (Hameed and Guo, 2009; Idris et al., 2013; Ji et al., 2014; Zheng et al., 2015; Liu et al., 2017; Zhang et al., 2017b). As such, there has been a growing demand to develop new solvents for keratin dissolution that are able to overcome the disadvantages associated with the traditional/existing solvents.

Ionic liquids have naturally been examined as solvents for the post-processing of keratin (Xie et al., 2005; Hameed and Guo, 2009; Sun et al., 2009; Zhao et al., 2010b; Lovejoy et al., 2012; Wang and Cao, 2012; Idris et al., 2013, 2014a,b; Li and Wang, 2013; Chen et al., 2014, 2015; Ghosh et al., 2014; Ji et al., 2014; Plowman et al., 2014; Wang et al., 2014, 2016; Zheng et al., 2015; Kammiovirta et al., 2016; Sharma and Gupta, 2016; Tran and Mututuvari, 2016; Liu et al., 2017, 2018; Zhang et al., 2017a;

FIGURE 1 | Representative ionic liquid cation and anion structures presented throughout the text.
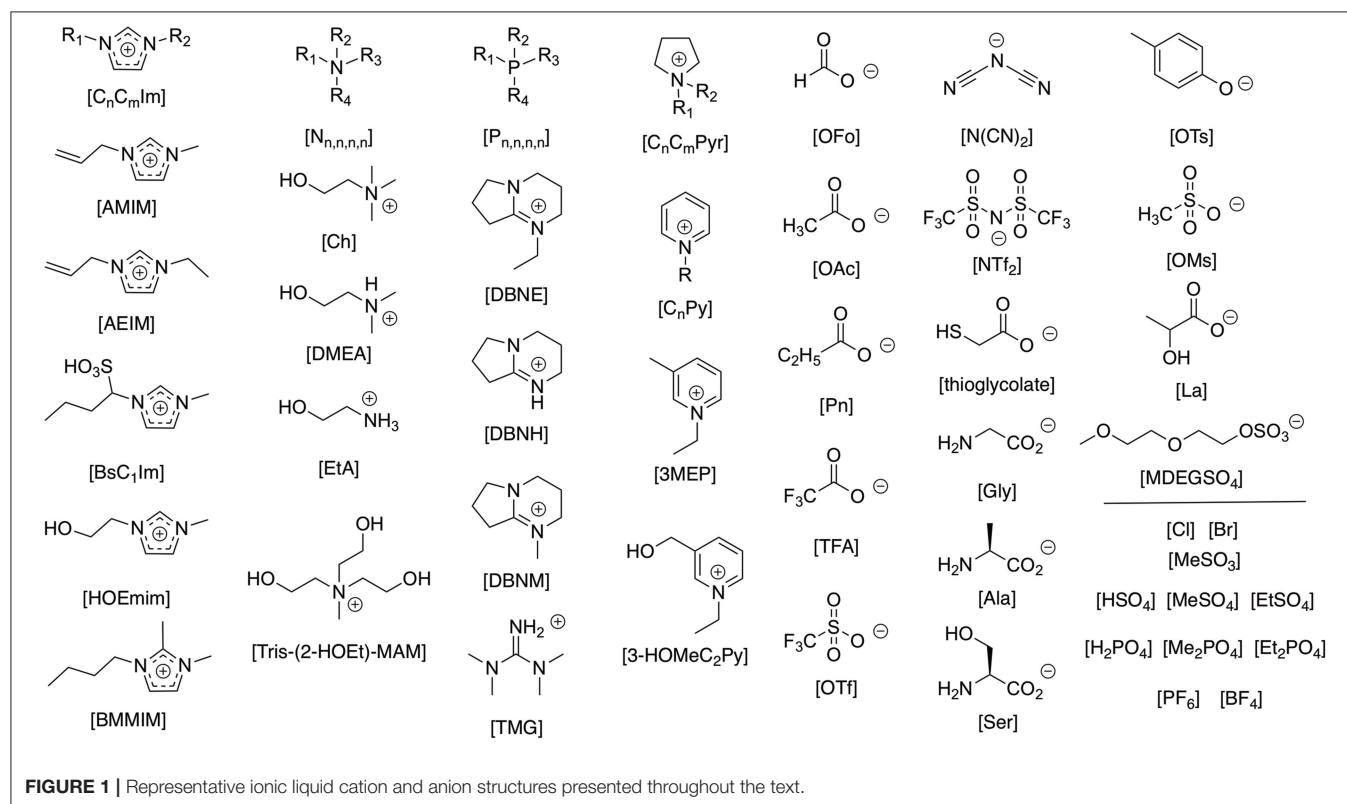
Zhang et al., 2017b). The dissolution process of keratin fiber starts with the swelling of the cuticle (outer layer) followed by the swelling and preferential dissolution of the cortex (inner layer). Of the two components, the cuticle generally takes longer to dissolve due to the high number of disulfide bonds present (Chen et al., 2014), however, selective swelling of the cuticle retaining the cortex intact is possible through careful control of conditions (Chen et al., 2015). According to Wang et al. (2014) for imidazolium cation and chloride anion-based ionic liquids, the combined effect of the anion and cation is responsible for breaking the covalent and non-covalent interactions in keratin, with each component participating through different interactions with the substrate (Ghosh et al., 2014).

An extensive array of ionic liquids has been tested with keratins (**Table 1**), reflecting the interest in reprocessing this protein. Early on, [C_4C_1Im][Cl] gained significant traction as the ionic liquid of choice for keratin dissolution (Xie et al., 2005; Hameed and Guo, 2009; Sun et al., 2009; Lovejoy et al., 2012; Idris et al., 2013; Li and Wang, 2013; Chen et al., 2014; Ghosh et al., 2014; Ji et al., 2014; Plowman et al., 2014; Wang et al., 2014; Zheng et al., 2015; Tran and Mututuvari, 2016; Zhang et al., 2017a; Liu et al., 2018), being effective for a broad range of keratin types, including human hair, hooves, goat and sheep wool, and duck, turkey and chicken feathers. Other small-cation imidazolium ionic liquids, primarily [AMIM], [C_2C_1Im] and [C_4C_1Im]-based derivatives have also been extensively trialed. It is the role of the anion, however, that appears to be key in the quality of regenerated keratin, with the nucleophilicity of chloride being suggested as the reason behind the degradation particularly of the disulfide bonds, and subsequent formation of cysteic acid (Ghosh et al., 2014). Acetate has also been strongly implicated in this process and was more effective than chloride, both for keratin and model systems (Zhang et al., 2017a). The differences between different cations with the same anion may potentially be attributed to the differences in ion-ion interactions providing a different effective availability of the corresponding anion. The wider ionic liquid organizational structure, combined with the specific structuring of the keratin, may also have implications for selectivity of different disulfides in the degradation process (Karimi et al., 2016).

There has been a growing drive to expand the range of suitable solvents for keratin to those that have specific properties useful for larger-scale processing, and, as such, both distillable and protic ionic liquids have been utilized with good effect (Chen et al., 2014, 2015; Idris et al., 2014a), alongside those containing potentially more benign, bio-compatible (Lovejoy et al., 2012; Zheng et al., 2015) and bio-derived (Idris et al., 2013; Chen et al., 2014, 2015), cations. Ionic liquids that have been tested and were reported to show either very poor or no detectable solubility of keratins include: [C_4C_1Im][PF_6] (Xie et al., 2005), [C_1Im][Cl] (Zhang et al., 2017a), [C_4Py][Cl] (Zheng et al., 2015; Zhang et al., 2017a), [C_4C_1Im][Br] (Zhang et al., 2017a), [C_4C_1Im][DBP] (Zhang et al., 2017a), [$P_{4,4,4,4}$][Cl] (Zheng et al., 2015; Zhang et al., 2017a), [$N_{4,4,4,4}$][Cl] (Zheng et al., 2015; Zhang et al., 2017a), [C_4C_1Im][H_2PO_4] (Zhang et al., 2017a), [C_4C_1Pyr][NTf_2] (Lovejoy et al., 2012), [C_4C_1Im][$OctSO_4$] (Lovejoy et al., 2012), [$P_{6,6,6,14}$][N(CN)$_2$] (Lovejoy et al., 2012),

[$P_{1,sec-4,sec-4,sec-4}$][OTs] (Lovejoy et al., 2012), [C_8C_1Im][BF4] (Lovejoy et al., 2012), [$P_{6,6,6,14}$][Cl] (Lovejoy et al., 2012), [$P_{6,6,6,14}$][NTf_2] (Lovejoy et al., 2012), [$P_{6,6,6,14}$][BF_4] (Lovejoy et al., 2012), [C_1Im][BF_4] (Lovejoy et al., 2012), [C_4C_1Im][BF_4] (Xie et al., 2005; Lovejoy et al., 2012) and [C_4C_1Im][$FeCl_4$] (Zheng et al., 2015). The ionic liquids [DMEA][OAc] and [DMEA][Cl] were also identified as potential candidates for dissolution, but because they had poor processing parameters, have not been tested for solubility (Idris et al., 2014a).

Recently a more systematic approach to determining useful ionic liquids for keratin dissolution was successfully applied, exploiting computational prediction of ionic liquid properties (Keaveney et al., 2015), based on the parametrised COSMO-RS methodology, with subsequent experimental verification (Liu et al., 2018). Here the σ-potential, a measure indicating the hydrogen bond acceptor-donor interactions of the model substrate, was matched for each model to generate the logarithmic activity coefficient (ln γ, proportional to the ionicity of the solution; Marsh et al., 1955), calculated against ionic liquid ion pairs. By testing 621 ion pairs and ranking these by cation and anion, a strong reliance on the anion was identified with a much more subdued contribution from the cation. Cations with additional hydrogen bonding groups, such as hydroxyethyl-methylimidazolium, acted to improve solubility over that predicted, and highlighted the role of hydrogen bond disruption in solubilisation.

Collagens

Unlike the disulfide-reinforced, arginine/glutamate-rich keratins, collagens are predominantly glycine-rich proteins, featuring also proline and/or hydroxyproline. Collagens contribute a range of structural roles in skin, ligaments, cartilage and tendons, as well as in bones, teeth and the cornea (Chen et al., 2017). Three strands of collagen-protein are able to form stable triple-helicies, with macrostructural alignment further imparting specific mechanical properties (Chen et al., 2017), attractive for biomaterials development (Defrates et al., 2018). Since collagen has different hierarchical, ordered layers to keratin, it provides an alternative framework for understanding the interactions of different ionic liquids on peptide dissolution and stabilization.

Choline salts have been examined in the context of collagen, because they provide potential for more biologically benign interaction agents suitable for biological implants. Cross-linking has been achieved in [Ch][lactate] and [Ch][levulinate] (Vijayaraghavan et al., 2010), along with the related, non-liquid, [Ch][tartrate] (Vijayaraghavan et al., 2010) and [Ch][H_2PO_4] (Vijayaraghavan et al., 2010; Mehta et al., 2015). The primary mechanism of the cross-linking is facilitated by the strong electrostatic interactions between the protein (Meng et al., 2012), postulated as from the arginine residues, and the ionic liquid, specifically the anion (Mehta et al., 2015). This was further explored both experimentally and theoretically with [Ch]$_2$[SO_4] (Tarannum et al., 2018a), and subsequently a selection of amino acid-based cholinium salts, [Ch][Ser], [Ch][Thr], [Ch][Lys], and [Ch]Phe (Tarannum et al., 2018b). In all these cases, the cholinium-based ionic liquids showed some variation in their interaction with collagen, based on features such as increases

TABLE 1 | Summary of keratin solubility in selected ionic liquids.

Ionic liquid	Keratin type	Solubility	Dissolution conditions	References
[AMIM][Cl]	Wool keratin	8 wt%	130°C, N_2, 10 h	Xie et al., 2005
	Turkey feathers	50 wt%	130°C, N_2, 10 h	Idris et al., 2013
	Wool keratin	21 wt%	130°C, 10.5 h	Li and Wang, 2013
	Merino Wool	200 mg/g	130°C, N_2, 10 h	Idris et al., 2014b
	Duck feather	5 wt%	120°C, 60 min	Ji et al., 2014
	Human hair	19 wt%	130°C	Wang et al., 2014
	Goat wool keratin	9 wt%	120°C, 30 min	Zhang et al., 2017a
	Wool keratin	13 wt%	120°C, 24 h	Liu et al., 2018
[AMIM][N(CN)$_2$]	Merino Wool	475 mg/g	130°C, N_2, 10 h	Idris et al., 2014b
[BsC$_1$Im][HSO$_4$]	Duck feather	4 wt%	120°C, 60 min	Ji et al., 2014
[C$_1$Im][OTf]	Duck feather	<1 wt%	120°C, 60 min	Ji et al., 2014
[C$_2$C$_1$Im][OAc]	Wool keratin	38 wt%	120°C, 24 h	Liu et al., 2018
	Chicken Feathers	5 wt%	130°C, 2.5 h	Kammiovirta et al., 2016
	Goat wool keratin	9 wt%	120°C, 30 min	Zhang et al., 2017a
[C$_2$C$_1$Im][Cl]	Wool keratin	14 wt%	120°C, 24 h	Liu et al., 2018
	Goat wool keratin	9 wt%	120°C, 30 min	Zhang et al., 2017a
[C$_2$C$_1$Im][Et$_2$PO$_4$]	Goat wool	8 wt%	120°C, 1.5 h	Liu et al., 2017
	Goat wool keratin	9 wt%	80-140°C,[c] 30–180 min	Zhang et al., 2017a
	Wool keratin	22 wt%	120°C	Liu et al., 2018
[C$_2$C$_1$Im][Me$_2$PO$_4$]	Wool keratin	8 wt%	130°C, 1.5 h	Zheng et al., 2015
	Wool keratin	9 wt%	130°C	Zhang et al., 2017b
[C$_4$C$_1$Im][OAc]	Goat wool keratin	9 wt%	120°C, 30 min	Zhang et al., 2017a
	Goat wool	8 wt%	120°C, 2.5 h	Liu et al., 2017
	Wool keratin	8 wt%	130°C, 10 min	Zheng et al., 2015
	Wool	single fibers	120°C, 3 min	Chen et al., 2014
	Merino Wool	Cuticle removal	75°C, 35 min	Chen et al., 2015
	Goat wool keratin	9 wt%	120°C, 30 min	Zhang et al., 2017a
[C$_4$C$_1$Im][BF$_4$][†]	Wool keratin	n/d	130°C, N_2, 24 h	Xie et al., 2005
	Human hair	insoluble	130°C	Wang et al., 2014
[C$_4$C$_1$Im][Br]	Wool keratin	2 wt%	130°C, N_2, 10 h	Xie et al., 2005
	Duck feather	4 wt%	120°C, 60 min	Ji et al., 2014
	Human hair	10 wt%	130°C	Wang et al., 2014
[C$_4$C$_1$Im][Cl]	Wool keratin	11 wt%	130°C, N_2, 10 h	Xie et al., 2005
	Wool	5 wt%	100°C	Hameed and Guo, 2009
	Chicken feather	23 wt%	100°C, N_2, 48 h	Sun et al., 2009
	Pig hoof powder	1 wt%	130°C, 10 h	Lovejoy et al., 2012
	Turkey feathers	50 wt%	130°C, N_2, 10 h	Idris et al., 2013
	Wool keratin	15 wt%	130°C, 9 h	Li and Wang, 2013
	Duck feather	5 wt%	120°C, 60 min	Ji et al., 2014
	Human hair	13 wt%	130°C	Wang et al., 2014
	Wool	single fibers	120°C, 90 min	Chen et al., 2014
	Merino Wool	5 wt%	99°C, 18 h	Plowman et al., 2014
	Merino Wool fabric	14 wt%	120, 150, and 180°C, 30 min	Ghosh et al., 2014
	Merino Wool	250 mg/g	130°C, N_2, 10 h	Idris et al., 2014b
	Wool keratin	8 wt%	130°C, 5 h	Zheng et al., 2015
	Raw wool	6 wt%	125–130°C, 6–8 h	Tran et al., 2016
	Goat wool keratin	9 wt%	120°C, 30 min	Zhang et al., 2017a
	Wool keratin	35 wt%	120°C, 24 h	Liu et al., 2018
[C$_4$C$_1$Im][Bu$_2$PO$_4$]	Wool	5.0%[a]	120°C, N_2, 12 h	Wang et al., 2016
[C$_4$C$_1$Im][N(CN)$_2$]	Wool keratin	1.5 wt%	120°C, 24 h	Liu et al., 2018

(Continued)

TABLE 1 | Continued

Ionic liquid	Keratin type	Solubility	Dissolution conditions	References
$[C_4C_1Im][Me_2PO_4]$	Wool keratin	8 wt%	130°C, 1.5 h	Zheng et al., 2015
$[C_4C_1Im][H_2PO_4]$	Wool	5.0% [a]	120°C, N_2, 10.5 h	Wang et al., 2016
	Wool	5.0% [a]	120°C, N_2, 17 h	Wang et al., 2016
$[C_4C_1Im][HSO_4]$	Wool	5.0% [a]	120°C, N_2, 13.5 h	Wang et al., 2016
$[C_4C_1Im][NO_3]$	Duck feather	4 wt%	120°C, 60 min	Ji et al., 2014
$[C_4C_1Im][SCN]$	Wool keratin	8 wt%	130°C, 15 h	Zheng et al., 2015
	Wool keratin	<1 wt%	120°C, 24 h	Liu et al., 2018
$[C_4C_1Pyr][Cl]$	Wool keratin	40 wt%	120°C, 24 h	Liu et al., 2018
	Pig hoof powder	1 wt%	130°C, 10 h	Lovejoy et al., 2012
$[C_4Py][Cl]$	Wool keratin	36 wt%	120°C, 24 h	Liu et al., 2018
$[Ch][thioglycolate]$	Turkey feathers	45 wt%	130°C, N_2, 10 h	Idris et al., 2013
	Merino Wool	225 mg/g	130°C, N_2, 10 h	Idris et al., 2014b
	Wool	single fibers	120°C, 10 min	Chen et al., 2014
$[Ch][Pn]$	Wool	single fibers	120°C, 45 min	Chen et al., 2014
	Merino Wool	Cuticle removal	75°C, 35 min	Chen et al., 2015
$[DBNE][Et_2PO_4]$	Goat wool	8 wt%	120°C, 3 h	Liu et al., 2017
$[DBNH][OAc]$	Goat wool	8 wt%	120°C, 20 min	Liu et al., 2017
$[DBNM][Me_2PO_4]$	Goat wool	8 wt%	120°C, 3.5 h	Liu et al., 2017
$[DMEA][HCO_2]$	Turkey feathers	150 mg/g	100°C, 7 h	Idris et al., 2014a
$[HOEmim][Cl]$	Wool keratin	3 wt%	120°C, 24 h	Liu et al., 2018
$[HOEmim][NTf_2]$	Chicken feathers	21.75% [b]	80°C, 4 h	Wang and Cao, 2012
$[N_{2,2,1}][Me_2PO_4]$	Wool keratin	8 wt%	130°C, 3 h	Zheng et al., 2015
$[P_{4,4,4,4}][Cl]$	Pig hoof powder	1 wt%	130°C, 10 h	Lovejoy et al., 2012
$[TMG][Pn]$	Wool	single fibers	100°C, 6.5 h, partial dissolution	Chen et al., 2014
	Merino Wool	Cuticle removal	75°C, 35 min	Chen et al., 2015

[a] wool fiber/ionic liquid mass ratio.

[b] extraction yield based on 1:45 mass ratio.

[c] No dissolution reported below 110°C.

Bs, 1-sulfobutyl; Pn, propionate; OAc, acetate; DBNE, 1-Ethyl-1,5-diazabicyclo[4.3.0]-non-5-enium; DBNH, 1,5-diazabicyclo [4.3.0]non-5-enium; DBNM, 1-methyl-1,5-diazabicyclo[4.3.0]non-5-enium; DMEA, N,N-dimethylethanolammonium; TMG, 1,1,3,3-Tetramethylguanidinium.

[†] Hydrolysable ionic liquid.

in the thermal denaturation temperature, fibril morphology, and changes in FTIR spectra, with more destabilization of the structure indicated for the lysinate and phenylalanate anions.

This dominance of the anionic interaction in governing stabilization is, however, challenged by the observation that $[P_{4,4,4,1}][Et_2PO_4]$, $[P_{4,4,4,1}][MeSO_3]$, and $[HN_{2,2,1}][MeSO_3]$ can result in structural deformation (Tarannum et al., 2018b), with $[C_4C_1Im][Me_2PO_4]$ resulting in collagen structural degradation (Tarannum et al., 2018a), rather than strengthening of the interactions. The implication is that both the nature of the anion is strongly important, and that the cation must also play a not insignificant role. Physicochemical impacts, including on thermal denaturation, were also observed for aqueous solutions of imidazolium chlorides $[C_2C_1Im][Cl]$, $[C_4C_1Im][Cl]$, and $[C_{10}C_1Im][Cl]$ (Mehta et al., 2014).

Collagen fiber solution has been utilized extensively in a broader range of imidazolium ionic liquids. In addition to $[C_4C_1Im][Cl]$ (Meng et al., 2012; Wang et al., 2013a; Mehta et al., 2014), where around 6 wt% collagen could be solubilised, $[C_2C_1Im][OAc]$ (Hu et al., 2013; Zhang et al.,

2014) showed temperature-dependant solubilisation ranging from 3.1 to 7.4 wt% going from 25 to 45°C, respectively, which was also impacted, and sometimes improved (up to *ca*. 10 wt%) by addition of sodium salts (Hu et al., 2013). This ionic liquid has been utilized in extracting collagen from waste fish scales (Muhammad et al., 2017). Aqueous mixtures of $[C_2C_1Im][EtSO_4]$ have been used with gelatin (partially hydrolysed collagen) to prepare nanoparticle-embedded ionogels with a variety of attractive properties. Other biomedical applications have included composite hydrogels for skin dressings (Iqbal et al., 2017), and composite hydrogels for bone applications (Iqbal et al., 2018a), prepared with collagen using the protic $[C_1Im][OAc]$ as a carrier. The protic, non-imidazolium $[NH(CH_2CH_2OH)_3][OAc]$ has similarly been used for preparation of bone filler composites (Iqbal et al., 2018b).

Similar to the work in keratin, COSMO has been utilized in the calculation of activity coefficients with ionic liquids and a collagen model (Muhammad et al., 2017). Here a range of imidazolium cations; $[C_2C_1Im]$, $[C_4C_1Im]$, $[C_6C_1Im]$, $[C_8C_1Im]$, $[C_{10}C_1Im]$; with a large selection of corresponding

anions was trialed, with lowest ln γ values obtained consistently for the smallest cation, especially in combination with small organic acid anions (acetate, propionate, formate, butanoate and crotonate, respectively). This was followed by the chloride anion, which interestingly had the largest variation in effect with cation, with a dramatic difference in ln γ values on going from $[C_2C_1Im]$ to $[C_4C_1Im]$ and again to $[C_6C_1Im]$, compared with other cation-anion combinations. Amino acid anions $[Gly]^-$, $[Arg]^-$, and $[Glu]^-$ afforded intermediate predictions, with more hydrophobic anions giving poor predictions for interaction, with high ln γ values. As a result, $[C_2C_1Im][OAc]$ was selected in this study as extraction solvent of choice.

Plant Proteins

The use of ionic liquids with plant proteins is less extensive than for those proteins from animals. The huge scale of soybean production worldwide means that soy protein is readily accessible (Nishinari et al., 2014). In practice soy protein is a mixture of different proteins of different sizes and properties, with two dominant, multimeric constituents, β-conglycinin and glycinin. These proteins are particularly rich in glutamate and aspartate, as well as arginine, lysine, serine, and proline, with higher quantities of leucine and phenylalanine in more hydrophobic subunits (Riblett et al., 2001). Soy protein has been used in a wet spinning method through dissolution in $[C_4C_1Im][Cl]$/DMSO mixtures (Deng et al., 2014), and blend films of soy protein with cellulose have been prepared with [AMIM][Cl] as the solvent (Wu et al., 2009).

The poorly-soluble zein protein is obtained as a by-product of industrial corn processing, most recently through bioethanol production (Gupta et al., 2016), and comprises around 7–8 wt% of the corn kernel (Shukla and Cheryan, 2001). Although rich in glutamate, leucine, alanine, and proline, it is low in basic amino acids such as arginine and deficient in lysine and tryptophan, making it poor quality for human nutrition. In an attempt to improve accessibility to reaction, nearly 15 wt% of zein was shown to be soluble in $[C_4C_1Im][Cl]$, with practical viscosities in the range of 10 wt% when dissolved at 120°C for 60 min, and benzoylation able to be demonstrated (Biswas et al., 2006). The ionic liquid $[C_4C_1Im][N(CN)_2]$ was reported to be similarly effective with solubilities of 10 wt%, whereas [Ch][Cl] deep eutectic mixtures were not effective at dissolving zein. With a focus on assessing green solvents, the imidazolium ionic liquids $[C_2C_1Im][OAc]$ and $[C_2C_1Im][Br]$ were compared with bioderived organic solvents. Here 1,4-dioxane and 2,3-butanediol were indicated as more promising for zein extraction applications (Gupta et al., 2016), although other ionic liquids may have performed better had they been assessed.

In 2014, Tomlinson et al. (2014) examined zein solubility in seven imidazolium ionic liquids; four non protic: ($[C_2C_1Im][OAc]$, $[C_2C_1Im][N(CN)_2]$, $[C_4C_1Im][OAc]$, and $[C_4C_1Im][Cl]$) and three protic: ($[C_1Im][OAc]$, $[C_1Im][OFo]$, and $[C_1Im][HSO_4]$), and related their results to the Linear Free Energy parameters α, β, and π* through multivariate regression. This model gave polarisability (π*) as the key contributor, increasing in importance at higher temperatures alongside the $E_T(30)$ polarity scale. They concluded that good solvents for zein would possess low hydrogen-bond accepting ability (β), low polarisability (π*) and weak hydrogen-bond donating ability (α), and that increases in water content within the ionic liquids had little impact on solubility. In line with this, they concluded that $[C_1Im][HSO_4]$ was an extremely poor solvent and that $[C_1Im][OAc]$ and $[C_2C_1Im][N(CN)_2]$ were their preferred solvents for zein, with solubilities measured at *ca.* 25 wt% zein at 60°C. Other protic ionic liquids were also shown to be successful in solubilising zein with $[NH_3(CH_2CH_2OH)][OFo]$ and $[NH_3(CH_2CH_2OH)][OAc]$ producing highly viscous 70 wt% solutions (Choi and Kwon, 2011). More practical solutions of 20 wt% zein could be produced either by microwave heating, or by conventional heating at 120°C.

Silks

Silk from the larval form of the silk moth *Bombyx mori* is a material that has been used by humanity for thousands of years. Whilst predominantly used for its properties as a textile, it has desirable mechanical properties (Pérez-Rigueiro et al., 2000), as well as potential biomedical applications (Reviewed Altman et al., 2003; Kapoor and Kundu, 2016), and is attracting significant research therefore in identifying mechanisms for reprocessing. Similar to the complex, layered structures of keratins, silk fibers are formed of two monofilaments called brins that are spun by the spinneret of the silk moth larve into a single fiber (bave). Each brin consists of two different proteinaceous substances: the core consists of fibroins and these are coated by serecins. For the sake of clarity when discussing solubility in ionic liquids, "silk" here will refer to fibroin obtained from *B. mori* with the serecin removed, unless explicitly stated.

The superlative mechanical characteristics of silk derive from a glycine- and alanine-rich repeating motif of the hexapeptide GAGAGX (where X = S, Y, A), periodically broken up by a GAAS motif (Zhou et al., 2001). Within silk fibers, these repeat regions make up a β-sheet structure interspersed with less structured regions. Further examinations of silk structure with small angle electron diffraction have shown that the β-sheets are organized into crystallites with dimensions of 66 ± 34 nm and 10 ± 3 nm with the major axis being aligned with the fiber axis (Shen et al., 1998), and it is this macrostructuring from the secondary level upwards that provides the underpinning mechanical properties of silk.

Previous attempts at solubilisation have required harsh solvents such as either hexafluoroisopropanol (HFIP) (Park et al., 2006), or aqueous inorganic salts, most commonly lithium bromide (Iizuka and Yang, 1966), that require subsequent dialysis to remove them afterward. Other methods have been explored for the dissolution of silk including calcium chloride in formic acid as well as mixtures of inorganic salts, water and alcohols (Yue et al., 2014; Cheng et al., 2015). In 2004, Phillips et al. (2004) published the first communication on the use of ionic liquids for silk dissolution, demonstrating $[C_4C_1Im]$ and $[C_2C_1Im]$-based ionic liquids as effective solvents. Ionic liquids have since proven great utility in dissolving *B. mori* silk for a range of applications (Phillips et al., 2004, 2005; Gupta et al., 2007; Mantz et al., 2007; Goujon et al., 2012, 2013; Silva et al., 2012, 2013; Wang et al., 2012, 2013b; Zhou et al., 2013; Yao et al.,

TABLE 2 | Ionic liquid data for silk solubility found in the literature.

IL	[Silk]/wt%	References
[AMIM][Cl]	1–15	Wang et al., 2012
$[C_1Im][Cl]$	Insoluble	Mantz et al., 2007
$[C_2Im][Cl]$	Insoluble	Lozano-Pérez et al., 2015
$[C_1C_1Im][Cl]$	>12	Lozano-Pérez et al., 2015
$[C_1C_1Im][NO_3]$	Insoluble	Mantz et al., 2007
$[C_2C_1Im][Cl]$	25	Lozano-Pérez et al., 2015
	23.3	Mantz et al., 2007
$[C_2C_1Im][NO_3]$	Insoluble	Mantz et al., 2007
$[C_2C_1Im][OAc]$	0.1–20	Zhang et al., 2016a
$[C_2C_1Im][SCN]$	Insoluble	Mantz et al., 2007
$[C_2C_1Im][OTf]$	Insoluble	Mantz et al., 2007
		Lozano-Pérez et al., 2015
$[C_2C_1Im][EtSO_4]$	Insoluble	Lozano-Pérez et al., 2015
$[C_2C_1Im][BF_4]$	Insoluble	Mantz et al., 2007
$[C_2C_1Im][AlCl_4]$	Insoluble	Mantz et al., 2007
$[C_2C_1Im][Gly]$	26.3	Mantz et al., 2007
$[C_2C_1Im][Ala]$	>20	Mantz et al., 2007
$[C_2C_1Im][Ser]$	>20	Mantz et al., 2007
$[C_3C_1Im][Cl]$	>15	Lozano-Pérez et al., 2015
$[C_4C_1Im][Cl]$	>12	Lozano-Pérez et al., 2015
	13.2	Phillips et al., 2004; Mantz et al., 2007
$[C_4C_1Im][Br]$	0.7	Phillips et al., 2004; Mantz et al., 2007[a]
$[C_4C_1Im][I]$	0.2	Phillips et al., 2004; Mantz et al., 2007[a]
$[C_4C_1Im][OAc]$	15	Li et al., 2015; Susanin et al., 2018
$[C_4C_1Im][BF_4]$[†]	Insoluble	Phillips et al., 2004; Mantz et al., 2007[a]
$[C_4C_1Im][PF_6]$[†]	Insoluble	Lozano-Pérez et al., 2015
$[C_4C_1Im][OctSO_4]$	Insoluble	Lozano-Pérez et al., 2015
$[C_4C_1Im][Cl]$	8.3	Phillips et al., 2004; Mantz et al., 2007
$[C_6C_1Im][Cl]$	>11	Lozano-Pérez et al., 2015
$[C_8C_1Im][Cl]$	Insoluble	Lozano-Pérez et al., 2015
$[C_{10}C_1Im][Cl]$	Insoluble	Lozano-Pérez et al., 2015
$[3\text{-}MEP][EtSO_4]$	Insoluble	Lozano-Pérez et al., 2015
EtAN	Insoluble	Lozano-Pérez et al., 2015
$[N_{4,4,4,4}][Gly]$	Insoluble	Mantz et al., 2007

[a] Solubility data obtained from whole cocoons including serecin.

3-MEP, 3-methyl ethylpyridinium; EtAN, Ethanolammonium nitrate.

[†] Hydrolysable ionic liquid.

2014a,b, 2018; Li et al., 2015; Lozano-Pérez et al., 2015; Zhang et al., 2016a; Susanin et al., 2017, 2018; Stanton et al., 2018; **Table 2**). Successful dissolution has been achieved with a range of 1-methyl-3-alkylimidazolium ionic liquids, particularly when partnered with chloride or carboxylate anions. In a similar fashion to other proteins, maximal solubility is achieved with the small methyl and ethyl alkyl groups on these cations. This trend for smaller side chains does not extend to the protic $[C_1Im][Cl]$, in which silk is insoluble. Alkylation at the 2-position of the imidazole ring also decreases silk solubility. As this is a known site of H-bonding within the imidazolium ionic liquids, it implies that cation H-bonding is also a critical interaction in stabilizing silk solutions.

From the surveyed ionic liquids, only three classes of anion have shown good solubilising properties: chloride, acetate, and amino acid anions. Although halides have shown to be effective anions, a direct comparison regarding solubility in [Cl]-based ionic liquids is difficult, as the $[C_4C_1Im][X]$ (X = Br⁻, I⁻) ionic liquids were tested on whole cocoons including the serecin. These ionic liquids, as well as the hydrolysable $[C_4C_1Im][BF_4]$ (Freire et al., 2010), are capable of dissolving serecin whilst displaying minimal to no fibroin solubility, a trend also confirmed in later work (Mantz et al., 2007). The imidazolium acetates have been utilized extensively in cellulose dissolution (Swatloski et al., 2002), but interestingly it was not until 2016 before $[C_2C_1Im][OAc]$ was used on silk (Zhang et al., 2016a). Particular anions (NO_3^-, SCN^-, TfO^-, $EtSO_4^-$, $OctSO_4^-$, BF_4^-, $AlCl_4^-$, PF_6^-) do not appear to sufficiently perturb the H-bonding of silk to act as useful solvents.

Amino acid-based ionic liquids, where the $[C_2C_1Im]$ cation was paired with the carboxylate anion form of the 20 natural amino acids, were initially developed by Fukumoto et al. (2005) with a subset of these ionic liquids characterized for their silk dissolution capacity (**Table 2**; Mantz et al., 2007). These amino acid anion-based ionic liquids provide some of the highest dissolution capacities for silk, showing promise in the area for more biocompatible dissolution solvents. One consideration however is whether the marginal gains in dissolution capacity, coupled to enhanced biocompatibility, are sufficient to justify the added complexity of their synthesis.

Solubility characterization has a direct impact on mechanisms of processing to afford silk in a desired functional form, such as the non-exhaustive examples highlighted in **Table 3**, which include composite formation for biomedical use (Silva et al., 2012). Silk coagulation from solution, although unsuccessful, also provides information on the underlying multi-way interactions between solvent, silk and coagulant. In general, small alcohols have been the most popular choice of coagulant, due to their ability to reform the β-sheet network critical to the strength of the silk II polymorph (Asakura et al., 1985). Water too has been utilized with differing levels of success where a regenerated silk will either not form at all ($[C_4C_1Im][Cl]$ and 9.51 wt% silk, consistent with amorphous silk being soluble in water) or form brittle films, unless both cellulose is used as an additive and the correct ionic liquid ($[C_2C_1Im][OAc]$ or [AMIm][Cl]) is chosen. Typical antisolvent choices for polar systems seem to yield either no coagulation or a brittle film or fiber (**Table 3**; Phillips et al., 2005). These observations emphasize that both solvent choice and the choice of coagulant are of paramount importance, with dominant options well-explored in the literature.

In contrast to water or alcohols as the coagulant for the regeneration of silk from solution, the tunability of ionic liquids offers an alternative approach to regeneration, and highlights the potential of these solvents. Protic ionic liquids (pILs) have been used to develop an all ionic liquid process for the dissolution and regeneration of silk (Goujon et al., 2012). Initially 5% w/w silk solutions in HFIP were regenerated using pILs based around the triethylammonium (TEA⁺) cation with differing anions: lactate (La⁻), triflate (OTf⁻), mesylate (OMs⁻) and dihydrogenphosphate ($H_2PO_4^-$), each of which

TABLE 3 | A representative sample of methods by which silk is dissolved and subsequently reformed listing silk concentrations, additives, coagulants and processing methods.

IL	[Silk] (wt%)	Additives	Coagulant	Processing method	RSF morphology	References
[C$_2$C$_1$Im][Cl]	10.4	7% water	MeOH	Pipetted into coagulant bath, soaked for 24 h.	Fibers	Mantz et al., 2007
	10.4	7% water	EtOH	Pipetted into coagulant bath, soaked for 24 h.	Precipitate	Mantz et al., 2007
	10.4	7% water	0.1 M H$_3$Ct−0.1 M NaH$_2$Ct pH 2.96	Pipetted into coagulant bath, soaked for 24 h.	-	Mantz et al., 2007
	10.4	7% water	0.1 M NaH$_2$Ct−0.1 M Na$_2$HCt pH 4.29	Pipetted into coagulant bath, soaked for 24 h.	Precipitate	Mantz et al., 2007
	10.4	7% water	0.14 NaH$_2$Ct−0.06M Na$_2$HCt pH 4.05	Pipetted into coagulant bath, soaked for 24 h.	Precipitate	Mantz et al., 2007
	10	-	MeOH	Wet spinning.	Solid, clear fibers	Phillips et al., 2005
	10	-	MeCN	Wet spinning.	Solid, white crusted, brittle fibers	Phillips et al., 2005
	10	-	Water	Wet spinning.	Dissolved leaving small residual fiber	Phillips et al., 2005
	10	-	Acetone	Wet spinning.	Formed immiscible droplets, no precipitation	Phillips et al., 2005
	10	-	Ethyl Acetate	Wet spinning.	Formed immiscible droplets, no precipitation	Phillips et al., 2005
	10	-	Hexanes	Wet spinning.	Formed immiscible droplets, no precipitation	Phillips et al., 2005
	1	Cellulose 9 wt%	Water	Cast film between glass slides in coagulant bath.	Clear, solid film	Stanton et al., 2018
[C$_2$C$_1$Im][OAc]	0.1–20	-	Water	Gellation.	Gel	Zhang et al., 2016a
	5–10	-	Water	Gellation.	Conductive Gel	Yao et al., 2018
	5–10	-	Water/EtOH	Gellation.	Conductive Gel	Yao et al., 2018
	1	Cellulose 9 wt%	Water	Cast film between glass slides in coagulant bath.	Clear, solid film	Stanton et al., 2018
[AMIM][Cl]	1	Cellulose 9 wt%	Water	Cast film between glass slides in coagulant bath.	Clear, solid film	Stanton et al., 2018
[C$_4$C$_1$Im][Cl]	9.51	-	MeOH	Cast film in coagulant bath.	Transparent film, high crystallinity	Phillips et al., 2004, Mantz et al., 2007
	9.51	-	MeCN	Cast film in coagulant bath.	White film due to surface light scattering, low crystallinity	Phillips et al., 2004, Mantz et al., 2007
	9.51	-	Water	Cast film in coagulant bath.	Dissolved	Phillips et al., 2004, Mantz et al., 2007
	5	-	MeOH	Electrospun into coagulant bath with subsequent rinsing.	Fibers	Mantz et al., 2007
	1	Cellulose 9 wt%	Water	Cast film between glass slides in coagulant bath.	Clear, solid film	Stanton et al., 2018
	10	Water 25 wt%	MeOH	Spin Coating and immersion in coagulant.	Clear film	Gupta et al., 2007
	10	-	MeOH Vapor	Cast film in vacuum oven with MeOH vapor, then water rinse and pressed between glass plates and dried under reduced pressure.	Clear film	Zhou et al., 2013
	7.5	Cellulose 2.5 wt%	MeOH Vapor	Cast film in vacuum oven with MeOH vapor, then water rinse and pressed between glass plates and dried under reduced pressure.	Clear film	Zhou et al., 2013
	5	Cellulose 5 wt%	MeOH Vapor	Cast film in vacuum oven with MeOH vapor, then water rinse and pressed between glass plates and dried under reduced pressure.	Clear film	Zhou et al., 2013

(Continued)

TABLE 3 | Continued

IL	[Silk] (wt%)	Additives	Coagulant	Processing method	RSF morphology	References
	2.5	Cellulose 7.5 wt%	MeOH Vapor	Cast film in vacuum oven with MeOH vapor, then water rinse and pressed between glass plates and dried under reduced pressure.	Clear film	Zhou et al., 2013
	0	Cellulose 10 wt%	MeOH Vapor	Cast film in vacuum oven with MeOH vapor, then water rinse and pressed between glass plates and dried under reduced pressure.	Clear film	Zhou et al., 2013
$[C_4C_1Im][Br]$	1	Cellulose 9 wt%	Water	Cast film between glass slides in coagulant bath.	Translucent, brittle film	Stanton et al., 2018
$[C_4C_1Im][OAc]$	5	-	80% TMG.La: 20% water	Injected silk solution into coagulant bath, left for 1 hr and then rinsed 3x with water.	Silk foam	Goujon et al., 2012
	10	-	EtOH	Molds immersed in EtOH for 24 h then Soxhlet extraction with EtOH for 5 days then into MeOH/water (80/20 vol%) to form beta sheets.	Cast hydrogel	Silva et al., 2013
	2.8	Chitosan 1.2 wt%	EtOH	Molds immersed in EtOH for 24 h then Soxhlet extraction with EtOH for 3 days then into MeOH for 10 min to form beta sheets.	Cast hydrogel	Silva et al., 2012
	2	Chitosan 2 wt%	EtOH	Molds immersed in EtOH for 24 h then Soxhlet extraction with EtOH for 3 days.	Cast hydrogel	Silva et al., 2012
	1.2	Chitosan 2.8 wt%	EtOH	Molds immersed in EtOH for 24 h then Soxhlet extraction with EtOH for 3 days.	Cast hydrogel	Silva et al., 2012
	15	-	EtOH	1–2 h at 25°C 65% RH then into EtOH and finally into water.	Clear film	Li et al., 2015
$[C_4C_1Im][MeSO_3]$	1	Cellulose 9 wt%	Water	Cast film between glass slides in coagulant bath.	Translucent, brittle film	Stanton et al., 2018

was in an 80%:20% w/w ratio of pIL to water. Fourier self-deconvolution of the FTIR spectrum was used to determine the secondary structure content of the silk foams regenerated with each of these coagulant solutions. The different anions were able to generate silk foams with very different structures. SEM showed a much more open and porous morphology for silk in [TEA][OMs] and a major peak at 22° shown in the XRD spectrum. Conversely, $[TEA][H_2PO_4]$ showed a much tighter foam-like morphology and a single peak at 18.5° in the XRD spectrum, which is possibly a native-like structure (16.5°) but with a greater intersheet spacing. Focussing on the underlying secondary structure, $[TEA][H_2PO_4]$ yielded the most native-like secondary structure with 55% β-sheet content (1,621–1,630 cm^{-1}) and no α-helices (1,655–1,662 cm^{-1}) whereas [TEA][OMs] yielded a silk foam with a large amount of α-helical structure (45%) as well as a large β-sheet content (50%).

Previous work with the amyloid peptide Aβ(1-40), best known for its implied role in Alzheimer's disease, foreshadowed the helix-inducing properties of [TEA][OMs] (Debeljuh et al., 2011). Through CD spectroscopy the secondary structure of Aβ(1-40) was monitored under varying [TEA][OMs] content. From 0 to 50% w/w [TEA][OMs] in water, the Aβ(1-40) retained its β-sheet secondary structure and ability to form fibrils. At 50–90% w/w the Aβ(1-40) changed to an α-helix secondary structure and no fibrils were formed. Finally at 90–100% w/w the Aβ(1-40) adopted the random coil conformation. Two potential hypotheses have been given for the mechanism by which pILs drive these conformational changes: the first is

that the unique H-bonding network that pILs exhibit may drive proteins to preferentially form intermolecular bonds over intramolecular bonds. Alternatively, the microheterogeneity of pILs could be providing a membrane-like environment where a helical structure is preferred. Both of these hypotheses could help explain the preferential formation of α-helices by silk in [TEA][OMs].

For [TMG][La] (1,1,3,3-tetramethylguanidinium lactate) the general trend was that as water content increased, the β-sheet content fell, and the propensity for a microsphere morphology increased. Changes in the H-bonding network, alongside changes to the surface tension could drive the microsphere morphology. Yields decreased and coagulation time increased with increasing water content, consistent with amorphous silk being soluble in water. With this in mind an 80%:20% w/w [TMG][La]:water composition was used to coagulate silk from a 5% w/w solution in $[C_4C_1Im][OAc]$. The choice of both coagulant and solvent affects both morphology and secondary structure content. When HFIP was used to dissolve silk, a much finer foam structure was formed compared to $[C_4C_1Im][OAc]$, containing larger, disordered voids. The secondary structure differed also with HFIP showing 55% β-sheet, 14% silk I structure, 12% α-helix and 9% β-turns, whereas using $[C_4C_1Im][OAc]$ there was 64% β-sheet, 6% silk I, 27% α-helices and 2% β-turns. The demonstrated capability of pILs to alter protein conformation in a tunable sense is a compelling phenomenon and could provide good potential for generating precise morphology for future protein formulations.

ENZYMES

Potential applications for ionic liquids in the biotech-industry are numerous and an exhaustive list is not possible here. However, the limiting biocompatibility of these electrolytes has led to the emergence of very specific fields of implementation, whereby the advantage in overcoming issues of common chemical synthesis by deploying a reaction-selective biocatalyst outweighs the challenges of finding a suitable ionic liquid system. In this regard, the solubility of either the substrate or product can be identified as the primary driver that indicates use of an ionic liquid solvent may be valuable. The major focus areas of published research concerning biocatalysis in ionic liquids over the last decade have been in biofuel production, followed by the use as biosensors, and the production of enantiomerically-pure compounds (reviewed in Itoh, 2017b; Meyer et al., 2018). Protein stability in ionic liquids has been examined (Kumar and Venkatesu, 2014; Zhao, 2016), and provides part of the story, but cannot always accurately predict activity. A more thorough understanding of salt and enzyme interactions, including a classification of the impact of different anions and cations on enzyme activity, will enable applications that lie outside these dominating research fields, and is one of the rising areas of interest in the ionic liquid field. Some recent highlights for specific systems are provided here.

Cellulases

Cellulases and their use in aqueous ionic liquids have one major, documented application: the saccharification of cellulose from various lignocellulose biomass sources for the production of biofuels. The treatment of the biomass with ionic liquids and the saccharification by the enzymes can be performed simultaneously, limited by the stability of the biocatalyst in such media. Pretreatment can be established through alkali, steam, acid or aqueous ammonia soaking, used for different substrates and exhibiting different yields (Ruiz et al., 2008; Cho et al., 2013; Govumoni et al., 2013; Maurelli et al., 2013). Pretreatment with ionic liquids dissolves lignin and hemicellulose by disruption of the hydrogen bonds of the cellulose to reduce crystallinity, thereby facilitating access for the hydrolytic enzymes (Tan and Macfarlane, 2010).

There is not a great variety of ionic liquids used for this process, as they need to have the ability to effectively compete with existing intermolecular H-bond interactions to separate the polymer chains (**Table 4**; Pinkert et al., 2010). The most usual cations are $[C_4C_1Im]$ and $[C_2C_1Im]$, and occasionally [AMIM] or [HEMA] (tris-(2-hydroxyethyl)-methylammonium). Similar to the situation with proteins, increasing the chain length of the imidazolium cation also leads to a decrease in dissolution of the cellulose (Kosan et al., 2007; Vitz et al., 2009; Cao et al., 2017). The anions [Cl], [OAc] and $[BF_4]$ have been most commonly investigated, followed by $[Et_2PO_4]$ or $[Me_2PO_4]$ and $[MeSO_4]$. The hydrophobic $[NTf_2]$ ion is not capable of interacting strongly with the hydroxyl groups of the polymer chains. The H-bond acceptor ability and size of the anions primarily determine the ionic liquid dissolution ability

(Pinkert et al., 2009), with a loose ranking of [SCN] < [Br] < dialkylphosphates < [OFo] ∼ [OAc] ∼ [Cl].

A comprehensive overview of reports on enzymatic lignocellulose treatment is given in a publication by Wahlstroem and Suurnaeki (Wahlström and Suurnäkki, 2015). Early publications investigated *Trichoderma reesei* cellulase effectiveness in ionic liquids (Turner et al., 2003; Kamiya et al., 2008), and found very low enzymatic activity and stability. Following this, very interesting results were obtained by a study from Datta et al. (2010) on three structurally similar family-5-celullases obtained from the three different domains of life (Eukarya, Bacteria and Archaea; *Trichoderma viride* and thermophilic cellulases from *Thermogata maritime* and *Pyrococcus horikoshii,* respectively), which showed dramatically different activities in $[C_2C_1Im][OAc]$ over a concentration range of 0–50% (v/v) (Datta et al., 2010). Relative specific activity was vastly different between all three. While *T. viride* cellulase activity had already declined to a third at 5% (v/v) IL, a linear trend of decreasing activity was observed for the cellulase from *T. maritima*, with about a third of the activity remaining at 20% (v/v). Activity stayed almost constant and equally high in comparison to the absence of ionic liquid for *P. horikoshii* cellulase in up to 20% (v/v) ionic liquid. However, by 50% (v/v) $[C_2C_1Im][OAc]$, activity had completely declined for all enzymes, with only that from *P. horikoshii* showing the slightest activity.

Picking up on these differences Jaeger et al. (2015) conducted a MD study on those very same systems and found the impact of the ionic liquid derived in each case from individual local structural disturbances (Jaeger et al., 2015). Simulating a concentration of 0, 15, and 50%, they found that for *P. horikoshii* and *T. viride* only a few unstructured loops were displaced at both concentrations, while the secondary structure of the *T. maritima* cellulase is intensely disrupted. Moreover, results suggest that the secondary structure is more heavily disrupted at low to medium concentrations of around 15% and some kind of refolding or "reassuming of a prime-similar structure" occurs at 50%. The observation of refolding also held true for both of the other enzymes. RMSD values for these two enzymes indicated an even higher stability in 50% ionic liquid, compared to the buffer system. Their reported trajectories for the positively charged surface of *T. maritima* suggest that key salt bridges within the protein are broken and enable large structural changes. The RMSD values at 15% (v/v) suggest higher conformational stability, most likely due to the trapping of the enzyme in a less favorable conformation, reflected in the gradual decrease of activity in the study by Datta et al. (2010) For *T. viride* they suggest a likely competitive inhibition for substrate binding. Indeed, a recently published enzyme kinetic analysis of a commercially available cellulase cocktail finds competitive inhibition by $[C_4C_1Im][Cl]$ is highly likely (Nemestóthy et al., 2017). In the case of the halophilic *P. horikoshii* cellulase, a possible deactivation at 50% (v/v) due to aggregation is suggested, because no major structural changes occur in the simulation (Jaeger et al., 2015).

Although many enzymes of other classes do not display their best activities in ionic liquids comprising chloride ions, a great

TABLE 4 | Summary of selected cellulase reactions in ionic liquids.

Ionic Liquid	Organism	Concentration range	Experimental outcome	References
[AMIM][Cl]	*Hu*-CBH1	20–40% (v/v) aq, 2 M NaCl	~100–5% relative activity, respectively	Zhang et al., 2011
	Celluclast *T. reesei*	10% (v/v) aq	~ 25% relative residual activity (30 min)	Engel et al., 2010
	Cel5A from *T. tengcongensis*	2 M	50% relative residual activity after 5 h at room temperature	Liang et al., 2011
[AMIM][Me$_2$PO$_4$]	*T. reesei*	20, 50, and 100% (v/v) aq	34.36, 0.3, and 0% conversion, respectively, with ultrasonic heating pretreatment	Yang et al., 2010
[AEIM][Et$_2$PO$_4$]	*T. reesei*	20, 50, and 100% (v/v) aq	11.00, 0, and 0% conversion, respectively, with ultrasonic heating pretreatment	Yang et al., 2010
[C$_1$C$_1$Im][Me$_2$PO$_4$]	*T. reesei*	20, 50, 100% (v/v) aq	53.18, 1, and 0.3% conversion, respectively, with ultrasonic heating pretreatment	Yang et al., 2010
	Celluclast *T. reesei*	10% (v/v) aq	40% relative residual activity after 11 days	Engel et al., 2010
[C$_1$C$_1$Im][MeSO$_4$]	α-galactosidase *Thermatoga maritimia*	0, 9, 27, and 45% (v/v)	42.7, 33, 6.2, 5.8 k$_{cat}$/K$_m$ s^{-1}mM^{-1} respectively to the concentrations	Ferdjani et al., 2011
[C$_1$C$_1$MIm][MeSO$_4$]	α-galactosidase *T. maritimia*	0-33% (v/v)	Similar activity profile to [C$_1$C$_1$Im][MeSO$_4$] but less soluble	Ferdjani et al., 2011
[C$_2$C$_1$Im][Br]	Pseudoalteromonas sp. cellulase	1–20% (v/v) aq	115% relative activity at 5% (v/v)	Trivedi et al., 2013
[C$_2$C$_1$Im][CF$_3$CO]	CelA2	30% (v/v) aq	506 mU/mg	Ilmberger et al., 2012, 2013
[C$_2$C$_1$Im][Cl]	*Tm*Bgl1A	200, 500 mM	1.32 × 10^3 k$_{cat}$/K$_m$ (s^{-1} mM^{-1}) at 200 mM	Kudou et al., 2014
	S. cerevisiae MT8-1	50–1000 mM	0.7 g/l ethanol production after 200 h	Nakashima et al., 2011
	Hu-CBH1	20% (v/v) aq 2 M NaCl	~120% relative activity	Zhang et al., 2011
[C$_2$C$_1$Im][Et$_2$PO$_4$]	*S. cerevisiae* MT8-1	50–1,000 mM	1.4 g/l ethanol produced after 200 h	Nakashima et al., 2011
	T. reesei	≤ 40% (v/v) aq	*In situ* one pot synthesis	Kamiya et al., 2008
	T. reesei	20, 50, and 100% (v/v) aq	2.18, 0, and 0% conversion at respective concentrations in ultrasonic heating pretreatment	Yang et al., 2010
[C$_2$C$_1$Im][EtSO$_4$]	C. rugosa lipase	20% wt	Simulation revealed, that effect of altering enzyme charge is confined to short range (<1 nm) ordering of the IL	Burney et al., 2015
[C$_2$C$_1$Im][Me$_2$PO$_4$]	*T. reesei*	20, 50, and 100% (v/v) aq	48.14, 0.7, and 0% conversion at respective concentrations in ultrasonic heating pretreatment	Yang et al., 2010
[C$_2$C$_1$Im][MeSO$_3$]	Pseudoalteromonas sp. cellulase	1–20% (v/v) aq	98% relative activity at 5% (v/v)	Trivedi et al., 2013
[C$_2$C$_1$Im][OAc]	*T. maritimia* endogluconase	5, 10, 15, and 20% (v/v) aq	52% decrease in specific activity at 15% (v/v)	Datta et al., 2010
	T. viride celullase	5, 10, 15, and 20% (v/v) aq	100% decrease in specific activity at 15% (v/v)	Datta et al., 2010
	Pyrococcus horikoshii endogluconase	5, 10, 15, and 20% (v/v) aq	5% decrease in specific activity at 15% (v/v)	Datta et al., 2010
	Cellulases from *A. terreus*	5, 10, 15, and 20% (v/v) aq	100% relative activity at 10% (v/v)	Gunny et al., 2014
	*Tm*Bgl1A	200 and 500 mM	3.15 × 10^3 k$_{cat}$/K$_m$ (s^{-1} mM^{-1}) at 200 mM	Kudou et al., 2014
	S. cerevisiae MT8-1	50–1,000 mM	1 g/l ethanol production after 200 h	Nakashima et al., 2011
	Paenibacillus tarimensis	20% (v/v) aq	90 and 80% relative activity at 80 and 50°C, respectively	Raddadi et al., 2013
	Pseudoalteromonas sp. cellulase	1–20% (v/v) aq	105% relative activity at 5% (v/v)	Trivedi et al., 2013

(Continued)

TABLE 4 | Continued

Ionic Liquid	Organism	Concentration range	Experimental outcome	References
	β-glucosidase *T. reesei*	15 and 20% (w/v)	77 and 65% relative activity, respectively	Wang et al., 2011
	Hu-CBH1	20% (v/v) aq, 2 M NaCl	~ 100% relative activity	Zhang et al., 2011
[C$_2$C$_1$Im][OTf]	CelA2	30% (v/v) aq	54% relative activity	Ilmberger et al., 2012, 2013
	CelA3	30% (v/v) aq	68% relative activity	Ilmberger et al., 2012, 2013
	CelA *Thermatoga maritimia*	60% (v/v) aq	115% relative residual activity after 4 days	Ilmberger et al., 2012, 2013
[C$_2$C$_2$Im][Et$_2$PO$_4$]	*T. reesei*	20, 50, 100% (v/v) aq	18.55, 0.1, and 0% conversion at respective concentrations in ultrasonic heating pretreatment	Yang et al., 2010
[C$_4$C$_1$Im][BF4]	*Humicola insolens*	IL:Buffer 1:1	1.5 γ$_C$ (g/l) after 6 h	Paljevac et al., 2006
[C$_4$C$_1$Im][Cl]	Cellulases from *A. terreus*	5, 10, 15, and 20% (v/v) aq	60% relative activity at 10% (v/v)	Gunny et al., 2014
	Cel5A from *T. tengcongensis*	40% (v/v) aq	80% relative residual activity after 5 h	Liang et al., 2011
	*Tm*Bgl1A	200 and 500 mM	1.89×10^3 k$_{cat}$/K$_m$ (s^{-1} mM^{-1}) at 200 mM	Kudou et al., 2014
	T. reesei engineered	0–5% (v/v) aq	~ 33, 18, and 16% conversion of 0.25 wt% lignin by succinylated, acetylated and wt enzyme, respectively	Nordwald et al., 2014
	H. insolens	IL:Buffer 1:1	0.3 γ$_C$ (g/l) after 6 h	Paljevac et al., 2006
	Paenibacillus tarimensis	40% (v/v) aq	40 and 45% relative activity at 80 and 50°C, respectively	Raddadi et al., 2013
	P. tarimensis	20% (v/v) aq	75 and 70% relative activity at 80 and 50°C, respectively	Raddadi et al., 2013
	Hu-CBH1	20% (v/v) aq, 2 M NaCl	~105% relative activity	Zhang et al., 2011
	Pseudoalteromonas sp. cellulase	1–20% (v/v) aq	102% relative activity at 5% (v/v)	Trivedi et al., 2013
[C$_4$C$_1$Im][OAc]	Cellulases from *A. terreus*	5, 10, 15, and 20% (v/v) aq	60% relative activity at 10% (v/v)	Gunny et al., 2014
	*Tm*Bgl1A	200 and 500 mM	~23 U/mg at 200 mM (80°C)	Kudou et al., 2014
[C$_4$C$_1$Im][OTf]	89C12	30% (v/v) aq	111 mU/mg	Ilmberger et al., 2012, 2013
	Pseudoalteromonas sp. cellulase	1–20% (v/v) aq	94% relative activity at 5% (v/v)	Trivedi et al., 2013
[C$_4$C$_1$Im][PF$_6$]	*H. insolens*	IL:Buffer 1:1	1.8 γ$_C$ (g/l) after 6 h	Paljevac et al., 2006
[BMMIM][Cl]	CelA2	30% (v/v) aq	181 mU/mg	Ilmberger et al., 2012, 2013
	CelA3	60% (v/v) aq	79% relative residual activity after 4 days	Ilmberger et al., 2012, 2013
[C$_4$C$_1$Pyr][OTf]	CelA2	60% (v/v) aq	11% relative residual activity after 5 days	Ilmberger et al., 2012, 2013
	CelA84	30% (v/v) aq	8% relative activity	Ilmberger et al., 2012, 2013
	CelA84	60% (v/v) aq	81% relative residual activity after 4 days	Ilmberger et al., 2012, 2013
	CelA10	30% (v/v) aq	74% relative activity, 0.8% relative residual activity after 17 h	Pottkämper et al., 2009
	CelA24	30% (v/v) aq	2% relative activity	Pottkämper et al., 2009
	Pseudoalteromonas sp. cellulase	1–20% (v/v) aq	93% relative activity at 5% (v/v)	Trivedi et al., 2013
[Tris-(2-HOEt)-MAM][MeSO$_4$]	*A. niger* endo-1,4-β-D-glucanase	0, 10, 50, and 99% (v/v) aq	Higher than average thermal stability; up to 140% relative activity at 75°C	Bose et al., 2012

number of cellulases seem to be particularly affected by [Cl] (Paljevac et al., 2006; Salvador et al., 2010; Ilmberger et al., 2013; Yoshimoto et al., 2013; Jaeger et al., 2015). For the highly positively surface-charged *T. maritima* cellulase, which is also particularly enriched in α-helices, an investigative comparison between $[C_4C_1Im]$ and $[C_2C_1Im]$, in combination with [Cl] and [OAc], revealed that although conformational stability in low concentrations (0.2 M) of $[C_4C_1Im][Cl]$ was extremely similar to the aqueous system with 10 mM phosphate buffer, a considerably decreased conformational stability in 0.2–0.5 M $[C_4C_1Im][OAc]$ correlated with a considerably higher relative activity than for the other solvent systems, including the aqueous environment (Kudou et al., 2014). This relative activity was found to be highly temperature dependent and had an optimum at 80°C, which is unsurprising given it is a hyperthermophile-derived cellulase. Conformational restriction in $[C_2C_1Im][OAc]$ manifested as an increased stability but to the point where the lowest activity was observed, as the active site could no longer be accessed effectively. These results imply that, as long as either catalytic residues are not displaced or the active center is not inhibited, a decreased conformational stability is rather preferable to a "rock-solid" conformation, where the active center is not flexible enough. The k_{cat}/K_m values were also found to be considerably increased for $[C_4C_1Im][OAc]$, indicating higher enzyme-substrate affinity (Kudou et al., 2014). These findings complement the observations by Jaeger et al. (2015) and Datta et al. (2010).

Halophilic cellulases appear to be promising biocatalysts and a recent patent out of the research on *Halorhabdus utahensis* cellulase Hu-CBH1 highlights this. This particular cellulase was found to display the same activity at 20% (v/v) $[C_2C_1Im][OAc]$ and [AMIM][Cl] as in 2 M NaCl-buffer and activity was even slightly improved at 20% (v/v) $[C_2C_1Im][Cl]$ (Zhang et al., 2011). The molecular basis for this improvement was postulated as due to the highly elevated negative surface charge brought about by a high proportions of Glu and Asp residues. There has been increasing interest in the investigation of halophilic celullases since Zhang's pioneering study (Ilmberger et al., 2012; Raddadi et al., 2013; Gunny et al., 2014; Nordwald et al., 2014). Ilmberger et al. (2012) used a concentration of 30% (v/v) of $[C_4C_1Im][Cl]$ and [BMMIM][Cl] (1-butyl-2,3-diemthylimidazolium), which yielded moderate specific activities from newly isolated, moderately thermophilic and halotolerant enzymes CelA2 and CelA3 from a biogas plant.

Raddadi et al. (2013) assayed a crude lysate of *Paenibacillus tarimensis* and demonstrated a clear correlation between temperature and salt concentration, which was also found in other studies regarding halophilic enzymes (Zhang et al., 2011; Gunny et al., 2014). While an increase of salt concentration in aqueous buffer systems leads, at low-moderate temperatures, to a decrease in activity, at high temperatures the opposite is found. However, this does not apply to ionic liquid concentrations. Mixtures of aqueous solution of 20 and 40% (v/v) $[C_4C_1Im][Cl]$ without NaCl in the buffer showed lower activity for the higher concentration at higher temperatures (Raddadi et al., 2013). Interestingly, if the buffer-ionic liquid solution contained an additional 5 M NaCl, a slight increase

in activity at higher temperatures was effected at 20% (v/v) $[C_4C_1Im][Cl]$ and $[C_2C_1Im][OAc]$. The sodium ions are likely the essential mitigators, coordinating to the negatively charged surface residues. Systems with $[C_2C_1Im][OAc]$ displayed overall the highest activity with ∼90% relative activity. Optimum activity for an *Aspergillus terreus*-derived cellulase was reached in low to medium concentrations of 10% (v/v) $[C_2C_1Im][OAc]$ with almost the same relative activity compared to the buffer system (Gunny et al., 2014). This study also found a similar salt-mitigating temperature dependence as per the Raddadi study.

Finally, another study examining *T. reesei* cellulase once more, modified the enzyme surface charge by succinylation and acylation, finding a moderate improvement for succinylation and a slight negative effect for acylation in $[C_4C_1Im][Cl]$ (Nordwald et al., 2014). This adverse effect of acylation in comparison to natively, negatively-charged enzymes could be explained by, and at the same time verify, the theory that negatively-charged surface residues are not randomly placed, but rather "strategically" favorable (Madern et al., 2000). This placement acts either to have these residues repel and lend the protein more flexibility; or to coordinate positively charged ions to secondary structural regions of interest, e.g., to α-helices, which seem to be more affected by salt than β-sheets; or a combination of both.

In conclusion, the studies of cellulases in ionic liquids have demonstrated that small positively charged ions (Na^+, K^+) seem to be essential for structural integrity, at least to enzymes that possess a negatively-charged surface. If the surface charge is positive, symmetrical, smallish, negatively-charged ions (Cl^-) are attracted to the surface and disrupt the secondary structure substantially, with the coordinating strength of the anion to the surface depending on its H-bond acceptor ability. This disruption does not automatically lead to a major disturbance of the active center, unless inhibition by the ionic liquid ions occurs. Upon increasing ionic liquid concentrations, overall enzyme structure can get trapped by the charged molecules; this applies already at low to moderate concentrations for mesophilic proteins and at higher concentrations of ionic liquid for halophilic proteins. In the latter case, the negatively charged surface residues most likely repel the negatively charged ions of the solution.

Alcohol Dehydrogenases

Alcohol dehydrogenases (ADHs) are valuable biocatalysts due to their enantioselective reactions with prochiral ketones and alcohols. Productivity for a broad range of substrates, however, is limited by the incompatibility of the solubility of the required redox cofactor NAD(P)H in non-aqueous media and sparingly water-soluble ketone substrates. This makes ionic liquids an attractive medium for reaction, where compatibility with the enzyme can be established.

A range of ionic liquids, primarily based on either imidazolium or ammonium cations (**Table 5**), have been employed with ADHs. The mechanism of impact of ionic liquids on ADH can be interpreted through the prism of three ionic liquid classifications: (a) hydrophilic ionic liquids (b) water-immiscible ionic liquids, which drive the partition coefficients of substrates and products in favor of the enzyme without direct interaction and (c) water-miscible, amphiphilic ionic liquids,

TABLE 5 | Summary of ADH reactions in selected ionic liquids.

Ionic Liquid	Enzyme	Concentration ranges	Experimental outcomes	References
$[C_4C_1Im][PF_6]$	YADH	IL:EtOH:H$_2$O	Catalytic activities between 0.7 and 11 mol L^{-1} min^{-1} recorded, depending on (up to 0.55 IL)	Zhang et al., 2011
	YADH	IL:H$_2$O:TritonX-100	Catalytic activity 51 mol L^{-1} min^{-1} with ratios 0.1:0.3:0.6, respectively.	Zhang et al., 2011
	HL-ADH	0.025–0.4 g/ml	Enhanced activity (up to 145% at 0.025 g/ml) dropping to 95% and then <50% at 0.075 and 0.15 g/ml and above, respectively. Half-life 1.6 h with residual activity at 50 h.	Shi et al., 2006
	RE-ADH	10% v/v (aq)	Conversion rate 98.5%; Activity 28% Half-life 135 h.	Hussain et al., 2008
	R. ruber ADH-A	20, 50, and 80% v/v (aq)	Conversion rates ~30, 20, and 15%, respectively	De Gonzalo et al., 2007
$[C_4C_1Im][NTf_2]$	LB-ADH	Biphasic with 50 mM phosphate buffer	88% conversion; 61% conversion in MTBE/buffer	Eckstein et al., 2004
	W110A TE-ADH	50% v/v (aq)	Conversion 52% - >99% with a selection of substrates	Musa et al., 2008
	R. ruber ADH-A	20, 50, and 80% v/v (aq)	Conversion rates ~25, 10, 5%, respectively	De Gonzalo et al., 2007
$[C_4C_1Im][Cl]$	HL-ADH	0.025–0.4 g/ml	Enhanced activity (up to 155% at 0.05 g/ml) dropping to 90% and then <50% at 0.2 and 0.4 g/ml, respectively. Half-life 14.5 h with residual activity at 50 h.	Shi et al., 2006
	YADH	0.01–0.6 M	98–20%, respectively; enzyme parameters.	Dabirmanesh et al., 2011, 2012
$[C_4C_1Im][Br]$	HL-ADH	0.025–0.4 g/ml	Enhanced activity (up to 185% at 0.05 g/ml) dropping to 90% and then <50% at 0.15 and 0.4 g/ml, respectively. Half-life 5.3 h with residual activity at 50 h.	Shi et al., 2006
$[C_4C_1Im][BF_4]$	HL-ADH	0.025–0.4 g/ml	Activity ~30% at 0.025 g/ml dropping to ~0% at 0.075 g/ml. Half-life <0.5 h.	Shi et al., 2006
	RE-ADH	10% v/v (aq)	Conversion rate 99.5%; Activity 38% Half-life 82 h.	Hussain et al., 2008
	W110A TE-ADH	50% v/v (aq)	Conversion 40–96% with a selection of substrates	Musa et al., 2008
	YADH	0.01–0.4 M	95–20%, respectively; enzyme parameters.	Dabirmanesh et al., 2011, 2012
$[C_4C_1Im][OAc]$	*R. ruber* ADH-A	20, 50, and 80% v/v (aq)	Conversion rates ~40, 10, and 0%, respectively	De Gonzalo et al., 2007
$[C_4C_1Im][OTf]$	HL-ADH	0.025–0.4 g/ml	Activity ~25% between 0.025 and 0.1 g/ml dropping to ~0% at 0.15 g/ml. Half-life 1.5 h.	Shi et al., 2006
$[C_2C_1Im][OAc]$	*R. ruber* ADH-A	20, 50, and 80% v/v (aq)	Conversion rates ~ 45, 2, and 0%, respectively	De Gonzalo et al., 2007
$[C_2C_1Im][Cl]$	HL-ADH	0.025–0.4 g/ml	Enhanced activity (up to 155% at 0.025 g/ml) dropping to 95% and then <50% at 0.075 and 0.4 g/ml, respectively.	Shi et al., 2006
$[C_2C_1Im][Et_2PO_4]$	LB-ADH	10% v/v (aq)	Activity ~ 5%	Kohlmann et al., 2011
$[C_2C_1Im][Me_2PO_4]$	LB-ADH	10% v/v (aq)	Activity ~ 80%	Kohlmann et al., 2011
$[C_2C_1Im][EtSO_4]$	RE-ADH	10% v/v (aq)	Half-life 147 h.	Hussain et al., 2008
$[C_2C_1Im][MeSO_3]$	*R. ruber* ADH-A	20, 50, and 80% v/v (aq)	Conversion rates ~5, 0, and 0%, respectively	De Gonzalo et al., 2007
	LB-ADH	10% v/v (aq)	Activity ~ 105%	Kohlmann et al., 2011
$[C_2C_1Im][MDEGSO_4]$	RE-ADH	10% v/v (aq)	Half-life 22 h.	Hussain et al., 2008
	LB-ADH	10% v/v (aq)	Activity ~ 70%	Kohlmann et al., 2011
$[C_2C_1Im][OTs]$	RE-ADH	10% v/v (aq)	Conversion rate 89%; Activity 51% Half-life 45 h.	Hussain et al., 2008
$[C_1C_1Im][Me_2PO_4]$	RE-ADH	10% v/v (aq)	Conversion rate 38.5%; Activity 66% Half-life 182 h.	Hussain et al., 2008

(Continued)

TABLE 5 | Continued

Ionic Liquid	Enzyme	Concentration ranges	Experimental outcomes	References
$[C_1Im][BF_4]$	YADH	0.01–0.6 M	85–0%, respectively with zero activity from 0.4 M; enzyme parameters.	Dabirmanesh et al., 2011, 2012
$[C_1Im][Cl]$	YADH	0.01–0.2 M	80–0%, respectively; enzyme parameters.	Dabirmanesh et al., 2011, 2012
[3-HOMeC$_2$Py][EtSO$_4$]	RE-ADH	10% v/v (aq)	Conversion rate 100%; Half-life 266 h.	Hussain et al., 2008
$[C_4C_1Pyr][NTf_2]$	RE-ADH	10% v/v (aq)	Activity 43%; Half-life 144 h.	Hussain et al., 2008
AmmoEng^{TM} 100*	R. ruber ADH-A	70, 80, and 90%	Conversion rates 77.5, 73.1, and 27.0%, respectively	De Gonzalo et al., 2007
	LB-ADH	10% v/v (aq)	Activity ~ 150%	Kohlmann et al., 2011
AmmoEng^{TM} 101*	R. ruber ADH-A	70, 80, and 90%	Conversion rates 78.2, 77.4, and 28.3%, respectively	De Gonzalo et al., 2007
	LB-ADH	10% v/v (aq)	Activity ~ 180%	Kohlmann et al., 2011
AmmoEng^{TM} 102*	RE-ADH	10% v/v (aq)	Conversion rate 100%; Activity 9.4%; Half-life 12 h.	Hussain et al., 2008
	R. ruber ADH-A	70, 80, and 90%	Conversion rates 69.7, 67.1, and 7.5%, respectively	De Gonzalo et al., 2007
	LB-ADH	10% v/v (aq)	Activity ~ 110%	Kohlmann et al., 2011
AmmoEng^{TM} 110*	RE-ADH	10% v/v (aq)	Half-life 77 h.	Hussain et al., 2008
AmmoEng^{TM} 112*	LB-ADH	10% v/v (aq)	Activity ~ 100%	Kohlmann et al., 2011
AmmoEng^{TM} 120	RE-ADH	10% v/v (aq)	Half-life 40 h.	Hussain et al., 2008
AmmoEng^{TM} 140	LB-ADH	10% v/v (aq)	Activity ~ 90%	Kohlmann et al., 2011
$[N_{8,8,8,1}][NTf_2]$	R. ruber ADH-A	20, 50, and 80% v/v (aq)	Conversion rates ~40, 20, and 10%, respectively	De Gonzalo et al., 2007
[Tris-(2-HOEt)-MAM][MeSO$_4$]	LB-ADH	10% v/v (aq)	Activity ~ 120%	Kohlmann et al., 2011
	R. ruber ADH-A	70, 80, and 90%	Conversion rates 79, 76.4, and 65.3%, respectively	De Gonzalo et al., 2007

MDEGSO$_4$, 2-(2-methoxyethoxy)ethylsulfate; *REACH registered.

which provide H-bonding through the hydrophilic part and substrate solubility within their alkyl-tail-pockets.

a) **Hydrophilic ionic liquids**

i. *Ion effects*

The impact of hydrophilic ions, such as Me$_4$N, choline, and imidazolium cations, and Cl, Br, BF$_4$, PF$_6$, OTf, Me$_2$PO$_4$, Et$_2$PO$_4$, MeSO$_3$ anions, has been examined for a number of ADH systems, with the caveat that PF$_6$ or BF$_4$ ions can be hydrolysed in aqueous solutions. While PF$_6$ hydrolysis is mainly promoted only under acidic conditions so that the PF$_6$ ion can be suitable for use at moderate temperatures in aqueous solutions, activity in BF$_4$ might not be fully attributed to the biocatalyst, as it is not stable in water and will hydrolyse readily (Freire et al., 2010). The ionic liquids $[C_2C_1Im][Cl]$, $[C_4C_1Im][PF_6]$, $[C_4C_1Im][Cl]$ and $[C_4C_1Im][Br]$ were able to enhance activity of HlADH at low concentrations between 0.05 and 0.075 M, when compared to pure buffer systems (Shi et al., 2006). This finding may hold true for many more small-molecule ions, but unfortunately not many ADH studies in ionic liquids apply alternatives to imidazolium

cations or examine such low concentrations (see **Table 5**). Comparability of results in this field is also challenging as reported results vary between conversion rates, yields and residual activity. Regardless, conversion rates and half-life of enzymes seem to show considerable improvements upon addition of aqueous ionic liquids, relative to buffer solutions at low to moderate concentrations. In particular, improvements have been seen for $[C_4C_1Im][OAc]$ and $[C_2C_1Im][OAc]$ at 20% (v/v) (De Gonzalo et al., 2007), for $[C_2C_1Im][MDEGSO_4]$, $[C_2C_1Im][MeSO_3]$, and $[C_1C_1Im][Me_2PO_4]$ at 10% (v/v) with respect to conversion rates (Kohlmann et al., 2011), and for [EMP][ES], $[C_4C_1Im][BF_4]$, and $[C_2C_1Im][OTs]$ at 10% (v/v) with respect to half-life stability (Hussain et al., 2008). In contrast, imidazole and imidazolium derivatives, because of their similarity in structure to parts of the cofactor NADP$^+$ (Dabirmanesh et al., 2012), have been reported as exhibiting competitive inhibition of the active center of ADHs (Zhang et al., 2008), and with smaller alkyl chains lengths for these imidazolium-based ionic liquids the inhibitory effect increases (Dabirmanesh et al., 2012).

Chloride-ion based ionic liquids do not act as a challenge to ADH-systems. YADH assayed in $[C_4C_1Im][Cl]$ lead to a slight decrease in activity (~95%) at very low concentrations (~0.01 M), but activity (~20% remaining) was maintained up to a concentration of ~0.6 M ionic liquid, while for $[C_1C_1Im][Cl]$ only 80% remaining activity was observed at 0.01 M and activity had completely declined at ~ 0.2 M (Dabirmanesh et al., 2011). For HlADH assayed in $[C_4C_1Im][Cl]$ a maximum relative activity of 150% was observed at 0.075 M and decreased slowly to 25% at 0.4 M ionic liquid concentration. Use of $[C_2C_1Im][Cl]$ lead to a maximum relative activity of 150% at 0.05 M, but activity values were ~50% less on average at higher concentrations (0.1–0.3 M) than for $[C_4C_1Im][Cl]$ (Shi et al., 2006). However, activity ended up being about the same at 0.4 M in both ionic liquids, which was the highest concentration assayed. Of the other hydrophilic ionic liquid systems that have been assayed, $[C_2C_1Im][Et_2PO_4]$ is strikingly detrimental to the enzymatic activity of *L. brevis* ADH with only 5% relative activity left at 10% (v/v) for the reduction of 2-octanone. This contrasts with $[C_1C_1Im][Me_2PO_4]$, with 85% relative activity, and is comparable to the activity of YADH found for $[C_1C_1Im][Cl]$ (above), and $[C_2C_1Im][MeSO_3]$ with 105% relative activity (Kohlmann et al., 2011).

Simulation studies have been able to shed light on the specific interactions that may be at play in controlling activity. Ionic liquid ions with low charge density (most cations) do not tend to exhibit any preference of vicinity on the protein surface, since coulombic forces for these ions are less dominant due to delocalisation and are competitive with the van der Waals interactions of the alkyl chains. Thus, these ions tend to be more mobile on the protein surface, than those ions with high charge density (most anions) (Tomé et al., 2012; Lim and Klähn, 2018), and this gives a rationale for the relatively more significant impact ascribed ionic-liquid anions. At all concentrations, the cations with their alkyl chains are able to contact like-charged-ions, but at low concentrations, since there are only a few about, they will, as single ions or small clusters, be able to closely associate to the protein surface.

The shorter the alkyl chain, the smaller are the polar domains that can interact with other species meaning, $[C_1C_1Im]$ or $[C_2C_1Im]$ can associate more closely and individually onto the surface of the protein and more easily into the binding pocket, than, for example C_4C_1Im. The peak in activity at very low concentrations of ionic liquid, and the consequent decrease in activity at increasing concentrations of ionic liquid may be attributed to the different numbers of cations being able to aggregate on the protein surface. As the cations continue to coordinate to the protein surface at increasing concentrations (Lim and Klähn, 2018), the ions form ever bigger patches, that are still small enough to amass onto the protein surface, but with the increasing patch-size an increased rigidity of

the protein is conferred. The discrepancy of ~50% less activity between $[C_4C_1Im]$ and $[C_2C_1Im]$ at medium range concentrations (0.1–0.3) underlines the different interactions of the ions with the protein surface, as $[C_2C_1Im]$ having shorter chains will be able to associate more closely overall. This close association allows an optimum effect on the flexibility (and activity) of the protein at a slightly lower concentration (0.05 M), than $[C_4C_1Im]$ with 0.075 M, and at the same time having a much higher impact on constraining the protein flexibility at medium concentrations. At low ionic strength, the ring and tail of the imidazolium ions are equally often in contact with the protein surface, whereby the tail mainly has a steric interaction (fitting into clefts on the surface) and the ring has a mostly charged interaction, which becomes more pronounced and dominant at higher ionic strengths (Haberler et al., 2011). In comparison, high-charge density ions, if located on the surface, preferentially reside at positions with oppositely charged amino acids and hardly associate with like-ions. At low ionic liquid concentrations the number of low charge density ions populating the protein surface is far greater than the number of high charge density ions, which prefer the hydration of water molecules in the bulk phase (Haberler et al., 2011), leading to asymmetric influence at different concentrations on the protein.

Anions with high charge density, being dispersed in bulk water at low concentrations, may strip off a small number of tightly bound, structuring water molecules from the protein surface, leading to an increase in entropy and hence more flexibility and activity of the enzyme, up to the maximum point, upon thereafter the disruption of the secondary structure and subsequent rigidity of the protein (as seen for cellulases) becomes detrimental. This can affect the binding pocket significantly, as was proposed by the study on the enantioselectivity of *Thermoanaerobacter ethanolicus* ADH (Musa et al., 2008). In aqueous solution, the binding pocket of *T. ethanolicus* ADH includes a bound, ordered water molecule, which is displaced when a bulky (*R*)-substrate binds, yielding a substantial entropy increase (Heiss et al., 2001). For smaller substrates there is no enantioselective conversion in aqueous solution because they are unable to displace the water molecule. Addition of ~50% (v/v) of the hydrolysable ionic liquid $[C_4C_1Im][BF_4]$ was able to facilitate the asymmetric reduction of small phenyl-ring containing ketones, with this result suggested as indicating the expulsion of the tightly bound, structured water molecule by the ionic liquid (Musa et al., 2008). A similar result was obtained using ~50% (v/v) of the water immiscible $[C_4C_1Im][NTf_2]$, where the lower concentration of substrate in the aqueous phase was used to account for the increase in enantioselectivity, highlighting that a more microscopic view of the reaction may be required to fully interpret the role of the ions.

ii. *Water-effects*

The change in activity seen for ADHs, spiking around one mole fraction of water ($\chi_{H2O} \sim 0.9$) highlights the

finding of a "magic point," reported in a computational solvation study of a small zinc-finger protein in aqueous ionic liquids (Haberler et al., 2011). This point hints at a change in the organization of the ions and water molecules at *ca.* 0.075 M ionic liquid-aqueous mixture, which appears to correlate with a transition from dipolar screening (achieved by small water molecules intercalating between protein residues and attenuating residue-residue interactions) to charge screening (by ion-charge interactions) of electrostatic forces. At this transition point the protein is at its highest total energy and lowest level of ordering of the secondary structure (Haberler and Steinhauser, 2011; Haberler et al., 2011, 2012). At comparably high ionic strengths the mean residence times of ions, especially anions, on the protein surface, i.e., their interaction with specific residues, is raised from picoseconds to nanoseconds (Haberler et al., 2011), and a weakening effect on the binding affinity of the substrate to the enzymes is observed (Dabirmanesh et al., 2011, 2012).

Furthermore, at increasing concentrations of ionic liquids, simulation studies show that the water molecules change their behavior significantly (Gehrke et al., 2018). At relatively low mole fractions of water (0.38) water molecules tend to form larger clusters of around 12 molecules, and they are apparently present either as single molecules or on-average as dimers at higher mole fractions of ∼ 0.82 (Gehrke et al., 2018). Here, the underlying structuring force of the van der Waals-induced, tetrahedral-coordinating water molecules becomes replaced by an ionicity driven network, which removes interstitial water molecules as the number of high-charge density ions increases in the bulk. This is in agreement with the observation of an overall dielectric decrement at reduced mole fractions of water, which is especially consequential in the first hydration shell (Haberler et al., 2012).

b) **Water-immiscible ionic liquids (biphasic systems)**

The water-immiscible ionic liquid $[C_4C_1Im][NTf_2]$ was one of the first ionic liquids successfully implemented for improving the enantioselective reduction of ketones with ADH (Eckstein et al., 2004), and since then biocatalysis in multiphasic ionic liquid reaction systems has advanced to show the potential for industrial scale applications of these systems (Meyer et al., 2018). In comparison with hydrophilic ionic liquids, for which a maximum tolerance of around 20% (v/v) of $[C_2C_1Im][OAc]$ (the best candidate with regards to conversion rates), was found, biphasic systems can provide meaningful application maxima of ∼80% (v/v) and still retain the enzyme's hydration shell (De Gonzalo et al., 2007). Since the enzyme and the cofactor are in this case "immobilized" in the aqueous phase, it is the partition coefficient of the substrate and co-substrate in the ionic liquid and aqueous phase that drives the thermodynamics of the reaction. In this regard, these biphasic systems are optimal replacements for conventional organic co-solvents as they

can be ion-specifically selected to facilitate different partition coefficients for particular substrates and co-substrates, as has been shown for 1-hexyloxymethyl-3-methyl-imidazolium and 1, 3-dihexyloxymethyl-imidazolium based ionic liquids with alcohols, water, ketones and hydrocarbons (Domanska and Marciniak, 2007). In particular, programmes such as COSMO-RS have been successfully validated for predicting phase equilibria for such systems containing imidazolium and pyridinium-based ionic liquids (Freire et al., 2007).

c) **Water-miscible, amphiphilic ionic liquids**

Hydroxyl-functionalised ionic liquids, including the AmmoEng™ series of task-specific ionic liquids (**Figure 2**), have been shown to enhance the activity of ADHs even at very high concentrations of up to 90% (v/v) ionic liquid content (De Gonzalo et al., 2007), with the optimal concentration dependant on the experimental set-up. Up to 90% (v/v) is tolerated when whole cell-biocatalysts or lysates thereof are applied (De Gonzalo et al., 2007), whilst for purified enzyme, solution concentrations of 10% (v/v) AmmoEng™ 101 were shown to enhance the relative activity of *L. brevis* ADH by 180% (Kohlmann et al., 2011). A major advantage of the use of these amphiphilic ionic liquids is the much higher than usual solubility of difficult substrates, as has been demonstrated for, for example, 4'-Br-2,2,2-trifluoroacetophenone and 6-bromo-β-tetralone (Hussain et al., 2008). *Rhodococcus erythropolis* ADH and GDH 103 did not show any residual activity for those substrates when used in buffer, but GDH 103 showed 65% (w/w) residual activity in 10% (v/v) AmmoEng™ 102. Both ADH and GDH 103 enzymes showed 50% (w/w) residual activity in the water-immiscible ionic liquid $[C_4C_1Pyr][NTf_2]$ (Hussain et al., 2008). The amphiphilic oligoether-based ionic liquids AmmoEng™ 100 and 101, with a 14-carbon coconut oil-derived group, were found to either impart the most activity or increase conversion by 150 and 180%, respectively (De Gonzalo et al., 2007; Kohlmann et al., 2011), with the main difference being the anion [MeSO₄ (100) and Cl (101)]. AmmoEng™ 102, which has an 18-carbon tallow-derived group, a 5-fold longer oligio(ether-) chain than AmmoEng™ 101 and a greater ability to absorb water due to the higher ether content (Ribot et al., 2012), was found to increase activity of *L. brevis* ADH by 110%. In AmmoEng™ 140 only a 90% increase in activity was observed.

Lipases

Lipase biotransformations have significant application, and this is reflected in the ionic liquid field by a substantial literature (Itoh et al., 2002; Zhao et al., 2010a, 2018; Latif et al., 2014; Kim et al., 2016; Carvalho et al., 2018; Itoh, 2018; Lisboa et al., 2018; Park et al., 2018; Zhong et al., 2018). As such, lipase-catalyzed biotransformations have been the topic of recent reviews, covering enantioselective transesterification, biofuel production and polymer synthesis in ionic liquids (Itoh, 2017a; Elgharbawy et al., 2018), and ionic liquid-mediated activation of lipase-catalyzed reactions (Itoh, 2018). Further, for specific lipase-catalyzed reactions there has been a more extensive fine tuning of the use of ionic liquids than for other enzymatic systems. A
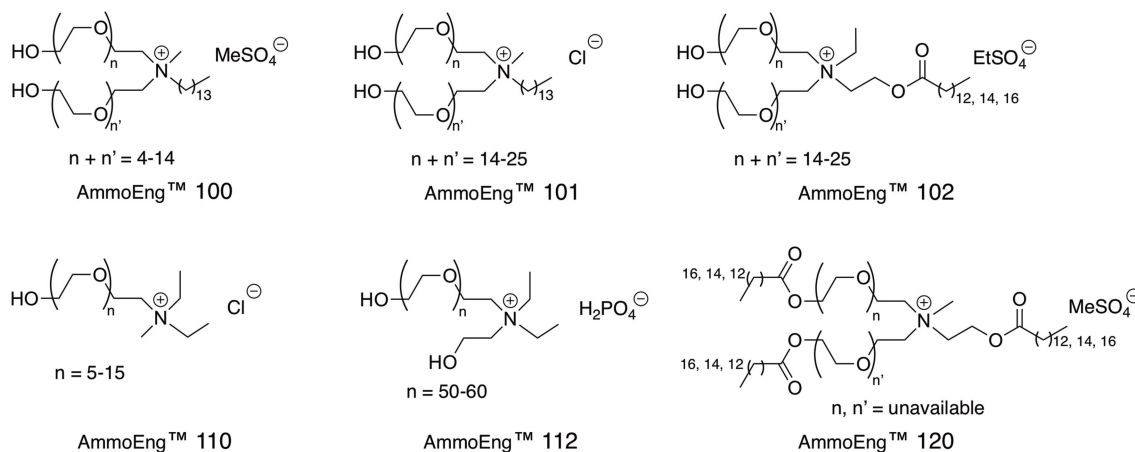
FIGURE 2 | The AmmoEng^{TM} series of ionic liquids.

prominent example is the deployment of [BDMIM] instead of [C_4C_1Im] in the prevention of oligomerisation of acetaldehyde, where the polymer product inhibits the reaction after repeated cycles (Itoh et al., 2002).

Dynamic kinetic resolution (DKR) can be enhanced through the use of lipase in ionic liquids. The polymerisable ionic liquid [VEIm][Br] (1-vinyl-3-ethylimidazolium bromide) was used to immobilize the lipase CalB as a hydrogel, with application for the kinetic resolution of 1-phenylethanol through transesterification (Grollmisch et al., 2018). Upon immobilization, the conversion after 5 h was nearly 15% higher and only the (R)-product was formed with an ee of > 99%, whilst the unreacted (S)-educt accumulated in the reaction mixture with twice the ee relative to the non-immobilized system (Grollmisch et al., 2018). Another immobilization study applying CalB focused on the catalytic selectivity toward diacylglycerols production (Zhong et al., 2018), where the immobilization substrate was modified with one of either [C_4C_1Im], [C_4C_4Im] or [C_4C_8Im]-like cations combined with either the [BF_4] or [PF_6] anion. Here the [BF_4] anion-modified material improved activities, whereas those coupled with the [PF_6] anion did not. Fish oil production has also been attempted with imidazolium-based ionic liquid–immobilized lipase systems utilizing the two hydrolysable ionic liquids [C_4C_1Im][BF_4] and [C_4C_1Im][PF_6], and the hydrophobic ionic liquid [C_4C_1Im][NTf_2] (Fu et al., 2018).

Revisiting the *Candida rugosa* lipase (CRL) for the enantioselective hydrolysis of racemic ketoprofen ethyl ester, Park et al. (2018) assessed six different [C_4C_1Im] derivatives, finding 5% (v/v) solution of [C_4C_1Im][$MeSO_4$] afforded highest conversion (47.3% after 23 h) and enantiomeric excess (ee$_p$ > 99%), but observed long term instability for this ionic liquid mixture (Park et al., 2018). A 20% (v/v) solution of [C_4C_1Im][PF_6] yielded a conversion of 48% with 96.9% ee$_p$ and the enzyme showed much higher long term stability. With the exception of [$MeSO_4$], for which an acid effect was attributed to the improved activity, decreasing H-bond basicity of the ionic

liquid anion correlated with an increase in enantioselectivity (Park et al., 2018).

Biodiesel production with lipase has had well-designed early strategies (Arai et al., 2010; Zhao et al., 2010a; Lozano et al., 2013), although inactivation of the enzyme through the effect of ethanol during transesterification is still an obstacle preventing large scale applications. This challenge may soon be overcome, with an effective model reaction to describe the inactivation of the lipase Novozyme 435 recently being proposed, and a circulating feed mixture being introduced into the reactor design to remove the by-product glycerine (Endo et al., 2018). The immobilization of *Burkholderia cepacia* lipase onto silica xerogel with protic ionic liquid (*N*-methylmonoethanolamine pentanoate) and in-depth characterization of the activity and operational stability could afford appropriate catalysts for such a circulating reactor (Carvalho et al., 2018). Experimental data of the physical adsorption of *B. cepacia* lipase on an aerogel-ionic liquid system based on [$N_{1,1,1,18}$][NTf_2], with an isotherm model fitted to the data, provides an alternative, characterized immobilization system (Lisboa et al., 2018).

Simulations of lipases in ionic liquids have been used to elucidate surface interactions between the enzyme and the cations and anions. Combining experimental and simulation techniques, chloride anions of [C_4C_1Im][Cl] were identified as inducing a conformational switch between an α-helix and turn in CalB, with a specific interaction with Lys290 leading to a narrow cavity entrance and directly reducing the activity (Kim et al., 2014). The transesterification of butyl alcohol was carried out in pure [C_4C_1Im][OTf], [C_4C_1Im][Cl], tert-butanol and 0.3 M NaCl, and simulation in these solvents showed that in water the cavity to the catalytic center can be opened and closed, in tert-butanol and [C_4C_1Im][OTf] it resumes the open conformation, but for [C_4C_1Im][Cl] the cavity is closed. The electrostatic energy between the anion and the enzyme was proposed as the driving force for the change in conformation. A follow-up study in 2016, using all-atom MD simulations to look at cation effects by varying the lengths of the alkyl tails of Imidazolium ions, found that

medium length (butyl–hexyl) alkyl chains disrupt the catalytic activity the least, while [C_2C_1Im], having a high ion coordination number, prevents the interaction between the key lysine and isoleucine residues controlling the cavity conformation. Longer alkyl chains (e.g., octyl) exhibit strong hydrophobic interactions with a nearby leucine, which leads to the complete loss of the secondary structure of the α-helix. Interaction of [C_8C_1Im] with the hydrophobic leucine next to the catalytic center induces an opening up of the pocket and allows [NTf_2] to locate and interact with the catalytic residues (Kim et al., 2016).

The role of water is important in understanding the action of aqueous ionic liquids on enzyme activity. Simulations of *Candida antarctica* lipase B (CalB) and CRL in the [C_4C_1Im]-based ionic liquid systems, with the counter-ions [PF_6], [BF_4], [Cl], [OTf], and [NTf_2], respectively, found a bell-shaped dependency of enzyme structural deviations (RMSD values) mirroring water-content (Latif et al., 2014), as had been previously reported for organic solvents and other ionic liquid-enzyme systems (Laszlo and Compton, 2001; Micaêlo and Soares, 2008). Non-localized water molecules were stripped off the enzyme surface with the degree of observed removal related to the solubility and hydrophobicity of the anions (Latif et al., 2014). Ions with high charge density (most anions studied) are preferentially dispersed in bulk water at low concentrations (Haberler and Steinhauser, 2011; Haberler et al., 2012), and are those that strip the non-localized water molecules. Chloride ions in aqueous solution require six water molecules to form a first hydration shell; in a study of the behavior of [C_8C_1Im][Cl] at both the interface and in bulk solution, the calculated water to ion pair molar fraction was found to be 3.6 at ∼20 wt%, meaning that the chloride ion was preferentially surrounded by one cation and 3-4 water molecules (Cheng et al., 2018). This structuring, and rearrangement of anionic coordination sphere could also have implications for the nature of the interaction of ions with a protein surface at different water contents. In addition, different surface topologies could also produce differential hydrogen-bond and ion-interaction dynamics (Dahanayake and Mitchell-Koch, 2018), leading to localized effects, individual to each protein and for particular solvation conditions.

Laccases

Solubilizing wood-derived biomass really dictates the need for ionic liquids, in the same way as these solvents are required for cellulases to access the cellulose substrate. Protein engineering to enhance activity and stability of laccase in the required ionic liquids is an attractive approach, as engineering of the ionic liquid-based reaction media can be challenging within the constraints of lignin solubility. Alternatively, two-phase systems have been successfully utilized (Xue et al., 2011).

Liu et al. (2013) reported the directed evolution of a laccase from *Trametes versicolor*, which increased its stability and its activity by 4.5-fold in 15% (v/v) [C_2C_1Im][EtSO$_4$], relative to buffer. Upon alteration of two residues, activity was also increased in buffer, but only by 3.5-fold. Fungal laccases comprise of three domains, whereby domains 2 and 3 are connected *via* an exceptionally long loop (Bertrand et al., 2002). A synergistic substitution of a residue in the connecting loop and a residue

in the catalytic center led to an increase in hydrophobicity in the loop region, increasing stability and providing better access to the catalytic center of the protein (Liu et al., 2013). The increase in hydrophobicity is proposed to enhance interactions between domains 2 and 3 under the augmented ionicity of the ionic liquid solution. Based on the identified importance of the changes in hydrophobicity of the domain-connecting loop, a follow-up study focused on synergistic substitutions of alanine residues to (mainly) charged residues in the loop region (Wallraf et al., 2018). The improved rigidity imparted by removing the flexible alanine residues, afforded a particular synergistic improvement in activity at a concentration of 5–15% (v/v) [C_2C_1Im][EtSO$_4$] (Wallraf et al., 2018). Structural stability to improve activity has also been exploited for *Myceliophthora thermophile* laccase in [C_2C_1Im][EtSO$_4$], where immobilization on agarose also prevented inactivation of this enzyme by 50% (Fernández-Fernández et al., 2014).

Lysozyme

An experimental and MD simulation study by Ghosh et al. (2015) was able to show that the hydrodynamic radius of lysozyme decreased by more than a third when exposed to 1.5 M [C_3C_1Im][Br], while also conformational relaxation time decreases, implying structural stabilization and constraint by the ionic liquid. A preferential solvation of the protein surface by the cations over anions was demonstrated and further confirmed the much more compact structure and closer interaction between the two protein domains of lysozyme in ionic liquid, promoting the closed conformation (Ghosh et al., 2015). This finding underlines the importance of conformational entrapment of the protein by ions, with significant potential to alter reactivity.

Wijaya et al. (2016) highlighted the importance of the solvophobic effect and the role of ions by demonstrating favorable lysozyme stability and activity in highly concentrated or neat, non-aqueous solutions of protic ionic liquids. For those ionic liquids containing hydroxyl groups (ethanolammonium-based), a similarity to the effect of glycerol and its lower dielectric constant in creating additional stability was postulated. These hydroxyl moieties can result in stronger hydrogen bonds and screening of charged groups (Pérez and Griebenow, 2000), consistent with the results seen for ADH in ionic liquids. The effect of stabilization and destabilization on lysozyme followed the Hofmeister series (Kumar and Venkatesu, 2014), and the increased role of anions appeared to correlate with the positive surface charge of this enzyme (Wijaya et al., 2016). In a follow-up study Wijaya et al. (2018) further underlined the activity-increasing influence of reduced ion-protein interactions on lysozyme, as promoted by kosmotropic (ordering) ions, relative to the opposite impact that chaotropic (disordering) ions have on activity (Wijaya et al., 2018).

Other Proteins
Cytochrome c
Complementing the finding of positive influence of hydroxyl groups on the structural stability of lysozyme, Papadopoulou et al. (2016) found hydroxyl ammonium based ionic liquids to mitigate the denaturing effect of H_2O_2 on the metalloprotein

cytochrome c and increase the catalytic efficiency, relative to the buffer system. The combination of a more hydrophilic, and thus more chaotropic cation, such as hydroxyl alkyl ammonium cations, in combination with a kosmotropic anion was proposed to enhance cytochrome c peroxidase catalytic activity through perturbation structure and especially of the haem center. A considerable decrease in activation energy, and resultant increase in reaction rate, was observed when chaotropic cations were used (Papadopoulou et al., 2016).

Ikeda et al. (2018) used a bi-phasic system of $[P_{4,4,4,4}][TMBS]$ (2,4,6-trimethylbenzenesulfonate) and buffer to show a favorable residence distribution of reduced and oxidized cytochrome c in the buffer and the hydrophobic ionic liquid phase, respectively. Using temperature gradients and applying a potential, cytochrome c could be reversibly transferred between phases. They found the oxidized form of cytochrome c, which resides in the IL, was more thermodynamically stable (Ikeda et al., 2018).

Tyrosinases

Tyrosinase catalyzes the oxidation of tyrosine through a copper active site and is connected to processes as diverse as melanin production and the over-ripening of fruits. In this regard, mainly kinetic mechanisms and the inhibition of the active site are of interest. Heitz and coworkers carried out a combined experimental kinetics and molecular docking study on mushroom tyrosinase in imidazolium-based cations (Heitz and Rupp, 2018; Heitz et al., 2018), with anions covering the range of the Hofmeister series (Kumar and Venkatesu, 2014). An increase in hydrophobicity of the ions led to an increase in preferential site interactions with the protein surface and active site. The anion $[NO_3]$ had the least impact on activity and was equally distributed on the enzyme surface. In contrast, the anion $[MeSO_3]$ had three preferential sites of interaction, which were dominated by positively charged and polar amino acids. The presence of fluorine atoms in [TFMS] had significant impact on the anion behavior in comparison to $[MeSO_3]$, and this fluorinated ion was mainly localized around the active site. The most detrimental ion to activity was $[NTf_2]$, which showed both competitive inhibition and preferentially interacted with active site residues, due to its hydrophobicity and electronegative atom composition. A similar preferential interaction within the active site was found for all cations, regardless of alkyl chain length, but an increasing hydrophobicity of the cation was correlated to a slight energy decrease in the docking values, indicating worse predicted binding (Heitz and Rupp, 2018; Heitz et al., 2018).

Transaminases

Transaminases are catalysts for the production of enantiomerically pure compounds, and in this regard they are similar in value to ADH for biotechnological applications. Again, poor solubility of the substrate or product in water is an issue, that is mainly overcome by the use of organic solvent. An alternative to overcoming the issue of inactivation in organic solvent by applying ionic liquids has been not by using them as a replacement for the organic phase, but to coat the enzyme in ionic liquids. Grabner et al. (2018) demonstrated an improved method for the coating of enzymes by ionic liquids for application in organic solvents by deploying Ω-transaminases. Co-lyophilisation of enzyme, ionic liquid ([AMIM][Cl] or $[C_2C_1Im][Br]$) and buffer yielded the best results, affording an 8-fold higher activity than compared to that of the free enzyme. The $[C_2C_1Im][Br]$ coating was more favorable in increasing the yield for both enzymes in all solvents tested, relative to [AMIM][Cl], with the exception of the yields under the organic solvents Et_2O and MTBE for one of the assayed enzymes (Grabner et al., 2018).

Selenate Reductase

Selenate reductase catalyzes the NADPH-dependant reduction of selenate and selenite to elemental selenium, which has multiple applications including in batteries, glass production, and solar cells. In a study by Mesbahi-Nowrouzi and Mollania (2018) two imidazolium-based ionic liquids were tested and the enzyme showed increased residual activity (∼110%) in low concentrations of $[C_2C_1Im][Br]$ [5–10% (v/v)] relative to buffer, which linearly decreased to 30% residual activity in 30% (v/v) ionic liquid. The thermal stability in this ionic liquid was also increased, indicating stabilization of the enzyme structure. For $[C_4C_1Im][Cl]$ a linear decline in activity over all concentrations was observed (Mesbahi-Nowrouzi and Mollania, 2018), but this could be recovered on diluting the solution, suggesting an inhibition effect. Both ionic liquids also had an impact on the size of selenium nanoparticles that were produced by the enzyme, compared to the absence of ionic liquid.

Carbonic Anhydrases

Carbonic anhydrase enzymes have been attracting substantial interest because of their ability to "fix" CO_2 through hydration. These enzymes thus have potential in carbon capture, provided they can be made robust enough to withstand the conditions needed, so thermotolerant and halotolerant variants have been attractive targets. To this aim, rational engineering of a mesohalophilic carbonic anhydrase has been achieved to generate extremely halotolerant variants, and subsequently the activity tested in the ionic liquids ethanolammonium formate (ETAF), ethyl ammonium formate (EAF), ethyl ammonium nitrate (EAN) and $[C_1C_1Im][Me_2PO_4]$ (Warden et al., 2015). The ETAF protected against thermal unfolding for the most halotolerant variants with increasing concentration, consistent with the effects seen for lysozyme (Wijaya et al., 2016), and cytochrome c (Papadopoulou et al., 2016). The other ionic liquids tested had only a moderate impact on thermal stability of the extremely halotolerant enzyme.

FUTURE OF PROTEINS AND ENZYMES IN IONIC LIQUIDS

The scope with which ionic liquids have already been utilized with proteins and enzymes is substantial with many exciting application areas already emerging. This includes the ability to analyse and sequence recalcitrant proteins (Plowman et al., 2014; Deb-Choudhury et al., 2016), the use of enzyme-ionic liquid solutions for the restoration of heritage materials (Hrdlickova

Kuckova et al., 2014), the production of ionic gel-like materials (ionogels) that could be used in applications as diverse as biocatalysis, batteries, environmental applications, and soft robotics (Ribot et al., 2012; Shamsuri et al., 2012; Silva et al., 2012, 2013; Wang et al., 2013a; Kapoor and Kundu, 2016; Iqbal et al., 2017; Singh et al., 2017; Grollmisch et al., 2018; Yao et al., 2018), and extension to the spinning, casting, and 3D-printing of reprocessed materials (Phillips et al., 2005; Gupta et al., 2007; Meli et al., 2010; Deng et al., 2014; Gunasekera et al., 2016; Zavgorodnya et al., 2017; Gunasekera, 2019). Bio-sensing and stimuli-responsive applications also show significant scope (reviewed in Kavanagh et al., 2012). Clearly, there are still many unanswered questions and challenges in the selection and use of the correct ionic liquid for the correct application to ensure effective and productive outcomes.

Challenges With Protein Processing

A number of challenges still need to be progressed in the reformation of protein-based materials, especially because of their applications in biotechnology and tissue engineering (Dal Pra et al., 2005; Park et al., 2006; Gupta et al., 2007; Rouse and Van Dyke, 2010; Vijayaraghavan et al., 2010; Silva et al., 2012, 2014; Kapoor and Kundu, 2016; Tran et al., 2016; Egorova et al., 2017; Iqbal et al., 2017, 2018a,b; Mahmood et al., 2017), with work being carried out to develop practical processing techniques. Among these are the issues with ionic liquid toxicity (Zhao et al., 2007; Ostadjoo et al., 2018), and by extension removal (Gupta et al., 2007; Silva et al., 2012, 2013; Iqbal et al., 2017), to ensure that the final materials are reliably biocompatible. Already the work on more biocompatible ionic liquids, such as those based on either cholinium cations or amino acid anions shows promising results, and is an area that should be further explored, not only in the context of biocompatibility, but also in sustainability. Primary human epidermal keratinocytes have been demonstrated as being able to grow on patterned films of silk, spin-coated from a 7.5% (w/w) solution of $[C_4C_1Im][Cl]$ and 25% (w/w) water (added to reduce viscosity) (Gupta et al., 2007), and this study illustrated that tracking characteristic ionic liquid peaks in the ATR-FTIR spectrum (in this case, 1,463 cm^{-1} of $[C_4C_1Im][Cl]$) before and after methanol treatment, is able to confirm successful ionic liquid removal and simultaneous development of the β-sheet structures (indicated by a shift in the amide I peak from 1,650 to 1,622 cm^{-1}).

Several studies have investigated the stability of both silk and keratin during their processing with ionic liquids and both proteins are quite often found to be degraded upon regeneration, either at the molecular level or with respect to secondary structural elements (Goujon et al., 2012; Idris et al., 2013; Ji et al., 2014; Cheng et al., 2015; Zheng et al., 2015; Liu et al., 2017; Zhang et al., 2017a,b). For keratins, decomposition of the disulfide linkages within the protein is expected as a natural part of dissolution, as without this the protein chains are too strongly bound. The high temperatures (>100°C) required for dissolution of keratin in ionic liquid provide an impetus for decomposition, and the temperature impact has been systematically studied by characterization of amino acid compositions of regenerated wool (Ghosh et al.,

2014). Degradation of cysteine (comprising initially about 10% of the total keratin content) with some oxidative formation of cysteic acid and other derivatives increases with increasing temperature, with less than half remaining after 30 min treatment at 150°C (Ghosh et al., 2014). Cleavage of the disulfide bonds was attributed, at least in part, to the attack of chloride ion from the $[C_4C_1Im][Cl]$ solvent. Variation both in the degree of retention of disulfides and presence of free sulfhydryl groups is seen with changing ionic liquid, with the dissolution capability mirroring the capacity to cleave the disulfide bonds and inversely proportional to the recovery percentage on regeneration (Zhang et al., 2017a). A minimum level of 65% cleavage was proposed as a benchmark requirement for adequate keratin dissolution, based on these data. A minimum temperature of 110°C for dissolution in $[C_2C_1Im][Et_2PO_4]$ was also necessary.

The biggest issue with silk degradation seems to lie in the serecin removal stage, which is common to all silk processing methods. The prolonged heating of silk has an effect on the level of degradation observed, similar to keratin. To overcome this issue, Lozano-Pérez et al. (2015) utilized ultrasonication to dissolve silk in ionic liquids and determined the level of peptidic chain fragmentation with SDS-PAGE. Where conventional heating of silk in ionic liquid can take several hours for full dissolution, the use of ultrasound reduced this time substantially with $[C_2C_1Im][Cl]$, reaching 23 ± 0.3% w/w in 17 min. SDS-PAGE analysis, tryptic degradation, and HPLC/MS confirmed that the silk treated with sonication in ionic liquid retained both much more of its integrity and, in addition, the lower molecular weight components of the silk, indicating a reduction in the thermal degradation of the silk. Combination of ultrasonication with other tailored and characterized dissolution methods (Wang et al., 2013b), may provide much improved methodology for the preservation of silk structure and properties going forward, along with enhanced recovery and reuse of the ionic liquids involved.

Biomaterials and Composites Formation

The access to ionic liquid-soluble proteins, and other recalcitrant biomass, has naturally led to the production of composites in order to create materials with a great depth and breadth of physical and chemical properties (Mahmood et al., 2017). Popular have been combinations of protein and cellulosic derivatives (Xie et al., 2005; Hameed and Guo, 2009; Wu et al., 2009; Shang et al., 2011; Wang et al., 2013a, 2014; Yao et al., 2014a,b; Zhang et al., 2014; Kammiovirta et al., 2016; Tran and Mututuvari, 2016; Tran et al., 2016; Stanton et al., 2018), alongside other sugar polymers such as chitosan (Silva et al., 2012; Tran and Mututuvari, 2016), chitin (Park et al., 2006), and starch (Leroy et al., 2012). Both protein structuring and macrostructural morphology provide insight into the impact of ionic liquids in the formation of these materials.

Initial approaches to regeneration of keratin already focussed on composite formation with cellulose (Xie et al., 2005), with regeneration by soaking in methanol overnight. Fiber structuring was not seen for 1:5 mixtures of keratin (10 wt% in $[C_4C_1Im][Cl]$), with blending resulting instead in a homogenous membrane, as visualized by SEM. Cellulose acetate (CA) composites with wool at 20 and 40 wt% CA regenerated

in water, in contrast, were less homogenous, although separate composites could not be easily distinguished (Hameed and Guo, 2009), neither at these or higher CA:wool ratios of 60 and 80 wt%, respectively. For these higher CA ratios, DSC analysis indicated a single phase, with significantly higher glass transition temperatures, along with increased thermal stability, relative to the pure regenerated components. This implies cooperative interactivity and new, strong hydrogen bonding between the wool and CA components, and changes to the hydrogen bonding were confirmed by FTIR. Industrial chicken feathers and cellulose (5 wt% in $[C_2C_1Im][OAc]$) in ratios from 70:30 to 0:100, respectively, were wet-spun and coagulated in ethanol (Kammiovirta et al., 2016). At 10:90 ratio, the strength and tenacity of the spun fiber was at its highest, and reinforced the fiber strength over pure cellulose. FTIR analysis suggested an unfolding of the β-sheets of the protein in the regenerated material. Characterization by SEM indicated a lack of phase separation, as per previous studies, however, keratin was unevenly distributed at the highest ratios and afforded a more porous structure, ascribed to asynchronous regeneration relative to cellulose. With this in mind, this result highlights how changes to the ionic liquid solvent may impact on regenerated properties, and how also tuning the solvent might be exploited.

Tran and coworkers have carried out the most extensive experiments to date on keratin-based composites formed from $[C_4C_1Im][Cl]$, and regenerated with water with the ionic liquid recycled (Tran and Mututuvari, 2016; Tran et al., 2016). Similar to previous composite studies, the keratin-sugar-based composites had improved mechanical properties and were homogenous by SEM analysis, although displayed increased roughness with an increasing keratin content. Different sources of keratin, due to differences in their underlying primary and secondary structures, afforded different microcrystalline structures, as assessed by SEM, and their composites displayed different antimicrobial activities (Tran et al., 2016). This latter property was linked to the differences in secondary structure. On either chitosan or cellulose addition (Tran and Mututuvari, 2016; Tran et al., 2016), the α-helix content of the keratin reportedly dropped or stayed consistent, with an increase in β-sheet structuring, attributed to specific stabilization from the hydrogen-bonding of the sugar hydroxyl-moieties.

Silk-based biocomposites have attracted the strongest attention of the biocomposite studies, particularly in understanding the conditions for appropriate regeneration. Silk-cellulose composite films from $[C_4C_1Im][Cl]$ were exposed to methanol vapor and then dried under vacuum (Zhou et al., 2013), in contrast to non-composite silk films that are commonly exposed to humid conditions as part of their processing method (Li et al., 2015). Subsequent SEM analysis indicated that a more fibrous microstructure with larger pores was observed with increasing silk loading. Cellulose content drove the formation of β-sheets and turns, as indicated by the change from $13 \pm 4\%$ in the pure silk sample to $41 \pm 9\%$ in the 75:25 cellulose-silk film, monitored by using deconvolution of FTIR spectra. The shift in the β-sheet peak from 1,629 to 1,623 cm^{-1}, attributed to intramolecular and intermolecular β-sheets respectively (Hu et al., 2006), suggested that decreasing the silk content

and increasing the cellulose content promotes intermolecular associations between neighboring fibroin polymer chains. Alternatively, this could be ascribed to the interaction of nearby cellulose chains with the hydrogen bonding network of the β-sheets (Zhang et al., 2016a). The eradication of XRD peaks associated with silk I ($2\theta = 8°$) and silk II ($2\theta = 28°$) structures suggest a reduction in silk ordering, however previous WAXS data for silk have shown a peak at $2\theta = 21°$ that could be masked by the cellulose peaks ($2\theta = 22.4°$) (Stanton et al., 2018), especially considering the continued presence of a strong β-sheet peak in the FTIR (Phillips et al., 2004).

The mechanical strength of these composite films was also correlated with cellulose content with the dry films ranging from 49.8 ± 7.4 MPa breaking stress when the silk-cellulose ratio was 75:25 to 146.9 ± 18.8 MPa for pure cellulose. The hydrated films were much weaker ranging from 0.9 ± 0.1 MPa to 10.7 ± 3.1 MPa, respectively. A qualitative inspection of cell viability using murine fibroblast cells L929 was carried out for the composite films, with cell density correlated with silk content. Further work in this area would help to establish key composite parameters for viability of cell adhesion and proliferation.

The effects of different ILs on composite films made from a 9% w/w cellulose and 1% w/w silk solution (**Table 3**), indicated that $[C_4C_1Im][Br]$ and $[C_4C_1Im][MeSO_3]$-derived composites formed translucent and brittle films, while all the others were solid and clear (Stanton et al., 2018). The brittle films exhibited the highest β-sheet content (58.6% for $[C_4C_1Im][Br]$ and 58.9% for $[C_4C_1Im][MeSO_3]$, respectively), as determined by Fourier self-deconvolution of the amide I region of the FTIR spectra of the films and the H-bonding capability of the anion was inversely proportional to the degree of β-sheet formation. The rationale provided was that the high β-sheet formation was driven by stronger interactions between the biopolymer components relative to those with the anions of the ionic liquid, allowing the reformation of original, albeit disrupted, β-sheets, as well as new ones upon coagulation.

Surface topography of silk-cellulose blends seems also to be very closely linked to anion character; regeneration with chloride-ionic liquid displayed a smooth surface for the biocomposite film, whereas the acetate-derived film had small pores and the $[MeSO_3]$ and bromide-derived films both showed a fibrous structure. A role for the cation was indicated by X-ray scattering data, where moving from [AMIM][Cl] to $[C_2C_1Im][Cl]$ increased the amorphous nature of the blend, shown by the backbone spacing between the cellulose and the silk. X-ray scattering peaks for $[C_2C_1Im][OAc]$ broadened, indicating an increase in the interaction with the anion and a resultant rise in the blending of the silk and cellulose chains in the film. For the $[C_4C_1Im][MeSO_3]$ and the $[C_4C_1Im][Br]$ there were clear peaks for both the cellulose crystallites and the β-sheets, which, combined with the high crystallinity shown in the FTIR spectra, are indicative of separated microphases. This could be the basis for the brittle nature of the films made with these ionic liquids. Previous studies with $[C_4C_1Im][Br]$ have demonstrated that it is a poor solvent for silk providing a rationale for microphase formation (Phillips et al., 2004; Mantz et al., 2007; Stanton et al., 2018).

The similar solubilising properties [C$_4$C$_1$Im][OAc] possesses for chitin and silk also allows them to be blended into a single structure (Park et al., 2006). This builds on the previously determined solubility of chitosan in ionic liquids (initially by Mantz et al., 2007) toward the production of a blended hydrogel for evaluating the seeding of human Dermal Fibroblasts (hDFs). The different ratios of chitin and silk (**Table 3**) have differing properties; primarily a greater β-sheet structure when the silk to chitosan ratio was 70:30, as determined by FTIR measurements of the amide peaks. The higher silk ratio imbued the hydrogel with greater rigidity and superior elastic behavior over the frequencies tested. The chitosan in these hydrogels exhibited changes to its secondary structure that, along with the homogenous structure observed in SEM, indicate physical interactions between the two biomaterials most likely in the form of either direct hydrogen bonding or ionic liquid anions being locked into the structure of the hydrogel.

Ionogels and Ionic Liquid-Mediated Entrapment

Ionogels or gel-polymer electrolytes (GPEs) are conducting gel-like materials that can arise from confinement of ionic liquids within ordered matricies (Marr and Marr, 2016). Such gels have found potential application in the areas of environmental cleanup (Billeci et al., 2018), and batteries (Cerclier et al., 2015), with further scope for areas where flexible conductive gels would be useful, such as soft robotics and smart bioelectrochemical devices (Fujita et al., 2012). Desirable properties of such gels include responsiveness to stimuli [e.g., thermoresponsive (Ribot et al., 2010) and electrochromic gels (Benedetti et al., 2015)] and self-healing abilities. Proteins and their composites offer nanostructuring opportunities for ionic liquid ions through their hydrogen-bonding network and ionic interactions, consistent with the reported gel-formation of some wool and silk materials prior to regeneration.

Ion jelly®, formed from gelatine and ionic liquid (including a range of cholinium-based ionic liquids), has been shown to be extremely versatile, with applications including selective membranes, gas separation, conductive coatings for textiles, development of antimicrobial fibers, solid-state electrochromic systems, and as a gas sensor (Vidinha et al., 2008; Nuno et al., 2011; Couto et al., 2013, 2015; Rana et al., 2013; Santos et al., 2013; Carvalho et al., 2014; Benedetti et al., 2015). Gelatine-based ionogels have also been partnered with silver oxide nanoparticles to generate microbe-resistant and highly stretchable materials that are also self-healing and have shape-memory (Singh et al., 2017). Gelatine with a propionic acid-functionalised ionic liquid [(C$_2$CO$_2$H)C$_1$Im][Br] and embedded Eu^{3+} ions retained luminescence, in contrast to aqueous solutions of Eu^{3+}, and could be utilized in UV-emitting LEDs (Li et al., 2014). Entrapment of enzymes within ionic liquid gels also offers an alternative to standard immobilization, with the benefits imparted by the ionic liquid. The protection of horse-radish peroxidase by entrapment in Ion Jelly® formed from [C$_2$C$_1$Im][EtSO$_4$] is one such example (Lourenço et al., 2011). Similarly, glucose oxidase was able to be stabilized

and utilized as a gel-coating for the sensing of glucose with this system.

Hydrogel formation in silks is well established (Kapoor and Kundu, 2016), and has been extended to ionogel formation (Zhang et al., 2016a; Yao et al., 2018). By varying silk, water, and [C$_2$C$_1$Im][OAc] ratios, differing mechanical properties could be obtained with the best being 10% silk, 50% [C$_2$C$_1$Im][OAc] and 40% water (all w/w) (Yao et al., 2018). The major drawback to silk-IL-water hydrogels is the gelation times, which has also been an issue in previous work (Zhang et al., 2016a). The gelation times for the silk:[C$_2$C$_1$Im][OAc] (50% w/w): water (40% w/w) hydrogel ranged from 30 days for mixtures containing 5% w/w silk, to 9 days for 10% w/w silk. Depending upon amount of ethanol added to a gel with 10% w/w silk, the gelation times could be improved from approximately 40 h for 10% v/v in water to just over an hour with 60% v/v, with little difference in the mechanical performance of the final gel in the range of 0–40% v/v, with the exception of a slight improvement to tensile properties (except stiffness). Increasing ethanol concentration also increases the rate at which the β-sheet folding transition occurs, giving another mechanism for tuning the mechanical properties of silk hydrogels formed in this manner.

Beyond gelatine and silk, scope for developing ionic liquid-based ionogel formation with other proteins also remains (Zhu et al., 2016). Enzyme immobilization in the context of biosensors and stimuli-responsive materials, including entrapment in both ionogels and polymerisable ionic liquid matricies (Grollmisch et al., 2018), has been well-reviewed recently (Kavanagh et al., 2012; Zuliani et al., 2014; Marr and Marr, 2016; Zhang et al., 2016b). Commonly, sensors have utilized glucose oxidase (GOx) with a view to producing accessible glucose sensors, primarily in combination with imidazolium-based ionic liquids (Sharma et al., 2015). Lactate oxidase in [C$_2$C$_1$Im][EtSO$_4$] has been similarly employed for lactate sensing (Khodagholy et al., 2012). Cellulases (Hosseini et al., 2018) and lipases (Suo et al., 2019) have recently been used as immobilized catalytic components, where additional functionalities such as magnetism can also be incorporated. As per other ionic liquid-protein applications, more biocompatible ionic liquids, such as those based on cholinium cations and amino acid anions, have been recently demonstrated as being useful in developing laccase-based biosensors (Zappi et al., 2018) and more generic enzyme-based sensors (Zappi et al., 2017). Certainly, as dissolution and gelation technology advances, tailored ionic liquid-based immobilization incorporating alternative biopolymers, and with a broader range of sensing capabilities, offers exciting and sustainable opportunities.

Potential for Driving Reactions of Proteins

One of the future application areas for proteins will not only be the reprocessing of existing biopolymers, but the ability to derivatise these materials to create new materials properties. For Zein, proof of principle has been achieved in benzoylation (Biswas et al., 2006), and for silks sulfation has been effective (Liu et al., 2015). Such reactions could therefore readily be extended to other proteins. One key consideration, however, is how the ionic liquid solvent is organized around the protein (Hayes et al., 2015;

Sprenger et al., 2017). Beyond the demonstrated impact of these interactions in creating the initial solubilisation, as noted through the extensive experimental work in this review, it has been well established that the organization of an ionic liquid around a potential reactive center plays a significant role in directing reactions at that center (Yau et al., 2008, 2009a,b, 2012, 2013; Tanner et al., 2013a,b; Keaveney et al., 2016, 2017, 2018; Hawker and Harper, 2018; Hawker et al., 2018; Schaffarczyk Mchale et al., 2018; Gilbert et al., 2019). The surface site interactions, leading to potential inner site interactions if hydrogen bonds are disrupted, are governed by the relative affinity of the ionic liquid ions for specific amino acids (Sprenger et al., 2017). Ionic liquids should thus be able to be tailored to enhance specific interactions, and, in addition, cooperative effects based on sequence are likely to generate differential organization, leading to different accessibility of reactive residues. In this way, specificity for particular sites on an enzyme could be engendered that can afford some selectivity in reaction. Further, where competitive reaction mechanisms exist, then another level of selectivity can be applied through the appropriate selection of ionic liquid (Tanner et al., 2013b; Yau et al., 2013; Hawker and Harper, 2018). Still, however, much further work needs to be done to develop the predictive rules for these interactions, although initial work has begun in this regard (Sprenger et al., 2017).

SYNOPSIS

The areas of application at the intersection of protein biochemistry, enzymology and ionic liquids are extensive and show promise for future applications. A variety of ionic liquids have been trialed with both structural proteins and enzymes, often with the exact set differing depending on purpose. The focus to date in all areas has been primarily on imidazolium-based ionic liquids, presumably due to their wide accessibility and established effectiveness. For most purposes involving solubilisation of a protein component, short chain substituents on the imidazolium have been most successful. Some other classes of ionic liquid cation are represented, including ammonium-based ionic liquids, pyrrolidiniums, and increasingly more functional ionic liquids such as protic ionic liquids, and/or bio-derived ionic liquids (including cholinium and amino-acid based species). The limited, but promising, studies utilizing the latter classes leaves a broad scope for future studies with good potential for even greener and more sustainable methodologies and applications.

The properties of regenerated biopolymers show variation with the ionic liquid used for dissolution, and the antisolvent used to generate the material. Films, membranes, gels and nanoparticles can all be formed under different conditions, although in pure biopolymers the secondary structure disruption on dissolution and imperfect reconstitution on regeneration, for example the increase in β-sheet formation in keratins and silks, can impact on properties. This can be mitigated to some extent by blending with sugar-based biopolymers, which are able to stabilize the protein structures and impart enhanced mechanical properties on the final composite, relative to the initial pure components, once regenerated.

Progress is also being made on the predictive understanding of ionic liquid-protein interactions in order to optimize them. In the enzyme sphere, the Hofmeister series provides an initial benchmark, with more detailed molecular simulation studies supporting a more detailed insight per enzyme feeding into more generalized principles. For solubility, increasingly sophisticated methods based on computational screening, such as use of COSMO to calculate $\ln \gamma$ values, appears to be effective, and other more general computational approaches are being developed that should allow more detailed interrogation of how structure is impacted by interactions with ions. A near future can be envisaged, whereby a pick-and-mix approach, included tailored binary and ternary mixtures, could be achieved to rapidly match a desired application.

AUTHOR CONTRIBUTIONS

All authors listed have made a substantial, direct and intellectual contribution to the work, and approved it for publication.

FUNDING

ACKNOWLEDGMENTS

REFERENCES

Altman, G. H., Diaz, F., Jakuba, C., Calabro, T., Horan, R. L., Chen, J., et al. (2003). Silk-based biomaterials. *Biomaterials* 24, 401–416. doi: 10.1016/S0142-9612(02)00353-8

Alves, R. R. N., Medeiros, M. F. T., Albuquerque, U. P., and Rosa, I. L. (2013). "From past to present: medicinal animals in a historical perspective," in *Animals in Traditional Folk Medicine,* eds R. R. N. Alves and I. L. Rosa (Berlin; Heidelberg: Springer-Verlag), 11–23. doi: 10.1007/978-3-642-29026-8_2

Arai, S., Nakashima, K., Tanino, T., Ogino, C., Kondo, A., and Fukuda, H. (2010). Production of biodiesel fuel from soybean oil catalyzed by fungus whole-cell biocatalysts in ionic liquids. *Enzyme Microb. Technol.* 46, 51–55. doi: 10.1016/j.enzmictec.2009.08.008

Asakura, T., Kuzuhara, A., Tabeta, R., and Saito, H. (1985). Conformation characterization of bombyx mori silk fibroin in the solid state by high-frequency13c cross polarization-magic angle spinning nmr, x-ray diffraction, and infrared spectroscopy. *Macromolecules* 18, 1841–1845. doi: 10.1021/ma00152a009

Benedetti, T. M., Carvalho, T., Iwakura, D. C., Braga, F., Vieira, B. R., Vidinha, P., et al. (2015). All solid-state electrochromic device consisting of a water soluble viologen dissolved in gelatin-based ionogel. *Sol. Energy Mater. Sol. Cells* 132, 101–106. doi: 10.1016/j.solmat.2014.08.037

Bertrand, T., Jolivalt, C., Briozzo, P., Caminade, E., Joly, N., Madzak, C., et al. (2002). Crystal structure of a four-copper laccase complexed with an arylamine: insights into substrate recognition and correlation with kinetics. *Biochemistry* 41, 7325–7333. doi: 10.1021/bi0201318

Billeci, F., D'anna, F., Gunaratne, H. Q. N., Plechkova, N. V., and Seddon, K. R. (2018). "Sweet" ionic liquid gels: materials for sweetening of fuels. *Green Chem.* 20, 4260–4276. doi: 10.1039/C8GC01615A

Biswas, A., Shogren, R. L., Stevenson, D. G., Willett, J. L., and Bhowmik, P. K. (2006). Ionic liquids as solvents for biopolymers: acylation of starch and zein protein. *Carbohydr. Polym.* 66, 546–550. doi: 10.1016/j.carbpol.2006.04.005

Bose, S., Barnes, C. A., and Petrich, J. W. (2012). Enhanced stability and activity of cellulase in an ionic liquid and the effect of pretreatment on cellulose hydrolysis. *Biotechnol. Bioeng.* 109, 434–443. doi: 10.1002/bit.23352

Burney, P. R., Nordwald, E. M., Hickman, K., Kaar, J. L., and Pfaendtner, J. (2015). Molecular dynamics investigation of the ionic liquid/enzyme interface: application to engineering enzyme surface charge. *Proteins* 83, 670–680. doi: 10.1002/prot.24757

Cao, Y., Zhang, R., Cheng, T., Guo, J., Xian, M., and Liu, H. (2017). Imidazolium-based ionic liquids for cellulose pretreatment: recent progresses and future perspectives. *Appl. Microbiol. Biotechnol.* 101, 521–532. doi: 10.1007/s00253-016-8057-8

Carvalho, N. B., Vidal, B. T., Barbosa, A. S., Pereira, M. M., Mattedi, S., Freitas, L. D. S., et al. (2018). Lipase immobilization on silica xerogel treated with protic ionic liquid and its application in biodiesel production from different oils. *Int. J. Mol. Sci.* 19:1829. doi: 10.3390/ijms19071829

Carvalho, T., Vidinha, P., Vieira, B. R., Li, R. W. C., and Gruber, J. (2014). Ion jelly: a novel sensing material for gas sensors and electronic noses. *J. Mater. Chem. C* 2, 696–700. doi: 10.1039/C3TC31496K

Cerclier, C. V., Zanotti, J. M., and Le Bideau, J. (2015). Ionogel based on biopolymer-silica interpenetrated networks: dynamics of confined ionic liquid with lithium salt. *Phys. Chem. Chem. Phys.* 17, 29707–29713. doi: 10.1039/C5CP04889C

Chen, J., Ahn, T., Colón-Bernal, I. D., Kim, J., and Banaszak Holl, M. M. (2017). The relationship of collagen structural and compositional heterogeneity to tissue mechanical properties: a chemical perspective. *ACS Nano* 11, 10665–10671. doi: 10.1021/acsnano.7b06826

Chen, J., Vongsanga, K., Wang, X., and Byrne, N. (2014). What happens during natural protein fibre dissolution in ionic liquids. *Materials (Basel).* 7, 6158–6168. doi: 10.3390/ma7096158

Chen, J., Vongsanga, K., Wang, X., and Byrne, N. (2015). Rapid and effective cuticle removal from wool fibers using ionic liquid. *Fibers Polym.* 16, 1289–1293. doi: 10.1007/s12221-015-1289-x

Cheng, G., Wang, X., Tao, S., Xia, J., and Xu, S. (2015). Differences in regenerated silk fibroin prepared with different solvent systems: from structures to conformational changes. *J. Appl. Polym. Sci.* 132:41959. doi: 10.1002/app.41959

Cheng, H.-W., Weiss, H., Stock, P., Chen, Y.-J., Reinecke, C. R., Dienemann, J.-N., et al. (2018). Effect of concentration on the interfacial and bulk structure of ionic liquids in aqueous solution. *Langmuir* 34, 2637–2646. doi: 10.1021/acs.langmuir.7b03757

Cho, S., Chae, J.-I., Seo, K.-S., and Jin-Choi, N. (2013). Effect of hemicellulase, cellulase, xylanase and alkali pretreatment on the saccharification of miscanthus sacchariflorus var. No. 1. *Afr. J. Agric. Res.* 8, 2778–2785. doi: 10.5897/AJAR12.1618

Choi, H.-M., and Kwon, I.-C. (2011). Dissolution of zein using protic ionic liquids: N-(2-hydroxyethyl) ammonium formate and n-(2-hydroxyethyl) ammonium acetate. *Ind. Eng. Chem. Res.* 50, 2452–2454. doi: 10.1021/ie1007745

Couto, R., Neves, L., Simoes, P., and Coelhoso, I. (2015). Supported ionic liquid membranes and ion-jelly® membranes with [BMIM][DCA]: comparison of its performance for CO_2 separation. *Membranes* 5, 13–21. doi: 10.3390/membranes5010013

Couto, R. M., Carvalho, T., Neves, L. A., Ruivo, R. M., Vidinha, P., Paiva, A., et al. (2013). Development of ion-jelly® membranes. *Sep. Purif. Technol.* 106, 22–31. doi: 10.1016/j.seppur.2012.12.026

Dabirmanesh, B., Khajeh, K., Akbari, J., Falahati, H., Daneshjoo, S., and Heydari, A. (2011). Mesophilic alcohol dehydrogenase behavior in imidazolium based ionic liquids. *J. Mol. Liq.* 161, 139–143. doi: 10.1016/j.molliq.2011.05.007

Dabirmanesh, B., Khajeh, K., Ranjbar, B., Ghazi, F., and Heydari, A. (2012). Inhibition mediated stabilization effect of imidazolium based ionic liquids on alcohol dehydrogenase. *J. Mol. Liq.* 170, 66–71. doi: 10.1016/j.molliq.2012.03.004

Dahanayake, J. N., and Mitchell-Koch, K. R. (2018). Entropy connects water structure and dynamics in protein hydration layer. *Phys. Chem. Chem. Phys.* 20, 14765–14777. doi: 10.1039/C8CP01674G

Dal Pra, I., Freddi, G., Minic, J., Chiarini, A., and Armato, U. (2005). De novo engineering of reticular connective tissue *in vivo* by silk fibroin nonwoven materials. *Biomaterials* 26, 1987–1999. doi: 10.1016/j.biomaterials.2004.06.036

Datta, S., Holmes, B., Park, J. I., Chen, Z., Dibble, D. C., Hadi, M., et al. (2010). Ionic liquid tolerant hyperthermophilic cellulases for biomass pretreatment and hydrolysis. *Green Chem.* 12, 338–345. doi: 10.1039/b916564a

De Gonzalo, G., Lavandera, I., Durchschein, K., Wurm, D., Faber, K., and Kroutil, W. (2007). Asymmetric biocatalytic reduction of ketones using hydroxy-functionalised water-miscible ionic liquids as solvents. *Tetrahedron* 18, 2541–2546. doi: 10.1016/j.tetasy.2007.10.010

Deb-Choudhury, S., Plowman, J. E., and Harland, D. P. (2016). Isolation and analysis of keratins and keratin-associated proteins from hair and wool. *Meth. Enzymol.* 568, 279–301. doi: 10.1016/bs.mie.2015.07.018

Debeljuh, N., Barrow, C. J., Henderson, L., and Byrne, N. (2011). Structure inducing ionic liquids-enhancement of alpha helicity in the abeta(1-40) peptide from alzheimer's disease. *Chem. Commun.* 47, 6371–6373. doi: 10.1039/c1cc10377f

Defrates, K. G., Moore, R., Borgesi, J., Lin, G., Mulderig, T., Beachley, V., et al. (2018). Protein-based fiber materials in medicine: a review. *Nanomaterials* 8:457. doi: 10.3390/nano8070457

Deng, S., Cheng, J., Guo, X., Jiang, L., and Zhang, J. (2014). Fiber spinning of polyacrylonitrile grafted soy protein in an ionic liquid/dmso mixture solvent. *J. Polym. Environ.* 22, 17–26. doi: 10.1007/s10924-013-0617-8

Domanska, U., and Marciniak, A. (2007). Phase behaviour of 1-hexyloxymethyl-3-methyl-imidazolium and 1, 3-dihexyloxymethyl-imidazolium based ionic liquids with alcohols, water, ketones and hydrocarbons: the effect of cation and anion on solubility. *Fluid Phase Equilib.* 260, 9–18. doi: 10.1016/j.fluid.2006.07.005

Eckstein, M., Villela Filho, M., Liese, A., and Kragl, U. (2004). Use of an ionic liquid in a two-phase system to improve an alcohol dehydrogenase catalysed reduction. *Chem. Commun.* 40, 1084–1085. doi: 10.1039/b401065e

Egorova, K. S., Gordeev, E. G., and Ananikov, V. P. (2017). Biological activity of ionic liquids and their application in pharmaceutics and medicine. *Chem. Rev.* 117, 7132–7189. doi: 10.1021/acs.chemrev.6b00562

Elgharbawy, A. A., Riyadi, F. A., Alam, M. Z., and Moniruzzaman, M. (2018). Ionic liquids as a potential solvent for lipase-catalysed reactions: a review. *J. Mol. Liq.* 251, 150–166. doi: 10.1016/j.molliq.2017.12.050

Endo, Y., Hatanaka, T., Maeda, K., Arafune, K., Yamamoto, T., Itoh, K., et al. (2018). Use of ethanol with triolein for fatty acid ethyl ester as biodiesel fuel in a novozym® 435 fixed-bed reactor. *Biomass Bioenergy* 108, 433–438. doi: 10.1016/j.biombioe.2017.11.023

Engel, P., Mladenov, R., Wulfhorst, H., Jäger, G., and Spiess, A. C. (2010). Point by point analysis: how ionic liquid affects the enzymatic hydrolysis of native and modified cellulose. *Green Chem.* 12, 1959. doi: 10.1039/c0gc00135j

Ferdjani, S., Ionita, M., Roy, B., Dion, M., Djeghaba, Z., Rabiller, C., et al. (2011). Correlation between thermostability and stability of glycosidases in ionic liquid. *Biotechnol. Lett.* 33, 1215–1219. doi: 10.1007/s10529-011-0560-5

Fernández-Fernández, M., Moldes, D., Domínguez, A., Sanromán, M. Á., Tavares, A. P. M., Rodríguez, O., et al. (2014). Stability and kinetic behavior of immobilized laccase from myceliophthora thermophila in the presence of the ionic liquid 1-ethyl-3-methylimidazolium ethylsulfate. *Biotechnol. Prog.* 30, 790–796. doi: 10.1002/btpr.1910

Freire, M. G., Neves, C. M., Marrucho, I. M., Coutinho, J. A., and Fernandes, A. M. (2010). Hydrolysis of tetrafluoroborate and hexafluorophosphate counter ions in imidazolium-based ionic liquids. *J. Phys. Chem. A* 114, 3744–3749. doi: 10.1021/jp903292n

Freire, M. G., Santos, L. M., Marrucho, I. M., and Coutinho, J. A. (2007). Evaluation of cosmo-rs for the prediction of lle and vle of alcohols+ ionic liquids. *Fluid Phase Equilib.* 255, 167–178. doi: 10.1016/j.fluid.2007.04.020

Fu, H., Li, M., Ni, R., and Lo, Y. M. (2018). Enzymatic catalysis for sustainable production of high omega-3 triglyceride oil using imidazolium-based ionic liquids. *Food Sci. Nutr.* 6, 2020–2027 .doi:10.1002/fsn3.733

Fujita, K., Murata, K., Masuda, M., Nakamura, N., and Ohno, H. (2012). Ionic liquids designed for advanced applications in bioelectrochemistry. *RSC Adv.* 2, 4018. doi: 10.1039/c2ra01045c

Fukumoto, K., Yoshizawa, M., and Ohno, H. (2005). Room temperature ionic liquids from 20 natural amino acids. *J. Am. Chem. Soc.* 127, 2398–2399. doi: 10.1021/ja043451i

Gehrke, S., Von Domaros, M., Clark, R., Hollóczki, O., Brehm, M., Welton, T., et al. (2018). Structure and lifetimes in ionic liquids and their mixtures. *Faraday Discuss.* 206, 219–245. doi: 10.1039/C7FD00166E

Ghosh, A., Clerens, S., Deb-Choudhury, S., and Dyer, J. M. (2014). Thermal effects of ionic liquid dissolution on the structures and properties of regenerated wool keratin. *Polym. Degrad. Stab.* 108, 108–115. doi: 10.1016/j.polymdegradstab.2014.06.007

Ghosh, S., Parui, S., Jana, B., and Bhattacharyya, K. (2015). Ionic liquid induced dehydration and domain closure in lysozyme: Fcs and md simulation. *J. Chem. Phys.* 143, 09B622_621. doi: 10.1063/1.4931974

Gilbert, A., Haines, R. S., and Harper, J. B. (2019). Understanding the effects of ionic liquids on a unimolecular substitution process: correlating solvent parameters with reaction outcome. *Org. Biomol. Chem.* 17, 675–682. doi: 10.1039/C8OB02460J

Goujon, N., Rajkhowa, R., Wang, X., and Byrne, N. (2013). Effect of solvent on ionic liquid dissolved regenerated antheraea assamensis silk fibroin. *J. Appl. Polym. Sci.* 128, 4411–4416. doi: 10.1002/app.38666

Goujon, N., Wang, X., Rajkowa, R., and Byrne, N. (2012). Regenerated silk fibroin using protic ionic liquids solvents: towards an all-ionic-liquid process for producing silk with tunable properties. *Chem. Commun.* 48, 1278–1280. doi: 10.1039/C2CC17143K

Govumoni, S. P., Koti, S., Kothagouni, S. Y., Venkateshwar, S., and Linga, V. R. (2013). Evaluation of pretreatment methods for enzymatic saccharification of wheat straw for bioethanol production. *Carbohydr. Polym.* 91, 646–650. doi: 10.1016/j.carbpol.2012.08.019

Grabner, B., Nazario, M., Gundersen, M., Loïs, S., Fantini, S., Bartsch, S., et al. (2018). Room-temperature solid phase ionic liquid (rtspil) coated ω-transaminases: development and application in organic solvents. *Mol. Catal.* 452, 11–19. doi: 10.1016/j.mcat.2018.03.012

Grollmisch, A., Kragl, U., and Großeheilmann, J. (2018). Enzyme immobilization in polymerized ionic liquids-based hydrogels for active and reusable biocatalysts. *SynOpen* 02, 0192–0199. doi: 10.1055/s-0037-1610144

Gunasekera, D. H. A. T. (2019). Three *dimensional printing of biopolymers* (Ph.D. thesis), University of Nottingham.

Gunasekera, D. H. Kuek, S., Hasanaj, D., He, Y., Tuck, C., et al. (2016). Three dimensional ink-jet printing of biomaterials using ionic liquids and co-solvents. *Faraday Discuss.* 190, 509–523. doi: 10.1039/C5FD00219B

Gunny, A. A., Arbain, D., Edwin Gumba, R. E., Jong, B. C., and Jamal, P. (2014). Potential halophilic cellulases for *in situ* enzymatic saccharification of ionic liquids pretreated lignocelluloses. *Bioresour. Technol.* 155, 177–181. doi: 10.1016/j.biortech.2013.12.101

Gupta, J., Wilson, B. W., and Vadlani, P. V. (2016). Evaluation of green solvents for a sustainable zein extraction from ethanol industry ddgs. *Biomass Bioenergy* 85, 313–319. doi: 10.1016/j.biombioe.2015.12.020

Gupta, M. K., Khokhar, S. K., Phillips, D. M., Sowards, L. A., Drummy, L. F., Kadakia, M. P., et al. (2007). Patterned silk films cast from ionic liquid solubilized fibroin as scaffolds for cell growth. *Langmuir* 23, 1315–1319. doi: 10.1021/la062047p

Haberler, M., Schröder, C., and Steinhauser, O. (2011). Solvation studies of a zinc finger protein in hydrated ionic liquids. *Phys. Chem. Chem. Phys.* 13, 6955–6969. doi: 10.1039/c0cp02487b

Haberler, M., SchröDer, C., and Steinhauser, O. (2012). Hydrated ionic liquids with and without solute: the influence of water content and protein solutes. *J. Chem. Theor. Comput.* 8, 3911–3928. doi: 10.1021/ct300191s

Haberler, M., and Steinhauser, O. (2011). On the influence of hydrated ionic liquids on the dynamical structure of model proteins: a computational study. *Phys. Chem. Chem. Phys.* 13, 17994–18004. doi: 10.1039/c1cp22266j

Hameed, N., and Guo, Q. (2009). Natural wool/cellulose acetate blends regenerated from the ionic liquid 1-butyl-3-methylimidazolium chloride. *Carbohydr. Polym.* 78, 999–1004. doi: 10.1016/j.carbpol.2009.07.033

Hawker, R. R., Haines, R. S., and Harper, J. B. (2018). Rational selection of the cation of an ionic liquid to control the reaction outcome of a substitution reaction. *Chem. Commun.* 54, 2296–2299. doi: 10.1039/C8CC00241J

Hawker, R. R., and Harper, J. B. (2018). Organic reaction outcomes in ionic liquids. *Adv. Phys. Org. Chem.* 52, 49–85. doi: 10.1016/bs.apoc.2018.09.001

Hayes, R., Warr, G. G., and Atkin, R. (2015). Structure and nanostructure in ionic liquids. *Chem. Rev.* 115, 6357–6426. doi: 10.1021/cr500411q

Heiss, C., Laivenieks, M., Zeikus, J. G., and Phillips, R. S. (2001). The stereospecificity of secondary alcohol dehydrogenase from thermoanaerobacter e thanolicus is partially determined by active site water. *J. Am. Chem. Soc.* 123, 345–346. doi: 10.1021/ja005575a

Heitz, M., Rupp, J., and Horn, K. (2018). Biocatalytic activity of mushroom tyrosinase in ionic liquids: specific ion effects and the hofmeister series. *Insights Enzyme Res.* 2:12. doi: 10.21767/2573-4466.100012

Heitz, M. P., and Rupp, J. W. (2018). Determining mushroom tyrosinase inhibition by imidazolium ionic liquids: a spectroscopic and molecular docking study. *Int. J. Biol. Macromol.* 107, 1971–1981. doi: 10.1016/j.ijbiomac.2017.10.066

Holkar, C. R., Jain, S. S., Jadhav, A. J., and Pinjari, D. V. (2018). Valorization of keratin based waste. *Process Saf. Environ. Prot.* 115, 85–98. doi: 10.1016/j.psep.2017.08.045

Hosseini, S. H., Hosseini, S. A., Zohreh, N., Yaghoubi, M., and Pourjavadi, A. (2018). Covalent immobilization of cellulase using magnetic poly(ionic liquid) support: improvement of the enzyme activity and stability. *J. Agric. Food Chem.* 66, 789–798. doi: 10.1021/acs.jafc.7b03922

Hrdlickova Kuckova, S., Crhova Krizkova, M., Pereira, C. L., Hynek, R., Lavrova, O., Busani, T., et al. (2014). Assessment of green cleaning effectiveness on polychrome surfaces by maldi-tof mass spectrometry and microscopic imaging. *Microsc. Res. Tech.* 77, 574–585. doi: 10.1002/jemt.22376

Hu, X., Kaplan, D., and Cebe, P. (2006). Determining beta-sheet crystallinity in fibrous proteins by thermal analysis and infrared spectroscopy. *Macromolecules* 39, 6161–6170. doi: 10.1021/ma0610109

Hu, Y., Liu, L., Dan, W., Dan, N., and Gu, Z. (2013). Evaluation of 1-ethyl-3-methylimidazolium acetate based ionic liquid systems as a suitable solvent for collagen. *J. Appl. Polym. Sci.* 130, 2245–2256. doi: 10.1002/app.39298

Hussain, W., Pollard, D. J., Truppo, M., and Lye, G. J. (2008). Enzymatic ketone reductions with co-factor recycling: improved reactions with ionic liquid co-solvents. *J. Mol. Catal. B Enzym.* 55, 19–29. doi: 10.1016/j.molcatb.2008.01.006

Idris, A., Vijayaraghavan, R., Patti, A. F., and Macfarlane, D. R. (2014a). Distillable protic ionic liquids for keratin dissolution and recovery. *ACS Sustainable Chem. Eng.* 2, 1888–1894. doi: 10.1021/sc500229a

Idris, A., Vijayaraghavan, R., Rana, U. A., Fredericks, D., Patti, A. F., and Macfarlane, D. R. (2013). Dissolution of feather keratin in ionic liquids. *Green Chem.* 15, 525–534. doi: 10.1039/c2gc36556a

Idris, A., Vijayaraghavan, R., Rana, U. A., Patti, A. F., and Macfarlane, D. R. (2014b). Dissolution and regeneration of wool keratin in ionic liquids. *Green Chem.* 16, 2857–2864. doi: 10.1039/C4GC00213J

Iizuka, E., and Yang, J. T. (1966). Optical rotatory dispersion and circular dichroism of the b-form of silk fibroin in solution. *Proc. Natl. Acad. Sci. U.S.A.* 55, 1175–1182. doi: 10.1073/pnas.55.5.1175

Ikeda, K., Ikari, R., Nakamura, N., Ohno, H., and Fujita, K. (2018). Distribution of cytochrome c in lcst-type ionic liquid/water mixtures controlled by

applied potential and temperature. *J. Electrochem. Soc.* 165, G96–G100. doi: 10.1149/2.1071807jes

Ilmberger, N., Meske, D., Juergensen, J., Schulte, M., Barthen, P., Rabausch, U., et al. (2012). Metagenomic cellulases highly tolerant towards the presence of ionic liquids—linking thermostability and halotolerance. *Appl. Microbiol. Biotechnol.* 95, 135–146. doi: 10.1007/s00253-011-3732-2

Ilmberger, N., Pottkämper, J., and Streit, W. R. (2013). Cellulases in ionic liquids—the long term stability of aspergillus sp. *Cellulase. Catalysts* 3, 584–587. doi: 10.3390/catal3020584

Iqbal, B., Muhammad, N., Jamal, A., Ahmad, P., Ul Haq Khan, Z., Rahim, A., et al. (2017). An application of ionic liquid for preparation of homogeneous collagen and alginate hydrogels for skin dressing. *J. Mol. Liq.* 243, 720–725. doi: 10.1016/j.molliq.2017.08.101

Iqbal, B., Muhammad, N., Rahim, A., Iqbal, F., Sharif, F., Safi, S. Z., et al. (2018a). Development of collagen/pva composites patches for osteochondral defects using a green processing of ionic liquid. *Int. J. Polym. Mater. Polym. Biomater.* 29, 1168–1184. doi: 10.1080/00914037.2018.1474358

Iqbal, B., Sarfaraz, Z., Muhammad, N., Ahmad, P., Iqbal, J., Khan, Z. U. H., et al. (2018b). Ionic liquid as a potential solvent for preparation of collagen-alginate-hydroxyapatite beads as bone filler. *J. Biomater. Sci., Polym. Ed.* 29, 1168–1184. doi: 10.1080/09205063.2018.1443604

Itoh, T. (2017a). "Biotransformation in ionic liquid," in *Future Directions in Biocatalysis, 2nd Edn*, ed T. Matsuda (Oxford, UK: Elsevier), 27–67. doi: 10.1016/B978-0-444-63743-7.00002-0

Itoh, T. (2017b). Ionic liquids as tool to improve enzymatic organic synthesis. *Chem. Rev.* 117, 10567–10607. doi: 10.1021/acs.chemrev.7b00158

Itoh, T. (2018). "Activation of lipase-catalyzed reactions using ionic liquids for organic synthesis," in *Advances in Biochemical Engineering/Biotechnology* (Berlin; Heidelberg: Springer), 1–26.

Itoh, T., Akasaki, E., and Nishimura, Y. (2002). Efficient lipase-catalyzed enantioselective acylation under reduced pressure conditions in an ionic liquid solvent system. *Chem. Lett.* 31, 154–155. doi: 10.1246/cl.2002.154

Jaeger, V., Burney, P., and Pfaendtner, J. (2015). Comparison of three ionic liquid-tolerant cellulases by molecular dynamics. *Biophys. J.* 108, 880–892. doi: 10.1016/j.bpj.2014.12.043

Ji, Y., Chen, J., Lv, J., Li, Z., Xing, L., and Ding, S. (2014). Extraction of keratin with ionic liquids from poultry feather. *Sep. Purif. Technol.* 132, 577–583. doi: 10.1016/j.seppur.2014.05.049

Kamiya, N., Matsushita, Y., Hanaki, M., Nakashima, K., Narita, M., Goto, M., et al. (2008). Enzymatic in situ saccharification of cellulose in aqueous-ionic liquid media. *Biotechnol. Lett.* 30, 1037. doi: 10.1007/s10529-008-9638-0

Kammiovirta, K., Jaaskelainen, A.-S., Kuutti, L., Holopainen-Mantila, U., Paananen, A., Suurnakki, A., et al. (2016). Keratin-reinforced cellulose filaments from ionic liquid solutions. *RSC Adv.* 6, 88797–88806. doi: 10.1039/C6RA20204G

Kapoor, S., and Kundu, S. C. (2016). Silk protein-based hydrogels: promising advanced materials for biomedical applications. *Acta Biomater.* 31, 17–32. doi: 10.1016/j.actbio.2015.11.034

Karimi, M., Ignasiak, M. T., Chan, B., Croft, A. K., Radom, L., Schiesser, C. H., et al. (2016). Reactivity of disulfide bonds is markedly affected by structure and environment: implications for protein modification and stability. *Sci. Rep.* 6:38572. doi: 10.1038/srep38572

Kavanagh, A., Byrne, R., Diamond, D., and Fraser, K. J. (2012). Stimuli responsive ionogels for sensing applications-an overview. *Membranes* 2, 16–39. doi: 10.3390/membranes2010016

Keaveney, S. T., Haines, R. S., and Harper, J. B. (2017). Ionic liquid solvents: The importance of microscopic interactions in predicting organic reaction outcomes. *Pure Appl. Chem.* 89, 745–757. doi: 10.1515/pac-2016-1008

Keaveney, S. T., Harper, J. B., and Croft, A. K. (2015). Computational approaches to understanding reaction outcomes of organic processes in ionic liquids. *RSC Adv.* 5, 35709–35729. doi: 10.1039/C4RA14676J

Keaveney, S. T., Harper, J. B., and Croft, A. K. (2018). Ion - reagent interactions contributing to ionic liquid solvent effects on a condensation reaction. *Chemphyschem* 19, 3279–3287. doi: 10.1002/cphc.201800695

Keaveney, S. T., White, B. P., Haines, R. S., and Harper, J. B. (2016). The effects of an ionic liquid on unimolecular substitution processes: the importance of

the extent of transition state solvation. *Org. Biomol. Chem.* 14, 2572–2580. doi: 10.1039/C5OB02598B

Khodagholy, D., Curto, V. F., Fraser, K. J., Gurfinkel, M., Byrne, R., Diamond, D., et al. (2012). Organic electrochemical transistor incorporating an ionogel as a solid state electrolyte for lactate sensing. *J. Mater. Chem.* 22, 4440. doi: 10.1039/c2jm15716k

Kim, H. S., Eom, D., Koo, Y.-M., and Yingling, Y. G. (2016). The effect of imidazolium cations on the structure and activity of the candida antarctica lipase b enzyme in ionic liquids. *Phys. Chem. Chem. Phys.* 18, 22062–22069. doi: 10.1039/C6CP02355J

Kim, H. S., Ha, S. H., Sethaphong, L., Koo, Y.-M., and Yingling, Y. G. (2014). The relationship between enhanced enzyme activity and structural dynamics in ionic liquids: a combined computational and experimental study. *Phys. Chem. Chem. Phys.* 16, 2944–2953. doi: 10.1039/c3cp52516c

Kohlmann, C., Robertz, N., Leuchs, S., Dogan, Z., Lütz, S., Bitzer, K., et al. (2011). Ionic liquid facilitates biocatalytic conversion of hardly water soluble ketones. *J. Mol. Catal. B Enzym.* 68, 147–153. doi: 10.1016/j.molcatb.2010.10.003

Kosan, B., Michels, C., and Meister, F. (2007). Dissolution and forming of cellulose with ionic liquids. *Cellulose* 15, 59–66. doi: 10.1007/s10570-007-9160-x

Kudou, M., Kubota, Y., Nakashima, N., Okazaki, F., Nakashima, K., Ogino, C., et al. (2014). Improvement of enzymatic activity of β-glucosidase from *Thermotoga maritima* by 1-butyl-3-methylimidazolium acetate. *J. Mol. Catal. B Enzym.* 104, 17–22. doi: 10.1016/j.molcatb.2014.02.013

Kumar, A., and Venkatesu, P. (2014). Does the stability of proteins in ionic liquids obey the hofmeister series? *Int. J. Biol. Macromol.* 63, 244–253. doi: 10.1016/j.ijbiomac.2013.10.031

Laszlo, J. A., and Compton, D. L. (2001). A-chymotrypsin catalysis in imidazolium-based ionic liquids. *Biotechnol. Bioeng.* 75, 181–186. doi: 10.1002/bit.1177

Latif, M. A. M., Micaêlo, N. M., and Rahman, M. B. A. (2014). Influence of anion–water interactions on the behaviour of lipases in room temperature ionic liquids. *RSC Adv.* 4, 48202–48211. doi: 10.1039/C4RA07460B

Leroy, E., Jacquet, P., Coativy, G., Reguerre, A. L., and Lourdin, D. (2012). Compatibilization of starch-zein melt processed blends by an ionic liquid used as plasticizer. *Carbohydr. Polym.* 89, 955–963. doi: 10.1016/j.carbpol.2012.04.044

Lewis, D. M., and Rippon, J. A. (eds.). (2013). *The Coloration of Wool and Other Keratin Fibres*. Chichester: John Wiley & Sons.

Li, L., Xiong, Y., Yu, S., Liu, S., Liu, F., and Xie, C. (2015). Facile preparation for robust and freestanding silk fibroin films in a 1-butyl-3-methyl imidazolium acetate ionic liquid system. *J. Appl. Polym. Sci.* 132, 2–8. doi: 10.1002/app.42822

Li, M., Wang, Y., Chen, Y., and Zhang, S. (2014). A luminescent ionogel based on an europium(iii)-coordinated carboxyl-functionalized ionic liquid and gelatin. *Photochem. Photobiol. Sci.* 13, 1025–1030. doi: 10.1039/C4PP00076E

Li, R., and Wang, D. (2013). Preparation of regenerated wool keratin films from wool keratin-ionic liquid solutions. *J. Appl. Polym. Sci.* 127, 2648–2653. doi: 10.1002/app.37527

Liang, C., Xue, Y., Fioroni, M., Rodríguez-Ropero, F., Zhou, C., Schwaneberg, U., et al. (2011). Cloning and characterization of a thermostable and halo-tolerant endoglucanase from thermoanaerobacter tengcongensis mb4. *Appl. Microbiol. Biotechnol.* 89, 315–326. doi: 10.1007/s00253-010-2842-6

Lim, G. S., and Klähn, M. (2018). On the stability of proteins solvated in imidazolium-based ionic liquids studied with replica exchange molecular dynamics. *J. Phys. Chem. B* 122, 9274–9288. doi: 10.1021/acs.jpcb.8b06452

Lisboa, M., Rodrigues, C., Barbosa, A., Mattedi, S., Freitas, L., Mendes, A., et al. (2018). New perspectives on the modification of silica aerogel particles with ionic liquid used in lipase immobilization with platform in ethyl esters production. *Process Biochem.* 75, 157–165. doi: 10.1016/j.procbio.2018.09.015

Liu, H., Zhu, L., Bocola, M., Chen, N., Spiess, A. C., and Schwaneberg, U. (2013). Directed laccase evolution for improved ionic liquid resistance. *Green Chem.* 15, 1348–1355. doi: 10.1039/c3gc36899h

Liu, X., Nie, Y., Liu, Y., Zhang, S., and Skov, A. L. (2018). Screening of ionic liquids for keratin dissolution by means of cosmo-rs and experimental verification. *ACS Sustainable Chem. Eng.* 6, 17314–17322. doi: 10.1021/acssuschemeng.8b04830

Liu, X., Nie, Y., Meng, X., Zhang, Z., Zhang, X., and Zhang, S. (2017). Dbn-based ionic liquids with high capability for the dissolution of wool keratin. *RSC Adv.* 7, 1981–1988. doi: 10.1039/C6RA26057H

Liu, X., Xu, W., Zhang, C., Liu, H., and Fang, J. (2015). Homogeneous sulfation of silk fibroin in an ionic liquid. *Mater. Lett.* 143, 302–304. doi: 10.1016/j.matlet.2014.12.140

Lourenço, N. M. T., Österreicher, J., Vidinha, P., Barreiros, S., Afonso, C.a,.M., Cabral, J. M. S., and Fonseca, L.P. (2011). Effect of gelatin–ionic liquid functional polymers on glucose oxidase and horseradish peroxidase kinetics. *React. Funct. Polym.* 71, 489–495. doi: 10.1016/j.reactfunctpolym.2011.01.006

Lovejoy, K. S., Lou, A. J., Davis, L. E., Sanchez, T. C., Iyer, S., Corley, C. A., et al. (2012). Single-pot extraction-analysis of dyed wool fibers with ionic liquids. *Anal. Chem.* 84, 9169–9175. doi: 10.1021/ac301873s

Lozano, P., Bernal, J. M., Sánchez-Gómez, G., López-López, G., and Vaultier, M. (2013). How to produce biodiesel easily using a green biocatalytic approach in sponge-like ionic liquids. *Energy Environ. Sci.* 6, 1328–1338. doi: 10.1039/c3ee24429f

Lozano-Pérez, A. A., Montalbán, M. G., Aznar-Cervantes, S. D., Cragnolini, F., Cenis, J. L., and Víllora, G. (2015). Production of silk fibroin nanoparticles using ionic liquids and high-power ultrasounds. *J. Appl. Polym. Sci.* 132, 1–8. doi: 10.1002/app.41702

Madern, D., Ebel, C., and Zaccai, G. (2000). Halophilic adaptation of enzymes. *Extremophiles* 4, 91–98. doi: 10.1007/s007920050142

Mahmood, H., Moniruzzaman, M., Yusup, S., and Welton, T. (2017). Ionic liquids assisted processing of renewable resources for the fabrication of biodegradable composite materials. *Green Chem.* 19, 2051–2075. doi: 10.1039/C7GC00318H

Mantz, R. A., Fox, D. M., Green, J. M., Iii, F.ylstra, P. A., De Long, H. C., and Trulove, P.C. (2007). Dissolution of biopolymers using ionic liquids. *Z. Naturforsch. A Phys. Sci.* 62, 275–280. doi: 10.1515/zna-2007-5-608

Marr, P. C., and Marr, A. C. (2016). Ionic liquid gel materials: applications in green and sustainable chemistry. *Green Chem.* 18, 105–128. doi: 10.1039/C5GC02277K

Marsh, R. E., Corey, R. B., and Pauling, L. (1955). An investigation of the structure of silk fibroin. *Biochim. Biophys. Acta* 16, 1–34. doi: 10.1016/0006-3002(55)90178-5

Maurelli, L., Ionata, E., La Cara, F., and Morana, A. (2013). Chestnut shell as unexploited source of fermentable sugars: Effect of different pretreatment methods on enzymatic saccharification. *Appl. Biochem. Biotechnol.* 170, 1104–1118. doi: 10.1007/s12010-013-0264-5

Mckittrick, J., Chen, P. Y., Bodde, S. G., Yang, W., Novitskaya, E. E., and Meyers, M. A. (2012). The structure, functions, and mechanical properties of keratin. *JOM* 64, 449–468. doi: 10.1007/s11837-012-0302-8

Mehta, A., Raghava Rao, J., and Fathima, N. N. (2015). Electrostatic forces mediated by choline dihydrogen phosphate stabilize collagen. *J. Phys. Chem. B* 119, 12816–12827. doi: 10.1021/acs.jpcb.5b07055

Mehta, A., Rao, J. R., and Fathima, N. N. (2014). Effect of ionic liquids on the different hierarchical order of type i collagen. *Colloids Surf. B* 117, 376–382. doi: 10.1016/j.colsurfb.2014.03.014

Meli, L., Miao, J., Dordick, J. S., and Linhardt, R. J. (2010). Electrospinning from room temperature ionic liquids for biopolymer fiber formation. *Green Chem.* 12, 1883–1883. doi: 10.1039/c0gc00283f

Meng, Z., Zheng, X., Tang, K., Liu, J., Ma, Z., and Zhao, Q. (2012). Dissolution and regeneration of collagen fibers using ionic liquid. *Int. J. Biol. Macromol.* 51, 440–448. doi: 10.1016/j.ijbiomac.2012.05.030

Mesbahi-Nowrouzi, M., and Mollania, N. (2018). Purification of selenate reductase from alcaligenes sp. Ckcr-6a with the ability to biosynthesis of selenium nanoparticle: Enzymatic behavior study in imidazolium based ionic liquids and organic solvent. *J. Mol. Liq.* 249, 1254–1262. doi: 10.1016/j.molliq.2017.10.117

Meyer, L.-E., Von Langermann, J., and Kragl, U. (2018). Recent developments in biocatalysis in multiphasic ionic liquid reaction systems. *Biophys. Rev.* 10, 901–910. doi: 10.1007/s12551-018-0423-6

Micaêlo, N. M., and Soares, C. M. (2008). Protein structure and dynamics in ionic liquids. Insights from molecular dynamics simulation studies. *J. Phys. Chem. B* 112, 2566–2572. doi: 10.1021/jp0766050

Muhammad, N., Gonfa, G., Rahim, A., Ahmad, P., Iqbal, F., Sharif, F., et al. (2017). Investigation of ionic liquids as a pretreatment solvent for extraction of collagen biopolymer from waste fish scales using cosmo-rs and experiment. *J. Mol. Liq.* 232, 258–264. doi: 10.1016/j.molliq.2017.02.083

Musa, M. M., Ziegelmann-Fjeld, K. I., Vieille, C., and Phillips, R. S. (2008). Activity and selectivity of w110a secondary alcohol dehydrogenase from *Thermoanaerobacter ethanolicus* in organic solvents and ionic liquids: Mono- and biphasic media. *Org. Biomol. Chem.* 6, 887–892. doi: 10.1039/b717120j

Nakashima, K., Yamaguchi, K., Taniguchi, N., Arai, S., Yamada, R., Katahira, S., et al. (2011). Direct bioethanol production from cellulose by the combination of cellulase-displaying yeast and ionic liquid pretreatment. *Green Chem.* 13, 2948. doi: 10.1039/c1gc15688h

Nemestóthy, N., Megyeri, G., Bakonyi, P., Lakatos, P., Koók, L., Polakovic, M., et al. (2017). Enzyme kinetics approach to assess biocatalyst inhibition and deactivation caused by [bmim][cl] ionic liquid during cellulose hydrolysis. *Bioresour. Technol.* 229, 190–195. doi: 10.1016/j.biortech.2017.01.004

Nishinari, K., Fang, Y., Guo, S., and Phillips, G. O. (2014). Soy proteins: a review on composition, aggregation and emulsification. *Food Hydrocoll.* 39, 301–318. doi: 10.1016/j.foodhyd.2014.01.013

Nordwald, E. M., Brunecky, R., Himmel, M. E., Beckham, G. T., and Kaar, J. L. (2014). Charge engineering of cellulases improves ionic liquid tolerance and reduces lignin inhibition. *Biotechnol. Bioeng.* 111, 1541–1549. doi: 10.1002/bit.25216

Nuno, M. T., LourençoO., Ana, V. M., Nunes Duarte, C. M. M., and Vidinha, P. (2011). "Ionic liquids gelation with polymeric materials: the ion jelly approach," in *Applications of Ionic Liquids in Science and Technology*, ed S. Handy (London: InTech), 155–172.

Ostadjoo, S., Berton, P., Shamshina, J. L., and Rogers, R. D. (2018). Scaling-up ionic liquid-based technologies: How much do we care about their toxicity? Prima facie information on 1-ethyl-3-methylimidazolium acetate. *Toxicol. Sci.* 161, 249–265. doi: 10.1093/toxsci/kfx172

Paljevac, M., Habulin, M., and Knez, Ž. (2006). Ionic liquids as (co) solvents for enzymatic reactions. *Chem. Ind. Chem. Eng. Q.* 12, 181–186. doi: 10.2298/CICEQ0603181P

Papadopoulou, A. A., Tzani, A., Alivertis, D., Katsoura, M. H., Polydera, A. C., Detsi, A., et al. (2016). Hydroxyl ammonium ionic liquids as media for biocatalytic oxidations. *Green Chem.* 18, 1147–1158. doi: 10.1039/C5GC02381E

Park, K. E., Jung, S. Y., Lee, S. J., Min, B. M., and Park, W. H. (2006). Biomimetic nanofibrous scaffolds: Preparation and characterization of chitin/silk fibroin blend nanofibers. *Int. J. Biol. Macromol.* 38, 165–173. doi: 10.1016/j.ijbiomac.2006.03.003

Park, S., Doan, T. T. N., Koo, Y.-M., Oh, K. K., and Lee, S. H. (2018). Ionic liquids as cosolvents for the lipase-catalyzed kinetic resolution of ketoprofen. *Mol. Catal.* 459, 113–118. doi: 10.1016/j.mcat.2018.09.001

Pérez, C., and Griebenow, K. (2000). Fourier-transform infrared spectroscopic investigation of the thermal denaturation of hen egg-white lysozyme dissolved in aqueous buffer and glycerol. *Biotechnol. Lett.* 22, 1899–1905. doi: 10.1023/A:1005645810247

Pérez-Rigueiro, J., Viney, C., Llorca, J., and Elices, M. (2000). Mechanical properties of single-brin silkworm silk. *J. Appl. Polym. Sci.* 75, 1270–1277. doi: 10.1002/(SICI)1097-4628(20000307)75:10<1270::AID-APP8>3.0.CO;2-C

Phillips, D. M., Drummy, L. F., Conrady, D. G., Fox, D. M., Naik, R. R., Stone, M. O., et al. (2004). Dissolution and regeneration of bombyx mori silk fibroin using ionic liquids. *J. Am. Chem. Soc.* 126, 14350–14351. doi: 10.1021/ja046079f

Phillips, D. M., Drummy, L. F., Naik, R. R., Long, H. C. D., Fox, D. M., Trulove, P. C., et al. (2005). Regenerated silk fiber wet spinning from an ionic liquid solution. *J. Mater. Chem.* 15, 4206–4206. doi: 10.1039/b510069k

Pinkert, A., Marsh, K. N., and Pang, S. (2010). Reflections on the solubility of cellulose. *Ind. Eng. Chem. Res.* 49, 11121–11130. doi: 10.1021/ie1006596

Pinkert, A., Marsh, K. N., Pang, S., and Staiger, M. P. (2009). Ionic liquids and their interaction with cellulose. *Chem. Rev.* 109, 6712–6728. doi: 10.1021/cr9001947

Plowman, J. E., Clerens, S., Lee, E., Harland, D. P., Dyer, J. M., and Deb-Choudhury, S. (2014). Ionic liquid-assisted extraction of wool keratin proteins as an aid to ms identification. *Anal. Methods* 6, 7305–7311. doi: 10.1039/C4AY01251H

Pottkämper, J., Barthen, P., Ilmberger, N., Schwaneberg, U., Schenk, A., Schulte, M., et al. (2009). Applying metagenomics for the identification of bacterial cellulases that are stable in ionic liquids. *Green Chem.* 11, 957. doi: 10.1039/b820157a

Raddadi, N., Cherif, A., Daffonchio, D., and Fava, F. (2013). Halo-alkalitolerant and thermostable cellulases with improved tolerance to ionic liquids and organic solvents from *Paenibacillus tarimensis* isolated from the chott el fejej, sahara desert, tunisia. *Bioresour. Technol.* 150, 121–128. doi: 10.1016/j.biortech.2013.09.089

Rana, S., Carvalho, T., Fangueiro, R., and Vidinha, P. (2013). Silk-ion jelly: a novel ion conducting polymeric material with high conductivity and excellent mechanical stability. *Polym. Adv. Technol.* 24, 191–196. doi: 10.1002/pat.3069

Riblett, A. L., Herald, T. J., Schmidt, K. A., and Tilley, K. A. (2001). Characterization of β-conglycinin and glycinin soy protein fractions from four selected soybean genotypes. *J. Agric. Food Chem.* 49, 4983–4989. doi: 10.1021/jf0105081

Ribot, J. C., Guerrero-Sanchez, C., Greaves, T. L., Kennedy, D. F., Hoogenboom, R., and Schubert, U. S. (2012). Amphiphilic oligoether-based ionic liquids as functional materials for thermoresponsive ion gels with tunable properties via aqueous gelation. *Soft Matter* 8, 1025–1032. doi: 10.1039/C1SM06468A

Ribot, J. C., Guerrero-Sanchez, C., Hoogenboom, R., and Schubert, U. S. (2010). Aqueous gelation of ionic liquids: Reverse thermoresponsive ion gels. *Chem. Commun.* 46, 6971–6973. doi: 10.1039/c0cc01671c

Rogers, R. D., and Seddon, K. R. (2003). Ionic liquids—solvents of the future ? *Science* 302, 792–793. doi: 10.1126/science.1090313

Rouse, J. G., and Van Dyke, M. E. (2010). A review of keratin-based biomaterials for biomedical applications. *Materials (Basel).* 3, 999–1014. doi: 10.3390/ma3020999

Ruiz, E., Cara, C., Manzanares, P., Ballesteros, M., and Castro, E. (2008). Evaluation of steam explosion pre-treatment for enzymatic hydrolysis of sunflower stalks. *Enzyme Microb. Technol.* 42, 160–166. doi: 10.1016/j.enzmictec.2007.09.002

Salvador, Â. C., Santos, M. D. C., and Saraiva, J. A. (2010). Effect of the ionic liquid [bmim] cl and high pressure on the activity of cellulase. *Green Chem.* 12, 632–635. doi: 10.1039/b918879g

Santos, R. D., Rocha, Â., Matias, A., Duarte, C., S.á-,Nogueira, I., et al. and Vidinha, P. (2013). Development of antimicrobial ion jelly fibers. *RSC Adv.* 3, 24400. doi: 10.1039/c3ra44258f

Schaffarczyk Mchale, K. S., Haines, R. S., and Harper, J. B. (2018). Ionic liquids as solvents for s_N^2 processes. Demonstration of the complex interplay of interactions resulting in the observed solvent effects. *ChemPlusChem* 83, 1162–1168. doi: 10.1002/cplu.201800510

Shamsuri, A. A., Abdullah, D. K., and Daik, R. (2012). Fabrication of agar/biopolymer blend aerogels in ionic liquid and co-solvent mixture. *Cellul. Chem. Technol.* 46, 45–52.

Shang, S., Zhu, L., and Fan, J. (2011). Physical properties of silk fibroin/cellulose blend films regenerated from the hydrophilic ionic liquid. *Carbohydr. Polym.* 86, 462–468. doi: 10.1016/j.carbpol.2011.04.064

Sharma, A., Rawat, K., Solanki, P. R., and Bohidar, H. B. (2015). Electrochemical response of agar ionogels towards glucose detection. *Anal. Methods* 7, 5876–5885. doi: 10.1039/C5AY01310K

Sharma, S., and Gupta, A. (2016). Sustainable management of keratin waste biomass: applications and future perspectives. *Braz. Arch. Biol. Technol.* 59:e16150684. doi: 10.1590/1678-4324-2016150684

Shen, Y., Johnson, M. A., and Martin, D. C. (1998). Microstructural characterization of *Bombyx mori* silk fibers. *Macromolecules* 31, 8857–8864. doi: 10.1021/ma980281j

Shi, X. A., Zong, M. H., and Lou, W. Y. (2006). Effect of ionic liquids on catalytic characteristics of horse liver alcohol dehydrogenase. *Chin. J. Chem.* 24, 1643–1647. doi: 10.1002/cjoc.200690307

Shukla, R., and Cheryan, M. (2001). Zein: the industrial protein from corn. *Ind. Crops Prod.* 13, 171–192. doi: 10.1016/S0926-6690(00)00064-9

Silva, N. H. C. S., Vilela, C., Marrucho, I. M., Freire, C. S. R., Pascoal Neto, C., and Silvestre, A. J. D. (2014). Protein-based materials: from sources to innovative sustainable materials for biomedical applications. *J. Mater. Chem. B* 2, 3715. doi: 10.1039/c4tb00168k

Silva, S. S., Popa, E. G., Gomes, M. E., Oliveira, M. B., Nayak, S., Subia, B., et al. (2013). Silk hydrogels from non-mulberry and mulberry silkworm cocoons processed with ionic liquids. *Acta Biomater.* 9, 8972–8982. doi: 10.1016/j.actbio.2013.06.044

Silva, S. S., Santos, T. C., Cerqueira, M. T., Marques, A. P., Reys, L. L., Silva, T. H., et al. (2012). The use of ionic liquids in the processing of chitosan/silk hydrogels for biomedical applications. *Green Chem.* 14, 1463–1463. doi: 10.1039/c2gc16535j

Simpson, W. S., and Crawshaw, G. H. (eds.). (2002). *Wool: Science and Technology*. Cambridge, UK; Boca Raton, FL: Woodhead Publishing; CRC Press.

Singh, G., Singh, G., Damarla, K., Sharma, P. K., Kumar, A., and Kang, T. S. (2017). Gelatin-based highly stretchable, self-healing, conducting, multiadhesive, and antimicrobial ionogels embedded with Ag$_2$O nanoparticles. *ACS Sustainable Chem. Eng.* 5, 6568–6577. doi: 10.1021/acssuschemeng.7b00719

Sprenger, K. G., Plaks, J. G., Kaar, J. L., and Pfaendtner, J. (2017). Elucidating sequence and solvent specific design targets to protect and stabilize enzymes for biocatalysis in ionic liquids. *Phys. Chem. Chem. Phys.* 19, 17426–17433. doi: 10.1039/C7CP03013D

Stanton, J., Xue, Y., Pandher, P., Malek, L., Brown, T., Hu, X., et al. (2018). Impact of ionic liquid type on the structure, morphology and properties of silk-cellulose biocomposite materials. *Int. J. Biol. Macromol.* 108, 333–341. doi: 10.1016/j.ijbiomac.2017.11.137

Sun, P., Liu, Z. T., and Liu, Z. W. (2009). Particles from bird feather: a novel application of an ionic liquid and waste resource. *J. Hazard. Mater.* 170, 786–790. doi: 10.1016/j.jhazmat.2009.05.034

Suo, H., Gao, Z., Xu, L., Xu, C., Yu, D., Xiang, X., et al. (2019). Synthesis of functional ionic liquid modified magnetic chitosan nanoparticles for porcine pancreatic lipase immobilization. *Mat. Sci. Eng. C* 96, 356–364. doi: 10.1016/j.msec.2018.11.041

Susanin, A. I., Sashina, E. S., Novoselov, N. P., and Zaborskii, M. (2017). Study of the rheological characteristics of solutions of silk fibroin in 1-butyl-3-methylimidazolium acetate and films based on them. *Fibre Chem.* 49, 88–96. doi: 10.1007/s10692-017-9849-z

Susanin, A. I., Sashina, E. S., Ziółkowski, P., Zakharov, V. V., Zaborski, M., Dziubinski, M., et al. (2018). A comparative study of solutions of silk fibroin in 1-butyl-3-methylimidazolium chloride and acetate. *Russ. J. Appl. Chem.* 91, 647–652. doi: 10.1134/S1070427218040171

Swatloski, R. P., Spear, S. K., Holbrey, J. D., and Rogers, R. D. (2002). Dissolution of cellose with ionic liquids. *J. Am. Chem. Soc.* 124, 4974–4975. doi: 10.1021/ja025790m

Tan, S. S., and Macfarlane, D. R. (2010). Ionic liquids in biomass processing. *Top. Curr. Chem.* 290, 311–339. doi: 10.1007/128_2008_35

Tanner, E. E. L., Hawker, R. R., Yau, H. M., Croft, A. K., and Harper, J. B. (2013a). Probing the importance of ionic liquid structure: a general ionic liquid effect on an snar process. *Org. Biomol. Chem.* 11, 7516–7521. doi: 10.1039/c3ob41634h

Tanner, E. E. L., Yau, H. M., Hawker, R. R., Croft, A. K., and Harper, J. B. (2013b). Does the cation really matter? The effect of modifying an ionic liquid cation on an S$_N^2$ process. *Org. Biomol. Chem.* 11, 6170-6175. doi: 10.1039/c3ob41038b

Tarannum, A., Adams, A., Blümich, B., and Fathima, N. N. (2018a). Impact of ionic liquids on the structure and dynamics of collagen. *J. Phys. Chem. B* 122, 1060–1065. doi: 10.1021/acs.jpcb.7b09626

Tarannum, A., Rao, J. R., and Fathima, N. N. (2018b). Choline-based amino acid ils-collagen interaction: Enunciating its role in stabilization/destabilization phenomena. *J. Phys. Chem. B* 122, 1145–1151. doi: 10.1021/acs.jpcb.7b10645

Tomé, L. I., Jorge, M., Gomes, J. R., and Coutinho, J. A. (2012). Molecular dynamics simulation studies of the interactions between ionic liquids and amino acids in aqueous solution. *J. Phys. Chem. B* 116, 1831–1842. doi: 10.1021/jp209625e

Tomlinson, S. R., Kehr, C. W., Lopez, M. S., Schlup, J. R., and Anthony, J. L. (2014). Solubility of the corn protein zein in imidazolium-based ionic liquids. *Ind. Eng. Chem. Res.* 53, 2293–2298. doi: 10.1021/ie403659x

Tran, C. D., and Mututuvari, T. M. (2016). Cellulose, chitosan and keratin composite materials: Facile and recyclable synthesis, conformation and properties. *ACS Sustainable Chem. Eng.* 4, 1850–1861. doi: 10.1021/acssuschemeng.6b00084

Tran, C. D., Prosencyes, F., Franko, M., and Benzi, G. (2016). Synthesis, structure and antimicrobial property of green composites from cellulose, wool, hair and chicken feather. *Carbohydr. Polym.* 151, 1269–1276. doi: 10.1016/j.carbpol.2016.06.021

Trivedi, N., Gupta, V., Reddy, C. R., and Jha, B. (2013). Detection of ionic liquid stable cellulase produced by the marine bacterium *Pseudoalteromonas* sp. Isolated from brown alga *Sargassum polycystum* c. *Agardh. Bioresour. Technol.* 132, 313–319. doi: 10.1016/j.biortech.2013.01.040

Turner, M. B., Spear, S. K., Huddleston, J. G., Holbrey, J. D., and Rogers, R. D. (2003). Ionic liquid salt-induced inactivation and unfolding of cellulase from *Trichoderma reesei*. *Green Chem.* 5, 443–447. doi: 10.1039/b302570e

Vidinha, P., Lourenco, N. M., Pinheiro, C., Bras, A. R., Carvalho, T., Santos-Silva, T., et al. (2008). Ion jelly: a tailor-made conducting material for smart electrochemical devices. *Chem. Commun.* 44, 5842–5844. doi: 10.1039/b811647d

Vijayaraghavan, R., Thompson, B. C., Macfarlane, D. R., Kumar, R., Surianarayanan, M., Aishwarya, S., et al. (2010). Biocompatibility of choline salts as crosslinking agents for collagen based biomaterials. *Chem. Commun.* 46, 294–296. doi: 10.1039/B910601D

Vitz, J., Erdmenger, T., Haensch, C., and Schubert, U. S. (2009). Extended dissolution studies of cellulose in imidazolium based ionic liquids. *Green Chem.* 11, 417–424. doi: 10.1039/b818061j

Wahlström, R., and Suurnäkki, A. (2015). Enzymatic hydrolysis of lignocellulosic polysaccharides in the presence of ionic liquids. *Green Chem.* 17, 694–714. doi: 10.1039/C4GC01649A

Wallraf, A.-M., Liu, H., Zhu, L., Khalfallah, G., Simons, C., Alibiglou, H., et al. (2018). A loop engineering strategy improves laccase lcc2 activity in ionic liquid and aqueous solution. *Green Chem.* doi: 10.1039/C7GC03776G

Wang, J., Wei, L., Ma, Y., Li, K., Li, M., Yu, Y., et al. (2013a). Collagen/cellulose hydrogel beads reconstituted from ionic liquid solution for cu(ii) adsorption. *Carbohydr. Polym.* 98, 736–743. 20, 2801–2812. doi: 10.1016/j.carbpol.2013.06.001

Wang, L., Nie, Y., Zhang, X., Zeng, S., Zhang, S., and Zheng, S. (2016). Synergistic effects of cosolvents on the dissolution of wool keratin using ionic liquids. *Chem. Eng. Technol.* 39, 979–986. doi: 10.1002/ceat.201500646

Wang, M., Zhao, T., Wang, G., and Zhou, J. (2014). Blend films of human hair and cellulose prepared from an ionic liquid. *Text. Res. J.* 84, 1315–1324. doi: 10.1177/0040517514521123

Wang, Q., Chen, Q., Yang, Y., and Shao, Z. (2013b). Effect of various dissolution systems on the molecular weight of regenerated silk fibroin. *Biomacromolecules* 14, 285–289. doi: 10.1021/bm301741q

Wang, Q., Yang, Y., Chen, X., and Shao, Z. (2012). Investigation of rheological properties and conformation of silk fibroin in the solution of amimcl. *Biomacromolecules* 13, 1875–1881. doi: 10.1021/bm300387z

Wang, Y., Radosevich, M., Hayes, D., and Labbé, N. (2011). Compatible ionic liquid-cellulases system for hydrolysis of lignocellulosic biomass. *Biotechnol. Bioeng.* 108, 1042–1048. doi: 10.1002/bit.23045

Wang, Y.-X., and Cao, X.-J. (2012). Extracting keratin from chicken feathers by using a hydrophobic ionic liquid. *Process Biochem.* 47, 896–899. doi: 10.1016/j.procbio.2012.02.013

Warden, A. C., Williams, M., Peat, T. S., Seabrook, S. A., Newman, J., Dojchinov, G., et al. (2015). Rational engineering of a mesohalophilic carbonic anhydrase to an extreme halotolerant biocatalyst. *Nat. Commun.* 6:10278. doi: 10.1038/ncomms10278

Wijaya, E. C., Separovic, F., Drummond, C. J., and Greaves, T. L. (2016). Activity and conformation of lysozyme in molecular solvents, protic ionic liquids (pils) and salt–water systems. *Phys. Chem. Chem. Phys.* 18, 25926–25936. doi: 10.1039/C6CP03334B

Wijaya, E. C., Separovic, F., Drummond, C. J., and Greaves, T. L. (2018). Stability and activity of lysozyme in stoichiometric and non-stoichiometric protic ionic liquid (PIL)-water systems. *J. Chem. Phys.* 148, 193838. doi: 10.1063/1.5010055

Wu, R.-L., Wang, X.-L., Wang, Y.-Z., Bian, X.-C., and Li, F. (2009). Cellulose/soy protein isolate blend films prepared via room-temperature ionic liquid. *Ind. Eng. Chem. Res.* 48, 7132–7136. doi: 10.1021/ie9001052

Xie, H., Li, S., and Zhang, S. (2005). Ionic liquids as novel solvents for the dissolution and blending of wool keratin fibers. *Green Chem.* 7, 606–608. doi: 10.1039/b502547h

Xue, L., Qiu, H., Li, Y., Lu, L., Huang, X., and Qu, Y. (2011). A novel water-in-ionic liquid microemulsion and its interfacial effect on the activity of laccase. *Colloids Surf.* 82, 432–437. doi: 10.1016/j.colsurfb.2010.09.016

Yang, F., Li, L., Li, Q., Tan, W., Liu, W., and Xian, M. (2010). Enhancement of enzymatic *in situ* saccharification of cellulose in aqueous-ionic liquid media by ultrasonic intensification. *Carbohydr. Polym.* 81, 311–316. doi: 10.1016/j.carbpol.2010.02.031

Yao, M., Su, D., Wang, W., Chen, X., and Shao, Z. (2018). Fabrication of air-stable and conductive silk fibroin gels. *ACS Appl. Mater. Interfaces* 10, 38466–38475. doi: 10.1021/acsami.8b14521

Yao, Y., Xia, X., Mukuze, K. S., Zhang, Y., and Wang, H. (2014a). Study on the temperature-induced sol–gel transition of cellulose/silk fibroin blends in 1-butyl-3-methylimidazolium chloride via rheological behavior. *Cellulose* 21, 3737–3743. doi: 10.1007/s10570-014-0349-5

Yao, Y., Zhang, E., Xia, X., Yu, J., Wu, K., Zhang, Y., et al. (2014b). Morphology and properties of cellulose/silk fibroin blend fiber prepared with 1-butyl-3-methylimidazolium chloride as solvent. *Cellulose* 22, 625–635. doi: 10.1007/s10570-014-0520-z

Yau, H. M., Barnes, S. A., Hook, J. M., Youngs, T. G. A., Croft, A. K., and Harper, J. B. (2008). The importance of solvent reorganisation in the effect of an ionic liquid on a unimolecular substitution process. *Chem. Commun.* 44, 3576–3578. doi: 10.1039/b805255g

Yau, H. M., Chan, S. J., George, S. R., Hook, J. M., Croft, A. K., and Harper, J. B. (2009a). Ionic liquids: just molten salts after all? *Molecules* 14, 2521–2534. doi: 10.3390/molecules14072521

Yau, H. M., Croft, A. K., and Harper, J. B. (2012). Investigating the origin of entropy-derived rate accelerations in ionic liquids. *Faraday Discuss.* 154, 365–371. doi: 10.1039/C1FD00060H

Yau, H. M., Howe, A. G., Hook, J. M., Croft, A. K., and Harper, J. B. (2009b). Solvent reorganisation as the driving force for rate changes of menschutkin reactions in an ionic liquid. *Org. Biomol. Chem.* 7, 3572–3575. doi: 10.1039/b909171h

Yau, H. M., Keaveney, S. T., Butler, B. J., Tanner, E. E. L., Guerry, M. S., George, S. R. D., et al. (2013). Towards solvent-controlled reactivity in ionic liquids. *Pure Appl. Chem.* 85, 1979–1990. doi: 10.1351/pac-con-12-10-22

Yoshimoto, M., Tanimura, K., Tokunaga, K., and Kamimura, A. (2013). Hydrolysis of insoluble cellulose to glucose catalyzed by cellulase-containing liposomes in an aqueous solution of 1-butyl-3-methylimidazolium chloride. *Biotechnol. Prog.* 29, 1190–1196. doi: 10.1002/btpr.1779

Yue, X., Zhang, F., Wu, H., Ming, J., Fan, Z., and Zuo, B. (2014). A novel route to prepare dry-spun silk fi bers from CaCl₂-formic acid solution. *Mater. Lett.* 128, 175–178. doi: 10.1016/j.matlet.2014.04.116

Zappi, D., Caminiti, R., Ingo, G. M., Sadun, C., Tortolini, C., and Antonelli, M. L. (2017). Biologically friendly room temperature ionic liquids and nanomaterials for the development of innovative enzymatic biosensors. *Talanta* 175, 566–572. doi: 10.1016/j.talanta.2017.07.081

Zappi, D., Masci, G., Sadun, C., Tortolini, C., Antonelli, M. L., and Bollella, P. (2018). Evaluation of new cholinium-amino acids based room temperature ionic liquids (RTILs) as immobilization matrix for electrochemical biosensor development: proof-of-concept with *Trametes versicolor* laccase. *Microchem. J.* 141, 346–352. doi: 10.1016/j.microc.2018.05.045

Zavgorodnya, O., Shamshina, J. L., Bonner, J. R., and Rogers, R. D. (2017). Electrospinning biopolymers from ionic liquids requires control of different solution properties than volatile organic solvents. *ACS Sustainable Chem. Eng.* 5, 5512–5519. doi: 10.1021/acssuschemeng.7b00863

Zhang, C., Chen, X., and Shao, Z. (2016a). Sol-gel transition of regenerated silk fibroins in ionic liquid/water mixtures. *ACS Biomater. Sci. Eng.* 2, 12–18. doi: 10.1021/acsbiomaterials.5b00149

Zhang, D.-H., Xu, H.-X., Chen, N., and Che, W.-C. (2016b). The application of ionic liquids in enzyme immobilization and enzyme modification. *Austin J. Biotech. Bioeng.* 3, id1060.

Zhang, M., Ding, C., Chen, L., and Huang, L. (2014). The preparation of cellulose/collagen composite films using 1-ethyl-3-methylimidazolium acetate as a solvent. *BioResources* 9, 756–771. doi: 10.15376/biores.9.1.756-771

Zhang, T., Datta, S., Eichler, J., Ivanova, N., Axen, S. D., Kerfeld, C. A., et al. (2011). Identification of a haloalkaliphilic and thermostable cellulase with improved ionic liquid tolerance. *Green Chem.* 13, 2083–2090. doi: 10.1039/c1gc15193b

Zhang, Y., Huang, X., and Li, Y. (2008). Negative effect of [bmim][PF₆] on the catalytic activity of alcohol dehydrogenase: mechanism and prevention. *J. Chem. Technol. Biotechnol.* 83, 1230–1235. doi: 10.1002/jctb.1931

Zhang, Z., Nie, Y., Zhang, Q., Liu, X., Tu, W., Zhang, X., et al. (2017a). Quantitative change in disulfide bonds and microstructure variation of regenerated wool keratin from various ionic liquids. *ACS Sustainable Chem. Eng.* 5, 2614–2622. doi: 10.1021/acssuschemeng.6b02963

Zhang, Z., Zhang, X., Nie, Y., Wang, H., Zheng, S., and Zhang, S. (2017b). Effects of water content on the dissolution behavior of wool keratin using 1-ethyl-3-methylimidazolium dimethylphosphate. *Sci. China Chem.* 60, 934–941. doi: 10.1007/s11426-016-9019-8

Zhao, D., Liao, Y., and Zhang, Z. D. (2007). Toxicity of ionic liquids. *Clean Soil Air Water* 35, 42–48. doi: 10.1002/clen.200600015

Zhao, H. (2016). Protein stabilization and enzyme activation in ionic liquids: specific ion effects. *J. Chem. Technol. Biotechnol.* 91, 25–50. doi: 10.1002/jctb.4837

Zhao, H., Song, Z., Olubajo, O., and Cowins, J. V. (2010a). New ether-functionalized ionic liquids for lipase-catalyzed synthesis of biodiesel. *Appl. Biochem. Biotechnol.* 162, 13–23. doi: 10.1007/s12010-009-8717-6

Zhao, J., Frauenkron-Machedjou, V. J., Fulton, A., Zhu, L., Davari, M. D., Jaeger, K.-E., et al. (2018). Unraveling the effects of amino acid substitutions enhancing lipase resistance to an ionic liquid: a molecular dynamics study. *Phys. Chem. Chem. Phys.* 20, 9600–9609. doi: 10.1039/C7CP08470F

Zhao, L., Tang, Y.-X., Zhao, R.-F., Mao, W.-K., Chen, S., and Hua, J. (2010b). Dissolution and regeneration of feather keratins in ionic liquids. *Maofang Keji* 38, 1–5. doi: 10.1039/C2GC36556A

Zheng, S., Yi, N., Zhang, S., Zhang, X., and Wang, L. (2015). Highly efficient dissolution of wool keratin by dimethylphosphate ionic liquids. *ACS Sustainable Chem. Eng.* 3, 2925–2932. doi: 10.1021/acssuschemeng.5b00895

Zhong, N., Li, Y., Cai, C., Gao, Y., Liu, N., Liu, G., et al. (2018). Enhancing the catalytic performance of candida antarctica lipase b by immobilization onto the ionic liquids modified sba-15. *Eur. J. Lipid Sci. Technol.* 120:1700357. doi: 10.1002/ejlt.201700357

Zhou, C.-Z., Confalonieri, F., Jacquet, M., Perasso, R., Li, Z.-G., and Janin, J. (2001). Silk fibroin: Structural implications of a remarkable amino acid sequence. *Proteins* 44, 119–122. doi: 10.1002/prot.1078

Zhou, L., Wang, Q., Wen, J., Chen, X., and Shao, Z. (2013). Preparation and characterization of transparent silk fibroin/cellulose blend films. *Polymer (Guildf).* 54, 5035–5042. doi: 10.1016/j.polymer.2013.07.002

Zhu, M., Tan, C., Fang, Q., Gao, L., Sui, G., and Yang, X. (2016). High performance and biodegradable skeleton material based on soy protein isolate for gel polymer electrolyte. *ACS Sustainable Chem. Eng.* 4, 4498–4505. doi: 10.1021/acssuschemeng.6b01218

Zoccola, M., Aluigi, A., and Tonin, C. (2009). Characterisation of keratin biomass from butchery and wool industry wastes. *J. Mol. Struct.* 938, 35–40. doi: 10.1016/j.molstruc.2009.08.036

Zuliani, C., Curto, V. F., Matzeu, G., Fraser, K. J., and Diamond, D. (2014). "Comprehensive materials processing," in *Properties and Customization of Sensor Materials for Biomedical Applications*, ed M. S. J. Hashmi (Oxford, UK: Elsevier), 221–243. doi: 10.1016/B978-0-08-096532-1.01308-X

Ionic Liquid-Based Electrolytes for Supercapacitor and Supercapattery

Linpo Yu[1] and George Z. Chen[1,2]*

[1] Department of Chemical and Environmental Engineering, Faculty of Science and Engineering, Key Laboratory of More Electric Aircraft Technology of Zhejiang Province, University of Nottingham Ningbo China, Ningbo, China, [2] Department of Chemical and Environmental Engineering, Faculty of Engineering, University of Nottingham, Nottingham, United Kingdom

There is a strong desire to replace or complement aqueous and organic electrolytes by ionic liquids (ILs) in electrochemical energy storage (EES) devices to achieve high operating voltages and hence high energy capacity. ILs are regarded as the inherent and competitive electrolytes since they were introduced to the electrochemical research community because they can overcome many disadvantages of the conventional aqueous and organic electrolytes, such as narrow potential windows, volatility, and flammability. This paper reviews critically the recent literatures of IL-based electrolytes used in supercapacitor, supercapattery, and micro-supercapacitor. Supercapattery is a generic term for various hybrid devices combining the merits of rechargeable battery and supercapacitor and often shows capacitive behavior. Fundamentals of supercapattery are briefly explained with typical examples. Micro-supercapacitor falls in the same scope of supercapacitor and supercapattery and shares the same fundamental concerns besides topology or structure. The future of IL-based electrolytes for the capacitive EES devices are also prospected.

Keywords: supercapacitor, supercapattery, micro-supercapacitor, ionic liquids, electrolytes, interfaces

INTRODUCTION

Electrochemical energy storage (EES) technologies are currently playing the dominant and prospective roles in the globe effort to tackle the challenges to renewable energy supply (Dutta et al., 2014). One of the challenges is to efficiently store and supply energy harvested from the renewable sources at affordable cost compared with the traditional non-renewable options. All successful EES devices charge (storage) and discharge (release) electric charges reversibly, but their charging-discharging mechanisms are different in how and where the charges are stored. Based on these differences, there are three main types of EES technologies: (1) rechargeable batteries, including redox flow batteries, (2) supercapacitors, also known as electrochemical capacitors, and (3) various hybrids of battery and supercapacitor which are called supercapattery and supercabattery which have been discussed in the previous reviews (Chae et al., 2012; Akinwolemiwa et al., 2015; Yu and Chen, 2016b; Chen, 2017; Xia et al., 2017; Akinwolemiwa and Chen, 2018). Rechargeable batteries are recognized for their high energy capacity, whilst supercapacitors are perceived to have high power capability and long cycle life measured against the common ground (Chen, 2013; Simon and Gogotsi, 2013). Either the batteries or supercapacitors alone cannot satisfy the current commercial needs based on the consumption of fossil fuels. On this condition, several EES hybrid devices have been proposed and demonstrated in many studies that combine a battery

electrode and a supercapacitor electrode into one device. Such hybrid device is a supercapattery if it has a capacitive performance exhibiting an enhanced energy capacity or it is a supercabattery if its performance is close to that of a battery. Supercabattery commonly possesses higher power capability and longer cycle life than battery. The performance of the hybrid devices mainly depends on the pairing of electrode materials. **Table 1** summarizes the electrode compositions of supercapacitor, supercapattery, supercabattery and battery based on the charge storage mechanisms of electrode materials. The performance metrics of the typical cells, especially the ones using IL-based electrolytes are also concluded.

Electrolytes, normally in liquid phase, are indispensable parts in all types of EES devices. They do not only help conduct electricity by means of transporting ions and keep an electronic insulation between positive and negative electrodes (positrode and negatrode), but also play a key role in exploiting the potentialities of EES devices. Generally, aqueous electrolytes are of high ionic conductivity and operational safety, but the maximum charging voltage (MCV) of an aqueous cell is limited by the splitting voltage of water. There is a strong desire to replace aqueous electrolytes by organic ones to achieve higher MCVs because the energy capacity can be dramatically promoted by the increased MCVs as described in Equation (1).

$$W_{max} = \frac{1}{2} C U_{max}^2 \qquad (1)$$

where C is the capacitance of a capacitive EES cell, W_{max} represents the maximum energy capacity of the cell, and U_{max} is the symbol of MCV. Nowadays, organic electrolytes have been widely used in commercial Li-ion batteries and supercapacitors. However, traditional organic electrolytes have several inevitable disadvantages, like maintenance difficulty (tedious purification processes for the volatile and flammable solvents), high environmental impact, high cost, safety issues, and relatively low ionic conductivity, each of which can compromise the application of capacitive EES devices. There is strong desire to develop a new kind of electrolytes that can overcome these disadvantages.

Ionic liquids (ILs) are pure liquid salts in nature. They are specially featured by their practically zero or negligible volatility, highly ionized environment, broad liquid temperature ranges, and wide operating voltage windows. These features have brought about unique opportunities, where ILs have been used as the electrolytes for electrolysis (Sun et al., 2005; Yu et al., 2007, 2013), thermochromic materials (Wei et al., 2008, 2009; Yu and Chen, 2014), and the electrolytes in capacitive EES devices (Akinwolemiwa et al., 2015; Guan et al., 2016; Yu and Chen, 2016a,b; Xia et al., 2017; Shahzad et al., 2018).

There are several reviews related to those three kinds of electrolytes for different devises (Xia et al., 2017), such as battery (Chen et al., 2018), supercapacitor (Shahzad et al., 2018), etc. This article intends to review the recent progress of the IL-based electrolytes for capacitive EES devices, including supercapacitor, supercapattery, and micro-supercapacitor. The opportunity and challenge of these IL-based electrolytes are prospected based on the current knowledge.

SUPERCAPACITORS

Electrical double layer capacitors (EDLCs) are part of supercapacitors and they store charges on the surface of electrode materials in principle. When a cell voltage is applied, the ions electrostatic adsorbed at the electrode/electrolyte interface contribute the charges stored by EDLCs. It is perceived that there should be no chemical reaction in EDLCs, and the charge storage process is widely considered to be physical in nature. Such mechanism has been proved by the fact that an EDLC using porous carbon electrodes can output a very high power of 90 kW kg^{-1}, but its energy capacity is limited to 2~8 Wh kg^{-1} (Stevenson et al., 2015). Ions are always solvated in a bulk solution, but less so when they are adsorbed at the electrode | electrolyte interface. Solvation effect cannot be neglected when investigating the relationship between the pore size and the specific capacitance of porous carbons in aqueous or organic electrolytes. ILs have been used in the studies of EDLCs to avoid the effect of solvation because ILs are purely comprised of cations and anions.

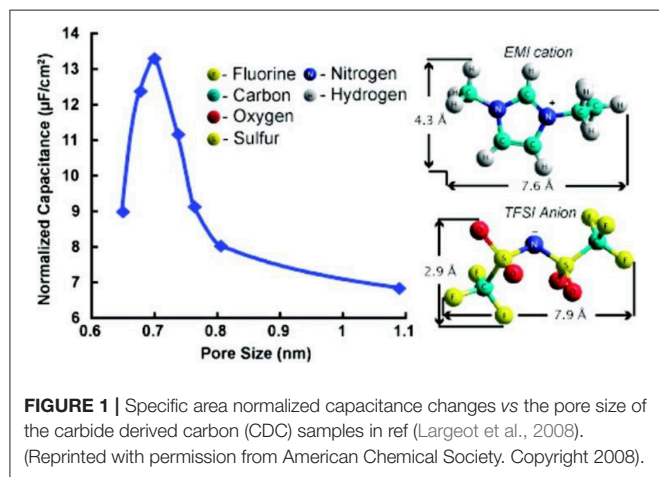## Neat IL Electrolytes for Supercapacitors

Amongst past attempts, an IL, 1-ethyl-3-methylimidazolium bis(trifluoromethylsulfonyl)imide (EMI-TFSI), was chosen to avoid solvation effect (Largeot et al., 2008). The longest dimensions of the EMI$^+$ and TFSI$^-$ ions are 0.76 and 0.79 nm, respectively, based on the calculation by using a HyperChem model. Because the average pore widths of carbide derived carbons (CDCs) can be easily modified from 0.65 to 1.1 nm by controlling the chlorination temperature from 400 to 1000°C, CDCs were used to fabricate the EDLC electrodes. Both EMI$^+$ and TFSI$^-$ ion sizes are within the range of the CDC pore sizes. **Figure 1** clearly shows the pore size effect on the capacitance and the molecular structures of EMI$^+$ and TFSI$^-$ with the ion sizes corrected by using HyperChem. It was concluded that the maximum EDL capacitance could be achieved when the pore size of CDCs was very close to the ion size, suggesting that the ions entering sub nanometre pores would greatly promote the capacitance of EDLCs (Largeot et al., 2008). The mechanism of this enhancement was further studied in a molecular dynamic simulation of an IL, 1-butyl-3-methylimidazolium hexafluorophosphate (BMI-PF$_6$), which was adsorbed inside the realistically modeled CDC electrodes (Merlet et al., 2012). The simulation showed the separated cations and anions inside the porous disordered carbons can yield a much higher capacitance than the ones with simple electrode geometries. A 3 V MCV was reached in the tests of these EDLCs and the specific capacitance reached 165 F g^{-1} (Largeot et al., 2008) and 125 F g^{-1} (Merlet et al., 2012) in EMI-TFSI and BMI-PF$_6$, respectively.

It should be mentioned that the normalized capacitance in **Figure 1** was calculated based on the specific capacitance and area of the CDCs. However, the area data were derived from the Brunauer-Emmet-Teller (BET) analysis (Largeot et al., 2008). IUPAC recommends the Non-Local Density Functional Theory (NLDFT) method for calculating the total surface area of microporous materials (Rouquerol et al., 1994) because this area is underestimated by using the

TABLE 1 | Summary of pairing the electrode materials of different charge storage mechanisms[*] into supercapacitor, supercapattery, supercabattery, and battery, and the performance metrics of the representative cells using different electrolytes (Yu and Chen, 2016b).

Device	Supercapattery							Battery
	Supercapacitor			Hybrid				Battery
	EDLC	Pseudocapacitor		Capacitive Hybrid		Others (Supercabattery)		
Electrode Material	NFCS	NFCS	CFS	NFCS	CFS	NFCS	CFS	NCFS
	+	+	+	+	+	+	+	+
	NFCS	CFS	CFS	NCFS	NCFS	NCFS	NCFS	NCFS
Specific energy (Wh kg^{-1})	102 (IL), 6.7 (aq.)	3.6	26.6	230	261	–	208.6	250
Max specific power (kW kg^{-1})	111.6	24.7	13	59	25	–	3	1.5
Cycling life (cycles)	>10,000	>5,000	>5,000	>1,000	>10,000	–	>1,000	<1,200
Electrolyte type	IL, aq.	aq.	aq.	IL	IL	–	organic	organic
References	Lewandowski et al., 2010; Hou et al., 2015	Zhou et al., 2012	Huang et al., 2015	Zhang F. et al., 2013; Zhang L. et al., 2013; Yu and Chen, 2016a	Ortaboy et al., 2017	–	Zhou et al., 2016	**

*NFCS, Non-Faradaic Capacitive Storage = Electrical Double Layer Capacitance) Storage; CFS, Capacitive Faradaic Storage = Pseudocapacitive Storage; NCFS, Non-Capacitive Faradaic Storage = Battery-Type Storage; ** data from web: https://en.wikipedia.org/wiki/Lithium-ion_battery#cite_note- 7. The colors represent different charge storage mechanisms and relevant devices.

FIGURE 1 | Specific area normalized capacitance changes *vs* the pore size of the carbide derived carbon (CDC) samples in ref (Largeot et al., 2008). (Reprinted with permission from American Chemical Society. Copyright 2008).

BET method (Centeno and Stoeckli, 2010). The anomalous increase of the normalized capacitance below 1 nm pore size shown in **Figure 1** was criticized afterwards by the other researchers who tested the different porous carbon materials in an organic electrolyte, tetraethylammonium tetrafluoroborate (TEA-BF$_4$) in acetonitrile (AN) (Centeno et al., 2011). It was found that the surface-normalized capacitance of the different carbon samples is fairly constant from 0.7 to 15 nm pore size if the specific area was calculated by the NLDFT approach. Similar constant surface-normalized capacitance was found in a study of activated carbons (Act-Cs) in an organic electrolyte (Feng et al., 2010). Later,

the NLDFT method has been always used when calculating the specific area of microporous carbons (Centeno and Stoeckli, 2011; Feng and Cummings, 2011; Hsieh et al., 2015; Galhena et al., 2016).

Carbon nanotubes (CNTs) are another important type of carbon used in EDLC. Specifically, the vertically aligned CNTs (ACNTs) was used to further improve the rate capability and the MCV of EDLCs in IL electrolytes. The specific capacitance of ACNTs in an IL electrolyte, EMI-TFSI, was found to be 24 F g^{-1}, which was lower than expected and approximate to the one of raw CNTs (Lu et al., 2009). However, the ACNTs after oxygen plasma etching presented a dramatically increased specific capacitance, up to 440 F g^{-1}. These highly capacitive ACNTs were used as the electrode materials and EMI-TFSI was the electrolyte. The resultant supercapacitor has high cell voltage (up to 4 V), energy capacity (up to 148 Wh kg^{-1}), and power capability (315 kW kg^{-1}) (Lu et al., 2009). For comparison, Act-Cs were used as the reference materials in this work. Cyclic Voltammograms (CVs) of the ACNT and Act-C electrodes in the EMI-TFSI electrolyte were collected at different scan rates as shown in **Figure 2**. The MCV, energy capacity and power capability of this symmetrical supercapacitor are very promising even nowadays. It was noticed that the specific capacitance of ACNTs doubled the theoretical one based on the specific surface area, indicating there is another charge storage mechanism. Meanwhile, the ability of charge accumulation at the electrode | electrolyte interface strongly depends on the mesoporosity, pore size, and surface nature of CNTs and the accessibility of electrolyte. It was believed that the high capacitance in this IL should be related to the unique
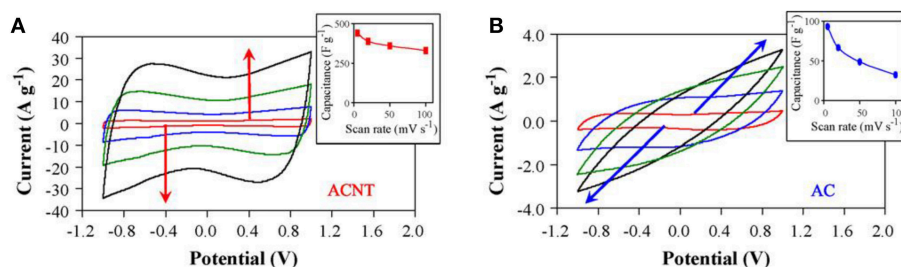
FIGURE 2 | CVs obtained in EMI-TFSI for an ACNT electrode **(A)** and an Act-C electrode **(B)** at the scan rate increasing from 5, 20, 50, to 100mV s^{-1} as indicated by arrows. Insets show capacitance change of the electrodes upon increasing the scan rate (Lu et al., 2009). (Reprinted with permission from Elsevier. Copyright 2008).
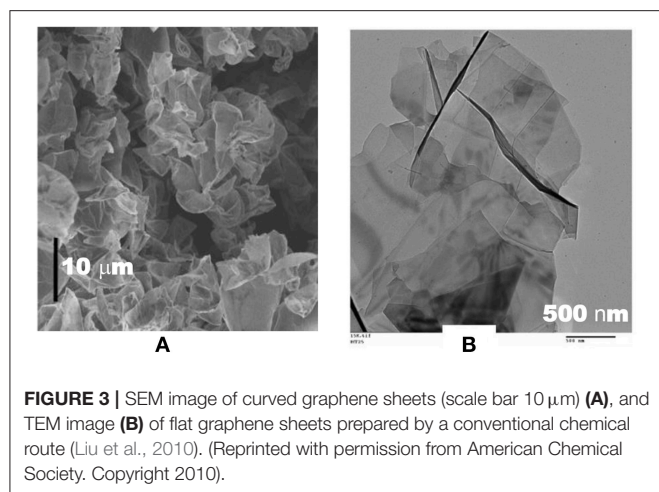
property of the plasma etched ACNTs. Pseudocapacitance can explain this phenomenon.

Graphene possesses exceptionally a high specific surface area up to 2,675 m^2 g^{-1}. Like CNTs, graphene and its derivatives have attracted a great attention of the EDLC community. ILs have been used in the graphene based EDLCs to achieve high energy capacity. However, the reported specific energy of the graphene samples varies from one to another. Before explaining these phenomena, an important question should be raised that if the exceptionally large specific surface area of graphene has been fully utilized for the capacitance charge storage. For example, the specific capacitance of the curved graphene samples fell in the range of 10 to 250 F g^{-1} at 1 A g^{-1} in the EMI-BF$_4$ electrolyte (Liu et al., 2010). It was explained that the morphology difference between the curved graphene sheets and the other conventional graphene sheets as shown in **Figure 3** leads to the different specific capacitance, which ranges from 250 F g^{-1} to <10 F g^{-1} in the same IL electrolyte. **Figure 3A** shows a representative scanning electron microscopy (SEM) image of the curved graphene sheets, exhibiting a morphology that is favorable for preventing the graphene sheets from closely restacking with one another when they are packed or compressed into an electrode. In contrast, **Figure 3B** presents a typical transmission electron microscopy (TEM) image of the graphene sheets that were prepared by a conventional chemical route. The inter-graphene spacing is likely <1 nm as observed from **Figure 3B**. The TEM image also indicates that the flat graphene sheets tend to restack with one another, leading to a decrease of the effective surface area. A supercapacitor using the curved graphene sheets as the electrode materials and EMI-BF$_4$ as the electrolyte exhibited a specific energy of 85.6 Wh kg^{-1} at 1 A g^{-1} at room temperature, and 136 Wh kg^{-1} at 80°C (Liu et al., 2010). It should be mentioned that the curved graphene sample shown in **Figure 3** is actually a kind of reduced graphene oxide (r-GO) that contains many defects and oxygen containing groups (OCGs) on the surface. Perfect graphene in principle can only be prepared by a physical method and it is mostly favored by physicists. In most studies, the graphene-based materials consist of r-GOs that could be obtained from either the partial oxidation of graphene or, in the majority cases, the partial reduction of graphene oxide (GO). In the early studies, graphene and r-GO were used interchangeably by researchers, especially by chemists.

Nowadays, r-GO is the preferred term if the sample is synthesized by the reduction of GO.

The study of the capacitance behavior of r-GO in ILs is still on-going. For example, GO could be partially reduced by a weak reductant, like HBr, to produce r-GO which has a maximum specific capacitance of 158 F g^{-1} at 0.2 A g^{-1} in BMI-PF$_6$ (Chen et al., 2011). There are still some OCGs in such r-GO sample. The OCGs offer an affinity between r-GOs and water and hence enable the r-GO to disperse well in water. The lateral dimension of the thinnest r-GO sheet containing 2-3 graphene layers was found to be about 150–250 nm. Thus, the corrugation and scrolling may exist simultaneously on the r-GO sheets. This r-GO material was capable of a better capacitive performance in the aqueous electrolyte than BMI-PF$_6$. The specific capacitance of r-GO at the same specific current reached to 348 and 158 F g^{-1} in aqueous and BMI-PF$_6$ electrolytes, respectively. However, in a recent study of the thick r-GO supercapacitor electrodes, the supercapacitor using the BMI-BF$_4$ electrolyte exhibited a better capacitive performance than the one using an aqueous electrolyte because the pores of the r-GO sample were precisely modified to accommodate the ions of the IL (Li et al., 2016). From the examples above, it can be noticed that the accessibility of IL electrolytes to the r-GO surface can greatly affect the capacitive performance of r-GO materials. Some more efforts have been made to increase the effective porosity and the accessibility of IL electrolytes by adding CNTs as spacers (Cheng et al., 2011; Lin et al., 2013; Pham et al., 2015) or using a special treatment (Yu et al., 2016b).

It is believed that the interposed CNTs in the inter-graphene spacing can prevent the graphene sheets to restack with one another. Researchers found that there was always an increase of specific capacitance of the CNT/r-GO composite (which is actually a hybrid material) after long time charging-discharging cycling (Cheng et al., 2011). They called this phenomenon electro-activation. The electro-activation occurs because the repeated charging-discharging cycling could help ions intercalate into the graphene layers where the electrolyte cannot fully access originally. After cycling, the inner-graphene spacing may be enlarged by the intercalation and the enlarged spacing can provide a larger effective surface area for capacitance. For the same CNT/r-GO composite, the specific capacitance can be increased by 18% after a long time cycling in an

FIGURE 3 | SEM image of curved graphene sheets (scale bar 10 μm) **(A)**, and TEM image **(B)** of flat graphene sheets prepared by a conventional chemical route (Liu et al., 2010). (Reprinted with permission from American Chemical Society. Copyright 2010).

aqueous electrolyte, whilst the increasement was found to be 29% in the EMI-TFSI electrolyte (Cheng et al., 2011). Meanwhile, a supercapacitor using the CNT/r-GO composite electrodes and the EMI-TFSI electrolyte reached a specific energy of 155.6 Wh kg^{-1}, which was very high when the result was published. In addition, the 3D structures of such CNT/r-GO composites do not only help increase the energy capacity, but also increase the power capability. In a recently published paper, it was claimed that a supercapacitor comprising two 3D CNT/r-GO (called CNT/graphene in original paper) composite electrodes and the EMI-BF$_4$ electrolyte exhibited an outstanding capacitive performance. The maximum energy density of the cell reached 117.2 Wh L^{-1} (110.6 Wh kg^{-1} for specific energy) at the maximum power density of 424 kW L^{-1} (400 kW kg^{-1} for specific power) based on the active materials (Pham et al., 2015).

In addition to CNTs and r-GOs, the other porous carbon materials also play an important role in supercapacitors. High surface Act-Cs are the predominant electrode materials in the commercial supercapacitors because they are easy to produce. The Act-Cs produced by pyrolyzing polypyrrole has a specific capacitance up to 300 F g^{-1} in the EMI-BF$_4$ electrolyte and, more interestingly, 5–8% of the performance improvement was achieved after 10,000 charging-discharging cycles at a high specific current of 10 A g^{-1} (Wei et al., 2012) (Note that in this and some other literatures, the unit of A g^{-1} was often incorrectly linked with current density, which should be corrected as specific current). When ILs were used as the electrolytes in supercapacitors, the pore and ion sizes and the accessibility of the IL ions to the surface of Act-Cs must be considered. The changes of microstructure were considered during the synthesis of the Act-Cs. It was concluded that the optimal pore size should be perfectly adapted to the size of ions for efficient adsorption, whilst larger or smaller pores would reduce the gravimetric capacitance (i.e., specific capacitance). Another work indicated that the sub-nanometre pores may slow down the ion diffusion rate and they didn't contribute the capacitance in the EDLCs using IL electrolytes (Largeot et al., 2008).

In fact, the precursors of Act-Cs are not limited to the artificial polymers, like polypyrrole mentioned above, various biomasses can be used to prepare the high-value Act-C materials. For example, natural silk was used to produce hierarchical porous nitrogen-doped carbon nanosheets through a one-step and facile large-scale synthesis route using ZnCl$_2$ and FeCl$_3$ as the effective activation-graphitization agents. The nanosheets exhibited a specific capacitance of 242 F g^{-1}, an energy density of 48 Wh L^{-1} (102 Wh kg^{-1} for specific energy), and a capacity retention of 81% after 10,000 cycles in the EMI-BF$_4$ electrolyte (Hou et al., 2015). The biomass algae, Enteromorpha, was used to synthesize nitrogen and oxygen co-doped hierarchical porous carbons (Yu et al., 2016a), which possessed a sponge-like 3D interconnected structure with combined macro-/meso-/micro-pores. The specific surface area of the carbons was estimated up to 2,073 m^2 g^{-1}. The supercapacitor comprising two sponge-like carbon electrodes and the EMI-BF$_4$ electrolyte exhibited a specific capacitance of 201 F g^{-1} at 1 A g^{-1} at 20°C. Rice straws were also used to produce the porous carbons as supercapacitor electrode materials (Sudhan et al., 2017). Although the capacitive performance of these carbons in EMI-BF$_4$ was not outstanding, this study proposed a feasible process dealing with the excess rice straws, which are the most common biowaste materials from different agriculture sectors. The porous carbons made from bamboo exhibited a remarkable specific capacitance of 192 F g^{-1} at 100 A g^{-1} whilst the corresponding EES device using an aqueous electrolyte only had a specific energy of 6.1 Wh kg^{-1} under the specific power of 26 kW kg^{-1} based on the active materials (Tian et al., 2015). However, when the aqueous electrolyte was replaced by an IL, EMI-TFSI, the energy capacity and power capability of the supercapacitor consisting of the same carbon electrodes were enhanced and the specific energy and power reached 43.3 Wh kg^{-1} and 42 kW kg^{-1}, respectively.

Based on the examples given above, there are several keynotes for using IL electrolytes in supercapacitors: (1) a wider operating voltage range leading to a higher MCV, up to 4.5 V; (2) a possible increase of specific capacitance due to the controversial hypothesis of the accessibility of ILs to the porous carbons; (3) the carbon morphology, especially the macro/meso/microporous structure, affects the capacitive behavior significantly. Obviously, it must be noted that in addition to porous carbon materials, the other materials with similar macro/meso/microporous structure can also be used as the supercapacitor electrode materials. 2D microporous covalent triazine-based frameworks showed a great potential in IL-based supercapacitors, and the rational design of electrode structures *via* bottom-up strategies could help further understand the capacitive EES mechanisms as well as better design the capacitive EES devices (Hao et al., 2015). A highly porous diamond foam was introduced as a kind of promising electrode material for supercapacitors because of the unmatched potential windows of the boron-doped polycrystalline diamond in aqueous solutions (Gao et al., 2014) or ILs (Gao et al., 2015). The porous boron-doped polycrystalline diamond can grow on the silica or silicon substrates. Consequently, the silicon nanowires (SiNWs) with and without coating materials were used in on-chip supercapacitors where ILs were used as the electrolytes (Berton et al., 2014; Thissandier et al., 2014;

Aradilla et al., 2015a,b, 2016a,b; Gao et al., 2015; Gaboriau et al., 2017). These micro-power source devices with IL electrolytes had the high MCVs up to 4.0 V, which can hardly be reached when the traditional organic electrolytes were used (Thissandier et al., 2012). Furthermore, these micro-supercapacitors can be integrated into the miniaturized devices which have been highly demanded by the development of micro-electronics. Some more details on micro-supercapacitors will be discussed in the latter section.

In fact, the studies of the electric double layer capacitance mechanisms have been done in the EDLC models consisting of the different carbon materials and ILs. Different from the traditional EDLC model, an electric double-cylinder capacitor (EDCC) model for microporous carbon materials in organic electrolytes was proposed to take the pore curvature into account when the model was simulated by using a DFT method (Huang et al., 2008). The simulation results based on the EDCC model are consistent with the results obtained from the molecular dynamic simulations of the porous CNT electrodes in ILs, such as $EMI-BF_4$ (Shim and Kim, 2010) and EMI-TFSI (Ma et al., 2017). A further agreement between the experimental and simulation results was achieved when the realistic atomistic structure of micropores and the electrode atomic polarization caused by ionic charges were considered in a simulation work based on the model of CDCs in $BMI-PF_6$ (Merlet et al., 2012). Meanwhile, the instinct characteristics of ILs as electrolytes were also studied to improve the understanding of the ILs which are considered as the charged interfaces (Gebbie et al., 2013, 2015). Differential capacitance is directly related to the capacity of EDLCs. A simulation of the electrode | IL interface was done to correlate the change of differential capacitance with surface potential (Vatamanu et al., 2010; Ma et al., 2014). It was also found that small ions, like Li^+, in an IL solution will change the original ionic composition of the IL and construct different electrode | IL interfaces leading to a smaller differential capacitance compared with the one of the neat IL (Zhao et al., 2010).

IL-Mixture Electrolytes for Supercapacitors

ILs are liquid salts and they can be used alone as the electrolytes in supercapacitors. Meanwhile, they can also be used as the supporting electrolytes in solvent-based electrolytes. As supporting electrolytes, ILs have the same function as the other salts, providing cations and anions in the organic solutions mostly for the charge transport. Theoretical and experimental studies have been focused on the relationship between the specific capacitance of porous carbons and their pore size, especially the capacitance contribution from micropores (Largeot et al., 2008; Jiang et al., 2011; Griffin et al., 2015; Zhu et al., 2016). IL Solutions comprising AN or propylene carbonate (PC) were the typical electrolytes used in previous research. The activated graphene was found to be useful for the EES devices and exhibited a specific capacitance of 200 F g^{-1} at 0.7 A g^{-1} in BMI-TFSI and 166 F g^{-1} at 5.7 A g^{-1} in the BMI-TFSI/AN electrolyte (Zhu et al., 2011). Although the specific capacitance in BMI-TFSI was larger than that in the BMI-TFSI/AN electrolyte, the CVs of the graphene in BMI-TFSI were distorted from the

rectangular shape whilst the ones in the ILs/AN electrolytes were still rectangular. It was suggested that the large ion size of the ILs caused the high viscosity and large charge transfer resistance of the electrolytes, leading to the distorted CVs. Similar findings were also reported about the activated graphene in the EMI-TFSI/AN electrolyte (Kim et al., 2013; Zhang F. et al., 2013; Zhang L. et al., 2013) and the graphene sheets-cotton cloth composite in the $EMI-BF_4$/AN electrolyte (Liu et al., 2012). A micro-supercapacitor made of graphene quantum dots exhibited a higher frequency response in the $EMI-BF_4$/AN electrolyte in comparison with the ones in aqueous electrolytes (Liu et al., 2013).

It is perceived the IL-solvent mixtures keep a wider operational voltage range and a higher ionic conductivity compared to the neat ILs. Thus, they are the good candidates for the electrolytes of supercapacitors. However, the liquid temperature ranges of these mixtures are narrower than the ones of the corresponding ILs due to the existence the traditional solvent (Ruiz et al., 2012). It is necessary to identify the temperature limits before an IL-solvent mixture is utilized as the electrolyte of capacitive EES devises. In addition to the temperature range issue, the risk from the flammable organic solvent is also a challenge to the further applications of IL-solvent mixture.

The IL-mixture electrolytes are not limited to the mixtures of ILs and molecular solvents. A eutectic mixture of ILs can dramatically decrease the melting point or show no melting point but a glass transition. For example, N-propyl-N-methylpiperidinium bis(fluorosulfonyl)imide (PMPip-FSI) and N-butyl-N-methylpyrrolidinium bis(fluorosulfonyl)imide (BMPyrr-FSI) were mixed at the 1:1 wt. ratio to make a eutectic mixture, which was used as the electrolyte in supercapacitors (Tsai et al., 2013). The eutectic IL electrolyte keeps liquid in the investigated temperature range from −50 to 80 °C. When the temperature was increased from room temperature to 80°C, a supercapacitor comprising two activated graphene electrodes and the eutectic IL electrolyte exhibited a increasing specific capacitance up to 180 F g^{-1} but a decreasing MCV from 3.5 to 2.8 V.

In supercapacitors, ILs can also contribute to the energy capacity of capacitive EES devices. A recent report about the biredox ILs presented a good example. BMI-TFSI was mixed with a biredox IL, which comprises a perfluorosulfonate anion bearing anthraquinone (AQ-PFS$^-$) and a methyl imidazolium cation bearing 2,2,6,6-tetramethylpiperidinyl-1-oxyl (TEMPO$^{\bullet}$-MI$^+$) (Mourad et al., 2017). This IL mixture was used as a supercapacitor electrolyte. **Figure 4** shows the molecular structures of the ILs. When the supercapacitor was charging, the cations and anions of BMI-TFSI were drawn into the negatrode and positrode, respectively, and they were adsorbed on the carbon surface without invoking any Faradaic reaction. In contrast, when the redox-active AQ-PFS$^-$ and TEMPO$^{\bullet}$-MI$^+$ were electro-adsorbed on the surface of the carbon electrodes, they underwent fast faradaic reactions. It is perceived that a dissolved redox species in electrolytes can result in a serious self-discharging problem in EES devices, especially supercapacitors.
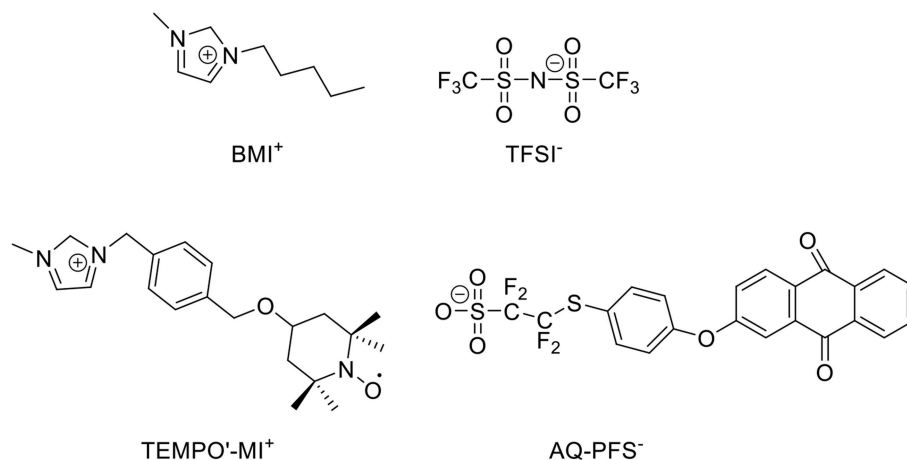
FIGURE 4 | Structure of BMI-TFSI and the biredox IL with anthraquinone and 2,2,6,6-tetramethylpiperidinyl-1-oxyl group (Mourad et al., 2017).

The mixture of the biredox IL and BMI-TFSI solved this problem because of their bulky size and high viscosity.

To study the biredox IL mixture in supercapacitor, Act-Cs (PICA) and r-GO were chosen as the electrode materials. **Figure 5** presents the CVs of the carbon-based supercapacitors with 0.5 mol L^{-1} biredox IL in BMI-TFSI and pure BMI-TFSI at 5 mV s^{-1}. PICA contained both micro- and mesopores, while r-GO offered an open surface with theoretically unrestricted access for the IL ions. In the CVs of the two carbons, the current amplitude doubled when the electrolyte was changed from BMI-TFSI to 0.5 mol L^{-1} biredox IL electrolyte. Broad oxidation and reduction peaks were observed at the intermediate voltages, indicating the redox processes of the biredox IL. In summary, the biredox IL was found to be able to increase the energy capacity of supercapacitors, by storing a significant amount of charge and retaining the redox species in the pores of electrodes. More detailed discussion about the contribution to energy capacity from the redox electrolytes can be found in the literature (Akinwolemiwa et al., 2015).

SUPERCAPATTERIES

The discussions above are mainly related to the IL-based electrolytes for supercapacitors, particularly EDLCs. Theoretically, there is no redox reaction involved in the charge storage of EDLCs. Thus, only the specific capacitance of electrode materials and the MCVs should be considered when calculating the specific energy of EDLCs. The IL-based electrolytes are favored in EDLCs because the MCVs is usually equal to the decomposition voltages of electrolytes and hence the wide operating potential windows of ILs are beneficial to the specific energy of EDLCs as we discussed in section Supercapacitors. The modified or doped materials were also used for supercapacitors and they had a higher specific capacitance than the un-modified or un-doped ones because of the redox activity induced by the modification or doping in the materials. Transition metal oxides (TMOs) and electronically conducting polymers (ECPs)

are another typical pseudocapacitance materials because of their redox nature. Although the specific capacitance of these pseudocapacitance materials are higher than the one of EDLCs, the potential ranges of these pseudocapacitance materials are usually narrower than 1.0 V. In this case, the symmetrical devices made of pseudocapacitance materials are not favorable for high energy capacity EES devices and the asymmetrical devices have been proposed to achieve high voltage. There are two main designs of asymmetrical devices. One is so called asymmetrical supercapacitors, which were first proposed and constructed by the positrode and negatrode capable of capacitive charge storage, typically the permutation and combination of the EDL and pseudocapacitance electrodes. The other design of asymmetrical devices is using a hybrid configuration that combines a supercapacitor electrode and a battery electrode into one device. Such hybrids have been reported under different names which are mainly corresponding to the different electrode materials. The word hybrid is obviously not a suitable unified expression for the future development of these asymmetrical devices as it is too abstract whilst supercapattery or supercabattery can be a general term to represent these asymmetrical devices vividly. In general, supercapattery takes advantages of the Faradaic charge storages typically the non-capacitive Faradaic store. Thus, pseudocapacitors fall in the scope of supercapatteries in a broad sense. More often, the battery-type storage should be involved in supercapatteries.

First, we hypothesized a supercapattery with a negatrode of lithium (Li) metal and a positrode of Act-Cs and then predicted the behavior of the electrodes and the cell as shown by the galvanostatic charging and discharging (GCD) plots in **Figure 6A**. The behavior of the cell is highly capacitive and hence Equation (1) is still valid to calculate the energy capacity of the hypothetic cell. The minimum potential of the Act-C electrode was set to 0.5 V *vs.* Li/Li$^+$ to prevent the lithiation of the Act-C electrode during discharge.

The balance of the electrode masses or charges is important for all the EES devices. The charges passed through the positrode
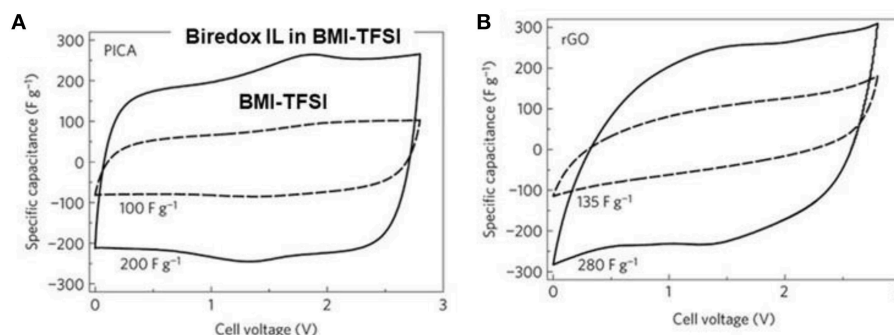
FIGURE 5 | CVs of supercapacitors made of PICA (Act-Cs) **(A)** and r-GO **(B)** at 5 mV s^{-1} with 0.5 mol L^{-1} biredox IL in BMI-TFSI (solid line) and pure BMI-TFSI (dash line), respectively (Mourad et al., 2017). (Reprinted with permission from Springer Nature. Copyright 2016).
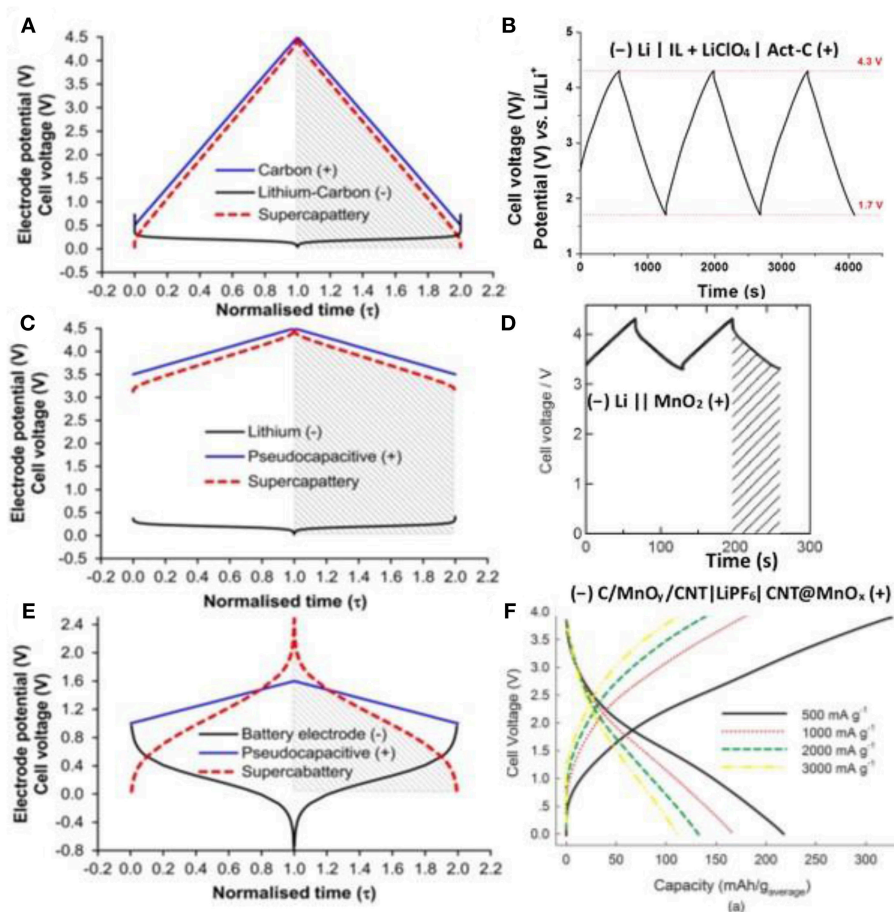

FIGURE 6 | Calculated electrode potential (black and blue lines for negatrode and positrode) and cell voltage (red dashed lines) as a function of normalized time for galvanostatic charging and discharging (GCD) of three types of hypothetical supercapattery and the GCD plots of the related experimental demonstration of supercapatteries. **(A)** a hypothetical supercapattery with a negatrode of lithium metal or lithiated carbon and a positive positrode of activated carbon; **(B)** an experimental demonstration of **(A)** (−) Li | IL + LiClO$_4$ | Act-C (+) (Yu and Chen, 2016a); **(C)** a hypothetical supercapattery with a negatrode of lithium metal or lithiated carbon and a pseudocapacitive positrode; **(D)** an experimental demonstration of **(C)** (−) Li | PEO-LiTFSI | LTAP | 1.0 M LiCl aq. | MnO$_2$ (+) (Makino et al., 2012) (Reprinted with permission from the Royal Society of Chemistry. Copy right 2012); **(E)** a hypothetical supercapattery with a negatrode of the typical battery type and a pseudocapacitive positrode; and **(F)** an experimental demonstration of **(E)** (−) C/MnO$_y$/CNT | LiPF6 | CNT@MnO$_x$ (+) (Zhou et al., 2016) (Reprinted with permission from the Electrochemical Society. Copyright 2016). **(A)**, **(C)** and **(E)** are adapted from the reference (Chen, 2017).

and negatrode in a supercapattery must be the same. In this case the masses of the positrode and negatrode were fixed according to the charges passed through as demonstrated in Equation (2).

$$Q_- = m_- Q_{sp-} = m_+ C_{sp+} \Delta E_+ = Q_+ \qquad (2)$$

where Q represents the charge, m the mass of the electrode, C_{sp} the specific capacitance of the electrode, ΔE the potential range, and the subscript $_+$ and $_-$ the positrode and negatrode, respectively. In the case of the lithium metal negatrode described in **Figure 6A**, $Q_{sp,Li} = nF/M_{Li} = 13900$ C g^{-1} = 3861 mAh g^{-1}, where $n = 1$, $F = 96485$ C mol^{-1}, and $M_{Li} = 6.941$ g mol^{-1}. As to the Act-C positrode, we hypothesis $C_{sp,C} = 200$ F g^{-1} and $\Delta E = 4.0$ V. After rearranging Equation (2) and filling in all the data above, we calculated the mass ratio of the positrode and negatrode, $m_C/m_{Li} = Q_{sp,Li}/C_{sp,C}\Delta E = \frac{13900}{200 \times 4.0} = 17.4$. When the total mass of this supercapattery was evaluated, the mass of the lithium metal negatrode was negligible compared to that of the Act-C positrode. In this case, the capacitance of the cell is equal to the one of the Act-C positrode approximately. Because the minimum potential of the Act-C electrode was set to 0.5 V *vs.* Li/Li$^+$, instead of zero, Equation (1) must be modified to Equation (3).

$$W_{\max} = \frac{1}{2}C(U_{\max}^2 - U_{\min}^2) \qquad (3)$$

Taking $C \approx C_{sp,C} = 200$ F g^{-1}, $U_{\max} = 4.5$ V and $U_{\min} = 0.5$ V into Equation (3), we calculated the specific energy of the hypothetic cell that $W_{\max} = 555.6$ Wh kg^{-1}.

On the experimental side, a supercapattery consisting of an Act-C positrode, a Li/Li$^+$ negatrode, and an IL electrolyte of 1-butyl-1-methylpyrrolidinium tri(pentafluoroethyl)trifluorophosphate (BMPyrrFAP) with dissolved gamma-butyrolactone (γ-GBL) and LiClO$_4$ was successfully demonstrated. The IL solution did not only provide cations and anions for non-Faradaic capacitive storage at the Act-C surface, but also enable the Li/Li$^+$ redox reaction on the negatrode for non-capacitive Faradaic or Nernstian storage. The GCD plot of this supercapattery is shown in **Figure 6B**, demonstrating a typical capacitive charging and discharging feature. The specific energy of the supercapattery reached 230 Wh kg^{-1} at a GCD current density of 1 mA cm^{-2} (based on active materials), which was the highest record for supercapatteries using Act-Cs as the electrode materials (Yu and Chen, 2016a).

When constructing the second hypothetic supercapattery as shown by the GCD plots in **Figure 6C**, we replaced the EDLC positrode by a pseudocapacitive electrode whose specific capacitance is higher than EDLC e.g., $C_{sp} = 500$ F g^{-1}, whilst the potential range is narrower e.g. $\Delta E = 1.0$ V. The mass ratio of the positrode and negatrode is $m_C/m_{Li} = Q_{sp,Li}/C_{sp,C}\Delta E = \frac{13900}{500 \times 1.0} = 27.8$, which is also big enough to neglect the mass of the lithium metal negatrode when evaluating the energy capacity as we calculated above. Similarly, taking $C \approx C_{sp,C} = 500$ F g^{-1}, $U_{\max} = 4.5$ V and $U_{\min} = 3.5$ V into Equation (3), we calculated

the specific energy capacity of the second hypothetic cell that $W_{\max} = 555.6$ Wh kg^{-1}.

Some recent studies on the cell of $(-)$ Li | PEO-LiTFSI | LTAP | 1.0 mol L^{-1} LiCl (60 °C) | MnO$_2$ (+) (Makino et al., 2012), where PEO-LiTFSI is a buffer layer and LTAP is a solid electrolyte made of LISICON-type solid glass ceramic, presented the GCD plot as shown in **Figure 6D** which is very comparable with the calculated plot shown in **Figure 6C**.

The lithium metal electrode works reversibly at the most negative potential among all the battery electrode materials. In contrast, the sluggish GCD plots can be observed for most battery electrodes as demonstrated in **Figure 6E**. Similar to the second hypothetic supercapattery, a pseudocapacitance positrode and a battery negatrode was combined to fabricate the third hypothetic device. The battery negatrode in the third hypothetic device works at more positive potential and its GCD is more sluggish than the lithium metal negatrode. It can be observed from **Figure 6E** that the GCD plot of the third hypothetic device is not a straight line in either charging or discharging, and hence it does not represent a simple capacitive behavior. As a result, we had to integrate the
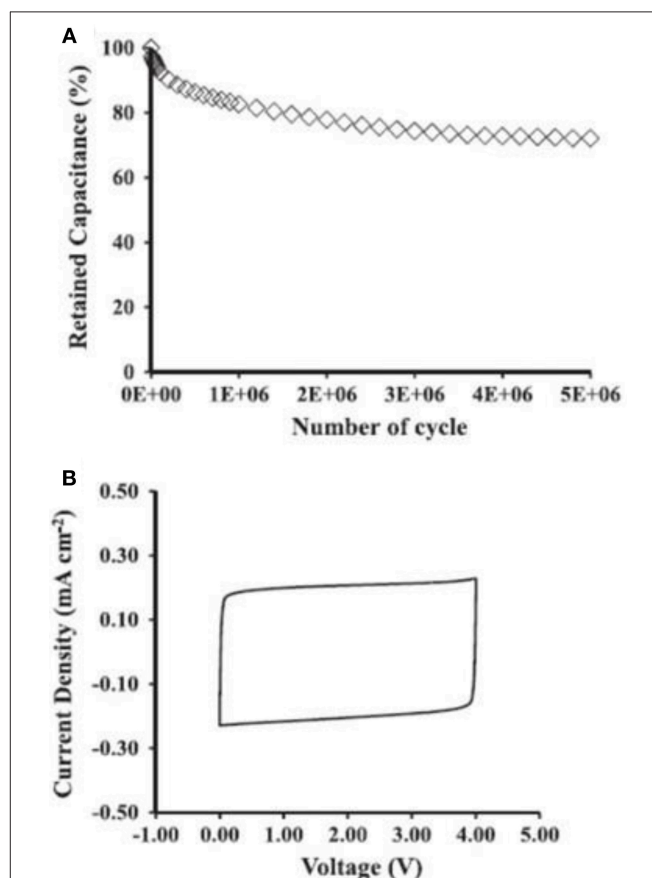
FIGURE 7 | Performance of the SiNWs micro-supercapacitors: **(A)** plots of capacitance retention ratio against the complete GCD cycles at 2 mA cm^{-2} between 0 and 4 V. **(B)** CVs after the GCD test at 20 V s^{-1} between 0 and 4 V (Aradilla et al., 2015b). (Reprinted with permission from Aradilla et al. (2015b) under the terms of the Creative Commons Attribution 3.0 license).
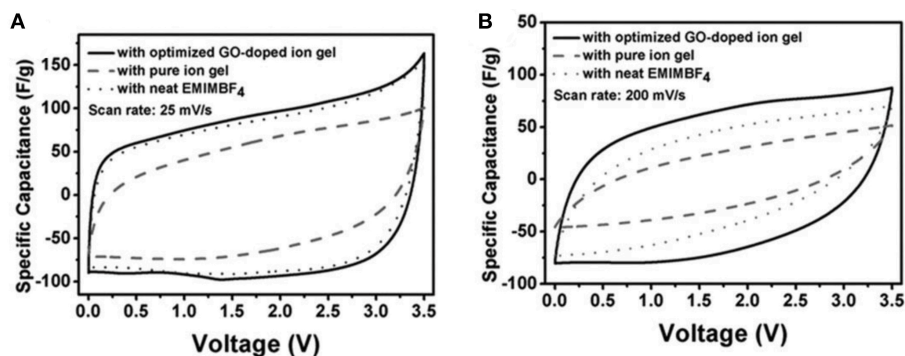
FIGURE 8 | Comparison of CVs from all-solid-state supercapacitors with GO-doped ion gel and pure ion gel, and conventional supercapacitor with neat EMI-BF$_4$ at a scan rate of 25 mV s^{-1} **(A)** and 200 mV s^{-1} **(B)**, respectively (Yang et al., 2013). (Reprinted with permission from John Wiley and Sons. Copyright 2013).

GCD of the cell to evaluate the cell energy capacity, instead of using Equation (3). The shadows shown in **Figure 6E** cover the area under the discharging branch of the GCD plot and the shadow area is proportional to the energy capacity of the cell. We can notice that the behavior of the cell is more like a battery and supercabattery is a more proper term for the cell.

The GCD plot of a typical example of supercabattery is shown in **Figure 6F**. ACNT@MnO$_x$ was synthesized by the reaction of ACNTs and KMnO$_4$ and the composite was used as the positrode material demonstrating a capacitive behavior in the supercabattery. ACNT@MnO$_x$ was further coated by the carbons using CVD in C$_2$H$_2$ atmosphere to produce C/MnO$_y$/ACNT, which was used as the negatrode materials in the supercabattery. The supercabattery reached a specific energy up to 208.6 Wh kg^{-1} and remained 105.8 Wh kg^{-1} under an ultrahigh specific power of 3,000 W kg^{-1} (Zhou et al., 2016).

According to the discussion above, the concept of supercapattery can easily clarify the Faradaic storage in the specified capacitive EES devices. For now, the expression of supercapacitor or hybrid device can be easily found from the literatures for the capacitive EES devices possessing Faradaic charge storage (Lukatskaya et al., 2016; Chen, 2017). Supercapattery is gradually accept by the EES community (Chen, 2017), and the number of the papers on supercapattery increased exponentially in the past 5 years. However, the aqueous or organic electrolytes were still used for the most reported supercapattery demonstrations and the typical examples of supercapattery using IL electrolytes are still rare. Consequently, only one supercapattery demonstration using the lithium metal negatrode, Act-C positrode and IL-based electrolyte was exemplified in **Figure 6B**. Another two experimental devices as exemplified in **Figures 6D,F** were based on the aqueous/solid hybrid electrolyte and organic electrolyte, respectively.

In the example of **Figure 6B**, the IL-mixture electrolyte does not only supply the Li$^+$ for the redox reaction related to the Faradaic charge storage, but also possess lower viscosity than the neat IL. This strategy was also applied in another reported supercapattery using EMI-TFSI/AN as the IL-mixture electrolyte (Ortaboy et al., 2017). In this study,
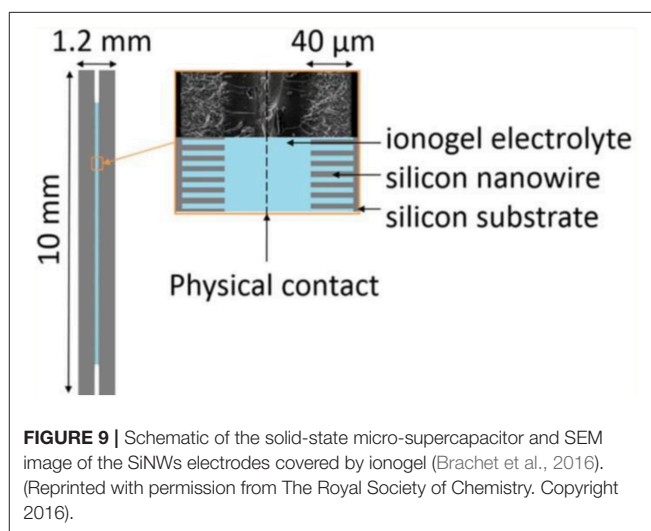
FIGURE 9 | Schematic of the solid-state micro-supercapacitor and SEM image of the SiNWs electrodes covered by ionogel (Brachet et al., 2016). (Reprinted with permission from The Royal Society of Chemistry. Copyright 2016).

manganese oxide-decorated carbonized porous silicon nanowire (MnO$_x$/C/PSiNWs) arrays were used as the Faradaic storage positrode materials, while PSiNWs as the EDL negatrode materials. The supercapattery (described as hybrid in the published paper) exhibited an excellent specific power of 25 kW kg^{-1} and specific energy of 261 Wh kg^{-1} at a current density of 0.2 mA cm^{-2} within 3.6 V. The capacity retention of the device kept higher than 80% after 10,000 CV cycles. It is a promising result, whilst the challenge of these electrolytes remains that there is still a volatile organic solvent in the electrolyte.

It should be mentioned that the Faradaic charge storage can also be obtained by dissolving a redox component in the electrolytes of a supercapacitor, typically EDLC as mentioned in section IL-Mixture Electrolytes for Supercapacitors. A cell using the biredox IL electrolyte demonstrated an increase of the energy capacity by adding the redox IL in another IL as shown in **Figure 5**. Because both Faradaic charge storage and EDL storage are exist in one device, this cell is also a special type of supercapattery.
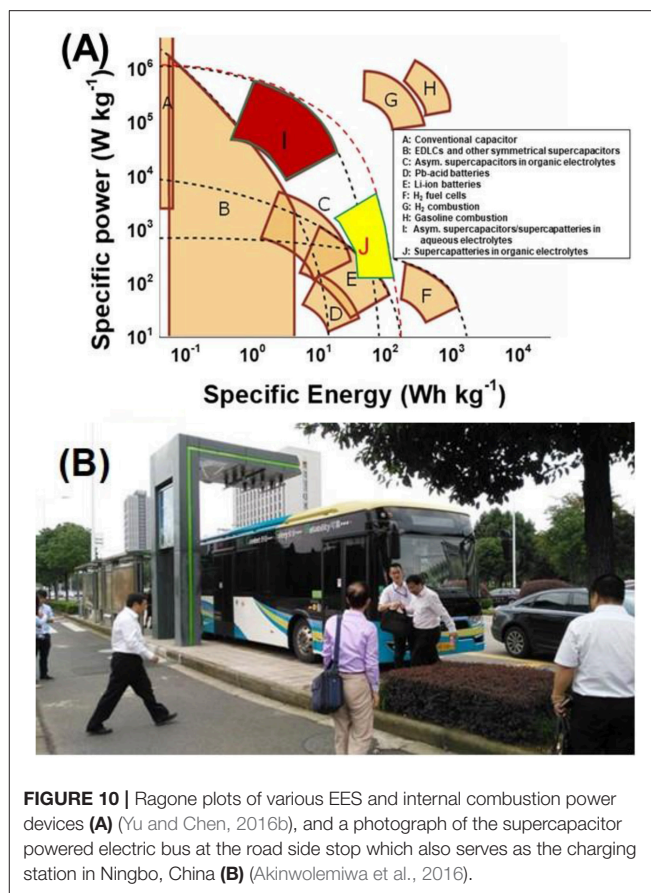
MICRO-SUPERCAPACITORS

Micro-supercapacitors fall in the scope of supercapacitors and supercapatteries in terms of the charge storage mechanism and the choices of electrode materials and electrolytes. The energy capacity and power capability of these miniaturized EES devices do not only depend on the choices of materials but also the topology or configuration of the devices. In general, a supercapacitor or supercapattery has a sandwich structure, whilst a micro-supercapacitor is a miniaturized EES device standing on a substrate of several square millimeters. As discussed in the previous section, the energy capacity and power capability of supercapacitors or supercapatteries are generally evaluated by the relevant gravimetric values. This strategy is not very useful for micro-supercapacitor because these small size devices are surface dependent. The areal metrics are more popular for micro-supercapacitors. Quite a lot of supercapacitor electrode materials have been utilized in micro-supercapacitors. Although it is a challenge to fabricate the electrode materials on a substrate of tiny area, the main technological barrier restraining the transfer of micro-supercapacitors from laboratory demonstration to pilot production is still the electrolytes issue (Lethien et al., 2019).

The energy capacity is always the first consideration of supercapacitors, so do micro-supercapacitors. When ILs are used as the electrolytes in micro-supercapacitor, the MCV can be increased up to the decomposition voltages of ILs. **Figure 7** shows the performance of a micro-supercapacitor made of the SiNWs electrodes and an IL, triethylammonium bis(trifluoromethylsulfonyl)imide. The SiNWs are ~35 μm in length. It was found that the micro-supercapacitor only lost 27% of the original capacitance after 5×10^6 complete GCD cycles in a voltage range from 0 to 4.0 V as shown in **Figure 7A**. After the GCD, the micro-supercapacitor was further examined by cyclic voltammetry. The CVs kept rectangular as shown in **Figure 7B** demonstrating an outstanding stability of the micro-supercapacitor.

Micro-supercapacitors with IL electrolytes possess high energy capacity due to the wide operating voltage of ILs. In practice, these on-chip supercapacitors would be integrated in the miniaturized devices, especially the wearable and portable devices. Thus, all-solid-state micro power sources devices would be favorable.

All-solid-state EES devices are gradually attracting attentions from both academia and industry, because they do not require high standard safety encapsulation materials compared with the other EES devices using liquid electrolytes. Consequently, their geometric shape can be variable, which is favored by designers and customers. High conductive solid electrolytes are the most essential component in all-solid-state EES devices. At present, solid electrolytes based on pure oxides and polymers are still suffered by their low or ultralow ionic conductivity at room temperature.

Many efforts have been dedicated to gel polymer electrolytes (GPEs), where ions are conducted through a polymer matrix. In a reported all-solid-state flexible supercapacitor, bacterial nanocellulose, CNTs, and an IL, EMI-TFSI, were used to fabricate an IL-based GPE. The copolymer consisting of bacterial

FIGURE 10 | Ragone plots of various EES and internal combustion power devices **(A)** (Yu and Chen, 2016b), and a photograph of the supercapacitor powered electric bus at the road side stop which also serves as the charging station in Ningbo, China **(B)** (Akinwolemiwa et al., 2016).

nanocellulose and CNTs was used to make the electrodes. The specific capacitance was estimated up to 50 F g^{-1} based on the CVs of the all-solid-state flexible supercapacitor (Kang et al., 2012). In another work, GO was regarded as an ionic conduction promoter for the GPE made of EMI-BF$_4$ and poly(vinylidene fluoride-hexafluoro propylene) [P(VDF-HFP)]. The demonstrated GO-doped GPE exhibited higher ionic conductivity than the pure GPE (Yang et al., 2013). The promoted ionic conductivity was attributed to the decrease of crystallinity in the GO-doped GPE compared with the pure GPE. This explanation was further proved by the differential scanning calorimetry data. It was also suggested that the degree of crystallinity in the GO-doped GPE should not be further reduced with more mass fraction of GO because a higher GO content was expected to deteriorate the ionic conductivity due to the restacking of GO sheets and the blocking effect by the excessive GO. **Figure 8** compares the CVs from these all-solid-state supercapacitors with the GPEs (indicated as ion gel in the figure) with and without GO, and the conventional supercapacitor using neat EMI-BF$_4$ at two scan rates. It was found that the CV from supercapacitor with GO-doped GPE was less distorted when the scan rate was increased, indicating the GO-doped GPE had lower internal resistance than the other two.

Ionogels resulted from a confinement of ILs in silica-like networks were also utilized as the solid electrolytes in

micro-supercapacitors. The scan rate of the CVs of micro-supercapacitors can reach 10 V s^{-1}, which demands a high ionic conductive electrolyte. An ionogel comprising an IL, EMI-TFSI, resisted a solder reflow which is an important process in the fabrication of micro-electronic devices (Brachet et al., 2016). **Figure 9** shows the schematics of a micro-supercapacitor and the SEM image of a SiNWs electrode covered by a layer of the ionogel electrolyte. The ionogel layer was fabricated on the top of the SiNWs as seen from the SEM image in **Figure 9**. In this case, there is no need to add a membrane separator or fill a liquid electrolyte in the micro-supercapacitor. It was found that the all-solid-state micro-supercapacitor consisted of the silicon nanowire electrodes and the ionogel electrolyte exhibited the same capacitive performance as the one using the IL electrolyte. The ionogel have been proofed to be applicable in various micro-supercapacitors made of different electrode materials, like CNTs (Hsia et al., 2014), photoresist-derived porous carbons (Wang et al., 2014), etc.

Ionogels are not limited to the silica networks as described above. The other nano-porous solids with large surface area and strong surface interaction to ILs can also be used as matrix materials, such as titanium oxide, alumina, CNTs, GO, etc. In all the EES devices, the non-conductive matrix materials are favorable in ionogels because the electronic conductive materials may cause some serious problems, like short-circuit and self-discharge . The ionic conductivity and stability of ionogels and the wettability between ionogels and electrode materials should also be considered in the choice of matrix materials and ILs.

PROSPECTS

In this review, we have introduced the recent progress on the capacitive EES devices from the perspective of IL electrolytes. The capacitive EES devices include supercapacitor, supercapattery and micro-supercapacitor (or EDLC, supercapattery and micro-supercapacitor from the view of charge storage mechanism) as described here and in the other reviews (Akinwolemiwa et al., 2015; Yu and Chen, 2016b; Chen, 2017; Xia et al., 2017). ILs have catered the trend for developing the high energy capacity EES devices. As described in the previous review on the redox electrode materials for supercapattery (Yu and Chen, 2016b) and shown in the Ragone plots of various electrochemical and internal combustion power devices from **(Figure 10A)**, EDLCs have remained advantageous in terms of power capability, although they are still fallen behind the other EES devices when the values of specific energy are considered. Supercapatteries including pseudocapacitors and capacitive EES hybrids using

aqueous electrolytes have also offered the high-power capability, while the organic electrolyte supercapatteries (block J in **Figure 10A**) are approaching the Li-ion batteries. The IL electrolytes have played an important role as a kind of organic electrolytes in this progress as introduced in this review. ILs containing large cations and anions may have some drawbacks when charge transport must be considered in some cases where high-power outputs are needed, while these drawbacks can be reasonably utilized to promote the energy capacity of capacitive EES devices, such as those supercapacitors using the biredox ILs. Supercapatteries using IL-based electrolytes are gradually becoming competitive compared with other EES devices when high-performance energy storage devices are strongly required nowadays. Following the continuous development in electrode materials for the capacitive EES devices, more and in-depth research efforts in the development of advanced electrolytes, especially those based on ILs, are needed to better understand the mechanism and kinetics of charge storage processes at the electrode | IL electrolyte interface for the technological advancement. The established market and public awareness can also stimulate the research on next generation of capacitive EES devices using IL electrolytes. On one hand, electric buses using supercapacitors (organic electrolytes) as the main power source have been serving the inner-city public transportation in Ningbo as shown in **Figure 10B** since 2015. On the other hand, the price for making and using ILs have been gradually reduced to an acceptable level along with the increasing demand from the global market. All progresses and efforts made from the research and industrial communities so far are promising a bright future for supercapacitor and supercapattery, and the fundamental research on IL-based electrolytes and the relevant technological innovation would be essential for the future development of supercapacitor and supercapattery.

AUTHOR CONTRIBUTIONS

All authors listed have made a substantial, direct and intellectual contribution to the work, and approved it for publication. GC supervised the work.

FUNDING

REFERENCES

Akinwolemiwa, B., and Chen, G. Z. (2018). Fundamental consideration for electrochemical engineering of supercapattery. *J. Braz. Chem. Soc.* 29, 960–972. doi: 10.21577/0103-5053.20180010

Akinwolemiwa, B., Peng, C., and Chen, G. Z. (2015). Redox electrolytes in supercapacitors. *J. Electrochem. Soc.* 162, A5054–A5059. doi: 10.1149/2.0111505jes

Akinwolemiwa, B., Yu, L., Hu, D., Jin, X., Slattery, J. M., and Chen, G. Z. (2016). Highlights from liquid salts for energy and materials - faraday discussion, Ningbo, China, 11-13 May 2016. *Chem. Commu.* 52, 12538–12554. doi: 10.1039/C6CC90442D

Aradilla, D., Gaboriau, D., Bidan, G., Gentile, P., Boniface, M., Dubal, D., et al. (2015a). An innovative 3-D nanoforest heterostructure made of polypyrrole coated silicon nanotrees for new high performance hybrid micro-supercapacitors. *J. Mater. Chem. A* 3, 13978–13985. doi: 10.1039/C5TA03435C

Aradilla, D., Gao, F., Lewes-Malandrakis, G., Muller-Sebert, W., Gaboriau, D., Gentile, P., et al. (2016a). A step forward into hierarchically nanostructured materials for high performance micro-supercapacitors: diamond-coated SiNW electrodes in protic ionic liquid electrolyte. *Electrochem. Commun.* 63, 34–38. doi: 10.1016/j.elecom.2015.12.008

Aradilla, D., Gao, F., Lewes-Malandrakis, G., Muller-Sebert, W., Gentile, P., Boniface, M., et al. (2016b). Designing 3D multihierarchical heteronanostructures for high-performance on-chip hybrid supercapacitors: poly(3,4-(ethylenedioxy)thiophene)-coated diamond/silicon nanowire electrodes in an aprotic ionic liquid. *ACS Appl. Mater. Interfaces* 8, 18069–18077. doi: 10.1021/acsami.6b04816

Aradilla, D., Gentile, P., Ruiz, V., Gomez-Romero, P., Wimberg, J., Iliev, B., et al. (2015). SiNWs-based electrochemical double layer micro-supercapacitors with wide voltage window (4V) and long cycling stability using a protic ionic liquid electrolyte. *Adv. Nat. Sci. Nanosci. Nanotechnol.* 6. doi: 10.1088/2043-6262/6/1/015004

Berton, N., Brachet, M., Thissandier, F., Le Bideau, J., Gentile, P., Bidan, G., et al. (2014). Wide-voltage-window silicon nanowire electrodes for micro-supercapacitors via electrochemical surface oxidation in ionic liquid electrolyte. *Electrochem. Commun.* 41, 31–34. doi: 10.1016/j.elecom.2014.01.010

Brachet, M., Gaboriau, D., Gentile, P., Fantini, S., Bidan, G., Sadki, S., et al. (2016). Solder-reflow resistant solid-state micro-supercapacitors based on ionogels. *J. Mater. Chem. A* 4, 11835–11843. doi: 10.1039/C6TA03142K

Centeno, T. A., Sereda, O., and Stoeckli, F. (2011). Capacitance in carbon pores of 0.7 to 15 nm: a regular pattern. *Phys. Chem. Chem. Phys.* 13, 12403–12406. doi: 10.1039/c1cp20748b

Centeno, T. A., and Stoeckli, F. (2010). The assessment of surface areas in porous carbons by two model-independent techniques, the DR equation and DFT. *Carbon* 48, 2478–2486. doi: 10.1016/j.carbon.2010.03.020

Centeno, T. A., and Stoeckli, F. (2011). Surface-related capacitance of microporous carbons in aqueous and organic electrolytes. *Electrochim. Acta* 56, 7334–7339. doi: 10.1016/j.electacta.2011.06.040

Chae, J. H., Zhou, X., and Chen, G. Z. (2012). From electrochemical capacitors to supercapatteries. *Green* 2, 41–54. doi: 10.1515/green-2011-0007

Chen, G. Z. (2013). Understanding supercapacitors based on nano-hybrid materials with interfacial conjugation. *Progress Nat. Sci. Mater. Int.* 23, 245–255. doi: 10.1016/j.pnsc.2013.04.001

Chen, G. Z. (2017). Supercapacitor and supercapattery as emerging electrochemical energy stores. *Int. Mater. Rev.* 62, 173–202. doi: 10.1080/09506608.2016.1240914

Chen, N., Zhang, H., Li, L., Chen, R., and Guo, S. (2018). Ionogel electrolytes for high-performance lithium batteries: a review. *Adv. Energy Mater.* 8:1702675. doi: 10.1002/aenm.201702675

Chen, Y., Zhang, X. O., Zhang, D. C., Yu, P., and Ma, Y. W. (2011). High performance supercapacitors based on reduced graphene oxide in aqueous and ionic liquid electrolytes. *Carbon* 49, 573–580. doi: 10.1016/j.carbon.2010.09.060

Cheng, Q., Tang, J., Ma, J., Zhang, H., Shinya, N., and Qin, L. C. (2011). Graphene and carbon nanotube composite electrodes for supercapacitors with ultra-high energy density. *Phys. Chem. Chem. Phys.* 13, 17615–17624. doi: 10.1039/c1cp21910c

Dutta, S., Bhaumik, A., and Wu, K. C. W. (2014). Hierarchically porous carbon derived from polymers and biomass: effect of interconnected pores on energy applications. *Energy Environ. Sci.* 7, 3574–3592. doi: 10.1039/C4EE01075B

Feng, G., and Cummings, P. T. (2011). Supercapacitor capacitance exhibits oscillatory behavior as a function of nanopore size. *J. Phys. Chem. Lett.* 2, 2859–2864. doi: 10.1021/jz201312e

Feng, Z., Xue, R., and Shao, X. (2010). Highly mesoporous carbonaceous material of activated carbon beads for electric double layer capacitor. *Electrochim. Acta* 55, 7334–7340. doi: 10.1016/j.electacta.2010.06.071

Gaboriau, D., Boniface, M., Valero, A., Aldakov, D., Brousse, T., Gentile, P., et al. (2017). Atomic layer deposition alumina-passivated silicon nanowires: probing the transition from electrochemical double-layer capacitor to electrolytic capacitor. *ACS Appl. Mater. Interfaces* 9, 13761–13769. doi: 10.1021/acsami.7b01574

Galhena, D. T. L., Bayer, B. C., Hofmann, S., and Amaratunga, G. A. J. (2016). Understanding capacitance variation in sub-nanometer pores by in situ tuning of interlayer constrictions. *ACS Nano* 10, 747–754. doi: 10.1021/acsnano.5b05819

Gao, F., Lewes-Malandrakis, G., Wolfer, M. T., Muller-Sebert, W., Gentile, P., Aradilla, D., et al. (2015). Diamond-coated silicon wires for supercapacitor applications in ionic liquids. *Diam. Relat. Mater.* 51, 1–6. doi: 10.1016/j.diamond.2014.10.009

Gao, F., Wolfer, M. T., and Nebel, C. E. (2014). Highly porous diamond foam as a thin-film micro-supercapacitor material. *Carbon* 80, 833–840. doi: 10.1016/j.carbon.2014.09.007

Gebbie, M. A., Dobbs, H. A., Valtiner, M., and Israelachvili, J. N. (2015). Long-range electrostatic screening in ionic liquids. *Proc. Natl. Acad. Sci. U.S.A.* 112, 7432–7437. doi: 10.1073/pnas.1508366112

Gebbie, M. A., Valtiner, M., Banquy, X., Fox, E. T., Henderson, W. A., and Israelachvili, J. N. (2013). Ionic liquids behave as dilute electrolyte solutions. *Proc. Natl. Acad. Sci. U.S.A.* 110, 9674–9679. doi: 10.1073/pnas.1307871110

Griffin, J. M., Forse, A. C., Tsai, W. Y., Taberna, P. L., Simon, P., and Grey, C. P. (2015). In situ NMR and electrochemical quartz crystal microbalance techniques reveal the structure of the electrical double layer in supercapacitors. *Nat. Mater.* 14, 812–820. doi: 10.1038/nmat4318

Guan, L., Yu, L., and Chen, G. Z. (2016). Capacitive and non-capacitive faradaic charge storage. *Electrochim. Acta* 206, 464–478. doi: 10.1016/j.electacta.2016.01.213

Hao, L., Ning, J., Luo, B., Wang, B., Zhang, Y. B., Tang, Z. H., et al. (2015). Structural evolution of 2D microporous covalent triazine-based framework toward the study of high-performance supercapacitors. *J. Am. Chem. Soc.* 137, 219–225. doi: 10.1021/ja508693y

Hou, J. H., Cao, C. B., Idrees, F., and Ma, X. L. (2015). Hierarchical porous nitrogen-doped carbon nanosheets derived from silk for ultrahigh-capacity battery anodes and supercapacitors. *ACS Nano* 9, 2556–2564. doi: 10.1021/nn506394r

Hsia, B., Marschewski, J., Wang, S., In, J. B., Carraro, C., Poulikakos, D., et al. (2014). Highly flexible, all solid-state micro-supercapacitors from vertically aligned carbon nanotubes. *Nanotechnology* 25:055401. doi: 10.1088/0957-4484/25/5/055401

Hsieh, W., Horng, T.-L. A., Huang, H.-C., and Teng, H. (2015). Facile simulation of carbon with wide pore size distribution for electric double-layer capacitance based on Helmholtz models. *J. Mater. Chem. A* 3, 16535–16543. doi: 10.1039/C5TA04125B

Huang, J., Sumpter, B. G., and Meunier, V. (2008). A universal model for nanoporous carbon supercapacitors applicable to diverse pore regimes, carbon materials, and electrolytes. *Chem. Euro. J.* 14, 6614–6626. doi: 10.1002/chem.200800639

Huang, Z.-H., Song, Y., Xu, X.-X., and Liu, X.-X. (2015). Ordered polypyrrole nanowire arrays grown on a carbon cloth substrate for a high-performance pseudocapacitor electrode. *ACS Appl. Mater. Interfaces* 7, 25506–25513. doi: 10.1021/acsami.5b08830

Jiang, D. E., Jin, Z. H., and Wu, J. Z. (2011). Oscillation of capacitance inside nanopores. *Nano Lett.* 11, 5373–5377. doi: 10.1021/nl202952d

Kang, Y. J., Chun, S. J., Lee, S. S., Kim, B. Y., Kim, J. H., Chung, H., et al. (2012). All-solid-state flexible supercapacitors fabricated with bacterial nanocellulose papers, carbon nanotubes, and triblock-copolymer ion gels. *ACS Nano* 6, 6400–6406. doi: 10.1021/nn301971r

Kim, T., Jung, G., Yoo, S., Suh, K. S., and Ruoff, R. S. (2013). Activated graphene-based carbons as supercapacitor electrodes with macro- and mesopores. *ACS Nano* 7, 6899–6905. doi: 10.1021/nn402077v

Largeot, C., Portet, C., Chmiola, J., Taberna, P. L., Gogotsi, Y., and Simon, P. (2008). Relation between the ion size and pore size for an electric double-layer capacitor. *J. Am. Chem. Soc.* 130, 2730–2731. doi: 10.1021/ja7106178

Lethien, C., Le Bideau, J., and Brousse, T. (2019). Challenges and prospects of 3D micro-supercapacitors for powering the internet of things. *Energy Environ. Sci.* 12, 96–115. doi: 10.1039/C8EE02029A

Lewandowski, A., Olejniczak, A., Galinski, M., and Stepniak, I. (2010). Performance of carbon–carbon supercapacitors based on organic, aqueous and ionic liquid electrolytes. *J. Power Sources* 195, 5814–5819. doi: 10.1016/j.jpowsour.2010.03.082

Li, H., Tao, Y., Zheng, X. Y., Luo, J. Y., Kang, F. Y., Cheng, H. M., et al. (2016). Ultra-thick graphene bulk supercapacitor electrodes for compact energy storage. *Energy Environ. Sci.* 9, 3135–3142. doi: 10.1039/C6EE00941G

Lin, J., Zhang, C. G., Yan, Z., Zhu, Y., Peng, Z. W., Hauge, R. H., et al. (2013). 3-Dimensional graphene carbon nanotube carpet-based microsupercapacitors with high electrochemical performance. *Nano Lett.* 13, 72–78. doi: 10.1021/nl3034976

Liu, C. G., Yu, Z. N., Neff, D., Zhamu, A., and Jang, B. Z. (2010). Graphene-based supercapacitor with an ultrahigh energy density. *Nano Lett.* 10, 4863–4868. doi: 10.1021/nl102661q

Liu, W. W., Feng, Y. Q., Yan, X. B., Chen, J. T., and Xue, Q. J. (2013). Superior micro-supercapacitors based on graphene quantum dots. *Adv. Funct. Mater.* 23, 4111–4122. doi: 10.1002/adfm.201203771

Liu, W. W., Yan, X. B., Lang, J. W., Peng, C., and Xue, Q. J. (2012). Flexible and conductive nanocomposite electrode based on graphene sheets and cotton cloth for supercapacitor. *J. Mater. Chem.* 22, 17245–17253. doi: 10.1039/c2jm32659k

Lu, W., Qu, L. T., Henry, K., and Dai, L. M. (2009). High performance electrochemical capacitors from aligned carbon nanotube electrodes and ionic liquid electrolytes. *J. Power Sources* 189, 1270–1277. doi: 10.1016/j.jpowsour.2009.01.009

Lukatskaya, M. R., Dunn, B., and Gogotsi, Y. (2016). Multidimensional materials and device architectures for future hybrid energy storage. *Nat. Commun.* 7:12647. doi: 10.1038/ncomms12647

Ma, K., Wang, X. W., Forsman, J., and Woodward, C. E. (2017). Molecular dynamic simulations of ionic liquid's structural variations from three to one layers inside a series of slit and cylindrical nanopores. *J. Phys. Chem. C* 121, 13539–13548. doi: 10.1021/acs.jpcc.7b03319

Ma, K., Woodward, C. E., and Forsman, J. (2014). Classical density functional study on interfacial structure and differential capacitance of ionic liquids near charged surfaces. *J. Phys. Chem. C* 118, 15825–15834. doi: 10.1021/jp504001u

Makino, S., Shinohara, Y., Ban, T., Shimizu, W., Takahashi, K., Imanishi, N., et al. (2012). 4 V class aqueous hybrid electrochemical capacitor with battery-like capacity. *RSC Adv.* 2, 12144–12147. doi: 10.1039/c2ra22265e

Merlet, C., Rotenberg, B., Madden, P. A., Taberna, P. L., Simon, P., Gogotsi, Y., et al. (2012). On the molecular origin of supercapacitance in nanoporous carbon electrodes. *Nat. Mater.* 11, 306–310. doi: 10.1038/nmat3260

Mourad, E., Coustan, L., Lannelongue, P., Zigah, D., Mehdi, A., Vioux, A., et al. (2017). Biredox ionic liquids with solid-like redox density in the liquid state for high-energy supercapacitors. *Nat. Mater.* 16, 446–454. doi: 10.1038/nmat4808

Ortaboy, S., Alper, J. P., Rossi, F., Bertoni, G., Salviati, G., Carraro, C., et al. (2017). MnOx-decorated carbonized porous silicon nanowire electrodes for high performance supercapacitors. *Energy Environ. Sci.* 10, 1505–1516. doi: 10.1039/C7EE00977A

Pham, D. T., Lee, T. H., Luong, D. H., Yao, F., Ghosh, A., Le, V. T., et al. (2015). Carbon nanotube-bridged graphene 3D building blocks for ultrafast compact supercapacitors. *Acs Nano* 9, 2018–2027. doi: 10.1021/nn507079x

Rouquerol, J., Avnir, D., Fairbridge, C. W., Everett, D. H., Haynes, J. H., Pernicone, N., et al. (1994). Recmmendations for the characterization of porous solids. *Pure Appl. Chem.* 66, 1739–1758. doi: 10.1351/pac199466081739

Ruiz, V., Huynh, T., Sivakkumar, S. R., and Pandolfo, A. G. (2012). Ionic liquid–solvent mixtures as supercapacitor electrolytes for extreme temperature operation. *RSC Adv.* 2, 5591–5598. doi: 10.1039/c2ra20177a

Shahzad, S., Shah, A., Kowsari, E., Iftikhar, F. J., Nawab, A., Piro, B., et al. (2018). Ionic liquids as environmentally benign electrolytes for high-performance supercapacitors. *Global Challenges* 3:1800023. doi: 10.1002/gch2.201800023

Shim, Y., and Kim, H. J. (2010). Nanoporous carbon supercapacitors in an ionic liquid: a computer simulation study. *ACS Nano* 4, 2345–2355. doi: 10.1021/nn901916m

Simon, P., and Gogotsi, Y. (2013). Capacitive energy storage in nanostructured carbon-electrolyte systems. *Acc. Chem. Res.* 46, 1094–1103. doi: 10.1021/ar200306b

Stevenson, A. J., Gromadskyi, D. G., Hu, D., Chae, J., Guan, L., Yu, L., et al. (2015). Supercapatteries with hybrids of redox active polymers and nanostructured carbons. *Nanocarb. Adv. Energy Stor.* 1, 79–210. doi: 10.1002/9783527680054.ch6

Sudhan, N., Subramani, K., Karnan, M., Ilayaraja, N., and Sathish, M. (2017). Biomass-derived activated porous carbon from rice straw for a high-energy symmetric supercapacitor in aqueous and non-aqueous electrolytes. *Energy Fuels* 31, 977–985. doi: 10.1021/acs.energyfuels.6b01829

Sun, H., Yu, L., Jin, X., Hu, X., Wang, D., and Chen, G. Z. (2005). Unusual anodic behaviour of chloride ion in 1-butyl-3-methylimidazolium hexafluorophosphate. *Electrochem. Commun.* 7, 685–691. doi: 10.1016/j.elecom.2005.04.020

Thissandier, F., Dupre, L., Gentile, P., Brousse, T., Bidan, G., Buttard, D., et al. (2014). Ultra-dense and highly doped SiNWs for micro-supercapacitors electrodes. *Electrochim. Acta* 117, 159–163. doi: 10.1016/j.electacta.2013.11.097

Thissandier, F., Le Comte, A., Crosnier, O., Gentile, P., Bidan, G., Hadji, E., et al. (2012). Highly doped silicon nanowires based electrodes for micro-electrochemical capacitor applications. *Electrochem. Commun.* 25, 109–111. doi: 10.1016/j.elecom.2012.09.019

Tian, W. Q., Gao, Q. M., Tan, Y. L., Yang, K., Zhu, L. H., Yang, C. X., et al. (2015). Bio-inspired beehive-like hierarchical nanoporous carbon derived from bamboo-based industrial by-product as a high performance supercapacitor electrode material. *J. Mater. Chem. A* 3, 5656–5664. doi: 10.1039/C4TA06620K

Tsai, W. Y., Lin, R. Y., Murali, S., Zhang, L. L., Mcdonough, J. K., Ruoff, R. S., et al. (2013). Outstanding performance of activated graphene based supercapacitors in ionic liquid electrolyte from-50 to 80 degrees C. *Nano Energy* 2, 403–411. doi: 10.1016/j.nanoen.2012.11.006

Vatamanu, J., Borodin, O., and Smith, G. D. (2010). Molecular insights into the potential and temperature dependences of the differential capacitance of a room-temperature ionic liquid at graphite electrodes. *J. Am. Chem. Soc.* 132, 14825–14833. doi: 10.1021/ja104273r

Wang, S., Hsia, B., Carraro, C., and Maboudian, R. (2014). High-performance all solid-state micro-supercapacitor based on patterned photoresist-derived porous carbon electrodes and an ionogel electrolyte. *J. Mater. Chem. A* 2, 7997–8002. doi: 10.1039/C4TA00570H

Wei, L., Sevilla, M., Fuertes, A. B., Mokaya, R., and Yushin, G. (2012). Polypyrrole-derived activated carbons for high-performance electrical double-layer capacitors with ionic liquid electrolyte. *Adv. Funct. Mater.* 22, 827–834. doi: 10.1002/adfm.201101866

Wei, X., Yu, L., Jin, X., Wang, D., and Chen, G. Z. (2009). Solar-thermochromism of pseudocrystalline nanodroplets of ionic liquid-NiII complexes immobilized inside translucent microporous PVDF films. *Adv. Mater.* 21, 776–780. doi: 10.1002/adma.200801816

Wei, X., Yu, L., Wang, D., Jin, X., and Chen, G. Z. (2008). Thermo-solvatochromism of chloro-nickel complexes in 1-hydroxyalkyl-3-methyl-imidazolium cation based ionic liquids. *Green Chem.* 10, 304–313. doi: 10.1039/b715763k

Xia, L., Yu, L., Hu, D., and Chen, G. Z. (2017). Electrolytes for electrochemical energy storage. *Mater. Chem. Front.* 1, 584–618. doi: 10.1039/C6QM00169F

Yang, X., Zhang, F., Zhang, L., Zhang, T. F., Huang, Y., and Chen, Y. S. (2013). A high-performance graphene oxide-doped ion gel as gel polymer electrolyte for all-solid-state supercapacitor applications. *Adv. Funct. Mater.* 23, 3353–3360. doi: 10.1002/adfm.201203556

Yu, L., and Chen, G. Z. (2014). Cryo-solvatochromism in ionic liquids. *RSC Adv.* 4, 40281–40285. doi: 10.1039/C4RA08116A

Yu, L., and Chen, G. Z. (2016a). High energy supercapattery with an ionic liquid solution of LiClO4. *Faraday Discuss.* 190, 231–240. doi: 10.1039/C5FD00232J

Yu, L., and Chen, G. Z. (2016b). Redox electrode materials for supercapatteries. *J. Power Sources* 326, 604–612. doi: 10.1016/j.jpowsour.2016.04.095

Yu, L., Jin, X., and Chen, G. Z. (2013). A comparative study of anodic oxidation of bromide and chloride ions on platinum electrodes in 1-butyl-3-methylimidazolium hexafluorophosphate. *J. Electroanalyt. Chem.* 688, 371–378. doi: 10.1016/j.jelechem.2012.07.034

Yu, L., Sun, H., He, J., Wang, D., Jin, X., Hu, M., et al. (2007). Electro-reduction of cuprous chloride powder to copper nanoparticles in an ionic liquid. *Electrochem. Commun.* 9, 1374–1381. doi: 10.1016/j.elecom.2007.01.050

Yu, W. H., Wang, H. L., Liu, S., Mao, N., Liu, X., Shi, J., et al. (2016a). N, O-codoped hierarchical porous carbons derived from algae for high-capacity supercapacitors and battery anodes. *J. Mater. Chem. A* 4, 5973–5983. doi: 10.1039/C6TA01821A

Yu, X., Kang, Y., and Park, H. S. (2016b). Sulfur and phosphorus co-doping of hierarchically porous graphene aerogels for enhancing supercapacitor performance. *Carbon* 101, 49–56. doi: 10.1016/j.carbon.2016.01.073

Zhang, F., Zhang, T., Yang, X., Zhang, L., Leng, K., Huang, Y., et al. (2013). A high-performance supercapacitor-battery hybrid energy storage device based on

graphene-enhanced electrode materials with ultrahigh energy density. *Energy Environ. Sci.* 6, 1623–1632. doi: 10.1039/c3ee40509e

Zhang, L., Zhang, F., Yang, X., Long, G. K., Wu, Y. P., Zhang, T. F., et al. (2013). Porous 3D graphene-based bulk materials with exceptional high surface area and excellent conductivity for supercapacitors. *Sci. Rep.* 3:1408. doi: 10.1038/srep01408

Zhao, D., Huang, Q., Jin, X. B., Wei, X. J., and Chen, Z. G. (2010). Capacitance at the electrode/Ionic liquid interface. *Wuli Huaxue Xuebao/ Acta Physico - Chimica Sinica* 26, 1239–1248. doi: 10.3866/PKU.WHXB201 00506

Zhou, H. T., Wang, X. H., Sheridan, H., Gao, H. Q., Du, J., Yang, J. H., et al. (2016). Boosting the energy density of 3D dual-manganese oxides-based Li-ion supercabattery by controlled mass ratio and charge injection. *J. Electrochem. Soc.* 163, A2618–A2622. doi: 10.1149/2.0691613jes

Zhou, X. H., Peng, C., and Chen, G. Z. (2012). 20 V stack of aqueous supercapacitors with carbon (-), titanium bipolar plates and CNT-polypyrrole composite (+). *Aiche J.* 58, 974–983. doi: 10.1002/aic. 12632

Zhu, J. Y., Childress, A. S., Karakaya, M., Dandeliya, S., Srivastava, A., Lin, Y., et al. (2016). Defect-engineered graphene for high-energy- and high-power-density supercapacitor devices. *Adv. Mater.* 28, 7185–7192. doi: 10.1002/adma.201602028

Zhu, Y. W., Murali, S., Stoller, M. D., Ganesh, K. J., Cai, W. W., Ferreira, P. J., et al. (2011). Carbon-based supercapacitors produced by activation of graphene. *Science* 332, 1537–1541. doi: 10.1126/science.1200770

Conflict of Interest Statement: The authors declare that the research was conducted in the absence of any commercial or financial relationships that could be construed as a potential conflict of interest.

Microscopic Structural and Dynamic Features in Triphilic Room Temperature Ionic Liquids

Fabrizio Lo Celso[1], Giovanni B. Appetecchi[2], Elisabetta Simonetti[2], Man Zhao[3], Edward W. Castner Jr.[3], Uwe Keiderling[4], Lorenzo Gontrani[5], Alessandro Triolo[6]* and Olga Russina[5]*

[1] Dipartimento di Fisica e Chimica, Università di Palermo, Palermo, Italy, [2] ENEA, Laboratory SSPT-PROMAS-MATPRO, Rome, Italy, [3] Department of Chemistry and Chemical Biology, Rutgers University, The State University of New Jersey, Newark, NJ, United States, [4] Soft Matter and Functional Materials, Helmholtz-Zentrum für Materialien und Energie GmbH, Berlin, Germany, [5] Department of Chemistry, University of Rome Sapienza, Rome, Italy, [6] Laboratorio Liquidi Ionici, Istituto Struttura della Materia, Consiglio Nazionale delle Ricerche (ISM-CNR), Rome, Italy

Here we report a thorough investigation of the microscopic and mesoscopic structural organization in a series of triphilic fluorinated room temperature ionic liquids, namely [1-alkyl,3-methylimidazolium][(trifluoromethanesulfonyl)(nonafluorobutylsulfonyl)imide], with alkyl=ethyl, butyl, octyl ([$C_n$mim][IM_{14}], $n = 2, 4, 8$), based on the synergic exploitation of X-ray and Neutron Scattering and Molecular Dynamics simulations. This study reveals the strong complementarity between X-ray/neutron scattering in detecting the complex segregated morphology in these systems at mesoscopic spatial scales. The use of MD simulations delivering a very good agreement with experimental data allows us to gain a robust understanding of the segregated morphology. The structural scenario is completed with determination of dynamic properties accessing the diffusive behavior and a relaxation map is provided for [C_2mim][IM_{14}] and [C_8mim][IM_{14}], highlighting their natures as fragile glass formers.

Keywords: fluorous tail, triphilic, ionic liquid, neutron scattering, molecular dynamics (MD)

INTRODUCTION

Ionic liquids (ILs) constitute an interesting class of compounds, composed solely of ionic species and with a melting point below 100°C. Although some debate exists on their environmental compatibility, they are attracting a great deal of attention as they are considered potential replacements for noxious solvents and flammable electrolytes. Their fascinating chemical and physical properties can be widely modulated upon slight chemical modification of constituent ionic species. In the framework of their potential application in a variety of fields, the possibility of introducing a fluorous moiety into either the cation or the anion (e.g., by replacing an alkyl with an equivalent length perfluoroalkyl chain) is quite attractive, as it allows accessing further modulation of properties and performances. In these cases, the already appealing properties of conventional ILs, including non-flammability, negligible vapor pressure, high thermal, chemical and electrochemical stability, are maintained and can be further fine-tuned by introduction of fluorous moieties leading to high hydrophobicity, enhanced surface activity, interesting gas uptake properties etc. Fluorinated Ionic Liquids (FILs) show properties arising from both their fluorous and ionic natures, thus introducing interesting variations into the more conventional IL landscape. As both fluorinated compounds and ILs are considered neoteric solvents with the potential to

impact sustainable processes and green chemistry, it can be envisaged that their merging into the FILs technology will soon be of high impact (Merrigan et al., 2000; van den Broeke et al., 2002; Kim et al., 2004; Xue and Shreeve, 2005; Xue et al., 2006; Almantariotis et al., 2010, 2017; Smith et al., 2010; Kunze et al., 2011; Yoshida and Saito, 2011; Jeremias et al., 2013; Pereiro et al., 2013a, 2018; Weber et al., 2013; Hollóczki et al., 2015; Suarez et al., 2015; Wu et al., 2016; Rauber et al., 2017; Bastos et al., 2018).

Among other peculiar features in FILs, their mesoscopic structural organization is quite interesting. It is well-known that alkyl chain bearing ILs are characterized by a distinct degree of nm-scale order, associated to the spatial segregation of apolar domains (viz. alkyl chains) with respect to a polar matrix (viz. anion and cation heads) (Urahata and Ribeiro, 2004; Wang and Voth, 2005, 2006; Canongia Lopes and Padua, 2006; Canongia Lopes et al., 2006; Pádua et al., 2007; Triolo et al., 2007; Almantariotis et al., 2010, 2017; Smith et al., 2010). Such a structural organization can be experimentally detected by means of X-ray and/or neutron scattering techniques, as it is fingerprinted by a distinct low momentum transfer (Q) peak (that is centered at a position reflecting the characteristic size of the segregated domain), as it was both experimentally and computationally found (Triolo et al., 2007, 2008, 2009; Atkin and Warr, 2008; Russina et al., 2009, 2012, 2017a,b; Hayes et al., 2011; Zheng et al., 2011; Li et al., 2012; Macchiagodena et al., 2012; Russina and Triolo, 2012, 2017; Song et al., 2012; Rocha et al., 2013). When introducing a fluorous moiety, as it is incompatible with both polar moieties and alkyl tails, it will tend to segregate into a third further kind of domain, where fluorous tails alone tend to cluster. This will lead to a characteristic mesoscopically organized morphology where three different, macroscopically incompatible, domains are forced to co-exist at the nm spatial scale: this led some of us to term such a kind of compounds as triphilic IL (Russina et al., 2013; Hollóczki et al., 2015). Such a scenario (Shen et al., 2012; Greaves et al., 2013; Pereiro et al., 2013b; Hettige et al., 2014; Brehm et al., 2015; Vieira et al., 2015; Ferreira et al., 2017; Shimizu et al., 2017) opens the way to simultaneous solvation of completely incompatible components into the homogeneous FIL, as each

compound (e.g., a salt, an oil, and a fluorous compound) can be simultaneously dissolved into the same mesoscopically organized medium (Weiss et al., 2017; Tsurumaki and Ohno, 2018). In this contribution, we report on the structural properties of a series of 1-alkyl-3-methylimidazolium ([$C_n$mim], where n indicates the number of carbon atoms along the side alkyl chain, with $n = 2$, 4, and 8) (trifluoromethanesulfonyl)(nonafluorobutylsulfonyl) imide ([IM_{14}], 1 and 4 represent the number of carbon atoms on the two sides of the imide anion) [see e.g., (Johansson et al., 2010; Montanino et al., 2012; Jeremias et al., 2013; Russina et al., 2013, 2017a; Castiglione et al., 2014; Paolone et al., 2018)], at ambient conditions. **Scheme 1** represents the chemical structure of the probed FILs.

EXPERIMENTAL DETAILS

Samples Synthesis

The imidazolium-based, (trifluoromethanesulfonyl)(nonafluorob utylsulfonyl)imide ionic liquids were synthesized through a procedure developed at ENEA and described in detail elsewhere (Jeremias et al., 2013; Montanino et al., 2013). The chemicals, i.e., 1-methylimidazole (99 wt.%), bromoethane (99 wt.%), 1-bromobutane (99 wt.%), 1-bromooctane (99 wt.%), were purchased by Sigma-Aldrich and used as received. The sorbent materials, i.e., activated carbon (Darco-G60, Sigma-Aldrich) and alumina (acidic, Brockmann I, Sigma-Aldrich), were previously rinsed in deionized water according to a route reported elsewhere (Palumbo et al., 2017). Acidic (trifluoromethanesulfonyl)(nonafluorobutylsulfonyl)imide, HIM_{14} (59 wt.% solution in water), was purchased by 3M and used as received. Deionized water, used as the processing solvent, was obtained with a Millipore ion-exchange resin deionizer.

The imidazolium precursor was synthesized by reacting the 1-methylimidazole, previously dissolved in deionized water, with the appropriate amount of bromoethane (or 1-bromobutane or 1-bromooctane). A concentrated aqueous solution of imidazolium bromide was obtained, which was then purified through activated carbon and acidic alumina. The liquid fraction (clear and colorless) was separated from the solid one
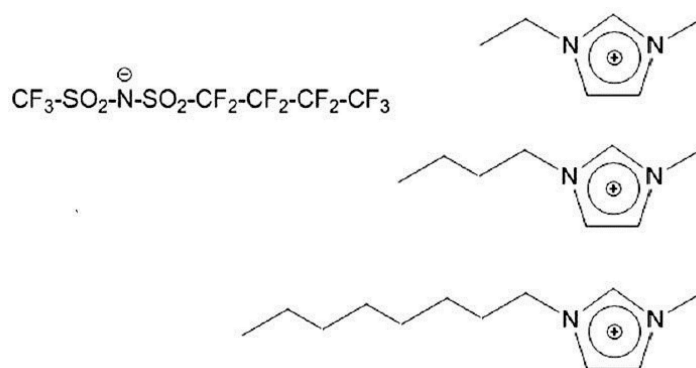
SCHEME 1 | Description of chemical nature of the investigated ionic liquids. On the **(Left)**, the anion's structure is shown, while the **(Right)** part of the Scheme shows the different cations [1-alkyl-3-methylimidazolium, with alkyl = ethyl **(Top)**, butyl **(Middle)**, and octyl **(Bottom)**].

(sorbent materials) by vacuum filtering and separately collected. Successively, the solid phase was rinsed with deionized water to recover the precursor trapped through the purifying materials, obtaining a further aqueous solution (clear and colorless) which was unified to the previous one.

The imidazolium IM_{14} ionic liquids were obtained by reacting the precursor water solutions and the suitable amount of HIM_{14}. The reaction (anion exchange) led to fast formation of hydrophobic ionic liquid and hydrophilic HBr (in water). After 1 h the mixing was interrupted and phase separation was allowed for a few minutes. The upper phase was mostly composed of water, HBr and HIM_{14} excess whereas the lower one was constituted of the ionic liquid with traces of water and HBr. After removal of the aqueous phase, the imidazolium IM_{14} ionic liquid was rinsed several times with deionized water to remove the HBr and HIM_{14} impurities. The ionic liquids were then housed in a vacuum rotary evaporator at 90°C to remove most of the water and, finally, vacuum dried at 120°C. The ionic liquid materials were stored in sealed glass tubes within a dry room.

The Li^+ and Br^- content was checked by atomic absorption analysis (SpetcrAA mod. 220 atomic absorption Spectrometer) and X-ray fluorescence spectrometry (Shimadzu energy-dispersion EDX-720 spectrometer), respectively. Less than 2 ppm of lithium and bromide were detected in the ionic liquid samples.

X-Ray Scattering

Small-Medium Angle X-ray scattering data were collected at the 11-ID-C beamline at the Argonne Photon Source (Ren, 2012). A monochromatic beam at a wavelength of 0.11165 A was used, with a beam size of 0.7×0.7 mm^2. Samples were contained in a 2 mm diameter quartz capillary purchased from WJM-Berlin. Thirty consecutive data acquisitions were collected for a total acquisition time of 200 sec. Before merging the different data sets, care was taken that no radiation damage occurred to samples. Raw 2D data sets were integrated and transformed into intensities using the FIT2D software (Hammersley et al., 1996). The scattering structure factor S(Q) was calculated using the PDFgetX2 software (Qiu et al., 2004), correcting for background contribution, absorption, Compton scattering, and multiple scattering.

Additionally Small-Medium-Wide Angle X-ray scattering data were collected at beamline BL04B2 SPring-8 (Japan Synchrotron Radiation Research Institute, JASRI, Japan) (Kohara et al., 2001; Ohmura et al., 2009; Aoun et al., 2010). Measurements were conducted at ambient conditions. A monochromatized X-ray (61.6 keV) was obtained using a Si(220) monochromator. The observed scattering intensity of the X-ray was corrected for absorption, polarization, and incoherent scatterings (Cromer, 1969) to obtain coherent scattering intensities.

Small Angle Neutron Scattering

Small Angle Neutron Scattering experiments (SANS) measurements on $[C_n mim][IM_{14}]$ (n = 2, 4, 8) were performed at the small-angle scattering instrument V4 which is placed in the cold neutron guide of Helmholtz-Zentrum Berlin (HZB). The

magnitude of the scattering vector is defined as $Q = (4\pi/\lambda)(\sin\theta)$ with λ being the wavelength and 2θ the scattering angle. The measured neutron flux of the V4 is $\sim 10^6$ cm^{-2}.s^{-1} for the wavelength used, $\lambda = 4.5$ Å (Keiderling and Wiedenmann, 1995). The scattering data were obtained at one sample detector distance of 1.0 m, which yields a total momentum transfer range of 0.5 nm^{-1} < Q < 8 nm^{-1}. For further information regarding the V4 instrument and its resolution the reader is referred to Keiderling and Wiedenmann (1995)and Gilles et al. (2000). The sample was placed into a circular quartz cuvette with inner spacing of 1 mm and placed in the beam for measurement. A Cd aperture of 13 mm was used for the scattering measurements. The 2D scattering data were reduced to a scattering curve [dΣ/dΩ(Q) vs. Q; hereinafter indicated as I(Q) vs. Q] by means of the BerSANS software. The raw data is then corrected for transmission, the quartz cell background scattering subtracted and converted to absolute units taking into account the scattering from water (Keiderling, 2002).

Wide Angle Neutron Scattering

Neutron diffraction measurements on $[C_2 mim][IM_{14}]$ were performed on the SANDALS diffractometer at ISIS. The neutron wavelength range is 0.05–4.95 Å. Data were collected over the momentum transfer (Q) range between ca. 0.3 and 50 Å^{-1}. The sample was contained in chemically inert, null scattering $Ti_{0.68}Zr_{0.32}$ flat cans (with size $3.5 \times 3.5 \times 1$ mm^3) sealed with Teflon O-rings. Measurements were also collected on the empty cell, so to properly subtract empty cell contribution. Furthermore, a measurement on a vanadium standard sample was also collected for data normalization purposes. Diffraction experiments were conducted at 298 K under vacuum. The diffraction pattern was measured for approximately 6 h at conditions of fully operating source. Data analysis was carried out using the GUDRUN software available at the facility that allows the application of (a) normalization to the incident flux, absorption and multiple scattering corrections, empty can subtraction, and normalization to absolute units by dividing the measured differential cross section by the scattering of a vanadium standard and (b) corrections for single atom scattering and hydrogen inelasticity effects.

Diffusivity Measurements From PG-SE NMR

Self-diffusion coefficients for the anions and cations were measured using pulsed gradient spin-echo (PG-SE) NMR methods. Anionic diffusivities were measured from ^{19}F NMR signals, and cationic diffusivities were obtained from ^{1}H signals. The Diffusion-ordered bipolar pulse pair stimulated echo (DBPPSTE) pulse sequence was used (Wu et al., 1995). NMR samples were prepared from ionic liquids dried for 48 h on a Schlenk vacuum line, and prepared in an argon glovebox with water and oxygen levels below 0.1 and 0.4 ppm, respectively. Samples were prepared in 3 mm O.D. NMR tubes, capped in the glovebox, and flame-sealed immediately after removal from the glovebox. A Doty Scientific diffusion probe was installed

on a 400 MHz Varian DirectDrive spectrometer for the PG-SE NMR measurements. PG-SE experiments had temperature uncertainties of ±1 K.

Additional details of our NMR diffusion protocols have been described previously (Liang et al., 2015; Wu et al., 2015, 2018).

Viscosity Measurements

Temperature-dependent viscosity measurements of the ionic liquid samples were made using a Cambridge Viscosity ViscoLab 4100 instrument, as described previously (Funston et al., 2007; Mariani et al., 2017). Temperatures for the viscosity measurements were controlled to ±0.1 K by water flow from a Lauda Brinkmann RMT-6 recirculating chiller/heater.

Dielectric Spectroscopy Measurements

Dielectric spectroscopy data were collected between 160 and 280 K in the range 2 10^{-2} – 3 10^6 Hz, applying the gain-phase analysis technique with a Solartron SI-1260 analyser and a Novo-Control BDS 4000 spectrometer. The sample was sandwiched between two gold plated flat electrodes, with diameter of 20 mm and with a sample thickness of 50 μm. The temperature was controlled by a Quatro cryosystem.

Computational Details

Molecular dynamic simulations were performed using the GROMACS 5.1.1 package (Van Der Spoel et al., 2005; Hess et al., 2008). Interactions were described using an all-atoms potential (Lopes and Padua, 2004; Shimizu et al., 2010). The simulations for [$C_n$mim][IM_{14}] ILs were performed using a cubic box of 900, 800, and 700 ion pairs for n = 2, 4, and 8, respectively; periodic boundary conditions were applied. Force field parameter files and initial configuration were created by DLPGEN software (Bernardes and Joseph, 2015); initial density was fixed 10% higher than the experimental one. A procedure of energy minimization has been performed starting from the initial configuration prior to the first NPT equilibration. The steepest descent algorithm implemented in Gromacs has been used and convergence has been obtained when every force on each atom would not exceed 1,000 kJ/mol/nm. Cutoff for the short range electrostatics and Van der Waals interaction were set to 1.0 nm. The equilibration procedure was done in several steps, starting from a series of NPT simulation at high temperatures and scaled partial charges, followed by lowering progressively the temperature and increasing the charges to their final value at 298,15 K and 1 bar, after a 15 ns run. This procedure was repeated two further times until an equilibrated system was obtained. After the equilibration phase, the system was run for a total of 50 ns for a production run, and then the trajectory of the last 5 ns was saved at a frequency of 1 ps, for calculation of the structural properties. The simulations were always checked vs. the experimental density and the energy profile. During the production runs for the temperature coupling, we used a velocity rescaling thermostat (Bussi et al., 2007) (with a time coupling constant of 0.1 ps), while for the pressure coupling, we used a Parrinello–Rahman barostat (Parrinello and Rahman, 1981) (1 ps for the relaxation constant). The Leap-Frog algorithm with a 1 fs time step was used for integrating the equations of motion. Cut-offs for the Lennard- Jones and real space part of

the Coulombic interactions were set to 15 Å. For the electrostatic interactions, the Particle Mesh Ewald (PME) summation method (Darden et al., 1993; Essmann et al., 1995) was used, with an interpolation order of 6 and 0.08 nm of FFT grid spacing. Selected graphs were done using Matplotlib (Hunter, 2007). Weighted and partial structure factors were computed by using in-house developed software, accordingly to text book formulas as highlighted in Margulis's work (Kashyap et al., 2012), while selected pair correlation function, angular distribution function were obtained by TRAVIS (Brehm and Kirchner, 2011; Hollóczki et al., 2015). Ion aggregation analysis was performed using the AGGREGATES software (Bernardes, 2017).

RESULTS AND DISCUSSION

The chemical structure of [$C_n$mim][IM_{14}] samples with n = 2, 4, 8 that have been studied in this report is shown in **Scheme 1**. These samples differ only on the length of the side alkyl chain in the cation, the anion remaining unaltered. [C_2mim][IM_{14}] has been previously reported to be an homogeneous liquid at ambient conditions (Appetecchi et al., 2011). Analogously, [C_4mim][IM_{14}] and [C_8mim][IM_{14}] are liquid at ambient conditions and their synthesis and properties are here reported for the first time.

Viscosity

The values for the viscosities for [C_2mim][IM_{14}] measured between 1.5 and 90°C spanned the range from 520 down to 12 cP. For [C_8mim][IM_{14}], the viscosities ranged from 1,011 to 28 cP over the temperature range from 3.7 to 70°C. As with all of our previous recorded viscosities for ionic liquids the data are best fit to the well-known Vogel-Fulcher-Tammann (VFT) equation in logarithmic form, given by: ln ($\eta(T)$, cP) = ln (η_{VFT})+B/(T−T$_o$); where η_{VFT}, B, and T$_o$ are fitting parameters, representing infinite temperature viscosity, an equivalent activation energy and a characteristic temperature, respectively.

The primary significance of these fits is that they provide an excellent representation of the data, permitting us to calculate an extrapolated viscosity for any arbitrary temperature in order to match the viscosity/temperature point for comparison with the diffusivities measured at different temperatures via PG-SE NMR. While the viscosity data does not fit as well to the Arrhenius equation as it does to the VFT equation, the Arrhenius fits are adequate for a qualitative discussion. The viscosity activation energies were found to be 37.2 kJ/mol for [C_2mim][IM_{14}] and 44.1 kJ/mol for [C_8mim][IM_{14}].

The fits of the viscosity data to the VFT and the Arrhenius equations are given in **Figures S1**, **S2**.

Anion and Cation Diffusivities From PG-SE NMR

PG-SE NMR measurements were used to obtain the anionic and cationic diffusivities over the temperature range from 5 to 75°C for both [C_2mim][IM_{14}] and [C_8mim][IM_{14}]. Cationic diffusivities were observed to always larger than anionic diffusivities for both [C_2mim][IM_{14}] and [C_8mim][IM_{14}],
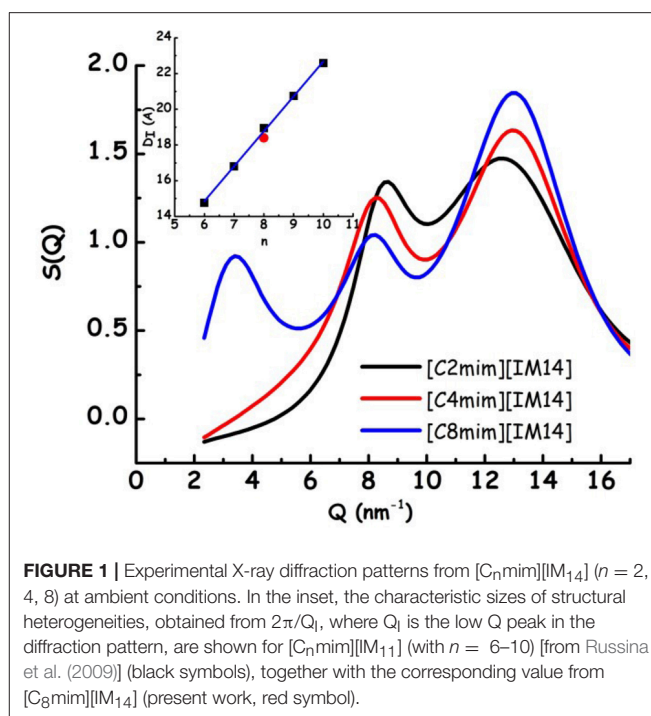
though the difference is more pronounced for the former case. For the [C_2mim][IM_{14}] IL, the anion is significantly larger than the cation, while the opposite is true for [C_8mim][IM_{14}]. It is worth noting that the mass of the [IM_{14}] anion (430 g/mol) is roughly four times that of the [C_2mim] cation ($F_w = 111$ g/mol) and twice that of the [C_8mim] cation ($F_w = 195$ g/mol). For [C_2mim][IM_{14}], the diffusivities range from 3.4×10^{-12} m^2s^{-1} for the [IM_{14}] anion at 5°C up to 1.1×10^{-10} m^2s^{-1}. For comparison, we note that the diffusivity of neat water is 1.26×10^{-9} m^2s^{-1} at 4°C.

As is the case for viscosities, the ionic self-diffusivities can also be fit by both Arrhenius and VFT laws, with the latter always providing somewhat superior fit statistics, albeit at the cost of one additional fit parameter. Considering the activation energies from the Arrhenius fits, one finds that the E_a values for [C_2mim][IM_{14}] are slightly less than that for the viscosity: 32.5 and 35.4 kJ/mol for the cation and anion, respectively, as compared with 37.2 kJ/mol for the viscosity. The E_a values for [C_8mim][IM_{14}] self-diffusion coefficients are larger than [C_2mim][IM_{14}], but again, less than the E_a value for the viscosity: E_a(cation) = 35.9 kJ/mol and E_a(anion) = 37.7 kJ/mol, vs. 44.1 kJ/mol (viscosity).

Harris showed that hydrodynamic scaling is not exact for any molecular fluids considered, including ionic liquids (Harris, 2009). Specifically, the Stokes-Einstein prediction that the diffusivities should be proportional to the ratio of temperature over viscosity does not hold exactly. Rather, a scaled or fractional Stokes-Einstein law does hold, where $D = (T/\eta)^\alpha$, where α is an exponent between 0.9 and 1.0. By using the VFT fit parameters, we can calculate precise viscosities in order to make graphs of the ionic diffusivities vs. the ratio of T/η These plots of D vs. T/η are shown in **Figure S3**.

Structure

In **Figure 1**, the X-ray diffraction patterns from the three samples are shown: in the reported Q range they are characterized by the presence of three peaks (Q_{I-III}, in order of increasing Q position), that fingerprint the existence of different kinds of correlations (Q_I is better discernible in the case of [C_8mim][IM_{14}]). In particular, in order of decreasing Q position, these peaks have been shown to reflect the existence of: (a) adjacency, (b) charge, and (c) polar correlations (Annapureddy et al., 2010; Araque et al., 2015). It appears that, similarly to other cases, the peak that is most affected by increase in chain length is Q_I that reflects the establishment of polar-apolar correlations (Triolo et al., 2007, 2009; Russina and Triolo, 2012; Russina et al., 2012): this peak has negligible amplitude for short chain length and it grows in amplitude and shifts to lower Q value upon increasing n. Such a behavior has been reported for a multitude of ILs and reflects the progressive increase in size of the apolar domain embedded into the polar matrix that can be qualitatively quantified as $D_I \sim 2\pi/Q_I$. In the inset of **Figure 1**, the characteristic domain sizes obtained for the case of [$C_n$mim][IM_{11}] (where [IM_{11}] is the commonly used anion bistriflamide, [Tf_2N]), reported by some of us in the past (Russina et al., 2009), are shown as a function of n. It can be observed

FIGURE 1 | Experimental X-ray diffraction patterns from [$C_n$mim][IM_{14}] ($n = 2$, 4, 8) at ambient conditions. In the inset, the characteristic sizes of structural heterogeneities, obtained from $2\pi/Q_I$, where Q_I is the low Q peak in the diffraction pattern, are shown for [$C_n$mim][IM_{11}] (with $n = 6$–10) [from Russina et al. (2009)] (black symbols), together with the corresponding value from [C_8mim][IM_{14}] (present work, red symbol).

that the corresponding quantity for the case of [C_8mim][IM_{14}] (for which Q_I peak position can be easily determined) is quite similar to the value reported for [C_8mim][IM_{11}], thus suggesting that X-ray scattering is a good reporter of the alkyl domain heterogeneities, whose size is only marginally affected by the different anion's nature. On the other hand, **Figure 2** reports Small Angle Neutron Scattering (SANS) data from the same [$C_n$mim][IM_{14}] samples at ambient conditions, over the Q range up to 8 nm^{-1} (thus covering only the Q range where Q_I typically occurs, see **Figure 1** for comparison). It clearly appears that while [C_8mim][IM_{14}] is characterized by a peak centered at ca. 3 nm^{-1} and [C_4mim][IM_{14}] shows a broad peaks superposition between 1 and 6 nm^{-1}, [C_2mim][IM_{14}] is instead characterized by a distinct peak centered at ca. 4.5 nm^{-1}. The latter peak has no analogous counterpart in the X-ray diffraction pattern shown in **Figure 1**. Moreover, the inset of **Figure 2** shows a comparison between the SANS data from [C_2mim][IM_{14}] and [C_2mim][IM_{11}]: it is clear that while [C_2mim][IM_{11}] is essentially featureless in the probed Q range, on the other hand [C_2mim][IM_{14}] shows a distinct peak. The featureless pattern from [C_2mim][IM_{11}] is rationalized considering that the side alkyl chain in the cation (an ethyl moiety) is too short to deliver a clustering of chains segregating from the polar moieties, accordingly no polar-apolar separation occurs in this system. On the other hand the clear existence of low Q peak in the case of [C_2mim][IM_{14}] fingerprints the existence of mesoscopic structural heterogeneities that, due to contrast reasons, neutrons can detect. As recently reported in a series of papers (Shen et al., 2012; Russina et al., 2013; Hettige et al., 2014; Hollóczki et al., 2015; Lo Celso et al., 2017, 2018a,b), neutron scattering (and occasionally, X-ray scattering, *vide infra*) succeed in detecting the occurrence of fluorous tails clusters embedded into the

charged matrix: the results presented in **Figures 1**, **2** confirm this observation, indicating that the perfluorobutyl chains in the $[IM_{14}]$ anions tend to associate into small fluorous domains and in the rest of the manuscript we will further explore this structural feature in the probed FILs.

In order to better address the issue of microscopic and mesoscopic structural organization in $[C_n mim][IM_{14}]$ FILs, we undertook a series of detailed Molecular Dynamics simulations
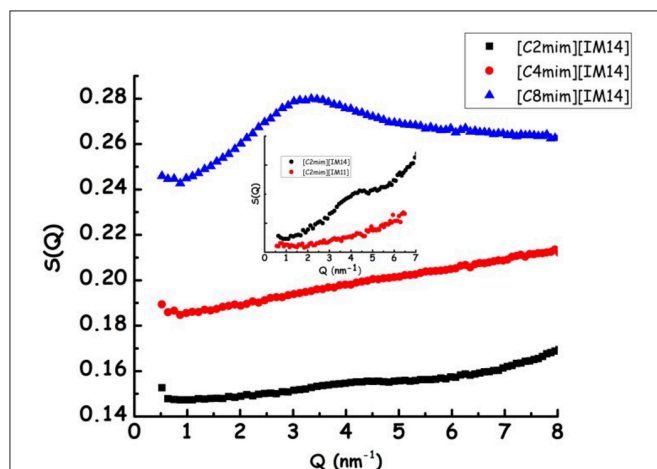

FIGURE 2 | Experimental small angle neutron scattering data from $[C_n mim][IM_{14}]$ (n = 2, 4, 8) at ambient conditions. In the inset a comparison between SANS data from $[C_2 mim][IM_{14}]$ and $[C_2 mim][IM_{11}]$ is shown.

on these compounds, aiming to extract information at atomistic level. In the experimental part, we described the procedure and other details used for these simulations. In the case of $[C_2 mim][IM_{14}]$, the computed neutron and X-ray diffraction patterns have been directly compared with experimentally derived data sets. **Figures 3A,B** show such a comparison, while **Figures 3C,D** describe the comparison between the experimental SANS data and the corresponding computed quantities for the case of $[C_n mim][IM_{14}]$, with n = 4 and 8: we consider the overall agreement between experimental and computational diffraction pattern very satisfactory. As a matter of fact, the simulations (along with the chosen interatomic potentials) succeed in accounting for all the structural features fingerprinted in the experimental diffraction patterns and this makes us confident that we can reliably interrogate the MD simulations to extract structural details at atomistic level.

Figure 4 show representative snapshots of simulation boxes for the three different samples $[C_n mim][IM_{14}]$ (n = 2, 4, 8), where polar moieties (imidazolium ring and SO_2-N-SO_2 moieties, belonging to cation and anion, respectively), alkyl tails and fluorous moieties are identified. A distinct mutual spatial segregation can be observed for these moieties, depending on the alkyl side chain length and we will better clarify this issue later on.

The characteristic alternation of oppositely charged layers around a chosen reference ion that is encountered in ILs, can be observed also in the present choice of compounds. **Figure 5** shows the representative case of $[C_2 mim][IM_{14}]$ (different
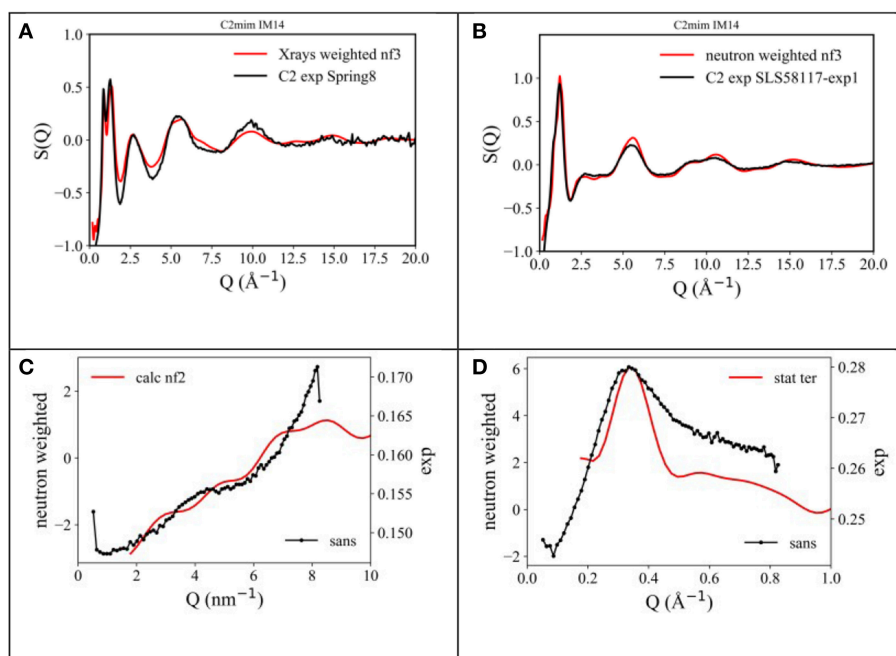
FIGURE 3 | Comparison between **(A)** X-ray and **(B)** neutron diffraction data and the output from present MD simulations for the case of $[C_2 mim][IM_{14}]$ at ambient conditions. Also, comparison between experimental (black line) and un-normalized MD-computed (red line) SANS data from $[C_n mim][IM_{14}]$, with **(C)** n = 4 and **(D)** n = 8, respectively, at ambient conditions.
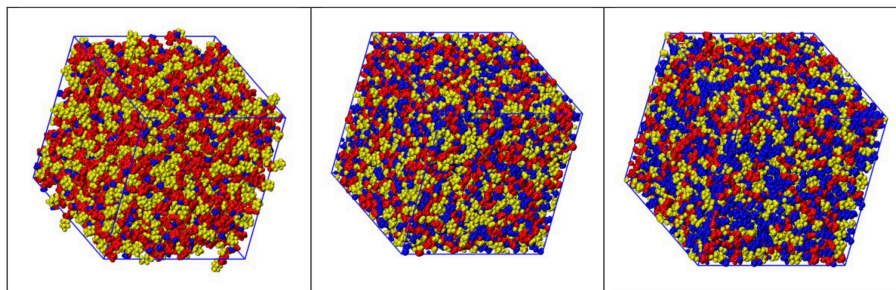
FIGURE 4 | Representative snapshots derived from MD simulations from $[C_n \text{mim}][IM_{14}]$, with $n = 2, 4, 8$ (left, center, and right, respectively), where color distinction of charged (red), alkyl (blue), and fluorous (yellow) moieties has been applied.

values of n lead to qualitatively similar results), where pair distribution functions (pdf) for: (a) center of mass of the imidazolium ring (ir) – ir; (b) ir – N_{anion} and (c) N_{anion} – N_{anion}, N_{anion} being the nitrogen atom in the anion, are reported. It appears that cation-anion correlations are the shorter ones, occurring at ca. 4 Å, in agreement with the nature of coulombic interactions. Spatial correlations between similarly charged ions occur at a larger distance (ca. 10 Å) and such correlations are out of phase with opposite charges correlations (their maxima fall where opposite charge pdf has minima).

We notice that the cation-cation correlation (ir-ir) is characterized by a short distance correlation (red line in **Figure 5** left) with two maxima at ca. 7 and 10 Å. In order to better rationalize this correlation, the combined distribution function (cdf), containing in abscissa the distance between neighbor imidazolium rings and in ordinate the angle (°) formed by vectors perpendicular to the imidazolium rings, has been evaluated and shown in **Figure 5** right. We can then envisage that the observed splitting of the first solvation shell of imidazolium rings around a reference ring is the consequence of different packing of neighbor rings: the hottest lobes in **Figure 5** right are found at ca. 8.2 Å for parallel or anti-parallel neighbor rings; however, non-negligible population is detected for perpendicular rings at distances of order of 7 and 10 Å.

Following an analysis approach introduced for the case of ILs by Margulis et al. (Annapureddy et al., 2010; Kashyap et al., 2012, 2013; Hettige et al., 2014; Araque et al., 2015), here we decompose the computed X-ray/neutron diffraction patterns in their components arising from structural correlations between polar and apolar moieties in the samples. While several examples exist of such a decomposition for the case of conventional ILs, where charged moieties and long alkyl tails represent the polar and apolar moieties, respectively, in the present case, similarly to recent analogous situations (Hettige et al., 2014), two different kinds of apolar moieties have been identified: namely, the alkyl and the fluorous tails. Such an approach stems from the quantitative interpretation of the visual situation depicted in **Figure 4**, where polar moieties as well as apolar alkyl and fluorous moieties tend to mutually exclude each other, thus introducing a complex triphilic structural scenario, with

three different classes of nm-scale domains, whose size and mutual distribution determines the experimentally determined diffraction patterns. In the simple case of polar (P) and one (e.g., the alkyl moieties) apolar (A) domains, Margulis' group has shown that a characteristic decomposition can be achieved for the low Q peak, in terms of P-P, A-A, and A-P contributions, the two former terms manifesting into a positive amplitude peak and the latter into a negative amplitude one at the experimental peak position (Annapureddy et al., 2010; Kashyap et al., 2012, 2013; Hettige et al., 2014; Araque et al., 2015). In the case of two different apolar (Aa and Af, where the subscript a and f stand for alkyl and fluorous, respectively) domains coexisting with the polar (P) one, all the different self and distinct contributions should be considered to contribute to the overall experimental pattern (Hettige et al., 2014). **Figure 6** report such decompositions of computed X-ray and neutron diffraction patterns; in the figures, the self-terms P-P (indicated therein as P), Aa-Aa (indicated therein as Aa), and Af-Af (indicated therein as Af) are shown together with the summation of the different distinct terms P-Aa, P-Af, Aa-Af (the combination of the latter terms being indicated as "cross"): the combination of these contributions leads to the total diffraction pattern. Overall, due to contrast reasons (contrast acts as a scale factor for each contribution and depends on either electron densities or scattering length densities for X-ray and neutron, respectively), the contribution of P/Aa alternation appears evident only in the case of $[C_8 \text{mim}][IM_{14}]$, where a positive amplitude peak is found for Aa-Aa and a negative amplitude one is found for P-Aa, both centered at a position $Q_{P/Aa} \sim 3.5$ nm^{-1}, fingerprinting the existence of the P/Aa alternation and its characteristic size of the order of $2\pi/Q_{P/Aa} \sim 18$ Å. The decomposition of both X-ray and neutron scattering allows detecting in a very clear way the structural alternation P/Af, between polar and fluorous domains. For example in **Figure 7**, the contributions P (Polar-Polar), Af (Af-Af), and cross (P-Af) to X-ray and neutron scattering are shown for $[C_4 \text{mim}][IM_{14}]$. It appears that both in the case of X-ray and neutron scattering, peaks and anti-peaks related to both P-P and Af-Af and P-Af alternations, exist, respectively and fall at a position $Q_{P/Af} \sim 4$ nm^{-1}. It is noteworthy that while in the case of X-ray scattering (**Figure 7** left), the combination of these three contributions essentially vanishes, thus leading to no
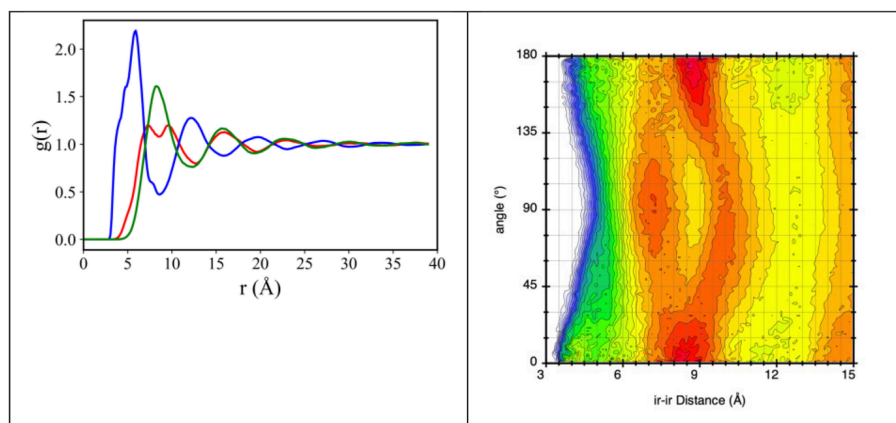
FIGURE 5 | (Left) MD-derived pair distribution functions for ir-ir (red line), ir-N_{anion} (blue line), and N_{anion}-N_{anion} (green line), where ir is the imidazolium ring center of mass and N_{anion} is the anion's nitrogen atom, from MD simulation of [C_2mim][IM_{14}] at ambient conditions. **(Right)** combined distribution function with abscissa the ir-ir distance and ordinate the angle between vector ir-ir and the vector normal to the imidazolium ring, from MD simulation of [C_2mim][IM_{14}] at ambient conditions. The plot explains the two maxima features occurring in the ir-ir pdf between 7 and 11 Å.

net contribution of the P/Af alternation to the total diffraction pattern, on the other hand, in the case of neutron scattering, the combination of the three terms leads to an overall non-zero contribution, that results into the low Q peak observed in the experimental neutron scattering data set (see **Figures 1**, **2**).

An estimation of the degree of clustering of both alkyl and perfluoroalkyl tails can be also be obtained by monitoring the sizes of the clusters of such moieties. Using an approach developed by Bernardes et al. (2011, 2014), Shimizu et al. (2014) we analyzed our MD trajectories using the AGGREGATES software made available by Bernardes (2017) We considered CH_2/CH_3 moieties as belonging to an alkyl domain when neighbor carbon atoms were 5 Å apart, while we considered CF_2/CF_3 groups belonging to a fluorous domain when neighbor carbon atoms were 6 Å apart (Shimizu et al., 2017). Under these conditions, we monitored the tendency of both alkyl and fluorous chains to segregate into clusters. **Figure 8** shows the trends observed for the dependence of (alkyl or fluorous) aggregates distribution sizes on the alkyl side chain length. It can be noticed that alkyl tails tend to form limited size clusters for the case of [$C_n$mim][IM_{14}] with $n = 2$ and 4 (clusters containing up to ∼10 and ∼30 methyl groups, respectively), while in [C_8mim][IM_{14}], octyl chains tend to percolate, as the size of aggregates reaches ∼700 (representing the total number of anions present in the simulation box). Accordingly a gradual transition from finite size to percolating clusters is observed. In the case of anion's perfluorobutyl chains, [$C_n$mim][IM_{14}] with $n = 2$ and 4 show percolating nature of the chains clusters, while, in the case of [C_8mim][IM_{14}] a finite size distribution with maximum size of ∼25 members is found, indicating also in this case the existence of a gradual transition from finite size to percolating clusters, though, with opposite trend with respect to n. When alkyl tails form finite size clusters, perfluorobutyl chain succeed in percolating the simulating box and, vice versa, when the latter chains form only finite clusters, it will be the alkyl chains that will percolate across the simulation box. Recently [$C_n$mim]-based

FILs with a fluorous anion have been simulated by Canongia-Lopes et al. (Pereiro et al., 2013b; Vieira et al., 2015; Ferreira et al., 2017; Shimizu et al., 2017). They found a behavior that is nice agreement with the present observations: while monitoring the aggregates detected in [$C_n$mim][$C_4F_9SO_3$], they also found that by increasing the side alkyl chain length of the cation, the alkyl domains tend to grow in size until they eventually percolate and this process is inverse in trend to the one observed for the fluorous domains sizes that instead decrease from the percolating regime to finite size clusters. Herein, on the basis of experimental results, supported by MD simulations, we further (Lo Celso et al., 2017, 2018b) validate this proposal.

Main Relaxation Process

We aim now at providing a preliminary description of relaxation phenomena occurring in selected [$C_n$mim][IM_{14}] ILs, on the basis of experimental data. The nature of relaxation processes occurring in both [C_2mim][IM_{14}] and [C_8mim][IM_{14}] has been explored using a range of techniques. **Figure 9** reports dielectric spectroscopy data collected for [C_2mim][IM_{14}] in the form of isochronal temperature dependence of the imaginary part of the electrical modulus, M″. This formalism is commonly used when dealing with conducting samples, as it allows suppressing the contribution from conductivity and detecting the main α process. The latter process is generally associated to diffusive dynamics in glass formers and has equivalent signatures when monitored with other complementary techniques, such as viscosity or conductivity. In this case it is customary to account for the overall temperature dependence of the process by using the time/temperature superposition (tTS) that would provide a complete picture of the relaxation map of the chosen material. In **Figure 10**, we then report the relaxation map built up by the merging of different experimental data sets obtained for the case of [C_2mim][IM_{14}] as well as [C_8mim][IM_{14}]. While a more extended interpretation of these experimental results will be presented elsewhere, here we compare data arising
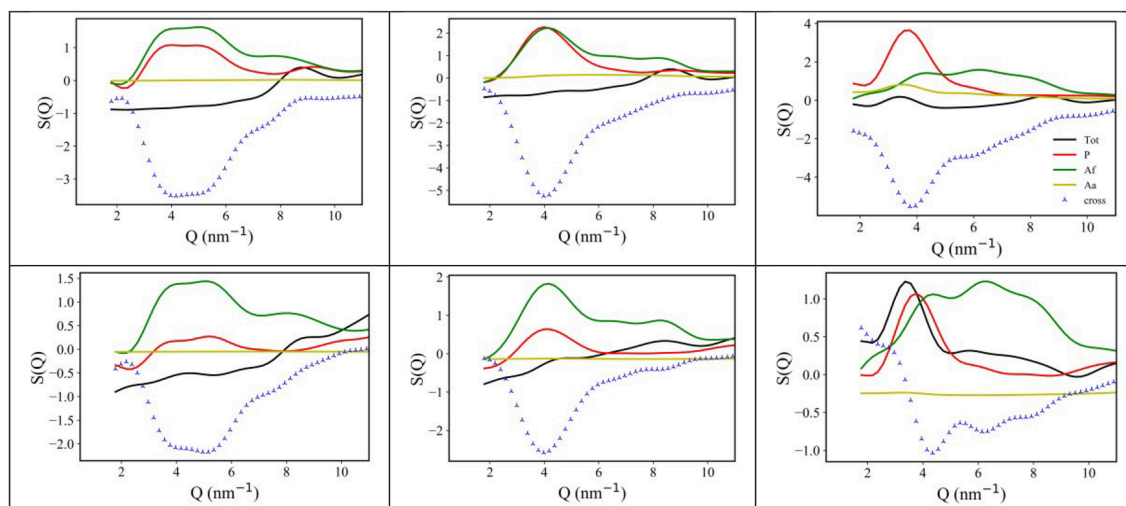
FIGURE 6 | **(Top)** X-ray MD-computed diffraction patterns for [$C_n$mim][IM$_{14}$], with $n = 2, 4, 8$ (left, center, and right, respectively) and their decomposition into polar-polar (P), alkyl-alkyl (Aa), 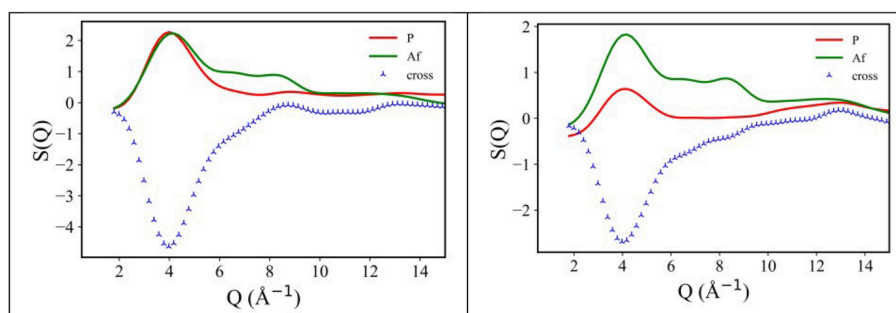and fluorous-fluorous (Af-Af), total and cross terms; **(Bottom)** neutron MD-computed diffraction patterns for [$C_n$mim][IM$_{14}$], with $n = 2, 4, 8$ (left, center, and right, respectively) and their decomposition into polar-polar (P), alkyl-alkyl (Aa), and fluorous-fluorous (Af), total and cross terms.

FIGURE 7 | X-ray **(Left)** and neutron **(Right)** MD-computed diffraction patterns decomposition into polar-polar (P), fluorous-fluorous (Af), and polar-fluorous (cross) terms, for [C_4mim][IM$_{14}$] at ambient conditions.
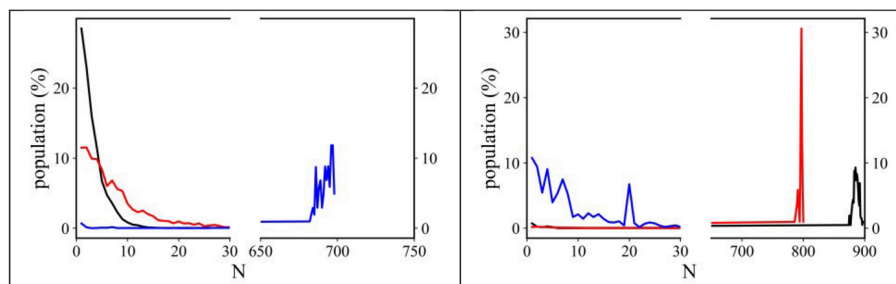
FIGURE 8 | Normalized distribution functions for the alkyl **(Left)** and fluorous **(Right)** domain sizes from MD simulations of [$C_n$mim][IM$_{14}$] ($n = 2, 4, 8$, black, red, and blue, respectively) at ambient conditions. The highest value of the abscissa corresponds to the number of ion pairs contained in the simulation boxes.

from the above mentioned dielectric spectroscopy experiment, from previously published (Appetecchi et al., 2011) and new (this work) viscosity experiments. Using the tTS approach, data referring to the viscosities of the two ILs are combined with

the characteristic times extracted from the M'' data sets (once properly vertically scaled) and are jointly modeled in terms of a Vogel-Fulcher-Tamman (VFT) temperature dependence (Fulcher, 1925; Tammann and Hesse, 1926): $\log x = \log$
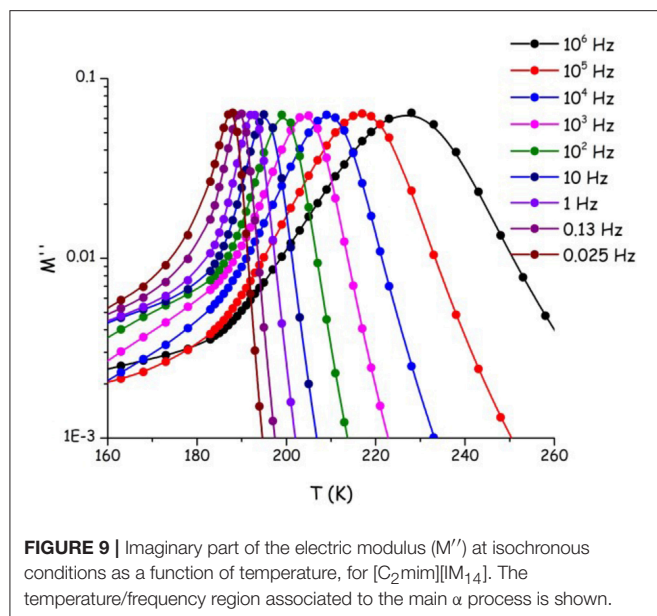
FIGURE 9 | Imaginary part of the electric modulus (M″) at isochronous conditions as a function of temperature, for [C$_2$mim][IM$_{14}$]. The temperature/frequency region associated to the main α process is shown.
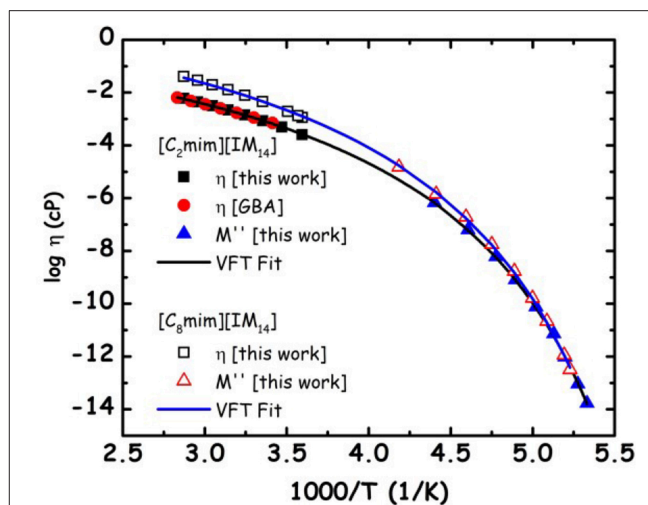
FIGURE 10 | Relaxation map for the primary α-process for [C$_2$mim][IM$_{14}$] and [C$_8$mim][IM$_{14}$]. Viscosity data obtained in the present work and from the literature [GBA refers to Appetecchi et al. (2011)] and characteristic times from the imaginary part of the electrical modulus, M″, are reported. The latter data sets have been vertically shifted in the logarithmic scale, taking advantage of the tTS that applies when dealing with different techniques probing the same relaxation process. Lines refer to the VFT fitting of the experimental data sets.

x$_o$+B/(T−T$_o$), where x refers to a given quantity (e.g., viscosity, relaxation time etc.), x$_o$, B, and T$_o$ are fitting parameters, accounting for the temperature dependence of the observed property. The VFT formalism nicely accounts for the divergence of diffusion-related quantities (viscosity and characteristic time for the main α-process in the dielectric spectrum), when approaching the glass transition. The dielectric data sets indicate that characteristic times of 100 s are reached at 187 and 190 K for [C$_2$mim][IM$_{14}$] and [C$_8$mim][IM$_{14}$], respectively. These are then considered to be the dielectric glass transitions (T$_{g,diel}$) for these compounds. On the basis of the VFT fitting parameters and the obtained T$_{g,diel}$'s, one can derive the corresponding fragility indexes (Angell, 1985, 1991; Böhmer and Angell, 1992; Böhmer et al., 1993), after: m = B/ln(10) T$_g$/(T$_g$−T$_o$)^2: we obtain then values of 84 and 76 for [C$_2$mim][IM$_{14}$]'s and [C$_8$mim][IM$_{14}$]'s fragilities, respectively. These are relatively large values for the fragility index and reflect some degree of fragility in this class of compounds [the larger m, the more fragile is the compound, according to the definition proposed by Angell (1985, 1991), Böhmer and Angell (1992), Böhmer et al. (1993). The trend toward decreasing fragility (m) upon increasing alkyl chain length in ILs has been shown elsewhere, e.g., Sippel et al. (2015), Leys et al. (2008), Tao et al. (2017), where m values for a series of [C$_n$mim]-based ILs with [BF$_4$] and [PF$_6$] anions have been reported and its relevance for energy applications highlighted.

CONCLUSION

Here we have reported a detailed characterization of the triphilic nature of morphology in a series of imidazolium based ILs bearing a fluorinated anion. In particular samples with an alkyl chain in the cation and a perfluorobutyl moiety in the anion have been investigated. The synergic exploitation of complementary scattering techniques and Molecular Dynamics

simulations allows extracting precise structural information at atomistic level. The complementarity of X-ray and neutron scattering is crucial to assess a specific feature of this class of FILs: It is clear that due to contrast reasons, X-ray scattering can detect only the existence of segregated clusters formed by alkyl chains. Neutron scattering instead allows detection of the existence of both alkyl and perfluoro alkyl segregated domains. Our careful MD simulations were able to accurately reproduce this behavior as well as the whole experimental data sets. Complementary approaches based on either diffraction pattern decomposition or aggregates analysis allowed to quantify the extent of (alkyl or perfluoroalkyl) chains clustering: upon increasing the alkyl chain length a complex transition from small to percolating alkyl chain clusters is observed; such a transition develops simultaneously with the inverse transition from percolating to small perfluoroalkyl chains clusters.

We also accounted for experimental determination of the diffusion related relaxation process for the case of [C$_2$mim][IM$_{14}$] and [C$_8$mim][IM$_{14}$], by determining their relaxation map and the fragility index, indicating their fragile behavior.

AUTHOR CONTRIBUTIONS

FLC developed MD simulations. GA and ES synthetized and characterized samples. MZ and EC executed viscosity and NMR measurements. UK, AT, and OR executed SANS experiments. AT and OR executed x-ray/neutron experiments. FLC, GA, EC, AT, and OR discussed the results. FLC,

SUPPLEMENTARY MATERIAL

The Supplementary Material for this article can be found online at: https://www.frontiersin.org/articles/10.3389/fchem.2019.00285/full#supplementary-material

REFERENCES

Almantariotis, D., Gefflaut, T., Pádua, A. A. H., Coxam, J.-Y., and Costa Gomes, M. F. (2010). Effect of fluorination and size of the Alkyl side-chain on the solubility of carbon dioxide in 1-alkyl-3-methylimidazolium Bis(Trifluoromethylsulfonyl)Amide ionic liquids. *J. Phys. Chem. B* 114, 3608–3617. doi: 10.1021/jp912176n

Almantariotis, D., Pensado, A. S., Gunaratne, H. Q. N. N., Hardacre, C., Pádua, A. A. H. H., Coxam, J.-Y., et al. (2017). Influence of fluorination on the solubilities of carbon dioxide, ethane, and nitrogen in 1- n -fluoro-alkyl-3-methylimidazolium Bis(n -Fluoroalkylsulfonyl)Amide ionic liquids. *J. Phys. Chem. B* 121, 426–436. doi: 10.1021/acs.jpcb.6b10301

Angell, C. (1991). Relaxation in liquids, polymers and plastic crystals — strong/fragile patterns and problems. *J. Non. Cryst. Solids* 131–133, 13–31. doi: 10.1016/0022-3093(91)90266-9

Angell, C. A. (1985). Spectroscopy simulation and scattering, and the medium range order problem in glass. *J. Non. Cryst. Solids* 73, 1–17. doi: 10.1016/0022-3093(85)90334-5

Annapureddy, H. V. R., Kashyap, H. K., De Biase, P. M., and Margulis, C. J. (2010). What is the origin of the prepeak in the X-ray scattering of imidazolium-based room-temperature ionic liquids? *J. Phys. Chem. B* 114, 16838–16846. doi: 10.1021/jp108545z

Aoun, B., Goldbach, A., Kohara, S., Wax, J.-F., Gonzalez, M. A., and Saboungi, M.-L. (2010). Structure of a prototypic ionic liquid: ethyl-methylimidazolium bromide. *J. Phys. Chem. B* 114, 12623–12628. doi: 10.1021/jp1070715

Appetecchi, G. B., Montanino, M., Carewska, M., Moreno, M., Alessandrini, F., and Passerini, S. (2011). Chemical–physical properties of Bis(Perfluoroalkylsulfonyl)Imide-based ionic liquids. *Electrochim. Acta* 56, 1300–1307. doi: 10.1016/j.electacta.2010.10.023

Araque, J. C., Hettige, J. J., and Margulis, C. J. (2015). Modern room temperature ionic liquids a simple guide to understanding their structure and how it may relate to dynamics. *J. Phys. Chem. B* 119, 12727–12740. doi: 10.1021/acs.jpcb.5b05506

Atkin, R., and Warr, G. G. (2008). The smallest amphiphiles: nanostructure in protic room-temperature ionic liquids with short alkyl groups. *J. Phys. Chem. B* 112, 4164–4166. doi: 10.1021/jp801190u

Bastos, J. C., Carvalho, S. F., Welton, T., Canongia Lopes, J. N., Rebelo, L. P. N., Shimizu, K., et al. (2018). Design of task-specific fluorinated ionic liquids: nanosegregation: versus hydrogen-bonding ability in aqueous solutions. *Chem. Commun.* 54, 3524–3527. doi: 10.1039/C8CC00361K

Bernardes, C. E. S. (2017). AGGREGATES: finding structures in simulation results of solutions. *J. Comput. Chem.* 38, 753–765. doi: 10.1002/jcc.24735

Bernardes, C. E. S., and Joseph, A. (2015). Evaluation of the OPLS-AA force field for the study of structural and energetic aspects of molecular organic crystals. *J. Phys. Chem. A* 119, 3023–3034. doi: 10.1021/jp512349r

Bernardes, C. E. S., Minas da Piedade, M. E., and Canongia Lopes, J. N. (2011). The structure of aqueous solutions of a hydrophilic ionic liquid: the full concentration range of 1-ethyl-3-methylimidazolium ethylsulfate and water. *J. Phys. Chem. B* 115, 2067–2074. doi: 10.1021/jp1113202

Bernardes, C. E. S., Shimizu, K., Lobo Ferreira, A. I. M. C., Santos, L. M. N. B. F., and Canongia Lopes, J. N. (2014). Structure and aggregation in the 1,3-dialkyl-imidazolium Bis(Trifluoromethylsulfonyl)Imide ionic liquid family: 2. From single to double long alkyl side chains. *J. Phys. Chem. B* 118, 6885–6895. doi: 10.1021/jp502968u

Böhmer, R., and Angell, C. A. (1992). Correlations of the nonexponentiality and state dependence of mechanical relaxations with bond connectivity in Ge-As-Se supercooled liquids. *Phys. Rev. B* 45, 10091–10094. doi: 10.1103/PhysRevB.45.10091

Böhmer, R., Ngai, K. L., Angell, C. A., and Plazek, D. J. (1993). Nonexponential relaxations in strong and fragile glass formers. *J. Chem. Phys.* 99, 4201–4209. doi: 10.1063/1.466117

Brehm, M., and Kirchner, B. (2011). TRAVIS - a free analyzer and visualizer for monte carlo and molecular dynamics trajectories. *J. Chem. Inf. Model.* 51, 2007–2023. doi: 10.1021/ci200217w

Brehm, M., Weber, H., Thomas, M., Hollóczki, O., and Kirchner, B. (2015). Domain analysis in nanostructured liquids: a post-molecular dynamics study at the example of ionic liquids. *Chem. Phys. Chem.* 16, 3271–3277. doi: 10.1002/cphc.201500471

Bussi, G., Donadio, D., and Parrinello, M. (2007). Canonical sampling through velocity rescaling. *J. Chem. Phys.* 126:014101. doi: 10.1063/1.2408420

Canongia Lopes, J. N., Costa Gomes, M. F., and Pádua, A. A. H. (2006). Nonpolar, polar, and associating solutes in ionic liquids. *J. Phys. Chem. B* 110, 16816–16818. doi: 10.1021/jp063603r

Canongia Lopes, J. N., and Padua, A. A. H. (2006). Nanostructural organization in ionic liquids. *J. Phys. Chem. B* 110:3330–3335. doi: 10.1021/jp056006y

Castiglione, F., Famulari, A., Raos, G., Meille, S. V., Mele, A., Appetecchi, G. B., et al. (2014). Pyrrolidinium-based ionic liquids doped with lithium salts: how does Li+coordination affect its diffusivity? *J. Phys. Chem. B* 118, 13679–13688. doi: 10.1021/jp509387r

Cromer, D. T. (1969). Compton scattering factors for aspherical free atoms. *J. Chem. Phys.* 50, 4857–4859. doi: 10.1063/1.1670980

Darden, T., York, D., and Pedersen, L. (1993). Particle mesh ewald: an N·log(N) method for ewald sums in large systems. *J. Chem. Phys.* 98, 10089–10092. doi: 10.1063/1.464397

Essmann, U., Perera, L., Berkowitz, M. L., Darden, T., Lee, H., and Pedersen, L. G. (1995). A smooth particle mesh ewald method. *J. Chem. Phys.* 103, 8577–8593. doi: 10.1063/1.470117

Ferreira, M. L., Pastoriza-Gallego, M. J., Araújo, J. M. M., Canongia Lopes, J. N., Rebelo, L. P. N. M., Piñeiro, M., et al. (2017). Influence of nanosegregation on the phase behavior of fluorinated ionic liquids. *J. Phys. Chem. C* 121, 5415–5427. doi: 10.1021/acs.jpcc.7b00516

Fulcher, G. S. (1925). Analysis of recent measurements of the viscosity of glasses. *J. Am. Ceram. Soc.* 8, 339–355. doi: 10.1111/j.1151-2916.1925.tb16731.x

Funston, A. M., Fadeeva, T. A., Wishart, J. F., and Castner, E. W. (2007). Fluorescence probing of temperature-dependent dynamics and friction in ionic liquid local environments. *J. Phys. Chem. B* 111, 4963–4977. doi: 10.1021/jp068298o

Gilles, R., Keiderling, U., Strunz, P., Wiedenmann, A., and Fuess, H. (2000). Silver behenate as a standard for instrumental resolution and wavelength calibration for small angle neutron scattering. *Mater. Sci. Forum* 321–323, 264–269. doi: 10.4028/www.scientific.net/MSF.321-324.264

Greaves, T. L., Kennedy, D. F., Shen, Y., Hawley, A., Song, G., and Drummond, C. J. (2013). Fluorous protic ionic liquids exhibit discrete segregated nano-scale solvent domains and form new populations of nano-scale objects upon primary alcohol addition. *Phys. Chem. Chem. Phys.* 15, 7592–7598. doi: 10.1039/c3cp44589e

Hammersley, A. P., Svensson, S. O., Hanfland, M., Fitch, A. N., and Hausermann, D. (1996). Two-dimensional detector software: from real detector to idealised image or two-theta scan. *High Press. Res.* 14, 235–248. doi: 10.1080/08957959608201408

Harris, K. R. (2009). The fractional stokes–einstein equation: application to lennard-jones, molecular, and ionic liquids. *J. Chem. Phys.* 131:054503. doi: 10.1063/1.3183951

Hayes, R., Imberti, S., Warr, G. G., and Atkin, R. (2011). Amphiphilicity determines nanostructure in protic ionic liquids. *Phys. Chem. Chem. Phys.* 13, 3237–3247. doi: 10.1039/C0CP01137A

Hess, B., Kutzner, C., Van Der Spoel, D., and Lindahl, E. (2008). GRGMACS 4: algorithms for highly efficient, load-balanced, and scalable molecular simulation. *J. Chem. Theory Comput.* 4, 435–447. doi: 10.1021/ct700301q

Hettige, J. J., Araque, J. C., and Margulis, C. J. (2014). Bicontinuity and multiple length scale ordering in triphilic hydrogen-bonding ionic liquids. *J. Phys. Chem. B* 118, 12706–12716. doi: 10.1021/jp5068457

Hollóczki, O., Macchiagodena, M., Weber, H., Thomas, M., Brehm, M., Stark, A., et al. (2015). Triphilic ionic-liquid mixtures: fluorinated and non-fluorinated aprotic ionic-liquid mixtures. *Chem. Phys. Chem.* 16, 3325–3333. doi: 10.1002/cphc.201500473

Hunter, J. D. (2007). Matplotlib: a 2D graphics environment. *Comput. Sci. Eng.* 9, 90–95. doi: 10.1109/MCSE.2007.55

Jeremias, S., Carewska, M., Conte, L., Passerini, S., and Appetecchi, G. B. (2013). Asymmetry effect of novel per(Fluoroalkylsulfonyl)Imide anions in pyrrolidinium ionic liquids. *RSC Adv.* 3:17755. doi: 10.1039/c3ra42980f

Johansson, P., Fast, L. E., Matic, A., Appetecchi, G. B., and Passerini, S. (2010). The conductivity of pyrrolidinium and sulfonylimide-based ionic liquids: a combined experimental and computational study. *J. Power Sources* 195, 2074–2076. doi: 10.1016/j.jpowsour.2009.10.029

Kashyap, H. K., Hettige, J. J., Annapureddy, H. V. R., and Margulis, C. J. (2012). SAXS anti-peaks reveal the length-scales of dual positive-negative and polar-apolar ordering in room-temperature ionic liquids. *Chem. Commun.* 48, 5103–5105. doi: 10.1039/c2cc30609c

Kashyap, H. K., Santos, C. S., Daly, R. P., Hettige, J. J., Murthy, N. S., Shirota, H., et al. (2013). How does the ionic liquid organizational landscape change when nonpolar cationic alkyl groups are replaced by polar isoelectronic diethers? *J. Phys. Chem. B* 117, 1130–1135. doi: 10.1021/jp311032p

Keiderling, U. (2002). The new "BerSANS-PC" software for reduction and treatment of small angle neutron scattering data. *Appl. Phys. A Mater. Sci. Process.* 74, s1455–s1457. doi: 10.1007/s003390201561

Keiderling, U., and Wiedenmann, A. (1995). New SANS instrument at the BER II reactor in Berlin, Germany. *Phys. B* 213–214, 895–897. doi: 10.1016/0921-4526(95)00316-2

Kim, J., Singh, R. P., and Shreeve, J. M. (2004). Low melting inorganic salts of alkyl-, fluoroalkyl-, alkyl ether-, and fluoroalkyl ether-substituted oxazolidine and morpholine. *Inorg. Chem.* 43, 2960–2966. doi: 10.1021/ic049916n

Kohara, S., Suzuya, K., Kashihara, Y., Matsumoto, N., Umesaki, N., and Sakai, I. (2001). A horizontal two-axis diffractometer for high-energy X-ray diffraction using synchrotron radiation on bending magnet beamline BL04B2 at SPring-8. *Nucl. Instruments Methods Phys. Res. Sect. A Accel. Spectrometers Detect. Assoc. Equip.* 467–468, 1030–1033. doi: 10.1016/S0168-9002(01)00630-1

Kunze, M., Paillard, E., Jeong, S., Appetecchi, G. B., Sch, M., Winter, M., et al. (2011). Inhibition of self-aggregation in ionic liquid electrolytes for high-energy electrochemical devices. *J. Phys. Chem. C* 115, 19431–19436. doi: 10.1021/jp2055969

Leys, J., Wübbenhorst, M., Preethy Menon, C., Rajesh, R., Thoen, J., Glorieux, C., et al. (2008). Temperature dependence of the electrical conductivity of imidazolium ionic liquids. *J. Chem. Phys.* 128:064509. doi: 10.1063/1.2827462

Li, S., Bañuelos, J. L., Guo, J., Anovitz, L., Rother, G., Shaw, R. W., et al. (2012). Alkyl chain length and temperature effects on structural properties of pyrrolidinium-based ionic liquids: a combined atomistic simulation and small-angle X-ray scattering study. *J. Phys. Chem. Lett.* 3, 125–130. doi: 10.1021/jz2013209

Liang, M., Khatun, S., and Castner, E. W. (2015). Communication: unusual structure and transport in ionic liquid-hexane mixtures. *J. Chem. Phys.* 142, 12–16. doi: 10.1063/1.4916388

Lo Celso, F., Appetecchi, G. B., Jafta, C. J., Gontrani, L., Canongia Lopes, J. N., Triolo, A., et al. (2018a). Nanoscale organization in the fluorinated room temperature ionic liquid: tetraethyl ammonium (Trifluoromethanesulfonyl)(Nonafluorobutylsulfonyl)Imide. *J. Chem. Phys.* 148:193816. doi: 10.1063/1.5016236

Lo Celso, F., Yoshida, Y., Castiglione, F., Ferro, M., Mele, A., Jafta, C. J., et al. (2017). Direct experimental observation of mesoscopic fluorous domains in fluorinated room temperature ionic liquids. *Phys. Chem. Chem. Phys.* 19, 13101–13110. doi: 10.1039/C7CP01971H

Lo Celso, F., Yoshida, Y., Lombardo, R., Jafta, C., Gontrani, L., Triolo, A., et al. (2018b). Mesoscopic structural organization in fluorinated room temperature ionic liquids. *Comptes Rendus Chim.* 21, 757–770. doi: 10.1016/j.crci.2018.02.001

Lopes, J. N. C., and Padua, A. A. H. (2004). Molecular force field for ionic liquids composed of triflate or bistriflyimide anions. *J. Phys. Chem. B* 108, 16893–16898. doi: 10.1021/jp0476545

Macchiagodena, M., Ramondo, F., Triolo, A., Gontrani, L., and Caminiti, R. (2012). Liquid structure of 1-ethyl-3-methylimidazolium alkyl sulfates by X-ray scattering and molecular dynamics. *J. Phys. Chem. B* 116, 13448–13458. doi: 10.1021/jp306982e

Mariani, A., Bonomo, M., Wu, B., Centrella, B., Dini, D., Castner, E. W., et al. (2017). Intriguing transport dynamics of ethylammonium nitrate-acetonitrile binary mixtures arising from nano-inhomogeneity. *Phys. Chem. Chem. Phys.* 19, 27212–27220. doi: 10.1039/C7CP04592A

Merrigan, T. L., Bates, E. D., Dorman, S. C., and Davis, J. H. (2000). New fluorous ionic liquids function as surfactants in conventional room-temperature ionic liquids. *Chem. Commun.* 2051–2052. doi: 10.1039/b005418f

Montanino, M., Alessandrini, F., Passerini, S., and Appetecchi, G. B. (2013). Water-based synthesis of hydrophobic ionic liquids for high-energy electrochemical devices. *Electrochim. Acta* 96, 124–133. doi: 10.1016/j.electacta.2013.02.082

Montanino, M., Moreno, M., Alessandrini, F., Appetecchi, G. B., Passerini, S., Zhou, Q., et al. (2012). Physical and electrochemical properties of binary ionic liquid mixtures: (1–x) PYR14TFSI–(x) PYR14IM14. *Electrochim. Acta* 60, 163–169. doi: 10.1016/j.electacta.2011.11.030

Ohmura, A., Sato, K., Hamaya, N., Isshiki, M., and Ohishi, Y. (2009). Structure of pressure-induced amorphous form of SnI4 at high pressure. *Phys. Rev. B* 80:054201. doi: 10.1103/PhysRevB.80.054201

Pádua, A. A. H., Costa Gomes, M. F., and Canongia Lopes, J. N. A. (2007). Molecular Solutes in Ionic Liquids: A Structural Perspective. *Acc. Chem. Res.* 40, 1087–1096. doi: 10.1021/ar700050q

Palumbo, O., Trequattrini, F., Appetecchi, G. B., and Paolone, A. (2017). A study of the conformers of the (Nonafluorobutanesulfonyl)Imide ion by means of infrared spectroscopy and Density Functional Theory (DFT) calculations. *Challenges* 8:7. doi: 10.3390/challe8010007

Paolone, A., Palumbo, O., Trequattrini, F., and Appetecchi, G. B. (2018). Relaxational dynamics in the PYR14-IM14 ionic liquid by mechanical spectroscopy. *Mater. Res.* 21, 1–6. doi: 10.1590/1980-5373-mr-2017-0870

Parrinello, M., and Rahman, A. (1981). Polymorphic transitions in single crystals: a new molecular dynamics method. *J. Appl. Phys.* 52, 7182–7190. doi: 10.1063/1.328693

Pereiro, A. B., Araújo, J. M. M., Esperança, J. M. S. S., and Rebelo, L. P. N. (2018). "Chapter 4, Surfactant fluorinated ionic liquids," in *RSC Smart Materials*, eds A. Eftekhari, Vol. 2018 (The Royal Society of Chemistry) 79–102. doi: 10.1039/9781788011839-00079

Pereiro, A. B., Araújo, J. M. M., Martinho, S., Alves, F., Nunes, S., Matias, A., et al. (2013a). Fluorinated ionic liquids: properties and applications. *ACS Sustain. Chem. Eng.* 1, 427–439. doi: 10.1021/sc300163n

Pereiro, A. B., Pastoriza-Gallego, M. J., Shimizu, K., Marrucho, I. M., Lopes, J. N. C., Piñeiro, M. M., et al. (2013b). On the formation of a third, nanostructured domain in ionic liquids. *J. Phys. Chem. B* 117, 10826–10833. doi: 10.1021/jp402300c

Qiu, X., Thompson, J. W., and Billinge, S. J. L. (2004). PDFgetX2 : a GUI-driven program to obtain the pair distribution function from X-ray powder diffraction data. *J. Appl. Crystallogr.* 37, 678–678. doi: 10.1107/S0021889804011744

Rauber, D., Zhang, P., Hempelmann, R., and Huch, V. (2017). Lamellar structures in fluorinated phosphonium ionic liquids : the roles of fluorination and chain length. *Phys. Chem. Chem. Phys.* 19, 27251–27258. doi: 10.1039/C7CP04814A

Ren, Y. (2012). High-energy synchrotron X-ray diffraction and its application to *in situ* structural phase-transition studies in complex sample environments. *JOM* 64, 140–149. doi: 10.1007/s11837-011-0218-8

Rocha, M. A. A., Neves, C. M. S. S., Freire, M. G., Russina, O., Triolo, A., Coutinho, J. A. P., et al. (2013). Alkylimidazolium based ionic liquids: impact of cation symmetry on their nanoscale structural organization. *J. Phys. Chem. B* 117, 10889–10897. doi: 10.1021/jp406374a

Russina, O., Lo Celso, F., Di Michiel, M., Passerini, S., Appetecchi, G. B., Castiglione, F., et al. (2013). Mesoscopic structural organization in triphilic room temperature ionic liquids. *Faraday Discuss.* 167, 499–513. doi: 10.1039/c3fd00056g

Russina, O., Lo Celso, F., Plechkova, N., Jafta, C. J., Appetecchi, G. B., and Triolo, A. (2017a). Mesoscopic organization in ionic liquids. *Top. Curr. Chem.* 375:58. doi: 10.1007/s41061-017-0147-2

Russina, O., Lo Celso, F., Plechkova, N. V., and Triolo, A. (2017b). Emerging evidences of mesoscopic-scale complexity in neat ionic liquids and their mixtures. *J. Phys. Chem. Lett.* 8, 1197–1204. doi: 10.1021/acs.jpclett.6b02811

Russina, O., and Triolo, A. (2012). New experimental evidence supporting the mesoscopic segregation model in room temperature ionic liquids. *Faraday Discuss.* 154, 97–109. doi: 10.1039/C1FD00073J

Russina, O., and Triolo, A. (2017). "Ionic liquids and neutron scattering," in *Experimental Methods in the Physical Sciences*, Vol. 49, eds F. Fernandez-Alonso and D. L. Price (Academic Press), 213–278. doi: 10.1016/B978-0-12-805324-9.00004-2

Russina, O., Triolo, A., Gontrani, L., and Caminiti, R. (2012). Mesoscopic structural heterogeneities in room-temperature ionic liquids. *J. Phys. Chem. Lett.* 3, 27–33. doi: 10.1021/jz201349z

Russina, O., Triolo, A., Gontrani, L., Caminiti, R., Xiao, D., Hines Jr., L. G., et al. (2009). Morphology and intermolecular dynamics of 1-alkyl-3-methylimidazolium Bis{(Trifluoromethane)Sulfonyl}amide ionic liquids: structural and dynamic evidence of nanoscale segregation. *J. Phys. Condens. Matter* 21:424121. doi: 10.1088/0953-8984/21/42/424121

Shen, Y., Kennedy, D. F., Greaves, T. L., Weerawardena, A., Mulder, R. J., Kirby, N., et al. (2012). Protic ionic liquids with fluorous anions: physicochemical properties and self-assembly nanostructure. *Phys. Chem. Chem. Phys.* 14, 7981–7992. doi: 10.1039/c2cp40463j

Shimizu, K., Almantariotis, D., Gomes, M. F. C., Pádua, A. A. H., and Canongia Lopes, J. N. (2010). Molecular force field for ionic liquids V: hydroxyethylimidazolium, dimethoxy-2- methylimidazolium, and fluoroalkylimidazolium cations and Bis(Fluorosulfonyl)Amide, perfluoroalkanesulfonylamide, and fluoroalkylfluorophosphate anions. *J. Phys. Chem. B* 114, 3592–3600. doi: 10.1021/jp9120468

Shimizu, K., Bernardes, C. E. S., and Canongia Lopes, J. N. (2014). Structure and aggregation in the 1-alkyl-3-methylimidazolium Bis(Trifluoromethylsulfonyl)Imide ionic liquid homologous series. *J. Phys. Chem. B* 118, 567–576. doi: 10.1021/jp409987d

Shimizu, K., Freitas, A. A., and Canongia Lopes, J. N. (2017). Structural characterization of the [CnC1im][C4F9SO3] ionic liquid series:

alkyl versus perfluoroalkyl side chains. *J. Mol. Liq.* 226, 28–34. doi: 10.1016/j.molliq.2016.08.014

Sippel, P., Lunkenheimer, P., Krohns, S., Thoms, E., and Loidl, A. (2015). Importance of liquid fragility for energy applications of ionic liquids. *Sci. Rep.* 5:13922. doi: 10.1038/srep13922

Smith, G. D., Borodin, O., Magda, J. J., Boyd, R. H., Wang, Y., Bara, J. E., et al. (2010). A comparison of fluoroalkyl-derivatized imidazolium:TFSI and Alkyl-derivatized imidazolium:TFSI ionic liquids: a molecular dynamics simulation study. *Phys. Chem. Chem. Phys.* 12, 7064–7076. doi: 10.1039/c001387k

Song, X., Hamano, H., Minofar, B., Kanzaki, R., Fujii, K., Kameda, Y., et al. (2012). Structural heterogeneity and unique distorted hydrogen bonding in primary ammonium nitrate ionic liquids studied by high-energy X-ray diffraction experiments and MD simulations. *J. Phys. Chem. B* 116, 2801–2813. doi: 10.1021/jp209561t

Suarez, S. N., Rúa, A., Cuffari, D., Pilar, K., Hatcher, J. L., and Ramati, S. F. (2015). Do TFSA anions slither? Pressure exposes the role of TFSA conformational exchange in self-diffusion. *J. Phys. Chem. B* 119, 14756–14765. doi: 10.1021/acs.jpcb.5b08658

Tammann, G., and Hesse, W. (1926). Die abhängigkeit der viscosität von der temperatur bie unterkühlten flüssigkeiten. *Zeitschrift Anorg. Allg. Chemie* 156, 245–257. doi: 10.1002/zaac.19261560121

Tao, R., Gurung, E., Cetin, M. M., Mayer, M. F., Quitevis, E. L., and Simon, S. L. (2017). Fragility of ionic liquids measured by flash differential scanning calorimetry. *Thermochim. Acta* 654, 121–129. doi: 10.1016/j.tca.2017.05.008

Triolo, A., Russina, O., Bleif, H.-J., and Di Cola, E. (2007). Nanoscale segregation in room temperature ionic liquids. *J. Phys. Chem. B* 111, 4641–4644. doi: 10.1021/jp067705t

Triolo, A., Russina, O., Fazio, B., Appetecchi, G. B., Carewska, M., and Passerini, S. (2009). Nanoscale organization in piperidinium-based room temperature ionic liquids. *J. Chem. Phys.* 130:164521. doi: 10.1063/1.3119977

Triolo, A., Russina, O., Fazio, B., Triolo, R., and Di Cola, E. (2008). Morphology of 1-alkyl-3-methylimidazolium hexafluorophosphate room temperature ionic liquids. *Chem. Phys. Lett.* 457, 362–365. doi: 10.1016/j.cplett.2008.04.027

Tsurumaki, A., and Ohno, H. (2018). Dissolution of Oligo(Tetrafluoroethylene) and preparation of Poly(Tetrafluoroethylene)-based composites by using fluorinated ionic liquids. *Chem. Commun.* 54, 409–412. doi: 10.1039/C7CC08449H

Urahata, S. M., and Ribeiro, M. C. C. (2004). Structure of ionic liquids of 1-alkyl-3-methylimidazolium cations: a systematic computer simulation study. *J. Chem. Phys.* 120, 1855–1863. doi: 10.1063/1.1635356

van den Broeke, J., Winter, F., Deelman, B., and van Koten, G. (2002). A highly fluorous room-temperature ionic liquid exhibiting fluorous biphasic behavior and its use in catalyst recycling. *Org. Lett.* 4, 3851–3854. doi: 10.1021/ol026700l

Van Der Spoel, D., Lindahl, E., Hess, B., Groenhof, G., Mark, A. E., and Berendsen, H. J. C. (2005). GROMACS: fast, flexible, and free. *J. Comput. Chem.* 26, 1701–1718. doi: 10.1002/jcc.20291

Vieira, N. S. M., Reis, P. M., Shimizu, K., Cortes, O. A., Marrucho, I. M., Araújo, J. M. M., et al. (2015). A thermophysical and structural characterization of ionic liquids with alkyl and perfluoroalkyl side chains. *RSC Adv.* 5, 65337–65350. doi: 10.1039/C5RA13869H

Wang, Y., and Voth, G. A. (2005). Unique spatial heterogeneity in ionic liquids. *J. Am. Chem. Soc.* 127, 12192–12193. doi: 10.1021/ja053796g

Wang, Y., and Voth, G. A. (2006). Tail aggregation and domain diffusion in ionic liquids. *J. Phys. Chem. B* 110, 18601–18608. doi: 10.1021/jp063199w

Weber, H., Hollóczki, O., Pensado, A. S., and Kirchner, B. (2013). Side chain fluorination and anion effect on the structure of 1-butyl-3-methylimidazolium ionic liquids. *J. Chem. Phys.* 139:084502. doi: 10.1063/1.4818540

Weiss, H., Mars, J., Li, H., Kircher, G., Ivanova, O., Feoktystov, A., et al. (2017). Mesoscopic correlation functions in heterogeneous ionic liquids. *J. Phys. Chem. B* 121, 620–629. doi: 10.1021/acs.jpcb.6b11220

Wu, B., Liang, M., Maroncelli, M., and Castner, E. W. (2015). Photoinduced bimolecular electron transfer from cyano anions in ionic liquids. *J. Phys. Chem. B* 119, 14790–14799. doi: 10.1021/acs.jpcb.5b09216

Wu, B., Liang, M., Zmich, N., Hatcher, J., Lall-Ramnarine, S. I., Wishart, J. F., et al. (2018). Photoinduced bimolecular electron transfer in ionic liquids: cationic electron donors. *J. Phys. Chem. B* 122, 2379–2388. doi: 10.1021/acs.jpcb.7b12542

Wu, B., Yamashita, Y., Endo, T., Takahashi, K., and Castner, E. W. (2016). Structure and dynamics of ionic liquids: trimethylsilylpropyl-substituted cations and Bis(Sulfonyl)Amide anions. *J. Chem. Phys.* 145:244506. doi: 10.1063/1.4972410

Wu, D. H., Chen, A., and Johnson, C. S. (1995). An improved diffusion-ordered spectroscopy experiment incorporating bipolar-gradient pulses. *J. Magn. Reson. Ser. A* 115, 260–264. doi: 10.1006/jmra.1995.1176

Xue, H., and Shreeve, J. M. (2005). Ionic liquids with fluorine-containing cations. *Eur. J. Inorg. Chem.* 13, 2573–2580. doi: 10.1002/ejic.200500129

Xue, H., Verma, R., and Shreeve, J. M. (2006). Review of ionic liquids with fluorine-containing anions. *J. Fluor. Chem.* 127, 159–176. doi: 10.1016/j.jfluchem.2005.11.007

Yoshida, Y., and Saito, G. (2011). Ionic liquids based on Diethylmethyl(2-Methoxyethyl)Ammonium cations and Bis(Perfluoroalkanesulfonyl)Amide anions: influence of anion structure on liquid properties. *Phys. Chem. Chem. Phys.* 13, 20302–20310. doi: 10.1039/c1cp21783f

Zheng, W., Mohammed, A., Hines, L. G., Xiao, D., Martinez, O. J., Bartsch, R. A., et al. (2011). Effect of cation symmetry on the morphology and physicochemical properties of imidazolium ionic liquids. *J. Phys. Chem. B* 115, 6572–6584. doi: 10.1021/jp1115614

An *ab initio* Study of the Structure and Energetics of Hydrogen Bonding in Ionic Liquids

Kaycee Low, Samuel Y. S. Tan and Ekaterina I. Izgorodina *

Monash Computational Chemistry Group, School of Chemistry, Monash University, Melbourne, VIC, Australia

Unlike typical hydrogen-bonded networks such as water, hydrogen bonded ionic liquids display some unusual characteristics due to the complex interplay of electrostatics, polarization, and dispersion forces in the bulk. Protic ionic liquids in particular contain close-to traditional linear hydrogen bonds that define their physicochemical properties. This work investigates whether hydrogen bonded ionic liquids (HBILs) can be differentiated from aprotic ionic liquids with no linear hydrogen bonds using state-of-the-art *ab initio* calculations. This is achieved through geometry optimizations of a series of single ion pairs of HBILs in the gas phase and an implicit solvent. Using benchmark CCSD(T)/CBS calculations, the electrostatic and dispersion components of the interaction energy of these systems are compared with those of aprotic ionic liquids. The inclusion of the implicit solvent significantly influenced geometries of single ion pairs, with the gas phase shortening the hydrogen bond to reduce electrostatic interactions. HBILs were found to have stronger interactions by at least $100 \, \mathrm{kJ \, mol^{-1}}$ over aprotic ILs, clearly highlighting the electrostatic nature of hydrogen bonding. Geometric and energetic parameters were found to complement each other in determining the extent of hydrogen bonding present in these ionic liquids.

Keywords: ionic liquids, hydrogen bonding, *ab initio*, protic ionic liquids, interaction energy, electrostatics, dispersion

1. INTRODUCTION

Hydrogen bonding, an intermolecular interaction which is crucial to a myriad of chemical systems, is as diverse and varied as it is common. Although easily identifiable in many systems, the modern definition of what constitutes hydrogen bonding is not straightforward. The IUPAC recommend six requirements for hydrogen bonding, which cumulate in the definition, *"an attractive interaction between a hydrogen atom from a molecule or molecular fragment X—H in which X is more electronegative than H, and an atom or a group of atoms in the same or a different molecule, in which there is evidence of bond formation"* (Arunan et al., 2011).

While hydrogen bonding may be quite recognizable, it can be difficult to define— and even harder to quantify (Weinhold and Klein, 2012). Steiner's (Steiner, 2002) review meticulously covered an extensive range of different hydrogen bond manifestations including the energy, charge density, spectroscopic properties, strength (strong, moderate, and weak), directionality (of both the donor and acceptor), and bond lengths. He concluded that the hydrogen bond is *"a complex interaction composed of several constituents that are different in their natures."* This leads to hydrogen bonding affecting *all* components of the total

interaction energy, and not simply electrostatics, induction, and exchange. Since hydrogen bonding is a very broad phenomenon, it cannot be strictly contained, but instead transitions and merges into other effects.

One of the quintessential examples of hydrogen bonding, the hydrogen bonded network in water, is largely driven by electrostatics and polarization effects (Lee and Rick, 2011). Other examples, such as Watson-Crick hydrogen bonding in DNA are electrostatic in nature (with significant charge transfer), and others may still be dispersion driven, such as the CH...π bond interactions in benzene crystals (Aida, 1988; Perutz, 1993). Hydrogen bond systems are traditionally defined as an interaction of the type: A...H−D, where H is the hydrogen atom, A is the acceptor, and D is the donor. H is bonded covalently to a donor atom, which is more electronegative than the hydrogen itself. This imbues hydrogen with a slight positive charge, which interacts attractively with the acceptor. According to Steiner, to qualify as a hydrogen bond, this interaction must fulfill two criteria (Steiner, 2002): (1) it is a local bond, and (2) D−H acts as a proton donor to A.

By these conditions, hydrogen bonding occurs in many ionic liquids, especially protic ionic liquids. The fields of both hydrogen bonding and ionic liquids are rich and complex, with significant overlap (Hunt et al., 2015). The characterization of hydrogen bonding in ionic liquids is by no means an easy task, with ionic liquids being a cocktail of manifold interactions. The medley of polar, nonpolar, organic, and inorganic constituents that can be incorporated into ionic liquids result in a complex representation from both electrostatic and dispersion forces present in these compounds, which have been studied from a range of computational viewpoints (Hunt et al., 2006; Bedrov et al., 2010). Dong et al. found that hydrogen bonding is a "major intermolecular structural feature" through DFT calculations of $[C_2mim][BF_4]$ and $[C_4mim][PF_6]$, examples of typical ionic liquids (Dong et al., 2012). Compared to protic ionic liquids, aprotic types are less likely to form directional hydrogen bonds (Stoimenovski et al., 2011). The C2-H bond, which is the most acidic proton on the imidazolium cation, is often involved in these non-directional hydrogen bonds. Conversely, protic ionic liquids, which are formed via a proton transfer reaction from a Brønsted acid to Brønsted base (Greaves et al., 2008; Simons et al., 2016), are more likely to form directional hydrogen bonds. This proton can subsequently be involved in a hydrogen bonding interaction with the anion. *Ab initio* molecular dynamics (AIMD) has been shown as necessary to identify these hydrogen bonds, as there are cases where classical molecular dynamics do not locate them (Maginn, 2007). For example, Del Pópolo, who was the first to run AIMD calculations for ionic liquids, used it to predict the structure of $[C_1mim]Cl$ and model the proton transfer from HCl. Strong in-plane hydrogen bonding with the C2-H bond has been observed in AIMD but not in classical molecular dynamics; further confirmed by Bühl et al. (2005), Del Pópolo et al. (2005), and Bhargava and Balasubramanian (2006).

Our recent review on quantum chemical methods for ionic liquids looked into the nature of hydrogen bonding within these semi-Coulombic systems in a great detail (Izgorodina et al., 2017). No significant energetic differences were found in a series of single ion pairs of aprotic ionic liquids consisting of imidazolium- and pyrrolidinium-based ionic liquids, with the former showing slightly larger dispersion components (Izgorodina and MacFarlane, 2011; Tan and Izgorodina, 2016). In terms of transport properties, the low viscosity of imidazolium ionic liquids has been largely attributed to the hydrogen bonding that occurs between the C2-H hydrogen and the anion (Fumino et al., 2009; Wulf et al., 2010; Dong et al., 2012). These studies have led to suggest that hydrogen bonding in ionic liquids might require a different treatment to typical cation-anion interactions when studied with classical force fields. This has motivated many to develop either different approaches to describing hydrogen bonding in ionic liquids in molecular dynamics force fields, or entirely new force fields solely for ionic liquids (Dommert et al., 2014; McDaniel et al., 2016). Protic ionic liquids in particular have linear hydrogen bonds as observed in their crystal structures (Henderson et al., 2012). Compared to aprotic ionic liquids, these directional hydrogen bonds also make them less viscous and result in higher dielectric constants (Weingärtner, 2014). Some of the hydrogen bonds can form extended hydrogen bonded networks, resulting in high melting points above 100 °C (Stoimenovski et al., 2010).

Regardless of the composition of ionic liquids, it has been established that the ions become strongly polarized in the bulk (Del Pópolo et al., 2005; Prado et al., 2006; Rigby and Izgorodina, 2013; Halat et al., 2017) and therefore, their geometry and energetics is strongly affected by the presence of neighboring ions (Wendler et al., 2011; Pensado et al., 2012). This study seeks to determine whether hydrogen bonding in ionic liquids results in interaction energies that differ from those of typical (i.e., non-specific) inter-ionic interactions. Single ion pairs of protic ionic liquids (PILs) were optimized in both the gas phase and implicit solvent and their energetic parameters were compared with those of archetypical ionic liquids based on imidazolium and pyrrolidinium cations. In addition, interaction energies of PILs in the gas phase and an implicit solvent were decomposed into electrostatic and dispersion components. Although the use of single ion pairs of hydrogen bonded ionic liquids cannot truly encapsulate the complexities of a bulk ionic liquid in which there would be multiple possible particle-particle interactions and various hydrogen bonded geometries, this article aims to provide a broad snapshot of several likely hydrogen bonding interactions that would be present in ionic liquids, and analyze their energetic components without claiming to represent all possible configurations that would be present in a bulk hydrogen bonded ionic liquid. Nevertheless, the obtained data provide an insight into the types of interactions within a hydrogen bonding ionic liquid and are used to comment on the debate whether hydrogen bonded ionic liquid requires special treatment. Equally important, we investigated the use of implicit solvent models to predict hydrogen-bonded structures of ionic liquids—as the gas phase tends to unrealistically reduce the hydrogen bond length between the cation and anion—thus rendering their energetic analysis possible.

2. THEORETICAL PROCEDURES

To study a range of hydrogen bonded ionic liquids with varying ions, the HBIL dataset was created from the following sets of six cations and six anions: dimethylethylammonium (DMEA$^+$), ethylmethylammonium (EtMeNH$_2^+$), ethylammonium (EtNH$_3^+$), trimethylethylammonium (TMEA$^+$), 1-methylimidazolium (mim$^+$) and N-methylpyrrolidinium (mpyr$^+$)—and anions: trifluoroacetate (CF$_3$COO$^-$), trifluoromethyl sulfonate (CF$_3$SO$_3^-$), methylsulfate (CH$_3$SO$_3^-$), methylsulfonate (MeOSO$_3^-$), nitrate (NO$_3^-$), and chloride (Cl$^-$). All cations are protonated on the nitrogen center bases and were chosen as they form protic ionic liquids.

Similar to the previously established IL174 dataset (Rigby and Izgorodina, 2014a), all systems here consist of combinations of a cation and an anion to form a single ion pair with a hydrogen bond between the N−H bond on the cation and an oxygen atom on the anion. Examples of these configurations are given in **Figure 1** for the six different cations and the methylsulfonate anion. In the case of the mim$^+$ and mpyr$^+$ cations, multiple interaction sites are present on the cation (Izgorodina and MacFarlane, 2011; Izgorodina et al., 2011). For example, 1-methylimidazolium can interact with the C2-H bond in the plane of the ring, or above the ring. These configurations form a subset of the HBIL dataset, and their analysis is included separately from the rest of the HBIL set. Some combinations only have one configuration, such as in most chloride systems. All initial geometries were chosen to best reflect energetically preferred ion pair configurations observed in imidazolium- and pyrrolidinium-based ionic liquids (Izgorodina et al., 2014) and maximize the hydrogen bond interaction. In systems were both hydrogen bonded, and non-hydrogen bonded interactions were possible, multiple initial configurations were chosen and optimized. However, the scope of this article is to study several, and not all, possible configurations of single ion pair ionic liquids to give an insight into the different types of energetics and bonding of hydrogen bonded ionic liquids.

Geometry optimizations were performed using the M06-2X functional (Zhao and Truhlar, 2008) and the cc-pVTZ basis set, in both the gas phase and implicit solvent. Ground state geometries were confirmed by frequency calculations indicating no imaginary frequencies present. All optimized structures can be found in the **Supplementary Material**.

The Conductor-like Polarizable Continuum Model (CPCM) (Klamt and Schüürmann, 1993; Barone and Cossi, 1998) was used to model implicit solvent, which was represented by the dielectric constant of ethanol. Ethanol was chosen as the solvent as its dielectric constant is representative of ionic liquids, which usually fall between 10 and 16, and up to 25–50 for protic ionic liquids (Singh and Kumar, 2008; Weingärtner, 2008). Previously we have shown that ethanol was a good model of the ionic liquid bulk for geometry optimizations, (Chen and Izgorodina, 2017) producing already reliable geometries for single ion pairs of aprotic ionic liquids. Geometry optimizations were performed using the Gaussian09 software, and single-point energy calculations were carried out in PSI4 (Frisch et al., 2009; Turney et al., 2012). To calculate and decompose the total interaction energy into its electrostatic and dispersion components, first the electronic energy of the entire ion pair was calculated. The individual electronic energies of the cation and anion were then subtracted from the total energy, leaving behind only the energy of interaction between the cation and anion. Counterpoise-corrected Hartree-Fock energies (HF/aug-cc-pVQZ) energies were used to calculate the electrostatic contribution to the interaction energy, and Halkier's (Halkier et al., 1999) method of extrapolating to the complete basis set (CBS) was applied to MP2 and coupled-cluster results to calculate the correction to the correlation energy [MP2/CBS + ΔCCSD(T)]; giving the contribution from electron-correlated effects, i.e., dispersion. The Boys and Bernardi method were used to calculate counterpoise correction with HF, MP2, and CCSD(T) levels of theory (Boys and Bernardi, 1970). The total CCSD(T)/CBS interaction energy was calculated as follows:

$$E(CCSD(T)/CBS) = E_{HF/aug-cc-pVQZ} + E_{MP2/CBS} \\ + \Delta CCSD(T)/CBS \quad (1)$$

The interaction energy is decomposed into two main components: electrostatic (represented by the HF energy) and dispersion (represented by the CCSD(T)/CBS correlation energy).

3. RESULTS AND DISCUSSION

3.1. Gas and Solvent Phase Geometry Optimizations

Geometry optimizations are frequently done in the gas phase to avoid additional computational costs. For condensed systems— be it liquid or solid—this approach may result in geometries that differ from those found experimentally, such as through X-ray crystallography. This might be particularly evident for systems driven by electrostatic interactions such as protic ionic liquids. This is a result of the gas phase calculations not taking into consideration the stabilizing effect of the surrounding ions, thus producing shorter intermolecular distances (Chen and Izgorodina, 2017). Although this may not pose a problem if the focus of a study is on the *nature* of the intermolecular interaction and less on ideal geometries, there may be times where inadequate geometries are used for purposes that warrant higher accuracy. It is well-known that the gas phase destabilizes electrostatic interactions and therefore seeks to reduce them, usually by favoring the back proton transfer from the cation to the anion in protic ionic liquids, thus forming neutral species. The use of implicit solvent has been demonstrated to lead to more energetically stable complexes of predominantly ionic nature (Mackerell et al., 2004; Chesman et al., 2014). A well-known example is the preference of amino acids to adopt the zwitterionic form in aqueous media, whereas in the gas phase they are optimized to be neutral (Stover et al., 2012). Polar solvent molecules may interact more strongly with ions and thus shift the balance toward the formation of charged species. In the gas phase, this does not occur as no additional stabilization is available for charge-separated ions.
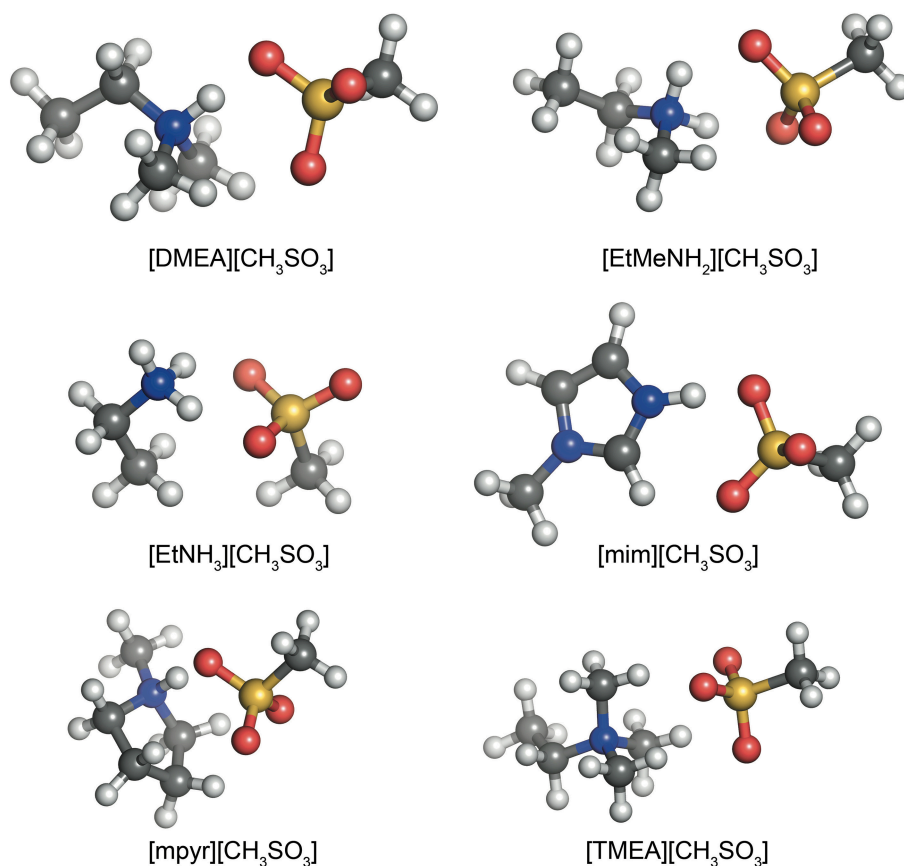
FIGURE 1 | The various cations in the HBIL dataset, paired with the methylsuphonate anion.
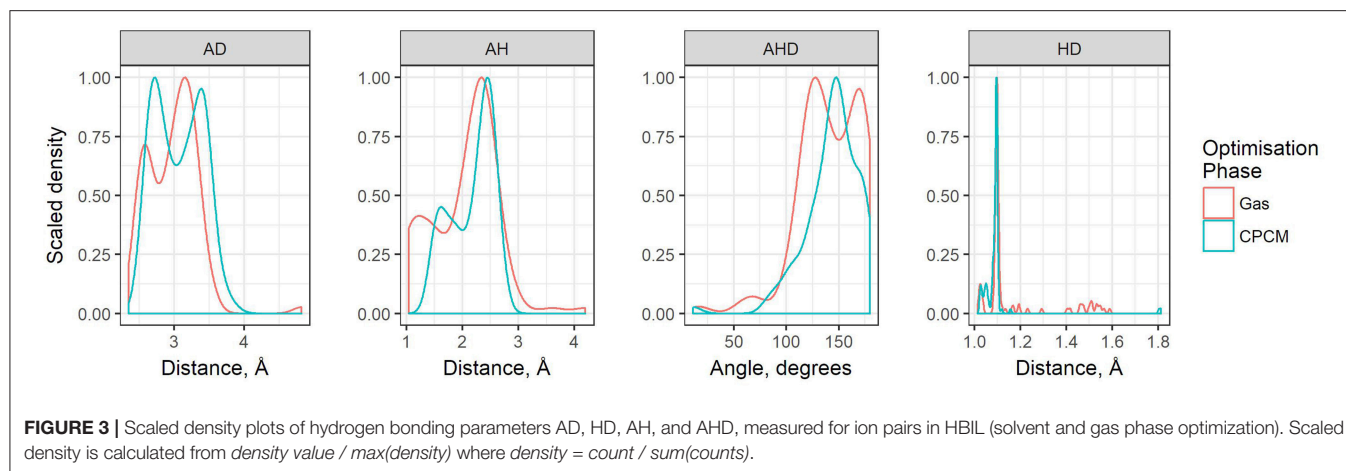
For the purposes of studying differences in geometries optimized in the gas phase and implicit solvent, the hydrogen bonded ionic liquids dataset (further in the text referred to as the HBIL dataset) were optimized under both conditions, using the same starting geometries. These were constructed with a linear hydrogen bond between the N-H bond on the cation and an electronegative atom (such as oxygen) on the anion. Some systems had more than one ion-pair configuration to reflect the different potential interactions possible, such as the chloride ion interacting either in-plane or above the plane of the imidazolium cation. The latter configuration does not have hydrogen bonding between the ions but is a known configuration in these systems (Izgorodina and MacFarlane, 2011).

This section discusses the geometries resulting from both the gas phase and implicit solvent optimizations, their differences, and significance. Further in the text, the following notation is used. D denotes the donor atom (which "donates" the hydrogen to the electronegative atom), and A, the acceptor atom as shown in **Figure 2**. Possible acceptor atoms consisted of either oxygen or chlorine, and possible donor atoms were either carbon or nitrogen. A hydrogen bond system, A...H−D, is defined by any three of the following four parameters: the hydrogen bond distance (AH), the length of the hydrogen donor bond (HD), the distance from the acceptor to the donor (AD), and the

FIGURE 2 | Hydrogen bonding parameters AD, AH, AHD, and HD measured in this study.
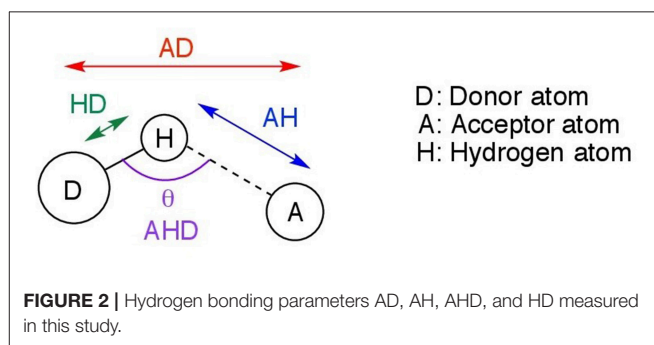
hydrogen bond angle (AHD). All four predicted parameters are discussed below.

The geometric parameters obtained from both modes of optimization is plotted as scaled density plots in **Figure 3**. For the acceptor-donor distance (AD), both distributions are similar in shape, with gas-phase distances shifted to shorter numbers by 1.3 Å on average. This is also seen in the distributions for the hydrogen bond distances, AH. These distances may be up to 0.7 Å longer in implicit solvent for methylpyrrolidinium-based ionic liquids; due to back proton transfer occurring from the anion to cation when optimized in the gas phase (see **Figure 4**). The

FIGURE 3 | Scaled density plots of hydrogen bonding parameters AD, HD, AH, and AHD, measured for ion pairs in HBIL (solvent and gas phase optimization). Scaled density is calculated from *density value / max(density)* where *density = count / sum(counts)*.

second peak in the distribution for AH relates to ionic liquids, for which the back-proton transfer has not occurred in the gas phase. AH tends to be shorter by an average of only 0.1 Å compared to implicit solvent, with good agreement for the methylimidazolium and pyrrolidinium-based cations in particular. Interestingly, for the hydrogen bond angle, AHD, implicit solvent has a peak at 150°, whereas the gas phase distribution is split into two peaks on either side of the solvent one. This suggests that gas phase optimizations tend to be more "extreme," resolving systems into either clearly hydrogen bonded, or not, whereas implicit solvent tends to produce a structure in between. The distance between the hydrogen atom and a donor atom, HD, is a parameter which highlights the difference between the two different optimization modes. While implicit solvent bond lengths fall in a very narrow range, around 1.1 Å, there are several instances of the gas phase HD lengths which vary as much as 1.8 Å. In fact, there are cases optimized in the gas phase where the hydrogen bond length is much longer than that in implicit solvent. One such example is ethylmethylammonium trifluoroacetate (**Figure 4**), whose AH length was found to be 1.06 Å and the HD length—1.53 Å. In implicit solvent, these distances are 1.52 and 1.10 Å respectively. Back proton transfer occurred during the gas phase optimization, thus producing neutral species and disfavoring the formation of a protic ionic liquid. The anions that are more likely to result in the back-proton transfer during gas-phase optimizations are chloride, methylsulfate, trifluoromethylsulfonate, and in some cases trifluoroacetate.

In terms of differences between the gas phase and implicit solvent geometric parameters, gas phase optimizations tend to give shorter AD distances in the majority of cases, though there are some instances where AD is overestimated by more than 0.5 Å. Similarly, the AH distance becomes longer when a solvent model is applied. On the other hand, the HD bond length has smaller deviations relative to the other parameters due to the covalent nature of either the N−H bond or the C−H bond in the case of either TMEA or mim$^+$ cations. This is the reason for why optimizations usually agree on the predicted bond length (except in cases where back proton transfer occurs). For the hydrogen bond angle, agreement between gas and solvent

optimizations are good when the angles are nearly linear (around 175°). However, when implicit solvent optimizations predicted lower bond angles around 150°, gas phase optimizations both over- and under-estimated bond angles. Overestimation tends to happen more for nitrogen donors, though there are exceptions such as [EtMeNH$_2$][MeOSO$_3$], which has an angle of 158° in implicit solvent and 123° in gas phase.

The graph shown in **Figure 5** compares the donor-hydrogen HD bond distance between the gas phase and implicit solvent optimizations. The gas phase parameters are plotted on the vertical axis, whereas the implicit solvent ones on the horizontal axis. Points are colored by the element of the acceptor atom and the shape of the point indicates the element of the donor. The diagonal black line is added as a visual guide only. The better the agreement between the two optimization modes, the closer to the diagonal line the predicted points should fall. As can be seen, two clusters are delineated by the gas phase distances. Implicit solvent bond lengths have a very narrow range, with the vast majority falling between 1 and 1.2 Å, due to the proton transfer from the acid to the base being strongly favored. There are a few outliers involving hydrogen bonds with the chloride anion which have a typical distance of 1.8 Å: this occurs for the bulky quaternary ammonium cation TMEA, as well as the EtNH$_3$ cation. In these cases, the longer bond length indicates the relatively weaker hydrogen-bonding interaction between the chloride and primary or quaternary amine, compared to the secondary amine or imidazolium/pyrrolidinium-based cations.

When an oxygen acceptor is involved (e.g., methylsulfate or nitrate), there is remarkable agreement on the C−H bond length between both optimization modes, with most of its points being tightly clustered on the line. This is expected, as it is usually understood to be a covalent bond. On the other hand, when the hydrogen is attached to a nitrogen donor, the points appear to follow a different trend. They agree for shorter distances, probably due to weaker interactions with the acceptor atom. Gas phase optimizations clearly struggle when the inter-ionic interaction becomes stronger, leading to instances for which the back-proton transfer occurs and hence no anion is formed. Examples of back-protonation include
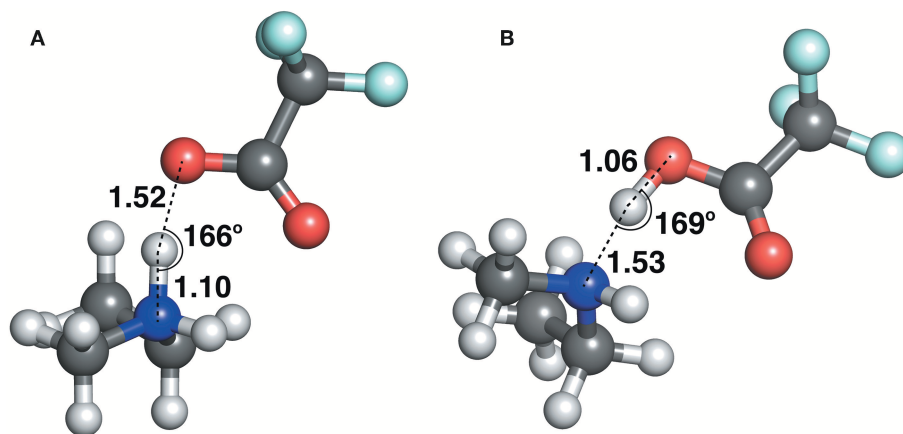
FIGURE 4 | Ethylmethylammonium trifluoroacetate structure, optimized with **(A)** CPCM in ethanol (left) and **(B)** in the gas phase (right).
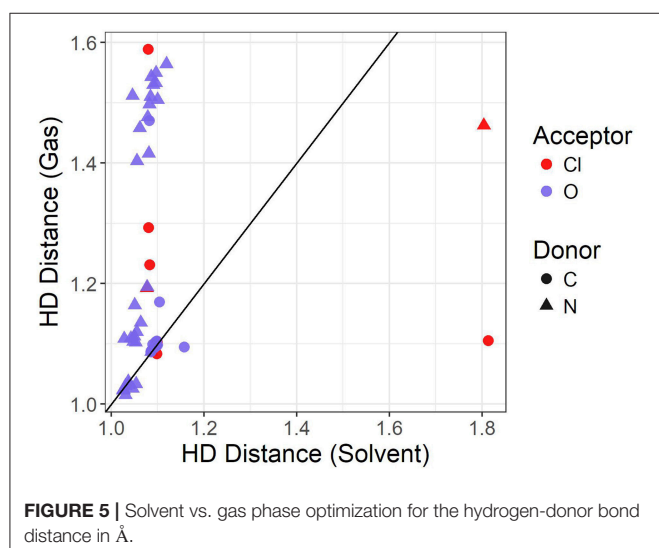

FIGURE 5 | Solvent vs. gas phase optimization for the hydrogen-donor bond distance in Å.

1-methylimidazolium chloride and dimethylethylammonium when coupled with $CH_3SO_3^-$, SO_3^-, TFA, and similarly for 1-methylpyrollidinium with NO_3^- and TFA.

3.1.1. Comparison With Crystal Structures of Similar Ionic Liquids

While data for the particular systems in HBIL have not yet been obtained, it is still insightful to compare experimental data from crystal structures of similar ionic liquids with solvent and gas phase calculations. These can be used to provide a sense of the typical hydrogen bond length in these ionic liquids.

Table 1 presents some available experimental hydrogen bond parameters. At least two interactions are shown for each ionic liquid. Comparing the typical distances and angles obtained through geometry optimizations with those obtained from experimental crystal structures, experimental values fall in a relatively narrow range. For example, the hydrogen bond distance (as defined by AH) ranges from 1.6 to 2.7 Å. All

four hydrogen bonding parameters from both optimization modes are shown in **Table 2**. Comparing the HD distance from geometry optimizations, the gas phase bond lengths are longer, except for the N...Cl donor-acceptor pair. The shorter bond distances for N...O and C...O systems from implicit solvent optimizations agree better with the experimental distances than gas optimizations. Most experimental data indicate that (all but 4) N−H or C−H distances fell below 1 Å, with the longest distance being 1.19 Å. In the optimized HBILs, the longest C−H bond with an O acceptor is 1.2 Å for both gas and CPCM optimizations. Similarly for the N−H bond, the longest distance in implicit solvent is found to be 1.1 or 1.2 Å in the gas phase, showing that both optimization modes have good agreement with experiment for this particular parameter. However, for the hydrogen bond distance parameter, AH, in the C...O systems, the range of experimental distances (1.9–2.6 Å) is much closer to the implicit solvent values (1.5–2.7 Å) compared to the gas phase values (1.5–4.2 Å). For N...O donor-acceptor pairs, the hydrogen bond is stronger than the systems with a carbon donor. This is reflected in the shorter average bond lengths, ranging from 1.6 to 2.5 Å. This is also observed in both optimization modes, but again implicit solvent optimizations (1.5–2.5 Å) tend to fare better than the gas phase ones (1.3–3.6 Å).

Experimental donor-acceptor distances are only available for the C...O and N...O systems. For the C...O cases, experimental values range from 2.7 to 3.4 Å which is closely reflected in the range of implicit solvent donor-acceptor distances of 2.6–3.6 Å. Gas phase has a higher maximum value, ranging from 2.7 to 4.8 Å. Once again, the experimental DA distances for the N...O systems are shorter and closer to the implicit solvent ones.

Hydrogen bond angles are an important indicator of hydrogen bonding, since directionality is a well-recognized characteristic of the interaction. For C...Cl systems, the implicit solvent average of 160° is much closer to the angles seen in experimental data (157° and 168°), compared to the gas phase average of 137°. For C...O systems, experimental angles range from 100° to 166°. While both optimization modes have similar averages, the implicit solvent values are closer to experiment (81°–178°), compared to

TABLE 1 | Hydrogen bonding parameters taken from experimental ionic liquid crystal structures.

Ionic liquid	Donor	Acceptor	HD	AH	AD	AHD
1-(2-hydroxyethyl) yrrolidine-1-ium	N	O	1.06	1.61	2.651	165
benzoate	C	O	0.99	2.53	3.382	145
1-(2-hydroxy-ethyl)pyrrolidinium	N	O	0.99	2.50	3.418	153
2,5-dihydroxy-benzoate	C	O	0.99	1.91	2.778	162
1-(2-hydroxyethyl) yrrolidine-1-ium	N	O	0.99	1.81	2.697	169
2-hydroxy-benzoate	C	O	0.99	2.51	3.391	148
(3s,5s,7s)-adamantan-1-ammonium	N	O	0.99	1.80	2.777	170
benzoate	N	O	1.19	1.60	2.278	169
	C	O	0.95	2.42	2.749	100
(3s,5s,7s)-adamantan-1-ammonium	N	O	1.03	1.76	2.781	170
2,5-dihydroxy-benzoate	N	O	0.91	1.93	2.809	162
(3s,5s,7s)-adamantan-1-ammonium	N	O	0.93	1.90	2.814	168
2-hydroxybenzoate	N	O	1.01	1.85	2.825	162
	C	O	0.97	2.58	3.440	148
heptan-2-ammonium	O	O	0.98	1.70	2.662	167
2,5-dihydroxy-benzoate	N	O	0.97	1.81	2.777	173
	O	O	0.82	1.77	2.544	157
	N	O	0.98	1.90	2.848	163
	N	O	0.87	2.42	2.979	122
	N	O	0.87	2.27	2.905	130
	C	O	0.95	2.57	3.225	126
butyl dimethyl imidazolium	C	O		2.41	3.360	147
hydrogen sulphate	C	O		2.45	3.230	166
butyl dimethyl imidazolium	C	Cl		2.68		157
chloride	C	Cl		2.59		168

Benzoate ionic liquids from Stoimenovski et al. (2011), and butyl dimenthyl imidazolium structures from Kölle and Dronskowski (2004).

the gas phase ones which unsurprisingly contain more outliers in the range of (17°–176°). Systems with nitrogen as a donor and oxygen as an acceptor show characteristics of a stronger hydrogen bond, with experimental data having higher angles, ranging from 122° to 173°. The gas phase seems to be a poor fit overall, ranging from 58 to 179° with an average of 135°. However, implicit solvent values did not perform much better, ranging from 11 to 178°, with a slightly higher average of 145°.

Overall, it is not too surprising that these results indicate that an implicit solvent model is necessary when performing geometry optimizations involving polar interactions such as hydrogen bonding. The CPCM model clearly stabilizes the charges on the ionic species, leading to more relaxed geometries. Gas phase geometries often result in shorter separations, which may not be a major issue if the goal is to qualitatively understand possible interaction configurations. However, there are many systems, including ionic liquids, where configurations exist only due to stabilizing effects from the environment. The use of implicit solvent models can help to replicate these effects and locate more accurate geometries without the need to perform large-scale calculations.

3.2. Energetic Differences in Hydrogen Bonded Ionic Liquids

As one of the major goals of this work was to determine whether it is possible to identify and characterize hydrogen bonding in protic ionic liquids by its energy decomposition, interaction energy calculations were performed for the HBILs

and compared with available data for the IL174 dataset, a dataset consisting of 174 single ion pairs of (mostly non-hydrogen bonding) aprotic ionic liquids (Rigby and Izgorodina, 2014b) based on imidazolium and pyrrolidinium cations and widely used anions. Full interaction energy data are available in the **Supplementary Material**. Only the solvent-optimized HBIL structures are included in the energetic calculations. The two components of total interaction energy of both datasets are plotted as distributions in **Figure 6**. The vertical axis represents a relative (in percentage) count for each energy value. Distributions that have a larger range, such as electrostatics in HBILs, seem smaller, but the area under the curves still represents the total percentage of systems.

Immediately noticeable is how significant the electrostatic energies are for hydrogen bonded ionic liquids. This is to be expected, as the nature of hydrogen bonding is predominantly electrostatic and polarizable in nature (Stoimenovski et al., 2011). This therefore translates to higher electrostatic energies and hence, stronger total interaction energies. For HBILs, electrostatic contributions range between -482.7 to $-262.3 \, \text{kJ mol}^{-1}$, and dispersion between -49.5 and $-16.3 \, \text{kJ mol}^{-1}$. The latter is more comparable with that of archetypical ionic liquids for which the dispersion contribution is between -70.0 and $-27.5 \, \text{kJ mol}^{-1}$. Probably the most striking observation is how the total interaction energy can span a very wide range of $230 \, \text{kJ mol}^{-1}$ in hydrogen-bonded ionic liquids, whereas archetypical ionic liquids tend to have their total interaction energy clustered around the $-370.1 \, \text{kJ mol}^{-1}$ value.

TABLE 2 | Hydrogen bond parameters by donor acceptor pairs for the gas phase and implicit solvent optimization modes.

Phase	Donor	Acceptor	MAE	SD	Min	Max	MAE	SD	Min	Max
			HD Distance				**HA Distance**			
CPCM	C	Cl	1.181	0.255	1.080	1.813	2.294	0.360	1.866	2.667
Gas	C	Cl	1.146	0.082	1.084	1.293	2.204	0.466	1.536	2.747
CPCM	N	Cl	1.440	0.514	1.077	1.803	1.896	0.010	1.889	1.903
Gas	N	Cl	1.193				1.631			
CPCM	C	O	1.096	0.009	1.082	1.157	2.373	0.230	1.539	2.703
Gas	C	O	1.099	0.011	1.087	1.170	2.335	0.354	1.529	4.196
CPCM	N	O	1.059	0.026	1.025	1.119	1.811	0.323	1.454	2.547
Gas	N	O	1.075	0.055	1.015	1.195	1.989	0.613	1.304	3.598
			DA Distance				**HBA Angle**			
CPCM	C	Cl	3.358	0.364	2.948	3.829	160.6	11.7	151.4	178.4
Gas	C	Cl	3.031	0.382	2.349	3.358	137.2	37.2	67.4	178.8
CPCM	N	Cl	2.969	0.007	2.964	2.974	172.5	4.7	169.2	175.8
Gas	N	Cl	2.822				176.5			
CPCM	C	O	3.237	0.237	2.628	3.646	138.7	19.6	81.3	177.9
Gas	C	O	3.186	0.278	2.695	4.819	134.0	23.7	16.5	175.8
CPCM	N	O	2.705	0.096	2.556	2.950	145.3	35.2	11.4	178.4
Gas	N	O	2.718	0.244	2.495	3.472	134.8	35.9	57.8	178.8

All distances are given in Å.
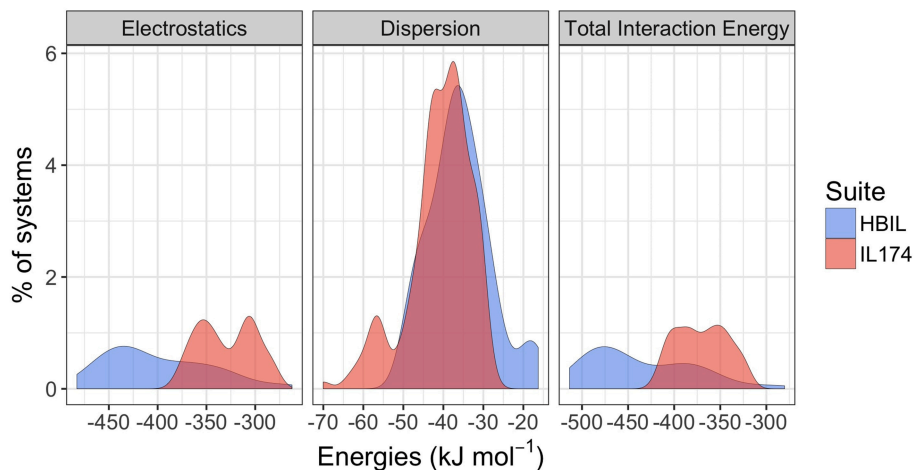
FIGURE 6 | Comparison of gas-phase interaction energy distributions between the IL174 and HBILs datasets.

This is at least $75 \, \text{kJ} \, \text{mol}^{-1}$ lower in energy than the average value for the HBILs, attributed predominantly to the electrostatic component. To complement **Figure 6**, the average, standard deviation, minimum and maximum values of each energetic component is shown in **Table 3**. Comparison of interaction energies between the gas phase and implicit solvent geometries is also included in **Table 4**.

These numbers once again highlight the discrepancy in interaction energy results when failing to include an implicit solvent model when optimizing single ion pairs of ionic liquids. The energetics of the gas phase structures have a much larger range for total energy, between -56.4 and

$-760.3 \, \text{kJ} \, \text{mol}^{-1}$. These values present both extremes of the spectrum, with the close to zero interaction energy indicating that the ions have little attractive force between them, which would naturally occur in cases when back proton transfer takes place and there are two neutral species. Conversely, the several hundred $\text{kJ} \, \text{mol}^{-1}$ interaction energy occurs in gas phase by bringing the ions closer together than what is representative of reality, due to there being no solvent present to offset some of the attractive charge. To illustrate, the system with the largest interaction energy in gas phase, [EtMeNH$_2$][TFA] ($-760.3 \, \text{kJ} \, \text{mol}^{-1}$), has its value of interaction energy reduced by almost a half ($-492.4 \, \text{kJ} \, \text{mol}^{-1}$) when a solvent model is

TABLE 3 | Comparison of interaction energy statistics (kJ mol^{-1}) for the HBIL (implicit solvent optimization) and IL174 datasets.

Dataset	Energy type	Mean	Std Dev	Min	Max
HBIL	Electrostatics	−399.3	±53.0	−482.7	−262.3
	Dispersion	−36.0	±7.8	−49.5	−16.3
	Total	−435.2	±56.6	−513.6	−280.3
IL174	Electrostatics	−329.2	±28.3	−378.7	−278.1
	Dispersion	−40.9	±7.9	−70.0	−27.5
	Total	−370.1	±27.2	−417.7	−319.3

TABLE 4 | Interaction energy statistics (kJ mol^{-1}) for the HBIL dataset for gas phase optimization.

Phase	Energy type	Mean	Std Dev	Min	Max
Gas	Electrostatics	−301.0	±184.4	−730.9	−34.9
	Dispersion	−39.9	±10.8	−55.9	−16.3
	Total	−340.0	±191.4	−760.3	−56.3
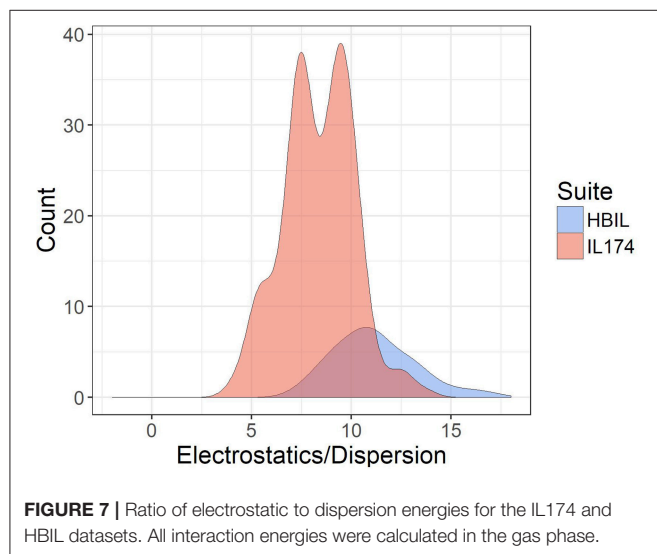
FIGURE 7 | Ratio of electrostatic to dispersion energies for the IL174 and HBIL datasets. All interaction energies were calculated in the gas phase.

used during optimization. Back-protonation occurs in the gas-optimized system, bringing the ions in close proximity. On the other hand, for system where back-protonation does not occur, [DMEA][CH$_3$OSO$_3$], interaction energy values are relatively more in agreement between the gas (−480.6 kJ mol^{-1}) and solvent (−455.1 kJ mol^{-1}) phases.

The ratio of electrostatic interaction energy is compared with dispersion energy in **Figure 7**. The majority of HBILs have a broad distribution of electrostatic interaction energy falling between 5 and 15 times the magnitude of the dispersion energy. This is similar to the IL174 dataset, for which the electrostatic interaction energy is clustered in the range of 5–10 times the dispersion energy.

In the following discussion, the relative energy of each component is discussed. This is defined as the energy of the

component divided by the total interaction energy. **Figure 8** plots the electrostatic interaction energy and dispersion energy against their contribution to the total interaction energy. While IL174 ionic liquids tend to be clustered in one area, its slope is sharper, indicating that the contributions from electrostatics decreases with increasing dispersion. Contrary to this trend, HBILs tend to maintain a relatively constant electrostatic contribution of about 92% to the total interaction energy. The relative contribution from the dispersion energy (**Figure 8,** right) shows a clear difference between the HBIL and IL174 datasets. The gains in the total interaction energy from hydrogen bonding do not come from the dispersion component, hence lower contributions are seen for the HBILs, with the majority falling around 10%.

Plots depicting components of the interaction energy and their relative contributions all reflect the same trends: hydrogen bonding leads to stronger interactions, but these increases do not come from one component alone. Determining whether a system is hydrogen bonded based on its energetics does not seem to be a reliable method in this implementation. While hydrogen bonded ionic liquids do follow different energetic trends, it could be difficult to decide which category a system falls into since there is a major overlap in the energy distributions. Thus far, the best indicator to detect hydrogen bonding in ionic liquids is to compare the electrostatic and dispersion energies. The dispersion component is largely unaffected by hydrogen bonding, whereas the electrostatic components are usually larger. Comparing the differences or ratios of the electrostatic and dispersion energies appears to be a good, though not completely bulletproof, method to determine hydrogen bonding in an ionic liquid system.

3.3. Relationship Between Energies and Geometries

The final part of the results considers the relationship between the geometric parameters for hydrogen bonding and interaction energy decomposition.

Figure 9 plots the distance between the acceptor and donor atoms against the hydrogen bond distance of the HBILs optimized in gas phase and implicit solvent. Points are colored by the strength of electrostatic interaction energy. Generally, the points follow a linear trend, which is expected as the electrostatic interaction is governed by the Coulomb's law confirming that an increase in the hydrogen bond length corresponds linearly to an increase in the acceptor-donor distance. The predicted points that do not follow this linear trend have bond angles that deviate significantly from 180°, often falling below 160°. The electrostatic interaction energy is higher for systems that are clearly hydrogen bonded, i.e., those with lower distances presented in the lower left corner of the graph. As the distance increases, the electrostatic interaction energy also decreases, due to a weakening interaction. However, this trend is not without exceptions. Several systems at longer separations, and indeed, non-linear bond angles, have strong electrostatic interaction energies. These systems include [EtNH$_3$][TFA], which has a bond angle of 167° and is shown in **Figure 10**. Other examples include DMEA coupled with MeSO$_3^-$ and TFA, [EtMeNH$_2$][TFA], EtNH$_3^+$ with NO$_3^-$ and TFA$^-$. Notably, these all have SO$_3$ or NO$_3$ groups,
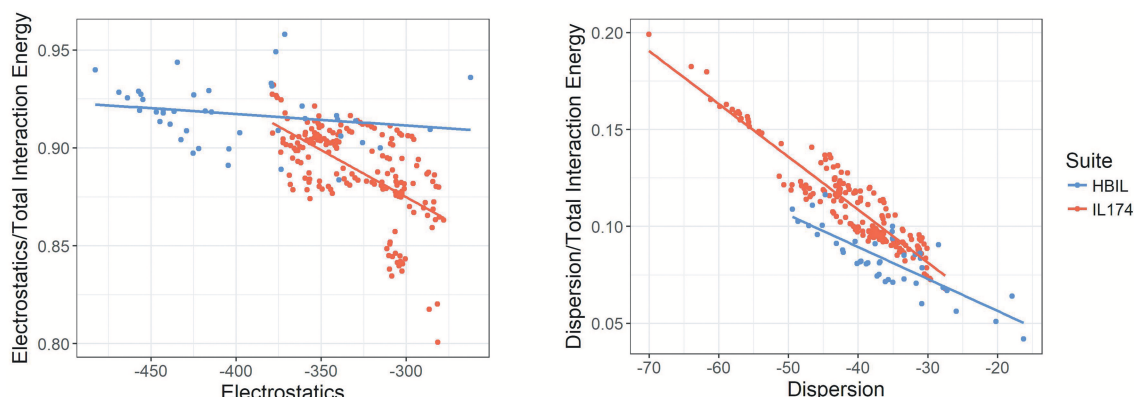
FIGURE 8 | Electrostatics **(left)** and dispersion **(right)** against their relative contribution to the total gas-phase interaction energy for IL174 and HBIL datasets in kJ mol^{-1}.
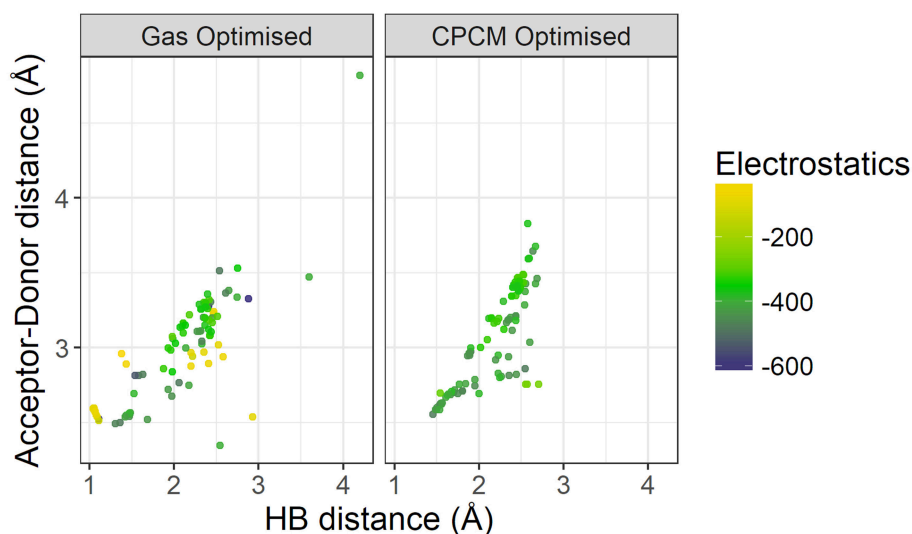

FIGURE 9 | Comparison of Acceptor-Donor distance against hydrogen bond distances for gas phase and implicit solvent optimized geometries, colored by strength of electrostatics.

electronegative groups that are able to form a strong hydrogen bond. This reflects the complicated nature of hydrogen bonded ionic liquids, where non-conventional lengths and angles can still result in significant electrostatic interactions.

On the left hand side of **Figure 9**, a comparison of the energetics of the implicit solvent optimized structures with those optimized in gas phase clearly highlights the failings of gas phase optimizations to capture the energetics of hydrogen bonding. There are a number of points with very weak electrostatic interaction energy (depicted in light yellow-green color) and are representative of structures for which the back-proton transfer occurs to form a neutral species. Gas-phase optimized structures clearly have weaker electrostatics compared to that of implicit solvent optimized ones, further highlighting the reduction of electrostatic interactions by gas phase in the absence of the stabilizing field of neighboring ions.

3.3.1. Difference Between Gas and Solvent Optimizations and Total Interaction Energy

In this section, the hydrogen bond parameters from the gas phase and implicit solvent geometry optimizations are contrasted, while examining the strength of the electrostatic interaction in the two optimization modes. In the following plots, the shape of the point denotes the four possible donor-acceptor pairings: Cl−C, O−C, Cl−N, and O−N. The total interaction energy is chosen as it can be easily calculated using a variety of methods, and since electrostatics is the largest component of the total interaction energy (as shown previously), this hopefully means that any effect that hydrogen bonding has on electrostatics will be reflected in the total energy.

Figure 11 contrasts the HA distances observed in gas phase and implicit solvent. If we take the total energy as indicative of the hydrogen bond strength, then at shorter distances there

is a strong correlation. These shorter distances are clearly hydrogen bonds in the conventional sense. It is noteworthy that most, if not all, are formed with nitrogen as the donor atom. As highlighted above, gas phase optimizations tend to underestimate these distances. However, at longer distances, solvent and gas phase optimizations agree better, with the gas phase optimizations tending to produce a wider range of HA distances > 3 Å, particularly for the sulphate-containing ionic liquids such as [DMEA][CF$_3$SO$_3$] and [DMEA][CH$_3$SO$_2$], [mim][CH$_3$SO$_3$], and [EtNH$_3$][CH$_3$OSO$_3$]. These points are seen to lie closer to the diagonal line, likely due to the diffusive nature of these sulfur-containing anions compared to the others chosen such as TFA. Naturally, the stronger charge-localized ions are more likely to have shorter HA distances in the gas phase.

At these longer distances, there are also some systems with strong electrostatic interactions. In certain cases, there is more than one interaction occurring. For example, in [EtNH$_3$][TFA], there is a clear hydrogen bond of 1.45 Å, and also another interaction involving the second oxygen of the anion and the same hydrogen, measuring at 2.4 Å (see **Figure 12**). The latter interaction is evidently not as strong; however due to the energy calculation encompassing the entire system, the resulting point appears to have a high energy even at a longer separation. A further analysis of these exceptions reveals that a few of these come from hydrogens attached to a carbon atom, and some of them from those attached to a nitrogen. This effect becomes very pronounced in the presence of multiple oxygen atoms on the anions such as TFA, CH$_3$SO$_3^-$, NO$_3^-$, interacting with other hydrogen atoms around a hydrogen bonds that is already short and strong, for primary and secondary amine cations EtNH$_3^+$ and EtMeNH$_2^+$ where there are multiple hydrogens available for hydrogen bonding. In regard to other cations such as imidazolium and pyrrolidinium, there is only one acidic proton available for interaction. This explains why several of the carbon donor systems have stronger Coulomb interactions, while occurring at longer separations. In general, carbon donor systems tend to form much weaker hydrogen bonds with energies between -300 and -350 kJ mol^{-1}. In contrast, it is remarkable

FIGURE 10 | Ethylammonium trifluoroacetate, optimized with the CPCM model.

FIGURE 12 | The two hydrogen bonds in [EtNH$_3$][TFA](CPCMoptimized).

FIGURE 11 | Gas vs. solvent optimized hydrogen bond distance in Angstrom, colored by strength of the total CPCM interaction energy **(left)**, and the total gas interaction energy **(right)**.

FIGURE 13 | Gas vs. solvent optimized hydrogen-Donor distance in Å, colored by strength of the total CPCM interaction energy **(left)**, and the total gas interaction energy **(right)**.

FIGURE 14 | Gas vs. solvent optimized hydrogen-Donor distance in Å, colored by ratio of the electrostatic contribution to total CPCM interaction energy **(left)**, and the total gas interaction energy **(right)**.

that all of the systems involving nitrogen as a donor have fairly strong electrostatics.

In **Figure 13**, the gas phase optimized HD bond lengths are plotted against the implicit solvent ones. This is typically a covalent bond, however in gas phase optimizations it can sometimes be noticeably long. In some cases, it tends to be longer than a typical hydrogen bond itself. As discussed above, this is due to a number of systems undergoing the back-proton transfer. Only a small number of systems have agreement from both optimization modes. This includes all of the systems with weaker interactions, *i.e.,* having carbon donors and long hydrogen bonds as discussed previously. However, a significant number of hydrogen bonding systems, judging from both shorter bond lengths and stronger interaction energies observed in implicit

solvent geometries, are relegated to longer bond lengths in gas phase due to the back-proton transfer. The nature of the acceptor atom seems to play a crucial role in determining whether gas phase geometries are adequate. It has to noted that the majority of the ionic liquids for which gas phase results favor neutral species, exist predominantly in their ionic form, such as [EtNH$_3$][TFA] and [EtNH$_3$][NO$_3$] which have been experimentally observed to exhibit a significant extent of ionization. (Capelo et al., 2012; Greaves and Drummond, 2015).

To further investigate the relationship between the interaction energy and the hydrogen bond parameters, additional plots were made, this time colored by the *relative* electrostatics contribution to total energy. As much of the hydrogen bonding in ionic liquids is electrostatic, this could grant further insight into

FIGURE 15 | Gas vs. solvent optimized hydrogen bond distance in Å, colored by ratio of the electrostatic contribution to total CPCM interaction energy **(left)**, and the total gas interaction energy **(right)**.
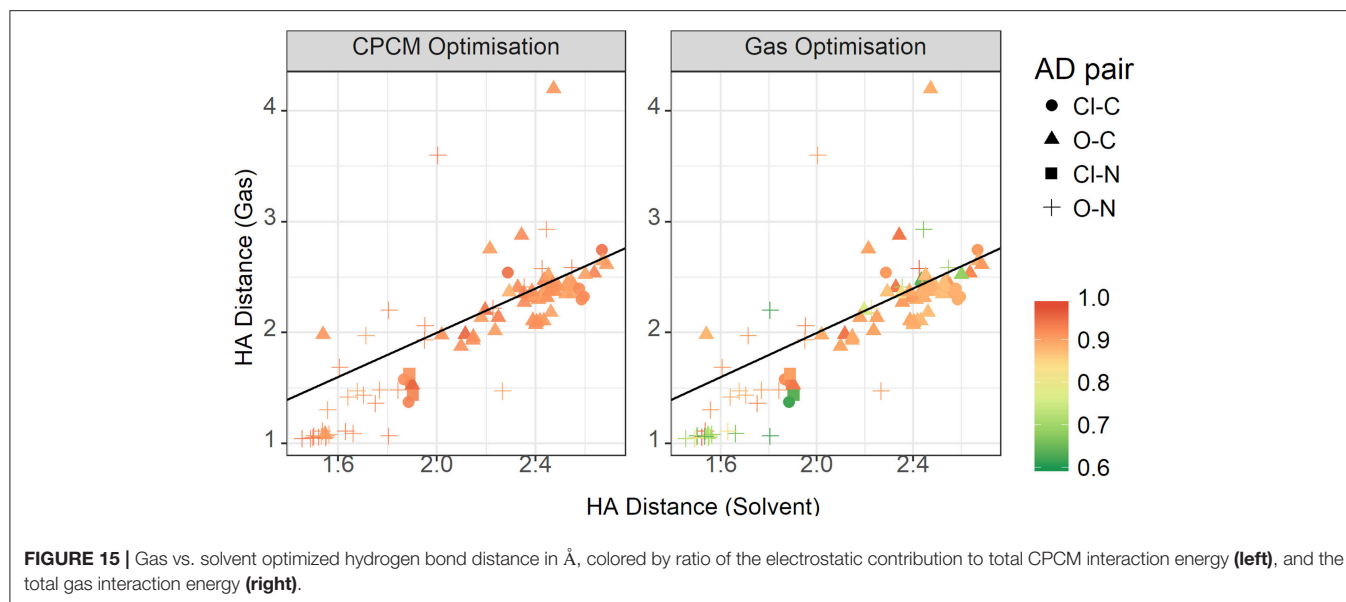
the energetics of hydrogen bonding. Since the electrostatics interaction is responsible for a significant part of the total interaction energy, these two energies are highly correlated. In **Figure 14**, the plot contrasts the HD bond lengths in both gas phase and implicit solvent, and the contribution of electrostatic interaction energy to the total interaction energy is given for both modes of optimization. Interestingly, for many of systems with the oxygen atom as an acceptor and the nitrogen atom as a donor, the relative electrostatic interaction energy is *negatively* correlated with increasing HD distance for gas phase optimized geometries. In particular, with increasing HD distance, the relative contribution from electrostatics also increases which is counter-intuitive to what is expected according to the Coulomb's law. As the solvent geometries have the HD bond distributed over a very narrow range of 1.03–1.81 Å, the length of this bond is likely not responsible for the change in the relative contribution from electrostatics. Referring to the relative contribution of electrostatics in gas phase optimized geometries, which is shown in the right-hand side of **Figure 14**, it is clear that gas phase optimizations may not account for all the electrostatic contributions present. The average relative contribution of electrostatics in gas-phase optimized structures is 85% compared to 91% for implicit solvent optimizations. As expected, the energy decomposition obtained using gas-phase geometries shows that an elongated donor-hydrogen bond is accompanied by a lower electrostatics component (exemplified by the two light red points in the Figure at longer HD distance).

The plot for the HA distances is shown in **Figure 15**, colored by the relative contribution of the electrostatic interaction to total interaction energy. This relative Coulomb force is strongest at short hydrogen bond distances, below approximately 1.8 Å. Additionally, there are some points around the 2.4 Å point that also have strong relative electrostatics. These points are not constrained to a particular acceptor-donor pair, but have a few representative each from oxygen-carbon,

chloride-nitrogen, and oxygen-nitrogen. They are also not cation or anion specific. The strongest anions, from strongest to weakest, are trifluoroacetate, chloride, methylsulfate, trifluoromethanesulfonate, and methanesulfonate. Cations are even more diverse, with various members of the ammonium-based cations present, as well as N,N'-dimethyl pyrrolidinium and 1,3-dimethylimidazolium. The striking difference between the gas phase and implicit solvent geometries is the reduced contribution from electrostatics in the former.

Altogether, geometry and energies give a better picture of hydrogen bonding and its complexities. Solvent-optimized structures are shown again to be vital to produce the most accurate geometries, which would in hand produce reliable values when analyzing interaction energy.

4. CONCLUSIONS

Hydrogen bonding can be a difficult interaction to model, and even more so when present in ionic liquids. In this study of protic ionic liquids with clearly directional hydrogen bonding, geometry optimizations of single ion pairs were compared between gas phase and implicit solvent optimizations. Gas phase optimizations were found to produce shorter hydrogen bonding distance at least 0.7 Å on average. In many cases, geometries of ions pairs were destabilized in gas phase to such a degree that back proton transfer became preferred, resulting in the formation of neutral species. Implicit solvent optimizations, with ethanol as solvent, produced geometries that were in good agreement with available crystal structures of previously studied protic ionic liquids. The majority of the hydrogen bonding did not have perfectly linear hydrogen bonds, with the average angle being found at 150° experimentally, 143° with CPCM optimization, and 141° in gas phase optimizations.

Compared to aprotic ionic liquids, HBILs optimized in implicit solvent tend to have higher electrostatic energies, leading

to a larger total interaction energy. In particular, the average value for total interaction energy is $-409.1\,\text{kJ mol}^{-1}$ for the HBIL dataset, whereas this number decreases to $-329.2\,\text{kJ mol}^{-1}$ on average for the IL174 dataset. The distribution of the interaction energy is much broader in HBILs, with the relative contribution remaining practically constant at 92%. In contrast to this, the IL174 dataset show a steeper dependence between the electrostatic interaction and total energy. The dispersion component was found to be similar in magnitude for both groups $-36.3\,\text{kJ mol}^{-1}$ on average for HBIL and $-40.9\,\text{kJ mol}^{-1}$ for IL174. In addition, for HBILs the electrostatic contribution was established to be 10 to 15 times greater than that for the dispersion energy. In the case of aprotic ionic liquids, the electrostatic contribution was 5–10 times greater than dispersion, thus making another clear energetic difference between the two classes of ionic liquids. In summary, geometric parameters and energetic components complement each other to better determine the presence of hydrogen bonding in ionic liquid systems. In particular, the total interaction energy and its electrostatic component can be reliably used to clearly classify the existence of hydrogen bonding as highlighted in **Table 3**.

Gas phase optimizations resulted in weaker interaction energies due to the fact that the gas phase tends to significantly reduce the electrostatic interaction. In this study we confirmed this commonly used rule, with the electrostatic contribution showing a decrease by $100\,\text{kJ mol}^{-1}$ on average, compared to implicit solvent geometries. In addition, for many systems, especially imidazolium- and trimethyl ethyl ammonium-cation based ones, the absence of a stabilizing continuum model results in the ions becoming destabilized, resulting in the back proton transfer from the base to the acid. For some systems such as $[\text{EtMeNH}_2][\text{TFA}]$, the interaction energy was as strong as $-760.3\,\text{kJ mol}^{-1}$ observed due to the significantly decreased hydrogen bonding distance. Therefore, we conclude that gas phase optimizations should be avoided for studying hydrogen bonding in ionic liquids and protic ionic liquids as it produces

unreliable geometries and energetics. Based on the data presented in this study, it is still inconclusive whether the hydrogen bond requires a special treatment in molecular dynamics simulations. The presence of a stronger electrostatic interaction might not necessary support this idea. Perhaps the only aspect that can be considered is the deviation from linearity of the hydrogen bond angle. Another aspect that has not been considered in this work is the charge distribution on the electronegative atoms partaking in hydrogen bonding. The presence of similar dispersion interactions might indicate that the charges in protic ionic liquids might have a similar distribution as that in aprotic ionic liquids.

AUTHOR CONTRIBUTIONS

SYST and KL ran calculations, which were analyzed by SYST, KL, and EII. SYST and KL equally edited the manuscript. KL, SYST, and EII approved the manuscript for publication.

FUNDING

ACKNOWLEDGMENTS

SUPPLEMENTARY MATERIAL

The Supplementary Material for this article can be found online at: https://www.frontiersin.org/articles/10.3389/fchem.2019.00208/full#supplementary-material

REFERENCES

Aida, M. (1988). Characteristics of the watson-crick type hydrogen-bonded DNA base pairs: an *ab initio* molecular orbital study. *J. Comput. Chem.* 9, 362–368. doi: 10.1002/jcc.540090411

Arunan, E., Desiraju, G. R., Klein, R. A., Sadlej, J., Scheiner, S., Alkorta, I., et al. (2011). Definition of the hydrogen bond (IUPAC recommendations 2011). *Pure Appl. Chem.* 83, 1637–1641. doi: 10.1351/PAC-REC-10-01-02

Barone, V., and Cossi, M. (1998). Quantum calculation of molecular energies and energy gradients in solution by a conductor solvent model. *J. Phys. Chem. A* 102, 1995–2001. doi: 10.1021/jp9716997

Bedrov, D., Borodin, O., Li, Z., and Smith, G. D. (2010). Influence of polarization on structural, thermodynamic, and dynamic properties of ionic liquids obtained from molecular dynamics simulations. *J. Phys. Chem. B* 114, 4984–4997. doi: 10.1021/jp911670f

Bhargava, B. L., and Balasubramanian, S. (2006). Intermolecular structure and dynamics in an ionic liquid: a car-parrinello molecular dynamics simulation study of 1,3-dimethylimidazolium chloride. *Chem. Phys. Lett.* 417, 486–491. doi: 10.1016/j.cplett.2005.10.050

Boys, S. F., and Bernardi, F. d. (1970). The calculation of small molecular interactions by the differences of separate total energies. Some procedures with reduced errors. *Mol. Phys.* 19, 553–566. doi: 10.1080/00268977000101561

Bühl, M., Chaumont, A., Schurhammer, R., and Wipff, G. (2005). *Ab initio* molecular dynamics of liquid 1,3-dimethylimidazolium chloride. *J. Phys. Chem. B* 109, 18591–18599. doi: 10.1021/jp0518299

Capelo, S. B., Méndez-Morales, T., Carrete, J., López Lago, E., Vila, J., Cabeza, O., et al. (2012). Effect of temperature and cationic chain length on the physical properties of ammonium nitrate-based protic ionic liquids. *J. Phys. Chem. B* 116, 11302–11312. doi: 10.1021/jp3066822

Chen, S., and Izgorodina, E. I. (2017). Prediction of 1h nmr chemical shifts for clusters of imidazolium-based ionic liquids. *Phys. Chem. Chem. Phys.* 19, 17411–17425. doi: 10.1039/C7CP02951A

Chesman, A. S., Hodgson, J. L., Izgorodina, E. I., Urbatsch, A., Turner, D. R., Deacon, G. B., et al. (2014). Anion–anion interactions in the crystal packing of functionalized methanide anions: an experimental and computational study. *Cryst. Growth Design* 14, 1922–1932. doi: 10.1021/cg500051m

Del Pópolo, M. G., Lynden-Bell, R. M., and Kohanoff, J. (2005). *Ab initio* molecular dynamics simulation of a room temperature ionic liquid. *J. Phys. Chem. B* 109, 5895–5902. doi: 10.1021/jp044414g

Dommert, F., Wendler, K., Qiao, B., Delle Site, L., and Holm, C. (2014). Generic force fields for ionic liquids. *J. Mol. Liquids* 192, 32–37. doi: 10.1016/j.molliq.2013.09.001

Dong, K., Song, Y., Liu, X., Cheng, W., Yao, X., and Zhang, S. (2012). Understanding structures and hydrogen bonds of ionic liquids at the electronic level. *J. Phys. Chem. B* 116, 1007–1017. doi: 10.1021/jp205435u

Frisch, M. J., Trucks, G. W., Schlegel, H. B., Scuseria, G. E., Robb, M. A., Cheeseman, J. R., et al. (2009). *Gaussian09 Revision A.02*. Wallingford, CT: Gaussian Inc.

Fumino, K., Wulf, A., and Ludwig, R. (2009). The potential role of hydrogen bonding in aprotic and protic ionic liquids. *Phys. Chem. Chem. Phys.* 11, 8790–8794. doi: 10.1039/b905634c

Greaves, T. L., and Drummond, C. J. (2015). Protic ionic liquids: Evolving structure-property relationships and expanding applications. *Chem. Rev.* 115, 11379–11448. doi: 10.1021/acs.chemrev.5b00158

Greaves, T. L., Weerawardena, A., Krodkiewska, I., and Drummond, C. J. (2008). Protic ionic liquids: physicochemical properties and behavior as amphiphile self-assembly solvents. *J. Phys. Chem. B* 112, 896–905. doi: 10.1021/jp0767819

Halat, P., Seeger, Z. L., Barrera Acevedo, S., and Izgorodina, E. I. (2017). Trends in two-and three-body effects in multiscale clusters of ionic liquids. *J. Phys. Chem. B* 121, 577–588. doi: 10.1021/acs.jpcb.6b10101

Halkier, A., Helgaker, T., Jørgensen, P., Klopper, W., and Olsen, J. (1999). Basis-set convergence of the energy in molecular hartree-fock calculations. *Chem. Phys. Lett.* 302, 437–446. doi: 10.1016/S0009-2614(99)00179-7

Henderson, W. A., Fylstra, P., De Long, H. C., Trulove, P. C., and Parsons, S. (2012). Crystal structure of the ionic liquid etnh3no3-insights into the thermal phase behavior of protic ionic liquids. *Phys. Chem. Chem. Phys.* 14, 16041–16046. doi: 10.1039/c2cp43079g

Hunt, P. A., Ashworth, C. R., and Matthews, R. P. (2015). Hydrogen bonding in ionic liquids. *Chem. Soc. Rev.* 44, 1257–1288. doi: 10.1039/C4CS00278D

Hunt, P. A., Kirchner, B., and Welton, T. (2006). Characterising the electronic structure of ionic liquids: an examination of the 1-butyl-3-methylimidazolium chloride ion pair. *Chem. Eur. J.* 12, 6762–6775. doi: 10.1002/chem.200600103

Izgorodina, E. I., Golze, D., Maganti, R., Armel, V., Taige, M., Schubert, T. J. S., et al. (2014). Importance of dispersion forces for prediction of thermodynamic and transport properties of some common ionic liquids. *Phys. Chem. Chem. Phys.* 16, 7209–7221. doi: 10.1039/C3CP53035C

Izgorodina, E. I., and MacFarlane, D. R. (2011). Nature of hydrogen bonding in charged hydrogen-bonded complexes and imidazolium-based ionic liquids. *J. Phys. Chem. B* 115, 14659–14667. doi: 10.1021/jp208150b

Izgorodina, E. I., Maganti, R., Armel, V., Dean, P. M., Pringle, J. M., Seddon, K. R., et al. (2011). Understanding the effect of the c2 proton in promoting low viscosities and high conductivities in imidazolium-based ionic liquids: Part I. weakly coordinating anions. *J. Phys. Chem. B* 115, 14688–14697. doi: 10.1021/jp208573y

Izgorodina, E. I., Seeger, Z. L., Scarborough, D. L. A., and Tan, S. Y. S. (2017). Quantum chemical methods for the prediction of energetic, physical, and spectroscopic properties of ionic liquids. *Chem. Rev.* 117, 6696–6754. doi: 10.1021/acs.chemrev.6b00528

Klamt, A., and Schüürmann, G. (1993). COSMO: a new approach to dielectric screening in solvents with explicit expressions for the screening energy and its gradient. *J. Chem. Soc. Perkin Trans.* 799–805. doi: 10.1039/P29930000799

Kölle, P., and Dronskowski, R. (2004). Hydrogen bonding in the crystal structures of the ionic liquid compounds butyldimethylimidazolium hydrogen sulfate, chloride, and chloroferrate(II,III). *Inorgan. Chem.* 43, 2803–2809. doi: 10.1021/ic035237l

Lee, A. J., and Rick, S. W. (2011). The effects of charge transfer on the properties of liquid water. *J. Chem. Phys.* 134:184507. doi: 10.1063/1.3589419

Mackerell, A. D., Feig, M., and Brooks, C. L. (2004). Extending the treatment of backbone energetics in protein force fields: limitations of gas-phase quantum mechanics in reproducing protein conformational distributions in molecular dynamics simulations. *J. Comput. Chem.* 25, 1400–1415. doi: 10.1002/jcc.20065

Maginn, E. J. (2007). Atomistic simulation of the thermodynamic and transport properties of ionic liquids. *Acc. Chem. Res.* 40, 1200–1207. doi: 10.1021/ar700163c

McDaniel, J. G., Choi, E., Son, C. Y., Schmidt, J. R., and Yethiraj, A. (2016). *Ab initio* force fields for imidazolium-based ionic liquids. *J. Phys. Chem. B* 120, 7024–7036. doi: 10.1021/acs.jpcb.6b05328

Pensado, A. S., Brehm, M., Thar, J., Seitsonen, A. P., and Kirchner, B. (2012). Effect of dispersion on the structure and dynamics of the ionic liquid 1-ethyl-3-methylimidazolium thiocyanate. *ChemPhysChem* 13, 1845–1853. doi: 10.1002/cphc.201100917

Perutz, M. F. (1993). The role of aromatic rings as hydrogen-bond acceptors in molecular recognition. *Philos. Trans. R. Soc. Lond. A* 345, 105–112. doi: 10.1098/rsta.1993.0122

Prado, C. E. R., Pópolo, M. G. D., Youngs, T., Kohanoff, J., and Lynden-Bell, R. (2006). Molecular electrostatic properties of ions in an ionic liquid. *Mol. Phys.* 104, 2477–2483. doi: 10.1080/00268970600765748

Rigby, J., and Izgorodina, E. I. (2013). Assessment of atomic partial charge schemes for polarisation and charge transfer effects in ionic liquids. *Phys. Chem. Chem. Phys.* 15:1632. doi: 10.1039/C2CP42934A

Rigby, J., and Izgorodina, E. I. (2014a). Il174 dataset.

Rigby, J., and Izgorodina, E. I. (2014b). New SCS- and SOS-MP2 coefficients fitted to semi-coulombic systems. *J. Chem. Theor. Comput.* 10, 3111–3122. doi: 10.1021/ct500309x

Simons, T. J., Verheyen, T., Izgorodina, E. I., Vijayaraghavan, R., Young, S., Pearson, A. K., et al. (2016). Mechanisms of low temperature capture and regeneration of co 2 using diamino protic ionic liquids. *Phys. Chem. Chem. Phys.* 18, 1140–1149. doi: 10.1039/C5CP05200A

Singh, T., and Kumar, A. (2008). Static dielectric constant of room temperature ionic liquids: internal pressure and cohesive energy density approach. *J. Phys. Chem. B* 112, 12968–12972. doi: 10.1021/jp8059618

Steiner, T. (2002). The hydrogen bond in the solid state. *Angew. Chem. Int. Edn.* 41, 48–76. doi: 10.1002/1521-3773(20020104)41:1<48::AID-ANIE48>3.0.CO;2-U

Stoimenovski, J., Dean, P. M., Izgorodina, E. I., and MacFarlane, D. R. (2011). Protic pharmaceutical ionic liquids and solids: aspects of protonics. *Faraday Discuss.* 154, 335–352. doi: 10.1039/c1fd00071c

Stoimenovski, J., Izgorodina, E. I., and MacFarlane, D. R. (2010). Ionicity and proton transfer in protic ionic liquids. *Phys. Chem. Chem. Phys.* 12, 10341–10347. doi: 10.1039/c0cp00239a

Stover, M. L., Jackson, V. E., Matus, M. H., Adams, M. A., Cassady, C. J., and Dixon, D. A. (2012). Fundamental thermochemical properties of amino acids: gas-phase and aqueous acidities and gas-phase heats of formation. *J. Phys. Chem. B* 116, 2905–2916. doi: 10.1021/jp207271p

Tan, S. Y., and Izgorodina, E. I. (2016). Comparison of the effective fragment potential method with symmetry-adapted perturbation theory in the calculation of intermolecular energies for ionic liquids. *J. Chem. Theor. Comput.* 12, 2553–2568. doi: 10.1021/acs.jctc.6b00141

Turney, J. M., Simmonett, A. C., Parrish, R. M., Hohenstein, E. G., Evangelista, F. A., Fermann, J. T., et al. (2012). Psi4: an open-source *ab initio* electronic structure program. *Wiley Interdisc. Rev. Comput. Mol. Sci.* 2, 556–565. doi: 10.1002/wcms.93

Weingärtner, H. (2008). Understanding ionic liquids at the molecular level: Facts, problems, and controversies. *Angew. Chem. Int. Edn.* 47, 654–670. doi: 10.1002/anie.200604951

Weingärtner, H. (2014). *Dielectric Properties of Ionic Liquids: Achievements So Far and Challenges Remaining*. Hoboken, NJ: Wiley-Blackwell, 235–258.

Weinhold, F., and Klein, R. A. (2012). What is a hydrogen bond? mutually consistent theoretical and experimental criteria for characterizing h-bonding interactions. *Mol. Phys.* 110, 565–579. doi: 10.1080/00268976.2012.661478

Wendler, K., Zahn, S., Dommert, F., Berger, R., Holm, C., Kirchner, B., et al. (2011). Locality and fluctuations: trends in imidazolium-based ionic liquids and beyond. *J. Chem. Theor. Comput.* 7, 3040–3044. doi: 10.1021/ct200375v

Wulf, A., Fumino, K., and Ludwig, R. (2010). Spectroscopic evidence for an enhanced anion-cation interaction from hydrogen bonding in pure imidazolium ionic liquids. *Angew. Chem. Int. Edn.* 49, 449–453. doi: 10.1002/anie.200905437

Zhao, Y., and Truhlar, D. G. (2008). The m06 suite of density functionals for main group thermochemistry, thermochemical kinetics, noncovalent interactions, excited states, and transition elements: two new functionals and systematic testing of four m06-class functionals and 12 other functionals. *Theor. Chem. Acc.* 120, 215–241. doi: 10.1007/s00214-007-0310-x

Ionic Liquids: A Simple Model to Predict Ion Conductivity Based on DFT Derived Physical Parameters

Jonathan Nilsson-Hallén, Bodil Ahlström[†], Maciej Marczewski[†] and Patrik Johansson*

Department of Physics, Chalmers University of Technology, Gothenburg, Sweden

A model able to a priori predict ion conductivities of ionic liquids (ILs) is a desired design tool. We here propose a set of simple conductivity models for ILs composed of small ions by only using data easily derived from standard DFT calculations as input; ion volume, ion mass, ion moment of inertia, and the ion-ion interaction strength. Hence these simple models are totally without any need for experimental parametrization. All model are made from fits of 22 ILs based on 12 different cations and 5 different anions, resulting in correlations vs. experiment of $R^2 \approx 0.95$ and MAE of 25–36%. Given their (very) simple layout and how fast they can be applied (and re-used), the models allow for ample screening of new IL designs, while not aimed for perfect predictions *per se*.

Keywords: ionic liquid, conductivity, DFT, model, ion

INTRODUCTION

Ionic liquids (ILs) represent an interesting class of materials that during the last few decades have been intensely studied (Plechkova and Seddon, 2008; Castner and Wishart, 2010; Thematic issue: Physical chemistry of ionic liquids, 2010; Thematic issue: Ionic liquids, 2012), partly driven by the many potential applications suggested, such as electrolytes in electrochemical energy storage and conversion devices e.g., batteries, fuel cells, solar cells, etc (Armand et al., 2009; Lewandowski and Swiderska-Mocek, 2009; Thematic issue: Ionic liquids for energy applications, 2013). Due to the large number of possible ILs, often estimated to 10^{12}-10^{14}, or even up to 10^{18}(!) (Plechkova and Seddon, 2008), methods for predicting the properties of ILs *a priori* to any time-consuming synthesis attempts are highly desirable. Any such method needs to take stance at the ion level and should preferably be general, accurate, non-empirical, and fast. Indeed, there are many different standard modeling approaches applied to ILs from *ab initio*, DFT, MD, to *ab initio* molecular dynamics (AIMD) (Del Pópolo et al., 2005; Tsuzuki et al., 2005; Borodin, 2009; Kirchner, 2009; Maginn, 2009; Angenendt and Johansson, 2010; Johansson et al., 2010; Ueno et al., 2010; Liu and Maginn, 2012; Tsuzuki, 2012), and more analytical methods (Abbott, 2004, 2005; Matsuda et al., 2007; Slattery et al., 2007; Tochigi and Yamamoto, 2007; Preiss et al., 2010; Eiden et al., 2011). All aim at predicting/estimating melting points (Slattery et al., 2007; Preiss et al., 2010), viscosities (Abbott, 2004; Matsuda et al., 2007; Slattery et al., 2007; Tochigi and Yamamoto, 2007; Ueno et al., 2010; Eiden et al., 2011), and not the least the ionic conductivities (Abbott, 2005; Del Pópolo et al., 2005; Tsuzuki et al., 2005; Matsuda et al., 2007; Slattery et al., 2007; Tochigi and Yamamoto, 2007; Borodin, 2009; Johansson et al., 2010; Ueno et al., 2010; Eiden et al., 2011; Liu and Maginn, 2012; Tsuzuki, 2012). While in general highly successful for their purposes, they often, however, have either limited accuracy, are time-consuming or require ion-specific or empirical parameters.

From an experimental point of view ion conductivity data are most often provided as Arrhenius plots, $\sigma = f(1/T)$, and can for ILs be accurately fitted using the Vogel-Tamman-Fulcher (VTF) equation (Vila et al., 2006),

$$\sigma = \sigma_\infty \exp\left(-\frac{E_a}{k_b\,(T - T_0)}\right) \qquad (1)$$

where σ_∞ is the conductivity at infinite temperature, E_a is the activation energy, and T_0 is a constant related to transformation of the observed glass transition temperature, T_g, to the ideal.

The general features of the VTF equation, together with a lot of other types of expressions, were here used as starting points to generate models for the ionic conductivity of ILs. Many previous IL conductivity models have shown a strong dependency on the ion volumes, but require ion-specific, most often anion-specific, parameters (Tsuzuki et al., 2005; Matsuda et al., 2007; Slattery et al., 2007; Borodin, 2009; Angenendt and Johansson, 2010; Ueno et al., 2010; Tsuzuki, 2012) or resort to analyzing ILs with very similar anions (Johansson et al., 2010). In order to avoid this, which severely limits the generality, we have included not only the ion volumes, but also ion (reduced) masses—as proven to affect the viscosity (Abbott, 2004, 2005; Matsuda et al., 2007), and ion moments of inertia as input parameters to a wide variety of (VTF-based) models. Furthermore, as a combination of (at least) two ions, a cation and an anion, is needed to create any IL, the strength of the specific ion-ion interaction was used as another parameter—more or less as a proxy for the activation energy (E_a) in the VTF expression—even if the connection between these is far from obvious (Tsuzuki et al., 2005; Borodin, 2009; Angenendt and Johansson, 2010; Johansson et al., 2010; Ueno et al., 2010; Tsuzuki, 2012). We would also like to stress that we here avoid any additional complexity of IL nano-structuration by only studying ILs with rather short cation alkyl chain lengths. We have also chosen to include imidazolium based ILs with the C2 position methylated as these seem to introduce a specific behavior in terms of ion-ion interaction. All the parameters are obtained starting from standard density functional theory (DFT) calculations on ions and cation-anion ion pairs—and can thus be used to create models totally without any experimental parametrization—one major advantage of the approach chosen.

The various models developed in this study have been fitted and evaluated against in-house measured ionic conductivities. While this clearly limits the statistics of the study in terms of quantity, it improves the quality as it avoids the errors that can result from gathering data from many different sources—important as reported IL conductivities are very sensitive to impurities, not the least water, and the set-up/sample history. From this approach the best fits are reported as largely phenomenological models using some few statistical measures and then discussed in terms of e.g., sensitivity vs. the different input parameters computed and the ILs chosen to study.

MATERIALS AND METHODS

In total 22 different ILs were used as received from Solvionic with the highest purity available (99.9 or 99.5%). The temperature

TABLE 1 | Name (acronym), volume (V), mass (M), and moment of inertia (I) of ions.

Name	V [Å³]	M [u]	I [Å²u]
1-ethyl-3-methylimidazolium (EMI)	156	111	315
1-butyl-3-methylimidazolium (BMI)	196	139	577
1-hexyl-3-methylimidazolium (HMI)	246	167	1,041
1,3-dimethyl-2-propylimidazolium (PMMI)	204	139	536
1,3-dimethyl-2-butylimidazolium (BMMI)	224	153	760
trimethyl-butylammonium (Me₃BuN)	111	193	429
trimethyl-hexylammonium (Me₃HexN)	148	240	934
diethylmethylpropylammonium (Et₂MeProN)	212	130	438
1-propyl-1-methylpyrrolidinium (MPPyr)	199	128	409
1-butyl-1-methylpyrrolidinium (BMPyr)	222	142	638
1-pentyl-1-methylpyrrolidinium (MPePyr)	242	156	896
1-propyl-1-methylpiperidinium (MPPip)	221	142	483
tetrafluoroborate (BF₄)	71	87	95
hexafluorophosphate (PF₆)	96	145	201
trifluoromethanesulfonate (Tf)	115	149	276
bis(fluorosulfonyl)imide (FSI)	136	180	446
bis(trifluoromethanesulfonyl)imide (TFSI)	199	280	1,214

dependent ionic conductivity was measured using a Novocontrol broadband dielectric spectrometer in the frequency range 10^{-1}-10^7 Hz. A liquid parallel plate cell, BDS 1308 Novocontrol, with two stainless steel electrodes with a Teflon spacer (Ø = 13.2 mm, d = 0.99 mm) was assembled in an Ar glove box (H_2O and O_2 < 1 ppm) and loaded into a cryo-furnace with N_2 gas flow. Data were collected during heating from 298.15 to 368.15 K in steps of 10 K and stabilization times of 30 min. The DC conductivities were obtained from the low frequency plateau of the conductivity isotherms by plotting the real part of the complex conductivity as a function of frequency.

Computationally low-energy conformers of all cations (12) and anions (5) (**Table 1**) constituting the totally 22 ILs investigated experimentally were initially generated by the molecular mechanics based scan routine in Spartan 06[1]. Amongst the cations we use the most popular families: imidazolium, EMI etc., and pyrrolidinium, MPPyr (Pyr13) etc. From these the geometries and energies were optimized by DFT, first at the B3LYP/6-311+G* level and subsequently further with M06-2X/6-311+G* (Vosko et al., 1980; Lee et al., 1988; Becke, 1993; Zhao and Truhlar, 2007), and their 2nd derivatives calculated to ensure the geometries to be local minima energy structures. From the DFT results the ion volumes were calculated as averages of 10 runs using a Monte Carlo (MC) integration scheme of a 0.001 e/bohr³ density envelope and 100 integration points/bohr³. The moments of inertia of the ions were calculated as the arithmetic mean of the three principal eigenvalues obtained from the routine in the VMD software (Humphrey et al., 1996).

The lowest energy conformers (B3LYP) for each of the ions were used to generate cation-anion ion pairs, with 20 starting

[1]Spartan '06, Wavefunction Inc.

Cation-Anion	E_{int} (M06-2X/6-311+G*)[kJmol^{-1}]	T_g[K]
EMI-Tf	−378.9	−
EMI-FSI	−362.3	−
EMI-TFSI	−360.5	181 (Fredlake et al., 2004)
BMI-BF$_4$	−385.0	188 (Fredlake et al., 2004)
BMI-PF$_6$	−363.6	197 (Fredlake et al., 2004)
BMI-Tf	−376.5	191 (Tokuda et al., 2006)
BMI-TFSI	−367.3	187 (Fredlake et al., 2004)
HMI-PF$_6$	−362.2	195 (Harris et al., 2007)
HMI-Tf	−374.6	189 (Gómez et al., 2013)
HMI-TFSI	−363.7	189 (Gómez et al., 2013)
PMMI-TFSI	−364.2	−
BMMI-TFSI	−363.7	−
Me$_3$BuN-TFSI	−343.9	199 (Tokuda et al., 2006)
Me$_3$HexN-TFSI	−353.5	202 (Taggougui et al., 2008)
Et$_2$MeProN-FSI	−340.7	−
MPPyr-FSI	−343.3	190 (Zhou et al., 2008)
MPPyr-TFSI	−346.8	188 (Calvar et al., 2013)
BMPyr-Tf	−361.5	197 (Calvar et al., 2013)
BMPyr-TFSI	−351.2	191 (Calvar et al., 2013)
MPePyr-TFSI	−352.1	−
MPPip-FSI	−332.9	−
MPPip-TFSI	−338.5	192 (Paduszynski et al., 2011)

configurations for each pair generated by our in-house developed software SECIL (Angenendt and Johansson). All structures were optimized in two steps; i) B3LYP/6-311+G* - providing a selection of 10 structures/ion pair based on energy and transferred to ii) M06-2X/6-311+G*. Not all SECIL generated configurations reach SCF convergence, but most B3LYP minima produce M06-2X minima, as verified by the 2nd derivatives. All DFT and MC calculations were made using the Gaussian 03 and 09 program packages (Frisch et al., 2004, 2010). From the M06-2X/6-311+G* data the ion-ion interaction energy, E_{int} = $E_{(ion\ pair)}$-Σ(E_{cation}+E_{anion}), was calculated—as a measure of specific ion-ion interaction strength (**Table 2**). Due to the main aim of arriving at a proof-of-concept method, and not the most performant, and the many other model omissions and simplifications, no comparisons to other DFT functionals (or higher *ab initio* methods) nor any basis set size effect investigations or basis set super-position error corrections were made.

Using the ion volume (V), mass (M), moment of inertia (I) and ion pair (E_{int}, reduced mass) data generated, potential models for the conductivity as function of temperature were formulated and tested with OriginPro 2015[2], using the Levenberg-Marquardt iteration algorithm to fit the data to a predefined function. The most promising models were further combined to achieve better fits, while kept physically sound.
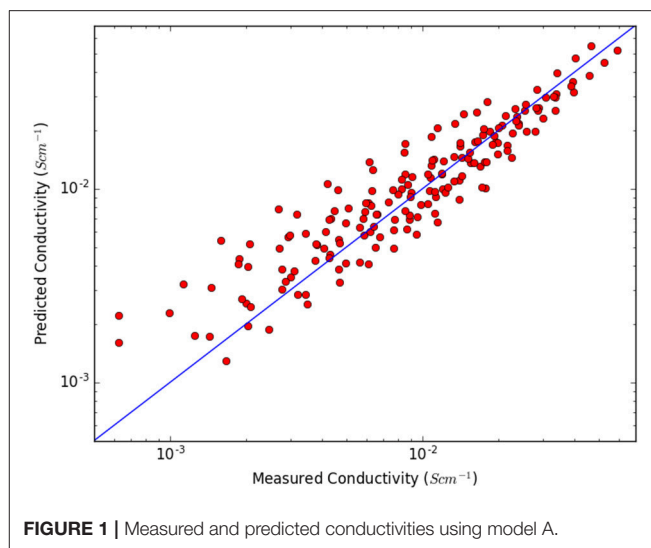
FIGURE 1 | Measured and predicted conductivities using model A.

RESULTS AND DISCUSSION

The computational data generated span an appreciable range of IL ion volumes (71–246 Å^3), masses (87–280 u), moments of inertia (95–1214 Å^{2}u), and interaction energies (−333 to −385 kJmol^{-1}). The first model found with an appreciable fit to the conductivity data, 176 data points for the 22 ILs, is **A** (**Figure 1**):

$$\sigma = \frac{b}{V_{tot}^2 I_+} \exp\left(c\frac{Eint}{T - T_0}\right) \quad \textbf{(A)}$$

where the input parameters V_{tot} is the sum of the cation and anion volumes, I_+ is the moment of inertia of the cation, and E_{int} is the interaction energy, while b, c, and T_0 are fitting parameters. That the conductivity is inversely proportional to the ion volumes, as in **A**, can easily be understood as larger ions both move slower and hinder movement of other ions and this has indeed been found previously (Slattery et al., 2007; Johansson et al., 2010; Tsuzuki, 2012), but why it should be proportional to the inverse of the volume squared is unclear.

It has previously been shown that the viscosity of ILs is affected by the IL ion masses (Abbott, 2004, 2005; Matsuda et al., 2007) and as the conductivity is related to the fluidity, the inverse of the viscosity through the fractional Walden rule, it is reasonable to assume that these could affect the conductivity. The reduced masses, M_{red}, are indeed almost linearly proportional to the volumes V_{tot} (**Figure 2**).

why a second model, **A2**, with one of the terms exchanged, was investigated—with almost equally good fit (**Figure 3**):

$$\sigma = \frac{b}{V_{tot}M_{red}I_+} \exp\left(c\frac{Eint}{T - T_0}\right) \quad \textbf{(A2)}$$

In both models **A** and **A2** T_0 has to some extent been treated as a normal fitting parameter. This enables a true prediction of conductivity without any prior IL synthesis, but given the coupling of T_0 to T_g, experimental T_g data as input might
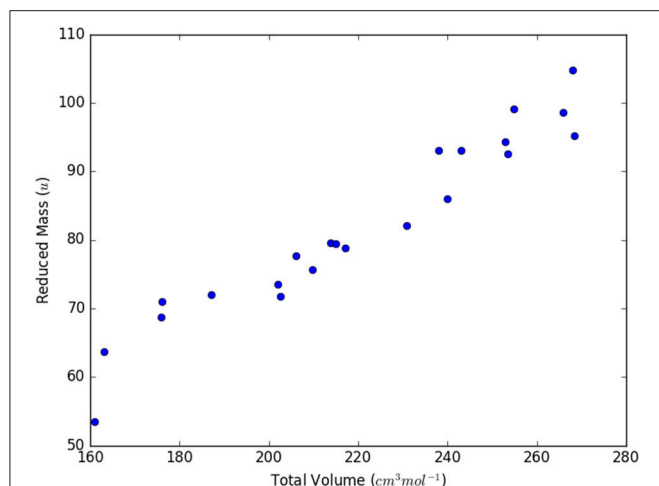
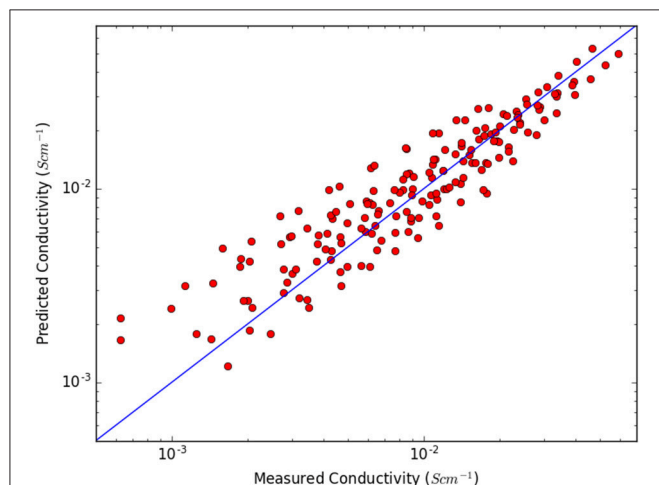**FIGURE 2 |** Correlation between total volume and reduced mass for the IL ion pairs.

FIGURE 3 | Measured and predicted conductivities using model **A2**.

improve the fits and models. In the literature T_g for 15 of the 22 ILs used were found (**Table 2**) covering the range 181-202 K (which arguably is a rather limited span in temperature). Applying these data to **A** and **A2** result in models **B** and **B2**, respectively:

$$\sigma = \frac{b}{V_{tot}^2 I_+} \exp\left(c\frac{Eint}{T-(T_g+d)}\right) \quad (\mathbf{B})$$

$$\sigma = \frac{b}{V_{tot}M_{red}I_+} \exp\left(c\frac{Eint}{T-(T_g+d)}\right) \quad (\mathbf{B2})$$

where d is an additional fitting parameter and indeed the fits are slightly improved. Using the reduced data set (15/22) in **A** and **A2** did not improve their fits and thus the improvement indeed comes from the inclusion of T_g (keeping in mind the limited T range). All models with their parameter values and statistical measures are summarized in **Table 3**.

TABLE 3 | Fitting parameter values, correlation coefficients (R^2), and mean absolute errors (MAE) for the four IL conductivity models.

Model	b [Scm^{-1}Å^{8}u]	c [KkJ^{-1}]	T$_0$/d [K]	R^2	MAE [%]
A	$1.29 \pm 0.45 \times 10^7$	-1.01 ± 0.26	204 ± 18.0	0.9538	35.3
A2	$2.52 \pm 0.88 \times 10^6$	-0.90 ± 0.25	211 ± 18.0	0.9508	36.5
B	$1.09 \pm 0.38 \times 10^7$	-0.82 ± 0.23	34.6 ± 15.9	0.9627	24.8
B2	$3.19 \pm 1.22 \times 10^6$	-1.01 ± 0.28	22.6 ± 17.6	0.9600	26.1

CONCLUDING REMARKS

Two VFT based models for IL conductivity without any experimental input have been developed using volume, mass, and moment of inertia of the constituting ions and the energy of the interaction between cation and anion. In contrast to earlier models there are no anion-specific parameters needed, and in addition moments of inertia of the cations are for the first time included. For the latter feature we initially believed a larger principal moment of inertia to be likely to have a decisive influence due to the elongated shape of many of the ions. However, no such behavior was found in the fits why the arithmetic mean of the three principal values is used. The main influence by the cation moment of inertia is due to many anions being close to spherical. All models without I_+ performed much worse than the fits here obtained and the inclusion of experimental glass transition temperatures improves the fit, but not to any large extent. From a physical point of view, the ion mass may influence the conductivity, why both A2 and B2, replacing one of the volume terms with the reduced masses of the ion pairs, could improve the fit if applied to a larger and more diverge data set (even if they here actually reduce the goodness of the fit). As VFT models in general captures ion conductivities of ILs (and other systems) quite well all of the above in terms of overall agreement come as no major surprise. Phenomenonlogically all the four (VFT) models show the expected behavior; as the volumes, moments of inertia, and masses of the ions increase, the conductivity will approach zero (0), and if they decrease the conductivity will increase. Likewise, if the ion-ion interaction energy increases to infinity the conductivity will approach zero and the conductivity increases with temperature. The inclusion of experimental glass transition temperatures did improve the fit, but there is a rather narrow temperature range for the T_g used. We stress that we do refrain from trying to connect the input parameters to any direct physical interpretation—such as why the prefactor in the VFT equations seem to relate to the ion volume squared, and how in the exponential the ion-ion interaction energy relate to the activation energy, etc. We do, however, believe it to be straightforward to produce input to these models for any IL of choice—remembering our deliberatively set limits of no nano-structured ILs—for which this model is likely to fail—dependent on how the ion mobility is affected. The DFT calculations will be the time-determining step, even if most data required only needs to be calculated once for each ion, the interaction energy of each ion pair must be obtained separately for each IL.

AUTHOR CONTRIBUTIONS

ACKNOWLEDGMENTS

REFERENCES

Abbott, A. P. (2004). Application of hole theory to the viscosity of ionic and molecular liquids. *Chem. Phys. Chem* 5, 1242–1246. doi: 10.1002/cphc.200400190

Abbott, A. P. (2005). Model for the conductivity of ionic liquids based on an infinite dilution of holes. *Chem. Phys. Chem*. 6, 2502–2505. doi: 10.1002/cphc.200500283

Angenendt, K., and Johansson, P. SECIL- Software Engine for Configuration of Ionic Liquids.

Angenendt, K., and Johansson, P. (2010). Ionic liquid structures from large density functional theory calculations using mindless. Configurations *J. Phys. Chem. C* 114, 20577–20582. doi: 10.1021/jp104961r

Armand, M., Endres, F., MacFarlane, D. R., Ohno, H., and Scrosati, B. (2009). Ionic-liquid materials for the electrochemical challenges of the future. *Nat. Mater*. 8, 621. doi: 10.1038/nmat2448

Becke, A. D. (1993). Density-functional thermochemistry. III. The role of exact exchange. *J. Chem. Phys*. 98, 5648.

Borodin, O. (2009). Relation between heat of vaporization, ion transport, molar volume, and cation–anion binding energy for ionic liquids. *J. Phys. Chem. B* 113, 12353–12357. doi: 10.1021/jp9070357

Calvar, N., Gómez, E., Macedo, E. A., and Domínguez, Á. (2013). Thermal analysis and heat capacities of pyridinium and imidazolium ionic liquids. *Thermochim. Acta* 565, 178–182. doi: 10.1016/j.tca.2013.05.007

Castner, E. W. Jr. and Wishart, J. F. (2010). Spotlight on ionic liquids. *J. Chem. Phys*. 132, 120901. doi: 10.1063/1.3373178

Del Pópolo, M. G., Lynden-Bell, R. M., and Kohanoff, J. (2005). *Ab Initio* molecular dynamics simulation of a room temperature ionic liquid. *J. Phys. Chem. B* 109, 5895–5902. doi: 10.1021/jp044414g

Eiden, P., Bulut, S., Köchner, T., Friedrich, C., Schubert, T., Krossing, I., et al. (2011). *In silico* predictions of the temperature-dependent viscosities and electrical conductivities of functionalized and non-functionalized ionic liquids. *J. Phys. Chem. B* 115, 300–309. doi: 10.1021/jp108059x

Fredlake, C. P., Crosthwaite, J. M., Hert, D. G., Aki, S. N. V. K., and Brennecke J, F. (2004). Thermophysical properties of imidazolium-based ionic liquids. *J. Chem. Eng. Data* 49, 954–964. doi: 10.1021/je034261a

Frisch, M. J., Trucks, G. W., Schlegel, H. B., Scuseria, G. E., Robb, M. A., Cheeseman, J. R., et al. (2004). *Gaussian 03* . (Wallingford, CT).

Frisch, M. J., Trucks, G. W., Schlegel, H. B., Scuseria, G. E., Robb, M. A., Cheeseman, J. R., et al. (2010). *Gaussian 09*. (Wallingford, CT).

Gómez, E., Calvar, N., Domínguez, Á., and Macedo, E. A. (2013). Thermal analysis and heat capacities of 1-Alkyl-3-methylimidazolium ionic liquids with NTf2–, TFO–, and DCA– anions. *Ind. Eng. Chem. Res*. 52, 2103–2110. doi: 10.1021/ie3012193

Harris, K. R., Kanakubo, M., and Woolf, L. A. (2007). Temperature and pressure dependence of the viscosity of the ionic liquids 1-hexyl-3-methylimidazolium hexafluorophosphate and 1-butyl-3-methylimidazolium bis(trifluoromethylsulfonyl)imide. *J. Chem. Eng. Data* 52, 1080–1085. doi: 10.1021/je700032n

Humphrey, W., Dalke, A., and Schulten, K. (1996). VMD: visual molecular dynamics. *J. Mol. Graph*. 14, 33–38.

Johansson, P., Fast, L. E., Matic, A., Appetecchi, G. B., and Passerini, S. (2010).The conductivity of pyrrolidinium and sulfonylimide based ionic liquids: A combined experimental and computational study. *Power Sources J*. 195, 2074–2076. doi: 10.1016/j.jpowsour.2009.10.029

Kirchner, B. (2009). Ionic liquids from theoretical investigations. *Top. Curr. Chem*. 290, 213–262. doi: 10.1007/128_2008_36

Lee, C., Yang, W., and Parr, R. G. (1988). Development of the Colle-Salvetti correlation-energy formula into a functional of the electron density. *Phys. Rev. B* 37, 785.

Lewandowski, A., and Swiderska-Mocek, A. (2009). Ionic Liquids as electrolytes for li-ion batteries—an overview of electrochemical studies. *Power Sources J*. 194, 601–609. doi: 10.1016/j.jpowsour.2009.06.089

Liu, H., and Maginn, E. (2012). An MD study of the applicability of the walden rule and the nernst–einstein model for ionic liquids. *Chem. Phys. Chem*. 13, 1701–1707. doi: 10.1002/cphc.201200016

Maginn, E. J. (2009). Molecular simulation of ionic liquids: current status and future opportunities. *J. Phys. Cond. Matt*. 21:373101. doi: 10.1088/0953-8984/21/37/373101

Matsuda, H., Yamamoto, H., Kurihara, K., and Tochigi, K. (2007). Prediction of the ionic conductivity and viscosity of ionic liquids by QSPR using descriptors of group contribution type. *J. Comp. Aid Chem*. 8, 114–127. doi: 10.2751/jcac.8.114

Paduszynski, K., Chiyen, J., Ramjugernath, D., Letcher, T. M., and Domanska U (2011). Liquid–liquid phase equilibrium of (piperidinium-based ionic liquid+ an alcohol) binary systems and modelling with NRHB and PCP-SAFT. *Fluid Phase Equilibria* 305, 43–52. doi: 10.1016/j.fluid.2011.03.005

Plechkova, N. V., and Seddon, K. R. (2008). Applications of ionic liquids in the chemical industry. *Chem. Soc. Rev*. 37, 123. doi: 10.1039/B006677J

Preiss, U., Bulut, S., and Krossing, I. (2010). *In silico* prediction of the melting points of ionic liquids from thermodynamic considerations: a case study on 67 salts with a melting point range of 337°C. *J. Phys. Chem. B* 114, 11133–11140. doi: 10.1021/jp104679m

Slattery, J. M., Daguenet, C., Dyson, P. J., Schubert, T. J. S., and Krossing, I. (2007). How to predict the physical properties of ionic liquids: a volume-based approach. *Angew. Chem*. 119, 5480–5484. doi: 10.1002/anie.200700941

Taggougui, M., Diaw, M., Carré, B., Willmann, P., and Lemordant, D. (2008). Solvents in salt electrolyte: Benefits and possible use as electrolyte for lithium-ion battery. *Electrochim. Acta* 53, 5496–5502. doi: 10.1016/j.electacta.2008.03.012

Thematic issue: Ionic liquids (2012). *Faraday Discuss*. 154.

Thematic issue: Ionic liquids for energy applications (2013). *MRS Bull*. 38.

Thematic issue: Physical chemistry of ionic liquids (2010). *Phys. Chem. Chem. Phys*. 12.

Tochigi, K., and Yamamoto, H. (2007). Estimation of ionic conductivity and viscosity of ionic liquids using a QSPR model. *J. Phys. Chem. C* 111, 15989–15994. doi: 10.1021/jp073839a

Tokuda, H., Tsuzuki, S., Susan, M. A., Hayamizu, K., and Watanabe, M. (2006). How ionic are room-temperature ionic liquids? an indicator of the physicochemical properties. *J. Phys. Chem. B* 110, 19593–19600. doi: 10.1021/jp064159v

Tsuzuki, S. (2012).Factors controlling the diffusion of ions in ionic liquids. *Chem. Phys. Chem*. 13, 1664–1670. doi: 10.1002/cphc.201100870

Tsuzuki, S., Tokuda, H., Hayamizu, K., and Watanabe, M. (2005). Magnitude and directionality of interaction in ion pairs of ionic liquids: relationship with ionic conductivity. *J. Phys. Chem. B* 109, 16474–16481. doi: 10.1021/jp0533628

Ueno, K., Tokuda, H., and Watanabe, M. (2010). Ionicity in ionic liquids: correlation with ionic structure and physicochemical properties. *Phys. Chem. Chem. Phys* 12, 1649–1658. doi: 10.1039/b921462n

Vila, J. Ginés, P., Pico, J. M., Franjo, C., Jiménez, E., Varela, L.M., et al. (2006). Temperature dependence of the electrical conductivity in EMIM based ionic liquids. Evidence of Vogel-Tamman-Fülcher behavior. *Fluid Phase Equilibria* 242, 141–146. doi: 10.1016/j.fluid.2006.01.022

Vosko, S. H., Wilk, L., and Nusair, M. (1980). Accurate spin-dependent electron liquid correlation energies for local spin density calculations: a critical analysis. *Can. J. Phys*. 58, 1200.

Zhao, Y., and Truhlar, D. G. (2007). The M06 suite of density functionals for main group thermochemistry, thermochemical kinetics, noncovalent interactions, excited states, and transition elements: two new functionals and systematic testing of four M06-class functionals and 12 other functionals. *Theor. Chem. Acc.* 120, 215–241. doi: 10.1007/s00214-007-0310-x

Zhou, Q., Henderson, W. A., Appetecchi, G. B., Montanino, M., and Passerini, S. (2008). Physical and electrochemical properties of N-alkyl-N-methylpyrrolidinium bis(fluorosulfonyl)imide ionic liquids: PY13FSI and PY14FSI. *J. Phys. Chem. B* 112, 13577–13580. doi: 10.1021/jp805419f

Utilizing Water Activity as a Simple Measure to Understand Hydrophobicity in Ionic Liquids

Qi Han*, Xungai Wang and Nolene Bynre*

Institute for Frontier Materials, Deakin University, Geelong, VIC, Australia

Ionic liquids (ILs) are regarded as designable solvents finding use in a variety of applications. One of the challenges of the design and selection process is to understand the ionic liquid properties. In this work, we selected seven ILs containing three types of hydrophilic anions and examined several key properties, which are correlated to hydrophobicity. In particular, we measured the hydrogen bond basicity β and water activity a_w of IL and IL-water mixtures, and suggested that these two properties are linearly correlated particularly in hydrated ILs. We then used NMR to evaluate the chemical shift of H_2O in hydrated ILs. Correlating the outcomes of each of these techniques with respect to understanding the hydrophobicity of the ILs is discussed. It is shown that water activity a_w is the most facile technique to represent and understand hydrophobicity of ILs.

INTRODUCTION

Ionic liquids (ILs) are salts with melting points below $100°C$. One of the most attractive properties of ILs is the tunability of the component ions, and extensive efforts have been devoted to understanding the properties of various ILs (Welton, 1999; Forsyth et al., 2004; Plechkova and Seddon, 2008; Freemantle, 2010; Hallett and Welton, 2011). Some key IL properties include polarity, hydrophobicity, viscosity, purity, and Kamlet Taft parameters (Olivier-Bourbigou et al., 2010). However, some of the important properties of ILs such as hydrophobicity cannot be easily measured, while a few of these properties may be correlated but require more studies.

Hydrophobicity of ILs is considered in a wide range of applications. It has been demonstrated that the IL hydrophobicity influences its solvation ability, reaction rates, reaction mechanisms, product yields, and enzyme activity, etc. (van Rantwijk and Sheldon, 2007; Hallett and Welton, 2011). While water is the most universal solvent and considered as impurity or co-solvent of ILs (Li et al., 2010, 2012; Patel et al., 2014; Han et al., 2017), hydrophobicity represents the miscibility with water. However, there is no normalized scale for the hydrophobicity. Generally, the Log P scale has been used to quantify the hydrophobicity of ILs, which is defined as the logarithm of their partition coefficient P of un-ionized ILs between octanol and water. Whereas in some cases, an IL partitions in an octanol/water mixture as an ion pair, and hence the log P value may depend not only on the concentration of the cation but also on that of the anion, and of ion pairing in both phases (Kaar et al., 2003; Yang and Pan, 2005). Conversely, a number of researchers predicted IL Log P by computation (Chapeaux et al., 2007; Mutelet et al., 2011). Thus, Log P can hardly be measured and present the hydrophobicity of ILs, but it can be a useful value for the prediction of the hydrophobicity.

The hydrophobicity can be regarded as a subset concept of polarity. The polarity is associated to the solubility of substrates/products and water association between solvent and solute (Zaks and Klibanov, 1988).The polarity of ILs can be quantified as Kamlet-Taft (KT) solvatochromic parameters, which is based on the analysis of the UV-Vis spectral band shifts of solvatochromic probes (Kamlet et al., 1981) (Oehlke et al., 2006). The KT parameters include hydrogen bond acidity α, hydrogen bond basicity β and dipolarity/polarizability π*, while β is considered as a significant parameter, since it specifically describes the solvent ability to donate electron density to form a hydrogen bond with protons of a solute (Ab Rani et al., 2011). Thus, β is related to the tendency of ILs to form hydrogen bonds with the water molecule and can be considered as an important indicator of hydrophobicity of ILs. Meanwhile, the nucleophilicity is related to polarity and particularly β (Zhao, 2016), but it cannot be measured and will be incorporated in the concept of polarity. KT parameters are measurable, however, the major drawback of their measurement is that the measurement depends on the set of probe dyes used, and it is sensitive to measurement conditions, such as the color and purity levels of the ILs and procedures employed. Recently, numerous studies utilized water as a co-solvent of ILs to modulate β and thus hydrogen bonding interaction, e.g., hydrated ILs by adding a small amount of water (∼75 mol%) (Ohno et al., 2015) and IL-water mixtures (∼90 mol%) (Lai et al., 2011; Han et al., 2016).

From the aspect of water, the contribution of water is associated with the free water rather than the water content added in the solvent (Zaks and Klibanov, 1988). And this can be quantified by the thermodynamic water activity (a_w). a_w is defined as the ratio of the partial pressure of aqueous salt solutions (p) to that of pure water ($p0$) (i.e., $a_w = p/p0$) (Cauvain and Young, 2009). Nowadays, a_w can be measured using certain instruments (Ohno et al., 2015). Besides, another property of ILs, kosmotropicity, describes an ion's ability to facilitate the structuring of nearby water molecules. Previous studies have suggested that the hydration state of an IL correlates with its stabilization effect on the dissolved proteins (Fujita et al., 2007). And recent studies have shown that the chemical shift of H_2O in ILs using nuclear magnetic resonance is related to the state of the hydrogen bonding network (Sare et al., 1973; Saihara et al., 2015) and even the kosmotropicity (Nikawa et al., 2017).

It has been demonstrated that the chemical structure of the ILs such as the chain length of cation and unique structure of anion [e.g., bis(trifluoromethylsulfonyl)imide (Tf_2N^-) and hexafluorophosphate (PF_6^-)] influences the hydrophobicity of ILs (Cammarata et al., 2001). Since most ILs tend to be hydrophilic (water-miscible), to investigate the rule of their hydrophobicity was the focus of this work. In the present work, we selected seven simple ILs to understand the correlation between measured properties and hydrophobicity of ILs. The ammonium cations coupled with hydrophilic anions including propionate, mesylate and dihydrogen phosphate were selected (**Figure 1**). The hydrogen bond basicity β and water activity of the ILs and hydrated ILs were explored, and the chemical shift of

H_2O in hydrated ILs was subsequently measured. Then the Log P of the conjugated base and acid was evaluated. By correlating the results of these measurements, the hydrophobicity of the ILs is discussed.

METHODS

Synthesis of ILs
All starting reagents were commercially obtained unless further mentioned, and used without further purifications. The ILs [ethylammonium mesylate (EaMs), triethylammonium mesylate (TeaMs), choline mesylate (ChoMs), ethylammonium propionate (EaPn), ethanolammonium propionate (EoaPn), choline propionate (ChoPn), choline dihydrogen phosphate (ChoDHP)] were synthesized according to the reported method (Belieres and Angell, 2007; Han et al., 2016). In brief, the ILs were synthesized by neutralizing equimolar amounts of the corresponding acid and base. A typical example of the procedure is as follows. Triethylamine (5.06 g, 0.05 mol) was added drop-wise to methanesulfonic acid (4.80 g, 0.05 mol) in a round bottom flask (250 mL) whilst stirring with a magnetic stir bar in an ice bath for 2 h. The mixture was allowed to stir overnight at room temperature and then dried under reduced pressure for 8 h at 40°C. After drying, a transparent clear liquid (9.85 g) was obtained. The water content of the synthesized ILs (<1 wt%) was measured by a Karl Fisher coulometer (Metrohm 899, MEP Instruments). The water content of EaMs, TeaMs, ChoMs, EaPn, EoaPn, ChoPn, ChoDHP was 0.50, 0.81, 0.89, 0.10, 0.93, 1.00, and 0.60 wt%, respectively. NMR samples of synthesized ILs were prepared in deuterated dimethyl sulfoxide (DMSO-d6). NMR experiments were acquired at 298 K (20°C) using 500 MHz Bruker Avance III nuclear magnetic resonance spectrometer (^{1}H at 500.130 MHz) equipped with a 5 mm broad-band probe. Chemical shifts (δ) are expressed in ppm with reference to the residual solvent signal (2.500 ppm for DMSO).

Characterization
The hydrogen bond basicity β of ILs and IL-water mixtures was measured and calculated as reported (Hauru et al., 2012; Debeljuh et al., 2013). Experimental conditions were slightly modified based on methanol and water, and the obtained values of methanol and water were in good agreement with the literature (Deye et al., 1990). First, a specified amount of ILs was gravimetrically mixed with MilliQ water to reach the required concentrations. The stock solutions of 4-nitroaniline (NA, 1 mol/L) and *N,N*-diethyl-4-nitroaniline (DENA, 1 mol/L) were dissolved in methanol prior to use. A 1 µL portion of the stock solution was transferred to 1 mL IL solutions (neat, 25 mol% or 8.3 mol% ILs) and the mixture was vigorously agitated using a vortex. The λmax of each sample was obtained from using UV/vis spectrophotometry. Deionized water or blank IL samples were measured and were background subtracted. UV/vis measurements for each sample were measured at room temperature and were repeated at least twice. The peak of the spectra was fitted with a Gaussian function in order to precisely locate the maxima
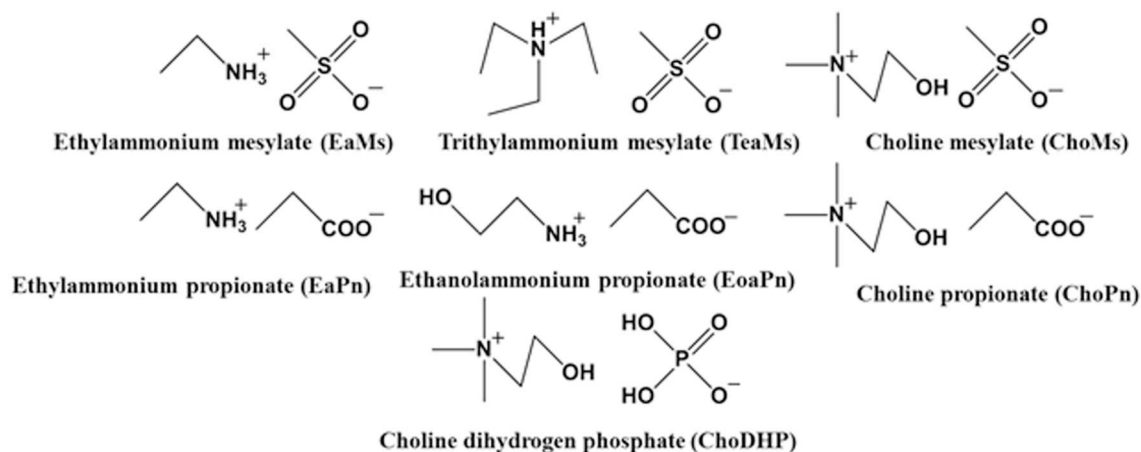
FIGURE 1 | Structure of ionic liquids used in this study.

(λmax). The result was a resolution exceeding that of the instrument (1 nm). The β was calculated according to equations 1 and 2,

$$vmax/1000 \; cm^{-1} = \frac{1}{0.0001 \lambda max/nm} \qquad (1)$$

$$\beta = \frac{1.035 \; vmax \, (DENA) + 2.64 - vmax(NA)}{2.8} \qquad (2)$$

where λmax (nm) is the maximum wavelength, while $v$max (DENA) and $v$max (NA) are the wavenumbers (1,000 cm^{-1}) at maximum absorbance for 4-nitroaniline and *N,N*-diethyl-4-nitroaniline, respectively (Kamlet and Taft, 1976). The mean deviations for β were $< \pm$ 0.01. The water activity of 3 mL IL-water mixtures (at 8.3 mol%, 10 mol%, 12.5 mol%, 16.7 mol%, 25 mol%, 33.3 mol% or neat ILs) was measured using a water activity instrument (LabSwift-a$_w$, Novasina AG). The solutions were placed in the container of the instrument and placed in the panel for readings. All the measurements were determined in a nitrogen atmosphere (Aldrich AtmosBag, Sigma-Aldrich) with triplicate readings (mean deviations $< \pm$ 0.03). The NMR experiments of the hydrated ILs were prepared in CDCl$_3$ using a coaxial insert. The predicted Log P and ALogP of the ILs in this study was estimated Chemicalize (ChemAxon)[1] and VCCLab (VCCLAB),[2] respectively.

RESULTS AND DISCUSSION

Hydrogen Bond Basicity β of the ILs

Since the hydrogen bond basicity β is possibly an important indicator for the evaluation of hydrophobicity, β of the seven ILs was initially evaluated. **Table 1** shows β of the ILs including

[1]*ChemAxon Chemicalize*. Available online at: https://chemicalize.com (accessed May, 11 2018).
[2]*VCCLAB Virtual Computational Chemistry Laboratory*. Available online at: http://www.vcclab.org (accessed May 11, 2018).

TABLE 1 | β values of ILs and IL-water mixtures in this study.

ILs	β of neat ILs	β of hydrated ILs (25 mol%)	β of ILs at 8.3 mol%
EaMs	–	0.57	0.29
TeaMs	0.74	0.59	0.42
ChoMs	–	0.46	0.18
EaPn	1.02	0.64	0.40
EoaPn	0.91	0.63	0.36
ChoPn	0.98	0.70	0.57
ChoDHP	–	0.26	0.25

–, unmeasurable due to the high melting point of the ILs.

neat ($\sim$100% IL), hydrated (25 mol%) and IL-water mixtures (8.3 mol%). In particular, the last two concentrations have been identified as the boundary of different states of ILs. ILs at $\sim$25 mol% presented as typical hydrated ILs where molar ratio of IL and H$_2$O is 1:3 with no free water, while IL-water mixtures ($\sim$8.3 mol% ILs) contained incompletely dissociated ions (Zhang et al., 2008; Kohno and Ohno, 2012; Stange et al., 2013; Ohno et al., 2015; Han et al., 2017). As the some of the ILs were not room-temperature ILs, the β of neat ILs was not obtained. As reported, β is mainly controlled by the IL anion (Ab Rani et al., 2011), and hence the seven ILs were categorized as three groups based on the anions.

It is seen that the intrinsic β values of four neat ILs were up to 0.7, while the three propionate-based ILs had similar β ($\sim$1.0). β of ChoPn was slightly higher than other two ILs, whereas the difference among the three ILs was not distinguishable. Regarding hydrated ILs (25 mol%), the β values decreased along with the dilution effect on the ILs. β of propionate-based ILs was in the range of 0.63–0.7 and was higher than that of mesylate-based ILs (0.46–0.59), while ChoDHP showed the lowest β value (0.26). Another study has also reported the similar order in neat or concentrated ILs (Zhao, 2016). In IL-water mixtures (8.3 mol%), the β values further reduced, while the trend of β was

observed as same as it in hydrated ILs, i.e., propionate-based ILs > mesylate-based ILs > ChoDHP. Notably, β of ChoPn still showed the highest value among the ILs, and this larger β value implies that choline has a greater tendency to accept protons from the probe dye when coupled with propionate than other combinations of cations and anions. β of mesylate-based ILs varied from 0.18 to 0.42, while ChoMs showed the lowest β in the seven ILs. Generally, the decreasing rate of β values as a function of IL concentration was different. For example, from 25 to 8.3 mol%, β of ChoMs dropped from 0.46 to 0.18, however, it was 0.26–0.25 for ChoDHP. This may be due to the incompletely dissociated ions of ILs in 8.3 mol% and such dissociation varies with different types of ILs (Zhang et al., 2008; Stange et al., 2013). In addition, it has been reported that β of aqueous ILs was not linear as a function of water, while the tendance was slightly different for ILs holding the same anion (Debeljuh et al., 2013). However, it observes that ChoDHP remained ∼0.25 over the dilution, indicating that choline cation may become a weaker hydrogen bond acceptor when coupling with dihydrogen phosphate.

Considering that β refers to the solvent ability to form a hydrogen bond (Ab Rani et al., 2011), it can be implied that mesylate-based ILs with lower β have a lower tendency to form hydrogen bonds with water molecule, and hence they are less hydrophilic than propionate-based ILs, while ChoDHP has the lowest measured β values and therefore is likely to have less hydrogen bonding interactions. It can be proposed that this rule can also be applied to the evaluation of the affinity of ILs with water and hence hydrophobicity of ILs. It is noticeable that the anion dominates the β values, and propionate anion tends to be basic while mesylate anion tends to be neutral as reported (Pagni, 2003; MacFarlane et al., 2006).

Water Activity as a Function of IL Concentration

The role of water in ionic liquids is important and many applications of IL use water as a co-solvent. Strong interactions of water molecules with the ions of ILs reduce the vapor pressure, which can be measured by water activity a_w. Thus, the high values of a_w (up to 1) refers to low interaction/affinity of ILs with water, and vice versa. In **Figure 2**, it is observed that the water activity a_w decreased from 1 to almost 0 as a function of the molar concentration of ILs in the solution. At low IL concentrations (0–20 mol%), water activity a_w decreased rapidly, while the decreasing rate was relatively steady in IL solutions with more than 20 mol% ILs. This indicates that the interaction between water and ILs becomes stronger in the hydrated state (<25 mol%), while the decreasing rate of a_w was reduced probably owing to the weakened interaction between water and ILs and the partial dissociation of ions. Meanwhile, the differences of a_w among the seven ILs was more distinguishable within this range (around 25 mol% ILs). This range has been highlighted as the hydrated state of IL, which contains no free water and has been applied as biological systems (Ohno et al., 2015; Han et al., 2016). Thus, the comparison among the ILs was focused in this region, i.e., 25 mol%.
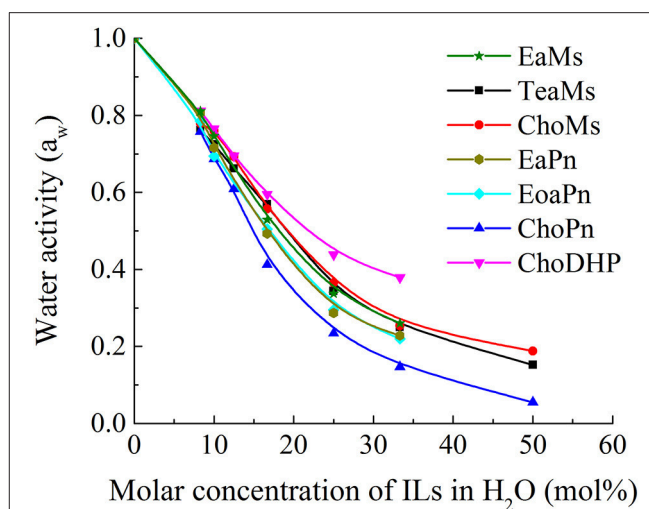
FIGURE 2 | Water activity of ILs as a function of molar concentration.

For the seven ILs particularly at 25 mol%, the overall trend for water activity as function of water concentration is very similar to β values measured above. The order of a_w shows ChoDHP > propionate-based ILs > mesylate-based ILs, suggesting that ChoDHP showed the lowest affinity with water, and ChoPn had the highest affinity. The three mesylate-based ILs showed very similar values across the entire water concentration range measured. The two ILs EaPn and EoaPn had similar trend along the IL concentrations, while they were slightly higher than ChoPn. It is known that ChoPn possesses strong hydrogen bonding capabilities (β = 0.98) and thus is the most hydrophilic among the seven ILs (Fukaya et al., 2007; Patinha et al., 2015). In addition, while TeaMs and ChoMs with chemically different cations shared a similar a_w, this indicates that the anion mesylate significantly influenced the hydrophobicity. This is in agreement with previous studies, which showed that the anion plays an important role on the IL properties (MacFarlane et al., 2006; Sate et al., 2007), and is primarily involved in the formation of hydrogen bonding (Cammarata et al., 2001). However, for ILs holding the same anion, the hydrophobicity of ILs cannot be easily identified as a function of cation.

Since **Figure 2** shows the clear trend of a_w in hydrated ILs (25 mol%), we correlated β with a_w at the same concentration of ILs (**Figure 3**). In particular, at 25 mol%, the molar ratio of IL and water is 1:3, which forms hydrated condition of ILs without free water. In this case, depending on the hydrophobicity, the properties of hydrated ILs such as β, a_w are impacted. **Figure 3** demonstrated the inverse linear relationship between β with a_w, where R^2 reached 0.9021. It should be noted that in the seven points, there are no critical points i.e., extreme high beta with low a_w or extreme low beta with high a_w, we suggest that this relationship is a linear relationship in such range. ChoPn showed the highest β up to 0.70 and the lowest a_w (0.234), while ChoDHP had the lowest β reaching 0.26 and highest a_w (0.438). The order of hydrophobicity can be described as ChoPn < EaPn ≈ EoaPn

FIGURE 3 | The linear correlation between hydrogen bond bacisity β and water activity a_w of hydrated ILs (25 mol%).

FIGURE 4 | NMR diagram of the hydrated ILs (25 mol%) at 20°C. The asterisk (*) refers to the signal of H_2O in the ILs. The NH peaks of protic ILs were marked. The dotted vertical line represents the signal of neat H_2O (4.80 ppm).
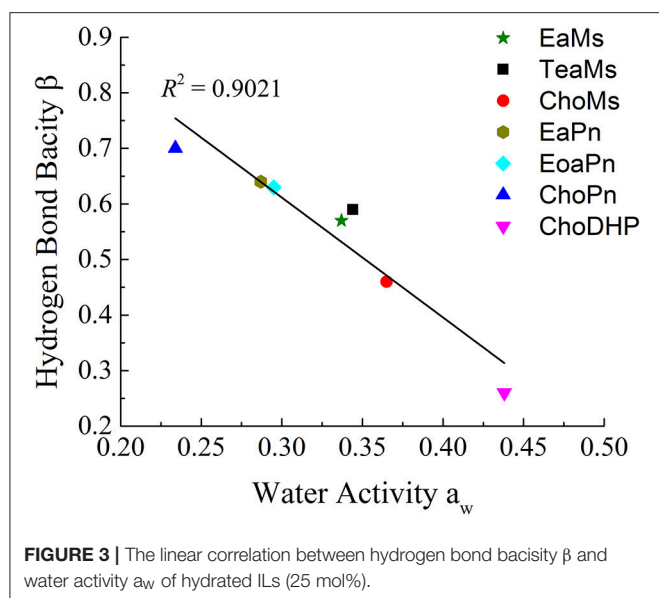
< EaMs ≈ TeaMs < ChoMs < ChoDHP. Again, the anion plays a key role on these two properties, however, the differences between EaPn and EoaPn, EaMs and TeaMs were relatively indistinctive. This may be because they shared the similar cations and same anions. Considering the nature of β and a_w as discussed above and their linear correlation, it can be suggested that the trend of water activity directly represents the different hydrogen bond network (expressed by β) in IL solutions, and hence hydrophobicity of ILs.

In general, both β and a_w of the seven ILs have a clear trend at 25 mol%, which is useful to understand the hydrophobicity of ILs. However, for a_w of diluted ILs (lower than 15 mol%) and β of neat ILs, the difference among the ILs was not significant (**Table 1** and **Figure 1**). Taken the test method into consideration, the measurement of β has a few drawbacks, such as the sensitivity of ILs to the set of probe dyes used and to measurement conditions. The evaluation of a_w at 25 mol% ILs is likely to be a more facile approach to understand the hydrophobicity of ILs.

Chemical Shift of H_2O in Hydrated Ionic Liquids

Here, NMR is used to evaluate the formation of hydrogen bonding networks between ionic liquids and water molecules. The chemical shift of H_2O in hydrated ILs can reveal hydration state of the ions, which also represented the kosmotropicity (Nikawa et al., 2017). In **Figure 4**, it is observed that the chemical shift of H_2O in hydrated ILs (25 mol%) varied based on the chemical shift relative to that of neat water (4.81 ppm).

It is evident that the chemical shift of H_2O in EaMs and TeaMs shifted slightly upfield to 4.73 and 4.50 ppm, respectively. As reported, the upfield shift suggests that the formation of hydrogen bonding network was promoted by the ILs (Nikawa et al., 2017). However, these two ILs are protic ILs
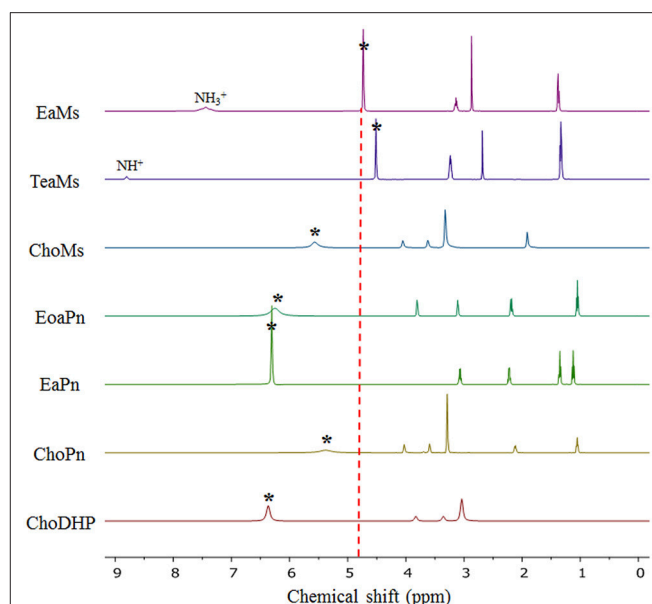
with transferred protons, which may be not comparable with other aprotic ILs. Moreover, the upfield shift of NH peak was noted, suggesting the water may influence the proton transfer. Interestingly, the other two protic ILs, EoaPn and EaPn showed the water peak in downfield, and their NH peaks were merged into the signal of water. This may imply that water was fast exchanged with the transfer proton in EoaPn and EaPn, and hence the merge with NH peak led to the downfield shift of water peak. Therefore, these two ILs formed stronger hydrogen bonding with water than EaMs and TeaMs. This result is supported by the β and a_w curves of ILs (**Table 1** and **Figure 2**). In other words, EoaPn and EaPn were more hydrophilic than EaMs and TeaMs.

Furthermore, chemical shift of H_2O can be correlated with a_w, as seen in **Figure 5**. In the four protic ILs, no clear trend was observed due to the interaction of NH peak with the exchangeable proton of H_2O. However, based on the anion, the ILs can be classified into the two regions, i.e., EaPn and EoaPn (I) vs. EaMs and TeaMs (II). Region I was coupled with propionate anion showing the merged peak of NH and H_2O, while region II had single peak of H_2O (**Figure 4**). However, comparing EaPn with EoaPn or EaMs with TeaMs, no noticeable difference on the hydrophobicity was observed (**Figures 3**, **5**). This implies that the anion impacts significantly for these two groups of protic ILs.

In terms of the aprotic ILs (region III including ChoMs, ChoPn and ChoDHP), it can be seen that all the H_2O signals were shifted downfield, suggesting the disruption of the hydrogen bonding network in these ILs. ChoDHP showed the highest shift to downfield, demonstrating the weakest hydrogen bonding with water. This is agreed with the lowest β values and highest

FIGURE 5 | The correlation between chemical shift of H_2O and water activity a_w of hydrated ILs (25 mol%). Region I and II refers to protic ILs with and without H_2O peak merged with NH peak, respectively, and Region III represented aprotic ILs with linear correlation of chemical shift of H_2O and a_w, while the straight line is a guide of the tendency.

TABLE 2 | Log P-values of the conjugated base and acid of ILs in this study.

ILs	ALogP	Log P	
	Base/acid	**Base/acid**	**Cation/anion**
Ethylamine	−0.2	−0.27	−0.27
Triethylamine	1.57	1.26	1.26
Ethanolamine	−1.53	−1.32	−0.98
Choline hydroixde	−1.5	−4.66	−4.66
Propionic acid	0.31	0.48	0.48
Methanesulfonic acid	−2.02	−0.96	−0.96
Phosphoric acid	–	−1.02	−1.02

a_w of ChoDHP. In general, the order of chemical shift of H_2O also followed the order of a_w, i.e., ChoDHP, ChoMs and ChoPn (**Figure 5**). However, ChoMs and ChoPn, have a similar trend with respect to the water peak, while significant differences in β values and a_w curves were observed for these two ILs. It is reported that the chemical shift of H_2O in hydrated aprotic ILs reflected the formation of hydrogen bonding networks between ions and water molecules (Nikawa et al., 2017). Whereas, the relationship between chemical shift of H_2O and a_w in region III showed noticeable deviation on the fitted regression line, it can be suggested that the water peak of aprotic ILs measured by NMR may be not an accurate indicator of hydrophobicity.

Log P of ILs

Log P has been previously used as a reliable indicator of hydrophobicity (Kaar et al., 2003), however, with respect to the ILs investigated here, Log P via the experimental method could not obtain any useful information. Therefore, the Log P of conjugated base and acid of ILs is considered here. **Table 2** shows two Log P values of conjugated base and acid of ILs acquired from two databases. It can be seen that ALog P (a predicted Log P from the database) was generally in good agreement with Log P. However, it is noted that Log P of choline hydroxide was −1.5, which was much higher than its ALog P-value (−4.66). In this case, the prediction is probably in the approximation. The Log P of ethanolamine, choline hydroxide and methanesulfonic acid was below −1, indicating that these precursors tend to be hydrophilic. And this low value means 99% of the IL can partition in water and 1% in octanol. For ethylamine and propionic acid with their Log P around 0, they may be slightly hydrophilic. On the contrary, Log P of triethylamine was above 1, indicating that it is hydrophobic. And it is well-acknowledged that triethylamine is water-immiscible. Even though the Log

P values for the conjugated base show significant difference i.e., Choline hydroxide (−1.5) and Triethylamine (1.57), the ILs ChoMs and TeaMs both tend to be hydrophilic (**Figure 2**). This again shows the dominance of the anion determining the hydrophobic nature of the ILs. For the conjugated acids, an inverse relationship exists. For example, propionic acid showed the highest Log P (most hydrophobic), while the propionate-based ILs were the most hydrophilic ILs (**Figures 2**, **3**). This may be due to the spatial conformation change of the anion by the introduction of cations. Unlike the molecular solvents, it is known that ILs network possesses not only hydrogen bonding, but also ionic interactions and Van der Waals forces (MacFarlane et al., 2017). In addition, it is reported that the cation and anion did not contribute equally to the physiochemical properties of ILs (Yang, 2009), and hence the Log P of conjugated base and acid observed in this study do not seem to be relevant for the hydrophobicity of ILs.

In relation to the chemical structure of these ILs, propionic acid/propionate has carboxylic group (**Figure 1**), which is prone to hydrogen bonds with water. Due to the length of alkyl chain, its Log P was slightly high (slightly hydrophobic). When it forms the IL with hydrophilic cations (ethylammonium, ethanolammonium or choline), the hydrophobicity of these ILs significantly decreased. For example, ChoPn was the most hydrophilic ILs among the IL in this study. This may be because the cation forms stronger electrostatic interaction with propionate (and van der Waals dispersion forces), and hence changes the conformation of both cation and anion as well as the hydrogen bonding. Therefore, the hydrogen bonds of IL with water would be different as those of single conjugated base or acid. ChoDHP is the most hydrophilic IL in this study, although it is formed by hydrophilic cation and hydrophilic anion based on their Log P (**Table 2**). Previous studies have shown that ChoDHP has an extended network of hydrogen bonding particularly though the DHP anions containing two protons (Fujita et al., 2009; Cahill et al., 2010). The proton of DHP anion transports via the reorganization of hydrogen bonds (Rana et al., 2010), and it is possible that this infinite and complicated network of hydrogen bonds hinder the interaction with water, compared with other ILs in this study. Therefore, it would be valuable to compare the measured properties including a_w and β to understand hydrophobicity of ILs, rather than just considering Log P or their chemical structure.

CONCLUSION

In this work, we evaluated hydrogen bond basicity β and water activity a_w as a function of molar concentrations. We suggested these two key measured properties were linearly correlated to each other and related to the hydrophobicity. In addition, the anion dominated these two properties. The order of the hydrophobicity of these ILs can be identified as ChoDHP, mesylate-based ILs, and propionate-based ILs. Then by examining the chemical shift of H_2O in hydrated ILs from NMR, the hydrophobicity of ILs can be recognized, and we showed that the water peak of hydrated aprotic ILs shifted downfield possibly due to the higher hydrophobicity.

AUTHOR CONTRIBUTIONS

QH conducted the experiments, analyzed the data, and wrote the paper. NB and XW supervised the project and critically revised the paper. Both NB and XW were chief investigators of the project. All authors commented on the manuscript and approved the final version to be published.

ACKNOWLEDGMENTS

REFERENCES

Ab Rani, M. A., Brant, A., Crowhurst, L., Dolan, A., Lui, M., Hassan, N. H., et al. (2011). Understanding the polarity of ionic liquids. *Phys. Chem. Chem. Phy.* 13, 16831–16840. doi: 10.1039/C1cp21262a

Belieres, J. P., and Angell, C. A. (2007). Protic ionic liquids: preparation, characterization, and proton free energy level representation. *J. Phys. Chem. B*. 111, 4926–4937. doi: 10.1021/jp067589u

Cahill, L. S., Rana, U. A., Forsyth, M., and Smith, M. E. (2010). Investigation of proton dynamics and the proton transport pathway in choline dihydrogen phosphate using solid-state NMR. *Phy. Chem. Chem. Phy.* 12, 5431–38 doi: 10.1039/b916422g

Cammarata, L., Kazarian, S. G., Salter, P. A., and Welton, T. (2001). Molecular states of water in room temperature ionic liquids. *Phy. Chem. Chem. Phy.* 3, 5192–5200. doi: 10.1039/B106900d

Cauvain, S. P., and Young, L. S. (2009). *Bakery Food Manufacture and Quality: Water Control and Effects*. Buckinghamshire: John Wiley & Sons.

Chapeaux, A., Simoni, L. D., Stadtherr, M. A., and Brennecke, J. F. (2007). Liquid phase behavior of ionic liquids with water and 1-octanol and modeling of 1-octanol/water partition coefficients. *J. Chem. Eng. Data* 52, 2462–2467. doi: 10.1021/Je7003935

Debeljuh, N. J., Sutti, A., Barrow, C. J., and Byrne, N. (2013). Phase transition of Poly(N-isopropylacrylamide) in aqueous protic ionic liquids: kosmotropic versus chaotropic anions and their interaction with water. *J. Phy. Chem. B*. 117, 8430–8435. doi: 10.1021/Jp4043232

Deye, J. F., Berger, T. A., and Anderson, A. G. (1990). Nile Red as a solvatochromic dye for measuring solvent strength in normal liquids and mixtures of normal liquids with supercritical and near critical fluids. *Anal. Chem.* 62, 615–622. doi: 10.1021/ac00205a015

Forsyth, S. A., Pringle, J. M., and MacFarlane, D. R. (2004). Ionic liquids - an overview. *Austr. J. Chem.* 57, 113–119. doi: 10.1071/Ch03231

Freemantle, M. (2010). *An Introduction to Ionic Liquids*. Cambridge: Royal Society of Chemistry.

Fujita, K., MacFarlane, D. R., Forsyth, M., Yoshizawa-Fujita, M., Murata, K., Nakamura, N., et al. (2007). Solubility and stability of cytochrome c in hydrated ionic liquids: effect of oxo acid residues and kosmotropicity. *Biomacromolecules* 8, 2080–2086. doi: 10.1021/bm070041o

Fujita, K., Macfarlane, D. R., Noguchi, K., and Ohno, H. (2009). Choline dihydrogen phosphate. *Acta Crystallogr. Sect. E. Struct. Rep. Online* 65(Pt 4), o709–o709. doi: 10.1107/S1600536809007259

Fukaya, Y., Iizuka, Y., Sekikawa, K., and Ohno, H. (2007). Bio ionic liquids: room temperature ionic liquids composed wholly of biomaterials. *Green Chem.* 9, 1155–1157. doi: 10.1039/B706571j

Hallett, J. P., and Welton, T. (2011). Room-temperature ionic liquids: solvents for synthesis and catalysis. 2. *Chem. Rev.* 111, 3508–3576. doi: 10.1021/Cr1003248

Han, Q., Wang, X., and Byrne, N. (2016). Understanding the influence of key ionic liquid properties on the hydrolytic activity of thermomyces lanuginosus lipase. *Chem. Cat. Chem.* 8, 1551–1556. doi: 10.1002/cctc.201600014

Han, Q., Wang, X., and Byrne, N. (2017). A simple approach to achieve self-buffering protic ionic liquid-water mixtures. *Chem. Select* 2, 4294–4299. doi: 10.1002/slct.201700651

Hauru, L. K. J., Hummel, M., King, A. W., Kilpeläinen, I., and Sixta, H. (2012). Role of solvent parameters in the regeneration of cellulose from ionic liquid solutions. *Biomacromolecules* 13, 2896–2905. doi: 10.1021/Bm300912y

Kaar, J. L., Jesionowski, A. M., Berberich, J. A., Moulton, R., and Russell, A. J. (2003). Impact of ionic liquid physical properties on lipase activity and stability. *J. Am. Chem. Soc.* 125, 4125–4131. doi: 10.1021/Ja028557x

Kamlet, M. J., Abboud, J. L. M., and Taft, R. W. (1981). "An examination of linear solvation energy relationships," in *Progress in Physical Organic Chemistry*. (John Wiley & Sons, Inc.), 485–630. doi: 10.1002/9780470171929.ch6

Kamlet, M. J., and Taft, R. (1976). The solvatochromic comparison method. I. The. beta.-scale of solvent hydrogen-bond acceptor (HBA) basicities. *J. Am. Chem. Soc.* 98, 377–383. doi: 10.1021/ja00418a009

Kohno, Y., and Ohno, H. (2012). Ionic liquid/water mixtures: from hostility to conciliation. *Chem. Commun.* 48, 7119–7130. doi: 10.1039/C2cc31638b

Lai, J. Q., Li, Z., Lu, Y. H., and Yang, Z. (2011). Specific ion effects of ionic liquids on enzyme activity and stability. *Green Chem.* 13, 1860–1868. doi: 10.1039/C1gc15140a

Li, Z., Liu, X., Pei, Y., Wang, J., and He, M. (2012). Design of environmentally friendly ionic liquid aqueous two-phase systems for the efficient and high activity extraction of proteins. *Green Chem.* 14, 2941–2950. doi: 10.1039/c2gc35890e

Li, Z., Pei, Y., Wang, H., Fan, J., and Wang, J. (2010). Ionic liquid-based aqueous two-phase systems and their applications in green separation processes. *TrAC Trends Anal. Chem.* 29, 1336–1346. doi: 10.1016/j.trac.2010.07.014

MacFarlane, D. R., Kar, M., and Pringle, J. M. (2017). *Fundamentals of Ionic Liquids: From Chemistry to Applications*. John Wiley & Sons.

MacFarlane, D. R., Pringle, J. M., Johansson, K. M., Forsyth, S. A., and Forsyth, M. (2006). Lewis base ionic liquids. *Chem. Commun.* 18, 1905–1917. doi: 10.1039/B516961p

Mutelet, F., Ortega-Villa, V., Moise, J. C., Jaubert, J. N., and Acree, W. E. (2011). Prediction of partition coefficients of organic compounds in ionic liquids using a temperature-dependent linear solvation energy relationship with parameters calculated through a group contribution method. *J. Chem. Eng. Data* 56, 3598–3606. doi: 10.1021/Je200454d

Nikawa, Y., Fujita, K., and Ohno, H. (2017). Quantitative assessment of kosmotropicity of hydrated ionic liquids by nuclear magnetic resonance. *Phys. Chem. Chem. Phys.* 19, 8148–8151. doi: 10.1039/C6CP07463D

Oehlke, A., Hofmann, K., and Spange, S. (2006). New aspects on polarity of 1-alkyl-3-methylimidazolium salts as measured by solvatochromic probes. *New. J. Chem.* 30, 533–536. doi: 10.1039/B516709D

Ohno, H., Fujita, K., and Kohno, Y. (2015). Is seven the minimum number of water molecules per ion pair for assured biological activity in ionic liquid-water mixtures? *Phys. Chem. Chem. Phy.* 17, 14454–14460. doi: 10.1039/C5CP00768B

Olivier-Bourbigou, H., Magna, L., and Morvan, D. (2010). Ionic liquids and catalysis: recent progress from knowledge to applications. *Appl. Catal. Gen.* 373, 1–56. doi: 10.1016/j.apcata.2009.10.008

Pagni, R. M. (2003). "Ionic liquids as alternatives to traditional organic and inorganic solvents," in *Green Industrial Applications of Ionic Liquids*. (Knoxville, TN: Springer), 105–127.

Patel, R., Kumari, M., and Khan, A. (2014). Recent advances in the applications of ionic liquids in protein stability and activity: a review. *Appl. Biochem. Biotechnol.* 172, 3701–3720. doi: 10.1007/s12010-014-0813-6

Patinha, D. J., Tom,é, L. C., Garcia, H., Ferreira, R., Pereira, C. S., Rebelo, L. P. N., et al. (2015). The role of water in cholinium carboxylate ionic liquid's aqueous solutions. *J. Chem. Thermodynam.* 84, 93–100. doi: 10.1016/j.jct.2014.12.020

Plechkova, N. V., and Seddon, K. R. (2008). Applications of ionic liquids in the chemical industry. *Chem. Soc. Rev.* 37, 123–150. doi: 10.1039/B006677J

Rana, U. A., Bayley, P. M., Vijayaraghavan, R., Howlett, P., MacFarlane, D. R., and Forsyth, M. (2010). Proton transport in choline dihydrogen phosphate/H3PO4 mixtures. *Phy. Chem. Chem. Phys.* 12, 11291–11298. doi: 10.1039/C0cp00156b

Saihara, K., Yoshimura, Y., Ohta, S., and Shimizu, A. (2015). Properties of water confined in ionic liquids. *Sci. Rep.* 5:10619. doi: 10.1038/srep10619

Sare, E. J., Moynihan, C. T., and Angell, C. A. (1973). Proton magnetic resonance chemical shifts and the hydrogen bond in concentrated aqueous electrolyte solutions. *J. Phys. Chem.* 77, 1869–1876. doi: 10.1021/j100634a011

Sate, D., Janssen, M. H. A., Stephens, G., Sheldon, R. A., Seddon, K. R., and Lu, J. R. (2007). Enzyme aggregation in ionic liquids studied by dynamic light scattering and small angle neutron scattering. *Green Chem.* 9, 859–867. doi: 10.1039/B700437K

Stange, P., Fumino, K., and Ludwig, R. (2013). Ion speciation of protic ionic liquids in water: transition from contact to solvent-separated ion pairs. *Angew. Chem. Int. Ed.* 52, 2990–2994. doi: 10.1002/anie.201209609

van Rantwijk, F., and Sheldon, R. A. (2007). Biocatalysis in ionic liquids. *Chem. Rev.* 107, 2757–2785. doi: 10.1021/Cr050946x

Welton, T. (1999). Room-temperature ionic liquids. *Solvents for synthesis and catalysis. Chem. Rev.* 99, 2071–2083. doi: 10.1021/Cr980032t

Yang, Z. (2009). Hofmeister effects: an explanation for the impact of ionic liquids on biocatalysis. *J. Biotechnol.* 144, 12–22. doi: 10.1016/j.jbiotec.2009.04.011

Yang, Z., and Pan, W. B. (2005). Ionic liquids: Green solvents for nonaqueous biocatalysis. *Enzyme Microb. Technol.* 37, 19–28. doi: 10.1016/j.enzmictec.2005.02.014

Zaks, A., and Klibanov, A. M. (1988). The effect of water on enzyme action in organic media. *J. Biol. Chem.* 263, 8017–8021

Zhang, L., Xu, Z., Wang, Y., and Li, H. (2008). Prediction of the solvation and structural properties of ionic liquids in water by two-dimensional correlation spectroscopy. *J. Phys. Chem. B* 112, 6411–6419 doi: 10.1021/jp8001349

Zhao, H. (2016). Protein stabilization and enzyme activation in ionic liquids: specific ion effects. *J. Chem. Technol. Biotechnol.* 91, 25–50 doi: 10.1002/jctb.4837

Check for updates

Investigating Intermolecular Interactions in a DME-Based Hybrid Ionic Liquid Electrolyte by HOESY NMR

Derick Gyabeng[1], Pierre-Alexandre Martin[1,2], Urbi Pal[1], Michaël Deschamps[2], Maria Forsyth[1] and Luke A. O'Dell[1]*

[1] Institute for Frontier Materials, Deakin University, Geelong, VIC, Australia, [2] CEMHTI, CNRS UPR 3079, Orléans University, Orléans, France

The intermolecular interactions in a hybrid electrolyte based on various compositions of the ionic liquid N-methyl-N-propyl pyrrolidinium bis-fluorosulfonylimide (C_3mpyrFSI), LiFSI salt and an ether-based additive, 1,2-dimethoxy ethane (DME), have been investigated using the HOESY (Heteronuclear Overhauser Effect SpectroscopY) NMR experiment. This NMR technique allows a quantification of the intermolecular interactions in ionic liquids (ILs) by measuring the cross-relaxation rate (σ) between different pairs of nuclei. Thereby, we compare the cross-relaxation rates between the cations, anions and DME in these hybrid electrolyte systems using ^{1}H-^{7}Li and ^{1}H-^{19}F HOESY experiments, and interpret the measured parameters in terms of ionic and molecular associations. The results give insights into the local coordination environment of the Li$^+$ cations and their solvation by the FSI anions and DME.

Keywords: ionic liquid electrolytes, ion interactions, Nuclear Overhauser Effect, HOESY NMR, cross-relaxation rates

INTRODUCTION

Ionic liquids (ILs), typically consisting of an organic cation and an inorganic anion, have gained a lot of attention from researchers over the last two decades (Weingärtner, 2013). ILs are generally liquids below 100°C and have shown a lot of promise as electrolytes in batteries and other energy storage applications due to their versatile properties including low volatility, high thermal and electrochemical stability as well as high ionic conductivity (Macfarlane et al., 2014). Lithium-ion batteries play a very crucial role among current energy storage technologies due to their high energy and power densities (Bruce et al., 2012). They are commonly used in consumer electronics and increasingly in electric vehicles, and hence are very important in addressing global energy concerns. However, current lithium ion battery technologies still pose a safety risk primarily due to the volatile and flammable nature of the commonly used organic electrolytes (Wongittharom et al., 2014; Zhou et al., 2017). IL electrolytes are promising materials to replace these battery electrolytes in particular because of their low volatility and non-flammability. However, these properties typically coincide with lower ionic conductivities compared to traditional electrolyte systems.

In order to advance the design of ILs with improved ionic conductivities for battery applications, their molecular interactions need to be understood (Damodaran, 2016). The location and local environment of Li$^+$ relative to the other ions in the electrolyte will play a very important role in

the charge transport mechanisms and other processes occurring in the electrolyte (Martin et al., 2018b), which will in turn be major factors in determining the overall performance of the device. It is therefore vital to understand the molecular level structure and dynamics of ILs in order to improve their properties by tailoring their structure and composition.

Nuclear magnetic resonance (NMR) spectroscopy is a useful tool that has helped researchers to probe the structure and dynamics of ionic liquids. Pulsed field gradients (Pope et al., 2016; Hilder et al., 2017), relaxation measurements (Han et al., 2012; Filippov et al., 2015), and dynamic nuclear polarization (Sani et al., 2018) are some NMR techniques that have been used to investigate the structure and dynamics of ILs. Nuclear Overhauser Effect (NOE) based experiments are particularly useful to probe nanostructured arrangements in ILs through the transfer of nuclear spin polarization by cross-relaxation (Damodaran, 2016). In particular, the Heteronuclear Overhauser Effect SpectroscopY (HOESY) pulse sequence (Lingscheid et al., 2012; Bai et al., 2013; Chiappe et al., 2013; Castiglione et al., 2014, 2015; Giernoth et al., 2014; Tripathi and Saha, 2014) has been used to probe the various molecular interactions in ILs and their interactions with other solvents.

In our recent work on HOESY (Martin et al., 2018b), we demonstrated the importance of taking into account both the longitudinal relaxation times and self-diffusion coefficients of the nuclear spins when fitting HOESY build-up curves, as well as the normalization of the measured signals to the equilibrium magnetization. This analysis allows the quantitative comparison of NOEs (quantified as cross-relaxation rates) among different ILs, concentrations or temperatures. There have however been controversies regarding the interpretation of the intermolecular NOEs measured using this technique, owing to the fact that the internuclear distances are dependent on both the rotational and translational dynamics of the ions. Gabl et al. (2013) proposed that intermolecular NOEs measured between nuclear spins with similar frequencies, such as ^{1}H and ^{19}F, are sensitive to longer distances than nuclear spins whose frequencies are far apart. Our very recent work corroborates this prediction (Martin et al., 2018a), demonstrating the validity of interpreting intermolecular NOEs in terms of distances provided that such effects are taken into consideration.

Herein, we apply the HOESY NMR technique to a class of hybrid ionic liquid electrolytes recently reported (Pal et al., 2018) by our group that shows promise for applications in lithium electrochemistry with low polysulfide dissolution that is of importance for Li-S batteries. The addition of DME in these hybrid electrolytes has been shown to increase the relative mobility of the lithium ion through the formation of a chelate compound with lithium. Further understanding of the structure and dynamics in these electrolytes is of interest in terms of their future development. Herein, we quantitatively measure the Overhauser cross-relaxation rates in this DME-based hybrid ionic liquid electrolyte system for the intermolecular heteronuclear spin pairs ^{1}H-^{19}F and ^{1}H-^{7}Li. The results provide insights into the ionic associations and lithium cation solvation environment via the interactions between the

Li$^+$/FSI$^-$ and the different hydrogen environments on the pyrrolidinium cations and DME molecules.

EXPERIMENTAL DETAILS

Sample Preparation

The ionic liquid N-methyl-N-propyl pyrrolidinium bis-fluorosulfonylimide (C$_3$mpyrFSI) was purchased from Solvionic (France) with 99.5% purity, 1,2-dimethoxy ethane (DME) was purchased from Sigma-Aldrich with 99.9% purity (anhydrous), and the Li salt of bis-fluorosulfonylimide (LiFSI) was purchased from Nippon Shokubai (Japan) with 99.5% purity and used without further purification. The structures of these compounds are shown in **Figure 1**. These components were mixed together at different molar ratios as specified in **Table 1**. A neat sample of the C$_3$mpyrFSI IL was also studied. All the materials were stored and packed in an Argon filled glove box. For the NMR experiments, the samples were packed in 3 mm capillary tubes inside the glove box to avoid contamination with water. The samples were then flame-sealed externally and inserted into 5 mm NMR tubes with D$_2$O as outer layer for field lock and to minimize thermal convection effects.

Diffusion Coefficient Measurements

Self-diffusion measurements for ^{1}H, ^{7}Li, and ^{19}F were performed at 20°C using a pulsed field gradient stimulated echo NMR pulse sequence with a Bruker Avance III 7.05 T spectrometer equipped with a 5 mm Bruker Diff50 probe with a maximum gradient strength of 3,000 G/cm. The gradient pulse length used in the experiment was 2 ms and the diffusion time was 25 ms. To extract the diffusion coefficients, which are displayed in **Table 2** below, the data were fitted in the Bruker Topspin software using the Stejskal-Tanner equation:

$$I = I_o \exp\left(-D\gamma^2 g^2 \delta^2 \left(\Delta - \frac{\delta}{3}\right)\right) \quad (1)$$

where, I is the observed signal intensity, I_o is the maximum signal intensity, γ is the gyromagnetic ratio of the nucleus under observation, g is the gradient strength, δ is the gradient pulse duration and Δ is the diffusion time.

Longitudinal Relaxation (T_1) Measurements

Longitudinal relaxation times (T_1) for ^{1}H, ^{7}Li, and ^{19}F were measured at 20°C at a magnetic field strength of 11.7 T (500 MHz ^{1}H frequency) using an inversion recovery pulse sequence and a Bruker Avance III spectrometer equipped with a 5 mm HX solution state probe. The data were fitted to an exponential curve using home-written Maple code.

Cross-Relaxation Time Measurements

Cross-relaxation rates for ^{7}Li-^{1}H and ^{19}F-^{1}H for each sample were measured at 20°C using a ^{1}H-detected HOESY pulse sequence, following an identical procedure to that previously reported (Martin et al., 2018a) and with the same NMR spectrometer and probe used for the longitudinal relaxation measurements. Mixing times for the HOESY build-up curves were varied over 22 values ranging from 3.7 ms to 4.5 s and
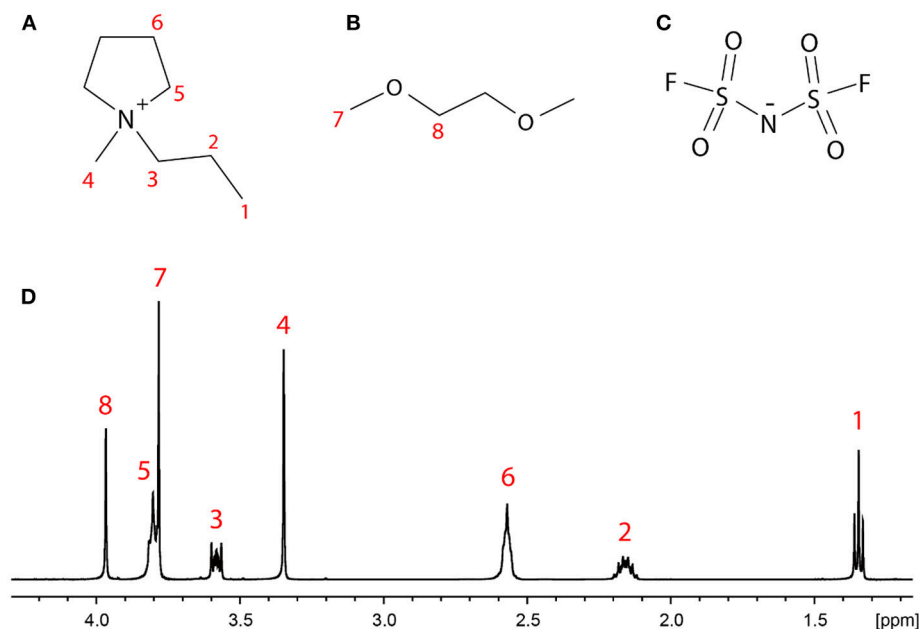
FIGURE 1 | Structures of **(A)** the C_3mpyr$^+$ cation and **(B)** the DME molecule, with the eight groups of distinct protons labeled, **(C)** the FSI$^-$ anion, and **(D)** the ^{1}H NMR spectrum of LiDME-0.5 with peak assignment.

440 scans were recorded for each mixing time. A recycle delay between 5.0 and 6.0 s was used to ensure quantitative measurements. The HOESY build-up curves were fitted to the following expression with σ (the cross-relaxation rate) as the sole variable:

$$M(\tau) = M_0 \sigma \frac{2\sinh(K\tau)}{K} e^{\frac{-(R_I + R_S)\tau}{2}} e^{-(D_I + D_S)\gamma_I \gamma_S g^2 \delta^2 (\Delta - \frac{\delta}{3})} \quad (2)$$

where $M(\tau)$ is the observed ^{1}H signal, M_0 is the thermal equilibrium magnetization of the ^{7}Li or ^{19}F spin, $R_{I/S}$ are the longitudinal relaxation rates of the two spins, $D_{I/S}$ are the diffusion coefficients of the ions containing the spins, $\gamma_{I/S}$ are the nuclear gyromagnetic ratios, g is the gradient pulse strength, δ the gradient pulse length, Δ the delay time between the first and last gradient pulses, and:

$$K = \frac{\sqrt{R_I^2 - 2R_I R_S + R_S^2 + 4\sigma^2}}{2} \quad (3)$$

A complete description of the signal normalization and HOESY curve fitting procedure can be found in our previous publication (Martin et al., 2018b).

RESULTS AND DISCUSSION

^{7}Li-^{1}H Cross-Relaxation Rates

The single-pulse excitation ^{1}H NMR spectrum of the LiDME-0.5 sample is shown in **Figure 1D** with the peaks assigned according to the structures in **Figures 1A,B**. All of the peaks are well-resolved with the exception of sites 5 (the ring CH$_2$ protons

closest to the nitrogen on the C$_3$mpyr cation) and 7 (the DME methyl protons), which show partial overlap. In the ^{1}H-^{7}Li HOESY experiments, the observed signals were much weaker, and the HOESY signal from site 5 was found to be generally less intense than that from site 7 in most cases. This made the extraction of the ^{1}H-^{7}Li cross-relaxation rates of the protons of site 5 from the DME-containing samples extremely difficult. The peak at around 3.8 ppm in the HOESY spectra was therefore fitted to a single cross-relaxation rate assumed to reflect only that of the site 7 protons on the DME molecule. For the ^{1}H-^{19}F HOESY experiments, higher signal intensities were obtained and these peaks were therefore able to be deconvoluted with separate HOESY build-up curves fitted for sites 5 and 7.

The ^{7}Li-^{1}H cross-relaxation rates $(\times 10^{-4}\ \text{s}^{-1})$ measured at 20°C from all three samples are presented in **Table 3**, and example fitted HOESY build-up curves from which these parameters were extracted are shown in **Figure 2**. The larger the value of the cross-relaxation rate, the stronger the NOE interaction between the two spins and this is typically interpreted as a closer average distance between the two nuclei. However, it should be noted here that variations in dynamics (specifically of the internuclear vector) will also play a role in determining the σ-value.

Considering first the interaction between the Li$^+$ and the C$_3$mpyr cation in sample LiMDE-0, the largest NOE is observed between the ^{7}Li and the methyl proton on the carbon directly attached to the nitrogen site. This is consistent with a previous DNP NMR and molecular dynamics (MD) study of a glassy-state LiFSI-containing C$_3$mpyrFSI sample in which measured C-Li distances suggested that the lithium cations are preferentially located on the side of the pyrrolidinium ring with this methyl

Sample	Li$^+$	FSI$^-$	C$_3$mpyr$^+$	DME	Li:DME
LiDME-0	0.25	0.50	0.25	0	1:0
LiDME-0.5	0.25	0.50	0.25	0.125	1:0.5
LiDME-1	0.25	0.50	0.25	0.25	1:1

TABLE 2 | Diffusion coefficient values of the various species in the pure IL and hybrid electrolytes, measured at 20°C.

	D (×10^{-11})/m^2.s^{-1}			
Sample	^{1}H (C$_3$mpyr$^+$)	^{1}H (DME)	^{7}Li(Li$^+$)	^{19}F(FSI$^-$)
Neat C$_3$mpyrFSI	2.63	–	–	3.11
LiDME-0	0.41	–	0.29	0.30
LiDME-0.5	0.96	0.85	0.83	0.93
LiDME-1	1.73	1.61	1.56	1.84

TABLE 3 | ^{7}Li-^{1}H cross-relaxation rates measured from the hybrid electrolytes at 20°C.

		^{1}H-^{7}Li σ/10^{-4} s^{-1}		
Peak number	Site	LiDME-0	LiDME-0.5	LiDME-1
1	Cation N-CH$_2$-CH$_2$-**CH$_3$**	0.46	2.04	1.52
2	Cation N-CH$_2$-**CH$_2$**-CH$_3$	0.44	0.41	0.35
3	Cation N-**CH$_2$**-CH$_2$-CH$_3$	0.43	0.36	0.27
4	Cation N-**CH$_3$**	1.79	1.82	1.41
5	Cation ring N-**CH$_2$**-CH$_2$	0.51	*	*
6	Cation ring N-CH$_2$-**CH$_2$**	0.56	0.66	0.51
7	DME **CH$_3$**	–	5.41	18.5
8	DME **CH$_2$**	–	16.0	37.2

*Uncertainties in these values are estimated at ± 10%. *Values for peak 5 could not be obtained from the samples containing DME due to low intensity and overlap with peak 7.*

FIGURE 2 | Fits of the ^{1}H-^{7}Li HOESY build-up curves from all of the ^{1}H peaks of sample LiDME-0.5 at 20°C (site numbers refer to the structures/peaks shown in **Figure 1**).

group (Sani et al., 2018). The smallest NOEs are observed for the protons on the propyl chain. Interestingly, upon addition of DME to this system, the NOEs between the lithium and the various sites on the C$_3$mpyr cation remain roughly the same, with the notable exception of the terminal methyl protons on the propyl chain (site 1), which show a significant increase in the cross relaxation rate.

With regards to the interactions between the Li$^+$ cations and DME molecules, the σ-values in **Table 3** show Li-DME NOEs that are larger by an order of magnitude or more than the Li-C$_3$mpyr NOEs. This could be expected given the solvation of the Li$^+$ cations by the ether oxygen groups of the DME molecules, as well as the fact that DME is a neutral molecule and hence will not show any charge repulsion from the Li. LiDME-1 shows the highest Li-DME NOEs and the lowest Li-C$_3$mpyr NOEs (with the exception of the propyl CH$_3$ group). It can be noted here that the diffusion coefficients of the Li$^+$ and FSI$^-$ ions are very similar in LiDME-0 (**Table 2**) indicating strong solvation of the lithium cations by the anions, but with the addition of DME the diffusion coefficient

of the Li$^+$ is closer to that of the DME molecules while the FSI anions diffuse faster. In combination with the HOESY results, this suggests that the DME solvates the Li$^+$ by displacing (at least partially) the FSI$^-$ ions. The solvation of the Li$^+$ by the DME molecules and the displacement of the FSI anions around the Li$^+$ means that there will be more repulsion between the Li and the C$_3$mpyr (e.g., a Li-DME-FSI cluster will have a net neutral charge compared to an Li(FSI)$_2^-$ cluster that will be more attracted to the C$_3$mpyr), and this can explain the reduced Li-C$_3$mpyr NOEs as the DME concentration increases. It was not possible to obtain reliable ^{7}Li-^{1}H cross-relaxation rates for the CH$_2$ on the IL cation ring near N$^+$ because it strongly overlaps with the terminal DME proton peak. Finally, the Li-DME NOEs are stronger for the CH$_2$ protons on the DME molecule than for the CH$_3$ protons. This may reflect the conformation of the DME molecule when solvating the lithium, however, the different dynamics of the two groups of protons (e.g., the rotation of the methyl group) may also play a role in the different NOE efficiencies.

^{19}F-^{1}H Cross-Relaxation Rates

The cross-relaxation rates extracted from ^{19}F-^{1}H HOESY build-up curves are displayed in **Table 4**, including values obtained from the neat C$_3$mpyrFSI IL (without LiFSI) for comparison. These values give insights into the interactions between the FSI anions and the C$_3$mpyr$^+$ cation/DME species, and once again we make the assumption that larger NOEs reflect closer average

TABLE 4 | ^{1}H-^{19}F cross-relaxation rates measured from the neat C_3mpyrFSI ionic liquid and the three hybrid electrolyte samples at 20°C.

Peak number	Site	^{1}H-^{19}F σ/10^{-4} s^{-1}			
		Neat IL	LiDME-0	LiDME-0.5	LiDME-1
1	Cation N-CH$_2$-CH$_2$-**CH$_3$**	1.67	8.62	7.79	2.46
2	Cation N-CH$_2$-**CH$_2$**-CH$_3$	3.05	7.64	4.34	1.91
3	Cation N-**CH$_2$**-CH$_2$-CH$_3$	3.81	8.04	5.14	2.41
4	Cation N-**CH$_3$**	16.1	16.7	17.5	7.92
5	Cation ring N-**CH$_2$**-CH$_2$	3.51	6.48	2.67	1.27
6	Cation ring N-CH$_2$-**CH$_2$**	1.12	6.39	3.97	1.27
7	DME **CH$_3$**	–	–	21.8	10.09
8	DME **CH$_2$**	–	–	38.4	12.02

Uncertainties in these values are estimated at ± 10%.

distances between these anions and the different proton sites. In the neat IL, the ^{19}F-^{1}H cross-relaxation rate is largest for the N-CH$_3$ group and the values decrease as the proton sites become more distant from this central nitrogen site. This can be interpreted in terms of the localized positive charge at this region of the cation which acts to attract the FSI anions. Upon addition of the LiFSI salt (i.e., sample LiDME-0), the σ-values increase for all proton sites. Rather than a net increase in the FSI-C$_3$mpyr interaction strength, we interpret this as being due to a change in the overall dynamics of the system, as it is well known that adding lithium salts to ionic liquids results in a significant increase in viscosity (Bose et al., 2018). This phenomenon is confirmed by the decrease in diffusion coefficients of both ions by around an order of magnitude upon the addition of LiFSI salt in LiDME-0 as shown in **Table 2**. The LiDME-0 sample also shows the largest ^{19}F-^{1}H NOE for the N-CH$_3$ protons which is again consistent with the picture established by DNP NMR and MD simulations (Sani et al., 2018) of a negatively charged Li(FSI)$_n$ cluster existing close to this part of the cation.

Upon addition of DME to this system, the σ-values can be seen to decrease overall, and once again this can be attributed at least in part to a reduction in the sample viscosity and an increase in the overall dynamics of the liquid (reflected also by an increase in the diffusion coefficients in **Table 2**). With regards to the FSI-C$_3$mpyr interactions, the overall trends remain similar to the LiDME-0 sample with the strongest interaction still being between the FSI and the N-CH$_3$ group. The fact that the interaction between the FSI anions and the terminal methyl group on the propyl chain of the cation does not appear to increase upon DME addition suggests that the increased interactions between the lithium cations and this particular group

may be due to the presence of Li(DME)$_n$ clusters. However, the much larger ^{19}F-^{1}H NOE values observed for the protons on the DME molecules strongly indicate the presence of lithium cations that are simultaneously solvated by both FSI and DME. MD simulations are currently being carried out on this system and should help with the further interpretation of these NOE values.

CONCLUSIONS

We have measured ^{7}Li-^{1}H and ^{19}F-^{1}H Overhauser cross-relaxation rates from several pyrrolidinium-based ionic liquid electrolytes containing lithium salt and the 1,2-dimethoxy ethane additive in different ratios. These parameters allow a quantitative comparison of the interactions of the Li$^+$ and FSI$^-$ ions with the IL cation and DME molecules in the different electrolytes. Both FSI-C$_3$mpyr and Li-C$_3$mpyr NOEs decrease overall as the DME content increases. The Li-DME and FSI-DME NOEs were found to be the largest, indicating the solvation of Li$^+$ by both of these species. Strong FSI-DME NOEs indicate simultaneous solvation of a Li$^+$ by both DME and FSI. Li-C$_3$mpyr and FSI-C$_3$mpyr interactions were strongest for the N-CH$_3$ protons which is consistent with a previous study that concluded that Li(FSI)$_n^-$ clusters preferentially locate close to that region of the cation (Sani et al., 2018). The measured diffusion coefficients assisted greatly in interpreting the NOE values, providing additional evidence for ion associations while also reflecting composition-dependent changes in the overall dynamics that affect the sizes of the measured NOE values. These results help to quantify the ionic interactions and the role that the additive 1,2-dimethoxy ethane plays in the ionic liquid *N*-methyl-*N*-propyl pyrrolidinium bis-fluorosulfonylimide. Further measurements as a function of temperature, along with the correlation to molecular dynamics simulation data, will allow a more detailed interpretation of these cross-relaxation rates, and such work is currently underway.

AUTHOR CONTRIBUTIONS

DG carried out the experiments, data analysis and interpretation, and wrote the paper. P-AM, UP, MD, MF, and LO contributed to the interpretation of the results and edited the paper.

ACKNOWLEDGMENTS

REFERENCES

Bai, T., Ge, R., Gao, Y., Chai, J., and Slattery, J. M. (2013). The effect of water on the microstructure and properties of benzene/[Bmim][AOT]/[Bmim][BF4] microemulsions. *Phys. Chem. Chem. Phys.* 15, 19301–19311. doi: 10.1039/c3cp53441c

Bose, P., Deb, D., and Bhattacharya, S. (2018). Ionic liquid based nanofluid electrolytes with higher lithium salt concentration for high-efficiency, safer, lithium metal batteries. *J. Power Sour.* 406, 176–184. doi: 10.1016/j.jpowsour.2018.10.050

Bruce, P. G., Freunberger, S. A., Hardwick, L. J., and Tarascon, J. M. (2012). Li–O$_2$ and Li–S batteries with high energy storage. *Nat. Mater.* 11, 19–29. doi: 10.1038/nmat3191

Castiglione, F., Appetecchi, G. B., Passerini, S., Panzeri, W., Indelicato, S., and Mele, A. (2015). Multiple points of view of heteronuclear NOE: long range vs

short range contacts in pyrrolidinium based ionic liquids in the presence of li salts. *J. Mol. Liquids* 210, 215–222. doi: 10.1016/j.molliq.2015.05.036

Castiglione, F., Famulari, A., Raos, G., Meille, S. V., Mele, A., Appetecchi, G. B., et al. (2014). Pyrrolidinium-based ionic liquids doped with lithium salts: how does Li+ coordination affect its diffusivity? *J. Phys. Chem. B* 118, 13679–13688. doi: 10.1021/jp509387r

Chiappe, C., Sanzone, A., Mendola, D., Castiglione, F., Famulari, A., Raos, G., et al. (2013). Pyrazolium- versus imidazolium-based ionic liquids: structure, dynamics and physicochemical properties. *J. Phys. Chem. B* 117, 668–676. doi: 10.1021/jp3107793

Damodaran, K. (2016). *Recent NMR Studies of Ionic Liquids. Annual Reports on NMR Spectroscopy, 1st Edn., Vol. 88.* London: Elsevier Ltd. doi: 10.1016/bs.arnmr.2015.11.002

Filippov, A., Azancheev, N., Taher, M., Shah, F. U., Rabét, P., Glavatskih, S., et al. (2015). Self-diffusion and interactions in mixtures of imidazolium bis(mandelato)borate ionic liquids with polyethylene glycol: 1H NMR study. *Magn. Reson. Chem.* 53, 493–497. doi: 10.1002/mrc.4232

Gabl, S., Steinhauser, O., and Weingärtner, H. (2013). From short-range to long-range intermolecular NOEs in ionic liquids: frequency does matter. *Angew. Chem. Int. Edn.* 52, 9242–9246. doi: 10.1002/anie.201302712

Giernoth, R., Bröhl, A., Brehm, M., and Lingscheid, Y. (2014). Interactions in ionic liquids probed by *in situ* NMR spectroscopy. *J. Mol. Liquids* 192, 55–58. doi: 10.1016/j.molliq.2013.07.010

Han, K. S., Li, S., Hagaman, E. W., Baker, G. A., Cummings, P., and Sheng, D. (2012). Rotational and translational dynamics of N -Butyl-N -methylpiperidinium trifluoromethanesulfonimide ionic liquids studied by NMR and MD simulations. *J. Phys. Chem. C* 116, 20779–20786. doi: 10.1021/jp3069283

Hilder, M., Gras, M., Pope, C. R., Kar, M., Macfarlane, D. R., Forsyth, M., et al. (2017). Effect of mixed anions on the physicochemical properties of a sodium containing alkoxyammonium ionic liquid electrolyte. *Phys. Chem. Chem. Phys.* 19, 17461–17468. doi: 10.1039/c7cp03318d

Lingscheid, Y., Arenz, S., and Giernoth, R. (2012). Heteronuclear NOE spectroscopy of ionic liquids *Chem. Phys. Chem.* 13, 261–266. doi: 10.1002/cphc.201100622

Macfarlane, D. R., Tachikawa, N., Forsyth, M., Pringle, J. M., Howlett, P. C., Elliott, G. D., et al. (2014). Energy applications of ionic liquids. *Energy Environ. Sci.* 7, 232–250. doi: 10.1039/c3ee42099j

Martin, P. A., Chen, F., Forsyth, M., Deschamps, M., and O'Dell, L. A. (2018a). Correlating intermolecular cross-relaxation rates with distances and coordination numbers in ionic liquids. *J. Phys. Chem. Lett.* 9, 7072–7078. doi: 10.1021/acs.jpclett.8b03021

Martin, P. A., Salager, E., Forsyth, M., O'Dell, L. A., and Deschamps, M. (2018b). On the measurement of intermolecular heteronuclear cross relaxation rates in ionic liquids. *Phys. Chem. Chem. Phys.* 20, 13357–13364. doi: 10.1039/c8cp00911b

Pal, U., Girard, G. M. A., O'Dell, L. A., Roy, B., Wang, X., Armand, M., et al. (2018). Improved Li-ion transport by DME chelation in a novel ionic liquid-based hybrid electrolyte for Li–S battery application. *J. Phys. Chem. C* 122, 14373–14382. doi: 10.1021/acs.jpcc.8b03909

Pope, C. R., Kar, M., MacFarlane, D. R., Armand, M., Forsyth, M., and O'Dell, L. A. (2016). Ion dynamics in a mixed-cation alkoxy-ammonium ionic liquid electrolyte for sodium device applications. *Chem. Phys. Chem.* 17, 3187–3195. doi: 10.1002/cphc.201600692

Sani, M. A., Martin, P. A., Yunis, R., Chen, F., Forsyth, M., Deschamps, M., et al. (2018). Probing ionic liquid electrolyte structure via the glassy state by dynamic nuclear polarization NMR spectroscopy. *J. Phys. Chem. Lett.* 1007–1011. doi: 10.1021/acs.jpclett.8b00022

Tripathi, N., and Saha, S. (2014). Unraveling the heterogeneity in N Butyl-N-methylpiperidinium trifluromethanesulfonimide ionic liquid by 1D and 2D NMR spectroscopy. *Chem. Phys. Lett.* 607, 57–63. doi: 10.1016/j.cplett.2014.05.046

Weingärtner, H. (2013). NMR studies of ionic liquids: structure and dynamics. *Curr. Opin. Coll. Interface Sci.* 18, 183–189. doi: 10.1016/j.cocis.2013.04.001

Wongittharom, N., Lee, T. C., Wang, C. H., Wang, Y. C., and Chang, J. K. (2014). Electrochemical performance of Na/NaFePO4 sodium-ion batteries with ionic liquid electrolytes. *J. Mater. Chem. A* 2:5655. doi: 10.1039/c3ta15273a

Zhou, Y., Wang, X., Zhu, H., Armand, M., Forsyth, M., Greene, G. W., et al. (2017). N-ethyl-N-methylpyrrolidinium bis(fluorosulfonyl)imide-electrospun polyvinylidene fluoride composite electrolytes: characterization and lithium cell studies. *Phys. Chem. Chem. Phys.* 19, 2225–2234. doi: 10.1039/c6cp07415d

Effect of β-Cyclodextrin on Physicochemical Properties of an Ionic Liquid Electrolyte Composed of N-Methyl-N-Propylpyrrolidinium bis(trifluoromethylsulfonyl)amide

Mio Suzuki, Naoya Kurahashi, Yuko Takeoka, Masahiro Rikukawa and Masahiro Yoshizawa-Fujita*

Department of Materials and Life Sciences, Sophia University, Tokyo, Japan

Ionic liquids (ILs) are promising electrolyte materials for developing next-generation rechargeable batteries. In order to improve their properties, several kinds of additives have been investigated. In this study, β-cyclodextrin (β-CD) was chosen as a new additive in IL electrolytes because it can form an inclusion complex with bis(trifluoromethylsulfonyl)amide (TFSA) anions. We prepared the composites by mixing N-methyl-N-propylpyrrolidinium bis(trifluoromethylsulfonyl)amide/LiTFSA and a given amount of triacetyl-β-cyclodextrin (Acβ-CD). The thermal behaviors and electrochemical properties of the composites were analyzed by several techniques. In addition, pulse field gradient NMR measurements were conducted to determine the self-diffusion coefficients of the component ions. The addition of Acβ-CD to the IL electrolytes results in the decrease in the conductivity value and the increase in the viscosity value. In contrast, the addition of Acβ-CD to the IL electrolytes induced an improvement in the anodic stability because of the formation of an inclusion complex between the Acβ-CD and TFSA anions. CDs are potential candidates as additives in IL electrolytes for electrochemical applications.

Keywords: ionic liquids, pyrrolidnium, TFSA, β-cyclodextrin, inclusion complex

INTRODUCTION

Ionic liquids (ILs) have been attractive as electrolyte materials because of their unique properties such as high ionic conductivity at room temperature and wide potential window (Armand et al., 2009). In addition, as ILs have a low vapor pressure and low flammability, they will be suitable for developing safer electrolytes instead of organic solvents (Ohno, 2011). Among onium cations, pyrrolidinium-based ILs are primarily being used as electrolytes in rechargeable batteries (Ishikawa et al., 2006; Matsumoto et al., 2006; Seki et al., 2008; Yoon et al., 2015). Pyrrolidinium-based ILs are superior in thermal and electrochemical stability as compared to those of other onium-based ILs. However, it is difficult to realize target ion transport with ions such as lithium ions or sodium ions in ILs, because the component ions of ILs as solvents also migrate along the potential gradient. New designs of ILs that address such drawback has been proposed by many researchers. For example, one candidate is poly(IL)s, which fix cation or anion species on the polymer chain (Yuan et al., 2013; Nishimura and Ohno, 2014; Qian et al., 2017). Another candidate is zwitterions, which have

the cation and anion in the same molecule (Yoshizawa et al., 2004; Narita et al., 2006; Yoshizawa-Fujita et al., 2011). Nevertheless, it is still difficult to achieve a high ionic conductivity over 10^{-2} S cm^{-1} at room temperature and a high lithium transference number (t_{Li+}) over 0.5.

Rechargeable batteries, especially lithium-ion batteries (LIBs), employing ILs as the electrolyte materials have been developed (Ishikawa et al., 2006; Matsumoto et al., 2006; Seki et al., 2008; Ohno, 2011). For practical applications, a high energy density of LIBs is required. In order to improve the energy density of LIBs, the cells are needed to be operated at higher cut-off voltages. However, high cut-off voltages induce a significant decrease in the charge/discharge cycle stability of LIBs due to the decomposition of electrolytes. As a result, a passivation layer on the electrode is formed, even when ILs are used as electrolytes (Seki et al., 2008). The decomposition reaction of electrolytes should be suppressed at high cut-off voltages to allow the use of high-voltage cathode materials [e.g., LiCo$_{1/3}$Ni$_{1/3}$Mn$_{1/3}$O$_2$ (Yabuuchi and Ohzuku, 2003), LiNi$_{0.5}$Mn$_{1.5}$O$_4$ (Zhu et al., 2014)]. Various additives have been used to improve the anodic stability of electrolyte materials (Franco, 2015).

Cyclodextrin (CD) is a circular oligosaccharide composed of α-D(+)-glucopyranose units. The CD, which possesses seven glucose units, is called β-CD. They have a three-dimensional funnel-shaped architecture with a narrower rim molded by a hydrogen-bonding network built by primary OH groups (one group per glucose unit), and with a broader rim composed of secondary OH groups (two groups per glucose unit) (Crini, 2014). The two rims of the molecules are hydrophilic, while the interior of their cavity is hydrophobic. It is known that β-CD tends to form inclusion complexes with guest molecules with suitable characteristics of polarity and dimension in aqueous solutions (Silva et al., 2008; Baâzaoui et al., 2016). CD is among the most frequently used host molecule in supramolecular chemistry; this ability has been widely used in food and pharmaceutical studies (Szejtli, 1998; Crini, 2014). It has also been widely used in lithium battery research as a surfactant to effectively disperse solid substances in liquids and as an agent to promote complexation reactions, which is beneficial to material dispersion and molding (Chen et al., 2016).

Recently, Amajjahe et al. (2008) found that the anion of 1-butyl-3-vinylimidazolium bis(trifluoromethylsulfonyl)amide exclusively formed a host–guest complex with β-CD (Amajjahe and Ritter, 2008; Amajjahe et al., 2008). He et al. (2009) investigated the interaction of hydrophobic ILs and β-CD in detail (He et al., 2009). They found that the imidazolium cation did not interact with β-CD while its long alkyl side chain did. In addition, hydrophobic anions with fluorine atoms could interact with β-CD, and the interaction between the bis(trifluoromethylsulfonyl)amide (TFSA) anion and β-CD was stronger than those of BF$_4$ and PF$_6$ anions. These results prompted us to investigate the effect of β-CD on the physicochemical properties of ILs, and we expected that the anion trap ability of β-CD would contribute to the enhancement of the Li-ion conductivity and the improvement of the

FIGURE 1 | Chemical structures of [C$_3$mpyr][TFSA], and Acβ-CD.
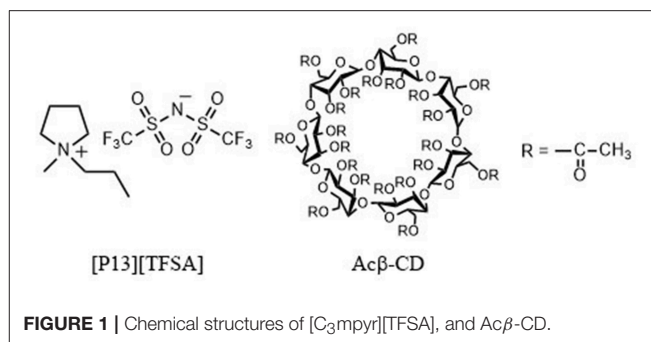
electrochemical stability. In this study, a pyrrolidinium-based IL with a TFSA anion, *N*-methyl-*N*-propylpyrrolidinium bis(trifluoromethylsulfonyl)amide ([C$_3$mpyr][TFSA]) (see **Figure 1**), was used as the electrolyte solution. Its LiTFSA composites were prepared and mixed with different amounts of β-CD, and their physicochemical and electrochemical properties were evaluated.

EXPERIMENTAL

Materials

N-Methylpyrrolidine (Tokyo Chemical Industry Co., Ltd., > 98.0%), 1-chloropropane (Tokyo Chemical Industry Co., Ltd., > 99.0%), and lithium bis(trifluoromethylsulfonyl)amide (LiTFSA) (Kishida Chemical Co., Ltd., 99.0%) were purchased. *N*-Methylpyrrolidine and 1-chloropropane were purified by distillation *in vacuo* prior to use. Triacetyl-β-cyclodextrin (Acβ-CD) (Tokyo Chemical Industry Co., Ltd., > 97.0%) (see **Figure 1**) was used after drying.

[C$_3$mpyr][TFSA] was prepared as follows. *N*-Methyl-*N*-propylpyrrolidinium chloride ([C$_3$mpyr][Cl]) was synthesized according to a previously published procedure (Laus et al., 2008). [C$_3$mpyr][Cl] and LiTFSA were separately dissolved in deionized water. LiTFSA aq. was added dropwise to [C$_3$mpyr][Cl] aq. The resulting liquid was purified by washing repeatedly with deionized water until no residual chloride was detected with the use of AgNO$_3$ aq. [C$_3$mpyr][TFSA] was obtained as a colorless liquid at room temperature and characterized by ^{1}H NMR, fast atom bombardment mass spectrometry (FAB-MS), and elemental analysis. ^{1}H NMR (CD$_2$Cl$_2$, 300 MHz): δ (ppm) = 3.50 (2H, ddd, *J* = 10.22, 5.58, 3.01 Hz), 3.26 (1H, dt, *J* = 8.59, 4.04 Hz), 3.04 (1.5H, s), 2.27 (2H, s), 1.83 (1H, tt, *J* = 12.20, 5.61 Hz), 1.06 (1.5H, t, *J* = 7.39 Hz). MS (FAB$^+$): m/z 128.2 [M], 536.4 [2M+X]$^+$, MS (FAB$^-$): m/z 280.0 [X], 688.0 [M+2X]$^-$. Anal. Calcd. for C$_{10}$H$_{18}$F$_6$N$_2$O$_4$S$_2$ (%): C, 29.4; H, 4.44; N, 6.86; S, 15.7; Found (%): C, 29.2; H, 4.42; N, 6.78; S, 16.1.

A given amount of LiTFSA was dissolved in [C$_3$mpyr][TFSA] [IL:LiTFSA = 18 : 1 (molar ratio)], and then a given amount of Acβ-CD was added into IL/LiTFSA composites at molar ratios LiTFSA:Acβ-CD = 1.0 : 0.5, 1.0 : 1.0, and 1.0 : 1.5. Four kinds of samples were prepared to investigate the effect of Acβ-CD on the properties of the IL electrolyte. Their composites are abbreviated

as the molar ratio of Acβ-CD. For example, the abbreviation of [C₃mpyr][TFSA] : LiTFSA : Acβ-CD = 18 : 1 : 1.5 is Acβ-CD1.5. These mixtures were stirred at 60°C for 24 h.

Measurements

Fourier-transform infrared (FT-IR) measurements were performed on a Nicolet 6700 (Thermo Fisher Scientific) by using KRS-5.

^{1}H and ^{19}F NMR measurements were carried out with a Bruker Avance III HD 400 MHz at 25°C. Thermogravimetric analysis was conducted using a TG-DTA instrument (TG/DTA7200, Hitachi High-Technologies Corp.) under a nitrogen atmosphere at temperatures ranging from 25 to 500°C at a heating rate of 10°C min^{-1}. The thermal behavior was examined using differential scanning calorimetry (DSC) (DSC7020, Hitachi High-Technologies Corp.) at temperatures between −150 and 100°C at a heating/cooling rate of 10°C min^{-1}.

Impedance measurements were carried out using a VSP-300 (Bio-Logic Science Instruments) at frequencies ranging from 100 mHz to 1 MHz and temperatures ranging from 80 to −40°C. The temperature was controlled by a constant-temperature oven (SU-642, Espec Corp.). The composites were enclosed in a homemade glass cell having two platinum electrodes. The measurements were carried out by maintaining the cells at each temperature for 30 min. Viscosity measurements were carried out using a stabinger viscometer (SVM3000, Anton Paar) and temperature ranging from 80 to 20°C.

Pulse field gradient nuclear magnetic resonance (PFG-NMR) measurements were carried out with a Bruker Avance III HD 400 MHz at 80°C for ^{1}H, ^{7}Li, and ^{19}F nucleus. The ILs were filled into 5-mm NMR tubes, which were sealed. The measurements were carried out in 16 gradient steps per diffusion experiment. The gradient strength was 1,700 G cm^{-1}. The diffusion coefficients were calculated from the peak integration attenuation according to Equation 1 (Tanner and Stejskal, 1968):

$$A = A_0 - \exp[(\gamma \delta G)^2 D(\Delta - \frac{\delta}{3})] \qquad (1)$$

where A is the signal at a certain gradient (G), A_0 is the signal at a gradient of 0, δ is the width of the gradient pulse, Δ is the diffusion time, D is the diffusion coefficient, and γ is the gyromagnetic ratio of the nuclei.

Linear sweep voltammetry (LSV) measurements were carried out by using a VSP-300 (Bio-Logic Science Instruments) in the potential range of −0.2 and 6 V at 60°C at a scan rate of 1.0 mV s^{-1}. Li foils were used as the reference and counter electrodes, while Ni and Pt plates were used as working electrodes in the potential ranges of −0.2–3.0, and 3.0–6.0 V, respectively. The electrodes were separated by a glass filter to prevent short-circuiting. The cyclic voltammetric measurements of [C₃mpyr][TFSA]:LiTFSA:Acβ-CD = 18:1:1.0 composites were carried out using a VSP-300 (Bio-Logic Science Instruments) in the potential range of −0.25–1.0 V at 25, at a scan rate of 1.0 mV s^{-1}, with Li foils as the reference and counter electrodes, and the Ni plate was used as the working electrode. The electrodes were separated by a glass filter to prevent short-circuiting.
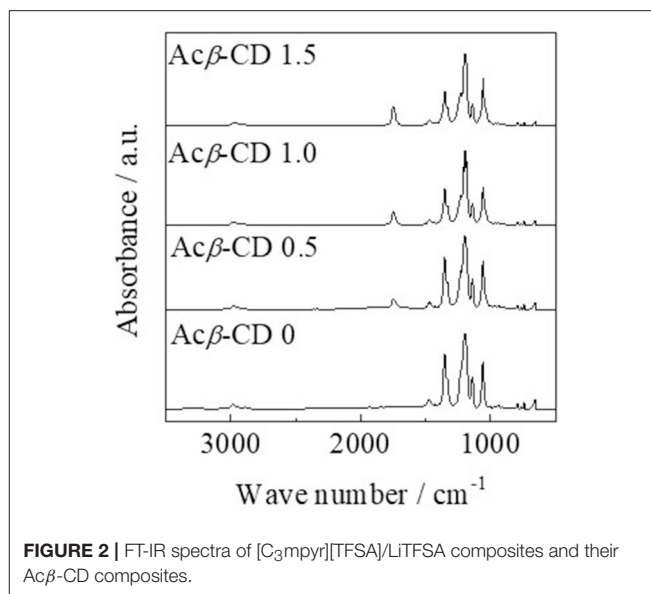
FIGURE 2 | FT-IR spectra of [C₃mpyr][TFSA]/LiTFSA composites and their Acβ-CD composites.

RESULTS AND DISCUSSION

Interaction Between Acβ-CD and TFSA Anion

A given amount of β-CD was initially added into [C₃mpyr][TFSA] and its LiTFSA mixture. Unfortunately, the IL electrolytes could not dissolve β-CD at any concentration. β-CD possesses hydroxyl groups, which form hydrogen bonds. The Lewis basicity of the TFSA anion is weak, and the TFSA anion cannot break the hydrogen bond. In fact, ILs with anions such as chloride and acetate, which exhibit a stronger Lewis basicity, can dissolve cellulose (Ohno and Fukaya, 2009) as such anions interact with the hydroxyl groups of cellulose because of the strong electron-donating ability. The TFSA anion could not dissolve even oligosaccharides. Therefore, Acβ-CD was used in this study instead of β-CD. A given amount of Acβ-CD was added into the IL electrolytes. [C₃mpyr][TFSA] with a weak Lewis-base anion could dissolve Acβ-CD, which has an acetyl group instead of a hydroxyl group.

FT-IR measurements were conducted, and each peak was assigned according to the literatures (Liu et al., 2009; Roy et al., 2016; Li et al., 2017; Wu et al., 2017). **Figure 2** presents FT-IR spectra of [C₃mpyr][TFSA]/LiTFSA and [C₃mpyr][TFSA]/LiTFSA/Acβ-CD composites. The FT-IR spectrum of [C₃mpyr][TFSA]/LiTFSA exhibits characteristic peaks for C-H stretching, CH₂ bending, and S=O stretching bands etc. The peaks in the range from 2,978 to 2,882 cm^{-1} can be assigned to the C-H stretching and CH₂ bending modes. In the case of TFSA anion, the peaks of S=O stretching band and C-SO₂-N bond are observed at 1,349 and 1,136 cm^{-1}, respectively. In addition, CF₃ symmetric stretching modes are located in 1,195 cm^{-1} and 1,056 cm^{-1}. For the spectrum of [C₃mpyr][TFSA]/LiTFSA/Acβ-CD, a new peak is observed at 1,746 cm^{-1}, which is assigned to C=O stretching mode for acetyl group, and the absorbance increases with increasing the Acβ-CD
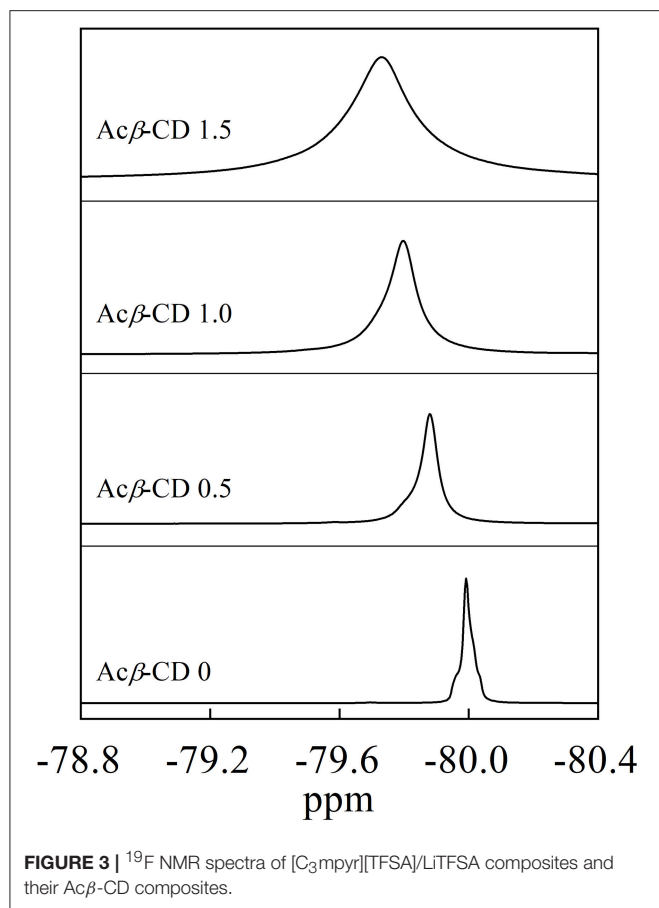
amount, indicating that the composites are formed by mixing [C$_3$mpyr][TFSA]/LiTFSA and Acβ-CD.

^{19}F NMR measurements were carried out to investigate the interaction between Acβ-CD and the TFSA anion. **Figure 3** presents ^{19}F NMR spectra of the CF$_3$ group in the TFSA anion for the [C$_3$mpyr][TFSA]/LiTFSA and [C$_3$mpyr][TFSA]/LiTFSA/Acβ-CD composites. The chemical shifts of the CF$_3$ group of the TFSA anion are -79.73, -79.80, -79.88, and -79.99 ppm for the Acβ-CD 1.5, 1.0, 0.5, and 0 composites, respectively. Zhang et al. (2014) performed ^{19}F NMR measurements of 1-ethyl-3-methylimidazolium bis(trifluoromethylsulfonyl)amide to detect the host–guest interaction between the β-CD and TFSA anion (Zhang et al., 2014). As the molar ratio of CD increases, downfield shifts for the fluorine atom of the CF$_3$ group in the TFSA anion are observed because of the formation of the complex for CD and the TFSA anion. In all the [C$_3$mpyr][TFSA]/LiTFSA/Acβ-CD composites, the CF$_3$ group chemically shifts to a lower magnetic field as compared to that of Acβ-CD 0, suggesting that Acβ-CD forms a complex with the TFSA anion.

Thermal Properties

To evaluate the thermal stability, onset thermal decomposition temperatures (T_d) were measured. **Figure 4** shows TGA traces for the [C$_3$mpyr][TFSA]/LiTFSA and
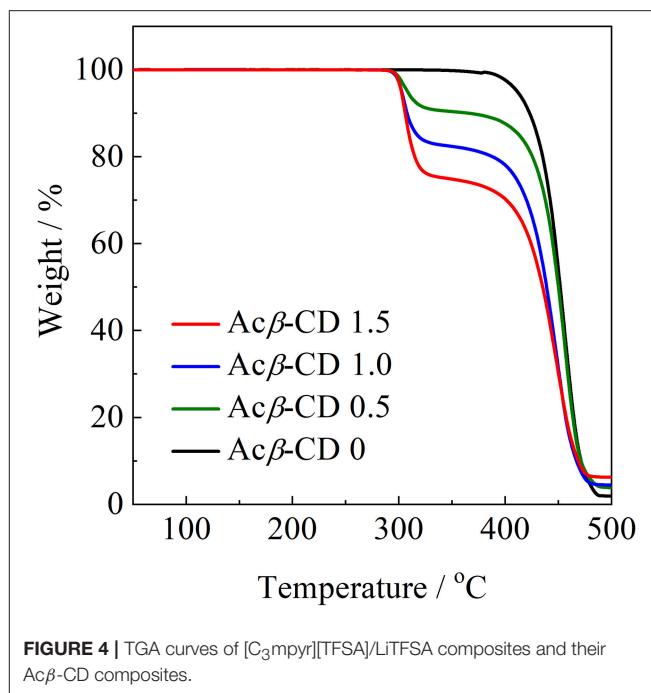
[C$_3$mpyr][TFSA]/LiTFSA/Acβ-CD composites. Acβ-CD 0 shows a T_d value at 386°C. Pyrrolidinium-based ILs with the TFSA anion are known to exhibit a higher thermal stability, and the T_d value of Acβ-CD 0 is consistent with the literature value (Yang et al., 2014). All the composites with Acβ-CD show similar T_d values, and their T_d values are about 300°C. This is due to the decomposition of Acβ-CD. The amount of weight loss is consistent with the amount of added Acβ-CD in the IL electrolytes.

DSC traces of the composites are presented in **Figure 5**. Acβ-CD 0 exhibits a melting point (T_m) of 8.0°C, which is consistent with the literature value (Wu et al., 2011). When the addition amount of Acβ-CD is 0.5 in the molar ratio, the glass transition temperature (T_g), two crystallization temperatures, and T_m are observed at -91, -33, -19, and 7.1°C, respectively. Acβ-CD 0.5 exhibits no crystallization temperature upon the cooling scan. In addition, the T_m value of Acβ-CD 0.5 slightly decreases as compared to that of Acβ-CD 0. The crystallization temperature and T_m cannot be observed in the composites in which the added amount of Acβ-CD is larger than the amount of Li salt in the molar ratio. Acβ-CD 1.0 and 1.5 exhibits T_g only and maintains low values below -79°C. These results suggest that the interaction between the Acβ-CD and TFSA anion prevents the crystallization of the IL.

Conductivity and Viscosity

Arrhenius plots of the ionic conductivities for the composite electrolytes are presented in **Figure 6**. **Figure 7** exhibits a typical Nyquist plot for Acβ-CD 1.5 at 0°C. The ionic conductivity values were calculated from the touchdown point on the Z'-axis which exhibits the resistance of the compound. For Acβ-CD 0 and 0.5, the conductivity values were not obtained by means

FIGURE 5 | DSC charts of [C$_3$mpyr][TFSA]/LiTFSA composites and their Acβ-CD composites.

FIGURE 6 | Arrhenius plots of ionic conductivities for [C$_3$mpyr][TFSA]/LiTFSA composites and their Acβ-CD composites.
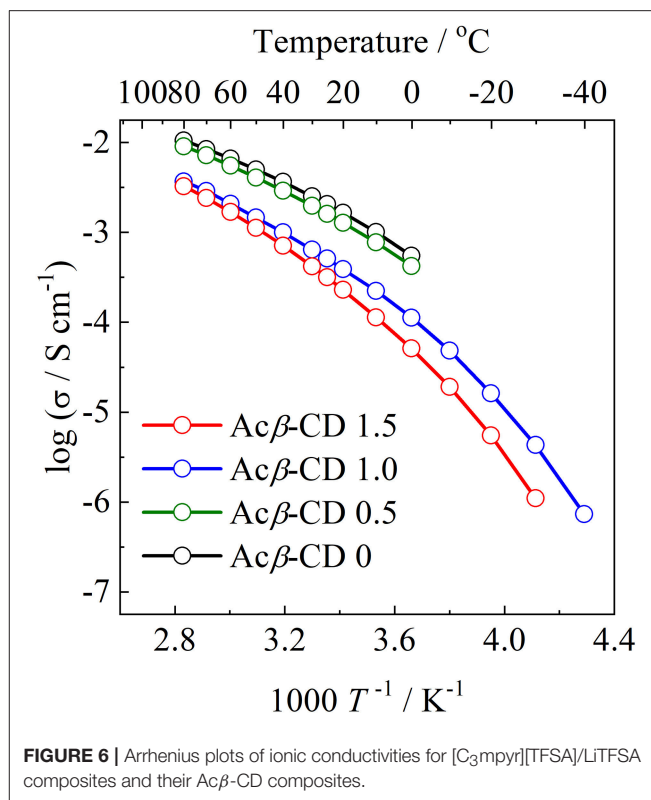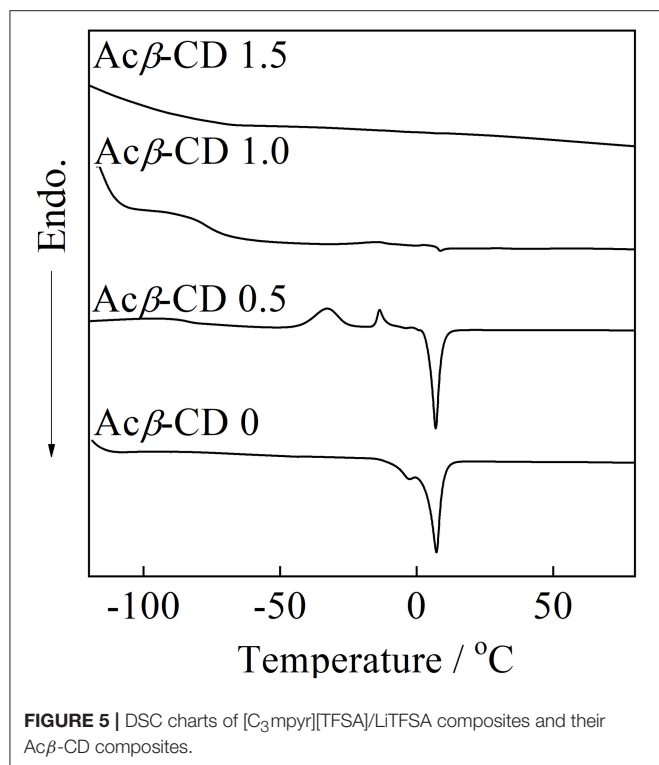
of our impedance apparatus, because of the crystallization of the electrolytes below 0°C, which is consistent with the DSC results. According to the DSC results, as Acβ-CD 1.0 and 1.5 are liquid in a wide temperature range, they exhibit a higher ionic conductivity even below 0°C, as shown in **Figure 5**. The ionic conductivities of the Acβ-CD 1.5, 1.0, 0.5, and 0 composites are 3.2×10^{-4}, 5.1×10^{-4}, 1.6×10^{-3}, and 2.1×10^{-3} S cm^{-1} at 25°C, respectively. The addition of Acβ-CD results in the decrease in the conductivity value, ascribable to the formation of an inclusion complex between Acβ-CD and the TFSA anion. This complex decreases the diffusivity of the component ions, thus decreasing the ionic conductivities. Roy and Roy (2017) used trihexyltetradecylphosphonium chloride as an IL, where a similar decrease in conductivity was observed as the amount of CD increased. The decrease in conductivity will be due to the encapsulation of guest molecules in the hydrophobic cavity of CD (Roy and Roy, 2017).

Figure 8 shows the ionic conductivity at 25°C and viscosity at 30°C as a function of the molar ratio of Acβ-CD. The ionic conductivity monotonously decreases with the Acβ-CD content as mentioned above. The viscosity values of the Acβ-CD 1.5, 1.0, 0.5, and 0 composites are 19,000, 1,700, 250, and 60 mPa s at 30°C, respectively. The viscosity values increase steeply as Acβ-CD is added to the composites. In addition, the conductivities and viscosities are inversely proportional (Salminen et al., 2007). The viscosity increases with CD concentration probably because of the IL and CD interactions and solvation (Roy et al., 2016). Thus, it is considered that the ionic conductivities decrease because of the increase in the viscosities of the composites.

FIGURE 7 | A typical Nyquist plot for Acβ-CD 1.5 at 0°C.
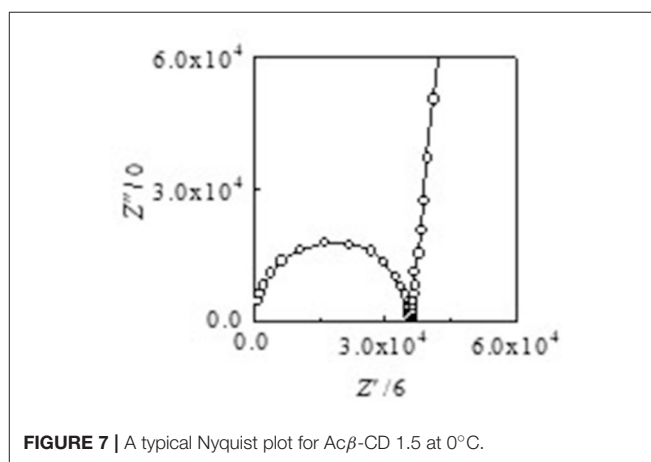
Diffusion Coefficients

The self-diffusion coefficients of C$_3$mpyr$^+$ (D_H), Li$^+$ (D_{Li}), and TFSA$^-$ (D_{TFSA}) for the [C$_3$mpyr][TFSA]/LiTFSA and [C$_3$mpyr][TFSA]/LiTFSA/Acβ-CD composites were determined by means of PFG-NMR at 80°C, as shown in **Figure 9**. The D_H and D_{TFSA} values of these composites are almost the same at 80°C, while the D_{Li} value is lower than those of the D_H and D_{TFSA} values. The increase in the Acβ-CD content induces a large difference between the D_{Li} value and other values. The apparent lithium transfer number (t_{Li+}) was calculated from the diffusion coefficient values using Equation (2):
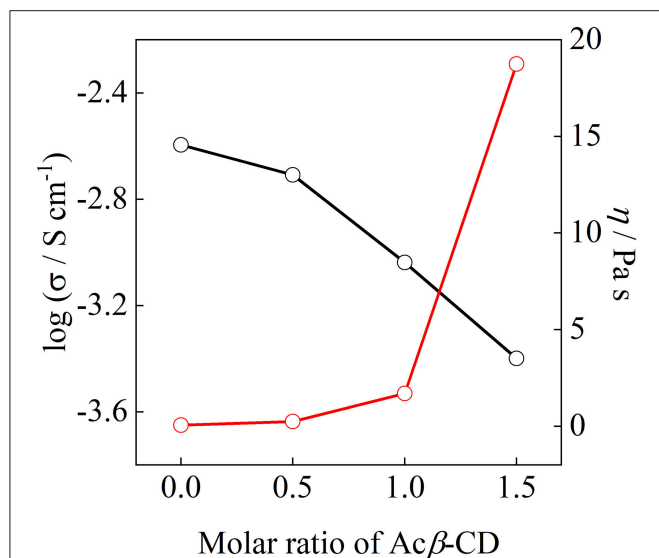
FIGURE 8 | Correlation between ionic conductivity and viscosity for [C$_3$mpyr][TFSA]/LiTFSA composites and their Acβ-CD composites.
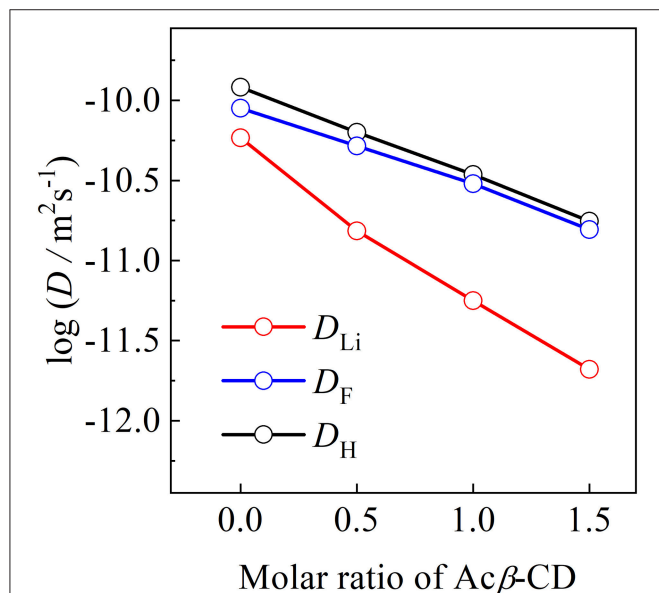

FIGURE 9 | Diffusion coefficients of [C$_3$mpyr][TFSA]/LiTFSA composites and their Acβ-CD composites as a function of mole ratio of Acβ-CD.
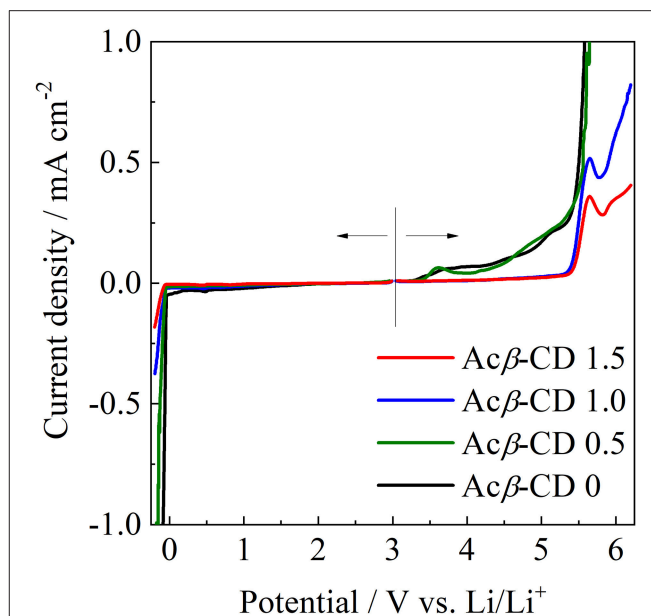

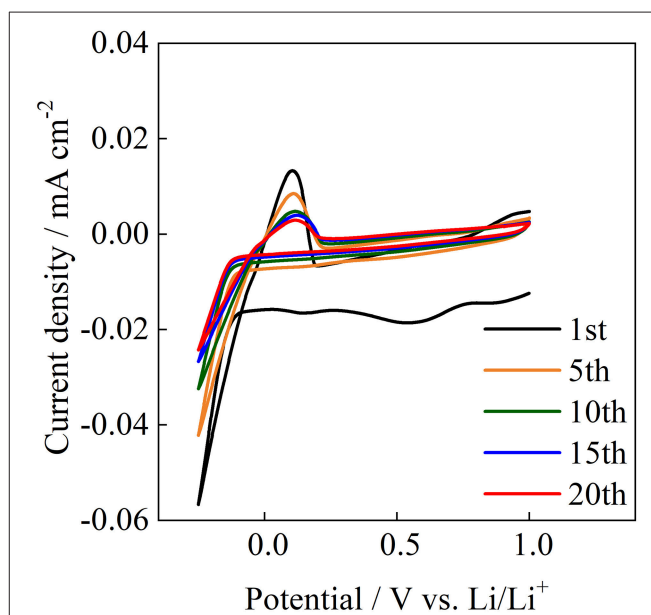**FIGURE 10 |** Linear sweep voltammograms of [C$_3$mpyr][TFSA]/LiTFSA composites and their Acβ-CD composites.

FIGURE 11 | Cyclic voltammograms of Acβ-CD 1.0 at 25°C.

$$t_{Li^+} = \frac{D_{Li}}{D_{Li} + D_{TFSA} + D_H} \tag{2}$$

Unlike electrochemical techniques, the diffusion coefficients obtained using the PFG-NMR method are derived not only from ionic species but also from non-ionic species (Horiuchi et al., 2017). The t_{Li}^+ values of the Acβ-CD 1.5, 1.0, 0.5, and 0 composites were 0.06, 0.08, 0.12, and 0.22, respectively. The decrease in the t_{Li}^+ values with the increase in Acβ-CD content suggests that an inclusion complex will be formed between LiTFSA and Acβ-CD. In addition, Acβ-CD would form an

inclusion complex with not only LiTFSA but also the aggregation including a Li cation, similar to the combination of two TFSA anions and one Li cation because the large surface charge density of a Li cation induces the formation of cluster ions (Appetecchi et al., 2016).

Electrochemical Properties

The electrochemical stabilities of the [C$_3$mpyr][TFSA]/LiTFSA and [C$_3$mpyr][TFSA]/LiTFSA/Acβ-CD composites were investigated by LSV on a Ni electrode (from 3 to -0.2 V)

and Pt electrode (from 3 to 6 V) at 60°C. The LSV results are presented in **Figure 10**. The electrochemical window ($EW = E_{anodic}\text{-}E_{cathodic}$) of all the IL electrolytes was determined from the values for the cathodic ($E_{cathodic}$) limit at $-0.1\,\mathrm{mA\ cm}^{-2}$ and anodic (E_{anodic}) limit at $0.1\,\mathrm{mA\ cm}^{-2}$. The EW value of Acβ-CD 0 is 4.6 V vs. Li/Li$^+$ and that of Acβ-CD 0.5 is 4.6 V vs. Li/Li$^+$, which is almost the same as that of Acβ-CD 0. The EW values are about 5.5 V vs. Li/Li$^+$ for both Acβ-CD 1.0 and 1.5 composites. As the addition amount of Acβ-CD increases, the oxidation stability improves. This improvement should be based on the formation of an inclusion complex between Acβ-CD and the TFSA anion because the anodic stability significantly improves, and the cathodic stability is almost the same regardless of the addition of Acβ-CD.

The reversible oxidation and reduction reactions of lithium were examined at room temperature for Acβ-CD 1.0. **Figure 11** shows the cyclic voltammogram for Acβ-CD 1.0 on a Ni electrode. Acβ-CD 1.0 exhibits reduction and oxidation peaks for Li at about -0.1 and 0.1 V vs. Li/Li$^+$, respectively. The current density decreases with the cycling number from 1st to 10th. After that, the current density maintains a constant value, and stable reversible redox reactions are observed during 20 cycles. At the initial anodic sweep, an anodic current is observed. This behavior is also observed for pyrrolidinium-based ILs (Towada et al., 2015; Horiuchi et al., 2016). In addition, the maximum current density of the anodic peak slightly shifts to a higher potential value with the increase in cycle number. These results suggest that a solid electrolyte interphase film is formed on the Ni electrode surface (Grande et al., 2015), even in the presence of Acβ-CD.

CONCLUSIONS

The effect of Acβ-CD on the properties of [C$_3$mpyr][TFSA]/LiTFSA was investigated by means of several techniques. The chemical shift of the CF$_3$ group of the TFSA anion shifted to a lower magnetic field with the increase in the Acβ-CD content. With the addition of Acβ-CD to the IL electrolyte, the T_m of the IL disappeared and the viscosity increased. These results suggest that an inclusion complex is formed between Acβ-CD and the TFSA anion. In contrast, the t_{Li+} and D_{Li} values decreased with the increase in the Acβ-CD content in the composites. The anodic stability of [C$_3$mpyr][TFSA]/LiTFSA was significantly improved after adding a certain amount of Acβ-CD. Li plating and stripping in the [C$_3$mpyr][TFSA]/LiTFSA/Acβ-CD composite were repeatedly observed. According to these results, Acβ-CD will be an interesting additive for improving the electrochemical stability of ILs. It is known that there are three kinds of CD, α-CD, β-CD, and γ-CD, which have different cavity sizes. The physicochemical properties of various ILs with different anions could be controlled by choosing suitable CD derivatives.

REFERENCES

Amajjahe, S., Choi, S., Munteanu, M., and Ritter, H. (2008). Pseudopolyanions based on poly(NIPAAM-co-beta-cyclodextrin methacrylate) and ionic liquids. *Angew. Chem. Int. Ed. Engl.* 47, 3435–3437. doi: 10.1002/anie.200704995

Amajjahe, S., and Ritter, H. (2008). Anion complexation of vinylimidazolium salts and its influence on polymerization. *Macromolecules* 41, 716–718. doi: 10.1021/ma702271p

Appetecchi, G. B., D'Annibale, A., Santilli, C., Genova, E., Lombardo, L., Navarra, M. A., et al. (2016). Novel functionalized ionic liquid with a sulfur atom in the aliphatic side chain of the pyrrolidinium cation. *Electrochem. Commun.* 63, 26–29. doi: 10.1016/j.elecom.2015.12.009

Armand, M., Endres, F., MacFarlane, D. R., Ohno, H., and Scrosati, B. (2009). Ionic-liquid materials for the electrochemical challenges of the future. *Nat. Mater.* 8, 621–629. doi: 10.1038/nmat2448

Baâzaoui, M., Béjaoui, I., Kalfat, R., Amdouni, N., Hbaieb, S., and Chevalier, Y. (2016). Interfacial properties and thermodynamic behavior of cationic amphiphilic β-cyclodextrins substituted with one or seven alkyl chains. *RSC Adv.* 6, 72044–72054. doi: 10.1039/C6RA10597A

Chen, R., Lai, J., Li, Y., Cao, M., Chen, S., and Wu, F. (2016). β-Cyclodextrin coated lithium vanadium phosphate as novel cathode material for lithium ion batteries. *RSC. Adv.* 6, 103364–103371. doi: 10.1039/C6RA22400H

Crini, G. (2014). Review: a history of cyclodextrins. *Chem. Rev.* 114, 10940–10975. doi: 10.1021/cr500081p

Franco, A. A. (2015). *Rechargeable Lithium Batteries*. Cambridge: Woodhead/Elsevier Science.

Grande, L., von Zamory, J., Koch, S. L., Kalhoff, J., Paillard, E., and Passerini, S. (2015). Homogeneous lithium electrodeposition with pyrrolidinium-based ionic liquid electrolytes. *ACS Appl. Mater. Interfaces* 7, 5950–5958. doi: 10.1021/acsami.5b00209

He, Y., Chen, Q., Xu, C., Zhang, J., and Shen, X. (2009). Interaction between ionic liquids and β-cyclodextrin: a discussion of association pattern. *J. Phys. Chem. B* 113, 231–238. doi: 10.1021/jp80 8540m

Horiuchi, S., Yoshizawa-Fujita, M., Takeoka, Y., and Rikukawa, M. (2016). Physicochemical and electrochemical properties of *N*-methyl-*N*-methoxymethylpyrrolidinium bis(fluorosulfonyl)amide and its lithium salt composites. *J. Power Sources* 325, 637–640. doi: 10.1016/j.jpowsour.2016.06.087

Horiuchi, S., Zhu, H., Forsyth, M., Takeoka, Y., Rikukawa, M., and Yoshizawa-Fujita, M. (2017). Synthesis and evaluation of a novel pyrrolidinium-based zwitterionic additive with an ether side chain for ionic liquid electrolytes in high-voltage lithium-ion batteries. *Electrochim. Acta* 241, 272–280. doi: 10.1016/j.electacta.2017.04.165

Ishikawa, M., Sugimoto, T., Kikuta, M., Ishiko, E., and Kono, M. (2006). Pure ionic liquid electrolytes compatible with a graphitized carbon negative electrode in rechargeable lithium-ion batteries. *J. Power Sources* 162, 658–662. doi: 10.1016/j.jpowsour.2006.02.077

Laus, G., Bentivoglio, G., Kahlenberg, V., Griesser, U. J., Schottenberger, H., and Nauer, G. (2008). Syntheses, crystal structures, and polymorphism of quaternary pyrrolidinium chlorides. *CrystEngComm*. 10, 748–752. doi: 10.1039/b718917f

Li, X., Zhang, Z., Li, S., Yang, K., and Yang, L. (2017). Polymeric ionic liquid-ionic plastic crystal all-solid-state electrolytes for wide operating temperature range lithium metal batteries. *J. Mater. Chem. A*. 5, 21362–21369. doi: 10.1039/C7TA04204C

Liu, Z.-T., Shen, L.-H., Liu, Z.-W., and Lu, J. (2009). Acetylation of β-cyclodextrin in ionic liquid green solvent. *J. Mater Sci.* 44, 1813–1820. doi: 10.1007/s10853-008-3238-1

Matsumoto, H., Sakaebe, H., Tatsumi, K., Kikuta, M., Ishiko, E., and Kono, M. (2006). Safety assessment of ionic liquid-based lithium-ion battery prototypes. *J. Power Sources* 160, 1308–1313. doi: 10.1016/j.jpowsour.2006.02.018

Narita, A., Shibayama, W., Sakamoto, K., Mizumo, T., Matsumi, N., and Ohno, H. (2006). Lithium ion conduction in an organoborate zwitterion–LiTFSI mixture. *Chem. Commun.* 1926–1928. doi: 10.1039/B517019B

Nishimura, N., and Ohno, H. (2014). 15th anniversary of polymerised ionic liquids. *Polymer* 55, 3289–3297. doi: 10.1016/j.polymer.2014.02.042

Ohno, H. (2011). *Electrochemical Aspects of Ionic Liquids, Second Ed*. Hoboken, NJ: John Wiley & Sons, Inc.

Ohno, H., and Fukaya, Y. (2009). Task specific ionic liquids for cellulose technology. *Chem. Lett.* 38, 2–7. doi: 10.1246/cl.2009.2

Qian, W., Texter, J., and Yan, F. (2017). Frontiers in poly(ionic liquid)s: syntheses and applications. *Chem. Soc. Rev.* 46, 1124–1159. doi: 10.1039/C6CS00620E

Roy, A., and Roy, M. N. (2017). Cage to cage study of ionic liquid and cyclic oligosaccharides to form inclusion complexes. *RSC Adv.* 7, 40803–40812. doi: 10.1039/C7RA08397A

Roy, A., Saha, S., Datta, B., and Roy, M. N. (2016). Insertion behavior of imidazolium and pyrrolidinium based ionic liquids into α and β-cyclodextrins: mechanism and factors leading to host–guest inclusion complexes. *RSC Adv.* 6, 100016–100027. doi: 10.1039/C6RA19684E

Salminen, J., Papaiconomou, N., Kumar, R. A., Lee, J.-M., Kerr, J., Newman, J., et al. (2007). Physicochemical properties and toxicities of hydrophobic piperidinium and pyrrolidinium ionic liquids. *Fluid Phase Equilibria* 261, 421–426. doi: 10.1016/j.fluid.2007.06.031

Seki, S., Kobayashi, Y., Miyashiro, H., Ohno, Y., and Mita, Y., Terada, N., et al. (2008). Compatibility of *N*-methyl-*N*-propylpyrrolidinium cation room-temperature ionic liquid electrolytes and graphite electrodes. *J. Phys. Chem. C* 112, 16708–16713. doi: 10.1021/jp805403e

Seki, S., Ohno, Y., Miyashiro, H., Kobayashi, Y., Usami, A., Mita, Y., et al. (2008). Quaternary ammonium room-temperature ionic liquid/lithium salt binary electrolytes: electrochemical study. *J. Electrochem. Soc.* 155, A421–A427. doi: 10.1149/1.2899014

Silva, O. F., Fernández, M. A., Pennie, S. L., Gil, R. R., and de Rossi, R. H. (2008). Synthesis and characterization of an amphiphilic cyclodextrin, a micelle with two recognition sites. *Langmuir* 24, 3718–3726. doi: 10.1021/la702962f

Szejtli, J. (1998). Introduction and general overview of cyclodextrin chemistry. *Chem. Rev.* 98, 1743–1754. doi: 10.1021/cr970022c

Tanner, J. E., and Stejskal, E. O. (1968). Restricted self-diffusion of protons in colloidal systems by the pulsed-gradient, spin-echo method. *J. Chem. Phys.* 49, 1768. doi: 10.1063/1.1670306

Towada, J., Karouji, T., Sato, H., Kadoma, Y., Shimada, K., and Ui, K. (2015). Charge–discharge characteristics of natural graphite electrode in N, N-diethyl-N-methyl-N-(2-methoxyethyl)ammonium bis(trifluoromethylsulfonyl)amide containing lithium ion for lithium-ion secondary batteries. *J. Power Sources* 275, 50–54. doi: 10.1016/j.jpowsour.2014.10.101

Wu, A., Lu, F., Sun, P., Qiao, X., Gao, X., and Zheng, L. I. (2017). Low-molecular-weight supramolecular ionogel based on host–guest interaction. *Langmuir* 33, 13982–13989. doi: 10.1021/acs.langmuir.7b03504

Wu, T.-Y., Su, S.-G., Wang, H.-P., Lin, Y.-C., Gung, S.-T., Lin, M.-W., et al. (2011). Electrochemical studies and self diffusion coefficients in cyclic ammonium based ionic liquids with allyl substituents. *Electrochim. Acta* 56, 3209–3218. doi: 10.1016/j.electacta.2011.01.040

Yabuuchi, N., and Ohzuku, T. (2003). Novel lithium insertion material of $LiCo_{1/3}Ni_{1/3}Mn_{1/3}O_2$ for advanced lithium-ion batteries. *J. Power Sources* 119–121, 171–174. doi: 10.1016/S0378-7753(03)00173-3

Yang, B., Li, C., Zhou, J., Liu, J., and Zhang, Q. (2014). Pyrrolidinium-based ionic liquid electrolyte with organic additive and LiTFSI for high-safety lithium-ion batteries. *Electrochim. Acta* 148, 39–45. doi: 10.1016/j.electacta.2014.10.001

Yoon, H., Best, A. S., Forsyth, M., MacFarlane, D. R., and Howlett, P. C. (2015). Physical properties of high Li-ion content N-propyl-N-methylpyrrolidinium bis(fluorosulfonyl)imide based ionic liquid electrolytes. *Phys. Chem. Chem. Phys.* 17, 4656–4663. doi: 10.1039/C4CP05333H

Yoshizawa, M., Narita, A., and Ohno, H. (2004). Design of ionic liquids for electrochemical applications. *Aust. J. Chem.* 57, 139–144. doi: 10.1071/CH03240

Yoshizawa-Fujita, M., Tamura, T., Takeoka, Y., and Rikukawa, M. (2011). Low-melting zwitterion: effect of oxyethylene units on thermal properties and conductivity. *Chem. Commun.* 47, 2345–2347. doi: 10.1039/C0CC03754K

Yuan, J., Mecerreyes, D., and Antonietti, M. (2013). Poly(ionic liquid)s: an update. *Prog. Polym. Sci.* 38, 1009–1036. doi: 10.1016/j.progpolymsci.2013.04.002

Zhang, W., Yuan, C., Guo, J., Qiu, L., and Yan, F. (2014). Supramolecular ionic liquid gels for quasi-solid-state dye-sensitized solar cells. *ACS Appl. Mater. Interfaces* 6, 8723–8728. doi: 10.1021/am501523x

Zhu, Z., Qilu, Z. D., and Yu, H.,. (2014). Preparation of spherical hierarchical $LiNi_{0.5}Mn_{1.5}O_4$ with high electrochemical performances by a novel composite co-precipitation method for 5 V lithium ion secondary batteries. *Electrochim. Acta* 115, 290–296. doi: 10.1016/j.electacta.2013.10.167

Check for
updates

Systematic Synthesis and Properties Evaluation of Dicationic Ionic Liquids, and a Glance Into a Potential New Field

Luca Guglielmero, Andrea Mezzetta, Lorenzo Guazzelli, Christian S. Pomelli, Felicia D'Andrea and Cinzia Chiappe*

Department of Pharmacy, University of Pisa, Pisa, Italy

Dicationic ionic liquids (DILs), a subset of the ionic liquid (IL) family, have attracted growing interest in recent years, and the range of applications within which they are investigated is constantly expanding. However, data which allows structure to property correlation of a DIL is still limited, and thus selecting an appropriate salt to address a specific challenge can be problematic. In comparison to traditional ILs, DILs physico-chemical properties can be tuned by changing the length and type of spacer which connects the cationic heads as well as the type of cation. This in turn could give rise to symmetrical or asymmetrical DILs. In this work, a systematic study of a homogeneous class of 12 dibromide DILs and 12 di-carboxylate salts has been performed. The latter class of DILs were also compared to mono cation derivatives. The different traditional exchange methods to prepare carboxylate DILs have been evaluated and an insight into the drawbacks encountered is also presented. Prepared DILs were characterized (NMR, TGA, DSC) allowing the influence of the structure on their thermal stability to be understood. Most DILs were obtained as solid salts after careful drying. For some of these compounds, a new possible application was studied, namely their use as hydrogen bond acceptors (HBA) of deep eutectic mixtures, showing again some significant structural related effects.

Keywords: dicationic ionic liquids, thermal analyses, deep eutectic solvents, TGA, DSC

INTRODUCTION

Conventional room temperature ionic liquids (ILs) have been extensively studied starting from the beginning of this century by several authors due to their unique physico-chemical properties, which have allowed for their use in numerous applications (Welton, 2018). Low vapor pressure and high thermal stability, associated with possible catalytic actions, which emerge in particular when properly functionalized cations or anions were used (Chiappe and Pomelli, 2014), contributed to their application as innovative green solvents for a plethora of important processes going from (bio)polymer dissolution (Shen et al., 2016; Mezzetta et al., 2017a; Zhang et al., 2017), to chemical reactions (Hallett and Welton, 2011) and separations (Brown et al., 2017). Furthermore, the wide electrochemical window and the high conductivity enabled their use as electrolytes in solar cells and batteries (Watanabe et al., 2017). Generally, they are constituted by an asymmetric organic cation, imidazolium based ILs are the most investigated, associated to a polyatomic inorganic or organic

anion (Scalfani et al., 2018). Nonetheless, more recently a new branch of ILs has been proposed: the generally defined dicationic (or geminal) ionic liquids (DILs). These ILs seem to differ from the traditional monocationic ones in many ways offering a growing portfolio of possible applications, ranging from the "classical" use as solvents, catalysts or catalytic supports in organic reactions, to more specific applications as high temperature lubricants/heat transfer fluids, including a variety of roles in analytical sciences (Patil et al., 2016). Further development of these interesting materials in terms of improved performances or new applications are expected, especially if the impact that structural changes can bring upon physical, optical and chemical properties of these unusual material will be understood. Another crucial aspect of ILs is their potential toxicity, which has been scrutinized during the last 10 years. On this regard, the studies performed up to now showed promising toxicity profiles for DILs when compared with the corresponding monocationic ILs (Pretti et al., 2009; Frizzo et al., 2018; Montalbána et al., 2018).

Although a relevant number of DILs has been described in the literature and the number of papers on this topic is rapidly increasing, the relationship between the three-dimensional structure and physicochemical characteristics is, as yet, not well understood.

In analogy with the situation that has characterized simple ILs, the development of DILs chemistry has been much more supported by the creativity of synthetic chemists than by a rational design. Surely, the factors that control the physico-chemical properties of monocationic ILs (MILs), such as the interaction between anions and cations or the structural arrangements of long alkyl chains, play an important role also in the case of dicationic and/or dianionic ILs. However, in this case also the linker(s) between the charged moieties affect the three-dimensional structure of these systems and consequently their principal physical properties, i.e., their ability to solvate dissolved particles, to stabilize transition states or to allow for the formation of polar and apolar domains. Furthermore, asymmetry can be introduced not only by changing the alkyl chains on cations but also introducing two different cationic cores or two different anions. The greater structural variability in DILs is expected to result in an increased tunability and versatility of these salts, when compared to MILs.

Finally, it is noteworthy that the possibility to associate two covalently linked cations to multi-covalently linked anions allows for obtaining the so-called ionic supramolecular polymers by self-assembly, i.e., supramolecular systems with high viscosity and polymer properties arising from the reversible link of small molecules (Craig, 2009). In the last years, starting from the pioneering paper of Wathier and Grinstaff reporting the preparation of organic supramolecular ionic networks by mixing multi-cationic and multi-anionic compounds (Wathier and Grinstaff, 2008), several papers have been published on this topic: for example, using simple proton transfer reactions between citric acid and a diamine, Mecerreyes et al. have prepared (Aboudzadeh et al., 2012a,b, 2013, 2014) protic supramolecular systems based on ionic interactions and, more recently, ionic networks having improved (Aboudzadeh et al., 2015) thermal and chemical

stability, employing highly delocalized hydrophobic dianions combined with geminal imidazolium dications. It is to note that this kind of ionic supramolecular organization is generally considered different with respect to the well-known dynamic supramolecular organization of common ionic liquids, which present at the molecular level distinct ionic and non-ionic domains: the two phenomena have probably different time scales.

In order to obtain further information on these ionic media, which have already been used in few applications [e.g., *in situ* formation of DESs in an innovative procedure for the separation of phenols from oils (Youan et al., 2017, 2018), CO_2 cycloaddition reaction (Liu et al., 2015), elucidation of a reaction mechanism (Bortolini et al., 2014)] or could be used to develop stimuli responsive ionic polymers, a systematic investigation of a homogeneous class of 12 imidazolium based dicationic dibromides and related dicarboxylate salts has been performed. The thermal properties of this latter class of compounds were also compared to mono cation derivatives. The different traditional exchange methods to prepare carboxylate ILs have been evaluated and an insight into the drawbacks encountered is also presented. Prepared salts were characterized (NMR, TGA, DSC) allowing to ascertain the influence of the structure on their thermal behavior/characteristics.

For some of the prepared compounds, a new possible research area was studied, namely their use as hydrogen bond acceptors (HBA) of deep eutectic mixtures. In 2003 Abbott et al. were the first to report the ability of urea to form a deep eutectic solvent (DES) with a quaternary chloride salt (Abbott et al., 2003) Since then, much research has been done in this specific field of solvents which consist of a mixture of two or more components (one of which is a salt) and are characterized by a melting point lower than any of its individual components. The formation of a DES requires the establishment of hydrogen bonds between the salt, in particular its halide anion, and an organic compound acting as hydrogen bond donor (HBD). This determines the formation of a supramolecular complex able to modify the free energy of the solid phase with respect to the liquid one. Although choline chloride is probably the most applied salt to obtain DES, also imidazolium, ammonium and phosphonium salts have been recently used as alternative organic salt components (Florindo et al., 2014).

Thus, considering that all the investigated DILs have a strong hydrogen bond accepting anion, to verify the possibility to transform at least some of the synthesized salts which are solid at room temperature into liquids, we used two reference compounds (**4** and **20**) for the preparation of the corresponding DESs by adding increasing amounts of either glycerol or diethylene glycol.

EXPERIMENTAL SECTION

General Methods

^{1}H and ^{13}C NMR spectra were recorded with a Bruker Avance II operating at 250.13 and 62.9 MHz at 24°C. The assignments were made with the aid of HSQC and COSY experiments. The first order proton chemical shifts δ are referenced to either residual DMSO (δ_H 2.50, δ_C 39.5) or D_2O (δ_H 4.79) and J-values are given

in Hz. The chemical shifts are given in δ and *J*-values are given in Hz. The following abbreviations are used: s = singlet, m = multiplet, bs = broad singlet, t = triplet, bt = broad triplet, q = quartet, qui = quintuplet, sext = sextet.

TLC analyses were performed on Kieselgel 60 F$_{254}$ with detection by UV light (254 nm) and/or with ethanolic 10% phosphomolybdic and heating. All reagents were obtained commercially and used without further purification.

The thermal stability of the synthesized ILs was investigated by thermal gravimetric analysis (TGA), conducted in a TA Instruments Q500 TGA. ILs (15–20 mg) was heated in a platinum crucible as sample holders. First, the heating mode was set to isothermal at 50°C in N$_2$ (100 mL/min) for 30 min. Then, IL was heated from 40 to 600°C with a heating rate of 10°C/min under nitrogen (100 mL/min). Mass change was recorded as a function of temperature and time. TGA experiments were carried out in triplicate.

The thermal behavior of the ionic liquids was analyzed by a differential scanning calorimeter (TA DSC, Q250, USA). About 5–10 mg of sample was loaded in hermetic aluminum crucibles. DSC analyses were performed at 10°C/min in nitrogen flow in the temperature range going from −40 to 250°C, as generally reported in the literature for this class of ionic liquids (Lee et al., 2011). In the drying cycle, the sample was heated from 40 to 130°C and maintained at this temperature for 30 min. Then, it was cooled down from 130 to −40°C, at a rate of 10°C/min, and maintained at −40°C for 10 min (cooling run). Finally, the sample was heated to the selected temperature at a rate of 10°C/min to ensure the complete sample melting (heating run). DSC experiments were carried out in duplicate.

Electrospray ionization mass (ESI-MS) spectra were registered on a LCQ Advantage ThermoFinnigan spectrometer equipped with an ion trap analyzer (Thermo Electron Company, San Jose, Ca, USA). Samples were dissolved in methanol (10^{-3} M), spectra were acquired in both negative-ion and positive-ion mode.

General Procedure for the Synthesis of 3,3′-(alkane-1,n-diyl)bis(1-alkyl-1H-imidazolium) bromide (1-12)

Method A (in toluene)
1,n-Dibromoalkane (58 mmol, 1 equiv) and 10 mL of toluene were added in a three-necked flask. A solution of 1-alkylimidazole (122 mmol, 2.1 equiv) in toluene (10 mL) was added dropwise under magnetic stirring at 0°C. Other 10 mL of toluene were added, and the solution was stirred for 15 min. The reaction mixture was then heated up and stirred at 80°C for 12 h. A white solid precipitation (or liquid separation) was observed after half an hour. Solid precipitates were filtrated under vacuum, washed with toluene (3 × 50 mL), EtOAc (3 × 50 mL) and dried in vacuo, to afford white solids in excellent yields. Liquid products were decanted, washed with toluene and dried in vacuo, to afford colorless liquids in excellent yields.

Method B (in 4-methyl-2-pentanone)
Alternatively, compounds **1-12** were prepared according to the general procedure described above, replacing toluene with 4-methyl-2-pentanone (MIBK) as the solvent.

3,3′-(Propane-1,3-diyl)bis(1-methyl-1H-imidazolium) bromide (1). The preparation of **1** (97% yield, hygroscopic white solid) was performed according to the general procedure (Method A). ^{1}H NMR (D$_2$O) δ 8.93 (s, 2H, 2×H-2), 7.65, 7.40 (2s, each 2H, 2×H-4, 2×H-5), 4.35 (t, 4H, *J*=7.3 Hz, 2×C*H*$_2$N), 3.93 (s, 6H, 2×NC*H*$_3$), 2.56 (qui, 2H, *J*=7.2 Hz, C*H*$_2$);^{13}C NMR (D$_2$O) δ 136.4 (2×C-2), 124.1, 122.3 (2×C-4, 2×C-5), 46.5 (2×CH$_2$N), 36.1 (2×NCH$_3$), 30.0 (CH$_2$). NMR (^{1}H, ^{13}C) data were in agreement with those reported (Chen et al., 2015; Leclercq and Schmitzer, 2011; Fareghi-Alamdari et al., 2016).

3,3′-(Butane-1,4-diyl)bis(1-methyl-1H-imidazolium) bromide (2). The preparation of **2** (97% yield, white solid) was performed according to the general procedure (Method B). ^{1}H NMR (D$_2$O) δ 8.77 (s, 2H, 2×H-2), 7.56, 7.45 (2s, each 2H, 2×H-4, 2×H-5), 4.26 (bs, 4H, 2×C*H*$_2$N), 3.89 (s, 6H, 2×NC*H*$_3$), 1.94 (bs, 4H, C*H*$_2$C*H*$_2$); ^{13}C NMR (D$_2$O) δ 136.2 (2×C-2), 123.9, 122.3 (2×C-4, 2×C-5), 48.9 (2×CH$_2$N), 36.0 (2×NCH$_3$), 26.4 (CH$_2$CH$_2$). NMR (^{1}H, ^{13}C) data were in agreement with those reported (Nachtigall et al., 2008; Chen et al., 2015).

3,3′-(Pentane-1,5-diyl)bis(1-methyl-1H-imidazolium) bromide (3). The preparation of **3** (92% yield, hygroscopic white solid) was performed according to the general procedure (Method A). ^{1}H NMR (D$_2$O) δ 8.78 (s, 2H, 2×H-2), 7.88, 7.43 (2s, each 2H, 2×H-4, 2×H-5), 4.20 (t, 4H, *J*=7.1 Hz, 2×C*H*$_2$N), 3.89 (s, 6H, 2×NC*H*$_3$), 1.93 (qui, 4H, *J*=7.5 Hz, 2×NCH$_2$C*H*$_2$), 1.33 (m, 2H, C*H*$_2$). ^{13}C NMR (D$_2$O) δ 136.1 (2×C-2), 123.8, 122.4 (2×C-4, 2×C-5), 49.4 (2×CH$_2$N), 36.0 (2×NCH$_3$), 28.9 (2×NCH$_2$CH$_2$), 22.4 (CH$_2$). NMR (^{1}H, ^{13}C) data were in agreement with those reported (Nielsen et al., 2006; Chen et al., 2015).

3,3′-(Hexane-1,5-diyl)bis(1-methyl-1H-imidazolium) bromide (4). The preparation of **4** (97% yield, white solid) was performed according to the general procedure (Method B). ^{1}H NMR (D$_2$O) δ 8.62 (s, 2H, 2×H-2), 7.46, 7.36 (2bs, each 2H, 2×H-4, 2×H-5), 4.17 (t, 4H, *J*=7.1 Hz, 2×C*H*$_2$N), 3.87 (s, 6H, 2×NC*H*$_3$), 1.89 (m, 4H, 2×NCH$_2$C*H*$_2$), 1.33 (m, 4H, C*H*$_2$C*H*$_2$); ^{13}C NMR (D$_2$O) δ 136.0 (2×C-2), 123.7, 122.3 (2×C-4, 2×C-5), 49.6 (2×CH$_2$N), 36.8 (2×NCH$_3$), 29.2 (2×NCH$_2$CH$_2$), 25.0 (CH$_2$CH$_2$). NMR (^{1}H, ^{13}C) data were in agreement with those reported (Bortolini et al., 2017).

3,3′-(Propane-1,3-diyl)bis(1-butyl-1H-imidazolium) bromide (5). The preparation of **5** (87% yield, hygroscopic white solid) was performed according to the general procedure (Method B). ^{1}H NMR (D$_2$O) δ 8.86 (s, 2H, 2×H-2), 7.52 (bs, 4H, 2×H-4, 2×H-5), 4.32 (t, 4H, *J*=7.2 Hz, 2×C*H*$_2$N), 4.19 (t, 4H, *J*=7.2 Hz, 2×C*H*$_2$N), 2.56 (qui, 2H, *J*=7.3 Hz, NCH$_2$C*H*$_2$CH$_2$N), 1.84 (qui, 4H, *J*=7.3 Hz, NCH$_2$C*H*$_2$C$_2$H$_5$), 1.30 (sext, 4H, *J*=7.5 Hz, 2×C*H*$_2$CH$_3$), 0.90 (t, 6H, *J*=7.3 Hz, 2×CH$_3$); ^{13}C NMR (D$_2$O) δ 135.3 (2×C-2), 122.7, 122.1 (2×C-4, 2×C-5), 49.4, 46.4 (each 2×CH$_2$N), 31.1 (2×NCH$_2$CH$_2$C$_2$H$_5$), 29.6 (NCH$_2$CH$_2$CH$_2$N), 18.7 (2×CH$_2$CH$_3$), 12.6 (2×CH$_3$). NMR (^{1}H) data were in agreement with those reported (Lee et al., 2010; Priede et al., 2014).

3,3′-(Butane-1,4-diyl)bis(1-butyl-1H-imidazolium) bromide (6). The preparation of **6** (99% yield, highly viscous colorless liquid) was performed according to the general procedure (Method B). ^{1}H NMR (D$_2$O) δ 8.82 (s, 2H, 2×H-2),

7.48 (bs, 4H, 2×H-4, 2×H-5), 4.30-4.20 (m, 8H, 4×CH_2N), 1.90-1.75 (m, 8H, 4× NCH_2CH_2), 1.38 (m, 4H, 2×CH_3CH_2), 0.85 (t, 6H, J=7.3 Hz, 2×CH_3); ^{13}C NMR (D_2O) δ 135.1 (2×C-2), 122.4, 122.0 (2×C-4, 2×C-5), 49.3 (2×CH_2N), 48.6 (2×CH_2N), 31.1, 26.2 (2×N$CH_2CH_2C_2H_5$, 2×N$CH_2(CH_2)_2CH_2$N), 18.7 (2×CH_2CH_3), 12.6 (2×CH_3). NMR (^{1}H, ^{13}C) data were in agreement with those reported (Mata et al., 2004).

3,3′-(Pentane-1,5-diyl)bis(1-butyl-1H-imidazolium) bromide (7). The preparation of **7** (99% yield, highly viscous colorless liquid) was performed according to the general procedure (Method B). ^{1}H NMR (D_2O) δ 8.84 (s, 2H, 2×H-2), 7.52 (bs, 4H, 2×H-4, 2×H-5), 4.25-4.18 (m, 8H, 4×CH_2N), 2.00-1.80 (m, 8H, 4×CH_2CH_2N), 1.38-1.23 (m, 6H, N$(CH_2)_2CH_2(CH_2)_2$N, 2×CH_2CH_3), 0.91 (t, 6H, J=7.3 Hz, 2×CH_3); ^{13}C NMR (D_2O) δ 134.9 (2×C-2), 122.3, 122.2 (2×C-4, 2×C-5), 49.3 (2×CH_2N), 49.1 (2×CH_2N), 31.2 (2×NCH_2CH_2), 28.6 (2×NCH_2CH_2), 22.1 (CH_2), 18.7 (2×CH_2CH_3), 12.6 (2×CH_3). ESI-MS: positive mode, [C_5(BIM)$_2$-H]$^+$ m/z 317.22 (25%), [C_5(BIM)$_2$/Br]$^+$ m/z 397.12 (100%) 397.15 (100%); negative mode, Br$^-$ m/z 79.05 (100%) and 81.06 (100%), ([C_5(BIM)$_2$]$_2$/5Br)$^-$ m/z 1035.13 (100% and all the other isotopic peaks), ([C_5(BIM)$_2$]$_3$/7Br)$^-$ m/z 1515.30 (100% and all the other isotopic peaks).

3,3′-(Hexane-1,6-diyl)bis(1-butyl-1H-imidazolium) bromide (8). The preparation of **8** (93% yield, hygroscopic white solid) was performed according to the general procedure (Method B). ^{1}H NMR (D_2O) δ 8.77 (s, 2H, 2×H-2), 7.47 (bs, 4H, 2×H-4, 2×H-5), 4.21-4.14 (m, 8H, 4×CH_2N), 1.89-1.77 (m, 8H, 4×CH_2CH_2N), 1.36-1.21 (m, 8H, 2×N$(CH_2)_2CH_2$, 2×CH_2CH_3), 0.89 (t, 6H, J=7.3 Hz, 2×CH_3); ^{13}C NMR (D_2O) δ 135.0 (2×C-2), 122.3, 122.1 (2×C-4, 2×C-5), 49.3 (4×CH_2N), 31.1 (2×NCH_2CH_2), 29.0 (2×NCH_2CH_2), 24.7 (CH_2CH_2), 18.6 (2×CH_2CH_3), 12.5 (2×CH_3). NMR (^{1}H) data were in agreement with those reported (Yang et al., 2014).

3,3′-(Propane-1,3-diyl)bis(1-hexyl-1H-imidazolium) bromide (9). The preparation of **9** (94% yield, white solid) was performed according to the general procedure (Method B). ^{1}H NMR (D_2O) δ 8.87 (s, 2H, 2×H-2), 7.50 (s, 4H, 2×H-4, 2×H-5), 4.31 (m, 4H, 2×CH_2N), 4.16 (m, 4H, 2×CH_2N), 2.52 (m, 2H, CH_2), 1.83 (m, 8H, 2×$C_3H_9CH_2CH_2$N), 1.25 [s, 12H, 2×Me$(CH_2)_3$], 0.80 (bt, 6H, 2×CH_3); ^{13}C NMR (D_2O) δ 135.2 (2×C-2), 122.6, 122.0 (2×C-4, 2 × C-5), 49.6, 46.2 (each 2×CH_2N), 30.1 (2×$C_3H_9CH_2CH_2$N), 29.6 (CH_2), 28.9, 24.8, 21.6 (2×Me$(CH_2)_3$),13.1(2×CH_3).

3,3′-(butane-1,4-diyl)bis(1-hexyl-1H-imidazolium) bromide (10). The preparation of **10** (98% yield, viscous colorless liquid) was performed according to the general procedure (Method B). ^{1}H NMR (D_2O) δ 8.79 (s, 2H, 2×H-2), 7.48 (m, 4H, 2×H-4, 2×H-5), 4.23-4.14 (m, 8H, 4×CH_2N), 1.85 (m, 8H, 4× NCH_2CH_2), 1.24 [s, 12H, 2×Me$(CH_2)_3$], 0.80 (bt, 6H, 2×CH_3); ^{13}C NMR (D_2O) δ 135.1 (2×C-2), 122.5, 122.0 (2×C-4, 2×C-5), 49.5, 48.6 (each 2×CH_2N), 30.1 (2×$C_3H_9CH_2CH_2$N), 28.9, 24.8, 21.6 (2×Me$(CH_2)_3$), 26.1 (CH_2CH_2), 13.0 (2×CH_3). ESI-MS: positive mode, [C_4(HIM)$_2$-H]$^+$ m/z 359.36 (20%), [C_4(HIM)$_2$/Br]$^+$ m/z 439.25 (100%) 441.29 (100%); negative mode, Br$^-$ m/z 79.05 (100%) and 81.06 (100%), ([C_4(HIM)$_2$]$_2$/5Br)$^-$ m/z 1119.33 (100% and all the

other isotopic peaks), ([C_5(BIM)$_2$]$_3$/7Br)$^-$ m/z 1641.30 (100% and all the other isotopic peaks).

3,3′-(pentane-1,5-diyl)bis(1-hexyl-1H-imidazolum) bromide (11). The preparation of **11** (96% yield, white solid) was performed according to the general procedure (Method B). ^{1}H NMR (D_2O) δ 8.82 (s, 2H, 2×H-2), 7.49 (s, 4H, 2×H-4, 2×H-5), 4.21-4.14 (m, 8H, 4×CH_2N), 1.90-1.80 (m, 8H, 4×NCH_2CH_2), 1.24 [s, 14H, 2×Me$(CH_2)_3$, CH_2], 0.80 (bt, 6H, 2×CH_3); ^{13}C NMR (D_2O) δ 135.0 (2×C-2), 122.3, 122.2 (2×C-4, 2×C-5), 49.4, 49.0 (each 2×CH_2N), 30.1, 29.0 (each 2×CH_2CH_2N), 28.5, 24.8, 21.6 (2×Me$(CH_2)_3$), 22.0 (CH_2), 13.0 (2×CH_3). ESI-MS: positive mode, [C_5(HIM)$_2$-H]$^+$ m/z 373.12 (20%), [C_5(HIM)$_2$/Br]$^+$ m/z 453.06 (100%) and 455.05 (100%); negative mode, Br$^-$ m/z 79 (100%) and 81.06 (100%), ([C_5(HIM)$_2$]$_2$/5Br)$^-$ m/z 1149.13 (100% and all the other isotopic peaks), ([C_5(HIM)$_2$]$_3$/7Br)$^-$ m/z 1682.90 (100% and all the other isotopic peaks).

3,3′-(Hexane-1,6-diyl)bis(1-hexyl-1H-imidazolium) bromide (12). The preparation of **12** (98% yield, viscous colorless liquid) was performed according to the general procedure (Method B). ^{1}H NMR (D_2O) δ 8.82 (s, 2H, 2×H-2), 7.50 (m, 4H, 2×H-4, 2×H-5), 4.19 (t, 8H, J=xx Hz, 2×CH_2N), 1.84 (m, 8H, 4×NCH_2CH_2), 1.30-1.24 [m, 16H, 2×Me$(CH_2)_3$, CH_2CH_2], 0.80 (bt, 6H, 2×CH_3);^{13}C NMR (D_2O) δ 134.9 (2×C-2), 122.2 (2×C-4, 2×C-5), 49.4, 46.2 (each 2×CH_2N), 30.1 (2×$C_3H_9CH_2CH_2$N), 28.9, 24.8, 21.6 (2×Me$(CH_2)_3$), 24.6 (CH_2,CH_2), 13.1 (2×CH_3). ESI-MS: positive mode, [C_6(HIM)$_2$-H]$^+$ m/z 387.32 (20%), [C_6(HIM)$_2$/Br]$^+$ m/z 467.22 (100%) 469.35 (100%); negative mode, Br$^-$ m/z 79.05 (100%) and 81.06 (100%), ([C_6(HIM)$_2$]$_2$/5Br)$^-$ m/z 1175.02 (100% and all the other isotopic peaks), ([C_6(HIM)$_2$]$_3$/7Br)$^-$ m/z 1723.30 (100% and all the other isotopic peaks).

General Procedure for the Synthesis of 3,3′-(alkane-1,n-diyl)bis(1-alkyl-1H-imidazolium) carboxylate (13-24)

Method A (with silver hydroxide)

To a NaOH aqueous solution (10% w/w), AgNO$_3$ (1 equiv) was added and the mixture was stirred at room temperature in the dark, for 10 min. The resulting brown mixture was filtered under vacuum over through a Teflon filter and left drying in the dark. Selected 3,3′-(alkane-1,n-diyl)bis(1-alkyl-1H-imidazol-3ium) bromide (1 equiv) was dissolved in water to form a 10% w/w solution. AgOH (1.1 equiv) was added to the bromide solution and the resulting suspension was left under stirring at room temperature in the dark. After 12 h, the mixture was filtered over Celite. To the filtrated solution, opportune carboxylic acid (1 equiv) was added and the mixture was stirred overnight. In case a precipitate was observed, the suspension was filtered over Celite. Evaporation of solvent under reduced pressure afforded hygroscopic white solids or highly viscous yellowish liquids.

Method B (with Ag$_2$CO$_3$)

To a stirred solution of the carboxylic acid (malonic acid, succinic acid or glutaric acid) in water (20 mL/g), commercial Ag$_2$CO$_3$ (1.02 equiv) was added slowly, in the dark. At the

end of the effervescence, opportune 3,3′-(alkane-1,n-diyl)bis(1-alkyl-1*H*-imidazolium) bromide (1.0 equiv) was added and the reaction mixture was stirring at room temperature in the dark overnight. The resulting yellowish suspension was filtered over Celite and the clear solution was concentrated under diminished pressure affording either hygroscopic white solids or highly viscous yellowish liquids.

Method C (with ion exchange resin)
A suspension of Amberlite IRA400 ion exchange resin in 500 mL of an aqueous NaOH solution (4% w/w) was stirred at room temperature for 2 days. The pretreated resin was packed into a 3.5 cm diameter column and washed with water until clear washing waters were obtained. Three hundred milliliters of NaOH solution (4% w/w) were passed through the column and recycled for three times. The same procedure was repeated with other 300, 200, and 200 mL of NaOH 4% w/w. The column was then washed with water until neutrality of washing waters.

Selected 3,3′-(alkane-1,n-diyl)bis(1-alkyl-1*H*-imidazolium) bromide (18.6 mmol) was dissolved in 7:3 (v/v) CH_3OH-water (100 mL) and the solution was passed through the column. The eluted was recovered and passed through the column until absence of halogens (this step was repeated five times). The hydroxyl-bromide substitution was followed by checking the presence of bromide in the eluted solution using pure silver nitrate (AgBr test). The column was then washed with 200 mL of CH_3OH/water solution and the eluted was combined with the previous 100 mL of opportune 3′-(alkane-1,n-diyl)bis(1-alkyl-1*H*-imidazolium) hydroxide solution. A solution of the proper carboxylic acid (18.6 mmol) in 7:3 (v/v) CH_3OH-water (250 mL) was added under stirring to the prepared 3,3′-(alkane-1,n-diyl)bis(1-alkyl-1*H*-imidazolium) hydroxide solution. After 1 h at room temperature, the solvent was evaporated under reduced pressure affording, after drying in vacuo, hygroscopic white solids or highly viscous yellowish liquids.

3,3′-(Propane-1,3-diyl)bis(1-methyl-1*H*-imidazolium) malonate (13). The preparation of **13** (95% yield, hygroscopic white solid) was performed according to the general procedure (Method C). ^1H NMR (D_2O) δ 8.76 (s, 2H, 2×H-2), 7.46, 7.42 (2s, each 2H, 2×H-4, 2×H-5), 4.27 (t, 4H, *J*=7.3 Hz, 2×CH_2N), 3.85 (s, 6H, 2×NCH_3), 2.47 (m, 4H, CH_2, CH_2CO); ^{13}C NMR (D_2O) δ 177.1 (2×C=O), 136.0 (2×C-2), 123.9, 122.1 (2×C-4, 2×C-5), 47.3 (2×CH_2N, CH_2CO), 35.8 (2×NCH_3), 29.7 (CH_2). ESI-MS: positive mode, [C_3(MIM)$_2$-H]$^+$ *m/z* 204.96 (70%), [C_3(MIM)$_2$/Mal + H]$^+$ *m/z* 309.10 (30%), ([C_3(MIM)$_2$/Mal]$_2$ + H)$^+$ *m/z* 617.10 (100%); negative mode, (Mal + H)$^-$ *m/z* 102.86 (70%), [C_3(MIM)$_2$]/3(Mal + H)$^-$ *m/z* 515.20 (70%), 2[C_3(MIM)$_2$]/[Mal+ 3(Mal + H)]$^-$ *m/z* 823.20 (30%), 3[C_3(MIM)$_2$]/[Mal+ 5(Mal + H)]$^-$ *m/z* 1235.40 (100%).

3,3′-(Butane-1,4-diyl)bis(1-methyl-1*H*-imidazolium) malonate (14). The preparation of **14** (94% yield, hygroscopic white solid) was performed according to the general procedure (Method C). ^1H NMR (D_2O) δ 8.69 (s, 2H, 2×H-2), 7.25, 7.10 (2bs, each 2H, 2×H-4, 2×H-5), 3.95 (bs, 4H, 2×CH_2N), 3.61 (s, 6H, 2×NCH_3), 2.81 (s, 2H, CH_2CO), 1.58 (m, 4H, CH_2CH_2); ^{13}C NMR (D_2O) δ 176.9 (2×C=O), 135.9 (2×C-2), 123.6, 121.9 (2×C-4, 2×C-5), 48.5 (2×CH_2N), 47.7

(CH_2CO), 35.6 (2×NCH_3), 26.0 (CH_2CH_2). ESI-MS: positive mode, [C_4(MIM)$_2$-H]$^+$ *m/z* 219.00 (70%), [C_4(MIM)$_2$/Mal + H]$^+$ *m/z* 323.04 (30%), ([C_4(MIM)$_2$/Mal]$_2$ + H)$^+$ *m/z* 645.20 (100%); negative mode, (Mal + H)$^-$ *m/z* 102.86 (100%), [C_4(MIM)$_2$]/3(Mal + H)$^-$ *m/z* 528.90 (70%), 2[C_4(MIM)$_2$]/[Mal+ 3(Mal + H)]$^-$ *m/z* 850.87 (40%), 3[C_4(MIM)$_2$]/[Mal+ 5(Mal + H)]$^-$ *m/z* 1277.10 (100%).

3,3′-(Pentane-1,5-diyl)bis(1-methyl-1*H*-imidazolium) malonate (15). The preparation of **15** (95% yield, hygroscopic white solid) was performed according to the general procedure (Method C). ^1H NMR (D_2O) δ 8.68 (s, 2H, 2×H-2), 7.41, 7.39 (2bs, each 2H, 2×H-4, 2×H-5), 4.15 (t, 4H, *J*=7.2 Hz, 2×CH_2N), 3.84 (s, 6H, 2×NCH_3), 3.06 (s, 2H, CH_2CO), 1.87 (qui, 4H, *J*=7.5 Hz, 2×NCH$_2CH_2$), 1.27 (m, 2H, CH_2). ^{13}C NMR (D_2O) δ 177.1 (2×C=O), 136.0 (2×C-2), 123.6, 122.2 (2×C-4, 2×C-5), 49.2 (2×CH_2N), 47.4 (CH_2CO), 35.7 (2×NCH_3), 28.7 (2×NCH$_2CH_2$), 22.2 (CH_2). ESI-MS: positive mode, [C_5(MIM)$_2$-H]$^+$ *m/z* 232.90 (100%), [C_5(MIM)$_2$/Mal + H]$^+$ *m/z* 336.82 (50%), ([C_5(MIM)$_2$/Mal]$_2$ + H)$^+$ *m/z* 672.91 (20%); negative mode, (Mal + H)$^-$ *m/z* 102.86 (100%), [C_5(MIM)$_2$]/3(Mal + H)$^-$ *m/z* 542.67 (70%), 2[C_5(MIM)$_2$]/[Mal+ 3(Mal + H)]$^-$ *m/z* 850.87 (40%), 3[C_5(MIM)$_2$]/[Mal+ 5(Mal + H)]$^-$ *m/z* 1318.69 (65%).

3,3′-(Hexane-1,6-diyl)bis(1-methyl-1*H*-imidazolium) malonate (16). The preparation of **16** (94% yield, hygroscopic white solid) was performed according to the general procedure (Method C). ^1H NMR (D_2O) δ 8.67 (s, 2H, 2×H-2), 7.41, 7.38 (2m, each 2H, 2×H-4, 2×H-5), 4.13 (t, 4H, *J*=7.1 Hz, 2×CH_2N), 3.83 (s, 6H, 2×NCH_3), 3.04 (s, 2H, CH_2CO), 1.81 (m, 4H, 2×NCH$_2CH_2$), 1.38 (m, 4H, CH_2CH_2); ^{13}C NMR (D_2O) δ 176.5 (2×C=O), 135.3 (2×C-2), 123.0, 122.6 (2×C-4, 2×C-5), 48.8 (2×CH_2N), 47.2 (2×CH_2CO), 35.0 (2×NCH_3), 28.5 (2 ×NCH$_2CH_2$), 24.3 (CH_2CH_2).). ESI-MS: positive mode, [C_6(MIM)$_2$-H]$^+$ *m/z* 246.99 (100%), [C_6(MIM)$_2$/Mal + H]$^+$ *m/z* 350.88 (20%); negative mode, (Mal + H)$^-$ *m/z* 102.96 (100%), [C_6(MIM)$_2$]/3(Mal + H)$^-$ *m/z* 557.01 (70%), 2[C_6(MIM)$_2$]/[Mal+ 3(Mal + H)]$^-$ *m/z* 907.21 (30%).

3,3′-(Propane-1,4-diyl)bis(1-methyl-1*H*-imidazolium) succinate (17). The preparation of **17** (97% yield, hygroscopic white solid) was performed according to the general procedure (Method C). ^1H NMR (D_2O) δ 8.75 (s, 2H, 2×H-2), 7.46, 7.41 (2s, each 2H, 2×H-4, 2×H-5), 4.25 (t, 4H, *J*=7.2 Hz, 2×CH_2N), 3.83 (s, 6H, 2×NCH_3), 2.45 (m, 2H, CH_2), 2.26 (m, 4H, CH_2, 2×CH_2CO); ^{13}C NMR (D_2O) δ 181.2 (2×C=O), 136.2 (2×C-2), 124.0, 122.1 (2×C-4, 2×C-5), 46.3 (2×CH_2N), 35.8 (2×NCH_3), 34.2 (2×CH_2CO), 29.7 (CH_2). ESI-MS: positive mode, [C_3(MIM)$_2$-H]$^+$ *m/z* 205.15 (70%), [C_3(MIM)$_2$/Succ + H]$^+$ *m/z* 323.30 (100%), ([C_3(MIM)$_2$/Succ]$_2$ + H)$^+$ *m/z* 645.34 (70%); negative mode, (Succ + H)$^-$ *m/z* 117.00 (70%), [C_3(MIM)$_2$]/3(Succ + H)$^-$ *m/z* 557.10 (100%), 2[C_3(MIM)$_2$]/[Succ + 3(Succ + H)]$^-$ *m/z* 879.45 (80%).

3,3′-(Butane-1,4-diyl)bis(1-methyl-1*H*-imidazolium) succinate (18). The preparation of **18** (98% yield, hygroscopic white solid) was performed according to the general procedure (Method C). ^1H NMR (D_2O) δ 8.45 (s, 2H, 2×H-2), 7.18, 7.16 (2bs, each 2H, 2×H-4, 2×H-5), 3.96 (bs, 4H, 2×CH_2N),

3.60 (s, 6H, 2×NCH_3), 2.10 (s, 4H, 2×CH_2CO), 1.61 (m, 4H, CH_2CH_2); ^{13}C NMR (D$_2$O) δ 181.7 (2×C=O), 135.9 (2×C-2), 123.6, 121.9 (2×C-4, 2×C-5), 48.6 (2×CH$_2$N), 35.6 (2×NCH$_3$), 33.8 (2×CH$_2$CO), 26.0 (CH$_2$CH$_2$). ESI-MS: positive mode, [C$_4$(MIM)$_2$-H]$^+$ m/z 218.80 (55%), [C$_4$(MIM)$_2$/Succ + H]$^+$ m/z 336.79 (100%), ([C$_4$(MIM)$_2$/Succ]$_2$ + H)$^+$ m/z 672.89, (70%); negative mode, (Succ + H)$^-$ m/z 117.00 (78%), [C$_4$(MIM)$_2$]/3(Succ + H)$^-$ m/z 571.12 (40%), 2[C$_4$(MIM)$_2$]/[Succ + 3(Succ + H)]$^-$ m/z 907.02 (100%).

3,3′-(Pentane-1,5-diyl)bis(1-methyl-1H-imidazolium) succinate (19). The preparation of **19** (97% yield, hygroscopic white solid) was performed according to the general procedure (Method C). ^{1}H NMR (D$_2$O) δ 8.54 (s, 2H, 2×H-2), 7.28, 7.25 (2bs, each 2H, 2×H-4, 2×H-5), 4.00 (t, 4H, J=7.2 Hz, 2×CH_2N), 3.70 (s, 6H, 2×NCH_3), 2.19 (s, 4H, 2×CH_2CO), 1.73 (qui, 4H, J=7.5 Hz, 2×NCH$_2$CH_2), 1.23 (m, 2H, CH_2). ^{13}C NMR (D$_2$O) δ 181.8 (2×C=O), 135.9 (2×C-2), 123.6, 122.1 (2×C-4, 2×C-5), 49.2 (2×CH$_2$N), 35.7 (2×NCH$_3$), 34.0 (2×CH$_2$CO), 28.7 (2×NCH$_2$CH$_2$), 22.2 (CH$_2$). ESI-MS: positive mode, [C$_5$(MIM)$_2$-H]$^+$ m/z 233.15 (65%), [C$_5$(MIM)$_2$/Succ + H]$^+$ m/z 351.17 (100%), ([C$_5$(MIM)$_2$/Succ]$_2$ + H)$^+$ m/z 701.56 (70%); negative mode, (Succ + H)$^-$ m/z 117.00 (70%), [C$_5$(MIM)$_2$]/3(Succ + H)$^-$ m/z 585.32 (100%), 2[C$_5$(MIM)$_2$]/[Succ + 3(Succ + H)]$^-$ m/z 935.40 (80%).

3,3′-(Hexane-1,6-diyl)bis(1-methyl-1H-imidazolium) succinate (20). The preparation of **20** (hygroscopic white solid) was performed according to the general procedure (Method A: 61% yield; Method B: 98% yield; Method C: 92% yield). ^{1}H NMR (D$_2$O) δ 8.66 (s, 2H, 2×H-2), 7.49, 7.37 (2m, each 2H, 2×H-4, 2×H-5), 4.13 (t, 4H, J=7.0 Hz, 2×CH_2N), 3.83 (s, 6H, 2×NCH_3), 2.24 (s, 4H, 2×CH_2CO), 1.82 (m, 4H, 2×NCH$_2$CH_2), 1.28 (m, 4H, CH_2CH_2); ^{13}C NMR (D$_2$O) δ 181.4 (2×C=O), 135.3 (2×C-2), 123.0, 121.6 (2×C-4, 2×C-5), 48.8 (2×CH$_2$N), 35.1 (2×NCH$_3$), 33.6 (2×CH$_2$CO), 28.5 (2×NCH$_2$CH$_2$), 24.3 (CH$_2$CH$_2$). ESI-MS: positive mode, [C$_6$(MIM)$_2$-H]$^+$ m/z 247.30 (65%), [C$_6$(MIM)$_2$/Succ + H]$^+$ m/z 365.35 (100%), ([C$_6$(MIM)$_2$/Succ]$_2$ + H)$^+$ m/z 729.50 (70%); negative mode, (Succ + H)$^-$ m/z 117.00 (70%), [C$_6$(MIM)$_2$]/3(Succ + H)$^-$ m/z 599.38 (100%), 2[C$_6$(MIM)$_2$]/[Succ + 3(Succ + H)]$^-$ m/z 963.50 (70%).

3,3′-(Propane-1,3-diyl)bis(1-methyl-1H-imidazolium) glutarate (21). The preparation of **21** (99% yield, hygroscopic white solid) was performed according to the general procedure (Method C). ^{1}H NMR (D$_2$O) δ 8.75 (s, 2H, 2×H-2), 7.47, 7.44 (2s, each 2H, 2×H-4, 2×H-5), 4.28 (t, 4H, J=7.3 Hz, 2×CH_2N), 3.86 (s, 6H, 2×NCH_3), 2.48 (qui, 2H, J=7.2 Hz, CH_2), 2.16 (t, 4H, J=7.5 Hz, 2×CH_2CO), 1.74 (bq, 2H, J=7.6 Hz, CH_2CH$_2$CO); ^{13}C NMR (D$_2$O) δ 183.2 (2×C=O), 136.2 (2×C-2), 124.0, 122.1 (2×C-4, 2×C-5), 46.1 (2×CH$_2$N), 37.3 (2×CH$_2$CO), 35.8 (2×NCH$_3$), 29.8 (CH$_2$), 23.0 (CH$_2$CH$_2$CO). ESI-MS: positive mode, [C$_3$(MIM)$_2$-H]$^+$ m/z 204.82 (40%), ([C$_3$(MIM)$_2$/Glut]$_2$ + H)$^+$ m/z 673.02 (100%); negative mode, (Glut + H)$^-$ m/z 131.02 (100%), [C$_3$(MIM)$_2$]/3(Glut + H)$^-$ m/z 599.17 (70%), 2[C$_3$(MIM)$_2$]/[Glut+ 3(Glut + H)]$^-$ m/z 935.19 (70%).

3,3′-(Butane-1,4-diyl)bis(1-methyl-1H-imidazolium) glutarate (22). The preparation of **22** (98% yield, hygroscopic white solid) was performed according to the general procedure

(Method C). ^{1}H NMR (D$_2$O) δ 8.69 (s, 2H, 2×H-2), 7.41, 7.39 (2bs, each 2H, 2×H-4, 2×H-5), 4.19 (bs, 4H, 2×CH_2N), 3.83 (s, 6H, 2×NCH_3), 2.09 (t, 4H, J=7.4 Hz, 2×CH_2CO), 1.84 (m, 4H, CH_2CH_2), 1.72 (s, 2H, CH_2CH$_2$CO); ^{13}C NMR (D$_2$O) δ 182.3 (2×C=O), 135.4 (2×C-2), 123.2, 121.5 (2×C-4, 2×C-5), 48.1 (2×CH$_2$N), 36.8 (2×CH$_2$CO), 35.6 (2×NCH$_3$), 25.6 (CH$_2$CH$_2$), 22.5 (CH$_2$CH$_2$CO). ESI-MS: positive mode, [C$_4$(MIM)$_2$-H]$^+$ m/z 218.95 (40%), ([C$_4$(MIM)$_2$/Glut]$_2$ + H)$^+$ m/z 701.05 (100%); negative mode, (Glut + H)$^-$ m/z 131.00 (100%), [C$_4$(MIM)$_2$]/3(Glut + H)$^-$ m/z 613.15 (70%), 2[C$_4$(MIM)$_2$]/[Glut+ 3(Glut + H)]$^-$ m/z 963.50 (60%).

3,3′-(Pentane-1,5-diyl)bis(1-methyl-1H-imidazolium) glutarate (23). The preparation of **23** (97% yield, hygroscopic white solid) was performed according to the general procedure (Method C). ^{1}H NMR (D$_2$O) δ 8.67 (s, 2H, 2×H-2), 7.41, 7.38 (2bs, each 2H, 2×H-4, 2×H-5), 4.14 (t, 4H, J=7.2 Hz, 2×CH_2N), 3.83 (s, 6H, 2×NCH_3), 2.11 (t, 4H, J=7.4 Hz, 2×CH_2CO), 1.86 (m, 4H, 2×NCH$_2$CH_2), 1.70 (m, 2H, CH_2CH$_2$CO), 1.23 (m, 2H, CH_2); ^{13}C NMR (D$_2$O) δ 182.8 (2×C=O), 135.9 (2×C-2), 123.6, 122.2 (2×C-4, 2×C-5), 49.2 (2×CH$_2$N), 37.3 (2×CH$_2$CO), 35.7 (2×NCH$_3$), 28.8 (2×NCH$_2$CH$_2$), 23.0 (CH$_2$CH$_2$CO), 22.2 (CH$_2$). ESI-MS: positive mode, [C$_5$(MIM)$_2$-H]$^+$ m/z 233.10 (40%), ([C$_5$(MIM)$_2$/Glut]$_2$ + H)$^+$ m/z 729.01 (100%); negative mode, (Glut + H)$^-$ m/z 131.00 (100%), [C$_5$(MIM)$_2$]/3(Glut + H)$^-$ m/z 626.99 (70%), 2[C$_5$(MIM)$_2$]/[Glut+ 3(Glut + H)]$^-$ m/z 990.98 (50%).

3,3′-(Hexane-1,6-diyl)bis(1-methyl-1H-imidazolium) glutarate (24). The preparation of **24** (98% yield, hygroscopic white solid) was performed according to the general procedure (Method C). ^{1}H NMR (D$_2$O) δ 8.66 (s, 2H, 2×H-2), 7.41, 7.38 (2m, each 2H, 2×H-4, 2×H-5), 4.12 (t, 4H, J=7.1 Hz, 2×CH_2N), 3.83 (s, 6H, 2×NCH_3), 2.12 (t, 4H, J=7.4 Hz, 2×CH_2CO), 1.83-1.67 (m, 6H, 2×NCH$_2$CH_2, CH_2CH$_2$CO), 1.29 (m, 4H, CH_2CH_2); ^{13}C NMR (D$_2$O) δ 182.1 (2×C=O), 135.3 (2×C-2), 123.0, 121.6 (2×C-4, 2×C-5), 48.8 (2×CH$_2$N), 36.7 (2×CH$_2$CO), 35.1 (2×NCH$_3$), 28.5 (2×NCH$_2$CH$_2$), 24.3 (CH$_2$CH$_2$), 22.4 (CH$_2$CH$_2$CO).

3,3′-(Butane-1,4-diyl)bis(1-butyl-1H-imidazolium) succinate (25). The preparation of **25** (99% yield, hygroscopic white solid) was performed according to the general procedure (Method C). ^{1}H NMR (D$_2$O) δ 8.77 (s, 2H, 2×H-2), 7.46, 7.44 (2s, each 2H, 2×H-4, 2×H-5), 4.19-4.11 (m, 8H, 4×CH_2N), 2.34 (s, 4H, 2×CH_2CO), 1.85-1.76 (m, 8H, 4×CH_2CH$_2$N), 1.25 (sext, 4H, J=7.6 Hz, 2×CH_2CH$_3$), 0.85 (t, 6H, J=7.3 Hz, 2×CH_3); ^{13}C NMR (D$_2$O) δ 181.8 (2×C=O), 135.1 (2×C-2), 122.5, 122.0 (2×C-4, 2×C-5), 49.2, 48.6 (each 2×CH$_2$N), 33.9 (2×CH$_2$CO), 31.1 (2×NCH$_2$CH$_2$C$_2$H$_5$), 26.1 (NCH$_2$CH$_2$CH$_2$N), 18.6 (2×CH$_2$CH$_3$), 12.5 (2×CH$_3$). ESI-MS: positive mode, [C$_4$(BIM)$_2$-H]$^+$ m/z 303.20 (70%), [C$_4$(BIM)$_2$/Succ + H]$^+$ m/z 421.30 (100%), ([C$_4$(BIM)$_2$/Succ]$_2$ + H)$^+$ m/z 841.55 (70%); negative mode, (Succ + H)$^-$ m/z 117.00 (80%), [C$_4$(BIM)$_2$]/3(Succ + H)$^-$ m/z 655.27 (100%), 2[C$_4$(HIM)$_2$]/[Succ + 3(Succ + H)]$^-$ m/z 1075.40 (85%).

3,3′-(Butane-1,4-diyl)bis(1-hexyl-1H-imidazolium) succinate (26). The preparation of **26** (99% yield, hygroscopic white solid) was performed according to the general procedure

(Method C). ^{1}H NMR (250 MHz, D$_2$O) δ ^{1}H NMR (D$_2$O) δ 8.76 (s, 2H, 2×H-2), 7.48 (m, 4H, 2×H-4, 2×H-5), 4.20-4.10 (m, 8H, 4×CH_2N), 2.33 (s, 4H, 2×CH_2CO), 1.83 (m, 8H, 4× NCH$_2$CH_2), 1.21 [s, 12H, 2×Me(CH_2)$_3$], 0.77 (bt, 6H, 2×CH_3); ^{13}C NMR (D$_2$O) δ 181.9 (2×C=O), 135.2 (2×C-2), 122.6, 122.1 (2×C-4, 2×C-5), 49.6, 48.6 (each 2×CH$_2$N), 34.0 (2×CH$_2$CO), 30.1 (2×C$_3$H$_9$CH$_2$CH$_2$N), 29.0, 24.9, 21.7 (2×Me(CH$_2$)$_3$), 26.2 (CH$_2$CH$_2$), 13.1 (2×CH$_3$). ESI-MS: positive mode, [C$_4$(HIM)$_2$-H]$^+$ m/z 359.03 (90%), [C$_4$(HIM)$_2$/Succ + H]$^+$ m/z 476.89 (100%), ([C$_4$(HIM)$_2$/Succ]$_2$ + H)$^+$ m/z 953.10 (80%); negative mode, (Succ + H)$^-$ m/z 117.00 (70%), [C$_4$(HIM)$_2$]/3(Succ + H)$^-$ m/z 711.33 (100%), 2[C$_4$(HIM)$_2$]/[Succ + 3(Succ + H)]$^-$ m/z 1187.16 (80%).

General Procedure for the Synthesis of 3-butyl-1-methyl-1H-imidazolium carboxylate (27-29). To a commercial methanolic solution of 3-butyl-1-methyl-1H-imidazolium methylcarbonate (Proionic, 34% w/w), the opportune carboxylic acid (1 equiv) was added. The resulting mixture was stirred at room temperature for 1 h and the solvent was evaporated under reduced pressure to afford a yellow oil in quantitative yield.

3-Butyl-1-methyl-1H-imidazolium malonate (27). The preparation of **27** (99% yield, viscous yellow oil) was performed according to the general procedure. ^{1}H NMR (D$_2$O) δ 8.57 (s, 2H, 2×H-2), 7.31, 7.27 (2s, each 2H, 2×H-4, 2×H-5), 4.03 (t, 4H, J=7.7 Hz, 2×CH_2N), 3.73 (s, 6H, 2×NCH_3), 2.94 (bs, 2H, CH_2CO), 1.71-1.65 (m, 4H, 2×CH_2CH$_2$N), 1.19-1.10 (m, 4H, 2×CH_2CH$_3$), 0.75 (t, 6H, J=7.2 Hz, 2×CH_3); ^{13}C NMR (D$_2$O) δ 177.0 (2×C=O), 135.9 (2×C-2), 123.5, 122.2 (2×C-4, 2×C-5), 49.3 (2×CH$_2$N), 47.5 (CH$_2$CO), 35.6 (2× NCH$_3$), 31.3 (2×NCH$_2$CH$_2$), 18.8 (2×CH$_2$CH$_3$), 12.7 (2×CH$_3$). ESI-MS: positive mode, [BMIM]$^+$ m/z 139.04 (100%); negative mode, (Mal + H)$^-$ m/z 102.86 (20%), [BMIM/2(Mal + H)]$^-$ m/z 344.77 (100%).

3-Butyl-1-methyl-1H-imidazolium succinate (28). The preparation of **28** (99% yield, viscous yellow oil) was performed according to the general procedure. ^{1}H NMR (D$_2$O) δ 8.68 (s, 2H, 2×H-2), 7.42, 7.37 (2s, each 2H, 2×H-4, 2×H-5), 4.11 (bt, 4H, 2×CH_2N), 3.83 (s, 6H, 2×NCH_3), 2.29 (bs, 4H, 2×CH_2CO), 1.83-1.71 (m, 4H, 2×CH_2CH$_2$N), 1.28-1.19 (m, 4H, 2×CH_2CH$_3$), 0.85 (bt, 6H, 2×CH_3); ^{13}C NMR (D$_2$O) δ 181.7 (2×C=O), 135.7 (2×C-2), 123.3, 122.0 (2×C-4, 2×C-5), 49.1 (2×CH$_2$N), 35.5(2×NCH$_3$), 34.2 (2×CH$_2$CO), 31.1 (2×NCH$_2$CH$_2$), 18.6 (2×CH$_2$CH$_3$), 12.5 (2×CH$_3$). ESI-MS: positive mode, [BMIM]$^+$ m/z 139.04 (100%); negative mode, (Succ + H)$^-$ m/z 117.00 (50%), [BMIM/2(Succ + H)]$^-$ m/z 373.00 (100%).

3-Butyl-1-methyl-1H-imidazolium glutarate (29). The preparation of **29** (99% yield, viscous yellow oil) was performed according to the general procedure. ^{1}H NMR (D$_2$O) δ 8.65 (s, 2H, 2×H-2), 7.40, 7.35 (2s, each 2H, 2×H-4, 2×H-5), 4.11 (t, 4H, J=7.0 Hz, 2×CH_2N), 3.81 (s, 6H, 2×NCH_3), 2.08 (t, 4H, J=7.5 Hz, 2×CH_2CO), 1.81-1.62 (m, 6H, 2×NCH$_2$CH_2, CH_2CH$_2$CO), 1.30-1.15 (m, 4H, 2×CH_2CH$_3$), 0.83 (t, 6H, J=7.3 Hz, 2×CH_3); ^{13}C NMR (D$_2$O) δ 182.7 (2×C=O), 135.6 (2×C-2), 123.2, 122.0 (2×C-4, 2×C-5), 49.1 (2×CH$_2$N), 37.2

(2×CH$_2$CO), 35.5 (2×NCH$_3$), 31.0 (2×NCH$_2$CH$_2$), 22.8 (CH$_2$CH$_2$CO), 18.5 (2×CH$_2$CH$_3$), 12.4 (2×CH$_3$). ESI-MS: positive mode, [BMIM]$^+$ m/z 139.02 (100%); negative mode, (Glut + H)$^-$ m/z 131.00 (50%), [BMIM/2(Glut + H)]$^-$ m/z 400.98 (100%).

3,3′-(Hexane-1,6-diyl)bis(1-methyl-1H-imidazolium) bromide (4) diethylenglycol mixture 1:6. Derivative **4** (1 equiv) and diethylenglycol (6 equiv), previously dried at rotary evaporator at 80°C for 2 h, were mixed and stirred at 80°C under argon for 1 h. ^{1}H NMR (neat at 23°C) δ 8.63 (s, 2H, 2×H-2), 7.27, 7.18 (2bs, each 2H, 2×H-4, 2×H-5), 4.11 (bs, 12H, 12×OH), 3.71 (bs, 4H, 2×CH_2N), 3.40 (s, 6H, 2×NCH_3), 2.97 (bs, 24H, 12×CH_2O), 2.92 (bs, 24H, 12×CH_2OH), 1.29 (bs, 4H, 2×NCH$_2$CH_2), 0.76 (bs, 4H, CH_2CH$_2$); ^{13}C NMR (neat at 23°C) δ 135.7 (2×C-2), 122.8, 121.5 (2×C-4, 2×C-5), 71.3 (12×CH$_2$O), 59.8 (12×CH$_2$OH), 48.2 (2×CH$_2$N), 35.3 (2×NCH$_3$), 28.6 (2×NCH$_2$CH$_2$), 24.2 (CH$_2$CH$_2$).

3,3′-(Hexane-1,6-diyl)bis(1-methyl-1H-imidazolium) succinate (20) diethylenglycol mixture 1:2. Derivative **20** (1 equiv) and diethylenglycol (2 equiv), previously dried at rotary evaporator at 80°C for 2 h, were mixed and stirred at 80°C under argon for 1 h. ^{1}H NMR (neat at 63°C) δ 9.21 (s, 2H, 2×H-2), 7.41, 7.30 (2bs, each 2H, 2×H-4, 2×H-5), 6.04 (bs, 4H, 4×OH), 3.80 (bs, 4H, 2×CH_2N), 3.80 (s, 6H, 2×NCH_3), 2.89 (bs, 8H, 4×CH_2O), 2.80 (bs, 8H, 4×CH_2OH), 1.69 (s, 4H, 2×CH_2CO), 1.21 (bs, 4H, 2×NCH$_2$CH_2), 0.68 (bs, 4H, CH_2CH$_2$); ^{13}C NMR (neat at 63°C) δ 177.4 (2×C=O), 136.5 (2×C-2), 122.7, 121.5 (2×C-4, 2×C-5), 71.3 (4×CH$_2$O), 59.3 (4×CH$_2$OH), 47.7 (2×CH$_2$N), 34.5 (2×CH$_2$CO, 2×NCH$_3$), 28.3 (2×NCH$_2$CH$_2$), 23.8 (CH$_2$CH$_2$).

3,3′-(Hexane-1,6-diyl)bis(1-methyl-1H-imidazolium) bromide (4) glycerol mixture 1:3. Derivative **4** (1 equiv) and glycerol (3 equiv), previously dried at rotary evaporator at 80°C for 2 h, were mixed and stirred at 80°C under argon for 1 h. ^{1}H NMR (neat at 23°C) δ 8.34 (s, 2H, 2×H-2), 6.98, 6.90 (2bs, each 2H, 2×H-4, 2×H-5), 3.75-3.60 (m, 9H, 9×OH), 3.41 (bt, 4H, 2×CH_2N), 3.13 (s, 6H, 2×NCH_3), 2.79 (bs, 3H, 12×CHOH), 2.62 (bs, 12H, 6×CH_2OH), 0.98 (bs, 4H, 2×NCH$_2$CH_2), 0.44 (bs, 4H, CH_2CH$_2$); ^{13}C NMR (neat at 23°C) δ 135.4 (2×C-2), 122.5, 121.2 (2×C-4, 2×C-5), 71.4 (3×CHO), 61.9 (6×CH$_2$OH), 48.1 (2×CH$_2$N), 35.4 (2×NCH$_3$), 28.3 (2×NCH$_2$CH$_2$), 23.9 (CH$_2$CH$_2$).

3,3′-(Hexane-1,6-diyl)bis(1-methyl-1H-imidazolium) succinate (20) glycerol mixture 1:2. Derivative **20** (1 equiv) and glycerol (2 equiv), previously dried at rotary evaporator at 80°C for 2 h, were mixed and stirred at 80°C under argon for 1 h. ^{1}H NMR (neat at 63°C) δ 8.75 (s, 2H, 2×H-2), 7.14, 7.05 (2bs, each 2H, 2×H-4, 2×H-5), 5.25 (bs, 6H, 6×OH), 3.53 (bs, 4H, 2×CH_2N), 3.24 (s, 6H, 2×NCH_3), 2.84-2.60 (m, 10H, 2×CHO, 4×CH_2OH), 1.58 (s, 4H, 2×CH_2CO), 1.11 (bs, 4H, 2×NCH$_2$CH_2), 0.59 (bs, 4H, CH_2CH$_2$); ^{13}C NMR (neat at 63°C) δ 177.8 (2×C=O), 135.9 (2×C-2), 122.6, 121.3 (2×C-4, 2×C-5), 71.3 (2×CHOH), 62.2 (4×CH$_2$OH), 47.8 (2×CH$_2$N), 34.5 (2×NCH$_3$), 33.8 (2×CH$_2$CO), 28.1 (2×NCH$_2$CH$_2$), 23.8 (CH$_2$CH$_2$).

RESULTS AND DISCUSSION

Synthesis and Characterization of the Investigated DILs

Initially, a series of imidazolium bromide based DILs, four of which have never been reported before (**7, 10-12**), varying both in the alkyl linker length (from C3 to C6) and in the length of the substituent on the imidazolium ring (1-methyl-, 1-butyl and 1-hexyl), were synthesized (**Figure 1**).

The generally used Menshutkin reaction between the selected 1-alkylimidazole and the proper 1,*n*-dibromoalkane was carried out in toluene in the first experiments, following previously reported procedures (Kishore and Das, 2012). However, toluene was subsequently substituted with 4-methyl-2-pentanone (MIBK), following a protocol already tested in the case of monocationic ILs (Chiappe et al., 2016), without observing any drop of yield. MIBK has lower aquatic and air impacts than toluene according to the GSK's Solvent Sustainability Guide (Alder et al., 2016).

The four 1-methylimidazolium bromides DILs **1-4**, differing for the linker length, were transformed into the corresponding dicarboxylate salts (**Figure 2**), namely malonate, succinate, and glutarate whereas salts **6** and **10** were converted into the corresponding succinates DILs (**25** and **26**). 1-Methyl-3-butylimidazolium methyl carbonate was also used as starting material to prepare the corresponding malonate, succinate and glutarate salts (**27-29**) following known procedures (Mezzetta et al., 2017b). With the exception of **24** (Bortolini et al., 2014), all the prepared dicarboxylate salts have not yet been reported in the Literature.

To ascertain the most convenient approach for the preparation of the target dicarboxylates in high yield and degree of purity, three different largely used synthetic procedures (**Figure 3**) were tested employing **4** as the substrate for the synthesis of **20**.

In particular, as schematically shown in **Figure 3** path A, AgOH was employed for the bromide-hydroxide anion exchange.

Subsequently, after removal of AgBr by filtration, the target product was obtained by addition of a stoichiometric amount of succinic acid to the resulting clear water solution. Unfortunately, poor results in terms of recovered material and purity were reached through this approach, probably due to the formation in the relatively strong basic medium of silver imidazole carbene complexes.

Since this approach is normally used successfully to prepare water soluble ILs starting from bromide or chloride based ILs, the chelating properties of the bis-imidazole systems toward silver could probably explain the different behavior of mono and dicationic ILs in this reaction. The carbene species formed from dicationic DILs can find a stabilization despite the aqueous medium in the formation of the chelated silver complex. Thus, to avoid imidazolium ring deprotonation the less basic silver carbonate was employed instead of silver hydroxide (path B). After the formation of the dicarboxylate silver salt by reacting silver carbonate with a stochiometric amount of succinic acid, the metathesis reaction was performed by adding the bromide DIL, and the desired product was obtained in practically quantitative yield.

Finally, an ion exchange resin-based procedure was tried (path C). The resin, in its hydroxy form, was used to perform the complete bromide-hydroxy substitution and the desired product, after succinic acid addition, was obtained also in this case in quantitative yield.

This latter procedure was applied to obtain the dicarboxylate based DILs **13-26**. At least for an application at lab scale, the relatively high cost of the silver carbonate makes the more time requiring exchange resin-based procedure competitive.

Thermal Analysis

The short-term stability of all synthesized DILs was determined by using dynamic TGA. Thus, DILs were exposed to a continuous linear increase of temperature and the mass loss was monitored. Furthermore, before the analysis all samples, although previously accurately dried, were subjected to a further drying cycle

FIGURE 1 | Structures of the synthetized dibromide DILs.

R = CH$_3$	n = 1,	**1**	R = C$_4$H$_9$	n = 1,	**5**	R = C$_6$H$_{13}$	n = 1,	**9**
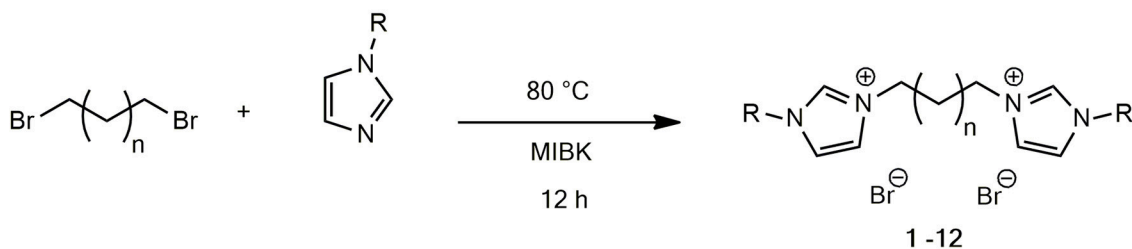
R = CH$_3$ n = 1,   **1**
R = CH$_3$ n = 2,   **2**
R = CH$_3$ n = 3,   **3**
R = CH$_3$ n = 4,   **4**

R = C$_4$H$_9$ n = 1,   **5**
R = C$_4$H$_9$ n = 2,   **6**
R = C$_4$H$_9$ n = 3,   **7**
R = C$_4$H$_9$ n = 4,   **8**

R = C$_6$H$_{13}$ n = 1,   **9**
R = C$_6$H$_{13}$ n = 2,   **10**
R = C$_6$H$_{13}$ n = 3,   **11**
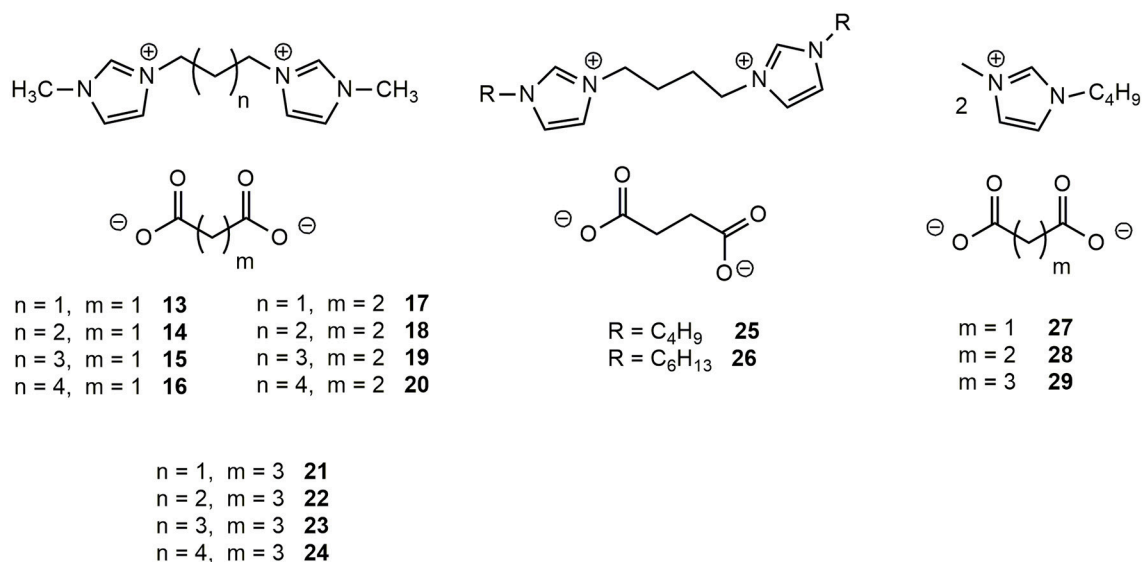R = C$_6$H$_{13}$ n = 4,   **12**

FIGURE 2 | Structures of the synthetized dicarboxylated dicationic and monocationic ILs.
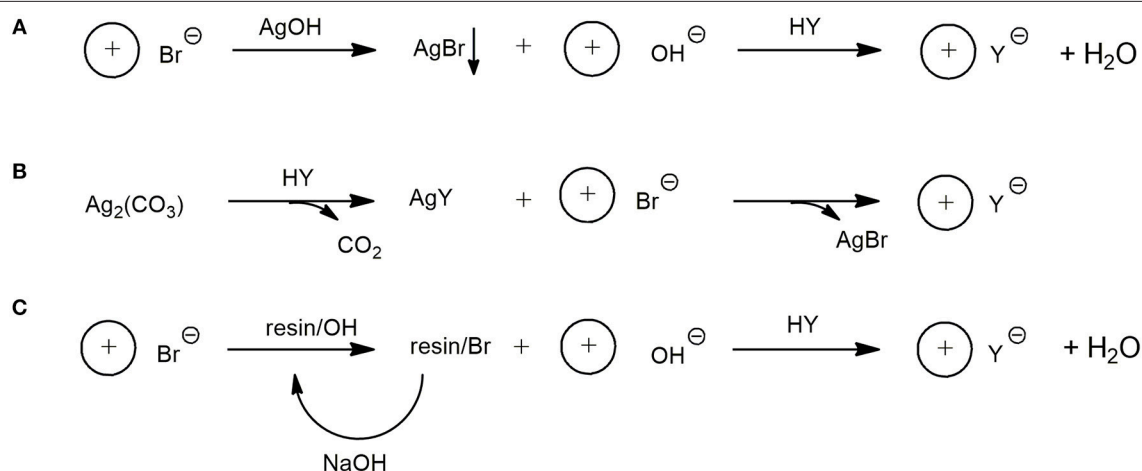

FIGURE 3 | Synthetic procedures for the preparation of dicarboxylate DILs using: AgOH **(A)**; Ag$_2$CO$_3$ **(B)**; Ion Exchange Resin **(C)**.

consisting in an isothermal run at 50°C for 30 min. Dynamic TGA curves were registered also for DILs previously investigated to avoid any effect related to the experimental conditions. From the thermographs, three characteristic temperatures of the short-term thermal stability were evaluated for each investigated DIL, T$_{start}$, T$_{onset}$, and T$_{peak}$ (**Table 1**). It should be noted that when the decomposition process occurs in more steps and the corresponding DTG curves are therefore characterized by two or more peaks, only the decomposition temperature corresponding to the highest peak was considered. **Figure 4** shows the dynamic curves for two typical DILs, while all the others are reported as **Supplementary Information**. For a more effective comparison, **Figure 5** shows the T$_{onset}$ of all investigated DILs.

All bromide based DILs display a similar thermal stability, with the onset degradation temperature ranging between 275°C, **6** [C$_4$(MIM)$_2$/2Br], and 298°C, **4** [C$_6$(MIM)$_2$/2Br]. Thus, in agreement with the Cao and Mu (Cao and Mu, 2014) classification, identifying five different classes of ionic liquids on the basis of their T$_{onest}$, these DILs can be defined as "less stable." The five classes are indeed the following: least stable (200°C<T$_{onest}$<250°C), less stable (250°C< T$_{onest}$<300°C), moderate (300°C<T$_{onest}$<350°C), more stable (350°C<T$_{onest}$<400°C), most stable (400°C<T$_{onest}$<450°C). Furthermore, based on the T$_{start}$, T$_{peak}$, and T$_{onest}$ values, the thermal stability of the investigated DILs having bromide as counteranion results affected (moderately) by the length of the lateral alkyl chain: DILs based on the 1-methylimidazolium

TABLE 1 | T_{start}, T_{onset}, and T_{peak} of the investigated ionic liquids (DILs and ILs) measured under a nitrogen atmosphere and with a heating rate of 10°C/min.

		T_{start} (°C)	T_{onset} (°C)	T_{peak} (°C)	Lit.
1	$C_3(MIM)_2/2Br$	271	288	308	$T_{start} = 283°C$[a]
					290°C[b]
					$T_{onset} = 311°C$[a]
2	$C_4(MIM)_2/2Br$	285	297	332	$T_{start} = 318°C$[c]
					281°C[a]
					250°C[d]
					$T_{onset} = 301°C$[a]
3	$C_5(MIM)_2/2Br$	272	282	303	
4	$C_6(MIM)_2/2Br$	287	298	326	
5	$C_3(BIM)_2/2Br$	251	280	315	$T_{start} = 250°C$[b]
6	$C_4(BIM)_2/2Br$	260	275	304	
7	$C_5(BIM)_2/2Br$	263	280	310	
8	$C_6(BIM)_2/2Br$	264	279	307	$T_{onset} = 297°C$[e]
9	$C_3(HIM)_2/2Br$	265	280	309	$T_{start} = 242°C$[f]
10	$C_4(HIM)_2/2Br$	260	277	308	
11	$C_5(HIM)_2/2Br$	259	284	314	
12	$C_6(HIM)_2/2Br$	260	279	309	
13	$C_3(MIM)_2/Mal$	190	229	245	
14	$C_4(MIM)_2/Mal$	144	227	253	
15	$C_5(MIM)_2/Mal$	175	232	255	
16	$C_6(MIM)_2/Mal$	201	225	256	
17	$C_3(MIM)_2/Succ$	166	235	261	
18	$C_4(MIM)_2/Succ$	156	242	262	
25	$C_4(BIM)_2/Succ$	174	245	280	
26	$C_4(HIM)_2/Succ$	208	240	270	
19	$C_5(MIM)_2/Succ$	187	239	260	
20	$C_6(MIM)_2/Succ$	215	240	261	
21	$C_3(MIM)_2/Glut$	143	236	252	
22	$C_4(MIM)_2/Glut$	209	241	261	
23	$C_5(MIM)_2/Glut$	226	241	261	
24	$C_6(MIM)_2/Glut$	238	243	262	
27	BMIM/ Mal	170	195	214	
28	BMIM/Succ	208	223	257	
29	BMIM/Glut	162	221	246	

[a]*Youan et al. (2017).* [b]*Priede et al. (2014).* [c]*Zhang et al. (2018).* [d]*Lee et al. (2010).* [e]*Yang et al. (2014).* [f]*Lee et al. (2011).*

cation are more stable than the corresponding salts based on 1-n-butyl and 1-n-hexyl imidazolium cations. The linker length instead appears practically unable to influence the thermal stability, only in the case of the 1-methyl imidazolium DIL subfamily, a small difference in the degradation temperatures between the alkyl linkers with an even or odd number of carbon atoms can be observed. DILs with an even number of carbon atoms show a degradation temperature higher than subsequent odd ones. This peculiar behavior was not observed in DILs with butyl or hexyl alkyl chain.

On the other hand, all the examined dicarboxylate based DILs show a lower thermal stability than the corresponding dibromides, with the onset degradation temperatures ranging between 225 and 245°C. These DILs belongs to the least stable class. Thus, comparing all the reported data, it is possible to state that the thermal stability of the investigated DILs depends primarily on the anion nature, bromides are significantly more stable than dicarboxylates, and a small effect can be also observed inside this latter class (Succinate ≈Glutarate>Malonate), whereas substituents on cation have a lower significant influence on the degradation temperature. It is also noteworthy that dicationic-dicarboxylated salts show a slightly higher thermal stability than the corresponding monocation dicarboxylated ILs (**27-29**). Finally, the dynamic TGA curves of the investigated dicarboxylate based DILs (**Figure 1** and **Supplementary Information**) evidence that the thermal decomposition of these salts generally takes place in multiple steps, however, further studies are required to properly understand the contribution of the different dicarboxylate frame to the decomposition events of the IL.

While TGA analysis does not show any prominent discernible trend throughout the DILs, DSC curves allowed for their division into distinct groups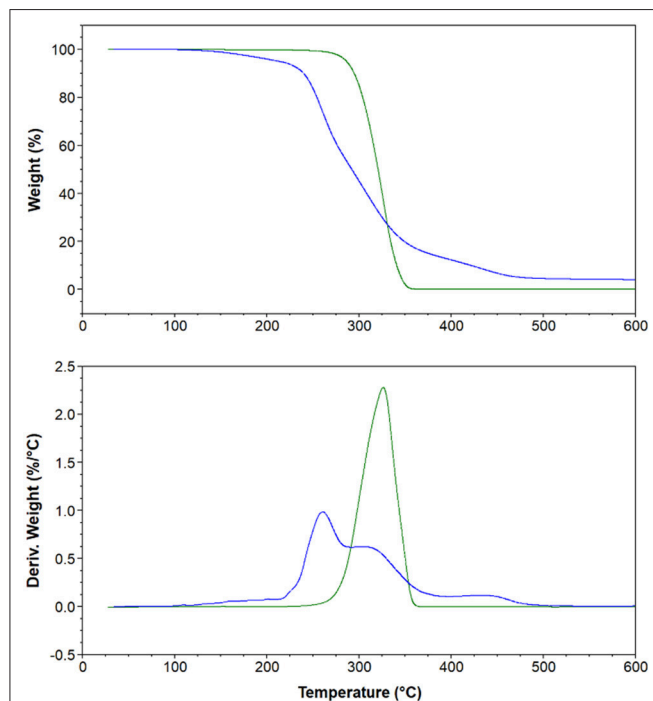. To favor comparison, also in this case the T_g and T_m have been plotted against the linker alkyl chain length (**Figure 6**).

It should be noted that compounds with an internal C3 alkyl linker and/or 1-methylimidazolium cation with dicarboxylate or Br anions are generally white solids at room temperature. For these DILs, all the observed transitions are reversible, unless the salt is heated to a temperature which determines thermal decomposition. The other dibromide DILs with n-butyl and n-hexyl lateral alkyl chains and C4, C5, and C6 alkyl linker are generally obtained as very viscous liquids at room temperature, with the exception of **8** [$C_6(BIM)_2/2Br$] which is a white solid. The phase transitions (DSC) of the synthesized bromide DILs are summarized in **Table 2**.

In agreement with the general trends reported by Gómez et al. (2015), three thermal behaviors have been observed for the investigated DILs: (i) DILs showing only glass transition temperatures (type I); (ii) DILs showing freezing transitions (giving crystals) upon cooling and a melting transition upon heating (type II); (iii) DILs that don't show a crystallization in the cooling run but exhibit a cold crystallization in the heating run (type III).

In particular, the five DILs which are liquid at room temperature, exhibit only glass transition(s) at low temperature without any phase transition, thus belonging to the type I. DIL **7** [$C_5(BIM)_2/2Br$] presents two different glass transitions, respectively at $-27.7°C$, $-11.1°C$ in the heating run, and one at $-13.9°C$ in the cooling run (**Figure 7A**). The other four salts, **6** [$C_4(BIM)_2/2Br$], **10** [$C_4(HIM)_2/2Br$], **11** [$C_5(HIM)_2/2Br$], and **12** [$C_6(HIM)_2/2Br$], show a single glass transition at $-24.2°C$, $-30.1°C$, $-27.6°C$, and $-29.8°C$, respectively. On the other

FIGURE 4 | Thermal gravimetric analysis (top) and derivative curves (bottom) of **4** [$C_6(MIM)_2/2Br$] (Green) and **20** [$C_6(MIM)_2/Succinate$] (Blue).
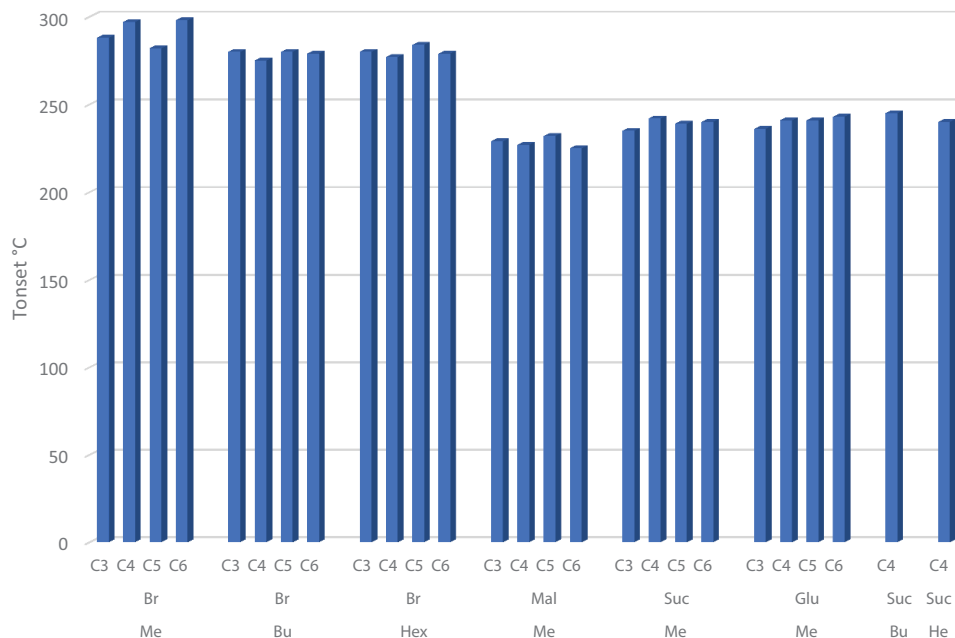
FIGURE 5 | T_{onset} values plotted against the linker alkyl chain length, grouped on the basis of the imidazole substituent (methyl, butyl or hexyl) for both bromide (Br) and dicarboxylate (Mal, Suc, Glu) DILs.
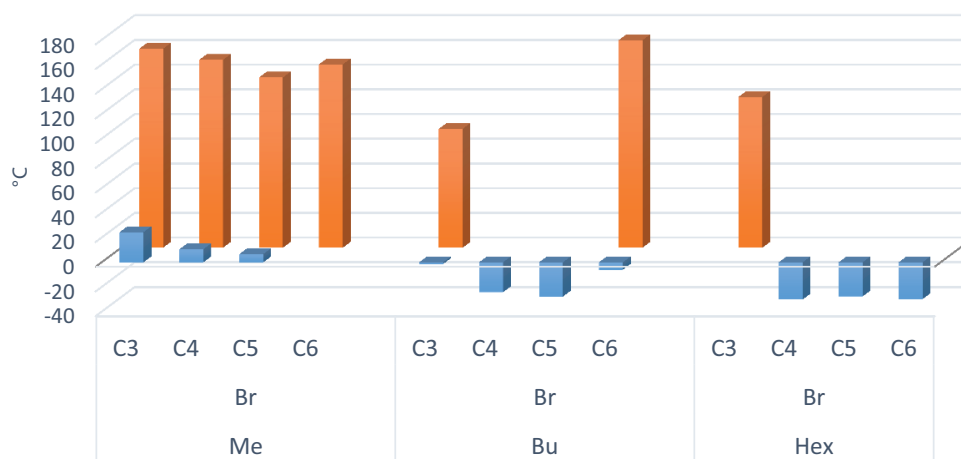
FIGURE 6 | T_m (orange) and T_g (blue) values plotted against the linker alkyl chain length, grouped on the basis of the imidazole substituent (methyl, butyl or hexyl) for bromide DILs.

TABLE 2 | Crystallization (T_c), glass transition (T_g), cold crystallization (T_{cc}), solid-solid transition (T_{ss}), and melting (T_m) temperatures for the synthesized bromide DILs.

| | | 2nd Cycle | | | | | | | |
| | | Cooling | | | Heating | | | | |
ILs	T_c (°C)	T_{ss} (°C)	T_g (°C)	T_g (°C)	T_{cc} (°C)	T_{ss} (°C)	T_m (°C)	T_m Lit. (°C)	T_g Lit. (°C)
1	$C_3(MIM)_2/2Br$			20.25	24.4	66.7	97.4(exo)	161.0; 164.5[a]	
2	$C_4(MIM)_2/2Br$				10.6	82.5	127.5 (endo)	152.5; 88.69[b]	115.45[c]
3	$C_5(MIM)_2/2Br$				6.71	90.4		137.8	
4	$C_6(MIM)_2/2Br$	123.9						148.4; 158.1[a]	
5	$C_3(BIM)_2/2Br$				−1.40	47.2		96.2	
6	$C_4(BIM)_2/2Br$				−24.2				
7	$C_5(BIM)_2/2Br$			−13.9	−27.7, −11.1				
8	$C_6(BIM)_2/2Br$	79.0			−6.0	40.5		167.9; 175.0[a]	151[d]
9	$C_3(HIM)_2/2Br$	116.0	24.1				23.3	122.6; 26.5[a]	104[e] −38[e]
10	$C_4(HIM)_2/2Br$				−30.1				
11	$C_5(HIM)_2/2Br$				−27.6			41.0[b]	
12	$C_6(HIM)_2/2Br$				−29.8				

[a] Data from 1st heating-cooling cycle. [b] Melting of dicationic ionic liquids hydrate form. [c] Zhang et al. (2018). [d] Yang et al. (2014) (supplementary). [e] Lee et al. (2011).

hand, **4** [$C_6(MIM)_2/2Br$] and **9** [$C_3(HIM)_2/2Br$] behave as low melting salts; they crystallize in the cooling run giving a sharp crystallization peak and a comparable melting peak in the heating run (type II). For **4** [$C_6(MIM)_2/2Br$] the single crystallization and melting events have been observed at 123.9 and 148.4°C, respectively. It is noteworthy that this latter DIL displays a higher melting point during the first heating-cooling cycle (158.1°C), a behavior which is generally attributed to the thermal history of the sample. DIL **9** [$C_3(HIM)_2/2Br$] instead presents two different exothermic transitions in the cooling run (116.0°C and 24.1°C) followed by two endothermic transitions in the heating run (23.3°C and 122.6°C), **Figure 7B**. Since this salt presents a melting point of 123°C, when determined using a Kofler hot bench apparatus, the endothermic transition at the lower temperature can be attributed to a solid-solid transition. Finally,

DILs **1** [$C_3(MIM)_2/2Br$], **2** [$C_4(MIM)_2/2Br$], **3** [$C_5(MIM)_2/2Br$], **5** [$C_3(BIM)_2/2Br$], and **8** [$C_6(BIM)_2/2Br$] exhibit an exothermic cold crystallization peak followed by a melting transition during the heating run (type III), **Figure 7D**. More in detail, **1** and **2** present also an exothermic and an endothermic solid-solid transition at 97.4°C and 127.5°C, respectively, whereas **8** is characterized by an even more peculiar behavior, **Figure 7C**. This salt shows indeed a partial crystallization at 79°C in the cooling run, followed by a small glass transition at −6.0°C, probably due to the residual amorphous part which undergoes to a cold crystallization in the heating run.

Finally, DILs based on dicarboxylated anions display simpler thermal behaviors as no transitions were observed either in the heating or in the cooling run in any of the three heating-cooling cycles. The sole transitions observed at higher temperatures can

FIGURE 7 | Differential scanning calorimetry (DSC) of compounds **7** [C$_5$(BIM)$_2$/2Br] **(A)**, **9** [C$_3$(HIM)$_2$/2Br] **(B)**, **8** [C$_6$(BIM)$_2$/2Br] **(C)**, and **2** [C$_4$(MIM)$_2$/2Br] **(D)**.
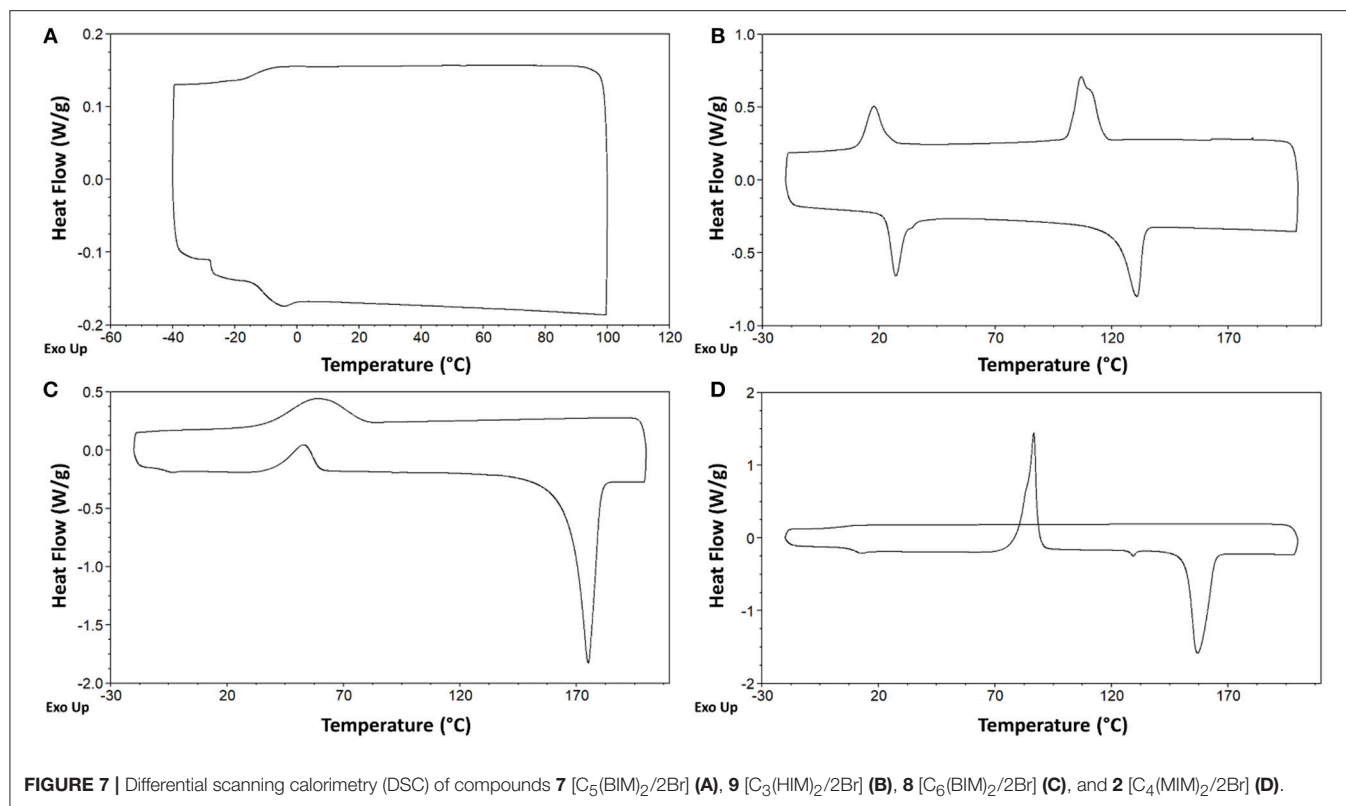
be attributed to degradation phenomena on the basis of the TGA analyses (**Figure S42–S53** see **Supporting Materials**).

DESs Preparation and Analyses

Following the generally reported protocol (Florindo et al., 2014), DESs were prepared by gently heating the selected components at 80°C, under stirring. Furthermore, since water can act as HBD and contribute to the formation of DES but, contemporaneously, it is able to modify all the physico-chemical properties of the resulting mixtures, all the components were accurately dried before use, and the contact with humidity was avoided during synthesis and storage. Liquid systems able to maintain this condition also during long term storage in the absence of humidity were obtained by mixing salts **4** and **20** with glycerol or diethylene glycol at the molar ratios reported in **Table 3**.

After further accurate drying, the four DESs studied in this work were analyzed by NMR as neat liquids to confirm that no reaction occurred under the employed conditions.

Interestingly, the ^{1}H-NMR spectra registered on the neat sample (coaxial tube) at 23°C in the case of C$_6$(MIM)$_2$/2Br:Glycerol 1:3 and C$_6$(MIM)$_2$/2Br:DiEG 1:6 and at 63°C in the case of C$_6$(MIM)$_2$/Succ:Glycerol 1:2 and C$_6$(MIM)$_2$/Succ:DiEG 1:2, due to the high viscosity of these latter DESs, show significative shifts of the signals of the OH groups of both employed HBD (**Figures S55–S58** see **Supporting Materials**). In particular, in the case of bromide based DESs an upfield shift of these signals (0.92 ppm for both OH groups of C$_6$(MIM)$_2$/2Br:Glycerol and

TABLE 3 | Glass transition (T$_g$) temperatures for the synthesized DESs.

		T$_{g\,heating}$ (°C)	T$_{g\,cooling}$ (°C)
1	C$_6$(MIM)$_2$/2Br:Glycerol 1:3	−79.7	
2	C$_6$(MIM)$_2$/2Br:DiEG 1:6	−86.6	
3	C$_6$(MIM)$_2$/Succ:Glycerol 1:2	−51.1	−54.8
4	C$_6$(MIM)$_2$/Succ:DiEG 1:2	−54.1	−50.0

0.56 ppm for C$_6$(MIM)$_2$/2Br:DiEG) has been observed, suggesting a decreased hydrogen bonding on going from pure glycols to DESs. On the other hand, downfield shifts characterized the same signals in the case of succinate based DESs (1.12 ppm for C$_6$(MIM)$_2$/Succ:Glycerol and 1.81 ppm for C$_6$(MIM)$_2$/Succ:DiEG), in agreement with the higher hydrogen bond acceptor ability of the carboxylates when compared with the bromide anion. Unfortunately, the NMR spectra of pure DILs cannot be obtained, however, as upfield shift of signals of the C(2)-H imidazolium protons can be estimated considering as reference values the chemical shift measured in aprotic solvents (C$_6$(MIM)$_2$/Succ 9.21 ppm in CDCl$_3$; C$_6$(MIM)$_2$/2Br 9.80 ppm in CDCl$_3$ or 9.30 ppm DMSO-d$_6$). This shift is attributable to decreased hydrogen bonding

acceptor ability on going from bromide or succinate to the oxygen of glycols. These data strongly support the formation of DESs.

TABLE 4 | T_{start}, T_{onset}, and T_{peak} of the investigated DESs measured under a nitrogen atmosphere and with a heating rate of 10°C/min.

		T_{start} (°C)	T_{onset} (°C)	T_{peak} (°C)
1	$C_6(MIM)_2$/2Br: Glycerol 1:3	198.3	202.0 337.0	252.8 357.8
2	$C_6(MIM)_2$/2Br: DiEG 1:6	121.2	133.7 325.6	173.6 347.8
3	$C_6(MIM)_2$/Succ: Glycerol 1:2	210.0	274.8	324.3
4	$C_6(MIM)_2$/Succ: DiEG 1:2	167.6	168.2 274.1	212.2 292.2 319.4

FIGURE 8 | DSC curves of selected DESs [$C_6(MIM)_2$/2Br - Glycerol 1:3 in blue, $C_6(MIM)_2$/succinate - Glycerol 1:2 in black).
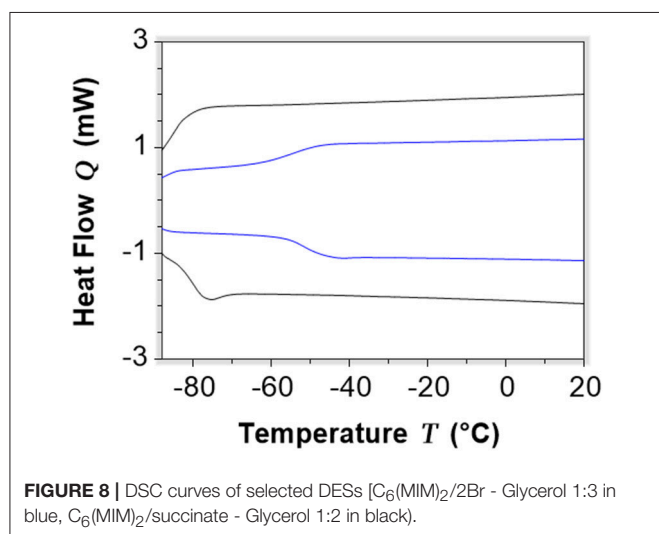
Subsequently, the thermal behavior of the obtained liquids was investigated by TGA and DSC.

Melting point and decomposition temperature are generally two important properties of DESs, particularly for the possible use of these liquids as solvents. Moreover, it was also interesting to evaluate if the thermal stability of the DILs might positively affect the decomposition temperature of the resulting DESs. The thermal properties are reported in **Tables 3, 4**.

The investigated DESs only present a glass transition at −79.7°C, −86.6°C, −51.1°C, and −54.1°C, respectively (**Table 3; Figure 8**), which confirm that these systems are supramolecular complexes with a liquid state over a wide range of temperatures.

For all the investigated DESs, the first decomposition event is strictly related to the more volatile component (**Figure 9**). Indeed, the lower decomposition temperatures were observed when diethylene glycol was used as the hydrogen bond donor for both DILs (133.7°C for $C_6(MIM)_2$/2Br:DiEG 1:6 and 168.2°C for $C_6(MIM)_2$/Succ:DiEG 1:2). It is also interesting to note how, for the same HBD, bromide dicationic based DESs resulted in being less stable than the succinate based DESs, which is the opposite of what was observed for pure DILs. This is probably due to either the stronger interaction between the carboxylate anion and the HBD than between the bromide anion and the HBD or to the higher amount of HBD required by dicationic bromide to form the DES or by a combination of the two.

CONCLUSIONS

A homogeneous class of 12 dibromide DILs has been prepared by performing the Menshutkin reaction in MIBK, a greener solvent than the frequently used toluene, between alkyl imidazoles and 1,n-dibromo alkanes. Methyl imidazolium bromide DILs, characterized by a different linker length between the cationic moieties (C3-C6), were converted into malonate, succinate, and glutarate dicarboxylate salts. The most common bromide-carboxylate anion exchange protocols were compared. In our

FIGURE 9 | Thermal gravimetric analysis (TGA) of prepared DESs with heating rate of 10°C/min.
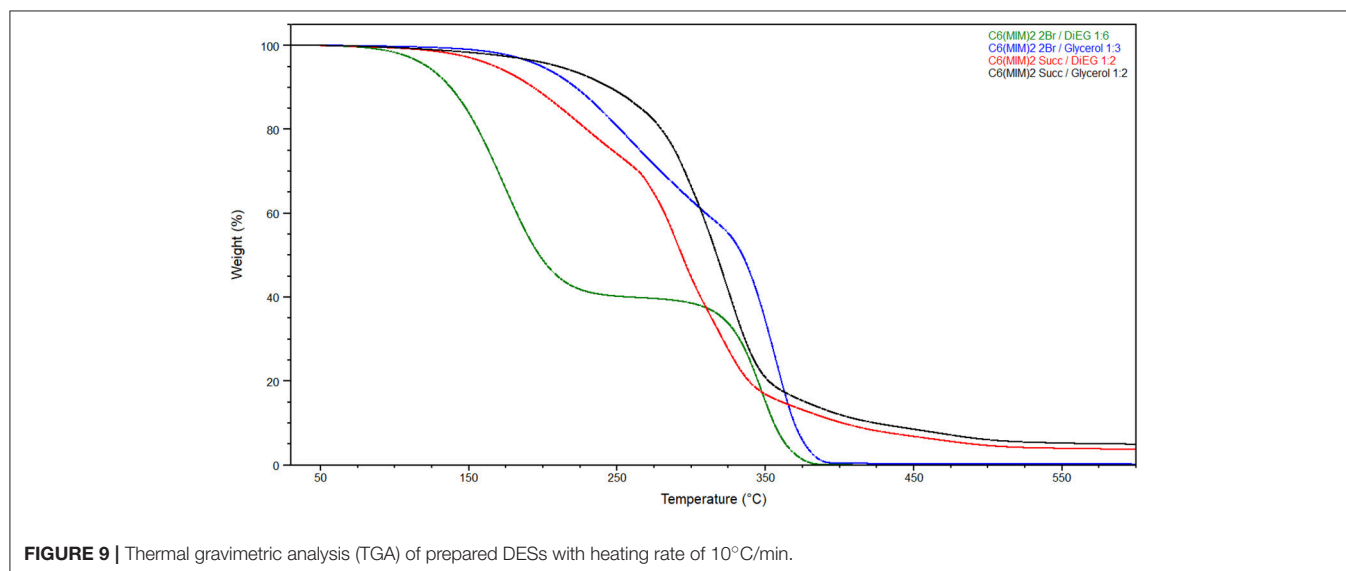
hands, the resin exchange procedure performed the best, and allowed for the preparation of all the desired dicarboxylate salts in high yield and purity. The thermal behaviors of the dibromide and dicarboxylate DILs were then investigated by TGA and DSC. For the dibromide DILs, TGA analysis showed an effect of the lateral alkyl substituent of the imidazolium cation on the thermal stability, while the internal linker seems to play a negligible role. DSC analysis revealed a quite complex picture of the thermal behavior, which confirmed how subtle structural changes affect phase transitions of ILs. As for the dicarboxylated DILs, lower thermal stabilities were found for all the prepared salts.

Two reference compounds, solids at room temperature, were also used as hydrogen bond acceptor (HBA) components for the preparation of DESs with either glycerol or diethylene glycol. The four liquid systems obtained were analyzed by ^{1}H NMR, which ascertained the formation of hydrogen bonds between the DES components, and by TGA and DSC, which showed the influence on the thermal stability of both the HBD and of the anion of the DIL. The systematic investigation of DILs thermal behavior as well as their use as potential DES components should allow for a future rational design of new liquid systems (DILs and DES) and their use in potential new applications. Studies to ascertain the (eco)toxicity of the proposed DILs are currently underway and will be presented in the due course.

AUTHOR CONTRIBUTIONS

LGug and AM worked on the presented work under the guide of LGua, CP, and FD. The manuscript was written by CC with the input from all authors.

ACKNOWLEDGMENTS

SUPPLEMENTARY MATERIAL

The Supplementary Material for this article can be found online at: https://www.frontiersin.org/articles/10.3389/fchem. 2018.00612/full#supplementary-material

REFERENCES

Abbott, A. P., Capper, G., Davies, D. L., Rasheeda, R. K., and Tambyrajaha, V. (2003). Novel solvent properties of choline chloride/urea mixtures. *Chem. Commun.* 70–71. doi: 10.1039/B210714G

Aboudzadeh, A., Fernandez, M., Muñoz, M. E., Santamaría, A., and Mecerreyes, D. (2014). Ionic supramolecular networks fully based on chemicals coming from renewable sources. *Macromol. Rapid. Commun.* 35, 460–465. doi: 10.1002/marc.201300732

Aboudzadeh, M. A., Muñoz, M. E., Santamaría, A., Fernández-Berridi, M. J., Irusta, L. D., and Mecerreyes, D. (2012a). Synthesis and rheological behavior of supramolecular ionic networks based on citric acid and aliphatic diamines. *Macromolecules* 45, 7599–7606. doi: 10.1021/ma300966m

Aboudzadeh, M. A., Muñoz, M. E., Santamaría, A., Marcilla, R., and Mecerreyes, D. (2012b). Facile synthesis of supramolecular ionic polymers that combine unique rheological, ionic conductivity, and self-healing properties. *Macromol. Rapid Commun.* 33, 314–318. doi: 10.1002/marc.201100728

Aboudzadeh, M. A., Muñoz, M. E., Santamaría, A., and Mecerreyes, D. (2013). New supramolecular ionic networks based on citric acid and geminal dicationic ionic liquids. *RSC Adv.* 3, 8677–8682. doi: 10.1039/C3RA40629F

Aboudzadeh, M. A., Shaplov, A. S., Hernandez, G., Vlasov, P. S., Lozinskaya, E. I., Pozo-Gonzalo, C., et al. (2015). Supramolecular ionic networks with superior thermal and transport properties based on novel delocalized di-anionic compounds. *J. Mater. Chem. A.* 3, 2338–2343. doi: 10.1039/C4TA05792A

Alder, C. M., Hayler, J. D., Henderson, R. K., Redman, A. M., Shukla, L., Shuster, L. E., et al. (2016). Updating and further expanding gsk's solvent sustainability guide. *Green Chem.* 18, 3879–3890. doi: 10.1039/C6GC00611F

Bortolini, O., Chiappe, C., Fogagnolo, M., Giovannini, P. P., Massi, A., Pomelli, C. S., et al. (2014). An insight into the mechanism of the aerobic oxidation of aldehydes catalyzed by N-heterocyclic carbenes. *Chem. Commun.* 50, 2008–2011. doi: 10.1039/C3CC48929A

Bortolini, O., Chiappe, C., Fogagnolo, M., Massi, A., and Pomelli, C. S. (2017). Formation, oxidation, and fate of the breslow intermediate in the *n*-heterocyclic carbene-catalyzed aerobic oxidation of aldehydes. *J. Org. Chem.* 82, 302–312. doi: 10.1021/acs.joc.6b02414

Brown, L., Earle, M. J., Gîlea, M. A., Pechkova, N. V., and Seddon, K. R. (2017). Ionic liquid-liquid chromatography: a new general purpose separation methodology. *Top. Curr. Chem.* 375, 1–41. doi: 10.1007/s41061-017-0159-y

Cao, Y., and Mu, T. (2014). Comprehensive Investigation on the Thermal Stability of 66 Ionic Liquids by Thermogravimetric Analysis. *Ind. Eng. Chem. Res.* 53, 8651–8664. doi: 10.1021/ie5009597

Chen, Y., Zhuo, K., Chen, J., and Bai, G. (2015). Volumetric and viscosity properties of dicationic ionic liquids in (glucose + water) solutions at T = 298.15 K. *J. Chem. Thermodynamics* 86, 13–19. doi: 10.1016/j.jct.2015.02.017

Chiappe, C., Mezzetta, A., Pomelli, C. S., Puccini, M., and Seggiani, M. (2016). Product as reaction solvent: an unconventional approach for ionic liquid synthesis. *Org. Proc. Res. Dev.* 20, 2080–2084. doi: 10.1021/acs.oprd. 6b00302

Chiappe, C., and Pomelli, C. S. (2014). Point-functionalization of ionic liquids: an overview of synthesis and applications. *Euro. J. Org. Chem.* 28, 6120–6139. doi: 10.1002/ejoc.201402093

Craig, S. L. (2009). From ionic liquids to supramolecular polymers. *Angew. Chem. Int. Ed.* 48, 2645–2647. doi: 10.1002/anie.200805603

Fareghi-Alamdari, R., Hatefipour, R., Rakhshi, M., and Zekri, N. (2016). Novel diol functionalized dicationic ionic liquids: synthesis, characterization and DFT calculations on H-bonding influence on thermophysical properties. *RSC Adv.* 6, 78636–78647. doi: 10.1039/C6RA17188E

Florindo, C., Oliveira, F. S., Rebelo, L. P. N., Fernandes, A. M., and Marrucho, I. M. (2014). Insights into the synthesis and properties of deep eutectic solvents based on cholinium chloride and carboxylic acids. *ACS Sustain. Chem. Eng.* 2, 2416–2425. doi: 10.1021/sc500439w

Frizzo, C. P., Bender, C. R., Salbego, P. R. S., Farias, C. A. A., da Silva, T. C., Stefanello, S. T., et al. (2018). Impact of anions on the partition constant, self-diffusion, thermal stability, and toxicity of dicationic ionic liquids. *ACS Omega* 3, 734–743. doi: 10.1021/acsomega.7b01873

Gómez, E., Calvarn, N., and Domínguez, A. (2015).Thermal behaviour of pure ionic liquids scott handy, intechopen, *Charter* 8, 199–228. doi: 10.5772/59271

Hallett, J. P., and Welton, T. (2011). Room-Temperature Ionic Liquids: Solvents for Synthesis and Catalysis. *Chem. Rev.* 111, 3508–3576. doi: 10.1021/cr100 3248

Kishore, R., and Das, S. K. (2012). Diversities of coordination geometry around the Cu^{2+} center in bis(maleonitriledithiolato)metalate complex anions: geometry controlled by varying the alkyl chain length of imidazolium cations. *Cryst. Growh Des.* 12, 3684–3699. doi: 10.1021/cg3004917

Leclercq, L., and Schmitzer, A. R. (2011). Influence of the Flexibility of the diimidazolium cations on their organization into crystalline materials. *Crys. Growth Des.* 11, 3828–3836. doi: 10.1021/cg200381f

Lee, M., Choi, U. H., Wi, S., Slebodnick, C., Colby, R. H., and Gibson, H. W. (2011). 1,2-Bis[N-(N'-alkylimidazolium)]ethane salts: a new class of organic ionic plastic crystals. *J. Mat. Chem.* 21, 12280–12287. doi: 10.1039/c1jm10995b

Lee, M., Niu, Z., Slebodnick, C., and Gibson, H. W. (2010). Structure and Properties of N,N-Alkylene Bis(N'-Alkylimidazolium) Salts. *J. Phys. Chem. B* 114, 7312–7319. doi: 10.1021/jp102370j

Liu, M., Liang, L., Lianga, T., Lin, X., Shi, L., Wang, F., et al. (2015). Cycloaddition of CO2 and epoxides catalyzed by dicationic ionic liquids mediated metal halide: Influence of the dication on catalytic activity. *J. Mol. Catal. A Chem.* 408, 242–249. doi: 10.1016/j.molcata.2015.07.032

Mata, J. A., Chianese, A. R., Miecznikowski, J. R., Poyatos, M., Peris, E., Faller, J. W., et al. (2004). Reactivity differences in the syntheses of chelating n-heterocyclic carbene complexes of rhodium are ascribed to ligand anisotropy. *Organometallics* 23, 1253–1263. doi: 10.1021/om034240

Mezzetta, A., Guazzelli, L., and Chiappe, C. (2017a). Access to cross-linked chitosans by exploiting CO$_2$ and the double solvent-catalytic effect of ionic liquids. *Green Chem.* 19, 1235–1239. doi: 10.1039/C6GC02935C

Mezzetta, A., Guazzelli, L., Seggiani, M., Pomelli, C. S., Puccini, M., and Chiappe, C. (2017b). A general environmentally friendly access to long chain fatty acid ionic liquids (LCFA-ILs). *Green Chem.* 19, 3103–3111. doi: 10.1039/C7GC00830A

Montalbána, M. G., Vílloraa, G., and Licence, P. (2018). Ecotoxicity assessment of dicationic versus monocationic ionic liquids as a more environmentally friendly alternative. *Ecotox. Environ. Safe* 150, 129–135. doi: 10.1016/j.ecoenv.2017.11.073

Nachtigall, F. M., Corilo, Y. E., Cassol, C. C., Ebeling, G., Morgon, N. H., Dupont, J., et al. (2008). Multiply Charged (Di-)Radicals. *Angew. Chem. Int. Ed.* 47, 151–154. doi: 10.1002/anie.200703858

Nielsen, D. J., Cavell, K. J., Skelton, B. W., and White, A. H. (2006). Silver(I) and Palladium(II) Complexes of an Ether-Functionalized Quasi-pincer Bis-carbene Ligand and Its Alkyl Analogue. *Organometallics* 25, 4850–4856. doi: 10.1021/om0605175

Patil, R. A., Talebi, M., Xu, C., Bhawal, S. S., and Armstrong, D. W. (2016). Synthesis of thermally stable geminal dicationic ionic liquids and related ionic compounds: an examination of physicochemical properties by structural modification. *Chem. Mater.* 28, 4315–4323. doi: 10.1021/acs.chemmater.6b01247

Pretti, C., Chiappe, C., Baldetti, I., Brunini, S., Monni, G., and Intorre, L. (2009). Acute toxicity of ionic liquids for three freshwater organisms: Pseudokirchneriella subcapitata, Daphnia magna and Danio rerio. *Ecotox. Environ. Safe.* 72, 1170–1176. doi: 10.1016/j.ecoenv.2008.09.010

Priede, E., Nakurte, I., and Zicmanis, A. (2014). Structure effect of imidazolium-based dicationic ionic liquids on claisen rearrangement. *Synthetic Comm.* 44, 1803–1809. doi: 10.1080/00397911.2013.873940

Scalfani, V. F., Al Alshaikh, A., and Bara, J. E. (2018). Analysis of the frequency and diversity of 1,3-dialkylimidazolium ionic liquids appearing in the literature. *Ind. Eng. Chem. Res.* 57, 15971–15981. doi: 10.1021/acs.iecr.8b02573

Shen, X., Shamshina, J. L., Berton, P., Bandomir, J., Wang, H., Gurau, G., et al. (2016). Comparison of hydrogels prepared with ionic-liquid-isolated vs commercial chitin and cellulose. *ACS Sustain. Chem. Eng.* 4, 471–480. doi: 10.1021/acssuschemeng.5b01400

Watanabe, M., Thomas, M. L., Zhang, S., Ueno, K., Yasuda, T., and Dokko, K. (2017). Application of ionic liquids to energy storage and conversion materials and devices. *Chem. Rev.* 117, 7190–7239. doi: 10.1021/acs.chemrev.6b00504

Wathier, M., and Grinstaff, M. W. (2008). Synthesis and properties of supramolecular ionic networks. *J. Am. Chem. Soc.* 130, 9648–9649. doi: 10.1021/ja803248q

Welton, T. (2018). Ionic liquid: a brief history. *Biophys. Rev.* 10, 691–706. doi: 10.1007/s12551-018-0419-2

Yang, M., Stapperta, K., and Mudring, A.-V. (2014). Bis-cationic ionic liquid crystals. *J. Mater. Chem. C.* 2, 458–473. doi: 10.1039/c3tc31368a

Youan, J., Yucui, H., Shuhang, R., Congfei, Y., and Weize, W. (2017). Highly efficient separation of phenolic compounds from oil mixtures by imidazolium-based dicationic ionic liquids via forming deep eutectic solvents. *Energy Fuels* 31, 10274–10282. doi: 10.1021/acs.energyfuels.7b01793

Youan, J., Yucui, H., Shuhang, R., Congfei, Y., and Weize, W. (2018). Highly efficient extraction of phenolic compounds from oil mixtures by trimethylamine-based dicationic ionic liquids via forming deep eutectic solvents. *Fuel Process. Technol.* 171, 183–191. doi: 10.1016/j.fuproc.2017.11.015

Zhang, H., Li, M., and Yang, B. (2018). Design, synthesis, and analysis of thermophysical properties for imidazolium-based geminal dicationic ionic liquids. *J. Phys. Chem. C.* 122, 2467–2474. doi: 10.1021/acs.jpcc.7b09315

Zhang, J., Wu, J., Yu, J., Zhang, X., He, J., and Zhang, J. (2017). Application of ionic liquids for dissolving cellulose and fabricating cellulose-based materials: state of the art and future trends. *Mater. Chem. Front.* 1, 1273–1290. doi: 10.1039/c6qm00348f/

Conflict of Interest Statement: The authors declare that the research was conducted in the absence of any commercial or financial relationships that could be construed as a potential conflict of interest.

Fluoride Ionic Liquids in Salts of Ethylmethylimidazolium and Substituted Cyclopropenium Cation Families

Owen J. Curnow[1]*, Douglas R. MacFarlane[2]* and Kelvin J. Walst[1]

[1] School of Physical and Chemical Sciences, University of Canterbury, Christchurch, New Zealand, [2] ARC Centre of Excellence for Electromaterials Science, Monash University, Melbourne, VIC, Australia

A series of solvent-stabilized ionic liquid fluorides were prepared, [EMIM]F.nCH$_3$COOH n = 1. 0, 1.6, 2.1, 2.4, and 3.2, either via exchange from the chloride salt using KF or AgF, or by neutralization of the hydroxide salt using HF. Azeotrope drying was used to remove water. Their viscosity, conductivity and density properties were determined. A diethanol solvate of the triaminocyclopropenium salt [C$_3$(NPr$_2$)$_3$]F was found to be stable and its viscosity, conductivity and density properties were also determined. The monoethanol solvate, however, was found to be unstable with trace water present. Intramolecular stabilization of fluoride was achieved by using OH functionalized cations: [C$_3$(NEt$_2$)$_2$N(CH$_2$CH$_2$OH)$_2$]F, [C$_3$(N(CH$_2$CH$_2$OH)$_2$)$_3$]F, and [Me$_3$NCH$_2$CH$_2$OH]F.H$_2$O, The first of these is an ionic liquid at ambient temperature and has a TGA mass loss onset at 175°C, indicating a useful range of liquid state stability.

Keywords: ionic liquids, fluoride, imidazolium, cyclopropenium, salts, solvate

INTRODUCTION

Research in Ionic Liquids (ILs) has explored a vast variety of anion types, revealing a wide range of properties and applications. Halide anion based ILs were some of the first known, especially those based on iodide due to the generally lower melting points with increasing size and polarizability in Group 17. Generally, fluoride salts are high melting and therefore have attracted little recent attention in this field. On the other hand, fluoride anions have the potential to make ionic liquids with interesting properties due to the reactivity of fluoride (Maiti et al., 2008; Mallik and Siepmann, 2010). Indeed, fluoride salts, such as tetrabutylammonium fluoride (TBAF), have many uses as fluorinating reagents and for the removal of silicon-based protecting groups. The more "naked" (higher donor ability) the fluoride anion is, the higher the reactivity (Christie and Jenkins, 2003). However, this reactivity causes difficulties with organic fluoride salts often being difficult to use, either because they become unstable due to the reactive fluoride (Sun and DiMagno, 2005) or they are insoluble in aprotic solvents.

Triaminocyclopropenium (TAC) cations have been considered as counter ions to fluoride for two reasons: firstly, there are no acidic protons, and secondly, TAC cations have a high energy HOMO that leads to weak cation-anion interactions and good ionic liquid properties (Weiss et al., 1995a,b; Butchard et al., 2006; Curnow et al., 2011, 2012; Wallace et al., 2015). Cations with acidic protons will easily be deprotonated by fluoride, which becomes a much stronger base as it becomes less solvated. This is predicted to occur in imidazolium fluoride salts: *ab initio* calculations on

1-ethyl-3-methylimidazolium fluoride, [EMIM]F, show that covalent bonding between the fluorine atom and a proton extracted from the 2 position of the imdazolium cation is preferred over the ionic form. The result is HF and a stable Arduengo carbene (Turner et al., 2003; Maiti et al., 2008). As a result, imidazolium-based ionic liquid fluorides have only been reported with solvated fluoride anions (Swatloski et al., 2003; Maiti et al., 2008). TAC cations might be more resistant to Hofmann elimination, which causes the decomposition of tetraalkylammonium fluorides. On the other hand, TAC cations are sensitive to strong nucleophiles, such as hydroxide, and possibly fluoride itself. For this reason, even if triaminocyclopropenium salts proved to be stable to fluoride, any kind of naked fluoride ionic liquid would be highly moisture sensitive.

A number of solvate salts of fluorides are known, for example the *t*-butanol solvate of tetrabutylammonium fluoride, TBAF(^{t}BuOH)$_4$, which is a fluoride solvate that has been investigated as an anhydrous source of fluoride (Kim et al., 2008). However, due to the symmetric shape of the ions and *t*-butanol, and the non-dispersed charges, it is a solid.

Larson (Larson and McMahon, 1983) carried out gas phase measurements of the binding energy of fluoride with a variety of Brönsted and Lewis acids. The binding energy of the ethanol to fluoride hydrogen bond was found to be 132 kJ mol^{-1}, a strong hydrogen bond that is not much weaker than that measured for hydrogen fluoride to fluoride (bifluoride) at 161 kJ mol^{-1}. Other measurements have suggested this was low and found a bond energy of 191 kJ mol^{-1} (Wenthold and Squires, 1995). The strong hydrogen bond suggests that the alcohol solvate can be thought of as a discrete species. Fluorohydrogenate ($[F(HF)_x]^-$) anions in ionic liquids are considered as a discrete species, and have received considerable attention in the literature due to high conductivities and low viscosities (Hagiwara et al., 1999, 2003).

In this paper, we report on TAC fluoride salts with inter- and intra-molecular alcohol solvate interactions. However, the solvate molecules do not need to be limited to alcohols, they just need to be good hydrogen bond donors. So, prompted by earlier work on dimeric and higher order oligomeric acetic acid anions (Johansson et al., 2008), acetic acid was also investigated as a solvate molecule with imidazolium fluoride salts. Both the [AcOHF]$^-$ and [(AcOH)$_2$F]$^-$ species, shown below, have been observed previously by NMR at sub-ambient temperature (Golubev et al., 2004).
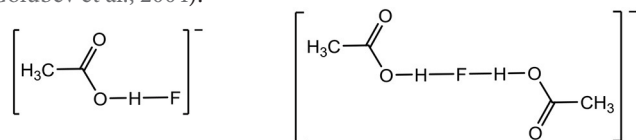
EXPERIMENTAL

General Procedures

All operations were performed using standard Schlenk techniques with a dinitrogen atmosphere in order to reduce exposure to water. ^{1}H-, ^{13}C{^{1}H}-NMR spectra were collected on a Varian Unity-300 operating at 300 and 75 MHz, respectively, or on a Varian INOVA-500 operating at 500 and 126 MHz,

respectively, in CDCl$_3$ or D$_2$O, referenced to residual solvent peaks or TMS. ^{19}F-NMR spectra were collected on a Varian Unity-300 operating at 282 MHz, in CDCl$_3$ or D$_2$O, referenced to C$_6$H$_5$F or CFCl$_3$. Electrospray mass spectrometry was carried out on a Micromass LCT, with samples dissolved in acetonitrile. Water contents were determined by Karl Fischer titration using a Metrohm 831 KF coulometer. Chloride contents were determined using a AutolabEco Chemie, with associated GPES software, under a dinitrogen atmosphere. The electrodes were either a glassy carbon (3 mm diameter) or platinum (1 mm diameter) working electrode, a platinum wire counter electrode and a silver reference electrode. Fluoride, Ag$^+$ and K$^+$ were determined similarly using ISEs. Mircoanalysis was performed by Campbell Microanalytical Laboratory, Dunedin. [C$_3$(NPr$_2$)$_3$]Cl (Curnow et al., 2011) and (Et$_2$N)$_2$C$_3$O (Curnow et al., 2012) were prepared by previously-published methods. Other reagents were used as obtained commercially.

Differential Scanning Calorimetry (DSC) was carried out on a TA Q100 DSC and a Perkin-Elmer DSC 8000. The DSC 8000 was calibrated with indium (156.60°C) and cyclohexane (−87.0 and 6.5°C). Three heating and cooling cycles were carried out with data collected from a repeatable second cycle. A scan rate of 10°C min^{-1} was used, over a temperature range of at least −100 to 50°C, with a greater range used as required. Transition temperatures are reported as the onset temperature. Enthalpy for a transition was found by integrating the peak area, with entropy then calculated using ΔS = ΔH/T. Sample size was ∼5–10 mg. Density measurements were carried out on an Anton Parr DMA 5000 instrument, an oscillating U-tube density meter, from 20 to 90°C in 10°C steps. All imidazolium fluoride acetic acid mixtures were measured on an Anton Parr AMVn automated microviscometer. The other samples were measured on a Brookfield DV-II+ Pro cone and plate viscometer. Samples that were measured using the cone and plate viscometer were examined for non-Newtonian behavior, although this was only over a limited shear rate range. All samples were measured from 20 (or above the melting point if solid) to 80 or 90°C, and performed sealed or under a dinitrogen gas flow. Conductivities were measured by AC impedance spectroscopy on a Solatron SI 1296 frequency response analyser, at ranges up to 0.01 Hz to 10 MHz. Measurements were carried out with a dip cell probe containing two platinum wires covered in glass. The resistance was identified using a Nyquist Plot, and conductivity then calculated using $\kappa = l/AR$, where l/A is the cell constant, which was determined using 0.01 mol L^{-1} KCl solution at 25°C. All samples were measured from 20 (or above the melting point if solid) to 80 or 90°C, and performed sealed or under a dinitrogen gas flow. Thermal Gravimetric Analysis (TGA) was carried out on a TA Q600 SDT (simultaneous DSC-TGA), using platinum pans. Temperature calibration carried out using zinc (419.6°C), and heat flow using a sapphire standard. Pans were cleaned after each TGA experiment by heating at 500°C under an air atmosphere, and if required cleaned with nitric acid. Sample size was ∼10 mg.

Syntheses

Tris(diethanolamino)cyclopropenium chloride, [C$_3$(N(C$_2$H$_4$OH)$_2$)$_3$]Cl (**1**)

Diethanolamine, $HN(C_2H_4OH)_2$, (97.1 g, 0.925 mol) was mixed with CH_2Cl_2 (250 mL), and the suspension was cooled to 0°C. Pentachlorocyclopropane, C_3Cl_5H (24.7 g, 0.115 mol) was added dropwise and the solution stirred at ambient temperature overnight. The mixture was then heated to reflux for 24 h. Dichloromethane was then removed *in vacuo*. The mixture was dissolved into ethanol (150 mL) and molecular sieves (13X, 10 Å pore size) were added slowly until the solution was completely absorbed into the sieves. The crude product was extracted from the molecular sieves by soaking in ethanol (100 mL for 3 h followed by 100 mL for 19 h). This was repeated using methanol (2 × 100 mL), but with overnight soakings. Alcohol from the four fractions was removed *in vacuo*, yielding a pale yellow viscous liquid (24 g). All fractions were ∼90% tris(diethanolamino)cyclopropenium chloride, with 10% $[H_2N(C_2H_4OH)_2]Cl$, as determined by NMR. The molecular sieves were washed with excess water to remove $[H_2N(C_2H_4OH)_2]Cl$, and the process was repeated to ultimately yield a pale yellow, extremely viscous liquid (7.0 g, 16%). ^1H NMR (D_2O, 300MHz): δ 3.81 (t, $J = 5.3$ Hz, 12H, NCH_2), 3.61 ppm (t, $J = 5.3$ Hz, 12H, NCH_2CH_2). ES$^+$ m/z 348.2158 (100%, M$^+$).

Bis(diethylamino)diethanolaminocyclopropenium iodide, $[C_3(NEt_2)_2N(C_2H_4OH)_2]I$ (**2**)

The cyclopropenone $(Et_2N)_2C_3O$ (7.68 g, 39.2 mmol) was dried using ethanol azeotropes (5 × 50 mL). Iodoethane (97.5 g, 625 mmol) was added and the solution heated to reflux for 18 h. After cooling to ambient temperature, $HN(C_2H_4OH)_2$ (8.44 g, 80.3 mmol) was added with stirring for 48 h. Excess iodoethane was removed *in vacuo* and water (100 mL) added. Cyclopropenone was extracted with dichloromethane (100 mL and 50 mL). The product was then back-extracted with water from this dichloromethane solution (2 × 100 mL) and recombined with the first water layer. The final product was then extracted with CH_2Cl_2 (3 × 100 mL) to yield a yellow liquid (3.50 g, 22%). ^1H NMR (300 MHz, D_2O): 3.73 (t, $J = 5.3$ Hz, 4H, NCH_2CH_2OH), 3.47 (t, $J = 5.3$ Hz, 4H, NCH_2CH_2OH), 3.37 (q, $J = 7.0$ Hz, 8H, NCH_2CH_3), 1.17 (t, $J = 7.2$ Hz, 12H, NCH_2CH_3). ^{13}C NMR (75 MHz, D_2O, methanol reference): 117.89 (C_1), 117.26 (C_2), 59.46 (NCH_2CH_2OH), 54.38 (NCH_2CH_2OH), 47.20 (NCH_2CH_3), 13.98 (NCH_2CH_3).

Tris(diethanolamino)cyclopropenium fluoride, $[C_3(N(C_2H_4OH)_2)_3]F$ (**3**) via HF

Tris(diethanolamino)cyclopropenium chloride (**1**) (7.0 g, 19 mmol) was dissolved in water (250 mL) and Ag_2O (7.0 g, 30 mmol) was added and stirred for 3 h in a blacked out flask. Water was partially (200 mL) removed *in vacuo*. AgCl was removed by filtration through Celite before the solution was neutralized to pH 7.5 with aqueous HF. Complete drying was achieved with additions (3 × 150 mL, 3 × 50 mL) of ethanol and isopropanol and removal of the solvent *in vacuo*. This was followed by extended drying under high vacuum with stirring and mild heat (40°C) to give a colorless solid (5.63 g, 84%). ^1H NMR as for $[C_3(N(C_2H_4OH)_2)_3]Cl$. ^{19}F NMR (282 MHz, D_2O, C_6H_5F): 122.05 (s). ^{13}C NMR (75 MHz, D_2O, acetonitrile reference): 118.18 (C_3), 59.38 (NCH_2CH_2OH), 54.29 (NCH_2CH_2OH).

Tris(diethanolamino)cyclopropenium fluoride, $[C_3(N(C_2H_4OH)_2)_3]F$ (**3**) via AgF

Compound **1**, $[C_3(C_2H_4OH)_3]Cl$ (3.0 g, 7.8 mmol) was dissolved in water (200 mL) and AgF (1.30 g, 10.2 mmol) added with stirring. AgCl was removed by filtration through Celite. Excess AgF was removed by removal of solvent *in vacuo*, followed by the addition of alcohol solvent (50 mL, 5 × ethanol then 5 × isopropanol), after each addition the solution was filtered through Celite and the solvent removed *in vacuo*. This yielded a light yellow, extremely viscous liquid (2.3 g, 80%). Found: C, 48.82; H, 8.09; N, 11.06%. Calc. for $C_{15}H_{30}N_3O_6F$: C, 49.04; H, 8.23; N, 11.44%. Cl$^-$ content: 1,600 ppm.

Bis(diethylamino)diethanolaminocyclopropenium fluoride diethanol, $[C_3(NEt_2)_2N(C_2H_4OH)_2]F$ (**4**)

Compound **2**, $[C_3(NEt_2)_2N(C_2H_4OH)_2]I$ (3.50 g, 8.52 mmol) was stirred in water (250 mL) in a blacked-out flask to which Ag_2O (3.0 g, 13 mmol) was added with stirring for 3 h. AgI was removed by filtration through Celite before the solution was neutralized to pH 7.5 with aqueous HF. The solution was reduced in volume to 20 mL *in vacuo*, with drying being completed with ethanol azeotrope drying (3 × 200 mL). This yielded the product as a viscous yellow liquid (2.5 g, 96%). ^{19}F NMR (282 MHz, D_2O, C_6H_5F reference): 121.94 (s).

Tris(dipropylamino)cyclopropenium fluoride diethanol, $[C_3(NPr_2)_3]F.1.9EtOH$ (**5.1.9EtOH**)

Tris(dipropylamino)cyclopropenium chloride, $[C_3(NPr_2)_3]Cl$ (10.6 g, 28.5 mmol) was stirred in water (450 mL), in a blacked-out flask, to which Ag_2O (6.70 g, 28.9 mmol) was added and then stirred for 3 h. AgCl was removed by filtering through Celite, before the solution was neutralized to pH 7.1 with aqueous HF. The solution was reduced in volume to 50 mL *in vacuo*, with drying being completed with ethanol azeotrope drying (3 × 500 mL), which yielded the product as an orange liquid (12.4 g, 97%). ^1H NMR (300 MHz, $CDCl_3$): 3.68 (q, $J = 7.0$ Hz, 3.81H, CH_3CH_2OH), 3.27 (t, $J = 7.9$ Hz, 12H, $NCH_2CH_2CH_3$), 1.67 (m, 12H, $NCH_2CH_2CH_3$), 1.21 (t, $J = 7.0$ Hz, 5.00H, CH_3CH_2OH), 0.94 (t, $J = 7.3$ Hz, 18H, $NCH_2CH_2CH_3$). ^{19}F NMR (282 MHz, D_2O, C_6H_5F): 122.03 (s). Found: C, 61.95; H, 12.48; N, 8.77%. Calc. for $C_{21}H_{42}N_3F.1.9EtOH.2.09H_2O$: C, 61.95; H, 12.07; N, 8.74%. H_2O content: 2,200 ppm. F$^-$ content: 44,300 ppm, calculated: 42,900 ppm.

1-Ethyl-3-methylimidazolium fluoride diethanol, $[EMIM]F.1.8EtOH$ (**6.1.8EtOH**)

To [EMIM]Cl (33.0 g, 225 mmol) in ethanol (500 mL) was added KF (30 g, 520 mmol) suspended in ethanol (250 mL). After stirring for 1 h, the solid was removed by filtration. Two further additions of KF (35 and 25 g), with stirring (1 h) and removal, were made. The solvent was reduced in volume *in vacuo*, and acetonitrile (250 mL) was added and the solution cooled. A precipitate formed, and was filtered off. Ethanol was added to the filtrate, and excess solvent removed *in vacuo*. Cl$^-$ content: 3,120 ppm. To the [EMIM]F ethanol solvate (52 g) in water (200 mL) was added AgF (550 mg, 4.34 mmol) in water (100 mL). AgCl precipitate was removed by filtration. The solvent volume was reduced *in vacuo* with drying completed using ethanol azeotropes. The product was a pale yellow liquid (41.9 g, 87%) with 1.83 ethanol solvate molecules per fluoride. ^1H NMR (400

MHz, D$_2$O): 8.63 (s, 1H, C*H*), 7.40 (d, *J* = 2.0 Hz, 1H, CH), 7.33 (d, *J* = 2.0 Hz, 1H, CH), 4.14 (q, *J* = 7.5 Hz, 2H, C*H*$_2$CH$_3$), 3.80 (s, 3H, C*H*$_3$), 3.56 (q, *J* = 7.3 Hz, 3.6H, CH$_3$C*H*$_2$OH), 1.41 (t, *J* = 7.5 Hz, 3H, CH$_2$C*H*$_3$), 1.09 (t, *J* = 7.3 Hz, 5.4H, C*H*$_3$CH$_2$OH). ^{19}F NMR (377 MHz, D$_2$O, CFCl$_3$): −121.22 (s). Cl$^-$ content: 69 ppm. K$^+$ content: <100 ppm. Ag$^+$ content: 821 ppm.

1-Ethyl-3-methylimidazolium fluoride acetic acid, [EMIM]F.1.0AcOH (**6**.1.0AcOH)

Acetic acid (1.77 g, 29.4 mmol) was added to [EMIM]F.1.8EtOH (6.31 g, 29.4 mmol). The mixture was dried with isopropanol (2 × 50 mL) and ethanol (50 mL) azeotropes. Additional acetic acid (0.111 g, 1.85 mmol) was then added. The product was a pale yellow liquid (5.04 g, 90%). ^{1}H

NMR (400 MHz, D$_2$O): 8.63 (s, 1H, C*H*), 7.41 (s, 1H, C*H*), 7.35 (s, 1H, C*H*), 4.15 (q, *J* = 7.3 Hz, 2H, C*H*$_2$CH$_3$), 3.82 (s, 3H, C*H*$_3$), 1.94 (s, 3H, C*H*$_3$CO$_2$HF), 1.43 (t, *J* = 7.3 Hz, 3H, CH$_2$C*H*$_3$). ^{19}F NMR (377 MHz, D$_2$O): −128.87 (s, CH$_3$CO$_2$H*F*), −142.77 (m, F$_2$H$^-$), 27.1:1 ratio. H$_2$O content: 1330 ppm.

1-Ethyl-3-methylimidazolium fluoride acetic acid, [EMIM]F.1.6AcOH (**6**.1.6AcOH)

Acetic acid (3.00 g, 50.0 mmol) was added to [EMIM]F.1.8EtOH (6.25 g, 29.2 mmol). The mixture was dried with an ethanol (50 mL) azeotrope, followed by drying for 5 h *in vacuo*. The product was a pale yellow liquid (6.50 g, 99%). ^{1}H NMR (400 MHz, D$_2$O): 8.63 (s, 1H, C*H*), 7.41 (s, 1H, C*H*), 7.35 (s, 1H, C*H*), 4.15 (q, *J* = 7.5 Hz, 2H, C*H*$_2$CH$_3$), 3.82 (s, 3H,
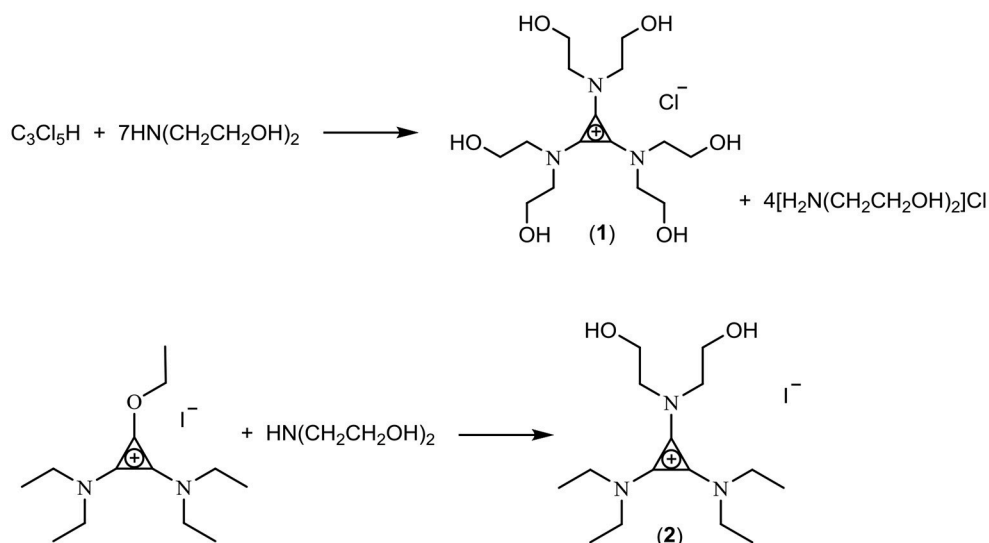
SCHEME 1 | Synthesis of hydroxyl-functionalized TAC salts.
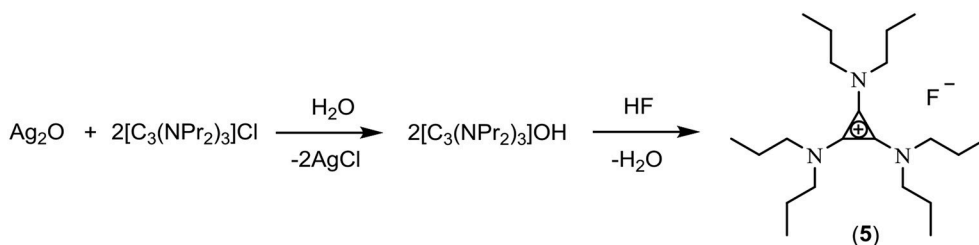
SCHEME 2 | Exchange using silver oxide.
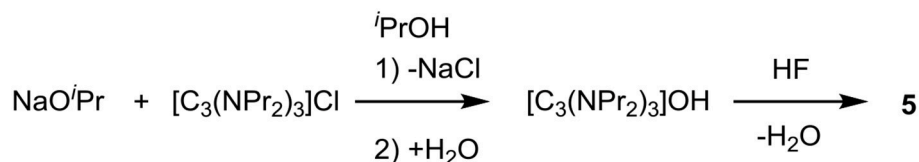
SCHEME 3 | Exchange using sodium isopropoxide.

CH_3), 1.95 (s, 4.8H, CH_3CO_2HF), 1.42 (t, $^3J_{HH} = 7.5$ Hz, 3H, CH_2CH_3). ^{19}F NMR (377 MHz, D_2O): −128.88 (s, CH_3CO_2HF), −142.49 (m, F_2H^-), 24.0:1 ratio. H_2O content: 1240 ppm.

1-Ethyl-3-methylimidazolium fluoride acetic acid, [EMIM]F.2.1AcOH (**6**.2.1AcOH)

Acetic acid (3.58 g, 59.6 mmol) was added to [EMIM]F.1.8EtOH (6.39 g, 29.8 mmol). The mixture was dried with ethanol (3 × 50 mL) azeotropes. Additional acetic acid (0.535 g, 8.91 mmol) was then added. The product was a pale yellow liquid (7.28 g, 96%). ^{1}H NMR (400 MHz, D_2O): 8.62 (s, 1H, CH), 7.40 (s, 1H, CH), 7.33 (s, 1H, CH), 4.14 (q, $J = 7.3$ Hz, 2H, CH_2CH_3), 3.80 (s, 3H, CH_3), 1.95 (s, 6.3H, CH_3CO_2HF), 1.41 (t, $J = 7.3$ Hz, 3H, CH_2CH_3). ^{19}F NMR (377 MHz, D_2O): −128.81 (s, CH_3CO_2HF), −142.48 (m, F_2H^-), 28.4:1 ratio. H_2O content: 1,030 ppm.

1-Ethyl-3-methylimidazolium fluoride acetic acid, [EMIM]F.2.4AcOH (**6**.2.4AcOH)

Acetic acid (4.09 g, 68.1 mmol) was added to [EMIM]F.1.8EtOH (5.83 g, 27.2 mmol). The mixture was dried with ethanol (2 × 50 mL) azeotropes. Additional acetic acid (0.495 g, 8.24 mmol) was then added. The product was a

pale yellow liquid (7.48 g, 99%). ^{1}H NMR (400 MHz, D_2O): 8.60 (s, 1H, CH), 7.39 (s, 1H, CH), 7.32 (s, 1H, CH), 4.13 (q, $^3J_{HH} = 7.3$ Hz, 2H, CH_2CH_3), 3.79 (s, 3H, CH_3), 1.95 (s, 7.2H, CH_3CO_2HF), 1.39 (t, $^3J_{HH} = 7.3$ Hz, 3H, CH_2CH_3). ^{19}F NMR (377 MHz, D_2O): −128.75 (s, CH_3CO_2HF), −142.46 (m, F_2H^-), 16.1:1 ratio. H_2O content: 1,580 ppm.

1-Ethyl-3-methylimidazolium fluoride acetic acid, [EMIM]F.3.2AcOH (**6**.3.2AcOH)

Acetic acid (3.76 g, 62.6 mmol) was added to [EMIM]F.1.8EtOH (4.47 g, 20.8 mmol). The mixture was dried with ethanol (2 × 50 mL) azeotropes. Additional acetic acid (0.825 g, 13.7 mmol) was then added. The product was a pale yellow liquid (5.20 g, 77%). ^{1}H NMR (400 MHz, D_2O): 8.62 (s, 1H, CH), 7.40 (s, 1H, CH), 7.34 (s, 1H, CH), 4.14 (q, $^3J_{HH} = 7.3$ Hz, 2H, CH_2CH_3), 3.81 (s, 3H, CH_3), 1.98 (s, 9.6H, CH_3CO_2HF), 1.42 (t, $^3J_{HH} = 7.3$ Hz, 3H, CH_2CH_3). ^{19}F NMR (377 MHz, D_2O): −128.80 (s, CH_3CO_2HF), −142.57 (m, F_2H^-), 20.4:1 ratio. H_2O content: 900 ppm.

(2-hydroxyethyl)trimethylammonium fluoride hydrate, choline fluoride hydrate (**7**.H_2O)

Choline chloride (10.2 g, 73.2 mmol) was dissolved into water (200 mL) in a blacked out flask. Ag_2O (12.7 g, 54.8 mmol) was added and the solution stirred for 4 h. AgCl was removed by filtration through Celite and the filtrate was neutralized to pH 7.5 with aqueous HF. Water was removed by drying *in vacuo* at 40°C for 72 h to yield a white solid (9.89 g, 91%). Found: C, 40.34; H, 11.24; N, 9.03%. Calc. for $C_5H_{14}NOF.1.43H_2O$: C, 40.34; H, 11.41; N, 9.41%.

SCHEME 4 | Synthesis of fluoride salts using KF in ethanol.

SCHEME 5 | Decomposition of $[C_3(NPr_2)_3]F$.

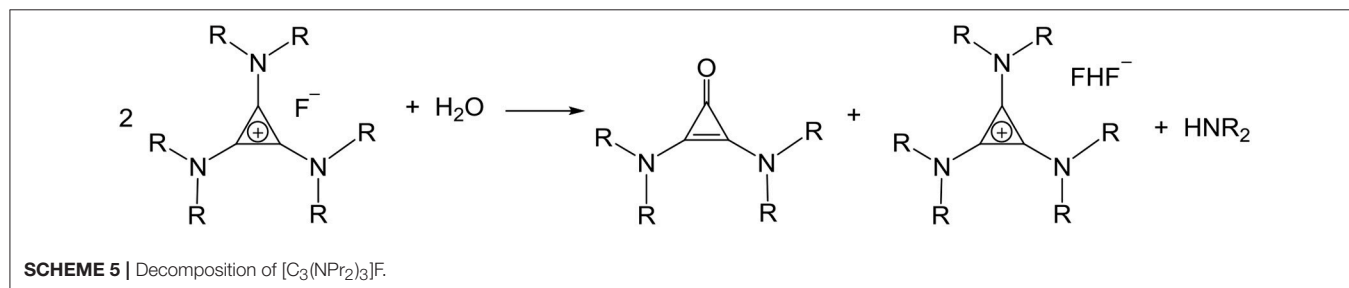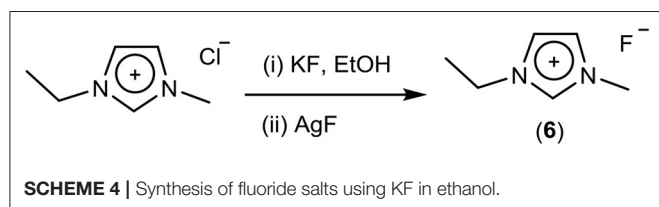**TABLE 1 |** Viscosity data for fluoride solvates (mPa s).

Salt	Temperature (°C)						
	20	25	30	35	40	45	50
5.1.9EtOH	49.6	40.3	32.7	26.8	22.1	18.1	15.4
$[C_3(NPr_2)_3]NTf_2$	220		127		78.3		50.1
$[C_3(NPr_2)_3]DCA$	107		59		35		21
6.1.0AcOH	30.2	24.7	20.2	17.2	14.7	12.7	11.1
6.1.6AcOH	20.5	17.1	14.8	12.7	11.1	9.71	8.58
6.2.1AcOH	17.6	14.8	12.7	11.0	9.61	8.45	7.47
6.2.4AcOH	15.9	13.4	11.5	9.92	8.65	7.60	6.71
6.3.2AcOH	13.8	11.8	10.1	8.82	7.73	6.81	6.03
[EMIM]DCA	19.1	16.1	14.0	11.9	10.4	9.1	8.2
[EMIM]NTf$_2$	38.6		27.1		19.4		14.9

RESULTS AND DISCUSSION

Synthesis

In this work, three classes of cations were studied for the preparation of fluoride ionic liquids: the tris(dialkylamino)cyclopropenium cation $[C_3(NPr_2)_3]^+$, the imidazolium cation $[EMIM]^+$, and hydroxyl-functionalized salts. Two hydroxy-functionalized TAC salts were prepared: Treatment of C_3Cl_5H with $HN(CH_2CH_2OH)_2$ yielded the hexaol TAC product $[C_3(N(CH_2CH_2OH)_2)_3]Cl$ (**1**) whereas a diol TAC salt was prepared by treatment of the alkoxydiamino TAC salt $[C_3(NEt_2)_2OEt]I$ (generated by addition of alkylation of the cyclopropenone $(Et_2N)_2C_3O$ with ethyliodide) with $HN(CH_2CH_2OH)_2$ to give $[C_3(NEt_2)_2N(CH_2CH_2OH)_2]I$ (**2**) (**Scheme 1**). Separation of the hexaol **1** from the excess starting amine and product ammonium salt proved challenging but was eventually achieved by trapping the smaller amine/ammonium salt in Zeolite 13X, which has a 10 Å pore size.

Three methods were investigated for the conversion of chloride salts to fluoride salts: anion metathesis with AgF, neutralization of hydroxide with HF acid, and metathesis with KF in ethanol.

Anion metathesis with AgF from the chloride salt is the most direct route (Maiti et al., 2008; Vitz et al., 2009): addition of AgF to an aqueous solution of a chloride IL precipitates AgCl. This method was used for one synthesis of $[C_3(N(C_2H_4OH)_2)_3]F$ (**3**) and resulted in a final chloride content of 1,600 ppm, ~3% of total anions.

A common and readily-accessible source of fluoride is HF. Since HF is a weak acid, direct metathesis with chloride is difficult, however, the chloride salt can be converted first to a hydroxide salt, which is then neutralized with HF. It should also be noted that TAC ILs are sensitive to concentrated or heated hydroxide solutions with the conversion of TAC cations to cyclopropenones. There were two methods trialed for the conversion of chloride to hydroxide anions: firstly, one using silver oxide and the other using sodium isopropoxide.

The exchange of chloride to hydroxide using Ag_2O (**Scheme 2**) involves mixing Ag_2O with an aqueous solution of the chloride salt in a blacked-out container. Using this method, chloride contents of 500 ppm were obtained. Solutions of **3**, $[C_3(NEt_2)_2N(C_2H_4OH)_2]F$ (**4**) and $[C_3(NPr_2)_3]F$ (**5**) were synthesized using this method.

The exchange of chloride to hydroxide via isopropoxide (**Scheme 3**) involves mixing isopropanol solutions of sodium isopropoxide and the chloride salt, which precipitates NaCl, leaving the cations in solution with isopropoxide. When this isopropoxide salt is added to water, hydroxide anions are formed and neutralization with aqueous HF then generates the fluoride salt. In the case of **5**, the chloride content was 8%, which would significantly affect physical properties.

The final method used for the exchange of chloride to fluoride was the use of KF in ethanol (**Scheme 4**; Dermeik and Sasson, 1989). This method is similar to that of the sodium isopropoxide exchange of chloride to hydroxide. It involves partially dissolving potassium fluoride in ethanol, followed by the addition of the chloride salt. The solubility ratio of potassium fluoride to

TABLE 2 | Fitting parameters for temperature dependence of viscosity.

Salt	η_0 mPa s	B K	T_0 K	D	δ mPa s	$A \times 10^{-3}$ mPa s	E_a kJ mol^{-1}	δ mPa s
5.1.9EtOH	0.020	1292	128	10.1	0.108	0.15	31	0.12
6.1.0AcOH	0.029	1290	106	12.1	0.024	0.60	26	0.28
6.1.6AcOH	0.030	1289	95	13.5	0.030	1.81	23	0.16
6.2.1AcOH	0.028	1289	93	13.9	0.015	1.76	22	0.12
6.2.4AcOH	0.024	1289	94	13.8	0.007	1.48	23	0.10
6.3.2AcOH	0.024	1289	90	14.3	0.004	1.85	22	0.06

TABLE 3 | Conductivity data and fitting parameters for fluoride solvates (mS cm^{-1}).

Salt	Temperature (°C)					$A \times 10^4$ mS cm^{-1}	E_a kJ mol^{-1}	δ mS cm^{-1}
	20	25	30	35	40			
5.1.9EtOH	1.89	2.28	2.74	3.24	3.75	9.19	26	0.03
$[C_3(NPr_2)_3]NTf_2$	0.50		0.86		1.32			
6.1.0AcOH	9.37	10.8	12.4	14.3	16.2	5.16	21	0.03
6.1.6AcOH	11.7	13.2	14.8	17.0	19.1	2.81	19	0.12
6.2.1AcOH	10.8	12.5	14.3	16.2	18.6	3.86	20	0.07
6.2.4AcOH	10.6	11.9	13.4	14.9	16.6	1.24	17	0.01
6.3.2AcOH	10.0	11.5	13.0	14.7	16.4	2.25	19	0.05
[EMIM]DCA	27							
[EMIM]NTf$_2$	7.73	9.12		12.29				

potassium chloride is 25, therefore, due to the lower solubility of potassium chloride, this precipitates out. The ethanol was then removed *in vacuo*, and acetonitrile was added. After cooling, a precipitate of potassium fluoride (and possibly residual chloride) was removed. Ethanol was added and acetonitrile removed *in vacuo* to yield the ethanol solvate. This method was used to synthesize the ethanol solvate of [EMIM]F (**6**), and after carrying out this exchange three times, the chloride content was 3,100 ppm, ~2.4% of total anions, and the potassium ion concentration was 220 ppm, ~0.15% of [EMIM]$^+$. Due to the chloride concentration being higher than preferred, a further step of adding silver fluoride was carried out. The amount of silver fluoride that was added was calculated to lower chloride to <100 ppm, without having excess silver present. The final chloride concentration was 70 ppm.

Once a solution of fluoride ionic liquid is obtained, the solvent needs to be removed, and this is a critical and delicate step. As the fluoride anion becomes less solvated, its basicity increases, which leads to decomposition. We will now discuss a variety of drying techniques that were trialed.
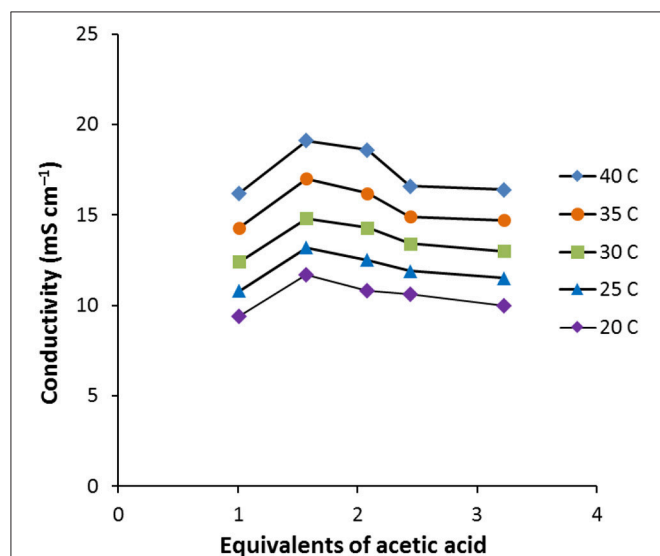
FIGURE 1 | Conductivity vs. equivalents of acetic acid for **6**.nAcOH (n = 1.0, 1.6, 2.1, 2.4, 3.2).

An aqueous solution of $[C_3(NPr_2)_3]F$ was dried on a rotary evaporator at 40°C. This reduced the water content to ~20%, about four water molecules per TAC fluoride. When the temperature or vacuum is increased more water is removed, however, due to the heat and the increasing basicity of the fluoride, the salt decomposed to bis(dipropylamino)cyclopropenone and $[C_3(NPr_2)_3]HF_2$ (**Scheme 5**). Freeze drying was also attempted, the water content dropped to 1.8% but there was 25% decomposition to cyclopropenone.

Heterogeneous azeotrope drying using toluene has been reported previously (Zhao et al., 2008), however, with the fluoride salts this still leads to the TAC fluoride salt being concentrated in a wet phase, and resulted in 30% cyclopropenone. Therefore, homogeneous azeotropes were investigated whereby water is removed before the ionic liquid is concentrated. Both ethanol and isopropanol will form lower boiling homogeneous azeotropes with water, and both were used successfully. Due to the potential of the ionic salt to break the azeotrope, a large excess of ethanol or isopropanol is used. Isopropanol has the advantage of having a higher percentage of water in the azeotrope, so water can be removed with less additional solvent.

Azeotrope drying was used to synthesize **3**, **4**.1.9EtOH, **5**.1.9EtOH, and **6**.1.8EtOH. During the synthesis of **5**.1.9EtOH, repeated additions of dry ethanol produced an ionic liquid fluoride with a water content of 2,200 ppm without cyclopropenone forming. The ethanol solvate could not easily be removed, because the strong hydrogen bonds between the alcohol solvate and fluoride anion provide stability to the IL fluoride.

Using another azeotrope, between benzene and ethanol, further ethanol can be removed from **5**.1.9EtOH to form a monoethanol solvate: one addition of dried benzene to a sample of the diethanol solvate leaves 1.36 ethanol molecules per fluoride. After two more additions, this drops to 1.1 ethanol molecule per fluoride. However, significant amounts (17%) of bis(dipropylamino)cyclopropenone were detected in this product.

A range of acetic acid solvates of an imidazolium fluoride were synthesized with ~1, 1.5, 2, 2.5, and 3 equivalents of acetic acid per fluoride anion. The acetic acid solvates were synthesized from the ethanol solvate **6**.1.8EtOH. Acetic acid was added and the mixture dried using ethanol or isopropanol azeotropes under reduced pressure with only small amounts of acetic acid

TABLE 4 | Density data for imidazolium fluoride solvates (g mL^{-1}).

Salt	Temperature (°C)						
	20	25	30	35	40	45	50
6.1.0AcOH	1.125	1.122	1.118	1.115	1.112	1.108	1.105
6.1.6AcOH	1.121	1.117	1.114	1.110	1.107	1.103	1.100
6.2.1AcOH	1.120	1.116	1.112	1.109	1.105	1.101	1.098
6.2.4AcOH^a	1.119	1.115	1.111	1.107	1.104	1.100	1.096
6.3.2AcOH	1.118	1.114	1.110	1.106	1.102	1.098	1.094

^{a}By interpolation.

being lost. Extra acetic acid was then added to give the desired HOAc/F$^-$ ratio. ^{1}H-NMR was used to determine the precise ratios of acetic acid to [EMIM]$^+$, which were found to be 1.0, 1.6, 2.1, 2.4, and 3.2.

The ^{13}C and ^{19}F NMR spectra also provide evidence for the formation of fluoride hydrogen-bonded anions. The ^{19}F NMR of **5**.1.9EtOH in D$_2$O shows a peak at -122.03 ppm and **6**.1.8EtOH at -121.22 ppm, which is the shift for sodium fluoride in D$_2$O. However, for the various acetic acid mixtures, the ^{19}F NMR peak is around -128.8 ppm. This compares to the shift for [FHF]$^-$, at -142 ppm, hence suggesting that [AcOHF]$^-$ is persisting, or at least a significant contribution, in the D$_2$O solution. A similar observation is made by examining the chemical shift of the methyl protons of the acetic acid. In D$_2$O, acetic acid is observed at 2.08 ppm and the acetate ion at 1.90 ppm (Gottlieb et al., 1997), whereas for the fluoride acetic acid mixtures the chemical shifts are between 1.94 and 1.98 ppm. A small signal for [FHF]$^-$ was also observed due to some dissociation of the fluoride solvate with the acetic acid then generating some H$^+$, which can hydrogen bond to two fluorides.

Properties

The viscosities of **5**.1.9EtOH and the [EMIM]F-acetic acid mixtures were measured over the temperature range 20–50°C

TABLE 5 | Fitting parameters for temperature dependence of density, $\rho = a - bT$.

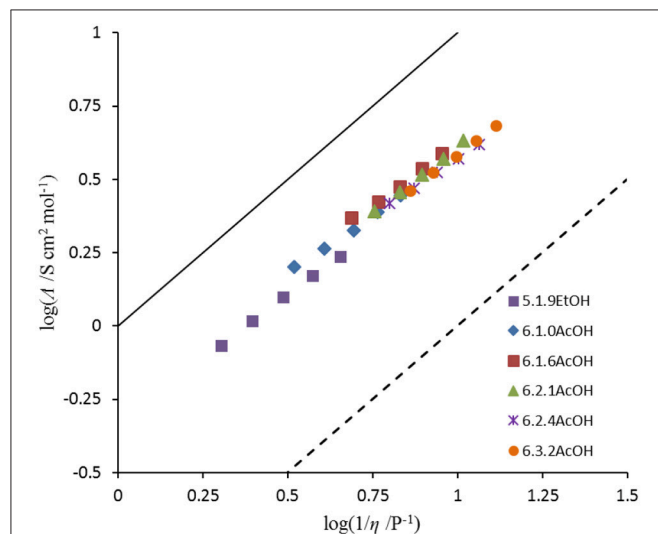| Salt	$b \times 10^4$ g mL^{-1} K^{-1}	a g mL^{-1}	$\delta \times 10^5$
6.1.0AcOH	6.7834	1.3238	2.5
6.1.6AcOH	7.0611	1.3276	2.6
6.2.1AcOH	7.2967	1.3335	2.6
6.3.2AcOH	7.6728	1.3424	2.8

FIGURE 2 | Walden plot of fluoride solvates.

(**Table 1**). Plots of viscosity and conductivity vs. temperature are provided in the **Supplementary Information**. The viscosity of **5**.1.9EtOH is lower than with DCA or NTf$_2^-$ anions (Walst et al., 2015) whereas the [EMIM]F acetic acid solvates are similar to the [EMIM]DCA salt. This is due to the acetic acid or ethanol being a co-solvent with much lower viscosity. While it is not possible to directly compare the viscosities of the acetic acid and ethanol solvates, due to the different cations and different number of solvate molecules, it is seems likely that the viscosity of the ethanol solvates is lower than the acetic acid solvates if the cation and number of solvate molecules is the same. Note that the viscosity of [C$_3$(NPr$_2$)$_3$]NTf$_2$ (**Table 1**) is approximately five times greater than that of [EMIM]NTf$_2$ (Walst et al., 2015), so an increase by a factor of about 2.2 from the EMIM acetic acid solvates to **5**.EtOH is small.

The temperature dependence (**Table 2**) was modeled with the VFT and Arrhenius equations (see **Supplementary Information**). D values (B/T_0) of between 12.1 and 14.3 were found for the acetic acid solvates and 10.1 for **5**.1.9EtOH, suggesting that these solvates are slightly less fragile than other ionic liquids with the same cations. The activation energies are between 22 and 31 kJ mol^{-1}.

Addition of acetic acid decreases the viscosity, for example, from 30.2 with 1.0AcOH to 13.8 mPa s with 3.2AcOH at 20°C. This is due to the acetic acid being a lower viscosity liquid and indicates the presence of increasing amounts of free HOAc.

The conductivities were measured over a temperature range of 20–40°C (**Table 3**). The conductivity of **5**.1.9EtOH is higher than the corresponding NTf$_2^-$ salt whereas the [EMIM]F acetic acid solvates have lower conductivity than the [EMIM]DCA ionic liquid. This is a reflection of the trends seen with the viscosity measurements. As with viscosity, it is not possible to directly compare their viscosities of the acetic acid and ethanol solvates, due to the different cations and different number of solvate molecules, it is probable that the conductivity of ethanol solvates is higher than the acetic acid solvates if the cation and number of solvate molecules is the same. The conductivity of the ethanol solvate is lower due to the large [C$_3$(NPr$_2$)$_3$]$^+$ cation, which causes higher viscosity and lowers the number of charge carriers in a given volume.

The temperature dependence of the conductivity (**Table 3**) was modeled with the Arrhenius equation (see **Supplementary Information**). The activation energies were between 17 and 26 kJ mol^{-1}. Due to the very limited temperature range and limited number of data points, the fitting to the

TABLE 6 | Walden product and deviation from ideal at 20°C.

Salt	Walden product	ΔW
5.1.9EtOH	0.43	0.37
6.1.0AcOH	0.48	0.32
6.1.6AcOH	0.48	0.32
6.2.1AcOH	0.43	0.36
6.2.4AcOH	0.42	0.38
6.3.2AcOH	0.40	0.40

VFT equation did not produce sensible results, so they are not reported here.

As the amount of acetic acid (**Figure 1**) increases, the conductivity increases from 9.4 mS cm^{-1} for [C$_2$MIM]F.1.0AcOH to 11.7 mS cm^{-1} for [C$_2$MIM]F.1.6AcOH, it then decreases to 10.0 mS cm^{-1} for [C$_2$MIM]F.3.2AcOH as further acetic acid is added. Initially, the molar conductivity increases, consistent with decreasing viscosity, but further acetic acid decreases the concentration of ions.

The densities for the [EMIM]F acetic acid mixtures were measured from 20 to 50°C (**Table 4**). As expected, density decreases as the relative concentration of acetic acid increases due to the lower density of acetic acid, and the density is linearly dependent on temperature (**Table 5**).

The ionicity of the fluoride solvates was assessed using a Walden plot (**Figure 2**; Xu et al., 2003). To complete the set of calculations, the density of **5**.1.9EtOH was approximated by that of [C$_3$(NPr$_2$)$_3$]DCA. The Walden product (= σ.η) and the deviation from ideal ionic behavior in the Walden plot, ΔW, are given in **Table 6**. The Walden products for the fluoride solvates

are between 0.40 and 0.48 S cm^2 P mol^{-1} and deviations from the ideal ionic behavior are between 0.32 and 0.40. Hence, all of the fluoride solvate ionic liquids can be classified as good ionic liquids in terms of the ionicity (Xu et al., 2003), with some degree of ion association or correlations evident suggesting some residual specific interaction between the cation and the anion solvate. There is a slight increase in ΔW as the amount of acetic acid increases. As a comparison, **6**.2.3HF has a higher Walden product of 0.76 and a lower ΔW of 0.12 (Hagiwara et al., 2003); in that case, there is the potential for a contribution from proton hopping, which increases molar conductivity.

Thermally stable ionic liquids would be desirable as they could be used in applications at elevated temperatures, however, the reactivity of fluoride and the volatility of acetic acid and ethanol are expected to hinder stability. The TGA of the TAC fluoride ethanol solvate **5**.1.9EtOH (**Figure 3**) shows steady weight loss from ∼50°C. Initially, this is likely to be loss of ethanol, which will lead to the decomposition of the cation.

The TGA of the dihydroxyl derivative **4** (**Figure 4**) shows a profile similar to that of [C$_3$(N(C$_2$H$_4$OH)$_2$)$_3$]F, with little
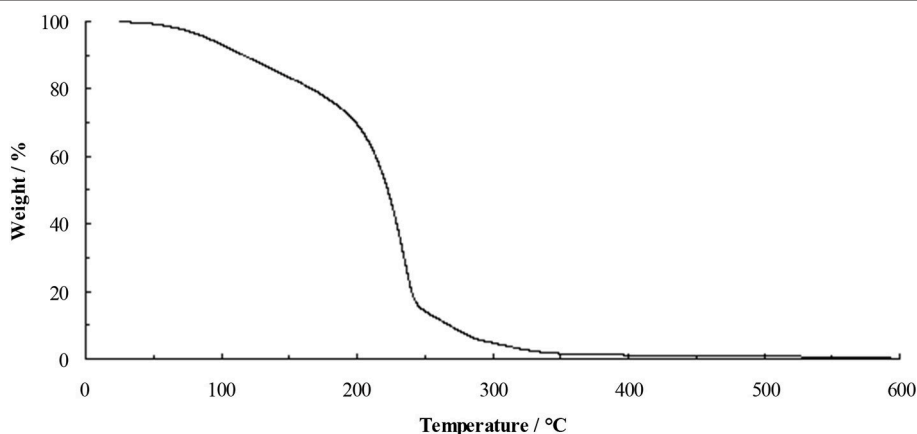
FIGURE 3 | TGA of **5**.1.9EtOH at 10°C min^{-1}.
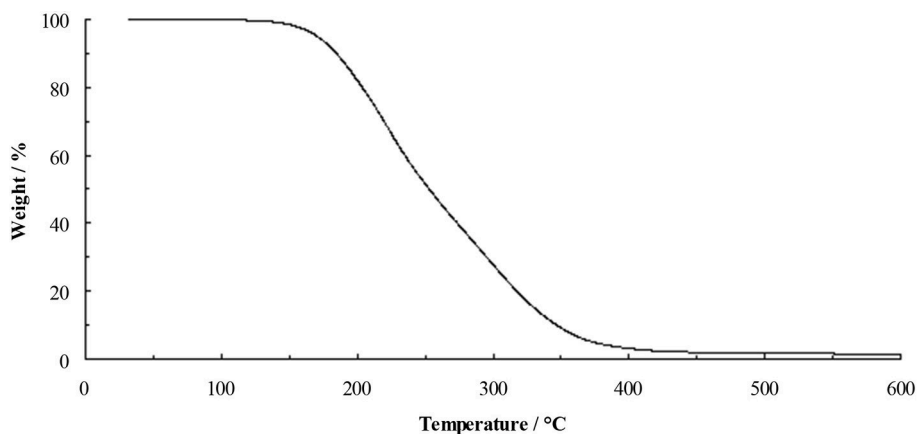
FIGURE 4 | TGA of [C$_3$(NEt$_2$)$_2$N(C$_2$H$_4$OH)$_2$]F **(4)** at 10°C min^{-1}.

weight loss before onset of decomposition at 175°C. This clearly indicates that hydroxyl functional groups do stabilize the fluoride anion. Salt **4** is a highly-viscous yellow liquid at ambient temperature, however, it is very sensitive to trace water and much care needs to be taken when drying this material.

The TGA of the hexahydroxyl derivative **3** shows an increase in stability compared to **4** with onset of decomposition at 191°C (**Supplementary Information**). The onset temperature is, as expected, much lower than other ionic liquids with non-coordinating anions such as NTf_2^-, which can exceed 400°C. Potentially useful is the observation of the melting point at 87°C, which indicates a stable ionic liquid range at elevated temperatures. It is notably less sensitive to moisture during the drying process compared to **4**. A sample of (2-hydroxyethyl)trimethylammonium (choline) fluoride hydrate (**7**.H_2O) was prepared from the chloride salt using silver oxide and aqueous HF. The TGA shows good thermal stability compared to the ethanol solvate of **5**, with an onset temperature of 139°C (**Supplementary Information**). However, this salt is a solid and no melting point is observed prior to decomposition.

The thermal behavior of **6**.1.6AcOH and **6**.3.2AcOH were examined using DSC: glass transitions were observed at −92 and −95°C, respectively, however, no melting points were observed.

CONCLUSIONS

Ionic liquid fluorides were synthesized by exchange of chloride to fluoride using one of three methods: anion metathesis with silver fluoride, anion metathesis using aqueous silver oxide followed by neutralization with HF acid or anion metathesis with potassium fluoride in ethanol. The fluoride salts were then isolated using homogeneous azetrope drying.

Whereas, naked fluoride salts are not stable in pure form, fluoride solvates with ethanol and acetic acid were found to be much more stable, probably due to strong hydrogen bond formation. Increasing amounts of acetic acid solvate decreases the viscosity and density, while the conductivity peaked at **6**.1.6AcOH.

The low decomposition temperature of **5**.1.9EtOH (starting at 50°C) led to the rational design of ionic liquids containing hydroxyl-functionalized cations; **3** and **4**. These liquids demonstrate improved thermal stability with higher decomposition temperatures of 175 and 191°C, respectively, consistent with stabilization by intramolecular hydroxyl-fluoride bonding, leading to ionic liquids that are stable as the unsolvated ionic liquid fluorides.

AUTHOR CONTRIBUTIONS

OC conceived of the project and directed the TAC work. DM conceived of the acetic acid solvate concept and directed this work. KW carried out the experimental work. All authors made critical contributions to the report, gave significant input into the report writing process and analysis of data herein.

ACKNOWLEDGMENTS

SUPPLEMENTARY MATERIAL

The Supplementary Material for this article can be found online at: https://www.frontiersin.org/articles/10.3389/fchem.2018.00603/full#supplementary-material

REFERENCES

Butchard, J. R., Curnow, O. J., Garrett, D. J., and Maclagan, R. G. (2006). Structure of a discrete dichloride hexahydrate cube as a tris(diisopropylamino)cyclopropenium salt. *Angew. Chem. Int. Ed.* 45, 7550–7553. doi: 10.1002/anie.200603547

Christie, K. O., and Jenkins, H. D. B. (2003). Quantitative measure for the "nakedness" of fluoride ion sources. *J. Am. Chem. Soc.* 125, 9457–9461. doi: 10.1021/ja035675r

Curnow, O. J., Holmes, M. T., Ratten, L. C., Walst, K. J., and Yunis, R. (2012). A facile route to functionalised, protic and chiral ionic liquids based on the triaminocyclopropenium cation. *RSC Adv.* 2, 10794–10797. doi: 10.1039/c2ra22078d

Curnow, O. J., MacFarlane, D. R., and Walst, K. J. (2011). Triaminocyclopropenium salts as ionic liquids. *Chem. Commun.* 47, 10248–10250. doi: 10.1039/c1cc13979g

Dermeik, S., and Sasson, Y. (1989). Synthesis of quaternary ammonium fluoride salts by a solid-liquid halogen exchange process in protic solvents. *J. Org. Chem.* 54, 4827–4829. doi: 10.1021/jo00281a024

Golubev, N. S., Tolstoy, P. M., Smirnov, S. N., Denisov, G. S., and Limbach, H.-H. (2004). Low-temperature NMR spectra of fluoride–acetic acid hydrogen-bonded complexes in aprotic polar environment. *J. Mol. Struct.* 700, 3–12. doi: 10.1016/j.molstruc.2004.01.024

Gottlieb, H. E., Kotlyar, V., and Nudelman, A. (1997). NMR chemical shifts of common laboratory solvents as trace impurities. *J. Org. Chem.* 62, 7512–7515. doi: 10.1021/jo971176v

Hagiwara, R., Hirashige, T., Tsuda, T., and Ito, Y. (1999). Acidic 1-ethyl-3-methylimidazolium fluoride: a new room temperature ionic liquid. *J. Fluorine Chem.* 99, 1–3. doi: 10.1016/S0022-1139(99)00111-6

Hagiwara, R., Matsumoto, K., Nakamori, Y., Tsuda, T., Ito, Y., Matsumoto, H., et al. (2003). Physicochemical properties of 1,3-Dialkylimidazolium fluorohydrogenate room-temperature molten salts. *J. Electrochem. Soc.* 150, D195–D199. doi: 10.1149/1.1621414

Johansson, K. M., Izgorodin, E. I., Forsyth, M., MacFarlane, D. R., and Seddon, K. R. (2008). Protic ionic liquids based on the dimeric and oligomeric anions: $[(AcO)_xH_{x-1}]^-$. *Phys. Chem. Chem. Phys.* 10, 2972–2978. doi: 10.1039/b801405a

Kim, D. W., Jeong, H.-J., Lim, S. T., and Sohn, M.-H. (2008). Tetrabutylammonium tetra(tert-butyl alcohol)-coordinated fluoride as a facile fluoride source. *Angew. Chem. Int. Ed.* 47, 8404–8406. doi: 10.1002/anie.200803150

Larson, J. W., and McMahon, T. B. (1983). Strong hydrogen bonding in gas-phase anions. An ion cyclotron resonance determination of fluoride binding energetics to Broensted acids from gas-phase fluoride exchange equilibrium measurements. *J. Am. Chem. Soc.* 105, 2944–2950. doi: 10.1021/ja00348a003

Maiti, A., Pagoria, P. F., Gash, A. E., Han, T. Y., Orme, C. A., Gee, R. H., et al. (2008). Solvent screening for a hard-to-dissolve molecular crystal. *Phys. Chem. Chem. Phys.* 10, 5050–5056. doi: 10.1039/B805169K

Mallik, B. S., and Siepmann, J. I. (2010). Thermodynamic, structural and transport properties of tetramethyl ammonium fluoride: first principles molecular dynamics simulations of an unusual ionic liquid. *J. Phys. Chem. B* 114, 12577–12584. doi: 10.1021/jp104261h

Sun, H., and DiMagno, S. G. (2005). Anhydrous tetrabutylammonium fluoride. *J. Am. Chem. Soc.* 127, 2050–2051. doi: 10.1021/ja0440497

Swatloski, R. P., Holbrey, J. D., and Rogers, R. D. (2003). Ionic liquids are not always green: hydrolysis of 1-butyl-3-methylimidazolium hexafluorophosphate. *Green Chem.* 5, 361–363. doi: 10.1039/b304400a

Turner, E. A., Pye, C. C., and Singer, R. D. (2003). Use of *ab initio* calculations toward the rational design of room temperature ionic liquids. *J. Phys. Chem. A* 107, 2277–2288. doi: 10.1021/jp021694w

Vitz, J., Erdmenger, T., Haensch, C., and Schubert, U. S. (2009). Extended dissolution studies of cellulose in imidazolium based ionic liquids. *Green Chem.* 11, 417–424. doi: 10.1039/b818061j

Wallace, A. J., Jayasinghe, C. D., Polson, M. I. J., Curnow, O. J., and Crittenden, D. L. (2015). Cyclopropenium cations break the rules of attraction to form closely bound dimers. *J. Am. Chem. Soc.* 137, 15528–15532. doi: 10.1021/jacs.5b10388

Walst, K. J. (2012). *Synthesis and Characterization of Triaminocyclopropenium Ionic Liquids.* Ph.D. thesis, University of Canterbury, Christchurch.

Walst, K. J., Yunis, R., Bayley, P. M., MacFarlane, D. R., Ward, C. J., Wang, R., et al. (2015). Synthesis and physical properties of tris(dialkylamino)cyclopropenium bistriflamide ionic liquids. *RSC Adv.* 5, 39565–39579. doi: 10.1039/C5RA05254H

Weiss, R., Brenner, T., Hampel, F., and Wolski, A. (1995a). The consequences of an electrostatic "forced marriage" between two electron-rich particles: strained ion pairs. *Angew. Chem. Int. Ed. Engl.* 34, 439–441. doi: 10.1002/anie.199504391

Weiss, R., Rechinger, M., Hampel, F., and Wolski, A. (1995b). Stable 1:1 adducts from iodoacetylenes and iodide ions: ion pair strain as an additional driving force? *Angew. Chem. Int. Ed. Engl.* 34, 441–443. doi: 10.1002/anie.199504411

Wenthold, P. G., and Squires, R. R. (1995). Bond dissociation energies of F_2^- and HF_2^-. A gas-phase experimental and G2 theoretical study. *J. Phys. Chem.* 99, 2002–2005. doi: 10.1021/j100007a034

Xu, W., Cooper, E. I., and Angell, C. A. (2003). Ionic liquids: ion mobilities, glass temperatures, and fragilities. *J. Phys. Chem. B* 107, 6170–6178. doi: 10.1021/jp0275894

Zhao, C., Burrell, G., Torriero, A. A. J., Separovic, F., Dunlop, N. F., MacFarlane, D. R., et al. (2008). Electrochemistry of room temperature protic ionic liquids. *J. Phys. Chem. B* 112, 6923–6936. doi: 10.1021/jp711804j

Conflict of Interest Statement: The authors declare that the research was conducted in the absence of any commercial or financial relationships that could be construed as a potential conflict of interest.

Physicochemical Properties of Various 2-Hydroxyethylammonium Sulfonate -Based Protic Ionic Liquids and Their Potential Application in Hydrodeoxygenation

Guangming Cai [1,2], Shaoqi Yang [1,2], Qing Zhou [1,2*], Lifei Liu [1], Xingmei Lu [1,2], Junli Xu [1] and Suojiang Zhang [1,2*]

[1] Beijing Key Laboratory of Ionic Liquids Clean Process, CAS Key Laboratory of Green Process and Engineering, State Key Laboratory of Multiphase Complex Systems, Institute of Process Engineering, Chinese Academy of Sciences, Beijing, China, [2] School of Chemical Engineering, University of Chinese Academy of Sciences, Beijing, China

In order to obtain the regularities of physicochemical properties of hydroxy protic ionic liquids (PILs) and broaden their potential application, a series of 2-hydroxyethylammonium sulfonate-based PILs were synthesized through proton transfer reaction and characterized by NMR and FT-IR and elemental analysis. Their phase transfer behavior (T_m) and initial decomposition point (T_d) were characterized by differential scanning calorimetry (DSC) and thermogravimetric analysis (TGA), respectively. Meanwhile, the regularities of density (ρ), viscosity (η) and electrical conductivity (σ) of synthesized PILs at different temperatures were measured. The results indicated that their physicochemical properties were tightly related with their structures and the interactions between cations and anions. In addition, the dissociation constants (pKa) of synthesized PILs were obtained by acid-base titration, which revealed that all synthesized PILs had pKa exceeding 7 and their cations were the crux of determining the pKa value. Moreover, several synthesized PILs with a low melting temperature also showed potential application in the deoxidation reaction of cyclohexanol, as they had conversion rates approximating 100% and the selectivity of cyclohexane or cyclohexene was about 80%.

Keywords: protic ionic liquids, density, viscosity, electrical conductivity, dissociation constants, deoxidation reaction

INTRODUCTION

Due to their unique and tunable characteristics, like low vapor pressure, high thermal stability, high conductivity and low flammability, ionic liquids (ILs), as a kind of functionalized solvents, have gained a lot of attention around the world (Wang et al., 2016; Miran et al., 2018; Xia et al., 2018; Yuan et al., 2018). In general, ILs can be classified in two categories, aprotic and protic ionic liquids (PILs), according to their structure characteristics (Greaves and Drummond, 2015; Shang et al., 2017). Among them, PILs are prepared by the neutralization reaction of certain Brønsted acids and Brønsted bases (generally from primary, secondary or tertiary amines, which are alkaline) and the fundamental feature of these kinds of ILs is that their cations have at least one available proton to

form hydrogen bond with anions (Vijayraghavan et al., 2013; Greaves and Drummond, 2015). In addition to the above aspects, the biggest advantage of PILs is the low-cost and simple synthetic procedure, which means that there is a great potential for large-scale applications (Brandt-Talbot et al., 2017; Sun et al., 2017). In recent years, PILs have been widely applied in electrochemistry (Armand et al., 2009; Vogl et al., 2014), natural products extraction (Tang et al., 2012), liquid-liquid extractions and separation (Elshwishin et al., 2014), gas capture (Shang et al., 2017), biomass processing (Elgharbawy et al., 2016; Brandt-Talbot et al., 2017; Sun et al., 2017; Yang et al., 2018), as well as catalytic processes (Vancov et al., 2012; Vekariya, 2017).

In order to meet the experimental or practical requirements, many attempts have been made to synthesize PILs with different anions and cations according to the desired properties (Brandt-Talbot et al., 2017; Shang et al., 2017; Sun et al., 2017; Qu et al., 2018; Yang et al., 2018). In this process, the type of PILs with hydroxy cation increasingly draws attention from academic and industrial application fields, because the hydroxy group in ILs facilitates the formation of strong hydrogen bonds between PILs and various substrates (Greaves and Drummond, 2015; Yang et al., 2018). This feature promotes hydroxy PILs to be applied in many fields. For example, S. Yang et al. used the hydroxy PILs to pretreat lignocelluloses and the results showed that PILs displayed good efficiency for extracting cellulose from corn straw (Yang et al., 2018). J. Sun et al. demonstrated that ethanolamine acetate was effective to produce cellulosic ethanol from switch grass in one-pot process (Sun et al., 2017). In addition to the consideration of cationic species, anions are also significant in the process of designing PILs in that the anions of PILs, as a kind of deprotonated acids, play crucial roles in many fields, like catalysis, gas absorption as well as biomass pretreatment and so on (Latos et al., 2018; Ren et al., 2018). Therefore, the combination of acidic anions and basic cations with various functional groups of PILs foreshadows a lot of meaningful and useful properties, which can widen potential applications of this type of PILs.

In recent years, a large number of hydroxy PILs have been reported in the literature along with their potential application (Sun et al., 2017; Ren et al., 2018; Yang et al., 2018). However, there is little exploration between molecular structures and physicochemical properties about hydroxy PILs, which has limited the further predication of physicochemical properties for this type of PILs (Xuedan Song et al., 2012). In this work, a series of 2-hydroxyethylammonium sulfonate-based PILs are synthesized and characterized by NMR, FT-IR, TGA, and DSC systematically. Also, their physicochemical properties, such as density (ρ), viscosity (η), electrical conductivity (σ) and acid-base property (pKa) are measured by density meter, viscometer, conductivity meter and acid-base titration, respectively. Moreover, the regularities of physicochemical properties about the PILs are explained through molecular structures and the interactions between cations and anions, which is helpful to predict the change law of similar PILs in the future. Furthermore, the deoxygenation is a very important reaction during lignin hydrodeoxygenation (HDO) processes (Yan et al., 2010; Chen et al., 2016, 2017). These reactions are

mostly catalyzed by using noble metal catalysts or protic acids according to the reported methods (Güvenatam et al., 2014). Herein, in order to explore the applicability of the synthesized ILs, several PILs with a low melting temperature are used as the potential catalysts for the deoxygenation reaction with cyclohexanol as the substrate.

## EXPERIMENTAL SECTION

Materials

The PILs presented in this manuscript were synthesized following the procedures described in the next section. N-methyldiethanolamine (>99%), N, N-dimethylethanolamine (>99%), triethanolamine (>99%), methanesulfonic acid (>99%), trifluoromethanesulfonic acid (>98%), benzenesulfonic acid (>98%), dodecane (GC, $\geq$99.0%), cyclohexanol (GC, >99.5%), cyclohexene (GC, >99.5%), cyclohexane (GC, >99.5%), and methyl tert-butyl ether (>99.5%) were from Aladdin Chemistry Co., Ltd. and were used as received. Ethanolamine (>99%) and diethanolamine (>99%) were from Xilong Chemical Co., Ltd. Ethyl acetate (>99.5%), ether (>99.5%) and methanol (>99.5%) were purchased from Sinopharm Chemical Reagent Co., Ltd. H_2 was provided by the Beijing Beiwen Gas Factory, and the purity was 99.999%.

Synthesis Procedures

All PILs were synthesized according to the same reaction mechanism, which was the neutralization reaction of Brønsted acids and Brønsted bases. Other references had reported the relevant synthesis procedures with similar structures (Xuedan Song et al., 2012; Cao et al., 2015; Hosseini et al., 2018), but the operation procedures were slightly different. The relevant structure of cations and anions of synthesized PILs are shown in **Figure 1** and their description and abbreviation are presented in **Table 1**. Among them, [MDEA][mesy], [DMEA][mesy], [TEA][mesy], [TEA][OTf], [TEA][Bsa], [ETA][OTf], and [DEA][OTf] have been reported in other studies (Xuedan Song et al., 2012; Gruzdev et al., 2017; Yang et al., 2018). The remaining PILs were reported for the first time in this study.

Synthesis of PILs Containing Methanesulfonate

A 500 mL one-neck flask and a 250 mL constant pressure dropping funnel were used to assemble the reaction apparatus. Using 200 mL methanol as the solvent, 0.1 mol of methanesulfonic acid was added in the equimolar alkanolamine solution (N-methyldiethanolamine, N, N-dimethylethanolamine, triethanolamine, ethanolamine, and diethanolamine) drop by drop in the condition of ice bath stirring (at 600 rpm) with a magnetic stirrer (**IKA**® **C-MAG** HS 7). The reaction was acted at room temperature for 48 h. Then, the methanol was removed by rotary evaporation (RE-2000E, Beijing Xingde Instrument Equipment Co., Ltd.) at 40°C and vacuum degree of 0.1 MPa for 2 h, thus the corresponding PILs were obtained. 200 mL Ethyl acetate and ether were used to wash the PILs three times, respectively. Then all PILs were

FIGURE 1 | The cations and anions structures of synthetized PILs.
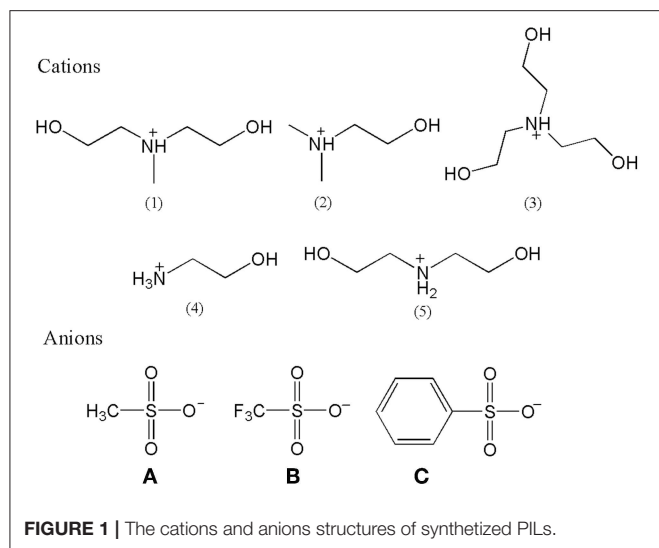
TABLE 1 | The description and abbreviation of synthesized PILs.

No.	Description	Abbreviation
1a	N-methyl- Bis(2-hydroxyethyl)ammonium methanesulfonate	[MDEA][mesy]
2a	N,N-dimethyl-2-hydroxyethylammonium methanesulfonate	[DMEA][mesy]
3a	Tris(2-hydroxyethyl)ammonium methanesulfonate	[TEA][mesy]
4a	2-hydroxyethylammonium methanesulfonate	[ETA][mesy]
5a	Bis(2-hydroxyethyl)ammonium methanesulfonate	[DEA][mesy]
1b	N-methyl- Bis(2-hydroxyethyl)ammonium trifluoromethanesulfonate	[MDEA][OTf]
2b	N,N-dimethyl-2-hydroxyethylammonium trifluoromethanesulfonate	[DMEA][OTf]
3b	Tris(2-hydroxyethyl)ammonium trifluoromethanesulfonate	[TEA][OTf]
4b	2-hydroxyethylammonium trifluoromethanesulfonate	[ETA][OTf]
5b	Bis(2-hydroxyethyl)ammonium trifluoromethanesulfonate	[DEA][OTf]
1c	N-methyl- Bis(2-hydroxyethyl)ammonium benzenesulfonate	[MDEA][Bsa]
2c	N,N-dimethyl-2-hydroxyethylammonium benzenesulfonate	[DMEA][Bsa]
3c	Tris(2-hydroxyethyl)ammonium benzenesulfonate	[TEA][Bsa]
4c	2-hydroxyethylammonium benzenesulfonate	[ETA][Bsa]
5c	Bis(2-hydroxyethyl)ammonium benzenesulfonate	[DEA][Bsa]

dried out in a vacuum drying oven (DZG-6021, Shanghai Sumsung Laboratory Instrument Co., Ltd.) in the condition of water absorbent P_2O_5 at $60°C$ and vacuum degree of 0.1 MPa for 120 h. To maintain high water absorption, P_2O_5 was replaced every 10 h.

Synthesis of PILs Containing Trifluoromethanesulphonate and Benzenesulfonate

As trifluoromethanesulfonic acid could easily absorb water in the air, the agent was quickly transferred and reacted in the

glove box. Also, before benzenesulfonic acid was used, 0.1 mol benzenesulfonic acid was dissolved in 100 mL of methanol to make the solution, because the acid was in a solid state at room temperature. The remaining procedures were similar to the procedures of the synthesis of methanesulfonate PILs.

Instrumental and Operation Procedures
NMR and FT-IR Spectroscopy as Well as CHNS Analysis

The synthesized PILs were characterized by ^{1}H and ^{13}C NMR (AVANCE III HD-600 MHz, Bruker, Switzerland) in deuterated dimethyl sulfoxide (DMSO-d_6) with reference of TMS. FT-IR (10,000–370 cm^{-1}, Thermo Nicolet 380 spectrometer, America) was used to verify the chemical bond vibration peaks of synthesized PILs. The range of scanning wavelength was 4,000–400 cm^{-1} at a repeat of 32 times with a KBr tablet. An elementar vario EL cube was used for the elemental analysis. Before the measurement, each PIL (2–3 mg) was capsuled in tin capsules (volume 0.05 mL) with three parallel samples. The final results were obtained by calculating the arithmetic mean values of the three samples.

Water Content

The water content of synthesized PILs were determined by Karl Fischer titrator (METTLER TOLEDO, C20 Coulometric KF Titrator). Before water measurement, the titrator was turned on and ran the baseline to make the water content balance at about 10 ppm. Approximately 3 mg PILs sample was then pipetted into the instrument using a plastic dropper to begin moisture measurements. The water was measured immediately after PILs were dried out in vacuum drying oven for 120 h.

Thermogravimetric Analysis (TGA)

TG/DTA6300 (Hitachi, JP) was used to get the TGA curves. About 15 mg PILs samples were heated in the TGA crucible from room temperature to $100°C$ at a rate of $10°C$/min at flow of 50 mL/min N_2 carrier first. It was set to remove any possible volatile impurities (such as water, washing solvents) in the PILs. When the crucible cooled to room temperatures again, the sample was heated to $800°C$ under the same conditions. The instrument recorded the weight residue percentage automatically.

Differential Scanning Calorimetry (DSC)

Differential scanning calorimetry (DSC) was performed using METTLER TOLEDO DSC 1 ST**A**R^e System in a sealed aluminum pan under nitrogen atmosphere (50 mL/min). Ultramicro electronic balance (METTLER TOLEDO, XS105 DualRange) was used to weigh about 5 mg PILs. Temperature programming was set from 25 to $100°C$ at a heating rate of $10°C$ min^{-1}, then keeping 10 min to evaporate the remaining water or any volatile impurities in the sample. Finally, the temperature was decreased to $-50°C$ and from there, the temperature programming started to increase from -50 to $350°C$ at the same heating rate.

Density (ρ) and Viscosity (η) Measurement

The density and viscosity of synthesized PILs were measured by an all-in-one machine comprised of Anton Paar DMA^{TM} 5000 M density meter and Anton Paar micro viscometer Lovis 2000 ME

at temperature (293.15–353.15) K. The density meter's accuracy is ± 0.000007 g/cm³ and the temperature in density chamber can accurate to 0.01 K. The micro viscometer's accuracy can up to ± 0.5% in the experiment and the temperature of glass capillaries can precise to ± 0.02 K. There are three kinds of glass capillaries (1.59, 1.8, 2.5) mm with viscosity range of (0.3–15,10–100 and 100–10,000) mPa·s, respectively. The capillaries were calibrated by Anton Paar company before using. All samples were degassed in the condition of 320 K before measuring. Every point was repeated at least three times and the calculated average was used as the final data.

Electrical Conductivity (σ)

The conductivity of all PILs samples was measured by conductivity meter (METTLER TOLEDO FiveEasy Plus) at the temperature range from (303.15 to 343.15) K. The maximum operating temperature of the conductivity cell was 353.15 K due to restrictions imposed by its plastic framework. Before measuring, the electrode of conductivity meter was calibrated using the standard solutions.

Thermodynamic Dissociation Constants (pK_a) Determination

The standard method of determining the pK_a of substance was described in the literature (Chen et al., 2014). The pK_a values of various PILs were obtained by acid–base titration. The specific operation steps were listed in the **Supplementary Material**. The dissociation constant was expressed as follows:

$$K_a = \frac{[Na^+] + [SH_2^+]}{[MSO_3^-] - [Na^+] - [SH_2^+]} * [SH_2^+] \tag{1}$$

where [X] stands for the concentration of each ion at any moment of titration and the [MSO_3^-] stands for the concentration of anion of each PIL in the experiments. The Equation (1) is applicable when the initial pH of solution is <7 and the only unknown value is [SH_2^+]. In order to obtain the value of the unknown [SH_2^+], the following equation was used to confirm its value:

$$[SH_2^+] = \frac{a[SH_2^+]}{f[SH_2^+]} \tag{2}$$

where $f[SH_2^+]$ is the activity coefficient and $a[SH_2^+]$ is the activity of [SH_2^+]. By using a series of volume and concentration data of titrant and titrand, the value of pK_a could be calculated. A more detailed derivation process can be seen in the **Supplementary Material**.

Catalytic Reaction for the Deoxidation of Cyclohexanol

The chemicals of cyclohexanol (1 mmol), ionic liquid (2 g) and n-dodecane (1 mmol) were added into an autoclave with a Teflon® cell. The reaction system was sealed and purged with high-purity hydrogen for at least three times in order to get the air out of the cell. Then the autoclave was pressurized with 4 MPa H₂ at room temperature. The autoclave was heated from room temperature to 120°C. When the temperature rose to the set

point, the agitator was opened about 600 rpm and timing started for 6 h. After the reaction finished, the autoclave was cooled in ice bath for about 2 h. The final products were extracted by 8 ml methyl tert-butyl ether (MBTE) and analyzed through gas chromatography mass spectrometry (GC-MS, Shimadzu GCMS-QP2020), and quantified with gas chromatography equipment (GC-2014, Shimadzu). The GC system was equipped with a capillary column from Agilent (RTX-5®, 30 m × 0.25 mm × 0.25 μm) connecting flame ionization detector (FID) for quantification. N-dodecane was used as the internal standard in the experiments.

RESULTS AND DISCUSSION

Characterization of Synthesized PILs

The ¹H and ¹³C NMR spectra are presented in **Figures S1–S15**. From the spectra, all H and C atoms shifts and peaks corresponded to the structures of PILs with reference of TMS. Meanwhile, the areas of peak were proportionable with the number of H atoms in the PILs. CHNS analysis indicated that the proportion of each element in synthesized PILs was consistent with the calculated values. The specific found values of CHNS analysis are listed in the **Supplementary Material**. In addition, all infrared spectra of explored PILs are presented in **Figures S16–S30** in the Supplementary Material and the infrared absorption peaks corresponded to the corresponding groups. What's more, The Karl Fischer titration results indicated that water was about (1,000–3,000) ppm for most part of samples. The specific water content of all samples are presented in **Table S1** in the Supplementary Material. Combining the analysis of ¹H NMR, ¹³C NMR, CHNS analysis and FT-IR spectra as well as Karl Fischer titration and elemental analysis, the purity of PILs containing methanesulfonate and trifluoromethanesulphonate was more than 99% and those containing benzenesulfonate exceeded 98%.

TGA and DSC Analysis

Thermogravimetric analysis (TGA) is an available way to characterize the thermostability of synthesized PILs and get their initial decomposition temperature (T_d) as well as to ascertain their feasible working temperature range. The regularities of weight loss of various PILs with the increase of temperature are shown in **Figure S31** and the temperature at 5 % weight loss of sample was identified as T_d (Castro et al., 2016; Huang et al., 2018). The T_d of all synthesized PILs are presented in **Table 2**. Among them, [ETA][OTf] had the highest T_d (314°C) and [DMEA][mesy] had the lowest one (156°C). In addition, it was noteworthy that the T_d was closely related to cations. In other words, PILs with the same cation have similar T_d. For example, the T_d of [TEA][mesy], [TEA][OTf] and [TEA][Bsa] were 266, 278, and 260°C, respectively. However, the T_d of [MDEA][mesy], [DMEA][mesy], [TEA][mesy], [ETA][mesy], and [DEA][mesy] were 205, 156, 266, 286, and 289°C, that varied greatly. Also, for the majority of synthesized PILs, they were degraded step by step as shown in **Figure S31**. The most probable reason for this phenomenon was that the thermostability of anions and cations were different because they consisted

of different groups. For example, for the cation containing hydroxyl, it was very easy to dehydrate at high temperature. Therefore, with the increase of temperature, the components that were thermal unstable degraded first and the components that were thermal stable decomposed later (Maton et al., 2013, Venkatraman and Alsberg, 2016).

Except for that, the melting points (T_m) of various PILs were explored making use of the DSC curve. The curves are shown in **Figure S32** in the Supplementary Material and the T_m are presented in **Table 2**. **Table 2** clearly shows that the T_m of most of synthesized PILs were below 0°C and only [DMEA][mesy] and [ETA][mesy] had T_m of more than 100°C. In addition, it was not hard to find that PILs containing ethanolamine cation had high T_m because **Table 2** shows that the T_m of [ETA][mesy], [ETA][OTf], and [ETA][Bsa] was 102, 85, and 96°C, respectively. The possible reason for this phenomenon might be that ethanolamine was a small cation compared to others and that lead to strong interactions between cations and anions, which were crucial in the process of determining T_m (Alan et al., 2001; Kireeva et al., 2012). Based on the discussion of T_d and T_m, it was found that the working temperature range, namely the range of being liquid and stable state, were wide for most of synthesized PILs. This property was helpful to the potential application in the field requiring high temperature.

Density (ρ)

As several PILs were in a solid state at room temperature, **Table S2** only summarizes the density data of 10 PILs which were in a liquid state at room temperature. In order to evaluate the influence of temperature to density of synthesized PILs, the following equation was used to characterize the change law of

density with the increase of temperature (Khan et al., 2017; Chen et al., 2018; Prasad et al., 2018b):

$$\rho = A^*T + B \tag{3}$$

where ρ stands for the density of PILs at specific temperature, T represents the Kelvin temperature, parameter A is the coefficient of density as a function of temperature and B is a constant.

Table 3 summarizes the coefficient A and constant B as well as the correlation coefficient R^2, which clearly indicated that the linearity of the curves was good, R^2 for all samples were approaching 1. Also, the fitting curves are shown in **Figure 2** and the change law of density as well as their distribution can be observed. Specifically, PILs with the anion of trifluoromethane sulfonate had a higher density. However, the density of PILs containing anions of benzene ring and methane sulfonate had overlaps to some extent. In addition, when synthesized PILs had the same anion, the PILs containing the cation of diethanolamine had the highest density, but those containing the cation of dimethylethanolamine had the lowest density. As the density of compound was codetermined by the molar mass as well as the molar volume (closely related with the structures of ions), PILs with the same anion and different cations would have different densities due to the different structures of cations.

The thermal expansion coefficient (α_P) was calculated using the density data through the following equation: (Khan et al., 2017; Prasad et al., 2018a; Sayah et al., 2018)

$$\alpha_P = -\frac{1}{\rho} \left(\frac{\partial \rho}{\partial T} \right)_P = -\frac{A}{AT + B} \tag{4}$$

where ρ represents the density of PILs at specific temperature and pressure, T is the Kelvin temperature, A and B are parameters calculated by the above function (3). The calculated α_P of different PILs at investigated temperatures from (293.15 to 353.15) K are summarized in **Table 4**. The increasing trend of α_P of PILs with the increase of temperature could be observed, which indicated that density of PILs changed more dramatically at a higher temperature. Among those PILs, [DMEA][OTf] had the highest thermal expansion coefficient

TABLE 2 | The melting point (T_m) and initial decomposition temperature (T_d) of synthesized PILs.
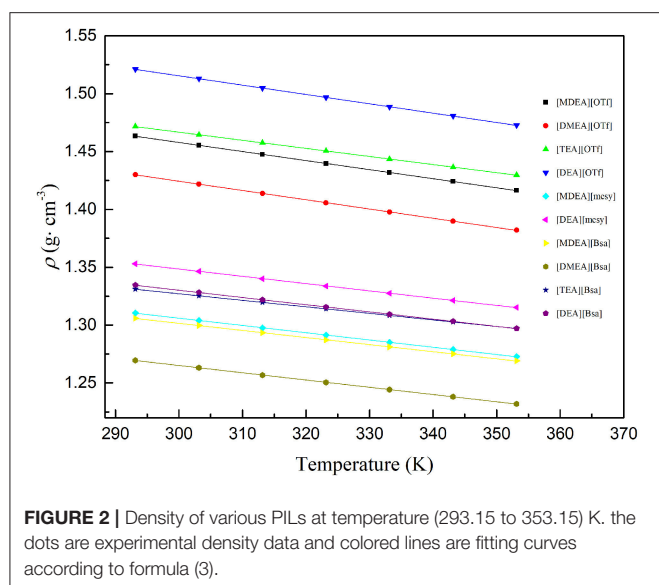
PILs	T_m (°C)[a]	T_d (°C)[b]
[MDEA][mesy]	< −50	205
[DMEA][mesy]	112	156
[TEA][mesy]	85	266
[ETA][mesy]	102	286
[DEA][mesy]	< − 50	289
[MDEA][OTf]	< −50	225
[DMEA][OTf]	37	167
[TEA][OTf]	< −50	278
[ETA][OTf]	85	314
[DEA][OTf]	26	305
[MDEA][Bsa]	< − 50	238
[DMEA][Bsa]	< −50	284
[TEA][Bsa]	−32	260
[ETA][Bsa]	96	310
[DEA][Bsa]	−39	294

[a] The melting point (T_m) of PILs was determined by the maximum endothermic peak of the DSC curve before the decomposition peak.
[b] The initial decomposition temperature of PILs was confirmed by the decomposition temperature at 5% loss of weight of samples.

TABLE 3 | Coefficient A and constant B as well as correlation coefficient R^2 of formula (3).

PILs	A (g·cm⁻³·K⁻¹)	B (g·cm⁻³)	R^2
[MDEA][OTf]	−7.83E-04	1.6927	0.9999
[DMEA][OTf]	−8.00E-04	1.6643	0.9999
[TEA][OTf]	−6.99E-04	1.6765	1.0000
[DEA][OTf]	−8.07E-04	1.7575	0.9999
[MDEA][mesy]	−6.28E-04	1.4943	0.9999
[DEA][mesy])	−6.30E-04	1.5374	0.9999
[MDEA][Bsa])	−6.13E-04	1.4855	0.9999
[DMEA][Bsa]	−6.27E-04	1.4532	0.9999
[TEA][Bsa]	−5.67E-04	1.4973	1.0000
[DEA][Bsa]	−6.27E-04	1.5182	0.9999

FIGURE 2 | Density of various PILs at temperature (293.15 to 353.15) K. the dots are experimental density data and colored lines are fitting curves according to formula (3).

from 5.59 $*10^{-4}$ K^{-1} at 293.15 K to 5.79 $*10^{-4}$ K^{-1} at 353.15 K and [TEA][Bsa] had the lowest ones from 4.26 $*10^{-4}$ K^{-1} to 4.37 $*10^{-4}$ K^{-1} at the same temperature range. In addition, when PILs had the same anion, they had the lowest α_P in the case of containing triethanolamine and the highest α_P in the case of containing dimethylethanolamine, such as α_P: $[DMEA][OTf]$ > [TEA][OTf] and [DMEA][Bsa] > [TEA][Bsa]. As triethanolamine had three hydroxyl groups and dimethylethanolamine only one, the regularities of α_P under the condition of same anion indicated that the number of hydroxyl group had great influence on the value of α_P. The more hydroxyl groups, the smaller α_P. The most likely cause of this phenomenon was that the more hydroxyl groups, the stronger the interactions between molecules, and the smaller the influence of temperature on the distance between molecules, the smaller the coefficient of thermal expansion. The variation of thermal expansion coefficients of investigated PILs were great as they changed from 4.26 $*10^{-4}$ K^{-1} to 5.79 $*10^{-4}$ K^{-1} at temperature (293.15 to 353.15) K. However, the values of PILs were much smaller than the general organic molecular solvents (10^{-3} K^{-1}) and greater than the typical molten salt ($1-2*10^{-4}$ K^{-1}) (Taravillo et al., 2007; Madhusudhan Rao et al., 2013; Khan et al., 2017).

Standard molar volume of substance stands for the volume of 1 mol pure material at a given temperature and pressure, and it can be calculated according to the following equation (Khan et al., 2017; Nie et al., 2017):

$$V_m = \frac{M}{\rho} \tag{5}$$

where V_m (cm$^3 \cdot$mol^{-1}) represents the molar volumes of investigated PILs at given temperature and pressure, M stands for the molar weight of PILs and ρ represents density of PILs at given temperature and pressure. The molar volumes were calculated and presented in **Table 5**.

The increasing molar volumes of synthesized PILs were noted at temperatures from (293.15 to 353.15) K. Among synthesized PILs, [TEA][Bsa] had the biggest molar volume and [DEA][mesy] had the smallest one. In the same anion, the molar volumes were directly related to cation size, like V_m: [TEA][OTf]>[MDEA][OTf]>[DEA][OTf]≈[DMEA][OTf] and [TEA][Bsa]>[MDEA][Bsa]>[DEA] [Bsa]>[DMEA] [Bsa]. The same change law was applicable to the case of the same cation but different anions. Since the V_m was largely determined by the molecular spacing, the size of the group had a direct effect on it. The larger the anion and cation, the more obvious the steric effect, the farther they were apart, the larger the V_m. In addition, a similar conclusion could be obtained from the change law of molecular volume, which was defined by the following formula: (Khan et al., 2017)

$$V = \frac{V_m}{N_A} \tag{6}$$

where V is the molecular volume of synthesized PILs, V_m is molar volume calculated by the above formula (5) and N_A is Avogadro's constant equaling to 6.02245×10^{23} molecule per mol. The calculated molecular volumes of PILs at temperatures from (293.15 to 353.15) K are presented in **Table 5**. The change law of molecular volumes corresponded to the change law of molar volumes listed in the same table. Resulting in the conclusion that the size of cations and anions decided the molecular volume. For example, [TEA][Bsa] had the biggest molecular volume among all PILs as it had large benzene ring and three ethanolamine groups. Also, the increase of temperature leaded to the increase of molecular volumes as same as molar volumes because they were relevant to the cation and anion thermal motion. With the increase of temperature, the van der Waal forces of interactions would decrease, which consequently caused an increase in the mobility of the ions (Tariq et al., 2009). Therefore, the higher the temperature, the more intense the thermal motion of the cation and anion, the further they were from each other and the bigger of their molecular volumes.

Viscosity (η)

The dynamic viscosity of PILs at the temperatures from (293.15 to 353.15) K are summarized in **Table S3**. At the investigated temperatures, η: [TEA][Bsa]>[DEA][Bsa]>[MDEA][Bsa]> [DMEA][Bsa]>[DEA][mesy]>[MDEA][mesy]>[DEA][OTf]≈ [TEA][OTf]>[MDEA][OTf] >[DMEA][OTf]. From the order of viscosity of PILs, it was clearly observed that the PILs containing [Bsa] anion had a higher viscosity in the same cation. At the same time, the PILs containing [TEA] cation had maximum viscosity at a given anion in most temperature ranges. However, the viscosity of [TEA][OTf] and [DEA][OTf] was similar at the whole temperature range. As liquid viscosity was caused by the cohesion of molecules, the viscosity change law of investigated PILs could be explained by the interactions of molecules (Yuan et al., 2018). Benzene ring was a large group. Thus, there were strong molecular interactions, specially van der Waals force, between each other. Therefore, PILs including benzene ring had a high viscosity. On the other hand, as [TEA] cation had three hydroxyethyl groups, it could generate strong hydrogen bond

TABLE 4 | The thermal expansion coefficient (α_P) of PILs at temperature (293.15 to 353.15) K.

	$\alpha \times 10^4$ (K^{-1})									
T (K)	[MDEA][OTf]	[DMEA][OTf]	[TEA][OTf]	[DEA][OTf]	[MDEA][mesy]	[DEA][mesy]	[MDEA][Bsa]	[DMEA][Bsa]	[TEA][Bsa]	[DEA][Bsa]
293.15	5.35	5.59	4.75	5.30	4.79	4.65	4.70	4.94	4.26	4.70
303.15	5.38	5.62	4.77	5.33	4.82	4.68	4.72	4.96	4.28	4.72
313.15	5.41	5.66	4.80	5.36	4.84	4.70	4.74	4.99	4.30	4.74
323.15	5.44	5.69	4.82	5.39	4.86	4.72	4.76	5.01	4.32	4.76
333.15	5.47	5.72	4.84	5.42	4.89	4.74	4.79	5.04	4.33	4.78
343.15	5.50	5.75	4.87	5.45	4.91	4.76	4.81	5.07	4.35	4.81
353.15	5.53	5.79	4.89	5.48	4.93	4.79	4.83	5.09	4.37	4.83

TABLE 5 | Molar volume (V_m) and molecular volume (V) of PILs at temperature (293.15 to 353.15) K.

T (K)	293.15	303.15	313.15	323.15	333.15	343.15	353.15
[MDEA][OTf]							
V_m (cm$^3 \cdot$mol^{-1})	184.0	185.0	186.0	187.0	188.0	189.1	190.1
V (nm^3)	0.305	0.307	0.309	0.311	0.312	0.314	0.316
[DMEA][OTf]							
V_m (cm$^3 \cdot$mol^{-1})	167.3	168.2	169.2	170.2	171.1	172.1	173.1
V (nm^3)	0.278	0.279	0.281	0.283	0.284	0.286	0.287
[TEA][OTf]							
V_m (cm$^3 \cdot$mol^{-1})	203.4	204.3	205.3	206.3	207.3	208.3	209.3
V (nm^3)	0.338	0.339	0.341	0.343	0.344	0.346	0.348
[DEA][OTf]							
V_m (cm$^3 \cdot$mol^{-1})	167.8	168.7	169.6	170.5	171.4	172.4	173.3
V (nm^3)	0.279	0.280	0.282	0.283	0.285	0.286	0.288
[MDEA][mesy]							
V_m (cm$^3 \cdot$mol^{-1})	164.3	165.1	165.9	166.7	167.5	168.3	169.1
V (nm^3)	0.273	0.274	0.275	0.277	0.278	0.279	0.281
[DEA][mesy])							
V_m (cm$^3 \cdot$mol^{-1})	148.7	149.5	150.2	150.9	151.6	152.3	153.0
V (nm^3)	0.247	0.248	0.249	0.251	0.252	0.253	0.254
[MDEA][Bsa])							
V_m (cm$^3 \cdot$mol^{-1})	212.4	213.4	214.4	215.5	216.5	217.5	218.5
V (nm^3)	0.353	0.354	0.356	0.358	0.359	0.361	0.363
[DMEA][Bsa]							
V_m (cm$^3 \cdot$mol^{-1})	194.8	195.8	196.8	197.8	198.8	199.8	200.8
V (nm^3)	0.323	0.325	0.327	0.328	0.330	0.332	0.333
[TEA][Bsa]							
V_m (cm$^3 \cdot$mol^{-1})	230.9	231.9	232.9	233.9	234.9	236.0	237.0
V (nm^3)	0.383	0.385	0.387	0.388	0.390	0.392	0.393
[DEA][Bsa]							
V_m (cm$^3 \cdot$mol^{-1})	197.3	198.2	199.2	200.2	201.1	202.1	203.0
V (nm^3)	0.328	0.329	0.331	0.332	0.334	0.336	0.337

between ions, which was thought an important factor affecting the viscosity of ILs (Yang et al., 2017). Hence, PILs containing hydroxyethyl group would have a higher viscosity and their viscosity would increase with the increase of the number of hydroxyethyl groups, as shown in **Table S3**.

Arrhenius law was used to the PILs viscosities within the measured temperatures from (293.15 to 353.15) K (Ghatee et al., 2012; Hou et al., 2018; Sayah et al., 2018):

$$\eta = \eta_0 e^{(E_{a,\eta}/RT)} \tag{7}$$

where η_0 is a fitting parameter, $E_{a,\eta}$ is the activation energy, R is the universal gas constant (8.314 J·K^{-1}·mol^{-1}) and T is the Kelvin temperature. The parameters are shown in **Table 6** and the fitting curves are depicted in **Figure 3**. From **Figure 3**, it was obvious that the dynamic viscosity decreased rapidly with the linear increase of temperature and the correlation coefficients (R^2) indicated the Arrhenius law fitted with experimental data very well. Energy of activation ($E_{a,\eta}$) was the least amount of energy required for the ions to move pass through other ones and therefore it could be linked with structure of PILs (Sayah

et al., 2018). As seen in **Table 6**, PILs containing benzene ring had higher $E_{a,\eta}$ universally and those containing trifluoromethane sulfonate had lower $E_{a,\eta}$, which corresponded with the change law of viscosity. In addition, $E_{a,\eta}$ increased with the increase of the number of hydroxyethyl groups when PILs had the same anion. These phenomena could be explained with the alkyl chain size, hydrogen bonding and electrostatic force. When there was a strong hydrogen bonding, electrostatic force or complex structure, it would be more difficult for ions to cross through each other. Thus, high $E_{a,\eta}$ would be measured.

Electrical Conductivity (σ)

The electrical conductivity of synthesized PILs are presented in **Table S4**. Arrhenius law was also used to the PILs electrical conductivity within the measured temperatures from (293.15 to 353.15) K:(Sayah et al., 2018)

$$\sigma = \sigma_0 e^{(-E_{a,\sigma}/RT)} \tag{8}$$

where σ_0 is a fitting parameter, $E_{\alpha,\sigma}$ is the activation energy for the electrical conductivity, R is the universal gas constant (8.314 J·K^{-1}·mol^{-1}) and T is the Kelvin temperature. The parameters are shown in **Table 7** and the fitting curves are depicted in **Figure 4**. As seen in **Table 7**, it was noted that the correlation coefficients (R^2) exceeded 0.99. These values indicated that the Arrhenius law fitted very well with the experimental data. As seen in **Figure 4**, all electrical conductivity of PILs increased with the increase of temperature, this trend fitted with other reports (Sayah et al., 2018; Yuan et al., 2018). In addition, among the synthesized PILs, [DMEA][OTf] had the highest conductivity at all investigated temperatures and [TEA][Bsa] had the lowest one at the same temperature range. Also, the PILs containing anion of benzene ring had lower conductivity and those containing anion of trifluoromethane sulfonate had higher conductivity among investigated PILs, this trend is the opposite of the change law of viscosity discussed in the above section. The calculated $E_{\alpha,\sigma}$ also supports the above discussion. Activation energy for electrical conductivity ($E_{\alpha,\sigma}$) was a parameter to characterize the difficulty level of ions migrating under the electric fields and it was often related to the size or polarity of ions. As seen in **Table 7**, it was noteworthy that PILs containing benzene ring had the highest $E_{\alpha,\sigma}$, in comparison to others, due to its large structure. Thus, it would be very difficult for this kind of PILs migrating in the liquid (Yuan et al., 2018). What's more, $E_{\alpha,\sigma}$ of PILs containing trifluoromethane sulfonates was low because the molecules were small and polarity was very strong. When PILs had the same anion, the number of hydroxyethyl group was of significance to $E_{\alpha,\sigma}$ and thus to electrical conductivity. For example, the order of $E_{a,\sigma}$: [TEA][OTf] ≈ [DEA][OTf]> [MDEA][OTf]>[DMEA][OTf] and [TEA][Bsa]>[DEA][Bsa]≈[MDEA][Bsa]>[DMEA][Bsa], which indicated that the more hydroxyethyl there is, the more difficult it is for ions to migrate. Because of the ions aggregation/pairing effect, the large ion size could cause the reduction of ion mobility and that could explain the phenomenon described above (Yuan et al., 2018). All activation energy for electrical conductivity of PILs corresponded to conductivity experimental data in the overall trend.

TABLE 6 | The parameter η_0 and activation energy ($E_{a,\eta}$) as well as correlation coefficients (R^2) of various PILs according to formula (7).

PILs	η_0 (mPa·s)	$E_{a,\eta}$ (kJ·mol^{-1})	R^2
[MDEA][OTf]	3.37E-06	45.57	0.9977
[DMEA][OTf]	5.84E-05	36.24	0.9953
[TEA][OTf]	5.69E-07	51.59	0.9978
[DEA][OTf]	5.93E-07	51.49	0.9985
[MDEA][mesy]	1.69E-07	57.01	0.9983
[DEA][mesy])	4.12E-07	54.91	0.9995
[MDEA][Bsa])	1.73E-08	65.45	0.9988
[DMEA][Bsa]	4.87E-09	66.87	0.9989
[TEA][Bsa]	9.10E-09	69.29	0.9985
[DEA][Bsa]	1.25E-08	66.83	0.9990

FIGURE 3 | Viscosity of various PIls at temperature (293.15 to 353.15) K. The dots are experimental viscosity data and colored lines are fitting curves according to formula (7).

TABLE 7 | The fitting parameter σ_0, activation energy for the electrical conductivity ($E_{\alpha,\sigma}$) and correlation coefficients (R^2) based on formula (8).

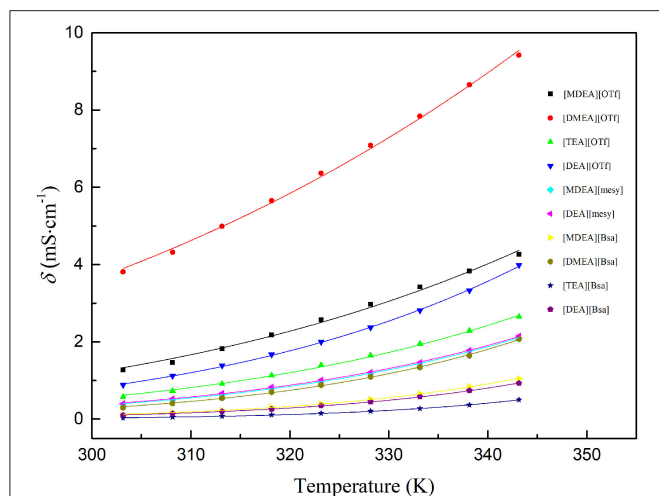| PILs	σ_0 (mS·cm^{-1})	$E_{a,\sigma}$ (kJ·mol^{-1})	R^2
[MDEA][OTf]	3.56E+04	25.70	0.9940
[DMEA][OTf]	8.42E+03	19.35	0.9979
[TEA][OTf]	1.82E+05	31.73	0.9977
[DEA][OTf]	2.70E+05	31.75	0.9995
[MDEA][mesy]	6.07E+05	35.87	0.9993
[DEA][mesy])	4.64E+05	35.06	0.9994
[MDEA][Bsa])	1.04E+07	45.94	0.9984
[DMEA][Bsa]	2.54E+06	40.01	0.9988
[TEA][Bsa]	1.97E+08	56.48	0.9995
[DEA][Bsa]	1.11E+07	46.47	0.9994

FIGURE 4 | Conductivity of various PILs at temperature (303.15 to 343.15) K. The dots are experimental electrical conductivity data and colored lines are fitting curves according to formula (8).

TABLE 8 | The dissociation constants (pKa) of various PILs at 25°C.

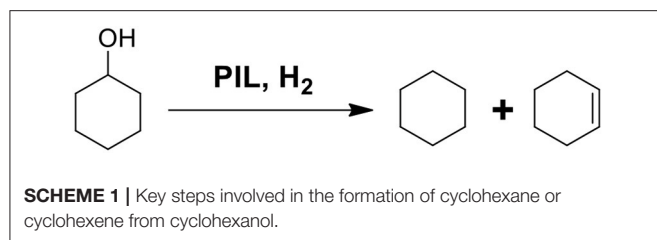| Abb.	[MDEA][mesy]	[DMEA][mesy]	[TEA][mesy]	[ETA][mesy]	[DEA][mesy]
pKa	8.56	9.23	7.72	9.51	8.79
Abb.	[MDEA][OTf]	[DMEA][OTf]	[TEA][OTf]	[ETA][OTf]	[DEA][OTf]
pKa	8.34	9.23	7.73	9.49	8.92
Abb.	[MDEA][Bsa]	[DMEA][Bsa]	[TEA][Bsa]	[ETA][Bsa]	[DEA][Bsa]
pKa	8.48	9.17	7.68	9.50	8.79

series cations of synthesized PILs, the amount of hydroxyethyl groups affected the charge distribution of the cation, which resulted in different pKa. This explanation was supported by the pKa of PILs containing the same hydroxyethyl groups, such as pKa: [DEA]>[MDEA] and [ETA]>[DMEA]. What they have in common was that they had the same number of hydroxyethyl groups. The other group was either methyl or hydrogen, which made them different pKa.

pKa is an important parameter because it indicates the acidity of PILs and has an important reference value in gas absorption (Chowdhury et al., 2013; Hayashi et al., 2014; Furukawa et al., 2017; Shang et al., 2017). As higher pKa denotes a stronger hydrogen bond accepting ability of PILs, they can be used for the absorption of acidic gases, like CO_2. At the same time, lower pKa value represents a stronger hydrogen bond donating of PILs and it is conducive to the absorption of basic gases, like NH_3 (Shang et al., 2017). Therefore, the high pKa of synthesized PILs foreshadows their potential applications in acid gas absorption.

Catalytic Effect for the Conversion of Cyclohexanol

Hydrodeoxygenation (HDO) is an important way to catalyze the conversion of lignin and its derivatives into high-calorific alkane. In this process, deoxygenation is crucial as it makes the whole reaction possible (Chen et al., 2016, 2017; Yang et al., 2019). Brønsted acid (like phosphoric acid), as a deoxidizer, is indispensable for facilitating the deoxygenation reaction in most catalytic systems (Güvenatam et al., 2014; Chen et al., 2016). However, it is noteworthy that acid is harmful to reactors, that inhibits the industrial utilization of lignin. Hence, developing acid free condition for the deoxygenation of lignin and its derivatives is highly desirable.

In order to investigate the potential deoxygenation effect of synthesized PILs, the conversion of cyclohexanol was selected as model reaction as shown in **Scheme 1**. **Table 9** presents catalytic activity of various PILs for deoxidization of cyclohexanol at 120°C for 6 h with the pressure of H_2 4 MPa. The GC chromatograms of catalytic results of various PILs are shown in **Figures S34–S43**. It was noted that all explored PILs showed catalytic activity to a certain extent. Among them, the conversion rate of cyclohexanol in the PILs [MDEA][OTf] and [DEA][OTf] were 100 % and the selectivity of cyclohexane and cyclohexene was 82.1 and 75.5%, respectively. In addition, [DEA][mesy], [MDEA][Bsa], [TEA][Bsa] and [DEA][Bsa] had a conversion rate of cyclohexanol of about 90% in experimental conditions. However, the total selectivity of cyclohexane and cyclohexene of these PILs did go not over 50%, it may be attributed to

Dissociation Constants (pKa)

Thermodynamic dissociation constants (pKa) are used to characterize the extent of dissociation of PILs in an aqueous solution, and the values are good parameters reflecting the degree of relative hydrogen bond donating ability, which are crucial in many chemical processes, like gas absorption and catalysis (Shang et al., 2017).

In general, the acid-base titration curve was used to calculate the pKa of explored substance (Xie et al., 2018). In the experiment, the titration curves (pH/V, black dot line) and their first derivative (ΔpH/ΔV, red dot line) curves of all synthesized PILs are shown in **Figure S33**. The maximum value of the first derivative was used to confirm the volume of titration end point, which was important to the calculation of pKa. All calculated pKa of investigated PILs are summarized in **Table 8**. Clearly, various PILs had pKa of more than 7.0 and PILs containing [ETA] cation had the highest pKa about 9.5 and containing [TEA] had the lowest value about 7.7. Meanwhile, it can be seen that PILs containing the same cation had similar pKa, but no apparent relation with anions. This phenomenon could be explained by the mechanism of pKa. As the exchangeable proton was on the cation of tertiary amine only, the type of anion did not make sense to pKa when its molar concentration was low (0.01 mol/L). Thus, the pKa of investigated PILs were related to cation only. However, what deserved our attention was that the number of hydroxyethyl group on tertiary amine was significant in deciding how hard it was for a proton to leave, and thus decide the high or low of pKa. Specifically, pKa: [ETA]>[DMEA]>[DEA]>[MDEA]>[TEA]. From the regularities of pKa, their values decreased with the increase of the number of hydroxyethyl groups. Particularly, PILs containing a [TEA] group had the lowest pKa and containing a [ETA] group had the highest pKa. In general, the charge distribution of ions was directly related with the interactions between proton and cation, which determined the pKa of PILs (Xie et al., 2018). For the

SCHEME 1 | Key steps involved in the formation of cyclohexane or cyclohexene from cyclohexanol.

TABLE 9 | Catalytic activity of different PILs for the deoxygenation of cyclohexanol.

PILs	Cyclohexane (%)	Cyclohexene (%)	Conversion (%)
[MDEA][OTf]	82.1	0	100
[DMEA][OTf]	7.2	0	59.8
[TEA][OTf]	3.9	0	74.8
[DEA][OTf]	0	75.5	100
[MDEA][mesy]	6.2	0	70.3
[DEA][mesy]	41.8	0	89.4
[MDEA][Bsa]	8.1	21.2	91.8
[DMEA][Bsa]	7.1	25.8	34.7
[TEA][Bsa]	11.2	32.1	97.8
[DEA][Bsa]	4.7	38.9	95.2

Reaction conditions: phenol, 1 mmol; ionic liquid, 2.0 g; H_2 pressure, 4 MPa; reaction temperature, 120°C (referred to the constant-temperature air bath temperature); reaction time, 6 h. The conversion and yields were determined by GC using n-dodecane as an internal standard.

the intermediate products or products of side-reaction (mainly dimer, cyclohexylcyclohexane) that dissolved in PILs. What's more, the conversation rate of cyclohexanol in [DMEA][OTf], [TEA][OTf], [MDEA][mesy] and [DMEA][Bsa] were 59.8, 74.8, 70.3, and 34.7% with almost <10% selectivity of cyclohexane, the result indicated low catalytic activity for these PILs in the conversion of cyclohexanol. In other reports, it was believed that the catalytic effect of ionic liquids was directly related to the acidity of the PILs (Yan et al., 2010). Therefore, the good catalytic effect of [MDEA][OTf] and [DEA][OTf] may also be attributed to their acidity. In brief, [MDEA][OTf] and [DEA][OTf] showed a promising application in deoxygenation of cyclohexanol during HDO of lignin derived chemicals.

CONCLUSION

A series of 2-hydroxyethylammonium sulfonate-based PILs were synthesized as well as characterized via NMR, FT-IR

and elemental analysis. The thermodynamics methods of TGA and DAS were used to determine T_m and T_d of synthesized PILs, results showed that most of PILs had T_m below 0°C. Also, the range of T_d for the synthesized PILs was wide, the value was mainly determined by cations and barely affected by anions. Meanwhile, the physicochemical properties, like density, viscosity and electrical conductivity, were also explored. The results indicated that these physicochemical properties were related to their structure tightly and the interactions between anions and cations played a crucial role in determining them. In addition, the thermodynamic dissociation constants of synthesized PILs confirmed that the values showed a strong relation with their cations' structure. Specifically, the regularities of pKa manifested that the more hydroxyethyl groups in cation, the lower the pKa for PILs. In general, the values of pKa of various synthesized PILs exceeded 7.0, which indicated a potential application in the field of acidic gases absorption. What's more, [MDEA][OTf] and [DEA][OTf] showed efficient catalytic activity in the reaction of deoxidation with cyclohexanol as the substrate at certain conditions, the conversion rate of cyclohexanol reached up to 100 % and the selectivity of cyclohexane and cyclohexene was 82.1 and 75.5%, respectively. The results indicated that these PILs had a great potential in the application of deoxygenation reaction during HDO processes.

AUTHOR CONTRIBUTIONS

GC designed the research. GC and LL prepared the samples and did determinations. GC and SY were involved in catalytic reactions. GC, SY, QZ, XL, JX, and SZ wrote the manuscript.

FUNDING

SUPPLEMENTARY MATERIAL

The Supplementary Material for this article can be found online at: https://www.frontiersin.org/articles/10.3389/fchem.2019.00196/full#supplementary-material

REFERENCES

Alan, R., Katritzky, R. J., Lomaka, A., Petrukhin, R., Maran, U., and Karelson, M. (2001). Perspective on the relationship between melting points and chemical structure. *Crystal Growth Design* 1, 261–265. doi: 10.1021/cg010009s

Armand, M., Endres, F., MacFarlane, D. R., Ohno, H., and Scrosati, B. (2009). Ionic-liquid materials for the electrochemical challenges of the future. *Nat. Mater.* 8, 621–629. doi: 10.1038/nmat2448

Brandt-Talbot, A., Gschwend, F. J. V., Fennell, P. S., Lammens, T. M., Tan, B., Weale, J., et al. (2017). An economically viable ionic liquid for the fractionation of lignocellulosic biomass. *Green Chem.* 19, 3078–3102. doi: 10.1039/c7gc00705a

Cao, Q., Lu, X., Wu, X., Guo, Y., Xu, L., and Fang, W. (2015). Density, viscosity, and conductivity of binary mixtures of the ionic liquid N-(2-Hydroxyethyl)piperazinium propionate with water, methanol, or ethanol. *J. Chem Eng. Data* 60, 455–463. doi: 10.1021/je500380x

Castro, M. C., Arce, A., Soto, A., and Rodríguez, H. (2016). Thermophysical characterization of the mixtures of the ionic liquid 1-Ethyl-3-methylimidazolium acetate with 1-propanol or 2-propanol. *J. Chem. Eng. Data* 61, 2299–2310. doi: 10.1021/acs.jced.5b01023

Chen, L., Fink, C., Fei, Z., Dyson, P. J., and Laurenczy, G. (2017). An efficient Pt nanoparticle–ionic liquid system for the hydrodeoxygenation of bio-derived phenols under mild conditions. *Green Chem.* 19, 5435–5441. doi: 10.1039/c7gc01870c

Chen, L., Xin, J., Ni, L., Dong, H., Yan, D., Lu, X., et al. (2016). Conversion of lignin model compounds under mild conditions in pseudo-homogeneous systems. *Green Chem.* 18, 2341–2352. doi: 10.1039/c5gc03121d

Chen, Y., Sun, Y., Li, Z., Wang, R., Hou, A., and Yang, F. (2018). Volumetric properties of binary mixtures of ionic liquid with tributyl phosphate and dimethyl carbonate. *J. Chem. Thermodynam.* 123, 165–173. doi: 10.1016/j.jct.2018.04.005

Chen, Y., Wang, H., and Wang, J. (2014). Effects of alkyl chain length and solvents on thermodynamic dissociation constants of the ionic liquids with one carboxyl group in the alkyl chain of imidazolium cations. *J. Phys. Chem. B* 118, 4630–4635. doi: 10.1021/jp501731j

Chowdhury, F. A., Yamada, H., Higashii, T., Goto, K., and Onoda, M. (2013). CO2 Capture by tertiary amine absorbents: a performance comparison study. *Industr. Eng. Chem. Res.* 52, 8323–8331. doi: 10.1021/ie400825u

Elgharbawy, A. A., Alam, M. Z., Moniruzzaman, M., and Goto, M. (2016). Ionic liquid pretreatment as emerging approaches for enhanced enzymatic hydrolysis of lignocellulosic biomass. *Biochem. Eng. J.* 109, 252–267. doi: 10.1016/j.bej.2016.01.021

Elshwishin, A., Köser, J., Schröer, W., and Qiao, B. (2014). Liquid–liquid phase separation of ionic liquids in solutions: ionic liquids with the triflat anion solved in aryl halides. *J. Mol. Liquids* 192, 127–136. doi: 10.1016/j.molliq.2013.07.012

Furukawa, Y., Koriki, H., Shuto, D., Sato, H., and Yamanaka, Y. (2017). 13C-NMR study of acid dissociation constant (pKa) effects on the CO2 absorption and regeneration of aqueous alkanolpiperidine. *Energy Proc.* 114, 1765–1771. doi: 10.1016/j.egypro.2017.03.1304

Ghatee, M. H., Bahrami, M., Khanjari, N., Firouzabadi, H., and Ahmadi, Y. (2012). A functionalized high-surface-energy ammonium-based ionic liquid: experimental measurement of viscosity, density, and surface tension of (2-Hydroxyethyl)ammonium formate. *J. Chem. Eng. Data* 57, 2095–2101. doi: 10.1021/je201055w

Greaves, T. L., and Drummond, C. J. (2015). Protic Ionic Liquids: Evolving Structure-Property Relationships and Expanding Applications. *Chem Rev* 115, 11379–11448. doi: 10.1021/acs.chemrev.5b00158.

Gruzdev, M. S., Shmukler, L. E., Kudryakova, N. O., Kolker, A. M., Sergeeva, Y. A., and Safonova, L. P. (2017). Triethanolamine-based protic ionic liquids with various sulfonic acids: Synthesis and properties. *J. Mol. Liquids* 242, 838–844. doi: 10.1016/j.molliq.2017.07.078

Güvenatam, B., Kurşun, O., Heeres, E. H. J., Pidko, E. A., and Hensen, E. J. M. (2014). Hydrodeoxygenation of mono- and dimeric lignin model compounds on noble metal catalysts. *Catalysis Today* 233, 83–91. doi: 10.1016/j.cattod.2013.12.011

Hayashi, K., Furukawa, Y., Sato, H., and Yamanaka, Y. (2014). 13C-NMR study of acid dissociation constant (pKa) effects on the CO2 absorption and regeneration of aqueous tertiary alkanolamines. *Energy Proc.* 63, 1876–1881. doi: 10.1016/j.egypro.2014.11.196

Hosseini, S. M., Alavianmehr, M. M., Gutiérrez, A., Khalifeh, R., Moghadasi, J., and Aparicio, S. (2018). On the properties and structure of 2-hydroxyethylammonium formate ionic liquid. *J. Mol. Liquids* 249, 233–244. doi: 10.1016/j.molliq.2017.10.122

Hou, H., Jiao, B., Li, Q., Lin, X., and Liu, S. (2018). Physicochemical properties, 1H-NMR, Ab initio calculations and molecular interaction in binary mixtures of N-methylimidazole with methanol. *J. Solu. Chem.* 47, 1875–1901. doi: 10.1007/s10953-018-0824-y

Huang, G., Lin, W.-C., He, P., Pan, Y., and Shu, C.-M. (2018). Thermal decomposition of imidazolium-based ionic liquid binary mixture: processes and mechanisms. *J. Mol. Liquids* 272, 37–42. doi: 10.1016/j.molliq.2018.09.058

Khan, A. S., Man, Z., Arvina, A., Bustam, M. A., Nasrullah, A., Ullah, Z., et al. (2017). Dicationic imidazolium based ionic liquids: synthesis and properties. *J. Mol. Liquids* 227, 98–105. doi: 10.1016/j.molliq.2016.11.131

Kireeva, N., Kuznetsov, S. L., and Tsivadze, A. Y. (2012). Toward navigating chemical space of ionic liquids: prediction of melting points using generative topographic maps. *Industr. Eng. Chem. Res.* 51, 14337–14343. doi: 10.1021/ie3021895

Latos, P., Culkin, A., Barteczko, N., Boncel, S., Jurczyk, S., Brown, L. C., et al. (2018). Water-tolerant trifloaluminate ionic liquids: new and unique lewis acidic catalysts for the synthesis of chromane. *Front. Chem.* 6:535. doi: 10.3389/fchem.2018.00535

Madhusudhan Rao, A. S., Narender, K., Kishan Rao, K. G., Gopi Krishna, N., (2013). Thermophysical properties of NaCl, NaBr and NaF by γ-ray attenuation technique. *J. Modern Phys.* 4, 208–214 doi: 10.4236/jmp.2013.42029

Maton, C., De Vos, N., and Stevens, C. V. (2013). Ionic liquid thermal stabilities: decomposition mechanisms and analysis tools. *Chem. Soc. Rev.* 42, 5963–5977. doi: 10.1039/c3cs60071h

Miran, M. S., Hoque, M., Yasuda, T., Tsuzuki, S., Ueno, K., and Watanabe, M. (2018). Key factor governing the physicochemical properties and extent of proton transfer in protic ionic liquids: deltapKa or chemical structure? *Phys. Chem. Chem. Phys.* 21, 418–426. doi: 10.1039/c8cp06973e

Nie, L.-R., Yao, S., Dong, B., Li, X.-L., and Song, H. (2017). Synthesis, characterization and physical properties of novel cholinium-based organic magnetic ionic liquids. *J. Mol. Liquids* 240, 152–161. doi: 10.1016/j.molliq.2017.05.044

Prasad, G., Muralidhar Reddy, K., Padamasuvarna, R., Madhu Mohan, T., Vijaya Krishna, T., and Ramesh Kumar, V. (2018a). Thermophysical properties of 1-butyl-3-methylimidazolium bis (trifluoromethylsulfonyl) imide with 2-ethoxyethanol from T = (298.15 to 323.15) K at atmospheric pressure. *J. Mol. Liquids* 251, 335–344. doi: 10.1016/j.molliq.2017.12.015

Prasad, G., Reddy, K. M., Padamasuvarna, R., Mohan, T. M., Krishna, T. V., and Rao, S. G. (2018b). Investigations of molecular interactions in the binary mixtures of 1-Butyl-3-methylimidazolium bis(Trifluoromethanesulfonyl) Amide and 2-Propoxyethanol from T = (298.15 to 323.15) K at Atmospheric Pressure. *J. Solu. Chem.* 47, 1980–2006. doi: 10.1007/s10953-018-0833-x

Qu, H., Zhou, Y., Ma, Y., Zhao, P., Gao, B., Guo, M., et al. (2018). A green catalyst for hydrolysis of cellulose: amino acid protic ionic liquid. *J. Taiwan Inst. Chem. Eng.* 93, 667–673. doi: 10.1016/j.jtice.2018.09.024

Ren, S., Hou, Y., Zhang, K., and Wu, W. (2018). Ionic liquids: functionalization and absorption of SO 2. *Green Energy Environ.* 3, 179–190. doi: 10.1016/j.gee.2017.11.003

Sayah, S., Ghamouss, F., Santos-Peña, J., Tran-Van, F., and Lemordant, D. (2018). The intriguing properties of 1-Ethyl-3-methylimidazolium bis(fluorosulfonyl)imide Ionic Liquid. *J. Solu. Chem.* doi: 10.1007/s10953-018-0814-0. [Epub ahead of print].

Shang, D., Zhang, X., Zeng, S., Jiang, K., Gao, H., Dong, H., et al. (2017). Protic ionic liquid [Bim][NTf2] with strong hydrogen bond donating ability for highly efficient ammonia absorption. *Green Chem.* 19, 937–945. doi: 10.1039/c6gc03026b

Sun, J., Konda, N. V. S. N. M., Parthasarathi, R., Dutta, T., Valiev, M., Xu, F., et al. (2017). One-pot integrated biofuel production using low-cost biocompatible protic ionic liquids. *Green Chem.* 19, 3152–3163. doi: 10.1039/c7gc01179b

Tang, B., Bi, W., Tian, M., and Row, K. H. (2012). Application of ionic liquid for extraction and separation of bioactive compounds from plants. *J. Chromatogr. B Analyt. Technol. Biomed. Life Sci.* 904, 1–21. doi: 10.1016/j.jchromb.2012.07.020

Taravillo, M., Pérez, F. J., Núñez, J., Cáceres, M., and Baonza, V. G. (2007). Thermodynamic properties of compressed liquid methanol in the vicinity of the freezing line. *J. Chem. Eng. Data* 52, 481–486. doi: 10.1021/je060415l

Tariq, M., Forte, P. A. S., Gomes, M. F. C., Lopes, J. N. C., and Rebelo, L. P. N. (2009). Densities and refractive indices of imidazolium- and phosphonium-based ionic liquids: effect of temperature, alkyl chain length, and anion. *J. Chem. Thermodynam.* 41, 790–798. doi: 10.1016/j.jct.2009.01.012

Vancov, T., Alston, A.-S., Brown, T., and McIntosh, S. (2012). Use of ionic liquids in converting lignocellulosic material to biofuels. *Renew. Energy* 45, 1–6. doi: 10.1016/j.renene.2012.02.033

Vekariya, R. L. (2017). A review of ionic liquids: applications towards catalytic organic transformations. *J. Mol. Liquids* 227, 44–60. doi: 10.1016/j.molliq.2016.11.123

Venkatraman, V., and Alsberg, B. K. (2016). Quantitative structure-property relationship modelling of thermal decomposition temperatures of ionic liquids. *J. Mol. Liquids* 223, 60–67. doi: 10.1016/j.molliq.2016.08.023

Vijayraghavan, R., Pas, S. J., Izgorodina, E. I., and MacFarlane, D. R. (2013). Diamino protic ionic liquids for CO2 capture. *Phys. Chem. Chem. Phys.* 15, 19994–19999. doi: 10.1039/c3cp54082k

Vogl, T., Menne, S., Kühnel, R.-S., and Balducci, A. (2014). The beneficial effect of protic ionic liquids on the lithium environment in electrolytes for battery applications. *J. Mater. Chem. A* 2, 8258–8265. doi: 10.1039/c3ta15224c

Wang, J., Petit, C., Zhang, X., and Park, A.-H. A. (2016). Simultaneous measurement of CO 2 sorption and swelling of phosphate-based ionic liquid. *Green Energy Environ.* 1, 258–265. doi: 10.1016/j.gee.2016.11.004

Xia, S. M., Chen, K. H., Fu, H. C., and He, L. N. (2018). Ionic liquids catalysis for carbon dioxide conversion with nucleophiles. *Front. Chem.* 6:462. doi: 10.3389/fchem.2018.00462

Xie, B., Xu, Y., Tang, X., Shu, H., Chen, T., and Zhu, X. (2018). Comparison of the alkalinity of hydroxypyridine anion-based protic ionic liquids and their catalytic performance for Knoevenagel reaction: the effect of the type of cation and the position of nitrogen atom of anion. *J. Mol. Liquids* 268, 610–616. doi: 10.1016/j.molliq.2018.07.094

Xuedan Song, R. K., Ishiguro, S.-I., and Umebayashi, Y. (2012). Physicochemical and acid-base properties of a series of 2-Hydroxyethylammonium-based protic ionic liquids. *Analyt. Sci.* 28, 469–474. doi: 10.2116/analsci.28.469

Yan, N., Yuan, Y., Dykeman, R., Kou, Y., and Dyson, P. J. (2010). Hydrodeoxygenation of lignin-derived phenols into alkanes by using nanoparticle catalysts combined with Bronsted acidic ionic liquids. *Angew. Chem. Int. Ed. Engl.* 49, 5549–5553. doi: 10.1002/anie.201001531

Yang, F., Ma, Q., Wang, X., and Liu, Z. (2017). Influence of aprotic cosolvents on the thermophysical properties of imidazolium-based ionic liquid. *J. Chem. Eng. Data* 62, 1628–1638. doi: 10.1021/acs.jced.7b00002

Yang, S., Lu, X., Yao, H., Xin, J., Xu, J., Kang, Y., et al. (2019). Efficient Hydrodeoxygenation of lignin-derived phenols and dimeric ethers with synergistic [Bmim]PF6-Ru/SBA-15 catalysis under acid free conditions. *Green Chem.* 21, 597–605. doi: 10.1039/c8gc03775b

Yang, S., Lu, X., Zhang, Y., Xu, J., Xin, J., and Zhang, S. (2018). Separation and characterization of cellulose I material from corn straw by low-cost polyhydric protic ionic liquids. *Cellulose* 25, 3241–3254. doi: 10.1007/s10570-018-1785-4

Yuan, W. L., Yang, X., He, L., Xue, Y., Qin, S., and Tao, G. H. (2018). Viscosity, conductivity, and electrochemical property of dicyanamide ionic liquids. *Front. Chem.* 6:59. doi: 10.3389/fchem.2018.00059

CO$_2$ Absorption by DBU-Based Protic Ionic Liquids: Basicity of Anion Dictates the Absorption Capacity and Mechanism

Feixiang Gao[1†], Zhen Wang[2†], Pengju Ji[1*] and Jin-Pei Cheng[1,3*]

[1] Department of Chemistry, Center of Basic Molecular Science, Tsinghua University, Beijing, China, [2] School of Chemical and Environmental Engineering, Anyang Institute of Technology, Anyang, China, [3] State Key Laboratory of Elemento-Organic Chemistry, Collaborative Innovation Center of Chemical Science and Engineering, Nankai University, Tianjin, China

PILs are promising solvent systems for CO$_2$ absorption and transformations. Although previously tremendous work has been paid to synthesize functionalized PILs to achieve a high-performance absorption, the underlying mechanisms are far less investigated and still not clear. In this work, a series of DBU-based PILs, i.e., [DBUH][X], with anions of various basicities were synthesized. The basicities of the anions were accurately measured in [DBUH][OTf] or extrapolated from the known linear correlations. The apparent kinetics as well as the capacities for CO$_2$ absorption in these PILs were studied systematically. The results show that the absorption rate and capacity in [DBUH][X] are in proportional to the basicity of PIL, i.e., a more basic PIL leads to a faster absorption rate and a higher absorption capacity. In addition, the spectroscopic evidences and correlation analysis indicate that the capacity and mechanism of CO$_2$ absorption in [DBUH][X] are essentially dictated by the basicities of anions of these PILs.

Keywords: protic ionic liquids, basicity, CO$_2$ absorption, linear correlation, absorption mechanism and capacity

INTRODUCTION

Being considered as one of the major long-lived greenhouse gases that is responsible for the ever-increasing global warming phenomenon as well as ocean acidification (Jenkinson et al., 1999; Joos et al., 1999), carbon dioxide (CO$_2$) has triggered tremendous research efforts in both academic and industry (Benson et al., 2009; Aresta et al., 2014; Goeppert et al., 2014; Sanna et al., 2014; Xia et al., 2018). To date a plethora of research attentions have been given to the processing, utilization and recycling of CO$_2$, and one of the most fundamental research area among these studies is to design high-performance materials and develop a number of practical and efficient processes for CO$_2$ capture and storage (CCS) (Haszeldine, 2009; Boot-Handford et al., 2014). Traditional chemical absorption of CO$_2$ by aqueous solution of amines is a well-established process in this regard, and currently is an indispensable technology because of its low cost and good reactivity (Rao and Rubin, 2002). However, there have been growing concerns on the environmental issues associated with the use of aqueous amine solutions for CO$_2$ absorption, such as high volatility and corrosive nature, etc. In addition, the degradation of amines during the absorption is also well-known, which significantly impairs the absorption capacity (Gouedard et al., 2012). Thus, discovering eco-friendly solvents/solvent systems or designing advanced materials as a potential replacement for the traditional CO$_2$ absorption is highly desirable.

Ionic liquids (ILs) are composed of entirely ions and exhibit a number of properties that are significantly different from those of conventional molecular solvents. In addition, the cations and anions of ILs can be varied or functionalized, which may endow them with one or several favorable properties, such as negligible vapor pressure, low flammability, high conductivity, and good thermal stability (Welton, 1999; Hallett and Welton, 2011). As an important subset of ILs, protic ILs (PILs) can be conveniently prepared from stoichiometric neutralization between Brönsted acids and bases. Due to the presence of dissociable proton(s), compared with aprotic ILs (AILs), PILs exhibit a stronger hydrogen bond donicity and higher ionic conductivity under neat condition (Greaves and Drummond, 2008, 2015). Due to these merits that are distinctive from those of molecular solvents, ILs are labeled as green solvents (Rogers and Seddon, 2003) and have been extensively applied to catalysis, material and biological science as well as energy storage, etc. (van Rantwijk and Sheldon, 2007; Bideau et al., 2011; Watanabe et al., 2017).

Since Brennecke and co-worker demonstrated that CO_2 has a good solubility in an imidazolium-based room temperature IL in 1999 (Blanchard et al., 1999), tremendous research efforts has been paid to utilize ILs or functionalized-ILs as media for physical and chemical CO_2 absorptions during the past decades (Bates et al., 2002; Gurkan et al., 2010; Luo et al., 2014; Xia et al., 2018). These pioneer explorations on the CO_2 absorptions in various ILs suggest that the absorption capacity and enthalpy are closely associated with the identity and structure of comprising cation and anion (Wang et al., 2010, 2012). By varying the structure of anions for these protic ILs, equimolar or even more than equimolar CO_2 absorption has been achieved (Wang et al., 2011; Chen et al., 2016). Although a high absorption capacity of CO_2 has been realized in ILs, the fundamental rules that govern the absorption mechanism and performances are still not clear, which may hamper a rational design and development of ILs in this respect. In addition, currently the rationales for the catalytic performance of PILs on CO_2 absorption were almost entirely based on the acidity data determined in molecular solvents, such as water or DMSO (Wang et al., 2010; Yang et al., 2016). It is known from both experimental results and theoretical calculations that the acidity obtained in molecular solvents may not explain acid/base behavior in ILs satisfactorily (Mihichuk et al., 2011). For example, the absorption capacity of phorsphonium-based ILs, i.e., $[R_4P][X]$ (R = alkyl), was found sigmoidally (Yasuda and Watanabe, 2013) or linearly (Wang et al., 2012) correlated with the basicity of anion in molecular solvents. Therefore, it is sensible to use the acidity data determined in the ILs to assess CO_2 absorption capacity, which may shed some lights on the intrinsic ability of ILs for CO_2 absorption.

Superbase DBU-derived PILs [DBU = 1,5-diazabicyclo[5.4.0]-5-undecene] are promising solvent systems for the CO_2 absorption, previous studies have shown that CO_2 has a considerable solubility in these PILs (Losetty et al., 2017; Zhu et al., 2017). In this work, in order to systematically investigate the relationship between the absorption capacity and thermodynamic properties of ILs, firstly we synthesized

11 DBU-based PILs, i.e., [DBUH][X], whose anions (X^-) are of different basicities (**Figure 1**), then the acidities of conjugated acids (HX) of these anions were determined or extrapolated from the known correlations obtained from previous study (Wang et al., 2018a). Next the apparent kinetics as well as capacity for CO_2 absorption in [DBUH][X] were measured, whereby the relationship between the basicity of anion X^- and CO_2 capture abilities of [DBUH][X] was established.

RESULTS AND DISCUSSION

Basicity Scale for the Anion (X^-) in [DBUH][X] (Figure 1)

In our previous work, we have successfully measured the acidities for several series of commonly seen organic acids in a DBU-based PIL, i.e., [DBUH][OTf] (OTf $^-$ = triflate) (Wang et al., 2018a). The regression analyses show that the acidities of structural and electronic different organic substrates, i.e., RO-H, N-H, N^+-H, and RCOO-H, linearly correlate with those in water. However, instead of forming a unified straight line, which is the case found for the analogous acidity correlation between a PIL EAN (ethylammonium nitrate) and water (Kanzaki et al., 2016), each individual series exhibits different slope and intercept (**Figure 2**) (Wang et al., 2018a). These linear acidity correlations between PILs and molecular solvent water are highly useful for accessing pK_a values of compounds in neat PILs that are difficult to determine due to the solvent leveling effect.

$$\text{For } N^+ - H \text{ acids}: pK_a^{[DBUH][OTf]} = 1.07 pK_a^{water} + 2.60 \quad (1)$$

$$\text{For } N - H \text{ acids}: pK_a^{[DBUH][OTf]} = 0.775 pK_a^{water} + 6.93 \quad (2)$$

$$\text{For } O - H \text{ acids}: pK_a^{[DBUH][OTf]} = 1.28 pK_a^{water} + 3.78 \quad (3)$$

$$\text{For } COO - H \text{ acids}: pK_a^{[DBUH][OTf]} = 1.34 pK_a^{water} + 5.26 \quad (4)$$

As shown in **Figure 2**, from the linear correlation of N^+-H series, the acidity of protonated DBU, i.e., $DBUH^+$ can be extrapolated as $pK_a = 15.1$ in neat [DBUH][OTf][1], which suggests that the acidities of these substrates with a pK_a close to and above this value (> ~14) are very difficult to be measured in neat [DBUH][OTf] by classical UV-vis spectroscopic approach (Yang et al., 2018). However, with the correlation equations provided in **Figure 2**, the basicities of a series of strong basic anions (**1–8**, **Figure 1**) for [DBUH][X] can be conveniently extrapolated from the linear correlation equations (Equations 1–4). Together with 3 experimentally determined basicities of less basic anions (**9–11**, **Figure 1**), a basicity scale that comprises totally 11 basicity values of anions (as expressed by the acidities of their anion precursors HX) involved in this work was established. Although

---

[1]From the correlation equation for N^+-H series (**Figure 2**), the autoprotolysis constant of [DBUH][OTf], $pK_{auto}^{[DBUH][OTf]} = [DBU]•[HOTf] = 14.5$ can also be derived as follow: $K_a = [DBU][H^+]/[DBUH^+] = K_{auto}^{[DBUH][OTf]}/[DBUH^+]$, therefore: $K_{auto}^{[DBUH][OTf]} = [DBUH^+]•K_a$, the molar concentration of [DBUH][OTf] at 25 °C (4.45 mol/L) can be calculated from the density [1.345 g/cm³ at 25°C (Miran et al., 2012)] and molecular weight (302.3 g/mol) of [DBUH][OTf]. $pK_{auto}^{[DBUH][OTf]}$ is about 0.5 or 4.5 pK units higher than that of water or EAN [$pK_{auto}^{EAN} = 10.0$ (Kanzaki et al., 2016)], respectively.
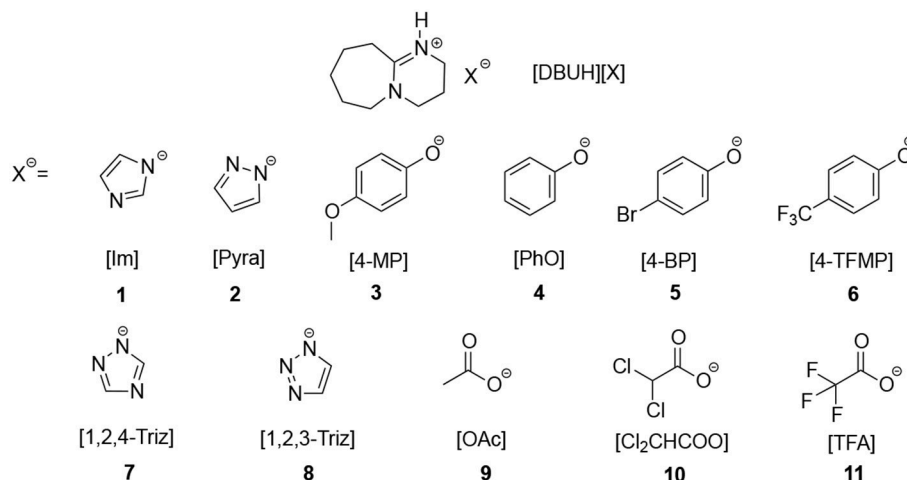
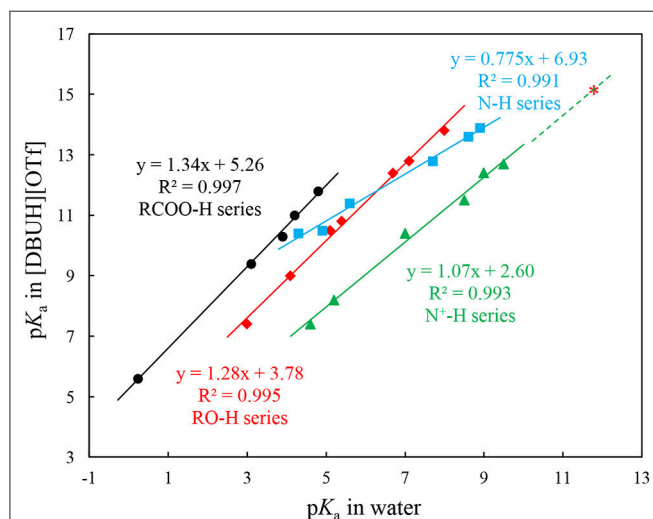**FIGURE 1 |** The structure of PILs [DBUH][X] involved in this work.

FIGURE 2 | Correlations between pK_as of N-H (■), N-H$^+$ (▲), RO-H (◆), and carboxylic (RCOO-H, ●) acids in [DBUH][OTf] and those in water. The red asterisk (✱) shows the extrapolated pK_a value of 15.1 for DBUH$^+$ [pK_a^{DBUH+} in water = 11.7, (Kaupmees et al., 2014)] in [DBUH][OTf] from the linear correlation of N$^+$-H series (Equation 1)[1]. Equations 1–4 were obtained from these linear correlations in **Figure 2** and used to extrapolate the pK_as of anion precursors HX (**1**–**8**, **Table 1**) in [DBUH][OTf] (**Table 1**), in specific, the pK_as of **1**, **2**, **7**, and **8** are from Equation 2 and those of **3**–**6** are from Equation 3.

these basicity values were acquired in [DBUH][OTf] and may be different from those in the PILs [DBUH][X], the relative basicity and nucleophilicity order of these anions are expected to be consistent between the DBU-based PILs. **Table 1** lists the acidity of anion precursor (HX) in [DBUH][OTf], together with those available data in molecular solvents. As shown in **Table 1**, the basicity scale for the anions of [DBUH][X] covers 13 pK units and the basicities of these anions in [DBUH][OTf] are similar to those in DMSO but significantly greater than in water.

CO$_2$ Absorption in [DBUH][X]

With the basicity scale for the anions in our hands, next we systematically measured the apparent kinetic of CO$_2$ absorption in [DBUH][X], with a control of temperature at constant 25°C by a thermostat and the measurement was performed under atmosphere pressure. The CO$_2$ absorption capacity in the individual [DBUH][X] is also determined as the molar ratio between the maximum amount of CO$_2$ absorbed and of [DBUH][X] used (**Table 1**). It is worth noting that the viscosity of [DBUH][X] increased with the increasing amount of CO$_2$ absorbed, forming a gel-like liquid which leads to a relatively large standard deviation (SD = ±0.05 of the absorption molar ratio). However, the volume of PILs did not have an obvious increase through CO$_2$ uptake, which is in line with the previous reported (Firaha and Kirchner, 2014). **Figure 3** shows the apparent kinetic profile of CO$_2$ absorption in these PILs, in general, the rates for CO$_2$ absorption in [DBUH][X] are slower than those observed in phosphonium-based aprotic ILs ([PR$_4$][X]), probably due to the hydrogen bonding between DBUH$^+$ and X$^-$ in [DBUH][X], which makes anions less reactive toward CO$_2$ than those in [PR$_4$][X] (Wang et al., 2011). As also can be seen from **Figure 3**, the rate of CO$_2$ absorption is faster in the [DBUH][X] with a more basic anion X$^-$ than in those with less basic ones. In addition, as shown from **Table 1**, the maximum absorption capacity of [DBUH][X] decreases with the decreasing basicity of anions. For examples, the amount of CO$_2$ uptake for the most basic [DBUH][Im] (**1**) is about twice as much as that for the less basic [DBUH][4-TFMP] (**6**). On the other hand, there is a sharp decrease in CO$_2$ absorption capacity in these weakly basic PILs (**8**–**11**), as for the least basic PILs, such as [DBUH][TFA] (**11**) and [DBUH][Cl$_2$CHCOO] (**10**), they both have a very limited absorption ability, despite of their obvious basicity difference.

In order to understand the absorption mechanism, the CO$_2$ absorption in [DBUH][X] was monitored by NMR and IR spectroscopies. The ^{13}C NMR and IR spectra for

TABLE 1 | The acidity of anion precursor (HX) in [DBUH][OTf] and the corresponding CO_2 absorption capacity in [DBUH][X].

Entry	[DBUH][X]	$^{a}pK_a^{[DBUH][OTf]}$ (HX)	$^{a,b}pK_a^{water}$ (HX)	$^{a,b}pK_a^{DMSO}$ (HX)	CO_2 absorption^c
1	[DBUH][Im]	18.2^d	14.5	18.6	1.19
2	[DBUH][Pyra]	17.7^d	13.9	19.8	1.15
3	[DBUH][4-MP]	16.8^d	10.2	19.1	0.90
4	[DBUH][PhO]	16.6^d	10.0	18.0	0.84
5	[DBUH][4-BP]	15.8^d	9.4	16.4	0.70
6	[DBUH][4-TFMP]	14.9^d	8.7	15.2	0.61
7	[DBUH][1,2,4-Triz]	14.7^d	10.0	14.7$_5$	0.55
8	[DBUH][1,2,3-Triz]	14.3^d	9.5	13.9	0.52
9	[DBUH][OAc]	11.8^e	4.7$_5$	12.5	0.24
10	[DBUH][Cl2CHCOO]	7.6^e	1.3$_5$	6.4	0.06
11	[DBUH][TFA]	5.6^e	0.23	3.6	0.05

^{a}The conjugated acid HX of the corresponding anion in [DBUH][X]. ^{b}pK$_a$ data is from: Internet Bond-energy Databank (iBonD), ibond.chem.tsinghua.edu.cn or ibond.nankai.edu.cn. ^{c}Mol CO_2 per mol PIL, the experiments were conducted at constant 25°C under atmospheric pressure, SD = ± 0.05, which is based on 3 individual absorption experiments. ^{d}Extrapolated values obtained from the corresponding linear correlations (**Figure 2** and Equations 1–4). ^{e}Determined experimentally, SD ≤ ± 0.05 pK units.
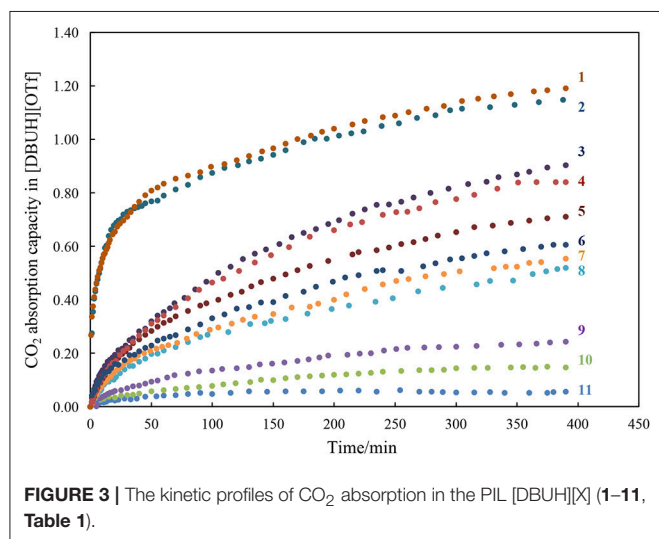
FIGURE 3 | The kinetic profiles of CO_2 absorption in the PIL [DBUH][X] (**1–11**, **Table 1**).

SCHEME 1 | Chemical absorption mechanism in the strong basic [DBUH][X] and the possible formation of hydrogen bonded complex (**1**-CO_2^-) after CO_2 uptake in [DBUH][Im] (**1**).

each [DBUH][X] before and after CO_2 absorption were recorded and compared (**Supplementary Material** provides full characterizations, herein only a representative example is presented). Spectroscopic results show that there is no change in both ^{13}C NMR and IR spectra before and after the absorption for [DBUH][X] with a relatively weak basic anion (**8–11**, **Table 1**, for details, see **Supplementary Material**). Presumably, this is due to the basicities of anions for these PILs are too weak to react with CO_2 to form the corresponding carboxylates (**Scheme 1**, vide infra), therefore a physical absorption mechanism likely dominates in these PILs (Izgorodina et al., 2015).

By contrast, the [DBUH][X] with relatively strong basic anions (**1–7**, **Figure 1**) clearly exhibit a different absorption mechanism as revealed by the results from ^{13}C NMR and IR spectra. Compared with those before CO_2 uptake, the IR and ^{13}C NMR spectra of **1–7** after CO_2 uptake show a new peak at ~1,700 cm^{-1} (C=O stretching) and a new signal at ~163 ppm
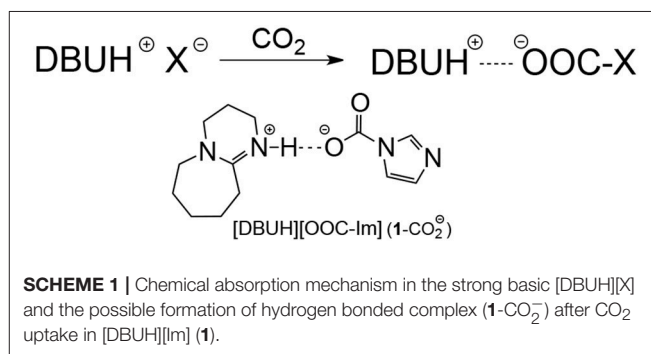
which are characteristic of carbonyl carbons in carbamates or carbonates, respectively (**Figures 4, 5, Supplementary Material**). As a representative example, the IR spectrum of [DBUH][Im] (**1**) after absorption shows a distinctive peak at 1,696 cm^{-1}, in addition, a new signal at 161.5 ppm was observed in ^{13}C NMR spectrum (**Figures 4, 5**).

These spectra results indicate that the mechanism for [DBUH][X] with a relatively strong basic anion (**1–7**) follows a chemical absorption mechanism (Wang et al., 2011; Chen et al., 2016). As illustrated in **Scheme 1**, the anions of **1–7** react with CO_2 through a nucleophilic attack process which yields the corresponding carboxylate adducts [DBUH][OOC-X], and the rate of forming carboxylate is in proportion to the basicity of anion which, under most circumstances, is paralleled with its nucleophilicity (**Figure 3**)[2].

Linear correlation can be a useful tool to reveal the underlying factors that govern the absorption kinetic and mechanism. In this connection, the correlation between the absorption capacity

---

[2]Although in some cases, there do exist discrepancies between nucleophilicity and basicity of nucleophile and the traditional Brönsted analysis fails (Mayr and Ofial, 2016). However, recent studies show that linear correlations were found between basicity and nucleophilicity of N-heterocyclic carbenes (NHCs) in the reactions that involving CO_2 as the substrate (Niu et al., 2017; Wang et al., 2018b).
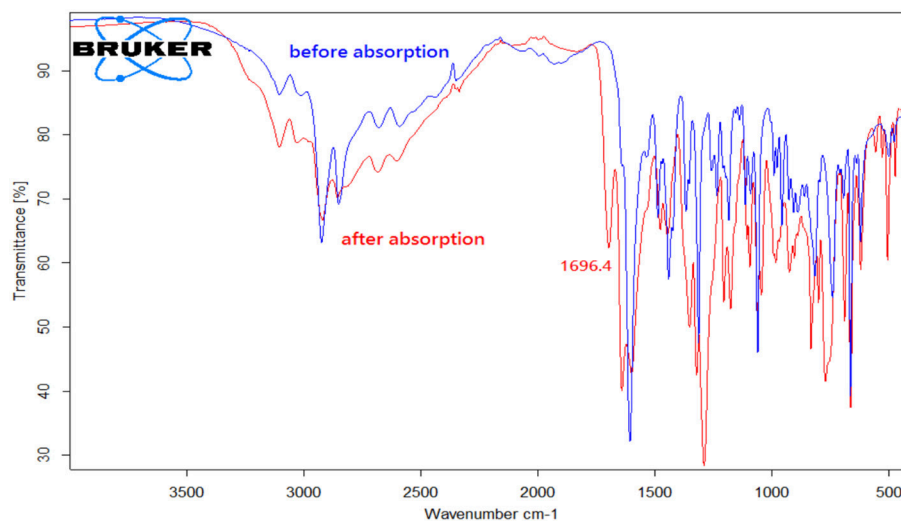
FIGURE 4 | IR spectra of [DBUH][Im] (**1**) before and after CO$_2$ absorption.

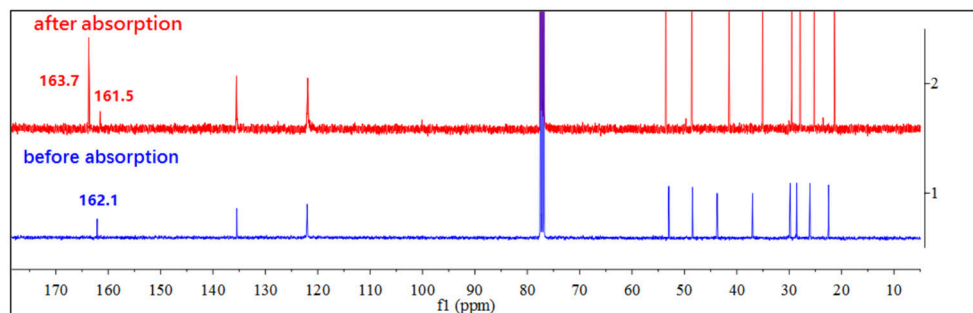**FIGURE 5 |** ^{13}C NMR spectra of [DBUH][Im] (**1**) before and after CO$_2$ absorption.
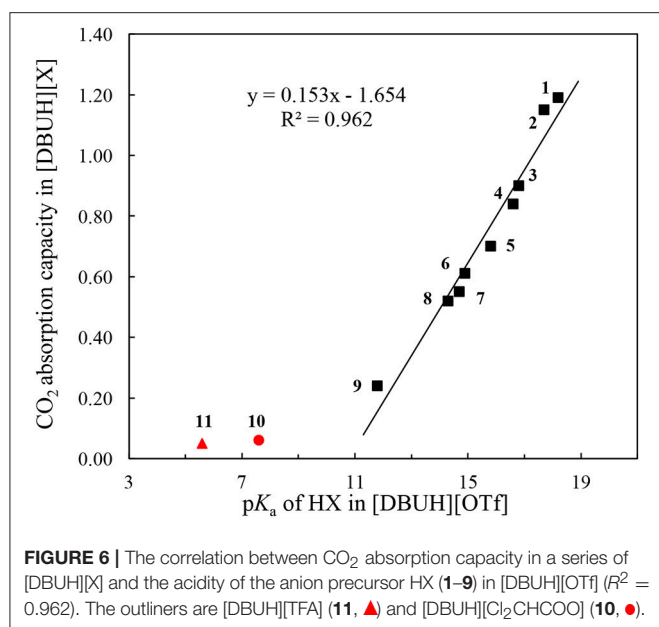
of [DBUH][X] and the basicity of anion in [DBUH][OTf] was performed. As shown in **Figure 6**, one can clearly notice a transition of CO$_2$ absorption capacity which is regulated by the basicity of anion. Specifically, there is a fairly good linear relationship ($R^2 = 0.962$) between the absorption capacity in [DBUH][X] (**1–9**) and the basicity of anion in [DBUH][OTf], excluding the data points of very weakly basic [DBUH][TFA] (**11**) and [DBUH][Cl$_2$CHCOO] (**10**). Combined with the evidences from the spectroscopic studies, we can conclude with confidence that a chemical absorption mechanism occurs in the [DBUH][X] (**1–7**) whose anion precursor HX has a pK_a > 15 in [DBUH][OTf], while the CO$_2$ absorption follows a physical absorption mechanism in [DBUH][X] (**10–11**) with an anion precursor's pK_a < 10. Presumably, a mixed chemical and physical mechanism occurs in these PILs with an anion precursor pK_a between 10 and 15, such as the CO$_2$ absorption in **8** and **9**. The quantum chemical calculations would be an ideal tool for the mechanism elucidation of CO$_2$ absorption in the PILs, however, currently some crucial physical and chemical parameters, such as dielectric constants, etc., for these PILs [DBUH][X] are not yet available, which hampers a detailed

and reliable theoretical calculation for the CO$_2$ absorption mechanism study in these PILs. It is worth noting that, by contrast, a similar correlation between absorption capacity and pK_a for precursor (**1–9**) of anion in molecular solvents, such as water and DMSO exhibits an inferior linear correlation ($R^2 = 0.874$ and 0.898, respectively, **Figures S36, S37**), which implies that the bond energetic data obtained in molecular solvents, though relatively abundant and well-established, may not be suitable to interpret the experimental observations in ILs. Therefore, cares should be taken when one attempts to utilize the thermodynamic parameters measured in *molecular solvents* to disclose the governing factors for the gas absorptions in *PILs*.

EXPERIMENTAL

Chemicals and CO$_2$ Gas

All the chemicals and solvents were purchased from commercially available sources, and used directly without further purification except otherwise noted. DBU was also from commercially available sources, but purified from multiple reduced pressure distillation. CO$_2$ gas was provided by the Linde

FIGURE 6 | The correlation between CO_2 absorption capacity in a series of [DBUH][X] and the acidity of the anion precursor HX (**1–9**) in [DBUH][OTf] (R^2 = 0.962). The outliners are [DBUH][TFA] (**11**, ▲) and [DBUH][Cl$_2$CHCOO] (**10**, ●).

Industrial Gases with a purity of >99.9995%, and was directly generated into [DBUH][X] for the CO_2 absorption.

Instrumentations

The IR spectra were recorded on a Bruker Tensor II FT-IR instrument. The ^1H NMR and ^{13}C NMR spectra were recorded on a Bruker AVANCE III HD 400 MHz spectrometer. The water content was determined by a Mettler Toledo V20S compact volumetric Karl-Fischer titrator. UV-vis spectra were obtained from an Agilent Cary 100 machine with the control of temperature at constant 25°C.

Preparation of [DBUH][X]

[DBUH][X] were synthesized by direct equal molar neutralization reactions between DBU and acids under neat condition or in methanol, **Supplementary Material** provides the detailed synthetic procedures. The structure of [DBUH][X] were confirmed by NMR and IR spectroscopies. The water content of prepared [DBUH][X] varies from 100 to 300 ppm, which was determined by a Karl-Fisher titration machine. It is worth noting that the water content of [DBUH][X] has only a limited effect on the CO_2 absorption in the range of 100 to 300 ppm, as the comparison experiments showed that nearly the identical amount of CO_2 was absorbed by the [DBUH][X] with a water content of 100 or 300 ppm.

[DBUH][Im] (**1**): ^1H NMR (400 MHz, CDCl$_3$) δ 11.49 (br, 1H), 7.64 (s, 1H), 7.06 (s, 2H), 3.57–2.96 (m, 6H), 2.39 (s, 2H), 1.90–1.74 (m, 2H), 1.72–1.32 (m, 6H); ^{13}C NMR (101 MHz, CDCl$_3$) δ 162.1, 135.5, 122.0, 53.0, 48.5, 43.7, 37.0, 29.8, 28.6, 26.0, 22.5 ppm; IR (neat): 3147, 2923, 2850, 2779, 2742, 2671, 2349, 1999, 1608 cm^{-1};

[DBUH][Pyra] (**2**): ^1H NMR (400 MHz, CDCl$_3$) δ 12.63 (br, 0.49H), 7.53 (d, J = 1.8 Hz, 2H), 6.24 (t, J = 1.8 Hz, 1H), 3.26

(t, J = 5.5 Hz, 2H), 3.20–3.08 (m, 4H), 2.42–2.26 (m, 2H), 1.82–1.70 (m, 2H), 1.68–1.41 (m, 6H); ^{13}C NMR (101 MHz, CDCl$_3$) δ 162.1, 133.3, 104.3, 52.9, 48.4, 43.5, 36.8, 29.7, 28.4, 25.8, 22.3 ppm; IR (neat): 3142, 3049, 2924, 2850, 2675, 2350, 1900, 1607 cm^{-1};

[DBUH][4-MP] (**3**): ^1H NMR (400 MHz, CDCl$_3$) δ 12.35 (br, 0.74H), 6.76–6.64 (m, 4H), 3.69 (s, 3H), 3.29–3.16 (m, 6H), 2.50–2.40 (m, 2H), 1.84–1.74 (m, 2H), 1.66–1.49 (m, 6H); ^{13}C NMR (101 MHz, CDCl$_3$) δ 163.0, 154.1, 151.5, 116.8, 114.7, 55.9, 53.1, 48.4, 42.0, 35.1, 29.6, 28.1, 25.5, 21.8 ppm; IR (neat): 2926, 2852, 2666, 2510, 2349, 2109, 1606 cm^{-1};

[DBUH][PhO] (**4**): ^1H NMR (400 MHz, CDCl$_3$) δ 13.26 (br, 0.85H), 7.18–7.05 (m, 2H), 6.88–6.75 (m, 2H), 6.66 (t, J = 7.3 Hz, 1H), 3.31–3.25 (m, 2H), 3.23 (t, J = 6.2 Hz, 4H), 2.56–2.37 (m, 2H), 1.89–1.75 (m, 2H), 1.72–1.47 (m, 6H). ^{13}C NMR (101 MHz, CDCl$_3$) δ 163.2, 160.8, 129.3, 117.0, 116.7, 53.2, 48.4, 41.8, 35.0, 29.6, 28.1, 25.4, 21.7 ppm; IR (neat): 3047, 2925, 2852, 2684, 2455, 2349, 2094, 1816, 1581 cm^{-1};

[DBUH][4-BP] (**5**): ^1H NMR (400 MHz, CDCl$_3$) δ 7.09 (d, J = 8.7 Hz, 2H), 6.67–6.56 (m, 2H), 3.24 (dd, J = 12.4, 6.9 Hz, 6H), 2.61–2.48 (m, 2H), 1.88–1.74 (m, 2H), 1.68–1.45 (m, 6H); ^{13}C NMR (101 MHz, CDCl$_3$) δ 164.7, 161.3, 131.8, 118.9, 107.4, 53.7, 48.4, 39.6, 33.3, 29.2, 27.3, 24.6, 20.4 ppm; IR (neat): 2926, 2853, 2449, 2349, 2101, 1860, 1640 cm^{-1};

[DBUH][4-TFMP] (**6**): ^1H NMR (400 MHz, CDCl$_3$) δ 12.51 (br, 1H), 7.31 (d, J = 8.6 Hz, 2H), 6.72 (d, J = 8.6 Hz, 2H), 3.33–3.23 (m, 6H), 2.60–2.52 (m, 2H), 1.92–1.81 (m, 2H), 1.73–1.54 (m, 6H); ^{13}C NMR (101 MHz, CDCl$_3$) δ 166.8, 164.3, 126.8(q, J C–F = 3.7 Hz), 125.6 (q, J = 270.0 Hz), 117.2, 116.8 (q, J C–F = 32.1 Hz), 53.6, 48.5, 40.5, 33.9, 29.4, 27.7, 25.0, 21.0 ppm; IR (neat): 2930, 2859, 2675, 2349, 2100, 1856, 1640, cm^{-1};

[DBUH][1,2,4-Triz] (**7**): ^1H NMR (400 MHz, CDCl$_3$) δ 14.81 (br, 1H), 8.06 (s, 2H), 3.48–3.14 (m, 6H), 2.78–2.41 (m, 2H), 1.93–1.82 (m, 2H), 1.72–1.54 (m, 6H); ^{13}C NMR (101 MHz, CDCl$_3$) δ 164.2, 148.3, 53.6, 48.5, 40.6, 34.2, 29.4, 27.7, 25.0, 21.0 ppm; IR (neat): 3078, 2925, 2855, 2473, 2350, 2072, 1898, 1638, 1611 cm^{-1};

[DBUH][1,2,3-Triz] (**8**): ^1H NMR (400 MHz, CDCl$_3$) δ 12.60 (br, 1H), 7.59 (d, J = 19.6 Hz, 2H), 3.63–3.02 (m, 6H), 2.90–2.56 (m, 2H), 1.93–1.80 (m, 2H), 1.58 (dd, J = 25.3, 3.8 Hz, 6H); ^{13}C NMR (101 MHz, CDCl$_3$) δ 165.1, 130.0, 53.8, 48.4, 39.1, 33.0, 29.1, 27.2, 24.4, 20.1 ppm; IR: 3234, 3101, 2926, 2857, 2672, 2117, 1881, 1637 cm^{-1};

[DBUH][OAc] (**9**): ^1H NMR (400 MHz, CDCl$_3$) δ 3.46–3.26 (m, 6H), 2.81 (d, J = 5.4 Hz, 2H), 1.99–1.85 (m, 5H), 1.68 (m, 4H), 1.60 (m, 2H); ^{13}C NMR (101 MHz, CDCl$_3$) δ 177.4, 165.6, 53.8, 48.3, 37.7, 31.6, 28.8, 26.8, 24.4, 23.9, 19.5 ppm; IR (neat): 3249, 2925, 2859, 2670, 2349, 2103, 1887, 1641, cm^{-1};

[DBUH][Cl$_2$CHCOO] (**10**): ^1H NMR (400 MHz, CDCl$_3$) δ 11.76 (br, 1H), 5.80 (s, 1H), 3.60–3.18 (m, 6H), 2.76 (d, J = 6.0 Hz, 2H), 2.08–1.78 (m, 2H), 1.75–1.55 (m, 6H); ^{13}C NMR (101 MHz, CDCl$_3$) δ 168.3, 166.2, 70.0, 54.4, 48.7, 38.3, 32.3, 29.1, 26.9, 24.2, 19.7 ppm; IR (neat): 3229, 2929, 2859, 2802,1632, 1377 cm^{-1};

[DBUH][TFA] (**11**): ^1H NMR (400 MHz, CDCl$_3$) δ 11.23 (br, 1H), 3.48–3.37 (m, 4H), 3.32 (dd, J = 7.8, 5.9 Hz, 2H), 2.79–2.65 (m, 2H), 2.00–1.89 (m, 2H), 1.63 (ddd, J = 14.7, 8.4, J = 5.4 Hz,

6H); ^{13}C NMR (101 MHz, CDCl$_3$) δ: 166.2, 161.3, 117.1, 54.3, 48.5, 38.1, 32.2, 28.9, 26.7, 23.9, 19.4 ppm; IR (neat): 3232, 3101, 3042, 2933, 2864, 2813, 1687, 1640 cm^{-1};

CO$_2$ Absorption in [DBUH][X]

The absorption capacity of CO$_2$ was measured according to the standard procedures reported (Wang et al., 2010, 2011). In specific, about 1.0 g [DBUH][X] was added to a 10 ml Schlenk tube which was pre-flushed with CO$_2$ gas. With agitation and control of temperature by a thermostat, a stream of CO$_2$ was bubbled into [DBUH][X] with a flow rate of 60 ml/min through a stainless steel needle (inner diameter = 10 mm) under atmosphere pressure. The weight of the tube was monitored from time to time until no further increment was detected by an electronic balance with an accuracy of ±0.1 mg. CO$_2$ absorption capacity in [DBUH][X] was then calculated based on the mass increasing of the Schlenk tube.

pK_a Determinations in [DBUH][OTf]

The UV-vis spectroscopic method was used the pK_a determination of the substrates involved in this work. The acidity ladder scale and indicator acids, the special UV cell and detailed procedures are similar to the previously reported (Wang et al., 2018a). The concentration of substrate acids was 10^{-4} to 10^{-3} M, the water content of [DBUH][OTf] was less than 100 ppm and the base used in the acidity determination in [DBUH][OTf] was DBU. The pK_a for each substrate was the average of 3 individual experiments, and the standard deviation (SD) is less than ±0.05 pK units.

CONCLUSIONS

In summary, we synthesized 11 DBU-based PILs with different basicity in [DBUH][OTf] and systematically investigated their CO$_2$ absorption kinetic and capacity in these PILs. The

basicity scale for the anion of these PILs in [DBUH][OTf] was established by extrapolation or direct determination. The CO$_2$ absorption in the weakly basic PILs are slow and practically have negligible absorption capacity, which is in line with a physical absorption mechanism. On the other hand, faster rates and higher absorption capacity were observed in the strongly basic PILs, and the spectroscopic studies support a chemical absorption mechanism in these PILs. The correlation between CO$_2$ absorption capacities and basicities of PILs, excluding those very weakly basic ones, in [DBUH][OTf] shows an excellent linear relationship, which indicates that the basicity of anion dictates the absorption ability and mechanism. We hope these results can be of help for a better understanding of structural implication of PILs on the CO$_2$ absorption, and also for a rational design of PILs in this connection.

AUTHOR CONTRIBUTIONS

PJ and J-PC conceived and designed the experiments and supervised the project; FG and ZW performed the experiments; FG, PJ, and J-PC prepared and revised the manuscript.

ACKNOWLEDGMENTS

SUPPLEMENTARY MATERIAL

The Supplementary Material for this article can be found online at: https://www.frontiersin.org/articles/10.3389/fchem. 2018.00658/full#supplementary-material

REFERENCES

Aresta, M., Dibenedetto, A., and Angelini, A. (2014). Catalysis for the valorization of exhaust carbon: from CO$_2$ to chemicals, materials, and fuels. Technological use of CO$_2$. *Chem. Rev.* 114, 1709–1742. doi: 10.1021/cr4002758

Bates, E. D., Mayton, R. D., Ntai, I., and Davis, J. H. (2002). CO$_2$ capture by a task-specific ionic liquid. *J. Am. Chem. Soc.* 124, 926–927.doi: 10.1021/ja017593d

Benson, E. E., Kubiak, C. P., Sathrum, A. J., and Smieja, J. M. (2009). Electrocatalytic and homogeneous approaches to conversion of CO$_2$ to liquid fuels. *Chem. Soc. Rev.* 38, 89–99. doi: 10.1039/B804323J

Bideau, J. L., Viau, L., and Vioux, A. (2011). Ionogels, ionic liquid based hybrid materials. *Chem. Soc. Rev.* 40, 907–925. doi: 10.1039/C0CS00059K

Blanchard, L. A., Hancu, D., Beckman, E. J., and Brennecke, J. F. (1999). Green processing using ionic liquids and CO$_2$. *Nature* 399, 28–29. doi: 10.1038/19887

Boot-Handford, M. E., Abanades, J. C., Anthony, E. J., Blunt, M. J., Brandani, S., MacDowell, N., et al. (2014). Carbon capture and storage update. *Energy Environ. Sci.* 7, 130–189. doi: 10.1039/C3EE42350F

Chen, F. F., Huang, K., Zhou, Y., Tian, Z. Q., Zhu, X., Tao, D. J., et al. (2016). Multi-molar absorption of CO$_2$ by the activation of carboxylate groups in amino acid ionic liquids. *Angew. Chem. Int. Ed.* 55, 7166–7170. doi: 10.1002/anie.201602919

Firaha, D. S., and Kirchner, B. (2014). CO$_2$ absorption in the protic ionic liquid ethylammonium nitrate. *J. Chem. Eng. Data* 59, 3098–3104. doi: 10.1021/je500166d

Goeppert, A., Czaun, M., Jones, J., Surya Prakash, G. K., and Olah, G. A. (2014). Recycling of carbon dioxide to methanol and derived products–closing the loop. *Chem. Soc. Rev.* 43, 7995–8048. doi: 10.1039/C4CS00122B

Gouedard, C., Picq, D., Launay, F., and Carrette, P. L. (2012). Amine degradation in CO$_2$ capture. I. A review. *Int. J. Greenh. Gas Con.* 10, 244–270. doi: 10.1016/j.ijggc.2012.06.015

Greaves, T. L., and Drummond, C. J. (2008). Protic ionic liquids: Properties and applications. *Chem. Rev.* 108, 206–237. doi: 10.1021/cr068040u

Greaves, T. L., and Drummond, C. J. (2015). Protic ionic liquids: Evolving structure–property relationships and expanding applications. *Chem. Rev.* 115, 11379–11448. doi: 10.1021/acs.chemrev.5b00158

Gurkan, B. E., de la Fuente, J. C., Mindrup, E. M., Ficke, L. E., Goodrich, B. F., Price, E. A., et al. (2010). Equimolar CO$_2$ absorption by anion-functionalized ionic liquids. *J. Am. Chem. Soc.* 132, 2116–2117. doi: 10.1021/ja909305t

Hallett, J. P., and Welton, T. (2011). Room-temperature ionic liquids. Solvents for synthesis and catalysis 2. *Chem. Rev.* 111, 3508–3576. doi: 10.1021/cr1003248

Haszeldine, R. S. (2009). Carbon capture and storage: how green can black be? *Science* 325, 1647–1652. doi: 10.1126/science.1172246

Izgorodina, E. I., Hodgson, J. L., Weis, D. C., Pas, S. J., and MacFarlane, D. R. (2015). Physical absorption of CO$_2$ in protic and aprotic ionic

liquids: an interaction perspective. *J. Phys. Chem. B* 119, 11748–11759. doi: 10.1021/acs.jpcb.5b05115

Jenkinson, D. S., Adams, D. E., and Wild, A. (1999). Model estimates of CO_2 emissions from soil in response to global warming. *Nature* 351, 304–306.

Joos, F., Plattner, G. K., Stocker, T. F., Marchal, O., and Schmittner, A. (1999). Global warming and marine carbon cycle feedbacks on future atmospheric CO_2. *Science* 284, 464–467. doi: 10.1126/science.284.5413.464

Kanzaki, R., Kodamatani, H., Tomiyasu, T., Watanabe, H., and Umebayashi, Y. (2016). A pH scale for the protic ionic liquid ethylammonium nitrate. *Angew. Chem. Int. Ed.* 55, 6266–6269. doi: 10.1002/anie.201511328

Kaupmees, K., Trummal, A., and Leito, I. (2014). Basicities of strong bases in water: a computational study. *Croat. Chem. Acta* 87, 385–395. doi: 10.5562/cca2472

Losetty, V., Matheswaran, P., and Wilfred, C. D. (2017). Synthesis, thermophysical properties and COSMO-RS study of DBU based protic ionic liquids. *J. Chem. Thermodyn.* 105, 151–158. doi: 10.1016/j.jct.2016.10.021

Luo, X. Y., Guo, Y., Ding, F., Zhao, H. Q., Cui, G. K., Li, H. R., et al. (2014). Significant improvements in CO_2 capture by pyridine-containing anion-functionalized ionic liquids through multiple-site cooperative interactions. *Angew. Chem. Int. Ed.* 53, 7053–7057. doi: 10.1002/anie.201400957

Mayr, H., and Ofial, A. R. (2016). Philicities, fugalities, and equilibrium constants. *Acc. Chem. Res.* 49, 952–965. doi: 10.1021/acs.accounts.6b00071

Mihichuk, L. M., Driver, G. W., and Johnson, K. E. (2011). Brönsted acidity and the medium: fundamentals with a focus on ionic liquids. *ChemPhysChem.* 12, 1622–1632. doi: 10.1002/cphc.201100087

Miran, M. S., Kinoshita, H., Yasuda, T., Md. Susan, A. B. H., and Watanabe, M. (2012). Physicochemical properties determined by ΔpK_a for protic ionic liquids based on an organic super-strong base with various Brønsted acids. *Phys. Chem. Chem. Phys.* 14, 5178–5186. doi: 10.1039/c2cp00007e

Niu, Y., Wang, N., Muñoz, A., Xu, J., Zeng, H., Rovis, T., et al. (2017). Experimental and computational gas phase acidities of conjugate acids of triazolylidene carbenes: rationalizing subtle electronic effects. *J. Am. Chem. Soc.* 139, 14917–14930. doi: 10.1021/jacs.7b05229

Rao, A. B., and Rubin, E. S. (2002). A technical, economic, and environmental assessment of amine-based CO_2 capture technology for power plant greenhouse gas control. *Environ. Sci. Technol.* 36, 4467–4475. doi: 10.1021/es0158861

Rogers, R. D., and Seddon, K. R. (eds) (2003). *Ionic Liquids as Green Solvents: Progress and Prospects.* Washington, DC: American Chemical Society; ACS Symposium Series, 856.

Sanna, A., Uibu, M., Caramanna, G., Kuusik, R., and Maroto-Valera, M. M. (2014). A review of mineral carbonation technologies to sequester CO_2. *Chem. Soc. Rev.* 43, 8049–8080. doi: 10.1039/C4CS00035H

van Rantwijk, F., and Sheldon, R. A. (2007). Biocatalysis in ionic liquids. *Chem. Rev.* 107, 2757–2785. doi: 10.1021/cr050946x

Wang, C. M., Luo, H. M., Jiang, D. E., Li, H. R., and Dai, S. (2010). Carbon dioxide capture by superbase-derived protic ionic liquids. *Angew. Chem. Int. Ed.* 49, 5978–5981. doi: 10.1002/anie.201002641

Wang, C. M., Luo, H. M., Li, H. R., Zhu, X., Yu, B., and Dai, S. (2012). Tuning the physicochemical properties of diverse phenolic ionic liquids for equimolar CO_2 capture by the substituent on the anion. *Chem. Eur. J.* 18, 2153–2160. doi: 10.1002/chem.201103092

Wang, C. M., Luo, X. Y., Luo, H. M., Jiang, D. E., Li, H. R., and Dai, S. (2011). Tuning the basicity of ionic liquids for equimolar CO_2 capture. *Angew. Chem. Int. Ed.* 50, 4918–4922. doi: 10.1002/anie.201008151

Wang, N., Xu, J., and Lee, J. K. (2018). The importance of N-heterocyclic carbene basicity in organocatalysis. *Org. Biomol. Chem.* 16, 8230–8244. doi: 10.1039/C8OB01667D

Wang, Z., Gao, F. X., Ji, P., and Cheng, J. P. (2018a). Unexpected solvation-stabilization of ions in a protic ionic liquid: insights disclosed by a bond energetic study. *Chem. Sci.* 9, 3538–3543. doi: 10.1039/C7SC05227H

Wang, Z., Wang, F., Xue, X. S., and Ji, P. (2018b). Acidity scale of N-heterocyclic carbene precursors: can we predict the stability of NHC-CO_2 adducts? *Org. Lett.* 20, 6041–6045. doi: 10.1021/acs.orglett.8b02290

Watanabe, M., Thomas, M. L., Zhang, S., Ueno, K., Yasuda, T., and Dokko, K. (2017). Application of ionic liquids to energy storage and conversion materials and devices. *Chem. Rev.* 117, 7190–7239. doi: 10.1021/acs.chemrev.6b00504

Welton, T. (1999). Room-temperature ionic liquids. Solvents for synthesis and catalysis. *Chem. Rev.* 99, 2071–2084. doi: 10.1021/cr980032t

Xia, S. M., Chen, K. H., Fu, H. C., and He, L. N. (2018). Ionic liquids catalysis for carbon dioxide conversion with nucleophiles. *Front. Chem.* 6:462. doi: 10.3389/fchem.2018.00462

Yang, J. D., Ji, P., Xue, X. S., and Cheng, J. P. (2018). Recent advances and advisable applications of bond energetics in organic chemistry. *J. Am. Chem. Soc.* 140, 8611–8623. doi: 10.1021/jacs.8b04104

Yang, Q., Wang, Z., Bao, Z., Zhang, Z., Yang, Y., Ren, Q., et al. (2016). New insights into CO_2 absorption mechanisms with amino–acid ionic liquids. *ChemSusChem.* 9, 806–812. doi: 10.1002/cssc.201501691

Yasuda, T., and Watanabe, M. (2013). Protic ionic liquids: fuel cell applications. *MRS Bull.* 38, 560–566. doi: 10.1557/mrs.2013.153

Zhu, X., Song, M. L., and Xu, Y. J. (2017). DBU-based protic ionic liquids for CO_2 capture. *ACS Sustain. Chem. Eng.* 5, 8192–8198. doi: 10.1021/acssuschemeng.7b01839

Conflict of Interest Statement: The authors declare that the research was conducted in the absence of any commercial or financial relationships that could be construed as a potential conflict of interest.

Simultaneous Separation of Antioxidants and Carbohydrates From Food Wastes Using Aqueous Biphasic Systems Formed by Cholinium-Derived Ionic Liquids

Catarina M. S. S. Neves[1], Marcos Figueiredo[1], Patrícia M. Reis[2], Ana C. A. Sousa[1], Ana C. Cristóvão[3], Mariana B. Fiadeiro[3], Luís Paulo N. Rebelo[2], João A. P. Coutinho[1], José M. S. S. Esperança[2]* and Mara G. Freire[1]*

[1] Department of Chemistry, CICECO – Aveiro Institute of Materials, University of Aveiro, Aveiro, Portugal, [2] LAQV/REQUIMTE, FCT-NOVA, Costa da Caparica, Portugal, [3] CICS-UBI – Health Sciences Research Centre, University of Beira Interior, Covilhã, Portugal

The food industry produces significant amounts of waste, many of them rich in valuable compounds that could be recovered and reused in the framework of circular economy. The development of sustainable and cost-effective technologies to recover these value added compounds will contribute to a significant decrease of the environmental footprint and economic burden of this industry sector. Accordingly, in this work, aqueous biphasic systems (ABS) composed of cholinium-derived bistriflimide ionic liquids (ILs) and carbohydrates were investigated as an alternative process to simultaneously separate and recover antioxidants and carbohydrates from food waste. Aiming at improving the biocompatible character of the studied ILs and proposed process, cholinium-derived bistriflimide ILs were chosen, which were properly designed by playing with the cation alkyl side chain and the number of functional groups attached to the cation to be able to create ABS with carbohydrates. These ILs were characterized by cytotoxicity assays toward human intestinal epithelial cells (Caco-2 cell line), demonstrating to have a significantly lower toxicity than other well-known and commonly used fluorinated ILs. The capability of these ILs to form ABS with a series of carbohydrates, namely monosaccharides, disaccharides and polyols, was then appraised by the determination of the respective ternary liquid-liquid phase diagrams at 25°C. The studied ABS were finally used to separate carbohydrates and antioxidants from real food waste samples, using an expired vanilla pudding as an example. With the studied systems, the separation of the two products occurs in one-step, where carbohydrates are enriched in the carbohydrate-rich phase and antioxidants are mainly present in the IL-rich phase. Extraction efficiencies of carbohydrates ranging between 89 and 92% to the carbohydrate-rich phase, and antioxidant relative activities ranging between 65 and 75% in the IL-rich phase were obtained. Furthermore, antioxidants from the IL-rich phase were recovered by solid-phase extraction, and the IL was recycled for two more times with

no losses on the ABS separation performance. Overall, the obtained results show that the investigated ABS are promising platforms to simultaneously separate carbohydrates and antioxidants from real food waste samples, and could be used in further related applications foreseeing industrial food waste valorization.

INTRODUCTION

According to the Food and Agriculture Organization of the United Nations (FAO), one third of the food worldwide produced for human consumption (1.3 billion tons per year) is lost or wasted (FAO, 2011). In Europe, *ca.* 88 million tons of food waste are generated *per* year, with associated costs of 143 billion euros (Fusions, 2016). Currently, food waste constitutes a relevant economic problem and is linked to negative societal and environmental impacts (Fusions, 2016), being responsible for about 8% of the Global Greenhouse Gas emissions (European Commission, 2018). As a result, the management of food waste, including its reuse, is a priority mitigation measure to reduce emissions intensity and the carbon footprint of the food production chain (IPCC, 2018). According to the Intergovernmental Panel on Climate Change (IPCC) this can be achieved through new technological solutions, e.g., by transforming food waste into products with marketable value (IPCC, 2018). These new solutions will not only reduce the environmental impact of the food industry, but will also contribute to improve its economic impact as the residues generated may contain value added compounds. Furthermore, sustainable food systems have a pivotal role in the UN Sustainable Developmental Goals (European Commission, 2018; Pradyumna, 2018). Overall, and in the framework of circular economy, these facts stress the need to develop sustainable and cost-effective technologies to recover value added compounds from food waste, aiming at contributing to a decrease of the environmental footprint and increased sustainability of this industrial sector.

Several extraction methods are currently applied for the valorization of food waste, including hydrothermal extraction, supercritical fluid extraction, pressurized liquid extraction, microwave-assisted extraction, and ultrasound-assisted extraction (see Arshadi et al., 2016 and references therein). However, some of these technologies display several drawbacks, including high capital investment and/or high operating costs, as well as potential negative environmental impacts associated to high-energy consumption and/or by the use of volatile organic solvents. In order to avoid the use of those and to decrease the economic burden, an increasing interest on the application of ionic liquids (ILs) as alternative solvents in the food industry sector has emerged (Toledo Hijo et al., 2016). Ionic liquids properties, including their ability to be tailored in terms of physicochemical properties and designed to a specific application through the manipulation of their ions (Rogers and Seddon, 2003; Ventura et al., 2017), make them ideal candidates

to be used in the valorization of food waste. Ionic liquids not only have the ability to dissolve and pretreat complex raw materials, but they can be also designed to selectively extract target compounds due to their tailoring ability. Nonetheless, when compared with their use in the extraction of value added products from biomass (Passos et al., 2014), few studies addressed the ILs application in the recovery of value added compounds from real food waste (Lateef et al., 2009; Bi et al., 2010; Qin et al., 2010; Bica et al., 2011; Guolin et al., 2012; Setoguchi et al., 2012; Cláudio et al., 2013, 2018; Jiao et al., 2013; Ge et al., 2014; Hernoux-Villière et al., 2014; Zhang et al., 2015, 2017; de Faria et al., 2017; Oberleitner et al., 2017; Mizuno and Usuki, 2018). Most of these studies employed imidazolium-based ILs to recover antioxidants, vitamins, fats, sugars, and essential oils from different types of food and food waste, such as tea, fruits, vegetables, crustaceans, or used oils. However, given the often moderate to high toxicity and poor biodegradability of imidazolium-based ILs, the application of novel and more biocompatible ILs, such as cholinium-based, started to emerge (Garcia et al., 2010; Ni et al., 2012; Wang et al., 2016; Oberleitner et al., 2017).

ILs can be used to form aqueous biphasic systems (ABS), which due to their water-rich media can be applied in sustainable and biocompatible separation processes. Most IL-based ABS are ternary systems formed by water, one IL and a third species with salting-out capacity, such as an inorganic salt with high-charge density (Freire et al., 2012). More recently, novel combinations to create IL-based ABS have been proposed by combining ILs with amino acids, polymers, or carbohydrates in aqueous media (Ventura et al., 2017). In addition to the characterization of their phase diagrams, a plethora of systems has been investigated in the extraction and separation of value added compounds from aqueous media (Freire et al., 2012). However, most of these studies were carried out with model systems, and the use of IL-based ABS for the recovery of target compounds from real matrices has seldom been studied (Ventura et al., 2017).

Although a large number of works on IL-based ABS have been reported (Freire et al., 2012; Ventura et al., 2017; Song et al., 2018; Yee et al., 2018), few works on the formation of IL-based ABS by the addition of carbohydrates are available since more hydrophobic (yet water-soluble) ILs are required (Zhang et al., 2007; Wu et al., 2008a,b,c; Chen et al., 2009, 2010, 2012; Chen and Zhang, 2010; Freire et al., 2011; Ferreira et al., 2016; Okuniewski et al., 2016; Quental et al., 2018). This trend is due to the weak salting-out aptitude of carbohydrates when compared to high-charge density salts. Therefore, imidazolium-based cations combined with tetrafluoroborate and triflate anions have been the

TABLE 1 | Cytotoxicity of ILs containing fluorinated anions toward the Caco-2 cell line evaluated through the MTT [3-(4,5-dimethylthiazol-2-yl)-2,5-diphenyltetrazolium bromide] assay.

Ionic liquid	Objective/Application	EC_{50} (mM)	References
$[C_4C_1im][BF_4]$	To compare the cytotoxicity of amino-acid- and imidazolium-based ILs	11.19 ($\pm$0.63)[a]	Egorova et al., 2015a
$[C_4C_1im][PF_6]$		11.50 ($\pm$1.08)[a]	Egorova et al., 2015a
$[Ala-OMe][BF_4]$	To address the citotoxicity of new drug delivery platforms based on imidazolium-based ILs	6.24 (4.32–8.17)[b]	Egorova et al., 2015b
$[C_2C_1im-OSal][BF_4]$		4.77 (3.27–6.27)[b]	Egorova et al., 2015b
$[C_8C_1im][PF_6]$	To evaluate the cytotoxicity of imidazolium-based ILs and application of models	5.12 ($\pm$31.81)[c]	García-Lorenzo et al., 2008
$[C_6C_1im][PF_6]$		15.67 ($\pm$3.78)[c]	García-Lorenzo et al., 2008

Only studies with a 24 h exposure period are provided in order to allow direct comparisons with our results.
[a]*Standard error of the mean (SEM).*
[b]*95% Confidence interval.*
[c]*Standard deviation (SD).*

most studied ILs (Freire et al., 2012). Nevertheless, these ILs may display some citotoxicity concerns, as summarized in **Table 1**. In this work, we demonstrate that less cytotoxic cholinium-derived ILs can form ABS with carbohydrates, achieved by a proper tailoring of the IL anion and cation alkyl side chain and number of attached functional groups. Taking into account the possibility of creating ABS with carbohydrates and more biocompatible cholinium-derived ILs, here established by cytotoxicity assays toward human intestinal epithelial cells (Caco-2 cell line), these systems may be anticipated as improved strategies to separate carbohydrates and antioxidants from food wastes.

In ABS formed by ILs and carbohydrates there is the spontaneous separation of the two-phase forming components above given concentrations, whereas previous works on ABS formed by ILs and salts support the preferential migration of antioxidants to the IL-rich phase (Cláudio et al., 2010, 2012, 2014). These patterns lead us to envision that both products (antioxidants and carbohydrates) may be enriched in separated phases in ABS formed by ILs and carbohydrates. This hypothesis was here validated under a perspective of resource efficiency and circular economy, in which ABS composed of cholinium-derived ILs and carbohydrates were investigated to simultaneously separate antioxidants and carbohydrates from food waste, namely from an expired commercial vanillin-rich pudding.

MATERIALS AND METHODS

Materials
The chemical structures of the ILs used in this work [*N*-methyl-*N,N,N*-tris(2-hydroxyethyl)ammonium bistriflimide, $[N_{1(2OH)(2OH)(2OH)}][NTf_2]$; *N*-ethyl-*N,N,N*-tris(2-hydroxyethyl) ammonium bistriflimide, $[N_{2(2OH)(2OH)(2OH)}][NTf_2]$; *N, N*-dimethyl-*N,N*-bis(2-hydroxyethyl) ammonium bistriflimide, $[N_{11(2OH)(2OH)}][NTf_2]]$ are presented in **Figure 1**. The ILs investigated were synthesized according to the protocol described by de Ferro et al. (2018). The $AgNO_3$ test was performed to all ILs to confirm the absence of halides (chloride

or bromide). Characterization analysis by ^1H and ^{19}F NMR and Elemental Analysis indicate that all ILs have a purity >99 wt%. These results are given in the **Supplementary Material**. Prior to their use, all ILs were dried for a minimum of 48 h at 35°C under vacuum ($\approx$0.1 Pa) with constant stirring. The water content of the dried ILs, measured by coulometric Karl Fischer titration, was below 500 ppm. Carbohydrates used in this work comprise monosaccharides, disaccharides and polyols, namely: D-maltitol ($\geq$95 wt%) and xylitol ($\geq$99 wt%) acquired from Acros Organics; D-(+)-maltose (99 wt%) acquired from BDH; D-sorbitol ($\geq$91 wt%) from Fisher BioReagents; D-(+)-sucrose ($\geq$99 wt%) and D-(+)-galactose ($\geq$98 wt%) from GPR Rectapur; D-(+)-glucose (99 wt%) from Scharlau; D-(-)-fructose ($\geq$99 wt%) and L-(+)-arabinose ($\geq$98 wt%) from PanReac AppliChem; D-(+)-mannose ($\geq$99 wt%) from Alfa Aesar; and D-(+)-xylose ($\geq$99 wt%) from Merck. The chemical structures of the investigated carbohydrates are depicted in **Figure 1**.

The water used was ultra-pure, double distilled, passed by a reverse osmosis system and further treated with a Milli-Q plus 185 water purification apparatus. For the antioxidant assays, the radical 2,2-diphenyl-1-picrylhydrazyl (DPPH) obtained from Sigma Aldrich was used. The Dubois method (Dubois et al., 1956) was used to determine the total content of carbohydrates in each phase, for which sulfuric acid (95 wt%) from Sigma-Aldrich and phenol (99.5 wt%) from Merck were used. A commercial vanillin-rich pudding from a Portuguese brand was used at a concentration of 18 wt% in water as the food waste sample. An Oasis HLB (200 mg) SPE cartridge from Waters was used in the solid-phase extractions to separate the IL from carbohydrates and antioxidants. Methanol of HPLC grade, acquired from Sigma-Aldrich, was used.

Cytotoxicity Assays
The cytotoxicity of each IL was evaluated in the human colon carcinoma cell line (Caco-2) using the 3-(4,5-dimethylthiazol-2-yl)-2,5-diphenyltetrazolium bromide (MTT) assay. The Caco-2 cell line was used since this cancer derived cell line is a well-established model of the intestinal epithelial barrier, being widely
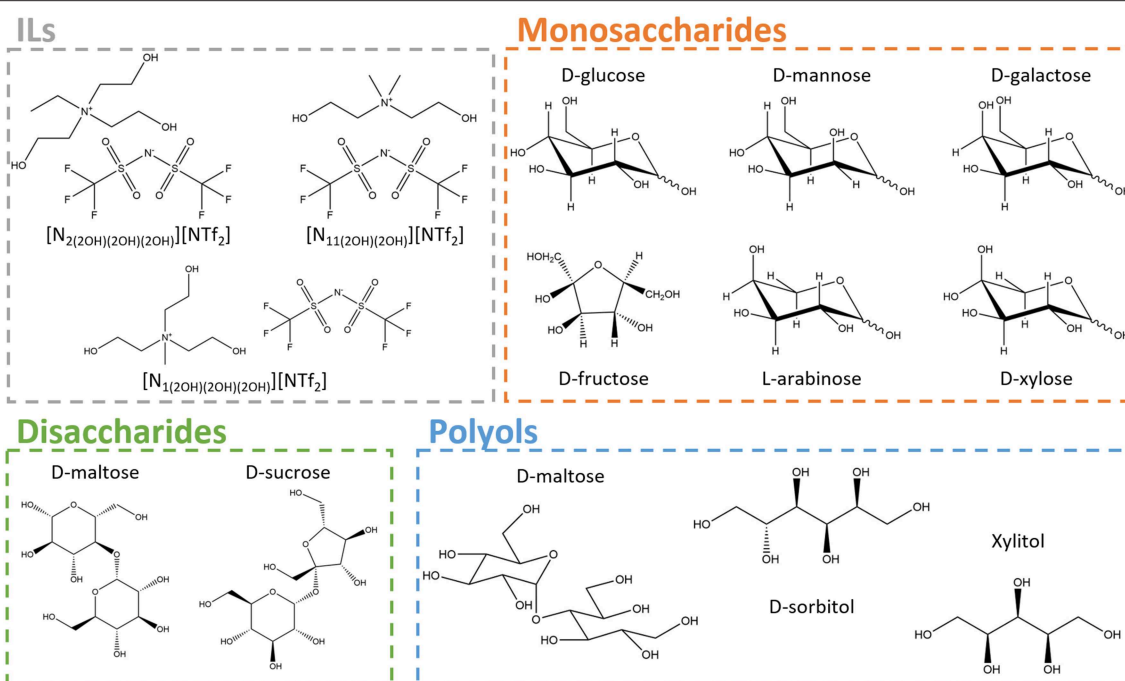
FIGURE 1 | Chemical structures of ionic liquids (ILs) and different classes of carbohydrates (monosaccharides, disaccharides, and polyols) studied.

used in the toxicological evaluation of pharmaceutical drugs (Meunier et al., 1995) and new food bioactive compounds (Lea, 2015). The MTT assay is based on the ability of viable cells to convert MTT into formazan, a water insoluble compound that can be colorimetrically quantified. It is a widely used assay to evaluate cytotoxicity being suitable for high throughput screening (HTS) (Riss et al., 2016; Sharma et al., 2018; Macário et al., 2019; Thamke et al., 2019). Furthermore, the available published studies performed with the same cell line (Caco-2 cell line) and the same incubation period (24 h) used MTT (García-Lorenzo et al., 2008; Egorova et al., 2015a,b); therefore, this assay also allows to perform comparisons with other fluorinated ILs used in the creation of ABS with carbohydrates.

Cells were grown in high glucose Dulbecco's modified Eagle's medium (DMEM-HG) with 10% (v/v) fetal bovine serum (FBS), 100 units penicillin, and 50 μg·mL^{-1} streptomycin in a humidified atmosphere of 5% CO_2 at 37°C. Different concentrations of ILs (0.01, 0.1, 1.0, 30, 60, and 90 g·L^{-1}) were prepared in saline [[NaCl] = 0.9% (m/w)] aqueous solutions. For the toxicological assays, cells were plated on polystyrene cell culture dishes at a density of 1 × 10^4 cells *per* well in 96 well culture plates. Upon 16 h after plating, cells were treated with different concentrations of the target ILs for 24 h. Afterwards, cell variability was assessed using the MTT assay. Caco-2 cells were incubated overnight at 37°C with 0.5 mg·L^{-1} of MTT, and the water-insoluble precipitate was dissolved in 10% (w/v) sodium dodecyl sulfate SDS for 4 h. The colorimetric detection was performed at 570 nm using a microplate spectrophotometer. Each concentration was tested in at least four replicates of three independent experiments ($n = 3$). The dose response curves and EC$_{50}$ calculations were performed using the GraphPad PRISM Software (version 5.01). The average effective concentration (EC$_{50}$), i.e., the concentration of IL at which 50% of cells are viable, was calculated using a sigmoidal dose response equation using the automatic outliers fitting method.

ABS Phase Diagrams and Their Application as Simultaneous Separation Strategies of Antioxidants and Carbohydrates

The ternary phase diagrams were determined at room temperature (≈25°C) and at atmospheric pressure by the cloud point titration method (Freire et al., 2011). Stock solutions of each carbohydrate (ranging from 40 to 70 wt%, depending on the carbohydrate solubility in water) and of each IL (≈70 wt%) were prepared and used for the determination of the phase diagrams. Repetitive drop-wise addition of each carbohydrate solution to each IL aqueous solution was carried out until the detection of a cloudy solution, followed by the drop-wise addition of ultra-pure water until the detection of a monophasic region (clear and limpid solution). All these additions were carried out under continuous stirring. When no more cloud points were detected, an inversion of the method was applied, i.e., with the repetitive addition of the IL solution to the carbohydrate solution aiming at gathering more experimental data points to better define each binodal curve. In both cases, the systems composition was determined by weight (±10^{-4} g). Not all the combinations of ILs and carbohydrates investigated are able to form ABS—a complete list of the combinations tested is given in **Supplementary Table S1**.

The ABS formed by ILs and carbohydrates were then investigated to simultaneously separate antioxidants and

carbohydrates from food waste. The food waste sample used corresponds to a vanilla pudding, thus rich in the antioxidant vanillin, of a Portuguese brand. The pudding was dissolved at room temperature (*ca.* 25°C) in distilled water for a minimum of 2 h under continuous agitation. This solution was then left for 20 min in order to allow the deposition of the non-water soluble solids, and further decanted. The obtained supernatant was centrifuged at 1,100 rpm for 10 min in an Eppendorf Centrifuge 5804, and the liquid fraction was filtered with PTFE membrane filters with a porosity of 0.45 μm. This aqueous solution, rich in both carbohydrates and antioxidants, was used in the ABS composition and formation. The mixture composition investigated corresponds to: 25 wt% D-glucose or D-sucrose + 50 wt% IL + 25 wt% aqueous solution of pudding. After mixing, each ABS was left overnight at 25°C, phases were separated, and the content of carbohydrates and antioxidants in each phase was quantitatively determined.

The content of antioxidants in each phase was appraised by the determination of the respective antioxidant activity using the DPPH radical scavenging assay, according to the method described by Sintra et al. (2015). Slight modifications were however introduced, in which methanol was substituted by ethanol in order to use more benign solvents. Briefly, 125 μL of DPPH solution (0.36 g·L^{-1} in ethanol) were mixed under dark conditions with each ABS phase (250 μL). Water was added up to 1 mL (final volume). All tubes were vortex mixed and kept for equilibrium in the dark for 30 min. Control samples were prepared and used. The absorbance of the samples was determined at 540 nm using a microplate spectrophotometer. Triplicate samples were prepared and the values given correspond to the average value and associated standard deviation.

The percentage antioxidant activity (%AA) was determined using Equation (1):

$$\%AA = \frac{A_0 - A_1}{A_0} \times 100 \tag{1}$$

where A_0 is the control absorbance and A_1 is the absorbance of the sample at the maximum wavelength.

The antioxidant relative activity (%ARA) in each ABS phase was calculated according to Equation (2):

$$\%ARA = \frac{AA_{phase}}{AA_{top} + AA_{bot}} \times 100 \tag{2}$$

where AA_{phase} is the antioxidant activity of the respective ABS phase, and AA_{top} and AA_{bot} are the antioxidant activity of the ABS top and bottom phases, respectively.

The total carbohydrates quantification in each ABS phase was performed through a colorimetric assay based on the Dubois method (Dubois et al., 1956). The colored product was quantified at 488 nm using a microplate spectrophotometer. The calibration curve was prepared with D-glucose. Triplicate samples were prepared and the values given correspond to the average value and associated standard deviation. The extraction efficiency (%EE) of carbohydrates was determined as the ratio between the

carbohydrates concentration in the respective ABS phase and the total concentration of carbohydrates in both phases, according to the Equation (3):

$$\%EE = \frac{[CH]_{phase}}{[CH]_{top} + [CH]_{bot}} \times 100 \tag{3}$$

where $[CH]_{phase}$ is the carbohydrates concentration in the ABS respective phase, and $[CH]_{top}$ and $[CH]_{bot}$ are the carbohydrates concentrations in the ABS top and bottom phases, respectively.
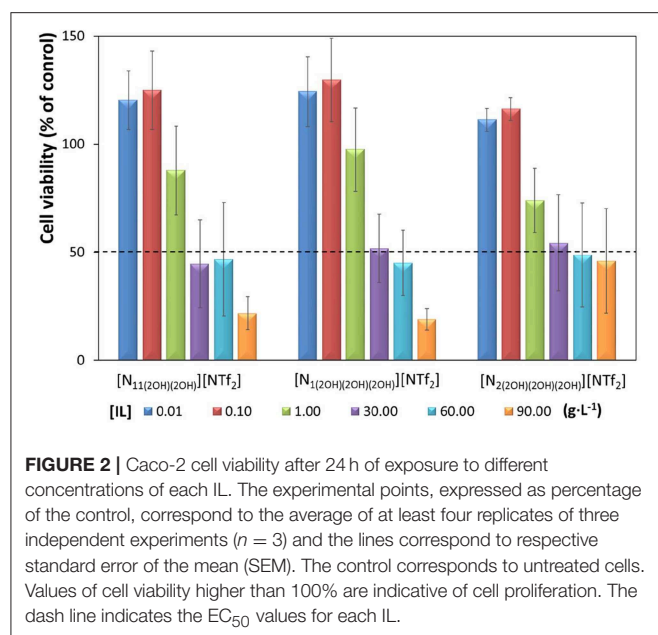
The separation of the IL from the antioxidants in the IL-rich phase was performed by solid-phase extraction, with Oasis HLB cartridges previously conditioned with methanol (1 mL) and equilibrated with acidic water (pH 2, 1 mL) (Waters, 2014). The IL-rich phase was loaded through the column, where carbohydrates and antioxidants are adsorbed, followed by the loading of 3 mL of acidic water to recover the IL. Then, 2 mL of a mixture of methanol/water (20:80, v:v) was used to desorb carbohydrates and antioxidants (Michalkiewicz et al., 2008). The IL purity after recovery was confirmed through ^{1}H NMR, and the respective losses determined gravimetrically ($\pm 10^{-4}$ g). After the separation through SPE, the fractions containing the IL were subjected to evaporation under vacuum at 60°C. The recovered non-volatile IL was then reused in the creation of novel ternary systems. The IL recycling was tested for two times. The carbohydrates quantification and the antioxidant activity were determined by the methods described above.

RESULTS AND DISCUSSION

ILs Cytotoxicity Analysis

In this work, we focused on the use of new cholinium-derived ILs with the bistriflimide anion, known to produce hydrophobic ILs, to create novel ABS with weak salting-out substances such as carbohydrates. We manipulated the chemical structure of the cholinium cation by grafting it with additional hydroxyethyl moieties to produce water soluble bistriflimide-based ILs. Complete water miscibility of the studied ILs (shown in **Figure 1**) is achieved due to the large number of OH groups at the cation, contributing to stronger hydrogen-bonding with water (de Ferro et al., 2018).

Given the hypothesis to be evaluated, i.e., if ABS formed by carbohydrates and ILs are platforms with potential to simultaneously separate carbohydrates and antioxidants from food waste, the evaluation of the ILs citotoxicity toward Caco-2 cells was here carried out as a first test to appraise their biocompatible nature. The cytotoxic profile of the investigated ILs toward the Caco-2 cell line is shown in **Figure 2**. The cytotoxic profile of $[N_{11(2OH)(2OH)}][NTf_2]$ and $[N_{1(2OH)(2OH)(2OH)}][NTf_2]$ is similar, where an increase in the IL concentration leads to an increase in cytotoxicity. For both ILs, an increase in the cell viability ($<30\%$) at the lowest concentrations tested (0.01 and 0.1 g·L^{-1}) is observed; however, this increase is not statistically significant ($p > 0.05$). The EC$_{50}$ and respective 95% confidence intervals (CI) values are also similar between these two ILs, with 29.19 g·L^{-1} (26.90–31.48 g·L^{-1}) for $[N_{11(2OH)(2OH)}][NTf_2]$ and 29.48 g·L^{-1} (28.35–30.61 g·L^{-1})

FIGURE 2 | Caco-2 cell viability after 24 h of exposure to different concentrations of each IL. The experimental points, expressed as percentage of the control, correspond to the average of at least four replicates of three independent experiments ($n = 3$) and the lines correspond to respective standard error of the mean (SEM). The control corresponds to untreated cells. Values of cell viability higher than 100% are indicative of cell proliferation. The dash line indicates the EC_{50} values for each IL.

for $[N_{1(2OH)(2OH)(2OH)}][NTf_2]$. For $[N_{2(2OH)(2OH)(2OH)}][NTf_2]$ a different cytotoxic pattern is seen. For this IL, concentrations higher than 30 g·L^{-1} do not lead to an increased toxicity. About 50% of viable cells are present for the higher concentrations investigated, namely 30, 60, and 90 g·L^{-1}, and for this reason it is not possible to calculate the EC_{50} value for this particular IL (*cf.* **Supplementary Figure S1**). However, this trend means that this IL exhibits low toxicity in the tested concentrations, and at least up to 90 g·L^{-1}. Overall, taking into account the EC_{50} values and respective standard errors shown in **Figure 2**, it is safe to admit that $[N_{2(2OH)(2OH)(2OH)}][NTf_2]$ has a similar cytotoxic impact when compared to the remaining ILs studied.

The comparison of the cytotoxic impact of the investigated ILs and of other ILs reported in the literature, whose data were obtained under the same experimental conditions (Caco-2 cell line and 24h of exposure period), is given in **Table 1** and **Supplementary Figure S2**. Ionic liquids comprising cations such as imidazolium and alanine derivatives combined with fluorinated anions are significantly more toxic than the cholinium-derived bistriflimide ILs investigated in this work. By combining the $[NTf_2]^-$ anion with cholinium derivatives cations, it is possible to reduce their average toxicity by *ca.* 10 times when comparing with the ILs O-methylalaninate tetrafluoroborate ($[Ala-OMe][BF_4]$), 1-(2-((2-hydroxybenzoyl)oxy)ethyl)-3-methylimidazolium tetrafluoroborate ($[C_2C_1im-OSal][BF_4]$) and 1-methyl-3-octylimidazolium hexafluorophosphate ($[C_8C_1im][PF_6]$) (Egorova et al., 2015a,b), and *ca.* 4 times when comparing with 1-hexyl-3-methylimidazolium hexafluorophosphate ($[C_6C_1im][PF_6]$) (García-Lorenzo et al., 2008). Such results demonstrate that it is possible to design new ILs based on the cholinium cation and fluorinated anions, such as bistriflimide, that are significantly less toxic than other fluorinated-based ILs

commonly used. Despite such promising results, it must be remarked that a complete risk assessment of these ILs always needs to be performed before their safety can be completely established. This evaluation should include more *in vitro* tests with other cell lines and different endpoints, as well as *in vivo* experiments with organisms from different taxa (including e.g., invertebrates and mammals).

ABS Phase Diagrams

The phase diagrams of each ternary system formed by water, IL and carbohydrate were determined at atmospheric pressure and 25°C. Three different classes of carbohydrates were tested to promote phase separation, namely monosaccharides (D-glucose, D-mannose, D-galactose, D-fructose, L-arabinose, and D-xylose), disaccharides (D-maltose and D-sucrose), and polyols (D-maltitol, D-sorbitol, and xylitol), combined with three ILs, namely $[N_{1(2OH)(2OH)2OH}][NTf_2]$, $[N_{2(2OH)(2OH)2OH}][NTf_2]$, and $[N_{11(2OH)(2OH)}][NTf_2]$. The chemical structures of the investigated ILs and carbohydrates are given in **Figure 1**. **Figure 3** depicts the binodal curves in molality units of each ABS determined by the cloud point titration method (Freire et al., 2011). Compositions of IL and carbohydrate above each binodal curve result in two-phase systems, whereas mixture compositions below fall within the monophasic region. In summary, a larger biphasic region corresponds to a higher ability of both the carbohydrate and the IL to induce phase separation, thus requiring lower amounts of these phase-forming components to create ABS. The detailed data and respective ternary phase diagrams in weight fraction are provided in **Supplementary Figures S3, S4** and **Supplementary Tables S2–S4**. Not all combinations of ILs and carbohydrates are able to form ABS at the studied conditions—a list of the successful combinations is provided in **Supplementary Table S1**.

Although all carbohydrates were tested with the three ILs, only the most hydrophobic, i.e., $[N_{11(2OH)(2OH)}][NTf_2]$, with a lower number of hydroxyl groups is able to form ABS with all the studied carbohydrates. This is an indication of the carbohydrates poor salting-out potential over ILs, in agreement with the literature (Freire et al., 2011). The lower the IL affinity for water, here achieved by reducing the number of hydroxyl groups and propensity for hydrogen-bonding with water, the easier it is to induce its salting-out and to create ABS. The general trend of the carbohydrates ability to salt-out the IL or to create ABS with $[N_{11(2OH)(2OH)}][NTf_2]$ shown in **Figure 3A**, obtained when the molality of IL equals the molality of carbohydrate in the binodal curve ($[IL] = [Carbohydrate]$, in mol·kg^{-1}), follows the order: D-maltitol > D-maltose ≈ D-sucrose ≈ xylitol > D-sorbitol > D-glucose > D-galactose > D-mannose ≈ D-fructose > D-xylose > L-arabinose. This trend is in good agreement to those previously reported in the literature (Freire et al., 2011), demonstrating that polyols are more effective than saccharides at promoting phase separation. Furthermore, it is shown that 6-sided ring carbohydrates are stronger salting-out agents than the 5-sided ring ones, as well as carbohydrates with a higher number of hydroxyl groups (increasing thus the propensity to hydrogen bond with water), being these more effective in the
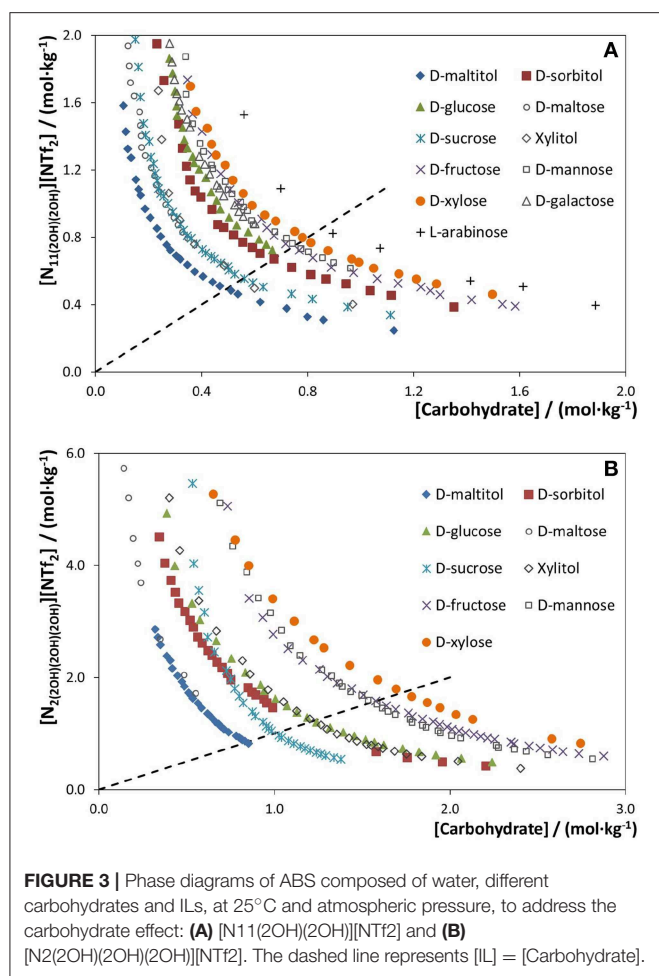
FIGURE 3 | Phase diagrams of ABS composed of water, different carbohydrates and ILs, at 25°C and atmospheric pressure, to address the carbohydrate effect: **(A)** [N11(2OH)(2OH)][NTf2] and **(B)** [N2(2OH)(2OH)(2OH)][NTf2]. The dashed line represents [IL] = [Carbohydrate].
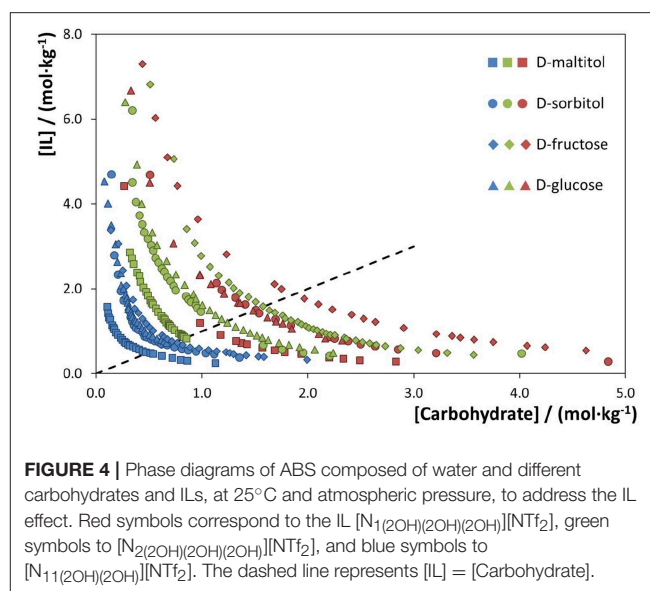

FIGURE 4 | Phase diagrams of ABS composed of water and different carbohydrates and ILs, at 25°C and atmospheric pressure, to address the IL effect. Red symbols correspond to the IL [N$_{1(2OH)(2OH)(2OH)}$][NTf$_2$], green symbols to [N$_{2(2OH)(2OH)(2OH)}$][NTf$_2$], and blue symbols to [N$_{11(2OH)(2OH)}$][NTf$_2$]. The dashed line represents [IL] = [Carbohydrate].

creation of ABS with ILs. A deeper discussion on these effects can be found in the literature (Freire et al., 2011; Ferreira et al., 2016). On the other hand, when the hydrophilicity of the IL is increased by the replacement of a methyl group in the cation by a hydroxyethyl group, the number of carbohydrates able to promote phase separation decreases. This trend is shown in **Figure 3B** for the second most hydrophobic IL investigated, [N$_{2(2OH)(2OH)(2OH)}$][NTf$_2$]. The binodal curves corresponding to the more hydrophilic IL [N$_{1(2OH)(2OH)(2OH)}$][NTf$_2$] are given in **Supplementary Figure S4**. The carbohydrates rank to form ABS with these ILs is as follows: D-maltitol ≈ D-maltose > D-sucrose > D-sorbitol > D-glucose ≈ xylitol > D-mannose ≈ D-fructose > D-xylose, being in close agreement with the previous one and to what has been found with other fluorinated ILs (Ferreira et al., 2016).

The binodal curves of ABS composed of different ILs and a fixed carbohydrate are provided in **Figure 4**. Examples with four carbohydrates are given. With a common carbohydrate, the IL ability to create ABS follows the order: [N$_{11(2OH)(2OH)}$][NTf$_2$] > [N$_{2(2OH)(2OH)(2OH)}$][NTf$_2$] > [N$_{1(2OH)(2OH)(2OH)}$][NTf$_2$]. The phase diagrams corresponding to a common carbohydrate and the most hydrophobic IL ([N$_{11(2OH)(2OH)}$][NTf$_2$]) are

the ones with the largest biphasic regions, whereas those corresponding to the ILs [N$_{2(2OH)(2OH)(2OH)}$][NTf$_2$] and [N$_{1(2OH)(2OH)(2OH)}$][NTf$_2$] display smaller biphasic regions. In general, an increase in the cation alkyl side chain from methyl to ethyl, i.e., from [N$_{1(2OH)(2OH)(2OH)}$][NTf$_2$] to [N$_{2(2OH)(2OH)(2OH)}$][NTf$_2$], increases the IL hydrophobicity and thus its ability to be salted-out by the carbohydrate and to create ABS. Moreover, when analyzing the overall trend, it is demonstrated that the number of hydroxyl groups at the IL cation has a stronger effect on phase separation in ABS than the effect of increasing the cation alkyl side chain length (from methyl to ethyl). ILs with a lower number of hydroxyl groups are more hydrophobic and more easily salted-out by each carbohydrate.

A comparison of ABS with other fluorinated ILs [1-butyl-3-methylimidazolium triflate, ([C$_4$C$_1$im][CF$_3$SO$_3$]) (Freire et al., 2011), 1-butyl-3-methylimidazolium tetrafluoroborate ([C$_4$C$_1$im][BF$_4$]) (Freire et al., 2011), and 1-ethyl-3-methylpyridinium perfluorobutanesulfonate [C$_2$C$_1$py][C$_4$F$_9$SO$_3$] (Ferreira et al., 2016)] and D-glucose is given in **Supplementary Figure S6**. Amongst all the studied ILs as phase-forming components of ABS with carbohydrates, it is shown that the IL [N$_{11(2OH)(2OH)}$][NTf$_2$] is the one that requires a lower amount of carbohydrates to undergo phase separation. This fact is relevant from an application point of view since lower quantities of IL and carbohydrate are required to form ABS, while reinforcing their higher biocompatible character due to their higher water content. On the other hand, the IL [N$_{1(2OH)(2OH)(2OH)}$][NTf$_2$] is the one that requires higher amounts of IL and carbohydrate to form ABS when compared with the remaining ILs reported in the literature, namely [C$_4$C$_1$im][BF$_4$], [C$_4$C$_1$im][CF$_3$SO$_3$], and [C$_2$C$_1$py][C$_4$F$_9$SO$_3$]. This opposite behavior reinforces the high tailoring ability of the investigated cholinium-derived ILs by only changing the size of the aliphatic moieties and number of hydroxyl groups at the

cation since they cover the whole hydrophobicity range showed up to date with ILs in ABS formation with carbohydrates.

ABS as Alternative Strategies for the Simultaneous Separation of Antioxidants and Carbohydrates From Food Waste

Given that in ABS formed by ILs and carbohydrates there is the spontaneous separation of the two phase-forming components above given concentrations, and that previous works on ABS formed by ILs and salts show a preferential partition of antioxidants to the IL-rich phase (Cláudio et al., 2010, 2012, 2014), we hypothesized the application of ABS formed by ILs and carbohydrates as one-step separation strategies of antioxidants and carbohydrates from food waste. After addressing the ILs cytotoxicity and their ability to create ABS, this hypothesis was here evaluated under a perspective of resource efficiency and circular economy. To this end, ABS composed of the three cholinium-derived ILs and two of the less expensive and most abundant carbohydrates (D-glucose and D-sucrose) were investigated to simultaneously separate antioxidants and carbohydrates from an expired commercial vanillin-rich pudding. However, with the IL $[N_{1(2OH)(2OH)(2OH)}][NTf_2]$ only D-glucose is able to promote phase separation, and consequently with this IL only ABS formed with D-glucose were evaluated. Based on the phase diagrams discussed above, a common mixture composition at the biphasic region of the several studied ABS was chosen, formed by 25 wt% of D-glucose or D-sucrose + 50 wt% of IL + 25 wt% of aqueous solution of pudding. The representation of this mixture composition is shown in **Supplementary Figure S5**.

The ABS extraction efficiency (%EE) for carbohydrates and antioxidant relative activity (%ARA) in each ABS phase were calculated using Equations (1–3), being shown in **Figure 5**. Detailed data and associated standard deviations are given in **Supplementary Table S5**. In all systems studied the top phase is mainly composed of carbohydrates and water, with the bottom phase corresponding to the IL-rich phase, as experimentally confirmed by conductivity measurements of both phases. The relative densities of the ABS phases on the studied systems are the opposite of most systems previously reported (Freire et al., 2012) due to the high density of the fluorinated ILs (Pereiro et al., 2013; Neves et al., 2014) used in this work.

In all studied systems, antioxidants majorly partition to the IL-rich phase, while carbohydrates are mainly present in the top phase. The separation of both types of compounds to opposite phases occurs in one-step, with %EE of carbohydrates to the carbohydrate-rich phase ranging between 89 and 92% for the systems formed by D-glucose and between 94 and 97% for the systems comprising D-sucrose. The %ARA of antioxidants to the IL-rich phase ranges between 65 and 75% in the systems with D-glucose and between 68 and 85% in the systems formed by D-sucrose. Being the pudding vanilla flavored, vanillin is one of the main antioxidants present. Previous studies demonstrated that vanillin preferentially migrates to the IL-rich phase (Cláudio et al., 2010) in ABS formed by ILs and a strong salting-out salt (K_3PO_4). Here, a class of weaker salting-out agents is used,
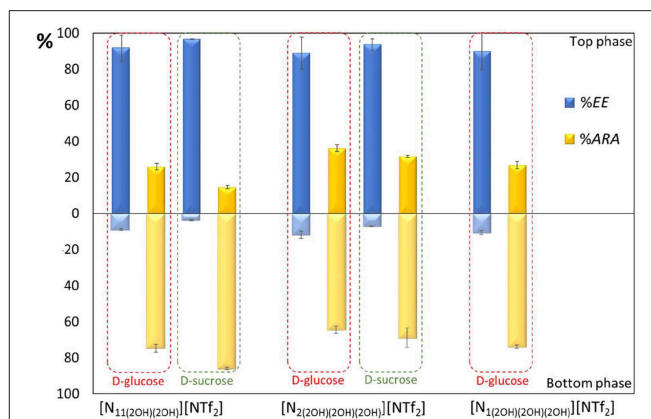
FIGURE 5 | Carbohydrates extraction efficiency (%EE) and antioxidant relative activity (%ARA) in each phase using ABS composed of 25 wt% D-glucose or D-sucrose + 50 wt% IL + 25 wt% aqueous solution of pudding.

namely carbohydrates, yet antioxidants still majorly partition to the IL-rich phase. On the opposite, sugars are preferentially enriched in the top phase, as expected given that these ILs were designed to be able to form ABS with carbohydrates and spontaneously separate at the concentrations used. Given that no significant differences exist in terms of separation performance between the three ILs investigated, we suggest $[N_{2(2OH)(2OH)(2OH)}][NTf_2]$ as the most adequate IL to be used since it has a lower cytotoxicity, being this the IL used in the recyclability studies discussed below.

Previous works employing ABS formed by ILs and carbohydrates focused on the separation of amino acids, alkaloids, terpenoids, and food colorants (Freire et al., 2011; Ferreira et al., 2016). These studies were carried out with model aqueous solutions, and their applicability in the separation of value added compounds from real samples, as carried out in this work, has not been attempted. Furthermore, this work on ABS constituted by ILs and carbohydrates takes advantage of the carbohydrates present and required for ABS formation in the design of a more integrated separation strategy, in which two classes of value added compounds (carbohydrates and antioxidants) are enriched in different phases. This strategy reduces the number of different compounds present in each phase and the number of purification steps. Overall, the investigated ABS composed of ILs and carbohydrates are promising platforms to separate carbohydrates and antioxidants from real food waste. The carbohydrates recovered may be reused by the food industry, while the antioxidants may be reused by the food or cosmetic industries, as summarized in **Figure 6**. It should be however remarked that although the toxicity of the investigated ILs toward human intestinal cell lines is substantially lower than those reported for other ILs based on fluorinated anions, we cannot conclude if the continuous exposure to these ILs is completely safe before a complete risk assessment is performed.

Foreseeing the described applications of the extracted antioxidants, it is of high significance to separate and recover

FIGURE 6 | Schematic representation of the proposed strategy for the separation and reuse of carbohydrates and antioxidants obtained from food waste. The IL recycling possibility is also shown.
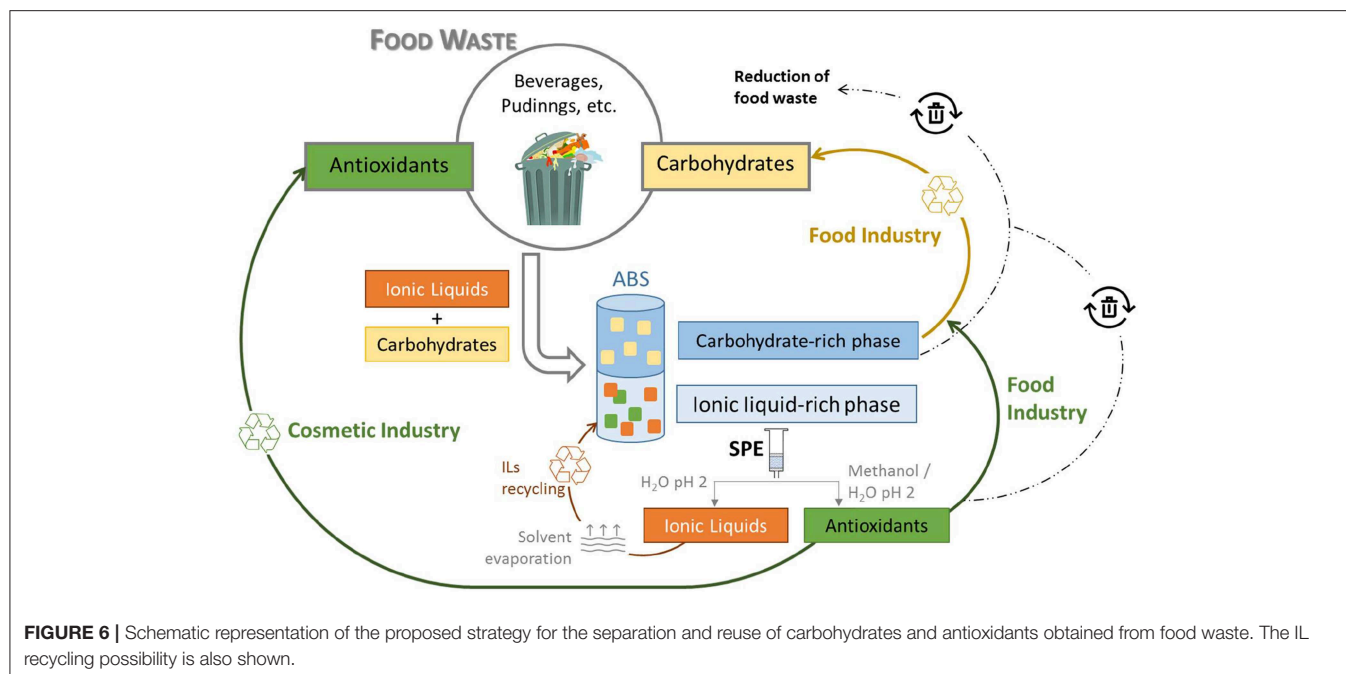
these compounds from the IL-rich fraction, while improving the sustainable character of the developed separation strategy by attempting the IL recycling. The recyclability of the IL-rich phase was performed for two times using the ABS composed of $[N_{2(2OH)(2OH)(2OH)}][NTf_2]$ and D-glucose. After the simultaneous separation of carbohydrates and antioxidants, SPE cartridges were used to separate the antioxidants from the IL-rich phase, allowing the IL recyclability and evaluation of the ABS separation performance for two more times. The use of the recycled IL in new ABS allows to obtain an %*ARA* of antioxidants to the IL-rich phase ranging between 72 and 82% and an %*EE* of carbohydrates to the carbohydrate-rich phase ranging between 89 and 91%. Detailed data are given in **Supplementary Figure S7** and **Supplementary Table S6**. The IL recycling possibility is depicted in **Figure 6**. In each recycling assay, 85 wt% of the IL was recovered; however, it should be stressed that this value can be increased when working at a large-scale and under optimized conditions of IL recovery and recycling. Overall, these results show that the IL can be recovered and recycled without losses on the ABS separation performance, while allowing the recovery of antioxidants from the IL-rich phase.

CONCLUSIONS

Food waste is an important economic, environmental and social problem that requires innovative solutions in order to reduce its burden. The management of food waste is a priority mitigation measure to reduce emissions intensity and the carbon footprint of the food production chain, which can be achieved through the implementation of new technological solutions such as by transforming food waste into products with marketable value. Accordingly, there is a relevant need to

develop sustainable and cost-effective technologies to recover value added compounds from food waste. Based on this need, we here proposed the use of ABS composed of ILs and carbohydrates to simultaneously separate two value added compounds from food waste.

We successfully demonstrated that cholinium-derived ILs, if properly designed, can form ABS with carbohydrates. These new ILs are substantially less toxic than other fluorinated ILs commonly used, as demonstrated by cytotoxicity assays toward the human colon carcinoma cell line (Caco-2). Based on the ability to create ABS with carbohydrates, these systems were finally evaluated as separation platforms of carbohydrates and antioxidants from food waste, namely from a vanilla pudding. The separation of these products occurs in one-step with the studied systems, where carbohydrates are enriched in a carbohydrate-rich phase and antioxidants are mainly present in the IL-rich phase. Extraction efficiencies of carbohydrates ranging between 89 and 97% to the carbohydrate-rich phase, and antioxidant relative activities ranging between 65 and 85% in the IL-rich phase were obtained. Furthermore, antioxidants from the IL-rich phase were recovered by solid-phase extraction, and the IL was recycled for two times with no losses on the ABS separation performance. Given that no significant differences exist in terms of separation performance between the three ILs investigated, $[N_{2(2OH)(2OH)(2OH)}][NTf_2]$ is proposed as the most adequate IL to be used since it has a lower cytotoxicity at higher IL concentrations. Overall, the investigated ABS composed of ILs and carbohydrates are promising platforms to simultaneously (one-step) separate carbohydrates and antioxidants from real food waste, in which ILs can be recovered and recycled under a circular economy approach.

DATA AVAILABILITY

The raw data supporting the conclusions of this manuscript will be made available by the authors, without undue reservation, to any qualified researcher.

AUTHOR CONTRIBUTIONS

MGF, JE, JC, and LR conceived and planed the work. PR synthesized and characterized all ILs. MBF, AC, and AS planned the cytotoxicity experiments, carried out the experimental assays, and analyzed the results. MF and CN carried out the experiments on the phase diagrams, and antioxidant activity and carbohydrates quantification assays. All authors contributed to the interpretation of the acquired data and to the manuscript preparation.

FUNDING

ACKNOWLEDGMENTS

SUPPLEMENTARY MATERIAL

The Supplementary Material for this article can be found online at: https://www.frontiersin.org/articles/10.3389/fchem.2019.00459/full#supplementary-material

REFERENCES

Arshadi, M., Attard, T. M., Lukasik, R. M., Brncic, M., da Costa Lopes, A. M., Finell, M., et al. (2016). Pre-treatment and extraction techniques for recovery of added value compounds from wastes throughout the agri-food chain. *Green Chem.* 18, 6160–6204. doi: 10.1039/C6GC01389A

Bi, W., Tian, M., Zhou, J., and Row, K. H. (2010). Task-specific ionic liquid-assisted extraction and separation of astaxanthin from shrimp waste. *J. Chromatogr. B* 878, 2243–2248. doi: 10.1016/j.jchromb.2010.06.034

Bica, K., Gaertner, P., and Rogers, R. D. (2011). Ionic liquids and fragrances - direct isolation of orange essential oil. *Green Chem.* 13, 1997–1999. doi: 10.1039/c1gc15237h

Chen, Y., Meng, Y., Yang, J., Li, H., and Liu, X. (2012). Phenol distribution behavior in aqueous biphasic systems composed of ionic liquids–carbohydrate–water. *J. Chem. Eng. Data* 57, 1910–1914. doi: 10.1021/je201290q

Chen, Y., Meng, Y., Zhang, S., Zhang, Y., Liu, X., and Yang, J. (2010). Liquid–Liquid equilibria of aqueous biphasic systems composed of 1-butyl-3-methyl imidazolium tetrafluoroborate + sucrose/maltose + water. *J. Chem. Eng. Data* 55, 3612–3616. doi: 10.1021/je100212p

Chen, Y., Wang, Y., Cheng, Q., Liu, X., and Zhang, S. (2009). Carbohydrates-tailored phase tunable systems composed of ionic liquids and water. *J. Chem. Thermodyn.* 41, 1056–1059. doi: 10.1016/j.jct.2009.04.008

Chen, Y., and Zhang, S. (2010). Phase behavior of (1-Alkyl-3-methyl imidazolium tetrafluoroborate + 6-(hydroxymethyl)oxane-2,3,4,5-tetrol + water). *J. Chem. Eng. Data* 55, 278–282. doi: 10.1021/je900473u

Cláudio, A. F. M., Cognigni, A., de Faria, E. L. P., Silvestre, A. J. D., Zirbs, R., Freire, M. G., et al. (2018). Valorization of olive tree leaves: extraction of oleanolic acid using aqueous solutions of surface-active ionic liquids. *Sep. Purif. Technol.* 204, 30–37. doi: 10.1016/j.seppur.2018.04.042

Cláudio, A. F. M., Ferreira, A. M., Freire, C. S. R., Silvestre, A. J. D., Freire, M. G., and Coutinho, J. A. P. (2012). Optimization of the gallic acid extraction using ionic-liquid-based aqueous two-phase systems. *Sep. Purif. Technol.* 97, 142–149. doi: 10.1016/j.seppur.2012.02.036

Cláudio, A. F. M., Ferreira, A. M., Freire, M. G., and Coutinho, J. A. P. (2013). Enhanced extraction of caffeine from guaraná seeds using aqueous solutions of ionic liquids. *Green Chem.* 15, 2002–2010. doi: 10.1039/c3gc40437d

Cláudio, A. F. M., Freire, M. G., Freire, C. S. R., Silvestre, A. J. D., and Coutinho, J. A. P. (2010). Extraction of vanillin using ionic-liquid-based aqueous two-phase systems. *Sep. Purif. Technol.* 75, 39–47. doi: 10.1016/j.seppur.2010.07.007

Cláudio, A. F. M., Marques, C. F. C., Boal-Palheiros, I., Freire, M. G., and Coutinho, J. A. P. (2014). Development of back-extraction and recyclability routes for ionic-liquid-based aqueous two-phase systems. *Green Chem.* 16, 259–268. doi: 10.1039/C3GC41999A

de Faria, E. L. P., Shabudin, S. V., Cláudio, A. F. M., Válega, M., Domingues, F. M. J., Freire, C. S. R., et al. (2017). Aqueous solutions of surface-active ionic liquids: remarkable alternative solvents to improve the solubility of triterpenic acids and their extraction from biomass. *ACS Sus. Chem. Eng.* 5, 7344–7351. doi: 10.1021/acssuschemeng.7b01616

de Ferro, A. M., Reis, P. M., Soromenho, M. R. C., Bernardes, C. E. S., Shimizu, K., Freitas, A. A., et al. (2018). Designing the ammonium cation to achieve a higher hydrophilicity of bistriflimide-based ionic liquids. *Phys. Chem. Chem. Phys.* 20, 19307–19313. doi: 10.1039/C8CP03398F

Dubois, M., Gilles, K. A., Hamilton, J. K., Rebers, P. A., and Smith, F. (1956). Colorimetric method for determination of sugars and related substances. *Anal. Chem.* 28, 350–356. doi: 10.1021/ac60111a017

Egorova, K. S., Seitkalieva, M. M., Posvyatenko, A. V., and Ananikov, V. P. (2015a). An unexpected increase of toxicity of amino acid-containing ionic liquids. *Toxicol. Res.* 4, 152–159. doi: 10.1039/C4TX00079J

Egorova, K. S., Seitkalieva, M. M., Posvyatenko, A. V., Khrustalev, V. N., and Ananikov, V. P. (2015b). Cytotoxic activity of salicylic acid-containing drug models with ionic and covalent binding. *ACS Med. Chem. Lett.* 6, 1099–1104. doi: 10.1021/acsmedchemlett.5b00258

European Commission (2018). *Food Waste.* Available online at: https://ec.europa.eu/food/safety/food_waste_en

FAO (2011). *Global Food Losses and Food Waste – Extent, Causes and Prevention.* Rome: Food and Agriculture Organization of the United Nations (FAO).

Ferreira, A. M., Esteves, P. D. O., Boal-Palheiros, I., Pereiro, A. B., Rebelo, L. P. N., and Freire, M. G. (2016). Enhanced tunability afforded by aqueous biphasic systems formed by fluorinated ionic liquids and carbohydrates. *Green Chem.* 18, 1070–1079. doi: 10.1039/C5GC01610J

Freire, M. G., Claudio, A. F. M., Araujo, J. M. M., Coutinho, J. A. P., Marrucho, I. M., Lopes, J. N. C., et al. (2012). Aqueous biphasic systems: a boost brought about by using ionic liquids. *Chem. Soc. Rev.* 41, 4966–4995. doi: 10.1039/c2cs35151j

Freire, M. G., Louros, C. L. S., Rebelo, L. P. N., and Coutinho, J. A. P. (2011). Aqueous biphasic systems composed of a water-stable ionic liquid + carbohydrates and their applications. *Green Chem.* 13, 1536–1545. doi: 10.1039/c1gc15110j

Fusions (2016). *Estimates of European Food Waste Levels.* Stockholm: IVL Swedish Environmental Research Institute.

Garcia, H., Ferreira, R., Petkovic, M., Ferguson, J. L., Leitão, M. C., Gunaratne, H. Q. N., et al. (2010). Dissolution of cork biopolymers in biocompatible ionic liquids. *Green Chem.* 12, 367–369. doi: 10.1039/b922553f

García-Lorenzo, A., Tojo, E., Tojo, J., Teijeira, M., Rodríguez-Berrocal, F. J., González, M. P., et al. (2008). Cytotoxicity of selected imidazolium-derived ionic liquids in the human caco-2 cell line. Sub-structural toxicological interpretation through a QSAR study. *Green Chem.* 10, 508–516. doi: 10.1039/b718860a

Ge, L., Xia, F., Song, Y., Yang, K., Qin, Z., and Li, L. (2014). Solubility of luteolin in several imidazole-based ionic liquids and extraction from peanut shells using selected ionic liquid as solvent. *Sep. Purif. Technol.* 135, 223–228. doi: 10.1016/j.seppur.2014.08.022

Guolin, H., Jeffrey, S., Kai, Z., and Xiaolan, H. (2012). Application of ionic liquids in the microwave-assisted extraction of pectin from lemon peels. *J. Anal. Methods Chem.* 2012:8. doi: 10.1155/2012/302059

Hernoux-Villière, A., Lévêque, J. M., Kärkkäinen, J., Papaiconomou, N., Lajunen, M., and Lassi, U. (2014). Task-specific ionic liquid for the depolymerisation of starch-based industrial waste into high reducing sugars. *Catal. Today* 223, 11–17. doi: 10.1016/j.cattod.2013.09.027

IPCC (2018). *Global Warming of 1.5°C an IPCC Special Report on the Impacts of Global Warming of 1.5 °C Above Pre-Industrial Levels and Related Global Greenhouse Gas Emission Pathways, in the Context of Strengthening the Global Response to the Threat of Climate Change, Sustainable Development, and Efforts to Eradicate Poverty.* IPCC.

Jiao, J., Ma, D. H., Gai, Q. Y., Wang, W., Luo, M., Fu, Y. J., et al. (2013). Rapid analysis of fructus forsythiae essential oil by ionic liquids-assisted microwave distillation coupled with headspace single-drop microextraction followed by gas chromatography–mass spectrometry. *Anal. Chim. Acta* 804, 143–150. doi: 10.1016/j.aca.2013.10.035

Lateef, H., Grimes, S., Kewcharoenwong, P., and Bailey, E. (2009). Ionic liquids in the selective recovery of fat from composite foodstuffs. *J. Chem. Technol. Biotechnol.* 84, 1681–1687. doi: 10.1002/jctb.2230

Lea, T. (2015). "Caco-2 cell line," in *The Impact of Food Bioactives on Health: in vitro and ex vivo Models,* eds K. Verhoeckx, P. Cotter, I. López-Expósito, C. Kleiveland, T. Lea, A. Mackie, T. Requena, D. Swiatecka, and H. Wichers (Cham: Springer International Publishing), 103–111.

Macário, I. P. E., Oliveira, H., Menezes, A. C., Ventura, S. P. M., Pereira, J. L., Gon?alves, A. M. M., et al. (2019). Cytotoxicity profiling of deep eutectic solvents to human skin cells. *Sci. Rep.* 9:3932. doi: 10.1038/s41598-019-39910-y

Meunier, V., Bourrié, M., Berger, Y., and Fabre, G. (1995). The human intestinal epithelial cell line caco-2; pharmacological and pharmacokinetic applications. *Cell Biol. Toxicol.* 11, 187–194. doi: 10.1007/BF00756522

Michalkiewicz, A., Biesaga, M., and Pyrzynska, K. (2008). Solid-phase extraction procedure for determination of phenolic acids and some flavonols in honey. *J. Chromatogr. A* 1187, 18–24. doi: 10.1016/j.chroma.2008.02.001

Mizuno, H., and Usuki, T. (2018). Ionic liquid-assisted extraction and isolation of cynaropicrin and cnicin from artichoke and blessed thistle. *ChemistrySelect* 3, 1781–1786. doi: 10.1002/slct.201703063

Neves, C. M. S. S., Kurnia, K. A., Shimizu, K., Marrucho, I. M., Rebelo, L. P. N., Coutinho, J. A. P., et al. (2014). The impact of ionic liquid fluorinated moieties on their thermophysical properties and aqueous phase behaviour. *Phys. Chem. Chem. Phys.* 16, 21340–21348. doi: 10.1039/C4CP02008A

Ni, X., Xing, H., Yang, Q., Wang, J., Su, B., Bao, Z., et al. (2012). Selective liquid–liquid extraction of natural phenolic compounds using amino acid ionic liquids: a case of α-tocopherol and methyl linoleate separation. *Ind. Eng. Chem. Res.* 51, 6480–6488. doi: 10.1021/ie201682h

Oberleitner, N., Ressmann, A. K., Bica, K., Gärtner, P., Fraaije, M. W., Bornscheuer, U. T., et al. (2017). From waste to value – direct utilization of limonene from orange peel in a biocatalytic cascade reaction towards chiral carvolactone. *Green Chem.* 19, 367–371. doi: 10.1039/C6GC01138A

Okuniewski, M., Paduszynski, K., and Domanska, U. (2016). Effect of cation structure in trifluoromethanesulfonate-based ionic liquids: density, viscosity, and aqueous biphasic systems involving carbohydrates as "Salting-Out" agents. *J. Chem. Eng. Data* 61, 1296–1304. doi: 10.1021/acs.jced.5b00931

Passos, H., Freire, M. G., and Coutinho, J. A. P. (2014). Ionic liquid solutions as extractive solvents for value-added compounds from biomass. *Green Chem.* 16, 4786–4815. doi: 10.1039/C4GC00236A

Pereiro, A. B., Araújo, J. M. M., Martinho, S., Alves, F., Nunes, S., Matias, A., et al. (2013). Fluorinated ionic liquids: properties and applications. *ACS Sustain. Chem. Eng.* 1, 427–439. doi: 10.1021/sc300163n

Pradyumna, A. (2018). Planetary health and food systems: insights from global SDGs. *Lancet Planet. Health* 2, e417–e418. doi: 10.1016/S2542-5196(18)30202-X

Qin, Y., Lu, X., Sun, N., and Rogers, R. D. (2010). Dissolution or extraction of crustacean shells using ionic liquids to obtain high molecular weight purified chitin and direct production of chitin films and fibers. *Green Chem.* 12, 968–971. doi: 10.1039/c003583a

Quental, M. V., Pereira, M. M., Ferreira, A. M., Pedro, S. N., Shahriari, S., Mohamadou, A., et al. (2018). Enhanced separation performance of aqueous biphasic systems formed by carbohydrates and tetraalkylphosphonium- or tetraalkylammonium-based ionic liquids. *Green Chem.* 20, 2978–2983. doi: 10.1039/C8GC00622A

Riss, T. L., Moravec, R. A., Niles, A. L., Duellman, S., Benink, H. A., Worzella, T. J., et al. (2016). "Cell viability assays," in *Assay Guidance Manual [Internet]*, eds G. S. Sittampalam, N. P. Coussens, and K. Brimacombe, et al. (Bethesda, MD: Eli Lilly & Company; National Center for Advancing Translational Sciences). Available online at: https://www.ncbi.nlm.nih.gov/books/NBK144065/

Rogers, R. D., and Seddon, K. R. (2003). Ionic liquids - solvents of the future? *Science* 302, 792–793. doi: 10.1126/science.1090313

Setoguchi, T., Kato, T., Yamamoto, K., and Kadokawa, J. (2012). Facile production of chitin from crab shells using ionic liquid and citric acid. *Int. J. Biol. Macromol.* 50, 861–864. doi: 10.1016/j.ijbiomac.2011.11.007

Sharma, V., Jaiswal, P. K., Saran, M., Yadav, D. K., Saloni, Mathur, M., et al. (2018). Discovery of C-3 Tethered 2-oxo-benzo[1,4]oxazines as potent antioxidants: bio-inspired based design, synthesis, biological evaluation, cytotoxic, and *in silico* molecular docking studies. *Front. Chem.* 6:56. doi: 10.3389/fchem.2018.00056

Sintra, T. E., Luis, A., Rocha, S. N., Lobo Ferreira, A. I. M. C., Goncalves, F., Santos, L. M. N. B. F., et al. (2015). Enhancing the antioxidant characteristics of phenolic acids by their conversion into cholinium salts. *ACS Sustain. Chem. Eng.* 3, 2558–2565. doi: 10.1021/acssuschemeng.5b00751

Song, C. P., Liew, P. E., Teh, Z., Lim, S. P., Show, P. L., and Ooi, C. W. (2018). Purification of the recombinant green fluorescent protein using aqueous two-phase system composed of recyclable CO2-based alkyl carbamate ionic liquid. *Front. Chem.* 6:529. doi: 10.3389/fchem.2018.00529

Thamke, V. R., Chaudhari, A. U., Tapase, S. R., Paul, D., and Kodam, K. M. (2019). *In vitro* toxicological evaluation of ionic liquids and development of effective bioremediation process for their removal. *Environ. Pollut.* 250, 567–577. doi: 10.1016/j.envpol.2019.04.043

Toledo Hijo, A. A. C., Maximo, G. J., Costa, M. C., Batista, E. A. C., and Meirelles, A. J. A. (2016). Applications of Ionic liquids in the food and bioproducts industries. *ACS Sustain. Chem. Eng.* 4, 5347–5369. doi: 10.1021/acssuschemeng.6b00560

Ventura, S. P. M., E Silva, F. A., Quental, M. V., Mondal, D., Freire, M. G., and Coutinho, J. A. P. (2017). Ionic-Liquid-mediated extraction and separation processes for bioactive compounds: past, present, and future trends. *Chem. Rev.* 117, 6984–7052. doi: 10.1021/acs.chemrev.6b00550

Wang, R., Chang, Y., Tan, Z., and Li, F. (2016). Applications of choline amino acid ionic liquid in extraction and separation of flavonoids and pectin from ponkan peels. *Sep. Sci. Technol.* 51, 1093–1102. doi: 10.1080/01496395.2016.1143006

Waters (2014). *Oasis HLB Cartridges and 96-Well Plates*. Care and Use Manual. Waters.

Wu, B., Zhang, Y., and Wang, H. (2008a). Phase behavior for ternary systems composed of ionic liquid + saccharides + water. *J. Phys. Chem. B* 112, 6426–6429. doi: 10.1021/jp8005684

Wu, B., Zhang, Y., Wang, H., and Yang, L. (2008b). Temperature dependence of phase behavior for ternary systems composed of ionic liquid + sucrose + water. *J. Phys. Chem. B* 112, 13163–13165. doi: 10.1021/jp805483k

Wu, B., Zhang, Y. M., and Wang, H. P. (2008c). Aqueous biphasic systems of hydrophilic ionic liquids + sucrose for separation. *J. Chem. Eng. Data* 53, 983–985. doi: 10.1021/je700729p

Yee, M. F., Emmel, G. N., Yang, E. J., Lee, E., Paek, J. H., Wu, B. M., et al. (2018). Ionic liquid aqueous two-phase systems for the enhanced paper-based detection of transferrin and escherichia coli. *Front. Chem.* 6:486. doi: 10.3389/fchem.2018.00486

Zhang, S., Li, Y., Liu, Z., Zhang, X., Wang, M., and Zhao, D. (2015). Ultrasonic-assisted extraction of total flavonoid from peanut hull using ionic liquid solution. *Asian J. Agric. Food Sci.* 3, 256–260.

Zhang, W., Feng, X., Alula, Y., and Yao, S. (2017). Bionic multi-tentacled ionic liquid-modified silica gel for adsorption and separation of polyphenols from green tea (*Camellia sinensis*) leaves. *Food Chem.* 230, 637–648. doi: 10.1016/j.foodchem.2017.03.054

Zhang, Y., Zhang, S., Chen, Y., and Zhang, J. (2007). Aqueous biphasic systems composed of ionic liquid and fructose. *Fluid Phase Equilib.* 257, 173–176. doi: 10.1016/j.fluid.2007.01.027

Efficient Fractionation of Lignin- and Ash-Rich Agricultural Residues Following Treatment With a Low-Cost Protic Ionic Liquid

Clementine L. Chambon[†], Meng Chen[†], Paul S. Fennell and Jason P. Hallett*

Laboratory of Sustainable Chemical Technology, Department of Chemical Engineering, Imperial College London, South Kensington Campus, London, United Kingdom

Agricultural residues from rice, wheat and sugarcane production are annually available at the gigaton-scale worldwide, particularly in Asia. Due to their high sugar content and ash compositions, their conversion to bioethanol is an attractive alternative to their present disposal by open-field burning and landfilling. In this work, we demonstrate application of the low-cost protic ionic liquid triethylammonium hydrogen sulfate ([TEA][HSO$_4$]) for pretreatment of rice straw, rice husk, wheat straw and sugarcane bagasse. The feedstocks had high ash (up to 13 wt%) and lignin content (up to 28 wt%). Pretreatment effectiveness was examined at 150 and 170°C and an optimal pretreatment time was identified and characterized by glucose release following enzymatic saccharification (i.e., hydrolysis), biomass delignification observed by compositional analysis, and lignin recovery. The isolated lignin fractions were analyzed by 2D HSQC NMR to obtain insights into the structural changes occurring following ionic liquid pretreatment. After treatment at 170°C for 30–45 min, enzymatic hydrolysis of three agroresidues gave near-quantitative glucose yields approaching 90% while rice husk gave 73% yield. Glucose release from the pulps was enhanced by saccharifying wet pulps without an air-drying step to reduce hornification. According to pulp compositional analysis, up to 82% of lignin was removed from biomass during pretreatment, producing highly digestible cellulose-rich pulps. HSQC NMR of the extracted lignins showed that delignification proceeded *via* extensive cleavage of β-O-4′ aryl ether linkages which was accompanied by condensation reactions in the isolated lignins. The high saccharification yields obtained indicate excellent potential for valorization of low-cost agroresidues in large volumes, which is promising for commercialization of biofuels production using the ionoSolv pretreatment technology.

Keywords: ionic liquids, biorefining, lignocellulose, agroresidues, pretreatment, enzymatic hydrolysis, lignin

INTRODUCTION

Agricultural residues (e.g., straws, husks, stalks, stovers and cobs) and residues originating from industrial processing (e.g., bagasse) are among the most abundant renewable resources on earth (nee' Nigam et al., 2009). These lignocellulosic materials are composed of up to 80 wt% polysaccharides, making them rich sources of energy (Reddy and Yang, 2005). Wheat, rice, maize

and sugarcane production generate the vast majority of residues, with global resources of 2.8 Gtons of dry matter available annually (IEA Bioenergy, 2015) after discounting ∼40% that must be left on the cropland to maintain the soil organic matter, carbon and nutrient balance (Scarlat et al., 2010). As such, agricultural crop residues represent a significant resource for bioenergy and biorefineries. Due to their abundance, high carbohydrate and ash content, agroresidues from rice, wheat and sugarcane production are most suitable for conversion to bioethanol. Kim and Dale (2004) have estimated that crop residues could be used to produce around 442 GL of bioethanol annually, of which 360 GL (>80%) could be produced from rice straw, wheat straw and bagasse alone. This amounts to over 14 times global bioethanol production (31 GL) (Kim and Dale, 2004). These feedstocks are most abundant in Asia (60%), which has the highest potential for bioethanol production from agricultural residues (Kim and Dale, 2004). As these are carbon-neutral resources that do not require additional land to produce, significant opportunities exist to reduce greenhouse gas emissions, increase domestic energy security and boost rural economies by displacing fossil fuels in the production of bioenergy and bio-based products.

Most agricultural residues are not optimally utilized at present, since their digestibility by animals and in established conversion processes is usually low (IEA Bioenergy, 2015). They are often considered waste materials and are disposed of by open-field burning, landfilling or incineration (Mehta and Pitt, 1976). Notably, open-field burning of rice, corn and wheat straws in South Asia and China has led to a pressing environmental crisis, releasing huge quantities of black carbon, the second-largest human emission causing climate change (Bond et al., 2013). Biomass burning also results in particulate and gaseous air pollution, with devastating consequences for public health and the environment (Shih et al., 2008). Accumulation of agricultural residues leads not only to the deterioration of the environment, but also to the loss of a potentially valuable feedstock which could be processed to yield a variety of fuels, chemicals and materials. If all rice straw that is currently burned were instead converted into bioethanol, it would become the single largest feedstock for lignocellulosic ethanol production (Satlewal et al., 2018). Despite their remarkable potential for conversion to bioethanol, these feedstocks are not presently used in commercial biofuels production processes due to low enzyme digestibility, linked to their high lignin content.

Pretreatment is an important tool for breakdown of the recalcitrant structures within agricultural residues prior to biochemical conversion. For bioethanol production, an effective and economical method is needed to separate polysaccharides from lignin, ash and other constituents in native biomass. However, the presence of high lignin and ash content in many agricultural feedstocks is problematic for conventional pretreatment processes, with sugar yields typically limited to 50–60% (Saha et al., 2005). Several important agricultural crops produce residues which are highly recalcitrant and also contain up to 30% ash by weight, notably rice straw and rice husk (Parikh et al., 2005). High ash concentrations are unfavorable for feedstock pre-processing and the extraction of cellulose. Silica, a

major ash constituent, wears down machinery used for feedstock grinding (Miles et al., 1996). Ash can also react with acids (i.e., the acidic pretreatment medium itself, or added acid catalyst) during dilute acid pretreatment, hot water or steam explosion pretreatment, increasing the amount of chemicals required for processing (Huang et al., 2017). Dilute acid pretreatment is a leading pretreatment process suitable for commercialization, but it is unable to delignify biomass with >10 wt% lignin, as is the case for many agroresidues (Fu et al., 2010). Steam explosion and hydrothermal pretreatments are somewhat suited for more lignified materials; however, the pretreated materials are poorly converted during enzymatic hydrolysis, presenting maximum glucose yields of around 60% at high solid to liquid ratio (i.e. solids loading) of 1:2 g/g wt% (Sun and Cheng, 2002). Delignifying pretreatments, such as treatment with alkali or with organic or aqueous-organic solvents ("organosolv" processing), have shown some success in pretreating the most recalcitrant agroresidue, rice husk (Singh et al., 2011; Singh and Dhepe, 2016), as well as rice straw (Zhang and Cai, 2008; Amiri et al., 2014). However, these methods have their respective drawbacks, including high reagent costs, and are considered economically unviable for bioethanol production from lignocellulose (Sánchez and Cardona, 2008). While alkaline pretreatment can be highly effective at delignifying a wide range of herbaceous feedstocks, performance suffers under high solids loadings representative of industrial biorefining, where glucose yields were limited to ∼50% (Cheng et al., 2010), thus high chemicals consumption is a major challenge for commercialization (Chen et al., 2013). In organosolv pretreatments, the organic solvents used are normally flammable and can generate explosive atmospheres, requiring strenuous safety precautions and leading to very high cost (Zhao et al., 2009). Generally, the use of agricultural residues is also hindered by their low bulk density and low energy density (Mani et al., 2004; Hoover et al., 2014) which require the development of high-efficiency pretreatment processes.

Ionic liquid biorefining has emerged as among the most promising technologies for large-scale economical conversion of agroresidues to bioethanol and fine chemicals (Yoon et al., 2011). Ionic liquids (ILs) are salts with low melting points that are thermally stable, non-volatile and non-flammable (Brandt et al., 2013). ILs are generally observed to have extremely low vapor pressures (Earle et al., 2006), avoiding environmental and safety hazards during handling. This also makes many ILs reusable and recyclable, offering a clean and safe alternative to conventional organic solvents (Brandt-Talbot et al., 2017). The recent surge of interest in ILs is due to their ability to decrystallize or dissolve cellulose (Swatloski et al., 2002). Cellulose-dissolving ILs have been reported to give high conversions with a variety of lignocellulose feedstocks (Li et al., 2010). Among these, the widely studied aprotic IL 1-ethyl-3-methylimidazolium acetate ([Emim][OAc]) has been shown to release over 90% of glucose from sugarcane bagasse at a moderate solids loading of 1:6.7 g/g (Fu et al., 2010). However, the high cost of alkylimidazolium ILs as well as their low thermal stability (Clough et al., 2013) and the requirement for dry conditions limits their ability to be economically recycled and reused in commercial processing (George et al., 2015). Therefore, a class of low-cost

amine-based protic ILs was developed by Hallett et al. (Chen et al., 2014). Among these, alkylammonium hydrogen sulfate ILs are significantly more thermally stable than [Emim][OAc] and can be recycled by distillation to regenerate a concentrated IL solution and reused (Chen et al., 2014; George et al., 2015; Brandt-Talbot et al., 2017).

IonoSolv pretreatment is a lignocellulose fractionation technology that uses IL-water mixtures to extract lignin and hemicellulose from biomass, leaving behind a cellulose-rich pulp (Brandt et al., 2011). It uses thermally stable, recyclable and inexpensive protic ILs that are suitable for large-scale biomass processing (Chen et al., 2014; George et al., 2015; Brandt-Talbot et al., 2017). Protic ILs can be produced by mixing a Brønsted acid with a Brønsted base in a single step (Greaves and Drummond, 2015). The solvent of choice in this study is triethylammonium hydrogen sulfate [TEA][HSO$_4$] that can be cheaply manufactured, with bulk cost as low as $1.24 kg^{-1} (Chen et al., 2014), at least 40 times cheaper than [Emim][OAc] (George et al., 2015). Brandt-Talbot et al. (2017) previously showed that [TEA][HSO$_4$] is a promising candidate protic IL for use in economically viable pretreatment processes. The IL was successfully recovered and reused four times for pretreatment of *Miscanthus*, and saccharification yields for *Miscanthus* were not affected by IL recycling (Brandt-Talbot et al., 2017). It has also been applied to pretreat sugarcane bagasse under mild temperature conditions (120°C, 4 h), resulting in glucose yields of up to 65% (Chambon et al., 2018). Recently, Gschwend et al. (2018) demonstrated that process temperatures up to 180°C improved lignin extraction and delignification and reduced residence times from hours to minutes, suggesting that this IL could be similarly applied to highly lignified feedstocks (up to 30 wt%). A major limitation of our previous work is that pretreated pulps were air-dried before enzymatic saccharification, severely limiting glucose yields. Therefore, in an attempt to reflect industrial practice, in this w we have avoided the energy-intensive air-drying step and directly hydrolyzed wet pulps to observe ionoSolv process performance on suitable candidate agricultural feedstocks for the future biorefinery.

In this work, we investigated the suitability of lignin-dissolving IL [TEA][HSO$_4$] for pretreatment of four agricultural residues, namely rice straw, rice husk, sugarcane bagasse and wheat straw. The four materials have high lignin (28 wt%) and ash content (up to 13 wt%) yet they are ideal feedstocks for biorefining as they are highly abundant, geographically diverse, low-cost and easily procured (Reddy and Yang, 2005). Here we apply ionoSolv processing at 150 and 170°C to establish optimal treatment times for cellulose valorization. Another novelty is the determination of the effect of pulp drying (pore collapse) on sugar yield. Successful pretreatment was characterized by high glucose release, delignification and lignin recovery, as gauged by enzymatic hydrolysis and compositional analysis of the recovered pulps. Subsequently, isolated lignin fractions were compared by 2D HSQC NMR to obtain insights into the structural changes occurring during ionoSolv pretreatment.

MATERIALS AND METHODS

Rice husk (*Oryza sativa*) was obtained from a rice mill in Bahraich district, Uttar Pradesh, India; rice straw was helpfully provided by the Institute of Chemical Technology, Mumbai, after harvesting in Tirunelveli district, Tamil Nadu, India; wheat straw (*Triticum aestivum*) was received from Glasgow, UK; depithed sugarcane bagasse (*Saccharum officinarum*) was kindly provided by Sugar Milling Research Institute, Durban, and originated from KwaZulu-Natal province, South Africa. All feedstocks were washed to remove adhering inorganic debris and air-dried at room temperature in order to prevent microbial degradation during shipping. Each feedstock was ground using a cutting mill (Retsch SM200, Germany) and then sieved using a vibratory shaker (Retsch AS200, Germany) to a particle size within 0.18–0.85 mm (US mesh scale −20/+80). The feedstocks were then stored air-dry in sealed plastic bags at ambient temperature. All chemical reagents were purchased from VWR International or Sigma-Aldrich and used as received. The Karl-Fischer titrator used to measure ionic liquid moisture content was a V20 volumetric Titrator (Mettler-Toledo). The analytical balance used in this study was a Sartorius CPA 1003S (±0.001 g).

Ionic Liquid Synthesis
The ionic liquid triethylammonium hydrogen sulfate ([TEA][HSO$_4$]) with an acid : base ratio of 1 : 1 (mol/mol) was synthesized according to a previously published protocol (Gschwend et al., 2018). The ionic liquid water content was adjusted to 20 wt% using a Karl-Fischer titrator (V20 volumetric titrator, Mettler-Toledo, USA) according to the standard operating procedure of our laboratory (Gschwend et al., 2016).

IonoSolv Pretreatment
Pretreatments, determination of oven-dried weight and pulp and lignin yields were conducted following the standard operating procedure of our laboratory (Gschwend et al., 2016). The solvent used for all experiments was a mixture of [TEA][HSO$_4$]:H$_2$O (4:1 wt/wt), i.e., with a final water content of 20 wt%. Pretreatments were carried out in triplicates using 10 g of solvent and 1 g of biomass (on an oven-dried basis), corresponding to a biomass loading of 1:10 g/g. Pretreatments were performed at 150° and 170°C for a pretreatment time varying between 30 and 180 min depending on the feedstock and operating temperature. For experiments *with* air-drying of the pulp, the cellulose-rich material (pulp) was washed four times with ethanol (40 mL) and Soxhlet extracted for 24 h using ethanol in cellulose thimbles before being air-dried overnight. The pulp was weighed before being subjected to saccharification. The collected ethanol washes and Soxhlet extractives were combined and ethanol removed by evaporation using a rotavapor, generating an ethanol-free IL-water liquor. Lignin was precipitated by addition of water (40 mL) as anti-solvent to the liquor and lignin was isolated by washing with water before being dried under vacuum at 45°C.

For experiments *without* air-drying of the pulp, the procedure was followed unchanged until the Soxhlet extraction step.

The pulp-containing thimbles were removed from the Soxhlet adapter after completion of the extraction and transferred to 50 mL Falcon tubes which were immediately filled with de-ionized water (40 mL). The pulp was left in the thimble inside the Falcon tube for at least an hour. The thimble was then taken out of the Falcon tube and the pulp transferred back to the Falcon tube using a spatula. The tubes were centrifuged (3,000 rpm or 2,000xg, 50 min) and the supernatant decanted; the washing step was repeated once more in de-ionized water. The wet pulp was weighed, its moisture content determined immediately and saccharification started the following day. Wet pulps were stored at 5°C.

Saccharification Assay

The enzymatic hydrolysis assay was carried out according to an adapted procedure entitled "Low Solids Enzymatic Saccharification of Lignocellulosic Biomass" published by the NREL (Resch et al., 2015). Saccharification assays were performed on native biomass, air-dried pulps and wet pulps, each in triplicate, using Cellic® CTec2 enzymes (Novozymes, Denmark).

100 ± 5 mg (on an oven-dried weight basis) of air-dried or wet biomass was placed into a Sterilin tube and the weight recorded. Three blanks were run with 100 µL of purified water in order to correct for sugar residues present in the enzyme solutions. 9.9 mL solution consisting of 5 mL 1 M sodium citrate buffer at pH 4.8, 40 µL tetracycline antibiotic solution (10 mg/mL in 70% ethanol), 30 µL cycloheximide antibiotic solution (10 mg/mL in purified water), 4.78 mL purified water and 50 µL of Novozymes experimental enzyme mixture NS-22201 was added, the tubes closed and placed into an Stuart Orbital Incubator (S1500) at 50°C and 250 rpm. Saccharification samples were obtained by filtering 1 mL of the saccharification mixture through a PTFE syringe filter. Samples were run on a Shimadzu HPLC with an AMINEX HPX-97P column (Bio rad, 300 x 7.8 mm) with purified water as mobile phase (0.6 mL/min). The column temperature was 85°C and acquisition was run for 20 min. Calibration standards with concentrations of 0.1, 1, 2 and 4 mg/mL of glucose, xylose, mannose, arabinose and galactose and 8 mg/mL of glucose were used. Glucose yields were calculated relative to the total glucan content of untreated biomass.

Feedstock and Pulp Characterization
Moisture Content
Moisture content determination of both native biomass and recovered pulp was determined according to published procedures (Gschwend et al., 2018).

Compositional Analysis
Compositional analysis was carried out in triplicates on native biomass and air-dried pulps, following the NREL protocol 'Determination of Structural Carbohydrates and Lignin in Biomass' (Sluiter et al., 2008). Details of the procedure used in our laboratory may be found in the **Supplementary Material**.

Delignification and Hemicellulose Removal
The pulp delignification was calculated using the following equation:

$$\text{Delignification} = \frac{Lignin_{untreated} - \left(Lignin_{pulp} \times Yield_{pulp}\right)}{Lignin_{untreated}} \cdot 100\% \quad (1)$$

where $Lignin_{untreated}$ is the total lignin content in untreated biomass, $Lignin_{pulp}$ is the total lignin content in the pulp and $Yield_{pulp}$ is the oven-dried pulp yield.

Hemicellulose removal can similarly be obtained from Equation 2, shown below:

$$\text{Hemicellulose removal} = \frac{Hem_{untreated} - (Hem_{pulp} \times Yield_{pulp})}{Hem_{untreated}} \cdot 100\% \quad (2)$$

Where $Hem_{untreated}$ is the hemicellulose sugar content of the untreated biomass and Hem_{pulp} is the hemicellulose content of the pulp.

Ash Content Determination
Ash samples were obtained from all four feedstocks (~0.5 g original sample weight) by ashing at 575°C in air to remove any organic material using a ramping program in a muffle furnace (Nabertherm + controller P 330). The heating program was as follows: heating from room temperature to 105°C; hold at 105°C for 12 min to remove moisture; heating to 250°C at 10°C/min; hold at 250°C for 30 min; heating to 575°C at 10°C/min; hold at 575°C for 3 h; cool to 105°C. Ash contents were determined in triplicate.

Elemental Analysis
CHNS analysis of untreated air-dried biomass was performed in duplicate by MEDAC Ltd. (Chobham, UK) by dynamic flash combustion analysis and thermal conductivity detection. Oxygen content was obtained by difference. Accuracy is ±0.30% absolute.

Lignin Analysis
Enzymatic Mild Acidolysis Lignin (EMAL)
Enzymatic mild acidolysis lignin (EMAL) was isolated from depithed sugarcane bagasse based on a three-stage protocol adapted from Wu and Argyropoulos (2003). First, depithed sugarcane bagasse was ground to <0.75 mm using a cutting mill. It was then acetone-extracted for 48 h and dried in a vacuum oven at 45°C. Approximately 60 g of dry extracted biomass was subjected to planetary ball milling (Retsch PM400, Germany) for 14 days at a rotation frequency of 150 rpm. It was ground in four 250 mL ball mill jars in the presence of four stainless steel balls which occupied ~50% of the active jar volume, using toluene as a grinding aid. The biomass was then allowed to dry in a fume cupboard overnight until the toluene had evaporated. Following ball-milling, enzymatic mild acid hydrolysis was performed in two separate stages. In the first stage, the ball-milled biomass was treated with cellulase enzymes (Ctec2, Novozymes, Denmark) in the amount of 190 mg protein per g biomass. The enzymatic hydrolysis was carried out at 50°C for 48 h at 3% consistency in the presence of 2% Tween 20 in 0.1 M citrate buffer (pH ~4.75). The slurry was stirred in a 2 L jacketed borosilicate

glass pressure vessel (polyclave, Büchiglasuster, Switzerland) that was agitated using an anchor impeller at 120 rpm. The process temperature was controlled using an oil recirculator equipped with a thermostat (Unistat 405, Huber, Germany). After 48 h had elapsed, the slurry was centrifuged at 3,000 rpm for 15 min with a high-speed centrifuge (Megastar 3.0, VWR, UK). The insoluble materials were re-suspended in a fresh batch of enzyme/citrate mixture for another 48 h at 50°C under the same reaction conditions. The insoluble materials were again collected by centrifugation and washed twice with acidified (pH 2.0) deionized water to remove soluble sugars. Residual proteins on the surface of the insoluble solids were washed twice with 6 M guanidine hydrochloride followed by freeze-drying for 72 h to obtain a crude lignin sample. In the second stage, the crude lignin was finely ground in a pestle and mortar and subjected to mild acid hydrolysis using an azeotrope of dioxane-water (96:4 v/v) containing 0.01 M HCl at 87°C under a nitrogen atmosphere. Butyl hydroxytoluene (BHT) was added as a radical scavenger and stabilizer to limit the formation of explosive peroxides. The crude lignin was suspended in the dioxane-water azeotrope with a solid-to-liquid ratio of 1:20 (g/mL) and refluxed for 2 h. After the reaction, the suspension was centrifuged and the supernatant was carefully withdrawn. The solid residue was washed with fresh dioxane-water until the supernatant was clear. The combined supernatants were then neutralized with sodium bicarbonate and then added drop-wise into 8 L acidified water (pH 2.0). The precipitated lignin was allowed to equilibrate with the aqueous phase overnight and was recovered by centrifugation and washed twice with deionized water. The solid was then washed once with hexane to dissolve any extractives and residual BHT and the purified solid was freeze-dried. The final yield of EMAL recovered through the entire procedure was 3 wt% based on dry bagasse starting material, and that based on the acid-insoluble lignin content of bagasse was 15 wt%.

HSQC NMR Spectroscopy of Lignins

^{13}C-^{1}H heteronuclear single quantum coherence (HSQC) NMR spectroscopy was performed in monoplicate for bagasse EMAL and for lignin precipitates generated under the optimized conditions for each of the following feedstocks: sugarcane bagasse (170°C, 45 min); rice husk (170°C, 45 min); rice straw (170°C, 30 min); wheat straw (170°C, 30 min). The analysis followed the same procedure described by Brandt-Talbot et al. (2017). The signal intensities were normalized to the total abundance of $G_2 + G_{2,cond}$ units. The total $(G_{2+} G_{2,cond})$ and $(S_2 + S_{2,cond})$ were used to calculate the S/G ratio, after halving the contribution from S units to avoid double-counting for the symmetrical syringyl unit. The degree of condensation was estimated as the proportion of G_2 units involved in condensation reactions, i.e. $G_{2,cond}$: $(G_{2+} G_{2,cond})$.

RESULTS AND DISCUSSION

Feedstock Characterization

In this study, four of the most abundant (>40 Mtpa) (FAOSTAT, 2018) lignocellulosic feedstocks available annually as crop waste were pretreated with a view to bioethanol production. The materials investigated were wheat straw, rice straw, rice husk and depithed sugarcane bagasse. For each material, the annual availability and geography, current uses and challenges for utilization, and appearance before pretreatment are presented in **Table 1**. All feedstocks were prepared by washing, air-drying and cutting to a standard size fraction (0.18–0.85 mm). Prior to pretreatment, the elemental and chemical composition of the feedstocks was determined (see **Table S1** in the Supplementary Material).

The biomass had compositions typical of grassy feedstocks (Parikh et al., 2005; Ang et al., 2012), though significant variation was seen in their lignin and ash contents. Rice husk (27%) and sugarcane bagasse (24%) had the highest lignin content while wheat straw (22%) and rice straw (18%) were less lignin-rich. The most ash-rich feedstocks were rice straw and rice husk (13 and 11% total inorganic matter, respectively) as determined by heating to 575°C, a method which tends to give higher ash values than compositional analysis. Acid hydrolysis in the latter method measures only water- and acid-insoluble inorganic species as metals, whereas inorganic matter from ashing of whole biomass is present as oxides. The straws showed greater discrepancies between their acid-insoluble ash and total ash contents, possibly because of higher alkali species content which are acid-soluble (Miles et al., 1996). Elemental composition of the biomass materials showed that feedstocks with higher ash contents had correspondingly lower carbon contents, another factor in the low energy densities of rice residues (Mehta and Pitt, 1976).

All materials had similar cellulose and hemicellulose contents (70–72 wt%) making them suitable for conversion into bioethanol; the exception is rice husk, which had a lower polysaccharide content of 62% on account of its high ash and lignin contents.
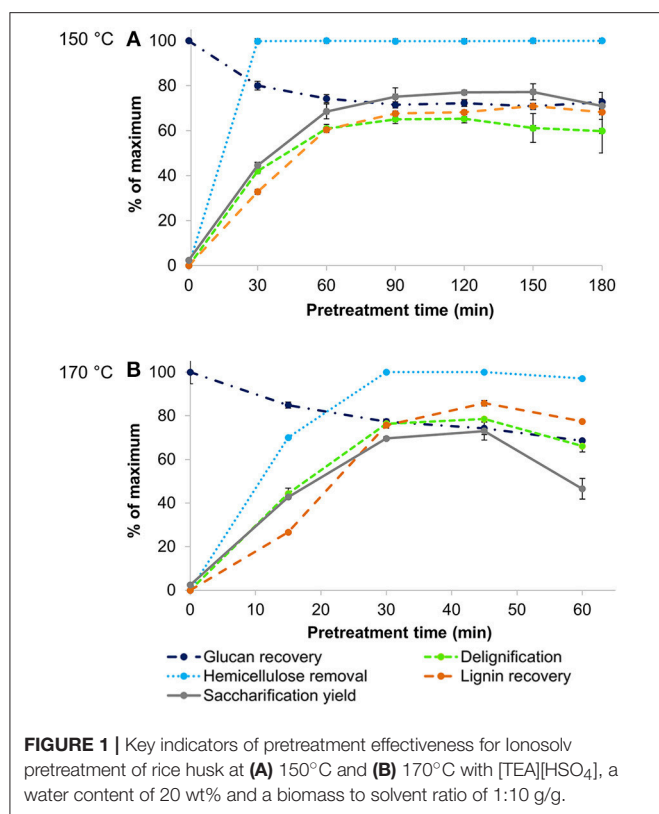
Fractionation Effectiveness for Rice Husk

Rice husk is naturally rich in lignin and has a significant ash content, which makes it the most recalcitrant and interesting feedstock to be studied. A first set of experiments was conducted by treating rice husk with the protic IL [TEA][HSO$_4$] at two different temperatures (150° and 170°C) for pretreatment times between 30 min and 180 min. These time courses enabled the identification of optimal pretreatment conditions, assessed via the maximum saccharification yield from wet pulps (reported as the glucose released relative to the glucan content in native biomass). **Figure 1** shows a number of pretreatment outcomes monitored over time for each temperature: lignin and hemicellulose removal from biomass, glucan retention in the pulp, and the yield of lignin precipitate as well as glucose yield after 7 days of enzymatic saccharification.

Pulp saccharification was the main indicator used to gauge pretreatment effectiveness. A number of studies have suggested that hornification, induced by air-drying, directly causes an irreversible pore shrinkage and collapse of pores within the cell wall, reducing internal surface area and, in turn, limiting enzyme accessibility and thereby lowering sugar yields (Luo et al., 2011). In this study, enzymatic saccharification was carried out for pretreated pulps both with and without an air-drying step. The

TABLE 1 | Agricultural residues investigated in the present study and their appearance after milling and before pretreatment.

Feedstock	Annual availability and major geography[a]	Current uses and challenges	Appearance
Wheat straw	43 Mtpa; Europe	Animal bedding (60%). Inefficient burning leads to alarming levels of environmental pollution	
Rice straw	501 Mtpa; Asia, notably China and India	Burning in open fields (50%); fodder; landfilled. Logistical challenges for utilization as mostly left in fields. Inefficient burning leads to alarming levels of environmental pollution	
Rice husk	125 Mtpa; Asia, notably China and India	Combustion and gasification after forming pellets or briquettes (unknown %). Resistant to burning; abrasive to grinding equipment; poor nutritive value; high ash content	
Sugarcane bagasse	157 Mtpa; Brazil, India and China	Combustion for combined heat and power production in sugar and ethanol mills (50%); remainder is stockpiled	

[a]*Based on 2017 data on crop production obtained from FAOSTAT (2018) and geographical availability from Satlewal et al. (2018). Key assumptions: bagasse to processed sugarcane ratio of 26:100 kg/kg (Li and Khanal, 2017); rice husk to rice paddy ratio of 22:100 kg/kg (Zafar, 2018); rice straw to paddy ratio of 400:100 kg/kg (IRRI, 2018); wheat straw to harvested wheat ratio of 43: 100 kg /kg available as straw (Agricultural Horticulure Development Board (AHDB), 2018); 40 wt% of available residues are plowed back into the soil for soil conservation (Scarlat et al., 2010).*

FIGURE 1 | Key indicators of pretreatment effectiveness for Ionosolv pretreatment of rice husk at **(A)** 150°C and **(B)** 170°C with [TEA][HSO$_4$], a water content of 20 wt% and a biomass to solvent ratio of 1:10 g/g.

outcomes (shown in **Figure S1**) confirmed that omitting an air-drying step for the pulp significantly increased the glucose yields by an average factor of 1.7. Very similar findings were obtained by Gschwend et al. (2019), whereby sugar release increased by 1.6× for pine treated under comparable conditions. Consequently, *wet* pulps were directly subjected to saccharification in the rest of the study. This is in line with industrial practice, where the cellulose pulp would be subjected to enzymatic hydrolysis immediately after its recovery as a wet solid, rather than undergoing an energy-intensive air-drying step. For both time courses, two different peaks in saccharification yields were observed at the following conditions: after 2 h at 150°C and only 45 min at 170°C, where glucose yields reached 77 and 73%, respectively.

Compositional analysis of the pulps confirmed that hemicellulose and lignin were rapidly removed from the pulp by the acidic IL at both temperatures, while glucan remaining in the pulp degraded slowly over time. At both temperatures, hemicellulose was completely extracted by the IL after 30 min of treatment. A strong relationship was observed between pulp delignification and saccharification yields (**Figure 1**). After the point of peak saccharification and delignification, the pulp lignin was seen to increase again. We attribute this to lignin re-deposition onto the pulp surface, limiting the accessibility of the cellulose and exerting a negative effect on pulp digestibility, as studied in detail in our previous work (Brandt-Talbot et al., 2017; Weigand et al., 2017; Gschwend et al., 2018). For lignin recoveries to reach a maximum, a longer pretreatment time was required, which is related both to condensation of small lignin

fragments dissolved in the ionic liquid yielding water-insoluble molecules that precipitate, and to pseudo-lignin formation (Gschwend et al., 2018). The formation of pseudo-lignin is expected at conditions when lignin recoveries exceed lignin removal, leading to a decrease in pulp accessibility and reduced sugar yields.

For the purpose of developing an industrially relevant process, the selected optimum condition for rice husk pretreatment was 45 min at 170°C, as shorter pretreatment times are desirable to reduce reactor volumes and hence capital cost (Gschwend et al., 2018).

Fractionation of Four Agricultural Residues

After observing the strong performance of ionoSolv fractionation for the recalcitrant material rice husk, similar pretreatments were conducted at 170°C to optimize fractionation conditions for three other abundant agricultural residues, namely rice straw, wheat straw and sugarcane bagasse. Optimal pretreatment conditions were again selected on the basis of peak cellulose digestibility (rather than hemicelluloses), as cellulose is the most abundant component with higher value and large and mature market.

As **Table 2** shows, the optimum glucose yields obtained from saccharification of wet pulps of all four feedstocks were very promising, as they are approaching the theoretical maximum glucose release based on the glucan content of untreated biomass. While 73% glucose yield was seen for rice husk, glucose release of nearly 90% was obtained for rice straw, wheat straw and sugarcane bagasse. We compared these yields to applications of the aprotic ionic liquid [Emim][OAc] for pretreatment of rice straw and rice husk, which gave maximal glucose yields of 75 and 40%, respectively (Ang et al., 2012; Poornejad et al., 2014). These findings show that [TEA][HSO$_4$] outperforms cellulose-dissolving ILs at 1/40th of the solvent cost (George et al., 2015).

Wheat straw (87%) and rice straw (89%) gave high glucose yields after only 30 min of treatment. We attribute this to their less dense and more porous cell wall structure as well as lower lignin content, meaning that fractionation is easier and less energy-intensive. Eighty-nine percent glucose recovery was obtained from sugarcane bagasse after 45 min of treatment, significantly higher than our previous optimum of 65% glucose yield from air-dried pulps at 120°C, presumably due to process intensification and direct saccharification of wet pulps reducing the effects of hornification. Rice husk gave 73% glucose yield, a 30-fold improvement over the very low glucose yield for untreated rice husk, which demonstrates that this material is highly recalcitrant (see **Table S2** in the Supplementary Material). The fact that rice husk and bagasse required more prolonged treatment (45 min rather than 30 min) is consistent with their higher lignin contents (see **Table S1**), and their dense and closed cell wall structures ((Real et al., 1996; Pu et al., 2013); Satlewal et al., 2018).

Figure 2 presents the key compositional changes of all four feedstocks under the optimal conditions for glucose hydrolysis identified in **Table 2**. Under these conditions, the hemicelluloses can be seen to have nearly completely hydrolysed into the IL solution. The hemicellulose solutes are known to react

TABLE 2 | Summary of maximal glucose yields obtained after Ionosolv pretreatment of for agroresidues at 170°C using [TEA][HSO$_4$], a water content of 20 wt% and a biomass to solvent ratio of 1:10 g/g.

Feedstock	Optimal pretreatment condition	Saccharification yield[a]		Increase in saccharification yield[b]
		With air drying (%)	Without air drying (%)	
Wheat straw	170°C, 30 min	80.5 ± 0.8	86.5 ± 1.9	5.6
Rice straw	170°C, 30 min	68.3 ± 0.5	88.8 ± 0.2	3.4
Rice husk	170°C, 45 min	58.8 ± 1.5	73.0 ± 4.3	30.4
Sugarcane bagasse	170°C, 45 min	78.4 ± 2.1	89.4 ± 5.5	8.1

[a]Calculated as a percentage of glucan content in untreated biomass.
[b]Calculated as ratio of wet pulp sugar yield compared to sugar yield for untreated biomass.

FIGURE 2 | Comparison of key pretreatment parameters for agricultural residues following Ionosolv pretreatment with [TEA][HSO$_4$] under optimized conditions.
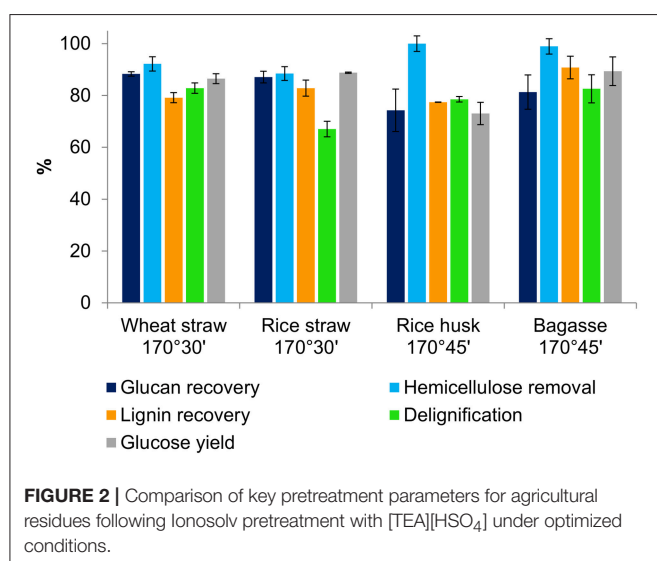
further in the acidic IL to form degradation products such as furfural and acetic acid, which can be separated quantitatively from the non-volatile IL by distillation (Brandt-Talbot et al., 2017). More prolonged treatments led to nearly quantitative hemicellulose removal, but this was accompanied by 10–20% glucan loss, as glucan degrades rapidly at 170°C. Cellulose degradation, rather than delignification, is suspected to be the limiting factor for glucose release. This was investigated by comparing the glucose yields as a percentage of glucan in the *pulp* (rather than in untreated biomass), shown in **Table S2** in the Supplementary Material. This analysis showed that glucan that survived the treatment was quantitatively released, suggesting that further optimization may be possible by adjusting reaction times between 30 and 45 min to maximize glucan recovery and hence glucose release from enzymatic saccharification. Lignin was also dissolved from the pulp by the acidic IL and recovered as a precipitate by addition of water to the IL liquor. All four feedstocks produced pulps that were highly delignified (67–82%), reflecting the strong link between lignin removal and glucose release; quantitative lignin removal is rarely observed (Brandt-Talbot et al., 2017). High lignin precipitate yields of ∼80–90% were obtained, with values similar to lignin removal from the

pulp for all feedstocks, except for rice straw and bagasse where the lignin recovery slightly exceeded delignification. The latter, which seems to indicate the "formation" of lignin, strongly suggests the occurrence of condensation reactions occurring between lignin fragments; upon further treatment, lignins form insoluble macromolecules that condense onto the pulp, reducing glucose yields, as seen in our previous work (Brandt-Talbot et al., 2017; Gschwend et al., 2018).

Lignin Characterization

As was shown in the previous section, pulp delignification is closely linked to the overall pretreatment performance represented by the saccharification yield. Compositional analysis does not provide information about changes in lignin structure and inter-unit linkages during pretreatment, which is key information for value-added applications of lignin. Therefore, we set out to analyze the lignin fractions isolated under the optimized pretreatment conditions at 170°C using HSQC NMR spectroscopy. Enzymatic mild acidolysis lignin (EMAL) was used to represent native lignin and as a benchmark against which the isolated ionoSolv lignins can be compared. **Figure 3A** shows the main lignin structural units present, while the two key regions of the NMR spectra for bagasse EMAL and bagasse ionoSolv lignin can be seen in **Figure 3B**. Full spectra of lignins isolated from all four agricultural feedstocks are available in **Figure S2** (see Supplementary Material).

A semi-quantitative technique was applied to quantify the changes in lignin sub-units following ionoSolv pretreatment. The results of volume integration are presented in **Figure 4**. All signal intensities were compared to the sum of the G$_2$ and G$_{2,\text{cond}}$ integrals, which can be used as an internal standard in the case of herbaceous biomass, according to the findings of Brandt-Talbot et al. (2017). It is thought to be the most stable C-H subunit in lignin and therefore representative of the total number of aromatic units in lignin (Zhang and Gellerstedt, 2007). Signal intensities were compared in **Figure 4** and the S/G ratios and degree of condensation of G$_2$ units are presented in **Table 3**. Within the side chain region of the spectrum (δH 6.5 – 2.5; δC 90 – 50) seen in **Figure 3B**, the most obvious change is the disappearance of signals corresponding to sugars from the pretreated lignin spectrum, reflecting high lignin purity. Delignification is known to proceed through cleavage of α-*O*-4′ and β-*O*-4′, linkages, facilitating dissolution of lignin into
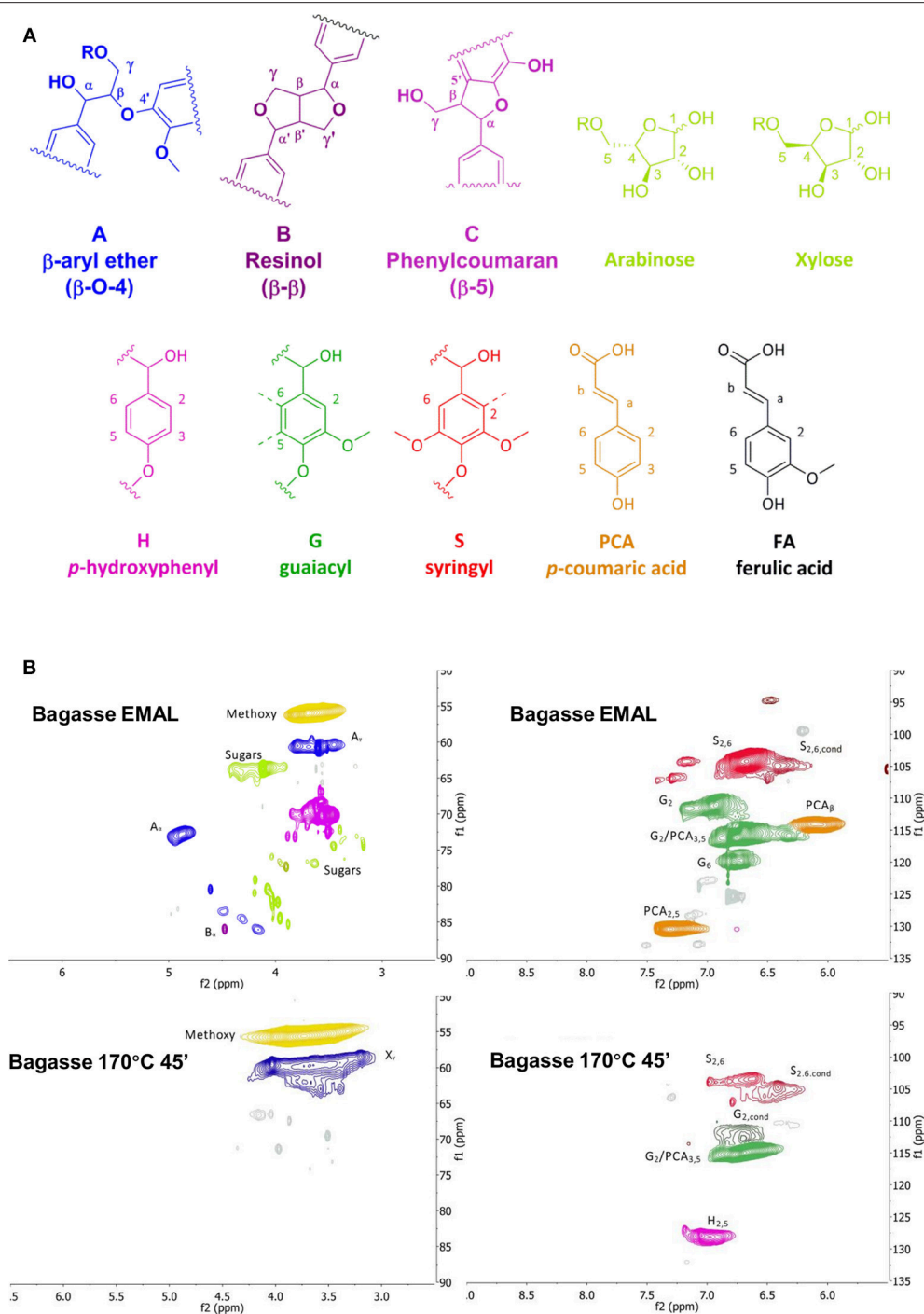
FIGURE 3 | (A) Lignin substructures found in grassy lignins, and **(B)** HSQC NMR spectra of bagasse enzymatic mild acidolysis lignin and lignin isolated with [TEA][HSO$_4$], with a water content of 20 wt% and a biomass to solvent ratio of 1:10 g/g. Side chain region (left) and aromatic region (right).

the IL (Brandt et al., 2015). The signals assigned to the major interunit linkages β-O-4′, β-5′, and β-β′ linkages disappeared after pretreatment, as they are rapidly cleaved or modified in acidic media. Among the three bonds, β-O-4′ ether linkages were the most readily removed during the acidic pretreatment,

with over 90% of bagasse ether bonds gone after pretreatment (**Figure 4**). Decreased signal intensities assigned to β-5′ and β-β′ linkages were attributed to their chemical alteration in acidic media rather than cleavage, as these linkages contain C–C bonds which are unlikely to have been broken (Brandt et al., 2015).

FIGURE 4 | HSQC NMR signal intensities of different lignin C-H units relative to 100 $G_2 + G_{2,cond}$ units, obtained for enzymatic mild acidolysis lignin (EMAL) isolated from sugarcane bagasse and for lignins isolated from four agricultural feedstocks with [TEA][HSO$_4$] with 20 wt% water and a biomass to solvent ratio of 1:10 g/g.
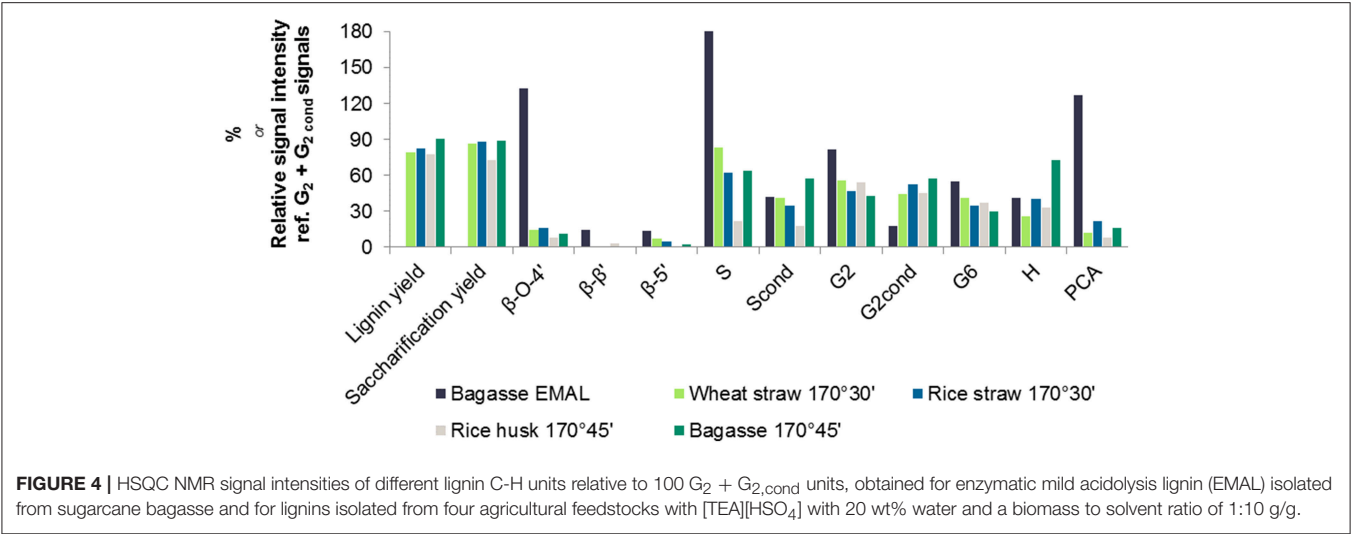
TABLE 3 | Degree of condensation as evidenced by S/G ratio and condensed: non-condensed G_2 ratios of enzymatic mild acidolysis lignin (EMAL) isolated from sugarcane bagasse and for lignins isolated from four agricultural feedstocks with [TEA][HSO$_4$] with 20 wt% water and a biomass to solvent ratio of 1:10 g/g.

Lignin	Sub-unit composition				S/G ratio[a]	Cond/Non-cond[b]
	G_2	$G_{2,cond}$	S_2	$S_{2,cond}$		
Bagasse EMAL	81.8	18.2	182.5	42.5	1.12	0.18
Wheat straw 170°30′	55.8	44.2	83.3	41.3	0.62	0.44
Rice straw 170°30′	47.1	52.9	62.0	34.9	0.48	0.53
Rice husk 170°45′	54.5	45.5	22.2	17.5	0.20	0.45
Bagasse 170°45′	42.9	57.1	64.3	57.9	0.61	0.57

[a]Calculated from HSQC NMR spectra signals as $0.5(S_2 + S_{2,cond})/(G_2 + G_{2,cond})$.
[b]Calculated as cond/non-cond $= G_{2,cond}/(G_2 + G_{2,cond})$.

FIGURE 5 | Chemical composition of untreated (UT) and pre-treated cellulose-rich pulps isolated from pretreatment of rice husk, sugarcane bagasse, wheat straw, and rice straw with [TEA] and [HSO$_4$] under optimized conditions.
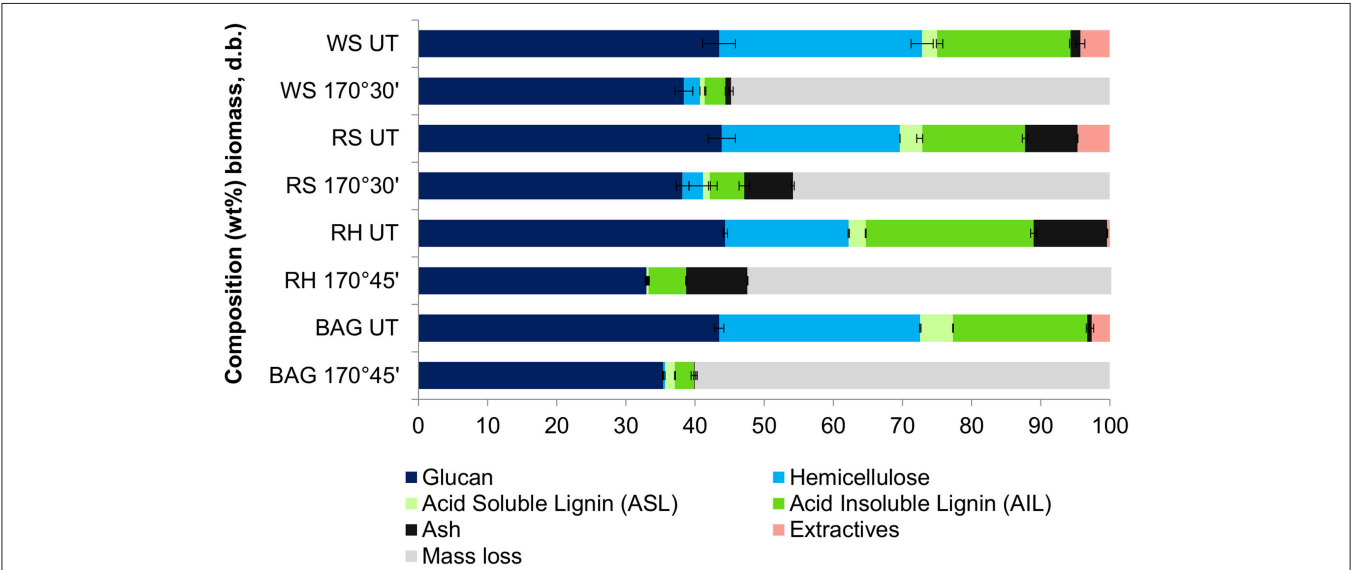
Within the aromatic region (δH 9.0 – 5.5; δC 135 – 90), extensive condensation between aromatic rings was observed. Condensation between aromatic rings is thought to occur at the 2- and 6- ring positions of G and S lignin units which are not fully substituted (Brandt et al., 2015). From **Figure 4**, evidence for C–C condensation reactions in bagasse lignin can be seen in the decrease in G_2 and S and increase in $G_{2,cond}$ and S_{cond} signals, relative to the sum of G_2 and $G_{2,cond}$ signals. Compared to native bagasse lignin (i.e. EMAL), the signal intensity of G_6 units was also reduced, which is similarly thought to stem from C–C condensation reactions occurring at this position. The degree of condensation of G_2 units, seen in **Table 3**, showed that around 50% of G_2 units had undergone condensation reactions in all pretreated feedstocks, compared to only 18% in bagasse EMAL. Rice straw and bagasse lignin appeared to be comparatively more condensed, as seen in their higher $G_{2,cond}$: G_2 ratios (**Figure 4**; **Table 3**), in agreement with the evidence for more advanced lignin condensation seen from compositional analysis (**Figure 2**). Another distinctive feature is the much lower S/G ratio observed for rice husk lignin, which could be a factor in its recalcitrance (Pu et al., 2013). Additionally, a significant drop in *p*-coumaric acid (PCA) subunit content and an apparent increase in H subunits were observed within this NMR region. This is in agreement with our previous findings, whereby interdependence of PCA and H units was explained by conversion of PCA units into "H-like" IL-soluble oligomers under acidic solutions, with these reactions occurring in parallel with condensation reactions (Brandt et al., 2015; Brandt-Talbot et al., 2017). Given that extensive condensation may preclude several value-added applications of lignin, such as carbon fiber or chemicals production (Ragauskas et al., 2014), further fine-tuning of the process conditions may be necessary to simultaneously optimize lignin properties and pulp digestibility, as demonstrated by Gschwend et al. (2018).

Fate of Ash Components

Ash recovery also needs to be considered when optimizing the pretreatment conditions, especially for rice straw and rice husk, which contain 13 and 11 wt% ash, respectively. Compositional analysis of the native biomass and pretreated pulps (**Figure 5**) revealed that ash mostly partitioned with the pulp, as expected from our previous study (Brandt-Talbot et al., 2017). This was most clearly observed for high-ash rice husk and rice straw, where 92 ± 5% and 84 ± 8% of ash were recovered in the pulp. It should be noted that chemical analysis reveals only acid-insoluble inorganic matter, whereas acid-soluble ash components are likely to have dissolved in the acidic ionic liquid medium during pretreatment (or later in the aqueous sulfuric acid medium during compositional analysis). The presence of ash in the pulp does not appear to have negatively impacted its enzymatic digestibility: between 88 and 100 wt% of the cellulose-rich material was hydrolyzed to glucose (see **Table S2**). The exception is rice husk, which was 58% hydrolyzed, presumably due to its greater residual lignin content and more packed cell wall structure (Real et al., 1996; Pu et al., 2013; Satlewal et al., 2018). As nearly all of the pulp can be hydrolyzed, the amount of post-hydrolysis solids would be desirably low, simplifying

processing. The inorganic matter, especially silica, could also be easily recovered in the post-hydrolysis solids. Facile separation of ash from the post-hydrolysis solids is helpful as the ash often has market value; for instance, rice husk ash is silica-rich and has various applications in cement production and waste-water treatment (Foo and Hameed, 2009). The effect of an additional ash product stream on process economics remains to be investigated.

CONCLUSIONS

Four of the world's most abundant agricultural residues, namely rice straw, rice husk, sugarcane bagasse and wheat straw, were pretreated using the ionoSolv process. The pretreatment solvent was the low-cost protic ionic liquid [TEA][HSO$_4$] with a water content of 20 wt% and a biomass to solvent ratio of 1:10 g/g. It was applied to four agricultural feedstocks with high lignin (up to 28 wt%) and ash content (up to 13 wt%), which were successfully pretreated to yield a highly digestible cellulose-rich pulp and lignin as co-products. Optimum pretreatment conditions were identified at a temperature of 170°C with the aim of maximizing enzymatic saccharification yields and minimizing residence time. Rice straw and wheat straw could be pretreated within 30 min while more prolonged treatment of 45 min was needed for rice husk and sugarcane bagasse, which have more dense and lignified structures. The glucose yields obtained following enzymatic saccharification of the pretreated pulps were 73% for rice husk and close to 90% glucose yields for rice straw, wheat straw and sugarcane bagasse. Glucose release from the pulps was enhanced by a factor of ∼1.7 by saccharifying wet pulps without an air-drying step to reduce hornification. Around 80–90% of lignin present in the feedstock could be recovered as a precipitate while the ash mostly partitioned within the solid pulp, enabling its recovery in the post-hydrolysis solids. According to both wet and dry pulp saccharification assays, [TEA][HSO$_4$] was demonstrated to obtain significantly higher glucose yields than aqueous [Emim][OAc] in the pretreatment of agricultural residues at the laboratory scale (process volumes of 10 mL), despite having a solvent cost of 1/40th that of [Emim][OAc].

A strong link between residual pulp lignin and saccharification yields was noted. Delignification was seen to proceed *via* extensive cleavage of β-*O*-4′ aryl ether linkages which was accompanied by condensation reactions in the lignin precipitate. This work has validated the potential use of the ionoSolv fractionation technology for conversion of abundant agricultural residues to bioethanol. Further work in this area should establish the energy requirements of grinding silica-rich materials such as rice husk and straw before pretreatment, and finding value-added applications for the inorganic components. Moreover, the process needs to be intensified to further reduce solvent and energy consumption, notably by use of larger particle sizes, higher solids loadings and direct pretreatment of moist raw feedstocks after harvesting to

eliminate the need for energy-intensive drying of feedstocks prior to pretreatment.

AUTHOR CONTRIBUTIONS

MC conducted all the major experiments and helped with the manuscript preparation. CC designed the study and wrote the manuscript. JH and PF provided valuable inputs for the study's development and helped with manuscript writing. All authors listed have made a substantial, direct and intellectual contribution to the work, and approved it for publication.

FUNDING

ACKNOWLEDGMENTS

SUPPLEMENTARY MATERIAL

The Supplementary Material for this article can be found online at: https://www.frontiersin.org/articles/10.3389/fchem.2019.00246/full#supplementary-material

REFERENCES

Agricultural and Horticulure Development Board (AHDB). (2018). *Straw - What It Is Good For?* Available online at: www.ahdb.org.uk/projects/Straw.aspx (accessed July 30, 2018).

Amiri, H., Karimi, K., and Zilouei, H. (2014). Organosolv pretreatment of rice straw for efficient acetone, butanol, and ethanol production. *Bioresour. Technol.* 152, 450–456. doi: 10.1016/j.biortech.2013.11.038

Ang, T. N., Ngoh, G. C., Chua, A. S. M., and Lee, M. G. (2012). Elucidation of the effect of ionic liquid pretreatment on rice husk via structural analyses. *Biotechnol. Biofuels* 5:67. doi: 10.1186/1754-6834-5-67

Bond, T. C., Doherty, S. J., Fahey, D. W., Forster, P. M., Berntsen, T., Deangelo, B. J., et al. (2013). Bounding the role of black carbon in the climate system: a scientific assessment. *J. Geophys. Res. Atmos.* 118, 5380–5552. doi: 10.1002/jgrd.50171

Brandt, A., Chen, L., Dongen, B. E., van Welton, T., and Hallett, J. P. (2015). Structural changes in lignins isolated using an acidic ionic liquid water mixture. *Green Chem.* 17, 5019–5034. doi: 10.1039/C5GC01314C

Brandt, A., Gräsvik, J., Hallett, J. P., Welton, T., Grasvik, J., Hallett, J. P., et al. (2013). Deconstruction of lignocellulosic biomass with ionic liquids. *Green Chem.* 15, 550–583. doi: 10.1039/c2gc36364j

Brandt, A., Ray, M. J., To, T. Q., Leak, D. J., Murphy, R. J., and Welton, T. (2011). Ionic liquid pretreatment of lignocellulosic biomass with ionic liquid–water mixtures. *Green Chem.* 13:2489. doi: 10.1039/c1gc15374a

Brandt-Talbot, A., Gschwend, F. J. V., Fennell, P. S., Lammens, T. M., Tan, B., Weale, J., et al. (2017). An economically viable ionic liquid for the fractionation of lignocellulosic biomass. *Green Chem.* 19, 3078–3102. doi: 10.1039/C7GC00705A

Chambon, C. L., Mkhize, T. Y., Reddy, P., Talbot, A. B., Deenadayalu, N., Fennell, P. S., et al. (2018). Pretreatment of South African sugarcane bagasse using a low-cost protic ionic liquid: a comparison of whole, depithed, fibrous and pith bagasse fractions. *Biotechnol. Biofuels* 11:237. doi: 10.1186/s13068-018-1247-0

Chen, L., Sharifzadeh, M., Dowell, N., Welton, T., Shah, N., and Hallett, J. P. (2014). Inexpensive ionic liquids: [HSO4]—based solvent production at bulk scale. *Green Chem.* 16, 3098–3106. doi: 10.1039/C4GC00016A

Chen, Y., Stevens, M. A., Zhu, Y., Holmes, J., and Xu, H. (2013). Understanding of alkaline pretreatment parameters for corn stover enzymatic saccharification. *Biotechnol. Biofuels* 6:8. doi: 10.1186/1754-6834-6-8

Cheng, Y. S., Zheng, Y., Yu, C. W., Dooley, T. M., Jenkins, B. M., and Vandergheynst, J. S. (2010). Evaluation of high solids alkaline pretreatment of rice straw. *Appl. Biochem. Biotechnol.* 162, 1768–1784. doi: 10.1007/s12010-010-8958-4

Clough, M. T., Geyer, K., Hunt, P. A., Mertes, J., and Welton, T. (2013). Thermal decomposition of carboxylate ionic liquids: trends and mechanisms. *Phys. Chem. Chem. Phys.* 15:20480. doi: 10.1039/c3cp53648c

Earle, M. J., Esperança, J. M. S. S., Gilea, M. A., Lopes, J. N. C., Rebelo, L. P. N., Magee, J. W., et al. (2006). The distillation and volatility of ionic liquids. *Nature* 439, 831–834. doi: 10.1038/nature04451

FAOSTAT (2018). *(Database) of Food and Agriculture Organization of the United Nations*. Available online at http://www.fao.org/faostat/en/ (accessed July 30, 2018).

Foo, K. Y., and Hameed, B. H. (2009). Utilization of rice husk ash as novel adsorbent: a judicious recycling of the colloidal agricultural waste. *Adv. Colloid Interface Sci.* 152, 39–47. doi: 10.1016/j.cis.2009.09.005

Fu, D., Mazza, G., and Tamaki, Y. (2010). Lignin extraction from straw by ionic liquids and enzymatic hydrolysis of the cellulosic residues. *J. Agric. Food Chem.* 58, 2915–2922. doi: 10.1021/jf903616y

George, A., Brandt, A., Tran, K., Zahari, S. M. S. N. S., Klein-Marcuschamer, D., Sun, N., et al. (2015). Design of low-cost ionic liquids for lignocellulosic biomass pretreatment. *Green Chem.* 17, 1728–1734. doi: 10.1039/C4GC01208A

Greaves, T. L., and Drummond, C. J. (2015). Protic ionic liquids: evolving structure-property relationships and expanding applications. *Chem. Rev.* 115, 11379–11448. doi: 10.1021/acs.chemrev.5b00158

Gschwend, F. J. V., Brandt, A., Chambon, C. L., Tu, W.-C., Weigand, L., and Hallett, J. P. (2016). Pretreatment of lignocellulosic biomass with low-cost ionic liquids. *J. Vis. Exp.* 114:e54246. doi: 10.3791/54246

Gschwend, F. J. V., Chambon, C. L., Biedka, M., Brandt-Talbot, A., Fennell, P. S., and Hallett, J. P. (2019). Quantitative glucose release from softwood after pretreatment with low-cost ionic liquids. *Green Chem.* 19, 692–703. doi: 10.1039/C8GC02155D

Gschwend, F. J. V., Malaret, F., Shinde, S., Brandt-Talbot, A., and Hallett, J. P. (2018). Rapid pretreatment of Miscanthus using the low-cost ionic liquid triethylammonium hydrogen sulfate at elevated temperatures. *Green Chem.* 20, 3486–3498. doi: 10.1039/C8GC00837J

Hoover, A. N., Tumuluru, J. S., Teymouri, F., Moore, J., and Gresham, G. (2014). Effect of pelleting process variables on physical properties and sugar yields of ammonia fiber expansion pretreated corn stover. *Bioresour. Technol.* 164, 128–135. doi: 10.1016/j.biortech.2014.02.005

Huang, C., Lai, C., Wu, X., Huang, Y., He, J., Huang, C., et al. (2017). An integrated process to produce bio-ethanol and xylooligosaccharides rich in xylobiose and xylotriose from high ash content waste wheat straw. *Bioresour. Technol.* 241, 228–235. doi: 10.1016/j.biortech.2017.05.109

IEA Bioenergy (2015). *Inter-Task Project Synthesis Report: Mobilizing Sustainable Bioenergy Supply Chains. Agricultural Residues for Bioenergy and Biorefineries.*

IRRI (2018). *Rice Knowledge Bank*. Available online at: http://www.knowledgebank.irri.org/ (accessed July 30, 2018).

Kim, S., and Dale, B. E. (2004). Global potential bioethanol production from wasted crops and crop residues. *Biomass Bioenergy* 26, 361–375. doi: 10.1016/j.biombioe.2003.08.002

Li, B., Asikkala, J., Filpponen, I., and Argyropoulos, D. S. (2010). Factors affecting wood dissolution and regeneration of ionic liquids. *Ind. Eng. Chem. Res.* 49, 2477–2484. doi: 10.1021/ie901560p

Li, Y., and Khanal, S. K. (2017). *Status and Potential for the Development of Biofuels and Rural Renewable Energy*. Hoboken, NJ: John Wiley and Sons.

Luo, X. L., Zhu, J. Y., Gleisner, R., and Zhan, H. Y. (2011). Effects of drying-induced fiber hornification on enzymatic saccharification of lignocelluloses. *Cellulose* 18, 1055–1062. doi: 10.1007/s10570-011-9541-z

Mani, S., Tabil, L. G., and Sokhansanj, S. (2004). Grinding performance and physical properties of wheat and barley straws, corn stover and switchgrass. *Biomass Bioenergy* 27, 339–352. doi: 10.1016/j.biombioe.2004.03.007

Mehta, P. K., and Pitt, N. (1976). Energy and industrial materials from crop residues. *Resour. Recover. Conserv.* 2, 23–38. doi: 10.1016/0304-3967(76)90015-9

Miles, T. R., Baxter, L. L., and Bryers, R. W. (1996). Boiler deposits from firing biomass fuels. *Biomass Bioenergy* 10, 125–138. doi: 10.1016/0961-9534(95)00067-4

nee' Nigam, P. S., Gupta, N., and Anthwal, A. (2009). "Chapter 2. Pretreatment of agro-industrial residues," in *Biotechnology for Agro-Industrial Residues Utilisation*, ed A. P. P. Singh nee' Nigam (Dordrecht: Springer Science+Business Media B.V.), 13–29.

Parikh, J., Channiwala, S. A., and Ghosal, G. K. (2005). A correlation for calculating HHV from proximate analysis of solid fuels. *Fuel* 84, 487–494. doi: 10.1016/j.fuel.2004.10.010

Poornejad, N., Karimi, K., and Behzad, T. (2014). Ionic liquid pretreatment of rice straw to enhance saccharification and bioethanol production. *J. Biomass Biofuel* 1, 8–15. doi: 10.11159/jbb.2014.002

Pu, Y., Hu, F., Huang, F., Davison, B. H., and Ragauskas, A. J. (2013). Assessing the molecular structure basis for biomass recalcitrance during dilute acid and hydrothermal pretreatments. *Biotechnol. Biofuels* 6:1. doi: 10.1186/1754-6834-6-15

Ragauskas, A. J., Beckham, G. T., Biddy, M. J., Chandra, R., Chen, F., Davis, M. F., et al. (2014). Lignin valorization: improving lignin processing in the biorefinery. *Science* 344:1246843. doi: 10.1126/science.1246843

Real, C., Alcala, M. D., and Criado, J. M. (1996). Preparation of silica from rice husks. *J. Am. Ceram. Soc.* 79, 2012–2016. doi: 10.1111/j.1151-2916.1996.tb08931.x

Reddy, N., and Yang, Y. (2005). Biofibers from agricultural byproducts for industrial applications. *Trends Biotechnol.* 23, 22–27. doi: 10.1016/j.tibtech.2004.11.002

Resch, M. G., Baker, J. O., and Decker, S. R. (2015). *Low Solids Enzymatic Saccharification of Lignocellulosic Biomass: Laboratory Analytical Procedure (LAP)*. Golden, CO: National Renewable Energy Laboratory, NREL/TP, 5100–63351.

Saha, B. C., Iten, L. B., Cotta, M. A., and Wu, Y. V. (2005). Dilute acid pretreatment, enzymatic saccharification, and fermentation of rice hulls to ethanol. *Biotechnol. Prog.* 21, 816–822. doi: 10.1021/bp049564n

Sánchez, O. J., and Cardona, C. A. (2008). Trends in biotechnological production of fuel ethanol from different feedstocks. *Bioresour. Technol.* 99, 5270–5295. doi: 10.1016/j.biortech.2007.11.013

Satlewal, A., Agarwal, R., Bhagia, S., Das, P., and Ragauskas, A. J. (2018). Rice straw as a feedstock for biofuels: availability, recalcitrance and chemical properties. *Biofuels Bioprod. Biorefining* 12, 83–107. doi: 10.1002/bbb.1818

Scarlat, N., Martinov, M., and Dallemand, J. F. (2010). Assessment of the availability of agricultural crop residues in the European Union: potential and limitations for bioenergy use. *Waste Manag.* 30, 1889–1897. doi: 10.1016/j.wasman.2010.04.016

Shih, S. I., Lee, W. J., Lin, L. F., Huang, J. Y., Su, J. W., and Chang-Chien, G. P. (2008). Significance of biomass open burning on the levels of polychlorinated dibenzo-p-dioxins and dibenzofurans in the ambient air. *J. Hazard. Mater.* 153, 276–284. doi: 10.1016/j.jhazmat.2007.08.048

Singh, A., Tuteja, S., Singh, N., and Bishnoi, N. R. (2011). Enhanced saccharification of rice straw and hull by microwave-alkali pretreatment and lignocellulolytic enzyme production. *Bioresour. Technol.* 102, 1773–1782. doi: 10.1016/j.biortech.2010.08.113

Singh, S. K., and Dhepe, P. L. (2016). Isolation of lignin by organosolv process from different varieties of rice husk: understanding their physical and chemical properties. *Bioresour. Technol.* 221, 310–317. doi: 10.1016/j.biortech.2016.09.042

Sluiter, A., Hames, B., Ruiz, R., Scarlata, C., Sluiter, J., Templeton, D., et al. (2008). *Determination of Structural Carbohydrates and Lignin in Biomass: Laboratory Analytical Procedure (LAP)*. NREL/TP-510-42618.

Sun, Y., and Cheng, J. (2002). Hydrolysis of lignocellulosic materials for ethanol production: a review. *Bioresour. Technol.* 83, 1–11. doi: 10.1016/S0960-8524(01)00212-7

Swatloski, R. P., Spear, S. K., Holbrey, J. D., and Rogers, R. D. (2002). Dissolution of cellose with ionic liquids. *J. Am. Chem. Soc.* 124, 4974–4975. doi: 10.1021/ja025790m

Weigand, L., Mostame, S., Brandt-Talbot, A., Welton, T., Hallett, J. P., Brandt, A., et al. (2017). Effect of pretreatment severity on the cellulose and lignin isolated from Salix using ionoSolv pretreatment. *Faraday Discuss.* 202, 331–349. doi: 10.1039/C7FD00059F

Wu, S., and Argyropoulos, D. (2003). An improved method for isolating lignin in high yield and purity. *J. Pulp Pap. Sci.* 29, 235–240. Available online at: https://repository.lib.ncsu.edu/bitstream/handle/1840.2/292/JPPS_29(7)_235_2003.pdf?sequence=1

Yoon, L. W., Ngoh, G. C., Seak, A., Chua, M., and Hashim, M. A. (2011). Comparison of ionic liquid, acid and alkali pretreatments for sugarcane bagasse enzymatic saccharification. *J. Chem. Technol. Biotechnol.* 86, 1342–1348. doi: 10.1002/jctb.2651

Zafar, S. (2018). *Rice Straw as Bioenergy Resource. BioEnergy Consult*. Available online at: https://www.bioenergyconsult.com/rice-straw-as-bioenergy-resource/ (accessed July 30, 2018).

Zhang, L., and Gellerstedt, G. (2007). Quantitative 2D HSQC NMR determination of polymer structures by selecting suitable internal standard references. *Magn. Reson. Chem.* 45, 473–483. doi: 10.1002/mrc.1914

Zhang, Q., and Cai, W. M. (2008). Enzymatic hydrolysis of alkali-pretreated rice straw by *Trichoderma reesei* ZM4-F3. *Biomass Bioenergy* 32, 1130–1135. doi: 10.1016/j.biombioe.2008.02.006

Zhao, X., Cheng, K., and Liu, D. (2009). Organosolv pretreatment of lignocellulosic biomass for enzymatic hydrolysis. *Appl. Microbiol. Biotechnol.* 82, 815–827. doi: 10.1007/s00253-009-1883-1

Task-Specific Organic Salts and Ionic Liquids Binary Mixtures: A Combination to Obtain 5-Hydroxymethylfurfural From Carbohydrates

Salvatore Marullo, Carla Rizzo and Francesca D'Anna*

Dipartimento di Scienze e Tecnologie Biologiche, Chimiche e Farmaceutiche, Università degli Studi di Palermo, Palermo, Italy

The increase in energy demand and depletion of fossil fuels are among major issues of modern society. Valorization and transformation of raw materials in products of industrial value represent a challenge. This justifies the growing interest of scientific research toward the identification of suitable media and methodologies able to pursue above goals, paying attention to matter of sustainability. On this subject, we studied sulfonic-acid functionalized diimidazolium salts as catalysts for the conversion of fructose and sucrose to 5-hydroxymethylfurfural (5-HMF) in an ionic liquid mixture. In general, using these salts allowed us to obtain 5-HMF in good yields from both substrates in mild conditions. Indeed, at 60°C and in the presence of 20 mol% of catalyst, 5-HMF yields of 60 and 30% were obtained from fructose and sucrose, respectively. The catalytic system was recycled and used up to six times observing no appreciable loss in yield for the first four cycles. Moreover, we gathered mechanistic information by *in situ* ^{1}H NMR monitoring the dehydration of fructose. To dissect the role of acidity on the reaction, we determined the Hammett acidity function of each salt. Comparison of these results with yields and reactivity observed in the presence of related monocationic salts and with a dicationic salt bearing only one sulfonic acid group, allowed stating that the reactivity observed is the result of the combined action of acidity and structural features of the catalysts. Overall, the approach proposed here could contribute to pave the way to increase sustainability in the raw material valorization processes.

Keywords: ionic liquids, carbohydrate conversion, 5-hydroxymethylfurfural, sustainable chemistry, task-specific organic salts

INTRODUCTION

The steady increase in energy demand in modern society has led researchers to tackle pressing challenges like global warming and the depletion of petroleum feedstocks together with the urgent need to reduce the generation of waste from industrial processes. As a result, the replacement of fossil fuels and energy sources with renewable alternatives features prominently in present-day chemical research. In this respect, the chemical conversion of vegetable biomasses in value-added chemicals represents a viable route to pursue these goals (Zhou et al., 2011; Brun et al., 2017; Den et al., 2018). Indeed, vegetable biomass is a naturally abundant, readily available resource

posing no environmental risk. Deriving from agricultural waste, vegetable biomass also provides a renewable resource at a negligible cost (Pierre, 2008). Accordingly, efficient conversion of biomass gives access to a wide range of chemical platforms, i.e., key intermediates for the synthesis of industrially relevant products. These include ethanol, succinic and 3-hydroxypropionic acids, levulinic acid, isoprene and so on (Chinnappan et al., 2016; Mika et al., 2018). In this context, 5-hydroxymethylfurfural (5-HMF) and its derivatives are among the most important chemical platforms obtained from the conversion of the carbohydrate rich fraction of biomasses (Rout et al., 2016). 5-HMF is a key intermediate to the production of solvents, biofuels and polymers (Zhang and Dumont, 2017) and is in principle easily obtained from the acid-catalyzed dehydration of fructose. However, obtaining 5-HMF from biomass is a more challenging task because the carbohydrate-based fraction of biomass is overwhelmingly richer in glucose-based materials. Hence, an intermediate step of isomerization of the glucose obtained by the breakdown of the biomass into fructose is required. The conventional methods for the production of 5-HMF require harsh reaction conditions with high temperatures and strong mineral acids like H_2SO_4 or metal based Lewis acids like $CrCl_3$ (Chheda et al., 2007).

Frequently, the use of harsh reaction conditions combined with corrosive or metal based catalysts is associated to the occurrence of undesired side reactions, entailing further problems when the greenness of the process is evaluated. The growing concerns for sustainability of chemical processes, embodied by the principles of Green Chemistry (Anastas and Eghbali, 2010) have led researchers to explore milder reaction conditions, shifting to safer and less environmentally impacting heterogeneous catalysts (De et al., 2016) such as zeolites (Taarning et al., 2011; Perego et al., 2017) and ionic exchange resins (Ramírez et al., 2017). Furthermore, applying analogous criteria to the selection of solvents has evidenced that non-conventional media such deep eutectic solvents (Vigier et al., 2015; Zuo et al., 2017) and ionic liquids (ILs) (Tim et al., 2011; Yoo et al., 2017; Zhang et al., 2017; Mika et al., 2018) can be suitable to carry out this process. ILs are organic salts with a low melting point (< 100°C) and often liquid at room temperature (Plechkova and Seddon, 2008; Hallett and Welton, 2011). They provide unique fully ionic reaction media with a distinct nanostructure (Dupont, 2011; Hayes et al., 2015). Regarding the topic of biomass conversion, some ILs stand out for their remarkable ability of solubilizing cellulose, the fraction of biomass richest in carbohydrates, by disrupting intra- and intermolecular hydrogen bonds (Sun et al., 2011).

Along these premises, in the framework of our interest in studying ILs properties and applications, (D'Anna et al., 2009b,c, 2011, 2013). We investigated the conversion of carbohydrates into 5-HMF, using IL binary mixtures as solvent system and the acidic ion exchange resin Amberlyst 15 as catalyst (D'Anna et al., 2014). We tested different IL binary mixtures, finding the 1-butyl-3-methylimidazolium chloride/tetrafluoroborate ([bmim][Cl]/[bmim][BF4]) mixture as the best solvent system for both mono (fructose and glucose) and disaccharides (sucrose) dehydration, under silent conditions

as well as ultrasound irradiation. In particular, we demonstrated that yield in 5-HMF changed as a function of binary mixture composition, with the best results obtained at $X_{Cl} \approx 0.5$. In the light of the above results, with the aim to use more active catalysts under milder conditions, we herein report on fructose and sucrose dehydration in the same IL mixture, testing the catalytic efficiency of acid-functionalized diimidazolium salts.

Endowing imidazolium or other ILs with catalytic moieties gives rise to the so-called Task Specific Ionic Liquids (TSILs) (Giernoth, 2010; Yue et al., 2011). A wide range of functionalities can be easily incorporated in ILs, (Chiappe and Pomelli, 2014) and in this context, we have successfully applied this approach for the obtainment of TSILs able to promote different reactions from the synthesis of aryl azides (D'Anna et al., 2008) to Michael addition (Rizzo et al., 2016a) and heterocyclic rearrangements (Rizzo et al., 2014). In particular, using acid-functionalized TSILs for the conversion of biomass can be a viable route to obtain value added chemicals under mild homogeneous conditions.

Functionalization of ILs with sulfonic acid groups is a widely used approach to enhance their acidity (Amarasekara, 2016; Chiappe et al., 2017) and promote the conversion of carbohydrates avoiding metal-based catalysts and mineral acids. However, to date the vast majority of the reports feature monocationic ILs, while the use of dicationic ILs has been less explored (Jadhav et al., 2012, 2014; Liu et al., 2015; Yaman et al., 2017). To the best of our knowledge only one report deals with supported sulfonic acid functionalized dicationic ILs as catalyst for the conversion of carbohydrates (Liu et al., 2015).

Dicationic ILs make for environmentally benign catalysts with high thermal stability (Fang et al., 2011). Moreover, dicationic ILs are generally less miscible with conventional organic solvents than corresponding monocationic ones (D'Anna and Noto, 2014). This could enable easier recycling of the solvent/catalyst system improving the whole eco-compatibility of studied processes.

Bearing this in mind, we herein report the use of some sulfonic acid-functionalized diimidazolium salts bearing 1,2- 1,3- and 1,4-xylilene spacers interposed between the charged heads (**Figure 1**) as catalysts for the conversion of fructose and sucrose into 5-HMF.

We tested all the isomers to evaluate how the different distance between charged heads, that could affect cation conformation, (D'Anna et al., 2009a, 2013) acts on the catalytic efficiency of our salts. Data collected in the presence of diimidazolium salts were compared with the ones obtained using 1-butyl-3-sulfobutyl-imidazolium chloride ([**b₂imS**][**Cl**], **Figure 1**) to verify whether the catalytic activity of dicationic salts derives simply from the combination of two acidic sites.

Moreover, to gain information on the effect exerted by the presence of a charged head devoid of sulfonic acid functionality, we also tested the salt 1-[1′-methylene-3′-butylimidazolium]-4-[1′-methylene-3′-sulfobutylimidazolium]benzene dichloride ([**p-Xyl-(bim)(bimS)**][**Cl**]₂, **Figure 1**). All reactions were carried out at 60°C (**Figure 2**).

To find the best reaction conditions, we analyzed the effect of operating parameters such as the amount of catalyst and reaction time. Finally, we determined the acid strength of the catalyst
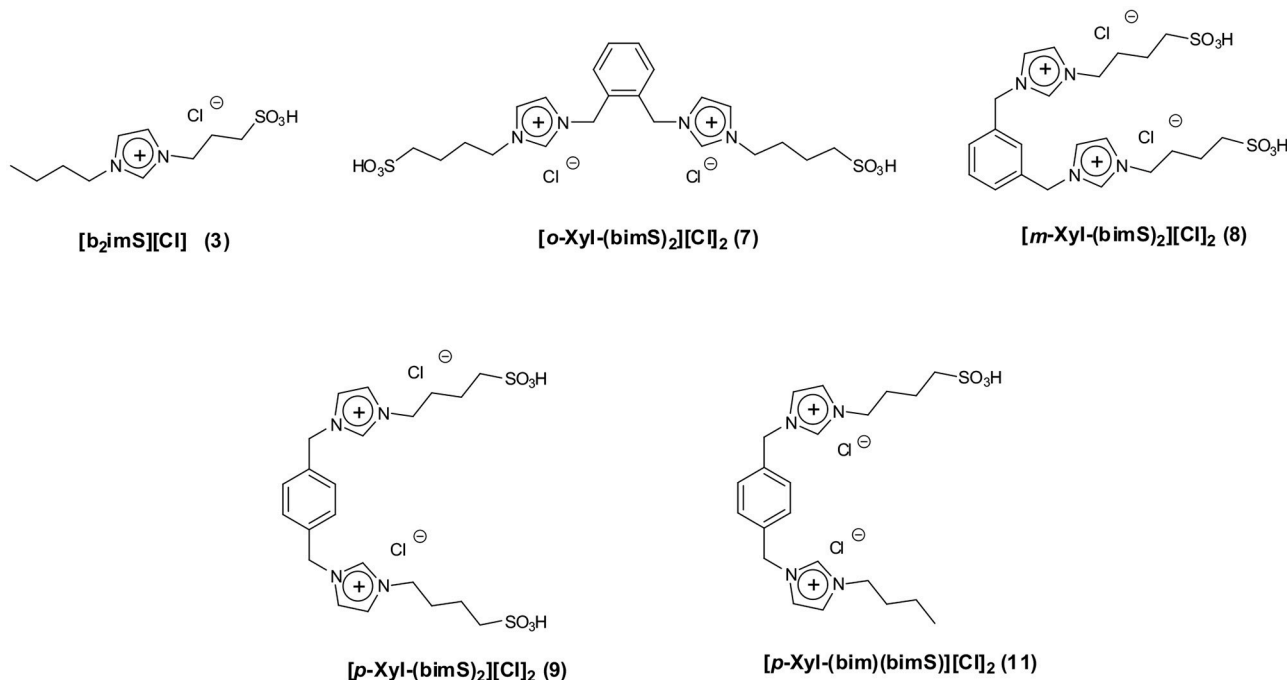
FIGURE 1 | Structures of sulfonic acid-functionalized mono- and dicationic imidazolium salts.

by means of the Hammett acidity function H_0 (Hammett and Deyrup, 1932) to dissect its role on the reaction outcome.

The results collected in this paper highlight the suitability of ILs binary mixtures to promote carbohydrate conversion into 5-HMF. Furthermore, they shed light on the good performance of acidic sulfonate TSILs whose action results from the balance of different factors besides acidity. The IL-based catalytic system could be recycled up to six times and mechanistic information were gathered by *in situ* ^{1}H-NMR monitoring the reaction.

MATERIALS AND METHODS

Materials

Commercially available 1-butylimidazole, 1-chlorobutane, 1,4-butanesultone, acetonitrile, fructose, and sucrose were used without further purification. ILs, 1-butyl-3-methylimidazolium tetrafluoroborate [bmim][BF₄] and 1-butyl-3-methylimidazolium chloride [bmim][Cl] obtained from commercial sources, were dried at 70°C in a vacuum line for 2 h. Then, they were lyophilized for 48 h at 0.06 mbar, and stored in a desiccator under argon and over calcium chloride prior each use. 1,2-, 1,3- and 1,4-bis(imidazolemethyl)benzene were prepared following reported procedures (D'Anna et al., 2012; Rizzo et al., 2016b).

The NMR spectra were recorded by using Bruker 300 or 250 MHz. ESI-MS spectra were recorded on a Q-TOF spectrometer in the positive ionization mode. Samples were prepared by dissolving suitable amounts of salts in methanol.

1,2-bis(Imidazolemethyl)Benzene (4)

1,2-bis(imidazolemethyl)benzene (**4**) was prepared according to a published procedure (D'Anna et al., 2013).

Imidazole (3.0 g, 0.045 mol) and potassium hydroxide (4.9 g, 0.09 mol) were dissolved in acetonitrile (300 mL) and stirred for 2 h at room temperature. Then, α,α'-o-dibromoxylene (5.9 g, 0.022 mol) was added to the mixture. The reaction mixture was stirred at room temperature for 1.5 h. The mixture was filtered through a Hirsch funnel to remove insoluble salts and the filtrate was concentrated in vacuo at 40°C. The residue was dissolved in CHCl₃ (1 L) and washed with water (4 × 150 mL) until the aqueous layer was neutral to p*H* paper. The organic layer was dried over anhydrous Na₂SO₄ and removal of the solvent afforded a pale yellow solid (2.4 g, 44%).

Synthesis of the Sulfonic Acid Functionalized Imidazolium Salts

1-Butyl-3-Sulfobutyl Imidazolium Chloride [b₂imS][Cl] (3)

To a stirred solution of 1-butylimidazole (**1**) (1g) in acetonitrile, 1.65 mL of 1,4-butanesultone (**2**) were added dropwise and the resulting mixture was stirred at 100°C for 24 h. Removal of the solvent afforded a yellow solid which was washed with several portions of acetone. The resulting solid was filtered off and dissolved in 20 mL of methanol. Then, the stoichiometric amount of HCl (37% w:w in water) was added and the resulting mixture was stirred at room temperature for 1 h. Subsequent removal of the solvent afforded a colorless oil (1.5 g, yield 68%).

FIGURE 2 | Reaction studied and IL mixture used as solvent.
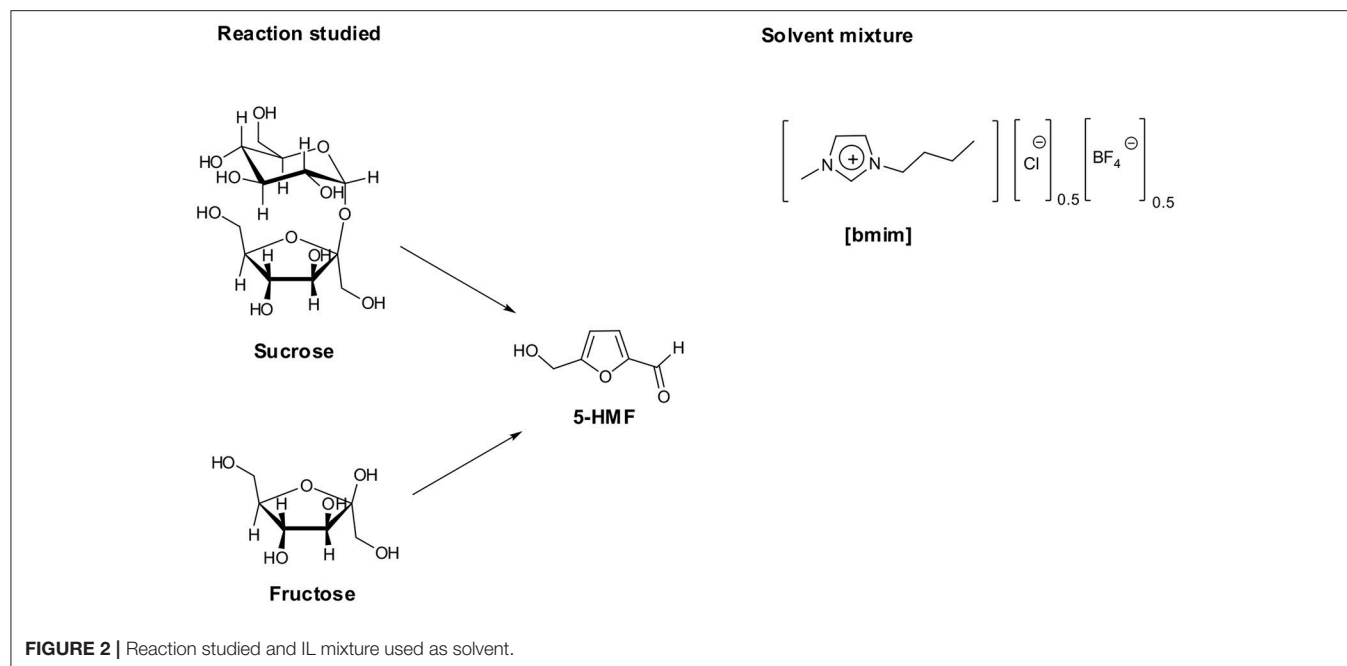
General Procedure for the Synthesis of Symmetrically Substituted Diimidazolium Salts

To a stirred solution of the suitable bis(imidazolemethyl)benzene (1 g, 4.2 mmol) in 30 mL acetonitrile, 1,4-butanesultone (**2**) was added (1.71 g, 12.6 mmol) and the resulting mixture was refluxed under inert atmosphere for 72 h. The reaction mixture was cooled down and acetone was added until complete precipitation of a colorless solid. The resulting solid was filtered, washed with acetone and then dissolved in methanol. To the resulting solution, the stoichiometric amount of HCl (37% w:w in water) was added and the mixture obtained was stirred at room temperature for 1 h. Subsequent removal of the solvent afforded the diimidazolium salts as colorless solids (All ^{1}H and ^{13}C NMR and mass spectra are reported in **Figures S2, S4**).

1,2-Bis-[1′-Methylene-3′-Sulfobutylimidazolium]Benzene Dichloride [o-Xyl-(bimS)₂][Cl]₂ (7)

Yield: 42%. Colorless solid; m. p.: 106°C. ^{1}H NMR (250 MHz, D₂O); δ (ppm): 8.64 (s, 2H, exch); 7.46 (m, 4H); 7.29 (m, 4H); 5.38 (s, 4H); 4.08 (t, J = 7.5 Hz, 4H); 2.78 (t, J = 7.5 Hz, 4H); 1.83 (quin, J = 7.5 Hz, 4H); 1.58 (quin, J = 7.5 Hz, 4H). ^{13}C NMR (250 MHz, D₂O); δ (ppm): 134.2; 133.6; 133.3; 125.5; 125.2; 52.6 (2C, overlapped); 51.9; 30.6; 23.6. *ESI (m/z)*: 511 [C-H]$^+$; 533 [C-2H+Na]$^+$.

1,3-Bis-[1′-Methylene-3′-Sulfobutylimidazolium]Benzene Dichloride [m-Xyl-(bimS)₂][Cl]₂ (8)

Yield: 100%. Colorless solid; m. p.: 74°C. ^{1}H NMR (250 MHz, D₂O); δ (ppm): 8.78 (s, 2H, exch); 7.39 (m, 8H); 5.32 (s, 4H); 4.16 (t, J = 7.5 Hz, 4H); 2.82 (t, J = 7.5 Hz, 4H); 1.95 (quin, J = 7.5 Hz,

4H); 1.61 (quin, J = 7.5 Hz, 4H). ^{13}C NMR (250 MHz, D₂O); δ (ppm): 138.3; 137.5; 133.0; 131.9; 130.8; 125.4; 55.1; 52.7; 51.8; 30.6; 23.6. *ESI (m/z)*: 511 [C-H]$^+$; 533 [C-2H+Na]$^+$.

3,3′-Di-Sulfobutyl-1,1′-(1,4-Phenylenedimethylene)Diimidazolium Dichloride [p-Xyl-(bimS)₂][Cl]₂ (9)

Yield: 100%. Colorless solid; m. p.: 112°C. ^{1} NMR (250 MHz, CD₃OD); δ (ppm): 9.14 (s, 2H); 7.67 (d, J = 9.0 Hz, 4H); 7.50 (s, 4H); 5.45 (s, 4H); 4.28 (t, J = 7.5 Hz, 4H); 2.82 (t, J = 7.5 Hz, 4H); 2.02 (quin, J = 7.5 Hz, 4H); 1.75 (quin, J = 7.5 Hz, 4H). ^{13}C NMR (250 MHz, CD₃OD); δ (ppm): 135.5 (2C, overlapped), 134.6, 129.3, 122.6, 105.4, 52.3, 49.9, 49.6, 28.1, 20.8. *ESI (m/z)*: 511 [C-H]$^+$; 533 [C-2H+Na]$^+$.

1-[1′-Methyleneimidazole]-4-[1′-Methylene-3′-Sulfobutylimidazolium]Benzene Inner Salt (10)

To a stirred solution of 1,4-bis(imidazolemethyl)-benzene (**6**) (1 g, 4.2 mmol) in acetonitrile (60 mL), 1,4-butanesultone (**2**) (0.57 g, 4.2 mmol) was added dropwise. The reacting mixture was kept at 90°C, for 72 h, under stirring. Subsequently, the solvent was removed and the residue was purified by flash chromatography on aluminum oxide eluting with ethyl acetate/methanol/water 2/2/1 mixture, affording 0.72 g of a yellow solid. Then, it was dissolved in 5 mL of methanol and, upon adding acetone, a white precipitate was obtained. The resulting solid was filtered off and further washed with acetone, then dissolved in anhydrous dichloromethane and treated with activated charcoal at room temperature overnight. The mixture was finally filtered through a pad of neutral aluminum oxide and solvent removal afforded 0.69 g of a colorless solid (^{1}H and ^{13}C NMR spectra are reported in **Figure S2**).

Yield: 44%. Colorless solid; m. p.: 105°C; ^{1}H NMR (250 MHz, CD$_3$OD); δ (ppm): 7.75 (s, 1H); 7.66 (d, J = 2.5 Hz, 1H); 7.61 (d, J = 2.5 Hz, 1H); 7.42 (d, J = 8.0 Hz, 2H); 7.32 (d, J = 8.0 Hz, 2H); 7.11 (s, 1H); 6.97 (s, 1H); 5.41 (s, 2H); 5.22 (s, 2H); 4.26 (t, J = 7.5 Hz, 2H); 2.83 (t, J = 7.5 Hz, 2H); 2.01 (quin, J = 7.5 Hz, 2H); 1.76 (quin, J = 7.5 Hz, 2H). ^{13}C NMR (250 MHz, CD$_3$OD); δ (ppm): 142.9; 138.4; 132.8; 132.6; 127.4; 127.1; 124.1; 62.2; 56.9; 54.4; 32.9; 25.9.

1-[1′-Methylene-3′-Butylimidazolium]-4-[1′-Methylene-3′-Sulfobutylimidazolium]Benzene Dichloride [p-Xyl-(bim)(bimS)][Cl]$_2$ (11)

1-chlorobutane (0.5 g, 5.4 mmol) and (**10**) (0.67 g, 1.8 mmol) were dissolved in 20 mL of 2-propanol and the resulting mixture was heated, at 90°C, for 72 h. Subsequently, the solvent was removed and the residue was purified by flash chromatography on aluminum oxide, eluting with ethyl acetate/methanol/water 2/2/1 mixture affording 0.54 g of a pale yellow solid. This latter was dissolved in 5 mL methanol and added with 90 μL of hydrochloric acid (37% w:w in water). Finally, removal of the solvent afforded 0.58 g of a pale yellow solid (^{1}H and ^{13}C NMR, and mass spectra are reported in **Figures S2, S4**).

Yield: 64%. Pale yellow solid; m. p.: 109°C. ^{1}H NMR (250 MHz, CD$_3$OD); δ (ppm): 9.16 (s, 1H, exch); 9.08 (s, 1H, exch); 7.78 (m, 4H); 7.51 (m, 4H); 5.49 (m, 8H); 4.28 (m, 6H); 3.31 (m, 2H); 2.82 (t, J = 7.5 Hz, 4H); 2.04 (quin, J = 7.5 Hz, 4H); 1.89 (quin, J = 7.5 Hz, 2H); 1.73 (quin, J = 7.5 Hz, 4H); 1.38 (sext, J = 7.5 Hz, 2H); 0.98 (t, J = 7.5 Hz, 3H). ^{13}C NMR (250 MHz, CD$_3$OD); δ (ppm): 150.5; 149.4 (2C); 149.3; 143.5; 143.4; 137.1; 136.9; 136.8; 136.3; 134.4; 66.5; 64.3; 63.7; 63.5; 45.9; 42.6; 35.5; 33.3; 26.6. ESI (m/z): 431[C–H]$^+$

General Procedure for Conversion of Carbohydrate in 5-HMF

A suitable amount of carbohydrate (0.025 g) was weighed in a round-bottom flask containing 0.5 g of IL binary mixture [bmim][Cl]$_{0.5}$[BF$_4$]$_{0.5}$. To favor carbohydrate dissolution, the mixture was stirred at 80°C for 30 min under argon. In all cases, the mixtures appeared homogeneous after this treatment.

For reactions carried out in conventional solvents, the substrates were dissolved in the suitable amount of solvent (500 μL) at room temperature.

After equilibration at the reaction temperature, the suitable amount of catalyst was added under argon atmosphere. The mixture was heated, at 60°C, under stirring. To monitor the amount of 5-HMF formed, a small aliquot of reaction mixture was withdrawn and diluted with methanol to reach a 5-HMF concentration ranging from $7 \cdot 10^{-6}$ M up to $7 \cdot 10^{-5}$ M. Hydrolysis of the 5-HMF dimer was carried out by adding 250 μL of ultrapure water and stirring for 20 min at room temperature. The concentration of 5-HMF was determined from UV absorbance recorded at 277 nm on the basis of a calibration curve previously determined. The presence of 5-HMF in the reaction mixture, as single UV absorbing product, was further verified by means of TLC on silica gel by comparison with a standard sample (eluent: ethyl acetate/methanol 5:1, v/v). To determine the amount of unreacted carbohydrates, an aliquot of

the reaction mixture was dissolved in methanol/water 80/20 v:v and injected in a HPLC system equipped with a SUPELCOSIL-C$_{18}$ column, using methanol/water 80/20 as eluting mixture. However, in all chromatograms the peaks of carbohydrates were not distinguishable from those of the ILs component and their amounts could not be determined. Conversely, 5-HMF was eluted after a retention time t_R = 5.0 min. Yields in 5-HMF determined by HPLC were in agreement with those measured by UV-vis spectroscopy within ± 3%.

Recycle of the IL

The reaction mixture was extracted under vigorous stirring with diethyl ether (4 × 20 mL), then the residual extraction solvent was removed by evaporation under reduced pressure at 70°C for 3 h. The resulting IL was then charged with fresh fructose and the reaction was carried out as described above. The amount of 5-HMF extracted was determined spectrophotometrically as described above.

In situ ^{1}H NMR Analysis

^{1}H NMR spectra were recorded on a 300 MHz spectrometer at 60°C. Samples were prepared by mixing in a NMR tube, a solution containing 25 mg of fructose with a solution containing the suitable amount of [**o-Xyl-(bimS)$_2$**][Cl]$_2$, both in the IL binary mixture [bmim][Cl]$_{0.5}$[BF$_4$]$_{0.5}$. The sample was rapidly transferred into the chamber of the spectrometer and spectra recorded at selected times. A coaxial capillary tube loaded with d$_6$-DMSO was used for the external lock of the NMR magnetic field/frequency, and its signal at δ =2.56 ppm was used as the ^{1}H NMR external reference.

Determination of the Acid Strength of the Salts (Hammett and Deyrup, 1932; Thomazeau et al., 2003)

The suitable amount of acidic imidazolium salt was added to a methanol solution of methyl orange ($2 \cdot 10^{-4}$ M). Upon adding the salts a color change in the solution was observed. The resulting solution was analyzed by UV-vis spectroscopy. The concentration of salts in the sample was $2 \cdot 10^{-3}$ M for the salts (**3**) and (**11**) and $1 \cdot 10^{-3}$ M for all the other salts. Acid strength was expressed by the H_0 acidity function defined by Equation (1):

$$H_0 = pK_I + log([I]/[HI^+]) \qquad (1)$$

where pK_I is the logarithm of the dissociation constant of the indicator used, [I] and [HI$^+$] are the concentration of the indicator and its conjugated acid, respectively. The [I]/[HI$^+$] ratio was determined spectrophotometrically after the evaluation of the ε value of the indicator.

RESULTS AND DISCUSSION

Synthesis of the Acidic Imidazolium Salts

All the salts considered in this work were prepared by modifications of a previously reported procedure (Ullah et al., 2016). The synthetic procedures followed are reported in **Figure 3**. In particular, the monocationic salt [**b$_2$imS**][**Cl**] (**3**) was

prepared by reacting 1-butylimidazole (**1**) with a stoichiometric amount of 1,4-butanesultone (**2**) followed by protonation with HCl. The symmetrically substituted salts [**o-Xyl-(bimS)₂**][**Cl**]₂, [**m-Xyl-(bimS)₂**][**Cl**]₂ and [**p-Xyl-(bimS)₂**][**Cl**]₂ (**7-9**) were prepared by following a two-step synthetic scheme. In the first step, the neutral diimidazole precursor (**4-6**) was reacted with excess of 1,4-butanesultone (**2**) to obtain the relevant sulfonate appended diimidazolium zwitterion, which in turn was treated with the stoichiometric amount of hydrochloric acid to yield the relevant sulfonic acid functionalized diimidazolium salt. The non-symmetrically substituted salt [**p-Xyl-(bim)(bimS)**][**Cl**]₂ (**11**) was prepared through a three-step synthesis. In the first step 1,4-bis-(imidazolemethyl)-benzene (**6**) was reacted with a stoichiometric amount of 1,4-butanesultone (**2**) to afford the relevant sulfonate imidazolium zwitterion (**10**).

In a subsequent step, **10** was further alkylated with chlorobutane. Finally, protonation with hydrochloric acid afforded the diimidazolium salt bearing one sulfonic acid functionality. Full synthetic details are reported in the experimental section.

Conversion of Carbohydrates in 5-HMF: Optimization of Reaction Conditions

Firstly, we searched for the possible catalytic activity of the IL binary mixture, performing both in the case of fructose and sucrose, the conversion in the absence of catalyst at 60°C. In both cases, we did not detect the formation of 5-HMF. Similar results were obtained using ethanol and DMSO as solvents. They were used to have a comparison with conventional organic solvents and chosen on the grounds of the eco-compatibility of the first one and the wide use of the latter in such kind of reactions.

Subsequently, we set out the optimal amount of catalyst by performing the conversion of sucrose and fructose at 60 °C in the presence of increasing amounts of [**b₂imS**][**Cl**], ranging from 5 to 50 mol% with respect to the substrate. Yields in 5-HMF were determined spectrophotometrically (see experimental section for details). Plots of yields in 5-HMF as a function of the amount of [**b₂imS**][**Cl**] are reported in **Figure 4**, while yield values are reported in **Table S1**.

In both cases, the suitable reaction time was chosen on the grounds of a kinetic investigation performed using 20 mol % of catalysts (see later).

Examination of the plots reported in **Figure 4** (blue trace) revealed that the yield in 5-HMF increased with the amount of catalyst until reaching a maximum value at 20 mol % of catalyst. Further increasing the amount of [**b₂imS**][**Cl**] led to a steady reduction in yields. Monitoring the reactions by TLC, we observed that the formation of 5-HMF was accompanied by the formation of a less polar by-product. Moreover, the formation of the by-product increased using higher amounts of [**b₂imS**][**Cl**].

We explained this finding by considering that under acidic conditions, 5-HMF can undergo dimerization forming 5,5′(oxy-bis(methylene))bis-2-furfural (Che et al., 2012; Galkin et al., 2016). Accordingly, the dimer can be converted back to 5-HMF simply by hydrolysis (Lewkowski, 2001). For this reason, we determined the yield in 5-HMF in both cases also after

performing hydrolysis by adding 250 µL of water and stirring for 20 min prior to the spectroscopic determination. As can be seen from the plots, (red trace) hydrolysis of the dimer afforded back 5-HMF. Moreover, an amount of catalyst of 20 mol % was sufficient to obtain good yields in 5-HMF in both cases. Similar conclusions can be drawn by examining the results of analogous experiments in the presence of the other catalysts. The relevant plots are reported in **Figure S1** and **Tables S2, S3**.

It is important to point out that the *p*-substituted salts, [**p-Xyl-(bimS)₂**][**Cl**]₂ and [**p-Xyl-(bim)(bimS)**][**Cl**]₂, were not soluble in the reaction mixture under the experimental conditions used, and acted as heterogeneous catalysts. In general, yields increased by raising the amount of catalyst until reaching a limiting value. However, in all cases a catalyst loading of 20 mol % represented a good compromise between yields and concentration of acidic imidazolium salts. Accordingly, we carried out all reactions using this amount of catalyst. It could be quite surprising the fact that, both in the case of mono- and dicationic salts, the same amount of catalyst gave rise to the best performance. However, in our opinion, this could be ascribed to the action of factors different from reaction media acidity that operate on the studied process (see later).

From now on, for the sake of clarity, we will deal with the conversion of fructose and sucrose separately.

Conversion of Fructose in 5-HMF

To gain information on the suitable reaction time, we carried out kinetic experiments monitoring the yield in 5-HMF as a function of time. It is worth noting that we did not perform kinetic investigations in the case of *p*-isomers as a consequence of their low solubility in the solvent mixture. Plots of yields in 5-HMF obtained from fructose as a function of time are reported in **Figure 5**, while yield values are reported in **Table S4**.

In general, the trends of yields as a function of time describe a curve, reaching a maximum yield at a given time and declining at longer reaction times. This drop in yield results from acid-catalyzed degradation processes of 5-HMF into humins or levulinic acid (Girisuta et al., 2006). Moreover, a closer inspection of the plots reported in **Figure 5** reveals that the maximum yield in 5-HMF is the same, 60%, irrespective of the catalyst used. Conversely, the nature of the catalyst affects the rate of the process. Indeed, the time needed to reach the best yield increases along the order: [**m-Xyl-(bimS)₂**][**Cl**]₂ < [**b₂imS**][**Cl**] < [**o-Xyl-(bimS)₂**][**Cl**]₂ (t_{max} = 90, 105, 150 min for [**m-Xyl-(bimS)₂**][**Cl**]₂, [**b₂imS**][**Cl**] and [**o-Xyl-(bimS)₂**][**Cl**]₂, respectively).

Anyway, to obtain a more meaningful comparison between homogeneous and heterogeneous catalysts, we chose to compare yields in 5-HMF obtained at the same time, 60 min, for all salts. For the sake of comparison, we performed the reactions also in ethanol and DMSO solution, using the [**o-Xyl-(bimS)₂**][**Cl**]₂ as catalyst, on the grounds of its good performance in the IL binary mixture. The results obtained in the IL binary mixture are reported in **Figure 6**.

The plot reported in **Figure 6** reveals that the *p*-substituted salts [**p-Xyl-(bimS)₂**][**Cl**]₂ and [**p-Xyl-(bim)(bimS)**][**Cl**]₂ are less efficient in enhancing the rate of the process compared
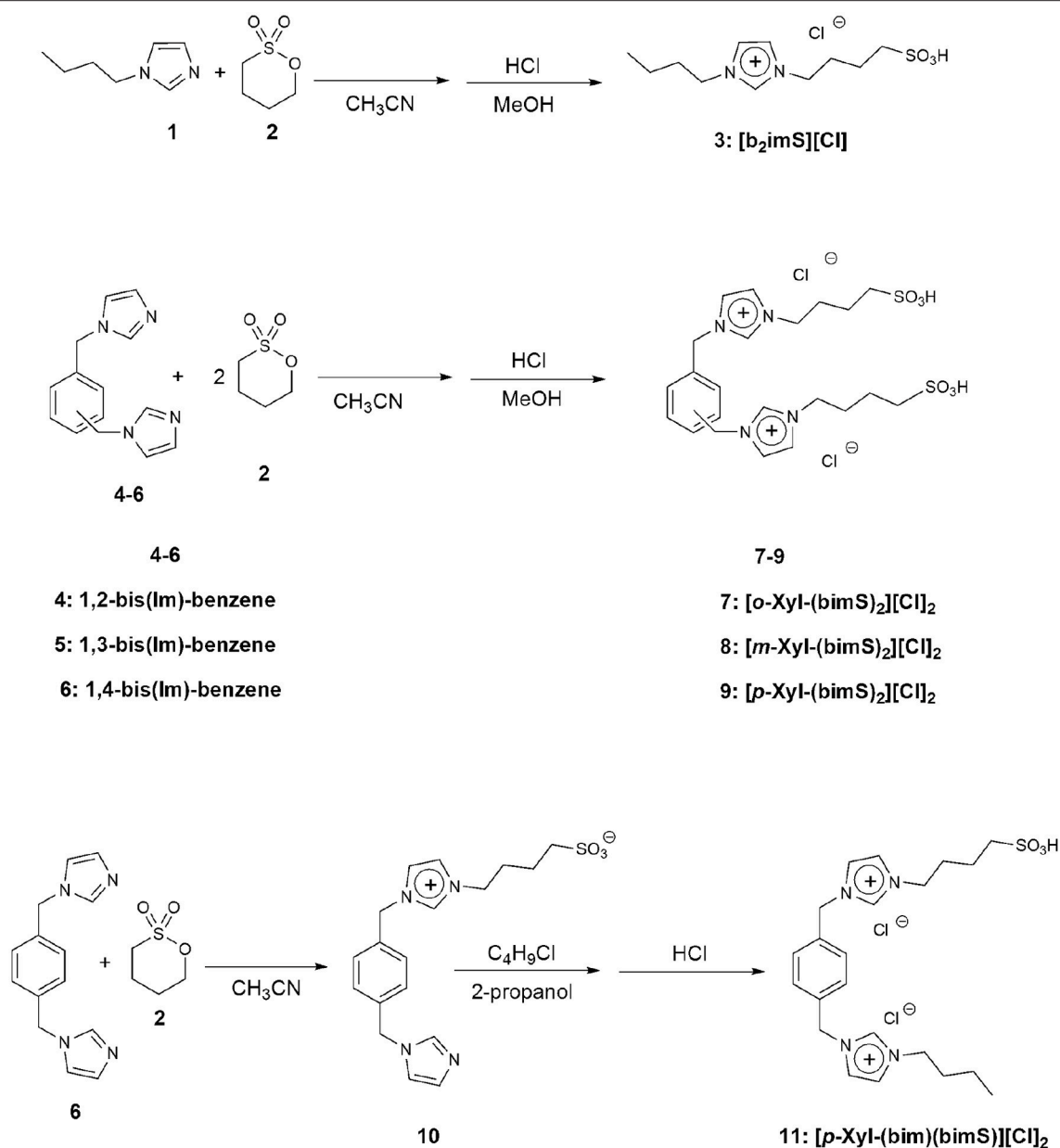
FIGURE 3 | Synthetic steps for the sulfonic acid functionalized imidazolium salts employed.

with the other salts. Indeed, for dicationic salts, yields decrease along the following order: $[o\text{-}Xyl\text{-}(bimS)_2][Cl]_2 \approx [m\text{-}Xyl\text{-}(bimS)_2][Cl]_2 > [p\text{-}Xyl\text{-}(bimS)_2][Cl]_2 \approx [p\text{-}Xyl\text{-}(bim)(bimS)][Cl]_2$. The above result could be easily explained by considering that, in the presence of p-isomers, the reaction takes place in a heterogeneous system. Furthermore, the different symmetry or the different acidity (see later) of the $[p\text{-}Xyl\text{-}(bim)(bimS)]^{2+}$ and $[p\text{-}Xyl\text{-}(bimS)_2]^{2+}$ cations does not appear to significantly affect the yield. Finally, considering the homogeneous catalysts, the dicationic salts give comparable yields with respect to monocationic one, suggesting that catalytic

efficiency cannot be directly ascribed to the presence of two acidic functionalities.

As far as the comparison with conventional organic solvents is concerned, in DMSO solution we obtained a lower yield with respect to the IL binary mixture (39 and 49 % in DMSO and IL binary mixture, respectively). Conversely, in ethanol, we did not detect 5-HMF formation, probably as a consequence of the very low solubility of the catalyst in this solvent.

Given that the best result were obtained in the presence of $[o\text{-}Xyl\text{-}(bimS)_2][Cl]_2$, we tested the recyclability of the IL-based catalytic system. To this aim, we tested different extracting
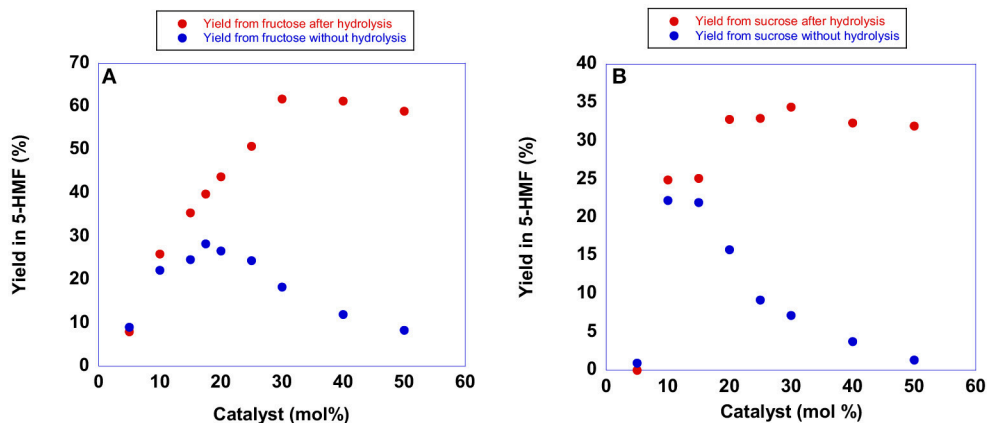
FIGURE 4 | Plots of yields in 5-HMF from **(A)** fructose obtained at 60°C after 105 min and **(B)** sucrose obtained at 60°C after 150 min in the presence of increasing amounts of **[b₂imS][Cl]**.
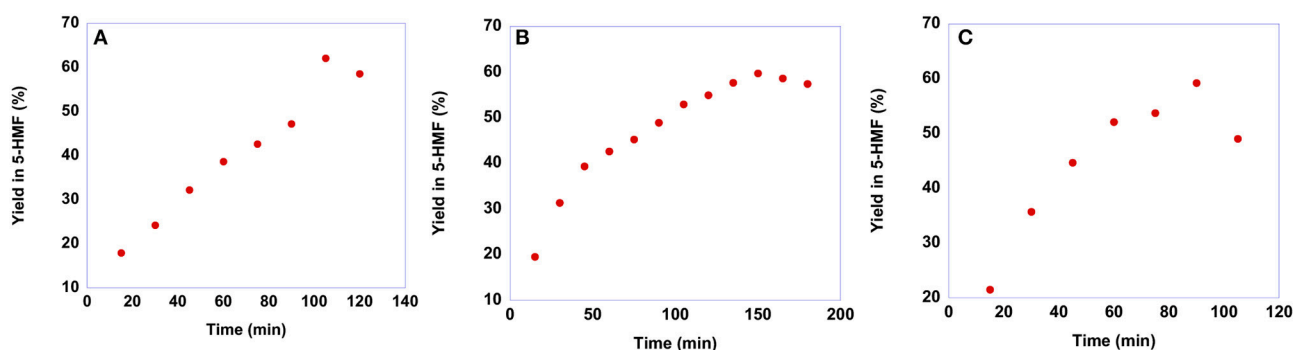
FIGURE 5 | Plots of yields in 5-HMF obtained at 60 °C from fructose in the presence 20 mol % of **(A) [b₂imS][Cl], (B) [o-Xyl-(bimS)₂][Cl]₂** and **(C) [m-Xyl-(bimS)₂][Cl]₂** as a function of time.
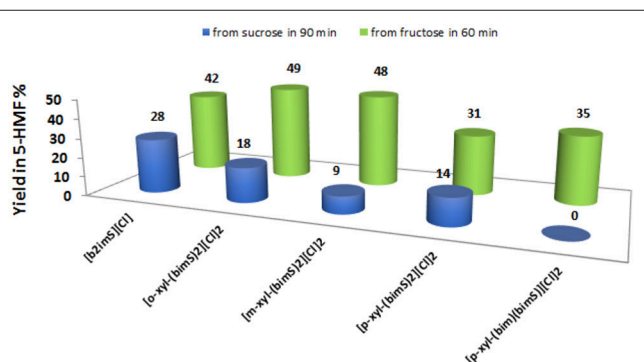
FIGURE 6 | Yields in 5-HMF from fructose (after 60 min) and from sucrose (after 90 min) at 60°C, at 20 mol % of catalyst and in the IL binary mixture.
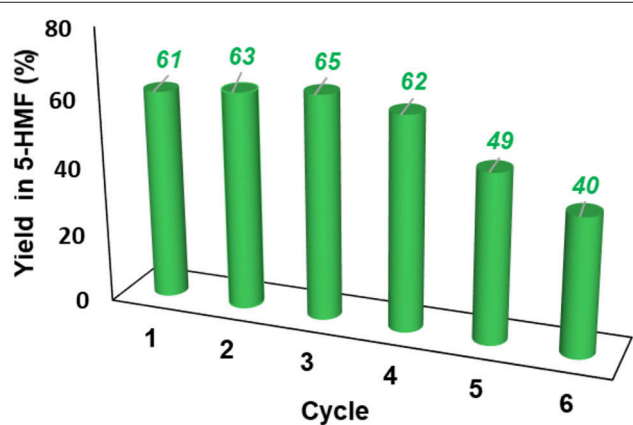
FIGURE 7 | Yield in 5-HMF obtained at 60°C from fructose in the presence 20 mol % of **[o-Xyl-(bimS)₂][Cl]₂** upon recycling of the catalytic system.

solvents and found that 5-HMF could be extracted using diethyl ether (4 × 20 mL). This amount of solvent is in line with what previously reported in the literature (Moreau et al., 2006) due to the known resistance of 5-HMF to be extracted from imidazolium-based ILs (Xiao and Huang, 2018). Using other solvents, like ethyl acetate, toluene, dimethyl carbonate or 2-methylpentanone resulted in insufficient recovery
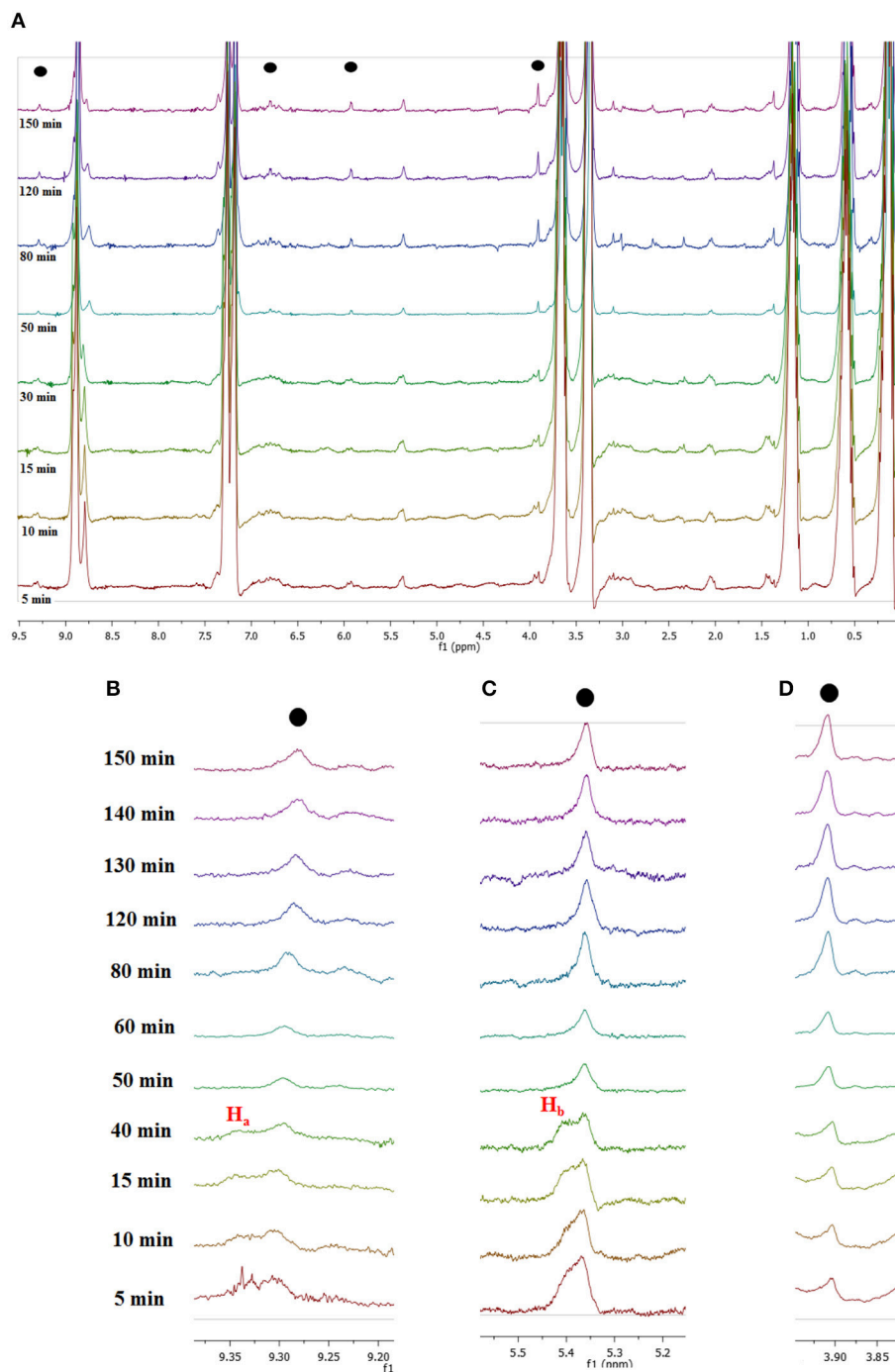
FIGURE 8 | (A) ^{1}H NMR spectra recorded for *in situ* conversion of fructose into 5-HMF at selected times and local enlargements of the chemical shifts region of **(B)** 9.20–9.40 ppm, **(C)** 5.20–5.50 ppm, and **(D)** 3.80–3.95 ppm.

of 5-HMF or loss of IL in the organic phase. Finally, adding water in the reaction mixture prior to extraction had a detrimental effect on the yield in the subsequent cycle, which plummeted to 20%.

Using only diethyl ether, allowed us to extract 5-HMF in the organic phase while leaving intact the catalyst in the IL phase.

The resulting IL mixture was then added with a fresh batch of fructose and the reaction was carried out as already described. The results obtained are summarized in **Figure 7**.

Results reported in **Figure 7** show that the IL mixture could be reused for 4 cycles without appreciable loss in yield. Even if further recycling led to a regular decrease in yield, the catalytic

system could be still reused for two additional cycles obtaining good yields.

To obtain mechanistic information, we carried out *in situ* ^{1}H-NMR measurements monitoring the dehydration of fructose into 5-HMF in a NMR-tube in the presence of **[*o*-Xyl-(bimS)$_2$][Cl]$_2$**, under the same experimental conditions described. Magnified ^{1}H-NMR spectra recorded at selected times and their enlargements are reported in **Figures 8, S3**.

A first glance at spectra reported in **Figure 8A** brings out the appearance and growth in intensity of the signals relevant to the protons of 5-HMF, labeled as (●). Furthermore, enlarging suitable regions of the spectra shows the presence of signals which gradually disappear with time and consequently can be attributed to the occurrence of intermediates. These can be observed at 9.35 ppm, (H$_a$, **Figure 8B**) and 5.40 ppm (H$_b$, **Figure 8C**). We explained these findings by hypothesizing the occurrence of a mechanism similar to that recently reported by Huang for the dehydration of fructose in a IL binary mixture, (Zhang et al., 2015; Xiao and Huang, 2018) featuring two cyclic intermediates (**Figure 9**).

In particular, the signal of the proton at 9.35 ppm which disappeared after 50 min, can be attributed to the aldehydic proton H$_a$ of intermediate I. Analogously, in the region of chemical shifts between 5.20 and 5.50 ppm in the first minutes of the reaction a broad resonance, resulting from the overlap of two signals can be observed (**Figure 8C**). After 50 min, the signal centered at 5.40 ppm disappeared, living a single peak centered at 5.30 ppm. We explain this finding by attributing the signal at 5.40 ppm to the H$_b$ proton of intermediate I. We observe the disappearance of these two signals, after the same time, 50 min. Their disappearance is therefore synchronous, which lends further support to the hypothesis that these signals belong to the same intermediate. Finally, in **Figure 8D** the appearance of the methylenic protons of 5-HMF can be observed at 3.95 ppm.

It is important to note that this is a simplified representation and that the full mechanistic picture can be much more complicated than that. However, a full mechanistic investigation is outside the scope of the present work.

Since the conversion of fructose into 5-HMF is an acid catalyzed process, we tried to understand the trend observed by measuring the acid strength of our sulfonic acid-functionalized imidazolium salts. To this aim, we assessed the acidity of our salts by determining the H_0 acidity function, using the Hammett indicator method (Hammett and Deyrup, 1932; Thomazeau et al., 2003). This approach has been applied to determine the acidity of sulfonic acid-functionalized imidazolium-based ILs (Kore and Srivastava, 2012; Yaman et al., 2017). In particular, we determined the H_0 function values for our salts using methyl orange as indicator in solution of methanol (pK_{aMeOH} = 3.8) (Kolthoff and Guss, 1938).

The choice of methanol was firstly due to the good solubility of all our catalysts in this solvent, differently from the case of water solution where *p*-isomers were not soluble at the concentration needed. Furthermore, as previously reported, polarity of imidazolium-based ILs is comparable to alcohols bearing shorter alkyl chains (Carmichael and Seddon, 2000).

We are aware that the acid strengths detected in methanol could be different than those occurring in solution of ILs. Nevertheless, this determination of the H_0 function can still give a qualitative understanding of the different acidities of our salts and their ability to promote the reaction. To obtain a meaningful comparison among salts bearing one and two sulfonic acid groups, all determinations were carried out in solutions containing the same total proton concentration. Full details of calculations are given in the experimental section, while H_0 values are reported in **Table 1**.

The analysis of results reported in **Table 1** reveals that our salts show comparable acidities. Furthermore, our dicationic TSILs exhibit acidity comparable to monocationic one **[b$_2$imS][Cl]**. The only exception is represented by **[*p*-Xyl-(bim)(bimS)][Cl]$_2$**, in which case a significantly lower acidity was detected.

However, trend in H_0 values does not allow rationalizing the reactivity trend, indicating that although the acidity plays a role, it is not able to explain alone the experimental data. Such inability to find a simple correlation between Hammet acidity or basicity and reactivity data has been already reported in literature. On this

TABLE 1 | H_0 values for each salt determined at 298 K using methyl orange as indicator [a].

Salt	H_0^b
[b$_2$imS][Cl]	3.8
[*o*-Xyl-(bimS)$_2$][Cl]$_2$	3.9
[*m*-Xyl-(bimS)$_2$][Cl]$_2$	4.1
[*p*-Xyl-(bimS)$_2$][Cl]$_2$	4.0
[*p*-Xyl-(bim)(bimS)][Cl]$_2$	5.9

[a]H_0 values were reproducible within ± 0.1.
[b]pK_a of methyl orange in MeOH = 3.80.

FIGURE 9 | Intermediates hypothesized for the dehydration of fructose into 5-HMF.
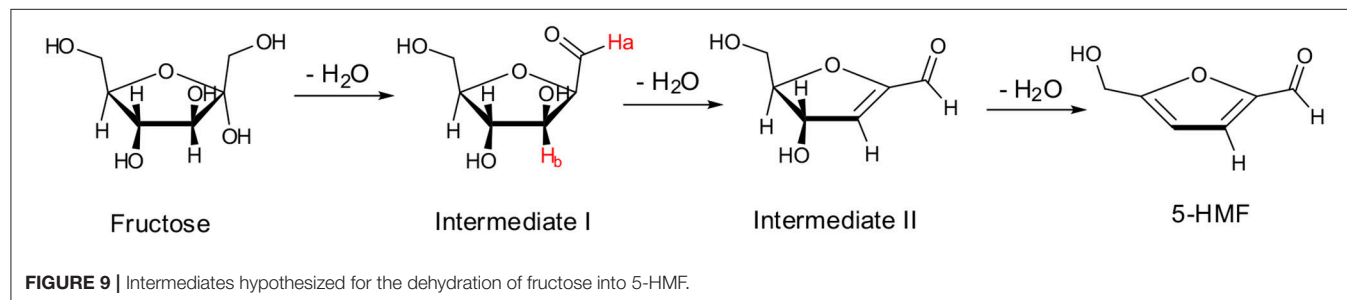
subject, we found a similar behavior performing the mononuclear rearrangement of heterocycles in the presence of dicationic TSILs (Rizzo et al., 2014). Previously, Chen et al. studying the Beckmann rearrangement in the presence of some acidic dicationic ILs, obtained comparable yields in amides regardless of the acidic strength of ILs, as accounted for by H_0 values (Liu et al., 2009). On the other hand, also for the dehydration of fructose, the trend in yield has been ascribed to the concomitant action of several factors on the transformation, different from the Hammett acidity (Dam et al., 1986).

Another parameter that can be affected by the relative position of the substituent in the phenyl ring is the dipole moment of the cation. In particular, for related dicationic isomeric salts, Yaman et al. reported that the dipole moment increases in the order para < meta < orto and that impacts on the acidity of the protons on the imidazolium rings (Yaman et al., 2017). However, in our case, this contribution is negligible, and the acidity of the isomeric dicationic salts is practically the same, due to the overwhelming effect of the strongly acidic -SO$_3$H function. For this reason, in our case, dipole moment does not play a significant role in explaining the reactivity observed.

Conversely, taking in consideration the catalysts soluble in the binary mixture of ILs, the concomitant action of cation structure and acidity could explain the reactivity trend. Indeed, the significant difference detected in the t_{max} values measured for [*m*-Xyl-(bimS)$_2$][Cl]$_2$ and [*o*-Xyl-(bimS)$_2$][Cl]$_2$ could be ascribed to the increased proximity of imidazolium heads on the *o*-xylilene spacer. This, could induce two different effects that decrease the catalytic ability of the corresponding TSIL. On the one hand, after the first deprotonation event, the second proton could be involved in hydrogen bonding interaction with the sulfonate group which, in turn, makes less probable its release in solution. On the other hand, the proximity of imidazolium heads could slow down the second deprotonation event, as a consequence of the electrostatic repulsion between sulfonate groups.

In this regard, it has been previously reported that for similar diimidazolium salts the isomeric substitution affects the conformations of cations and properties of the relevant IL (D'Anna et al., 2009a). Unfortunately, solubility issues do not allow drawing similar conclusions in the case of *p*-isomers.

In general, our task specific dicationic ILs show better performance in fructose conversion with respect to the ones previously reported by Jadhav et al. (2012) Indeed, in that case, yield values ranged from 70 up to 90 %, but using an equimolar amount of catalyst at 120°C.

Conversion of Sucrose in 5-HMF

As already said, the conversion of sucrose into 5-HMF is a more difficult process compared with that of fructose. Consequently, sucrose conversion often shows lower yields in 5-HMF and requires harsher conditions. To assess whether our salts are suitable for obtaining 5-HMF from sucrose, we conducted the reactions at 60°C, the same temperature used for the conversion of fructose, maintaining the same reaction conditions also in terms of catalyst loading, 20 mol %, with respect to the substrate. In particular, also in this case we monitored

the yield in 5-HMF as a function of time. Plots of yields in 5-HMF obtained from sucrose as a function of time are reported in **Figure 10**, while the yield values are reported in **Table S5**.

Looking at the plots reported in **Figure 10** reveals that even at this relatively low temperature, a yield of 30% is obtained after 90 min in the case of [**b$_2$imS**][**Cl**], 105 min in the case of [***m*-Xyl-(bimS)$_2$**][**Cl**]$_2$ and 135 min in the presence of [***o*-Xyl-(bimS)$_2$**][**Cl**]$_2$. These findings represent a marked improvement compared with our previous investigation of sucrose conversion in 5-HMF, in ILs, catalyzed by Amberlyst 15. In that case a lower yield, 23% was obtained after 120 min but required a much higher temperature, 90°C (D'Anna et al., 2014). Furthermore, notwithstanding in two cases the catalysts bear the same acidic functions, the TSILs used in this paper allowed us to operate under less acidic conditions compared with the analogous reaction carried out in the same ILs mixture in the presence of Amberlyst 15 (2.35·10^{-4} mol H$^+$ and 5.55·10^{-5} mol H$^+$ for Amberlyst 15 and dicationic TSILs, respectively) (D'Anna et al., 2014).

Notably, a comparable yield has been reported in literature for the obtainment of 5-HMF from sucrose in the presence of FePO$_4$ in THF/H$_2$O after 1h at 140°C (Yang et al., 2015). Some reports in the literature show the obtainment of higher yields in 5-HMF from sucrose (Tian et al., 2013; Qu et al., 2016; Yu et al., 2017). However, in all these cases either metal catalysts or very high temperatures and thus harsh reaction conditions are required. Consequently, we claim that the much milder reaction conditions and the absence of toxic metal catalyst make the use of our salts convenient from the standpoint of green chemistry.

Also in this case, we compared the rate of sucrose conversion in 5-HMF in the presence of all catalysts in the IL binary mixture and in ethanol and DMSO solution, using the [*o*-Xyl-(bimS)$_2$][Cl]$_2$ as catalyst, by considering the yield in 5-HMF obtained at the same time, 90 min. The results, collected in the IL binary mixture, are reported in **Figure 6**.

These findings show that yields in 5-HMF display a more articulate trend compared with the one observed in the case of fructose conversion. In particular, while the monocationic salt [**b$_2$imS**][**Cl**] affords the fastest conversion, no 5-HMF is formed after 90 min in the presence of the non-symmetrically substituted salt [***p*-Xyl-(bim)(bimS)**][**Cl**]$_2$. Furthermore, yields increase by following the order: [***m*-Xyl-(bimS)$_2$**][**Cl**]$_2$ < [***p*-Xyl-(bimS)$_2$**][**Cl**]$_2$ < [***o*-Xyl-(bimS)$_2$**][**Cl**]$_2$ < [**b$_2$imS**][**Cl**].

In the case of sucrose, the yield obtained in DMSO solution was comparable to the one obtained in the IL binary mixture.

Analogously to what happens in the case of fructose conversion, the trend obtained is not related to the acidity of the salts, as expressed by the H_0 function. However, in this case the solubility of the salts in the reacting mixture does not prove a limiting factor and no single parameter is able to account for the trend observed. This can be the result of the concomitant action of several factors on different mechanistic steps featuring this complex pathway.

As previously stated the use of dicationic organic salts to obtain 5-HMF from carbohydrates has been scarcely explored,
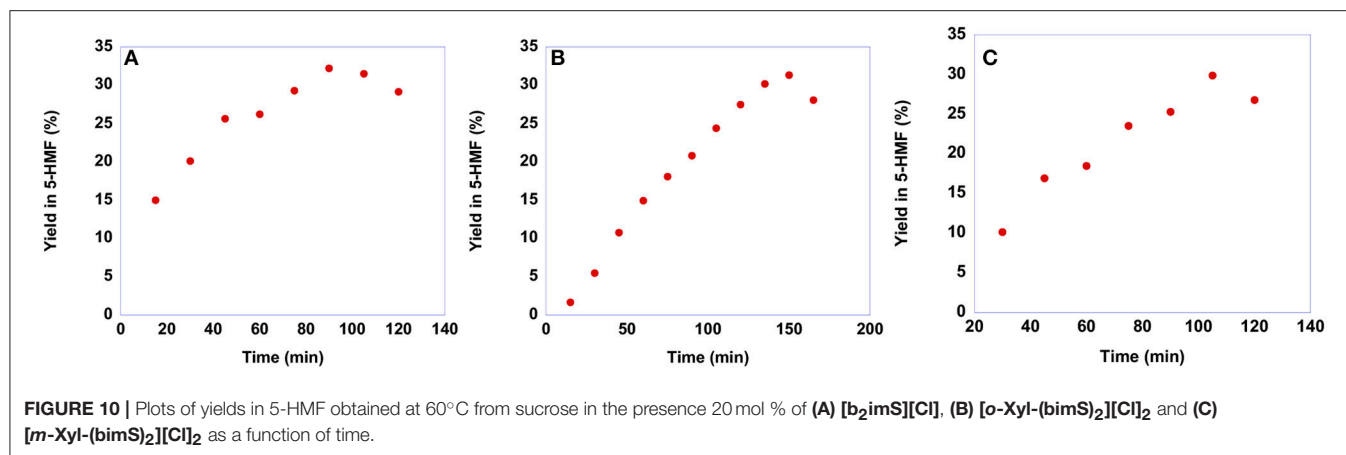
FIGURE 10 | Plots of yields in 5-HMF obtained at 60°C from sucrose in the presence 20 mol % of **(A) [b$_2$imS][Cl]**, **(B) [o-Xyl-(bimS)$_2$][Cl]$_2$** and **(C) [m-Xyl-(bimS)$_2$][Cl]$_2$** as a function of time.

TABLE 2 | Reaction conditions and yield values for fructose and sucrose conversion in 5-HMF in the presence of task specific dicationic ILs.

Catalyst	Fructose		Sucrose		
	Reaction temperature (°C)/Reaction time (min)	Yield (%)	Reaction temperature (°C)/Reaction time (min)	Yield (%)	References
[DiEG(mim)$_2$][OMs]$_2$	120/40	70	120/150	54	Jadhav et al., 2012
[TriEG(mim)$_2$][OMs]$_2$	120/40	77		61	
[TetraEG(mim)$_2$][OMs]$_2$	120/40	92		67	
A-ortho Cl	100/60	50			Yaman et al., 2017
B-para Cl	100/60	<40			
C-meta Cl	100/60	<50			
A-ortho HSO$_4$	100/60	90			
B-meta HSO$_4$	100/60	60			
B-para HSO$_4$	100/60	90			
[tetra(EG)(mim)trimethylamine][CH$_3$SO$_3$]	70/40	62			Jadhav et al., 2014
[tetra(EG) (mim)trimethylamo][Br]$_2$	70/40	57			
[tetra(EG)(mim) trimethylamo][HSO$_4$]$_2$	70/40	92			
[m-Xyl-(bimS)$_2$][Cl]$_2$	60/90	60	60/105	30	This work
[o-Xyl-(bimS)$_2$][Cl]$_2$	60/150	60	60/135	30	This work

above all as far as sucrose is taken in consideration as starting material. Consequently, at this point, comparison with data available in literature is mandatory (**Table 2**).

It is worth noting that, with only one exception in which the catalyst is used in DMSO solution, (Yaman et al., 2017) in the other cases reported in literature, task specific dicationic ILs are used both as solvent and catalyst; hence in a significantly higher amount. Bearing in mind this information, analysis of data reported in **Table 2** underlines how, in the case of fructose, the advantage in using our catalysts derives from the lower reaction temperature. Indeed, with the only exception of **[tetra(EG)(mim)trimethylamo][HSO$_4$]$_2$**, that gives significantly higher yield in 5-HMF at a slightly higher temperature, in all the other cases comparable yields were obtained, using a significantly higher reaction temperature.

On the other hand, in the case of sucrose, yields ranging from 54 up to 67% were reported, but working at 120°C for 150 min.

CONCLUSIONS

The study of fructose and sucrose conversion catalyzed by acid functionalized imidazolium salts in the [bmim][Cl]$_{0.5}$[BF$_4$]$_{0.5}$ IL mixture, demonstrated that our salts are effective catalysts for the obtainment of 5-HMF in very mild conditions. Indeed, working at 60°C and using 20 mol % of catalyst, we obtained 60 and 30 % of 5-HMF from fructose and sucrose, respectively. The reaction medium and catalyst could also be successfully recycled for 4 times without loss of yield and for further two cycles obtaining lower but still good yields. Furthermore, by *in situ* ^{1}H NMR monitoring of the reaction we hyphothesized the occurrence of a mechanistic pathway involving two intermediates.

The different substitution of the dicationic salts appeared to impact mainly the rate of the process and only marginally the overall yields. In particular, in the case of fructose the dicationic salts **[m-Xyl-(bimS)$_2$][Cl]$_2$** and **[o-Xyl-(bimS)$_2$][Cl]$_2$** lead to

faster and slower reaction compared with the monocationic [b₂imS][Cl]. Differently, in the case of sucrose, [b₂imS][Cl] proved the best catalyst.

Evaluation of the acidity of the salts revealed almost identical acid strength for all the salts, with the exception of [p-Xyl-(bim)(bimS)][Cl]₂. Finally, we identified the lower solubility of the p-substituted salts [p-Xyl-(bimS)₂][Cl]₂ and [p-Xyl-(bim)(bimS)][Cl]₂ as the reason for their poor catalytic performance in both cases.

On the whole, our results show that acidic TSILs do not behave as simple catalysts. Indeed, their performance cannot be attributed only to the amount of protons borne in the structure, but rather to the action of structural and conformational effects. Rather interestingly, in the ILs binary mixture used, our TSILs prove to be more efficient than some of previously reported catalytic systems both in terms of catalyst loading and reaction temperature, paving the way to more sustainable processes for the valorisation of raw materials.

For fructose conversion, the comparison with conventional organic solvents sheds light on a better efficiency of the tested catalyst, the [o-Xyl-(bimS)₂][Cl]₂, in the IL binary mixture with respect to DMSO solution. Probably, the increased efficiency can be ascribed to the different nature of the ion pair, representing the catalyst, in the two solvent systems, i.e., intimate and solvated ion pair in IL binary mixture and DMSO solution, respectively. Only in the first case, the TSIL could behave as a "bifunctional catalyst" that favors the carbohydrate dehydration both coordinating the hydroxyl group through hydrogen bond and favoring the water molecule departure as a consequence of the proton transfer.

AUTHOR CONTRIBUTIONS

All authors listed have made a substantial, direct and intellectual contribution to the work, and approved it for publication.

FUNDING

SUPPLEMENTARY MATERIAL

The Supplementary Material for this article can be found online at: https://www.frontiersin.org/articles/10.3389/fchem.2019.00134/full#supplementary-material

REFERENCES

Amarasekara, A. S. (2016). Acidic ionic liquids. *Chem. Rev.* 116, 6133–6183. doi: 10.1021/acs.chemrev.5b00763

Anastas, P., and Eghbali, N. (2010). Green chemistry: principles and practice. *Chem. Soc. Rev.* 39, 301–312. doi: 10.1039/B918763B

Brun, N., Hesemann, P., and Esposito, D. (2017). Expanding the biomass derived chemical space. *Chem. Sci.* 8, 4724–4738. doi: 10.1039/C7SC00936D

Carmichael, A. J., and Seddon, K. R. (2000). Polarity study of some 1-alkyl-3-methylimidazolium ambient-temperature ionic liquids with the solvatochromic dye, Nile Red. *J. Phys. Org. Chem.* 13, 591–595. doi: 10.1002/1099-1395(200010)13:10<591::AID-POC305>3.0.CO;2-2

Che, P., Lu, F., Zhang, J., Huang, Y., Nie, X., Gao, J., et al. (2012). Catalytic selective etherification of hydroxyl groups in 5-hydroxymethylfurfural over H4SiW12O40/MCM-41 nanospheres for liquid fuel production. *Bioresour. Technol.* 119, 433–436. doi: 10.1016/j.biortech.2012.06.001

Chheda, J. N., Roman-Leshkov, Y., and Dumesic, J. A. (2007). Production of 5-hydroxymethylfurfural and furfural by dehydration of biomass-derived mono- and poly-saccharides. *Green Chem.* 9, 342–350. doi: 10.1039/B611568C

Chiappe, C., and Pomelli, C. S. (2014). Point-functionalization of ionic liquids: an overview of synthesis and applications. *Eur. J. Org. Chem.* 2014, 6120–6139. doi: 10.1002/ejoc.201402093

Chiappe, C., Rodriguez Douton, M. J., Mezzetta, A., Pomelli, C. S., Assanelli, G., and de Angelis, A. R. (2017). Recycle and extraction: cornerstones for an efficient conversion of cellulose into 5-hydroxymethylfurfural in ionic liquids. *ACS Sustain. Chem. Eng.* 5, 5529–5536. doi: 10.1021/acssuschemeng.7b00875

Chinnappan, A., Baskar, C., and Kim, H. (2016). Biomass into chemicals: green chemical conversion of carbohydrates into 5-hydroxymethylfurfural in ionic liquids. *RSC Adv.* 6, 63991–64002. doi: 10.1039/C6RA12021K

Dam, H. E. V., Kieboom, A. P. G., and Bekkum, H. V. (1986). The conversion of fructose and glucose in acidic media: formation of hydroxymethylfurfural. *Starch Stärke* 38, 95–101.

D'Anna, F., Ferrante, F., and Noto, R. (2009a). Geminal ionic liquids: a combined approach to investigate their three-dimensional organisation. *Chem. Eur. J.* 15, 13059–13068. doi: 10.1002/chem.200901788

D'Anna, F., La Marca, S., and Noto, R. (2009b). p-Nitrophenolate: a probe for determining acid strength in ionic liquids. *J. Org. Chem.* 74, 1952–1956. doi: 10.1021/jo802473p

D'Anna, F., Marullo, S., and Noto, R. (2008). Ionic liquids/[bmim][N3] mixtures: promising media for the synthesis of Aryl Azides by SNAr. *J. Org. Chem.* 73, 6224–6228. doi: 10.1021/jo800676d

D'Anna, F., Marullo, S., Vitale, P., and Noto, R. (2011). The effect of the cation π-surface area on the 3D organization and catalytic ability of imidazolium-based ionic liquids. *Eur. J. Org. Chem.* 2011, 5681–5689. doi: 10.1002/ejoc.201100763

D'Anna, F., Marullo, S., Vitale, P., Rizzo, C., Lo Meo, P., and Noto, R. (2014). Ionic liquid binary mixtures: promising reaction media for carbohydrate conversion into 5-hydroxymethylfurfural. *Appl. Catal. A* 482, 287–293. doi: 10.1016/j.apcata.2014.05.039

D'Anna, F., Nimal Gunaratne, H. Q., Lazzara, G., Noto, R., Rizzo, C., and Seddon, K. R. (2013). Solution and thermal behaviour of novel dicationic imidazolium ionic liquids. *Org. Biomol. Chem.* 11, 5836–5846. doi: 10.1039/c3ob40807h

D'Anna, F., and Noto, R. (2014). Di- and tricationic organic salts: an overview of their properties and applications. *Eur. J. Org. Chem.* 2014, 4201–4223. doi: 10.1002/ejoc.201301871

D'Anna, F., Vitale, P., Marullo, S., and Noto, R. (2012). Geminal imidazolium salts: a new class of gelators. *Langmuir* 28, 10849–10859. doi: 10.1021/la301319u

D'Anna, F., Vitale, P., and Noto, R. (2009c). Determination of basic strength of aliphatic amines through ion pair formation in some ionic liquid solutions. *J. Org. Chem.* 74, 6224–6230. doi: 10.1021/jo901172j

De, S., Dutta, S., and Saha, B. (2016). Critical design of heterogeneous catalysts for biomass valorization: current thrust and emerging prospects. *Catal. Sci. Technol.* 6, 7364–7385. doi: 10.1039/C6CY01370H

Den, W., Sharma, V. K., Lee, M., Nadadur, G., and Varma, R. S. (2018). Lignocellulosic biomass transformations via greener oxidative pretreatment processes: access to energy and value-added chemicals. *Front. Chem.* 6:141. doi: 10.3389/fchem.2018.00141

Dupont, J. (2011). From Molten Salts to Ionic Liquids: A "Nano" Journey. *Acc. Chem. Res.* 44, 1223–1231. doi: 10.1021/ar2000937

Fang, D., Yang, J., and Jiao, C. (2011). Dicationic ionic liquids as environmentally benign catalysts for biodiesel synthesis. *ACS Catal.* 1, 42–47. doi: 10.1021/cs100026q

Galkin, K. I., Krivodaeva, E. A., Romashov, L. V., Zalesskiy, S. S., Kachala, V. V., Burykina, J. V., et al. (2016). Critical influence of 5-hydroxymethylfurfural aging and decomposition on the utility of biomass conversion in organic synthesis. *Angew. Chem. Int. Ed.* 55, 8338–8342. doi: 10.1002/anie.2016 02883

Giernoth, R. (2010). Task-specific ionic liquids. *Angew. Chem., Int. Ed.* 49, 2834–2839. doi: 10.1002/anie.200905981

Girisuta, B., Janssen, L. P. B. M., and Heeres, H. J. (2006). A kinetic study on the decomposition of 5-hydroxymethylfurfural into levulinic acid. *Green Chem.* 8, 701–709. doi: 10.1039/b518176c

Hallett, J. P., and Welton, T. (2011). Room-temperature ionic liquids: solvents for synthesis and catalysis. 2. *Chem. Rev.* 111, 3508–3576. doi: 10.1021/cr1003248

Hammett, L. P., and Deyrup, A. J. (1932). A series of simple basic indicators. i. the acidity functions of mixtures of sulfuric and perchloric acids with water1. *J. Am. Chem. Soc.* 54, 2721–2739. doi: 10.1021/ja01346a015

Hayes, R., Warr, G. G., and Atkin, R. (2015). Structure and nanostructure in ionic liquids. *Chem. Rev.* 115, 6357–6426. doi: 10.1021/ cr500411q

Jadhav, A. H., Chinnappan, A., Patil, R. H., Kostjuk, S. V., and Kim, H. (2014). Green chemical conversion of fructose into 5-hydroxymethylfurfural (HMF) using unsymmetrical dicationic ionic liquids under mild reaction condition. *Chem. Eng. J.* 243, 92–98. doi: 10.1016/j.cej.2013.12.054

Jadhav, A. H., Kim, H., and Hwang, I. T. (2012). Efficient selective dehydration of fructose and sucrose into 5-hydroxymethylfurfural (HMF) using dicationic room temperature ionic liquids as a catalyst. *Catal. Commun.* 21, 96–103. doi: 10.1016/j.catcom.2012.02.007

Kolthoff, I. M., and Guss, L. S. (1938). Ionization Constants of Acid-Base Indicators in Methanol. *J. Am. Chem. Soc.* 60, 2516–2522. doi: 10.1021/ ja01277a068

Kore, R., and Srivastava, R. (2012). Influence of –SO3H functionalization (N-SO3H or N-R-SO3H, where R=alkyl/benzyl) on the activity of Brönsted acidic ionic liquids in the hydration reaction. *Tetrahedron Lett.* 53, 3245–3249. doi: 10.1016/j.tetlet.2012.04.066

Lewkowski, J. (2001). Synthesis, chemistry and applications of 5-hydroxymethyl-furfural and its derivatives. *ARKIVOC* 2001, 17–54. doi: 10.3998/ark.5550190.0002.102

Liu, W., Wang, Y., Li, W., Yang, Y., Wang, N., Song, Z., et al. (2015). Polyethylene glycol-400-functionalized dicationic acidic ionic liquids for highly efficient conversion of fructose into 5-hydroxymethylfurfural. *Catal. Lett.* 145, 1080–1088. doi: 10.1007/s10562-015-1485-8

Liu, X., Xiao, L., Wu, H., Chen, J., and Xia, C. (2009). Synthesis of novel gemini dicationic acidic ionic liquids and their catalytic performances in the beckmann rearrangement. *Helv. Chim. Acta* 92, 1014–1021. doi: 10.1002/hlca.2008 00382

Mika, L. T., Cséfalvay, E., and Németh, Á. (2018). Catalytic conversion of carbohydrates to initial platform chemicals: chemistry and sustainability. *Chem. Rev.* 118, 505–613. doi: 10.1021/acs.chemrev.7b00395

Moreau, C., Finiels, A., and Vanoye, L. (2006). Dehydration of fructose and sucrose into 5-hydroxymethylfurfural in the presence of 1-H-3-methyl imidazolium chloride acting both as solvent and catalyst. *J. Mol. Catal. A: Chem.* 253, 165–169. doi: 10.1016/j.molcata.2006.03.046

Perego, C., Bosetti, A., Ricci, M., and Millini, R. (2017). Zeolite materials for biomass conversion to biofuel. *Energy Fuels* 31, 7721–7733. doi: 10.1021/acs.energyfuels.7b01057

Pierre, G. (2008). Catalytic conversion of biomass: challenges and issues. *ChemSusChem* 1, 734–737. doi: 10.1002/cssc.200800091

Plechkova, N. V., and Seddon, K. R. (2008). Applications of ionic liquids in the chemical industry. *Chem. Soc. Rev.* 37, 123–150. doi: 10.1039/B00 6677J

Qu, Y., Li, L., Wei, Q., Huang, C., Oleskowicz-Popiel, P., and Xu, J. (2016). One-pot conversion of disaccharide into 5-hydroxymethylfurfural catalyzed by imidazole ionic liquid. *Sci. Rep.* 6:26067. doi: 10.1038/ srep26067

Ramírez, E., Bringué, R., Fité, C., Iborra, M., Tejero, J., and Cunill, F. (2017). Role of ion-exchange resins as catalyst in the reaction-network of transformation of biomass into biofuels. *J. Chem. Technol. Biotechnol.* 92, 2775–2786. doi: 10.1002/jctb.5352

Rizzo, C., D'Anna, F., Marullo, S., and Noto, R. (2014). Task specific dicationic ionic liquids: recyclable reaction media for the mononuclear rearrangement of heterocycles. *J. Org. Chem.* 79, 8678–8683. doi: 10.1021/jo501451t

Rizzo, C., D'Anna, F., and Noto, R. (2016a). Functionalised diimidazolium salts: the anion effect on the catalytic ability. *RSC Adv.* 6, 58477–58484.doi: 10.1039/C6RA12037G

Rizzo, C., D'Anna, F., Noto, R., Zhang, M., and Weiss, R. G. (2016b). Insights into the formation and structures of molecular gels by diimidazolium salt gelators in ionic liquids or "Normal" Solvents. *Chem. Eur. J.* 22, 11269–11282. doi: 10.1002/chem.201600670

Rout, P. K., Nannaware, A. D., Prakash, O., Kalra, A., and Rajasekharan, R. (2016). Synthesis of hydroxymethylfurfural from cellulose using green processes: a promising biochemical and biofuel feedstock. *Chem. Eng. Sci.* 142, 318–346. doi: 10.1016/j.ces.2015.12.002

Sun, N., Rodriguez, H., Rahman, M., and Rogers, R. D. (2011). Where are ionic liquid strategies most suited in the pursuit of chemicals and energy from lignocellulosic biomass? *Chem. Commun.* 47, 1405–1421. doi: 10.1039/C0CC03990J

Taarning, E., Osmundsen, C. M., Yang, X., Voss, B., Andersen, S. I., and Christensen, C. H. (2011). Zeolite-catalyzed biomass conversion to fuels and chemicals. *Energy Environ. Sci.* 4, 793–804. doi: 10.1039/C004518G

Thomazeau, C., Olivier-Bourbigou, H., Magna, L., Luts, S., and Gilbert, B. (2003). Determination of an acidic scale in room temperature ionic liquids. *J. Am. Chem. Soc.* 125, 5264–5265. doi: 10.1021/ja0297382

Tian, G., Tong, X., Cheng, Y., and Xue, S. (2013). Tin-catalyzed efficient conversion of carbohydrates for the production of 5-hydroxymethylfurfural in the presence of quaternary ammonium salts. *Carbohydr. Res.* 370, 33–37. doi: 10.1016/j.carres.2013. 01.012

Tim, S., Wenjing, F., M, W.J., and Anders, R. (2011). Synthesis of 5-(Hydroxymethyl)furfural in ionic liquids: paving the way to renewable chemicals. *ChemSusChem.* 4, 451–458. doi: 10.1002/cssc.201000374

Ullah, Z., Bustam, M. A., Man, Z., Shah, S. N., Khan, A. S., and Muhammad, N. (2016). Synthesis, characterization and physicochemical properties of dual-functional acidic ionic liquids. *J. Mol. Liq.* 223, 81–88. doi: 10.1016/j.molliq.2016.08.018

Vigier, K. D. O., Chatel, G., and Jérôme, F. (2015). Contribution of deep eutectic solvents for biomass processing: opportunities, challenges, and limitations. *Chem. Cat. Chem.* 7, 1250–1260. doi: 10.1002/cctc.201500134

Xiao, Y., and Huang, X. (2018). The physicochemical properties of a room-temperature liquidus binary ionic liquid mixture of [HNMP][CH3SO3]/[Bmim]Cl and its application for fructose conversion to 5-hydroxymethylfurfural. *RSC Adv.* 8, 18784–18791. doi: 10.1039/C8RA03604G

Yaman, S., Mohamad, S., and Manan, N. S. A. (2017). How do isomeric ortho, meta and paradicationic ionic liquids impact the production of 5-hydroxymethylfurfural? *J. Mol. Liq.* 238, 574–581. doi: 10.1016/j.molliq.2017.02.076

Yang, L., Yan, X., Xu, S., Chen, H., Xia, H., and Zuo, S. (2015). One-pot synthesis of 5-hydroxymethylfurfural from carbohydrates using an inexpensive FePO4 catalyst. *RSC Adv.* 5, 19900–19906. doi: 10.1039/C4RA16145A

Yoo, C. G., Pu, Y., and Ragauskas, A. J. (2017). Ionic liquids: Promising green solvents for lignocellulosic biomass utilization. *Curr. Opin. Green Stustainable Chem.* 5, 5–11. doi: 10.1016/j.cogsc.2017.03.003

Yu, S.-B., Zang, H.-J., Yang, X.-L., Zhang, M.-C., Xie, R.-R., and Yu, P.-F. (2017). Highly efficient preparation of 5-hydroxymethylfurfural from sucrose using ionic liquids and heteropolyacid catalysts in dimethyl sulfoxide–water mixed solvent. *Chin. Chem. Lett.* 28, 1479–1484. doi: 10.1016/j.cclet.2017. 02.016

Yue, C., Fang, D., Liu, L., and Yi, T.-F. (2011). Synthesis and application of task-specific ionic liquids used as catalysts and/or solvents in organic unit reactions. *J. Mol. Liq.* 163, 99–121. doi: 10.1016/j.molliq.2011. 09.001

Zhang, D., and Dumont, M.-J. (2017). Advances in polymer precursors and bio-based polymers synthesized from 5-hydroxymethylfurfural. *J. Polym. Sci. Part A: Polym. Chem.* 55, 1478–1492. doi: 10.1002/ pola.28527

Zhang, J., Yu, X., Zou, F., Zhong, Y., Du, N., and Huang, X. (2015). Room-temperature ionic liquid system converting fructose into 5-hydroxymethylfurfural in high efficiency. *ACS Sustain. Chem. Eng.* 3, 3338–3345. doi: 10.1021/acssuschemeng.5b01015

Zhang, Z., Song, J., and Han, B. (2017). Catalytic transformation of lignocellulose into chemicals and fuel products in ionic liquids. *Chem. Rev.* 117, 6834–6880. doi: 10.1021/acs.chemrev.6b00457

Zhou, C.-H., Xia, X., Lin, C.-X., Tong, D.-S., and Beltramini, J. (2011). Catalytic conversion of lignocellulosic biomass to fine chemicals and fuels. *Chem. Soc. Rev.* 40, 5588–5617. doi: 10.1039/c1cs15124j

Zuo, M., Le, K., Li, Z., Jiang, Y., Zeng, X., Tang, X., et al. (2017). Green process for production of 5-hydroxymethylfurfural from carbohydrates with high purity in deep eutectic solvents. *Ind. Crops Prod.* 99, 1–6. doi: 10.1016/j.indcrop.2017.01.027

Influence of Anion and Cation Structure of Ionic Liquids on Carboxylic Acids Extraction

Ján Marták* and Štefan Schlosser

Institute of Chemical and Environmental Engineering, Faculty of Chemical and Food Technology, Slovak University of Technology, Bratislava, Slovakia

A recently proposed new mechanism and a model of reactive extraction of carboxylic acids by hydrophobic ionic liquids (ILs) was tested on five systems from published as well as from new equilibrium data on liquid-liquid extraction of butyric and lactic acids (BA and LA) from aqueous solutions. Two phosphonium and one ammonium ILs were used. The model describes experimental data for all systems with a good fit. The mechanism of acid extraction by ILs is very similar for all tested systems. This indicates a more general validity of the developed model. The model allows deeper understanding of regularities in carboxylic acid extraction by hydrophobic ILs. Stability constants of the first acid-IL bonds are by one to three orders of magnitude higher compared to that of acid-acid bonds. Values of stability constants related to two acid-IL bonds are sensitive to a cation and anion structure while stability constants for acid-acid bonds more distant from polar head of IL are not sensitive to IL structure. The stability constants of acid-IL bonds for LA and phosphonium ILs are by more than one order of magnitude lower compared to those for BA and are not influenced with an anion structure. The value of stability constant for the first BA-IL bond is for phosphonium IL with a decanoate anion only one third of those for IL with a phosphinate anion. Differences in the stability of acid-IL bonds for BA and LA can be attributed to hydrophobic interactions which almost do not occur in LA extraction. Ammonium IL also forms a less stable BA-IL bond than the phosphonium IL with the same phosphinate anion. A less stable BA-IL bond can favor the higher recovery of volatile acid from the solvent by vacuum evaporation where free acid is separated instead of acid salts as in classical processes what is a great advantage.

Keywords: extraction, carboxylic acids, ionic liquids, influence of structure, model, L/L equilibrium

INTRODUCTION

Phosphonium and ammonium ionic liquids (ILs) are effective solvents for extraction of carboxylic acids (Schlosser et al., 2018) which could be of interest as platform chemicals produced from renewable resources (Bozell and Petersen, 2010; Schlosser and Blahušiak, 2011). The mechanism of carboxylic acids extraction by hydrophobic ILs is rather complex (Sprakel and Schuur, 2019). Several phenomena participate in this process, e.g., competitive extraction of acid and water, coextraction of acid and water, aggregation and segregation in ILs, formation of reverse micelles in the organic phase, synergistic effect between the IL cation and anion, etc. (Schlosser et al., 2018). The structure of an anion and cation strongly influences the extraction performance

(Schlosser et al., 2018). A new mechanism and model of carboxylic acids extraction by hydrophobic ILs was proposed in paper (Marták and Schlosser, 2016) and tested on butyric acid (BA) extraction with a good fit.

The aim of this work was to test a new model of carboxylic acids extraction by hydrophobic ILs (Marták and Schlosser, 2016) on data for five systems: earlier published (Marták and Schlosser, 2007; Blahušiak et al., 2013) and new equilibrium data on liquid-liquid extraction of butyric and lactic acids (BA and LA) by two phosphonium and one ammonium ILs from aqueous solutions.

THEORY

The most important characteristics of the new extraction mechanism and model of liquid-liquid equilibrium developed in paper (Marták and Schlosser, 2016) are presented in this chapter with some actualizations enabling its more general applicability. A more detailed description of the model is in Marták and Schlosser (2016).

Reactive extraction of monocarboxylic acid, AH, by IL takes place by the formation of $(p, 1)$ complexes containing p molecules of acid and one ion pair of IL. In water saturated ILs with phosphinate and carboxylate anions water is associated around two H-bonding sites located on the carboxylate or phosphinate oxygens of IL anions. The H-bonds as an important and very general phenomenon in ILs was discussed in Hunt (2017). It is assumed that after the addition of AH, an acid-IL complex $(p, 1)$ is formed by the **competitive mechanism** resulting in the replacement of water surrounding these H-bonding sites with AH according to the following equation:

$$\text{AH} + \overline{(\text{AH})_{p-1}(\text{H}_2\text{O})_{k_{p-1}}\text{IL}} \rightleftharpoons \overline{(\text{AH})_p(\text{H}_2\text{O})_{k_p}\text{IL}}$$
$$+ \left(k_{p-1} - k_p\right)\text{H}_2\text{O} \qquad K_p = \frac{c_p}{c_{\text{F}}c_{p-1}} \qquad (1)$$
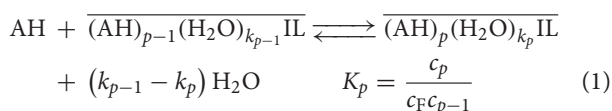
For $p = 1$ in Equation (1), c_0 is the concentration of water saturated acid-free IL in the organic phase. In the case of LA extraction by all tested ILs and BA extraction by ILs with phosphinate anions k_p for $p \geq 2$ is equal to zero so that in the complexes $(p, 1)$ with these p there is no water directly associated with IL. The same follows also for BA extraction by phosphonium decanoate with the exception that $p \geq 3$.

Once the constant k_p is equal to zero, binding of the next acid does not compete with water, but it forms H-bond with the acid already contained in complex. Therefore, the complexes with higher p are formed by a **non-competitive mechanism**. In the studied systems, this follows typically for complexes with $p > 2$ except for the system with BA and IL with decanoate anion where it is for $p > 3$. For the non-competitive mechanism, the following equation can be written

$$\text{AH} + \overline{(\text{AH})_{p-1}\text{IL}} \rightleftharpoons \overline{(\text{AH})_p\text{IL}} \qquad K_p = \frac{c_p}{c_{\text{F}}c_{p-1}} \qquad (2)$$
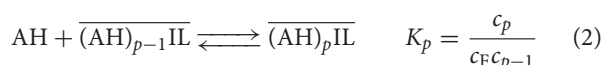
K_p in Equations (1, 2) are the stability constants (equilibrium constant) characterizing the stability of the bond between acid and IL in complexes (1, 1) and (2, 1), and between two acids

in complexes with $p > 2$. They are defined in terms of molar concentrations. For system with BA and decanoate IL one acid-acid bond is proposed also in complex (2, 1) as shown in **Figure 1**. The proposed structural formulas of $(p, 1)$ complexes were published in our previous works (Marták and Schlosser, 2016, 2017). For more hydrophobic acids, e. g. butyric acid (BA), the acid-IL and acid-acid hydrophobic interactions between hydrocarbon chains occur. In such case K_p is lumped constant including also van der Waals interactions.

Using Equations (1, 2), molar ratio of the $(p, 1)$ complex to IL is:

$$u_p = \frac{n_p}{n_{\text{I}}} = \frac{\left(\prod_{i=1}^{p} K_i\right) c_{\text{F}}^p}{1 + \sum_{p=1}^{n} \left(\prod_{i=1}^{p} K_i\right) c_{\text{F}}^p} \qquad (3)$$

Loading of IL by AH is defined as the molar ratio of reactively extracted acid and IL:

$$z_{\text{AH}} = \frac{n_{\text{S}}}{n_{\text{I}}} = \sum_{p=1}^{n} p u_p \qquad (4)$$

From Equations (3, 4) follows that the loading is independent of the IL concentration. The same applies to all monobasic acids. The values of K_p systematically decrease with the increasing p. For the mathematical expression of this dependence, an exponential decay according to the following empirical formula has been suggested:

$$\ln K_p = A + B e^{Cp} \qquad (5)$$

where A, B, and C are empirical parameters. The selection of this empirical dependence is elucidated in the previous work (Marták and Schlosser, 2016).

Fitting of equilibrium data from the AH extraction was done using z_{AH} as a function of c_{F}, which is the concentration of

FIGURE 1 | Proposed structural formula of BA-[$C_{14}C_6C_6C_6P^+$][C_9COO^-] complex (2, 1).
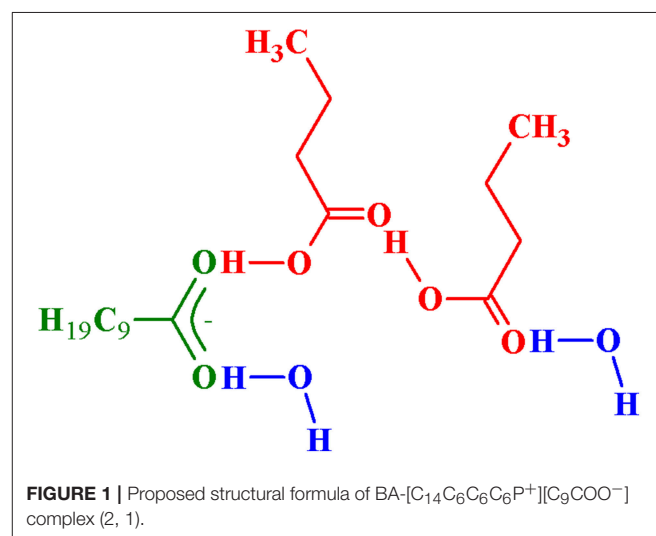
undissociated AH in the aqueous phase. The relation between the analytical AH concentrations in the aqueous phase c_{aF} and c_F can be derived using pK_a of AH and equilibrium pH as follows:

$$c_F = \frac{c_{aF}}{10^{(pH_F - pK_a)} + 1} \tag{6}$$

$pK_a = 4.821$ at the temperature of $298\,K$ was used for butyric acid (Partanen, 2004) and $pK_a = 3.86$ for lactic acid (Dawson et al., 1986).

Apart from water directly associated with IL which competes with acid according to Equation (1) another type of water is extracted to the organic phase together with acid by **coextraction mechanism**. In other words, the extracted acid is hydrated. Therefore, the total equilibrium loading of IL by water in the organic phase was defined as a sum of loadings by water directly associated with the IL which competes with AH, and water co-extracted (associated) with the acid

$$z_W = z_{W,\,comp} + z_{W,\,coext} \tag{7}$$

where

$$z_{W,\,comp} = k_0 u_{I,\,AHfree} + k_1 u_1 + k_2 u_2 \tag{8}$$
$$z_{W,\,coext} = K_{W,\,coext} z_{AH} \tag{9}$$

and

$$u_{I,\,AHfree} = \frac{n_{I,\,AHfree}}{n_I} = \frac{1}{1 + \sum_{p=1}^{n} \left(\prod_{i=1}^{p} K_i \right) c_F^p} \tag{10}$$

is the molar ratio of IL not associated with AH and the total IL. Experimental results indicated that the amount of coextracted water is linearly dependent on the amount of extracted acid. This is expressed by Equation (9) where $K_{W,coext}$ is the water coextraction constant. Fitting of equilibrium data on water extraction was done using z_W as a function of c_F by combining (Equations 7–10, 3).

Coefficients k_p represent only water extracted by the competitive mechanism (see Equation 1). All water associated with IL and AH in complexes (1, 1) and (1, 2) (Marták and Schlosser, unpublished manuscript) can be calculated as follows

$$k_{1,\,Wtot} = k_1 + K_{W,\,coext} \tag{11}$$
$$k_{2,\,Wtot} = k_2 + 2K_{W,\,coext} \tag{12}$$

Thus, the overall mechanism of simultaneous extraction of AH and water by IL can be divided into three sub-mechanisms:

a) Competitive extraction of acid and water
b) Non-competitive mechanism of AH extraction
c) Co-extraction of water with AH

MATERIALS AND METHODS

Ionic liquids (ILs) used in the experiments are summarized in **Table 1**. $[C_{14}C_6C_6C_6P^+][BTMPP^-]$ and $[C_{14}C_6C_6C_6P^+][C_9COO^-]$ are commercial products and $[C_nC_nC_nC_1N^+][BTMPP^-]$ was synthesized by metathesis from precursors $[C_nC_nC_nC_1N^+][Cl^-]$ and BTMPP-H (Blahušiak et al., 2013). Before use, all ILs were conditioned by washing with equal volumes of the aqueous solution of 0.5 and eventually 0.15 $kmol.m^{-3}$ NaOH and then typically more than 10 times with deionized water until a constant pH value of the aqueous phase was achieved. Also, the precursors were conditioned. The structural formulas of IL anions and cations are shown in **Figure 2**.

Lactic acid (LA, **Figure 2F**) extra pure was purchased from Merck (Germany) as a 90 wt. % aqueous solution. Before use it was five times diluted with deionized water and boiled under the total reflux of distillate for $>5\,h$ to split the acid dimer. Butyric acid (BA, **Figure 2E**) with the purity of >99 wt. % was also supplied by Merck. Dodecane with the purity of above 98 wt. % (Fluka, Switzerland) was used as a diluent.

All experiments were done at the temperature of $298.15\,K$. Liquid–liquid equilibrium experiments were carried out using 4, 10, or 25 cm^3 vials according to the final volume of the quaternary two-phase system (acid + water + IL + dodecane). The equilibrium was reached after more than $10\,h$ in a rotational shaking water bath (GFL, Germany). The intensity of shaking was optimized to ensure the dispersion of phases and to avoid the formation of stable emulsion.

Analysis of LA and BA in the aqueous phases was done by capillary electrophoresis using an analyzer EA 100 (Villa, Slovakia). In experiments with $[C_{14}C_6C_6C_6P^+][C_9COO^-]$, BA was analyzed on an Agilent Technologies 1260 Infinity HPLC system (USA). More detailed descriptions of used chemicals, experimental methods and analyses are provided in previous works (Marták and Schlosser, 2007, 2016).

TABLE 1 | Ionic liquids used.

IL short name	IL full name	Trade name	Producer	Purity wt. %
$[C_{14}C_6C_6C_6P^+][BTMPP^-]$	tetradecyltrihexylphosphonium bis-(2,4,4-trimethylpentyl) phosphinate	Cyphos IL-104	Cytec (Canada)	95
$[C_{14}C_6C_6C_6P^+][C_9COO^-]$	tetradecyltrihexylphosphonium decanoate	Cyphos IL-103	Cytec (Canada)	95+
$[C_nC_nC_nC_1N^+][BTMPP^-]$	trialkylmethylammonium bis-(2,4,4-trimethylpentyl) phosphinate, $n = 6$, 8, or 10	–	Synthetized (Blahušiak et al., 2013)	89+
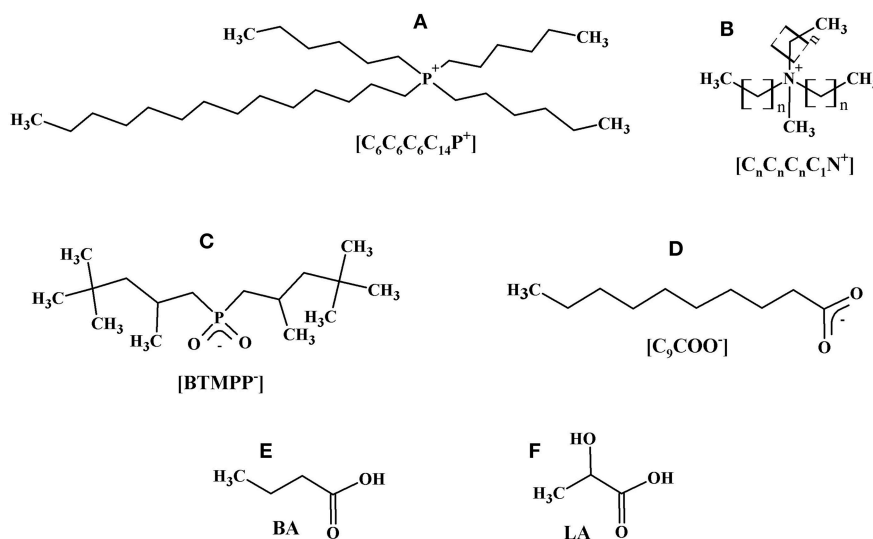
FIGURE 2 | Structural formulas of tetradecyltrihexylphosphonium **(A)** trialkylmethylammonium **(B)** cations, bis-(2,4,4-trimethylpentyl)phosphinate **(C),** and decanoate **(D)** anions, butyric **(E),** and lactic **(F)** acids. In panel **(B)** n = 6, 8, or 10.

RESULTS AND DISCUSSION

Differences between the new model of liquid-liquid equilibrium and the previous one used in papers (Marták and Schlosser, 2007, 2008) are explained in papers (Marták and Schlosser, 2016). Briefly, the main differences are that the stability constants of the previous model were the equilibrium constants of $(p, 1)$ complex formation from its free components (acid and IL) but in the new model, they express the equilibrium between complexes $(p – 1, 1)$ and $(p, 1)$. The advantage is that constant K_p now characterizes the stability of only one acid-IL or acid-acid bond (Equations 1 and 2) and it does not include all bonds of the complex. Second difference is that at higher acid loadings of IL , all complexes are considered (Equation 5) and not only those selected by the fitting method as it is in an older model.

Application of the new model on experimental data for lactic acid (LA) and $[C_{14}C_6C_6C_6P^+][BTMPP^-]$ is shown in **Figures 3**, **4**. After consideration, the data for a 30 % $[C_{14}C_6C_6C_6P^+][BTMPP^-]$ solution previously published in papers (Marták and Schlosser, 2007, 2017) were not used because of the formation of a dodecane-rich third phase as shown in paper (Marták and Schlosser, 2017). New data on LA extraction with $[C_{14}C_6C_6C_6P^+][C_9COO^-]$ are presented in **Figure 5**.

Even though lactic acid is stronger (pK_a = 3.86 at 298 K) than butyric acid (BA, pK_a = 4.82 at 298 K) it has been shown that its affinity to basic amine extractants is much lower compared to that of BA (Procházka et al., 1994; Sabolová et al., 2001). The same applies also for phosphonium ILs as it has been reported in the previous works (Marták and Schlosser, 2007, 2016, 2017) as well as for the new data on LA extraction by $[C_{14}C_6C_6C_6P^+][C_9COO^-]$ (**Figure 5**).

For LA, the values of constant K_1 (**Table 2**) representing the stability of acid-IL interaction includes mainly the strength of polar interactions between the acid and IL and the contribution of
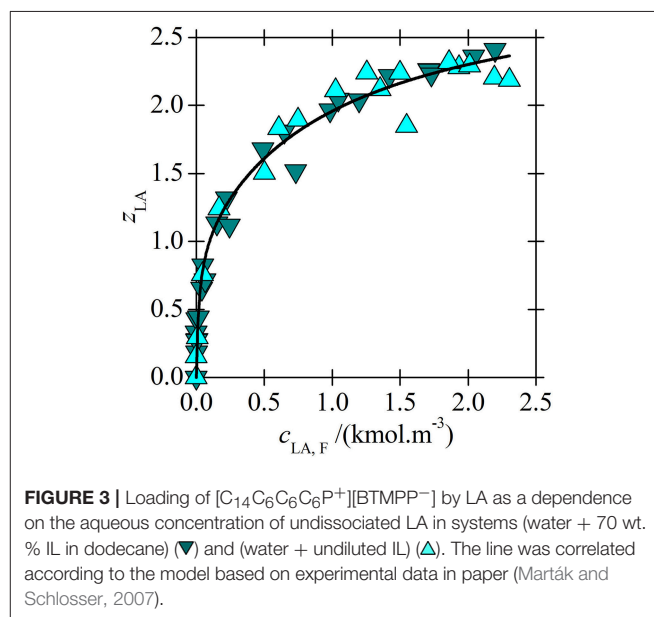
FIGURE 3 | Loading of $[C_{14}C_6C_6C_6P^+][BTMPP^-]$ by LA as a dependence on the aqueous concentration of undissociated LA in systems (water + 70 wt. % IL in dodecane) (▼) and (water + undiluted IL) (△). The line was correlated according to the model based on experimental data in paper (Marták and Schlosser, 2007).

hydrophobic interactions is rather insignificant since LA contains only one methyl group. For BA, constants K_1 are by more than one order of magnitude higher, which indicates rather high contribution of hydrophobic interactions between the acid and IL in complex (1, 1). Therefore, for BA extraction, K_1 should be a lumped constant, which includes both polar interactions represented by the strength of the BA-IL H-bond as well as the hydrophobic interactions. The same follows also for K_p for $p > 1$.

For LA, the values of K_1 are similar for phosphonium ILs with both phosphinate and decanoate anions (**Table 2**). The same can be said for K_2, indicating that the affinities of LA to both ILs
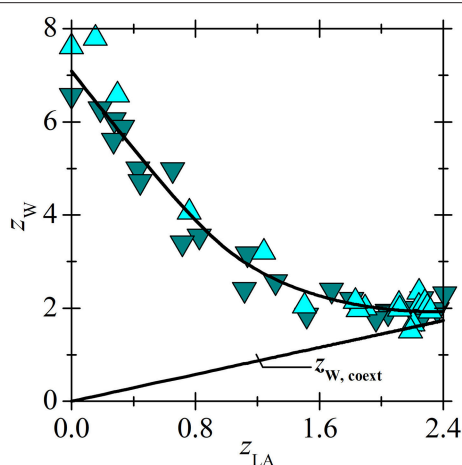
FIGURE 4 | Loading of $[C_{14}C_6C_6C_6P^+][BTMPP^-]$ by water vs. loading by LA in the same systems as in **Figure 3**. Lines represent the values calculated according to the model based on experimental data in paper (Marták and Schlosser, 2007). For $z_{W, coext}$ see Equation (9).
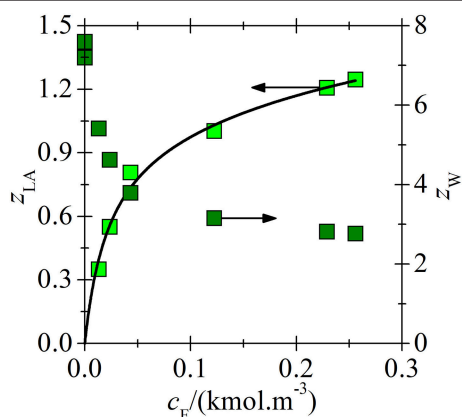
FIGURE 5 | Loading of $[C_{14}C_6C_6C_6P^+][C_9COO^-]$ by LA (▦) and water (▦) vs. equilibrium LA concentration of undissociated LA in the aqueous phase in system (water + undiluted $[C_{14}C_6C_6C_6P^+][C_9COO^-]$). The line correlates experimental data according to the model. Loading of IL by water was not correlated because of insufficient number of data points.

are almost the same. However, for BA, extraction by these ILs, the differences in constants K_1 as well as K_2 are larger, which can be attributed to differences in hydrophobic interactions between the alkyl chains of ILs and BA. The decanoate anion contains linear carbon chain and phosphinate anion includes two branched chains. The presence of branched alkyl chains usually increases the viscosity as a consequence of more intensive van der Waals interactions which can be reflected in higher values of stability constants for extraction of BA by phosphinate IL. Further investigation is needed to verify this idea.

The values of stability constant K_p are the highest for K_1 which are by one to three orders of magnitude higher compared to K_p for higher p. K_p decrease exponentially with the increasing

p (Equation 5, **Table 2**). This indicates that the acid-IL bonds are stronger than acid-acid bonds. The strength of the acid-acid bonds decreases as the acid distance from the polar head of IL increases approaching for $p > 5$ a similar value, around the unity, for all observed ILs in BA extraction. Therefore, the stability of acid-acid bonds more distant from the polar head of IL is independent of the IL structure.

Comparison of acid loadings of phosphonium ILs is shown in **Figure 6**. Since the overall acid loading of IL for LA exceeds the value of two only moderately even at high LA concentrations (**Figure 3**), the stability constant of the acid-acid bond in complex (3, 1) formed from complex (2, 1) is very low (**Table 2**) and hence the bond between the second and the third acid is weak. Due to the high polarity of LA it probably cannot form complexes with more than three molecules of LA.

In contrast to LA, BA with a C_3 hydrophobic tail can form big complexes with the tested ILs as it follows from the loadings in **Figures 6, 7**. These complexes are formed by non-competitive mechanism as follows from Equation (2). Even the values of K_p with the highest p are about twice higher than K_3 for LA, **Table 2**. However, due to the high values of constant K_1 (**Table 2**), i. e. high affinity of ILs to the first BA molecule, the recovery yield of BA from extract with $[C_{14}C_6C_6C_6P^+][BTMPP^-]$ by distillation in a short-path vacuum evaporator cannot achieve higher value than about 90% at 160°C (Blahušiak et al., 2011, 2012). It requires higher distillation temperature, which can be a problem when considering limit in temperature stability of IL. Much lower values of K_1 for $[C_{14}C_6C_6C_6P^+][C_9COO^-]$ with a decanoate anion or for ammonium IL with a phosphinate anion (**Table 2**) can be advantageous as it is suggested by the preliminary data for $[C_{14}C_6C_6C_6P^+][C_9COO^-]$. In the short path vacuum evaporator with wiped film operating continuously in the same way as in paper (Blahušiak et al., 2011), binary solutions of phosphonium ILs were distilled with 30 wt. % BA at 130°C and pressure of 2 kPa. The recovery of BA from phosphonium ILs with phosphinate and decanoate anions was about 88 and 94%, respectively, proving the advantage of ILs with a decanoate anion in regeneration.

The correlation between K_p values and extraction capability of ILs is not direct. For example, in extraction of BA K_1 decreases in order of ILs $[C_{14}C_6C_6C_6P^+][BTMPP^-] > [C_nC_nC_nC_1N^+][BTMPP^-] > [C_{14}C_6C_6C_6P^+][C_9COO^-]$ (**Table 2**). However, at low BA concentrations where the complex (1, 1) is mostly formed, the distribution coefficients indicating the extraction capability decreases in the order $[C_{14}C_6C_6C_6P^+][C_9COO^-] > [C_{14}C_6C_6C_6P^+][BTMPP^-] > [C_nC_nC_nC_1N^+][BTMPP^-]$ as shown in **Figure 8** so that IL providing lowest K_1 has the highest extraction capability. Such paradox can be explained as follows: for example, the densities and water mass fractions in water saturated $[C_nC_nC_nC_1N^+][BTMPP^-]$ and $[C_{14}C_6C_6C_6P^+][C_9COO^-]$ are very similar (about 0.9 g.cm⁻³ and 16%). However, the molecular weight of $[C_{14}C_6C_6C_6P^+][C_9COO^-]$ (655.1 g.mol⁻¹) is lower compared to $[C_{14}C_6C_6C_6P^+][BTMPP^-]$ (773.3 g.mol⁻¹) so that it has higher molarity. Due to higher molarity of $[C_{14}C_6C_6C_6P^+][C_9COO^-]$ the distribution coefficient can be higher although K_1 is lower. Comparing **Table 2** and **Figure 8**

TABLE 2 | Values of parameters K_p, A, B, C, k, k_1, k_2, $k_{1,Wtot}$, $k_{2,Wtot}$, and $K_{W,coext}$ resulting from the fitting of the data on (Liquid-Liquid) equilibrium in the system (IL + dodecane + acid + water) by the studied model.

Acid	LA	LA	BA (Marták and Schlosser, 2016)	BA (Marták and Schlosser, unpublished manuscript)	BA
IL	$[C_{14}C_6C_6C_6P^+]$ $[BTMPP^-]$	$[C_{14}C_6C_6C_6P^+]$ $[C_9COO^-]$	$[C_{14}C_6C_6C_6P^+]$ $[BTMPP^-]$	$[C_{14}C_6C_6C_6P^+]$ $[C_9COO^-]$	$[C_nC_nC_nC_1N^+]$ $[BTMPP^-]$ $n = 6, 8,$ or 10
P	$\dfrac{K_p}{m^3 \cdot kmol^{-1}}$	$\dfrac{K_p}{m^3 \cdot kmol^{-1}}$	$\dfrac{K_p}{m^3 \cdot kmol^{-1}}$	$\dfrac{K_p}{m^3 \cdot kmol^{-1}}$	$\dfrac{K_p}{m^3 \cdot kmol^{-1}}$
1	**51.4**	**47.0**	**1,610**	**524**	**638**
2	**1.89**	**1.77**	**85.4**	**62.2**	**20.6**
3	**0.467**	-	21.1	8.64	21.3
4	-	-	5.03	3.23	5.57
5	-	-	2.36	1.83	2.53
6	-	-	1.58	1.32	1.6
7	-	-	1.28	1.10	1.22
8	-	-	1.15	0.986	1.04
9	-	-	1.08	0.927	0.944
10	-	-	1.05	0.894	0.894
11	-	-	1.03	0.876	0.865
12	-	-	-	0.866	-
13	-	-	-	0.860	-
14	-	-	-	0.857	-
15	-	-	-	0.855	-
16	-	-	-	0.854	-
A	-	-	**0.0142**	**−0.160**	**−0.191**
B	-	-	**20.7**	**12.2**	**16.0**
C	-	-	**−0.639**	**−0.553**	**−0.532**
$\bar{R}^2_{BA}$	0.9740	0.9924	0.9987	0.9978	0.9948
K	**7.09**	-	**7.83**	**7.39**	**11.6**
k_1	**2.13**	-	**3.20**	**2.47**	**5.48**
k_2	**0**	-	**0**	**0.880**	**0**
k_1, W_{tot}	2.85	-	3.72	3.07	6.22
k_2, W_{tot}	1.44	-	1.05	2.07	1.48
			0.523[c]		
k_W, coext	**0.722[b]**	-	**0.410[d]**	**0.596[e]**	**0.738[f]**
$\bar{R}^2_W$	0.9419	-	0.9945	0.9726	0.9173

The fitted parameters are shown in bold. Other parameters were calculated from fitted ones using Equations (5, 11, 12). Temperature: $T = 298.15^a$ K, pressure: $P = 0.10$ MPa^a. R squared related to the data on acid extraction ($\bar{R}^2_{BA}$) and water extraction ($\bar{R}^2_W$) are also presented.

[a] Standard uncertainties u: $u(T) = 0.1$ K, $u_r(P) = 0.06$.

[b] Common value for systems with 70 wt. % IL in dodecane and undiluted IL. Concentrations c_F where the differences between $K_{W,coext}$ at various IL concentrations are apparent (higher z_{BA}) were not achieved.

[c] Value for undiluted IL.

[d] Value for 60 wt. % IL diluted in dodecane.

[e] Value for undiluted IL. No experiments were done for diluted IL.

[f] Value for undiluted IL. Experiments at high z_{BA} were not available for diluted IL.

the same can be said also for extraction of LA. In the future research the structure of IL providing low K_1, high extraction capability and low viscosity should be found. However, this is not an easy task because ILs composed from small ions providing higher molarity as well as low-viscosity ILs are usually more polar, and hence more soluble in water.

All studied ILs are hydrophobic but they can dissolve large amount of water (**Figures 9**, **10**) (Marták and Schlosser, 2007, 2016; Blahušiak et al., 2013). The differences in water solubility in $[C_{14}C_6C_6C_6P^+][BTMPP^-]$ for experiments with LA and BA, as follows from **Figure 9B** and values of constant k in **Table 2**, are probably due to different IL batches from the supplier. The
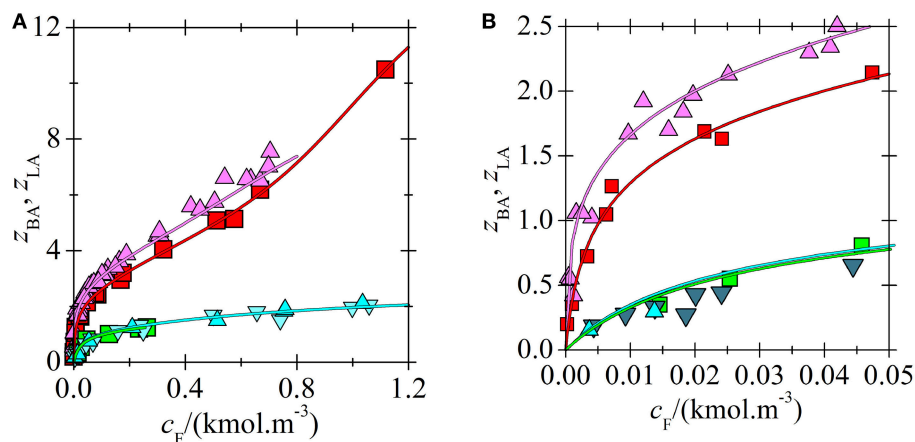
FIGURE 6 | Loading of phosphonium ILs by acids vs. aqueous equilibrium concentration of acid in systems (BA + undiluted [$C_{14}C_6C_6C_6P^+$][$BTMPP^-$]) (△) (Marták and Schlosser, 2016), (BA + undiluted [$C_{14}C_6C_6C_6P^+$][C_9COO^-]) (■) (Marták and Schlosser, unpublished manuscript), (LA + undiluted (△) or 70 wt. % (▽) [$C_{14}C_6C_6C_6P^+$][$BTMPP^-$] in dodecane) (Marták and Schlosser, 2007), and (LA + undiluted [$C_{14}C_6C_6C_6P^+$][C_9COO^-]) (■). Lines correlate with the experimental data according to the model. **(B)** An extended view of the lower concentration range of **(A)**.
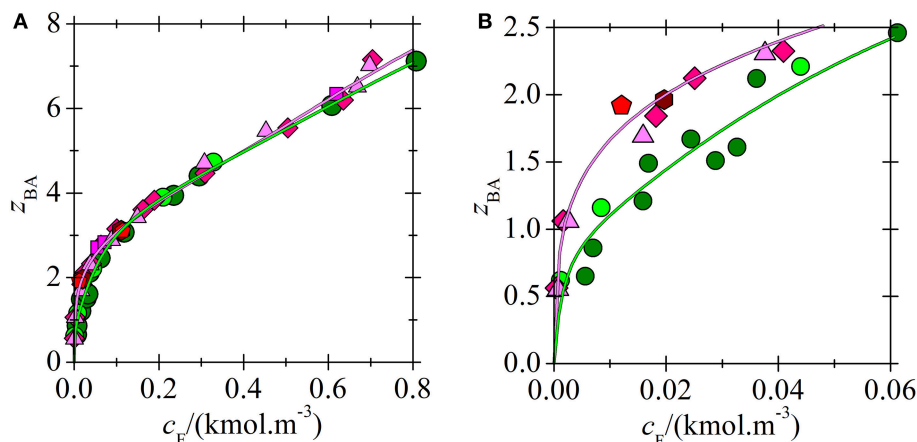
FIGURE 7 | Comparison of BA loading for phosphonium (Marták and Schlosser, 2016) and ammonium (Blahušiak et al., 2013) ILs vs. aqueous equilibrium concentration of acid in two-phase systems (water + IL dissolved in dodecane). Composition of dry solvent phase (wt. % of IL in dodecane): [$C_nC_nC_nC_1N^+$][$BTMPP^-$] 70 (●), undiluted (●), [$C_{14}C_6C_6C_6P^+$][$BTMPP^-$] 40 (●), 50 (⬠), 60 (◆), 70 (◼), undiluted (△). Lines correlate with the experimental data according to the model (green for ammonium and magenta for phosphonium IL). **(B)** An extended view of the lower concentration range of **(A)**.

dependence of water loading on the acid loading of ILs is similar for all tested ILs. In **Figure 10** it is shown that water content in ammonium IL is higher in the whole range of acid loadings of the IL compared to that in phosphonium IL, probably due to the higher polarity of the ammonium cation caused by higher charge density on nitrogen compared to phosphorus.

At lower acid concentrations when the acid-IL complexes are formed mainly by competitive mechanism (Equation 1) acid competes with water for H-bond sites situated on carboxylate or phosphinate oxygens of IL anions. The formation of H-bonds between water and oxygen located on IL anion has been already suggested and modeled by atomistic simulation, e.g., for tetraalkylphosphonium bis(oxalato)borate ionic liquid (Wang et al., 2015). With the increasing acid content, water

is substituted with acid (**Figures 9**, **10**). Typically, about half of the water amount is released from water saturated IL when complex (1, 1) is formed as it follows from the comparison of k and $k_{1,\,Wtot}$ in **Table 2** (see also Equation 11). In BA extraction, after reaching the minimum of IL loading by water, (p, 1) complexes are formed by non-competitive mechanism (Equation 2) and **Figure 9** documents that water content in the solvent phase increases linearly with the increasing acid loading of the IL. This increase indicates that such water is not associated directly with the IL (both H-bonding sites on IL anion are occupied by acid) but with the acid (also by H-bond), and the water to acid molar ratio is given by constant $K_{W,coext}$ as it follows from Equation (9) (Marták and Schlosser, 2016). As it can be seen in **Figure 9**, the dependence of water

loading on IL loading cannot reach the region of increasing water loading in LA extraction due to low acid loading of the IL. Anyway, it is assumed that similarly to BA, also extracted LA is hydrated and constant $K_{W,coext}$ was calculated as shown in **Table 2**. A comparison of the results with LA and BA extracted by $[C_{14}C_6C_6C_6P^+][BTMPP^-]$ shows that the value of $K_{W,coext}$ is higher for LA than for BA, which can be attributed to the higher polarity of LA.

The differences between coefficients k_p and $k_{p,Wtot}$ enable us to consider the distribution of water in individual complexes (Equations 11 and 12). As follows from Equation (11) and **Table 2**, in the complex of $[C_{14}C_6C_6C_6P^+][BTMPP^-]$ with LA (1, 1) there are typically two molecules of water bound to the IL and one to LA. For BA extraction, complex (1, 1) with $[C_{14}C_6C_6C_6P^+][BTMPP^-]$ contains about three molecules of water bound to the IL and only half water molecule was left to bond with the acid. This can be explained by the association of complexes via a water bridge as suggested in previous work (Marták and Schlosser, 2016). In BA extraction with $[C_{14}C_6C_6C_6P^+][C_9COO^-]$, a comparison of the values of
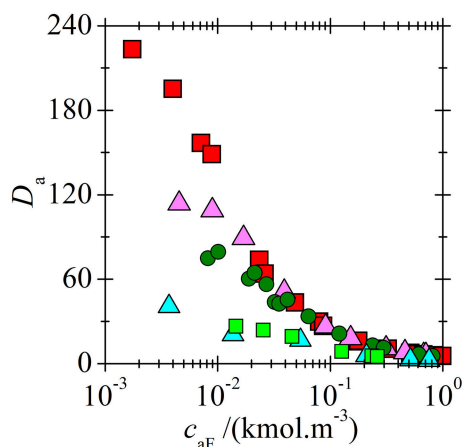
FIGURE 8 | Concentration dependences of acids distribution coefficients in two-phase systems (water + IL) for BA extracted by $[C_{14}C_6C_6C_6P^+][C_9COO^-]$ (■) (Marták and Schlosser, unpublished manuscript), $[C_{14}C_6C_6C_6P^+][BTMPP^-]$) (△) (Marták and Schlosser, 2016), $[C_{14}C_6C_6C_6P^+][BTMPP^-]$ (●) (Blahušiak et al., 2013) and LA extracted by $[C_{14}C_6C_6C_6P^+][C_9COO^-]$ (■) and $[C_{14}C_6C_6C_6P^+][BTMPP^-]$ (△) (Marták and Schlosser, 2007).
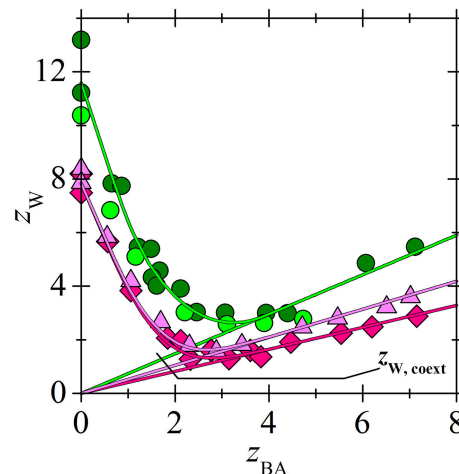
FIGURE 10 | Comparison of water loading of IL for phosphonium (Marták and Schlosser, 2016) and ammonium (Blahušiak et al., 2013) ILs vs. BA loading of IL for the selected systems in **Figure 7**. Composition of dry solvent phase (wt. % of IL in dodecane): $[C_nC_nC_nC_1N^+][BTMPP^-]$ 70 (●), undiluted (●), $[C_{14}C_6C_6C_6P^+][BTMPP^-]$ 60 (◆), undiluted (△). For $z_{W,coext}$ see Equation (9). Lines correlate with the experimental data according to the model.
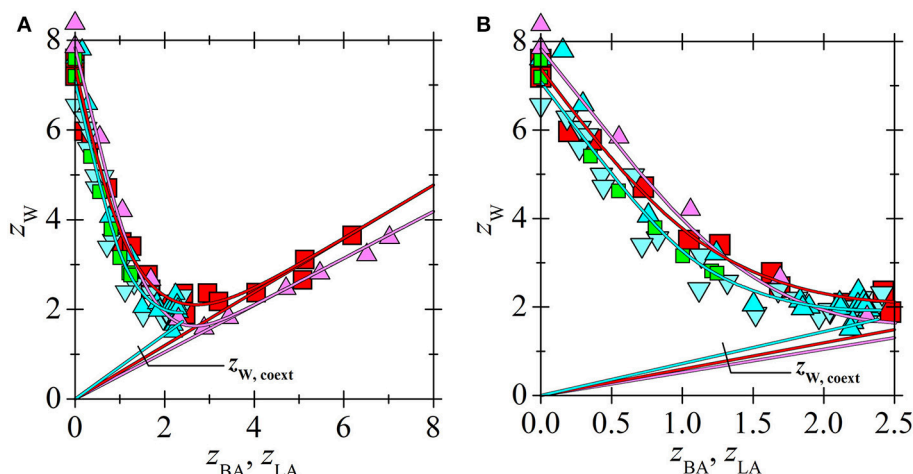
FIGURE 9 | Loading of phosphonium ILs by water vs. loading of IL by acid for the same systems as in **Figure 6**. (BA + undiluted $[C_{14}C_6C_6C_6P^+][BTMPP^-]$) (△) (Marták and Schlosser, 2016), (BA + undiluted $[C_{14}C_6C_6C_6P^+][C_9COO^-]$) (■) (Marták and Schlosser), (LA + undiluted $[C_{14}C_6C_6C_6P^+][BTMPP^-]$ (△) or 70 wt. % (▽) $[C_{14}C_6C_6C_6P^+][BTMPP^-]$ in dodecane) (Marták and Schlosser, 2007) and (LA + undiluted $[C_{14}C_6C_6C_6P^+][C_9COO^-]$) (■). Diluent was dodecane. For $z_{W,coext}$ see Equation (9). Lines correlate with the experimental data according to the model. **(B)** The extended view of the lower acid loading range of **(A)**.

k_1, $k_{1,\text{Wtot}}$, and $K_{W,\text{coext}}$ showed that complex $(1, 1)$ contains probably two or three water molecules associated with the IL and one water molecule can form a bridge between the complexes. In BA extraction with $[C_nC_nC_nC_1N^+][\text{BTMPP}^-]$, complex $(1, 1)$ contains about five or six water molecules associated with the IL and one with the acid.

A comparison of k_p and $k_{p,\text{Wtot}}$ also provides that complex $(2, 1)$ contains only water associated with acids in all tested systems except for BA with $[C_{14}C_6C_6C_6P^+][C_9\text{COO}^-]$, where constant k_2 (Equation 12, **Table 2**) has a non-zero value. The value of k_2 close to unity suggests one water molecule associated with IL. Hypothetical structure of the $(\text{BA} + [C_{14}C_6C_6C_6P^+][C_9\text{COO}^-])$ complex $(2, 1)$ is shown in **Figure 2** (Marták and Schlosser, unpublished manuscript).

CONCLUSIONS

New mechanism and a model of reactive extraction of carboxylic acids by hydrophobic ionic liquids (ILs) published in Marták and Schlosser (2016) was tested on a wider set of experimental data published earlier (Marták and Schlosser, 2007; Blahušiak et al., 2013) and new equilibrium data on liquid-liquid extraction of butyric and lactic acids (BA and LA) from aqueous solutions by two phosphonium and one ammonium ionic liquids (ILs). The model describes experimental data for five systems with a good fit which indicates its more general validity. It allows deeper understanding of regularities in carboxylic acid extraction by ILs.

The values of stability constants K_1 of acid-IL bond are one to three orders of magnitude higher compared to K_p with higher p. K_p decreases exponentially with the increasing p. Therefore, acid-IL bonds are stronger than acid-acid bonds. Differences in the stability of acid-IL bonds for BA and LA can be attributed to hydrophobic interactions which almost do not occur in LA extraction. Stability of acid-acid bonds with $p > 5$ are not sensitive to the IL structure.

The values of stability constants K_p of acid-IL bonds are more than one order of magnitude lower for LA compared to BA, despite LA being a stronger acid than BA. In addition to H-bonding, hydrophobic interactions of BA with IL contribute to the overall value of K_p which is lumped constant.

The loading of IL by LA exceeds the value of two only moderately so that the stability constant of acid-acid bonds between acids in complex $(3, 1)$ is very low. Due to the high polarity of LA it likely does not form complexes with $p > 3$. BA is more hydrophobic than LA so that it forms complexes with $p > 3$.

Substitution of an anion or cation in the IL influences the values of stability constants K_p, especially in BA extraction. The affinity of LA to both phosphonium ILs is almost the same since the values of appropriate stability constants are similar. BA has higher affinity to IL with $[\text{BTMPP}^-]$ which could be attributed to the more intensive van der Waals forces with the anion containing branched alkyls.

The correlation between the value of K_1 characterizing the affinity of acid to IL and extraction capability of IL is not proportional but more complex. For example, the value of K_1 for $[C_{14}C_6C_6C_6P^+][\text{BTMPP}^-]$ is higher than for $[C_{14}C_6C_6C_6P^+][C_9\text{COO}^-]$ but the extraction capability characterized by distribution coefficient is for $[C_{14}C_6C_6C_6P^+][C_9\text{COO}^-]$ higher due to its higher molarity.

The recovery yield of BA in short-path vacuum distillation from an extract with $[C_{14}C_6C_6C_6P^+][C_9\text{COO}^-]$ or $[C_nC_nC_nC_1N^+][\text{BTMPP}^-]$ can be higher compared to that with $[C_{14}C_6C_6C_6P^+][\text{BTMPP}^-]$ since the values of stability constant K_1 in BA extraction by these ILs are much lower. In this regeneration process free acid is recovered instead of acid salts in classical processes what is a great advantage.

DATA AVAILABILITY

The datasets generated for this study are available on request to the corresponding author.

AUTHOR CONTRIBUTIONS

JM and ŠS: model development and testing, manuscript writing; JM: measurement of equilibrium data.

FUNDING

REFERENCES

Blahušiak, M., Schlosser, Š., and Cvengroš, J. (2012). Simulation of a new regeneration process of solvents with ionic liquid by short-path distillation. *Separat. Purif. Technol.* 97, 186–194. doi: 10.1016/j.seppur.2012.03.010

Blahušiak, M., Schlosser, Š., Cvengroš, J., and Marták, J. (2011). New approach to regeneration of an ionic liquid containing solvent by molecular distillation. *Chem. Papers* 65, 603–607. doi: 10.2478/s11696-011-0053-y

Blahušiak, M., Schlosser, Š., and Marták, J. (2013). Extraction of butyric acid with a solvent containing ammonium ionic liquid. *Separat. Purif. Technol.* 119, 102–111. doi: 10.1016/j.seppur.2013.09.005

Bozell, J. J., and Petersen, G. R. (2010). Technology development for the production of biobased products from biorefinery carbohydrates-the US Department of Energy's "Top 10" revisited. *Green Chem.* 12, 539–554. doi: 10.1039/b922014c

Dawson, R. M. C., Elliott, D. C., Elliott, W. H., and Jones, K. M., (Eds.). (1986). *Data for Biochemical Research, 3rd Edn.* Oxford: Clarendon Press.

Hunt, P. A. (2017). Quantum chemical modeling of hydrogen bonding in ionic liquids. *Top. Curr. Chem.* 375:59. doi: 10.1007/s41061-017-0142-7

Marták, J., and Schlosser, Š. (2007). Extraction of lactic acid by phosphonium ionic liquids. *Separat. Purif. Technol.* 57, 483–494. doi: 10.1016/j.seppur.2006.09.013

Marták, J., and Schlosser, Š. (2008). Liquid-liquid equilibria of butyric acid for solvents containing a phosphonium ionic liquid. *Chem. Papers* 62, 42–50. doi: 10.2478/s11696-007-0077-5

Marták, J., and Schlosser, Š. (2016). New mechanism and model of butyric acid extraction by phosphonium ionic liquid. *J. Chem. Eng. Data* 61, 2979–2996. doi: 10.1021/acs.jced.5b01082

Marták, J., and Schlosser, Š. (2017). Density, viscosity, and structure of equilibrium solvent phases in butyric acid extraction by phosphonium ionic liquid. *J. Chem. Eng. Data* 62, 3025–3035. doi: 10.1021/acs.jced.7b00039

Partanen, J. I. (2004). Re-evaluation of stoichiometric dissociation constants from electrochemical cell data for propionic and n-butyric acids at (0 to 60) °C and for some other aliphatic carboxylic acids at (18 or 25)°C in aqueous sodium chloride solutions. *J. Chem. Eng. Data* 49, 394–406. doi: 10.1021/je030242p

Procházka, J., Heyberger, A., Bízek, V., Koušová, M., and Volaufová, E. (1994). Amine extraction of hydroxycarboxylic acids.2. *Comparison of equilibria for lactic, malic, and citric acids. Indust. Eng. Chem. Res.* 33, 1565–1573. doi: 10.1021/ie00030a016

Sabolová, E., Schlosser, S., and Marták, J. (2001). Liquid-liquid equilibria of butyric acid in water plus solvent systems with trioctylamine as extractant. *J. Chem. Eng Data* 46, 735–745. doi: 10.1021/je000323a

Schlosser, Š., and Blahušiak, M. (2011). Biorefinery for production of chemicals, energy and fuels. *Elektroenergetika* 4, 8–16. Available online at: https://eejournal.fei.tuke.sk/index.php/jeen/article/view/210/195

Schlosser, Š., Marták, J., and Blahušiak, M. (2018). Specific phenomena in carboxylic acids extraction by selected types of hydrophobic ionic liquids. *Chem. Papers* 72, 567–584. doi: 10.1007/s11696-017-0365-7

Sprakel, L. M. J., and Schuur, B. (2019). Solvent developments for liquid-liquid extraction of carboxylic acids in perspective. *Separat. Purif. Technol.* 211, 935–957. doi: 10.1016/j.seppur.2018.10.023

Wang, Y. L., Sarman, S., Gavatskth, S., Antzutkin, O. N., Rutland, M. W., and Laaksonen, A. (2015). Atomistic Insight into Tetraalkylphosphonium-Bis(oxalato)borate ionic liquid/water mixtures. *I. Local microscopic structure. J. Phys. Chem. B* 119, 5251–5264. doi: 10.1021/acs.jpcb.5b00667

Non-halogenated Ionic Liquid Dramatically Enhances Tribological Performance of Biodegradable Oils

Patrick Rohlmann [1†], Bulat Munavirov [1†], István Furó [2], Oleg Antzutkin [3], Mark William Rutland [2,4*] and Sergei Glavatskih [1,5]

[1] Machine Design, KTH Royal Institute of Technology, Stockholm, Sweden, [2] Department of Chemistry, KTH Royal Institute of Technology, Stockholm, Sweden, [3] Chemistry of Interfaces, Luleå University of Technology, Luleå, Sweden, [4] Surfaces, Processes and Formulation, RISE Research Institutes of Sweden, Stockholm, Sweden, [5] Department of Electrical Energy, Metals, Mechanical Constructions and Systems, Ghent University, Ghent, Belgium

It is demonstrated that a phosphonium orthoborate ionic liquid may serve as a wear reducing additive in biodegradable oils at steel-steel surfaces in the boundary lubrication regime. Tribological tests were performed in a ball-on-three plate configuration. A set of surface characterization techniques—SEM/EDS, FIB and white light interferometry were used to characterize surfaces following the tribotests and to observe the formation of any tribofilms. ^{11}B NMR was used to follow changes in the composition of the ionic-liquid-oil blends and to identify boron-containing decomposition products after the tribotests. The ionic liquid reduces the wear of steel surfaces by up to 92% compared to the neat oil at 90°C; it is shown that the reduction in wear can be correlated with the formation of boron enriched patches in the boundary films.

Keywords: biodegradable oil, ionic liquid, wear, friction, boundary lubrication, NMR

INTRODUCTION

The mounting pressure for a transition from mineral to biodegradable oils in many industrial applications implies a number of technological challenges. One of them is to identify the next generation of wear reducing additives. Most current anti-wear additives, such as zinc dialkyldithiophosphates (ZDDP) and tricresyl phosphates (TCP), were developed in late 1940s for use with mineral oils. Despite their good wear reducing properties for lubricated steel-steel contacts (Martin, 1999; Fujita and Spikes, 2004), there are environmental concerns regarding the use of ZDDP and TCP. ZDDP containing formulations tend to form zinc and phosphorus rich ashes in internal combustion engines, which poison catalysts and consequently worsen the exhaust quality (Xie et al., 2016). Similar problems are related to the use of TCP, which promotes formation of toxic species upon its decomposition at lubrication contacts at elevated temperatures (Michaelis, 2011; Ramsden, 2013), and it is intrinsically toxic in its pure form (Goldstein et al., 1988). Moreover, the wear reducing performance of these additives in biodegradable oils is rather moderate according to four-ball configuration mechanical tests for steel-steel contacts: it has been reported that vegetable oils with ZDDP additives result in only up to 13% reduction of the wear scar diameter when compared with the neat oil (Mahipal et al., 2014). Choi et al. have studied the performance of TCP in vegetable oils and reported up to 30% reduction in the wear scar diameters when compared to the neat oils (Choi et al., 1997).

A range of alternative additive approaches have been examined, including other phosphorus compounds (Johnson and Hils, 2013) and nanoparticles (Shahnazar et al., 2016). Hybrid approaches have also been used, for example when combining diamond nanoparticles with phosphoesters (Acharya et al., 2018). Another promising avenue to address the challenge is the use of ionic liquids (ILs). Knowledge of ILs in lubrication is rapidly expanding and the growing number of publications on ILs as neat lubricants or additives to oils (Zhou and Qu, 2017) is clear evidence of this. Ionic liquids also provide the opportunity to control the friction properties via the use of electric fields due to their ionic nature (Sweeney et al., 2012; Cooper et al., 2016)—so called tribotronics (Glavatskih and Höglund, 2008). However, a significant fraction of the published work is on halogenated ILs, which for historical reasons are commercially available, but are of limited interest to industry (Totten et al., 2003) due to environmental and health reasons. The "rear-view mirror" approach to the development of the ionic liquids field in general—that is to say the vicious circle of ionic liquid selection based on previous studies for benchmarking purposes—was highlighted at the recent Faraday Discussions on Ionic Liquids, and indeed formed the basis of the closing address (Jessop, 2018). A further key element concerning the "sustainability" of ionic liquids was a salutary reminder that one cannot consider the relative merits of ILs vs. their conventional counterparts in their application alone, but that the environmental impact of their manufacture should also be compared. Successful candidates for industrial applications in the field of tribology (the study of friction, lubrication, and wear) need to be non-halogenated ILs engineered to meet the requirements of the lubrication industry (Shah et al., 2011). The choice and structure of cations and anions are dictated by the application specifics such as the materials to be lubricated, the contact geometry and pressure, as well as the speed, ambient conditions and type of movement (sliding/rolling, reciprocating/continuous). An example of an exception to the use of halogenated ILs is the work of Kronberger et al. They investigated tribological performance of a number of neat ILs and IL solutions in glycerol (Kronberger et al., 2012) using sulfur based anions [sulfates (Pejakovic et al., 2012) and sulphonates] and nitrogen based cations (n-alkylammonium, cholines, pyrrolidinium). In some cases both friction and wear were reduced compared to neat glycerol, with neat ILs and solutions performing similarly. XPS analysis of the worn surfaces suggest that the performance is enhanced by formation of iron sulfide tribolayers on the metal surfaces. The same authors have also pointed out that miscibility of an IL with a carrier fluid is crucial for their deployment (Kronberger et al., 2014).

Xie et al. have recently compared ZDDP with phosphonium based ionic liquids (ILs) and concluded that ILs have less impact on the functionality of the catalysts (Xie et al., 2016). Phosphonium cations are known for their wear reducing performance and the anti-wear boundary films produced on the lubricated surfaces have been shown to contain phosphorus (Westerholt et al., 2015). A corrosion inhibition effect of phosphonium cations has also been observed (Kondo et al., 2012). It has also been reported that ILs containing phosphorus in both anion and cation are efficient anti-wear additives to non-polar oils (Qu et al., 2015). An enhancement in the anti-wear

FIGURE 1 | The structure of the C8-C6 monoester, hexyl-octanoate, denoted in the text as ME. Red, O; gray, C; white, H.
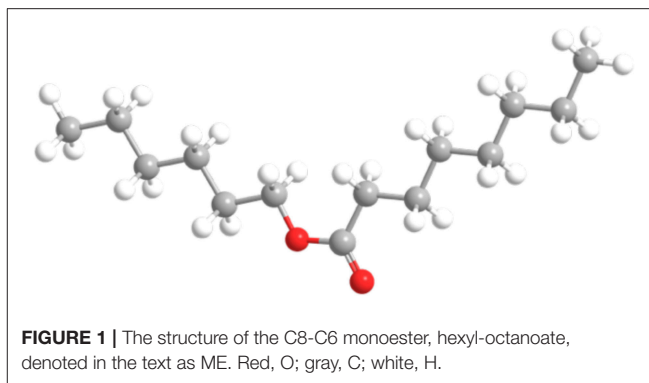
performance of phosphonium ILs as additives to a mineral oil was achieved by adding a borate ester (Sharma et al., 2016) to the oil blend. Boron is known to form friction and wear reducing compounds in lubricated contacts (Shah et al., 2013) and ILs consisting of phosphorus and boron based ions have thus been the target of synthesis (Shah et al., 2011). Such ILs have formed the focus of a range of nanotribology and model studies (Li et al., 2016; Cooper et al., 2017; Cowie et al., 2017) confirming this promise. In this work, boron and phosphorus are incorporated in a single IL, as the anion and cation respectively, trihexyltetradecylphosphonium bis(mandelato)borate (P-BMB), which is then used as an additive to biodegradable oils. The goal is to study how the IL additive improves oil lubrication performance on steel surfaces, and to relate this to the additive properties, and to any antiwear films generated on the surfaces.

MATERIALS AND METHODS

P-BMB was synthesized and characterized as previously described (Shah et al., 2011). The higher polarity of biodegradable oils compared to conventional mineral oils increases their affinity for the surface and may also have implications for the transport properties of the IL. Two representative biodegradable oils were selected for the tests. Oil soluble polyalkylene glycol (OPAG), UCON OSP46 (Dow Chemicals inherently biodegradable; more than 35% during 28 days), and a monoester (ME), Estisol 240 (Estichem, readily biodegradable; more than 60% during 28 days), were used in the lubrication tests. The exact chemical structure of OPAG is undisclosed which underlines some of the challenges of performing relevant tribological research from a chemical perspective. Estisol 240 is a C8-C6 monoester, hexyl-octanoate with a structure shown in **Figure 1** and has a non-polarity index of 32. To ensure homogeneous blends, the blends were ultrasonicated for at least 60 min at 50°C. **Table S1** shows viscosities of IL, oils and the blends of oils with IL. Viscosities were measured with a HR-2 rheometer, TA Instruments.

Solubility Tests of Ionic Liquids

Several IL-oil mixtures were prepared with IL concentrations varied within 0–20 wt.%. After having been thoroughly mixed, the samples were centrifuged at a speed of 6,500 rpm. An equal amount of supernatant was then carefully taken from

all mixtures, centrifuged and placed into separate NMR tubes. Quantitative ^{31}P and ^{1}H NMR were run on the resultant samples of the ME and OPAG blends. Obtained NMR spectra were processed: "0" and "1" order phase corrections were applied; the baseline was corrected using a first order polynomial correction. After that spectral regions corresponding to the IL liquid were integrated. The resultant integral values were normalized according to the integral value obtained from the sample with an IL concentration of 1 wt%. The initial concentrations were determined from the actual IL and oil weights used before the centrifugation.

Test Procedure

The same rheometer that was used for measuring lubricant viscosities was utilized for the lubrication tests. A set-up with a ball-on-three-plates configuration as shown in **Figure S1** was installed. (This setup allows high contact pressures, continuous sliding—typical for lubricated contacts, faster lubricant consumption and the plates are compatible with SEM analysis). The ball was pressed against the plates with an initial maximum Hertzian contact pressure of 1.11 GPa. This load, corresponding to 21 N per contact, was selected to place the contact in the boundary regime, for which this is an appropriate pressure; similar contact pressures have been used in related publications. 1.13 GPa was employed to study neat IL lubrication of steel (Garcia et al., 2014), while 1.0 GPa maximum pressure was used in two studies of IL as additives to glycerol (Kronberger et al., 2012; Pejakovic et al., 2012; Garcia et al., 2014). Each test was run with a sliding speed of 0.2 ms^{-1} for a sliding distance of 2000 m. (This sliding speed and distance provide a balance between experimental time and a suitable degree of wear). Normal and friction forces were recorded with an acquisition frequency of 1 Hz. Friction coefficients during 500 m of sliding were then averaged. Oil bath temperature, set to 90°C, was regulated by a Peltier element. A test run required 1.2 ml of lubricant and was repeated 4 times. Relative humidity, measured during the tests, was 40 ± 5% at an ambient temperature of 22 ± 2°C. The ⌀12.7 mm steel balls (AISI 52100, Rotera Kullager AB, Täby, Sweden), used in the lubrication tests, had a measured roughness of R$_a$ = 0.074 ± 0.006 μm and a hardness of 60–67 HRC (Rockwell Hardness, according to the supplier). The mating surface, AISI 52100 steel plates, had a measured hardness of 64 HRC and roughness of R$_a$ = 0.142 ± 0.028 μm. The roughness was measured with a Taylor Hobsen PGI 800 Profilometer from Talysurf. The hardness was determined by measuring indents with an optical microscope from Nikon (MM-60/L3). The plates were cut from the rolling bearing discs and had the following dimensions: 3 mm in thickness, 6 mm in width and 7 mm in length. Before each test, balls and plates were cleaned in several steps. First, they were ultrasonicated in acetone for 30 min and then dried under a dry air stream. Next, they were ultrasonicated in isopropanol for 30 min and finally dried by dry air stream again. After the tribological experiments balls and plates were rinsed with ethanol and ultrasonicated twice (30 min each time), using fresh heptane each time. Then they were dried under a dry air flow and placed in a vacuum oven for 3 days at 50°C.

Wear, Interfacial Film, and Oil Analysis

The wear volume of the plates was measured by using a contact profilometer (Taylor Hobson PGI800) and an optical profiler (Zygo7300). The average wear volume W_v was calculated for each set of three plates and used to obtain the wear coefficient:

$$k = W_v/(F_N \times s), \qquad (1)$$

where F_N is the normal contact force on a single plate and s is sliding distance (Archard, 1953).

A Scanning Electron Microscope (SEM), JEOL 7800F, was employed to take images of the wear tracks at a beam energy of 10 kV. Distributions of chemical elements for selected points inside and outside the wear tracks were obtained by using an Energy Dispersive X-ray Spectroscopy (EDS), Bruker Quantax system.

A focused ion beam (FIB-SEM FEI NOVA 600) was used to create cross section cuts through the boundary film. Prior to each cut EDS spectra were recorded with 10 kV, followed by a deposition of a thin layer ($\sim$500 nm) of platinum on top of the investigated area (100 pA current, 30 kV voltage). Thereafter, the focused ion beam with a beam current of 3 nA and 30 kV voltage was utilized to create a wedge cut-out with a maximum depth of 4 μm at the edge of cross section. SEM images of the cut-outs were recorded with a 5 keV beam voltage.

^{11}B NMR spectra of the oil blends before and after the lubrication tests were recorded at 160.5 MHz on a Bruker Avance III NMR spectrometer. A standard Broad Band probe from Bruker was used. Spectral width was set to 64 kHz and all NMR measurements were performed at 60°C. A 50 Hz exponential filter was applied to all spectra to reduce the noise level.

RESULTS AND DISCUSSION

The normalized spectral integral values obtained for the blends prepared at room temperature are shown in **Figure 2**. The IL NMR integral values (corresponding to the amount of IL in the supernatants) for the ME blends are proportional to the initial concentrations of IL in a mixture. For the OPAG blends, a plateau of the NMR integral values is observed for the initial concentrations higher than 5 wt%. Addition of IL above this concentration to OPAG resulted in the precipitation of the added IL during the centrifugation stage. It is thus concluded that the IL is soluble in ME within the concentration range studied, whereas it has a limited solubility (up to 5 wt% at RT) in OPAG.

The self-diffusion coefficients of the ions of the IL in oils were approximately one order of magnitude higher relative to their values in neat IL. Thus, the distribution of IL in the ME is considered stable and homogeneous and no liquid droplets exist.

Blends of 5 wt% IL with ME and OPAG were thus used for the lubrication tests (the concentrations of phosphorus and boron in the blends were 1,948 and 680 ppm, respectively). The results for all samples are shown in **Figure 3**. In the beginning of each test the running-in process resulted in a somewhat larger variation of the coefficient of friction. This variation decreased with time in all cases. However, for ME + IL more unstable friction returned toward the end of the test. Particularly after running-in it is clear that the OPAG+IL friction coefficients are

uniformly lower than for OPAG, by ~10% The full data sets are shown in **Figure S2**. The fact that the friction coefficient values are similar, despite a 6-fold difference in viscosity between ME and OPAG samples at 90°C strongly indicates that the contact indeed operates in the targeted boundary lubrication regime, as opposed to "full film lubrication," whereby a liquid film separates the surfaces. Since hydrodynamic effects are insignificant in boundary lubrication, it is concluded that surface protection is achieved through the interactions of oil molecules and additives with the lubricated surfaces.

Monoesters are recognized as surface active compounds and are often used as friction modifiers with an anti-wear functionality (Spikes, 2015). Consequently, in these experiments neat ME provided ~5 times lower wear compared to OPAG. Similar trends for ME and polyglycols have previously been reported (Chen et al., 2009). The wear coefficients are presented

in **Figure 4**. It can be seen that addition of IL resulted in significantly lower wear. The reduction was much larger (92%) for the OPAG/IL blend, reflecting the fact that OPAG has poorer intrinsic wear protection than ME. Optical images of the wear scars are shown in **Figure 5**. The wear scars attained with the neat oils are deep and are of a non-circular shape (see the ESI for details). Compared to the neat oils, the blends with IL produced much smaller and shallower wear scars. Scratches from the manufacturing process (polishing) were still visible on the plate surfaces after the tests. The depth of the scratches was similar to the wear scar depth for the oil/IL blends, emphasizing the mildness of the wear.

Biodegradable oils are designed to degrade if they leak into the environment but to remain stable in the lubrication system. However, due to high thermo-mechanical stresses in the lubricated interface, the oil *may* degrade in the contact producing compounds that can also be reactive toward ions, thus accelerating consumption of the IL and shortening lubricant service life. Note that reactivity can also have a positive effect
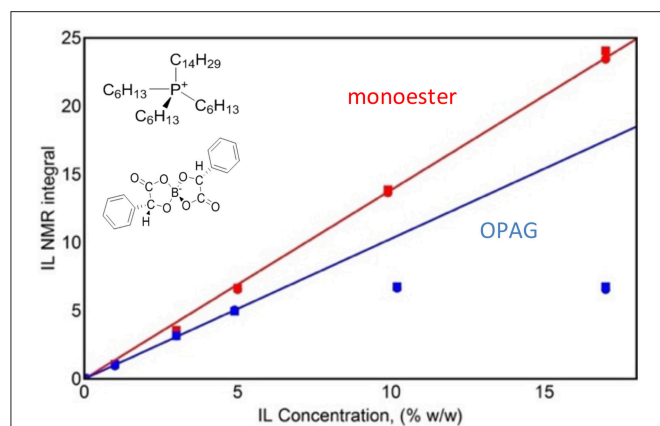
FIGURE 2 | IL NMR integral value for supernatants of centrifuged mixtures as a function of the initial concentration. Circles are for ^{31}P NMR and squares for ^{1}H NMR. Solid lines are linear fits to the low-concentration experimental data.
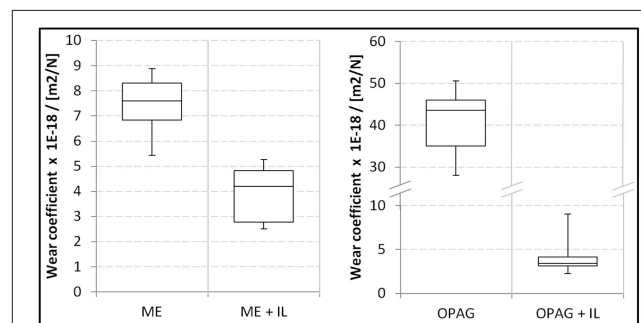
FIGURE 4 | Wear coefficients for the plates lubricated by ME, OPAG and their blends with IL. Note that the axis for OPAG has been broken since the wear for the neat oil was much larger.
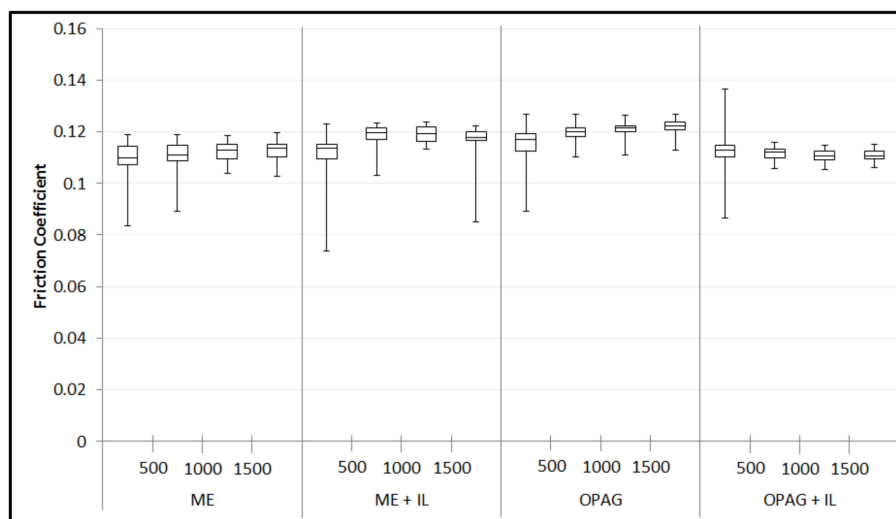
FIGURE 3 | Average friction coefficients over a sliding distance of 2,000 m. The data is divided into four intervals of the sliding distance to allow any distance or time dependent phenomena to be observed.
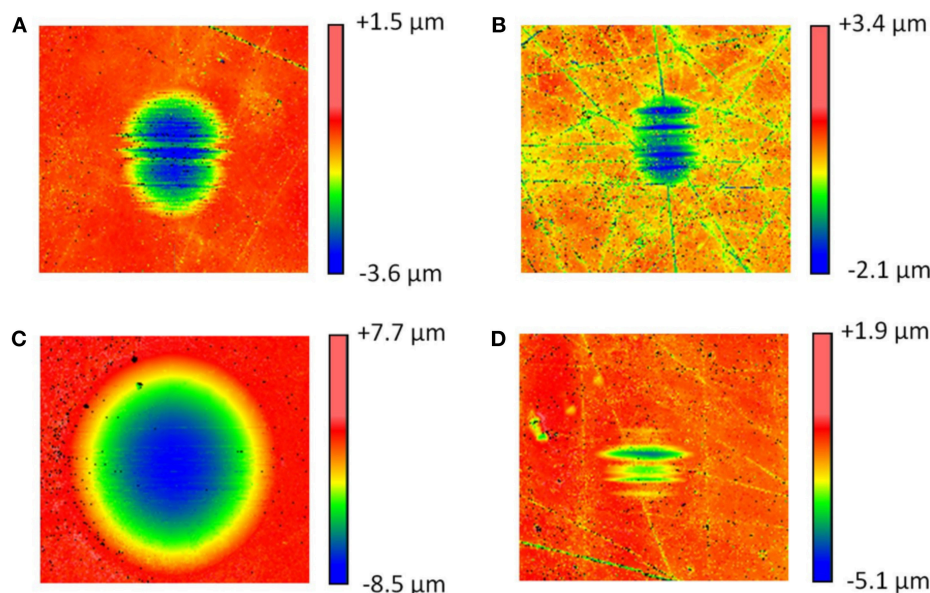
FIGURE 5 | Optical images (1 × 1 mm) of the wear scars for **(A)** ME, **(B)** ME + IL, **(C)** OPAG, **(D)** OPAG + IL.

if it contributes to the formation of stable, so called "antiwear" films on the surfaces in contact. Consumption of the IL in the blends was studied with NMR spectroscopy. The ^{11}B NMR spectra of ME/IL and OPAG/IL blends taken before and after the lubrication tests were compared. The spectra before the tests showed a single resonance line, **Figure 6**, corresponding to the neat IL but this changed after the tests. Additional spectral lines appeared, indicating the orthoborate anion reacting to yield boron in a new chemical environment. The overall signal intensity (obtained by integration between −100 and 100 ppm) also decreased, relative to the initial (before the lubrication tests) situation. Those relative values are shown in percent in **Figure 6**. This finding indicates a depletion of soluble boron-containing (including the original orthoborate anions) species from the oil blends during the lubrication tests.

This effect is particularly strong for the ME blend where, in addition, hardly any of the boron-containing solutes are in the form of the original orthoborate species (as indicated by the near disappearance of the original resonance line at ca. 11 ppm). For the OPAG blend, neither the depletion nor the chemical reaction is as pronounced. Since the amount of boron in the oil blends decreased during the lubrication tests, it can be assumed that boron accumulated in the boundary films.

To investigate the veracity of this assumption, both the unworn and worn steel surfaces were analyzed using SEM-EDS. SEM images (insets in **Figures 7**, **8**) revealed a patchy boundary film structure inside the wear track for both oil blends. The patches appeared to be larger in the case of OPAG/IL compared to the ME/IL blend. EDS spectra were recorded at a number of points located within the wear scar to probe the elemental composition of the patches. Reference EDS spectra were recorded at points located on the unworn surface outside
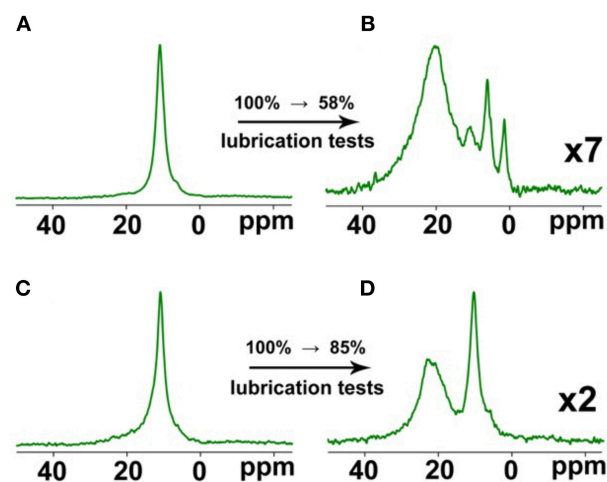
FIGURE 6 | ^{11}B NMR spectra and changes in the relative values of the spectral integral intensities for the ME + IL **(A,B)** and OPAG + IL (**C,D** blends). Intensities of the spectra recorded after the lubrication tests are amplified.

the wear scar. Point positions are marked by numbers in the insets in **Figures 7**, **8**. Spectra for the balls are not shown as no phosphorus or boron were detected in the wear scars on the ball surfaces. This is reasonable considering the less severe tribological conditions experienced by the ball surface due to the shorter contact time (see **Figure S1**).

The unworn plate surface contained iron, carbon, oxygen and traces of aluminum. Aluminum originates from the grinding and polishing process. Almost no aluminum was detected inside the wear scar, indicating that it was located within the very top
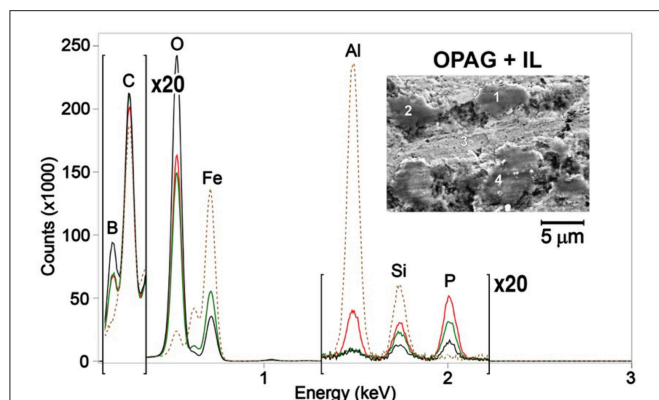
FIGURE 7 | EDS spectra for ME/IL obtained at several points as shown in the inserts. Spectra color codes are for different points: 1—red, 2—blue, 3—green, 4—black. The brown dashed line is for the unworn surface.
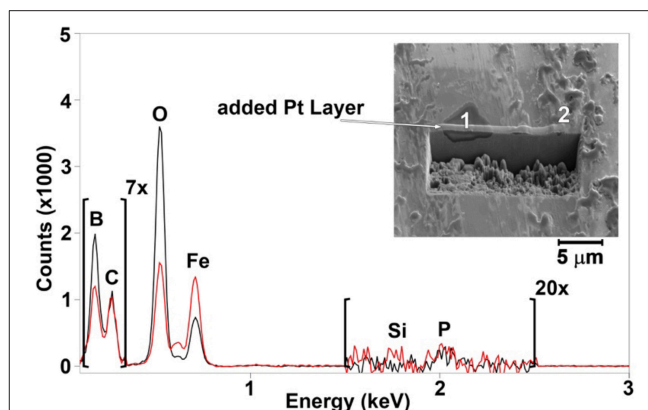

FIGURE 9 | EDS spectra for points 1 (in black) and 2 (in red) and the corresponding FIB cross sectional cut of a patch formed on the surface lubricated by the ME/IL blend.
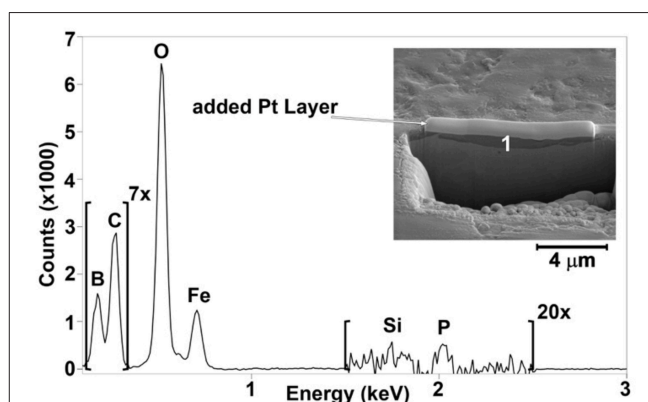

FIGURE 8 | EDS spectra for OPAG/IL obtained at several points as shown in the inserts. Spectra color codes are for different points: 1—red, 2—blue, 3—green, 4—black. The brown dashed line is for the unworn surface.

FIGURE 10 | EDS spectrum for point 1 in the FIB cross sectional cut of a patch formed on the surface lubricated by the OPAG/IL blend.

surface layer and was removed by rubbing during the lubrication tests. The worn surfaces also showed an increased amount of oxygen and a decreased amount of iron. The lower intensity of the iron peak indicates that the boundary film was formed on top of the metal surface during the rubbing process. EDS spectra for a majority of the points taken in the oil/IL sample boundary films, formed by the oil/IL blends, showed the presence of both boron and phosphorus. The presence of boron enriched patches and the reduced boron concentration seen by ^{11}B NMR appears to confirm that boron in the boundary films originated from the IL "consumed" during the lubrication tests.

It should be remembered however, that physically adsorbed IL at the lubricated surface can also contribute to the observations. The mechanism of boron mobility toward the lubricated surfaces and its surface activity includes a combination of processes. Since lubrication of steel can result in a locally positive surface charge (exo-electron emission; Nakayama et al., 1992), anions will consequently be preferentially attracted to the surface. It has been demonstrated for the same OPAG/IL mixture that such an electro-diffusion process is indeed controlled by the surface

charge (Hjalmarsson et al., under review). Thermomechanical stresses cause the anions to decompose and it is thought that decomposition starts with the cleavage of a B-O bond, which simulations demonstrate to be energetically most vulnerable (Golets et al., 2016). Boron may contribute to formation of B_2O_3 and BPO_4 while phosphorus may contribute to formation of phosphates and polyphosphates (Sharma et al., 2016). These compounds are known to provide wear resistant boundary films (McFadden et al., 1997; Shah et al., 2013). Compared to the case of borate ester addition to the IL/oil blend (Sharma et al., 2016), the use of orthoborate anions provides more boron in the boundary films enhancing the anti-wear performance. FIB-EDS was used to probe the thickness and composition of the selected patches, particularly since interfacially bound, unreacted IL might contribute to the EDS spectra in **Figures 7**, **8**.

Figure 9 shows results for the ME/IL blend. The boron containing patch is rather wide and thick. Judging by the peak intensity, the boron content is much higher than the phosphorus content. A cross sectional cut of the patch reveals a uniform structure of up to 1,600 nm in thickness, probably composed

largely of iron oxides, B_2O_3 and HBO_2-III (Sharma et al., 2016; Spadaro et al., 2018). Similar observations can be made for the patches formed by the OPAG/IL blend. **Figure 10** illustrates that the patch is once again enriched in boron with a smaller amount of phosphorus. Furthermore, the cross section of the patch reveals a homogeneous structure which is similar to, but much thinner than (800 nm), that formed by the ME/IL blend. This agrees well with the boron consumption trends revealed by the ^{11}B NMR results. Hence, it can be concluded that the protective boundary films are similar in nature regardless of the base oil in which the IL was dissolved.

CONCLUSION

The choice of IL as "next generation additive" to polar oils appears to be well-justified. It is clear that this non-halogenated IL forms stable, wear-reducing, boundary films in polar biodegradable oils. Importantly, it is the bis(mandelato)borate anion, rather than (as generally assumed) the tetraalkylphosphonium cation, which appears to answer for the majority of the composition of the boundary film.

The wear reduction is dramatic compared to the unformulated base oils in both cases, but there is a very strong dependence on the oil type, at least at the single, relevant temperature used here. The monoester performs better as a lubricant than the polyalkylglycol in the absence of IL, but this behavior is essentially reversed when IL is used as additive. In both cases reactions occur

and wear films are formed but the wear film is much thinner in the polyalkylglycol than in the monoester and much less IL is consumed.

The study shows that the fields of chemistry and tribology are inextricably linked and provides a clear path forward for the chemical design of IL based anti-wear additives in synergy with the biodegradable oil. The choice of anion is as important as that of the cation and should be matched to both the cation and the oil.

AUTHOR CONTRIBUTIONS

PR and BM performed and analyzed experiments. SG, OA, IF, and MR conceived the project. All authors contributed to the interpretation and writing of the manuscript.

ACKNOWLEDGMENTS

SUPPLEMENTARY MATERIAL

The Supplementary Material for this article can be found online at: https://www.frontiersin.org/articles/10.3389/fchem. 2019.00098/full#supplementary-material

REFERENCES

Acharya, B., Avva, K. S., Thapa, B., Pardue, T. P., and Krim, J. (2018). Synergistic effect of nanodiamond and phosphate ester anti-wear additive blends. *Lubricants* 18:56. doi: 10.3390/lubricants6020056

Archard, J. F. (1953). Contact and rubbing of flat surfaces. *J. Appl. Phys.* 24, 981–988. doi: 10.1063/1.1721448

Chen, C., Bosse, H., and Deters, L. (2009). Effects of various base oils and additives on the tribological behaviour of lubricated aluminium- on-aluminium and steel-on-aluminium contacts. *Proc. Inst. Mech. Eng. J.* 223, 571–580. doi: 10.1243/13506501JET511

Choi, U. S., Ahn, B. G., Kwon, O. K., and Chun, Y. J. (1997). Tribological behavior of some antiwear additives in vegetable oils. *Tribol. Int.* 30, 677–683. doi: 10.1016/S0301-679X(97)00039-X

Cooper, P. K., Li, H., Rutland, M. W., Webber, G. B., and Atkin, R. (2016). Tribotronic control of friction in oil-based lubricants with ionic liquid additives. *Phys. Chemist. Chem. Phys.* 18, 23657–23662. doi: 10.1039/C6CP04405K

Cooper, P. K., Wear, C. J., Li, H., and Atkin, R. (2017). Ionic liquid lubrication of stainless steel: friction is inversely correlated with interfacial liquid nanostructure. *ACS Sust. Chem. Eng.* 5, 11737–11743. doi: 10.1021/acssuschemeng.7b03262

Cowie, S., Cooper, P. K., Atkin, R., and Li, H. (2017). Nanotribology of ionic liquids as lubricant additives for alumina surfaces. *J. Phys. Chem. C* 121, 28348–28353. doi: 10.1021/acs.jpcc.7b09879

Fujita, H., and Spikes, H. A. (2004). The formation of zinc dithiophosphate antiwear films. *Proc. Instit. Mech. Eng. J.* 218, 265–277. doi: 10.1243/1350650041762677

Garcia, A., Gonzalez, R., Battez, A. H., Viesca, J. L., Monge, R., Fernandez-Gonzalez, A., et al. (2014). Ionic liquids as a neat lubricant applied to steel-steel contacts. *Tribol. Int.* 72, 42–50. doi: 10.1016/j.triboint.2013.12.007

Glavatskih, S., and Höglund, E. (2008). Tribotronics: towards active tribology. *Tribol. Int.* 41, 934–939. doi: 10.1016/j.triboint.2007.03.001

Goldstein, D. A., Mcguigan, M. A., and Ripley, B. D. (1988). Acute tricresylphosphate intoxication in childhood. *Human Exp. Toxicol.* 7, 179–182. doi: 10.1177/096032718800700213

Golets, M., Shimpi, M. R., Wang, Y. L., Antzutkin, O. N., Glavatskih, S., and Laaksonen, A. (2016). Understanding the thermal decomposition mechanism of a halogen-free chelated orthoborate-based ionic liquid: a combined computational and experimental study. *Phys. Chem. Chem. Phys.* 18, 22458–22466. doi: 10.1039/C6CP03191A

Jessop, P. G. (2018). Fundamental properties and practical applications of ionic liquids: concluding remarks. *Faraday Discuss.* 206, 587–601. doi: 10.1039/C7FD90090B

Johnson, D., and Hils, J. (2013). Phosphate esters, thiophosphate esters and metal thiophosphates as lubricant additives. *Lubricants* 18, 132–148. doi: 10.3390/lubricants1040132

Kondo, Y., Yagi, S., Koyama, T., Tsuboi, R., and Sasaki, S. (2012). Lubricity and corrosiveness of ionic liquids for steel-on-steel sliding contacts. *Proc. Instit. Mech. Eng. J.* 226, 991–1006. doi: 10.1177/1350650112456127

Kronberger, M., Pagano, F., Pejakovic, V., Igartua, A., Urbistondo, E., and Kalin, M. (2014). Miscibility and tribological investigations of ionic liquids in biodegradable esters. *Lubricat. Sci.* 26, 463–487. doi: 10.1002/ls.1274

Kronberger, M., Pejakovic, V., Gabler, C., and Kalin, M. (2012). How anion and cation species influence the tribology of a green lubricant based on ionic liquids. *Proc. Instit. Mech. Eng. J.* 226, 933–951. doi: 10.1177/1350650112459012

Li, H., Somers, A. E., Rutland, M. W., Howlett, P. C., and Atkin, R. (2016). Combined nano- and macrotribology studies of titania lubrication using the oil-ionic liquid mixtures. *ACS Sust. Chem. Eng.* 4, 5005–5012. doi: 10.1021/acssuschemeng.6b01383

Mahipal, D., and Krishnanunni, P., Mohammed Rafeekh, P., and Jayadas, N. H. (2014). Analysis of lubrication properties of zinc-dialkyl-dithio-phosphate

(ZDDP) additive on Karanja oil (Pongamia pinnatta) as a green lubricant. *Int. J. Eng. Res.* 3, 494–496. doi: 10.17950/ijer/v3s8/804

Martin, J. M. (1999). Antiwear mechanisms of zinc dithiophosphate: a chemical hardness approach. *Tribol. Lett.* 6, 1–8. doi: 10.1023/A:1019191019134

McFadden, C., Soto, C., and Spencer, N. D. (1997). Adsorption and surface chemistry in tribology. *Tribol. Int.* 30, 881–888. doi: 10.1016/S0301-679X(97)00075-3

Michaelis, S. (2011). Contaminated aircraft cabin air. *J. Biol. Phys. Chem,* 11, 132–145. doi: 10.4024/41111/11-4-abs1.jbpc.11.04

Nakayama, K., Suzuki, N., and Hashimoto, H. (1992). Triboemission of charged particles and photons from solid surfaces during frictional damage. *J. Phys. D Appl. Phys.* 25, 303–308. doi: 10.1088/0022-3727/25/2/027

Pejakovic, V., Kronberger, M., Mahrova, M., Vilas, M., Tojo, E., and Kalin, M. (2012). Pyrrolidinium sulfate and ammonium sulfate ionic liquids as lubricant additives for steel/steel contact lubrication. *Proc. Instit. Mech. Eng. J* 226, 923–932. doi: 10.1177/1350650112448978

Qu, J., Barnhill, W. C., Luo, H., Meyer, H. M., Leonard, D. N., Landauer, A. K., et al. (2015). Synergistic effects between phosphonium-alkylphosphate ionic liquids and zinc dialkyldithiophosphate (ZDDP) as lubricant additives. *Adv. Mater.* 27, 4767–4774. doi: 10.1002/adma.201502037

Ramsden, J. J. (2013). On the proportion of ortho isomers in the tricresyl phosphates contained in jet oil. *J. Biol. Phys. Chem* 13, 69–72. doi: 10.4024/03RA13L.jbpc.13.02

Shah, F. U., Glavatskih, S., and Antzutkin, O. N. (2013). Boron in tribology: from borates to ionic liquids. *Tribol. Lett.* 51, 281–301. doi: 10.1007/s11249-013-0181-3

Shah, F. U., Glavatskih, S., Macfarlane, D. R., Somers, A., Forsyth, M., and Antzutkin, O. N. (2011). Novel halogen-free chelated orthoborate-phosphonium ionic liquids: synthesis and tribophysical properties. *Phys. Chem. Chem. Phys.* 13, 12865–12873. doi: 10.1039/c1cp21139k

Shahnazar, S., Bagheri, S., and Abd Hamid, S. B. (2016). Enhancing lubricant properties by nanoparticle additives. *Int. J. Hydrogen Energy* 41, 3153–3170. doi: 10.1016/j.ijhydene.2015.12.040

Sharma, V., Doerr, N., Erdemir, A., and Aswath, P. B. (2016). Interaction of phosphonium ionic liquids with borate esters at tribological interfaces. *RSC Adv.* 6, 53148–53161. doi: 10.1039/C6RA11822D

Spadaro, F., Rossi, A., Ramakrishna, S. N., Lainé, E., Woodward, P., and Spencer, N. D. (2018). Understanding complex tribofilms by means of H_3BO_3-B_2O_3 model glasses. *Langmuir* 34, 2219–2234. doi: 10.1021/acs.langmuir.7b01795

Spikes, H. (2015). Friction modifier additives. *Tribol. Lett.* 60:5. doi: 10.1007/s11249-015-0589-z

Sweeney, J., Hausen, F., Hayes, R., Webber, G. B., Endres, F., Rutland, M. W., et al. (2012). Control of nanoscale friction on gold in an ionic liquid by a potential-dependent ionic lubricant layer. *Phys. Rev. Lett.* 109:155502. doi: 10.1103/PhysRevLett.109.155502

Totten, G. E., Shah, R. J., and Westbrook, S. R. (2003). *Fuels and Lubricants Handbook: Technology, Properties, Performance, and Testing.* Glen Bumie, MD: ASTM International.

Westerholt, A., Weschta, M., Bösmann, A., Tremmel, S., Korth, Y., Wolf, M., et al. (2015). Halide-free synthesis and tribological performance of oil-miscible ammonium and phosphonium-based ionic liquids. *ACS Sust. Chem. Eng.* 3, 797–808. doi: 10.1021/sc500517n

Xie, C., Toops, T. J., Lance, M. J., Qu, J., Viola, M. B., Lewis, S. A., et al. (2016). Impact of lubricant additives on the physicochemical properties and activity of three-way catalysts. *Catalysts* 6:54. doi: 10.3390/catal6040054

Zhou, Y., and Qu, J. (2017). Ionic liquids as lubricant additives – a review. *ACS Appl. Mater. Interfaces* 9, 3209–3222. doi: 10.1021/acsami.6b12489

Theoretical Elucidation of β-O-4 Bond Cleavage of Lignin Model Compound Promoted by Sulfonic Acid-Functionalized Ionic Liquid

Yaqin Zhang, Feng Huo, Yanlei Wang, Yu Xia, Xin Tan, Suojiang Zhang and Hongyan He*

Beijing Key Laboratory of Ionic Liquids Clean Process, CAS Key Laboratory of Green Process and Engineering, State Key Laboratory of Multiphase Complex Systems, Institute of Process Engineering, Chinese Academy of Sciences, Beijing, China

While the depolymerization of lignin to chemicals catalyzed by ionic liquids has attracted significant attention, the relevant molecular mechanism, especially the cleavage of specific bonds related to efficient depolymerization, still needs to be deeply understood for the complexity of this natural aromatic polymer. This work presents a detailed understanding of the cleavage of the most abundant β-O-4 bond in the model system, guaiacylglycerol β-guaiacyl ether, by a Brønsted acidic IL (1-methyl-3-(propyl-3-sulfonate) imidazolium bisulfate ([C_3SO_3Hmim][HSO_4]) using density functional theory calculation and molecular dynamics simulation. It has been found that [C_3SO_3Hmim][HSO_4] generates zwitterion/H_2SO_4 *via* proton transfer with an energy barrier of 0.38 kcal/mol, which plays a dominant role in the lignin depolymerization process. Subsequently, the reaction can be carried out *via* three potential pathways, including (1) the dehydration of α-C-OH, (2) dehydration of γ-C-OH, and (3) the protonation of β-O. The electrophilic attack of H_2SO_4 and the hydrogen-bonding interaction between GG and zwitterion are the two most important factors to promote the depolymerization reaction. In all steps, the dehydration of α-C-OH route is computed to be favored for the experiment. The relatively higher energy barrier for β-O-4 bond dissociation among these reaction steps is attributed to the hindrance of the self-assembled clusters of GG in the mixed system. Further, the dense distribution of H13([C_3SO_3Hmim]) surrounding O21(GG), indicated by sharp peaks in RDFs, reveals that -SO_3H in cations plays a substantial role in solvating lignin. Hopefully, this work will demonstrate new insights into lignin depolymerization by functionalized ILs in biomass conversion chemistry.

Keywords: lignin, ionic liquid, DFT, molecular dynamics, β-O-4 bond, reaction mechanism

INTRODUCTION

Lignin, a main aromatic component of lignocellulosic biomass accounting for 18–40 wt% of dry wood (Amen-Chen et al., 2001; Zhang et al., 2019), is an alternative feedstock to the depleting petroleum-based sources owing to its abundant reserves, renewability and low cost (Zakzeski et al., 2010). The basic building blocks of lignin are coniferyl, sinapyl, and *p*-coumaryl alcohols which

are mostly linked by β-O-4, 4-O-5, α-O-4, β-5, β-1, and 5-5 bonds to form a three-dimensional amorphous and irregular structure. The dominate bond between monomers is the β-O-4 ether bond, representing ∼50% of all linkages (Chatel and Rogers, 2014), and the main linkage is the key objective and the major challenge of most utilization studies (Jia et al., 2010a,b; Younker et al., 2011; Lu et al., 2016). Other bonds are becoming increasingly difficult to degrade during traditional processing methods because of strong carbon-carbon bond formation (Upton and Kasko, 2016). Owing to its complex structure, lignin is resistant to degradation, thus, it is generally burned to produce electricity after the bioethanol production (Zakzeski et al., 2010). Therefore, preparation of fine aromatic chemicals from lignin residues by target cleavage of β-O-4 bond is a promising strategy. Recently, efforts have been devoted to the decomposition of β-O-4 ether bond by solvolysis (Ma et al., 2014; Deepa and Dhepe, 2015; Katahira et al., 2016), oxidation (Prado et al., 2016), reduction (Shuai et al., 2016), pyrolysis (Jollet et al., 2014) etc. However, these technologies need to conduct under extreme reaction conditions to achieve degradation of lignin, and these processes mostly involve strong acid, caustic alkali, volatile toxic solvents, or noble metals (Venica et al., 2008). In this aspect, greener utilization of lignin is urged.

Ionic liquids (ILs) have attracted enormous attention as an environmental benign medium for solubilizing lignocelluloses (Mora-Pale et al., 2011; Brandt et al., 2013; D'Anna et al., 2014), owing to their unusual properties such as near-zero vapor pressure, tunable structure of cations and anions, and excellent solvent power for both organic and inorganic substances (Zhang et al., 2006, 2017a), etc. The recent experiments have elucidated the catalytic depolymerization of real lignin in ILs to aromatic compounds, through breaking β-O-4 ether bonds. Jia et al. reported that the hydrolysis of β-O-4 bonds of lignin dimer [guaiacylglycerol-β-guaiacyl ether (GG)], could be achieved in an acidic IL (1-H-3-methylimidazolium chloride), and a possible reaction mechanism accounting for the primary product (guaiacol) was speculated (Jia et al., 2010a). After that, Cox et al. demonstrated that the coordination of anions of ILs with hydroxyl groups can stabilize the intermediates, which facilitate the cleavage of β-O-4 ether bond and inhibit the condensation of lignin fragments during fragmentation (Cox et al., 2011). Further studies have shown that the combination of [Bmim][Cl] with metal chloride was effective for β-O-4 bond cleavage, which is attributed to hydrochloric acid formed by hydrolysis of metal chlorides (Jia et al., 2010b). Recent studies have presented that the selective tailor for ester bonds, rather than the ether bonds of lignin, yields methyl p-hydroxycinnamate with [Bmim][FeCl$_4$]. The high catalytic activity was attributed to the narrow HOMO-LUMO gap between ester lignin and [FeCl$_4$]$^-$ anion (Li et al., 2018). The efficient degradation of lignin using acidic IL, 1-(4- sulfobutyl)-3-methylimidazoliumhydrosulfate ([C$_4$H$_8$SO$_3$Hmim][HSO$_4$]), was investigated (Long et al., 2015), yielding useful fine aromatic chemicals such as guaiacol, phenol and 4-ethylphenol through dehydration and dealkylation of lignin. Amarasekara et al. reported that sulfuric acid functionalized IL exhibited better catalytic activity than pure sulfuric acid at the same H$^+$ ion concentration because it acts

as both a solvent and a catalyst (Amarasekara and Wiredu, 2011). Cai et al. developed an emulsion reactor containing butyl-3-(butyl-4-sulfonate) imidazolium hydrogen sulfate for lignin depolymerization, which exhibited high efficiency in product separation by automatic phase partition (Cai et al., 2015). Recently, Singh et al. compared the depolymerization of lignin in various ILs catalysts and sulfuric acid (Singh and Dhepe, 2016). Their results showed that [C$_3$SO$_3$Hmim][HSO$_4$] had a superior capacity to synthesize low molecular-weight aromatic products with a high conversion rate, indicating that IL is a promising substitute for metals and inorganic catalysts to depolymerize real lignin. The enhanced catalytic activity of –SO$_3$H functionalized ILs has resulted from the strong interaction between lignin moieties and ILs, which facilitates the hydrolysis of β-O-4 bonds (Janesko, 2014). Apart from the theoretical study of acid-promoted cleavage of β-O-4 bond (Qu et al., 2015), there are still some challenges to overcome as the reaction mechanism of ILs catalyzed depolymerization of lignin remains unclear. The acting mechanism of –SO$_3$H functionalized ILs has not been elucidated yet, and this encourages us to perform a DFT mechanistic study. Our previous work explained the geometric and energetic details between various ILs and the lignin model compound, GG. It was found that ILs with sulfonic acid group had the strongest interaction with GG via hydrogen bonding and π-π interaction. Furthermore, hydroxyl groups and ether oxygen of GG are the key sites for the interaction (Zhang et al., 2017b). To further elucidate the reaction mechanism and physicochemical phenomena of β-O-4 bond cleavage with sulfonic IL, the conversion of GG to guaiacol by a –SO$_3$H functionalized IL [C$_3$SO$_3$Hmim][HSO$_4$] was proposed in this article by density functional theory (DFT) calculations and molecular dynamics (MD) simulations. The Gibbs energies of reaction profiles in vacuum and solvent, electron density at bond critical points, bond dissociation energies and non-covalent interactions were specially investigated to study the nature of β-O-4 bond cleavage. The computed results are expected to be helpful for understanding the mechanism of –SO$_3$H functionalized IL-catalyzed transformation of lignin to small phenols.

THEORETICAL METHODS

Quantum Chemistry Calculations

In this study, all DFT calculations were performed by employing Gaussian 09 software package (Frisch et al., 2013). The stationary points including reactants, intermediates, products, and transition states were optimized using the M06-2x functional, which is proposed to be excellent for describing the dispersion effects within noncovalent interactions (Zhao and Truhlar, 2008), combined with the standard 6–31+g(d,p) basis set (Hariharan and Pople, 1973; Frisch et al., 1984). Harmonic frequency calculations were carried out at the same level of theory to verify the optimized structures as zero imaginary frequency for minima and one imaginary frequency for transition states. The intrinsic reaction coordinate (IRC) calculations were traced to confirm the reaction pathways of transition states (Fukui, 1981). Structures at the two ends of IRC paths were optimized to minima, which represent the stable geometrics of reactants

and products (A rigid scan of intermediates can be found in **Figure S7** and the energies in **Table S3**). Single point energies and Gibbs free energies of all structures were refined at the M06-2x/6-311+g(d,p) level. Additionally, to mimic the solvent effect on the reactions, the solvation model based on density (SMD) in methanol solvent was adapted for all gas phase structures (Marenich et al., 2009; Bernales et al., 2012).

Molecular Dynamics Simulations

MD simulations for GG-IL systems containing 400 GG and 430 pairs of [C$_3$SO$_3$Hmim][HSO$_4$] were performed with the Gromacs 5.1.1 software package. The number of GG and ion pairs were based on the dissolution experiment of Singh et al. (Singh and Dhepe, 2016). The CHARMM general force field was used for cations [C$_3$SO$_3$Hmim]$^+$ and anions [HSO$_4$]$^-$ (Jo et al., 2008; Vanommeslaeghe et al., 2010; Moyer et al., 2018), and the CHARMM parameters reported by Petridis and Smith (2009) were employed for lignin dimer GG. The starting structures of all the GG-IL systems were randomly built by PACKMOL (Martinez and Martinez, 2003). For the GG-IL mixtures, periodic boundary conditions (PBC) were used in x, y, z directions with an initial box size 90 × 90 × 90 Å, and the PME algorithm were used for electrostatic interactions. The systems were initially energy-minimized for 10,000 steps using the conjugate gradient algorithm to remove abnormal contacts between molecules. Subsequently, the systems were simulated for 5 ns under the NVT canonical ensemble with a V-rescale thermostat to increase the initial temperature to 500 K. Then, another 5 ns annealing were taken by decreasing the temperature from 500 to 300, 420, 440, 460, and 480 K under the NPT isothermal-isobaric ensemble with a V-rescale thermostat to reach equilibrium, respectively (Berendsen et al., 1984). Afterwards, the production runs were equilibrated for another 30 ns under canonical ensemble to collect the data of interest. The simulation results were obtained by analyzing the last 10 ns trajectory of production runs. For all MD simulations, the Lennard-Jones interaction was truncated at a radius of 1.2 nm, and the Coulombic interaction was treated using particle-mesh Ewald (PME) summation with a cutoff of 1.2 nm (Zheng et al., 2018).

RESULTS AND DISCUSSION

Generation of Zwitterion/H$_2$SO$_4$ Complex

[C$_3$SO$_3$Hmim][HSO$_4$] is one kind of sulfonic acid functionalized ILs (SAFILs). The class of Brønsted acidic ILs has displayed good characteristics for use as liquid catalysts in organic synthesis and for the hydrolysis of carbohydrates (Cole et al., 2002; Kitaoka et al., 2004; Qiao et al., 2004; Zare et al., 2012). It has also been reported that intermolecular hydrogen bonds were automatically formed between the anion and cation by the O-H...O hydrogen bonds (Liu et al., 2009), and the extremely strong hydrogen bonds resulted in proton transfer from cation to anion. Finally, the complex of zwitterion/H$_2$SO$_4$ was formed (Ohno et al., 2018). In the present work, the reaction barrier forming zwitterion/H$_2$SO$_4$ was investigated; H$_2$SO$_4$ was supposed to serve as better proton shuttle and zwitterion was expected to stabilize the intermediates or transition states. Here, a one-step reaction was identified

in **Figure 1**. The precursor of the reaction **BS1** is a pair of [C$_3$SO$_3$Hmim][HSO$_4$] bonded by O-H...O hydrogen bonds. The bond length of Oc-H (Oc, oxygen atom of cation) is 1.063 Å and the distance between Oa (Oa, oxygen atom of anion) and H (H, hydrogen atom of -SO$_3$H) is 1.438 Å. Due to the strong nucleophilic ability of the anion, [HSO$_4$]$^-$ extracts the proton from [C$_3$SO$_3$Hmim]$^+$ *via* Oc-H...Oa. In the transition state **BS-TS**, Oc-H bond is elongated to 1.153 Å and H...Oa gets closer to 1.272 Å. It is observed that the zwitterion/H$_2$SO$_4$ complex is formed by deprotonation of [C$_3$SO$_3$Hmim]$^+$ in **BS2**. One can see that the covalent bond Oa-H is 1.022 Å and the distance between Oc and H is 1.575 Å. In this step, the calculated energy barrier is only 0.38 kcal/mol, and the product is 2 kcal/mol more stable than the reactant, suggesting a slightly exothermic reaction for this route. The existence of zwitterion/H$_2$SO$_4$ is considered to be geometrically and thermodynamically feasible at ambient temperature (Sun et al., 2014). In the subsequent mechanism study, the zwitterion/H$_2$SO$_4$ complex was used as the main catalyst for the bond cleavage reactions. In the following sections, detailed mechanistic calculations of route A, B, and C were shown to understand the depolymerization of lignin with this zwitterion/H$_2$SO$_4$.

Route A: Dehydration of α-C-OH

The previous experimental studies have speculated that the depolymerization of lignin to phenols by acids or acidic ionic liquids experienced a dehydration process (Cox et al., 2011; Janesko, 2014), which is presented in route A. It is believed that route A involves dehydration of α-C-OH, followed by hydrolysis of the β-O-4 ether bond by the water molecules that were removed (**Scheme S1** in ESI). For the system studied with zwitterion/H$_2$SO$_4$ acting as a catalyst, the reaction profile of Gibbs free energy was shown in **Figure 2**. The bond cleavage process was conducted *via* three elementary steps: the elimination of α-C-OH, followed by the deprotonation of β-C and finally the hydrolysis of the β-O-4 bond. **Figure 2** displays the computed energy profile, where the zero-energy reference point, **a1,** is taken as the initial complex between a GG molecule and the zwitterion/H$_2$SO$_4$. The first transition state, **ts12,** represents the elimination of α-C-OH, where H$_2$SO$_4$ acts as a proton shuttle, donating a proton H75 at O71 of H$_2$SO$_4$. At this stage the distance between O71 and H75 is elongated to 1.815 Å. The proton H75 approaches O42 and protonation of O42 also leads to elongation of O42-C17, resulting in the removal of the hydroxyl group at C17 and the formation of an intermediate, **a2**. The distances of O42-H75, O42-C17, and C17-C19 are 0.980, 2.327, and 1.489 Å, respectively. The first protonation step involves an energy barrier of 20.55 kcal/mol. Before the subsequent deprotonation reaction, **a2** evolves into a more stable conformation (**a3**) *via* the rearrangement of GG and zwitterion. After that, **a3** is converted to **a4** through **ts34**, realizing the removal of H20 at C19 and the recovery of H$_2$SO$_4$ by another proton shuttle, H$_3$O$^+$. Noted, the H20 removed gets close to the eliminated H$_2$O molecule to form H$_3$O$^+$, then H$_3$O$^+$ returns H75 to [HSO$_4$]$^-$ and the dehydration step is complete. The energy barrier of **a3** to **a4** is 9.74 kcal/mol, which is considerably lower than that of the first protonation step (20.55 kcal/mol).
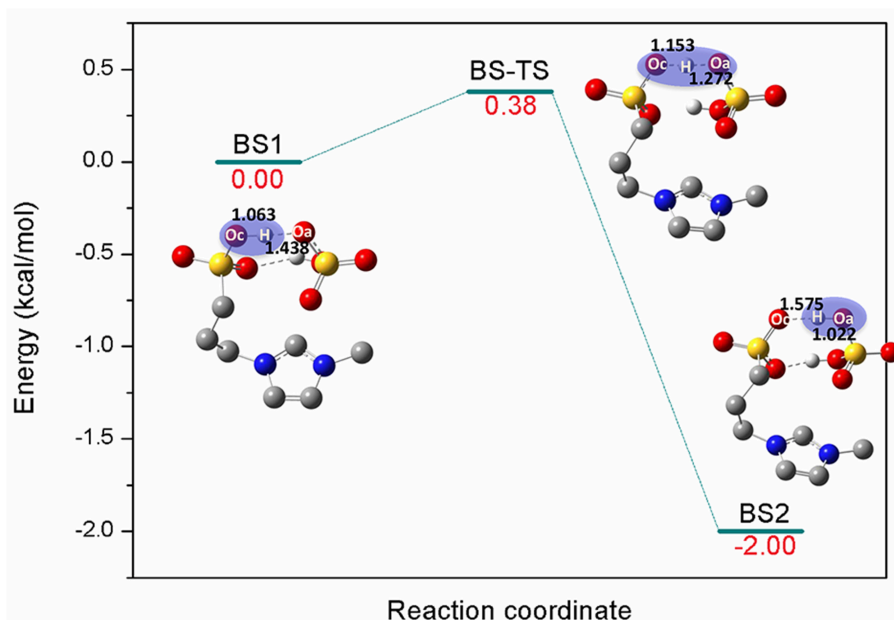
FIGURE 1 | Potential energy profile for the generation of zwitterion/H_2SO_4 complex. The unimportant hydrogen atoms are omitted for clarity and the bond lengths are labeled in Å.

Next, **a4** evolves into a more energetically stable structure, **a5**, which is geometrically feasible to conduct the bond cleavage step, **ta56**. In this step, the proton H75 of H_2SO_4 attacks O21 of β-O-4 bond, and the bond length of O71-H75 is elongated to 1.465 Å. Meanwhile, the adjacent water molecule approaches β-C, C19. Due to the formation of hydrogen bonds between O72 and H20, the covalent bond O42-H20 is weakened, causing H20 to transfer from O42 to O72, and the remaining part of the water molecule is added to C19. The final step 3 is to form the O21-H75, C19-O42 bonds and to break O21-C19 bond to yield the final phenolic products. The energy barrier of **a5** to **a6** is 52.25 kcal/mol, which is the highest among all steps in route A (all structures can be found in **Figure S1**). The possible reason for this high energy barrier is the steric hindrance that occurred in the β-O-4 site, which will be further discussed in the MD simulation section. Additionally, due to the flexibility of the lignin molecule (Upton and Kasko, 2016), π-π stacking interaction between imidazolium ring of zwitterion and benzene ring of lignin GG is considered to be the key factor which stabilizes the transition states and intermediates.

Route B: Dehydration of γ-C-OH

The major reaction steps of route B are identified in **Figure 3** and all geometric structures along this route can be found in **Figure S2**. Similarly, the bond cleavage is also carried out *via* three elementary steps: the elimination of γ-C-OH accompanied by intramolecular hydrogen rearrangement, followed by the deprotonation of γ-C, and finally the hydrolysis of the β-O-4 bond. The reaction steps start from the deprotonation of H_2SO_4. Once H_2SO_4 is deprotonated, the resulting H74 proton attacks O35 *via* the γ-C-OH site. The bond length of O72-H74

is elongated to 1.664 Å, and bond H74-O35 has the distance of 0.996 Å. At the same time, bond C32-O35 is weakened to 2.291 Å. As a result, the hydroxyl group O35-H and H74 leave the GG molecule in the form of one water molecule. In this step, conversion of **b1** to **b2** experiences the transition state, in the form of **tb12,** by overcoming an energy barrier of 47.42 kcal/mol, which is much higher than that of the protonation of α-C-OH in route A. One reason is that γ-C-OH tends to form intramolecular hydrogen bonds with the adjacent methoxy group, which make it difficult to break (Zhang et al., 2017b), and the other is probably owing to the rearrangement of hydrogen H20 from C19 to C32 in **tb12**. One can see that C32 is bonded with two hydrogen atoms after the removal of the hydroxyl group O35-H. The strong electronegativity of C32 attracted H20 of C19, which makes intermediate **b2** stable. Upon the transfer of H20 from C19 to C32, H20 forms H_3O^+ with the water molecule generated in the first step, and these changes suggest that C19-C32 is migrating from a C-C single bond to a C=C double bond in the dehydration intermediate **b2** (same with **b3**). The transition state **tb34** clearly reveals that H_3O^+ returns H74 to O72, and H20 leaves with O35-H in the form of a water molecule. At the same time, the bond length of C19 = C32 in **tb12** (1.392 Å) is shorter than that in **tb34** (1.408 Å). The departing of H20 overcomes an energy barrier of 3.59 kcal/mol. Afterwards, intermediate **b4** evolves into a more stable conformational isomer, **b5**, which is geometrically feasible to conduct the cleavage of the β-O-4 bond. Subsequently, **b5** is converted to the phenolic product **b6** through **tb56**, where the hydrogen atom H75 is abstracted by O21 of lignin; co-occurring with the proton H35 transfer from H_2O to $[HSO_4]^-$ and the addition of O35-H20 to C19. The energy barrier of this step is 49.09 kcal/mol. Comparing with that of **tb34**, the length of
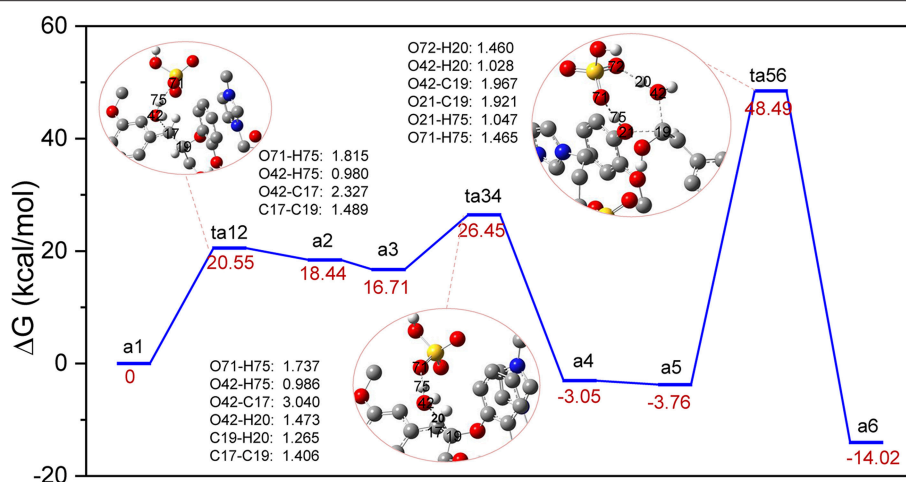
FIGURE 2 | Gibbs free energy profile for β-O-4 bond cleavage undergoing α-C-OH dehydration. The unimportant hydrogen atoms are omitted for clarity and the bond lengths are labeled in Å.

ether bond C19-O21 in **tb56** is elongated from 1.309 to 1.882 Å. **Figure 3** demonstrates that the overall process is exothermic by 10.68 kcal/mol, and the first protonation step is the rate-determining step. However, the bond cleavage step remains to be a high energy barrier due to the steric hindrance at the β-O-4 site.

Route C: Protonation of β-O

The conversion processes in Route A: Dehydration of α-C-OH and Route B: Dehydration of γ-C-OH have identified the three steps *via* protonation, elimination, and hydrolysis, and the hydrolysis process was generally speculated by the experimental work (Jia et al., 2010a; Cox et al., 2011; Singh and Dhepe, 2016). As reported by Loerbroks et al. (2013), cellobiose can be activated by acid hydrolysis of glycosidic linkage of cellobiose, with a low energy barrier of 33 kcal/mol. Here, we reported the mechanism of direct protonation of β-O-4 ether bond by zwitterion/H_2SO_4. A two-step reaction mechanism is shown in **Figure 4**, and the structures of route C can be found in **Figure S3**. Starting from protonated lignin GG, **c1**, the first step involves the dissociation of the O21-C19 bond, followed by a conformational change of the position between C17, C19, and C32. Due to the elongation of O21-C19, C19 gets too close to the carbon atom of the benzene ring which is originally bonded with C17, so that C19 replaces the position of C17. Consequently, C19 in structure **c2** becomes bonded to the carbon atom of the benzene ring, and both C17 and C32 become connected with C19. The computed energy barrier to form **tc12** is 27.98 kcal/mol. followed by the intermediate **c2**, at which point the hydroxyl group, O42-H43 at C17, gets close to the SO3 part of zwitterion. Accordingly, the hydrogen atom H43 transfers from O42 to O71 and the ion pair [C3SO3Hmim][HSO4] is re-obtained. The reaction barrier of the second step is estimated to be 1.71 kcal/mol. It is worth pointing out that there is experimental evidence showing that the activation of the O-glycosidic site could be hindered by the preferential protonation of O of hydroxyl group in cellulose (Palkovits et al., 2010; Rinaldi et al., 2010). Though route C

experiences the lowest energy barrier, a catalyst is likely to be hindered by the hydroxyl groups, so the dehydration processes displayed in route A and B are more likely to be initiated. These findings may be concerted to the mechanism speculated by Singh et al. (Singh and Dhepe, 2016). The relatively higher energy barriers in dehydration processes could be attributed to much larger bond dissociation energies of O-H bonds than those of β-C-O ether bond, which were verified to be 112.39 and 117.25 kcal/mol for (α-C-O)-H and γ-C-O-H, respectively, and 74.46 kcal/mol for the β-C-O bond (**Figure S4** and **Table S2** in ESI).

Solvent Effect

In order to evaluate the solvation effect on the reaction profiles, the Gibbs free energies were refined at the M06-2x/6-311+g(d,p) level of theory. According to experimental results, methanol was chosen as the SMD solvent because of its fine performance for lignin depolymerization (Singh and Dhepe, 2016; Li et al., 2018). The energy profiles of the three reaction routes are shown in **Figure 5**; the energies under vacuum are denoted in solid lines and those under solvent condition are denoted in dash lines. Overall, the energies for the species of **ta12**, **ta34**, **tb12,** and **tc12** under solvent condition are lower than that under vacuum condition, which suggests that the solvent effects strongly stabilize these transition states. However, the energies for the species of **ta56**, **tb34**, **tb56,** and **tc34** are relatively higher than that under vacuum condition. The different degrees of stabilization of intermediates and transition states causes the reaction kinetics to be significantly affected. In route A (α-C-OH), the relative activation energies of **ta12**, **ta34,** and **ta56** are reduced by 5.11 kcal/mol and increased by 3.78 and 2.73 kcal/mol, respectively. In route B (γ-C-OH), the energy barriers of **tb12** and **tb56** are lowered by 3.54 and 1.06 kcal/mol, respectively. The energy barrier of **tb34** rises by 3.03 kcal/mol. In route C, the energy barrier of **tc12** and **tc34** is reduced by 3.62 and 1.16 kcal/mol, respectively. The detailed activation energies of all the transition states are given in **Table 1**. Through comparing the energy profiles of possible pathways of β-O-4 bond cleavage, it
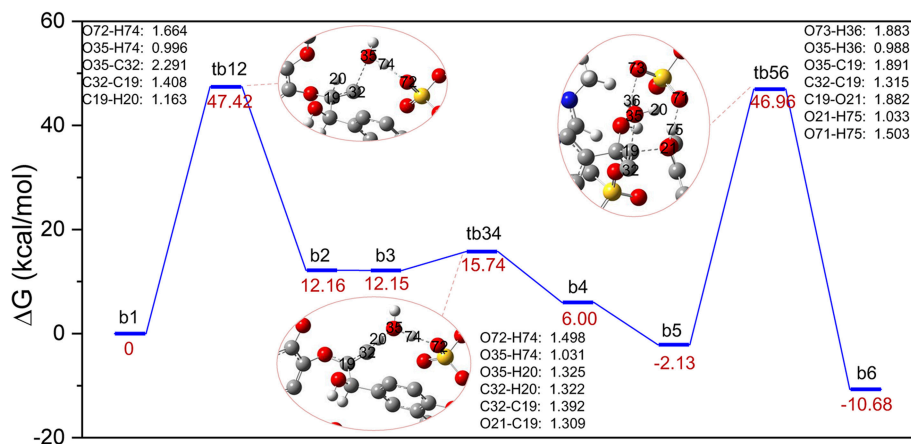
FIGURE 3 | Gibbs free energy profile for β-O-4 bond cleavage undergoing γ-C-OH dehydration. The unimportant hydrogen atoms are omitted for clarity and the bond lengths are labeled in Å.
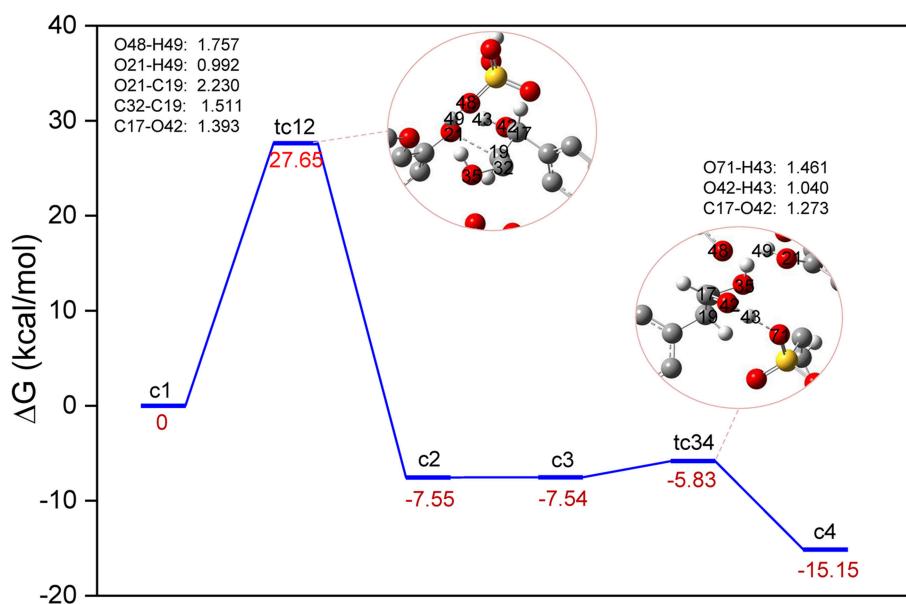

FIGURE 4 | Gibbs free energy profile for β-O-4 bond cleavage undergoing directly β-C-O protonation. The unimportant hydrogen atoms are omitted for clarity and the bond lengths are labeled in Å.

is clear that the most kinetically favored pathway could be route A, with the lowest activation energy of 15.44 kcal/mol. This is concerted to the calculation results in the gas phase. Furthermore, analysis of solvent effects on the β-O-4 bond cleavage reaction indicates that methanol solution has a better stabilization effect on the protonation of the hydroxyl group at α-C and γ-C, and the protonation of β-O in the initial steps. However, the solvent effects have a lower stabilization effect on the transition states in the hydrolysis steps and give little help to the bond cleavage, which may be attributed to the competition between methanol molecules and water molecules to form hydrogen bonds with H_2SO_4, especially in **ta56**. Therefore, water molecules have some difficulty in approaching the β-O-4 ether bond. Among the two

hydrolysis routes, the energy barrier of route A is generally lower than route B, which proves that α-C-OH is a better reaction site (Zhang et al., 2017b), among the two hydrolysis routes.

Non-covalent Interactions Analysis

Besides the reaction pathways, the non-covalent interactions between lignin GG and catalyst are investigated for the most important steps according to the atoms in molecules (AIM) theory (Cioslowski, 1991; Bader, 2002; Johnson et al., 2010). The inter- and intramolecular weak interactions are differentiated by the sign of second Hessian eigenvalue [sign(λ_2)ρ] in Reduced density gradient (RDG) analysis, and visualized by 3D plots with a color-scale from −0.03 to 0.02 a.u.. The description of
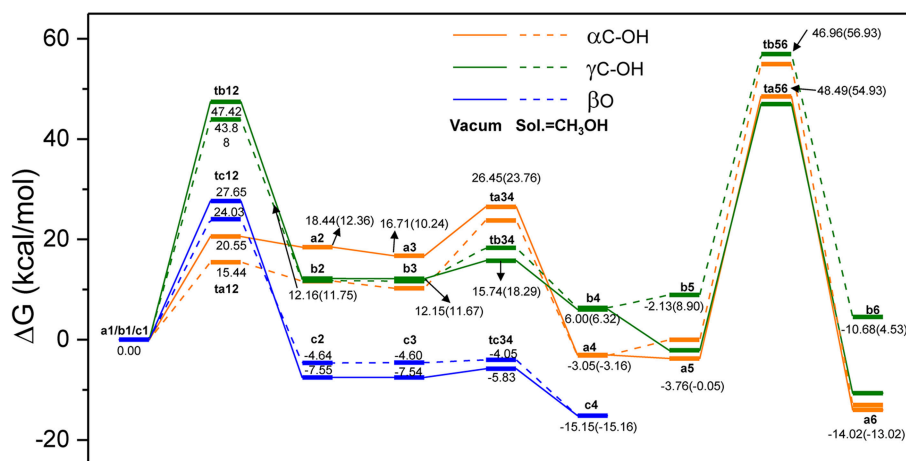
FIGURE 5 | The overall reaction pathways of route A: α-C-OH, route B: γ-C-OH, and route C: β-O with solid lines representing energies in vacuum condition and dash lines representing energies in solvent (SMD, sol. = CH$_3$OH).

TABLE 1 | Activation energies of transition states in **Figure 5**.

Route A (α-C-OH)	ta12	ta34	ta56
Energy barrier (kcal/mol)	20.55 (15.44)	9.74 (13.52)	52.25 (54.98)
Route B (γ-C-OH)	tb12	tb34	tb56
Energy barrier (kcal/mol)	47.42 (43.88)	3.59 (6.62)	49.09 (48.03)
Route C (β-O)	tc12	tc34	
Energy barrier (kcal/mol)	27.65 (24.03)	1.71 (0.55)	

Energies under solvent condition are displayed in parentheses.

noncovalent interactions can be found within these work (Yang et al., 2016; Zhang et al., 2017b). The electronic properties are shown for transition states of protonation steps (**ta12** and **tb12**) in **Figure 6** and bond cleavage steps (**ta56**, **tb56**, and **tc12**) in **Figure 7**. For the protonation steps, electron densities at the bond critical point of O42-C17 (α-C and O of hydroxyl group at α-C) and O35-C32 (γ-C and O of hydroxyl group at γ-C) are focused on the following analysis, relating to the departure of the hydroxyl group. While for the bond cleavage steps, electron densities at bond critical point of O21-C19 (β-C-O) are investigated with the scatter plots and their corresponding 3D plots. As can be seen, the electron density at O42-C17 is 0.032 a.u. with a positive Laplacian value of 0.092 a.u. (**Table S1** in ESI), and the blue surface denoted by yellow circle (**Figure 6C**) indicates that O42 still maintains a strong electrostatic-dominated noncovalent interaction with C17. The weak interaction also proves that protonation of the hydroxyl group at C17 strongly weakened the O42-C17 bond. Similarly, the electron density at O35-C32 is 0.081 a.u. with a negative Laplacian value of −0.142 a.u. The negative Laplacian value usually means that the electron density is locally concentrated, which is dominated by a covalent interaction. The site denoted by a yellow circle (**Figure 6D**) does not indicate that a noncovalent interaction surface is consistent with the presence of the O35-C32 covalent bond. Moreover, the lower electron density at O42-C17

than O35-C32 suggests that the hydroxyl group at α-C is more easily activated by H$_2$SO$_4$. Meanwhile, other large green surfaces are classified by π-π stacking interactions between benzene rings of lignin GG and the imidazolium ring of zwitterion.

In a quest to better understand the difference between the dehydration route and protonation route, the electron density properties at the bond critical point of O21-C19 (β-C-O ether bond), of transition states (**ta56**, **tb56**, and **tc12**) in the bond cleavage steps, are shown in **Figure 7**. One can see that, there are obvious spikes at where sign(λ$_2$)ρ equals to −0.079, −0.088, and −0.038 a.u. in **Figures 7A–C**, respectively. There is a dense distribution of spikes at a position where sign(λ$_2$)ρ approximately equals to zero, which indicates that the van der Waals dominated dispersive attractions between zwitterion and GG molecules. These interactions are shown by green surfaces in **Figures 7D–F**. However, the regions which correspond to the O21-C19 bond interaction for **ta56** and **tb56** are in red color, and that for **tc12** are in blue color. The bigger electron densities at BCP of O21-C19 of **ta56** and **tb56** suggest that O21 and C19 are strongly bonded, meaning there are obvious repulsive effects at the red regions. On the contrary, the electron density at BCP of O21-C19 of **tc12**, 0.038 a.u. is much smaller than the former, which demonstrates that the O21-C19 bond is greatly weakened in the protonation route. Additionally, the nonbonded atoms, O21 and C19 show a strong electrostatic attraction at the blue regions. Owing to the stronger attack of H$_2$SO$_4$ and dispersion effects of the zwitterion, route C has the lowest reaction barrier in the bond cleavage step.

Radical Distribution Functions

To gain a deeper understanding of how the location of ILs and GG molecules affects the cleavage of the β-O-4 bond, the structural properties of cations and anions close to the ether-oxygen atom are quantified by radical distribution functions between center of mass of GG and GG (GG-GG), cation [C$_3$SO$_3$Hmim]$^+$ and GG (C$_3$SO$_3$Hmim-GG), anion [HSO$_4$]$^-$
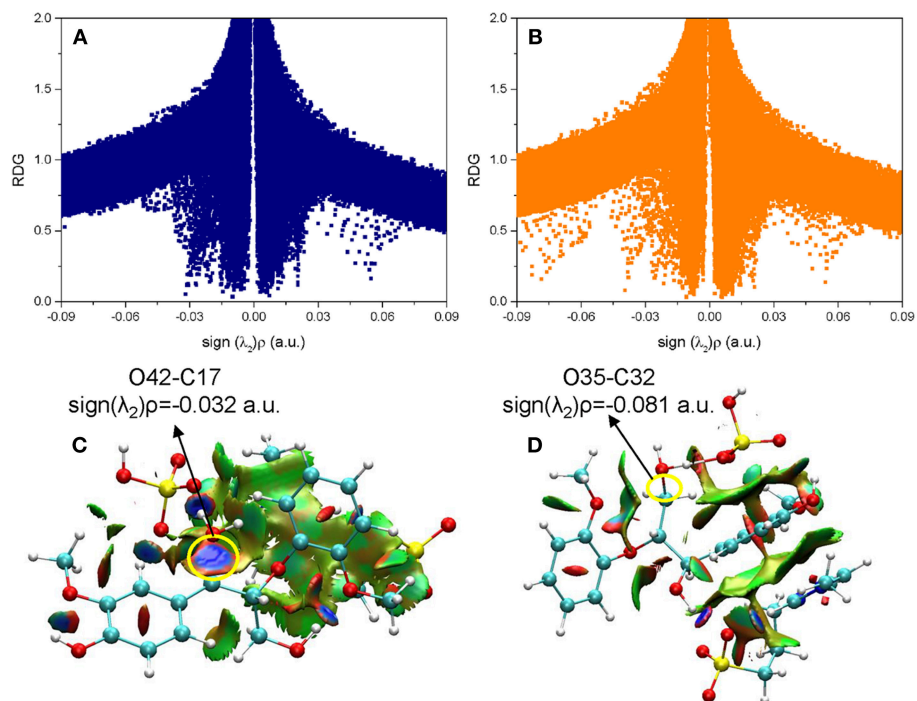
FIGURE 6 | The noncovalent interactions in the protonation steps in **(A)** ta12 and **(B)** tb12, and the corresponding 3D plots **(C,D)** are shown below with blue regions indicating strong electrostatic interactions, red regions indicating steric hindrance and green regions indicating more dispersive attractive interactions. The 3D plots are given with an isosurface of 0.7 a.u..
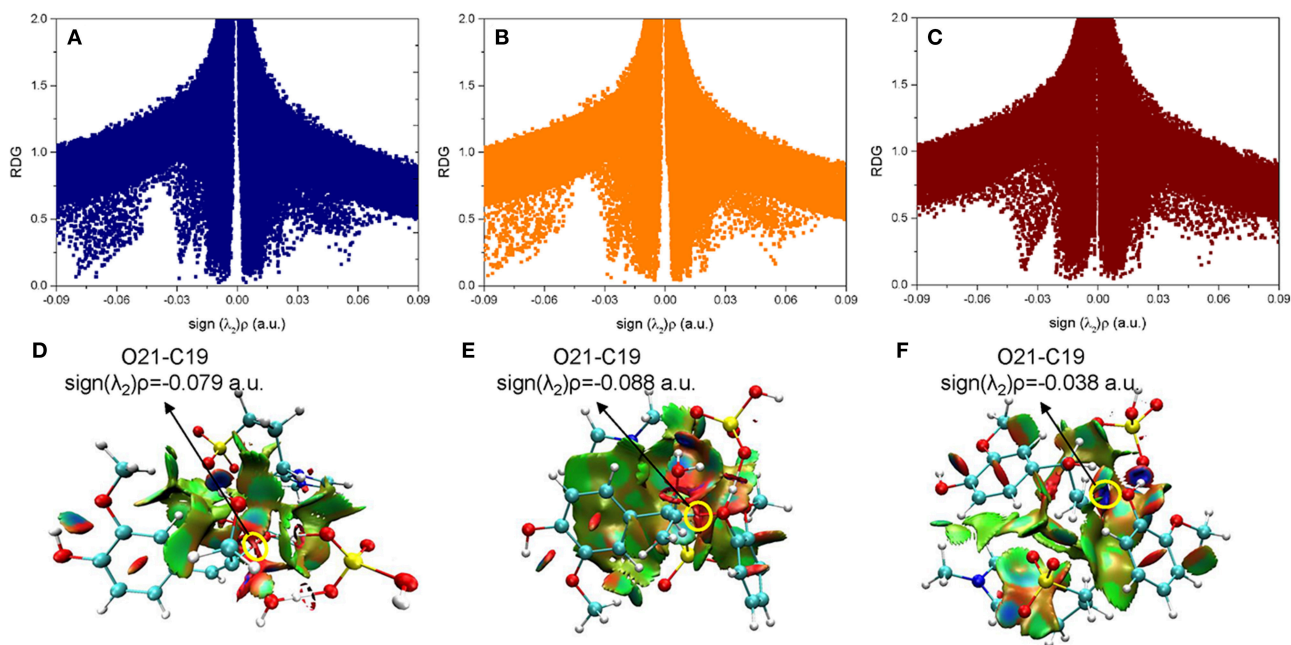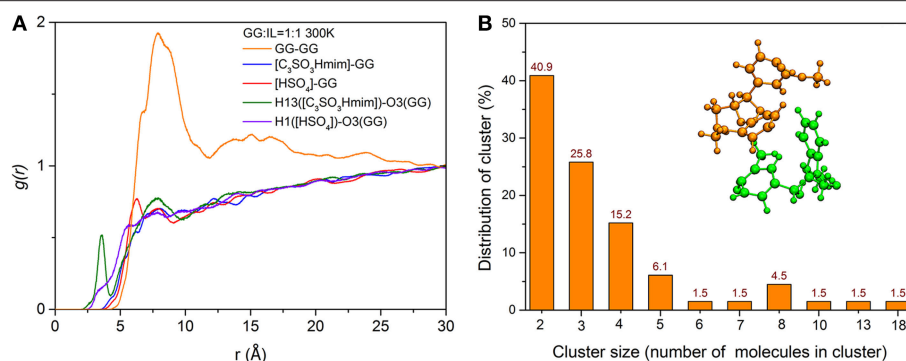

FIGURE 7 | The noncovalent interactions in the β-O-4 bond breaking steps in **(A)** ta56, **(B)** tb56, and **(C)** tc12, and the corresponding 3D plots **(D–F)** are shown below with blue regions indicating strong electrostatic interactions, red regions indicating steric hindrance, and green regions indicating more dispersive attractive interactions. The 3D plots are given with an isovalue of 0.7 a.u..

FIGURE 8 | (A) RDFs between center of mass of GG and GG, $[C_3SO_3Hmim]^+$ and GG, $[HSO_4]^-$ and GG, atom-atom RDFs between H13($[C_3SO_3Hmim]$) and O21(GG), H1($[HSO_4]$) and O21(GG); **(B)** The number distribution of clusters with different numbers of GG molecules in the system of 300 K, and the snapshot of a typical cluster with two GG molecules.

and GG ($[HSO_4]$-GG), and atom-atom distribution between H13 of $[C_3SO_3Hmim]^+$ and O3 of GG, H1 of $[HSO_4]^-$ and O3 of GG. Here, H13 is the hydrogen atom of -SO_3H group in $[C_3SO_3Hmim]^+$ and O21 is the ether-oxygen atom of GG. As shown in **Figure 8A**, the $[C_3SO_3Hmim]$-GG and $[HSO_4]$-GG RDFs do not show obvious peaks, indicating the less structured GG-IL orientation. One shoulder at ∼6 Å in **Figure 8A** suggests that there are more anions in the solvation layer than cations, and anions are closer to GG, which is in agreement with Moyer's results (Moyer et al., 2018). Though the RDFs of center of mass do not show a significant difference between $[C_3SO_3Hmim]$-GG and $[HSO_4]$-GG, the atom-atom RDFs in **Figure 8A** do. As shown, H13 has a dense distribution around O21, with a sharp maximum at ∼3.5 Å and a second maximum at ∼7.5 Å. The first sharp peak implies the solvation shell which is ascribed to the hydrogen-bonding interaction between ether-oxygen O21 and H13 of -SO_3H group. It is speculated that a mass of H-bonds are directly formed between O21 and H13, resulting in the very sharp peaks observed at ∼3.5 Å in the RDF curves. Meanwhile, the second peak is farther away from O21, which is possibly due to the occupancy by the acidic hydrogens of the imidazolium ring. The close contacts between the imidazolium ring and ether-oxygen lead to -SO_3H group locating at a far distance. In contrast to H13($[C_3SO_3Hmim]$)-O21(GG) RDFs, the H1($[HSO_4]$)-O21(GG) RDFs show little variation to $[HSO_4]$-GG, and only weak peaks are located at ∼7 Å, which implies that the -SO_3H group of cations are more closely located around GG. The unobvious RDF peaks between IL and GG are likely to be ascribed to strong self-aggregation of GG, as indicated by sharp peaks between GG and GG. The strong self-aggregation results in steric hindrance to direct protonation of β-O in route C. It was found that GG clusters are distributed with different numbers of GG molecules (**Figure S6** and **Figure 8**) and the majority of the clusters include two GG molecules (**Figure 8B**). With increasing temperature, a gradual loss of local solvation layers is observed, shown by the decrease in the solvation peaks (**Figure S5**). However, the shape of the first peak does not change a lot, proving the important role of -SO_3H in solvating lignin. Moreover, a significant rise in temperature is more conducive

to the dispersion of lignin in ionic liquids. Although the RDFs confirm that H13 of cation $[C_3SO_3Hmim]^+$ has more favorable distances to ether-oxygen, this phenomenon is not contradicted by the formation of zwitterions/H_2SO_4 between $[C_3SO_3Hmim]^+$ and $[HSO_4]^-$, because the reaction energy barrier is only 0.38 kcal/mol. In this case, protons get into inner solvation shells of ILs.

CONCLUSION

DFT calculations have shown the mechanism details of the conversion of lignin model compound, guaiacyl glycerol-β-guaiacyl ether (GG), to guaiacol by -SO_3H functionalized IL. Three possible pathways exist that contribute to the cleavage of the β-O-4 bond. Route A is characterized by the dehydration of α-C-OH, route B describes the dehydration of γ-C-OH, and route C involves the direct protonation of β-O of GG to form guaiacol species. H_2SO_4/zwitterion complexes are formed by basic steps, H_2SO_4 acts as a proton donor like a proton shuttle, while the zwitterion part provides a polar environment to stabilize the intermediates and transition states. The closer distance between H13($[C_3SO_3Hmim]$)-O21(GG) in RDFs also confirmed that -SO_3H in cations plays a substantial role in solvation of lignin. The computed energy barriers of the three routes indicated that the cleavage of the β-O-4 bond is more easily carried out through route C. However, the protonation of β-O-4 ether bond in route C could be hindered due to the steric effect of zwitterion, as pointed out by the experiments. Therefore, the dehydration routes A and B are more consistent with experimental results. In addition, the solvation model calculations strongly suggest that methanol is beneficial for protonation steps in routes A and B, not only for protonation of the β-O-4 bond in route C. These theoretical findings provide a mechanistic understanding of the cleavage of the β-O-4 bond of lignin with –SO_3H functionalized ILs.

AUTHOR CONTRIBUTIONS

HH and SZ designed the research. YZ, FH, and YW carried out the whole simulation. YZ, FH, YW, and

HH did data analysis. YZ, YX, and XT discussed the results and did the revisions. YZ, HH, and SZ wrote the manuscript.

SUPPLEMENTARY MATERIAL

The Supplementary Material for this article can be found online at: https://www.frontiersin.org/articles/10.3389/fchem.2019.00078/full#supplementary-material

REFERENCES

Amarasekara, A. S., and Wiredu, B. (2011). Degradation of cellulose in dilute aqueous solutions of acidic ionic liquid 1-(1-propylsulfonic)-3-methylimidazolium chloride, and p-toluenesulfonic acid at moderate temperatures and pressures. *Ind. Eng. Chem. Res.* 50, 12276–12280. doi: 10.1021/ie200938h

Amen-Chen, C., Pakdel, H., and Roy, C. (2001). Production of monomeric phenols by thermochemical conversion of biomass: a review. *Bioresource Technol.* 79, 277–299. doi: 10.1016/S0960-8524(00)00180-2

Bader, R. F. W. (2002). "Atoms in molecules," in *Encyclopedia of Computational Chemistry* (Hamilton, ON: JohnWiley & Sons, Ltd.).

Berendsen, H. J. C., Postma, J. P. M., Vangunsteren, W. F., Dinola, A., and Haak, J. R. (1984). Molecular-dynamics with coupling to an external bath. *J. Chem. Phys.* 81, 3684–3690. doi: 10.1063/1.448118

Bernales, V. S., Marenich, A. V., Contreras, R., Cramer, C. J., and Truhlar, D. G. (2012). Quantum mechanical continuum solvation models for ionic liquids. *J. Phys. Chem. B* 116, 9122–9129. doi: 10.1021/jp304365v

Brandt, A., Grasvik, J., Hallett, J. P., and Welton, T. (2013). Deconstruction of lignocellulosic biomass with ionic liquids. *Green Chem.* 15, 550–583. doi: 10.1039/c2gc36364j

Cai, Z. P., Li, Y. W., He, H. Y., Zeng, Q., Long, J. X., Wang, L. F., et al. (2015). Catalytic depolymerization of organosolv lignin in a novel water/oil emulsion reactor: lignin as the self-surfactant. *Ind. Eng. Chem. Res.* 54, 11501–11510. doi: 10.1021/acs.iecr.5b03247

Chatel, G., and Rogers, R. D. (2014). Review: oxidation of lignin using ionic liquids—an innovative strategy to produce renewable chemicals. *ACS Sustain. Chem. Eng.* 2, 322–339. doi: 10.1021/sc4004086

Cioslowski, J. (1991). Atoms in molecules: a quantum theory. *Science* 252, 1566–1568. doi: 10.1126/science.252.5012.1566-a

Cole, A. C., Jensen, J. L., Ntai, I., Tran, K. L. T., Weaver, K. J., Forbes, D. C., et al. (2002). Novel bronsted acidic ionic liquids and their use as dual solvent-catalysts. *J. Am. Chem. Soc.* 124, 5962–5963. doi: 10.1021/ja026290w

Cox, B. J., Jia, S., Zhang, Z. C., and Ekerdt, J. G. (2011). Catalytic degradation of lignin model compounds in acidic imidazolium based ionic liquids: hammett acidity and anion effects. *Polym. Degrad. Stabil.* 96, 426–431. doi: 10.1016/j.polymdegradstab.2011.01.011

D'Anna, F., Marullo, S., Vitale, P., Rizzo, C., Lo Meo, P., and Noto, R. (2014). Ionic liquid binary mixtures: promising reaction media for carbohydrate conversion into 5-hydroxymethylfurfural. *Appl. Catal. A-gen.* 482, 287–293. doi: 10.1016/j.apcata.2014.05.039

Deepa, A. K., and Dhepe, P. L. (2015). Lignin depolymerization into aromatic monomers over solid acid catalysts. *ACS Catal.* 5, 365–379. doi: 10.1021/cs501371q

Frisch, M. J., Pople, J. A., and Binkley, J. S. (1984). Self-consistent molecular-orbital methods.25. Supplementary functions for gaussian-basis sets. *J. Chem. Phys.* 80, 3265–3269. doi: 10.1063/1.447079

Frisch, M. J., Trucks, G. W., Schlegel, H. B., Scuseria, G. E., Robb, M. A., Cheeseman, J. R., et al. (2013). *Gaussian 09. Gaussian 09, Revision D. 01*, Wallingford CT: Gaussian, Inc.

Fukui, K. (1981). The path of chemical-reactions - the irc approach. *Accounts Chem. Res.* 14, 363–368. doi: 10.1021/ar00072a001

Hariharan, P. C., and Pople, J. A. (1973). The influence of polarization functions on molecular orbital hydrogenation energies. *Theor. Chim. Acta* 28, 213–222. doi: 10.1007/BF00533485

Janesko, B. G. (2014). Acid-catalyzed hydrolysis of lignin beta-O-4 linkages in ionic liquid solvents: a computational mechanistic study. *Phys. Chem. Chem. Phys.* 16, 5423–5433. doi: 10.1039/c3cp53836b

Jia, S., Cox, B. J., Guo, X., Zhang, Z. C., and Ekerdt, J. G. (2010a). Cleaving the beta-O-4 bonds of lignin model compounds in an acidic ionic liquid, 1-H-3-methylimidazolium chloride: an optional strategy for the degradation of lignin. *Chem. Sus. Chem.* 3, 1078–1084. doi: 10.1002/cssc.201000112

Jia, S., Cox, B. J., Guo, X., Zhang, Z. C., and Ekerdt, J. G. (2010b). Hydrolytic cleavage of β-O-4 ether bonds of lignin model compounds in an ionic liquid with metal chlorides. *Ind. Eng. Chem. Res.* 50, 849–855. doi: 10.1021/ie101884h

Jo, S., Kim, T., Iyer, V. G., and Im, W. (2008). Software news and updates - charnim-gui: a web-based grraphical user interface for charmm. *J. Comput. Chem.* 29, 1859–1865. doi: 10.1002/jcc.20945

Johnson, E. R., Keinan, S., Mori-Sanchez, P., Contreras-Garcia, J., Cohen, A. J., and Yang, W. (2010). Revealing noncovalent interactions. *J. Am. Chem. Soc.* 132, 6498–6506. doi: 10.1021/ja100936w

Jollet, V., Gissane, C., and Schlaf, M. (2014). Optimization of the neutralization of red mud by pyrolysis bio-oil using a design of experiments approach. *Energy Environ. Sci.* 7, 1125–1133. doi: 10.1039/C3EE43585G

Katahira, R., Mittal, A., McKinney, K., Chen, X. W., Tucker, M. P., Johnson, D. K., et al. (2016). Base-catalyzed depolymerization of biorefinery lignins. *ACS Sustain. Chem. Eng.* 4, 1474–1486. doi: 10.1021/acssuschemeng.5b01451

Kitaoka, S., Nobuoka, K., and Ishikawa, Y. (2004). The first utilization of acidic ionic liquid for preparation of tetraarylporphyrins. *Chem. Commun.* 17, 1902–1903. doi: 10.1039/b404241g

Li, Z., Cai, Z., Zeng, Q., Zhang, T., France, L. J., Song, C., et al. (2018). Selective catalytic tailoring of the H unit in herbaceous lignin for methyl p-hydroxycinnamate production over metal-based ionic liquids. *Green Chem.* 20, 3743–3752. doi: 10.1039/C8GC01252K

Liu, X. M., Song, Z. X., and Wang, H. J. (2009). Density functional theory study on the -SO₃H functionalized acidic ionic liquids. *Struct. Chem.* 20, 509–515. doi: 10.1007/s11224-009-9448-6

Loerbroks, C., Rinaldi, R., and Thiel, W. (2013). The electronic nature of the 1,4-beta-glycosidic bond and its chemical environment: DFT insights into cellulose chemistry. *Chem. Eur. J.* 19, 16282–16294. doi: 10.1002/chem.201301366

Long, J. X., Lou, W. Y., Wang, L. F., Yin, B. L., and Li, X. H. (2015). [C₄H₈SO₃Hmim]HSO₄ as an efficient catalyst for direct liquefaction of bagasse lignin: decomposition properties of the inner structural units. *Chem. Eng. Sci.* 122, 24–33. doi: 10.1016/j.ces.2014.09.026

Lu, J. M., Wang, M., Zhang, X. C., Heyden, A., and Wang, F. (2016). Beta-O-4 bond cleavage mechanism for lignin model compounds over Pd catalysts identified by combination of first-principles calculations and experiments. *ACS Catal.* 6, 5589–5598. doi: 10.1021/acscatal.6b00502

Ma, R., Hao, W. Y., Ma, X. L., Tian, Y., and Li, Y. D. (2014). Catalytic ethanolysis of kraft lignin into high-value small-molecular chemicals over a nanostructured alpha-molybdenum carbide catalyst. *Angew. Chem. Int. Edit.* 53, 7310–7315. doi: 10.1002/anie.201402752

Marenich, A. V., Cramer, C. J., and Truhlar, D. G. (2009). Universal solvation model based on solute electron density and on a continuum model of the solvent defined by the bulk dielectric constant and atomic surface tensions. *J. Phys. Chem. B* 113, 6378–6396. doi: 10.1021/jp810292n

Martinez, J. M., and Martinez, L. (2003). Packing optimization for automated generation of complex system's initial configurations for molecular dynamics and docking. *J. Comput. Chem.* 24, 819–825. doi: 10.1002/jcc.10216

Mora-Pale, M., Meli, L., Doherty, T. V., Linhardt, R. J., and Dordick, J. S. (2011). Room temperature ionic liquids as emerging solvents for the pretreatment of lignocellulosic biomass. *Biotechnol. Bioeng.* 108, 1229–1245. doi: 10.1002/bit.23108

Moyer, P., Smith, M. D., Abdoulmoumine, N., Chmely, S. C., Smith, J. C., Petridis, L., et al. (2018). Relationship between lignocellulosic biomass dissolution and physicochemical properties of ionic liquids composed of 3-methylimidazolium cations and carboxylate anions. *Phys. Chem. Chem. Phys.* 20, 2508–2516. doi: 10.1039/C7CP07195G

Ohno, H., Yoshizawa-Fujita, M., and Kohno, Y. (2018). Design and properties of functional zwitterions derived from ionic liquids. *Phys. Chem. Chem. Phys.* 20, 10978–10991. doi: 10.1039/C7CP08592C

Palkovits, R., Tajvidi, K., Procelewska, J., Rinaldi, R., and Ruppert, A. (2010). Hydrogenolysis of cellulose combining mineral acids and hydrogenation catalysts. *Green Chem.* 12, 972–978. doi: 10.1039/c000075b

Petridis, L., and Smith, J. C. (2009). A molecular mechanics force field for lignin. *J. Comput. Chem.* 30, 457–467. doi: 10.1002/jcc.21075

Prado, R., Brandt, A., Erdocia, X., Hallet, J., Welton, T., and Labidi, J. (2016). Lignin oxidation and depolymerisation in ionic liquids. *Green Chem.* 18, 834–841. doi: 10.1039/C5GC01950H

Qiao, K., Deng, Y. Q., Yokoyama, C., Sato, H., and Yamashina, M. (2004). Preparation of epsilon-caprolactam via beckmann rearrangement of cyclohexanone oxime: a mild and recyclable process. *Chem. Lett.* 33, 1350–1351. doi: 10.1246/cl.2004.1350

Qu, S. L., Dang, Y. F., Song, C. Y., Guo, J. D., and Wang, Z. X. (2015). Depolymerization of oxidized lignin catalyzed by formic acid exploits an unconventional elimination mechanism involving 3c-4e bonding: a DFT mechanistic study. *ACS Catal.* 5, 6386–6396. doi: 10.1021/acscatal.5b01095

Rinaldi, R., Meine, N., vom Stein, J., Palkovits, R., and Schuth, F. (2010). Which controls the depolymerization of cellulose in ionic liquids: the solid acid catalyst or cellulose? *Chem. Sus. Chem.* 3, 266–276. doi: 10.1002/cssc.200900281

Shuai, L., Amiri, M. T., Questell-Santiago, Y. M., Heroguel, F., Li, Y. D., Kim, H., et al. (2016). Formaldehyde stabilization facilitates lignin monomer production during biomass depolymerization. *Science* 354, 329–333. doi: 10.1126/science.aaf7810

Singh, S. K., and Dhepe, P. L. (2016). Ionic liquids catalyzed lignin liquefaction: mechanistic studies using TPO-MS, FT-IR, raman and 1D, 2D-HSQC/nosey NMR. *Green Chem.* 18, 4098–4108. doi: 10.1039/C6GC00771F

Sun, J., Yao, X. Q., Cheng, W. G., and Zhang, S. J. (2014). 1,3-dimethylimidazolium-2-carboxylate: a zwitterionic salt for the efficient synthesis of vicinal diols from cyclic carbonates. *Green Chem.* 16, 3297–3304. doi: 10.1039/c4gc00279b

Upton, B. M., and Kasko, A. M. (2016). Strategies for the conversion of lignin to high-value polymeric materials: review and perspective. *Chem. Rev.* 116, 2275–2306. doi: 10.1021/acs.chemrev.5b00345

Vanommeslaeghe, K., Hatcher, E., Acharya, C., Kundu, S., Zhong, S., Shim, J., et al. (2010). Charmm general force field: A force field for drug-like molecules compatible with the charmm all-atom additive biological force fields. *J. Comput. Chem.* 31, 671–690. doi: 10.1002/jcc.21367

Venica, A. D., Chen, C. L., and Gratzl, J. S. (2008). Soda-aq delignification of poplar wood. Part 1: Reaction mechanism and pulp properties. *Holzforschung* 62, 627–636. doi: 10.1515/HF.2008.118

Yang, H., Wang, X., Ma, Y., Wang, L., and Zhang, J. (2016). Quaternary ammonium-based ionic liquids bearing different numbers of hydroxyl groups as highly efficient catalysts for the fixation of CO_2: a theoretical study by QM and MD. *Catal. Sci. Technol.* 6, 7773–7782. doi: 10.1039/C6CY01045H

Younker, J. M., Beste, A., and Buchanan, A. (2011). Computational study of bond dissociation enthalpies for substituted β-O-4 lignin model compounds. *Chem. Phys. Chem.* 12, 3556–3565. doi: 10.1002/cphc.201100477

Zakzeski, J., Bruijnincx, P. C., Jongerius, A. L., and Weckhuysen, B. M. (2010). The catalytic valorization of lignin for the production of renewable chemicals *Chem. Rev.* 110, 3552–3599. doi: 10.1021/cr900354u

Zare, A., Moosavi-Zare, A. R., Merajoddin, M., Zolfigol, M. A., Hekmat-Zadeh, T., Hasaninejad, A., et al. (2012). Ionic liquid triethylamine-bonded sulfonic acid ([Et₃N-SO₃H]Cl) as a novel, highly efficient and homogeneous catalyst for the synthesis of beta-acetamido ketones, 1,8-dioxo-octahydroxanthenes and 14-aryl-14h-dibenzo[aj]xanthenes. *J. Mol. Liq.* 167, 69–77. doi: 10.1016/j.molliq.2011.12.012

Zhang, S., Sun, N., He, X., Lu, X., and Zhang, X. (2006). Physical properties of ionic liquids: database and evaluation. *J. Phys. Chem. Ref. Data* 35, 1475–1517. doi: 10.1063/1.2204959

Zhang, S., Wang, Y., He, H., Huo, F., Lu, Y., Zhang, X., et al. (2017a). A new era of precise liquid regulation: quasi-liquid. *Green Energy Environ.* 2, 329–330. doi: 10.1016/j.gee.2017.09.001

Zhang, Y., He, H., Dong, K., Fan, M., and Zhang, S. (2017b). A dft study on lignin dissolution in imidazolium-based ionic liquids. *RSC Adv.* 7, 12670–12681. doi: 10.1039/C6RA27059J

Zhang, Y., He, H., Liu, Y., Wang, Y., Huo, F., Fan, M., et al. (2019). Recent progress in theoretical and computational studies on the utilization of lignocellulosic materials. *Green Chem.* 21, 9–35. doi: 10.1039/C8GC02059K

Zhao, Y., and Truhlar, D. G. (2008). The m06 suite of density functionals for main group thermochemistry, thermochemical kinetics, noncovalent interactions, excited states, and transition elements: two new functionals and systematic testing of four m06-class functionals and 12 other functionals. *Theor. Chem. Acc.* 120, 215–241. doi: 10.1007/s00214-007-0310-x

Zheng, W., Huang, C. Z., Sun, W. Z., and Zhao, L. (2018). Microstructures of the sulfonic acid-functionalized ionic liquid/sulfuric acid and their interactions: a perspective from the isobutane alkylation. *J. Phys. Chem. B* 122, 1460–1470. doi: 10.1021/acs.jpcb.7b09755

Imidazolium Based Ionic Liquids: A Promising Green Solvent for Water Hyacinth Biomass Deconstruction

Jitendra Kumar Singh[1†], Rahul Kumar Sharma[2†], Pushpal Ghosh[2], Ashwani Kumar[1*] and Mohammed Latif Khan[1]

[1] Metagenomics and Secretomics Research Laboratory, Department of Botany, Dr. Harisingh Gour Central University, Sagar, India, [2] Department of Chemistry, School of Chemical Sciences and Technology, Dr. Harisingh Gour Central University, Sagar, India

Water hyacinth (WH) is a troublesome aquatic weed of natural and artificial water bodies of India and other tropical countries and causing severe ecological problems. The WH biomass is low in lignin content and contains high amount of cellulose and hemicellulose, making it suitable material for conversion into liquid fuels for energy production. This study highlighted that, how different imidazolium based ionic liquids (ILs) [1-alkyl-3-methylimidazolium bromide, $[C_nmim]Br$ (n = 2, 4, 6, 8, and 10)] with tunable properties can be employed for the degradation of WH biomass. Different characterizations techniques, such as XRD, FT-IR, SEM, and DSC are used to unravel the interplay between ILs and the biomass. In this study, it is observed that [Emim][Br] pretreated samples have maximum crystalline value (Crl = 26.38%) as compared to other ionic liquids pretreatments. FTIR data showed the removal of lignin from WH biomass by 12.77% for [Emim][Br] and 10.74% for [Edmim][Br]. SEM images have proven that [Emim][Br] pretreatment have altered the structure of biomass the most. Our results proved that IL pretreatment is a promising approach for effective treatment of WH biomass and causes high levels disruption of cellulose structure.

Keywords: water hyacinth, lignocellulosic biomass, ionic liquids, pretreatment, hydrolysis, crystallinity index

INTRODUCTION

The limited supply of fossil based fuels in recent time has become a serious concern globally. Further, their associated negative impacts of fossil fuels on global climate are also becoming environmental concerns in many countries. Biofuels *in lieu of* fossil fuels has drawn a tremendous attention as a source of renewable, and clean energy (Kumar et al., 2010; Kumar and Sharma, 2011; Singh et al., 2014a; Raghunandan et al., 2018). Therefore, the search of alternative renewable energy source for biofuel production has expanded (Rezania et al., 2015). Lignocellulose is most abundant, renewable, cost effective, carbon neutral, non-edible plant material (Saini et al., 2015) and can be used for bioethanol production (Zabed et al., 2016; Singh et al., 2018; Vyas et al., 2018). Lignocellulosic materials for biofuels production are of much interest due to its low cost and high availability.

Till date, many plants biomass have been explored for the production of advanced biofuel by passing through three different steps; pretreatment, saccharification and fermentation (Sindhu et al., 2016; Kothari et al., 2017). Lignocellulosic biomass is composed of crystalline cellulose fibers which are embedded in a solid matrix of lignin and hemicelluloses that restrict the entry
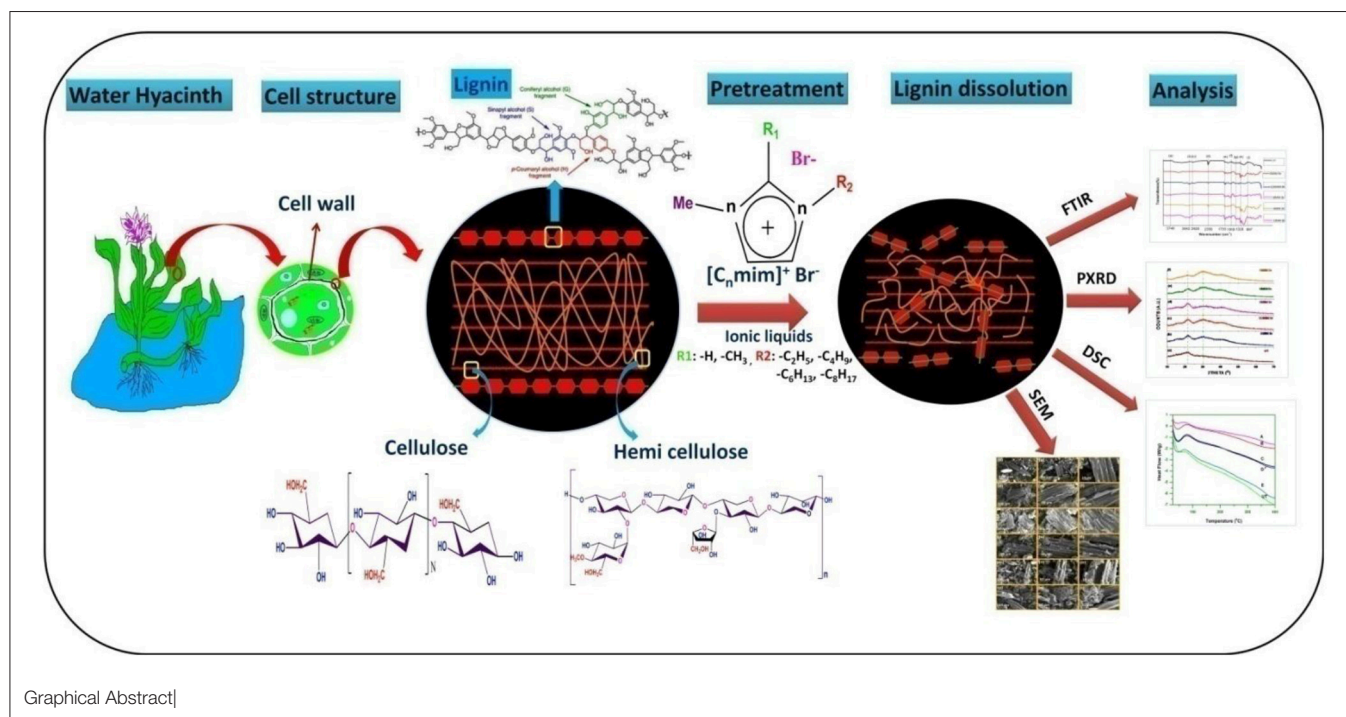
Graphical Abstract|

of microbial enzymes and also provide a barrier to microbial attack. Among all component of biomass, lignin is a highly branched, aromatic polymer, composed of phenylpropanoid units that serve as the glue that binds cellulose and hemicellulose, imparting rigidity and microbial resistance to lignocellulose (Chandra et al., 2007). Therefore, a proper pretreatment is required during the bioconversion process to disrupt the hydrogen bonds in crystalline cellulose to remove lignin and hemicellulose that surrounds the cellulose fibers and increase the porosity and surface area for enhanced enzymatic hydrolysis (Singh et al., 2014b).

Different types of pretreatment methods have been used in the past to overcome the recalcitrance of lignocellulosic biomass which are dilute acid (Schell et al., 2003; Lloyd and Wyman, 2005), ammonia fiber expansion (Lau et al., 2008), hot water (Liu and Wyman, 2004), lime (Sierra et al., 2011) and organic solvent (Zhang et al., 2007). Among various pretreatment methods available for biomass hydrolysis, the ionic liquids (ILs) pretreatment has gained more popularity due to its ability to dissolve lignocellulose under simpler conditions (Menon and Rao, 2012). ILs are organic salts that usually melt below 100°C and often called as "green" and "designer" solvent (Sheldon, 2002). Application of ILs offers several advantages than volatile organic solvents, such as insignificant vapor pressure, good dissolving and extracting ability, wide liquid range, good thermal stability, excellent microwave-absorbing abilities, and they can be modified as per the requirement (Aid et al., 2016). In addition,

physical and chemical properties of ILs can be effectively tuned by tuning the cation/anion combination; alkyl chain length, viscosity etc. and most importantly cellulose as well as the ILs can be recovered after the dissolution process with no toxic or odor emissions. The asymmetric nature of the cation part of ILs inhibits compact packing of the ions, and speedup the reactions that needs both high and low temperature. ILs display excellent characteristics in chemical processes with ability to dissolve polar and non-polar organic, inorganic, and polymeric compounds (Lee and Lee, 2005). Though, ILs is extensively used in catalysis, battery applications, inorganic synthesis, f-element separations etc., its application in biofuel production is still limited. Previously, several researchers have used variety of ILs for the dissolution of full lignocellulosic biomass using multistep processes followed by cellulose hydrolysis with acid or enzymes (Fort et al., 2007; Kilpeläinen et al., 2007; Li et al., 2009). Due to the protective feature of lignin, and its inability to undergo rapid degradation, different biomass pretreatment strategies have been focused on achieving a reduction in lignin contents. In dissolution process, ILs exhibit excellent physical characteristics including the ability to dissolve polar and non-polar organic, inorganic and polymeric compounds (Lee and Lee, 2005). They can dissolve the biomass due to the strong hydrogen bonding basicity of certain ions, such as Ac, Cl, Br, and NO₃. These anions can extensively disrupt the hydrogen bonding interactions present in the three dimensional network of lignocellulose, leading to either dissolution of biomass or selected individual components based on the nature of the anion (Wei et al., 2012).

In this study, we have used ILs for the biomass hydrolysis of water hyacinth (*Eichhornia crassipes*; Family- Pontederiaceae, related to Liliaceae family) and analyzed the structural changes

---

Abbreviations: FTIR, Fourier transform infrared; XRD, X-ray diffraction; SEM, scanning electron microscope; DSC, differential scanning calorimeter; CrI, crystallinity index

by FTIR, PXRD, DSC and SEM. Water hyacinth (WH), is a free floating troublesome aquatic weed plant that originates from Brazil and Ecuador. This plant multiply asexually (stolons) as well as sexually (seeds), at 25–35°C temperature and difficult to control due to its fast multiplication and long dormancy up to 20 years (Rezania et al., 2015, 2017). Single plant may produce 140 million individuals with fresh biomass weighing 28,000 tons each year under optimum conditions and aggravate eutrophication of water bodies, increases in CO_2 emission, increased BOD (Biological Oxygen Demand) of water bodies, block river ways, obstruct navigation and causes irreversible damage to ecological system. Generally plant biomass growing on land is composed of about 30–50% cellulose, 20–40% hemicelluloses and 15–30% lignin. On the other hand, in WH biomass the amount of lignin (10%) is less and cellulose (20%) and hemicelluloses (33%) is high (Bolenz et al., 1990; Gressel, 2008), with high growth rate and no competition with land plants has led WH to be suitable material for biofuel industry (Feng et al., 2017). Previously, report showed that, acid and alkali based pretreatment were most commonly used methods for the pretreatment of WH biomass. Though, ILs based method was less utilized for the biomass hydrolysis. Here in this study, we have used imidazolium based ILs with pendant alky chain length for WH biomass hydrolysis. The whole process of biomass hydrolysis is presented in graphical abstract. A special care has been taken to understand how the structures and intricate properties of ILs influence the biomass degradation.

MATERIALS AND METHODS

Procurement of Biomass Samples

The water hyacinth (WH) biomass collected from Lakhabanjara lake at Sagar (23.8388° N, 78.7378°E), Madhya Pradesh, India. Collected WH biomass was processed by following the method of Ganguly et al. (2013). The harvested WH biomass was washed with distilled water vigorously to remove all undesirable matters, such as sand particles and cut to get average particle size of 1–2 cm. The cut WH biomass was then dried in an oven with the temperature of 105°C for 24 h. Dried plant material was powdered by grinder mixture (Jaipan 1290–750 W) and sieved to 0.02 mm mesh size. Subsequently, WH biomass samples were stored in a air tight glass container in a freezer at −4°C to maintain the aseptic condition until subsequent experiments. The pulverized WH biomass was stored in sterile condition because micro-organism can modify the complex chemical structure or main organic groups that constitute the WH biomass.

Synthesis of Ionic Liquids

Five different ILs were synthesized and applied for WH biomass hydrolysis, which were based on imidazolium cation and bromide counter anion (**Figure 1**). The side chain of imidazolium cation is changed via varying the alkyl chain length. Furthermore, C (2) position of imidazolium ring is also substituted by methyl group in $[Edmim]^+[Br]^-$ in order to observe the role of acidic hydrogen on the degradation of cellulose of WH. The ionic liquids used in this study for the pretreatment of the WH sample are presented in **Table 1**.

FIGURE 1 | A general scheme of imidazolium based ionic liquids.
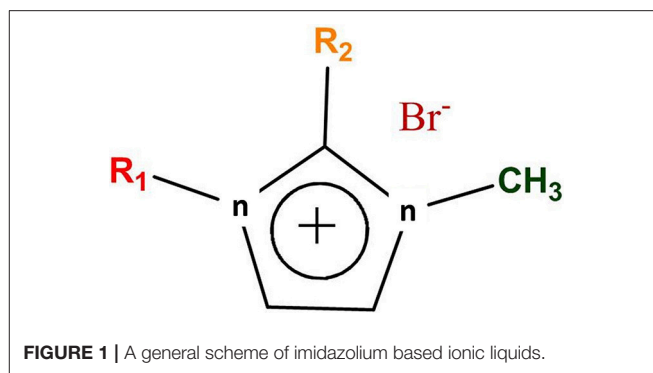
Chemicals

Tetra-methylammonium bromide (Loba Chemie, 98%), 1-methylimidazole ($C_4H_6N_2$) (Alfa Aesar, 99.0%), 1,2-dimethylimidazole (Sigma Aldrich, 98%), Bromoethane (C_2H_5Br) (99.0%), n-Butyl Bromide (C_4H_9Br) (96.0%), n-Hexyl Bromide ($C_6H_{13}Br$) (99.0%), Octyl Bromide ($C_8H_{17}Br$) (98.5%) of Himedia brand were used. Ethyl Acetate (99.5%), Acetonitrile (99.5%), Dichloromethane (99.5%) were purchased from Loba Chemie and Silver Nitrate from Fisher Scientific brands were used. 1-ethyl-3-methylimidazolium bromide [Emim][Br], 1-ethyl-2,3-dimethylimidazolium bromide [Edmim][Br], 1-butyl-3-methylimidazolium bromide [Bmim][Br], 1-hexyl-3-methylimidazolium bromide [Hmim][Br] and 1-octyl-3-methylimidazolium bromide [Omim][Br] were prepared by modifying the previously reported methods (Ghosh and Mudring, 2016; Kumar et al., 2017). Synthesis procedure of the above mentioned ionic liquids (ILs) in detail is followed as:

1-Ethyl-3-Methyl Imidazolium Bromide [Emim][Br]

Modified procedure, 12.376 ml of bromo ethane (0.166 mol) and 10 ml of N-methyl imidazole (0.126 mol) were taken in a 250 ml round bottom flask and refluxed at 40°C for 4 h under Ar atmosphere in order to get complete reaction. Obtained product was allowed to attain the room temperature (RT) and product was washed twice with ethyl acetate. Resultant product was vacuum dried at room temperature for 24 h to obtain white solid product and checked by ^{1}HNMR and ^{13}C NMR.

1-Ethyl-2,3-Methyl Imidazolium Bromide [Edmim][Br]

By using the similar procedure as stated above, [Edmim][Br] was synthesized, except 0.126 mol of 1, 2-dimethyl imidazole (Sigma Aldrich, 98%) was used instead of N-methyl imidazole.

1-Butyl-3-Methylimidazolium Bromide [Bmim][Br]

This IL was synthesized through the previously reported method in which (0.166 mol) 1-bromo butane was added drop wise to (0.126 mol) 1-methyl imidazole in ice bath for 30 min with stirring. After that, flask was covered with aluminum foil and kept the reaction for 96 h at room temperature. Obtained product was re-crystallized from acetonitrile and vacuum dried at room temperature. The as-obtained product is checked with ^{1}H NMR and ^{13}C NMR.

TABLE 1 | Types of as-prepared ionic liquids (ILs).

S. No.	Ionic liquids (ILs)	Alkyl group (R$_1$)	C(2) position (R$_2$)	Abbreviations
1	1-Ethyl-3-methyl imidazolium Bromide (IL1)	$-C_2H_5$	$-H$	[Emim][Br]
2	1-Ethyl-2,3-dimethyl imidazolium Bromide (IL2)	$-C_2H_5$	$-CH_3$	[Edmim][Br]
3	1-Butyl-3-methyl imidazolium Bromide (IL3)	$-C_4H_9$	$-H$	[Bmim][Br]
4	1-Hexyl-3-methyl imidazolium Bromide (IL4)	$-C_6H_{13}$	$-H$	[Hmim][Br]
5	1-Octyl-3-methyl imidazolium Bromide (IL5)	$-C_8H_{17}$	$-H$	[Omim][Br]

1-Hexyl-3-Methylimidazolium Bromide [Hmim][Br]

Modifying the previous literature procedure, 10 ml of N-methyl imidazole (0.126 mol) and 50 ml acetonitrile was taken in 250 ml round bottom flask, followed by drop wise addition of 23.22 ml (0.166 mol) of n-bromo-hexane in ice bath. After that reaction was allowed to be taken place at 60°C for 12 h. Obtained product was cooled at room temperature and washed with ethyl acetate two times. Obtained product was vacuum dried till golden yellow liquid being appeared.

1-Octyl-3-Methylimidazolium Bromide [Omim][Br]

By following similar procedure, 1-octyl-3-methyl imidazolium bromide was synthesized. The required concentration of n-bromo-octane was taken according to its molecular weight and reaction was kept for 48 h. Golden yellow viscous liquid was obtained.

Pretreatment of WH Biomass

A 6% (w/w) WH biomass samples were pretreated with different ionic liquids as mentioned in **Table 1**. A WH biomass solution comprised of 0.3 g of biomass with 4.7 g of ILs in a 50 ml glass tube and this mixture was placed in water bath without stirring at 100°C for 1 h. After 1 h incubation, 35 ml of distilled water (DW) was added into the biomass/ionic liquids slurry and then centrifuged at 10,000 rpm for 10 min for the removal of IL. After that ILs pretreated WH biomass was washed at least four times with distilled water and solids were oven dried at 60°C till constant weight was obtained and then kept in a sealed plastic container at −4°C for further investigation.

FTIR Analysis

FTIR analysis was performed to observe the changes in structural and functional group in pretreated WH biomass. FTIR spectroscopy was carried out using a Fourier Transform Infrared Spectrophotometer (8400S SHIMADZU). The solid WH biomass samples (10 mg) were first mixed with the spectroscopic grade KBr (200 mg) (Merk, Germany) and ground to a fine powder in air by using a motor and pestle and then pressed into pellets for IR transmission studies. In each run, a background (pure KBr) was recorded (Chen et al., 2016). Biomass samples were scanned using an average 25 scan in the range of 400–4,000 cm^{-1} at spectral resolution of 2 cm^{-1}. By using the FTIR data different values, such as lateral order index (LOI), hydrogen bond intensity (HBI) and total crystallinity index (TCI) (Hurtubise and Krassig, 1960; Nelson and O Connor, 1964; Nada et al., 2000) were calculated.

Powder X-ray Diffraction (PXRD)

PXRD was performed to observe the crystalline nature of the untreated and ILs pretreated WH biomass using a D8 Bruker Advance Cu-ray tube diffractometer (Cruz et al., 2013). The following parameter were set; $Cu_{K\alpha}$ ($\lambda = 1.54$ A°) voltage (30 kV), and current (30 mA), 2θ scan range (0–60°), with scanning rate (2°/min) and a step size of 0.05° at room temp and sample were positioned on a quartz sample holder. The crystallinity value was obtained from the ratio between the intensity of the (002) peak (I_{002}, 2θ = 22.5) and the minimum dip (I_{am}, 2θ = 18.5) between the (002) and the (101) peaks as by using Equation (1) (Segal et al., 1959; Rodrigues et al., 2007).

$$\%CrI = [(I_{002} - I_{am}/I_{002})] \qquad (1)$$

Where I_{002} is the intensity of plane belongs to (002) and I_{am} is related to the amorphous structure.

Scanning Electron Microscope (SEM)

The morphological changes in the pretreated biomass samples of WH before and after the ionic liquids pretreatment were observed by SEM. For sample preparation, the treated WH samples were fixed on stubs and gold layer coated using a Denton sputter coater system (Qiu et al., 2012). After gold coating samples were preserved in the desiccators till the analysis was performed. These samples were then imaged by FEI Nova Nano SEM^{TM} 450 operated with an acceleration voltage of 15 kV and working distance of 5 mm. Different SEM images at various magnifications (500×, 1,000×, 3,000×) were recorded.
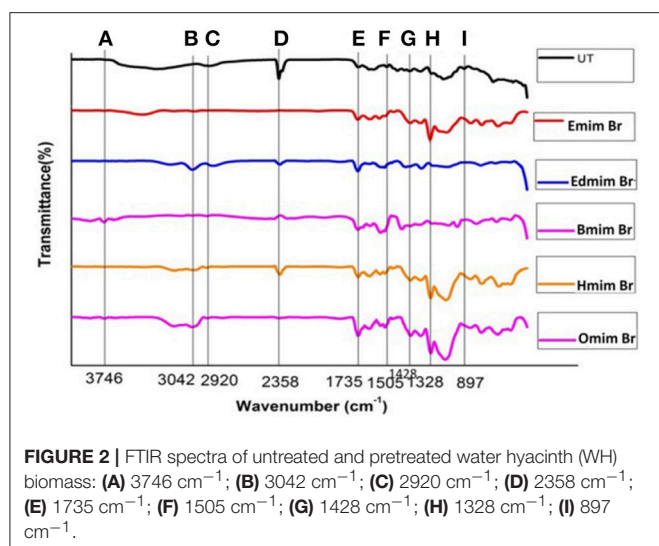
DSC Analysis

A differential scanning calorimeter having Simultaneous Thermal Analyzer (NETZSSCH): STA 449 F$_1$ Jupiter was used with a N$_2$ atmosphere in the range (25–450°C) at 10°C/min ramp. DSC curves were obtained with 3.3 mg untreated and pretreated WH biomass. The procedure used for DSC analysis was the same as described by Swatloski et al. (2002) and Bodirlau et al. (2010).

RESULT AND DISCUSSION

FTIR Analysis

FTIR spectroscopy was used to affirm the changes in untreated and ILs pretreated WH biomass at structural level (**Figure 2**). Data related to the percentage relative changes in WH biomass and FTIR intensity value for different ILS pretreated samples are presented in **Tables 2**, **3**, respectively. The main functional groups

FIGURE 2 | FTIR spectra of untreated and pretreated water hyacinth (WH) biomass: **(A)** 3746 cm^{-1}; **(B)** 3042 cm^{-1}; **(C)** 2920 cm^{-1}; **(D)** 2358 cm^{-1}; **(E)** 1735 cm^{-1}; **(F)** 1505 cm^{-1}; **(G)** 1428 cm^{-1}; **(H)** 1328 cm^{-1}; **(I)** 897 cm^{-1}.

of the WH biomass components are cellulose, hemicelluloses, and lignin. The bands ranging in FTIR spectra from 3,000 to 3,500 cm^{-1}, was assigned to the OH stretching vibration, which indicate the cellulose content in the sample. FTIR spectra at 3,348 cm^{-1} showed a significance reduction in the intensity of the band for ILs-pretreated WH sample, this peak is for O–H stretching vibrations and related to the hydrogen bonds in cellulose (Kumar et al., 2009) and changes related with this peak revealed changes in cellulose structure. Structurally, cellulose is having three hydroxyl groups which interact with other hydroxyl groups to form secondary valence bonds and responsible for cellulose crystallinity and chain structure by forming hydrogen bonding network. Changes in the peak intensity at 3,348 cm^{-1} showed the disruption of intermolecular and intra molecular hydrogen bonding (Alemdar and Sain, 2008; Yang et al., 2011). Comparative FTIR analysis revealed the efficacy of cellulosic hydrogen bond disruption by [Emim][Br] and [Edmim][Br] than the other ILs-pretreatment for WH biomass. Our results are supported by published report on pretreated switch grass (Li et al., 2010). Similarly the other band at 2,920 cm^{-1} is ascribed to C-H vibration for alkanes (Liu et al., 2006), and CH$_2$–(C$_6$)–bending vibration (Yang et al., 2011). The noticeable peak at 1,735 cm^{-1} which is ascribed to C=O stretching vibration in acetyl groups of the hemicelluloses was observed in untreated WH biomass (Karatzos et al., 2012), the intensity of this peak was very weak for the [Emim][Br] pretreated sample, as compared to the other ILs pretreated samples (**Figure 2**). The changes in the intensity of this peak could have been due to release of the acetyl groups in order of following treatments; [Emim][Br] pretreatment > [Edmim][Br] > [Bmim][Br] > [Hmim][Br] > [Omim][Br]. After IL pretreatment, this peak disappeared, indicated that some of hemicelluloses were removed in the dissolution process. The bands at 1,739 cm^{-1}, and around 1,321–1,317 cm^{-1} are assigned to characteristic bending or stretching vibrations of the different groups from cellulose (Popescu et al., 2009).

The bands between 1,595 and 1,230 cm^{-1} are assigned to characteristic bending or stretching of different groups of lignin.

To observe the changes in lignin removal, following peaks at 1,328 and 1,505 cm^{-1} were observed, these peaks attributable to aromatic skeletal vibrations in lignin. Additionally, the peaks presented in the range of 1,428–1,458 cm^{-1} were allocated to the C–H deformation in lignin and carbohydrates (Pandey and Pitman, 2003). The peak noticed at 1,428 cm^{-1} is assigned to bending vibration of CH$_2$ in cellulose and lignin. This band is strong in crystalline cellulose and weak in amorphous cellulose. Therefore, the amorphous cellulose in untreated, and ILs pretreated [Omim][Br], [Hmim][Br] and [Bmim][Br] samples is more than the samples treated by following ILs [Emim][Br] and [Edmim][Br]. The peaks located in the range 1,320–1,380 cm^{-1} in all untreated and pretreated ILs WH samples were ascribed to the bending vibration of C–H and C–O groups in the aromatic ring (Genestar and Palou, 2006). By applying different ILs pretreatment to WH biomass, we observed the decrease in intensity of the lignin linked peaks (peak at 1,514 cm^{-1} is associated with the aromatic skeletal modes of lignin and the peak at 1,328 cm^{-1} denotes the aromatic hydroxyl groups generated by the cleavage of ether bonds in lignin) which showed the effectiveness of the ILs pretreatment (Hsu et al., 2010). It was seen that the ILs pretreated WH biomass samples were delignified more in comparison to the untreated ones for the peak intensity changes at 1,328 and 1,514 cm^{-1} (**Figure 2; Table 4**). For example,[Emim][Br] pretreated WH biomass was delignified slightly more efficiently than the other ILs pretreatments. While, ILs pretreated samples showed the less intensity at 1,505 cm^{-1} over untreated one. The absorbance at 1,158 and 897 cm^{-1} correspond to C–O–C vibration in cellulose and hemicelluloses, and C–H deformation in cellulose, respectively (Pandey and Pitman, 2003). At 897 cm^{-1} the peak obtained showed changes with ILs used in the study. The band at 897 cm characterized by C–O–C stretching at β 1–4 glycosidic linkage, showed the amorphous nature of cellulose. The peak observed at 897 cm^{-1} was less intense in case of [Emim][Br] and [Edmim][Br] pretreated WH biomass compared to the other ILs ([Bmim][Br], [Hmim][Br], and[Omim][Br]) and untreated WH biomass samples. The presence of band at 897 cm^{-1} is strong and sharp that showed the presence of amorphous cellulose. So, from (**Figure 2; Table 3**) it is concluded that [Emim][Br] and [Edmim][Br] pretreated WH biomass samples have less amorphous cellulose than other ILs pretreated WH biomass samples used in this study.

We have compared the percentage changes in different spectra for untreated as well-pretreated WH biomass samples that are calculated by subtracting the intensity of the important peaks in the untreated WH biomass material from that of respective peaks in the pretreated WH biomass samples with different ILs (**Table 2**). The results of this calculation showed that the peak intensity at 1,510 cm^{-1} decreased by about 12.77% for the [Emim][Br] and by 10.74% for the [Edmim][Br]. Our results supported the efficacy of ILs pretreatment as appropriate method for removing lignin (**Figure 2; Table 3**).

This study showed the increased crystallinity index in the ILs pretreated WH biomass samples, which could have been due to the partial removal of hemicelluloses and lignin from the biomass.

Band position	Assignment	Pretreatment					
		UT	A	B	C	D	E
3,332	O–H stretching (indicate the hydrogen bonds breaking in cellulose)		15.10	20.89	17.73	8.31	−8.71
2,906	C–H stretching (breaking of methyl/ methylene group of cellulose)		3.35	2.43	2.75	0.36	5.50
2,359	C–H methyl and methylene groups		8.70	5.63	4.14	−12.64	−15.46
1,730	Carbonyl bonds (it is linked with removal of lignin side chain)		2.26	1.62	1.34	−2.98	−5.85
1,510	C–C stretching (vibrations in the aromatic ring of lignin)		2.61	1.91	1.71	1.42	−5.46
1,420	CH$_2$ scissoring at C(6) in cellulose		1.09	0.97	0.35	−4.91	−8.83
1,325	C–H deformation in hemicellulose		10.55	8.60	8.49	4.90	−9.41
1,058	C–O stretch		0.46	6.8	4.89	1.76	−15.80
897	C–O–C valence (vibration of β-glycosidic link)		4.82	3.51	1.55	−0.88	−7.12

Relative change (%) = 100 (intensity of UT solids – intensity of pretreated solids)/intensity of UT solids; where positive value of % relative change indicates reduction.*
UT, [Untreated]; A, [Emim][Br]; B, [Edmim][Br]; C, [Bmim][Br]; D, [Hmim][Br]; E, [Omim][Br].

TABLE 3 | FTIR intensity value obtained for different ILs pretreated water hyacinth (WH) samples.

Treatment	FTIR peaks (cm^{-1})								
	3,348	2,920	2,358	1,735	1,505	1,428	1,328	1,056	897
Untreated	89.644	92.379	93.470	91.286	91.450	94.193	87.626	80.497	89.647
[Emim][Br]	99.578	99.488	99.250	93.311	95.628	91.101	91.465	85.464	99.604
[Edmim][Br]	99.529	98.402	98.267	96.677	97.718	92.090	98.017	97.910	97.197
[Bmim][Br]	99.345	99.281	99.576	94.541	93.946	93.177	95.854	96.183	96.094
[Hmim][Br]	99.358	98.996	99.317	94.421	96.162	93.580	92.734	83.454	95.288
[Omim][Br]	99.246	99.047	99.650	94.659	96.938	93.791	94.709	88.338	95.082

TABLE 4 | LOI, TCI and HBI index of untreated, ionic liquid treated water hyacinth (WH) samples.

Samples	LOI 1,420/891 cm^{-1}	TCI 1,370/2,900 cm^{-1}	HBI 3,338/1,334 cm^{-1}
Untreated	0.980	0.940	1.870
[Emim][Br]	1.570	0.997	1.291
[Edmim][Br]	1.450	0.980	1.383
[Bmim][Br]	1.389	0.971	1.537
[Hmim][Br]	1.237	0.965	1.649
[Omim][Br]	1.190	0.953	1.779

LOI, lateral order index or crystallinity index; TCI, total crystallinity index; HBI, hydrogen bond intensity.

The TCI, LOI and HBI for untreated and ILs pretreated biomass are shown in **Table 4**. For marking the changes in cellulose structure the crystalline and amorphous regions, were indicated by two peaks at 1,428 and 896 cm^{-1} denoted (O'Connor et al., 1958). During the ILs pretreatment of WH biomass samples these two absorption bands showed changes due to the vibrating nature of cellulose in crystalline region and amorphous area. Therefore, the ratio of the intensities of these two bands was defined as an empirical "crystallinity index," and it was termed as the "Lateral Order Index" (LOI). Generally, decrease in LOI value indicate the decrease in crystallinity (Oh et al., 2005; Kljun et al., 2011). The ratio between the bands at

1,372 and 2,900 cm^{-1}, also proposed by Nelson and O Connor (1964) to be the total crystallinity index (TCI), was used to evaluate the infrared crystallinity (IR) ratio.

The value LOI and TCI for the ionic liquid pretreated WH biomass samples are shown in **Table 4**. WH biomass pretreated with different ILs, showed high LOI and TCI value as compared to untreated sample, indicating that untreated sample possessed a lower crystallinity value. Therefore, WH biomass pretreated with different ILs are indicative of biomass with a higher crystallinity and more ordered structure of cellulose as represented by the higher values of given index LOI and TCI.

In this study, an empirical index HBI and LOI were used to interpret qualitative changes in crystallinity for all WH biomass samples, and HBI was used to study the changes of hydrogen bonding between certain hydroxyl groups in cellulose, generally crystallinity decreases with increasing HBI value (Oh et al., 2005). Siroky et al. (2010) reported that the two peaks at 3,338 and 1,336 cm^{-1} were closely associated with the crystalline cellulose and intra-, inter- molecular regularity. The TCI value is comparative to the crystallinity degree of cellulose in the biomass (Carrillo et al., 2004) and LOI is proportional to the degree of order in cellulose (Corgiè et al., 2011). Ionic liquids [Emim][Br] pretreated WH biomass presented the more TCI and LOI values, which is directly correlated to degree of crystallinity and more ordered structure of cellulose in comparison to other ionic liquids pretreated WH biomass. On the other hand, ionic liquids [Omim][Br] presented the lowest TCI and LOI values, which

may indicate that the cellulose of this pretreated WH biomass is composed of more amorphous domains when compared with the other ionic liquids pretreated WH biomass. While ionic liquids [Edmim][Br], [Bmim][Br] and [Hmim][Br] pretreated WH biomass presented intermediate values. HBI value is another indicator of ordered nature of cellulose and high degree of intermolecular regularity. From **Table 4**, the decreasing HBI values for [Emim][Br] and [Edmim][Br] pretreated WH biomass samples recommended the increase in degree of intermolecular regularity during the conversion process.

PXRD Analysis

The Powder X-ray diffractometer (PXRD) was used to detect the effect of ILs pretreatment on WH biomass. The PXRD profile of untreated and ILs pretreated WH biomass have shown two well-defined peaks of cellulose around 2θ = 22.5° (for the 002 peak) and 2θ = 15° (for the 001 peak) (**Figure 3**). It is observed after the analysis that all the untreated and pretreated samples showed the typical PXRD patterns of cellulose. Our results of PXRD analysis of ILs pretreated WH biomass showed two peaks one with 2θ range at 21–23° corresponding to the crystallographic forms of cellulose and second broader peaks with 2θ range 15–19° for cellulose. In this study, ILs pretreatment induced some changes in the peak which was depicted in the PXRD patterns at the value of 2θ angle.

The untreated WH biomass revealed a lower crystallinity value (CrI = 18.63%) in comparison to the ILs pretreated samples. These ILs pretreated samples [Edmim][Br] (CrI = 25.41%) and [Emim][Br] (CrI = 26.38%). [Emim][Br] have maximum crystalline value as compared to other ILs pretreatments in this study (**Table 5**). Other study supported our findings, where they have mentioned that the increase in peak intensity could be due to the untreated raw fibers containing non-cellulosic amorphous constituents, such as hemicelluloses and lignin (Silvério et al., 2013; Mtibe et al., 2015). While in some cases the stem explosion pretreated biomass indicated increase in the value of this index (Tanahashi et al., 1983). The main reason behind increase in crystallinity is due to the removal of lignin and hemicelluloses fraction (amorphous substances) and not certainly due to changes in the crystalline structure of the biomass (**Table 4**).

These PXRD patterns generated here showed semi-crystalline substances with crystalline peaks and amorphous broad hump (Santos et al., 2013). In this study, it's clear that the CrI of ILs pretreated WH had a higher value than the untreated WH biomass. Zhao et al. (2011), in their study reported that crystalline structure of cellulose is more recalcitrant to microbial and enzymatic attack, compared to amorphous cellulose.

From PXRD patterns (**Figures 3A–F**) of the untreated and pretreated samples using various ILs, it can be evidently seen that how the ILs are playing a significant role in the dissolution of lignin of WH samples. Previously, it is illustrated that anion and imidazolium ring of IL plays a crucial role in the dissolution of lignin via hydrogen bonding and π-π stacking interaction, respectively (Hossain and Aldous, 2012). Here we have analyzed the influence of alkyl chain length on the interaction between imidazolium cation and lignin in which anion is same. The pendant alkyl chain (number of carbon atoms in alkyl group
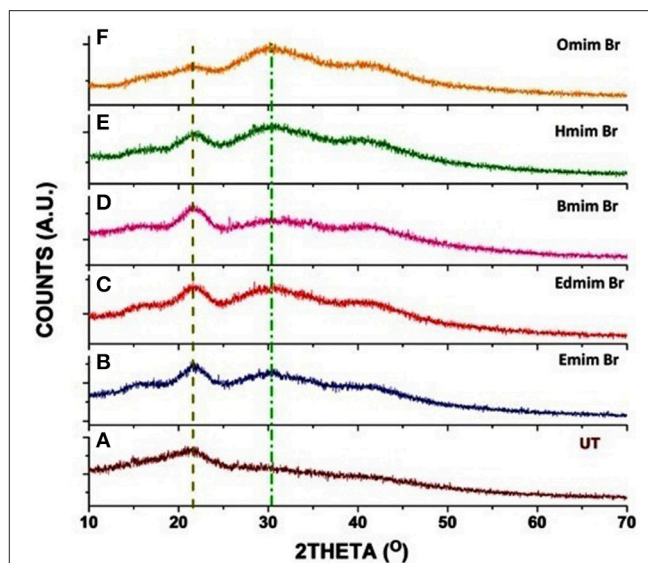

FIGURE 3 | PXRD patterns of untreated and pretreated water hyacinth (WH) biomass samples: **(A)** (UT) [Untreated]; **(B)** [Emim][Br] treated; **(C)** [Edmim][Br] treated; **(D)** [Bmim][Br] treated; **(E)** [Hmim][Br] treated and **(F)** [Omim][Br] treated.

TABLE 5 | CrI value of water hyacinth (WH) biomass.

S. No.	Treatments	Crystallinity index (%)	Increases (%)
1	Untreated	18.63	–
2	[Emim][Br] treated	26.38	41
3	[Edmim][Br] treated	25.41	36
4	[Bmim][Br] treated	22.01	18
5	[Hmim][Br] treated	21.32	14
6	[Omim][Br] treated	20.73	11

C = 2, 4, 6, and 8) length is increased to C-1 position of imidazolium cation. And the intensity of peak localized in the range of 15–25°, 2θ is substantially changing with alkyl chain length of IL. Here, intensity of peak centralized at 21.59° is gradually increasing up to [Bmim] Br (**Figures 3B–D**) however peak intensity is decreasing from [Hmim] Br and almost disappeared in the case of [Omim] Br (shown in **Figures 3E,F**). Further, hump like broad peak around 30–34° is simultaneously appearing as well-increasing with the alkyl chain length of imidazolium cations.

Moreover, it is clearly indicated that interaction between ILs and lignin molecules is dependent on the alkyl chain length of the cation. Longer the alkyl chain length more would be the steric hindrance. Consequently, lesser would be the attachment of IL cation over the surface of the WH; less amount of lignin will be dissolved in the IL. As the anion is common in case of all ILs, the role of anion on crystallinity value can be nullified.

Furthermore, the effect of IL is on the pretreatment sample can be quantitatively related to the crystallinity index (CrI) which is calculated using the Equation (1). The extent of dissolution of lignin can be indirectly determined through the CrI value. If
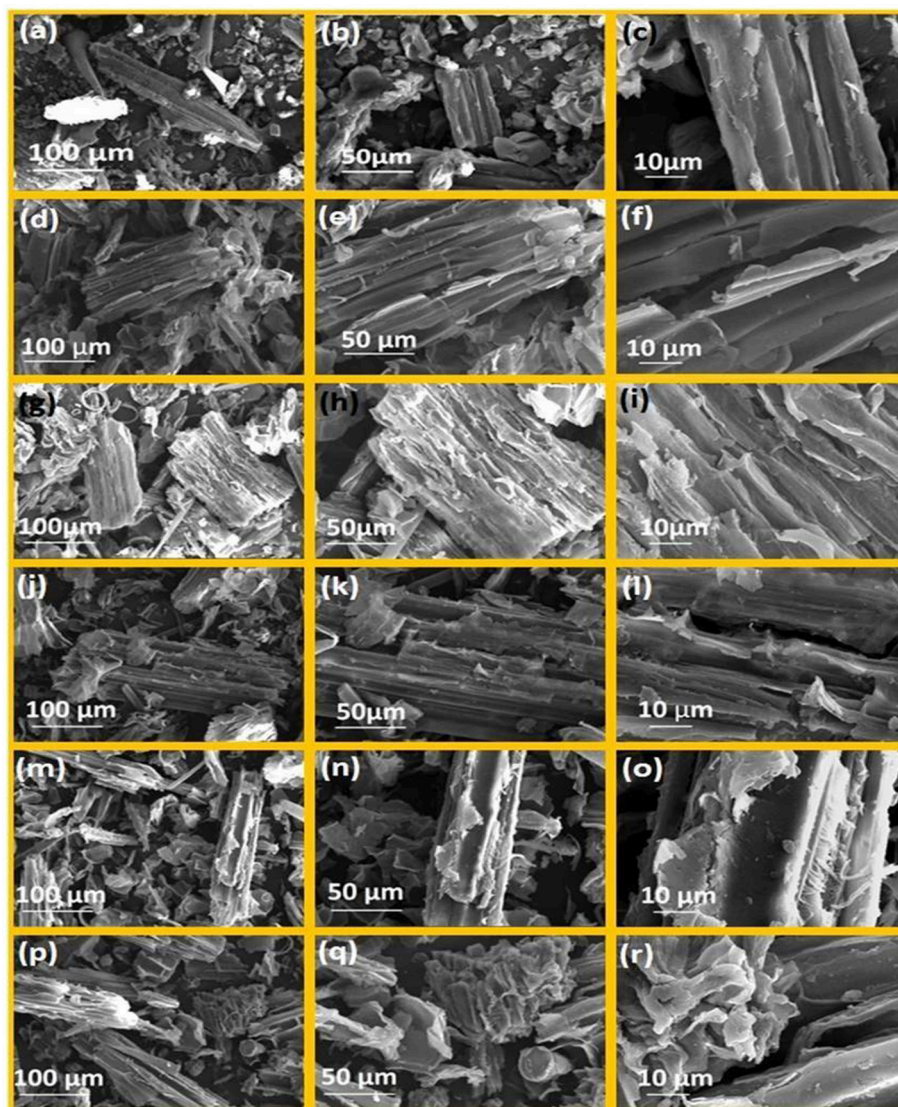
FIGURE 4 | SEM images of water hyacinth biomass at following magnification (500×, 1,000×, 3000×); **(a–c)** untreated biomass; **(d–f)** [Emim][Br]-pretreated water hyacinth biomass; **(g–i)** [Edmim][Br]-pretreated water hyacinth biomass; **(j–l)** [Bmim][Br]-pretreated water hyacinth biomass; **(m–o)** [Hmim][Br]-pretreated water hyacinth biomass; **(p-r)** [Omim][Br]-pretreated water hyacinth biomass.

the CrI value is decreasing with the alkyl chain length of the ILs, it means interaction between the IL and lignin will not be taken place to the significant extent. For instance, it is obtained highest for the sample pretreated with [Emim][Br] whereas this value is obtained very less for [Omim][Br] (20.73%) and least value is found for the untreated sample (18.63%). Same trend is also obtained for increasing the percentage of CrI of pretreated samples using different ILs with respect to the untreated sample (1) (as shown in **Table 4**), maximum value i.e., 41% is obtained for the [Emim][Br] and minimum for the [Omim][Br] (20.73%). Crystallinity index value is observed greater for the [Emim] [Br]. Similarly FTIR results also support PXRD results. Because, LOI and TCI is greater for [Emim] [Br] than that of [Omim] [Br].

SEM Analysis

The water hyacinth (WH) biomass was subjected to different ILs pretreatment and samples were analyzed by SEM to observe the changes in the surface structures of raw cellulose and the pretreated celluloses, and recognizable difference between raw cellulose biomass and the treated cellulose biomass which are shown in **Figures 4a–r** with different levels of magnifications (500×, 1,000×, and 3,000×). Image analysis revealed highly fibrillar and intact morphology (**Figures 4a–c**) in case of untreated biomass, while the pretreated samples showed change in surface morphology and marked damage caused by the ILs (**Figures 4d–r**). Among all the pretreatments used, the [Emim][Br] was the highly effective pretreatment which have altered the structure of biomass to swollen and loose and fibrous

structure has transformed into porous and amorphous form and been completely distorted (**Figures 4d–f**). Results shown in **Figure 4** clearly supported the findings observed in case of FTIR and PXRD analysis. IL pretreatment using [Edmim][Br] had similar effects on water hyacinth biomass (**Figures 4g–i**) leading to maximum alterations in water hyacinth biomass structure after [Emim][Br] pretreatment. SEM analysis showed that following ILs [Omim][Br], [Hmim][Br] and [Bmim][Br] showed lesser effect on physical structure which was incapable of making any significant alterations. Microscopic shape of cellulose was smooth and compact, but the shapes of pretreated cellulose biomass were absolutely lamellar. So it is clear that due to smaller size of [Emim] cation, it interacts with the biomass more in comparison to the other. This may be due to the π-π stacking interaction of aromatic ring and hydrogen bonding at C-2 position. So–CH_3 group are incorporated in [Edmim][Br], crystallinity and other degradation parameters are less. Moreover, when we are increasing the alkyl chain length etc. For example, [Bmim][Br], [Hmim][Br] and so on degradation of biomass is less. This might be due to the steric hindrance due to which imidazolium cannot interact with the biomass.

Structurally, cellulose is composed of the several cellulose strands run parallel and the large quantity of hydroxyls closed in a crystal cell, these parameters determine the CrI of raw cellulose. But after the treatment, change in microscopic structure of cellulose takes place that changes the CrI value. As a result, the pretreated cellulose biomass with ionic liquids had a looser microscopic shape. Our results are supported by Mood et al. (2014) where different sets of ionic liquids [Bmim][OTF], [MMIM][DMP], [BMIM][CL], [EMIM][DEP] and [EMIM][AC] are used to understand the physical and structural changes using SEM in barley straw.

DSC Analysis

The major components of biomass (cellulose, hemicellulose and lignin) degrade at different temperatures. Cellulose is highly crystalline, which makes it thermally stable. Hemicellulose and lignin on the other hand are amorphous and start to degrade before cellulose (Hill, 2006). Hemicelluloses are the least thermally stable components of biomass, due to the presence of acetyl groups (Bourgois et al., 1989). Lignin degrades partly over a wide temperature range, starting at relatively low temperatures (Nassar and MacKay, 2007).

DSC analysis was performed to determine the melt processing, which is due to change in the structural organization that influence the thermal behavior of cellulose, especially for its specific congregated structure. The DSC analysis validated the changes observed in the ILs pretreated biomass, including hydrogen bond strength, the CrI and microscopic changes. The thermal behavior can be assessed by TGA whilst the endothermic and exothermic reactions can be followed by DSC. The untreated and pretreated cellulose biomass was investigated by using DSC in a N_2 atmosphere.

DSC curves showed only one clear endothermic change within the temperature range of 30–400°C (**Figure 5**). The endotherm that occurred from 30 to 100°C represented the loss of water to evaporation. Untreated WH had the highest evaporization
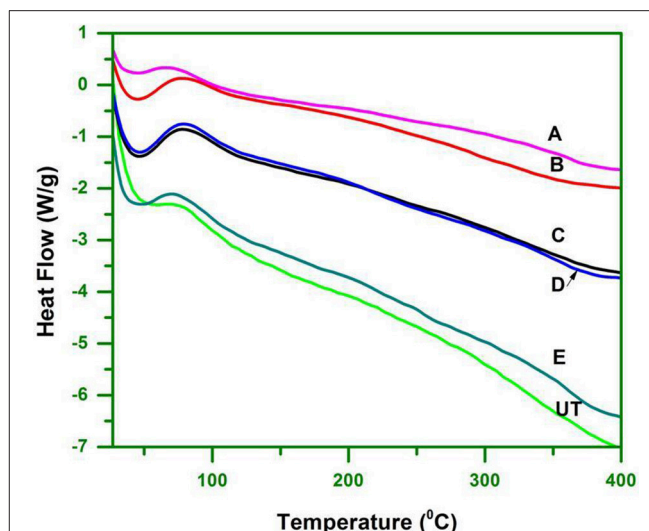
FIGURE 5 | DSC curve that indicate the energy consumption property of cellulose of hyacinth biomass.

temperature (T_{eva}) of 54°C, followed by [Bmim][Br] treated WH at 44°C. The obtained results were due to the hydrophilic substances, such as hemicelluloses, lignin, and non-cellulosic materials that retain moisture in untreated WH. The DSC curves of treated WH were found to be 42°C, 45°C, 47°C, and 40°C.

Mechanism of Dissolution of Lignin Using ILs

Several studies reported that imidazolium based ILs could effectively dissolve complex lignocellulosic biomass network (Zhang et al., 2005; Erdmenger et al., 2008). The mechanism for lignin dissolution in ILs seems unlike that for cellulose dissolution. Xue et al. (2016), reported that the change of the solvent property for GVL-based binary solvent systems [Binary solvent systems consisting of biomass derived γ-valerolactone (GVL) and one co-solvent (e.g., water, ionic liquids, DMSO, and DMF)] was beneficial for the break of the strong hydrogen bonding in lignin and the combination of the aromatic nucleus and aliphatic chain regions, and thus resulted in much higher lignin solubility. Alvira et al. (2010) reported that ILs with anion activity (e.g., the 1-butyl-3 methyl imidazolium cation [$C4mim$]$^+$) can dissolve the lignin and carbohydrate because ILs form hydrogen bonds between the non-hydrated chloride ions of the IL and the sugar hydroxyl protons in a 1:1 stoichiometry. As a result, the intricate network of non-covalent interactions among biomass polymers of cellulose, hemicellulose, and lignin is effectively disrupted while minimizing formation of degradation products (Alvira et al., 2010). Dissolution of lignin in ionic liquids is tremendously studied in which the effect of anions and their counter ion on the dissolution of lignin was reported by different workers. It is well-known that IL is fundamentally consisted of cation and anion parts. It is previously reported that nature of anions play a significant role in dissolving the lignin

through hydrogen-bonding. While, imidazolium based cation has aromatic ring system which interacts with aromatic structural moieties (for instance paracoumaryl alcohol, coniferyl alcohol and synapyl alcohol) of lignin via π-π interaction (Hossain and Aldous, 2012). The effect of alkyl chain length of ILs on the lignin dissolution is not reported to the best of our knowledge. Hereby different imidazolium based ILs with tunable alkyl chain length (such as ethyl in [Emim]$^+$ and [Edmim]$^+$, butyl in [Bmim]$^+$, hexyl [Hmim]$^+$ and octyl [Omim]$^+$) but with the same counter anion Br$^-$ are used in the present study. Therefore, the role of anion on the lignin dissolution can be neglected here. In addition, to understand the effect of acidic proton on the dissolution of lignin, C-2 position of imidazolium cation is substituted by methyl group in [Edmim][Br]. Mechanism of interaction between IL and sample can be described using the FESEM images and PXRD patterns of pretreated samples of WH, and it is found that [Emim][Br] IL is showing high crystallinity value while very less value of crystallinity index is in case of [Omim][Br]. The value of crystallinity index is gradually decreasing with alkyl chain length of ILs. In addition, similar trend was also obtained in FESEM images of the pretreatment samples. In FESEM images, sample pretreated with [Emim][Br] was found very much ruptured and inner layers were highly exposed and as a result fibril like structures were appeared (as shown in **Figures 4m–o**). Contrary to this, when the sample was pretreated with [Hmim] [Br] and [Omim] [Br] (**Figures 4j–l,g–i**), we did not find any noticeable changes than the untreated sample and fibril like structure was also absent. There are two ways through which IL is interacting with sample: a) via hydrogen bonding between acidic proton and lignin moiety and b) π-π interaction between imidazolium cation and aromatic groups of lignin that depends on the alkyl chain length at C-1 position of imidazolium cation (steric hindrance effect). Imidazolium based ionic liquids have significantly been used for synthesis of nano-materials specially in tuning the crystal phase and morphology of the nanoparticles. It has already been illustrated that during synthesis of nanoparticles, imidazolium based ionic liquids are bound at nucleation stage via aromatic π- (pi)-system or acidic proton via hydrogen bonding (Wang et al., 2008). Similarly, biomolecules often consist of aromatic system containing molecules like protein, amino acids, polypeptide chains, lignin, hemicellulose and so on. Therefore, the possibility of interaction between biomolecules and ionic liquid is increased. As a result, effect of ionic liquid on the biological system can also be noticed. Thus, from detailed studies of all pretreated samples, it was noticed that the alkyl chain length of ILs is playing a significant role in interaction which is to be occurred between ILs and lignin. It means smaller the pendant alkyl chain length greater would be the binding of the ILs on the surface of pretreated sample. As the alkyl chain length increases, binding of ILs on the surface of samples decreases resulting of lignin dissolution was found very less as in case of [Omim][Br] IL. In order to see the effect of acidic proton on C-2 position of IL, [Edmim][Br] IL was employed for pretreatment of WH biomass sample; in that case crystallinity index was found to be increased to

noticeable extent because crystallinity is strongly influenced by the lignocellulosic biomass complex composition. The raw lignocellulosic biomass has a lowest crystallinity because it has a higher content of lignin and hemicellulose which are amorphous in nature (Xu et al., 2007). In this study, the Crl of the untreated WH biomass was higher than that of the untreated WH biomass. This indicates that the higher value of crystallinity results from modification of the complex composition of the pretreated WH biomass. In other word, substitution of acidic proton by methyl group is also decreasing the attachment of the [Edmim][Br] on the surface of pretreated WH biomass sample due to steric hindrance effect (shown in **Table 4**). Perez-Pimienta et al. (2016) confirmed that [Emim][OAc] readily dissolved lignin in the tested biomass. The authors then compared the solubility of lignin in ILs with the same anion [OAc], but with different cations [Emim]$^+$, [Bmim]$^+$, [N$_{4448}$]$^+$, [Bm$_2$im]$^+$, and [Bpyr]$^+$, and noted that the solubility follows [Emim]$^+$ = [Bmim]$^+$ = [Bpyr]$^+$ > [Bm$_2$im]$^+$ > [N$_{4448}$]$^+$.

CONCLUSIONS

In summary, we have succeeded to develop an IL based methodology for lignin solubilization from WH, whose biomass is one of the most important feedstock for the production of fermentable sugar and bio-ethanol. Amongst 5 different imidazolium based ILs, 1-ethyl-3-methylimidazolium bromide [Emim][Br] is found most efficient in biomass conversion followed by 1-ethyl-2,3-dimethylimidazolium bromide [Edmim][Br]. Analysis reveals that imidazolium cation with lower alkyl chain length like [Emim]$^+$ can interact with the aromatic rings of lignin moieties via π stacking as well as H-bonding. However, ILs with higher alkyl chain length cannot interact so efficiently with the lignin due to steric hindrance and causes less dissolution. To the best of our knowledge, the effect of IL cation on the hydrolysis of WH biomass is not reported so far and can pave the way for an IL based promising approach for hydrolysis of other biomasses.

AUTHOR CONTRIBUTIONS

JS and RS have contributed equally to this manuscript under the guidance of AK and PG. PG and AK prepared and edited the manuscript. MK suggested some improvements to the manuscript.

ACKNOWLEDGMENTS

REFERENCES

Aid, T., Paist, L., Lopp, M., Kaljurand, M., and Vaher, M. (2016). An optimized capillary electrophoresis method for the simultaneous analysis of biomass degradation products in ionic liquid containing samples. *J. Chromatogr. A* 1447, 141–147. doi: 10.1016/j.chroma.2016.04.027

Alemdar, A., and Sain, M. (2008). Isolation and characterization of nanofibers from agricultural residues–wheat straw and soy hulls. *Bioresour. Technol.* 99, 1664–1671. doi: 10.1016/j.biortech.2007.04.029

Alvira, P., Tomás-Pejó, E., Ballesteros, M. J., and Negro, M. J. (2010). Pretreatment technologies for an efficient bioethanol production process based on enzymatic hydrolysis: a review. *Bioresour. Technol.* 101, 4851–4861. doi: 10.1016/j.biortech.2009.11.093

Bodirlau, R., Teaca, C.-A., and Spiridon, I. (2010). Influence of ionic liquid on hydrolyzed cellulose material: FT-IR spectroscopy and TG-DTG-DSC analysis. *Int. J. Polym. Anal. Charact.* 15, 460–469. doi: 10.1080/1023666X.2010.510112

Bolenz, S., Omran, H., and Gierschner, K. (1990). Treatments of water hyacinth tissue to obtain useful products. *Biol. Wastes* 33, 263–274. doi: 10.1016/0269-7483(90)90130-K

Bourgois, J., Bartholin, M. C., and Guyonnet, R. (1989). Thermal treatment of wood: analysis of the obtained product. *Wood Sci. Technol.* 23, 303–310. doi: 10.1007/BF00353246

Carrillo, F., Colom, X., and Su, J. J. (2004). Structural FTIR analysis and thermal characterisation of lyocell and viscose-type fibres. *Eur. Polym. J.* 40, 2229–2234. doi: 10.1016/j.eurpolymj.2004.05.003

Chandra, R. P., Bura, R., Mabee, W. E., Berlin, A., Pan, X., and Saddler, J. N. (2007). Substrate pretreatment: The key to effective enzymatic hydrolysis of lignocellulosics? *Adv. Biochem. Eng. Biotechnol.* 108, 67–93. doi: 10.1007/10_2007_064

Chen, L., Li, J., Lu, M., Guo, X., Zhang, H., and Han, L. (2016). Integrated chemical and multi-scale structural analyses for the processes of acid pretreatment and enzymatic hydrolysis of corn stover. *Carbohydr. Polym.* 141, 1–9. doi: 10.1016/j.carbpol.2015.12.079

Corgié, S. C., Smith, H. M., and Walker, L. P. (2011). Enzymatic Transformations of Cellulose Assessed by Quantitative High-Throughput Fourier Transform Infrared Spectroscopy (QHT-FTIR). *Biotechnol. Bioeng.* 108, 1509–1520. doi: 10.1002/bit.23098

Cruz, A. G., Scullin, C., Mu, C., Cheng, G., Stavila, V., Varanasi, P., et al. (2013). Impact of high biomass loading on ionic liquid pretreatment. *Biotechnol. Biofuels* 6:52. doi: 10.1186/1754-6834-6-52

Erdmenger, T., Vitz, J., Wiesbrock, F., and Schubert, U. S. (2008). Influence of different branched alkyl side chains on the properties of imidazolium-based ionic liquids. *J. Mater. Chem.* 18, 5267–5273. doi: 10.1039/b807119e

Feng, W., Xiao, K., Zhou, W., Zhu, D., Zhou, Y., Yuan, Y., et al. (2017). Analysis of utilization technologies for *Eichhornia crassipes* biomass harvested after restoration of wastewater. *Bioresour. Technol.* 223, 287–295. doi: 10.1016/j.biortech.2016.10.047

Fort, D. A., Remsing, R. C., Swatloski, R. P., Moyna, P., Moyna, G., and Rogers, R. D. (2007). Can ionic liquids dissolve wood? Processing and analysis of lignocellulosic materials with 1-n-butyl-3-methylimidazolium chloride. *Green Chem.* 9, 63–69. doi: 10.1039/B607614A

Ganguly, A., Das, S., Bhattacharya, A., Dey, A., and Chatterjee, P. K. (2013). Enzymatic hydrolysis of water hyacinth biomass for the production of ethanol: optimization of driving parameters. *Indian J. Exp. Biol.* 51, 556–566.

Genestar, C., and Palou, J. (2006). SEM–FTIR spectroscopic evaluation of deterioration in an historic coffered ceiling. *Anal. Bioanal. Chem.* 987–993. doi: 10.1007/s00216-005-0243-y

Ghosh, P., and Mudring, A. (2016). Phase selective synthesis of quantum cutting nanophosphors and the observation of a spontaneous room temperature phase transition. *Nanoscale* 8, 8160–9. doi: 10.1039/c6nr00172f

Gressel, J. (2008). Transgenics are imperative for biofuel crops. *Plant Sci.* 174, 246–263. doi: 10.1016/j.plantsci.2007.11.009

Hill, C. A. S. (2006). *Wood Modification: Chemical, Thermal and Other Processes.* Chichester, UK: John Wiley and Sons

Hossain, M. M., and Aldous, L. (2012). Ionic liquids for lignin processing: Dissolution, isolation, and conversion. *Aust. J. Chem.* 65, 1465–1477. doi: 10.1071/CH12324

Hsu, T. C., Guo, G. L., Chen, W. H., and Hwang, W. S. (2010). Effect of dilute acid pretreatment of rice straw on structural properties and enzymatic hydrolysis. *Bioresour. Technol.* 101, 4907–4913. doi: 10.1016/j.biortech.2009.10.009

Hurtubise, F. G., and Krassig, H. (1960). Classification of fine structural characteristics in cellulose by infrared spectroscopy. *Anal. Chem.* 32, 177–181. doi: 10.1021/ac60158a010

Karatzos, S. K., Edye, L. A., Orlando, W., and Doherty, S. (2012). Sugarcane bagasse pretreatment using three imidazolium-based ionic liquids; mass balances and enzyme kinetics. *Biotechnol. Biofuel.* 5, 1–12. doi: 10.1186/1754-6834-5-62

Kilpeläinen, I., Xie, H., King, A., Granstrom, M., Heikkinen, S., and Argyropoulos, D. S. (2007). Dissolution of wood in ionic liquids. *J. Agric. Food Chem.* 55, 9142–9148. doi: 10.1021/jf071692e

Kljun, A., Benians, T. A., Goubet, F., Meulewaeter, F., Knox, J. P., and Blackburn, R. S. (2011). Comparative analysis of crystallinity changes in cellulose I polymers using ATR-FTIR, X-ray diffraction, and carbohydrate-binding module probes. *Biomacromolecules* 12, 4121–4126. doi: 10.1021/bm201176m

Kothari, R., Pandey, A., Ahmad, S., Kumar, A., Pathak, V. V., and Tyagi, V. V. (2017). Microalgal cultivation for value-added products: a critical enviro-economical assessment. *3 Biotech.* 7, 243. doi: 10.1007/s13205-017-0812-8

Kumar, A., Kumar, K., Kaushik, N., Sharma, S., and Mishra, S. (2010). Renewable energy in India: current status and future potentials. *Renew. Sustain. Energy Rev.* 14, 2434–2442. doi: 10.1016/j.rser.2010.04.003

Kumar, A., and Sharma, S. (2011). Potential non-edible oil resources as biodiesel feedstock: an Indian perspective. *Renew. Sustain. Energy Rev.* 15, 1791–1800. doi: 10.1016/j.rser.2010.11.020

Kumar, R., Mago, G., Balan, V., and Wyman, C. E. (2009). Physical and chemical characterizations of corn stover and poplar solids resulting from leading pretreatment technologies. *Bioresour. Technol.* 100, 3948–3962. doi: 10.1016/j.biortech.2009.01.075

Kumar, R., Mudring, A., and Ghosh, P. (2017). Recent trends in binary and ternary rare-earth fluoride nanophosphors: how structural and physical properties influence optical behavior. *J. Lumin.* 189, 44–63. doi: 10.1016/j.jlumin.2017.03.062

Lau, M. W., Dale, B. E., and Balan, V. (2008). Ethanolic fermentation of hydrolysates from ammonia fiber expansion (AFEX) treated corn stover and distillers grain without detoxification and external nutrient supplementation. *Biotechnol. Bioeng.* 99, 529–539. doi: 10.1002/bit.21609

Lee, S. H., and Lee, S. B. (2005). The Hildebrand solubility parameters, cohesive energy densities and internal energies of 1-alkyl-3-methylimidazolium-based room temperature ionic liquids. *Chem. Commun.* 3469–3471. doi: 10.1039/b503740a

Li, C., Knierim, B., Manisseri, C., Arora, R., Scheller, H. V, Auer, M., et al. (2010). Comparison of dilute acid and ionic liquid pretreatment of switchgrass: biomass recalcitrance, delignification and enzymatic saccharification. *Bioresour. Technol.* 101, 4900–4906. doi: 10.1016/j.biortech.2009.10.066

Li, R., Fei, J., Cai, Y., Li, Y., Feng, J., and Yao, J. (2009). Cellulose whiskers extracted from mulberry: a novel biomass production. *Carbohydr. Polym.* 76, 94–99. doi: 10.1016/j.carbpol.2008.09.034

Liu, C., and Wyman, C. E. (2004). Impact of fluid velocity on hot water only pretreatment of corn stover in a flowthrough reactor. *Appl. Biochem. Biotechnol.* 113–116, 977–987. doi: 10.1385/ABAB:115:1-3:0977

Liu, C. C., Wang, M. K., Chiou, C. S., Li, Y. S., Lin, Y. A., and Huang, S. S. (2006). Chromium removal and sorption mechanism from aqueous solutions by wine processing waste sludge. *Ind. Eng. Chem. Res.* 45, 8891–8899. doi: 10.1021/ie060978q

Lloyd, T. A., and Wyman, C. E. (2005). Combined sugar yields for dilute sulfuric acid pretreatment of corn stover followed by enzymatic hydrolysis of the remaining solids. *Bioresour. Technol.* 96, 1967–1977. doi: 10.1016/j.biortech.2005.01.011

Menon, V., and Rao, M. (2012). Trends in bioconversion of lignocellulose: Biofuels, platform chemicals & biorefinery concept. *Prog. Energy Combust. Sci.* 38, 522–550. doi: 10.1016/j.pecs.2012.02.002

Mood, S. H., Golfeshan, A. H., Tabatabaei, M., Abbasalizadeh, S., Ardjmand, M., and Jouzani, G. S. (2014). Comparison of different ionic liquids pretreatment for corn stover enzymatic saccharification. *Prep. Biochem. Biotechnol.* 44, 451–63. doi: 10.1080/10826068.2013.833112

Mtibe, A., Linganiso, L. Z., Mathew, A. P., Oksman, K., John, M. J., and Anandjiwala, R. D. (2015). A comparative study on properties of micro and

nanopapers produced from cellulose and cellulose nanofibres. *Carbohydr. Polym.* 118, 1–8. doi: 10.1016/j.carbpol.2014.10.007

Nada, A. A. M. A., Kamel, S., and El-Sakhawy, M. (2000). Thermal behaviour and infrared spectroscopy of cellulose carbamates. *Polym. Degrad. Stab.* 70, 347–355. doi: 10.1016/S0141-3910(00)00119-1

Nassar, M. M., and MacKay, G. D. M. (2007). Mechanism of thermal decomposition of lignin. *Wood Fiber Sci.* 16, 441–453.

Nelson, and O Connor, R. T. O. (1964). Relation of certain infrared bands to cellulose crystallinity and crystal lattice type. part I. Spectra of lattice types I, II, III and of amorphous cellulose. *J. Appl. Polym. Sci.* 8, 1311–1324. doi: 10.1002/app.1964.070080323

O'Connor, R. T., DuPre, E. F., and Mitcham, D. (1958). Applications of infrared absorption spectroscopy to investigations of cotton and modified cottons: part I: physical and crystalline modifications and oxidation. *Text. Res. J.* 28, 382–392. doi: 10.1177/004051755802800503

Oh, S. Y., Dong, I. Y., Shin, Y., Hwan, C. K., Hak, Y. K., Yong, S. C., et al. (2005). Crystalline structure analysis of cellulose treated with sodium hydroxide and carbon dioxide by means of X-ray diffraction and FTIR spectroscopy. *Carbohydr. Res.* 340, 2376–2391. doi: 10.1016/j.carres.2005.08.007

Pandey, K. K., and Pitman, A. J. (2003). FTIR studies of the changes in wood chemistry following decay by brown-rot and white-rot fungi. *Int. Biodeterior. Biodegrad.* 52, 151–160. doi: 10.1016/S0964-8305(03)00052-0

Perez-Pimienta, J. A., Flores-Gómez, C. A., Ruiz, H. A., Sathitsuksanoh, N., Balan, V., da Costa Sousa, L., et al. (2016). Evaluation of agave bagasse recalcitrance using AFEX^{TM}, autohydrolysis, and ionic liquid pretreatments. *Bioresour. Technol*, 211, 216-223. doi: 10.1016/j.biortech.2016.03.103

Popescu, C. M., Singurel, G., Popescu, M. C., Vasile, C., Argyropoulos, D. S., and Willför, S. (2009). Vibrational spectroscopy and X-ray diffraction methods to establish the differences between hardwood and softwood. *Carbohydr. Polym.* 77, 851–857. doi: 10.1016/j.carbpol.2009.03.011

Qiu, Z. H., Aita, G. M., and Walker, M. S. (2012). Effect of ionic liquid pretreatment on the chemical composition, structure and enzymatic hydrolysis of energy cane bagasse. *Bioresour. Technol.* 117, 251–256. doi: 10.1016/j.biortech.2012.04.070

Raghunandan, K., Kumar, A., Kumar, S., Permaul, K., and Singh, S. (2018). Production of gellan gum, an exopolysaccharide, from biodiesel-derived waste glycerol by *Sphingomonas* spp. *3 Biotech.* 8, 71. doi: 10.1007/s13205-018-1096-3

Rezania, S., Fadhil, M., Din, M., Mohamad, S. E., Sohaili, J., Taib, S. M., et al. (2017). Review on pretreatment methods and ethanol production from cellulosic water hyacinth. *BioResources* 12, 2108–2124. doi: 10.15376/biores.12.1.Rezania

Rezania, S., Ponraj, M., Din, M. F. M., Songip, A. R., Sairan, F. M., and Chelliapan, S. (2015). The diverse applications of water hyacinth with main focus on sustainable energy and production for new era: an overview. *Renew. Sustain. Energy Rev.* 41, 943–954. doi: 10.1016/j.rser.2014.09.006

Rodrigues, G., de Assunção, R. M. N., Vieira, J. G., Meireles, C. da S., Cerqueira, D. A., da Silva Barud, H., et al. (2007). Characterization of methylcellulose produced from sugar cane bagasse cellulose: Crystallinity and thermal properties. *Polym. Degrad. Stab.* 92, 205–210. doi: 10.1016/j.polymdegradstab.2006.11.008

Saini, J. K., Saini, R., and Tewari, L. (2015). Lignocellulosic agriculture wastes as biomass feedstocks for second-generation bioethanol production: concepts and recent developments. *3 Biotech.* 5, 337–353. doi: 10.1007/s13205-014-0246-5

Santos, R. B., Hart, P. W., Jameel, H., and Chang, H. M. (2013). Wood based lignin reactions important to the biorefinery and pulp and paper industries. *BioResources* 8, 1456–1477. doi: 10.15376/biores.8.1.158-171

Schell, D. J., Farmer, J., Newman, M., and McMillan, J. D. (2003). Dilute-sulfuric acid pretreatment of corn stover in pilot-scale reactor: investigation of yields, kinetics, and enzymatic digestibilities of solids. *Appl. Biochem. Biotechnol.* 105–108, 69–85. doi: 10.1385/ABAB:105:1-3:69

Segal, L., Creely, L., Martin, A. E., and Conrad, C. M. (1959). An empirical method for estimating the degree of crystallinity of native cellulose using the X-ray diffractometer. *Text. Res. J.* 29, 786–794. doi: 10.1177/004051755902901003

Sheldon, R. A. (2002). Biocatalysis in ionic liquids. *Chem. Rev.* 107, 2757–2785. doi: 10.1021/cr050946x

Sierra, R., Holtzapple, M. T., and Granda, C. B. (2011). Long-term lime pretreatment of poplar wood. *AIChE J.* 57, 1320–1328. doi: 10.1002/aic.12350

Silvério, H. A., Flauzino Neto, W. P., Dantas, N. O., and Pasquini, D. (2013). Extraction and characterization of cellulose nanocrystals from corncob for application as reinforcing agent in nanocomposites. *Ind. Crops Prod.* 44, 427–436. doi: 10.1016/j.indcrop.2012.10.014

Sindhu, R., Binod, P., and Pandey, A. (2016). Biological pretreatment of lignocellulosic biomass–an overview. *Bioresour. Technol.* 199, 76–82. doi: 10.1016/j.biortech.2015.08.030

Singh, J. K., Vyas, P., Dubey, A., Upadhyaya, C. P., Kothari, R., Tyagi, V. V., et al. (2018). Assessment of different pretreatment technologies for efficient bioconversion of lignocellulose to ethanol. *Front. Biosci.* 10:521. doi: 10.2741/521

Singh, N. B., Kumar, A., and Rai, S. (2014a). Potential production of bioenergy from biomass in an Indian perspective. *Renew. Sustain. Energy Rev.* 39, 65–78. doi: 10.1016/j.rser.2014.07.110

Singh, R., Tiwari, S., Srivastava, M., and Shukla, A. (2014b). Microwave assisted alkali pretreatment of rice straw for enhancing enzymatic digestibility. *J. Energy* 2014:483813. doi: 10.1155/2014/483813

Siroky, J., Blackburn, R.S., Bechtold, T., Taylor, J., and White, P. (2010). Attenuated total reflectance Fourier-transform Infrared spectroscopy analysis of crystallinity changes in lyocell following continuous treatment with sodium hydroxide. *Cellulose.* 103–115. doi: 10.1007/s10570-009-9378-x

Swatloski, R. P., Spear, S. K., Holbrey, J. D., and Rogers, R. D. (2002). Dissolution of cellulose with ionic liquids. *J. Am. Chem. Soc.* 124, 4974–4975. doi: 10.1021/ja025790m

Tanahashi, M., Takada, S., Aoki, T., Goto, T., Higuchi, T., and Hanai, S. (1983). Characterization of explosion wood. *Wood Res.* 66, 36–51.

Tiwari, G., Sharma, A., Kumar, A., and Sharma, S. (2018). Assessment of microwave-assisted alkali pretreatment for the production of sugars from banana fruit peel waste. *Biofuel* 7269. doi: 10.1080/17597269.2018.1442665

Vyas, P., Kumar, A., and Singh, S. (2018). Biomass breakdown: a review on pretreatment, instrumentations and methods. *Front. Biosci.* 10:815. doi: 10.2741/815

Wang, L., Chang, L., Zhao, B., Yuan, Z., Shao, G., and Zheng, W. (2008). Systematic investigation on morphologies, forming mechanism, photocatalytic and photoluminescent properties of ZnO nanostructures constructed in ionic liquids. *Inorg. Chem.* 47, 1443–1452. doi: 10.1021/ic701094a

Wei, L., Li, K., Ma, Y., and Hou, X. (2012). Dissolving lignocellulosic biomass in a 1-butyl-3-methylimidazolium chloride–water mixture. *Indus. Crops Prod.* 37, 227–234. doi: 10.1016/j.indcrop.2011.12.012

Xu, Z., Wang, Q., Jiang, Z., Yang, X. X., and Ji, Y. (2007). Enzymatic hydrolysis of pretreated soybean straw. *Biomass Bioenergy* 31, 162–167. doi: 10.1016/j.biombioe.2006.06.015

Xue, Z., Zhao, X., Sun, R. C., and Mu, T. (2016). Biomass-derived γ-valerolactone-based solvent systems for highly efficient dissolution of various lignins: dissolution behavior and mechanism study. *ACS Sustain. Chem. Eng.* 4, 3864–3870. doi: 10.1021/acssuschemeng.6b00639

Yang, Q., Pan, X., Huang, F., and Li, K. (2011). Synthesis and characterization of cellulose fibers grafted with hyperbranched poly(3-methyl-3-oxetanemethanol). *Cellulose* 18, 1611–1621. doi: 10.1007/s10570-011-9587-y

Zabed, H., Sahu, J. N., Boyce, A. N., and Faruq, G. (2016). Fuel ethanol production from lignocellulosic biomass: An overview on feedstocks and technological approaches. *Renew. Sustain. Energy Rev.* 66, 751–774. doi: 10.1016/j.rser.2016.08.038

Zhang, H., Wu, J., Zhang, J., and He, J. (2005). 1-Allyl-3-methylimidazolium chloride room temperature ionic liquid: a new and powerful nonderivatizing solvent for cellulose. *Macromolecules* 38, 8272–8277. doi: 10.1021/ma0505676

Zhang, Y.-H. P., Ding, S.-Y., Mielenz, J. R., Cui, J.-B., Elander, R. T., Laser, M., et al. (2007). Fractionating recalcitrant lignocellulose at modest reaction conditions. *Biotechnol. Bioeng.* 97, 214–223. doi: 10.1002/bit.21386

Zhao, J., Zhang, H., Zheng, R., Lin, Z., and Huang, H. (2011). The enhancement of pretreatment and enzymatic hydrolysis of corn stover by FeSO$_4$ pretreatment. *Biochem. Eng. J.* 56, 158–164. doi: 10.1016/j.bej.2011.06.002

Activation of Electrophile/Nucleophile Pair by a Nucleophilic and Electrophilic Solvation in a S$_N$Ar Reaction

Bruno Sánchez[1], Cristian Calderón[2], Ricardo A. Tapia[3], Renato Contreras[1] and Paola R. Campodónico[2]*

[1] Departamento de Química, Facultad de Ciencias, Universidad de Chile, Santiago, Chile, [2] Centro de Química Médica, Facultad de Medicina, Clínica Alemana Universidad del Desarrollo, Santiago, Chile, [3] Facultad de Química, Pontificia Universidad Católica de Chile, Santiago, Chile

Nucleophilic aromatic substitution reactions of 4-chloroquinazoline toward aniline and hydrazine were used as a model system to experimentally show that a substrate bearing heteroatoms on the aromatic ring as substituent is able to establish intramolecular hydrogen bond which may be activated by the reaction media and/or the nature of the nucleophile.

Keywords: solvent effects, ionic liquids, catalysis, anion effect, preferential solvation

INTRODUCTION

The electrophilicity (ω^+) and nucleophilicity (ω^-) concepts (Ingold, 1929, 1933, 1934) are related to electron-deficient (electrophile) and electron-rich (nucleophile) species (Jaramillo et al., 2006). These concepts were early introduced by Ingold in 1934 and they are based on the valence electron theory of Lewis (Lewis, 1923) and the general acid-base theory of Brönsted and Lowry (Brönsted, 1923; Lowry, 1923; Cedillo et al., 2007).

The solvent effect at a microscopic scale could be studied considering the possible interactions using Lewis concepts. The solvent effects usually are studied in aromatic nucleophilic substitution (S$_N$Ar) reactions, because the reaction media involves the stabilization of species associated to the Potential Energy Surface (PES) such as: electrophile/nucleophile (E^+/Nu^-) pair, transition state (TS) and intermediate structures, respectively (Ormazábal-Toledo et al., 2013c; Gazitúa et al., 2014; Alarcón-Espósito et al., 2015, 2016, 2017). Specific interactions such as hydrogen bond (HB), π–π and p–π stacking are expected to shed insights on the responses of these species in the bulk and specific E^+/Nu^- pair-solvent interactions would determine selectivity, reaction rates and mechanisms (Ormazábal-Toledo et al., 2013c; Gazitúa et al., 2014; Alarcón-Espósito et al., 2015, 2016, 2017; Marullo et al., 2016).

Considering that the solvation and catalysis phenomena are mainly determined by HB interactions, would be more appropriate to use the Lewis acidity/basicity than Brönsted acidity/basicity concepts in order to perform scales. The main reason is because the Brönsted acidity/basicity scale is refers to different chemical processes where the acidic/basic hydrogen atom is completely transferred or accepted in the form of a proton, while the Lewis acidity/basicity scale is fundamentally a regional property and not a global one (Ormazábal-Toledo et al., 2013c; Gazitúa et al., 2014; Alarcón-Espósito et al., 2015, 2016, 2017; Marullo et al., 2016). Solvent effects can be split into two types: non-specific and specific interactions, including all the possible interactions that can occur between solvent and the E^+/Nu^- pair (Chiappe et al., 2011). Preferential solvation
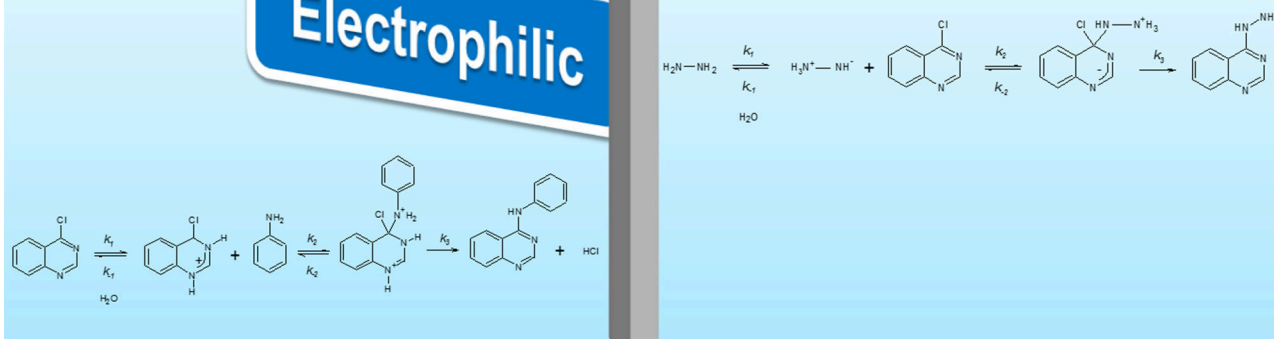
GRAPHICAL ABSTRACT |

(Mancini et al., 1999; Ormazábal-Toledo et al., 2013c; Alarcón-Espósito et al., 2015) may be defined into the form of specific E^+/Nu^- pair-solvent interactions that describes local solvation, defined as a "first solvation shell." Local solvation may be classified as "electrophilic" or "nucleophilic" solvation (Winstein et al., 1951; Olah and Klumpp, 2004; Ormazábal-Toledo et al., 2013c).

Electrophilic solvation represents the specific interaction through an HB with the hydrogen atom of the solvent, whereas nucleophilic solvation describes a specific interaction through a HB between an acidic hydrogen atom of the E^+/Nu^- pair and the solvent (Ormazábal-Toledo et al., 2013c). The effect of the HB in S_NAr was early studied by Bernasconi et al. (Bunnett et al., 1955; Bernasconi and De Rossi, 1976) and recently by our group (Ormazábal-Toledo et al., 2013a,b,c; Gallardo-Fuentes et al., 2014; Alarcón-Espósito et al., 2015; Contreras et al., 2015) from experimental and theoretical point of view in order to explain the observed reactivity trends (Parr et al., 1999; Contreras et al., 2003; Ormazábal-Toledo et al., 2013a).

Scheme 1 shows the S_NAr process considered in this work. Note that, the first step on the reaction pathway corresponds to the formation of a zwitterionic complex named Meisenheimer complex (MC) from which two processes for its decomposition have been postulated:(Banjoko and Babatunde, 2004; Um et al., 2007; Ormazábal-Toledo et al., 2013a,b,c Terrier, 2013; Gallardo-Fuentes et al., 2014; Gazitúa et al., 2014; Alarcón-Espósito et al., 2015, 2016, 2017; Contreras et al., 2015) (a) expulsion of the leaving group (LG) followed by fast proton loss to give the reaction product (k_2 in **Scheme 1**), and (b) the base-catalyzed

deprotonation of the MC that loss the LG to give the reaction product (k_3 in **Scheme 1**) (Alarcón-Espósito et al., 2017).

Solvent effects studies in S_NAr have been addressed experimentally in order to get detailed information about phenomena that are not observable and occurring at microscopic levels (Ormazábal-Toledo et al., 2013b,c; Alarcón-Espósito et al., 2015; Contreras et al., 2015). The model systems are the reactions between the substrate or electrophile named 4-chloroquinazoline and two amines of different nature (aniline and hydrazine), respectively (see **Scheme 1**).

The main goal of this work is to analyze the activation of the E^+/Nu^- pair by nucleophilic or electrophilic solvation given by conventional solvents like water and organic solvent and ionic liquids (IL). This article will be focused on the discussion of the solvent on the reactivity of the E^+/Nu^- pair based on a detailed kinetic study and its incidence on the reaction mechanisms.

ILs at room temperature (RTIL) are defined as molten salts (composed entirely of cations and anions) that melt below 100°C (Welton, 1999; Crowhurst et al., 2004; Weingärtner, 2008) with remarkable physicochemical properties (Freemantle, 1998). The high combinatorial flexibility has converted these materials into "design solvents" or "task specific" solvents (Welton, 1999; Weingärtner, 2008; Gazitúa et al., 2014) whose properties can be specified to suite the requirements of a particular reaction (Reichardt and Welton, 2011; Gazitúa et al., 2014; Alarcón-Espósito et al., 2016). Details of structures and acronyms of the IL used in this study are in **Scheme 1**. RTILs have been classified as Lewis acid/base with the ability of the anion to accept a HB and to donate an HB in the case of the cation forming the IL (Crowhurst

SCHEME 1 | General reaction mechanism for the S_NAr of 4-chloroquinazoline and the amines studied.
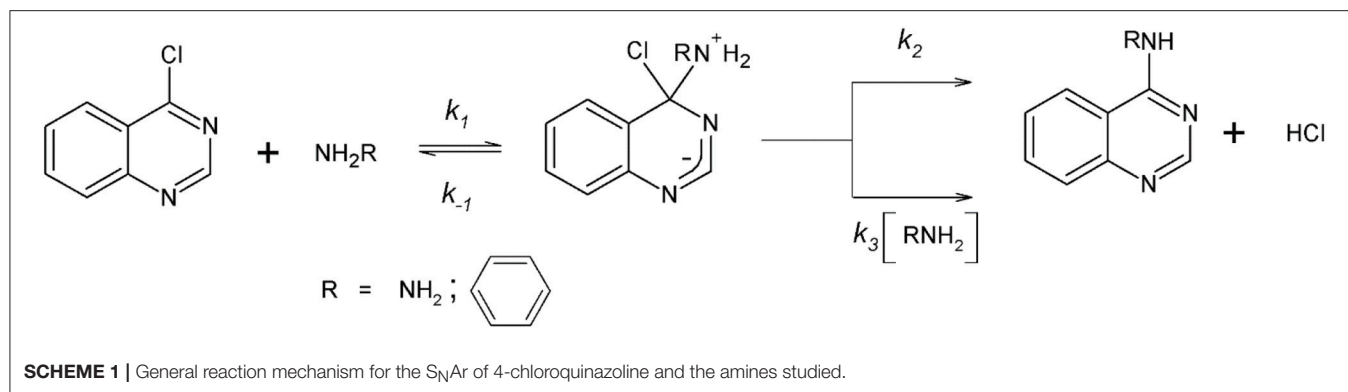
et al., 2003; Ab Rani et al., 2011; Contreras et al., 2013; Gazitúa et al., 2015).

MATERIALS AND METHODS

Reagents and Solvents

All reagents and solvents used were the commercially available from Sigma-Aldrich and Merck. The certificate of analysis guarantees purity ≥ 99%.

Purity of the Ionic Liquids

The series of ionic liquids used were purchased from Merck and used as delivered. The specifications are as follows: purity (HPLC) > 98%; identity (NMR) passed test; halides (IC) < 0.1%; water (KF) < 0.1%.

Kinetic Measurements

The kinetic of the reactions in aqueous media were measured by a diode array spectrophotometer HP 8453 at 25°C at an ionic strength 0.2 M in KCl. The kinetic measurements in conventional organic solvents and ionic liquids were made in the absence of KCl. The formation of a reaction product was monitored at 330 nm. The substrate concentration was 1.09×10^{-4} M. Under excess of nucleophile, pseudo-first-order rate coefficients k_{obs} were obtained. The reactions were carried out at three pH values (pH = pK_a and pH = $pK_a \pm 0.3$) thereby establishing an equilibrium between the free nucleophile and its protonated form. The total concentration of each nucleophile comes from free nucleophile and its protonated form (Gazitúa et al., 2014; Calfuman et al., 2017).

Spectroscopic Measurements

Polarity determinations were performed by monitoring the spectroscopic behavior of Reichardt's dye. A stock solution of the probe was prepared in ethanol, and aliquots of the respective dye solution was added to the studied RTILs, previously dried overnight (70°C, under vacuum), and the added volume of ethanol was removed by evaporation under vacuum, followed by treatment of the solutions with a nitrogen stream. Absorption spectra were recorded in an Agilent 8453 UV-Vis spectrometer using 1 cm path length quartz cells. Et30 was calculated from

the longest wavelength absorption maxima of Reichardt's dye, according to Equation 1.

$$Et_{30} = \frac{28591.5}{\lambda_{max}} \qquad (1)$$

C343 steady-state fluorescence measurements were performed using a Perkin Elmer LS-55 fluorescence spectrometer, using an excitation wavelength of 340 nm and 1 cm path length quartz cells. The final spectra considered for each measurement corresponds to the average between 20 collected spectra. The fluorescent probe was incorporated into the samples following the same procedure for Reichardt's dye (Sánchez et al., 2018).

Product Study

The presence of the kinetic reaction products: 4-anilinoquinazoline and 4-hydrazinoquinazoline (Asif, 2014), respectively were validated spectrophotometrically by comparison of the UV-vis spectra at the end of the reactions with those authentic samples under the same experimental conditions (Alarcón-Espósito et al., 2017).

Synthesis of 4-Anilinoquinazoline

A solution of 4-chloroquinazoline (164.6 mg, 1.0 mmol) and aniline (279.4 mg, 3.0 mmol) in n-butanol (5.0 mL) was heated at reflux for 1.5 h. After the reaction mixture was concentrated under reduced pressure, the residue was purified by chromatography on silica gel using ethyl acetate: chloroform 2:1 to afford 4-anilinoquinazoline (155 mg, 70% yield, mp. 222–223°C (Lit. 222-224 °C) (Shen et al., 2011). ^{1}H NMR (DMSO-d_6): 9.80 (s, 1H), 8.59 (s, 1H), 8.56 (d, 1H, J = 8.0 Hz), 7.90-7.75 (m, 4H), 7.64 (t, 1H, J = 8.0 Hz), 7.40 (t, 2H, J = 8.2 Hz), 7.15 (t, 1H, J = 7.4 Hz). ^{13}C NMR (DMSO-d_6): 158.8, 154.4, 149.5, 139.1, 133.0, 128.4 (2C), 127.7, 126.2, 123.8, 122.9, 122.5 (2C), 115.1.

RESULTS AND DISCUSSION

The studied reactions followed a stepwise mechanism, where the non-catalyzed route is the rate determining step (RDS). Under the experimental conditions, for the amines considered, single products (4-anilinoquinazoline and 4-hydrazine quinazoline, see **Scheme 2**), respectively were observed and monitored by UV-Vis
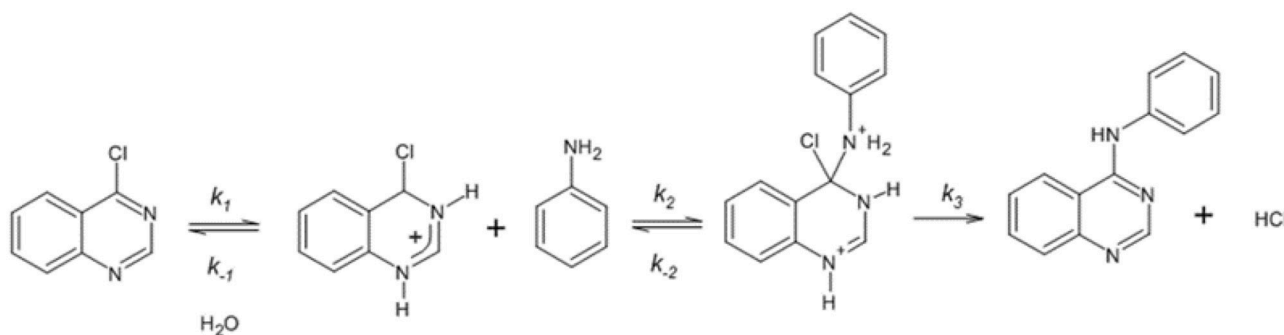
SCHEME 2 | Proposed reaction mechanism for the reaction between 4-chloroquinazoline and aniline.

spectrophotometry. The pseudo-first-order rate constant (k_{obs}) for the reactions can be expressed as Equation 2, in which [Nu] represents the concentration of nucleophile (Alarcón-Espósito et al., 2017).

$$\frac{k_{obs}}{[Nu]} = \frac{k_1(k_2 + k_3[Nu])}{(k_{-1} + k_2 + k_3 [Nu])} \tag{2}$$

The microconstants (k_1, k_{-1} and k_3, respectively) are associated to the reaction mechanism of an S_NAr reaction (see **Scheme 1**). Note that, the values of k_{obs} are in accordance with eq. 3 were k_0 and k_N are the rate coefficients for solvolysis and nucleophilic attack, respectively. These values are obtained as the intercept (k_0) and slope (k_N) of linear plots of E3 (Choi et al., 2002; Castro et al., 2009).

$$k_{obs} = k_0 + k_N [Nu] \tag{3}$$

S_NAr reactions may present two mechanistic trends: *(i)* assuming that: $k_2 + k_3 [Nu] << k_{-1}$, Equation 2 can be simplified to give Equation 4, where $K_1 = \frac{k_1}{k_{-1}}$. Plots of k_{obs} vs. [Nu] show curves upward in accordance with Equation 4, thereby indicating that the reaction proceeds through a rate-limiting proton transfer mechanism (Banjoko and Babatunde, 2004; Um et al., 2007; Ormazábal-Toledo et al., 2013a,b,c; Terrier, 2013; Gallardo-Fuentes et al., 2014; Gazitúa et al., 2014; Alarcón-Espósito et al., 2015, 2016, 2017; Contreras et al., 2015).

$$k_{obs} = K_1 k_2 [Nu] + K_1 k_3 [Nu]^2 \tag{4}$$

(ii) when $k_{-1} + k_2 \gg k_3$ the formation of the MC intermediate is the rate determining step, where k_{obs} is given by Equation 5: (Banjoko and Babatunde, 2004; Um et al., 2007; Ormazábal-Toledo et al., 2013a,b,c; Terrier, 2013; Gallardo-Fuentes et al., 2014; Gazitúa et al., 2014; Alarcón-Espósito et al., 2015, 2016, 2017; Contreras et al., 2015).

$$k_{obs} = k_N [Nu] \quad and \quad k_N = \frac{k_1 k_2}{k_{-1} + k_2} \tag{5}$$

Plots of k_{obs} vs. [Nu] show straight lines in accordance with Equation 5, thereby indicating that the reaction proceeds through a non-catalyzed mechanism (k_3 *channel in* **Scheme 1**).

TABLE 1 | Nucleophilic rate coefficients and pK_a values for aniline and hydrazine in aqueous media at 25°C and ionic strength 0.2 M in KCl.

Nucleophile	pK_a	pH	k_N ($s^{-1}M^{-1}$)
Aniline	4.73	4.43	0.617 ± 0.016
		4.73	0.381 ± 0.012
		5.03	0.225 ± 0.013
Hydrazine	8.10	7.80	0.015 ± 0.001
		8.10	0.025 ± 0.003
		8.40	0.033 ± 0.002

Table 1 shows the nucleophilic rate coefficients (k_N) and pK_a values for both amines in aqueous media at 25°C and ionic strength 0.2 M in KCl. Note that, the values accompanying k_N coefficients correspond to the error associated to the slope. From **Table 1** it is clear that the reaction is pH-dependent. The kinetic results for aniline suggest that k_N values are improved when the acidity of the media is increased. However, the inverse effect is observed with hydrazine. Note that, the nature and reactivity of the amines are different and their pK_a values were statistically corrected by using p (numbers of protons which can be deprotonated from the conjugate acid of the nucleophile) and q (numbers of nucleophilic sites of the nucleophile) (Bell, 1959; Um et al., 2007). **Tables S1–S6** show the kinetic data in **Supplementary Material**.

Figure 1 shows the plots of k_{obs} against free amine concentration expressed in Molar (M). Note that in **Figure 1**, the linear response for both amines in aqueous media discards a catalytic route exerted by a second molecule of nucleophile. **Figure 1** shows that each linear response has an intercept close to the origin. This result would suggest that the step *(i)* can be safely discarded and the contribution of the reaction media may be irrelevant (Um et al., 2007).

In summary, the kinetic data suggest that reactivity of the E^+/Nu^- pair is determined by an electrophilic & nucleophilic solvation, respectively. On other words, the HB that would be determining the reactivity of the studied reaction, could be established with the hydrogen atom of the solvent (electrophilic solvation) or between an acidic hydrogen atom of the E^+/Nu^-

FIGURE 1 | Plots of k_{obs} vs. free amine concentration in aqueous media **(A)** aniline and **(B)** hydrazine.
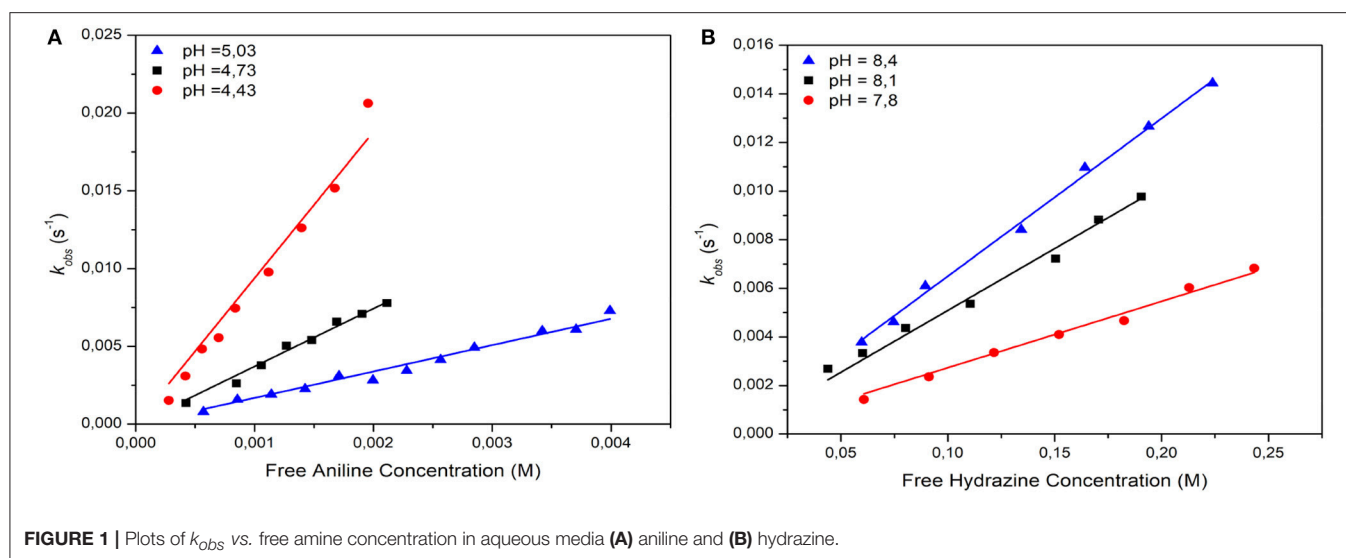
pair and the solvent (nucleophilic solvation) (Ormazábal-Toledo et al., 2013c). See **Scheme 3**.

The reaction between aniline and 4-chloroquinazoline in aqueous media (**Figure 1A**) suggests that the substrate, in more acidic conditions, is protonated (see **Table S7** and **Figure S1**). This electrophilic solvation promotes its reactivity toward aniline making it more susceptible to the nucleophilic attack. In order to validate this hypothesis, the reaction was performed in aprotic conventional organic solvents as: formamide, acetonitrile and dichloromethane, respectively. However, the kinetic studies under the same experimental conditions showed that the reaction did not proceed after 5 h in those solvents.

Based on these kinetic results it is possible to postulate at first glance that prior to the nucleophilic attack, there is a protonation step oriented toward the electrophile.(Campodónico et al., 2010) This step will induce an increased electrophilicity on the substrate making it susceptible to the attack of a nucleophile of low nucleophilic strength. Taking into account this additional step on the reaction mechanism, kinetic experiments were carried out in some RTILs such as: BMIMSO, EMIMDCN, BMIMDCN, BMIMPF$_6$, BMIMBF$_4$, and BMIMNTF$_2$. The observed response only was in 1-ethyl-3-methyl imidazolium methane sulfonate (BMIMSO). For the other studied RTILs, the reaction did not proceed after 5 h. The elapsed time was an arbitrary kinetic criterion considered in this study in order to discriminate when the reaction proceeds (or not) toward the formation of reaction products.

The relationship between k_N values were about 30 times slower than water (see **Table 1**, k_N value at pH = pK_a). The obtained k_N value for BMIMSO is of 0.0128 ± 0.0009 ($s^{-1}M^{-1}$). More details are in **Figure S2** and **Table S8**. This information suggests that the reaction would proceed better in a protic RTIL. Preliminary data showed that propyl ammonium nitrate (PAN) was 68 times more reactive than BMIMSO with a k_N value of 0.8740 ± 0.0359 ($s^{-1}M^{-1}$). See **Table S9** and **Figure S2**. These results shown that the nature of the cation/anion pair of the RTILs is determinant in the reaction pathway for this reaction

(Hallett and Welton, 2011). The cation moiety of PAN would be playing a significant influence over the studied reaction. This effect may be traced to its Lewis basicity and the insignificant effect of the anion over the course of this reaction. This statement is supported on the kinetic response of the studied reaction on the analyzed RTILs which adds to the "task specific" concept, where determined RTILs can be specified to suite the requirements of a particular reaction (Welton, 1999, Weingärtner, 2008; Gazitúa et al., 2014; Alarcón-Espósito et al., 2016). Then, the capacity to donate an HB by ammonium moiety of PAN toward the substrate would be emulating the electrophilic solvation toward the 4-chloroquinazoline suggested in aqueous media. **Scheme 2** shows the proposed mechanism for this reaction. In it is suggested a first step (K_1) that corresponds to the protonation of the electrophile leading to the formation of a positive intermediate (Banjoko and Babatunde, 2004). This intermediate will be enhancing the electrophilicity of the substrate thereby improving its reactivity toward aniline. Note that, this route does not follow the formation of the traditional MC intermediate typical in a S_NAr reaction. However, this positively charged intermediate will suggest that the nucleophilic attack of the aniline molecule (K_2) toward an activated substrate will be the slow step of the reaction pathway with a fast LG departure (k_3) and deprotonation of it. The suggested RDS associated to the nucleophilic attack is attributable to a poor nucleophile (aniline) and a good LG (chlorine atom) added to a first protonation step toward the electrophile. On the other hand, the mentioned deprotonation step is not considered here, because it is very fast in comparison with the others steps on the reaction pathway. Note that, based on the previous kinetic analysis (linear plots of k_{obs} vs. [Nu]) the catalyzed route was discarded (k_3 in **Scheme 1**). A definitive answer about the mechanism would be obtained through the full exploration of the PES that could contribute to add evidence on the proposed pathway.

On the other hand, the kinetic analysis for the reaction between 4-chloroquinazoline and hydrazine showed that it is improved at high pH values in aqueous media (see **Figure 1B**

SCHEME 3 | Proposed reaction mechanism for the reaction between 4-chloroquinazoline and hydrazine.
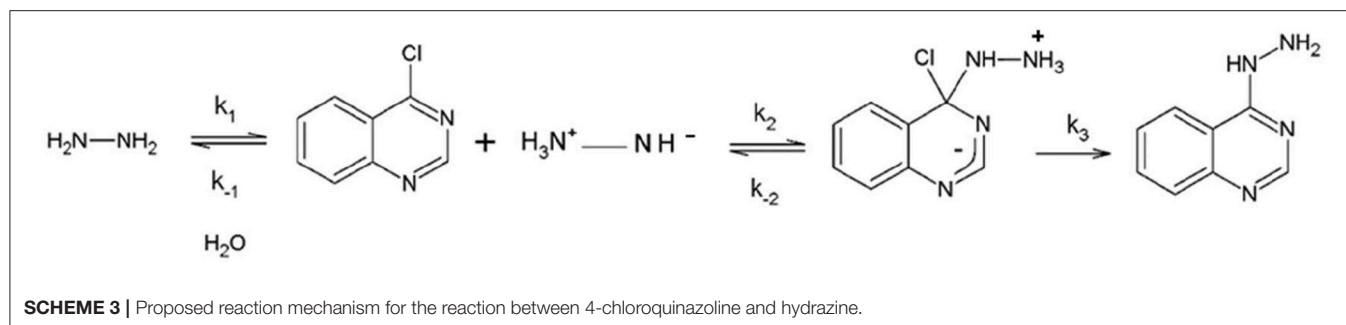
in the text). **Scheme 3** shows the proposed mechanism for this reaction. In this case, the nature of the amine changed in comparison to aniline. In **Scheme 3** is suggested a first step (K_1) corresponding to the nucleophilic solvation of hydrazine, where hydrazine, highly reactive in a second step, will act as dipole reacting with the electrophile (K_2) although the formation of a MC with a fast LG departure (k_3) and deprotonation of it. More details below in the analysis of this reaction.

From **Table 1** and considering k_N values at pH = pK_a for both amines, the relationships between k_N values was about 15 times slower than aniline. This fact is not in agreement with the pK_a values and the kinetic results. Hydrazine is an alpha nucleophile (Anderson and Jencks, 1960; Ormazábal-Toledo et al., 2013b; Gallardo-Fuentes et al., 2014). This compound has a lone pair vicinal to the attacking nitrogen atom (Ormazábal-Toledo et al., 2013b). Therefore, it should be expected an enhanced nucleophilicity toward the substrate. This fact, suggests that the reaction media has an improved effect over the reaction. Water molecule is polar, with high possibilities to establish HB interactions. Then, water molecules would be affecting the nucleophilic character of hydrazine via HB formation. However, the reaction of 4-chloroquinazoline with hydrazine in aqueous media (see **Table 1**) shows a catalytic behavior (see **Figure 1B**) similar to that found between 4-chloroquinazoline with aniline (see **Figure 1A**), but in an opposite acid/base conditions. This fact implies that the reaction media will be able to capture or/and to donate an hydrogen atom from the hydrazine molecule suggesting that the nucleophile will be acting as dipole (Kirby et al., 2006). This nucleophilic solvation will be promoting the reactivity of the hydrazine toward 4-chloroquinazoline through a strong nucleophile. Remember that, the substrate in more basic condition will be not activated. Then, this S_NAr reaction will follow the formation of an anionic intermediate. The same reaction in conventional organic solvents shown k_N values higher than water (see **Table 1**, k_N value at pH = pK_a). The studied solvents were: ethanol, butanol, dioxane and acetonitrile, respectively. **Tables S10–S13** and **Figure S3** are given in SM. Aprotic solvents show k_N values in the same range than water (see **Table 1** for hydrazine). The obtained values were 0.027 ± 0.002 and 0.012 ± 0.002 ($s^{-1}M^{-1}$) for dioxane and acetonitrile, respectively. However, ethanol showed an increased value of k_N (0.071 ± 0.001 $s^{-1}M^{-1}$) in comparison to water at pH = pK_a (0.025 $s^{-1}M^{-1}$). This

protic solvent would open the possibility to establish an HB with the hydrazine shifting the equilibria toward its zwitterionic form.

Finally, this reaction was performed in ILs showing that the nature of the anion improves the reactivity, being at least 10 times higher than water and conventional organic solvents (DÁnna et al., 2010). The k_N values obtained in 1-butyl-3-methylimidazolium dicyanamide (BMIMDCN) and 1-butyl-1-methylpyrrolidinium dicyanamide (BMPYRDCN) were of 0.239 ± 0.027 ($s^{-1}M^{-1}$) and 0.325 ± 0.039 ($s^{-1}M^{-1}$), respectively. More details are in **Tables S14, S15** and **Figure S4**. Note that, these RTILs have the same anion moiety. The selection is based on the high polarizability of the dicyanamide anion and its size (Gazitúa et al., 2014; Alarcón-Espósito et al., 2016). The aforementioned led us to analyze the solvation effect in terms of the kinetics in conventional solvents and its relationships on the reaction pathway. These results show a key role of the HB acidity (Lewis acidity) and the minor effect of the cation in the course of the reaction. In this way, this reaction is promoted when the anion moiety is able to capture an HB from the hydrazine emulating the same behavior of the reaction showed in aqueous media, enhancing the "anion effect" over the reaction (Alarcón-Espósito et al., 2016; Sánchez, 2018). The hypothesis of the zwitterionic form for hydrazine could be complemented with the report of one of our previous works, which describes a site activation problem for a pyrimidine derivative and benzohydrazide series in aqueous media (Gallardo-Fuentes et al., 2014). Both analysis allow us to suggest for this reaction an intramolecular HB formation that would operate as a perturbation that will produce a dual response at the reaction centers by enhancing the electrophilicity of 4-chloroquinazoline and the nucleophilicity of the hydrazine molecule (Gallardo-Fuentes et al., 2014). Then, the substrate that bear heteroatoms on the aromatic ring as substituent and the zwitterionic nucleophile would be able to establish an intramolecular HB between the α hydrogen atom on the $^+NH_3$- moiety of hydrazine molecule and the nitrogen atom of the quinazoline moiety; the rate determining step being nucleophilic attack. See more mechanistic details in **Scheme 3**.

In order to further analyze the performance of the RTILs used in this study, steady state fluorescence studies were performed. **Figure 2** shows the Stokes shift of the solvatochromic probe (coumarin 343, denoted C343) against to Et30 values for the

FIGURE 2 | Plot of Coumarin 343 stokes shift vs. the Et_{30} values of the studied ionic liquids.
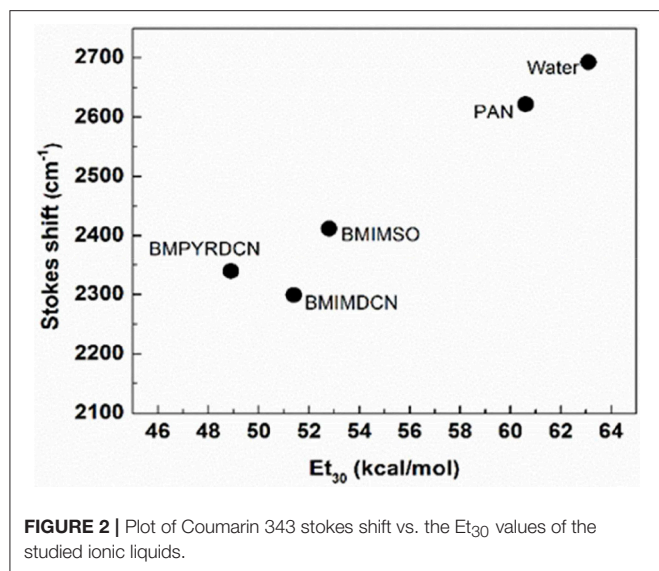
used RTILs. Note that, water is considered as the reference solvent. C343 belongs to a family of 7-aminocoumarin derivatives (Kuznetsova and Kaliya, 1992) which has been used extensively as laser dye and in studies regarding solvation dynamics in different media (Correa and Levinger, 2006; Sánchez et al., 2018), due to the sensitivity of both absorption and emission spectra to solvent polarity and the hydrogen bond donor capacity of the solvent molecules.

Figure 2 shows that the largest C343 Stokes shifts are observed in water and PAN. This result is in agreement with their polarities and HB abilities (Correa and Levinger, 2006; Gutierrez et al., 2010). This fact is associated to the first hypothesis established for the reaction between aniline and 4-chloroquinazoline in aqueous media. **Figure 2** suggests that the substrate in more acidic conditions is protonated. The high influence of PAN and water on the fluorescence spectra of C343 is related to the formation of HB, while BMIMSO does so in a lesser degree. The aforementioned response is attributed to its inability to establish HB interactions leading to a lesser red shift of the emission spectra of C343. On the other hand, BMIMDCN and BMPYRDCN in **Figure 2** displays a comparable response toward the fluorescence of C343. Remember that, these RTILs were used for the hydrazine reaction. BMIMDCN and BMPYRDCN bear the same anion moiety. Therefore, the only difference toward C343 might be associated with the nature of the cation moiety. However, dicyanamide anion presents a high π density, small size and high basicity (Gazitúa et al., 2014). All these features of these RTILs enable the abstraction of an HB from hydrazine favoring the zwitterionic form for hydrazine. Note that, the k_N value for BMPYRDCN with respect to BMIMDCN is increased by approximately one time. However, of these two solvents BMPYRDCN is the RTIL that induces the larger Stokes

shift of C343, in spite of BMIMDCN being more polar. On the other hand, $BMIM^+$ cation presents significant difference in electron delocalization patterns and number of nitrogen atoms compared with $BMPYR^+$ cation. Therefore, the reactivity observed suggests that the "anion effect" compensates the "cation solvent effect" (Alarcón-Espósito et al., 2016; Sánchez et al., 2018).

CONCLUSIONS

A kinetic study on a $S_N Ar$ reaction in a series of reaction media and two nucleophiles of different nature have been illustrated. The reactions have been studied because the electrophile bears heteroatoms on the aromatic ring as substituent able to establish intramolecular HB that may be activated by solvation or by the nucleophile. On the other hand, the kinetic analyses shown that solvent effects are affected under a change of amine nature, showing that both nucleophiles in aqueous media are pH-dependent. However, aniline shows that the reaction rate coefficients are amplified when the acidity of the media is increased, while the inverse effect is observed with hydrazine. The kinetic study for aniline showed that is possible to postulate at first glance that prior to the nucleophilic attack, there is a protonation step that improve the reactivity of the substrate. On the other hand, the solvent effects open the possibility to establish an HB with the hydrazine moving the equilibria toward its zwitterionic form. This step would be complemented with an intramolecular HB formation that will operate as a perturbation that produces a dual response at the reaction centers by enhancing the electrophilicity of the substrate and the nucleophilicity of one of the nitrogen atom of the hydrazine molecule.

AUTHOR CONTRIBUTIONS

BS, CC, RT, RC, and PC designed the experiments, analyzed the results, wrote, and revised the manuscript. All authors have approved the final revised manuscript. PC on behalf of The Collaborative Working Group.

FUNDING

SUPPLEMENTARY MATERIAL

The Supplementary Material for this article can be found online at: https://www.frontiersin.org/articles/10.3389/fchem.2018.00509/full#supplementary-material

REFERENCES

Ab Rani, M. A., Brant, A., Crowhurst, L., Dolan, A., Lui, M., Hassan, N. H., et al. (2011). Understanding the polarity of ionic liquids. *Phys. Chem. Chem. Phys.* 13, 16831–16840. doi: 10.1039/c1cp21262a

Alarcón-Espósito, J., Contreras, R., and Campodónico, P. R. (2016). Gutmann's Donor Numbers correctly assess the effect of the solvent on the kinetics of S$_N$Ar reactions in ionic liquids. *Chem. Eur. J.* 22, 13347–13351. doi: 10.1002/chem.201602237

Alarcón-Espósito, J., Contreras, R., and Campodónico, P. R. (2017). Iso-solvation effects in mixtures of ionic liquids on the kinetics of a model S$_N$Ar reaction. *New J. Chem.* 41, 13435–13441. doi: 10.1039/C7NJ03246C

Alarcón-Espósito, J., Tapia, R. A., Contreras, R., and Campodónico, P. R. (2015). Changes in the S$_N$Ar reaction mechanism brought about by preferential solvation. *RSC Adv.* 5, 99322–99328. doi: 10.1039/C5RA20779G

Anderson, B. M., and Jencks, W. P. (1960). The effect of structure on reactivity in semicarbazone formation. *J. Am. Chem. Soc.* 82, 1773–1777. doi: 10.1021/ja01492a057

Asif, M. (2014). Chemical characteristics, synthetic methods, and biological potential of quinazoline and quinazolinone derivatives. *Int. J. Med. Chem.* 2014:395637. doi: 10.1155/2014/395637

Banjoko, O., and Babatunde, I. A. (2004). Rationalization of the conflicting effects of hydrogen bond donor solvent on nucleophilic aromatic substitution reactions in non-polar aprotic solvent: reactions of phenyl 2,4,6-trinitrophenyl ether with primary and secondary amines in benzene–methanol mixtures. *Tetrahedron* 60, 4645–4654. doi: 10.1016/j.tet.2004.03.079

Bell, R. P. (1959). *The Proton in Chemistry*. London: Methuen.

Bernasconi, C., and De Rossi, R. H. (1976). Influence of the o-nitro group on base catalysis in nucleophilic aromatic substitution. Reactions in Benzene Solution. *J. Org. Chem.* 41, 44–49. doi: 10.1021/jo00863a010

Brönsted, J. N. (1923). Some remarks on the concept of acid and bases. *Recl. Trav. Chim. Pays-Bas.* 42, 718–728.

Bunnett, J. F., Morath, R. J., and Okamoto, T. (1955). The ortho: para Ratio in activation of aromatic nucleophilic substitution by the carboxylate group. *J. Am. Chem. Soc.* 77, 5055–5057. doi: 10.1021/ja01624a034

Calfuman, K., Gallardo-Fuentes, S., Contreras, R., Tapia, R. A., and Campodónico, P. R. (2017). Mechanism for the S$_N$Ar reaction of atrazine with endogenous thiols: experimental and theoretical study. *New J. Chem.* 41, 12671–12677. doi: 10.1039/C7NJ02708G

Campodónico, P. R., Aliaga, M. E., Santos, J. G., Castro, E. A., and Contreras, R. (2010). Reactivity of benzohydrazide derivatives towards acetylation reaction. *Exp. Theor. Stud. Chem. Phys. Lett.* 488, 86–89. doi: 10.1016/j.cplett.2010.01.052

Castro, E. A., Aliaga, M., Campodónico, P. R., Cepeda, M., Contreras, R., and Santos, J. G. (2009). Experimental and theoretical studies on the nucleofugality patterns in the aminolysis and phenolysis of S-aryl O-aryl thiocarbonates. *J. Org. Chem.* 74, 9173–9179. doi: 10.1021/jo902005y

Cedillo, A., Contreras, R., Galván, M., Aizman, A., Andrés, J., and Safont, V. S. (2007). Nucleophilicity index from perturbed electrostatic potentials. *J. Phys. Chem. A* 111, 2442–2447. doi: 10.1021/jp068459o

Chiappe, C., Pomelli, C. S., and Rajamani, S. (2011). Influence of structural variations in cationic and anionic moieties on the polarity of ionic liquids. *J. Phys. Chem. B* 115, 9653–9661. doi: 10.1021/jp2045788

Choi, J. H., Lee, B. C., Lee, H. W., and Lee, I. (2002). Competitive reaction pathways in the nucleophilic substitution reactions of aryl benzenesulfonates with benzilamines in acetonitrile. *J. Org. Chem.* 67, 1277–1281. doi: 10.1021/jo0161835

Contreras, R., Aizman, A., Tapia, R. A., and Cerda-Monje, A. (2013). Lewis molecular acidity of ionic liquids from empirical energy-density models. *J. Phys. Chem. B* 117, 1911–1920. doi: 10.1021/jp3114946

Contreras, R., Andrés, J., Safont, V. S., Campodónico, P. R., and Santos, J. G. (2003). A theoretical study on the relationship between nucleophilicity and ionization potentials in solution phase. *J. Phys. Chem. A* 107, 5588–5593. doi: 10.1021/jp0302865

Contreras, R., Campodonico, P. R., and Ormazábal-Toledo, R. (2015). *Arene Chemistry: Reaction Mechanism and Methods for Aromatic Compounds.* Hoboken, NJ: Willey.

Correa, N. M., and Levinger, N. (2006). What can you learn from a molecular probe? New insights on the behavior of C343 in homogeneous solutions and AOT reverse micelles. *J. Phys. Chem. B* 110, 13050–13061. doi: 10.1021/jp0572636

Crowhurst, L., Lancaster, N. L., Pérez-Arlandis, J. M., and Welton, T. (2004). Manipulating solute nucleophilicity with room temperature ionic liquids. *J. Am. Chem. Soc.* 126, 11549–11555. doi: 10.1021/ja046757y

Crowhurst, L., Mawdsley, P. R., Perez-Arlandis, J. M., Salter, P. A., and Welton, T. (2003). Solvent–solute interactions in ionic liquids. *Phys. Chem. Chem. Phys.* 5, 2790–2794. doi: 10.1039/B303095D

DÁnna, F., Marullo, S., and Noto, R. (2010). Aryl azides formation under mild conditions: a kinetic study in some ionic liquid solutions. *J. Org. Chem.* 75, 767–771. doi: 10.1021/jo9022952

Freemantle, M. (1998). Designer Solvent. Ionic liquids may boost clean technology development. *Chem. Eng. News* 76, 32–37. doi: 10.1021/cen-v076n013.p032

Gallardo-Fuentes, S., Tapia, R. A., Contreras, R., and Campodónico, P. R. (2014). Site activation effects promoted by intramolecular hydrogen bond interactions in S$_N$Ar reactions. *RSC Adv.* 4, 30638–30643. doi: 10.1039/C4RA04725G

Gazitúa, M., Fuentealba, P., Contreras, R., and Ormazábal-Toledo, R. (2015). Lewis acidity/basicity changes in imidazolium based ionic liquids brought about by impurities. *J. Phys. Chem. B* 119, 13160–13166. doi: 10.1021/acs.jpcb.5b05305

Gazitúa, M., Tapia, R. A., Contreras, R., and Campodónico, P. R. (2014). Mechanistic pathways of aromatic nucleophilic substitution in conventional solvents and ionic liquids. *New J. Chem.* 38, 2611–2618. doi: 10.1039/C4NJ00130C

Gutierrez, J. A., Falcone, R. D., Silber, J. J., and Correa, N. M. (2010). Role of the medium on the C343 inter/intramolecular hydrogen bond interactions. An absorption, emission, and ^{1}HNMR investigation of C343 in benzene/n-heptane mixtures. *J. Phys. Chem. A* 114, 7326–7330. doi: 10.1021/jp102136e

Hallett, J. P., and Welton, T. (2011). Room-temperature ionic liquids: solvents for synthesis and catalysis. *Chem. Rev.* 111, 3508–3576. doi: 10.1021/cr1003248

Ingold, C. K. (1929). The principles of aromatic substitution, from the standpoint of the electronic theory of valency. *Recl. Trav. Chim. Pays-Bas* 48, 797–812. doi: 10.1002/recl.19290480808

Ingold, C. K. (1933). Significance of tautomerism and of the reactions of aromatic compounds in the electronic theory of organic reactions. *J. Chem. Soc.* 1120–1127. doi: 10.1039/jr9330001120

Ingold, C. K. (1934). Principles of an electronic theory of organic reactions. *Chem. Rev.* 15, 225–274. doi: 10.1021/cr60051a003

Jaramillo, P., Pérez, P., Contreras, R., Tiznado, W., and Fuentealba, P. (2006). Definition of a nucleophilic scale. *J. Phys. Chem. A*, 110, 8181–8187. doi: 10.1021/jp057351q

Kirby, A. J., Davies, J. E., Brandao, T. A. S., Da Silva, P. F., Roccha, W. R., and Nome, F. (2006). Reaction mechanism and tautomeric equilibrium of 2-mercaptopyrimidine in the gas phase and in aqueous solution: a combined Monte Carlo and Quantum Mechanics study. *J. Am. Chem. Soc.* 128, 12374–12375. doi: 10.1021/ja065147q

Kuznetsova, N. A., and Kaliya, O. L. (1992). The photochemistry of coumarins. *Russ. Chem. Rev.* 61, 683–696. doi: 10.1070/RC1992v061n07ABEH000992

Lewis, G. N. (1923). *Valence and the Structure of Atoms and Molecules.* NewYork, NY: Chemical Catalog Co.

Lowry, T. M. (1923). The uniqueness of hydrogen. *J. Chem. Technol. Biotechnol.* 42, 43–47. doi: 10.1002/jctb.5000420302

Mancini, P. M. E., Terenzani, A. J., Adam, C., and Vottero, L. R. (1999). Characterization of solvent mixtures. Part 8 - Preferential solvation of chemical probes in binary solvent systems of a polar aprotic hydrogen-bond acceptor solvent with acetonitrile or nitromethane. Solvent effects on aromatic nucleophilic substitution reactions. *J. Phys. Org. Chem.* 12, 207–220.

Marullo, S., Dánna, F., Campodónico, P. R., and Noto, R. (2016). Ionic liquid binary mixtures: how different factors contribute to determine their effect on the reactivity. *RSC Adv.* 6, 90165–90171. doi: 10.1039/C6RA12836J

Olah, G. A., and Klumpp, D. A. (2004). Superelectrophilic solvation. *Acc. Chem. Res.* 37, 211–220. doi: 10.1021/ar020102p

Ormazábal-Toledo, R., Contreras, R., Tapia, R. A., and Campodónico, P. R. (2013b). Specific nucleophile-electrophile interactions in nucleophilic aromatic substitutions. *Org. Biomol. Chem.* 11, 2302–2309. doi: 10.1039/c3ob27450k

Ormazábal-Toledo, R., Contreras, R., Tapia, R. A. A. C., and Campodónico, P. R. (2013a). Reactivity indices profile: a companion tool of the potential energy surface for the analysis of reaction mechanism. Nucleophilic

aromatic substitution reactions as test case. *J. Org. Chem.* 78, 1091–1097. doi: 10.1021/jo3025048

Ormazábal-Toledo, R., Santos, J. G., Ríos, P., Castro, E. A., and Campodónico, P. R., and Contreras, R. (2013c). Hydrogen bond contribution to preferential solvation in S$_N$Ar reactions. *J. Phys. Chem. B* 117, 5908–5915. doi: 10.1021/jp4005295

Parr, R. G., Szentpály, L. V., and Liu, S. (1999). Electrophilicity Index. *J. Am. Chem. Soc.* 121, 1922–1924. doi: 10.1021/ja983494x

Reichardt, C., and Welton, T. (2011). *Solvents and Solvent Effects in Organic Chemistry*. Weinheim: John Wiley & Son.

Sánchez, B., Calderón, C., Garrido, C., Contreras, R., and Campodónico, P. R. (2018). Solvent effect on a model S$_N$Ar reaction in ionic liquid/water mixtures at different compositions. *New J. Chem.* 42, 9645–9650. doi: 10.1039/C7NJ04820C

Shen, Z., He, X., Dai, J., Mo, W., Hu, B., Sun, N., et al. (2011). An efficient HCCP-mediated direct amination of quinazolin-4(3H)-ones. *Tetrahedron* 67, 1665–1672. doi: 10.1016/j.tet.2010.12.067

Terrier, F. (2013). Modern nucleophilic aromatic substitution. Weinheim: John Wiley & Sons.

Um, I.-H., Min, S.-W., and Dust, M. J. (2007). Choice of solvent (MeCN vs H$_2$O) decides rate-limiting step in S$_N$Ar aminolysis of 1-fluoro-2,4-dinitrobenzene with secondary amines: importance of Brønsted-type analysis in acetonitrile. *J. Org. Chem.* 72, 8797–8803. doi: 10.1021/jo701549h

Weingärtner, H. (2008). Understanding ionic liquids at the molecular level: facts, problems, and controversies. *Angew. Chem. Int. Ed.* 47, 654–670. doi: 10.1002/anie.200604951

Welton, T. (1999). Room-temperature ionic liquids. Solvents for Synthesis and Catalysis. *Chem. Rev.* 99, 2071–2084. doi: 10.1021/cr980032t

Winstein, S., Grunwald, E., and Jones, H. W. (1951). The correlation of solvolysis rates and the classification of solvolysis reactions into mechanistic categories. *J. Am. Chem. Soc.* 73, 2700–2707. doi: 10.1021/ja01150a078

Water-Tolerant Trifloaluminate Ionic Liquids: New and Unique Lewis Acidic Catalysts for the Synthesis of Chromane

Piotr Latos[1], Alice Culkin[2], Natalia Barteczko[1], Sławomir Boncel[3], Sebastian Jurczyk[4], Lucy C. Brown[2], Peter Nockemann[2], Anna Chrobok[1]* and Małgorzata Swadźba-Kwaśny[2]*

[1] Department of Organic Chemical Technology and Petrochemistry, Silesian University of Technology, Gliwice, Poland, [2] The QUILL Research Centre, School of Chemistry and Chemical Engineering, Queen's University Belfast, Belfast, United Kingdom, [3] Department of Organic Chemistry, Bioorganic Chemistry and Biotechnology, Silesian University of Technology, Gliwice, Poland, [4] Institute for Engineering of Polymer Materials and Dyes, Gliwice, Poland

The first example of triflometallate ionic liquids, named in analogy to chlorometallate ionic liquids, is reported. Trifloaluminate ionic liquids, synthesized from 1-alkyl-3-methylimidazolium triflates and aluminum triflate, were characterized by multinuclear NMR spectroscopy and FT-IR spectroscopy, revealing the existence of oligonuclear, multiply-charged trifloaluminate anions, with multiple bridging triflate modes. Acceptor numbers were determined to quantify their Lewis acidity, rendering trifloaluminate ionic liquids as medium-strength Lewis acids (AN = *ca.* 65). Used as acidic catalysts in the cycloaddition of 2,4-dimethylphenol and isoprene (molar ratio 2:1) to prepare chromane, trifloaluminate systems outperformed literature systems, showing high activity (conversions 94–99%, selectivities 80–89%) and at low loadings (0.2 mol%) at 35°C. Using these new systems as supported ionic liquid phase (SILP) on multi-walled carbon nanotubes (ionic liquid loading 16 wt%) delivered a recyclable catalytic system, with activity enhanced with respect to the homogenous regime.

Keywords: trifloaluminate ionic liquids, metal triflates, chromane, carbon nanotubes, SILP

INTRODUCTION

Lewis acid catalysis is widely used, from multi-ton industrial processes to asymmetric synthesis of fine chemicals. However, traditional Lewis acids (AlCl$_3$ and BF$_3$) suffer from several drawbacks, in particular high corrosivity and propensity to hydrolysis. Therefore, many Lewis-acid catalyzed reactions must be carried out under strictly anhydrous conditions and using corrosion-resistant vessels. Furthermore, low stability toward water limits application of strong Lewis acids in reactions where water is eliminated, e.g., condensation.

Lewis acid catalysis in organic synthesis is typically carried out in an organic solvent, which comes with a set of challenges in terms of process sustainability, from flammability and issues of recycling/disposal, to difficulties in dissolving both the catalyst and the reactants at sufficient concentrations. Ionic liquids have been used to address some of these challenges: typically inflammable, they also offer enhanced separation and recycling strategies, from liquid biphasic systems to supported ionic liquid phases (SILPs) (Plechkova and Seddon, 2008).

Lewis acidic ionic liquids are nearly synonymous with chlorometallate ionic liquids, i.e., ionic liquids that contain Lewis acidic chlorometallate anions. They are synthesized by the reaction of a metal halide with an organic halide salt (e.g., 1-ethyl-3-methylimidazolium chloride) at various reactant ratios, commonly reported as the molar ratio of the metal halide, χ_{MClx}. Lewis acidic systems are typically associated with the excess of metal halide, resulting in the formation of oligonuclear, Lewis acidic anions (Estager et al., 2010, 2014; Hardacre et al., 2010; Atkins et al., 2011). Systems with chloroaluminate(III), chlorogallate(III) or chlorostannate(II) anions may be used to fine-tune the strength of Lewis acidity, and all have been implemented in organic syntheses, prominently in Friedel-Crafts chemistry and Diels-Alder reactions (Markiton et al., 2016; Matuszek et al., 2016). However, although solvent-related issues (flammability, limited solubility) have been addressed, chlorometallate ionic liquids share disadvantages of low stability toward moisture and high corrosivity with their respective metal chlorides. Although some chlorometallate ionic liquids are known as water-stable, most prominently chlorozincate(II) and chloroindate(III) ones (Abbott et al., 2001; Silveira Neto et al., 2004), they too pose corrosion issues due to high chloride content.

An alternative approach to tackling shortcomings of common Lewis acids utilizes Lewis acidic metal trifluoromethanesulfonates (triflates, OTf). Kobayashi and co-workers found that certain Lewis acidic metal triflates (M = Al, Ga, Ln) are stable in aqueous media (Kobayashi and Manabe, 2000; Kobayashi et al., 2002). Following this, such metal triflates were reported as water-tolerant Lewis acidic catalysts for a range of organic transformations: aldol condensations, Diels-Alder reactions, Friedel-Crafts acylations and alkylations, radical additions, aromatic nitrations and sulfonylations (Lub et al., 2005; Coulombel et al., 2009; Robertson and Wu, 2010; Williams and Lawton, 2010; Prakash et al., 2012; Lemière and Duñach, 2013; Markiton et al., 2018). The metal triflate catalysts were active at low concentrations, bearing the promise of cost-effective and efficient processes, but suffered from limitations in solubility. Namely, metal triflates dissolve well only in highly coordinating solvents, such as acetone or acetonitrile, which coordinate to the Lewis acid itself and weaken or disable its catalytic activity, and have very limited solubility in non-coordinating media. Again, ionic liquids have been tested as alternative solvents to overcome the solubility issue: for example, $Yb(OTf)_3$ dissolved in 1-butyl-3-methylimidazolium hexafluoroantimonate, $[C_4mim][SbF_6]$ at 0.1 M was not only well soluble and catalytically active, but possible recycle and reuse several times (Song et al., 2004; Binnemans, 2007; Sarma and Kumar, 2008; Rao et al., 2011).

In this work, we set out to combine these recent advances in Lewis acid catalysis, in the search of a robust, water-tolerant Lewis acidic catalytic system. Rather than solubilising metal triflates in organic solvents or ionic liquids, a family of triflometallate ionic liquids was synthesized. In analogy to chlorometallate systems, they contained metallate anions, but surrounded by triflate, rather than chloride, ligands. Following a multi-technique speciation study, trifloaluminate systems were

used as Lewis acidic catalysts in a model reaction: [3+3]-cycloaddition of 2,4-dimethylphenol and isoprene to prepare chromane. Seeking for the best recycling strategy, catalytic reactions were carried out homogenously, under solventless conditions, and heterogeneously, with trifloaluminate ionic liquids immobilized on the surface of carbon nanotubes (SILP).

EXPERIMENTAL SECTION

Materials and Methods

All air-sensitive materials were handled under an nitrogen or argon, using standard Schlenk line and glovebox techniques. Solvents were used without purification, or dried by purging with argon. $CDCl_3$, CD_3OD, and C_2D_6SO for NMR spectroscopy were purchased from Sigma Aldrich and used without purification.

2,4-Dimethylphenol, isoprene, and triflate salts of Al(III), Sn(II), Sc(III), In(III), Yb(III), Ga(III) Zn(II), La(III), Li(I), Ag(I), Er(III), Bi(III), Y(III), and Tl(III), and nitrobenzene were purchased from Sigma-Aldrich. Multiwalled carbon nanotubes, MWCNTs, were supplied from CheapTubes™ (USA). 1-Ethyl-3-methylimidazolium triflate, $[C_2mim][OTf]$, and 1-octyl-3-methylimidazolium triflate, $[C_8mim][OTf]$, were purchased from Sigma-Aldrich.

Analytical Methods

GC analyses were performed using a SHIMADZU GC-2010 Plus equipped with a Zebron ZB-5MSi column (30 m × 0.32 mm × 0.25 μm film). GC-MS analyses were performed using an Agilent GC 7890C (HP-5 MS capillary column, 30 m × 0.25 mm × 0.25 μm, conjugated with an Agilent mass spectrometer 5975C with EI ionization (70 eV). The products were identified using the NIST/EPA/NIH Mass Spectral Library.

Nitrogen adsorption/desorption isotherms for the carbon materials were obtained using a Micrometrics ASAP 2420M instrument at −196°C to calculate their specific surface areas (SBETs) and pore volumes. The size of the pores was obtained using the Barrett–Joyner–Halenda (BJH) method with the Kruk–Jaroniec–Sayari correction. Prior to the experiments, the samples were out-gassed at 200°C and $1.33 \cdot 10^{-3}$ Pa for 5 h.

The ionic liquid loadings on the surface of the CheapTubes™ MWCNTs were determined by thermogravimetry (TGA), using a Mettler-Toledo STAR851 thermobalance. Samples (5–10 mg) were placed in standard 70 μL Al_2O_3 crucibles and heated from 25°C to 800°C at a rate of 20°C min⁻¹, under nitrogen flow of 100 cm³ min⁻¹. TG, DTG and DTA curves were recorded (SD, **Figures S8-S12**).

Infrared spectra of neat ionic liquid samples were recorded on a Perkin Elmer Spectrum 100 Series FT-IR spectrometer with a universal ATR accessory. Eight scans were acquired for each sample.

NMR spectra of ionic liquids were recorded using Bruker AVANCE 400, at the following operating frequencies: ^{1}H 399.78 MHz, ^{31}P{^{1}H} 161.83 MHz, ^{19}F 376.17 MHz, ^{13}C{^{1}H} 100.53 MHz. NMR spectra of 2,4-dimethylphenol, isoprene and chromane were recorded using Agilent 400-MR, at the

following operating frequencies: ^{1}H 399.89 MHz, ^{13}C 150.90 MHz. Chemical shifts are quoted as parts per million.

Differential Scanning Calorimetry (DSC)

All scans were obtained using a TA DSC Q2000 model with a TA Refrigerated Cooling System 90 (RCS) and an autosampler. The samples were sealed in the glovebox in TA Tzero aluminum pans with hermetic lids. The temperature was ramped from -90 to 100°C at 5°C min^{-1}, then stabilized at 100°C for 5 min, and subsequently cooled to -90°C at 5°C min^{-1}, then stabilized for 5 min, and the whole cycle was repeated two more times; the DSC chamber was filled with dry nitrogen. Curves representative of glass transitions are shown in **Figure S6**.

Acceptor Number Determination

For each ionic liquid, three samples (*ca.* 1 g each; SD, **Tables S1–S2**) were weighed out in a glovebox, and mixed with a ^{31}P NMR probe molecule, triethylphosphine oxide (TEPO), at different TEPO concentrations (3–10 mol%). After dissolution of TEPO was ensured, the solutions were loaded into NMR tubes, containing sealed capillaries with d6-dimethylsulfoxide (an external lock).

^{31}P NMR spectra were recorded at 80°C, at 161.98 MHz, using a Bruker AvanceIII 400 MHz spectrometer. Phosphoric(V) acid, 85% solution in water, was used as an external reference. Three solutions of TEPO in hexane (*ca.* 5, 10 and 15 mol %) were prepared, and then measured at 27, 57, 87°C (**Tables S3, S4**). For each TEPO-ionic liquid system, the ^{31}P NMR chemical shift for the infinite dilution of TEPO, δ_{inf}, was determined by extrapolation from the ^{31}P NMR chemical shifts measured at different TEPO concentrations. The chemical shift of TEPO in hexane, extrapolated to infinite dilution, $\delta_{inf\ hex}$, was used as a reference ($\delta_{inf\ hex} = 0$ ppm). The AN values for all samples were calculated from the following formula: AN $= 2.348 \cdot \delta_{inf}$ (Gutmann, 1978; Estager et al., 2010).

Synthetic Procedures

Synthesis of Trifloaluminate Ionic Liquids

In the glove box, [C_2mim][OTf] or [C_8mim][OTf] and Al(OTf)$_3$ were weighed into a vial at various molar ratios, expressed as a molar fraction of Al(OTf)$_3$: $\chi_{Al(OTf)_3} = 0.15, 0.25, 0.33, 0.375, 0.40, 0.50$. The reactants were stirred at 85°C for 2 h to homogenize. Samples were prepared at 1 g scale and used without further purification (SD, **Tables S3–S4**). All ionic liquids were stored in the glovebox until used, and samples for NMR studies of neat ionic liquids and AN measurements were prepared in the glovebox. Typical NMR spectroscopic analyses are given below.

[C_2mim][OTf]-Al(OTf)$_3$, $\chi_{Al(OTf)_3} = 0.15$: ^{1}H NMR (DMSO, 400 MHz, 360 K): δ 8.05 (s, 1H), 6.87 (s, 1H), 6.81 (s, 1H), 3.58 (m, 2H), 3.26 (s, 3H), 0.83 (m, 3H); ^{13}C NMR (DMSO, 400 MHz, 360 K): δ 135.54, 122.97, 121.30, 119.51 (q, $^1J_{CF} = 318$ Hz), 44.15, 34.94, 13.49; ^{19}F NMR (DMSO, 400 MHz, 360 K): $\delta-79.42$ (s, -CF$_3$); ^{27}Al NMR (DMSO, 400 MHz, 360 K): $\delta-13.63$ (s, Al(OTf)$_6$).

[C_8mim][OTf]-Al(OTf)$_3$, at $\chi_{Al(OTf)_3} = 0.15$: ^{1}H NMR (DMSO, 400 MHz, 360 K): δ 8.05 (s, 1H), 6.87 (s, 1H), 6.81 (s, 1H), 3.58 (m, 2H), 3.26 (s, 3H), 0.83 (m, 3H); ^{13}C NMR (DMSO, 400 MHz, 360 K): δ 136.05, 123.16, 121.88, 119.77 (q, $^1J_{CF} = 318.1$ Hz, C$_{13}$), 49.21, 35.17, 30.79, 29.06, 28.01, 27.97, 25.26, 21.56, 12.68; ^{19}F NMR (DMSO, 400 MHz, 360 K): $\delta-79.12$ (s, -CF$_3$),-79.49 (shoulder, Al-OTf); ^{27}Al NMR (DMSO, 400 MHz, 360 K): $\delta-12.56$ (s, Al(OTf)$_6$).

Preparation of Immobilized Ionic Liquids

[C_2mim][OTf]-Al(OTf)$_3$], $\chi_{Al(OTf)_3} = 0.25$ (0.200 g), MWCNTs (0.400 g) and hexane (10 cm^3) were introduced into a 25 cm^3 round-bottom flask. The flask was sealed with a septum and mixed in an ultrasonic bath (20°C, 2 h). Then, the mixture was filtered through a Büchner funnel, washed with 15 cm^3 of hexane and dried at 50°C under vacuum (Schlenk line) for 2 h.

Synthesis of 2,2-Dimethyl-2,4-Dimethylchromane

The catalyst: Al(OTf)$_3$, trifloaluminate ionic liquids or immobilized trifloaluminate ionic liquids, used at 0.2–2 mol% per isoprene, was added to a stirred solution of 2,4-dimethylphenol (0.489 g, 4 mmol) and isoprene (0.272 g, 2 mmol), at 35°C. Reaction progress was monitored by GC. After completion, *n*-hexane (3 cm^3) was added to the reaction mixture to separate the catalyst: Al(OTf)$_3$ precipitated as white powder, ionic liquids phase-separated from the reaction mixture, and immobilized ionic liquids could be separated by filtration. After separation of the catalyst, the product was isolated as a colorless oil using column chromatography (SiO$_2$, *n*-hexane:AcOEt 100:1).

2,2-dimethyl-2,4-dimethylchromane: ^{1}H NMR (400 MHz, CDCl$_3$, TMS): δ 1.32 (s, 6H), 1.76-1.79 (t, J = 6.8 Hz, 2H), 2.14 (s, 3H), 2.23 (s, 3H), 2.72-2.75 (t, J = 6.8 Hz, 2H), 6.72 (s, 1H), 6.78 (s, 1H). ^{13}C NMR (150 MHz, CDCl$_3$): δ 16.07, 20.56, 22.78, 27.19, 33.12, 73.80, 120.10, 126.11, 127.26, 127.98, 129.24, 150.06; GC-MS: (EI) m/z (%) 190 (40, M$^{+\cdot}$), 175 (16), 135 (100), 134 (27), 106 (12), 91 (38), 77 (16), 65 (11), 41 (23), 39 (27).

Leaching Studies

To test for catalyst leaching from the support, the reaction was stopped after 15 min, the catalyst was filtered off, and the reaction was continued. Results were compared to these without the filtration step.

Recycling Studies

For recycling experiments, reactions were scaled up by a factor of five. After completion of the reaction, *n*-hexane was added (15 cm^3) and the catalyst was separated. Ionic liquids phase-separated (0.075 g) and was washed with *n*-hexane (3 × 5 cm^3). Al(OTf)$_3$ was filtered off (0.200 g) and washed with *n*-hexane (3 × 5 cm^3). When using supported ionic liquids, the addition of *n*-hexane resulted in phase-separation of the second liquid phase (the ionic liquid phase, 0.091 g), which was re-immobilized on the MWCNTs surface using standard procedure. Irrespective of the catalyst, in the final step *n*-hexane was removed from the catalyst (60°C under vacuum on Schlenk line, 1 h), and the catalyst was used in the next cycle of the reaction.

RESULTS AND DISCUSSION

Synthesis and Characterization of Trifloaluminate Ionic Liquids

A wide range of Lewis acidic metal triflates are commercially available: the most costly are $Sn(OTf)_2$, $Sc(OTf)_3$, and $Yb(OTf)_3$ (30–70 Euro per 1 g from Sigma-Aldrich), followed by $Bi(OTf)_3$, $Ga(OTf)_3$, and $In(OTf)_3$ (*ca.* 17 Euro per 1 g). $Al(OTf)_3$, priced at *ca.* 6 Euro per 1 g, is by far the least costly option. Bearing in mind that the success of chloroaluminate ionic liquids lied in their high Lewis acidity combined with low cost of the metal salt, it was found reasonable to select this least expensive triflate for this study.

The first examples of trifloaluminate ionic liquids (**Figure 1**) were synthesized, by analogy to chloroaluminate systems (Estager et al., 2010, 2014; Hardacre et al., 2010; Atkins et al., 2011)., through a solventless reaction of $[C_2mim][OTf]$ or $[C_8mim][OTf]$ with $Al(OTf)_3$, at various molar ratios of reactants, expressed as the molar fraction of $Al(OTf)_3$: $\chi_{Al(OTf)_3}$ = 0.15, 0.25, 0.33, 0.375, 0.40, 0.50 (see **Tables S1**, **S2** for experimental details).

Reactions were carried out for 2 h at 85°C, and the products' appearance varied from colorless, homogeneous liquids to pastes consisting of extremely viscous liquids and white solids. This trend, summarized in **Table 1**, is in stark contrast to chloroaluminate ionic liquid series, where viscosity decreases with increasing loading of $AlCl_3$, and which form homogenous liquids up to χ_{AlCl_3} = 0.67 (Welton, 1999; Estager et al., 2014). Despite several attempts, it has not been possible to record melting points for either system; in DSC scans all homogenous liquid samples featured weak glass transitions, with onsets between −75.15 and −13.15°C (**Figure S6**).

The investigation concerning the structure of newly synthesized trifloaluminate anions was carried out using different techniques, such as multinuclear NMR, variable temperature NMR and FT-IR spectroscopy. Such difference in physical properties indicates fundamental differences in anionic speciation between trifloaluminate and chloroaluminate ionic liquids. Multi-technique spectroscopic studies were employed to shed light on the speciation of the newly synthesized triflometallate systems.

NMR Spectroscopy

^{27}**Al NMR spectra** are often instrumental in elucidating the nature of aluminate species, with four-coordinate species commonly found at 40 to 140 ppm, five-coordinate at 25–60 ppm, and six-coordinate at −46 to 40 ppm (Olah et al., 1984; Atwood, 1998; Choi et al., 2009; Apblett, 2012; Tayade et al., 2015).

^{27}Al NMR spectra of three homogenous samples of the $[C_8mim][OTf]$-$Al(OTf)_3$ system ($\chi_{Al(OTf)_3}$ = 0.15, 0.25 and 0.33), recorded at 27°C, are shown in **Figure 2**. All spectra feature broad signals, with pronounced NMR probe signal at around 65 ppm. All samples feature a group of signals between−10 and 1 ppm, corresponding to multiple six-coordinate ^{27}Al species. Only for $\chi_{Al(OTf)_3}$ = 0.15, there is a singlet at 103 ppm (four-coordinate ^{27}Al), which is rather surprising given high excess of triflate anions in this sample. The prevalence of the six-coordinate species is expected for $\chi_{Al(OTf)_3}$ = 0.15 and 0.25, considering the excess of triflate ligands per each aluminum atom (around 8:1 and 6:1, respectively). However, mononuclear complexes at $\chi_{Al(OTf)_3}$ = 0.33 were expected to be five-coordinate, or to comprise a combination of four- and six-coordinate species, given triflate-to-Al ratio of 5:1.

Increasing temperature of NMR measurements may have profound effect on the spectrum: exchange rate between species increases (peaks merge), viscosity decreases (peaks are better resolved), species may appear/disappear. Variable temperature ^{27}Al NMR studies (SD, **Figures S1–S3**) were carried out, with spectra recorded between 27 and 87°C. In all cases, there were differences in shape and resolution of ^{27}Al NMR signals, which is unsurprising given temperature-induced changes in viscosity of the neat samples, and changes in rate of exchange between species, but no fundamental alterations in coordination numbers were found. Furthermore, variable temperature ^{27}Al NMR studies of the two homogenous, liquid samples of the $[C_2mim][OTf]$-$Al(OTf)_3$ system ($\chi_{Al(OTf)_3}$ = 0.15 and 0.25) featured only multiple six-coordinate environments of ^{27}Al (SD, **Figure S3**).

TABLE 1 | The appearance of trifloaluminates as a function of $\chi_{Al(OTf)3}$.

| Entry	$\chi_{Al(OTf)3}$	Physical state	
		$[C_2mim][OTf]$-$Al(OTf)_3$	**$[C_8mim][OTf]$-$Al(OTf)_3$**
1	0.15	Pale liquid	Pale liquid
2	0.25	Viscous liquid	Liquid
3	0.33	Viscous liquid with suspended solid	Viscous liquid
4	0.375	–	Very viscous liquid with suspended solid
5	0.40	Very viscous liquid with suspended solid	Very viscous liquid with suspended solid
6	0.50	Glass with suspended solid	Extremely viscous liquid with suspended solid
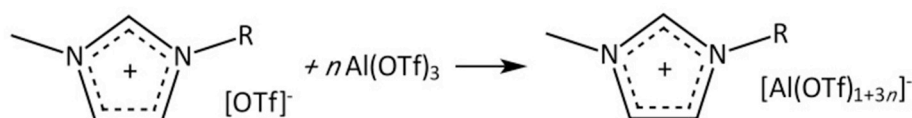
FIGURE 1 | The synthesis of $[C_2mim][OTf]$-$Al(OTf)_3$.
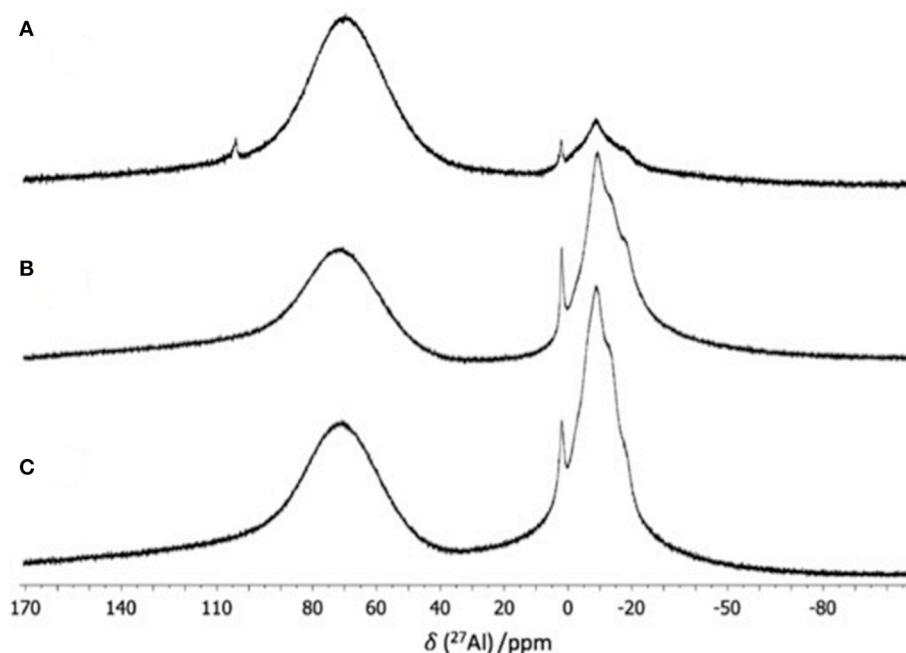
FIGURE 2 | ^{27}Al NMR spectra of [C_8mim][OTf]-Al(OTf)$_3$, $\chi_{Al(OTf)3}$ = **(A)** 0.15, **(B)** 0.25, and **(C)** 0.33 recorded neat, with d_6-dmso capillary, at 57°C).

^{27}Al NMR studies suggest that aluminum surrounded exclusively by triflate ligands shows strong propensity for six-coordinate environment, in contrast to four-coordinate environment in chloride-rich environment. This is in agreement with multiple crystallographic data, demonstrating that aluminum adopts coordination number of 6 when surrounded by O-donors (Finnegan et al., 1986). Multiple signals strongly suggest multiple hexacoordinate complexes, suggesting a variety of triflate coordination modes in aluminum complexes. Furthermore, six-coordinate environment at $\chi_{Al(OTf)3}$ = 0.33 indicates the presence of multinuclear species, with triflates in bridging coordination modes.

^{19}F NMR spectra were recorded for a range of [C_8mim][OTf]-Al(OTf)$_3$ compositions: $\chi_{Al(OTf)3}$ = 0.15-0.40, and for aluminum-free triflate ionic liquid, [C_8mim][OTf] ($\chi_{Al(OTf)3}$ = 0.00). Only the liquid part of the $\chi_{Al(OTf)3}$ = 0.40 composition was studied.

As shown in **Figure 3**, ^{19}F NMR spectrum of the neat ionic liquid features a singlet characteristic of free triflate at −80.2 ppm (Burger and Baumeister, 1999) which prevailed in trifloaluminate ionic liquids up to $\chi_{Al(OTf)3}$ = 0.33, with significant broadening as the Al(OTf)$_3$ loading increased, but was absent from the Al(OTf)$_3$-saturated sample, $\chi_{Al(OTf)3}$ = 0.40. Upon the addition of Al(OTf)$_3$ to [C_8mim][OTf] several new signals appeared, very slightly deshielded with respect to free triflate (range here −79.83 to−78.93 ppm). Also these signals broadened with increasing Al(OTf)$_3$ loading; four peaks noticeable at $\chi_{Al(OTf)3}$ = 0.15 merged into two peaks with a shoulder at $\chi_{Al(OTf)3}$ = 0.40. Intensity of the singlet originated from the free triflate group decreased with increasing mole fraction of Al(OTf)$_3$. The presence of free triflate at $\chi_{Al(OTf)3}$ = 0.33 (triflate-to-aluminum

ratio 5:1), together with the confirmed coordination number of 6 for all Al species, suggests that aluminum in a triflate-rich environment has the preference toward oligomeric clusters with multiple bridging triflates.

The general peak broadening likely results from the increasing viscosity of neat ionic liquids. Multiple signals from trifloaluminate anions corroborate with ^{27}Al NMR spectra, suggesting several coordination modes that triflate ligands adopt. Variable temperature ^{19}F NMR studies (SD, **Figure S4**), with spectra recorded between 27 and 87°C, show that signals merge progressively, to form sharp signals at 87°C, which indicates increased rate of dynamic exchange between free and coordinated triflate.

FT-IR Spectroscopy

Both [C_8mim][OTf]-Al(OTf)$_3$ and [C_2mim][OTf]-Al(OTf)$_3$ systems were analyzed with FT-IR spectroscopy across compositional range, and compared to the corresponding starting materials. The key triflate absorption were identified: asymmetric S-O stretch ca. 1,260 cm^{-1} and asymmetric C-F stretch at ca. 1,160 cm^{-1} (**Table 2**; Gejji et al., 1993; Johnston and Shriver, 1993).

Both set of results are similar, and follow the same trend. To facilitate the interpretation, a graphical representation of the results for [C_8mim][OTf]-Al(OTf)$_3$ has been plotted in **Figure 4**. At a glance, there are three value ranges adopted by both $\nu_{SO3\ ass}$ and $\nu_{CF3\ ass}$. Firstly, triflate in Al(OTf)$_3$ is characterized by red-shifted S-O vibrations (1,221.8 cm^{-1}) and blue-shifted C-F vibrations (1,180.3 cm^{-1}). Secondly, free triflate in the ionic liquid is characterized by slightly higher energy S-O vibrations (1,254.0 cm^{-1}) and red-shifted C-F vibrations (1,157.0
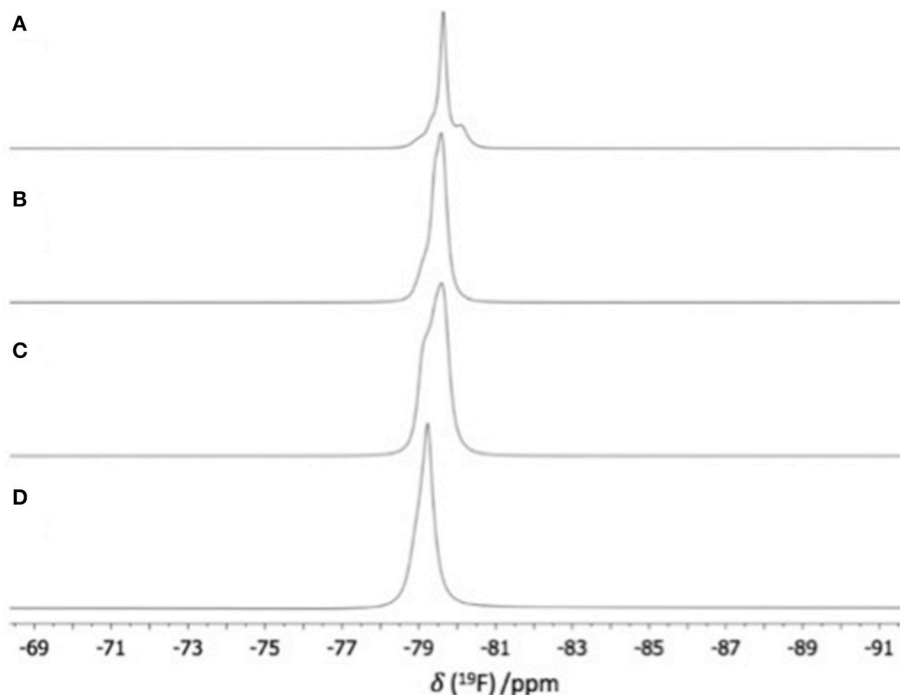
FIGURE 3 | ^{19}F NMR spectra of [C_8mim][OTf]-Al(OTf)$_3$, $\chi_{Al(OTf)3}$ = **(A)** 0.15, **(B)** 0.25, **(C)** 0.33, and **(D)** 0.40 (recorded neat, with d_6-dmso capillary, at 57°C).

TABLE 2 | Vibrational frequencies (cm^{-1}) of the key molecular vibrations in triflates, for Al(OTf)$_3$, [C_2mim][OTf] or [C_8mim][OTf], and their mixtures.

Assignment	$\chi_{Al(OTf)3}$ in [C_2mim][OTf]-Al(OTf)$_3$				
	0.00	**0.15**	**0.25**	**0.50**	**1.00**
$\nu_{SO3\ ass}$ (cm^{-1})	1252.4	1260.9	1289.1	1302.9	1221.8
$\nu_{CF3\ ass}$ (cm^{-1})	1154.7	1159.8	1162.8	1166.1	1180.3
	$\chi_{Al(OTf)3}$ in [C_8mim][OTf]-Al(OTf)$_3$				
$\nu_{SO3\ ass}$ (cm^{-1})	1254.0	1254.8	1287.6	1292.5	1221.8
$\nu_{CF3\ ass}$ (cm^{-1})	1157.0	1158.6	1163.1	1165.4	1180.3

cm^{-1}). Results for very low loading of Al(OTf)$_3$, $\chi_{Al(OTf)3}$ = 0.15, are the same as for free triflate; it appears that bands for trifloaluminate anions have been obscured by signals from free triflates. Thirdly, all compositions $\chi_{Al(OTf)3}$ = 0.25–0.50 (only liquid parts considered) share very similar spectroscopic features, with blue-shifted S-O vibrations ($\sim$1,290.5 cm^{-1}) and intermediate values for C-F vibrations ($\sim$1,164.5 cm^{-1}). It can be assumed that the last set of values corresponds to characteristic vibrations of trifloaluminate anions in ionic liquid.

Discussion on Speciation

Multiple signals corresponding to six-coordinate aluminum in ^{27}Al NMR spectra, combined with the presence of free triflates up to $\chi_{Al(OTf)3}$ = 0.33 (from ^{19}F NMR spectroscopy)

suggest propensity of aluminum to form a variety of oligomeric complexes with triflates in bridging modes. Viscosity visibly increasing with the increasing $\chi_{Al(OTf)3}$ value indicates the formation of multiply-charged species.

In discussing liquid-phase speciation, it is common to refer to relevant solid-state structures; however, these are not available for Al(OTf)$_3$, or any trifloaluminate anions. Indeed, no M(OTf)$_3$ crystal structures are known. The only single crystal structures recorded by conventional methods are these of Group 1, K(OTf) (Korus and Jansen, 2001) and Na(OTf) (Sofina et al., 2003), in addition to several M(OTf)$_2$ structures, recoded relatively recently by synchrotron X-ray powder diffraction data (Dinnebier et al., 2006). All of these feature triflate anions in complex binding modes, both terminal and bridging, with a single oxygen in triflate shared by one, two or three metal centers. In this work, multiple attempts to grow a single crystal suitable for structural studies, from any composition from the [C_2mim][OTf]-Al(OTf)$_3$ system, failed.

Clues provided from above data, both literature and spectroscopic, lead to conclusion that the homonuclear trifloaluminate anions are not the thermodynamically preferred. The nominal stoichiometry for the [Al(OTf)$_6$]$^{3-}$ anion is $\chi_{Al(OTf)3}$ = 0.25, but this composition was shown to contain free triflate and multiple environments of ^{27}Al, indicative of multinuclear species. Furthermore, it has not been possible to obtain a homogenous sample with $\chi_{Al(OTf)3}$ = 0.50 composition, where [Al(OTf)$_4$]$^-$ would be expected in analogy to [AlCl$_4$]$^-$.

The limit for accessing homogenous trifloaluminate ionic liquids appears to lie somewhere between $\chi_{Al(OTf)3}$ =

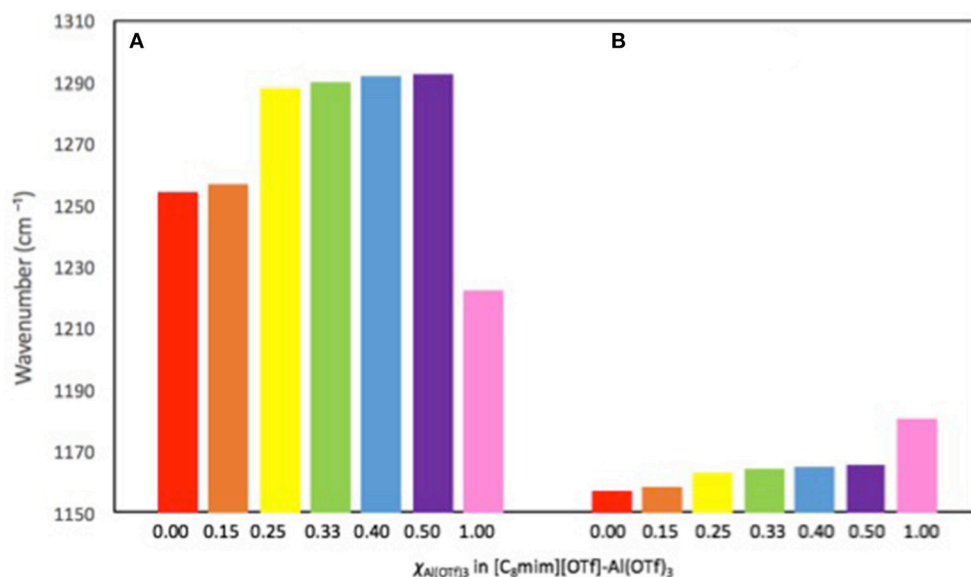**FIGURE 4 |** Wavenumbers (cm^{-1}) of the characteristic triflate molecular vibrations: **(A)** ν_{SO3ass} and **(B)** ν_{CF3ass} in Al(OTf)$_3$, [C$_8$mim][OTf], and their mixtures.

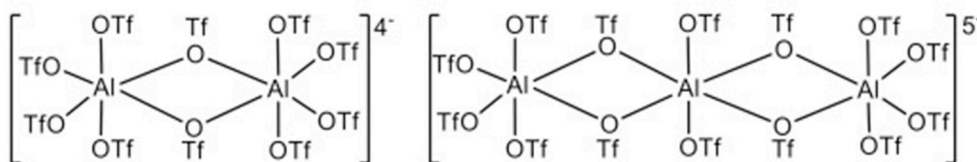**FIGURE 5 |** Plausible anionic species present in trifloaluminate ionic liquids, close to the maximum loading of Al(OTf)$_3$: [Al$_2$(OTf)$_{10}$]$^{4-}$ and [Al$_3$(OTf)$_{14}$]$^{5-}$.

0.33 and 0.375, which corresponds to oligomeric structures [Al$_2$(OTf)$_{10}$]$^{4-}$ and [Al$_3$(OTf)$_{14}$]$^{5-}$, respectively (**Figure 5**). It is not suggested that these are the only structures present in at these compositions, but plausible examples of dominant anionic species, consistent with gathered evidence.

Acceptor Numbers

Whereas, the synthetic goal of preparing liquids with high Al(OTf)$_3$ loadings was achieved, it was unsure whether the products would retain catalytic activity of Al(OTf)$_3$. In order to assess Lewis acidity of the trifloaluminate ionic liquids, Gutmann acceptor number (AN) approach was adopted, which commonly used for Lewis acidic ionic liquids (Gutmann, 1978; Estager et al., 2010). AN values are measured using a weakly basic ^{31}P NMR spectroscopic probe, triethylphosphine oxide (TEPO). Small amounts of TEPO were dissolved in each homogenous composition of both systems, and ^{31}P NMR spectra were measured at three temperatures, 27, 57 and 87°C.

At the two lower temperatures, two ^{31}P NMR signals were recorded across the compositional range, whereas one (probably averaged) signal was recorded at 87°C (SD, **Figure S5**). Following the approach adopted in our previous work (Hogg et al., 2017),

AN values were calculated based on the more deshielded signal, corresponding to the strongest Lewis acid in the system.

Acceptor numbers ranged from AN = 64.9 to 69.3 for [C$_8$mim][OTf]-Al(OTf)$_3$, and from AN = 65.8 to 69.3 for [C$_2$mim][OTf]-Al(OTf)$_3$. These values were lower than those measured for Lewis acidic chloroaluminate ionic liquids (AN = 96), but comparable to mildly Lewis acidic chlorozincate ionic liquids (Estager et al., 2011). Furthermore, compared to chlorometallate systems, there was little variability across measured compositions, which suggests that in all samples species of similar acidity are present.

Analyzing the small variations between studied samples (**Figure 6**, actual AN values SD, **Tables 1**, **2**), AN values increase with the increasing $\chi_{Al(OTf)3}$, and are on average slightly higher for [C$_2$mim][OTf]-Al(OTf)$_3$, compared to the analogous [C$_8$mim][OTf]-Al(OTf)$_3$ composition. Furthermore, AN values appear to decrease with temperature, which may relate to larger kinetic energy corresponding to lower propensity of the probe to bind to the aluminum center.

Aluminum surrounded exclusively by chloride ligands assumes maximum coordination of 4, and is 6-coordinate in the presence of *O*-donors. Lewis acidity in chloroaluminate ionic liquids arises from the coordinationally saturated [Al$_2$Cl$_7$]$^-$
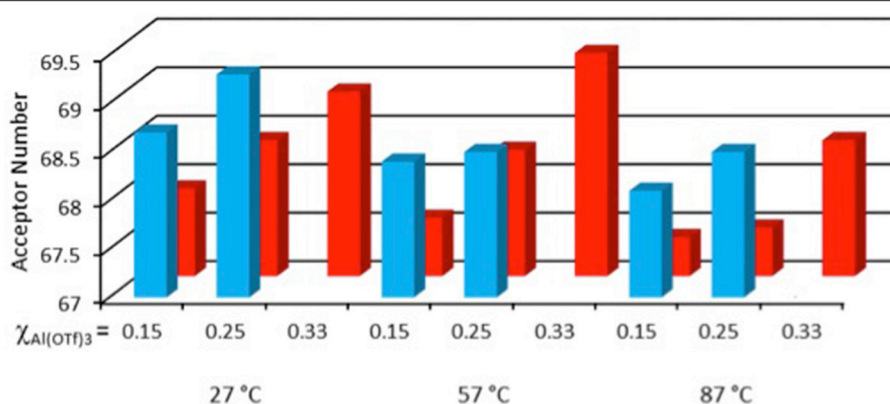
FIGURE 6 | Acceptor numbers for $[C_n mim][OTf]$-$Al(OTf)_3$ ($n = 2$, blue; $n = 8$, red), measured for $\chi_{Al(OTf)_3}$ = 0.15, 0.25 and 0.33, at three temperatures: 27, 57 and 87°C.

anion, where the bridging chloride bond must be broken to reveal latent Lewis acidic site. In analogy, it can be assumed that a bridging oxygen bond is severed in 6-coordinate a trifloaluminate anion, for the aluminum center to interact with a base. Difference in Lewis acidity is naturally explained by the presence of six O-donor ligands, which lower electrophilicity of the aluminum center more efficiently than four chloride ligands.

Hydrolytic Stability of Trifloaluminate Ionic Liquids

Metal triflates are reported to be water tolerant Lewis acids; some of them can be even recovered from the aqueous phases after the reaction and recycled without loss of activity, e.g., $La(OTf)_3$, $Zn(OTf)_2$, $Yb(OTf)_3$, and LiOTf (Kobayashi and Manabe, 2000; Kobayashi et al., 2002). Other metal triflates are known to slowly hydrolyse in water, releasing triflic acid, thus acting sometimes as a Brønsted acid–this includes $Al(OTf)_3$, $Sn(OTf)_2$, $Sc(OTf)_3$, and $In(OTf)_3$ (Baes and Mesmer, 1976; Noji et al., 2003; Markiton et al., 2018). As a rule of a thumb, metals at higher oxidation states are more prone to hydrolysis, with the exception of rare earth metal triflates, which are water-stable and act as Lewis acids in both aqueous and non-aqueous media (Kobayashi et al., 2002).

Trifloaluminate ionic liquids, in contrast to chloroaluminate analogs, do not react violently with water, but appear to be water-miscible in a wide range of proportions. Furthermore, trifloaluminate ionic liquids did not change their appearance upon overnight exposure to atmospheric moisture (air), neither showed marked change in their NMR spectra, whereas their chloroaluminate counterparts tend to undergo immediate hydrolysis evident by fuming and white crust forming on the interface of ionic liquid and air.

In order to check for traces of hydrolysis undetectable by NMR spectroscopy, trifloaluminate ionic liquids (used as synthesized, without previous drying, exposed to atmospheric moisture) generation of retinyl cations from retinyl acetate in the presence of ionic liquid dissolved in nitrobenzene was used as the probe reaction. Nitrobenzene provided adequate solubility and did not generate protons by O–H bond polarization. Reaction of retinol with a Brønsted acid results in the formation of a blue carbocation, which can be detected and quantified by UV/Vis spectroscopy **Figure 7**, SD, **Figure S7**) (Williams and Lawton, 2010).
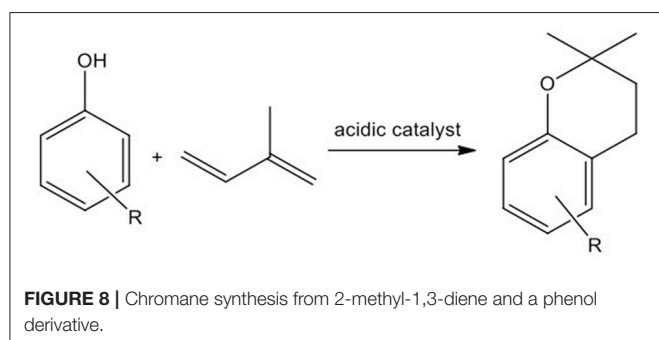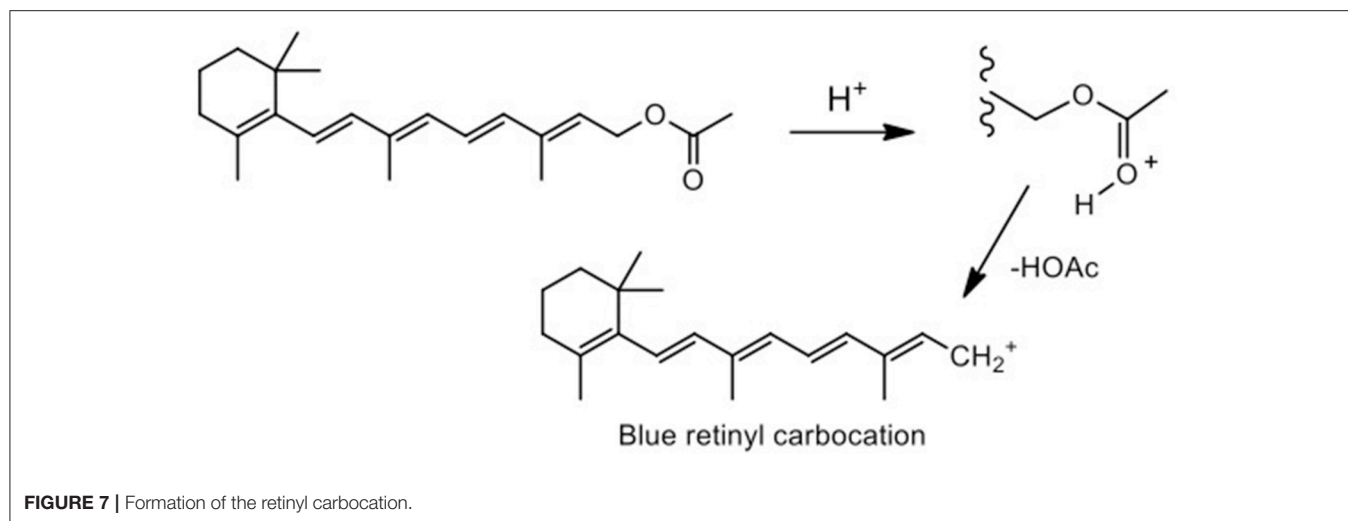
Three reactions involving $[C_2 mim][OTf]$-$Al(OTf)_3$, $\chi_{Al(OTf)_3}$ = 0.25, triflic acid and $Al(OTf)_3$ (as benchmarks) all turned blue, indicating the formation of the retinyl cation, related to the presence of hydronium ion (Brønsted acidity). In contrast, reaction with lanthanum triflate did not cause color change, which is associated with the absence of hydrolysis products. In conclusion, although trifloaluminate ionic liquids do not violently react with water, they may undergo very slow hydrolysis in the presence of atmospheric moisture.

Synthesis of a Model Chromane, Catalyzed by Metal Triflates

An important reaction typically catalyzed by metal triflates is the synthesis of chromans *via* the reaction of dienes with phenolic compounds (**Figure 8**; Youn and Eom, 2006; Bonrath et al., 2007; Adrio and Hii, 2008; Vece et al., 2010; Dang et al., 2011). The two-step reaction involves alkylation of a phenolic compound, followed by etherification reaction to form benzofuran or benzopyran. 2,2-Dimethylbenzopyran is found in the natural products, such as vitamin E (Schneider, 2005) and flavonoids (Middleton et al., 2000); some of the latter compounds are biologically active (Brown et al., 1990), for example as HIV protease inhibitors (Kashman et al., 1992).

Reaction carried out in the presence of conventional catalysts, both Lewis and Brønsted acids (Amberlyst® 15, H_3PO_4, $AlCl_3$) (Ahluwalia et al., 1982; Kalena et al., 1997; Bonrath et al., 2007) requires high temperatures and high catalyst loadings. Selectivity is also a challenge, with side-products forming *via* C-alkylation of phenol by diene, toward substituted alkylated phenols, as well as alkylated chromans.

Amongst the most promising catalysts are metal triflates; for example, AgOTf (5 mol% in dichloroethane, at ambient

FIGURE 7 | Formation of the retinyl carbocation.

FIGURE 8 | Chromane synthesis from 2-methyl-1,3-diene and a phenol derivative.

temperature) promoted the formation of a variety of dihydrobenzopyran and dihydrobenzofuran ring systems; for example, addition of isoprene to 4-methoxyphenol gave 61% of yield of benzopyran (Youn and Eom, 2006). Yet, although various Lewis acidic metal triflates have been used as catalysts for the synthesis of chromanes (Youn and Eom, 2006; Bonrath et al., 2007; Adrio and Hii, 2008; Vece et al., 2010; Dang et al., 2011), the literature lacks comparative studies of the activity of different metal triflates, which could guide the selection of best triflometallate ionic liquids.

In the preliminary screening, a wide range of metal triflates: Al(III), Sn(II), Sc(III), In(III), Li(I), Ag(I), Ga(III), Zn(II), La(III), Bi(III), Yb(III), Y(III), Tl(III) and Er(III), were tested as Lewis acidic catalysts in the synthesis of the model compound: 2,2-dimethyl-2,4-dimethylchromane, obtained through the reaction of 2,4-dimethylphenol with 2-methyl-1,3-butadiene (isoprene). There are two pathways leading to the chromane formation (**Figure 9**; Vece et al., 2010). The first route concerns Friedel–Crafts *C*-allylation to **4** followed by intramolecular cyclisation to chromane, **5**. The second sequence requires the formation of allyl-aryl ether, **3**, followed by a [3,3]-sigmatropic rearrangement to **4**, and further intramolecular cyclisation leading to **5**. Products **3** and **4** are the intermediates of this reaction.

The model reaction was carried out at 35°C, solventless, using 1:2 molar ratio of isoprene:2,4-dimethylphenol. In all cases,

the addition of 2 mol% of metal triflate gave a suspension of catalyst in the liquid reaction mixture, rather than a homogenous solution. Conversion of 2,4-dimethylphenol (α) was measured after 90 min of the reaction, using GC (**Table 3**).

Sn(OTf)$_2$, Sc(OTf)$_3$, Bi(OTf)$_3$, Ga(OTf)$_3$, and In(OTf)$_3$ exhibited the highest activity, achieving full conversion of 2,4-dimethylphenol, combined with high selectivities to chromane (81–92%) after 90 min. Rare-earth metals were found inactive under the reaction conditions, except for Yb(OTf)$_3$, which offered poor selectivity. Al(OTf)$_3$ gave intermediate results, with conversion of 82% (at 80% selectivity) achieved after 150 min. Two by-product were detected (GC-MS analysis, ESI) across all post-reaction mixtures: 2,4-dimethyl-1-[(3-methyl-3-buten-1-yl)oxy]benzene (**3**) and 2,4-dimethyl-6-(3-methyl-3-buten-1-yl)phenol (**4**); both of them are intermediates leading to the target chromane (**Figure 9**). Therefore, the challenge appears to lie in shifting the equilibrium toward the product formation, rather than avoiding unwanted by-products.

As already mentioned, the focus on triflometallate ionic liquids was dictated by the drive to find both chemically active and economically attractive system. Seeing that the most active metal triflates were also among the most expensive ones, in this work we set to explore whether the ionic liquid pathway may offer an enhancement of catalytic activity of the inexpensive Al(OTf)$_3$, before venturing into more expensive metal triflates.

Synthesis of a Model Chromane, Catalyzed by Trifloaluminate Ionic Liquids

AN values measured for all triflometallate ionic liquids were relatively similar, with small variations resulting from the length of alkyl chain on the cation, temperature of measurement or even on the $\chi_{Al(OTf)_3}$ value. Considering viscosity rising dramatically with increasing $\chi_{Al(OTf)_3}$, it was decided to select systems with lower Al(OTf)$_3$ loading: $\chi_{Al(OTf)_3}$ = 0.15 and 0.25, which bore promise of better mass transport in a biphasic liquid mixture, due to lower viscosity. By the same token, systems based on [C$_2$mim]$^+$ cation were selected over [C$_8$mim]$^+$ cation.
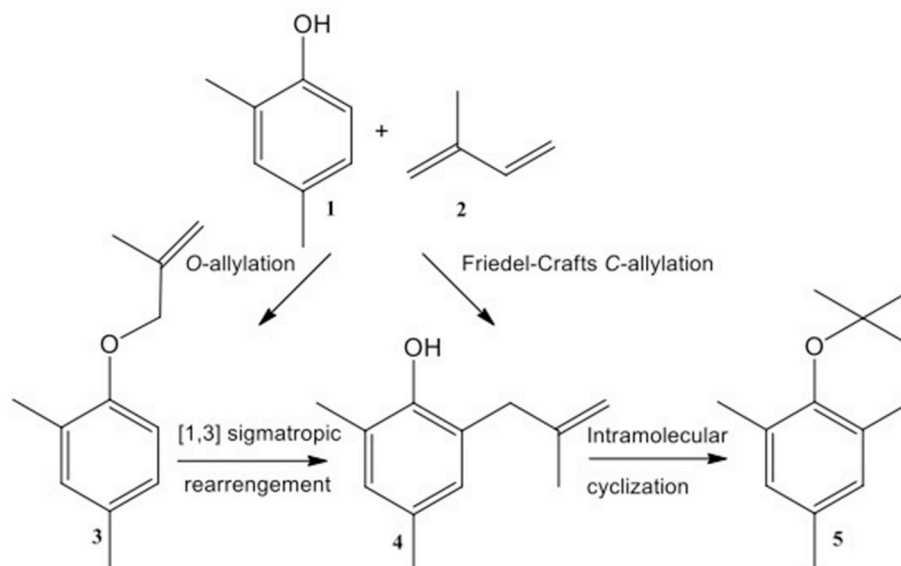
FIGURE 9 | The model reaction of 2,4-dimethylphenol with 2-methyl-1,3-butadiene.

TABLE 3 | The synthesis of model chromane in the presence of various metal triflates.

Entry	Metal triflate	α, %	Selectivity, %
1	Al(OTf)$_3$ (90 min)	70	80
	(120 min)	78	80
	(150 min)	82	80
	(180 min)	82	80
2	Sn(OTf)$_2$	100	81
3	Sc(OTf)$_3$	100	91
4	Bi(OTf)$_3$	100	92
5	Ga(OTf)$_3$	100	89
6	In(OTf)$_3$	97	81
7	Yb(OTf)$_3$	100	66
8	Ag(OTf)	30	42
9	Li(OTf)	10	14
10	Y(OTf)$_3$	7	14
11	Er(OTf)$_3$	6	100
12	Zn(OTf)$_2$, La(OTf)$_3$, Tl(OTf)$_3$	0	0

Reaction conditions: 35°C, 2,4-dimethylphenol (4 mmol), isoprene (2 mmol), catalyst loading 2 mol % per isoprene, 1,500 rpm, reaction time 90 min.

Reactants Ratio

In the first set of experiments, trifloaluminate ionic liquids were used as homogenous catalysts in the synthesis of chromane under solventless conditions, at 35°C, and molar ratio of isoprene to 2,4-dimethylphenol was varied between 1:2 and 2:1 (**Figure 10**). Best results were recorded for 2-fold molar excess of 2,4-dimethylphenol to isoprene, which allowed for reaching full conversion of 1 mol of 2,4-dimethylphenol per 1 mol of isoprene and high selectivities: 89% when using [C$_2$mim][OTf]-Al(OTf)$_3$, $\chi_{Al(OTf)3} = 0.25$, and 79% when using [C$_2$mim][OTf]-Al(OTf)$_3$, $\chi_{Al(OTf)3} = 0.15$. Using the catalyst with lower aluminum loading

resulted in longer reaction time required to reach full conversion (120 vs. 90 min), which can be justified in lower content of Lewis acidic aluminum centers per mole of the $\chi_{Al(OTf)3} = 0.15$ ionic liquid (calculated as mole of cation).

Reaction Conditions

The influence of reaction temperature and catalyst loading was studied, keeping the reactants ratio at two-fold molar excess of 2,4-dimethylphenol (**Table 4**). Selectivity to the main product (**5**) and the two by-products (**3, 4**) was reported. For the sake of comparison, reaction was carried out in the presence of HOTf and Al(OTf)$_3$, since both Lewis and Brønsted acid sites may be involved in catalysis (**Table 4**, entries 1-4). Ionic liquids with both cations: [C$_2$mim]$^+$ and [C$_8$mim]$^+$ were screened, at two compositions: $\chi_{Al(OTf)3} = 0.15$ and 0.25 (**Table 4**, entries 5–12). In general, increase of selectivity with reaction time was observed, as intermediates **3** and **4** were transformed to **5** in the course of reaction.

Comparing activity of Al(OTf)$_3$ and [C$_2$mim][OTf]-Al(OTf)$_3$, $\chi_{Al(OTf)3} = 0.25$, lower activity of the former is particularly visible under less favorable reaction conditions. At low reaction temperature (20°C) the ionic liquids retained high activity, in contrast to Al(OTf)$_3$ (**Table 4**, entries 2 and 6). Furthermore, at low catalyst loading (0.2 mol%) Al(OTf)$_3$ gave 30% conversion after 240 min, whereas the ionic liquid delivered 95% conversion after 180 min (**Table 4**, entries 4 and 9).

Comparing catalytic activity of different IL catalysts, the cation had no measurable influence on the catalytic performance. As expected, ILs with lower Al(OTf)$_3$ loading were less active under the same reaction conditions. Below 0.2 mol% loading, it was impossible to reach full conversion using [C$_2$mim][OTf]-Al(OTf)$_3$, $\chi_{Al(OTf)3} = 0.25$ under standard reaction conditions (reaction has stopped at 75% conversion).
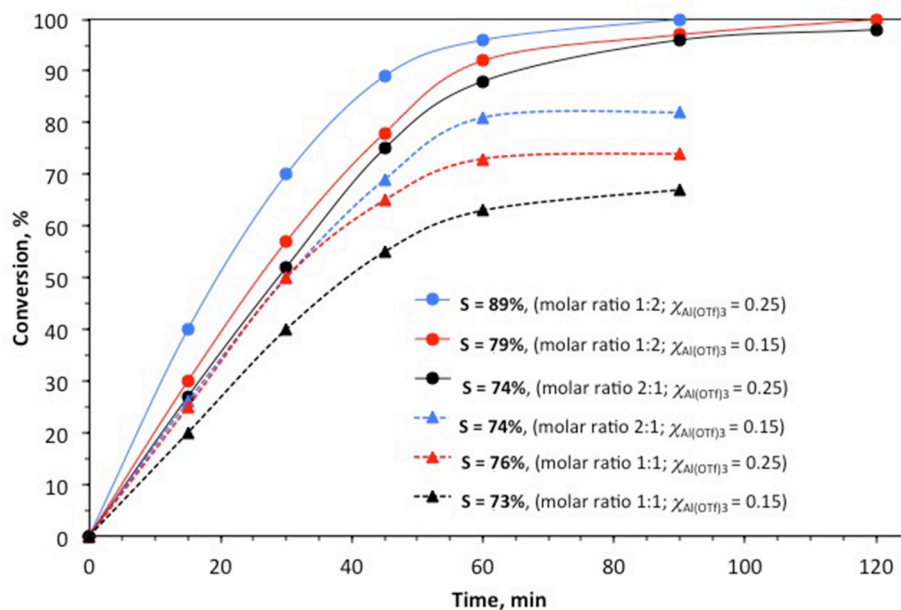
FIGURE 10 | The influence of molar ratio of isoprene to 2,4-dimethylphenol (in parentheses) on the conversion of 2,4-dimethylphenol and selectivity to chromane.
Reaction conditions: 35°C, catalyst loading 2 mol % per isoprene, 1,500 rpm. Catalyst: $[C_2mim][OTf]$-$Al(OTf)_3$.

TABLE 4 | The influence of the temperature and amount of various catalysts on the conversion of 2,4-dimethylphenol.

Entry	Catalyst	T°C	Catalyst loading, mol% per isoprene	Time, min	α,%	Selectivity,%
1	TfOH	35	0.2	180	81	82(**5**), 9 (**3**), 9 (**4**)
2	$Al(OTf)_3$	20	2.0	60	10	23
3		35	2.0	150	82	80 (**5**), 10 (**3**), 10 (**4**)
4		35	0.2	240	30	48
5	$[C_2mim][OTf]$-$Al(OTf)_3$, $\chi_{Al(OTf)3} = 0.15$	35	2.0	120	99	79 (**5**), 8 (**3**), 13 (**4**)
6	$[C_2mim][OTf]$-$Al(OTf)_3$, $\chi_{Al(OTf)3} = 0.25$	20	2.0	120	99	78 (**5**), 10 (**3**), 12 (**4**)
7		35	2.0	60	94	89 (**5**), 4 (**3**), 7 (**4**)
8		35	1.0	90	96	81 (**5**), 8 (**3**), 11 (**4**)
9		35	0.2	180	95	84 (**5**), 6 (**3**), 10 (**4**)
10		35	0.15	180	61	73 (**5**), 10 (**3**), 17 (**4**)
11	$[C_8mim][OTf]$-$Al(OTf)_3$, $\chi_{Al(OTf)3} = 0.15$	35	2.0	120	97	81 (**5**), 8 (**3**), 11 (**4**)
12	$[C_8mim][OTf]$-$Al(OTf)_3$, $\chi_{Al(OTf)3} = 0.25$	35	2.0	60	95	87 (**5**), 4 (**3**), 9 (**4**)
13	MWCNT-$[C_2mim][OTf]$-$Al(OTf)_3$, $\chi_{Al(OTf)3} = 0.25$	35	0.2	90	99	84 (**5**), 10 (**3**), 6 (**4**)
14	MWCNT-$[C_2mim][OTf]$-$Al(OTf)_3$, $\chi_{Al(OTf)3} = 0.25$	35	0.2[a]	120	66	80 (**5**), 13 (**3**), 7 (**4**)
15	MWCNT-$[C_2mim][OTf]$-$Al(OTf)_3$, $\chi_{Al(OTf)3} = 0.25$	35	0.15	90	76	78(**5**), 9 (**3**), 13 (**4**)

[a] *recycled catalyst. Reaction conditions: 35°C, 2,4-dimethylphenol (4 mmol), isoprene (2 mmol), 1,500 rpm.*

Moisture Sensitivity

Since no evidence for hydrolysis was found, either visually or through the NMR spectroscopy, chromane syntheses were carried out without protective atmosphere or drying precautions. However, following the retinyl cation test indicating the presence of acidic protons, it was decided to repeat two experiments with trifloaluminate ionic liquids (**Table 4**, entries 7 and 9) in a glovebox, under strictly anhydrous conditions. Nevertheless, no differences in conversion or selectivity were detected compared to unprotected experiments, indicating that

protic impurities must have been generated at trace levels only, and did not interfere with catalytic performance of ionic liquids.

Recycling

It was attempted to recycle the $[C_2mim][OTf]$-$Al(OTf)_3$, $\chi_{Al(OTf)3} = 0.25$ catalyst, from reaction carried out at 0.2 mol% loading. After completion, *n*-hexane was added to the reaction mixture and two phases formed. The lower (ionic liquid) phase was separated and re-used. Unfortunately, activity of the recycled

catalyst decreased (**Table 4**, entry 14), yielding 66% conversion of 2,4-dimethylphenol (and selectivity of 80%) after 120 min.

Seeking strategies for a more efficient recycle of trifloaluminate ionic liquids, it was attempted to use it as supported ionic liquid phase (SILP), with multi-walled carbon nanotubes (MWCNTs) used as the support.

Synthesis of Model Chromane, Catalyzed by Trifloaluminate Ionic Liquids Immobilized on Carbon Nanotubes

Carbon nanotubes (CNTs) have been described as versatile supports for immobilization of catalysts due to their small size, large surface area, as well as mechanical and thermal stability. Supporting catalysts on CNTs has had profound effect on both catalytic activity and selectivity, with major enhancements reported in the literature (Eder, 2010). The economy of CNT-based processes is increasingly favorable, with prices of industrial-grade MWCNTs as low as 100$ per 1 kg (Nanocyl™ NC7000 MWCNTs). Finally, in CNTs prepared *via* catalytic chemical vapor deposition (c-CVD), their integral feature is the presence of core-encapsulated ferromagnetic iron-based nanoparticles, which are typically irremovable under lower technological regimes. This characteristic allows for an easy removal of the catalysts from the post-reaction mixtures by means of a magnetic field, which is a significant advantage in light of the processing economy.

The superactive catalysts based on carbon nanomaterials as supports have been already demonstrated in our earlier studies (Markiton et al., 2017, 2018). Extremely high activity of $Sn(OTf)_2$ immobilized on MWCNTs in promoting the Baeyer-Villiger oxidation was related to spherical nanosize $Sn(OTf)_2$ particles (*ca.* 2 nm) dispersed along the outer nanotube walls.[13] In chemo-enzymatic Baeyer-Villiger reaction, the performance of lipase was significantly improved by immobilization on MWCNTs (Markiton et al., 2017).

Encouraged by the past results, we decided to support trifloaluminate ionic liquids on MWCNTs, in hope to develop a high-performance and recyclable SILP catalyst. To the best of our knowledge, it is the first attempt to use solid-immobilized metal triflate for chromans synthesis.

Comparison of Homogenous and SILP Systems

The best-performing ionic liquid, $[C_2mim][OTf]$-$Al(OTf)_3$, $\chi_{Al(OTf)_3} = 0.25$, was immobilized on the CheapTubes™ MWCNTs, at a mass ratio of MWCNTs to ionic liquid of 1:2. Suspension of the ionic liquid and MWCNTs was suspended in *n*-hexane by ultrasonication, and then filtered. Subsequent washing with *n*-hexane and solvent removal under reduced pressure yielded the heterogenised catalyst, MWCNT-$[C_2mim][OTf]$-$Al(OTf)_3$, $\chi_{Al(OTf)_3} = 0.25$. The quantity of the active phase (ionic liquid) was estimated by thermogravimetric analysis (TGA, SI, **Figures S8–S12**), and the SILP catalyst was characterized in comparison to neat MWCNTs. As compared in **Table S5**, both pore volumes (V_p) and overall surface area (S_{BET}) decreased in SILP compared to neat MWCNTs, as the result of interstitial channels–forming both pores and available surface–occupied by the adsorbed ionic liquid (33 wt%).

The trifloaluminate ionic liquid in the SILP form, MWCNTs-$[C_2mim][OTf]$-$Al(OTf)_3$, $\chi_{Al(OTf)_3} = 0.25$, was tested as the catalyst for chromane synthesis under solventless conditions, at low catalyst loading of 0.2 mol%, (**Table 4**, entry 13). It was found that immobilization of the trifloaluminate ionic liquid increased its catalytic activity, with the reaction time required for full conversion shortened to 90 min, compared to 180 min needed in analogous homogenous reaction (**Table 4**, entry 9).

Optimisation of the IL Loading

The original procedure used to prepare the SILP catalyst was modified to combine MWCNTs and the ionic liquid at mass ratios of 4:1 and 1:1. The sample prepared at 4:1 ratio contained only 16 wt% of ionic liquid, and required 0.2 mol% loading to work as a catalyst, which also caused stirring problems due to large volume of suspended MWCNTs in the synthesis of chromane. In contrast, the use of catalyst prepared at 1:1 ratio, contained 30 wt% of the ionic liquid (nearly the same as sample prepared with two-fold excess of ionic liquid) let efficient mixing of reaction system. In conclusion, it was found sufficient to use equal mass of the ionic liquid and MWCNTs to prepare "fully loaded" SILP catalyst.

Leaching and Recycling

Leaching was tested by repeating the benchmark reaction with the $[C_2mim][OTf]$-$Al(OTf)_3$, $\chi_{Al(OTf)_3} = 0.25$ catalyst (**Table 4**, entry 5), but filtering the catalyst off after 15 min (conversion 37%, selectivity 61%), and continuing the reaction in absence of the catalyst. After 30 min (15 min after the filtration) the reaction progressed slightly further (conversion 44%, selectivity 63%), but further progress was significantly halted, with conversion 51% and selectivity 65% reported after 90 min and no further change after 150 min. For comparison, the benchmark experiment (**Table 3**, entry 5) gave full conversion and 84% selectivity after 90 min. In conclusion, the slow progress of the reaction after SILP catalyst removal could be attributed to some amount of leaching.

Indeed, TGA analysis of the filtered-off catalyst sample revealed that *ca.* 27 wt% of the initial amount of ionic liquid was removed from the MWCNT surface. In agreement with this assessment, recycled catalyst gave lower performance than the fresh sample (conversion 45%, selectivity 56%), as shown in **Figure 11**.

Fortunately, it was found that the leached ionic liquid could be recovered from the post-reaction mixture and re-immobilized on the MWCNTs surface, which restored full catalytic activity. After each reaction cycle, the SILP catalyst was filtered off and *n*-hexane was added to the filtrate. Next, the lower phase (containing ionic liquid) was isolated and immobilized on the surface of the SILP sample that has been isolated by filtration. Such re-immobilized system contained 33 wt% of the ionic liquid loading (by TGA), and retained high catalytic activity and selectivity over four recycles (**Figure 11**).

Comparison to the Literature

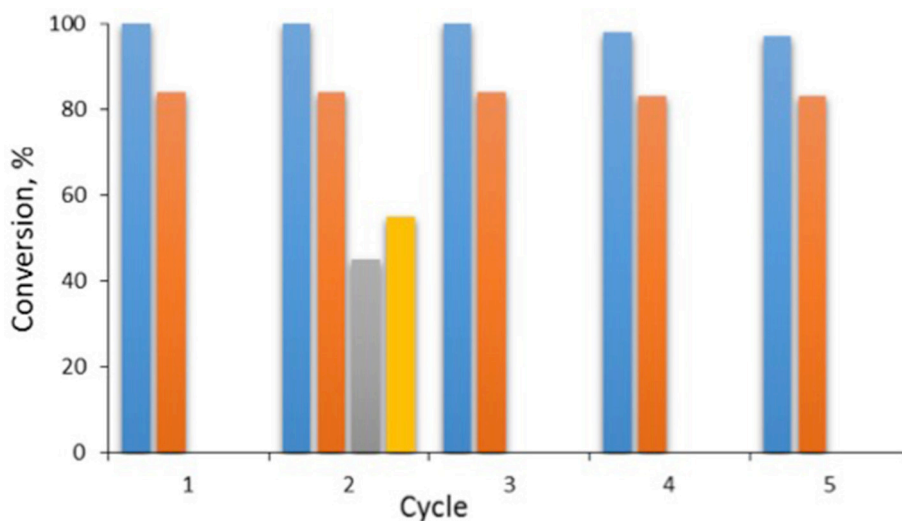Comparing literature reports on various tandem additions/cyclizations of phenols with dienes, it is evident that

FIGURE 11 | The recycle of catalyst MWCNT-[C$_2$mim][OTf]-Al(OTf)$_3$, $\chi_{Al(OTf)3}$ = 0.25 after regeneration; blue bars: conversion; orange bars: selectivity; gray bar: conversion and yellow bar: selectivity for the reaction carried out with the recycled catalyst without its regeneration. *Reaction conditions:* 35°C, 2,4-dimethylphenol (4 mmol), isoprene (2 mmol), catalyst loading 0.2 mol% per isoprene, 1,500 rpm, reaction time 90 min.

using trifloaluminate ionic liquids offers certain improvements, either in homogenous or SILP form.

For comparison, AgOTf was used at 5 mol% loading (RT, 1,2-dichroetane as a solvent), and gave 54–96% yields after 24 h (S. Youn and Eom, 2006). It was possible to reduce AgOTf loading to 1 mol%, but the addition of 4 mol% of ^{t}BuCl was required, which gave up to 86% conversion to dihydrobenzopyrans in 20 min. (Dang et al., 2011). Nevertheless, in both cases higher loadings of a more expensive catalyst are required, in addition to cancerogenic chlorinated solvents/co-catalysts.

In other examples, In(OTf)$_3$ was used at 1 mol% (RT, 2 h, average yield 80%; Vece et al., 2010), and Bi(OTf)$_3$ was used at 5 mol% (RT, 2 h or RT, 10-16 h, depending on reactants, gave 80% yield; Ollevier and Mwene-Mbeja, 2006). The lowest catalyst loadings were achieved with Cu(OTf)$_2$ promoted with PPh$_3$, which worked at 0.5 mol% loading (RT, 18 h; Adrio and Hii, 2008).

CONCLUSIONS

In this contribution, we report the first example of triflometallate ionic liquids. Trifloaluminate systems, in contrast to the chloroaluminate counterparts, contain hexacoordinate aluminum in multiply-charged, oligonuclear anionic complexes, featuring a variety of triflate bridging modes. As a consequence of this speciation, trifloaluminate ionic liquids are viscous, and it is only practical to use them at low Al(OTf)$_3$ loadings (up to $\chi_{Al(OTf)3}$ = 0.25). Their acidity is lower than that of chloroaluminate ionic liquids, and similar to chlorozincate ionic liquids.

Newly reported trifloaluminate systems have been found efficient catalysts in the chromane syntheses in solvent-free, one-pot process. In contrast to literature processes, the catalyst loadings were found to be truly catalytic (0.2 mol%) and the reaction times required for the full conversion were drastically shortened. The procedure is entirely chloride-free, and eliminates the requirement for chlorinated solvent/promoter, reported in some earlier works.

Further improvements were achieved by supporting trifloaluminate ionic liquids on multi-walled carbon nanotubes. In agreement with earlier reports, the activity of the catalyst was enhanced by the support, and recycling was facilitated by enabling simple filtration. Although some ionic liquid leached into the reaction mixture, it was possible to recover and re-support it, which resulted in a recyclable catalytic system.

AUTHOR CONTRIBUTIONS

PL and NB synthesis of chromane; AlC and LB synthesis and speciation of ionic liquids; SJ thermal analysis; SB preparation and analysis of supported ionic liquids; PN and MS-K supervision of PL, AlC and LB, contribution to manuscript writing; AnC supervision of PL and NB, contribution to manuscript writing.

FUNDING

SUPPLEMENTARY MATERIAL

The Supplementary Material for this article can be found online at: https://www.frontiersin.org/articles/10.3389/fchem. 2018.00535/full#supplementary-material

REFERENCES

Abbott, A. P., Capper, G., Davies, D. L., Munro, H. L., Rasheed, R. K., and Tambyrajah, V. (2001). Preparation of novel, moisture-stable, Lewis-acidic ionic liquids containing quaternary ammonium salts with functional side chains. *Chem. Commun.* 2010–2011. doi: 10.1039/B106357J

Adrio, L. A., and Hii, K. K. (2008). A recyclable copper(II) catalyst for the annulation of phenols with 1,3-dienes. *Chem. Commun.* 2325–2327. doi: 10.1039/B719465J

Ahluwalia, V. K., Arora, K. K., and Jolly, R. S. (1982). Acid-catalysed condensation of isoprene with phenols. Formation of 2,2-dimethylchromans. *J. Chem. Soc. Perkin Trans.* 1, 335–338.

Apblett, A. W. (2012). *Aluminum: Inorganic Chemistry Encyclopedia of Inorganic and Bioinorganic Chemistry*. Hoboken, NJ: John Wiley & Sons.

Atkins, M. P., Seddon, K. R., and Swadzba-Kwaśny, M. (2011). Oligomerisation of linear 1-olefins using a chlorogallate(III) ionic liquid. *Pure Appl. Chem.* 83, 1391–1406. doi: 10.1351/PAC-CON-10-12-03

Atwood, D. A. (1998). Cationic group 13 complexes. *Coordination Chem. Rev.* 176, 407–430. doi: 10.1016/S0010-8545(98)00127-1

Baes, C. F., and Mesmer, R. (1976). *The Hydrolysis of Cations*. New York, NY: John Wiley & Sons.

Binnemans, K. (2007). Lanthanides and actinides in ionic liquids. *Chem. Rev.* 107, 2592–2614. doi: 10.1021/cr050979c

Bonrath, W., Dittel, C., Giraudi, L., Netscher, T., and Pabst, T. (2007). Rare earth triflate catalysts in the synthesis of Vitamin E and its derivatives. *Catal. Today* 121, 65–70. doi: 10.1016/j.cattod.2006.11.022

Brown, P. E., Lewis, R. A., and Waring, M. A. (1990). Studies of chromenes. Part 9. syntheses of chromenequinones. *J. Chem. Soc. Perkin Trans. I* 2979–2988.

Burger, P., and Baumeister, J. M. (1999). Transition metal complexes with sterically demanding ligands. I. Synthesis and X-ray crystal structure of 1,5-cyclooctadiene palladium methyl triflate, (COD)Pd(Me)(OTf) and its cationic penta-coordinate adducts with sterically demanding 2,9-diaryl-substituted 1,10-phenanthroline ligands. *J. Organomet. Chem.* 575, 214–222. doi: 10.1016/S.0022-328X.(98)00997-8

Choi, M., Matsunaga, K., Oba, F., and Tanaka, I. (2009). ^{27}Al NMR chemical shifts in oxide crystals: a first-principles study. *J. Phys. Chem. C* 113, 3869–3873. doi: 10.1021/jp810484j

Coulombel, L., Weiwer, M., and Dunach, E. (2009). Aluminium triflate catalysed cyclisation of unsaturated alcohols: novel synthesis of rose oxide and analogues. *Eur. J. Org. Chem.* 33, 5788–5795. doi: 10.1002/ejoc.200900841

Dang, T. T., Boeck, F., and Hintermann, L. (2011). Hidden Brønsted acid catalysis: pathways of accidental or deliberate generation of triflic acid from metal triflates. *J. Org. Chem.* 76, 9353–9361. doi: 10.1021/jo201631x

Dinnebier, R., Sofina, N., Hildebrandt, L., and Jansen, M. (2006). Crystal structures of the trifluoromethyl sulfonates M(SO3CF3)(2) (M = Mg, Ca, Ba, Zn, Cu) from synchrotron X-ray powder diffraction data. *Acta. Cryst. B.* 62, 467–473. doi: 10.1107/S0108768106009517

Eder, D. (2010). Carbon nanotube–inorganic hybrids. *Chem. Rev.* 110, 1348–1385. doi: 10.1021/cr800433k

Estager, J., Holbrey, J., and Swadzba-Kwaśny, M. (2014). Halometallate ionic liquids-revisited. *Chem. Soc. Rev.* 43, 847–886. doi: 10.1039/C3CS60310E

Estager, J., Nockemann, P., Seddon, K. R., Swadzba-Kwaśny, M., and Tyrrell, S. (2011). Validation of speciation techniques: a study of chlorozincate(II) ionic liquids. *Inorg. Chem.* 50, 5258–5271. doi: 10.1021/ic200586u

Estager, J., Oliferenko, A. A., Seddon, K. R., and Swadzba-Kwaśny, M. (2010). Chlorometallate(III) ionic liquids as Lewis acidic catalysts-a quantitative study of acceptor properties. *Dalton Trans.* 39, 11375–11382. doi: 10.1039/c0dt00895h

Finnegan, M. M., Rettig, S. J., and Orvig, C. (1986). A neutral water-soluble aluminum complex of neurological interest. *J. Am. Chem. Soc.* 108, 5033–5055. doi: 10.1021/ja00276a069

Gejji, S. P., Hermansson, K., and Lindgren, J. (1993). Ab initio vibrational frequencies of the triflate ion, $(CF_3SO_3)^-$. *J. Phys. Chem.* 97, 3712–3715. doi: 10.1021/j100117a014

Gutmann, V. (1978). *The Donor-Acceptor Approach to Molecular Interactions*. New York, NY: Plenum Press.

Hardacre, C., Murphy, R. W., Seddon, K. R., Srinivasan, G., and Swadzba-Kwaśny, M. (2010). Speciation of chlorometallate ionic liquids based on

gallium(III) and indium(III). *Aust. J. Chem.* 63, 845–848. doi: 10.1071/CH10014

Hogg, J. M., Brown, L. C., Matuszek, K., Latos, P., Chrobok, A., and Swadzba-Kwaśny, M. (2017). Liquid coordination complexes of Lewis acidic metal chlorides: lewis acidity and insights into speciation. *Dalton Trans.* 46, 11561–11574. doi: 10.1039/C7DT02408H

Johnston, D. H., and Shriver, D. F. (1993). Vibrational study of the trifluoromethanesulfonate anion: unambiguous assignment of the asymmetric stretching modes. *Inorg. Chem.* 32, 1045–1047. doi: 10.1021/ic00058a050

Kalena, G. P., Jain, A., and Banerji, A. (1997). Amberlyst 15 catalyzed prenylation of phenols: one-step synthesis of benzopyrans. *Molecules* 2, 100–105. doi: 10.3390/20700100

Kashman, Y., Gustafson, K. R., Fuller, R. W., Cardellina, J. H., McMahon, J. B., Currens, M. J., et al. (1992). The calanolides, a novel HIV-inhibitory class of coumarin derivatives from the tropical rainforest tree, Calophyllum lanigerum. *J. Med. Chem.* 35, 2735–2743. doi: 10.1021/jm00093a004

Kobayashi, S., and Manabe, K. (2000). Green Lewis acid catalysis in organic synthesis. *Pure Appl. Chem.* 72, 1373–1380. doi: 10.1351/pac200072071373

Kobayashi, S., Sugiura, M., Kitagawa, H., and Lam, W. W.-L. (2002). Rare-earth metal triflates in organic synthesis. *Chem. Rev.* 102, 2227–2302. doi: 10.1021/cr010289i

Korus, G., and Jansen, M. (2001). Kristallstruktur, Phasenumwandlung und Kaliumionenleitfaehigkeit von Kaliumtrifluormethylsulfonat. *Z. Anorg. Allg. Chem.* 627, 1599–1605. doi: 10.1002/1521-3749(200107)627:7<1599::AID-ZAAC1599>3.0.CO;2-0

Lemière, G., and Duñach, E. (2013). Catalytic activation of olefins by metal triflates and triflimides: application to fragrance chemistry. *Chem. Eur. J.* 19, 3270–3280. doi: 10.1002/chem.201203903

Lub, S., Zhu, L., Talukdar, A., Zhang, G., Mi, X., Cheng, J., et al. (2005). Recent advances in rare earth-metal triflate catalyzed organic synthesis in green media. *Mini Rev. Org. Chem.* 2, 177–202. doi: 10.2174/1570193053544472

Markiton, M., Boncel, S., Janas,. D., and Chrobok, A. (2017). Highly active nanobiocatalyst from lipase noncovalently immobilized on multiwalled carbon nanotubes for Baeyer-Villiger synthesis of lactones. *ACS Sus. Chem. Eng.* 5, 1685–1691. doi: 10.1021/acssuschemeng.6b02433

Markiton, M., Chrobok, A., Matuszek, K., Seddon, K. R., and Swadzba-Kwasny, M. (2016). Exceptional activity of gallium(III) chloride and chlorogallate(III) ionic liquids for Baeyer–Villiger oxidation. *RSC Adv.* 6, 30460–30467. doi: 10.1039/C6RA03435G

Markiton, M., Szelwicka, A., Boncel, S., Jurczyk, S., and Chrobok, A. (2018). Superactive tin(II) triflate/carbon nanotube catalyst for the Baeyer-Villiger oxidation. *Appl. Catal.* 556, 81–91. doi: 10.1016/j.apcata.2018.02.033

Matuszek, K., Chrobok, A., Latos, P., Markiton, M., Szymanska, K., Jarzebski, A., et al. (2016). Silica-supported chlorometallate(III) ionic liquids as recyclable catalysts for Diels–Alder reaction under solventless conditions. *Catal. Sci. Technol.* 622, 8129–8137. doi: 10.1039/C6CY01771A

Middleton, E., Kandaswami, C., and Theoharide, T. C. (2000). The effects of plant flavonoids on mammalian cells: implications for inflammation, heart disease, and cancer. Pharmacol. *Rev.* 52, 673–751.

Noji, M., Ohno, T., Fuji, K., Futaba, N., Tajima, H., and Ishii, K. (2003). Secondary benzylation using benzyl alcohols catalyzed by lanthanoid, scandium, and hafnium triflate. *J. Org. Chem.* 68, 9340–9347. doi: 10.1021/jo034255h

Olah, G., Laali, K., and Farooq, O. (1984). Chemistry in superacids. 6. Perfluoroalkanesulfonic acid-boron perfluoroalkanesulfonates: new superacid systems for generation of carbocations and catalysts for electrophilic transformations of hydrocarbons. *J. Org. Chem.* 49, 4591–4594. doi: 10.1021/jo00198a004

Ollevier, T., and Mwene-Mbeja, T. M. (2006). Bismuth triflate catalyzed [1,3] rearrangement of aryl 3-methylbut-2-enyl ethers. *Synthesis* 23, 3963–3966. doi: 10.1055/s-2006-950326

Plechkova, N. V., and Seddon, K. R. (2008). Applications of ionic liquids in the chemical industry. *Chem. Soc. Rev.* 37, 123–150. doi: 10.1039/B006677J

Prakash, G. K. S., Mathew, T., and Olah, G. A. (2012). Gallium(III) triflate: an efficient and a sustainable Lewis acid catalyst for organic synthetic transformations. *Acc. Chem. Res.* 45, 565–577. doi: 10.1021/ar2002039

Rao, V. K., Rao, M. S., and Kumar A. (2011). Ytterbium(III) triflate: an efficient and simple catalyst for isomerization of 2′-hydroxychalcone and 2′-aminochalcones in ionic liquid. *J. Heterocycl. Chem.* 48, 1356–1360. doi: 10.1002/jhet.760

Robertson, F., and Wu, J. (2010). Convenient synthesis of allylic thioethers from phosphorothioate esters and alcohols. *Org. Lett.* 12, 2668–2671. doi: 10.1021/ol1009202

Sarma, D., and Kumar, A. (2008). Rare earth metal triflates promoted Diels-Alder reactions in ionic liquids. *Appl. Catal. A* 335, 1–6. doi: 10.1016/j.apcata.2007.10.026

Schneider, C. (2005). Chemistry and biology of vitamin E. *Mol. Nitur. Food Res.* 49, 7–30. doi: 10.1002/mnfr.200400049

Silveira Neto, B. A. da., Ebeling, G., Gonçalves, R. S., Gozzo, F. C., Eberlin, M. N., and Dupont, J. (2004). Organoindate Room temperature ionic liquid: synthesis, physicochemical properties and application. *Synthesis* 8, 1155–1158. doi: 10.1055/s-2004-822372

Sofina, N., Peter, E. M., and Jansen, M. (2003). Kristallstrukturanalyse und Natriumionenleitung von wasserfreiem alpha-Natriumtrifluoromethylsulfonat. *Z. Anorg. Allg. Chem.* 629, 1431–1436. doi: 10.1002/zaac.200300103

Song, C. E., Jung, D.-U., Choung, S. Y., Roh, E. J., and Lee, S.-G. (2004). Dramatic enhancement of catalytic activity in an ionic liquid: highly practical friedel-crafts alkenylation of arenes with alkynes catalyzed by metal triflates. *Angew. Chem. Int. Ed.* 43, 6183–6185. doi: 10.1002/anie.200460292

Tayade, K., Mishra, M., Munsamy, K., and Somani, R. S. (2015). Synthesis of aluminium triflate-grafted MCM-41 as a water-tolerant acid catalyst for the ketalization of glycerol with acetone. *Catal. Sci. Technol.* 5, 2427–2440. doi: 10.1039/C.4C.Y.01396D

Vece, V., Ricci, J., Poulain-Martini, S., Nava, P., Carissan, Y., Humbel, S., et al. (2010). In[III]-Catalysed tandem c–c and c–o bond formation between phenols and allylic acetates. *Eur. J. Org. Chem.* 2010, 6239–6248. doi: 10.1002/ejoc.201000738

Welton, T. (1999). Room-temperature ionic liquids. Solvents for synthesis and catalysis. *Chem. Rev.* 99, 2071–2084. doi: 10.1021/cr980032t

Williams, B. G., and Lawton, M. (2010). Metal triflates: on the question of Lewis versus Brønsted acidity in retinyl carbocation formation. *J. Mol. Catal. A* 317, 68–71. doi: 10.1016/j.molcata.2009.10.023

Youn, S. W., and Eom, J. I. (2006). Ag(I)-catalyzed sequential c–c and c–o bond formations between phenols and dienes with atom economy. *J. Org. Chem.* 71, 6705–6707. doi: 10.1021/jo061221b

Solid Contact Potentiometric Sensors Based on a New Class of Ionic Liquids on Thiacalixarene Platform

Pavel L. Padnya[1], Anna V. Porfireva[2], Gennady A. Evtugyn[2] and Ivan I. Stoikov[1]*

[1] Department of Organic Chemistry, A. M. Butlerov' Chemistry Institute, Kazan Federal University, Kazan, Russia,
[2] Department of Analytical Chemistry, A. M. Butlerov' Chemistry Institute, Kazan Federal University, Kazan, Russia

New solid-contact potentiometric sensors have been developed for hydrogen phosphate recognition on the basis of ionic liquids containing tetrasubstituted derivatives of thiacalix[4]arene in *cone* and *1,3-alternate* conformations with trimethyl- and triethylammonium fragments at the lower rim substituents. The recognition of selected anions including carbonate, hydrogen phosphate, perchlorate, oxalate, picrate, and EDTA was conducted using electrochemical impedance spectroscopy with ferricyanide redox probe. For the potentiometric sensor assembling, the ionic liquids were stabilized by multiwalled carbon nanotubes and carbon black deposited on the glassy carbon electrode. The influence of support, steric factors and modification conditions on the sensor performance has been investigated. As was shown, potentiometric sensors developed make it possible to selectively determine hydrogen phosphate anion within the concentration range from 1×10^{-2} to 1×10^{-6} M and limit of detection of $2 \times 10^{-7}-1 \times 10^{-6}$ M with unbiased selectivity coefficients varied from 1.2×10^{-1} to 1.0×10^{-8} (carbonate, acetate, oxalate, succinate, glutharate, glycolate, and malonate anions).

Keywords: ionic liquid, solid-contact potentiometric sensor, phosphate determination, thiacalix[4]arene, carbon nanotubes

INTRODUCTION

Ionic liquids (ILs) are organic salts with the melting point below 100°C (Sun and Armstrong, 2010). Most of the ILs have a large cation (imidazolium, pyridinium, phosphonium, ammonium etc.) combined with rather small inorganic (Cl^-, PF_6^-, BF_4^-) or organic (trifluoromethylsulfonate, trifluoroethanoate) anion. Relatively high difference in the ion size and their low symmetry result in rather low melting point of ILs. Besides, ILs offer some advantages of application in many areas, e.g., extraction, electrophoresis, liquid chromatography, and sensors. The ILs substitute conventional organic solvents in chemical synthesis and separation technologies. Due to extremely low volatility, thermal stability, non-flammability, low toxicity and reusability their application is considered as a green chemistry approach (Marr and Marr, 2016) though the synthesis of the ILs themselves utilizes some toxic species and reagents, which are not friendly for the environment. It is also important that many of the ILs features can be altered by design of the ions implemented in their content.

Regarding application of the ILs in electroanalytical chemistry (Sun and Armstrong, 2010; Tan et al., 2012) and in electrochemical sensors (Wei and Ivaska, 2009; Shiddiky and Torriero, 2011; Silvester, 2011), their undisputable advantages like ionic conductivity and chemical and

electrochemical inertness are mostly mentioned. The addition of the ILs to the carbon paste (Švancara et al., 2009) or to the mixtures of carbonaceous materials (Abo-Hamad et al., 2016; Valentini et al., 2016) instead of paraffin improve the performance of biosensors due to lower intrinsic resistance of the electrode material. The synergic influence of ILs and redox active additives was reported for the voltammetric determination of oxidizable compounds (Sanati et al., 2017; Mohammadian et al., 2018). Better conditions of the electron transfer, enhanced sensitivity of the sensor reported due to IL introduction are attributed to the microextraction of the analyte molecules into the electrode body, its pre-concentration on the analysis stage (Nawała et al., 2018) and to microstructuring and self-gelation of polymeric layers on the transducer surface (Carvalho et al., 2014).

In potentiometric sensors, the ILs that are melted slightly above ambient temperature can be easily implemented in the electrode material as an ionophore or ion-exchanger (Shvedene et al., 2011). Their use allows excluding polymeric matrices and, in some cases, lipophilic salts from the surface membrane content. This is especially important for the development of solid-contact sensors where ILs serve as ion-to-electron materials required to establish reliable reversible response to primary ions. Although, analytical characteristics of such IL based potentiometric sensors are comparable with those of conventional ion-selective electrodes with internal filling, they are much easier *to prepare and store*, do not require time consuming conditioning prior to use and do not offer additional requirements in miniaturization and automation of potentiometric measurement systems.

The number of primary ions determined with ILs based sensors is increasing every year. To date, the determination of I$^-$ (Shvedene et al., 2011; Mendecki et al., 2016), SO$_4^{2-}$ (Peng et al., 2008), Cl$^-$, I$^-$, and SCN$^-$ (Rzhevskaia et al., 2016), Cu^{2+} (Wardak and Lenik, 2013; Fan et al., 2017), Cd^{2+} (Afkhami et al., 2012; Wardak, 2015), Pb^{2+} (Wardak, 2011), Pr^{3+} (Ganjali et al., 2009), alkali metal cations (Xie et al., 2013). Besides, some organic species bearing charge or able to protonate/deprotonate have been determined with the IL based potentiometric sensors (triethylammonium-*closo*-dodecaborate ; Kopytin et al., 2012; Faridbod and Shafaat, 2017). In some of them, ILs are used as binding material in rather complex matrix consisting of ionophores and redox active species. Thus, tramadol was determined with carbon paste sensor involving nanographene particles, tramadol-imprinted polymer and 1-butyl-1-methylpyrrolidinium bis (trifluoromethylsulfonyl)imide (Bagheri et al., 2017). The same IL was introduced in the carbon paste together with graphene nanosheets for determination of losartan (Bagheri et al., 2015). Electronic tongue system consisted of low-selective potentiometric sensor with 1,3-dihexadecylimidazolium salts as ionophores was successfully applied for identification of mineral water samples and separate determination of iodide and chloride anions in such waters (Shvedene et al., 2017).

Potentiometric sensors for anion determination are of a special concern due to limited number of ionophores because of the more complex requirements to their structure and binding sites against cation receptors. In the above examples

of potentiometric sensors for anion detection, most of the ILs contain target anion to be detected in their structure as a counter ion. Meanwhile, the selectivity of their response remains moderate and the number of particular ions detected is rather limited. In some cases, variation of the lipophilic cation of the IL in a single sensor or assembling of the sensor array with different ILs were used to overcome this limitation.

Among inorganic anions, hydrogen phosphate anion is one of most frequently determined in the water and soil analysis as a part of mineral fertilizers and a marker of eutrophication and water contamination with stock farming wastes. Nevertheless, the number of ion-selective electrodes for hydrogen phosphate determination is rather limited. Insoluble salts and complexes of multivalent cations (Tonelli et al., 2013; Tafesse and Enemchukwu, 2015), oxyions (Wroblewski et al., 2000; Sessler et al., 2006), and polyamines (Carey and Riggan, 1994; Hartley et al., 2000) have been described in the assembly of appropriate sensors. Besides, molecular imprinting technology was recently proposed for the synthesis of polymeric membranes for phosphate recognition (Alizadeh and Atayi, 2018; Storer et al., 2018). The potentiometric sensors for HPO$_4^{2-}$ determination show satisfactory characteristics but need to be improved in selectivity and sensitivity of target ion determination.

Calixarenes and their thia-analogs are macrocyclic compounds that offer unique opportunities of ionophore design due to the variety of functional groups in the substituents of the lower and upper rim of the macrocycle and pre-determined rigid spatial configuration of binding sites easily adapted to the guest molecule (ion) (Patra et al., 2012). The advantages of calixarene based receptors have been applied in the design of hydrogen phosphate receptors with good selectivity and sensitivity of the response (Yan et al., 2007). Calix[4]arene modifier was proposed for determination of inorganic anions including phosphates in snow water by capillary electrophoresis (Fernández-Gutiérrez et al., 2000). Indirect determination of organic acids by polyaniline based solid-contact sensors with functionalized thiacalix[4]arenes was described for general assessment of beverages (Evtugyn et al., 2010). Besides, thiacalix[4]arene based ionophores were used for discrimination of some inorganic anions and detection of ionic content of mineral waters (Sorvin et al., 2018).

In this work, we have combined the advantages of macrocyclic ionophores and ILs in the assemblies of solid-contact potentiometric sensors and developed potentiometric sensor to hydrogen phosphate with carbonaceous materials (carbon black (CB), multi-walled carbon nanotubes (MWCNTs)) as the IL supports. To the best of our knowledge, this is a first example of application of ILs with calixarene core for potentiometric determination of hydrogen phosphate.

MATERIALS AND METHODS

Reagents and Materials

The ILs used in the work, i.e., 5,11,17,23-tetra-*tert*-butyl-25,26,27,28-tetrakis [(*N*-(3′,3′-dimethyl-3′-(pentoxycarbonylmethyl)ammoniumpropylcarbamoylmethoxy]-2,8,14,20- tetrathiacalix[4]arene tetra [bis(

trifluoromethylsulfonyl)imide] in *cone* (**1**) and *1,3-alternate* (**2**) conformation, and 5,11,17,23- tetra-*tert*-butyl—25,26,27,28-tetrakis[(*N*-(2′,2′-diethyl-2′-(pentoxycarbonylmethyl) ammoniumethyl)carbamoylmethoxy]-2,8,14,20-tetrathiacalix[4]arene tetra[bis(trifluoromethylsulfonyl)imide] in *cone* (**3**) and *1,3-alternate* (**4**) conformation, were synthesized at the Organic Chemistry Department of Kazan Federal University as described elsewhere (Padnya et al., 2017). The conformation and chemical structure of the compounds were confirmed by ^{1}H, ^{13}C NMR, and IR spectroscopy, MALDI-TOF mass spectrometry and elemental analysis. Chemical structures of the IL studied are presented in **Figure 1**.

Oxalic acid, potassium ferricyanides $K_3[Fe(CN)_6]$ and $K_4[Fe(CN)_6]$, MWCNTs were purchased from Sigma-Aldrich, Germany, CB from IMERYS, Belgium, succinic acid from VitaChim, Russia, glutaric and glycolic acids from TauRus, Russia, malonic acid from AquaChim, Russia. All the reagents were of analytical grade. All the solutions were prepared using deionized Milli-Q® water.

Home-made glassy carbon electrode consisted of 2 cm long rod 1.7 mm in diameter inserted in the polytetrafluoroethylene tube was used for solid-contact ion-selective electrode assembling. Threaded connection made of stainless steel was fixed from the opposite end of the electrode. All the potentials are given against double-junction Ag/AgCl/3 M KCl reference electrode (Metrohm Autolab).

Impedimetric Measurements

EIS measurements were performed in working cell containing 4.5 mL of 0.1 M KNO_3 and 0.5 mL of the mixture of 0.1 M $K_3[Fe(CN)_6]$ and 0.1 M $K_4[Fe(CN)_6]$ at 0.265 V using FRA2 module of the potentiostat-galvanostat PGSTAT 302N (Metrohm Autolab b.v., the Netherlands). The glassy carbon electrode was first mechanically polished and cleaned by acetone, sulfuric acid, NaOH and twice with deionized Milli-Q® water. Then, 2 µL of 1.0 mM solution of the IL in acetone were placed on the working surface and allowed to dry at ambient temperature. The amplitude of the applied sine potential was 5 mV and the frequency varied from 100 kHz to 0.04 Hz with a sampling rate of 12 points per decade. The capacitance and charge transfer resistance were calculated by fitting experimental data using Randles equivalent circuit (1) with the NOVA software (Metrohm Autolab).

(1)
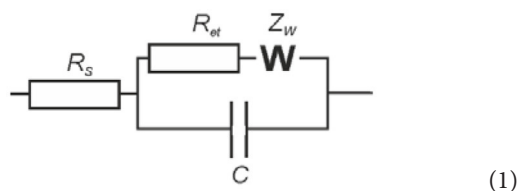
Here R_s is solution resistance, R_{et} charge transfer resistance, Z_W Warburg impedance and C is constant phase element which is here equal to interface capacitance.

Prior to measurement, freshly prepared electrode covered with the IL film was repeatedly heated to 80°C in solid-state thermostat and cooled to ambient temperature to equalize the surface layer. After equalization, an aliquot of the analyte solution was placed on the working surface for 10 min. Then the electrode was washed and the impedance was measured in the presence of the ferricyanide redox probe. The EIS parameters were calculated and averaged for three replications.

Potentiometric Sensor Preparation and Application

The glassy carbon electrode was first mechanically polished and cleaned as described above in section Impedimetric Measurements. In layer-by-layer deposition, 1 µL of 1 mg/mL CB suspension in dimethylformamide (DMF) was placed on its surface and dried at 60°C for 30 min. Then, 2 µL of 1.0 mM IL solution in acetone were placed on the electrode surface and dried again. Alternatively, a mixture of the CB suspension and IL solution in 10:1 or 20:1 v/v ratio was prepared and the same aliquot (2 µL) were spread on the working surface as described above.

MWCNTs were deposited on the surface of electrode in a similar manner. They were first mixed with concentrated H_2SO_4 and HNO_3 in 3:1 vol. ratio and sonicated at 40°C for 4 h (Tesla ultrasonic bath, 40 W). Then they were centrifuged, washed with distilled water and dried at 80°C for 2 h. The MWCNTs dispersion was prepared by 15 min unltrasonication of oxidized MWCNTs in DMF.

SEM images of the CB and MWCNTs coatings were obtained with the high-resolution field emission scanning electron microscope Merlin™ (Carl Zeiss). Highly ordered pyrolytic graphite plate 12 × 12 × 2 mm (Agar Scientific, cat. No AG3389-1212) was used as substrate for deposition of carbonaceous materials.

If not used, the potentiometric sensors were stored in dry conditions in alumina foil cover at ambient temperature. Prior to use, dry electrodes were conditioned in deionized water and appropriate salt containing the anion to be determined.

Potentiometric measurements were performed at ambient temperature in 5 mL non-thermostated working cell with four-channel digital ionomer Expert-001 (Econix-Expert, Moscow, Russia). For sensor calibration, a series of standard solutions with concentration varied from 0.1 µM to 10.0 mM was prepared in deionized water. The pH was adjusted to 8.0 with NaOH. The pH of solutions was measured using glass pH-electrode (Econix-Expert). Calibration curves were obtained by step addition of appropriate salt solutions to the working cell under continuous magnetic stirring. The unbiased potentiometric selectivity coefficients $K_{i,j}^{Sel}$ were determined by separate solution method (SSM). For this purpose, standard potentials of primary (E_i^0) and interfering (E_j^0) ions were calculated from the dependence of the electrode potential on their activities, S_i is the slope of calibration curve. The $K_{i,j}^{Sel}$ values were calculated from Equation (2) adapted for anion determination (Bakker, 1997) and averaged from five replications.

$$\log K_{i,j}^{Sel} = -\frac{(E_j^0 - E_i^0)}{S_i/z_i}$$

(2)

Besides, matched potential method (MPM) was used for selectivity coefficient determination to take into account non-ideal behavior of primary and interfering ions (Umezawa et al.,
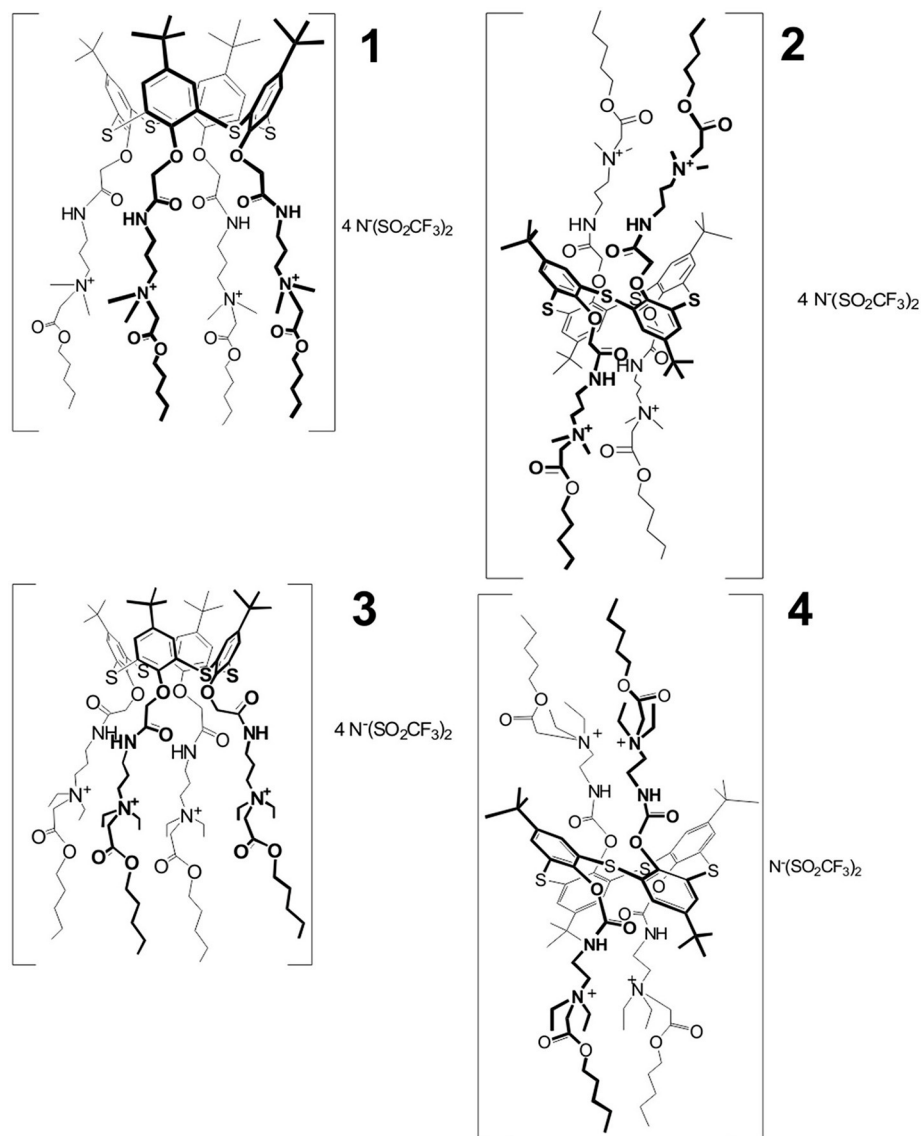
FIGURE 1 | Chemical structures of the ILs used in the assembly of potentiometric sensors.

1995). In this method, changes in the potential are measured by addition of the primary ion to its reference solution. After that, interfering ion is added to the same reference solution to reach the same potential shift. The $K_{i,j}^{Sel}$ values are calculated in accordance with Equation (3), where a_i^0 is the activity of the primary ion in reference solution, a_i is its activity after addition of an aliquot, a_j is the activity of interfering ion resulted in the same shift of the potential.

$$K_{i,j}^{Sel} = -\frac{a_i - a_i^0}{a_j} \tag{3}$$

Contrary to SSM, MPM is insensitive to the difference in the charge of the primary and interfering ion and can be applied for non-Nernstian behavior of the ions.

The content of ionic species in the samples of lake waters was determined by ion chromatography using two-channel ICS-5000 system (Dionex, CA, United States) with CD conductivity detector.

RESULTS

Impedimetric Investigation of Ionic Liquids Based on Thiacalix[4]Arene Core

Although, the ILs assume different mechanisms of potentiometric response toward target analytes, ion exchange remains most frequently discussed. To estimate the anion exchange capabilities of the ILs studied, EIS technique was used. In these experiments, the IL was deposited alone on the surface of glassy carbon electrode and the EIS spectra were recorded

in the presence of ferricyanide redox probe. Reproducible results were obtained after equalization of the freshly prepared sensor in water. Commonly, in consecutive measurements the charge transfer resistance R_{et} first monotonously increased by 10–20 kΩ. In deionized water, the R_{et} was stabilized at about 200 kΩ. In the salts of inorganic and organic acids, stationary value was remarkably higher and depended on the analyte nature. Increase in the concentration of sodium phosphate, oxalate and carbonate in the range from 1.0×10^{-6} to 1.0×10^{-2} M decreased the R_{et}. Between measurements, the potentiometric sensor was shortly heated above IL melting point (60–80°C) and sharply cooled to ambient temperature to accelerate the stabilization of the EIS parameters. Typical

Nyquist diagram and changes in the charge transfer resistance are shown in **Figure 2** for hydrogen phosphate and IL **1** as example. The slope of appropriate graphs in the plots of R_{et} vs. log$c$ increased from 21 to 24 kΩ/pC (hydrogen phosphate and oxalate anions) to 65–70 kΩ/pC (carbonate and EDTA). Other anions tested influenced the R_{et} value only at their high concentrations. Thus, perchlorate suppressed the R_{et} value in concentrations exceeding 1.0×10^{-3} M, thiocyanate, chloride, bromide anions in those higher than 1.0×10^{-2} M.

Changes in the R_{et} values can be attributed to the ion exchange on the surface of the IL film. Partial substitution of bis(trifluoromethylsulfonyl)imide (Tf_2N^-) anion with a smaller
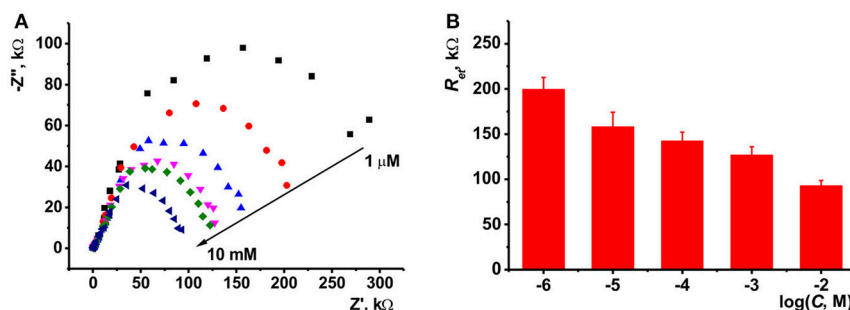
FIGURE 2 | (A) The Nyquist diagram of impedance spectra recorded with glassy carbon electrode covered with IL **1** in the presence of 1.0×10^{-2}, 1.0×10^{-3}, 1.0×10^{-4}, 1.0×10^{-5}, and 1.0×10^{-6} M Na_2HPO_4. Measurements in the presence of 0.01 M $K_3[Fe(CN)_6]$ and 0.01 M $K_4[Fe(CN)_6]$ at 265 mV vs. Ag/AgCl. Frequency range 0.04 Hz−100 kHz, amplitude 5 mV. **(B)** The dependence of the charge transfer resistance on the concentration of hydrophosphate anion, mean ± S.D. for three replications.
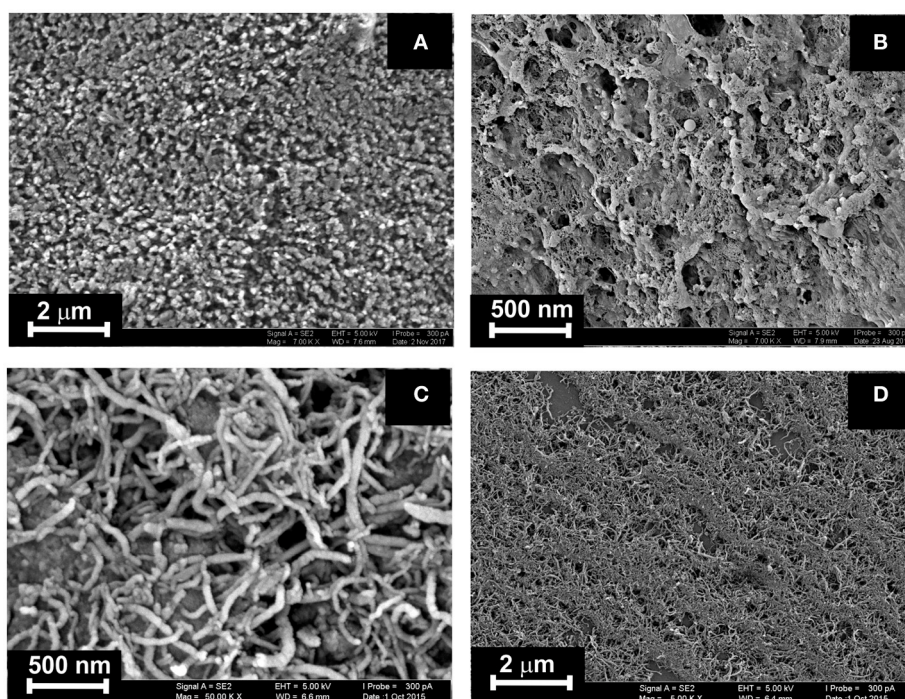
FIGURE 3 | SEM images obtained for highly oriented pyrolytic graphite covered with CB **(A,B)** and MWCNTs **(C, D)** prior to **(A, C)** and after deposition of IL **1 (B, D)**. Layer-by-layer deposition, 0.1 mg/mL of CB and MWCNTs (aliquot 1 μL) + 0.1 mM IL **1** (aliquot 2 μL).

ferricyanide ion bearing higher charge results in electrostatic repulsion of redox probe and hence increase of the R_{et} value. In the presence of other anions, the implementation of ferricyanide ions becomes lower and thus the resistance changes in the opposite direction. The lower the size of the anion and the higher its charge are the more the R_{et} value changes with its addition. The highest sensitivity corresponds to the three basic EDTA anion and carbonate. The latter one can additionally alter the accessibility of ferricyanide ion due to formation of molecular form $CO_2 \cdot H_2O$ in the measurement conditions. All the anions mentioned above affect the R_{et} value in the whole range of concentrations tested, i.e., from 1.0×10^{-6} to 1.0×10^{-2} M.

Direct deposition of the ILs on the glassy carbon electrode allowed impedimetric detection of some anions able to ion exchange on the electrode interface. However, the lifetime of the sensor was limited by 15–20 measurements due to partial deterioration of the surface layer especially on the stage of heating and following solidification. This calls for searching possible supports for mechanical hardening of the surface layer and improving its robustness in routine measurements.

Potentiometric Sensors Based on Ionic Liquids in the Matrix of Carbon Black or Carbon Nanotubes

Choice of the Supporting Material

Carbonaceous materials, e.g., CB (Paczosa-Bator, 2014), graphene nanosheets (Afkhami et al., 2015; Shirzadmehr et al., 2015, 2016; Bagheri et al., 2016) and MWCNTs (Afkhami et al., 2014; Roy et al., 2017), are used in solid-contact sensors together with ionophores to improve the conditions of the signal transduction due to electron-to-ion conductivity of such materials. Besides, they can be applied as mechanical support of the liquid components preventing their leaching from the surface film.

We have used CB and MWCNTs deposited on the glassy carbon electrode prior to or together with the ILs. No lipophilic salts and plasticizers were necessary to establish a reliable reproducible response to the anions tested previously with EIS.

The ILs studied were deposited on the surface of electrode after formation of the underlying layer of the carbonaceous particles (layer-by-layer deposition) or in one step by preliminary mixing of the suspension of CB (MWCNTs) in DMF and
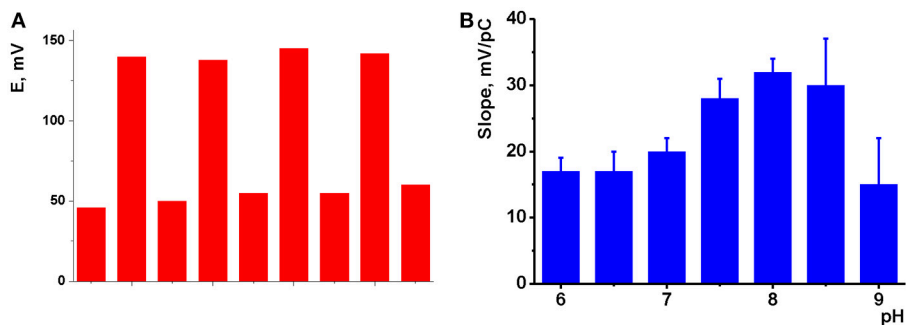

FIGURE 4 | (A) Reversibility of the response of potentiometric to 10.0 mM and 10.0 μM Na_2HPO_4, pH 8.0, intermediate washing in deionized water and short heating to 80°C; **(B)** pH dependence of the slope of linear part of hydrogen phosphate calibration curve (mean ± S.D. for three replications). Potentiometric sensor based on sensor based on CB and IL **1**.
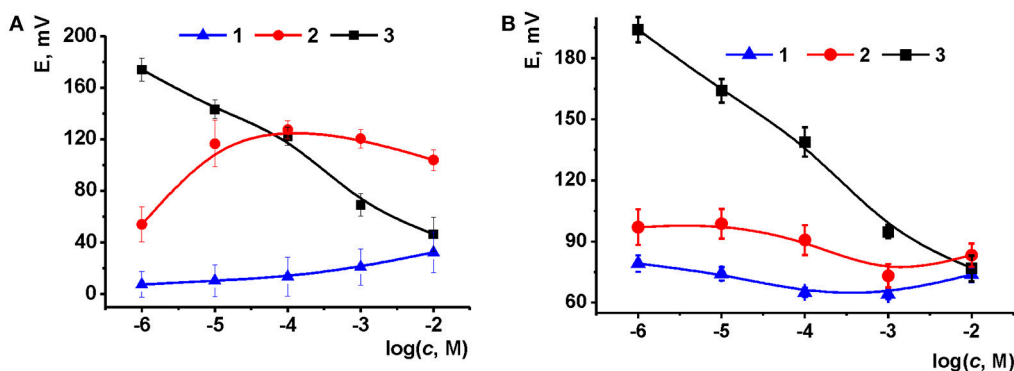

FIGURE 5 | Calibration curves of Na_2HPO_4 obtained with the potential sensors based on CB **(A)** and MWCNTs **(B)** support (2 μL of 1.0 mg/mL suspension) and IL **1** [aliquot of 1 μL of 0.1 mM solution (1), 1 μL of 1.0 mM solution (2) and 2 μL of 1.0 mM solution (3)]. Layer-by-layer deposition, pH 8.0. Average from three replications (mean ± S.D. for three replications).

IL solution in acetone. The amounts of CB and MWCNTs were chosen to reach full coverage of the electrode surface. Higher quantities of modifiers made worsen electron exchange conditions on the electrode interface and were less mechanically stable. In the series of consecutive drying-wetting steps, excessive amounts of particles left the electrode. This resulted in dramatic shift of the stationary potential of the sensor. As could be seen from **Figure 3**, the CB layer consisted of roundish particles 30–50 nm in size. Their coverage with the IL kept high porosity of the layer sufficient for a fast response. MWCNTs formed tangled three-dimensional layer with a high free internal volume then partially filled with the IL placed over.

The IL film improved the mechanical strength of the layer and about fully excluded deterioration of carbonaceous particles within the sensor lifetime. In some cases, crack appeared after washing the electrode, which could be removed by short heating them over 60°C and cooling to ambient temperature.

The potentiometric sensors were applied for the determination of Na_2HPO_4. Prior to use, freshly prepared sensor was conditioned overnight in 0.01 M solution of the analyte. The same results were obtained in series of heating—cooling steps as described above for impedimetric measurements. After addition of the hydrogen phosphate, the sensor potential shifts within 10–12 s in accordance with anionic sensitivity of the response. The dynamic response time insignificantly alters with the amounts of CB (MWCNTs) and IL present in the surface layer and tends to increase to 15–20 s with the analyte concentrations decreasing to 1.0×10^{-6} M. Reverse return after washing is slower but can be accelerated by melting IL in a short heating of the sensor to 80°C. The reversibility of the signal was demonstrated in measurements of alternating concentrations (10.0 mM and 10.0 μM) with the same sensor (**Figure 4A**).

pH Influence

The pH value of the test solution is an important factor influencing the performance of potentiometric sensors (Afkhami et al., 2015; Shirzadmehr et al., 2015, 2016; Bagheri et al., 2016). To investigate the pH effect on the potentiometric response, first the potentials of glassy carbon electrode covered with CB or MWCNTs were measured at different pH values. The

TABLE 1 | Analytical characteristics of hydrogen phosphate determination with solid-contact potentiometric sensor based on CB and IL **1**-**4**.

Surface layer content	E, mV = a + b×log(c, M)			Concentration range, M	LOD, M
	a	b	R^2		
CB/**1** layer-by-layer	3.5 ± 1.2	−32.8 ± 1.3	0.9934	1.0×10^{-6}−1.0×10^{-2}	2.0×10^{-7}
CB/**2** layer-by-layer	26 ± 1	−21.2 ± 0.3	0.9975	1.0×10^{-6}−1.0×10^{-3}	7.0×10^{-7}
Mixture of CB/**2** 10:1	27 ± 2	−9.9 ± 1.6	0.9479	1.0×10^{-6}−1.0×10^{-4}	1.0×10^{-6}
Mixture of CB/**2** 20:1	52 ± 5	−8.3 ± 1.1	0.9486	1.0×10^{-6}−1.0×10^{-3}	1.0×10^{-6}
CB/**3** layer-by-layer	16.1 ± 1.4	−27.7 ± 0.3	0.9987	1.0×10^{-6}−1.0×10^{-3}	5.0×10^{-7}
Mixture of CB/**3** 10:1	−290 ± 15	−73 ± 30	0.7216	1.0×10^{-6}−1.0×10^{-4}	1.0×10^{-6}
Mixture of CB/**3** 20:1	−270 ± 25	−69 ± 9	0.8472	1.0×10^{-6}−1.0×10^{-4}	1.0×10^{-6}
CB/**4** layer–by–layer	80 ± 9	−11.5 ± 2.1	0.9046	1.0×10^{-6}−1.0×10^{-3}	1.0×10^{-6}
Mixture of CB/**4** 10:1	63 ± 22	−17.4 ± 4.4	0.8808	1.0×10^{-6}−1.0×10^{-4}	1.0×10^{-6}
Mixture of CB/**4** 20:1	53 ± 32	−20.8 ± 6.3	0.8318	1.0×10^{-6}−1.0×10^{-4}	1.0×10^{-6}

TABLE 2 | Analytical characteristics of hydrogen phosphate determination with solid-contact potentiometric sensor based on MWCNTs and IL **1**-**4**.

Surface layer content	E, mV = a + b×log(c, M)			Concentration range, M	LOD, M
	a	b	R^2		
MWCNTs/**1** layer-by-layer	4.7 ± 3.1	−31.0 ± 1.9	0.9907	1.0×10^{-6}−1.0×10^{-2}	5.0×10^{-7}
Mixture of MWCNTs/**1** 10:1	−16.2 ± 3.9	−7.4 ± 0.8	0.9785	1.0×10^{-6}−1.0×10^{-4}	1.0×10^{-6}
Mixture of MWCNTs /**1** 20:1	−3.9 ± 3.7	−15.1 ± 0.7	0.9953	1.0×10^{-6}−1.0×10^{-4}	8.0×10^{-7}
MWCNTs/**2** layer-by-layer	7.1 ± 1.9	−27.1 ± 1.2	0.9943	1.0×10^{-6}−1.0×10^{-4}	2.0×10^{-7}
Mixture of MWCNTs/**2** 10:1	36 ± 3	−12.8 ± 2.7	0.9623	1.0×10^{-5}−1.0×10^{-3}	5.0×10^{-6}
Mixture of MWCNTs /**2** 20:1	18.7 ± 3.4	−19.3 ± 1.2	0.9893	1.0×10^{-6}−1.0×10^{-3}	1.0×10^{-6}
MWCNTs/**3** layer-by-layer	8.0 ± 2.8	−27.3 ± 1.8	0.9904	1.0×10^{-6}−1.0×10^{-2}	1.0×10^{-6}
Mixture of MWCNTs/**3** 10:1	−74 ± 7	−18.8 ± 2.2	0.9745	1.0×10^{-6}−1.0×10^{-4}	1.0×10^{-6}
Mixture of MWCNTs /**3** 20:1	−53 ± 6	−21.2 ± 5.0	0.9490	1.0×10^{-6}−1.0×10^{-3}	1.0×10^{-6}
MWCNTs/**4** layer-by-layer	−15.0 ± 4.6	−17.8 ± 1.3	0.9781	1.0×10^{-6}−1.0×10^{-3}	1.0×10^{-6}
Mixture of MWCNTs/**4** 10:1	−3.9 ± 1.0	−10.6 ± 0.7	0.9823	1.0×10^{-6}−1.0×10^{-2}	1.0×10^{-6}
Mixture of MWCNTs /**4** 20:1	−35 ± 3	−21.1 ± 2.1	0.9517	1.0×10^{-6}−1.0×10^{-3}	1.0×10^{-6}

pH value was adjusted by addition of diluted nitric acid or sodium hydrochloride in the range from 2.0 to 10.0. A linear dependency was found with no respect of the direction of the pH change with the slope of -10 ± 2 mV/pH for CB and -8 ± 2 mV/pH for MWCNTs layer. The pH dependency was attributed to the carboxylic groups located on the surface of the particles of carbonaceous materials used. In basic media, deterioration of the surface layer took place after long incubation of the sensors. The addition of the ILs to the surface layer suppressed the slope of the pH dependency of the potential to 2–5 mV/pH, which is comparable with the standard deviation of the above parameter determined for six experimental points measured in triplicate. The influence of the ILs can be explained by shielding of the acidic groups on the surface of the coating and buffering influence of the anion of the IL that made the pH influence more smoothen against bare CB (MWCNTs) layer.
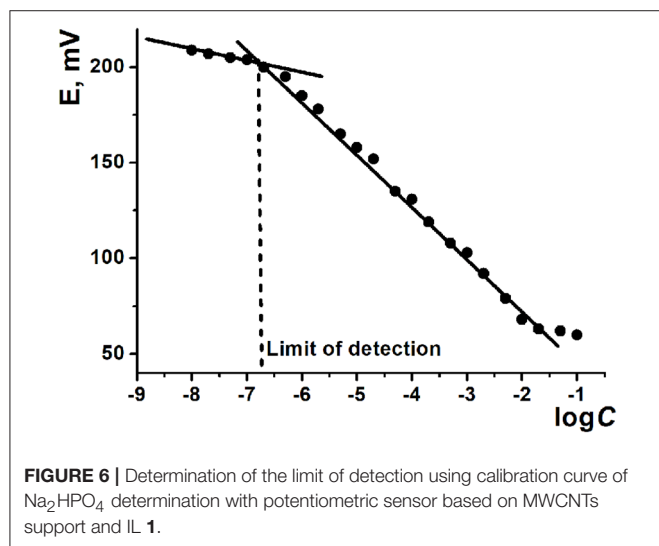
FIGURE 6 | Determination of the limit of detection using calibration curve of Na_2HPO_4 determination with potentiometric sensor based on MWCNTs support and IL **1**.

The response toward HPO_4^{2-} depended on the pH of solution to a much higher extent. The slopes of appropriate dependencies are presented in **Figure 4B** for CB based sensors as an example. One could see, they remain about constant at 16–18 mV/pC in neutral and weakly basic media, then increased to 30–32 mV/pH with maximum at pH 8.0 and then sharply decayed to 14–15 at higher pH values. The changes in the sensitivity of the response follow the distribution of phosphate ion forms and correspond to the domination of HPO_4^{2-} anions at pH > 8.0. The decrease of the slope value observed at higher pH was attributed to the mechanical deterioration of the film caused by electrostatic repulsion of negatively charged CB particles. In case of MWCNTs, maximal slope of the dependency remain constant in the pH range 8.0–10.0. However, the standard deviation of the slope increases to 10–14%. At pH < 8.0, dihydrogen phosphate becomes dominating and impedimetric measurements showed low sensitivity of the ILs to one-charge anions. Thus, the following measurements of the HPO_4^{2-} response were performed at pH 8.0.

Selection of the Surface Layer Content

The content of the surface layer was specified by variation in the quantities of ILs added to the carbonaceous support (**Figure 5**). For CB based support, a weak cationic response was observed at low volume of IL solution deposited. This might be due to uncompensated anionic charge of carboxylate groups on the surface of the CB particles and electrostatic attraction of sodium cation from the solution. With increasing IL quantities, the calibration curve changed its direction and finally the slope of -33 mV/pC was reached typical from double charged ions. The following increase of the IL loading did not dramatically alter the position of the curve though the deviation of the potential became higher (up to 12%). The behavior of potentiometric sensors based on MWCNTs was similar: the maximal slope of the curve obtained for 2 μL aliquot of IL **1** solution was equal to 26 mV/pC. Thus, the following experiments were

TABLE 3 | Comparison of the analytical characteristics of HPO_4^{2-} ions determination with potentiometric sensors.

Sensing layer	Dynamic range, M	LOD, M	Sample tested	References.
Mo acetylacetonate complex in PVC matrix	$1.0 \times 10^{-1} – 1.0 \times 10^{-7}$	6.0×10^{-8}	Fertilizers, Ba^{2+} titration	Ganjali et al., 2006
$Co/Co_3(PO_4)_2$	$1.0 \times 10^{-1} – 1.0 \times 10^{-5}$	7.5×10^{-6}	Microbial flocks	Lee et al., 2009
Tetraphenylazo macrocycle in PVC-polyurethane matrix	$1.0 \times 10^{-1} – 1.0 \times 10^{-6}$	8.4×10^{-7}	Standard reference material, titration	Kumar et al., 2010
Mg/Al hydrotalcite mineral in PVC matrix	$5.0 \times 10^{-5} – 2.0 \times 10^{-2}$	3.0×10^{-5}	Hydroxyapatite	Tonelli et al., 2013
$AlPO_4$	$1.0 \times 10^{-1} – 1.0 \times 10^{-6}$	1.0×10^{-1}	-	Tafesse and Enemchukwu, 2015
Co phosphates	$1.0 \times 10^{-1} – 1.0 \times 10^{-5}$	-	-	Hu et al., 2018
Polymer of methacrylate and vinyl pyridine with molecular imprints	$1.0 \times 10^{-1} – 1.0 \times 10^{-5}$	4.0×10^{-6}	La^{3+} titration	Alizadeh and Atayi, 2018
CB (MWCNTs) and IL with cations on thiacalixarene platform	$1.0 \times 10^{-2} – 1.0 \times 10^{-6}$	$(0.2–1.0) \times 10^{-6}$	Lake water	This work

performed with 2 µL of 0.1 mM IL solution in acetone at pH 8.0.

Hydrophosphate Ion Determination

The analytical characteristics of hydrogen phosphate determination are presented in **Tables 1**, **2** for CB and MWCNTs based potentiometric sensors, respectively. All the standard solutions contained 0.1 M NaCl to take into account significant difference in their ionic strength. The comparison of the slopes showed higher results near Nernstian 29 mV/pC for the sensors obtained by layer-by-layer deposition of the components. Probably, adsorption of the ILs onto carbonaceous materials partially blocks the cationic centers involved in the interaction with the analyte ions. In case of CB/IL **1** loading, their simultaneous deposition in the mixture did not allow measuring reproducible response to HPO_4^{2-} anions. Variation in the content of the mixture did not significantly alter the analytical characteristics of the sensor. In case of IL **3**, super-Nernstian response was obtained in a narrow range of concentrations when mixture with CB was loaded on the electrode. This might be a result of non-stationary distribution of ions in the membrane body. Indeed, several cycles of heating-cooling of the sensor resulted in decrease of the slope to more convenient 25–27 mV/pC.

The ILs based on thiacalix[4]arenes in *1,3-alternate* conformation are less sensitive to the deposition protocol but also demonstrate lower sensitivities of the HPO_4^{2-} determination against ILs on *cone* macrocycle platform. To some extent, the same refers to the difference between methyl- and ethylammonium derivatives (ILs **1**, **2** against **3**, **4**). In both cases, difference in the slopes of the curves can be attributed to different steric hindrance of the anion access to the cationic center of the IL. Contrary to that, CB and MWCNTs did not show significant difference in the hydrogen phosphate determination. Higher deviation of the signals observed for CB can be related to the lower reproducibility of the surface morphology and specific surface influencing the ion exchange. The LOD values were determined in accordance with the IUPAC recommendation (Buck and Linder, 1994) as interception point of the linear sections of the calibration plot (**Figure 6**).

The analytical characteristics of hydrogen phosphate determination are comparable or better than those reported for other potentiometric sensors (**Table 3**).

Measurement Precision, Sensor Lifetime, and Selectivity

The measurement precision toward 1.0×10^{-4} M HPO_4^{2-} ions was estimated using five individual sensors made with MWCNTs support from the same reagent set. Each sensor was used for five consecutive measurements of the hydrophosphate signal performed at pH 8.0 in the presence of 0.1 M NaCl. The measurement-to-measurement repeatability was equal to 1.5% and sensor-to-sensor repeatability to 2.5%. The lifetime

TABLE 4 | Potentiometric selectivity coefficients $K_{Phos,j}^{Sel}$ of solid-contact potentiometric sensors based on MWCNTs and ILs **1**-**4** calculated by SSM and MPM methods.

Interference	Potentiometric selectivity coefficients $K_{Phos,j}^{Sel}$ (SSM / PMP)			
	1	**2**	**3**	**4**
Carbonate	1.2×10^{-1} (2.5)	2.9×10^{-2} (0.3)	1.7×10^{-4} (4.4×10^{-2})	4.8 / 6.0 (2.5)
Chloride	5.2×10^{-9} (-)	1.0×10^{-6} (5.0×10^{-3})	1.0×10^{-7} (8.2×10^{-5})	2.8×10^{-6} (4.5×10^{-3})
Thiocyanate	4.2×10^{-7} (5.0×10^{-5})	4.9×10^{-5} (2.0×10^{-3})	1.5×10^{-8} (-)	1.1×10^{-5} (4.2×10^{-3})
Bromide	9.0×10^{-7} (2.0×10^{-5})	8.4×10^{-6} (1.0×10^{-4})	3.2×10^{-7} (5.8×10^{-5})	2.4×10^{-6} (6.1×10^{-5})
Acetate	1.2×10^{-8} (-)	1.4×10^{-5} (5.5×10^{-3})	1.0×10^{-8} (-)	7.8×10^{-4} (4.3×10^{-2})
Oxalate	2.8×10^{-7} (-)	3.2×10^{-5} (6.7×10^{-4})	4.8×10^{-6} (6.4×10^{-5})	1.9×10^{-5} (8.3×10^{-5})
Succinate	7.6×10^{-6} (1.5×10^{-4})	1.4×10^{-4} (1.5×10^{-3})	3.1×10^{-5} (4.7×10^{-4})	5.9×10^{-5} (3.9×10^{-4})
Glutarate	4.6×10^{-5} (3.0×10^{-3})	1.7×10^{-4} (1.2×10^{-3})	1.7×10^{-5} (7.2×10^{-3})	3.4×10^{-5} (2.0×10^{-4})
Glycolate	8.7×10^{-6} (6.0×10^{-4})	1.5×10^{-4} (6.5×10^{-4})	2.1×10^{-5} (9.0×10^{-4})	6.6×10^{-5} (8.6×10^{-4})
Malonate	6.1×10^{-6} (2.0×10^{-3})	1.2×10^{-4} (6.5×10^{-4})	1.1×10^{-5} (7.1×10^{-4})	2.2×10^{-5} (6.1×10^{-4})

'-', means that MPM method is not applicable.

TABLE 5 | Phosphate determination in lake water samples with the potentiometric sensor based on CB/IL **1**.

Anion	HCO_3^- mg/L	Cl^-, mg/L	NO_3^-, mg/L	NO_2^- mg/L	PO_4 (total), mg/L	
					Ion chromatography	Potentiometry (HPO_4^{2-} content)
Sample 1	80.5	1.2	4.0	0.15	0.1	0.07 ± 0.02
Sample 2	45.0	2.2	12.0	0.35	0.6	0.5 ± 0.1
Sample 3	50.0	1.5	25.0	0.8	0.8	0.6 ± 0.1

Other anions content was determined by ion chromatography.

of the sensor stored in dry conditions was assessed by every weak signal measurement. After 3 months, the signal toward 1.0×10^{-4} M HPO_4^{2-} ions decreased to 90% of its initial value. Thus, potentiometric sensor developed showed satisfactory stability and signal measurement precision convenient for real sample analysis. Similar experiments with the CB layer showed lower stability of sensing layer and life time of 6 weeks. Measurement-to-measurement and sensor-to-sensor repeatability were found to be 3.5 and 4.5%, respectively.

Using this potentiometric sensor, unbiased selectivity coefficients were determined by SSM and MPM methods (see section Potentiometric Sensor Preparation and Application). The results obtained are presented in **Table 4**. Except carbonate ion, most of the potentiometric sensors exhibited highly selective response to target analyte. MPM calculations result in higher selectivity coefficients especially in case of one-charged ions. This is a result of non-Nernstian behavior of interfering ions and incomplete consideration of different ion charges. In some cases with high difference in the signals of primary and interfering ions, the increment in the potential established for primary ion cannot be reached by addition of interfering ion. In such cases, dash sign in placed in brackets. The IL **3** can be considered as most selective receptor among other ILs studied. Selectivity of the solid-contact sensors developed makes it possible to determine hydrogen phosphate anions in natural and mineral water on the level of their permissible levels (5.0×10^{-6} M in Russian Federation).

Real Sample Analysis

The potentiometric sensors developed were tested in the determination of hydrogen phosphate anions in fresh waters samples taken from natural lakes in the suburb of Kazan City. The content of anions established by ionic chromatography and the results of potentiometric determination are presented in **Table 5**. CB/IL **1** was used in all the measurements, the results were averaged for three replications. As could be seen, the potentiometric sensor developed can be used for the assessment of the phosphate content in fresh waters. Minor underestimation against chromatography results can be attributed to the different sample treatment protocol including some other phosphate sources (organic esters, pyrophosphates) undetectable with potentiometric sensors. In potentiometric experiment, water samples were filtered to exclude organic phosphate sources and their pH was adjusted to 8.0 with NaOH solution.

DISCUSSION

Application of ILs in the assembly of solid-state potentiometric sensors offers some attractive advantages, e.g., small size, flexibility of the design, no need in internal filling and long conditions prior to use. Besides, the ILs do not need in additional implementation of lipophilic salt and plasticizers and are applicable with modern technologies of sensor manufacture (screen-printing technique). Meanwhile, the number of successful examples of IL based potentiometric sensors is rather limited due to difficulties in their synthesis and some difficulties of introduction in the sensor assembly including moderate solubility in water and in some cases insufficient mechanical durability of the surface layer.

In this work, we propose to use a new class of ILs which is based on thiacalix[4]arene platform with rather long hydrophobic substituents bearing cationic centers able to exchange. Previously we have shown that introduction of Tf_2N^- anion instead of bromide or nitrate decreased melting point to meet the IL definition (Padnya et al., 2017). Insolubility of the ILs tested in water is another advantage providing a long lifetime of the sensors and low potential drift during the operational period.

Direct EIS investigation of the films obtained by deposition of the ILs on electrode showed remarkable dependence of the charge transfer resistance to the anions present in the solution which was referred to the competition between the ferricyanide ions (redox probe) and those added to the solution for the binding sites of the IL layer. The comparison of the effect achieved for different salts made it possible to preliminarily conclude on the selective recognition of hydrogen phosphate anions. The following experiments with carbonaceous materials as supports for ILs confirmed the possibility for reliable and sensitive determination of HPO_4^{2-} anions in aqueous solutions. Ion exchange mechanism of potentiometric response toward HPO_4^{2-} anions was confirmed by EIS data. The comparison of the results obtained with *cone* and *1,3-alternate* conformations of macrocycle core as well as those with dimethyl- and diethyl-ammonium fragments in the substituents at the lower rim of the macrocycle confirmed the suggestion about predominant influence of steric factors on the recognition of the hydrogen phosphate anion. The conditioning of the freshly prepared sensor as well as its recovery after the contact with the sample can be accelerated by short heating to 80°C followed by solidification by cooling to ambient temperature. The sensor showed good mechanical durability and stable response toward $1.0 \times 10^{-2}-1.0 \times 10^{-6}$ M HPO_4^{2-} within at least 30 days with a standard deviation varied from 2.3% (MWCNTs) to 3.2% (CB) in the series of six individual sensors. The selectivity of the response makes it possible to directly determine the hydrogen phosphate anion in the presence of most inorganic and many organic anions commonly present in water samples and biological fluids. The potentiometric sensor was validated on real samples of surface waters containing some contaminants typical for rural area (high quantities of nitrite and nitrate salts and moderate mineralization level). The results obtained can be used for further miniaturization of the sensor and extension of its possible area of application to biological fluids and wastes containing biogenic and inorganic phosphate sources.

AUTHOR CONTRIBUTIONS

PP and IS synthesized ILs based on thiacalixarene platform, characterized their purity and conformation and participated

REFERENCES

Abo-Hamad, A., Al Saadi, M. A. H., Hayyan, M., Juneidi, I., and Hashim, M. A. (2016). Ionic liquid-carbon nanomaterial hybrids for electrochemical sensor applications: a review. *Electrochim. Acta* 193, 321–344. doi: 10.1016/j.electacta.2016.02.044

Afkhami, A., Bagheri, H., Shirzadmehr, A., Khoshsafar, H., and Hashemi, P. (2012). A potentiometric sensor for Cd^{2+} based on carbon nanotube paste electrode constructed from room temperature ionic liquid, ionophore and silica nanoparticles. *Electroanalysis* 24, 2176–2185. doi: 10.1002/elan.201200246

Afkhami, A., Shirzadmehr, A., Madrakian, T., and Bagheri, H. (2014). Improvement in the performance of a Pb^{2+} selective potentiometric sensor using modified core/shell SiO_2/Fe_3O_4 nano-structure. *J. Mol. Liquids* 199, 108–114. doi: 10.1016/j.molliq.2014.08.027

Afkhami, A., Shirzadmehr, A., Madrakian, T., and Bagheri, H. (2015). New nano-composite potentiometric sensor composed of graphene nanosheets/thionine/molecular wire for nanomolar detection of silver ion in various real samples. *Talanta* 131, 548–555. doi: 10.1016/j.talanta.2014.08.004

Alizadeh, T., and Atayi, K. (2018). Synthesis of nano-sized hydrogen phosphate-imprinted polymer in acetonitrile/water mixture and its use as a recognition element of hydrogen phosphate selective all-solid state potentiometric electrode. *J. Mol. Recogn.* 31:e2678. doi: 10.1002/jmr.2678

Bagheri, H., Shirzadmehr, A., and Rezaei, M. (2015). Designing and fabrication of new molecularly imprinted polymer-based potentiometric nano-graphene/ionic liquid/carbon paste electrode for the determination of losartan. *J. Mol. Liquids* 212, 96–102. doi: 10.1016/j.molliq.2015.09.005

Bagheri, H., Shirzadmehr, A., and Rezaei, M. (2016). Determination of copper ions in foodstuff products with a newly modified potentiometric carbon paste electrode based on a novel nano-sensing layer. *Ionics* 22, 1241–1252. doi: 10.1007/s11581-016-1646-9

Bagheri, H., Shirzadmehr, A., Rezaei, M., and Khoshsafar, H. (2017). Determination of tramadol in pharmaceutical products and biological samples using a new nanocomposite carbon paste sensor based on decorated nanographene/tramadol-imprinted polymer nanoparticles/ionic liquid. *Ionics* 24, 833–843. doi: 10.1007/s11581-017-2252-1

Bakker, E. (1997). Determination of unbiased selectivity coefficients of neutral carrier-based cation-selective electrodes. *Anal. Chem.* 69, 1061–1069. doi: 10.1021/ac960891m

Buck, R. P., and Linder, E. (1994). Recomendations for nomenclature of ion-selective electrodes. *Pure Appl. Chem.* 66, 2527–2536. doi: 10.1351/pac199466122527

Carey, C. M., and Riggan, W. B. (1994). Cyclic polyamine ionophore for use in a dibasic phosphate-selective electrode. *Anal. Chem.* 66, 3587–3591. doi: 10.1021/ac00093a009

Carvalho, T., Vidinha, P., Vieira, B. R., Li, R. W. C., and Gruber, J. (2014). Ion Jelly: a novel sensing material for gas sensors and electronic noses. *J. Mater. Chem. C* 2, 696–700. doi: 10.1039/C3TC31496K

Evtugyn, G. A., Belyakova, S. V., Shamagsumova, R. V., Saveliev, A. A., Ivanov, A. N., Stoikova, E. E., et al. (2010). Discrimination of apple juice and herbal liqueur brands with solid-state electrodes covered with polyaniline and thiacalixarenes. *Talanta* 82, 613–619. doi: 10.1016/j.talanta.2010.05.016

Fan, Y., Xu, C., Wang, R., Hu, G., Miao, J., Hai, K., et al. (2017). Determination of copper(II) ion in food using an ionic liquids-carbon nanotubes-based ion-selective electrode. *J. Food Compos. Anal.* 62, 63–68. doi: 10.1016/j.jfca.2017.05.003

Faridbod, F., and Shafaat, A. (2017). Ionic liquids based polymeric membrane drug sensors. *Curr. Anal. Chem.* 13, 52–61. doi: 10.2174/1573411012666160601150123

Fernández-Gutiérrez, A., Cruces-Blanco, C., Cortacero-Ramírez, S., and Segura-Carretero, A. (2000). Sensitive determination of inorganic anions at trace levels in samples of snow water from Sierra Nevada (Granada, Spain) by capillary ion electrophoresis using calix[4]arene as selective modifier. *Chromatographia* 52, 413–417. doi: 10.1007/BF02535712

Ganjali, M. R., Khoshsafar, H., Faridbod, F., Shirzadmehr, A., Javanbakht, M., and Norouzi, P. (2009). Room temperature ionic liquids (RTILs) and multiwalled carbon nanotubes (MWCNTs) as modifiers for improvement of carbon paste ion selective electrode response; A comparison study with PVC membrane. *Electroanalysis* 21, 2175–2178. doi: 10.1002/elan.200904642

Ganjali, M. R., Norouzi, P., Ghomi, M., and Salvati-Niasari, M. (2006). Highly selective and sensitive monohydrogen phosphate membrane sensor based on molybdenum acetylacetonate. *Anal. Chim. Acta* 567, 196–201. doi: 10.1016/j.aca.2006.03.026

Hartley, A. M., House, W. A., Callow, M. E., and Leadbeater, B. S. C. (2000). Application of a cylic polyamine ionophore in phosphate selective electrodes for environmental analysis. *Intern. J. Environ. Anal. Chem.* 76, 199–214. doi: 10.1080/03067310008034131

Hu, K., Kitazumi, Y., Kano, K., and Shirai, O. (2018). Phosphate ion sensor using a cobalt phosphate coated cobalt electrode. *Electrochimica Acta* 282, 242–246. doi: 10.1016/j.electacta.2018.06.021

Kopytin, A. V., Zhizhin, K., Yu., Urusov, Y. I., Mustyatsa, V. N., Kokunov, Yu,. V., and Kuznetsov, N. T. (2012). Potentiometric sensors with membranes based on ionic liquid tetradecylammonium triethylammonio-*closo*-dodecaborate. *J. Anal. Chem.* 67, 168–171. doi: 10.1134/S1061934812020074

Kumar, P., Kim, D. M., Hyun, M. H., and Shim, Y.-B. (2010). An all-solid-state monohydrogen phosphate sensor based on a macrocyclic ionophore. *Talanta* 82, 1107–1112. doi: 10.1016/j.talanta.2010.06.011

Lee, W. H., Seo,. Y., and Bishop, P. L. (2009). Characteristics of a cobalt-based phosphate microelectrode for in situ monitoring of phosphate and its biological application. *Sens. Actuators B* 137, 121–128. doi: 10.1016/j.snb.2008.10.032

Marr, P. C., and Marr, A. C. (2016). Ionic liquid gel materials: applications in green and sustainable chemistry. *Green Chem.* 18, 105–128. doi: 10.1039/c5gc02277k

Mendecki, L., Chen, X., Callan, N., Thompson, D. F., Schazmann, B., Granados-Focil, S., et al. (2016). Simple, robust, and plasticizer-free iodide-selective sensor based on copolymerized tiazole-based ionic liquid. *Anal. Chem.* 88, 4311–4317. doi: 10.1021/acs.analchem.5b04461

Mohammadian, A., Ebrahimi, M., and Karimi-Maleh, H. (2018). Synergic effect of 2D nitrogen doped reduced graphene nano-sheet and ionic liquid as a new approach for fabrication of anticancer drug sensor in analysis of doxorubicin and topotecan. *J. Mol. Liquids* 265, 727–735. doi: 10.1016/j.molliq.2018.07.026

Nawała, J., Dawidziuk, B., Dziedzic, D., Gordon, D., and Popiel, S. (2018), Applications of ionic liquids in analytical chemistry with a particular emphasis on their use in solid-phase microextraction. *TrAC. Trends Anal. Chem.* 105, 18–36. doi: 10.1016/j.trac.2018.04.010

Paczosa-Bator, B. (2014). Effects of type of nanosized carbon black on the performance of an all-solid-state potentiometric electrode for nitrate. *Microchim. Acta.* 181, 1093–1099. doi: 10.1007/s00604-014-1216-7

Padnya, P. L., Andreyko, E. A., Gorbatova, P. A., Parfenov, V. V., Rizvanov, I. Kh., and Stoikov, I. I. (2017). Towards macrocyclic ionic liquids: novel ammonium salts based on tetrasubstituted *p-tert*-butylthiacalix[4]arenes. *RSC Adv.* 7, 1671–1686. doi: 10.1039/c6ra24734b

Patra, S., Maity, D., Gunupuru, R., Agnihotri, P., and Paul, P. (2012). Calixarenes: Versatile molecules as molecular sensors for ion recognition study. *J. Chem. Sci.* 124, 1287–1299. doi: 10.1007/s12039-012-0329-y

Peng, B., Zhu, J., Liu, X., and Qin, Y. (2008). Potentiometric response of ion-selective membranes with ionic liquids as ion-exchanger and plasticizer. *Sens. Actuators B*. 133, 308–314. doi: 10.1016/j.snb.2008.02.027

Roy, S., David-Pur, M., and Hanein, Y. (2017). Carbon nanotube-based ion selective sensors for wearable applications. *ACS Appl. Mater. Interfaces*. 9, 35169–35177. doi: 10.1021/acsami.7b07346

Rzhevskaia, A. V., Shvedene, N. V., and Pletnev, I. V. (2016). Anion-selective electrodes based on solidified 1,3-dihexadecylimidazolium ionic liquids with halide and pseudohalide anions. *J. Electroanal. Chem.* 783, 274–279. doi: 10.1016/j.jelechem.2016.11.009

Sanati, A. L., Faridbod, F., and Ganjali, M. R. (2017). Synergic effect of graphene quantum dots and room temperature ionic liquid for the fabrication of highly sensitive voltammetric sensor for levodopa determination in the presence of serotonin. *J. Mol. Liquids* 241, 316–320. doi: 10.1016/j.molliq.2017.04.123

Sessler, J. L., Melfi, P. J., and Dan Pantos, G. (2006). Uranium complexes of multidentate N-donor ligands. *Coordination Chem. Rev*. 250, 816–843. doi: 10.1016/j.ccr.2005.10.007

Shiddiky, M. J. A., and Torriero, A. A. J. (2011). Application of ionic liquids in electrochemical sensing systems. *Biosens. Bioelectron*. 26, 1775–1787. doi: 10.1016/j.bios.2010.08.064

Shirzadmehr, A., Afkhami, A., and Madrakian, T. (2015). A new nano-composite potentiometric sensor containing an Hg^{2+}-ion imprinted polymer for the trace determination of mercury ions in different matrices. *J. Mol. Liquids* 204, 227–235. doi: 10.1016/j.molliq.2015.01.014

Shirzadmehr, A., Rezaei, M., Bagheri, H., and Khoshsafar, H. (2016). Novel potentiometric sensor for the tracelevel determination of Zn^{2+} based on a new nanographene/ion imprinted polymer composite. *Intern. J. Environ. Anal. Chem*. 96, 929–944. doi: 10.1080/03067319.2016.1210608

Shvedene, N. V., Avramenko, O. A., Baulin, V. E., Tomilova, L. G., and Pletnev, I. G. (2011). Iodide-selective screen-printed electrodes based on low-melting ionic solids and metallated phthalocyanine. *Electroanalysis* 23, 1067–1072. doi: 10.1002/elan.201000632

Shvedene, N. V., Rzhevskaia, A. V., Aksenova, V. A., and Pletnev, I. V. (2017). A potentiometric multisensor system of anion-selective electrodes based on ionic liquids. *Moscow Univ. Chem. Bull*. 72, 307–314. doi: 10.3103/S0027131418010078

Silvester, D. S. (2011). Recent advances in the use of ionic liquids for electrochemical sensing. *Analyst* 136, 4871–4882. doi: 10.1039/C1AN15699C

Sorvin, M., Belyakova, S., Stoikov, I., Shamagsumova, R., and Evtugyn, G. (2018). Solid-contact potentiometric sensors and multisensors based on polyaniline and thiacalixarene receptors for the analysis of some beverages and alcoholic drinks. *Front. Chem.* 6:134. doi: 10.3389/fchem.2018.00134

Storer, C. S., Coldrick, Z., Tate, D. J., Donoghue, J. M., and Grieve, B. (2018). Towards phosphate detection in hydroponics using molecularly imprinted polymer sensors. *Sensors* 18:531. doi: 10.3390/s18020531

Sun, P., and Armstrong, D. W. (2010). Ionic liquids in analytical chemistry. *Anal. Chim. Acta* 661, 1–16. doi: 10.1016/j.aca.2009.12.007

Švancara, I., Vytras, K., Kalcher, K., Walcarius, A., and Wang, J. (2009). Carbon paste electrodes in facts, numbers, and notes: a review on the occasion of the 50-years jubilee of carbon paste in electrochemistry and electroanalysis. *Electroanalysis* 21, 7–28. doi: 10.1002/elan.200804340

Tafesse, F., and Enemchukwu, M. (2015). Application of layered double hydroxide membranes as phosphate-sensitive electrodes. *Phosph. Sulf. Silicon* 190, 36–44. doi: 10.1080/10426507.2014.919294

Tan, Z., Liu, J., and Pang, L. (2012). Advances in analytical chemistry using the unique properties of ionic liquids. *TrAC Trenda Anal. Chem.* 39, 218–227. doi: 10.1016/j.trac.2012.06.005

Tonelli, D., Ghorbel, S., Colombari, M., Guadagnini, L., and Ghorbel, A. (2013). Monohydrogen phosphate selective electrode based on a synthetic hydrotalcite. *J. Electroanal. Chem*. 690, 25–31. doi: 10.1016/j.jelechem.2012.11.039

Umezawa, Y., Umezawa, K., and Sato, H. (1995). Selectivity coefficients for ion-selective electrodes – recommended methods for reporting values (technical report). *Pure Appl. Chem*. 67, 507–518. doi: 10.1351/pac199567030507

Valentini, F., Carbone, M., and Palleschi, G. (2016). Graphene oxide nanoribbons (GNO), reduced graphene nanoribbons (GNR), and multi-layers of oxidized graphene functionalized with ionic liquids (GO-IL) for assembly of miniaturized electrochemical devices. *Anal. Bioanal. Chem*. 405, 3449–3474. doi: 10.1007/s00216-012-6615-1

Wardak, C. (2011). A highly selective lead-sensitive electrode with solid contact based on ionic liquid. *J. Hazardous Mater*. 186, 1131–1135. doi: 10.1016/j.jhazmat.2010.11.103

Wardak, C. (2015). Solid contact cadmium ion-selective electrode based on ionic liquid and carbon nanotubes. *Sens. Actuators B*. 209, 131–137. doi: 10.1016/j.snb.2014.11.107

Wardak, C., and Lenik, J. (2013). Application of ionic liquid to the construction of Cu(II) ion-selective electrode with solid contact. *Sens. Actuators B*. 189, 52–59. doi: 10.1016/j.snb.2012.12.065

Wei, D., and Ivaska, A. (2009). Applications of ionic liquids in electrochemical sensors. *Anal. Chim. Acta* 607, 126–135. doi: 10.1016/j.aca.2007.12.011

Wroblewski, W., Wojciechowski, K., Dybko, A., Brzozka, Z., Egberink, R. J. M., Snellink-Ruel, B. H. M., et al. (2000). Uranyl salophenes as ionophores for phosphate-selective electrodes. *Sens. Actuators B* 68, 313–318. doi: 10.1016/S0925-4005(00)00450-0

Xie, L., Qin, Y., and Chen, H.-Y. (2013). Preparation of solid contact potentiometric sensors with self-plasticizing triblock polymer and ionic liquid-polymer composites. *Sens. Actuators B*. 186, 321–326. doi: 10.1016/j.snb.2013.06.026

Yan, Z., Li, X., and Ye, B. (2007). Amide and acyl-hydrazine functionalized calix[4]arenes as carriers for hydrogen phosphate selective electrodes. *Electroanalysis* 19, 958–963. doi: 10.1002/elan.200603810

Efficient Nucleophilic Degradation of an Organophosphorus Pesticide "Diazinon" Mediated by Green Solvents and Microwave Heating

Daniela Millán[1,2]*, Ricardo A. Tapia[1] and Paulina Pavez[1]

[1] Facultad de Química, Pontificia Universidad Católica de Chile, Santiago, Chile, [2] Centro Integrativo de Biología y Química Aplicada, Universidad Bernardo O'Higgins, Santiago, Chile

An efficient strategy for the degradation of organophosphate pesticide Diazinon was investigated. In this work, ionic liquids, bio-based solvents, and two conventional organic solvents were used as reaction media. Kinetics studies by means of half-life ($t_{1/2}$,h) were followed by ^{31}P NMR and the products analyzed by GC-MS, HPLC-MS and NMR techniques. These results have shown that $t_{1/2}$ values in ionic liquids were the lowest and also they were able to activate two electrophilic centers in Diazinon, whilst degradation in bio-based solvents occurred slowly by only an aromatic pathway. In addition, a study to estimate the influence of green activation techniques was carried out by using Ultrasound irradiation and Microwave heating in combination with greener solvents and two conventional organic solvents. Under Microwave heating, faster degradation than under ultrasound irradiation was found. Finally, considering both families of solvent used here and their behavior under green activation techniques, we propose that the more efficient way for degradation of Diazinon with piperidine is by microwave heating using ionic liquids as solvents.

Keywords: greener solvents, ionic liquids, organophosphate pesticides, ^{31}P NMR, microwaves, ultrasound

INTRODUCTION

Organophosphorus pesticides (OPPs) represent 38% of total pesticides used globally, due to their high insecticidal activity and other biological activities (Casida and Quistad, 2004; Singh, 2009). Considering the known toxicity of OPPs to humans, their presence in the environment is of great concern since most of them as well as their degradation products have been found both in surface and groundwater (Matouq et al., 2008). Therefore, degradation of these compounds is an important issue overall when some of the treatments to degrade OPPs may not be very efficient or are harmful to the environment due to the formation of by-products that have mild or acute toxicity (Ortiz-Hernández et al., 2003; Gan et al., 2006). Among the methods that have been developed for their degradation, microbiological and chemical processes are commonly used. Biological degradation takes place in soils when soil microorganisms or enzymes consume or break down pesticides (Richins et al., 1997; Deng et al., 2015), while chemical degradation occurs through reactions such

as photolysis, hydrolysis, oxidation or nucleophilic attack by using O and N nucleophiles (Menger and Rourk, 1999; Kodaka et al., 2003; Bavcon Kralj et al., 2007). The latter is a promising alternative to other remediation approaches used for their destruction (Onyido et al., 2005; Rougier et al., 2010; Singh et al., 2015).

In this context, the solvent is essential to carry out this process, and the replacement of conventional organic solvents (COS) by a suitable alternative, has become one of the main topics of modern chemistry (Sheldon, 2005). In this respect, ionic liquids and bio-based sustainable solvents have lately appeared as the most promising approaches for current solvent innovation (Hallett and Welton, 2011; Yang et al., 2012; MacMillan et al., 2013). Both kinds of solvents have been used previously by our group to study nucleophilic substitutions reactions of Paraoxon and Fenitrothion and the results provided useful information for the appropriate degradation of organophosphate pesticides (Pavez et al., 2013, 2016).

On the other hand, not only the solvent plays a key role in organic reactions but time and energy efficiency are also important, overall when the requirement for a sustainable and safe process is gaining much attention. In this context, the use of irradiation methods can be a further way to meet the demands of the Green Chemistry principles. In this sense, Ultrasound (US) and Microwave (MW) technologies have been recently used as green activation techniques (Cravotto and Cintas, 2007) to improve the outcome of several organic reactions as well as an analytical technique to determine organic pollutants (Cravotto and Cintas, 2006; Papadopoulos et al., 2016). Ultrasound technique has been used to investigate the degradation of some OPPs, for instance, Matouq et al. studied the effect of high ultrasound irradiation frequency techniques in degradation of Diazinon in aqueous solution, concluding that the kinetics of degradation fit well with a pseudo-first-order process (Matouq et al., 2008). Zhang et al. treated different samples of apple juice which contained malathion and chlorpyrifos with ultrasonic irradiation, and their results showed that ultrasonic treatment was effective for the degradation of malathion and chlorpyrifos in apple juice (Zhang et al., 2010). In another study by Yao et al., investigated the mechanism of sonolithic degradation of Parathion, and they demonstrated that the degradation rate increased proportionally with an increase in ultrasonic intensity (Yao et al., 2010).

Additionally, the synergetic effect of ionic liquids in combination with US has been of great interest, due that they have demonstrated to generate improvements in yield, rate, and selectivity compared to classical chemistry, or products expected (D'Anna et al., 2012; Chatel and MacFarlane, 2014). Nevertheless, to the best of our knowledge, there is no report about the degradation of OPPs using ILs and greener bio-based solvents in combination with US or MW.

The purpose of this work was to study the influence of the solvent in the nucleophilic substitution reactions of organophosphate pesticide Diazinon **1** (**Figure 1**) with piperidine as a nucleophile, in six ILs and eighth bio-based solvents (**Scheme 1**). Additionally, we are motivated to compare the

FIGURE 1 | Pesticide under study.
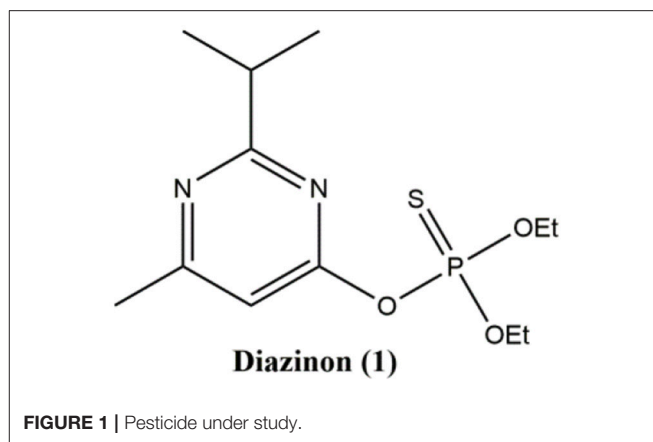
results obtained in ILs and bio-based solvents with those obtained under ultrasound and microwaves irradiation to search for a more efficient approach for the degradation of **1**.

EXPERIMENTAL SECTION

Materials

All bio-based solvents, conventional organic solvents (COS), piperidine and Diazinon® were purchased. All ionic liquids were dried before use on a vacuum oven at 70°C for at least 12 h and stored in a dryer under nitrogen and over calcium chloride. The water content in ILs was <0.1% by Karl Fisher titration.
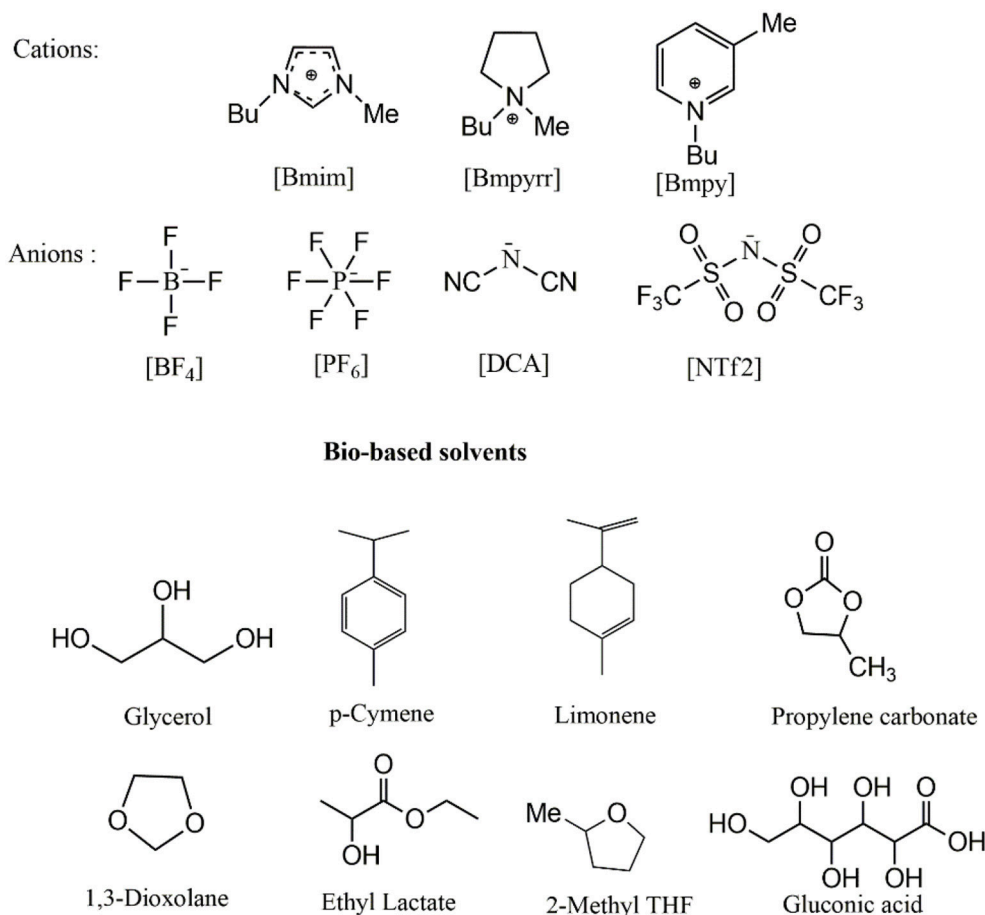
Kinetic Measurements

The kinetic study of the reaction of **1** with piperidine in all solvents was performed by ^{31}P NMR obtained on a 400 spectrometer, following the disappearing of the signal of **1**, at least a 10-fold excess of total amine over the substrate was employed and each measurement was made in triplicate.

Typical ^{31}P NMR kinetic experiment: an NMR tube containing 500 μL of solvent (COS, ILs or bio-based solvents) was thermostated at 25°C for 10 min. Then 10 μL of pesticide (0.5M in MeCN) and 40 μL of neat piperidine were added. Capillaries of deuterated water were used as reference solvent. The spectra were recorded at different reaction times and pseudo-first-order rate coefficients (k_{obsd}) were found for the different reaction routes. The overall k_{obsd} values obtained for degradation of **1** were obtained by integration of the NMR signals and then plotted log (integration) vs. time. To obtain the rate constants for the product formation, we multiplied k_{obsd} by the fraction of each product relative to the total products. The molar concentrations of the products at the end of the reactions were obtained by quantitative analysis of each product.

Microwave-Assisted Degradation

Microwave-assisted reactions were carried out in an Anton Paar Monowave 300 Microwave Synthesis Reactor (Anton Paar

SCHEME 1 | Greener solvents used in this study.

GmbH, Graz, Austria) in 10 mL sealed vials. To run a microwave experiment the same quantities of solvent, pesticide, and piperidine as kinetic measurements were used. Measurements were carried out at 50°C and 500 rpm, each measurement was made in triplicate. To evaluate the % of degradation of the pesticide the reaction mixture was analyzed by ^{31}P NMR.

Ultrasound-Assisted Degradation

The reactions were carried out in a thermostated ultrasonic cleaning bath (SB−3200 DTD) operating at a frequency of 40 kHz. The tank dimensions were 300 × 155 × 150 mm, with a liquid holding capacity of 6 L. The ultrasonic cleaner had an output power of 0–180 W through digital adjustment. The reactions were carried out in a round-bottomed flask of 20 mL capacity suspended at the center of the cleaning bath, 5 cm below the surface of the liquid. In a typical experiment 1,000 μL of solvent (COS, ILs or bio-based solvents), 20 μL of pesticide (0.5M in MeCN) and 80 μL of neat piperidine were added to the round-bottomed flask and then irradiated by 1 h. To evaluate the % of degradation of the pesticide the reaction

mixture was analyzed by ^{31}P NMR. Each measurement was made in triplicate.

Electrospray Ionization Mass Spectrometry (ESI-MS)

The detection of Compounds **1a**, **1b**, **1c,** and **1d** for degradation of **1** (See **Scheme 2**), were identified by an ABSciex Triple Quad 4500 (UHPLC-MS/MS) mass spectrometer equipped with a Turbo Ion Spray (AB Sciex) ion source. A microsyringe pump delivered the mixed reaction of **1** with piperidine in DMSO at infinite time dissolved in 10% (vol/vol) acetonitrile into the ESI source at a flow rate of 10 μL/min. ESI and the QQ (linear trap) mass spectrometer were operated in the negative-ion mode for detecting **1a** and **1c** and the positive mode for **1b** and **1d** by using the multiple reaction monitoring (MRM) scan types. Main conditions: curtain gas nitrogen flow = 10 mL min-1; ion spray voltage = −4,500 eV; declustering potential = −60 eV; entrance potential = −10 eV; collision cell exit potential = −12 eV; source temperature was set at 300°C and source gas GS1 and GS2 were set to 12 and 0, respectively. All data were acquired using Analyst 1.6.2 (AB Sciex).

RESULTS AND DISCUSSION

To investigate the degradation of Diazinon in solvents labeled as "greener solvents," we performed a kinetic study where by means of first-order rate constants (k_{obsd}) obtained from nucleophilic attack of piperidine to **1** in Ionic liquids, bio-based solvents, and some conventional solvents; we calculated half-life ($t_{1/2}$). The k_{obsd} were obtained by ^{31}P NMR technique in the presence of total piperidine excess and calculated from the slope of

a logarithmic plot of the ^{31}P NMR area due to degradation of substrate **1** at different times [**Table S1** in Electronic Supplementary Information (ESI)]. **Figure 2** shows the $t_{1/2}$ values obtained for degradation of **1** in all solvents used in this study.

As seen in **Figure 2**, the lowest $t_{1/2}$ value was found in BmimBF$_4$ (0.68 h), while the highest was in propylene carbonate (PC) (229 h). In fact, the ratio between highest and lowest is *ca* 327. In general, the highest values of $t_{1/2}$ were found in
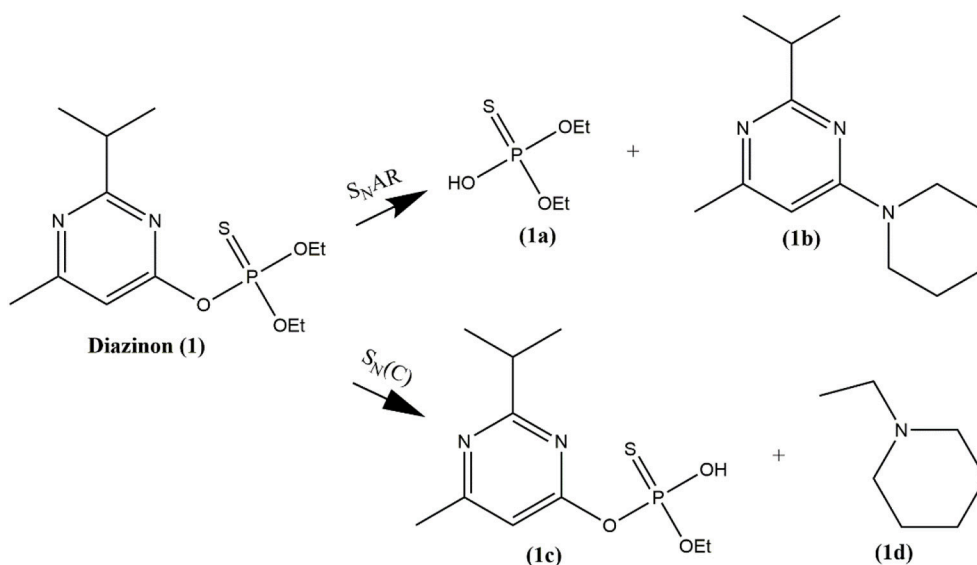
SCHEME 2 | Reaction pathways for degradation of **1** by piperidine in all ionic liquids, DMSO and MeCN.
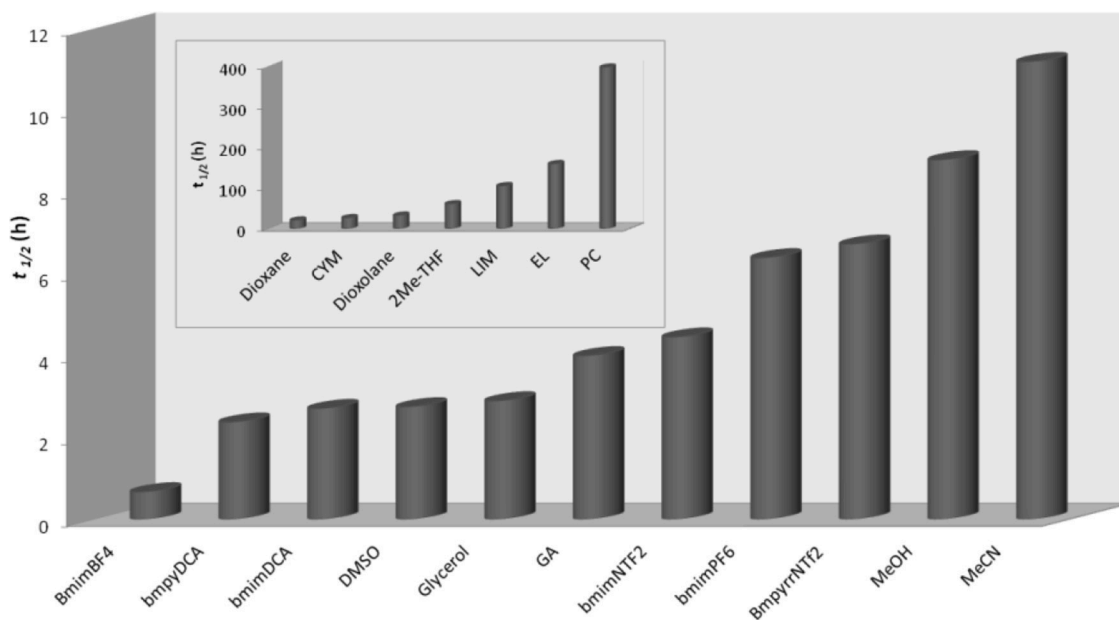
FIGURE 2 | Half-life ($t_{1/2}$,h) for degradation of **1** with piperidine (0.7 M) in several solvents. Each measurement was made in triplicate.

bio-based solvents (inset of **Figure 2**), intermediate values in conventional solvents (MeCN and MeOH) and smallest in ionic liquids, DMSO, glycerol (GLY), and gluconic acid (GA). These results in ILs agree with a recent study where the degradation of Fenitrothion was investigated in the same family of solvents (Pavez et al., 2016). In that study, it was also found that ionic liquids were the best solvents to degradation Fenitrothion.

In order to analyze the solvent effects on the degradation of Diazinon, it is necessary to identify the electrophilic centers where the nucleophilic attack by piperidine is occurring.

Therefore, to have an insight into the mechanism of degradation of **1** we performed a product analysis of this reaction by NMR and GC-MS techniques (**Figures S1–S3** in ESI). As an example, **Figure 3** shows the ^{31}P NMR spectra obtained for degradation of **1** with piperidine in BmpyrrNTF$_2$ at different times.

As can be observed from **Figure 3**, the signal for pesticide **1** at 60.3 ppm decreases and two other phosphorylated signals increase simultaneously. These two new signals were assigned to the formation of the two phosphorylated species, diethyl thiophosphate (**1a**) and O-ethyl O-[4-methyl-6-(propan-2-yl)pyrimidin-2-yl]thiophosphate diester (**1c**) at approximately 54 and 48 ppm, respectively (shown in **Scheme 2**) . Compound **1a** is formed by nucleophilic attack of piperidine at C-1 carbon of the aromatic ring of **1** via a S$_N$Ar pathway, and **1c** by an attack at the aliphatic carbon of the O-ethyl group, through a bimolecular nucleophilic substitution (S$_N$2(C)) mechanism. This behavior was found in all ionic liquids, DMSO and MeCN

(see **Figures S4–S10** in ESI), and the pathways are shown in **Scheme 2**.

In addition, the progressive ^{31}P NMR spectra obtained for degradation of **1** with piperidine in CYM, LYM, EL, PC, MeOH, GLY, GLU (see **Figures S11–S14**, in ESI), showed only one phosphorylated signal that appears at approximately 58 ppm, which it was assigned to the formation of the phosphorylated species **1a** (**Scheme 2**). It is worth to mention that all ILs used in this study were capable of activating two electrophilic centers, aromatic and aliphatic carbons (S$_N$Ar and S$_N$2 routes), in contrast with bio-based solvents where degradation only takes place through S$_N$2(C) route.

On the other hand, when 1,3-dioxolane, dioxane, and 2-MeTHF were the solvents as reaction media, the product distribution was different to those described in **Scheme 2**. As an example, **Figure 4** shows the progressive ^{31}P NMR spectra obtained for degradation of **1** in 1,3-dioxolane. It can be observed that while the signal of pesticide decreases (61 ppm) the same two signals assigned to the nucleophilic attack of piperidine to the aromatic carbon (57.5 ppm) and to the aliphatic carbon of **1** (51.5 ppm) increased. But, at very long reaction time it is possible to see a new signal at approximately 62.5 ppm, which increases at expenses of the signal at 51.5 ppm (**Figure 4**).

This new phosphorylated species (**1e**) was attributed to the product formed by a new piperidine attack at the phosphorus atom of compound **1c**, as shown in **Scheme 3**. Progressive ^{31}P NMR spectra obtained for degradation of **1** in Dioxane and 2-MeTHF are shown in **Figures S15**, **S16** in ESI.
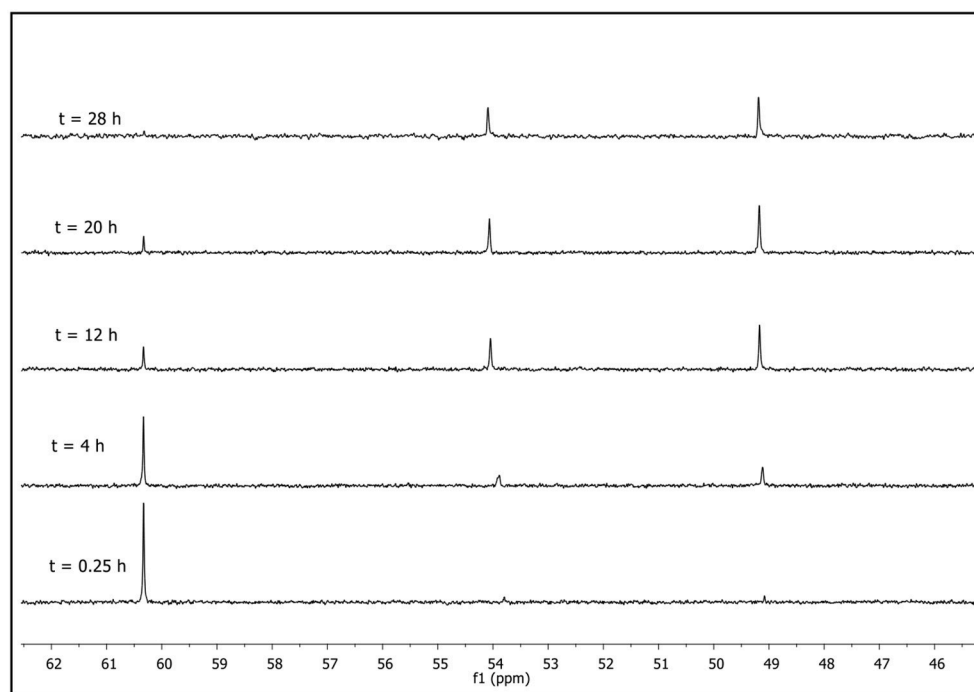

FIGURE 3 | Progressive ^{31}P NMR spectra obtained for degradation of **1** with piperidine (0.7M) at 25°C in BmpyrrNTF$_2$.
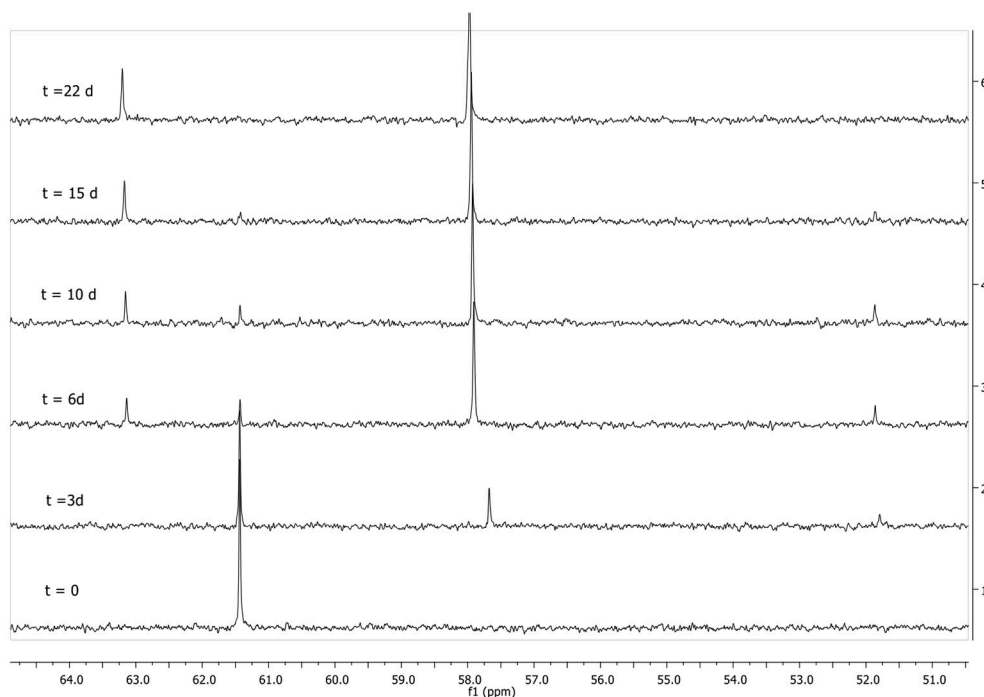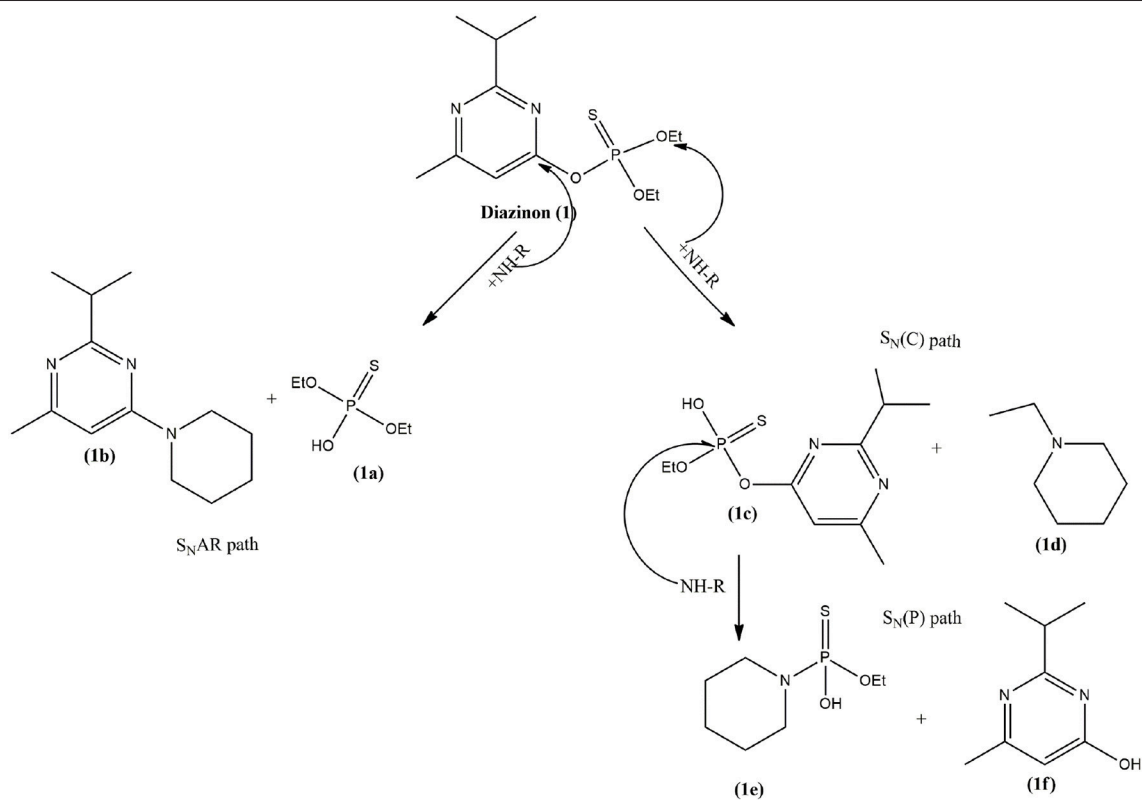
FIGURE 4 | Progressive ^{31}P NMR spectra obtained for degradation of **1** with piperidine (0.74 M) at 25°C in 1,3-Dioxolane.

SCHEME 3 | Reaction pathway for degradation of **1** by piperidine in 1,3-Dioxolane, Dioxane and 2-MeTHF.
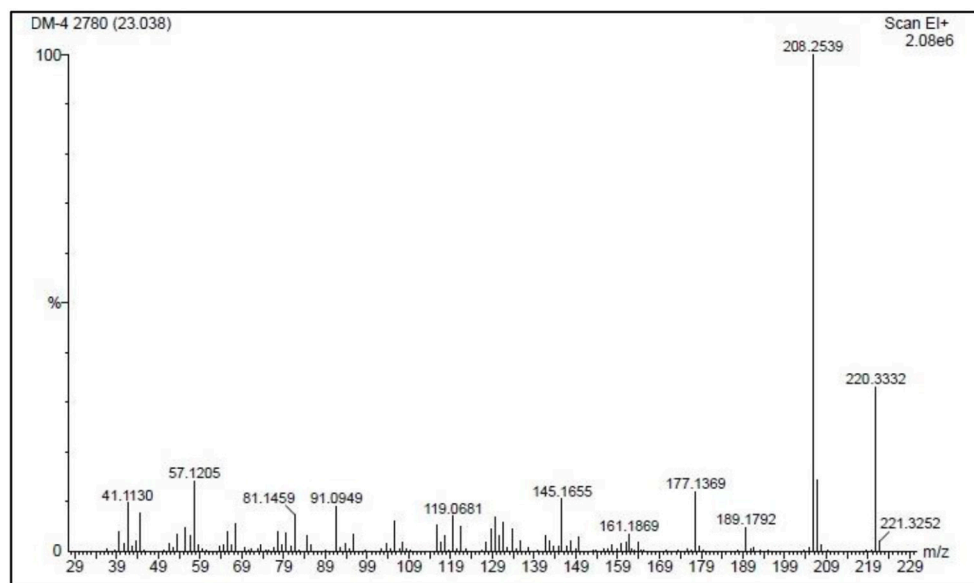
FIGURE 5 | Mass spectrum of compound **1e** (r.t. = 23.04 min, m/z = 208.25) from an extract of the reaction of **1** with piperidine in 2-MeTHF at 25°C.

The presence of compound **1e** as a reaction product was confirmed by GC/MS by means of an extraction with diethyl ether from the reaction medium and this extract was analyzed by GC/MS (compound **1e**: r.t. = 23.04 min, m/z = 208.25), the principal fragments are shown in **Figure 5**.

In addition, in order to confirm the structure of compound **1e** we also performed a 2D ^{31}P-^{1}H HMBC experiment. **Figure 6** shows the HMBC spectra obtained at the beginning (A) and at the end of the reaction (B) of Diazinon with piperidine in 2Me-THF as a solvent. As we can see, the only aromatic proton of Diazinon is lost when reacting with piperidine. When 2Me-THF is the solvent two phosphoryl compounds are observed at the end of the reaction: (a) compound **1a** where the correlation with aliphatic protons of Ethyl moiety are clear and (b) compound **1e** where the loss of one Ethyl group is evidenced at around 1.4 ppm, and the new correlation of a phosphorous atom with a proton is found at ~3.4 ppm which is assigned at one of the protons of piperidine.

On the other hand, from the integration of the ^{31}P NMR signals of the products formed by piperidine attack to the different electrophilic centers of **1** in all solvents used in this study (see **Figure 4** and **Figures S4–S16** in ESI), the relative products distribution was calculated in the different reaction media. **Figure 7** shows this behavior schematically.

It is clear from **Figure 7** that there are three different behaviors, and the selectivity of this reaction is strongly dependent on the nature of the solvent. ILs promote both S$_N$Ar and S$_N$2(C) pathways (blue and red columns, respectively), and the highest selectivity for S$_N$2(C) route was observed with BmimDCA (70%). For those ILs sharing Bmim cation preference for S$_N$2(C) path decreases on increasing the size of the anion from DCA>BF$_4$ >PF$_6$ >NTf$_2$. In addition,

fixing anion DCA and changing from imidazolium (Bmim) to pyridinium cation (Bmpy), selectivity to S$_N$2(C) route decreases. The enhanced selectivity to S$_N$Ar could be explained by means of higher aromaticity of Bmpy cation compared to aromaticity of Bmim cation. These results would suggest a higher π stacking interaction between aromatic cation of the IL and the leaving group of the pesticide, favoring the S$_N$Ar route. Note that the reaction in 1,3-dioxolane, dioxane and 2-MeTHF solvents have a different behavior, and in addition to S$_N$Ar and S$_N$2(C) pathways, a nucleophilic attack of piperidine to the phosphorus atom of **1c** by S$_N$2(P) (green columns) was observed. This three solvents are cyclic ethers present some structural similarities and show similar behaviors in S$_N$Ar reactions (Mancini et al., 1984).

In order to account the influence of the solvent in organic reactions Kamlet–Taft parameters (α, β, and π*) are frequently used, which assess hydrogen bond donating ability (β), hydrogen bond accepting ability (α), and a combination of dipolarity and polarizability (π*) (Kamlet et al., 1977, 1983).

Thus, to rationalize the influence of the solvent on the t$_{1/2}$ of degradation of Diazinon, we have performed a multiparameter linear solvation energy relationship (LSER) between the logarithm of t$_{1/2}$ values and several empirical solvent parameters. Considering the reaction mechanism shown in **Scheme 2**, we have obtained t$_{1/2}$ values for S$_N$Ar and S$_N$2(C) reaction routes by using the relative product distribution of **Figure 7** and **Table S2**. The t$_{1/2}$ values calculated for the different reaction pathways and the solvent parameters for each solvent used are reported in **Tables S1, S3** in ESI, respectively. **Table 1** shows the multiparametric regression analyses including Kamlet-Taft solvent parameters described above, viscosity (η), Hildebrandt's parameter (δ$_H$), and E_N^T polarity parameter. Each
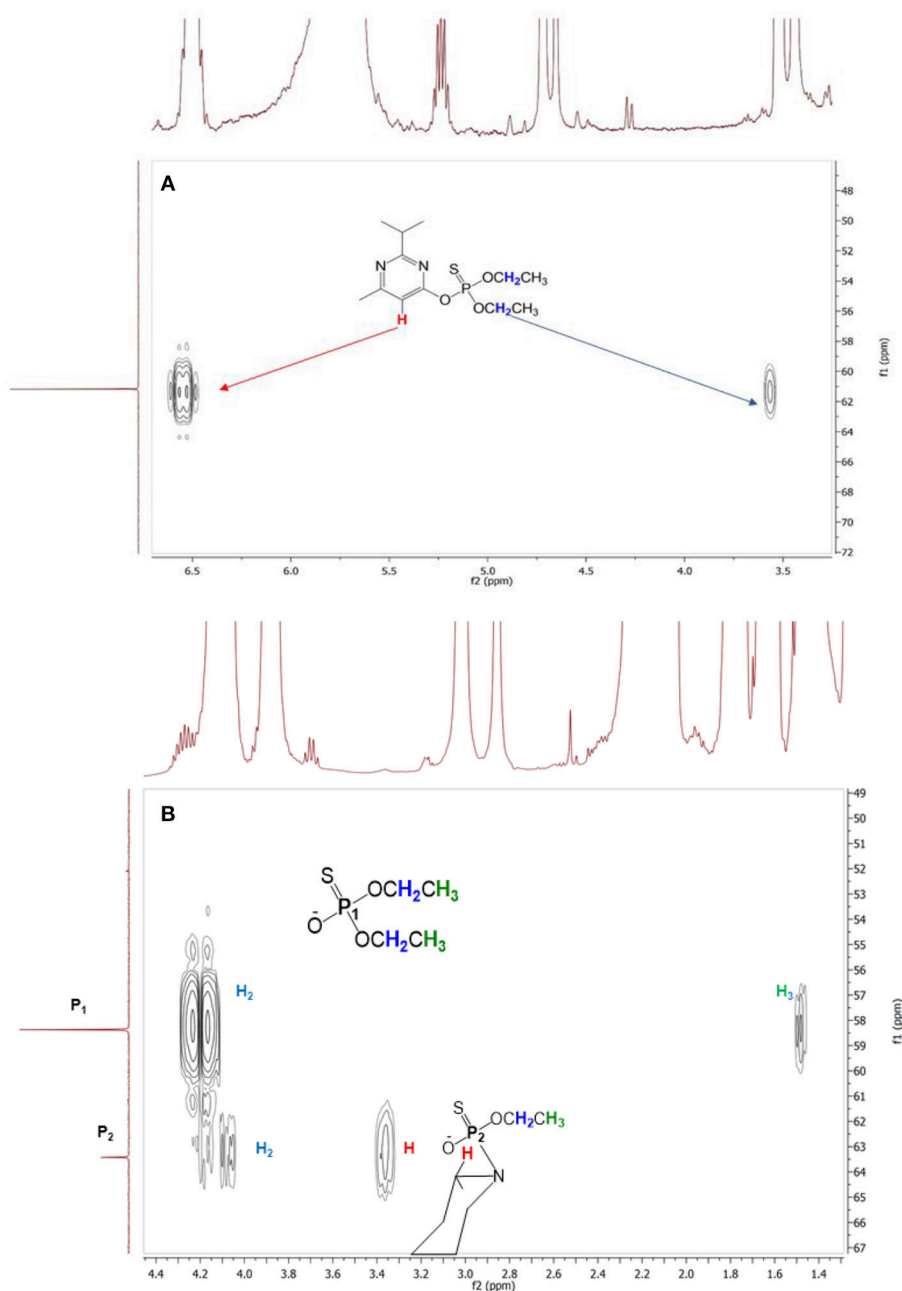
FIGURE 6 | 2D ^{31}P-^{1}H HMBC experiment of the reaction of Diazinon with piperidine in 2-Me THF at 25°C at the beginning **(A)** and at the end **(B)** of the reaction.

parameter is empirically obtained and has been measured in a wide range of solvents, including ionic liquids and bio-based solvents (Jessop et al., 2012).

As we can see in **Table 1** several equations were tested varying the number of parameters for the S_NAr route. The best correlation was found for a S_NAr pathway between log $t_{1/2}$ values and π^* parameter, **Figure 8** shows this comparison. On the other hand **Table S3** in ESI shows the same procedure for the $S_N2(C)$ pathway.

As we can see from **Figure 8**, degradation of pesticide Diazinon occurs faster via S_NAr in solvents with high π^* values. This could be explained because S_NAr route involves formation of Meisenheimer complex during addition-elimination process which leads to a dipolar intermediate which is large and highly polarizable, in addition, π^* parameter is related to the ability of a bulk solvent to stabilize a charged or a dipolar solute by means of charge-dipole or dipole-dipole interactions (Martinez et al., 1986), therefore, seems correct a good correlation between
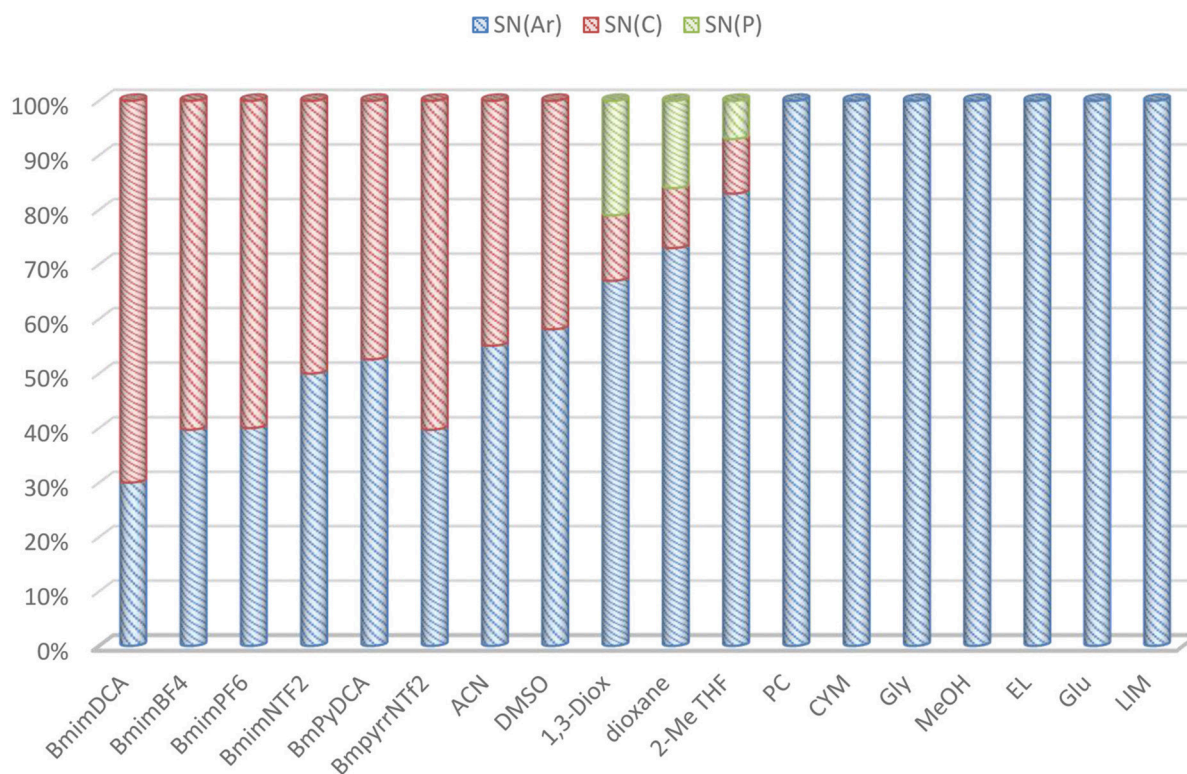
FIGURE 7 | Relative nucleophilic attack of piperidine to **1** in ILs, bio-based and conventional solvents. Attack of piperidine at phosphorus atom of **1c** (see **scheme 2**) by $S_N2(P)$ pathway (green columns), C-1 aromatic carbon by S_NAr pathway (blue columns), and aliphatic carbon by $S_N2(C)$ pathway (red columns).

TABLE 1 | Statistical data from the multiparametric regression procedure including viscosity (η), α, β, π^* Kamlet–Taft, Hildebrand solubility (δ_H^2) and E_N^T polarity parameters for solvents used in degradation of **1** by S_NAr route.

Equation	[a]F	[b]R^2	α	β	π^*	δ_H^2	η	E_N^T
1	0.49	−0.23	−15.5(47.4)	−53.7(55.1)	17.7(59.2)			
2	56.1	0.94	−5.9(16.1)	−9.61(20.7)	−195(18.8)	$9 \cdot 10^{-3}$(0.014)		
3	2.64	0.29			−138(69.3)	0.21(0.09)		
4	2.97	0.42			−238(89.5)	0.24(0.08)		113.6(73.1)
5	58.9	0.91			−175(24.1)			−15.0(25.1)
6	35.7	0.91			−174(25.5)		$4.96 \cdot 10^{-3}$(0.017)	−17.8(28.3)
7	302	0.95			−194.3(11.2)			

[a]Statistical F.
[b]Correlation coefficient.
Standard deviations are given in parentheses.

π^* parameter and log $t_{1/2}$ for the aromatic route. The same trend it has been described for rate and equilibrium constant for the formation of Meisenheimer complexes when changing from polar protic solvents to dipolar aprotic solvents (Vinson et al., 1983; El Guesmi et al., 2013; Gazitúa et al., 2014).

Finally, with the aim of achieving a more degradation, we have performed a study to investigate the effect of green activation techniques on the degradation of this pesticide in some conventional and greener solvents. Thus, the reaction under study was carried out in three ionic liquids, four bio-based solvents, and two conventional solvents under microwave

heating and ultrasonic waves. We tried to perform the reactions under MW and US during the same period of time, but after 1 h of MW irradiation many of the reactions had finished, for that reason, we chose to perform the experiments for 30 min at 50°C. To contrast with activation techniques, the reactions were carried out in silent conditions, *ie*, no irradiation at room temperature to 60 min.

Figure 9, illustrates the percentage (%) of resting Diazinon calculated by integration of signals of ^{31}P NMR after 60 min of silent conditions, 60 min of ultrasound waves and 30 min of microwave heating at 50°C.

FIGURE 8 | plot of log $t_{1/2}$ against π^* parameter, obtained for the degradation of 1 by S_NAr route in several solvents.

FIGURE 9 | Percentage (%) of resting Diazinon after 30 min of microwave (MW) heating and 60 min of ultrasound (US)waves and silent conditions.
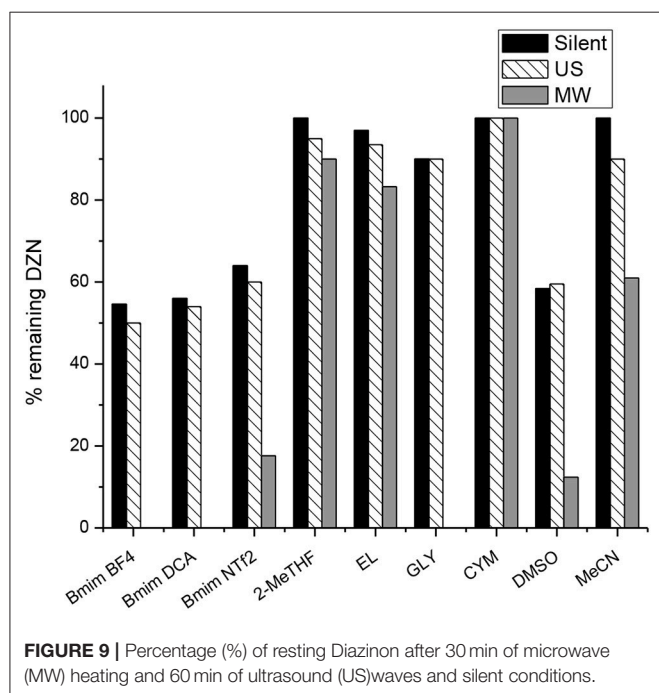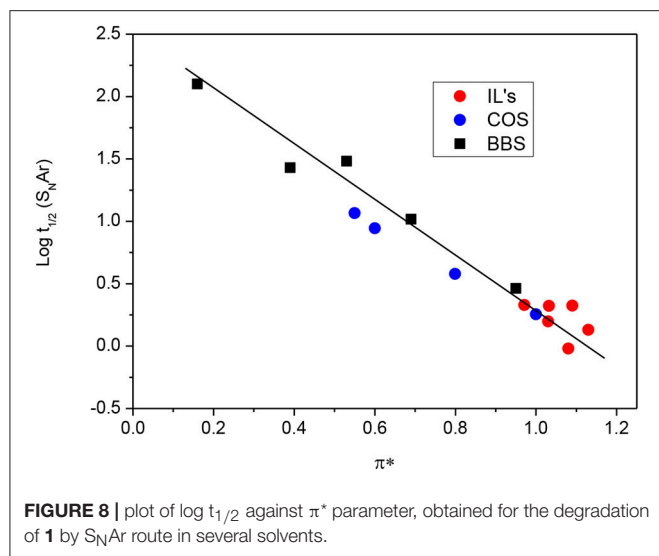
The comparative graph (**Figure 9**) shows that the best technique to degrade Diazinon was by MW irradiation, whilst the best solvents to carry out the degradation under microwave heating were Ionic Liquids and Glycerol. It can be observed that similar % of resting Diazinon are obtained in silent conditions and with the ultrasound bath. These results can be attributed to the low ultrasonic power delivered by the bath in comparison with MW.

Degradation assisted by US and MW in bio-based solvents, with exception of glycerol, shown that it occurs very slowly independent of the activation method used. For example, when CYM is the solvent there is no degradation during the experiment time, even with MW irradiation. It is worth to highlight the

contrasting behavior of glycerol under US and MW irradiation in this reaction. Since glycerol is a polar molecule with high viscosity, high acoustic impedance and a loss tangent of 0.651 in addition to its surface tension, it was expected a comparable performance under both activation techniques (Cintas et al., 2014; García et al., 2014). However, US waves seem not to affect degradation of Diazinon in this solvent. Despite the physical properties of glycerol enhances the cavitational collapse the viscosity is a drawback, which is usually overcome by conventional heating or microwave activation (Kappe, 2004). In this context, a great performance is observed under MW heating where 100% of degradation is obtained after 30 min of heating.

On the other hand, when DMSO and MeCN are the reaction media, degradation under US and silent conditions are quite close in these solvents, but again the polarizable DMSO takes advantage when heating under MW.

Regarding the ionic liquids used under MW irradiation, BmimBF$_4$ and BmimDCA showed a complete degradation in 30 min of heating whilst when BmimNTF$_2$ is the solvent still remains 18% of Diazinon after the time of irradiation.

Finally, results obtained in ILs and GLY with MW are in accordance with those reports where a synergetic behavior of ILs and GLY in combination with MW have been found (Hu et al., 2010; Cintas et al., 2014). Due to MW heat up molecules or ions through friction, the presence of ions and/or polar molecules is necessary for substances to be heated in the microwave (Hoffmann et al., 2003).

CONCLUSIONS

Degradation of Diazinon by nucleophilic reactions with piperidine in ILs, bio-based solvents and conventional solvents have been investigated at room temperature and under Ultrasound and Microwave irradiation. In silent conditions, the best solvents for degradation of Diazinon were ILs, which not only have the lowest $t_{1/2}$ values but show selectivity to the aliphatic route, reaching 70% of preference in BmimDCA. The $S_N2(C)$ pathway leads to phosphate products less lipophilic and therefore less toxic to the human being.

A comparison between Ultrasound and Microwaves activation techniques shows that degradation of Diazinon proceed faster under Microwave irradiation and furthermore it was found a synergetic combination when using ionic liquids and glycerol as reaction media.

Finally, it is difficult to choose the best solvent to carry out the degradation since both ionic liquids and glycerol have a good performance under MW heating, but considering that ionic liquids are versatile solvents which can be tuned to specific reactions, we conclude that the more efficient way for the degradation of Diazinon is the microwave-assisted using ionic liquids as solvents.

AUTHOR CONTRIBUTIONS

DM contributed conception and design of the study as well as experimental work. PP and DM organized the database and performed the statistical analysis. DM wrote the first draft. All

authors contributed to manuscript revision, read and approved the submitted version.

SUPPLEMENTARY MATERIAL

The Supplementary Material for this article can be found online at: https://www.frontiersin.org/articles/10.3389/fchem.2018.00669/full#supplementary-material

Electronic Supplementary Information (ESI)

Stacked ^{31}P NMR plot for the reaction of Diazinon with piperidine in all solvents, GC/MS and ESI-MS chromatograms and mass spectra, experimental procedure and kinetics results are available.

REFERENCES

Bavcon Kralj, M., Franko, M., and Trebše, P. (2007). Photodegradation of organophosphorus insecticides - investigations of products and their toxicity using gas chromatography-mass spectrometry and AChE-thermal lens spectrometric bioassay. *Chemosphere* 67, 99–107. doi: 10.1016/j.chemosphere.2006.09.039

Casida, J. E., and Quistad, G. B. (2004). Organophosphate toxicology: safety aspects of nonacetylcholinesterase secondary targets. *Chem. Res. Toxicol.* 17, 983–998. doi: 10.1021/tx0499259

Chatel, G., and MacFarlane, D. R. (2014). Ionic liquids and ultrasound in combination: synergies and challenges. *Chem. Soc. Rev.* 43, 8132–8149. doi: 10.1039/C4CS00193A

Cintas, P., Tagliapietra, S., Calcio Gaudino, E., Palmisano, G., and Cravotto, G. (2014). Glycerol: a solvent and a building block of choice for microwave and ultrasound irradiation procedures. *Green Chem.* 16:1056. doi: 10.1039/c3gc41955j

Cravotto, G., and Cintas, P. (2006). Power ultrasound in organic synthesis: moving cavitational chemistry from academia to innovative and large-scale applications. *Chem. Soc. Rev.* 35, 180–196. doi: 10.1039/B503848K

Cravotto, G., and Cintas, P. (2007). The combined use of microwaves and ultrasound: improved tools in process chemistry and organic synthesis. *Chem. A Eur. J.* 13, 1902–1909. doi: 10.1002/chem.200601845

D'Anna, F., Marullo, S., Vitale, P., and Noto, R. (2012). Synthesis of aryl azides: a probe reaction to study the synergetic action of ultrasounds and ionic liquids. *Ultrason. Sonochem.* 19, 136–142. doi: 10.1016/j.ultsonch.2011.06.010

Deng, S., Chen, Y., Wang, D., Shi, T., Wu, X., Ma, X., et al. (2015). Rapid biodegradation of organophosphorus pesticides by Stenotrophomonas sp. G1. *J. Hazard. Mater.* 297, 17–24. doi: 10.1016/j.jhazmat.2015.04.052

El Guesmi, N., Berionni, G., and Asghar, B. H. (2013). Electronic and solvent effects on kinetics of SNAr substitution reactions of substituted anilines with 2,6-bis(trifluoromethanesulfonyl)-4-nitroanisole in MeOH-Me2SO mixtures of varying composition: one reaction with two mechanistic pathways. *Monatshefte fur. Chem.* 144, 1537–1545. doi: 10.1007/s00706-013-1030-7

Gan, Q., Singh, R. M., and Jans, U. (2006). Degradation of naled and dichlorvos promoted by reduced sulfur species in well-defined anoxic aqueous solutions. *Environ. Sci. Technol.* 40, 778–783. doi: 10.1021/es051482n

García, J. I., García-Marín, H., and Pires, E. (2014). Glycerol based solvents: synthesis, properties and applications. *Green Chem.* 16:1007. doi: 10.1039/c3gc41857j

Gazitúa, M., Tapia, R. A., Contreras, R., and Campodónico, P. R. (2014). Mechanistic pathways of aromatic nucleophilic substitution in conventional solvents and ionic liquids. *New J. Chem.* 38:2611. doi: 10.1039/c4nj00130c

Hallett, J. P., and Welton, T. (2011). Room-temperature ionic liquids: solvents for synthesis and catalysis. 2. *Chem. Rev.* 111, 3508–76. doi: 10.1021/cr1003248

Hoffmann, J., Nüchter, M., Ondruschka, B., Wasserscheid, P., Dupont, J., Seddon, K. R., et al. (2003). Ionic liquids and their heating behaviour during microwave irradiation – a state of the art report and challenge to assessment. *Green Chem.* 5, 296–299. doi: 10.1039/B212533A

Hu, H., Hao, Y., Huang, P., Cui, D., Peng, Y., Zhang, J., et al. (2010). Unique role of ionic liquid in microwave-assisted synthesis of monodisperse magnetite nanoparticles. *Chem. Commun.* 46, 3866–3868. doi: 10.1039/b927321b

Jessop, P. G., Jessop, D. A., Fu, D., and Phan, L. (2012). Solvatochromic parameters for solvents of interest in green chemistry. *Green Chem.* 14, 1245–1259. doi: 10.1039/c2gc16670d

Kamlet, M. J., Abboud, J. L., and Taft, R. W. (1977). The solvatochromic comparison method. 6. The.pi.* scale of solvent polarities. *J. Am. Chem. Soc.* 99, 6027–6038. doi: 10.1021/ja00460a031

Kamlet, M. J., Abboud, J. L. M., Abraham, M. H., and Taft, R. W. (1983). Linear solvation energy relationships. 23. A comprehensive collection of the solvatochromic parameters, π^*, α, and β, and some methods for simplifying the generalized solvatochromic equation. *J. Org. Chem.* 48, 2877–2887. doi: 10.1021/jo00165a018

Kappe, C. O. (2004). Controlled microwave heating in modern organic synthesis. *Angew. Chemie Int. Ed.* 43, 6250–6284. doi: 10.1002/anie.200400655

Kodaka, R., Sugano, T., Katagi, T., and Takimoto, Y. (2003). Clay-catalyzed nitration of a carbamate fungicide diethofencarb. *J. Agric. Food Chem.* 51, 7730–7737. doi: 10.1021/jf0346049

MacMillan, D. S., Murray, J., Sneddon, H. F., Jamieson, C., Watson, A. J. B., Scott, J. P., et al. (2013). Evaluation of alternative solvents in common amide coupling reactions: replacement of dichloromethane and N,N-dimethylformamide. *Green Chem.* 15:596. doi: 10.1039/c2gc36900a

Mancini, P. M. E., Martinez, R. D., Vottero, L. R., and Nudelman, N. S. (1984). Solvent effects on aromatic nucleophilic substitutions. Part 3.1 The kinetics of the reaction of 2,4-dinitrochlorobenzene with piperidine in aprotic solvents. *J. Chem. Soc. Perkin Trans.* 2, 1133–1138.

Martinez, R. D., Mancini, P. M. E., Vottero, L. R., and Nudelman, N. S. (1986). Solvent effects on aromatic nucleophilic substitutions. Part 4. Kinetics of the reaction of 1-chloro-2,4-dinitrobenzene with piperidine in protic solvents. *J. Chem. Soc. Perkin Trans. 2* 0, 1427–1431. doi: 10.1039/P29860001427

Matouq, M. A., Al-Anber, Z. A., Tagawa, T., Aljbour, S., and Al-Shannag, M. (2008). Degradation of dissolved diazinon pesticide in water using the high frequency of ultrasound wave. *Ultrason. Sonochem.* 15, 869–874. doi: 10.1016/j.ultsonch.2007.10.012

Menger, F. M., and Rourk, M. J. (1999). Deactivation of mustard and nerve agent models via low-temperature microemulsions. *Langmuir* 15, 309–313. doi: 10.1021/la980910i

Onyido, I., Swierczek, K., Purcell, J., and Hengge, A. C. (2005). A concerted mechanism for the transfer of the thiophosphinoyl group from aryl dimethylphosphinothioate esters to oxyanionic nucleophiles in aqueous solution. *J. Am. Chem. Soc.* 127, 7703–7711. doi: 10.1021/ja0501565

Ortiz-Hernández, M. L., Quintero-Ramírez, R., Nava-Ocampo, A. A., and Bello-Ramírez, A. M. (2003). Study of the mechanism of *Flavobacterium* sp. for hydrolyzing organophosphate pesticides. *Fundam. Clin. Pharmacol.* 17, 717–723. doi: 10.1046/j.1472-8206.2003.00202.x

Papadopoulos, C., Frontistis, Z., Antonopoulou, M., Venieri, D., Konstantinou, I., and Mantzavinos, D. (2016). Sonochemical degradation of ethyl paraben in environmental samples: Statistically important parameters determining kinetics, by-products and pathways. *Ultrason. Sonochem.* 31, 62–70. doi: 10.1016/j.ultsonch.2015.12.002

Pavez, P., Millán, D., Morales, J. I., Castro, E., a., López, A., C., and Santos, J. G. (2013). Mechanisms of degradation of paraoxon in different ionic liquids. *J. Org. Chem.* 78, 9670–9676. doi: 10.1021/jo401351v

Pavez, P., Oliva, G., and Millán, D. (2016). Green solvents as a promising approach to degradation of organophosphorate pesticides. *ACS Sustain. Chem. Eng.* 4, 7023–7031. doi: 10.1021/acssuschemeng.6b01923

Richins, R. D., Kaneva, I., Mulchandani, A., and Chen, W. (1997). Biodegradation of organophosphorus pesticides by surface-expressed organophosphorus hydrolase. *Nat. Biotechnol.* 15, 984–987. doi: 10.1038/nbt1097-984

Rougier, N. M., Vico, R. V., de Rossi, R. H., and Buján, E. I. (2010). Reactivity of the insecticide fenitrothion toward O and N nucleophiles. *J. Org. Chem.* 75, 3427–3436. doi: 10.1021/jo100541y

Sheldon, R. A. (2005). Green solvents for sustainable organic synthesis: state of the art. *Green Chem.* 7, 267–278. doi: 10.1039/b418069k

Singh, B. K. (2009). Organophosphorus-degrading bacteria: ecology and industrial applications. *Nat. Rev. Microbiol.* 7, 156–164. doi: 10.1038/nrmicro2050

Singh, N., Karpichev, Y., Tiwari, A. K., Kuca, K., and Ghosh, K. K. (2015). Oxime functionality in surfactant self-assembly: an overview on combating toxicity of organophosphates. *J. Mol. Liq.* 208, 237–252. doi: 10.1016/j.molliq.2015.04.010

Vinson, J. A., Evans, J. F., and Holets, H. E. (1983). Spot test and colorimetric determination of amines with trinitrobenzene. *Mikrochim. Acta* 81, 301–306. doi: 10.1007/BF01196714

Yang, J., Tan, J.-N., and Gu, Y. (2012). Lactic acid as an invaluable bio-based solvent for organic reactions. *Green Chem.* 14:3304. doi: 10.1039/c2gc36083g

Yao, J., Gao, N., Deng, Y., Ma, Y., Li, H., Xu, B., et al. (2010). Ultrasonics sonochemistry sonolytic degradation of parathion and the formation of byproducts. *Ultrason. Sonochem.* 17, 802–809. doi: 10.1016/j.ultsonch.2010.01.016

Zhang, Y., Xiao, Z., Chen, F., Ge, Y., Wu, J., and Hu, X. (2010). Ultrasonics Sonochemistry Degradation behavior and products of malathion and chlorpyrifos spiked in apple juice by ultrasonic treatment. *Ultrason. Sonochem.* 17, 72–77. doi: 10.1016/j.ultsonch.2009.06.003

Nano- and Macroscale Study of the Lubrication of Titania Using Pure and Diluted Ionic Liquids

Peter K. Cooper[1][†], Joe Staddon[1][†], Songwei Zhang[2], Zachary M. Aman[3], Rob Atkin[1]* and Hua Li[1]*

[1] School of Molecular Sciences, University of Western Australia, Crawley, WA, Australia, [2] State Key Laboratory of Solid Lubrication, Lanzhou Institute of Chemical Physics, Chinese Academy of Sciences, Lanzhou, China, [3] Fluid Science and Resources, Department of Chemical Engineering, University of Western Australia, Crawley, WA, Australia

Titanium is a strong, corrosion-resistant light—weight metal which is poised to replace steel in automobiles, aircraft, and watercraft. However, the titanium oxide (titania) layer that forms on the surface of titanium in air is notoriously difficult to lubricate with conventional lubricants, which restricts its use in moving parts such as bearings. Ionic liquids (ILs) are potentially excellent lubricants for titania but the relationship between IL molecular structure and lubricity for titania remains poorly understood. Here, three-ball-on-disk macrotribology and atomic force microscopy (AFM) nanotribology measurements reveal the lubricity of four IL lubricants: trioctyl(2-ethylhexyl)phosphonium bis(2-ethylhexyl)phosphate ($P_{8,8,8,6(2)}$ BEHP), trihexyl(tetradecyl)phosphonium bis(2-ethylhexyl)phosphate ($P_{6,6,6,14}$ BEHP), trihexyl(tetradecyl)phosphonium bis(2,4,4-trimethylpentyl)phosphinate ($P_{6,6,6,14}$ ($^{i}C_8)_2PO_2$), and trihexyl(tetradecyl)phosphonium bis(trifluoromethylsulfonyl)imide ($P_{6,6,6,14}$ TFSI). The macrotribology measurements demonstrated that friction decreased in $P_{6,6,6,14}$ TFSI by four times ($\mu = 0.13$) compared to in hexadecane, even at 60°C and loads up to 10 N. On the other hand, $P_{8,8,8,6(2)}$ BEHP reduced friction most effectively in the AFM nanotribology measurements. The results were interpreted in terms of the lubrication regime. The lower viscosity of $P_{6,6,6,14}$ TFSI coupled with its good boundary lubrication made it the most effective IL for the macrotribology measurements, which were in the mixed lubrication regime. Conversely, the cation structure of $P_{8,8,8,6(2)}$ BEHP allowed it to adsorb strongly to the surface and minimized energy dissipation in the nanotribology measurements, although its high bulk viscosity inhibited its performance in the mixed regime. These results reinforce the importance of carefully selecting IL lubricants based on the lubrication regime of the sliding surfaces.

Keywords: titanium, lubrication, friction mechanism, atomic force microscopy, nanotribology, light-weight metal

INTRODUCTION

Recent interest in optimizing efficiency in machines has led to a strong desire to replace steel with light—weight materials. Titanium is an attractive candidate, with the highest strength-to-density ratio of any metallic element, and excellent resistance to corrosion and heat (Budinski, 1991). These properties make titanium an exceptional material for stationary parts in machinery and are why it

is increasingly adopted in automobiles, aircraft, and watercraft (Schutz and Scaturro, 1991; Boyer, 1996; Faller and Froes, 2001).

A critical drawback of titanium is its poor lubrication. Conventional lubricant additives such as zinc dialkyldithiophosphate (ZDDP) do not lubricate titanium well, which restricts its use in moving parts such as bearings (Rabinowicz and Kingsbury, 1955; Tian et al., 1989). Furthermore, titanium tends to strongly adhere to other surfaces, resulting in adhesive wear known as galling (Budinski, 1991; Dong, 2010). Presently, the best anti-wear protection comes from oxidizing the surface under very high temperatures ($>800°C$) to form a corrosion resistant titanium dioxide (titania) film (Qu et al., 2009; Bailey and Sun, 2013). Apart from being expensive, this treatment is potentially ineffective over long periods of time (Bansal et al., 2013). A more desirable solution involves using a liquid lubricant which can reduce friction and wear, as well as dispersing wear particles and dissipating heat generated from friction.

Ionic liquids (ILs) are potentially excellent lubricants for titania. ILs are pure salts that are liquid at low temperatures. Their exceptional physical properties including high thermal stability and negligible vapor pressures mean that they can be used in high temperature or low pressure environments such as outer space (Kobayashi et al., 2015; Nancarrow and Mohammed, 2017). Furthermore, ILs interact strongly with themselves and surfaces via electrostatic, van der Waals, h-bonding and solvophobic interactions (Jiang et al., 2018). This rich range of interactions enables them to act as highly effective boundary lubricants, where both the cation and anion adsorb strongly to a wide variety of surfaces and form a protective lubricating film. Both nano- and macroscale friction and wear measurements have demonstrated that ILs effectively lubricate steel, alumina, silica and diamond—like carbon (Somers et al., 2013; Qu et al., 2015; Li et al., 2016a; Cooper et al., 2017; Cowie et al., 2017; Zhou and Qu, 2017).

In contrast to the extensive studies of ILs lubricating other surfaces, very few studies have been carried out into IL lubrication for titanium surfaces (Jiménez and Bermúdez, 2009, 2010a,b). Li et al. showed that the IL trihexyl(tetradecyl)phosphonium bis(2,4,4-trimethyl)pentylphosphinate ($P_{6,6,6,14}$ ($^iC_8$)$_2$PO$_2$) reduced the friction coefficient five times more effectively than a base oil without additives (Li et al., 2016b). Importantly, diluting the IL in a hydrocarbon oil above 2 mol% showed reduced friction almost to the same extent as the pure IL.

While some ILs have been shown to be good lubricants for titania, the relationship between IL structure and lubrication remains only partially understood. Under low loads, ILs, like conventional lubricants, protect sliding surfaces by physically separating them via hydrodynamic pressure. This is known as hydrodynamic lubrication. If the viscosity of the lubricant is too high, however, hydrodynamic drag leads to high friction. At higher loads, the surfaces intermittently come into direct contact with each other, and friction results from a combination of hydrodynamic friction and energy lost through the surface contact. This is referred to as mixed or elastohydrodynamic lubrication. At very high loads, the liquid separating the surfaces is squeezed out, and lubrication comes from a molecularly thin layer of lubricant between the surface, and is known as boundary lubrication.

In this study, macroscale three-balls-on-disk and nanoscale AFM friction force microscopy (FFM) tribology measurements reveal that the lubricity of the IL depends strongly on the bulk viscosity as well as the IL structure. Whereas the macroscale experiment measures the average friction over a relatively large area, AFM FFM measures the friction between single asperities on the surfaces (Enachescu et al., 1998; Enachescu, 2012). Four quaternary phosphonium ILs with subtle differences in their structure were selected. Quaternary phosphonium—based ILs have attracted considerable attention as lubricants in recent years as they can dissolve in apolar hydrocarbon oils including mineral oil (Yu et al., 2012; Zhou and Qu, 2017). As an additional benefit, quaternary phosphonium—based ILs are generally very stable, hydrophobic and do not lead to severe corrosion observed in other IL lubricants (Somers et al., 2013; Zhou and Qu, 2017). In addition to the measurements of the pure ILs, measurements of the ILs diluted in a model hydrocarbon oil were also carried out to investigate their effectiveness as additives.
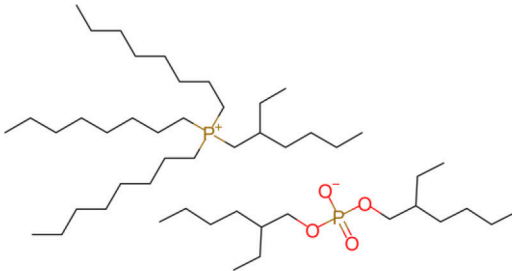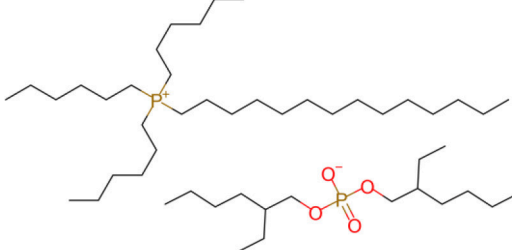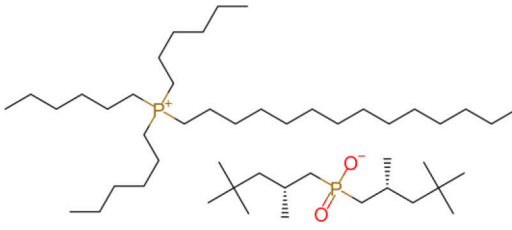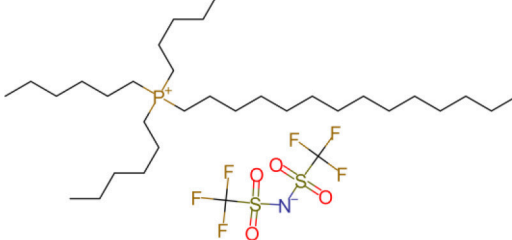
MATERIALS AND METHODS

Ionic Liquids

The ILs trihexyl(tetradecyl)phosphonium bis(2-ethylhexyl)phosphate ($P_{6,6,6,14}$ BEHP) (purity >98 %), trihexyl(tetradecyl)phosphonium bis(2,4,4-trimethylpentyl)phosphinate (henceforth referred to as $P_{6,6,6,14}$ ($^iC_8$)$_2$PO$_2$) (purity >95 %), and trihexyl(tetradecyl)-phosphonium bis(trifluoromethylsulfonyl)imide (henceforth referred to as $P_{6,6,6,14}$ TFSI) (purity >98 %) were all supplied by IoLiTec and used as received. Trioctyl(2-ethylhexyl)phosphonium bis(2-ethylhexyl)phosphate ($P_{8,8,8,6(2)}$ BEHP) was synthesized by adding an equimolar amount of trioctylphosphine dropwise to trioctylphosphate. The reaction was carried out under nitrogen at a temperature between 180 and 200°C over 30 h. The product was purified through high pressure distillation, with a yield of $\sim$75% and viscosity measured to be $\sim$1,050 mPa · s. The viscosity and molecular structure of all the ILs are provided in **Table 1**. Hexadecane (purity >99%), purchased from Sigma Aldrich was used as a hydrocarbon oil with which the friction coefficients using the ILs could be compared to.

Titanium Surface

The titanium surfaces used in the experiments were cut from a single sheet of unpolished titanium metal (Airport Metals Australia). After initial investigations on a polished titanium surface, it was decided that an unpolished, commercially available titanium surface should be used. This is a more industrially relevant surface for lubrication, and thus more suitable for macroscale friction measurements. The RMS roughness for a 5 × 5 μm scan of the titanium surface was measured to be 108 ± 16 nm by AFM.

TABLE 1 | The viscosities and molecular structures of the ILs used in this study.

Ionic liquid	Viscosity (mPa s)	Molecular structure
$P_{8,8,8,6(2)}$ BEHP	1050	
$P_{6,6,6,14}$ BEHP	1045[a] (Barnhill et al., 2014)	
$P_{6,6,6,14}$ $(^iC_8)_2PO_2$	1007[b] (Li et al., 2016a)	
$P_{6,6,6,14}$ TFSI	312[b] (Fraser et al., 2007)	

[a] Measured at 23°C.
[b] Measured at 25°C.

Macrotribology

Macroscale friction measurements were taken using a TA Instruments HR-2 rheometer with a three-balls on plate geometry using stainless-steel balls (diameter = 12.7 mm) on the titanium surface. The sliding speed was a constant 15 mm s^{-1}, and the motor mode set to "Stiff." Varying environmental conditions were used, with the temperature of the base set to 25 and 60°C, and the axial force set to 5 and 10 N. The coefficient of friction, μ, was recorded as the ratio between the lateral and normal force. Each condition was recorded for 9 m of sliding. The test in $P_{6,6,6,14}$ TFSI at 5 and 10 N was recorded for 25 m to investigate the strength of the boundary layer. The titanium surfaces were cleaned with ethanol and air dried before reuse. The friction coefficient was measured in air after cleaning to ensure that it was consistent with the friction coefficient of the fresh surface before the sliding tests. The ILs were used on different surfaces to prevent contamination.

Atomic Force Microscopy

A Veeco Nanoscope IV AFM with an EV scanner was used in contact mode. Sharp silicon tips with a spring constant of 0.8 ± 0.2 N m^{-1} as measured by the Sader method (Sader et al., 1999) and a nominal tip radius of 8 nm (HQ:NSC36/ AL BS, Mikromasch) were used in these experiments. The measurements were performed inside an AFM fluid cell (Bruker). Before each experiment the tip was irradiated with ultraviolet light for 10 min to remove any organic matter, and the surface and cell washed with ethanol and deionized water before being dried with nitrogen.

Friction measurements were performed with a scan angle of 90° (with respect to the cantilever long axis), a scan size of 500 nm and a scan rate of 5.92 Hz with the slow scan axis disabled while the normal load was increased from 0 to 200 nN. The lateral deflection signal (i.e., cantilever twist) was converted to lateral force using a customized function produced in MATLAB. This function converts the lateral voltage trace and retrace data into friction force by taking into account the torsional spring constant, and the lateral and normal deflection sensitivity. More details are provided in Pettersson and Dédinait (2008). The lateral deflection sensitivity was calculated by the method described by Schwarz et al. (1996). The friction coefficient, μ, of each data set was extracted from the linear region of the lateral force vs. normal load graph, in accordance with Amontons' Law, $F_L = \mu F_N + F_L(0)$, where $F_L(0)$ is the lateral force at zero normal load (Enachescu et al., 1999). At least three runs of increasing and decreasing load were performed for each liquid, and each run performed on a different area of the titanium. Increasing and decreasing load showed the same trend, so the decreasing load data have been omitted for clarity.

Force separation profiles were recorded for each liquid by moving the surface toward the tip and detecting the cantilever deflection as a function of separation, with at least 60 normal force curves recorded from a ramp size of 30 nm, at a scan rate of 0.2 Hz. Standard methods were used to convert deflection vs. separation data to normal force vs. apparent separation curves.

RESULTS AND DISCUSSION

Macrotribology

The macrotribology of the ILs $P_{6,6,6,14}$ BEHP, $P_{8,8,8,6(2)}$ BEHP, $P_{6,6,6,14}$ $(^iC_8)_2PO_2$ and $P_{6,6,6,14}$ TFSI was studied with a three-balls on disk tribometer. The coefficient of friction was measured over 9 m for each IL at 5 and 10 N of load at both 25 and 60°C. The balls were spun at a speed of 15 mm s^{-1}. 5 N load corresponds to a Hertzian contact stress of 0.5 GPa for each ball, while 10 N corresponds to 0.6 GPa (see **Supplementary Materials** for calculations). For comparison, the same tests were performed with hexadecane as a model, additive-free hydrocarbon oil.

The friction coefficient vs. sliding distance measured in the ILs and hexadecane is shown in **Figure 1**. Over the first 1 m, the friction coefficient varies significantly before reaching a stable value. This initial period of instability is referred to as the "break-in" period (Neale, 1995). In hexadecane, the friction coefficient increases rapidly as the unprotected surfaces are quickly worn down before it stabilizes at ~0.5 regardless of the load or temperature. This is consistent with the friction coefficient of titania in hexadecane measured in previous work (Qu et al., 2005; Li et al., 2016b). Hexadecane still lubricates the surfaces better than in air (c.f. **Figure S1**), where friction continues to increase with sliding distance since the wear debris is not transported away from the sliding zone as it is in a liquid.

Under a load of 5 N at 25°C (**Figure 1A**), the friction coefficient decreased up to 2–5 times in ILs compared to the friction coefficient in hexadecane. $P_{6,6,6,14}$ TFSI and $P_{8,8,8,6(2)}$ BEHP reduced the friction coefficient to 0.13 almost immediately

without any significant break-in period. On the other hand, in $P_{6,6,6,14}$ $(^iC_8)_2PO_2$, friction initially increased, then decreased, with low friction ($\mu = 0.13$) only observed after 2 m of sliding. Of the four ILs tested, $P_{6,6,6,14}$ BEHP was the least effective ($\mu = 0.22$), albeit still much more effective than hexadecane.

To investigate the effectiveness of the ILs under more demanding conditions, the same measurements were performed under a higher load of 10 N and the temperature increased from 25 to 60°C. Under 10 N at 25°C (**Figure 1B**), the ILs $P_{6,6,6,14}$ TFSI and $P_{6,6,6,14}$ $(^iC_8)_2PO_2$ reduced friction as effectively as they did at 5 N ($\mu = 0.13$), albeit the break-in period increased significantly from that at 5 N. Conversely, the friction coefficient for the ILs $P_{8,8,8,6(2)}$ BEHP at 10 N was much higher than at 5 N ($\mu = 0.28$ vs. 0.13). Similarly, $P_{6,6,6,14}$ BEHP demonstrated a higher friction coefficient under 10 N of load than 5 N ($\mu = 0.35$ vs. 0.22).

The tests at 60°C also revealed differences in the performance of the ILs which were not observed at 25°C. At 60°C and 5 N (**Figure 1C**), $P_{6,6,6,14}$ TFSI lubricates as well as at 25°C ($\mu = 0.13$), albeit only after 2 m of sliding. The friction coefficient in $P_{6,6,6,14}$ $(^iC_8)_2PO_2$ varied, from an initial increase to 0.30 over the first 2 m, followed by a gradual decrease in friction coefficient, eventually reaching 0.15 after 9 m. $P_{6,6,6,14}$ BEHP and $P_{8,8,8,6(2)}$ BEHP were less effective at reducing friction, with $\mu = 0.35$ in both cases. At 10 N of load (**Figure 1D**), the trends were similar to 5 N, only differing in a slightly higher friction coefficient for $P_{6,6,6,14}$ $(^iC_8)_2PO_2$, $P_{6,6,6,14}$ BEHP and $P_{8,8,8,6(2)}$ BEHP.

The measurements at higher loads and temperatures demonstrate that $P_{6,6,6,14}$ TFSI lubrication reduces friction more effectively than any of the other ILs. Longer tests reveal the durability of $P_{6,6,6,14}$ TFSI lubricity at 60°C and 10 N and are presented in **Figure 2**. Between 2 and 20 m of sliding, the friction coefficient in $P_{6,6,6,14}$ TFSI is low and stable. However, after 20 m of sliding the friction coefficient increases until it seems to stabilize at 0.25. The breakdown in lubrication has been observed previous for IL macrotribology (Li et al., 2016a). The sudden increase in friction suggests that the ball suddenly ruptures the boundary layer, which is subsequently unable to reform. Even still, after the breakdown the friction coefficient in lubrication is half of that measured in hexadecane. This indicates that lubrication between the surfaces persists, albeit perhaps only via hydrodynamic lubrication.

Mixtures of the ILs with hexadecane did not reduce friction as effectively as the pure ILs. 1 mol% mixtures of $P_{6,6,6,14}$ $(^iC_8)_2PO_2$, $P_{8,8,8,6(2)}$ BEHP and $P_{6,6,6,14}$ BEHP with hexadecane were measured at 25°C under 5 N of load and are presented in **Figure S2**. $P_{6,6,6,14}$ TFSI is immiscible with hexadecane and therefore could not be used. The mixtures did not reduce friction more effectively than hexadecane. Measurements of the mixtures at 60°C and 10 N did not show any signs of improvement over hexadecane.

While the results demonstrate that $P_{6,6,6,14}$ TFSI lubricates most effectively under all the tested conditions, it is not immediately obvious why. The thickness of the IL films was estimated to be between 18 and 74 nm by the Hamrock and Dowson model, as shown in **Table S1** (Stachowiak and Batchelor, 2005), which suggests that the ILs are in a mixed lubrication
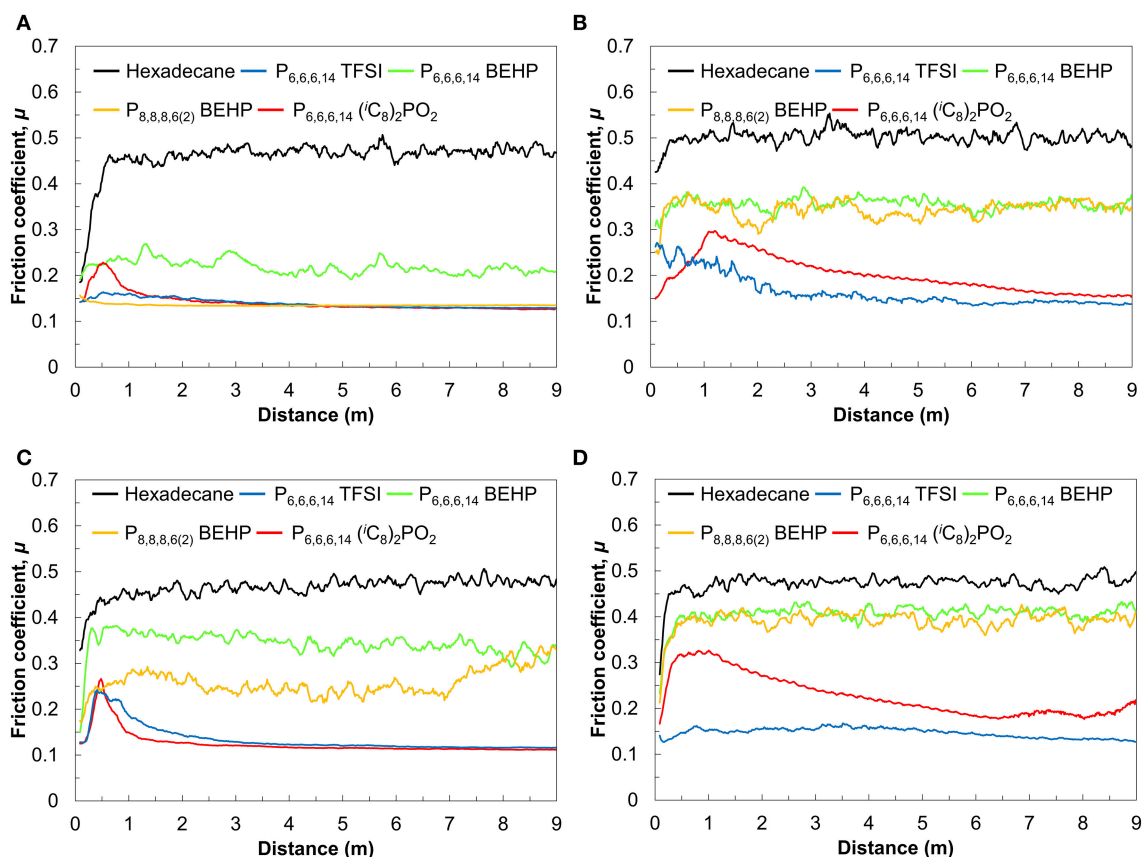
FIGURE 1 | Friction coefficient as a function of sliding distance at **(A)** 25°C and 5 N, **(B)** 25°C and 10 N, **(C)** 60°C, and 5 N, **(D)** 60°C and 10 N.
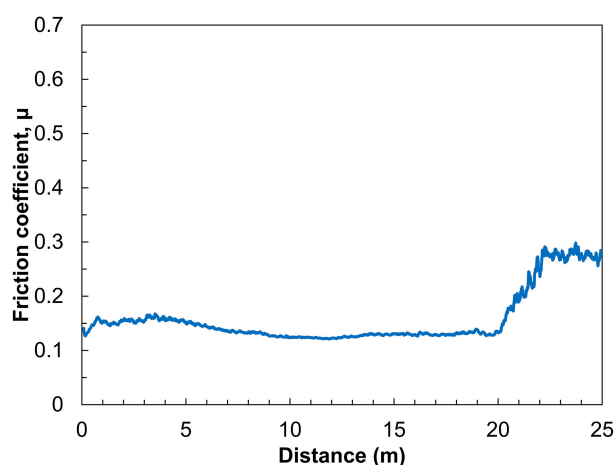

FIGURE 2 | Friction coefficient as a function of sliding distance for three stainless steel balls sliding on a titanium surface in $P_{6,6,6,14}$ TFSI. Sliding was carried out under 10 N of normal load and a temperature of 60°C.

regime (calculations provided in the **Supplementary Material**). Additionally, measuring μ vs. velocity for $P_{6,6,6,14}$ TFSI and hexadecane (c.f. **Figure S3**) reveals that the experiments were

carried out at the "trough" of the Stribeck curve i.e., in the mixed region (Stachowiak and Batchelor, 2005). In the mixed lubrication regime, friction results from a combination of intermittent direct contact between the surfaces as well as hydrodynamic losses. However, the trends in friction coefficient data do not correlate with the trends in viscosity provided in **Table 1**. This means that the ILs lubricate the direct contact between the surfaces differently via boundary lubrication, and that it is not purely hydrodynamic losses via viscosity.

Nanotribology

AFM friction force microscopy measurements were performed to disentangle the contribution from boundary layer lubrication and that of mixed layer lubrication in the macrotribology measurements. A sharp Si tip was used with the same type of titanium surface used in the macrotribology. The lateral (friction) force was recorded up to 200 nN. A 200 nN load equals a Hertzian contact stress of 18.7 GPa, assuming that the tip dimensions are not significantly altered during the friction experiments. These forces correspond to the boundary regime; calculation of the film thickness revealed an impossibly thin film (<1 pm), consistent with previous AFM boundary layer studies (Li et al., 2016a,b). In the boundary regime, the bulk of the liquid lubricant has been squeezed out, and lubrication is effected by a layer of molecules

adsorbed at the surface, called the boundary layer. Boundary lubrication is therefore independent of the bulk viscosity of the liquid.

The lateral forces experienced by the tip as it slides on the surface as a function of normal load are shown in **Figure 3**. The gradient of these data is the friction coefficient μ as per Amontons' law $F_L = F_A + \mu F_N$, where F_L is the lateral force, F_A is the force of adhesion, and F_N is the normal load. In hexadecane, the friction force increases rapidly with increasing normal load, with $\mu = 0.33$. This reveals that hexadecane is, as expected, a poor lubricant. As the tip and the surface come into contact any weakly adsorbed hexadecane is expelled resulting in direct contact between the tip and surface and high friction.

In contrast to hexadecane, $P_{8,8,8,6(2)}$ BEHP is an excellent boundary lubricant. Lateral forces increase at a lower rate with increasing normal force, resulting in a friction coefficient of 0.08, approximately four times lower than in hexadecane. $P_{6,6,6,14}$ $(^iC_8)_2PO_2$ and $P_{6,6,6,14}$ TFSI, the most effective ILs at reducing friction on the macroscale, reduced friction by about half of that measured in hexadecane ($\mu = 0.16$ and 0.17 respectively). $P_{6,6,6,14}$ BEHP did not reduce friction any more effectively than hexadecane ($\mu = 0.33$), which is consistent with it being the poorest lubricant on the macroscale. A summary of the friction coefficients measured by AFM are presented in **Table 2**.

As with the macroscale tests, 1 mol % mixtures of $P_{8,8,8,6(2)}$ BEHP, $P_{6,6,6,14}$ $(^iC_8)_2PO_2$ and $P_{6,6,6,14}$ BEHP in hexadecane did not significantly reduce friction (**Figure 3**). Previous studies of IL/oil mixtures on surfaces including titania have shown that 1–2 mol% mixtures can reduce the friction coefficient as effectively as the pure IL (Li et al., 2014, 2016b; Cooper et al., 2016). However, these reductions in friction only occur after the bulk concentration reaches a critical concentration (Li et al., 2014). Surfactant adsorption studies with titania have found that the surfactant surface excess may be half of that compared to another oxide surface such as silica (Favoriti et al., 1996). A lower surface excess means that the adsorbed boundary layer of IL will be patchy, and unable to reduce friction as effectively.

The trends in the AFM nanotribology results presented in **Figure 3** can be explained by considering the mechanisms in which energy dissipation (i.e., friction) occurs. In the boundary regime, energy dissipates mainly via (i) expulsion of the near surface IL layers from the space between the tip and the surface, and (ii) by deformations and rotations of ions in the boundary layer (Salmeron, 2001; Sweeney et al., 2014). A common feature of many ILs is the presence of layers of adsorbed ions at solid surfaces which are preferentially oriented based on the polar and apolar domains of the IL. Number of observed layers varies significantly with IL molecular structure. Previous AFM nanotribology measurements have demonstrated that the presence of these layers in ILs is inversely proportional to friction; that is, the greater the number of near surface layers, the more energy dissipates via (i) (Sweeney et al., 2014; Cooper et al., 2017).

To investigate how significant the near surface structure is in these ILs, a series of AFM normal force—separation profiles were measured for the pure ILs and the mixtures and are
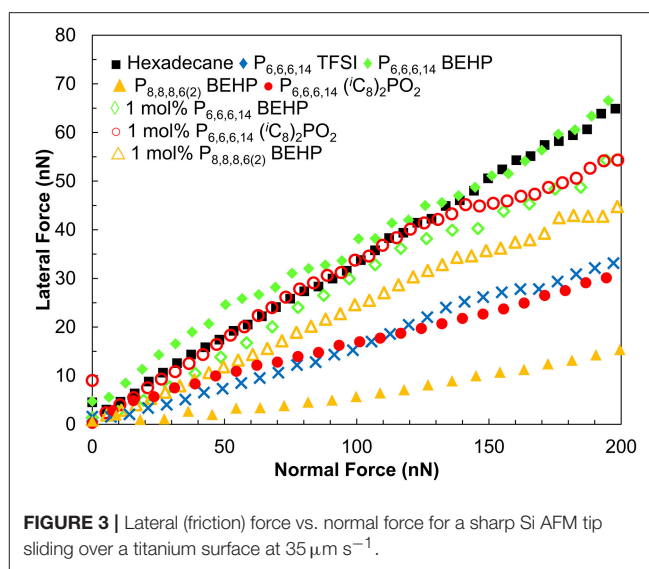

FIGURE 3 | Lateral (friction) force vs. normal force for a sharp Si AFM tip sliding over a titanium surface at $35\,\mu\mathrm{m\,s^{-1}}$.

TABLE 2 | The calculated friction coefficients of the ILs measured by AFM.

Liquid	Friction coefficient, μ
$P_{8,8,8,6(2)}$ BEHP	0.08
$P_{6,6,6,14}$ BEHP	0.33
$P_{6,6,6,14}$ $(^iC_8)_2PO_2$	0.16
$P_{6,6,6,14}$ TFSI	0.17

presented in **Figure 4**. For each IL and mixture, no significant force was measured beyond 2 nm of apparent separation between the tip and the surface. The "steps" in the force profile at closer separations indicate the presence of a single near surface layer in some cases, however, all ILs in this study are generally weakly unstructured. Based on the weak structure observed by AFM, energy dissipation via (i) cannot explain the large differences in lateral forces measured in the ILs.

The differences in the lateral forces measured by nanotribology may instead be explained by considering how the ions adsorb and pack onto the surface, which determines energy dissipation via (ii). The isoelectric point of titania is 5.7, and therefore one might expect the cation to preferentially adsorb to the surface. Nevertheless, neutron reflectometry measurements and MD simulations have revealed that oppositely charged ions still contribute to the adsorbed layer (Lauw et al., 2012; Wang et al., 2017; Cooper et al., 2018).

Considering the cations first, **Figure 2** shows that $P_{8,8,8,6(2)}$ BEHP reduces friction far more effectively than $P_{6,6,6,14}$ BEHP. The $P_{8,8,8,6(2)}^+$ cation can pack more neatly with the bulky BEHP$^-$ ion than $P_{6,6,6,14}^+$ with its long 14 C chain potentially sterically hindering one of the ions or both from adsorbing strongly on the surface. For the anions, comparing $P_{6,6,6,14}$ BEHP, $P_{6,6,6,14}$ $(^iC_8)_2PO_2$ and $P_{6,6,6,14}$ TFSI, the TFSI$^-$ and $(^iC_8)_2PO_2^-$ were approximately equally effective. This result is consistent with the results from a previous study on stainless steel (Cooper et al., 2017). The BEHP$^-$ anion in this case was the worst
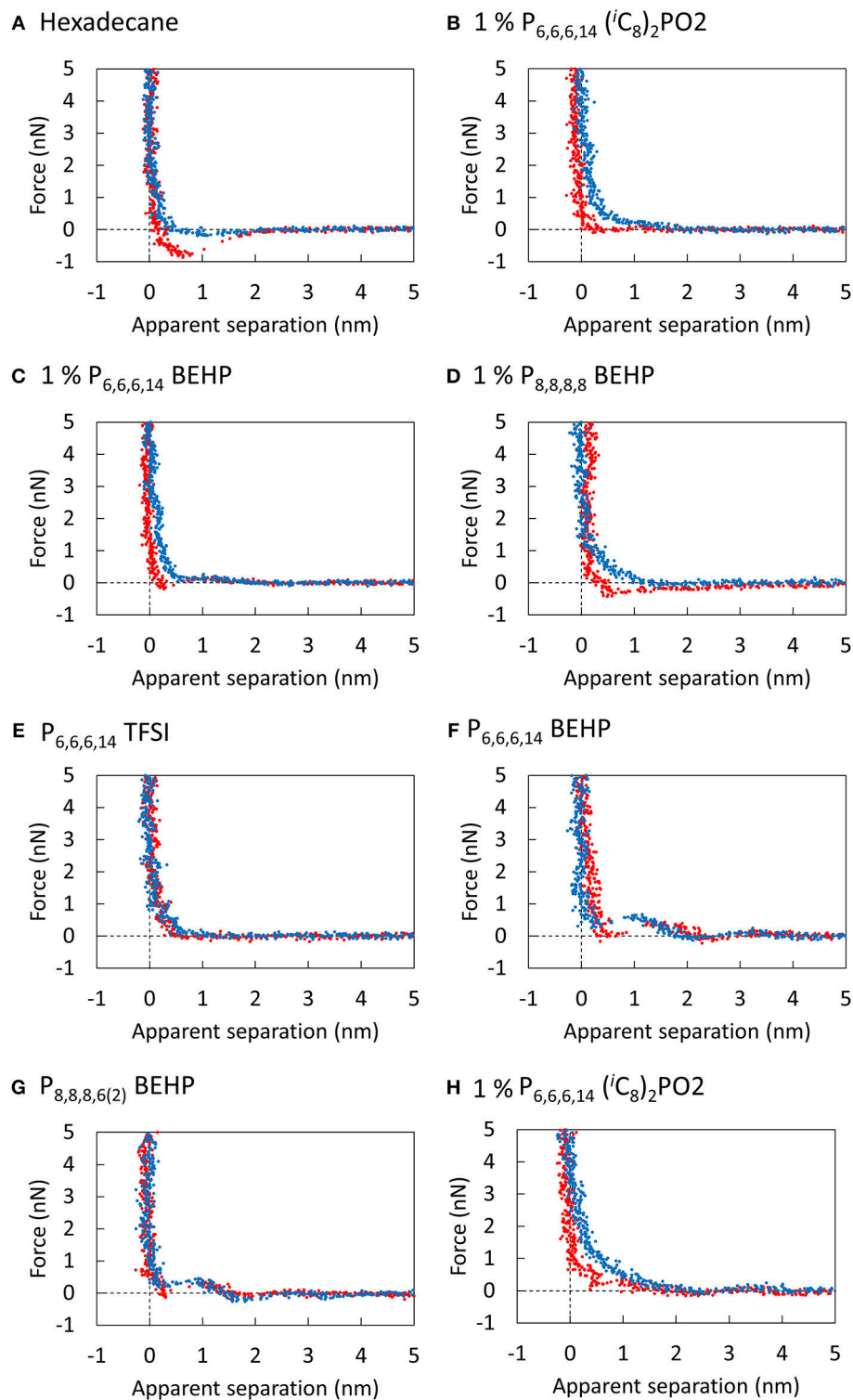
FIGURE 4 | Force curves of the silicon AFM tip approaching (blue) and retracting (red) from the unpolished titanium surface submerged in **(A)** Hexadecane, **(B)** 1% $P_{6,6,6,14}$ $(^iC_8)_2PO_2$, **(C)** 1% $P_{6,6,6,14}$ BEHP, **(D)** 1% $P_{8,8,8,6(2)}$ BEHP, **(E)** $P_{6,6,6,14}$ TFSI, **(F)** $P_{6,6,6,14}$ BEHP, **(G)** $P_{8,8,8,6(2)}$ BEHP, and **(H)** 1% $P_{6,6,6,14}$ $(^iC_8)_2PO_2$. Scan size: 30 nm.

performing of the three. Despite having an apparently similar structure to $(^iC_8)_2PO_2^-$, the longer alkyl chains of the BEHP$^-$ restrict its packing compared to the more dense $(^iC_8)_2PO_2^-$ and TFSI$^-$ anions. Indeed, MAS NMR, FITR and Raman spectroscopy measurements have shown that the interaction between the anions of quaternary phosphonium ILs and metal

oxide surfaces can vary significantly, despite similar molecular structures (Shah et al., 2018).

CONCLUSIONS

Combining the results from the macroscale tribology experiments and the nanotribology experiments gives remarkable insight into the role of IL structure on friction across both length scales. All ILs in this study were generally good lubricants for titania. However, IL lubrication performance in the nanotribology tests varied from the macrotribology tests. For the AFM nanotribology, only the structure of the ILs determines boundary lubrication. More specifically, the ability of the ions to pack into a neat, robust layer largely determined their success as nanoscale lubricants. On the other hand, for the macroscale three-ball-on-disk experiments, a combination of bulk physical properties and adsorbed boundary layer govern mixed layer lubrication. This difference is illustrated by $P_{8,8,8,6(2)}$ BEHP, which was the most effective IL in the nanotribology tests, but only the third most effective in the macrotribology tests.

For lubrication in the boundary regime lubrication, the ideal IL will adsorb strongly to the surface and form a robust film which minimizes energy dissipation. Importantly, for boundary regime lubrication the viscosity of the IL does not need to be considered. For lubrication in the mixed or hydrodynamic regime, the macrotribology measurements here show the importance of both viscosity and boundary layer lubrication. Ultimately, this work demonstrates the importance of the judicious selection of IL based on the lubrication regime operating in the sliding surfaces.

AUTHOR CONTRIBUTIONS

ACKNOWLEDGMENTS

SUPPLEMENTARY MATERIAL

The Supplementary Material for this article can be found online at: https://www.frontiersin.org/articles/10.3389/fchem.2019.00287/full#supplementary-material

Data Sheet 1 | These include the macrotribology friction coefficient vs. sliding distance measured in air, the friction coefficient vs. sliding distance measured in the 1 mol% mixtures of IL in hexadecane, the AFM force—separation curves, and the AFM lateral force vs. normal force data for the 1 mol% mixtures of the ILs.

REFERENCES

Bailey, R., and Sun, Y. (2013). Unlubricated sliding friction and wear characteristics of thermally oxidized commercially pure titanium. *Wear* 308, 61–70. doi: 10.1016/j.wear.2013.09.020

Bansal, D. G., Kirkham, M., and Blau, P. J. (2013). Effects of combined diffusion treatments and cold working on the sliding friction and wear behavior of Ti−6Al−4V. *Wear* 302, 837–844. doi: 10.1016/j.wear.2013.01.034

Barnhill, W. C., Qu, J., Luo, H., Meyer, H. M., Ma, C., Chi, M., et al. (2014). Phosphonium-organophosphate ionic liquids as lubricant additives: effects of cation structure on physicochemical and tribological characteristics. *ACS Appl. Mater. Interf.* 6, 22585–22593. doi: 10.1021/am506702u

Boyer, R. (1996). An overview on the use of titanium in the aerospace industry. *Mater. Sci. Eng. A* 213, 103–114. doi: 10.1016/0921-5093(96)10233-1

Budinski, K. G. (1991). Tribological properties of titanium alloys. *Wear* 151, 203–217. doi: 10.1016/0043-1648(91)90249-T

Cooper, P. K., Li, H., Rutland, M. W., Webber, G. B., and Atkin, R. (2016). Tribotronic control of friction in oil-based lubricants with ionic liquid additives. *Phys. Chem. Chem. Phys.* 18, 23657–23662. doi: 10.1039/C6CP04405K

Cooper, P. K., Li, H., Yepuri, N. R., Nelson, A., Webber, G. B., Le Brun, A. P., et al. (2018). Ionic liquid adsorption at the silica–oil interface revealed by neutron reflectometry. *J. Phys. Chem. C* 122, 24077–24084. doi: 10.1021/acs.jpcc.8b05952

Cooper, P. K., Wear, C. J., Li, H., and Atkin, R. (2017). Ionic liquid lubrication of stainless steel: friction is inversely correlated with interfacial liquid nanostructure. *ACS Sustain. Chem. Eng.* 5, 11737–11743. doi: 10.1021/acssuschemeng.7b03262

Cowie, S., Cooper, P. K., Atkin, R., and Li, H. (2017). Nanotribology of ionic liquids as lubricant additives for alumina surfaces. *J. Phys. Chem. C* 121, 28348–28353. doi: 10.1021/acs.jpcc.7b09879

Dong, H. (2010). "3–Tribological properties of titanium-based alloys," in *Surface Engineering of Light Alloys,* ed H. Dong (Cambridge: Woodhead Publishing), 58–80.

Enachescu, M. (2012). "Nanoscale effects of friction, adhesion and electrical conduction in AFM experiments," in *Atomic Force Microscopy—Imaging, Measuring and Manipulating Surfaces at the Atomic Scale*, ed V. Bellitto (Rijeka: Intech), 99–146.

Enachescu, M., Van Den Oetelaar, R. J. A., Carpick, R. W., Ogletree, D. F., Flipse, C. F. J., and Salmeron, M. (1998). Atomic force microscopy study of an ideally hard contact: the diamond(111)/tungsten carbide interface. *Phys. Rev.Lett.* 81, 1877–1880. doi: 10.1103/PhysRevLett.81.1877

Enachescu, M., Van Den Oetelaar, R. J. A., Carpick, R. W., Ogletree, D. F., Flipse, C. F. J., and Salmeron, M. (1999). Observation of proportionality between friction and contact area at the nanometer scale. *Tribol. Lett.* 7:73. doi: 10.1023/A:1019173404538

Faller, K., and Froes, F. H. (2001). The use of titanium in family automobiles: current trends. *J. Minerals* 53, 27–28. doi: 10.1007/s11837-001-0143-3

Favoriti, P., Monticone, V., and Treiner, C. (1996). Coadsorption of naphthalene derivatives and cetyltrimethylammonium bromide on alumina/water, titanium dioxide/water, and silica/water interfaces. *J. Coll. Interface Sci.* 179, 173–180. doi: 10.1006/jcis.1996.0199

Fraser, K. J., Izgorodina, E. I., Forsyth, M., Scott, J. L., and Macfarlane, D. R. (2007). Liquids intermediate between "molecular" and "ionic" liquids: liquid ion pairs? *Chem. Commun.* 37, 3817–3819. doi: 10.1039/B710014K

Jiang, H. J., Atkin, R., and Warr, G. G. (2018). Nanostructured ionic liquids and their solutions: recent advances and emerging challenges. *Curr. Opin. Green Sustain. Chem.* 12, 27–32. doi: 10.1016/j.cogsc.2018.05.003

Jiménez, A. E., and Bermúdez, M.-D. (2009). Ionic liquids as lubricants of titanium–steel contact. *Tribol. Lett.* 33, 111–126. doi: 10.1007/s11249-008-9396-0

Jiménez, A. E., and Bermúdez, M. D. (2010a). Ionic liquids as lubricants of titanium–steel contact. part 2: friction, wear and surface interactions at high temperature. *Tribol. Lett.* 37, 431–443. doi: 10.1007/s11249-009-9539-y

Jiménez, A. E., and Bermúdez, M. D. (2010b). Ionic liquids as lubricants of titanium–steel contact. part 3. ti6al4v lubricated with imidazolium ionic liquids with different alkyl chain lengths. *Tribol. Lett.* 40, 237–246. doi: 10.1007/s11249-010-9633-1

Kobayashi, K., Suzuki, A., Fujinami, Y., Nogi, T., Obara, S., and Masuko, M. (2015). Lubrication performance of ionic liquids as lubricants for space mechanisms under high vacuum and low temperature. *Tribol. Online* 10, 138–146. doi: 10.2474/trol.10.138

Lauw, Y., Horne, M. D., Rodopoulos, T., Lockett, V., Akgun, B., Hamilton, W. A., et al. (2012). Structure of [C4mpyr][NTf2] room-temperature ionic liquid at charged gold interfaces. *Langmuir* 28, 7374–7381. doi: 10.1021/la3005757

Li, H., Cooper, P. K., Somers, A. E., Rutland, M. W., Howlett, P. C., Forsyth, M., et al. (2014). Ionic liquid adsorption and nanotribology at the silica–oil interface: hundred-fold dilution in oil lubricates as effectively as the pure ionic liquid. *J. Phys. Chem. Lett.* 5, 4095–4099. doi: 10.1021/jz5021422

Li, H., Somers, A. E., Howlett, P. C., Rutland, M. W., Forsyth, M., and Atkin, R. (2016a). Addition of low concentrations of an ionic liquid to a base oil reduces friction over multiple length scales: a combined nano- and macrotribology investigation. *Phys. Chem. Chem. Phys.* 18, 6541–6547. doi: 10.1039/C5CP07061A

Li, H., Somers, A. E., Rutland, M. W., Howlett, P. C., and Atkin, R. (2016b). Combined nano-and macrotribology studies of titania lubrication using the oil-ionic liquid mixtures. *ACS Sustain. Chem. Eng.* 4, 5005–5012. doi: 10.1021/acssuschemeng.6b01383

Nancarrow, P., and Mohammed, H. (2017). Ionic liquids in space technology – current and future trends. *ChemBioEng Rev.* 4, 106–119. doi: 10.1002/cben.201600021

Neale, M. J. (1995). *The Tribology Handbook.* Oxford; Boston, MA: Elsevier Science.

Pettersson, T., and Dédinait,é, A. (2008). Normal and friction forces between mucin and mucin–chitosan layers in absence and presence of SDS. *J. Coll. Interface Sci.* 324, 246–256. doi: 10.1016/j.jcis.2008.04.055

Qu, J., Blau, P. J., Howe, J. Y., and Meyer, H. M. (2009). Oxygen diffusion enables anti-wear boundary film formation on titanium surfaces in zinc-dialkyl-dithiophosphate (ZDDP)-containing lubricants. *Scripta Mater.* 60, 886–889. doi: 10.1016/j.scriptamat.2009.02.009

Qu, J., Blau, P. J., Watkins, T. R., Cavin, O. B., and Kulkarni, N. S. (2005). Friction and wear of titanium alloys sliding against metal, polymer, and ceramic counterfaces. *Wear* 258, 1348–1356. doi: 10.1016/j.wear.2004.09.062

Qu, J., Meyer, H. M., Cai, Z.-B., Ma, C., and Luo, H. (2015). Characterization of ZDDP and ionic liquid tribofilms on non-metallic coatings providing insights of tribofilm formation mechanisms. *Wear* 332–333, 1273–1285. doi: 10.1016/j.wear.2015.01.076

Rabinowicz, E., and Kingsbury, E. P. (1955). Lubricants for Titanium. *Metal Progress* 67, 112–114.

Sader, J. E., Chon, J. W. M., and Mulvaney, P. (1999). Calibration of rectangular atomic force microscope cantilevers. *Rev. Sci. Instrum.* 70, 3967–3969. doi: 10.1063/1.1150021

Salmeron, M. (2001). Generation of defects in model lubricant monolayers and their contribution to energy dissipation in friction. *Tribol. Lett.* 10, 69–79. doi: 10.1023/A:1009026312732

Schutz, R. W., and Scaturro, M. R. (1991). An overview of current and candidate titanium alloy applications on US navy surface ships. *Naval Eng. J.* 103, 175–191. doi: 10.1111/j.1559-3584.1991.tb00948.x

Schwarz, U. D., Köster, P., and Wiesendanger, R. (1996). Quantitative analysis of lateral force microscopy experiments. *Rev. Sci. Instrum.* 67, 2560–2567. doi: 10.1063/1.1147214

Shah, F. U., Holmgren, A., Rutland, M. W., Glavatskih, S., and Antzutkin, O. N. (2018). Interfacial behavior of orthoborate ionic liquids at inorganic oxide surfaces probed by NMR, IR, and raman spectroscopy. *J. Phys. Chem. C* 122, 19687–19698. doi: 10.1021/acs.jpcc.8b06049

Somers, A., Howlett, P., Macfarlane, D., and Forsyth, M. (2013). A review of ionic liquid lubricants. *Lubricants* 1:3. doi: 10.3390/lubricants1010003

Stachowiak, G. W., and Batchelor, A. W. (2005). *Engineering Tribology.* Amsterdam; Boston, MA: Elsevier Butterworth-Heinemann.

Sweeney, J., Webber, G. B., Rutland, M. W., and Atkin, R. (2014). Effect of ion structure on nanoscale friction in protic ionic liquids. *Phys. Chem. Chem. Phys.* 16, 16651–16658. doi: 10.1039/C4CP02320J

Tian, H., Saka, N., and Suh, N. P. (1989). Boundary lubrication studies on undulated titanium surfaces. *Tribol. Transact.* 32, 289–296. doi: 10.1080/10402008908981891

Wang, Y.-L., Golets, M., Li, B., Sarman, S., and Laaksonen, A. (2017). Interfacial structures of trihexyltetradecylphosphonium-bis(mandelato)borate ionic liquid confined between gold electrodes. *ACS Appl. Mater. Interfaces* 9, 4976–4987. doi: 10.1021/acsami.6b14429

Yu, B., Bansal, D. G., Qu, J., Sun, X., Luo, H., Dai, S., et al. (2012). Oil-miscible and non-corrosive phosphonium-based ionic liquids as candidate lubricant additives. *Wear* 289, 58–64. doi: 10.1016/j.wear.2012.04.015

Zhou, Y., and Qu, J. (2017). Ionic liquids as lubricant additives: a review. *ACS Appl. Mater. Interfaces* 9, 3209–3222. doi: 10.1021/acsami.6b12489

Dispersion and Stabilization of Exfoliated Graphene in Ionic Liquids

Emilie Bordes [1], Bishoy Morcos [2], David Bourgogne [1], Jean-Michel Andanson [1], Pierre-Olivier Bussière [1], Catherine C. Santini [2], Anass Benayad [3], Margarida Costa Gomes [4]* and Agílio A. H. Pádua [4]*

[1] Centre National de la Recherche Scientifique, SIGMA Clermont, Institut de Chimie de Clermont-Ferrand, Université Clermont Auvergne, Clermont-Ferrand, France, [2] UMR 5265 Centre National de la Recherche Scientifique, Université de Lyon, Villeurbanne, France, [3] Université Grenoble Alpes and CEA, LITEN, Grenoble, France, [4] École Normale Supérieure de Lyon, Centre National de la Recherche Scientifique, Laboratoire de Chimie, Lyon, France

The liquid-phase exfoliation of graphite is one of the most promising methods to increase production and commercial availability of graphene. Because ionic liquids can be easily obtained with chosen molecular structures and tuneable physicochemical properties, they can be use as media to optimize the exfoliation of graphite. The understanding of the interactions involved between graphite and various chemical functions in the solvent ions will be helpful to find liquids capable of dissociating and stabilizing important quantities of large graphene layers. After a step of sonication, as a mechanical precursor, samples of suspended exfoliated graphene in different ionic liquids have been characterized experimentally in terms of flake size, number of layers, total concentration and purity of the exfoliated material. Nine different ionic liquids based on imidazolium, pyrrolidinium and ammonium cations and on bis(trifluoromethylsulfonyl)imide, triflate, dicyanamide, tricyanomethanide, and methyl sulfate anions have been tested. UV-vis, Raman and X-ray photoelectron in addition to high resolution transmission electron and atomic force microscopy have been selected to characterize suspended exfoliated graphene in ionic liquids. The number of layers in the flakes exfoliated, the size and concentration depend of the structure of the ionic liquid selected. In order to obtain large flake sizes, ionic liquids with bis(trifluoromethylsulfonyl)imide anions and a cation with an alkyl chain of medium length should be selected. Smaller cation and anion favors the exfoliation of graphene. The exfoliation caused the formation of C-H bonds and the oxidation of the graphitic surface.

Keywords: exfoliation, graphene, graphite, ionic liquids, suspension

1. INTRODUCTION

Since its isolation in 2004 (Novoselov, 2004), graphene has showed superior mechanical (Lee et al., 2008), electrical (Mayorov et al., 2011), and thermal (Mak et al., 2010) properties (Novoselov et al., 2012). Graphene is the first 2D-material available to us. Its remarkable properties make it useful in many applications in diverse fields such as energy storage with batteries (Raccichini et al., 2014), electronics with transistors (Kelly et al., 2017), photonics with photodetectors (Blake et al., 2008), coating with composites (Young et al., 2012) or biomedical with drug delivery (Nair et al., 1993). Graphite is a stack of graphene sheets bound by van der Waals interactions, each graphene layer being made of sp² carbons distributed in a hexagonal crystal structure. Today, two approaches are

known to produce graphene: in "bottom-up" methods, such as chemical vapor deposition (CVD), graphene is synthesized, whereas in "top-down" methods, for example liquid-phase exfoliation, graphene sheets are separated from bulk material. The first approach produces low quantities with high quality and large flakes. The second method (top-down) using graphite is low in cost and yields a high concentration of suspended flakes but fabricates limited-size sheets with a low yield of mono-layer graphene. The development of technologies to produce large quantities of high-quality exfoliated graphene is important. One way to achieve a large scalable production is to improve methods of the liquid-phase exfoliation of graphite.

Direct exfoliation of graphite in liquid media using a mechanical precursor is a promising approach in order to increase the production and the commercial availability of high-quality graphene. Various techniques (ultrasound Hernandez et al., 2008, ball-milling Zhao et al., 2010, microwaves Wang et al., 2011) and solvents such organic solvents (Hernandez et al., 2008), water/surfactants (Lotya et al., 2009), supercritical fluids Pu et al., 2009, or ionic liquids (ILs) Wang et al., 2010 have been studied in order to produce a large graphene sheets in high quality and concentration. To determine the best solvents to overcome the van der Walls interactions between two graphene layers, the surface tension of different liquids has been investigated. Hernandez et al. (2008) and Coleman (2013) have studied forty molecular solvents as media to exfoliate graphite *via* sonication and characterized them by the fraction of graphite/graphene remaining after centrifugation. They observed that solvents with a high ability to disperse graphite are the ones having a surface tensions between 40 and 50 mNm^{-1}. N-methyl-2-pyrrolidone (NMP) has stabilized a high concentration of graphene flakes compared to other solvents (Coleman, 2013). However some solvents with a surface tension in the 40–50 mN m^{-1} range do not necessary achieve high level of exfoliation. Interfacial energies graphite-solvent are thus not the only descriptor to predict a good candidate for exfoliation of graphite. ILs have demonstrated efficiency to disperse graphene derivatives such as carbon nanotubes (Chen et al., 2007; Fukushima and Aida, 2007; Wang et al., 2008; Shim and Kim, 2009; Peng et al., 2013) or fullerene (Szala-Bilnik et al., 2016). The electrostatic interactions present in the ILs would be responsible for the solvating results of the graphitic planes through favorable interactions between ions and the polarisable electrons in graphene, in particular cation-π interactions.

Ionic liquids (ILs) are liquid salts below 373 K (Seddon, 1997; Hallett and Welton, 2011), generally constituted of a bulky organic cation with an inorganic or organic anion. ILs can be easily obtained with chosen molecular structures in function of the intended application. Their very low vapor pressure makes the ILs less hazardous (reduction of flammability) than organic solvents in general. Among the most representative properties are their ionicity (Hollóczki et al., 2014), their chemical and thermal stability, their large electrochemical window (Armand et al., 2009) and ease of recycling. A large number of ion combinations is possible, leading to a wide range of physicochemical properties (Deetlefs et al., 2006). Inks (Kelly et al., 2017), supercapacitors (Chen et al., 2011, 2012; Tsai et al., 2013; Li et al., 2016; Liu et al.,

2017), filter sponges (Zambare et al., 2017), graphene-polymer composites (Peng et al., 2013; Saurín et al., 2016; Wang et al., 2017) belong to the list where graphene and graphite meet ionic liquids for application purposes.

The direct exfoliation of graphite (without an oxydation step) has been reported in ILs with promising results. In 2010, Wang et al. (2010) were the first group to study the exfoliation of graphite using two ILs; 1-butyl-3-methylimidazolium bis(trifluoromethanesulfonyl)imide ([C$_4$C$_1$im][Ntf$_2$]) and 1-butyl-1-methylpyrrolidinium bis(trifluoromethanesulfonyl)imide ([Pyrr$_{4,1}$][Ntf$_2$]). The exfoliation conditions are summed up in **Table 1**. According to the results obtained by X-ray photoelectron spectroscopy (XPS), the exfoliation did not lead to any major oxidation to graphene flakes. In the same year, 1-hexyl-3-methyl-imidazolium hexafluorophosphate ([C$_6$C$_1$im][PF$_6$]) was also used to exfoliate graphite using an ultrasound technique (Nuvoli et al., 2011). The authors demonstrated that a longer sonication time and a high initial concentration are favorable conditions to achieve higher concentrations of exfoliated graphene.

New ILs have been synthesized for the specific needs of graphene exfoliation. The approach of Bari et al. (2014) was to functionalise an imidazolium cation with one or two benzyl groups in order to create π-π interactions in contact with graphenic planes. Ultrasound was used to supply energy for exfoliation of graphite into suspensions. Four different ILs were investigated: 1-benzyl-3-methylimidazolium bis(trifluoromethylsulfonyl)imide ([BnzC$_1$im][Ntf$_2$]), [C$_4$C$_1$im][Ntf$_2$], 1-benzyl-3-metylimidazolium bromide ([BnzC$_1$im][Br]) and 1,3-bis(phenylmethyl)imidazolium bis(trifluoromethylsulfonyl)imide ([(Bnz)$_2$im][Ntf$_2$]). The concentration of graphene in suspension was measured by UV-vis absorbance spectroscopy. [BnzC$_1$im][Br] has a viscosity that was judged too high to disperse graphite. The concentration of suspended graphene in the [C$_4$C$_1$im][Ntf$_2$] was too low to be detected by absorbance with the author's set up. [(Bnz)$_2$im][Ntf$_2$] stabilized a larger amount of graphene over [BnzC$_1$im][Ntf$_2$] (values are listed in **Table 1**). This results were explained by *ab initio* calculations, as both benzyl groups of [(Bnz)$_2$im][Ntf$_2$] were found oriented parallel to the surface of graphene unlike the single benzyl substituent in [BnzC$_1$im][Ntf$_2$] (Bari et al., 2014). No statistical study was actually carried out to characterize this heterogeneous suspension, either in terms of lateral size of the flakes or the number of layers of exfoliated graphene. A better understanding of the efficacy of ILs to exfoliate graphene is needed.

In 2015, Matsumoto et al. (2015) developed a fast and effective method to exfoliate natural graphite. A 25 mg mL^{-1} suspension of graphite powder in an oligomeric IL with repeating units of [(ethoxy)im][PF$_6$], was exfoliated using microwaves during 0.5 h. The mixture reached the temperature of 443 K. By proton NMR the authors showed that 10% of the IL was degraded. Graphene had no additional structural defects and 95% of the flakes produced were single-layer graphene. The same protocol was used in [C$_4$C$_1$im][PF$_6$] but with a lower exfoliation rate.

In 2016, Elbourne et al. (2016) explored the spontaneous exfoliation of a highly oriented pyrolytic graphite (HOPG)

TABLE 1 | Comparison of ILs used for the direct exfoliation of graphite in the liquid phase.

ILs	Exfoliation set up	Yield	Size	Nbr. layer
$[C_4C_1im][Ntf_2]$ (Wang et al., 2010)	Ultrasound(750 W)/1 h + 10,000 rpm/1 h	47.5%	$\approx \mu m$	1–5
$[Pyrr_{4,1}][Ntf_2]$ (Wang et al., 2010)	"	"	"	"
$[C_6C_1im][PF_6]$ (Nuvoli et al., 2011)	Ultrasound(550 W)/24 h + 4,000 rpm/0.33 h	8.17%	3-4 μm	1–5
$[C_4C_1im][Ntf_2]$ (Bari et al., 2014)	Ultrasound(10 W)/1 h + 5,000 rpm/6 h	unstable	n/a	n/a
$[BnzC_1im][Ntf_2]$ (Bari et al., 2014)	"	0.81%	n/a	n/a
$[(Bnz)_2im][Ntf_2]$ (Bari et al., 2014)	"	58%	n/a	2-5
$[C_4C_1im][PF_6]$ (Shang et al., 2012)	Grinding/4 h + 3,000 rpm/0.5 h	20%	9 nm	2-7
$[(ethoxy)im][PF_6]$ (Matsumoto et al., 2015)	Microwaves(30 W)/0.5 h	92%	1–5 μm	1

Description of the methods used to produce exfoliated graphene, mass yield, lateral size of the flakes and number of exfoliated layers. ("n/a" means non available information).

immersed into five ILs without mixing or sonication. Two of the 5 ILs studied, $[C_2C_1im][Ntf_2]$ and $[C_2C_1im][acetate]$, degraded the surface of the HOPG and exfoliated graphene layers after 72 and 190 min, respectively. To confirm these observations, atomic force microscopic (AFM) was used to analyse the surface showing that the IL intercalated between graphene layers and that the cation preferentially interacts with the surface of graphene compared to the anion. One explanation is that the $C_2C_1im^+$ cation is not very large and can be interposed between two layers of graphene. Also the interfacial energy between the IL and graphene is comparable to that between two stacked graphene sheets.

It is not possible to compare two solvents without using the same exfoliation conditions. In this study we compared the graphite exfoliation in nine different commercial ILs in order to establish structure/property rules for the exfoliation process. We make use of a number of characterization techniques to assess the concentration of suspended graphene, flake size, number of layers, and chemical integrity of the exfoliated material.

2. METHODS

2.1. Materials

The ionic liquids (ILs) studied in this work are listed in **Table 2**. All are liquids at room temperature. The ILs were dried under primary vacuum for 24 h at room temperature. The water content was determined with a Karl Fisher coulometer DL32 from Metter Toledo in a Hydranal solution and is listed in **Table S1**.

Natural graphite flakes were purchased from Alpha Aesar with a 99.8% purity and a size inferior to 325 mesh. Raman spectroscopy and X-ray diffraction (XRD) were performed, without any treatment, to verify the initial purity (see in the **Figure S1A**).

In order not to degrade the IL and to work at low temperature with a scalable technique, ultrasound was selected as a mechanical precursor technique. The chemical stability of the IL during sonication was verified by XPS (see **Figure S6**). To have a significant evaluation of the stabilization of graphene in ILs, a high rate of centrifugation was employed. The concentration was estimated by UV-visible spectroscopy. The lateral size of the flakes was measured by transmission electron microscopy (TEM) and AFM. The number of layer was identified by AFM

and Raman spectroscopy. The purity of the exfoliated graphene was determined by XPS.
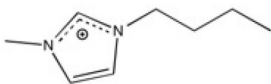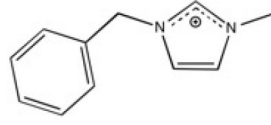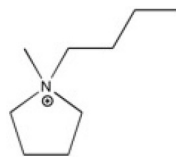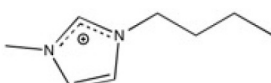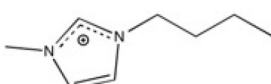
2.2. Sample Preparation
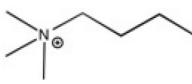
Suspended exfoliated graphite (SEG) solutions were prepared by adding graphite flakes to 2 mL of IL at an initial concentration of 5 mg.mL^{-1}. To produce a high concentration suspension of a few layers or monolayer graphene, these dispersions were then sonicated in a low power sonicator bath (Branson 2510, 40 kHz, 130 W) for 24 h. The ultrasonic water bath warmed up during use and reached a maximum temperature of 328 K. This thermal energy expanded the graphite layers and made the exfoliation process easier. As we worked with ILs, this temperature increase did not cause degradation of the solvent. Thus, the water bath was not cooled but was maintained at 323 $\pm$ 5 K. The horizontal distribution of the ultrasound is not homogeneous in the bath (Nascentes et al., 2001). In order to obtain reproducible results we developed a rotating holder (80 rpm) to support the samples, which eliminates the arbitrary position of the sample in the bath. For the graphene suspensions to exhibit long term stability, the dispersions were centrifuged at 10,000 rpm for 1 h at 298 K using a centrifuge (Thermoscinetic Sorval biofuge Primo R), (G-force equals to 9,727 g). After centrifugation of the supernatants or SEG, *ca.* 1.5 mL was carefully removed and retained for further use. A set of ten dispersions of graphite flakes in $[C_4C_1im][Ntf_2]$ were prepared in order to determine the repeatability of the experiment. Six different sonication experiments were conduced under the same conditions. After the centrifugation steps, the absorptions of the supernatants at 660 nm were measured. The standard deviation of those absorption values was 40%.

For the remaining ILs, two samples were prepared at the same time. We tried to exfoliate graphite flakes in 1-butyl-3-methylimidazolium bis(2-ethylhexyl)sulfosuccinate ($[C_4C_1im][AOT]$) from Brown et al. (2012), but because of its high viscosity, the flakes could not be suspended in the IL.

2.3. Sample Characterization

To estimate the quantities of SEG in the nine ILs, we used UV-vis spectroscopy. The absorption measurements were performed by a spectrophotometer Jasco V-650 at 660 nm (Hernandez et al., 2008; Lotya et al., 2009; Khan et al., 2010; Nuvoli et al., 2012) with a 1 cm optical path quartz cuvette at ambient temperature. The signal from the IL was systematically subtracted. Just after mixing

TABLE 2 | Structure, name and origin of the ILs selected for the liquid phase exfoliation of graphite.

Structure		Abbreviation	Origin
		$[C_4C_1im][Ntf_2]$	Iolitec (99 %)
		$[C_{10}C_1im][Ntf_2]$	Iolitec (98%)
		$[BnzmC_1im][Ntf_2]$	Iolitec (99%)
		$[Pyrr_{4,1}][Ntf_2]$	Iolitec (99%)
		$[N_{4,1,1,1}][Ntf_2]$	Iolitec (99%)
		$[C_4C_1im][C(CN)_3]$	Iolitec (98%)
		$[C_2C_1im][N(CN)_2]$	Iolitec (98%)
		$[C_4C_1im][C_1SO_4]$	Iolitec (99%)
		$[C_2C_1im][Otf]$	Iolitec (99%)

the graphite flakes with the IL, the suspensions were shaken and the absorbances of the solutions were quickly measured to prevent any sedimentation. After the sonication and the centrifugation steps, the absorbances of SEG were determined. The ratio of the two absorbances gives us the amount of material stabilized in IL.

All samples were analyzed by high resolution transmission electron microscopy (HRTEM) using a MET JEOL 2100FEF (field effect gun energy filtering) microscope with a point resolution of 0.23 nm without removing the IL. First, a thin film of SEG in IL was deposited on a copper mesh 200 grid coated with a layer of formvar/carbon. The grid was then dried gently with a filter paper. The liquid films were observed using an acceleration voltage of 200 kV. For each sample, five squares of the grid were analyzed. High resolution transmission electron microscopy, HRTEM, analysis was also performed on some particles using the same microscope. Subsequently, the HRTEM images and their crystal structure were determined from the diffraction pattern seen in the Fourier Transform images.

A volume of 1 mL of SEG was filtered through a polyvinylidene fluoride (PVDF) hydrophobic membrane (from Durapore) with a 220 nm pore size. The membrane was washed with dichloromethane and isopropanol (IPA) to remove the IL from the exfoliated graphite. Then, the filter was dried at 463 K during 12 h. This filter with exfoliated graphite was analyzed by Raman spectroscopy. Raman spectra were recorded at 294 K on a Jobin Yvon T64000 spectrophotometer equipped with a Olympus confocal microscope (100× objective lens) with

a CDD multichannel detector cooled with liquid nitrogen. The excitation source was a 514.5 nm ionized argon laser (Spectra Physics) line. The laser power was adjusted to 200 mW (minimal power). Spectral resolution is at 0.7 cm^{-1} in the range of 1,200–2,900 cm^{-1}.

The membrane filter with exfoliated graphite was washed from the opposite side with 2 mL of IPA to remove the nanomaterial. Ten drops of IPA suspension (20 μL per drop every 1 min) were casted by spin coating at 1,000 rpm onto a silicium wafer (Si/SiO$_2$). The Si/SiO$_2$ wafer had been previously washed in IPA during 30 min in an ultrasonic bath. After coating with the exfoliated graphene, the wafer was dried at 463 K for 2 h. The lateral and vertical size of the particles on the wafer were measured by AFM (**Table S3**). A minimum area of 600 μm^2 was explored on the silicium wafer where the homogeneous deposition is visible in the **Figure S3**. The arithmetic mean roughness (Ra) was estimated on a area of 1,500 μm^2 of the SiO$_2$/Si wafer after receiving ten drops of IPA followed by drying for 2 h at 463 K. The Ra obtained is 0.234 nm.

AFM measurements were carried out on a Bruker Mutlimode 8 equiped with a Nanoscope 5 using Tapping Mode and Peak Force Tapping based (Bruker Nano Inc., 2017) on real time force distance curve analysis recorded at a frequency of about 2.0 kHz. This allows us to locally measure the height of the sample. In addition, the Peak Force QNM mode controls the force applied to the sample by the tip, this decreasing the contact area between the tip and sample as well as deformation depths. So there is minimal damage to the probe or sample. The analyses were
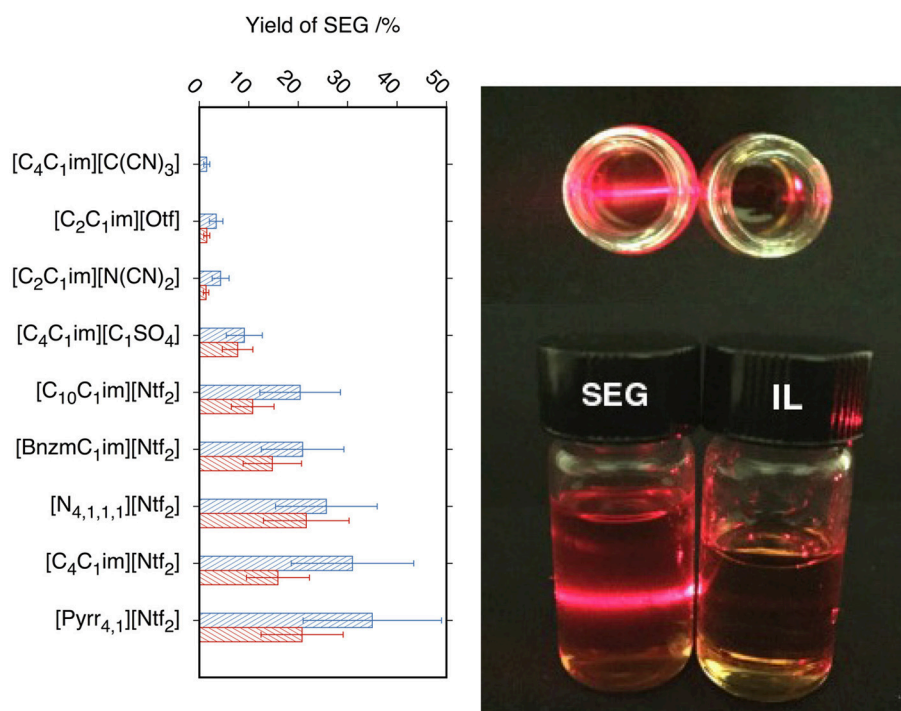

FIGURE 1 | On the left, the histogram represents the percentage of remaining suspended exfoliated graphite (SEG) in ionic liquid (IL) after centrifugation (blue) and after filtration of particles with a flakes size above 220 nm (red). On the right, pictures show Tyndall effect on SEG in [C$_4$C$_1$im][Ntf$_2$], using a red laser.
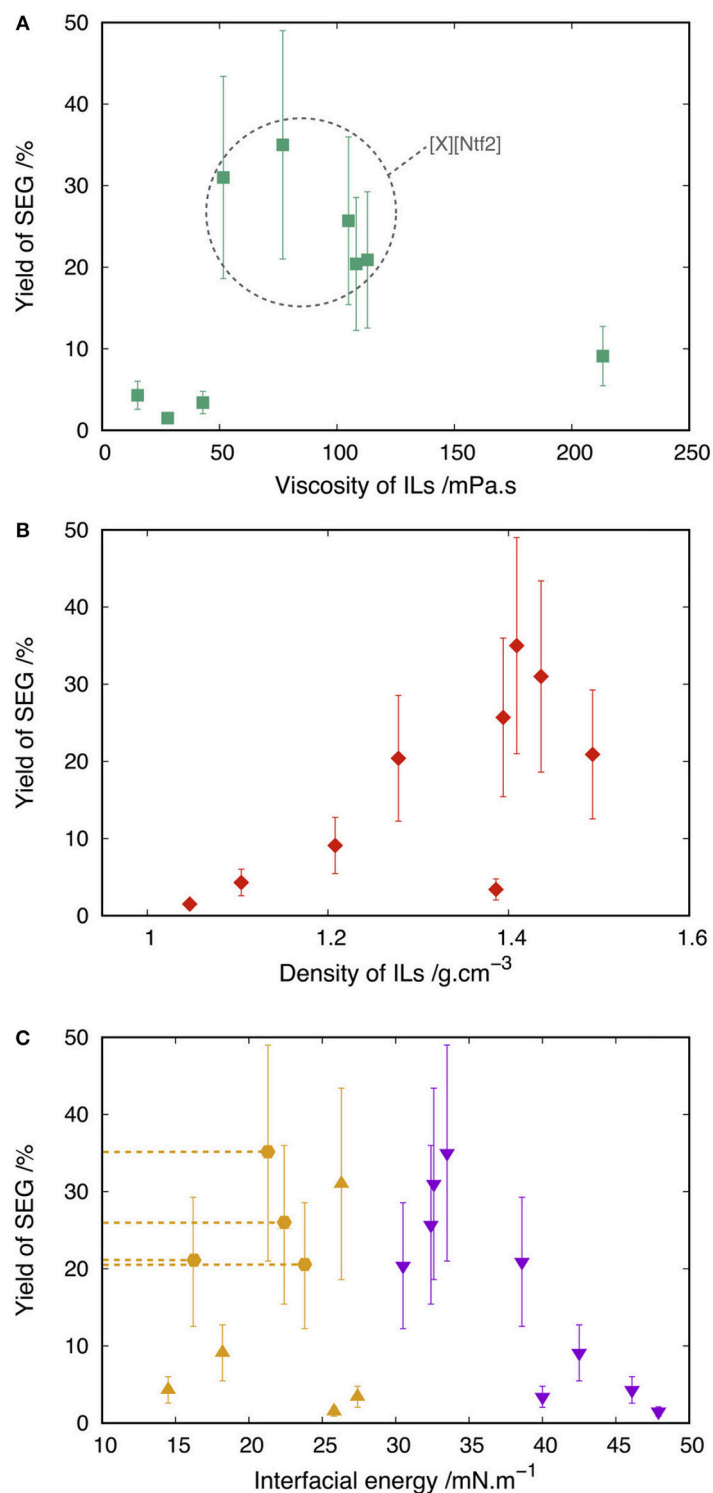
FIGURE 2 | Concentration of suspended graphite in ILs as function of properties of ILs at 298 K: **(A)** viscosity of ILs (Dzyuba and Bartsch, 2002; Seddon et al., 2002; Jacquemin et al., 2006; Pereiro et al., 2007; Ahosseini and Scurto, 2008; Fröba et al., 2008; Harris et al., 2011; Almeida et al., 2016) (green squares), **(B)** density of ILs (Seddon et al., 2002; Jacquemin et al., 2006; Pereiro et al., 2007; Fröba et al., 2008; Kolbeck et al., 2010; Tao et al., 2014; Almeida et al., 2016) (red diamonds), **(C)** ILs-argon surface tension (Bordes et al., 2017) (purple triangles), graphite-ILs interfacial energy (Bordes et al., 2017) (orange triangles) and upper bound to the graphite-ILs interfacial energy (orange hexagons) (Bordes et al., 2017).

performed using a RTESPA tip (300 kHz) from Bruker. The given characteristics of the RTESPA tip corresponded to a spring constant of $40 \, N \, m^{-1}$ and a curvature radius of 8 nm. The scan rate of the sample is 0.5 Hz with 512 scan lines.

XPS analysis was performed with Versaprobe II PHI 5000(ULVAC-PHI) spectrometer using a 100 μm focused monochromatic Al-Kα X-ray source (1486.6 eV) beam. The high-resolution spectral analysis was performed using a pass energy of 23 eV allowing an energy resolution of 0.5 eV. The XPS spectra were fitted by using Multipak $V_{9.1}$ software in which a Shirly background is assumed. The fitting peaks of the experimental spectra are defined by a combinaison of Gaussian (80%) and Lorentzian (20%) distributions. The analyzed covered a surface of approximately 100 μm^2 with a depth of 5 nm.

The Potentiel of Mean Force (PMF), calculated in this work, corresponds to the reversible work required to peel one layer of graphene from a stack of four layers in different ILs. The method and set up of these PMF calculations by molecular dynamics have been described in a previous paper (Bordes et al., 2018). The ionic liquids were modeled by the CL&P atomistic force field (Canongia Lopes and Pádua, 2012) and graphene/graphite by the OPLS-AA force field for aromatic carbon materials (Severance and Jorgensen, 1990). These are fully-atomistic force fields representing the covalently bonded structures with full flexibility, through harmonic covalent bonds and valence angles, and also torsion energy profiles that determine molecular conformations and the flexibility of the 2D nanomaterial. Non-bonded interactions included Lennard-Jones potentials and electrostatic partial charges placed on each atom. The periodic simulation boxes consisted of a stack of five stacked layers of graphite (each sheet about 5 by 4 nm) surrounded by at least 2 nm of ionic liquid, in such a way that the stack does not interact with its periodic images. The systems contain about 25,000 atoms. Simulations were carried out using the LAMMPS (Plimpton, 1995) molecular dynamics package, at 423 K and 1 bar using Nosé-Hoover thermostat and barostat. Long-range electrostatic interactions were computed using the PPPM method. The length of covalent bonds terminated by H atoms were constrained using the SHAKE algorithm in order to allow for a timestep of 1 fs. Trajectories of 5 ns were generated after 1 ns equilibration. The reversible work of peeling the top layer from the stack, in vacuum and in the presence of ionic liquid, was evaluated using a potential of mean force technique (umbrella sampling with the weighed histogram analysis method). The authors have used similar methods studying exfoliation of different nanomaterials in molecular and ionic solvents (Sresht et al., 2015, 2017; Bordes et al., 2018), with further simulation details provided in these previous publications.
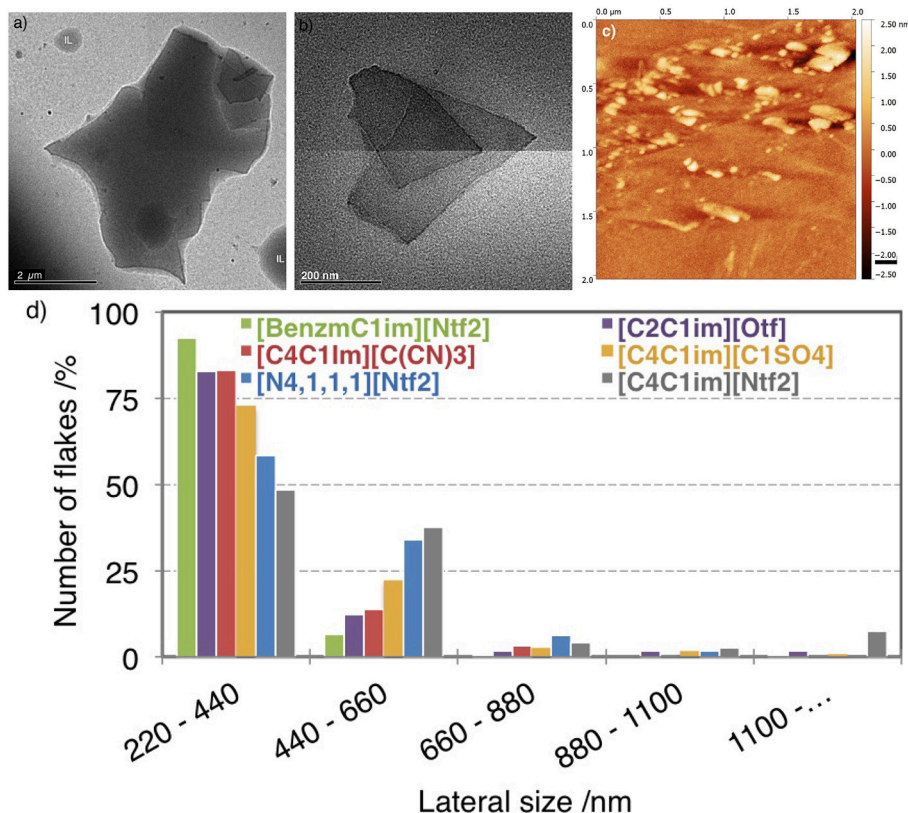
FIGURE 3 | TEM images of multilayer graphene after centrifugation in **(a)** $[C_4C_1im][Ntf_2]$ and **(b)** $[C_2C_1im][Otf]$. **(c)** Topographical AFM image of flakes produced in $[C_2C_1im][Otf]$ and deposited on Si/SiO$_2$ substrates by spin-coating. **(d)** Histogram of the percentage of flakes found in the dispersions as a function of the lateral size of flakes.

3. RESULTS AND DISCUSSION

3.1. Concentration of SEG in ILs

The total concentration of carbon material in suspension in ILs was estimated by absorbance spectroscopy at 660 nm. The concentration represents the surface of exfoliated graphite flakes that absorb light. In **Figure 1**, pictures of a SEG solution and corresponding ILs representing the Tyndall effect are presented and the scattered light in the suspension is seen. Thus, it is clear that exfoliated graphite can be dispersed in ILs.

In order to have a first assessment of the solvent ability of ILs, after the sonication and the centrifugation step, we have measured the absorbance of the supernatant suspensions containing exfoliated graphite. After filtration of the supernatant suspensions through a PVDF filter with 220 nm pores, the absorbance of filtrated suspensions were measured and subtracted to the absorbance of the supernatant suspensions. The **Figure 1** represents the yields of SEG in supernatant suspension (blue histogram) and the yield of SEG above 220 nm of size (red histogram). The yield of SEG corresponds to the ratio of the absorbance of nano-carbon in ILs after exfoliation to the absorbance measured before exfoliation. Quantities of suspended graphite are given in **Table S2**.

The $[C_4C_1im][Ntf_2]$, $[N_{4,1,1,1}][Ntf_2]$ and the $[Pyrr_{4,1}][Ntf_2]$ presented the highest yield of SEG (the concentration is around 1.8 mg.mL^{-1}) among the nine studied ILs. In the ILs with
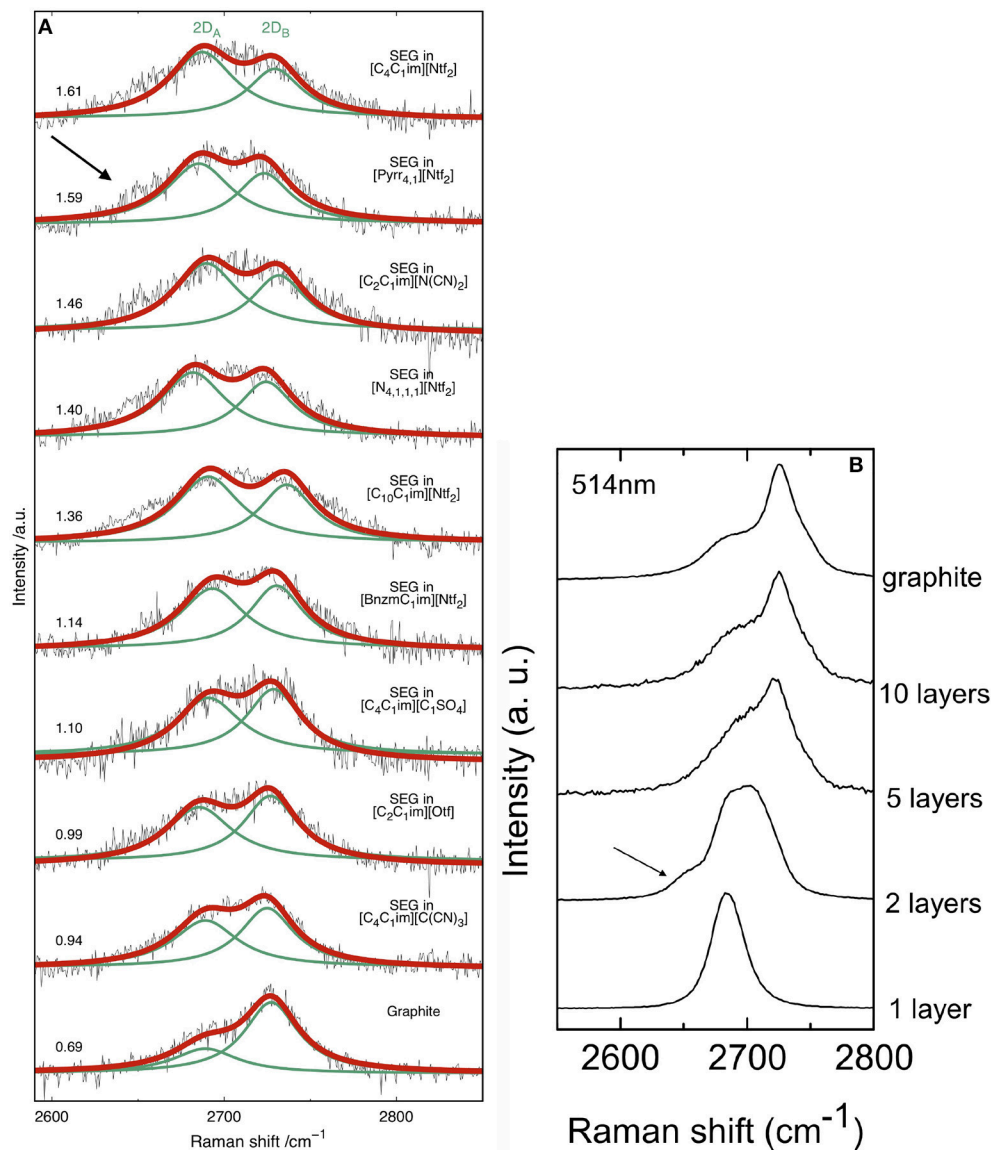

FIGURE 4 | (A) Raman spectra (2D band) using a 514.5 nm laser for bulk graphite and suspended exfoliated graphite in different ionic liquids after filtration on a PVDF membrane. The values on the left correspond to the ratio of the areas of the two Lorentzian functions used to fit the 2D band. **(B)** Evolution of the 2D band with the number of graphene layers (514.5 nm). Reproduced with permission from Ferrari et al. (2006). Arrows indicate a shoulder present in the case of bilayer graphene.

other anions, the concentrations are below 0.5 mg.mL^{-1} and lower than in ILs with the Ntf_2^- anion. The [C_4C_1im][$C(CN)_3$], [C_2C_1im][Otf] and [C_2C_1im][N(CN)$_2$] ILs presented the lowest concentrations of SEG. The relatively high error bars make the distinction between ILs with the Ntf_2^- anion but different cations difficult. Bari et al. (2014) exfoliated graphene in [BnzC$_1$im][Ntf$_2$] and also in [C_4C_1im][Ntf$_2$] with a different set up. After exfoliation, no nano-carbon object was found in [C_4C_1im][Ntf$_2$] and 0.81% of SEG in [BnzC$_1$im][Ntf$_2$]. The low and similar concentrations of SEG reported in these two ILs hinders comparison with our results. Our main conclusion is that using a Ntf_2^- anion instead of other anions is favorable to stabilize exfoliated graphene.

In **Figure 2** is presented the yield of SEG as function of the viscosity, density, surface tension of the studied ILs and of the interfacial energy between graphite and the ILs. The concentration of SEG in ILs is not correlated to their viscosity. For example, [C_4C_1im][C_1SO_4] which is the IL with the highest viscosity, the concentration of SEG is lower than in the ILs based on the Ntf_2^- anion which have lower viscosities. These results validate the experimental method followed and prove that the chosen rate of centrifugation is sufficiently high to balance the IL viscosity during the stabilization of the SEG. The ILs based on Ntf_2^- that lead to the highest concentration of SEG have a density between 1.4 and 1.5 g.cm^{-3}. ILs with densities around 1.4 g.cm^{-3} seem to be favorable to suspend exfoliated graphite, this conclusion being a simple observation and does not necessarily imply causation.

The same observations hold for the surface tension. Having an IL with a surface tension around 34 mN.m^{-1} leads to higher concentrations of SEG. In a previous work (Bordes et al., 2017), the interfacial energy between graphite and different ILs was calculated. On **Figure 2C**, we could not correlate this interfacial energy with the concentration of SEG in the studied ILs, because as it was discussed in a previous work (Bordes et al., 2017), for four ILs, the graphite-ILs interfacial energy is not a value but instead just an upper bound. We also investigated the speed of sound in four ILs, in order to correlate a quantity related to compressibility and cavitation with the concentration of SEG. We could not find a valuable trend because of the lack of values in literature (the results are presented in **Figure S2**). Coleman et al. (Hernandez et al., 2008) studied forty molecular solvents and predicted that good solvents are characterized by surface tensions in the region of 40–50 mN.m^{-1}. In the case of ILs, surface tensions between 30 and 40 mN.m^{-1} lead to better stabilization of exfoliated graphite.

3.2. Lateral Size of Flakes

We measured the lateral size of SEG in ILs using TEM and AFM. **Figures 3a–c** displays examples of flakes. At least fifty flakes of SEG, were analyzed to generate statistical results that are presented in the histogram of the **Figure 3d**. With our exfoliation process (24 h sonication plus centrifugation at 10,000 rpm) most of the SEG have sizes between 220 and 440 nm. Our results reveal that the lateral size of flakes exfoliated is larger in [C_4C_1im][Ntf$_2$] than in [BnzmC$_1$im][Ntf$_2$].

Flakes of exfoliated graphite have larger sizes in [C_4C_1im][Ntf$_2$] than in [$N_{4,1,1,1}$][Ntf$_2$], and also appear to be present in suspension in larger quantity, in agreement with the measurement of concentration determined by absorption spectroscopy (**Figure 1**). The ionic liquids [C_2C_1im][Otf] and [C_4C_1im][$C(CN)_3$] lead to similar lateral size profiles and to approximately the same amounts of suspended material. We conclude that ILs with the Ntf_2^- anion favor the stabilization of larger exfoliated graphite flakes.

3.3. Number of Graphene Layers

In order to determine the number of layers in the exfoliated flakes we measured their Raman spectra in nine ILs and compared those with the spectrum of bulk graphite (**Figure 4**). The flakes of SEG were obtained by filtering the suspensions though a PVDF membrane, but even after washing the filter (with dichloromethane and isopropanol) residual amounts of IL were found and caused some fluorescence during the acquisition of spectra.

The Raman spectra of graphene or graphite is mainly composed of D, G and 2D peaks corresponding to in-plane vibration (Ferrari and Basko, 2013). The G band appearing at 1582 cm^{-1} is assigned to the stretching of the C-C bond in graphitic materials. The D band (around 1350 cm^{-1}) is due to the breathing modes of the carbon atoms and requires a defect, such as oxydation, to be activated. The intense 2D band at about 2,700 cm^{-1} is one of the D-band overtones characteristic of sp^2 carbon materials (Malard et al., 2009). The Raman spectrum of graphite is given in the (**Figure S1B**).

Due to residual ionic liquid at the surface of graphite, inducing extra fluorescence, the resolution of the spectra is not sufficient to characterize properly the intensity of the D peak. In these conditions, the most relevant information obtained from the spectra is the shape of the 2D band. This is the reason why the relative 2D/D intensity is not described in this study. Accumulation of spectra between 2,600 and 2,850 cm^{-1} (corresponding to the 2D band) enabled us to reach a sufficient resolution for our analysis. The exact number of layers was

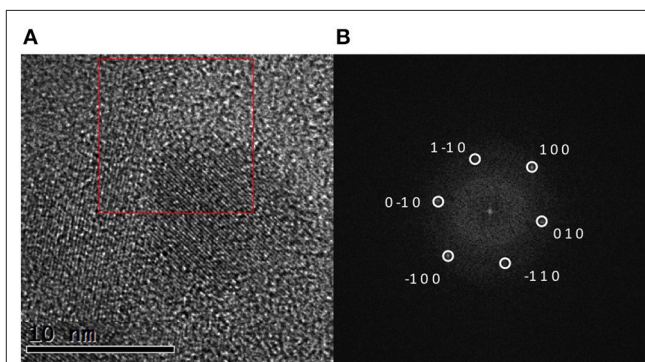**FIGURE 5 | (A)** Exemplary HRTEM image of graphene generated by exfoliation of graphite by sonication in [C_4C_1im][Ntf$_2$] and **(B)** FFT of the area in the red square indexed by a hexagonal structure along the (001) zone axis with a lattice parameter of 2.5 and 6.7 Å corresponding to graphene.
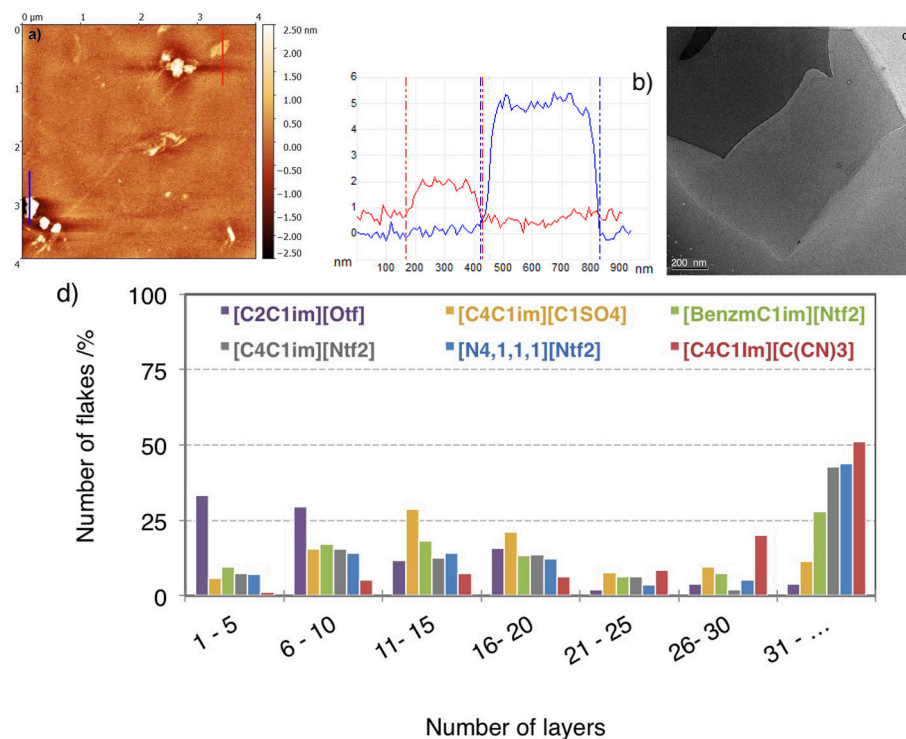
FIGURE 6 | (a) Topographical AFM image of flakes produced in [C_2C_1im][Otf] and deposited on Si/SiO$_2$ substrates by spin-coating. **(b)** Height profile of bi-layers graphene (red) and fourteen layers graphene (bleue). **(c)** TEM image of multilayer graphene in [C_4C_1im][Ntf$_2$] **(d)** Histogram of the percentage of flakes as a function of the number of layers obtained statistical thickness analysis by AFM.

measured using AFM and the presence of impurities was detected using XPS, as reported below.

We will focus on the shape on the 2D band, which changes significantly in shape and intensity when moving from graphene to graphite (Ferrari et al., 2006). Depending on the number of graphene layers, the 2D band can be fitted with a different number of Lorentzian function (Ferrari et al., 2006; Zhu et al., 2014). Comparing our spectra of **Figure 4A** with those of the literature (**Figure 4B**), we can see our samples are not monolayer graphene because the bands are too broad.
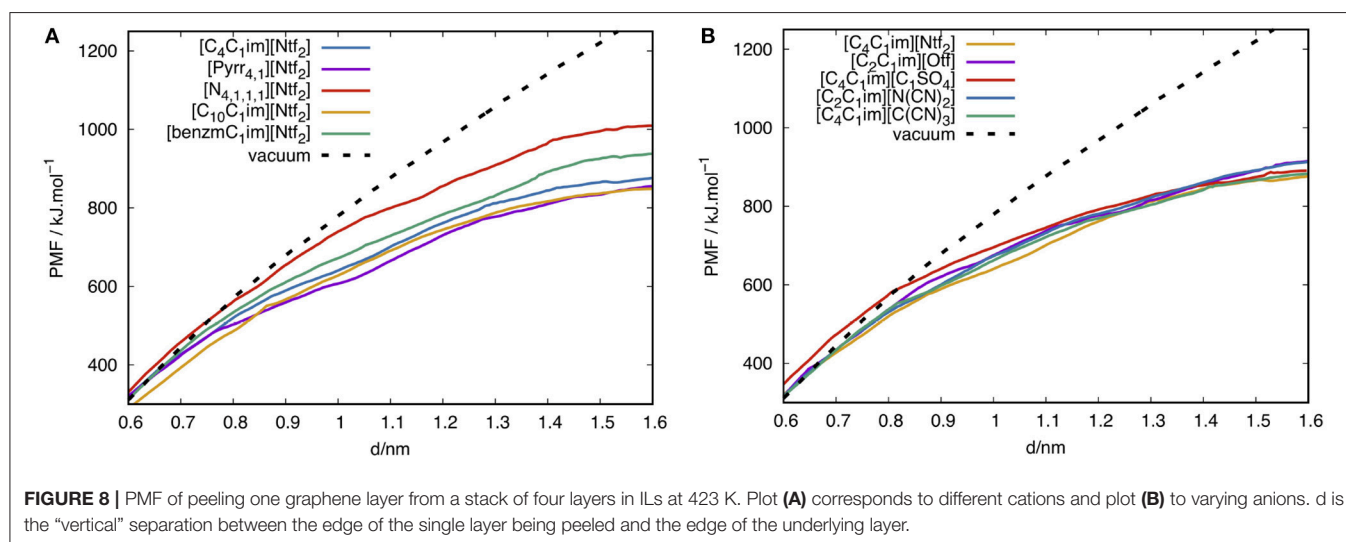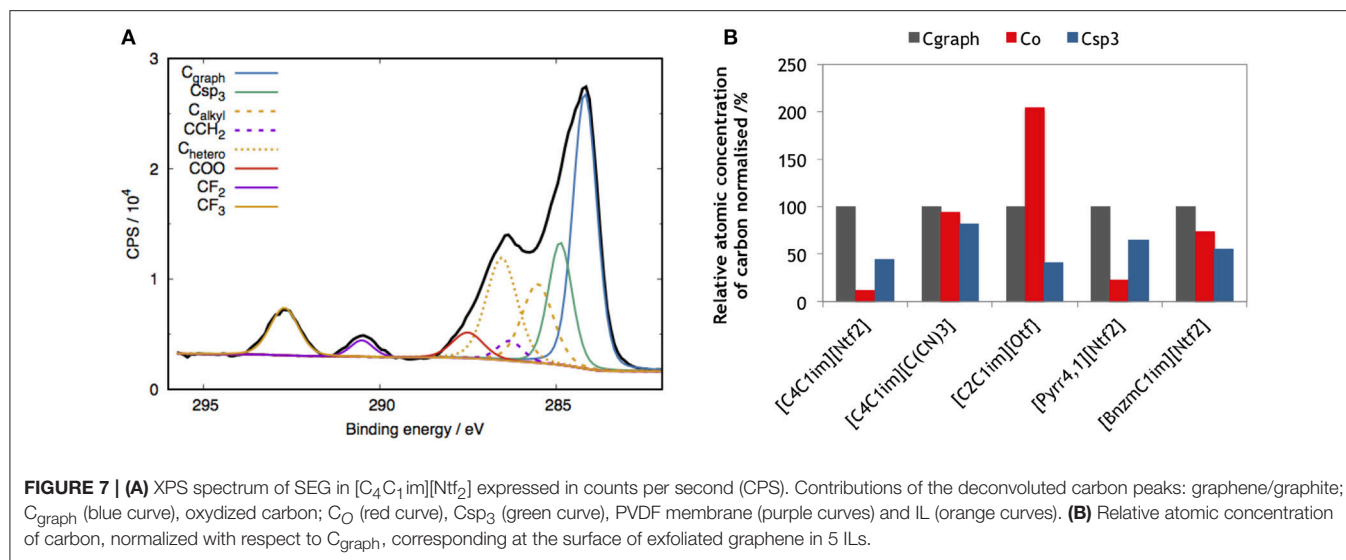
According to the literature (Malard et al., 2009), the number of Lorentzian functions needed to fit the 2D peak is linked to the number of graphene layers, although not in a monotonous way. In order to establish a direct comparison between the SEG in the nine ILs, we chose to fit the band with two Lorentzian functions, called 2D$_A$ and 2D$_B$, as our Raman spectra are too noisy to fit accurately with more functions. The half-width at half-maximum (hwhm) of 2D$_A$ and 2D$_B$ have been kept fixed for every spectrum. The ratio of the areas of the two Lorentzian functions used for fitting this band are given in the **Figure 4** with each spectrum. Raman spectra have been recorded at three different positions for each sample. The spectrum with the highest area 2D$_A$/2D$_B$ ratio is given in the **Figure 4**. Where we see that a correlation exists between the number of layers of graphene and the area ratio. In graphite, this ratio has a value of 0.69. For SEG obtained in the five ILs with an area ratio

above 1.14, we can observe an shoulder on the left of the band at 2650 cm^{-1}. This does not correspond to 5–10 graphene layers because the ratio of the two band is to high. The 2D band of the Raman spectra of SEG in [C_4C_1im][Ntf$_2$], [Pyrr$_{4,1}$][Ntf$_2$], [C_2C_1im][N(CN)$_2$], [$N_{4,1,1,1}$][Ntf$_2$] and [$C_{10}C_1$im][Ntf$_2$] are similar to that of bi-layer graphene, as we can observe a shoulder in **Figure 4**.

The as-prepared graphene sheets were analyzed by high resolution HRTEM. The pictures contrast allowed an easy recognition of single to very few layered graphene from residual graphite existing in the sample. Additionally, graphene sheets exhibited a well-defined crystalline structure under HRTEM as shown in **Figure 5A**. As a result, fast-Fourier transform (FFT) analysis of the pictures yielded a pattern of clearly defined spots in the reciprocal space. This pattern was compared to the typical hexagonal close-packed (hcp) structure of graphene.

In all cases, spots corresponding to an interplanar distance of about 2.1 Å were observed. It could correspond to the (100) distance in the hcp structure. Indeed, it is shown in **Figure 5B** that the pattern in the FFT image can be completely indexed using this structure. The real electron diffraction pattern measured (in **Figure S4**) also supported the same crystal structure.

AFM is one of the most direct and precise methods to quantify the degree of exfoliation of graphene by measuring the height of the deposited flakes. Between 50 and 150 flakes were

FIGURE 7 | (A) XPS spectrum of SEG in [C_4C_1im][Ntf_2] expressed in counts per second (CPS). Contributions of the deconvoluted carbon peaks: graphene/graphite; C_{graph} (blue curve), oxydized carbon; C_O (red curve), Csp_3 (green curve), PVDF membrane (purple curves) and IL (orange curves). (B) Relative atomic concentration of carbon, normalized with respect to C_{graph}, corresponding at the surface of exfoliated graphene in 5 ILs.

FIGURE 8 | PMF of peeling one graphene layer from a stack of four layers in ILs at 423 K. Plot (A) corresponds to different cations and plot (B) to varying anions. d is the "vertical" separation between the edge of the single layer being peeled and the edge of the underlying layer.

analyzed for each sample (**Figures 6a,b**). The superposition of layers illustrated in **Figure 6c**), would result in over-estimation of the number of graphene layers in AFM measurements. The estimation of the height of SEG *via* AFM depends on the substrate and on the experimental conditions (i.e., relative humidity and temperature). For example, on Si/SiO$_2$, graphene can show an apparent height of 1 nm (Ishigami et al., 2007; Eredia et al., 2017). In this work, graphene height is estimated by assuming that the apparent thickness of the thinnest graphene sheet observed on our images amounts to 0.9 nm and the distance between two layers of graphene is 0.315 nm.

The SEG were also analyzed by high resolution TEM to identify monolayers of graphene. **Figure 6d** shows a histogram of the distribution of flake thickness for six samples. In all the liquids, graphene or few-layers graphene ($\leq$ 5 layers) was found. A poorly exfoliated suspension was produced in [C_4C_1im][$C(CN)_3$]. Fifty percent of the exfoliated graphene is in fact graphite with more than 30 flakes while in [C_2C_1im][Otf],

30% of graphene with <5 layers is found. Using **Figure 6d** a ranking can be estimated to find the IL, amongst those studied, which exfoliates the most of graphite: [C_2C_1im][Otf] > [C_4C_1im][C_1SO_4] > [BnzmC_1im][Ntf_2] > [$N_{4,1,1,1}$][Ntf_2] $\simeq$ [C_4C_1im][Ntf_2] > [C_4C_1im][$C(CN)_3$].

The choice of the anion seems important to control the degree of exfoliation of SEG. Adding a benzyl function instead of an alkyl chain on an imidazolium head group will reduce the lateral size of flakes but will favor a higher concentration of graphene.

3.4. Purity of Exfoliated Graphene

The purity of graphene after exfoliation in different ILs was investigated by XPS. In order to probe the relative amount of sp^2, sp^3 and oxydated carbon atoms at the surface of exfoliated graphite, XPS measurements were performed in samples of washed SEG deposited on a PVDF membrane. Based on references samples studies, we performed C1s core level fitting for

exfoliated graphite in different ILs media. In exfoliated graphite, we assigned five main contributions, graphitic carbon (CC_{graph}) at 284.3 eV, IL related carbon (C_{alkyl}, C_{hetero} and CF_3 at 285.6, 286.5 and 292.7 eV), PVDF related peaks (CCH_2 and CF_2 at 286.3 and 290.5 eV), carbon sp^3 at 284.9 eV and carbon oxyde related peak (C–O and COO at 286.0 and 287.5 eV). **Figure 7A** shows peak fitting for SEG in $[C_4C_1im][Ntf_2]$. The XPS spectrum of natural graphite is presented in the (**Figure S5**) for comparison. Since IL is present in relatively large quantities at the surface of graphene, the IL contributions were inferred from the pure IL XPS spectra. Hence the Csp^3 contribution, where the binding energy is closed to alkyl and hetero carbon of ILs, was identified. Based on this peak fitting protocol, the relative concentrations of C_{graph}, C–O and Csp^3 are reported in the chart of **Figure 7**.

The purity of SEG in $[C_4C_1im][Ntf_2]$ and $[Pyrr_{4,1}][Ntf_2]$ is similar in terms of the presence of Csp^3 and C–O at the surface. For the rest of the ILs studied, the oxydation at the surface is significant. Specially in the case of exfoliated graphite in $[C_2C_1im][Otf]$: more than two every three carbons are not graphitic. This result can be correlated with the number of graphene layers determined by AFM measurements in **Figure 6d**. $[C_2C_1im][Otf]$ produced the most exfoliated graphite among the ILs we studied and it is known that one method to produce graphene form graphite is to oxidize the graphite (Zhu et al., 2010), so the high content of graphene in $[C_2C_1im][Otf]$ could be due to oxydation at the surface of graphene. In the presence of $[bnzmC_1im][Ntf_2]$ and $[C_4C_1im][C(CN)_3]$, formation of C–H bonds and oxidation of at least 60% of carbon were found at the surface of the carbon material.

The eventual degradation of pure IL due to sonication was investigated by XPS. A volume of 2 mL of $[Pyrr_{4,1}][Ntf_2]$ was sonicated during 24 h. No differences were found between the XPS spectra of the IL before and after sonication, as shown in the (**Figure S6**). This oxidation at the surface of graphene could be due to the presence of a few ppm of water in the ILs, to the gas dissolved in ILs or to the step of washing the filter with dichloromethane.

3.5. Free Energies of Peeling

In order to quantify the energy needed to exfoliate one graphene layer in the nine ILs, the reversible work (PMF) of peeling graphene in ILs was calculated from MD simulations and is plotted in **Figure 8**. The reversible work required to exfoliate graphene is higher in vacuum than in any of the ILs at 423 K. Thus, ILs are favorable solvents since they reduce the free energy for the exfoliation of graphene. Some results have been discussed in a previous work (Bordes et al., 2018).

In **Figure 8**, PMF curves obtained in different anions are closer than those obtained in different cations. Changing the anion leads to PMF curves that are too close to be completely distinguishable in our simulations, whereas different cations lead to PMF curves which are clearly distinguishable. The choice of the cation appears therefore more significant. The presence of a benzyl group is not beneficial toward the graphene peeling process, a conclusion in line with the absorbance measurements reported above (see **Figure 1**). Increasing the alkyl chain of the imidazolium cation decreases the free energy of peeling.

The pyrrolidinium head group leads to an improvement in solvent quality compared to imidazolium and also to ammonium. This result was also expected from the concentrations of SEG in ILs. However, since the imidazolium head group is aromatic we expected stronger interactions with graphene for imidazolium ILs. $[N_{4,1,1,1}][Ntf_2]$ has demonstrated worst results than $[C_4C_1im][Ntf_2]$, in term of concentration, lateral size and number of exfoliated layers. The PMF curves also indicate that the intercalation of $[N_{4,1,1,1}][Ntf_2]$ between two layers of graphene requires more energy than $[C_4C_1im][Ntf_2]$.

4. CONCLUSION

In order to attain a more complete view of suspended graphene in ILs, different techniques were used to characterize graphene flakes produced by solvent exfoliation of graphite.

The concentration of suspended exfoliated graphene (SEG) is related to the stabilization step. UV-visible spectroscopy measurements reveal that the ILs with Ntf_2^- anions stabilize higher concentrations of exfoliated graphite. Higher concentrations of SEG are produced in ILs with medium-length alkyl side chains in cations and without functionalisation by benzyl groups. Density and surface tension of the ILs seem to be good descriptors to choose ionic liquids capable of stabilizing larger concentrations of SEG.

AFM and TEM measurements allowed to determine the lateral size of graphene flakes, showing that $[C_4C_1im][Ntf_2]$ and $[N_{4,1,1,1}][Ntf_2]$ lead to larger flakes compared to $[BnzmC_1im][Ntf_2]$ whereas smaller SEG flakes were found in $[C_2C_1im][Otf]$. A bulky anion seems to be an advantage to stabilize larger flakes. The number of stacked layers in flakes determined by AFM was smaller in $[C_2C_1im][Otf]$.

Exfoliation of graphene in ILs using ultrasound caused surface changes mainly oxydation but also sp^3 hybridization of carbon. $[C_2C_1im][Otf]$ leads to the highest degree of oxidation compared to the others ILs studied. This result could explain the efficiency of this IL to exfoliate graphite down to single layers. Using an ultrasonic bath to process the exfoliation of graphite does not seems to be the best technique to produce a high concentration of pristine graphene. To optimize the exfoliation process, we need first to increase the reproducibility of the sonication/centrifugation procedure used in this work in order to increase the initial concentration and size of graphite flakes significantly.

Adding π-π interactions between the IL and the carbon material does not seem to improve the exfoliation process. With these results, the design of the IL can be optimized by choosing a Ntf_2^- anion to increase the stabilization and the purity of SEG with a 1-ethyl-2-methylpyrrolidinium cation to increase the intercalation and the dispersion of graphene flakes.

AUTHOR CONTRIBUTIONS

EB conducted the experiments jointly with BM (TEM), CS (TEM and EIS), DB and P-OB (AMF), AB (XPS, EIS). MG and AP supervised the project. The manuscript

was written by EB, MG, and AP with inputs from all authors.

ACKNOWLEDGMENTS

SUPPLEMENTARY MATERIAL

The Supplementary Material for this article can be found online at: https://www.frontiersin.org/articles/10.3389/fchem.2019.00223/full#supplementary-material

REFERENCES

Ahosseini, A., and Scurto, A. M. (2008). Viscosity of imidazolium-based ionic liquids at elevated pressures: cation and anion effects. *Int. J. Thermophys.* 29, 1222–1243. doi: 10.1007/s10765-008-0497-7

Almeida, H. F., Carvalho, P. J., Kurnia, K. A., Lopes-da Silva, J. A., Coutinho, J. A. P., and Freire, M. G. (2016). Surface tensions of ionic liquids: non-regular trend along the number of cyano groups. *Fluid Phase Equilib.* 409, 458–465. doi: 10.1016/j.fluid.2015.10.044

Armand, M., Endres, F., MacFarlane, D. R., Ohno, H., and Scrosati, B. (2009). Ionic-liquid materials for the electrochemical challenges of the future. *Nat. Mater.* 8, 621–629. doi: 10.1038/nmat2448

Bari, R., Tamas, G., Irin, F., Aquino, A. J., Green, M. J., and Quitevis, E. L. (2014). Direct exfoliation of graphene in ionic liquids with aromatic groups. *Colloids Surfaces Physicochem. Eng. Asp.* 463, 63–69. doi: 10.1016/j.colsurfa.2014.09.024

Blake, P., Brimicombe, P. D., Nair, R. R., Booth, T. J., Jiang, D., Schedin, F., et al. (2008). Graphene-based liquid crystal device. *Nano Lett.* 8, 1704–1708. doi: 10.1021/nl080649i

Bordes, E., Douce, L., Quitevis, E. L., Pádua, A. A. H., and Gomes, M. C. (2017). Ionic liquids at the surface of graphite : wettability and structure. *J. Phys. Chem.* 148:193840. doi: 10.1063/1.5010604

Bordes, É., Szala-Bilnik, J., and Pádua, A. A. H. (2018). Exfoliation of graphene and fluorographene in molecular and ionic liquids. *Faraday Discuss.* 206, 61–75. doi: 10.1039/c7fd00169j

Brown, P., Butts, C. P., Eastoe, J., Fermin, D., Grillo, I., Lee, H. C., et al. (2012). Anionic surfactant ionic liquids with 1-Butyl-3-methyl-imidazolium cations: Characterization and application. *Langmuir* 28, 2502–2509. doi: 10.1021/la204557t

Bruker Nano Inc. (2017). *PeakForce QNM (Quantitative Nanomechanical Property Mapping) | Bruker*. Available online at: https://www.bruker.com/products/surface-and-dimensional-analysis/atomic-force-microscopes/modes/modes/imaging-modes/peakforce-qnm.html, (accessed April 02, 2019).

Canongia Lopes, J. N., and Pádua, A. A. H. (2012). CL&P: a generic and systematic force field for ionic liquids modeling. *Theor. Chem. Acc.* 131, 1–11. doi: 10.1007/s00214-012-1129-7

Chen, S., Wu, G., Sha, M., and Huang, S. (2007). Transition of Ionic liquid [bmim][PF 6] from liquid to high-melting-point crystal when confined in multiwalled carbon nanotubes. *Jacs* 129, 2416–2417. doi: 10.1021/ja067972c

Chen, Y., Zhang, X., Zhang, D., and Ma, Y. (2012). High power density of graphene-based supercapacitors in ionic liquid electrolytes. *Mater. Lett.* 68, 475–477. doi: 10.1016/j.matlet.2011.11.008

Chen, Y., Zhang, X., Zhang, D., Yu, P., and Ma, Y. (2011). High performance supercapacitors based on reduced graphene oxide in aqueous and ionic liquid electrolytes. *Carbon N. Y.* 49, 573–580. doi: 10.1016/j.carbon.2010.09.060

Coleman, J. N. (2013). Liquid exfoliation of defect-free graphene. *Acc. Chem. Res.* 46, 14–22. doi: 10.1021/ar300009f

Deetlefs, M., Seddon, K. R., and Shara, M. (2006). Predicting physical properties of ionic liquids. *Phys. Chem. Chem. Phys.* 8, 642–649. doi: 10.1039/B513453F

Dzyuba, S. V., and Bartsch, R. A. (2002). Influence of Structural Variations in 1-Alkyl(aralkyl)-3-Methylimidazolium Hexafluorophosphates and Bis(trifluoromethylsulfonyl)imides on Physical Properties of the Ionic Liquids. *ChemPhysChem* 3, 161–166. doi: 10.1002/1439-7641(20020215)3:2<161::AID-CPHC161>3.0.CO;2-3

Elbourne, A., McLean, B., Voïtchovsky, K., Warr, G. G., and Atkin, R. (2016). Molecular Resolution *in situ* Imaging of Spontaneous Graphene Exfoliation. *J. Phys. Chem. Lett.* 7, 3118–3122. doi: 10.1021/acs.jpclett.6b01323

Eredia, M., Bertolazzi, S., Leydecker, T., El Garah, M., Janica, I., Melinte, G., et al. (2017). Morphology and electronic properties of electrochemically exfoliated graphene. *J. Phys. Chem. Lett.* 8, 3347–3355. doi: 10.1021/acs.jpclett.7b01301

Ferrari, A. C., and Basko, D. M. (2013). Raman spectroscopy as a versatile tool for studying the properties of graphene. *Nat. Nanotechnol.* 8, 235–246. doi: 10.1038/nnano.2013.46

Ferrari, A. C., Meyer, J. C., Scardaci, V., Casiraghi, C., Lazzeri, M., Mauri, F., et al. (2006). Raman spectrum of graphene and graphene layers. *Phys. Rev. Lett.* 97, 1–4. doi: 10.1103/PhysRevLett.97.187401

Fröba, A. P., Kremer, H., and Leipertz, A. (2008). Density, refractive index, interfacial tension, and viscosity of ionic liquids [EMIM][EtSO4], [EMIM][NTf2], [EMIM][N(CN) 2], and [OMA][NTf2] in dependence on temperature at atmospheric pressure. *J. Phys. Chem. B* 112, 12420–12430. doi: 10.1021/jp804319a

Fukushima, T., and Aida, T. (2007). Ionic liquids for soft functional materials with carbon nanotubes. *Chem. A Eur. J.* 13, 5048–5058. doi: 10.1002/chem.200700554

Hallett, J. P., and Welton, T. (2011). Room-temperature ionic liquids: solvents for synthesis and catalysis. 2. *Chem. Rev.* 111, 3508–3576. doi: 10.1021/cr1003248

Harris, K. R., Woolf, L. A., Kanakubo, M., and Rüther, T. (2011). Transport Properties of N -Butyl- N -methylpyrrolidinium Bis(trifluoromethylsulfonyl)amide. *J. Chem. Eng. Data* 56, 4672–4685. doi: 10.1021/je2006049

Hernandez, Y., Nicolosi, V., Lotya, M., Blighe, F. M., Sun, Z., De, S., et al. (2008). High-yield production of graphene by liquid-phase exfoliation of graphite. *Nat. Nanotechnol.* 3, 563–568. doi: 10.1038/nnano.2008.215

Holló czki, O., Malberg, F., Welton, T., and Kirchner, B. (2014). On the origin of ionicity in ionic liquids. ion pairing versus charge transfer. *Phys. Chem. Chem. Phys.* 16, 16880–16890. doi: 10.1039/C4CP01177E

Ishigami, M., Chen, J. H., Cullen, W. G., and Fuhrer, M. S. (2007). Atomic structure of graphene on SiO$_2$. *Nano Lett.* 7, 1643–1648. doi: 10.1021/nl070613a

Jacquemin, J., Husson, P., Padua, A. A. H., and Majer, V. (2006). Density and viscosity of several pure and water-saturated ionic liquids. *Green Chem.* 8, 172–180. doi: 10.1039/B513231B

Kelly, A. G., Hallam, T., Backes, C., Harvey, A., Esmaeily, A. S., Godwin, I., et al. (2017). All-printed thin-film transistors from networks of liquid-exfoliated nanosheets. *Science* 356, 69–73. doi: 10.1126/science.aal4062

Khan, U., O'Neill, A., Lotya, M., De, S., and Coleman, J. N. (2010). High-concentration solvent exfoliation of graphene. *Small* 6, 864–871. doi: 10.1002/smll.200902066

Kolbeck, C., Lehmann, J., Lovelock, K. R. J., Cremer, T., Paape, N., Wasserscheid, P., et al. (2010). Density and surface tension of ionic liquids. *J. Phys. Chem. B* 114, 17025–17036. doi: 10.1021/jp1068413

Lee, C., Wei, X., Kysar, J. W., and Hone, J. (2008). Measurement of the elastic properties and intrinsic strength of monolayer graphene. *Science* 321, 385–388. doi: 10.1126/science.1157996

Li, X. L., Qiao, X. F., Han, W. P., Zhang, X., Tan, Q. H., Chen, T., et al. (2016). Determining layer number of two-dimensional flakes of transition-metal dichalcogenides by the Raman intensity from substrates. *Nanotechnology* 27, 145704. doi: 10.1088/0957-4484/27/14/145704

Liu, Z., Li, G., Cui, T., Borodin, A., Kuhl, C., and Endres, F. (2017). A battery-supercapacitor hybrid device composed of metallic zinc, a biodegradable ionic liquid electrolyte and graphite. *J. Solid State Electrochem.* 22:91. doi: 10.1007/s10008-017-3725-x

Lotya, M., Hernandez, Y., King, P. J., Smith, R. J., Nicolosi, V., Karlsson, L. S., et al. (2009). Liquid phase production of graphene by exfoliation of graphite in surfactant/water solutions. *J. Am. Chem. Soc.* 131, 3611–3620. doi: 10.1021/ja807449u

Mak, K. F., Lui, C. H., and Heinz, T. F. (2010). Thermal conductance at the graphene-SiO2 interface measured by optical pump-probe spectroscopy. *Appl. Phys. Lett.* 97:221904. doi: 10.1063/1.3511537

Malard, L. M., Pimenta, M. A., Dresselhaus, G., and Dresselhaus, M. S. (2009). Raman spectroscopy in graphene. *Phys. Rep.* 473, 51–87. doi: 10.1016/j.physrep.2009.02.003

Matsumoto, M., Saito, Y., Park, C., Fukushima, T., and Aida, T. (2015). Ultrahigh-throughput exfoliation of graphite into pristine 'single-layer' graphene using microwaves and molecularly engineered ionic liquids. *Nat. Chem.* 7, 730–736. doi: 10.1038/nchem.2315

Mayorov, A. S., Gorbachev, R. V., Morozov, S. V., Britnell, L., Jalil, R., Ponomarenko, L. A., et al. (2011). Micrometer-scale ballistic transport in encapsulated graphene at room temperature. *Nano Lett.* 11, 2396–2399. doi: 10.1021/nl200758b

Nair, R. R., Anissimova, S., Zan, R., Blake, P., Blake, J. R., Geim, A. K., et al. (1993). Graphene as a transparent conductive support for studying biological molecules by transmission electron microscopy. *IEEE Trans. Inf. Theory* 39, 1057–1064. doi: 10.1063/1.3492845

Nascentes, C. C., Korn, M., Sousa, C. S., and Arruda, M. A. (2001). Use of ultrasonic baths for analytical applications: a new approach for optimisation conditions. *J. Braz. Chem. Soc.* 12, 57–63. doi: 10.1590/S0103-50532001000100008

Novoselov, K. S. (2004). Electric field effect in atomically thin carbon films. *Science* 306, 666–669. doi: 10.1126/science.1102896

Novoselov, K. S., Falko, V. I., Colombo, L., Gellert, P. R., Schwab, M. G., and Kim, K. (2012). A roadmap for graphene. *Nature* 490, 192–200. doi: 10.1038/nature11458

Nuvoli, D., Alzari, V., Sanna, R., Scognamillo, S., Piccinini, M., Peponi, L., et al. (2012). The production of concentrated dispersions of few-layer graphene by the direct exfoliation of graphite in organosilanes. *Nanoscale Res. Lett.* 7, 674–681. doi: 10.1186/1556-276X-7-674

Nuvoli, D., Valentini, L., Alzari, V., Scognamillo, S., Bon, S. B., Piccinini, M., et al. (2011). High concentration few-layer graphene sheets obtained by liquid phase exfoliation of graphite in ionic liquid. *J. Mater. Chem.* 21, 3428–3431. doi: 10.1039/C0JM02461A

Peng, R., Wang, Y., Tang, W., Yang, Y., and Xie, X. (2013). Progress in imidazolium ionic liquids assisted fabrication of carbon nanotube and graphene polymer composites. *Polymers* 5, 847–872. doi: 10.3390/polym5020847

Pereiro, A. B., Legido, J. L., and Rodríguez, A. (2007). Physical properties of ionic liquids based on 1-alkyl-3-methylimidazolium cation and hexafluorophosphate as anion and temperature dependence. *J. Chem. Thermodyn.* 39, 1168–1175. doi: 10.1016/j.jct.2006.12.005

Plimpton, S. (1995). Fast parallel algorithms for short-range molecular dynamics. *J. Comput. Phys.* 117, 1–19. doi: 10.1006/jcph.1995.1039

Pu, N. W., Wang, C. A., Sung, Y., Liu, Y. M., and Ger, M. D. (2009). Production of few-layer graphene by supercritical CO2 exfoliation of graphite. *Mater. Lett.* 63, 1987–1989. doi: 10.1016/j.matlet.2009.06.031

Raccichini, R., Varzi, A., Passerini, S., and Scrosati, B. (2014). The role of graphene for electrochemical energy storage. *Nat. Mater.* 14, 271–279. doi: 10.1038/nmat4170

Saurín, N., Sanes, J., and Bermúdez, M. D. (2016). New graphene/ionic liquid nanolubricants. *Mater. Today Proc.* 3, 227–232. doi: 10.1016/j.matpr.2016.02.038

Seddon, K. R. (1997). Ionic liquids for clean technology. *J. Chem. Technol. Biotechnol.* 68, 351–356. doi: 10.1002/(SICI)1097-4660(199704)68:4<351::AID-JCTB613>3.0.CO;2-4

Seddon, K. R., Stark, A., and Torres, M.-J. (2002). "Viscosity and density of 1-Alkyl-3-methylimidazolium ionic liquids," in *ACS Symposium Series* Vol. 819, 34–49. doi: 10.1021/bk-2002-0819.ch004

Severance, D. L. and Jorgensen, W. L. (1990). Aromatic-Aromatic interactions: free energy profiles for the benzene dimer in water, chloroform, and liquid benzene. *J. Am. Chem. Soc.* 112, 4768–4774. doi: 10.1021/ja00168a022

Shang, N. G., Papakonstantinou, P., Sharma, S., Lubarsky, G., Li, M., McNeill, D. W., et al. (2012). Controllable selective exfoliation of high-quality graphene nanosheets and nanodots by ionic liquid assisted grinding. *Chem. Commun.* 48, 1877–1879. doi: 10.1039/c2cc17185f

Shim, Y., and Kim, H. J. (2009). Solvation of carbon nanotubes in a room-temperature ionic liquid. *ACS Nano* 3, 1693–1702. doi: 10.1021/nn900195b

Sresht, V., Govind Rajan, A., Bordes, E., Strano, M. S., Pádua, A. A., and Blankschtein, D. (2017). Quantitative Modeling of MoS2-Solvent Interfaces: Predicting Contact Angles and Exfoliation Performance using Molecular Dynamics. *J. Phys. Chem. C* 121, 9022–9031. doi: 10.1021/acs.jpcc.7b00484

Sresht, V., Pádua, A. A. H., and Blankschtein, D. (2015). Liquid-phase exfoliation of phosphorene: design rules from molecular dynamics simulations. *ACS Nano* 9, 8255–8268. doi: 10.1021/acsnano.5b02683

Szala-Bilnik, J., Costa Gomes, M. F., and Pádua, A. A. H. (2016). Solvation of C_{60} Fullerene and $C_{60}F_{48}$ Fluorinated Fullerene in Molecular and Ionic Liquids. *J. Phys. Chem. C* 120, 19396–19408. doi: 10.1021/acs.jpcc.6b05140

Tao, R., Tamas, G., Xue, L., Simon, S. L., and Quitevis, E. L. (2014). Thermophysical properties of imidazolium-based ionic liquids: the effect of aliphatic versus aromatic functionality. *J. Chem. Eng. Data* 59, 2717–2724. doi: 10.1021/je500185r

Tsai, W. Y., Lin, R., Murali, S., Li Zhang, L., McDonough, J. K., Ruoff, R. S., et al. (2013). Outstanding performance of activated graphene based supercapacitors in ionic liquid electrolyte from -50 to 80C. *Nano Energy* 2, 403–411. doi: 10.1016/j.nanoen.2012.11.006

Wang, C., Han, X., Xu, P., Zhang, X., Du, Y., Hu, S., et al. (2011). The electromagnetic property of chemically reduced graphene oxide and its application as microwave absorbing material. *Appl. Phys. Lett.* 98, 072906. doi: 10.1063/1.3555436

Wang, J., Chu, H., and Li, Y. (2008). Why single-walled carbon nanotubes can be dispersed in imidazolium-based ionic liquids. *ACS Nano* 2, 2540–2546. doi: 10.1021/nn800510g

Wang, L., Wang, W., Fan, P., Zhou, M., Yang, J., Chen, F., et al. (2017). Ionic liquid-modified graphene/poly(vinyl alcohol) composite with enhanced properties. *J. Appl. Polym. Sci.* 134, 1–10. doi: 10.1002/app.45006

Wang, X., Fulvio, P. F., Baker, G. A., Veith, G. M., Unocic, R. R., Mahurin, S. M., et al. (2010). Direct exfoliation of natural graphite into micrometre size few layers graphene sheets using ionic liquids. *Chem. Commun.* 46, 4487–4489. doi: 10.1039/c0cc00799d

Young, R. J., Kinloch, I. A., Gong, L., and Novoselov, K. S. (2012). The mechanics of graphene nanocomposites: a review. *Compos. Sci. Technol.* 72, 1459–1476. doi: 10.1016/j.compscitech.2012.05.005

Zambare, R., Song, X., Bhuvana, S., Antony Prince, J. S., and Nemade, P. (2017). Ultrafast dye removal using ionic liquid-graphene oxide sponge. *ACS Sustain. Chem. Eng.* 5, 6026–6035. doi: 10.1021/acssuschemeng.7b00867

Zhao, W., Fang, M., Wu, F., Wu, H., Wang, L., and Chen, G. (2010). Preparation of graphene by exfoliation of graphite using wet ball milling. *J. Mater. Chem.* 20, 5817–5819. doi: 10.1039/c0jm01354d

Zhu, A. Y., Yi, F., Reed, J. C., Zhu, H., and Cubukcu, E. (2014). Optoelectromechanical multimodal biosensor with graphene active region. *Nano Lett.* 14, 5641–5649. doi: 10.1021/nl502279c

Zhu, Y., Murali, S., Cai, W., Li, X., Suk, J. W., Potts, J. R., et al. (2010). Graphene and graphene oxide: synthesis, properties, and applications. *Adv. Mater.* 22, 3906–3924. doi: 10.1002/adma.201001068

Advantages of publishing in Frontiers

OPEN ACCESS
Articles are free to read
for greatest visibility
and readership

FAST PUBLICATION
Around 90 days
from submission
to decision

HIGH QUALITY PEER-REVIEW
Rigorous, collaborative,
and constructive
peer-review

TRANSPARENT PEER-REVIEW
Editors and reviewers
acknowledged by name
on published articles

Frontiers
Avenue du Tribunal-Fédéral 34
1005 Lausanne | Switzerland

Visit us: www.frontiersin.org
Contact us: info@frontiersin.org | +41 21 510 17 00

REPRODUCIBILITY OF RESEARCH
Support open data
and methods to enhance
research reproducibility

DIGITAL PUBLISHING
Articles designed
for optimal readership
across devices

FOLLOW US
@frontiersin

IMPACT METRICS
Advanced article metrics
track visibility across
digital media

EXTENSIVE PROMOTION
Marketing
and promotion
of impactful research

LOOP RESEARCH NETWORK
Our network
increases your
article's readership